Texture Evolution and Its Relationship with Strain Path of Mg-Ca-Zn Lean Alloys

Zhiyu Quan

School of Chemical, Materials and Biological Engineering

The University of Sheffield

Thesis submitted for the degree of Doctor of Philosophy

February 2025

Abstract

The project was based on magnesium-calcium-zinc (Mg-Ca-Zn) alloys, a topical study the area of Mg alloys. There has been extensive research, leading to many explanations for the mechanism of texture weakening in the Mg-Ca-Zn alloys. However, the explanations of the texture weakening remain controversial. Different materials and different processing routes (extrusion and rolling) lead to different results. Different processing routes cause different strain paths in the materials. The role of the strain path on the texture weakening mechanism is unknown and is therefore important to investigate. The aim of this project was to discover the relationship between the different strain paths and the mechanism of the weakening effect in Mg-Zn-Ca alloy. The relationship between strain/strain rate and mechanism of the weakening effect was also investigated. While the role of the Ca and Zn in weakening the texture of the Mg alloys is clearer, the relationship between the Ca/Zn ratio and the texture weakening in Mg-Ca-Zn alloy still needs further investigation and is also the subject of this work.

A group of lean Mg-Ca-Zn alloys (Mg-0.5Ca, Mg-0.4Ca-0.1Zn, Mg-0.2Ca-0.3Zn, Mg-0.1Ca-0.4Zn, Mg-0.5Zn (at%)), cast in-house, were used as the experimental materials. For the strain path study and the strain/strain rate study, channel die compression and double truncated cone specimen compression experiments were conducted. The double truncated cone specimen experiment was suspended due to the unexpected nonuniform deformation of the specimens. In the channel die compression, the one-direction compression and two-direction compression were conducted on the specimens to generate different strain paths. Due to time constraints, these experiments were only undertaken on the Mg-0.2Ca-0.3Zn, Mg-0.1Ca-0.4Zn, Mg-0.5Zn alloys.

The channel die compression experiments revealed distinctly different recrystallization behaviour between one-direction and two-direction compression specimens. In one-direction compression, recrystallization initiated earlier due to higher deformation energy and stress concentration in a single direction, which provided a strong driving force for the recrystallization process. Conversely, two-direction compression resulted in a more uniform distribution of stress and deformation, leading to a delayed onset of recrystallization. Despite this delay, two-direction compressed specimens exhibited faster and more uniform growth of recrystallized grains, facilitated by their higher fraction of tensile twins and additional nucleation sites at shear bands and grain boundaries. After annealing, two-direction compressed specimens showed weaker texture, particularly in Ca-containing alloys, due to the random orientation of grains originating from the consumption of tensile twins and shear bands during recrystallization.

The addition of Ca significantly increased the fraction of twin boundaries and slowed recrystallization due to solute drag effects and Ca segregation at grain boundaries. These trends in recrystallization rates and texture weakening were observed consistently in both one-direction and two-direction compression specimens, with higher Ca content contributing to a more dispersed grain orientation and reduced stacking fault energy. In contrast, the specimen without Ca displayed the expected strong basal texture. This was attributed to the absence of significant solute segregation and lattice distortion, resulting in a microstructural response similar to that of pure magnesium.

Contents

Acknowledgment

First and foremost, I would like to express my heartfelt gratitude to my first supervisor, Prof. W. Mark Rainforth, and my second supervisor, Dr. Dikai Guan, for their invaluable guidance and support throughout my doctoral research. Their expertise and encouragement have been crucial to my academic development. I am also deeply grateful for their constant care and concern for my mental health.

I am thankful to the University of Sheffield and the Henry Royce Institute for providing the equipment necessary for my PhD research study.

I am very grateful to my close friends Xingjian Zhao, Haoran Yi, Yanheng Xie, Zhicheng Lin and Daniel Olguin, as well as to Dr. John Nutter and Dr. Jiawei Xi, the postdocs in our research group. I have learned many valuable skills and much knowledge from them, and I will always cherish the time we spent together at the university.

Special thanks go to Dr. Yunus Azakli, who has always been so kind and available to help whenever I encountered problems. He taught me how to cast my experimental materials, which gave me a strong start to my PhD studies. I am also thankful to Dr. William Pulfrey in the same lab, who helped me complete the rolling process of my materials.

I am grateful to the technical staffs at the Micropreparation Lab, the Thermomechanical Processing Lab and the Quarrell Lab. Sylwester Mikula and Tesoro Monaghan provided excellent training on how to prepare high-quality samples. Dean Haylock provided perfect training on how to run a compression test and helped me to contact manufacturer to make my samples and channel die. Dr. Lisa Hollands, Neil Hind, and Tesoro Monaghan were incredibly generous with their time and assistance in helping me complete nearly a hundred heat treatment experiments.

I also appreciate the training and support I received from the technical staffs at the Sorby Centre. Dr. Le Ma gave me outstanding training on the equipment, and Dr. Ian Ross, Dr. Cheryl Shaw, Stuart Creasey-Gray, and Dr. Jiahui Qi were all incredibly helpful when I faced difficulties.

I would like to extend my heartfelt thanks to my family for their unwavering encouragement and support throughout my studies abroad. A special thanks must go to my grandmother, whose financial assistance played a significant role in my journey.

Lastly, I want to express my deepest appreciation to my girlfriend and our two adorable little bears, Xionxiong and Xiongzai, for their companionship and support throughout my doctoral studies. They have played a vital role in helping me complete my PhD, and I could not have done it without them.

1. Introduction

1.1 Background

Magnesium alloys have a good strength to weight ratio, which also are the lightest commercial structural metal. The density of steel is about four times higher than that of magnesium and the density of aluminium is 50% higher than that of magnesium [1-4]. Mg alloys show a good stiffness to strength ratio while maintaining a low weight [1,2]. Mg alloys are highly recyclable which means they have a high potential for commercial use e.g. automobile industry, aviation industry. However, the poor room temperature formability of Mg alloys restricts their usage. The use of hot working processes to improve the performance of Mg alloys [5,6] have been investigated but the strong basal texture has always been found after hot working causing low ductility [7-9]. There has been extensive use of rare earth (RE) elements, such as yttrium (Y) as an alloying element in Mg alloys to improve the formability [7,10,11]. The addition of RE elements to Mg alloys changes the texture from the strong basal texture found in for example Mg-Zn alloys to a weaker, so called RE texture, which improves formability. However, the cost of RE is relatively high, making these alloys too expensive for many applications. Therefore, there is much focus on the development of formable non-RE containing Mg alloys but with comparable properties to those Mg-RE alloys [12,13].

Based on this background, an interesting area of controversy was found in the studies of Mg-Ca-Zn alloys. With different processing methods (extrusion and rolling), different (even opposite) explanations have been proposed for the texture weakening in the Mg-Ca-Zn alloys. This strongly suggests that there must be additional factors affecting the texture weakening in the Mg alloys in addition to the alloy composition. Specifically, the processing method has also a strong effect on texture evolution. The basic difference between the extrusion and the rolling is the strain path in the processed materials. Thus, it is important to investigate the unknown relationship between the strain path and the texture weakening in the Mg-Ca-Zn alloys. In addition, the effect of the Ca/Zn ratio to the texture weakening in Mg alloys is also not very clear. By making different Mg-Ca-Zn alloys with different Ca/Zn ratios, the role that Ca/Zn ratio plays in the texture weakening may also be discovered.

1.2 Main techniques used

1. The main method for the material production was the induction melting combined with mould casting.
2. The main method for the specimen deformation was the channel die compression.

3. For the microstructure characterization, optical microscope, scanning electron microscope (SEM) including energy dispersive X-Ray spectroscopy (EDX) and electron backscattered diffraction (EBSD) were used to investigate the specimens.

1.3 Main objectives

1. To investigate the relationship between the strain path and the microstructural evolution in the Mg lean alloys, particularly recrystallisation kinetics and mechanisms and consequent effect on texture evolution.
2. To study the effect of the Ca and Zn additions in the Mg lean alloys on recrystallisation kinetics and mechanisms and consequent effect on texture evolution.

2. Literature review

2.1 Introduction to magnesium

2.1.1 Basic information of magnesium

Magnesium, the eighth most abundant element in the earth's crust, occupies about 2.0% of crustal content [1-3]. Magnesium is found in nature exclusively as part of compounds rather than in its elemental state due to it being an alkaline earth metal. It is primarily refined from minerals such as magnesite ($MgCO_3$, containing 27% Mg), dolomite ($MgCO_3 \cdot CaCO_3$, containing 13% Mg), and carnallite ($KCl \cdot MgCl_2 \cdot 6H_2O$, containing 8% Mg). Additionally, seawater contains 0.13% magnesium, equivalent to 1.1 kg per cubic meter, making it the third most abundant dissolved mineral in the ocean. The primary methods for recovering magnesium include the electrolysis of molten anhydrous $MgCl_2$, the thermal reduction of dolomite, and the extraction of magnesium oxide from seawater [2,3].

2.1.2 Basic physical properties of magnesium

The atomic number of Mg is 12. The atomic mass of Mg is 24.305u. The pure Mg has a density of 1.738g/cm^3 with a melting point of 650℃ (1202°F) and boiling point of 1090℃ (1994°F). It has a silvery-white metallic appearance [2,3]. The more detailed properties of Mg are shown below in Figure 2-1.

Crystal Structure	hdp
Density	1,738 g/cm^3 at RT
	1,584 g/cm^3 at T_m
Young's Modulus	45 GPa
Ultimate Tensile Strength	80-180 MPa
Fracture Elongation	1-12 %
Melting Point	650 +/- 0,5°C
Boiling Point	1090°C
Specific Heat Capacity	1,05 kJ/(kg K)
Fusion Heat	195 kJ/kg
Heat Conductivity	156 W/(m·K) (RT)
Linear Expansion Coefficient	26·10^{-6} K^{-1} (RT)
Shrinkage (solid-liquid)	4,2 %
Shrinkage (T_s-RT)	ca. 5%
Specific Electrical Conductivity	22,4 m/(Ω mm^{-2}) (RT)
Normal Potential	-2,37 V

Figure 2-1 Properties of pure magnesium [2]

2.1.3 Crystallography of magnesium

The crystal structure of pure Mg is hexagonal close packed (hcp) at room temperature. The lattice parameters a and c are 0.32092nm and 0.52105nm, respectively [2,3]. As a result, the c/a ratio of pure Mg is 1.6236 which is very close to the ideal close packed

ratio 1.633. For the atomic packing, the coordination number and the atomic packing factor (APF) of magnesium is 12 and 0.74, respectively [2,3]. As a hcp material, the unit cell of magnesium contains two atoms, and the stacking sequence of the atomic layers follows the ABAB pattern. The unit cell and the major slip planes of magnesium are shown below in Figure 2-2.

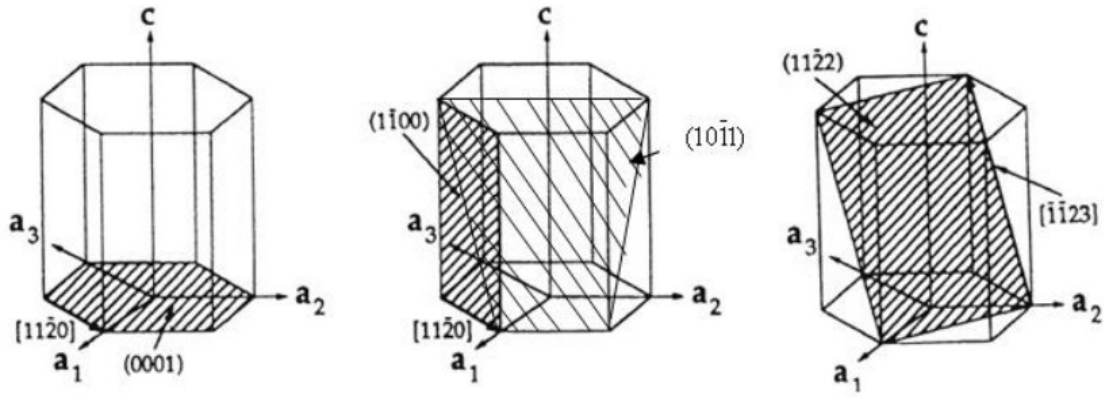

Figure 2-2 The unit cell and the major slip planes in magnesium [3]

The deformation behaviour of magnesium alloys is closely related to their hexagonal close-packed (hcp) crystal structure. During room-temperature deformation (<200°C), the primary mechanisms are basal slip (on the (0001) plane along the <11-20> direction) and twinning (including {10-12} tensile twins and {10-11} compressive twins). However, basal slip provides only three independent slip systems, insufficient to meet the requirement for uniform polycrystalline deformation (which demands at least five systems as dictated by the von Mises criterion), resulting in poor plasticity and pronounced anisotropy. At elevated temperatures (>200°C), the critical resolved shear stress (CRSS) for non-basal slip systems—such as prismatic slip ({10-10} planes) and pyramidal slip ({11-22} planes)—significantly decreases, activating additional slip systems and enhancing ductility. Concurrently, dynamic recrystallization (DRX) refines the grain structure, while grain boundary sliding (facilitated by diffusion accommodation) dominates superplastic deformation, markedly improving formability. Elevated temperatures also suppress twinning, reducing localized stress concentrations [1, 3].

2.1.4 Recrystallisation, grain growth and deformation

Recrystallization and grain growth are core processes in the microstructural evolution of materials. Recrystallization is driven by the strain energy stored during cold deformation (due to high dislocation density, which elevates the system energy) and occurs in three stages: In the recovery phase at low temperatures, internal stresses are partially released through dislocation rearrangement; during the recrystallization phase,

new defect-free grains nucleate and grow within the deformed matrix, significantly reducing dislocation density and restoring material plasticity; finally, grain growth takes place, driven by the minimization of grain boundary energy, where larger grains coarsen the microstructure by consuming smaller ones via grain boundary migration. The influence of deformation on these processes is manifested by the necessity of exceeding a critical deformation threshold (typically >5%) to provide sufficient strain energy for recrystallization, with higher deformation lowering the recrystallization temperature and increasing nucleation rates. Also, deformation-induced textures (e.g. rolling-preferred orientations) potentially being inherited or altered during recrystallization, affecting material anisotropy and uniform deformation (e.g. rolling) promoting homogeneous recrystallization, while localized high-strain zones (e.g. shear bands) preferentially nucleate new grains, leading to microstructural heterogeneity. Additionally, dynamic recrystallization occurring during high-temperature deformation (e.g. hot rolling) simultaneously combines deformation and recrystallization, suppressing grain growth and refining the microstructure (e.g. Mg alloys can be refined to the micrometer scale), making it a critical strategy for balancing strength and toughness in materials design [1-3].

2.2 Magnesium alloys development

The development of magnesium alloys dates back to the early 19th century, with their commercialization beginning in the early 20th century and significant advancements occurring in the mid to late 20th century. The discovery of magnesium can be traced to 1808 when British chemist Sir Humphry Davy isolated metallic magnesium through electrolysis. In 1828, French scientist Antoine Bussy produced pure magnesium by reducing molten anhydrous magnesium chloride. By 1910, global magnesium production was only 10 tons per year [14]. However, by 1930, Germany pioneered the use of magnesium alloys in automobiles, marking an initial industrial application. In the 1950s, magnesium alloys were widely adopted in the automotive industry, primarily to reduce vehicle weight and improve fuel efficiency. Notably, in 1957, Volkswagen used die-cast magnesium alloys to manufacture engine transmission components for the Beetle. Magnesium alloys also found applications in the aerospace sector due to their lightweight properties, which help reduce aircraft weight. During this period, casting technologies for magnesium alloys, such as high-pressure die casting and gravity casting, saw significant advancements. By the 1990s, with growing environmental awareness, the recycling and reuse of magnesium alloys gained attention. Additionally, new magnesium alloys were developed, such as WE43, which is used in high-strength and high-temperature applications.

Over the past three decades, the rapid development of magnesium alloys has been widely recognized. To expand their application prospects in manufacturing and construction, particularly in the automotive and aerospace industries, extensive research has been conducted on magnesium alloys, ranging from their composition and deformation mechanisms to processing and production methods.

2.2.1 The texture of the magnesium alloys

Magnesium (Mg) alloys are known for their lightweight properties and potential for applications in industries such as automotive and aerospace. Enhancing their mechanical properties, grain size control, and texture weakening has been a key area of research. As one of the important factors affecting the properties of Mg alloys, the texture naturally attracts a lot of attention. Texture in Mg alloys refers to the crystallographic orientation of grains in the material, which develops during various manufacturing processes such as casting, rolling, extrusion, and forging [2, 15]. Because magnesium has a hcp crystal structure with limited slip systems [3], it is inherently anisotropic due to the unequal number of slip systems available along different crystallographic planes and directions. The basal (0001) plane, which is the most densely packed, is the primary plane for deformation [16]. During processes like rolling and extrusion, most grains align such that their basal planes (0001) become parallel to the plane of the material or the processing direction. This results in the "basal texture," where the c-axis (perpendicular to the basal plane) aligns perpendicular to the deformation direction [15-17]. Figure 2-3 shows the pole figures and pole intensities of an annealed AZ61 alloy studied by Perez-Prado [18]. All specimens showed a very strong basal texture after the annealing process. A strong basal texture significantly affects the deformation behavior and comprehensive performance of Mg alloys. Yield strength and ductility are higher along specific directions, while fracture toughness and fatigue resistance vary depending on loading orientation [16, 17]. In terms of deformation mechanisms, the strong texture leads to dominant basal slip with only three independent slip systems, which fails to meet the requirements for coordinated polycrystalline deformation and exacerbates anisotropy. Particularly under loading perpendicular to the basal plane, deformation relies on high-stress twinning (e.g. {10-12} tensile twins), leading to localized strain concentration. Although non-basal slip systems are partially activated at elevated temperatures, dynamic recrystallization (DRX) may still retain residual texture features. In terms of mechanical properties, this manifests as pronounced anisotropy (higher strength and plasticity in the direction parallel to the basal plane compared to the perpendicular direction) and tendency to brittleness (twin bands or slip bands acting as crack propagation paths, reducing fatigue life and fracture toughness). These issues result in increased risks of cracking and

challenges in springback control during deep drawing processes. As the most straightforward way to improve the performance of the Mg alloys, people extensively studied how to weaken the basal texture i.e. acquiring random orientated grains.

For weakening the strong basal texture in Mg alloys, different techniques were developed e.g. changing alloying elements (adding rare-earth elements like yttrium (Y), gadolinium (Gd), cerium (Ce) neodymium (Nd) etc.), conducting thermomechanical processing (cross-rolling, asymmetric rolling, or multi-axial forging etc.) and changing heat treatment parameters etc. [2, 3, 97, 98]. Among them, the addition of rare-earth elements was regarded as an effective means to weaken the texture of magnesium alloys, many studies were carried out based on the Mg-RE alloys [7-11, 21-28]. The influence of RE elements on texture in magnesium alloys can be attributed to several mechanisms. Firstly, RE elements increase the critical resolved shear stress (CRSS) for basal slip while reducing it for non-basal slip systems, such as prismatic (10-10⟨a⟩) and pyramidal (10-11⟨c+a⟩) slips. This adjustment facilitates uniform deformation across multiple crystallographic planes, thereby reducing the alignment of basal planes and weakening the strong basal texture typically observed in magnesium alloys [21-23]. Secondly, RE elements act as solute atoms in the magnesium matrix, exerting a "solute drag" effect during recrystallization [21, 24]. This effect slows grain boundary motion, resulting in grains with random orientations and further weakening the overall texture. Additionally, RE elements tend to segregate at grain boundaries, altering their energy and mobility, which promotes the growth of grains with non-basal orientations during recrystallization. Lastly, the introduction of RE elements leads to the formation of Mg-RE intermetallic precipitates, which interact with dislocations and grain boundaries, hindering basal slip and encouraging deformation via non-basal slip systems, ultimately modifying the texture. Meanwhile, random orientated grains related to particle-stimulated nucleation (PSN) was also reported [21]

On the other hand, there is not a universal drive to completely weaken the texture in magnesium alloys. Some researchers have taken advantage of the characteristics of texture, that is, by generating specific textures through special processing techniques to enhance the performance of the material in a certain aspect to meet certain special product requirements. The equal channel angular extrusion (ECAE) and the extruded fine-grain size Mg alloys was reported by Agnew et al. [19] and Wang et al. [20].

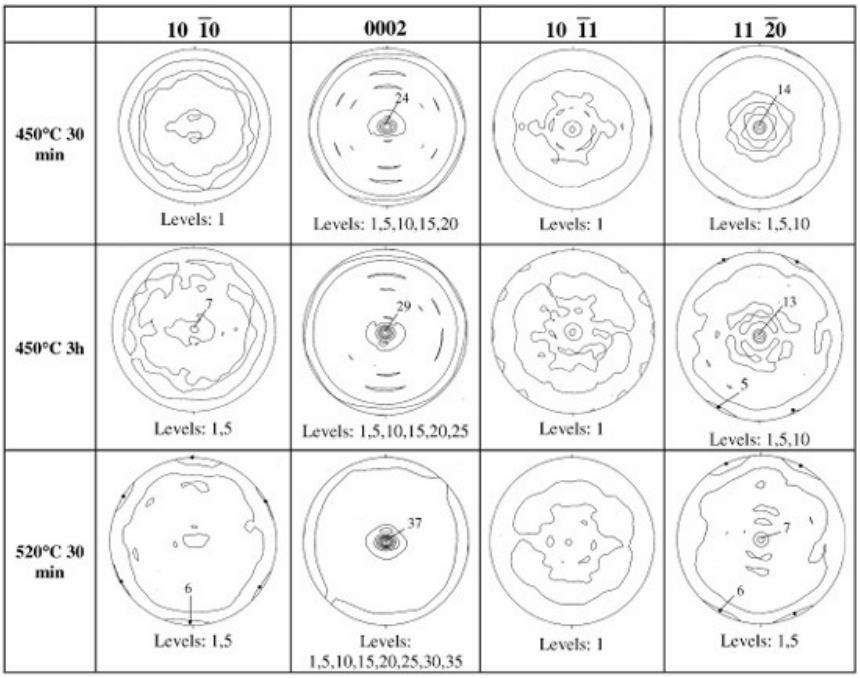

	450 °C/30 min	450 °C/3 h	520 °C/30 min
{10$\bar{1}$0}	4.8	7.0	2.0
{0002}	24.0	28.7	36.9
{10$\bar{1}$1}	2.0	0	1.0
{11$\bar{2}$0}	13.8	13.0	7.0

Figure 2-3 Pole figures and pole intensities of annealed AZ61 alloy [18]

2.2.2 Introducing calcium in magnesium alloys

Although adding the RE additions can help Mg alloys obtain a weaker texture, the Mg-RE alloys have consistently faced the challenge of high costs. Calcium (Ca), once considered a minor alloying element, has emerged as a potential alternative to Rare-Earth elements in Mg alloys. In 2010, Stanford [12] was among the pioneers to report that adding Ca to Mg alloys reduced grain size and weakened texture, leading to improved mechanical properties. The Mg-1.3Mn-Ca, Mg-1.3Mn (wt.%) and binary Mg-Ca alloys were chosen as the experimental alloys. After the hot extrusion, Stanford found that an increase in the Ca concentration resulted in a decrease in the grain size of the extruded material (shown in Figure 2-4(a)). Meanwhile, the additional Ca in Mg alloys was found to reduce the texture strength, the result is shown in Figure 2-4(b). This transition stems from the similar atomic radius of Ca and RE elements, which allows Ca to play comparable roles in weakening the extrusion texture of Mg alloys. This study also sparked a surge of interest in Ca-contained Mg alloys and their mechanisms of texture modification.

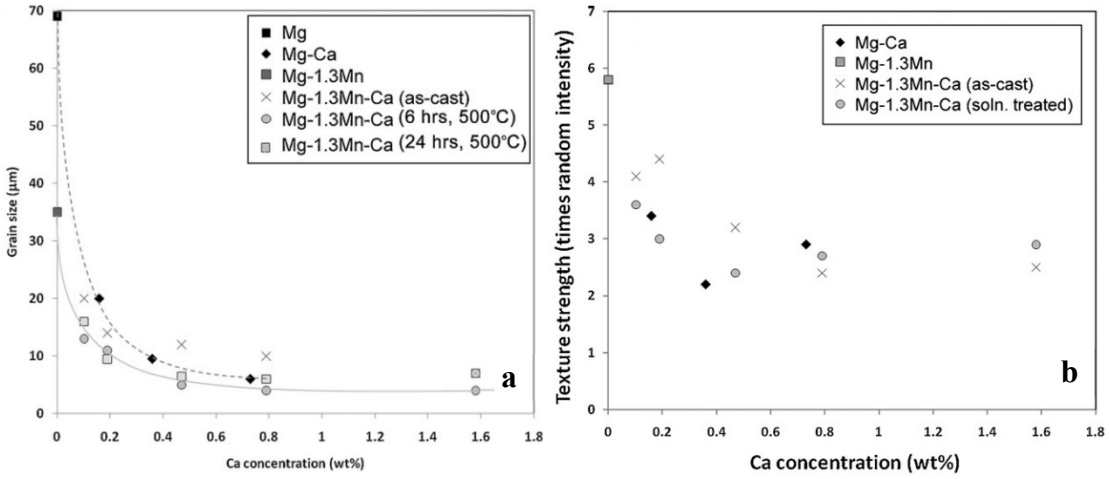

Figure 2-4 (a) Relationship between Ca concentration and grain size (b) Relationship between Ca concentration and texture strength [12]

Further investigations by Zhang et al. [29] and Chino et al. [30] built on these findings, showing how Ca interacts with other alloying elements like Zn and Al. For the extruded Mg-Ca-Zn sample, Zhang indicated that the grain refinement and the unique extrusion texture could be the reason for the improved properties, and these changes could have a close connection with Ca concentrations. On the other hand, Chino et al. found that both hot-rolled Mg-Zn-Ca and Mg-Al-Ca alloys showed a weaker basal texture than their binary alloys which without Ca addition. Compared with the Mg-Al-Ca alloys, the Ca addition showed a better performance on weakening texture in Mg-Zn-Ca alloys (shown in Figure 2-5). The reports from Stanford [12], Zhang et al. [29] and Chino et al. [30] all mentioned that the Ca addition might play an important role in weakening the texture of Mg alloys. However, they did not mention the mechanisms as to what precise role that Ca addition plays in the Mg alloys. Zeng et al. [31] explored the influence of Ca in the Mg-Zn alloys during the cold rolling. They found that the Ca addition in Mg alloys did not directly affect the texture weakening but performed as a delay process to retard deformation twin growth, hindering the formation of a strong basal texture.

In addition to the studies into binary Mg-Ca alloys and the ternary Mg-Ca-X (Zn/Al) alloys, many researchers also explored the combination of Ca addition and the commercial Mg alloys (AZ series etc.). Bian et al. [32] and Kim et al. [33] both studied the hot-rolled AZ series Mg alloys with Ca addition (AXMZ1000 and AZ61+Ca, respectively). A much finer grain size and different texture compared to the original alloy were reported by both papers. The better hot-workability and finer grain size were also reported by Rabbi et al. [34] and Takabayashi et al. [35] when studying the AZ61

alloy with Ca addition. Besides, Yuasa et al. [36] and Ashokan et al. [37] reported better corrosion properties of AZ61 alloy with Ca addition under solution treatment and AZ31 alloy with Ca addition, respectively. Ashokan also mentioned better mechanical properties (UTS, hardness and elongation rate etc.) of AZ31 after adding the Ca, which revealed the potential medical usage of this alloy. With in-depth research on the addition of Ca to Mg alloys, the advantages of calcium-containing magnesium alloys have been gradually discovered, and people have begun to consider the possibility of replacing rare earth elements with Ca in Mg alloys.

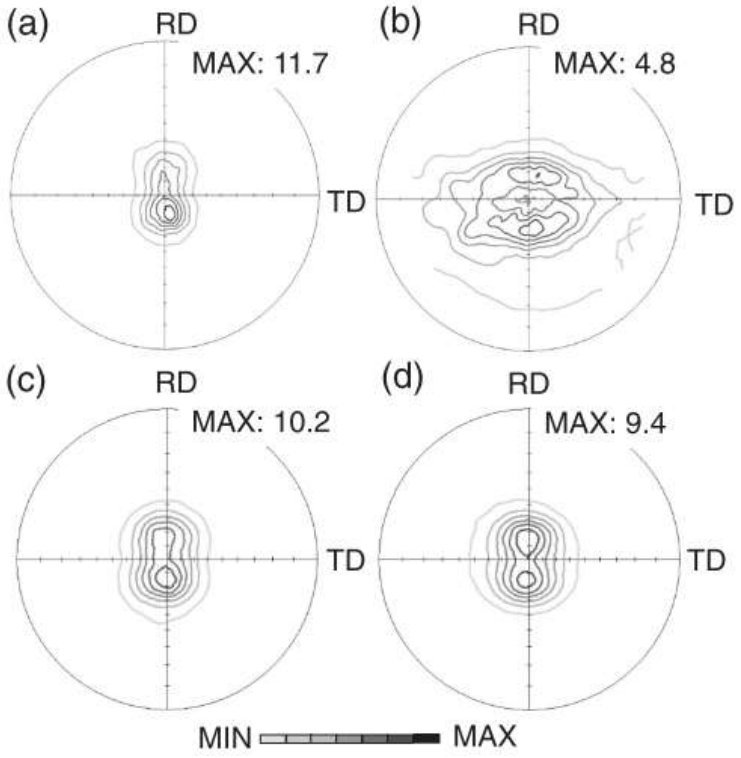

Figure 2-5 The (0002) pole figures of as-rolled: (a) Mg-1.5Zn, (b) Mg-1.5Zn-0.1Ca, (c) Mg-3Al, (d) Mg-3Al-0.1Ca [30]

2.2.3 Calcium's role compared to Rare Earth (RE) elements

Given its cost-effectiveness and availability, Ca is increasingly being considered a substitute for RE elements in Mg alloys. Jung et al. [21] reported their review and study (using CALPHAD databases) about the role of RE and Ca in magnesium alloys. They summarized the similarities of Ca and RE elements, noting that both kinds of element enhance solute drag/pinning effect and reduce stacking fault energy (SFE), thereby promoting non-basal slip systems. Although Jung et al. did not mention the mechanisms by which Ca segregates to grain boundaries and influences recrystallization, most consider it associated with the large atomic size compared to Mg which always leads to segregation.

Bohlen et al. [38] investigated the texture development in Mg-0.91Zn-0.52Ca and Mg-0.86Zn-0.51Ca-0.08Zr (wt%) alloys during rolling and annealing. They observed that Ca in Mg alloys plays a role similar to RE elements, contributing to random-oriented textures due to the presence of twins. Furthermore, the addition of Zr retarded texture development, although the mechanism remained unclear.

Further study by Ding et al. [39] found that Ca weakens texture by widening texture orientation, akin to RE effects. The comparison among the hot-extruded binary Mg alloys (Mg-Ca/Zn/RE) and ternary alloys (Mg-Zn-Ca/RE) presented a similar mechanical properties and texture between the Ca-contained samples and RE-contained samples. The reduced c/a ratio and SFE were considered as the possible reasons for the weakened texture in Mg-Ca-Zn samples.

Although the reason for the weakened texture in Mg-Ca-Zn alloys was not very clear, this effective behaviour makes a strong case for using Ca as a viable alternative to RE elements. Additionally, it indicates that the Mg-Ca-Zn alloys have significant application potential to be further investigated to optimize behaviour [29, 30, 38, 39].

2.2.4 The research of calcium and zinc in magnesium alloys

Research into Mg-Ca-Zn alloys has shown a synergy between Ca and Zn and this has emerged as one of the focal points for current research. Du et al. [40] explored the microstructure and mechanical properties of Mg-6Zn (Z6), Mg-6Zn-0.4Ca (ZX604), and Mg-6Zn-0.8Ca (ZX608) (wt%) alloys. They found that increasing Ca concentration replaced the Mg_4Zn_7 phase with $Ca_2Mg_6Zn_3$, effectively pinning grain boundaries and enhancing dynamic recrystallization. This refinement resulted in improved strength in ZX604 and ZX608 alloys compared to Z6.

Jiang et al. [41] also examined dilute Mg alloys (Mg-0.21Zn-0.30Ca-0.14Mn wt%) processed by extrusion at various temperatures. Their findings corroborated Du et al.'s findings that Ca-containing precipitates refined dynamic recrystallized grains and weakened basal textures. However, the precise mechanisms causing texture weakening remained elusive.

Zeng et al. [42] proposed that the addition of Zn and Ca affects recrystallization kinetics. Investigating Mg-0.4Zn, Mg-0.1Ca, and Mg-0.3Zn-0.1Ca (wt%) alloys, they observed weaker textures in ternary alloys. Recrystallized grains with random orientations from grain boundaries and solute segregation of Ca and Zn at grain boundaries contributed to this behavior. A similar result was also reported by Wang et al. [43].

Nakata et al. [44] explored Zn's influence in Mg-8Al-1Zn-1Ca-0.3Mn (wt%) alloys, revealing that Zn addition increased precipitate density and weakened textures. While the mechanisms were not detailed, further research into Zn's synergy with Ca

was recommended.

Incesu and Gungor [45] highlighted the Zn/Ca ratio's impact on microstructure in Mg-Zn-Ca alloys. Excessive Ca content led to the formation of Mg_2Ca phases, deteriorating mechanical properties. Conversely, $Ca_2Mg_6Zn_3$ phases enhanced grain refinement and corrosion resistance. Studies by Nie et al. [46] and Wang et al. [47] further refined this understanding by examining how the Zn/Ca ratio affects particle distribution, grain size, and texture. The findings consistently pointed to a "sweet spot" for Zn/Ca ratios, emphasizing the importance of balanced alloying.

Zhou et al. [48] compared Ca and Sr additions, confirming Ca's superior role in grain refinement and texture weakening. Go et al. [49] demonstrated that Ca and Gd additions to Mg alloys produced fine-grained structures with improved tensile properties due to particle-stimulated nucleation (PSN).

In addition to the studies about texture weakening in Mg-Ca-Zn alloys detailed above, the research about aging hardening [50-52], grain refinement/abnormal growth [53-55] and corrosion resistance [58-61] were also reported.

2.2.5 Exploring mechanisms: recovery and recrystallization

Diverging views on the role of Ca emerged as researchers delved deeper into the mechanisms behind its effects. Zhang et al. [62] focused on the PSN effect, observing Ca-containing precipitates within grains during hot extrusion. These precipitates restricted dislocation motion and stimulated recrystallization, leading to finer grains and weakened textures. Meanwhile, the texture weakening by the PSN in the Mg alloys were also reported by many other researchers [21, 40, 41, 46, 47, 49, 50, 63].

In contrast, Nakano et al. [64] and Lee et al. [65] highlighted the role of twinning. They found that Ca additions promote twinning, particularly compression and double twinning, which act as nucleation sites for recrystallization. These twinning mechanisms create grains with varied orientations, further contributing to texture weakening. The pole figures of the samples (Mg–3Al–1Zn (AZ31) and Mg–3Zn–0.5Ca (ZX31) (wt.%)) from Lee et al.'s research are shown below in Figure 2-6. The importance of twinning in the texture weakening of Mg alloys was also reported by many other researchers [48, 63, 66-68]. The studies of twins including enhanced formability by twins [69], twinning during rolling [70] and twins in hcp material [71] etc. [72-79] further developed the understanding of the twins.

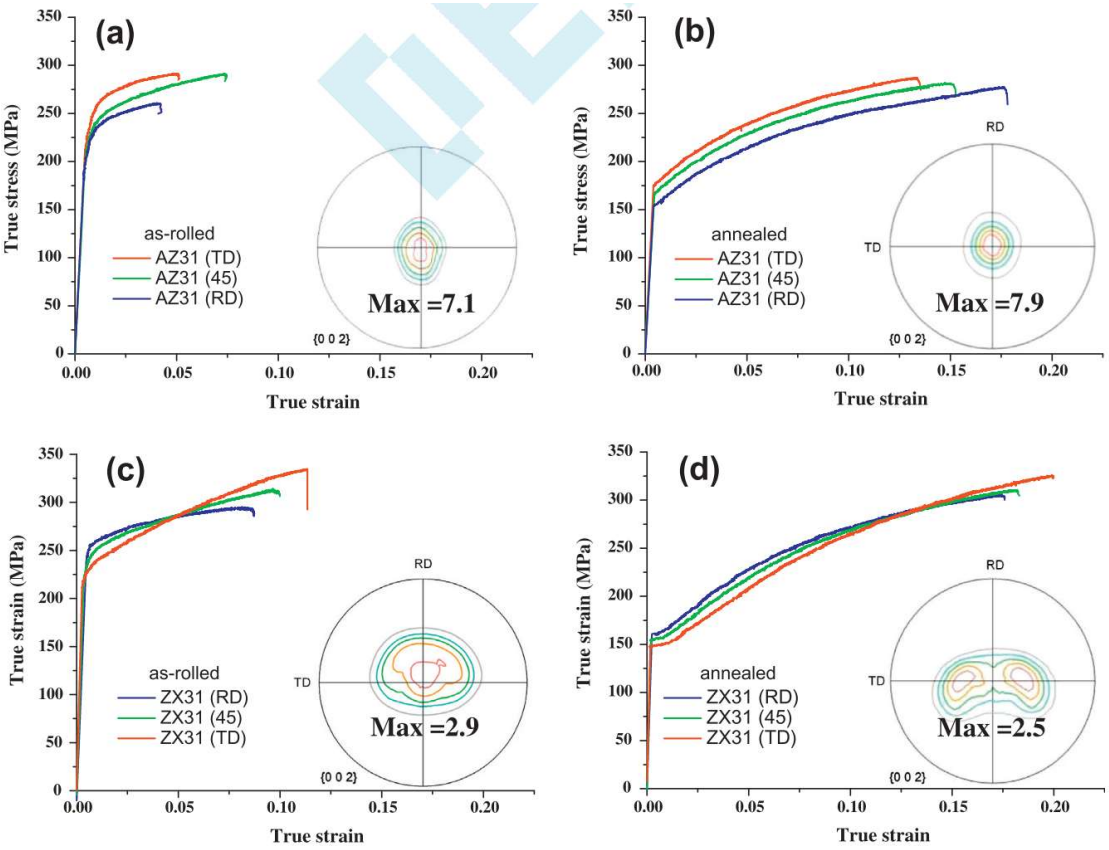

Figure 2-6 Pole figures of: (a) as-rolled AZ31, (b) 350°C 30min annealed AZ31; (c) as-rolled ZX31, (d) 350°C 30min annealed ZX31 [64]

Guan et al. [66, 82] employed quasi-in-situ EBSD and HAADF-STEM to analyze Mg-6.6Zn-0.2Ca (ZX70) alloys [66] (shown in Figure 2-7) and Mg-0.8Zn-0.2Ca (ZX10) [82]. They identified the role of each twin type in recrystallisation and texture evolution [66]. Double twins which rapidly transformed from compressive twins were the main deformation mechanism. The nucleation of recrystallisation from double twins and compressive twins were both confirmed, and the double twins were identified as the main nucleation site in the sample. Tensile twins rarely became the nucleation site due to "minimal accumulation of dislocations and consequently low elastic strain energy along mobile twin boundaries" [66]. The ratio of PSN was too low compared to the nucleation from double twins, while the nucleation from grain boundaries was restricted by the second phase particles on prior grain boundaries and retarded by the concurrent precipitation along the grain boundaries. Guan et al.'s subsequent studies [82] emphasized Ca and Zn co-segregation at grain boundaries, and the concurrent precipitation playing a similar role in recrystallization and grain growth as mentioned in last study. The precipitates decreased the frequency of recrystallization by pinning the prior grain boundaries. They also limited the grain growth of the grains with basal texture orientation. The double twins and twinning-related shear bands were identified

as the main nucleation site and were found to affect the final recrystallized structure. Guan et al.'s work indicate that double twins and twinning-related shear bands are critical to RE-like textures i.e. the random orientated grains were found mainly from double twins, with solute segregation and concurrent precipitation preserving these weak textures.

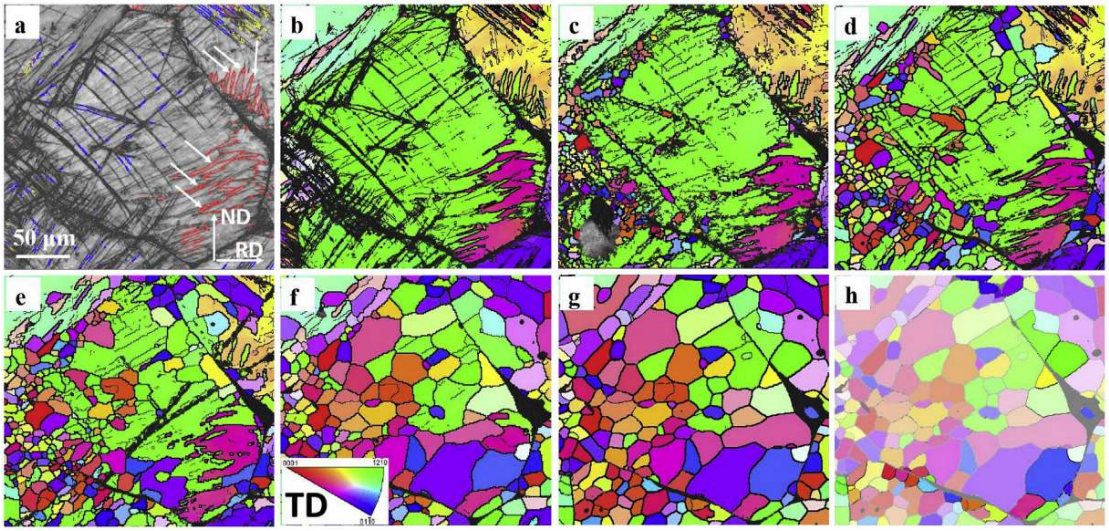

Figure 2-7 (a) Band contrast map with various twin boundaries (red: TTW, yellow: CTW, blue: DTW), (b) Quasi-in-situ EBSD IPF of the same area, (c)-(g) Quasi-in-situ EBSD IPF of the same area at different time of the recrystallization process (385s, 1030s, 1630s, 3430s and 7030s), (h) PSN grains along the GB (highlighted) [66]

The reports from Wang [63], Basu et al. [83] and Stanford [84] also mentioned that the shear bands play an important role as the nucleation site of the random orientated grains in Mg alloys. On the other hand, Zeng et al. [42] and Wang [63] also mentioned the random orientated grains from grain boundaries. Moreover, the weakened texture related to the activation of the non-basal slip system and the solution drag was also reported by many researchers [54, 85-90]. They believe the alloying elements in matrix plays an important role in modifying the strong texture of Mg alloys.

Compared with the extensive research in recrystallization mentioned above, there was much less research in recovery of Mg alloys [91]. The recovery studies in aluminium alloys were considered potential references for understanding the recovery in Mg alloys [92-94].

The studies mentioned above highlighted many mechanisms contributing to the texture weakening in Mg alloys: PSN, recrystallization from twinning, shear bands or grain boundaries and solute in matrix. The experimental materials used in these studies vary in composition. It was normal for materials to have different recrystallization mechanisms. However, among these studies, there were another point of difference i.e. the two processing methods: rolling and extrusion. Thus, a question arises: does the

processing method affect the recrystallization of Mg alloys, causing different reasons for the texture weakening?

2.2.6 Processing methods: extrusion & rolling

Except a few studies using wrought materials as the test specimens [7, 10, 56], most of the research used as-extruded [11-13, 29, 39-41, 43, 46, 52-54,58, 59, 62, 95-97] or as-rolled materials [9, 30, 31, 38, 42, 44, 45, 47-49, 57, 64-66, 68, 82, 85, 98-101] as the test samples. By making the comparison between these studies, it is clear that the processing method significantly influences the texture weakening effect in Mg alloys. Researchers observed distinct outcomes based on whether extrusion or rolling was used. For instance, Lee et al. [85] attributed texture weakening to Ca atoms in the Mg solid solution matrix during rolling, while Zhang et al. [62] emphasized PSN during extrusion. These contrasting views highlight the complexity of texture modification mechanisms under different processing conditions.

Cold rolling, as investigated by Zeng et al. [47], revealed that Ca additions delayed the formation of strong basal textures. However, greater thickness reductions eventually resulted in texture intensification, a phenomenon absent in hot rolling studies. This discrepancy underscores the need for comparative studies of different processing methods.

Li et al. [98] studied Mg-2Zn-1.2Ca (wt.%) plates under unidirectional rolling (UR) and cross-rolling (CR) methods (shown in Figure 2-8), while Du et al. [97] also focused on the influence of the UR and CR to the Mg-4.5Zn-1.1Ca (wt.%) alloy. Li et al. reported that UR led to more shear bands and uniform grain sizes, whereas CR induced a distinct texture. Du indicated that the rolling process refined the second phase particles in as-extruded samples and the CR sample had a finer second phase particles than UR sample. Thus, the CR sample had the strongest pole intensity followed by UR sample and original sample. These studies demonstrated the critical role of processing in texture evolution.

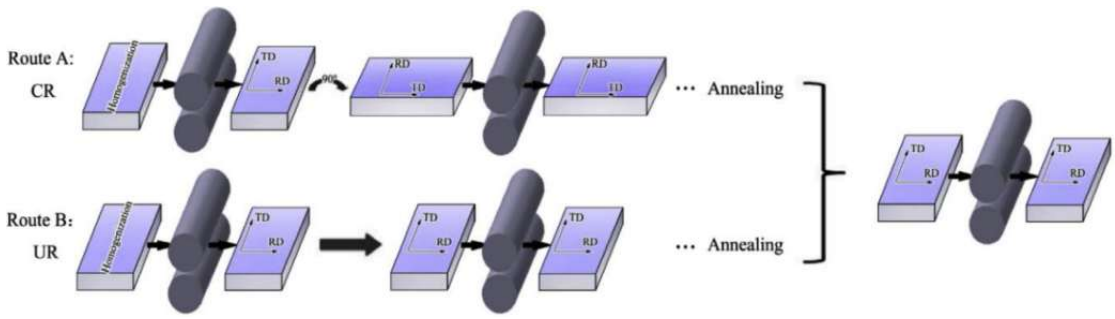

Figure 2-8 The CR processing and the UR processing [98]

In a similar vein, Hofstetter et al. [95] highlighted the impact of processing methods on microstructure using Mg–1Zn–0.3Ca (ZX10) and Mg–0.5Zn–0.15Ca (ZX00) alloys. Employing deformation dilatometry and semi-industrial extrusion, they demonstrated that post-deformation heat treatments could yield highly recrystallized structures. The recrystallization volume fraction, while influenced by processing methods, remained critical for studying the role of Ca in Mg alloys.

Victoria-Hernández et al. [68] attributed transverse direction (TD)-split textures in hot-rolled Mg alloys to extended recovery reactions. Their work underscored processing differences, as hot rolling favored discontinuous static recrystallization and reduced texture intensity.

Pan et al. [96] studied extrusion temperatures in Mg–1.0Ca–1.0Al–0.2Zn–0.1Mn alloys, finding that higher temperatures improved ductility by reducing coarse particles and basal textures while promoting sub-grain refinement. Similarly, Wang et al. [99] linked elliptical annular textures in hot-rolled Mg-Al-Zn-Mn-Ca alloys to contraction twins and non-basal slip mechanisms, shaped by grain boundary segregation of Al, Zn, and Ca.

2.2.7 Emerging techniques and future directions

Recent studies have introduced advanced techniques and concepts to refine our understanding the role of Ca in Mg alloys. For instance, Pan et al. [96] explored how extrusion temperature influences microstructure and ductility, revealing that higher temperatures result in fewer coarse particles and improved mechanical properties.

Khrustalyov et al. [102] reported using nanodiamond (ND) and the ultrasonic treatment (US) to improve the performance of the Mg alloy. With the ultrasonic treatment, the yield strength, ultimate tensile strength and ductility of the Mg-Ca-Zn (US) alloy and the Mg-Ca-Zn-ND alloy were all better than original Mg-Ca-Zn alloy.

For the computer aided analysis, Beyerlein et al. [103] and Chen et al. [104] used digital modelling to study twins and alloy deformation mechanism. Beyerlein indicated that the twin numbers in a grain is strongly related to the grain size, and the grain orientation has minimal relevance to twin variant selection. By using the new model, Chen successfully plotted the activation energy map, which can identify the optimal deformation conditions and analyze the deformation mechanism. Meanwhile, some other researchers reported the usage of the machine learning in deformation mechanism prediction/analysis and alloy design [105, 106].

Looking ahead, key research gaps include understanding the interplay of Ca and Zn in optimizing Zn/Ca ratios and developing processing methods that maximize texture weakening. Comparative studies of rolling and extrusion in identical Mg alloys could also yield critical insights. For the issue mentioned above, machine learning and

numerical modeling have significant development potential. For the present study, microstructure evolution requires continuous monitoring to track variations, such as nucleation sites and grain growth. Machine learning can help track these changes and provide more reliable and accurate results.

2.2.8 Summary

Calcium has proven to be a transformative element in Mg alloys, offering a cost-effective pathway to grain refinement and texture weakening [107]. Despite the progress made, the exact mechanisms remain partially understood, and varying processing methods continue to yield different results. The solute segregation, concurrent precipitation, particle-stimulated nucleation, twinning or shear bands, anyone could be the answer. As research advances, the different explanations from different processing methods also require more investigation. The difference between rolling and extrusion can be regarded as the difference in the strain path of the material. Thus, it is worth investigating the relationship between the strain path and the texture evolution in the Mg alloys. Furthermore, the combination of Ca with other elements like Zn and novel processing techniques holds the promise of unlocking the full potential of Mg alloys for high-performance applications, and the machine learning plus modeling could be an efficient way to push the study one step ahead.

2.3 Studying the strain path and texture evolution in magnesium alloys

As mentioned above, the relationship between the strain path and the texture evolution in Mg alloys is still not clear. Although some investigations were related to the “strain path and texture evolution” [98, 108], they did not determine the relationship between strain path and texture evolution but focused more on the texture evolution. Some researchers reported their studies about strain path and microstructure evolution [109-117], they mainly focused on the variation of twinning [109-112], numerical simulation [113-116] or fracture in Mg alloys [117], but less talked about the connection to the strain path. The role of other mechanisms (PSN, shear band and solute drag etc.) was also not investigated. On the other hand, few papers report studies on the relationship between texture evolution and strain/strain rate. Many studies about strain and Mg focused on strain hardening to the Mg alloys [118, 119] or Mg composites [120-122]. The studies about strain rate and Mg alloys did report some related results, but they are either studying the pure Mg and different strain rates [123, 124] or studying the twins in Mg alloys and different strain rates [125]. However, the different strains/strain rates affecting the texture evolution of Mg alloys is still not clear. Considering the similar deformation methods in actual production such as multi-directional rolling or

progressive die stamping process, it is clearly important to understand the role of strain path and strain/strain rate played in affecting the microstructure evolution of Mg alloys. It can help formulate new processing techniques or develop magnesium alloys with higher performance.

Moreover, the experimental materials were deformed by using rolling or tensile test machine. The deformation of the specimens were all carried out in three dimensions. The EBSD can only acquire the information from a surface [126] i.e. the deformation information in one dimension cannot be obtained in those specimens. The experimental method used by Xiong et al. [127] could be a good reference for simplifying the deformation by restricting deformation in two directions in the specimens. By using a channel die (shown in Figure 2-9), the deformation in two sides of the specimen (contact to the die) can be controlled, generating an almost two-dimension deformation in the specimen. Thus, the information lost in the third dimension could be avoided in EBSD. Furthermore, the channel die compression can generate different strain paths compared to the rolling process, i.e. the thickness reduction direction can be made on the TD of the compressed specimen, which cannot be produced via the rolling process. Besides, using channel die compression can save experimental material. Only a small piece of material is needed to complete the experiment, which the same volume of the material may not be able to be rolled.

On the other hand, considering the influence of the strain and strain rate to the deformation [123-130], the relationship between strain/strain rate and texture evolution is also worth investigating. The specimen with a double truncated cone shape [131] (shown in Figure 2-10) is considered as the ideal test sample to study the strain and the texture evolution in Mg alloys in one sample. The reason for using this sample geometry is simple. Compared to the traditional test method (making a large number of specimens for each alloying composition and running tests with different settings to generate different strains and strain rates), the compression on double truncated cone specimen can generate different strains and different strain rates within one specimen in different areas with only one compression. It can save a lot of time, especially for multi-group specimens.

This study aims to investigate the relationship between the strain path and the microstructure evolution in lean Mg alloys, particularly recrystallisation kinetics and mechanisms and consequent effect on texture evolution. The study also aims to study the effect of the Ca and Zn additions in the Mg lean alloys on recrystallisation kinetics and mechanisms and consequent effect on texture evolution.

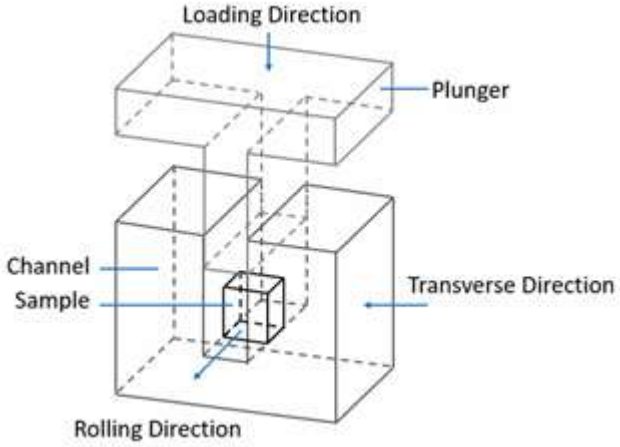

Figure 2-9 The channel die compression [127]

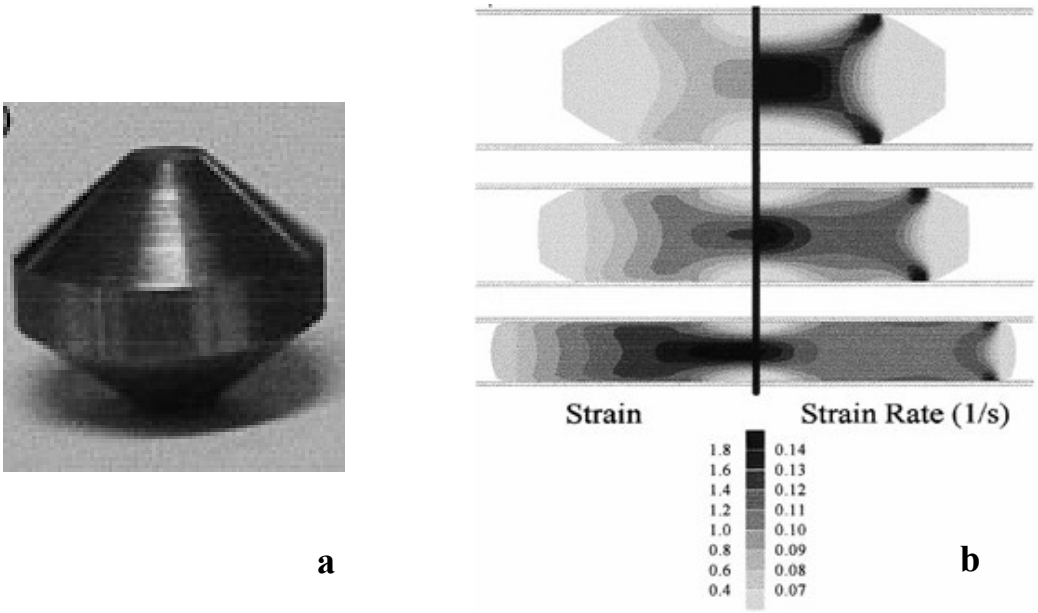

Figure 2-10 (a)The double truncated cone sample, (b) The strain/strain rate in the sample during the compression [131]

3. Methods

3.1 Ingot casting

Five ingots were prepared with the specific compositions: Mg-0.5Ca, Mg-0.4Ca-0.1Zn, Mg-0.2Ca-0.3Zn, Mg-0.1Ca-0.4Zn, Mg-0.5Zn (at%). High purity raw materials were used for casting: Mg rods (99.95% purity, $\emptyset\, 9.5\text{mm} \times 300mm$, from NewMet), Ca grains (99.5% purity, $\emptyset\, 2-5\text{mm}$, from NewMet), Zn pieces (99.999% purity, $\emptyset\, 4-8\text{mm}$, from NewMet). The ingots were manufactured using the Arcast SC100 Strip Caster (shown in Figure 3-1). Melting was undertaken using ceramic crucible induction melting combined with mould casting.

Figure 3-1 The Arcast SC100 Strip Caster

Based on the cavity size of the casting mould, the size and the volume of the Mg alloy ingots were determined as $7.4cm \times 5.4cm \times 4.0cm$ and $159.8cm^3$. The quantity of the ingredients for each ingot are shown below in Table 3-1. The original length of the pure Mg rod was 30cm which was too long to fit into the crucible and could reduce the melting efficiency. Thus, the rods were cut by hacksaw manually into 10-15cm sticks in length to give sufficient materials to fill the crucible. Based on the calculation, the specific weight of the pure Ca grains (99.5% purity, $\emptyset\, 2-5\text{mm}$) and pure Zn pieces (99.999% purity, $\emptyset\, 4-8\text{mm}$) were prepared by using the high-precision electronic scale.

Table 3-1 The ingredients of the experimental Mg alloys

at%	wt.%	Mg/g	Ca/g	Zn/g
MgCa0.5	Mg99.18Ca0.82	275.53	2.28	0
MgCa0.4Zn0.1	Mg99.08Ca0.66Zn0.27	275.84	1.84	0.75
MgCa0.2Zn0.3	Mg98.89Ca0.36Zn0.75	276.440	1.04	2.10
MgCa0.1Zn0.4	Mg98.77Ca0.16Zn1.07	276.85	0.45	3.00
MgZn0.5	Mg98.67Zn1.33	277.17	0	3.74

After finishing, the preparation of the raw materials and the preparation of the casting process were carried out. Firstly, boron nitride (BN) spray was used to coat the inner surface of the crucible and the outer surface of the stopper (a long bar which physically stops the melted material flowing through the nozzle into the cast mould). This is to prevent the raw materials sticking to the crucible and the stopper. Secondly, the stopper was put into the crucible to block the nozzle at the bottom of the crucible. It also acts as a switch to allow control of when to release the melted alloy down to the mould. Then, the raw materials were placed into the crucible. Before the assembly was moved into the chamber of the Arcast SC100, the moving distance of the lifting mechanism was adjusted to make sure the stopper could lift high enough, making melted material flow down smoothly. Next, the whole assembly was moved into the well-cleared chamber of the Arcast SC100. An induction coil was set around the crucible followed by the placement of the casting mould where beneath the assembly and direct towards the nozzle. After linking the stopper to the lifting mechanism and putting the K-type thermal couple into the stopper, the chamber was evacuated using the roughing pump to 500mTorr first and then fine evacuated to 5mTorr. Both readings were acquired from the vacuum gauge. The chamber was then backfilled with Ar gas to -7inHg. This reading was acquired from the chamber pressure gauge.

The next step was the heating process. To avoid breaking the crucible, the heating rate was controlled at no faster than $20℃/min$. When the temperature reached the target temperature ($750℃$), it was held for another 20 minutes. This is to make sure the alloying components are entirely melted and well-mixed. Then, the stopper was lifted by the lifting mechanism so that the melted Mg alloy flowed through the nozzle and down to the mould. After 2-3 hours cooling inside the chamber, the chamber was refilled with air and the ingot was acquired from the mould. Figure 3-2 shows the Arcast SC100 and the casting assembly. Figures 3-3 show the first batch and the second batchof five ingots acquired by this casting process.

Figure 3-2 The Arcast SC100 and the casting assembly (before closing the door)

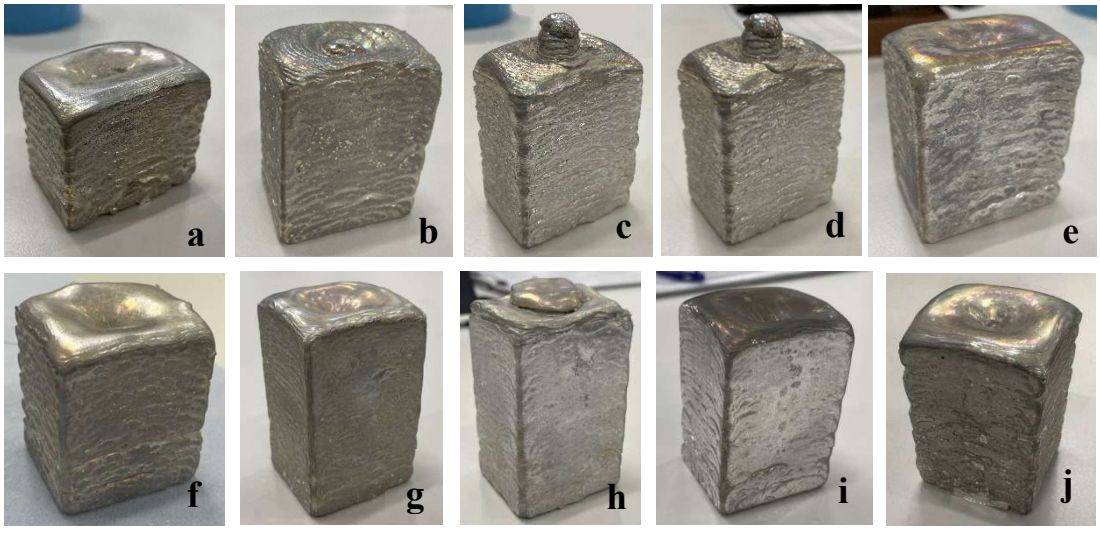

Figure 3-3 The first batch cast Mg ingots: (a) Mg-0.5Ca, (b) Mg-0.4Ca-0.1Zn, (c) Mg-0.2Ca-0.3Zn, (d) Mg-0.1Ca-0.4Zn, (e) Mg-0.5Zn
The second batch cast Mg ingots: (f) Mg-0.5Ca, (g) Mg-0.4Ca-0.1Zn, (h) Mg-0.2Ca-0.3Zn, (i) Mg-0.1Ca-0.4Zn, (j) Mg-0.5Zn

Unfortunately, this ingot casting process had disadvantages, some of which have been solved, but some were not. For example, in the first casting of the Mg-0.5Ca alloy, the BN coating was not applied to the crucible and the stopper. This resulted in the pure Mg rods sticking onto the surface of the crucible and the stopper (shown in Figure 3-4). Meanwhile, some of the rods did not melt and appeared to have had no contact with any surface and were tilted at a large angle to the vertical direction. Clearly, the unmelted rods led to the failure of the casting. This problem was solved by the application of the BN coating spray and by placing all rod feedstock vertically into the crucible.

During the fifth casting process (Mg-0.5Zn alloy), after holding for 20 minutes, the stopper did not move when the lifting mechanism was activated, resulting in the need to cool down the melted alloy inside the crucible. The reason for this malfunction was attributed to a loose screw in the lifting mechanism. After a full check of the casting system and correction of the screw, the crucible charge was remelted at 750℃ and the Mg-0.5Zn alloy was successfully produced after the routine casting operation. The screw check has been added into the standard operating procedure of the Arcast SC100 ceramic crucible melting.

Figure 3-4 The unmelted pure Mg rods inside the crucible after the casting of the Mg-0.5Ca alloy

There is an unavoidable problem of evaporation of the Mg during the heating process. The solution to this was to use to a higher Ar gas pressure in the chamber to suppress the evaporation as well as adding excess pure Mg when preparing the raw materials. However, this unwanted consumption of pure Mg through evaporation was never fully prevented when using the Arcast SC100 to do the ingot casting.

Another problem was controlling the heating rate. The heating method in the Arcast SC100 was coil induction heating. The heating rate was controlled by changing the voltage applied to the coil. The most difficult point was that the voltage needs real-time control i.e. the voltage needed to be changed manually based on the reading from the thermocouple to make sure the heating rate did not exceed 20℃/min. This is an inevitable problem as the induction coupling efficiency continuously changes as the materials heat up, giving fluctuations in the heating rate. The only solution was to continuously monitor the temperature reader and quickly adjust the voltage of the coil to get the desired heat rate.

3.2 Heat treatment & ingot quality check

3.2.1 Heat treatment of the first batch ingots (without hot rolling)

Following casting the first batch of ingots with 5 compositions, the ingots were then homogenized in the Lenton 21-501808 tube furnace (shown in Figure 3-5). The as-cast ingots were homogenized at 450℃ under Ar inert gas for 8 hours. The microstructure was then investigated using Nikon optical microscope (shown in Figure 3-6 (a)). Optical microscope (OM) was used for checking the grain size and the second phase content. An FEI Inspect F50 (shown in Figure 3-6(b)), with Oxford energy-dispersive X-ray spectroscopy (EDS) was used to further look at the microstructure and the chemical composition to make sure they are as designed in all the ingots.

3.2.2 Heat treatment and hot rolling of the second batch ingots

Besides the first batch ingots, the second batch of 5 ingots were manufactured using the same process as the first batch. These ingots were then hot rolled using the Fenn Rolling Mill 081 (shown in Figure 3-7). For rolling, the ingots were pre-heated at 350℃ for 30 minutes. The temperature of the rolls was also maintained at 350℃ during the process to give near isothermal rolling. Then, the hot rolling was conducted at a 10% thickness reduction per pass and 5 passes in total i.e. 50% thickness reduction (from 4cm to 2cm) of the sample after the hot rolling. The temperature and the time duration of the intermediate heat treatment were 350℃ and 10 minutes, respectively. A water quench was used after the final rolling pass. The microstructure of the hot-rolled ingots was then investigated using the same techniques as for the first batch of ingots.

Figure 3-5 The Lenton 21-501808 tube furnace

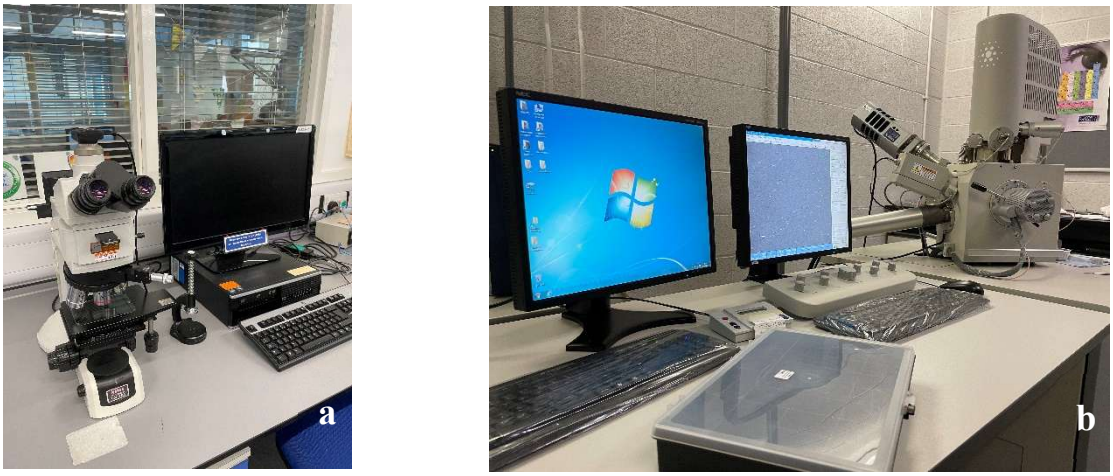

Figure 3-6 (a) The Nikon optical microscope, (b) The FEI Inspect F50

Figure 3-7 The Lenton tube furnace

3.2.3 OM sample preparation and OM check

To prepare the samples for optical microscopy, a Buehler Abrasimet 250 (shown in Figure 3-8 (a)) and Struers Secotom 50 (shown in Figure 3-8 (b)) were used to cut the test samples from the as-cast ingots and the homogenized ingots after the heat treatment. To avoid the influence of heat during the sample mounting process, the cold mounting method (with epoxy resin) was chosen to replace the hot mounting method (with Bakelite powder). The Struers EpoFix Resin and EpoFix Hardener were mixed with a ratio of 25:3 by weight to mount the samples in the specimen mould. Before the mounting, Vaseline was thinly coated on the inner surface of the specimen mould to facilitate the release of the specimen after the curing of resin. The sample was then placed at the bottom of the specimen mould followed by the filling of the mixed resin. Finally, the specimen mould was placed in a vacuum chamber for 10 minutes to remove

any bubbles from inside of the resin. The size of the cold mounted specimens was 32mm in radius and 20mm in height.

After 8 hours of curing, all the cold mounting specimens were given an identification mark at the bottom and then the grinding and polishing was performed on a Buehler Automet 250 Grinder-Polisher (shown in Figure 3-8 (c)). The procedure took some time to perfect given the soft nature of magnesium alloys and the need for a very high standard of finish for subsequent EBSD investigation. The top surface of the specimen (without sample) was first ground to flat followed by the bottom surface (with sample) using 2500P grinding paper and water lubrication (2 min in total). This was for removing the cured epoxy resin flash around the top surface and the extra epoxy resin beneath the sample on the bottom surface. The parallelism of the top and the bottom surface of the specimens was also secured by this process. The 4000P grinding paper was applied to grind the specimens for around 5 minutes with 5N force combined with an OM check of surface condition every minute. After this step, two Struers DP-Suspension A oil-based diamond polishing suspensions (1micron and 0.25micron) were used in the order to achieve a high polish on the sample surface. Isopropanol (IPA) was used as the lubricant during the whole polishing stage. At least 10 minutes polishing was required with each kind of suspension for samples to acquire a well-polished surface. The OM check was also carried out every 2.5 minutes in this stage.

The specimens were then etched in 2% nital for the optical microscopy. Three beakers were prepared with 15ml 2% nital, 20ml isopropanol and 20ml isopropanol, respectively. The polished specimens were cleaned with water and isopropanol before etching. After the specimens were dried, the test surface of the sample was immersed in the 2% nital for 20-30 seconds. Cleaning was undertaken in the second beaker of isopropanol. After 10 seconds, the specimens were moved into the third beaker of isopropanol for 20 seconds to further reduce the concentration of the remaining 2% nital. Finally, the specimens were cleaned with water and isopropanol, followed by cold air dry. The etched samples were then investigated by OM to check the surface condition. For acquiring a clear view of the grain boundaries under OM, the etching process was normally repeated two to three times for each sample.

Besides the cold mounting, a series of specially designed sample holders (shown in Figure 3-9) were also used to clamp the sample for grinding and polishing. Two or three layers of paper tape were first attached to the two semicircular surfaces which are on the two sides of the gap. Next, the sample was set on a flat surface with the grinding or polishing surface facing downwards. The sample was then covered from above by the sample holder and placed in the gap. After the position of the sample was adjusted to the centre of the sample holder, two screws were used to tighten the sample followed by the removal of the tapes. Thus, the sample surface was given a slight height

difference from the sample holder surface by tapes for the grinding and polishing work. The following sample preparation process was the same as that of the cold mounting specimens.

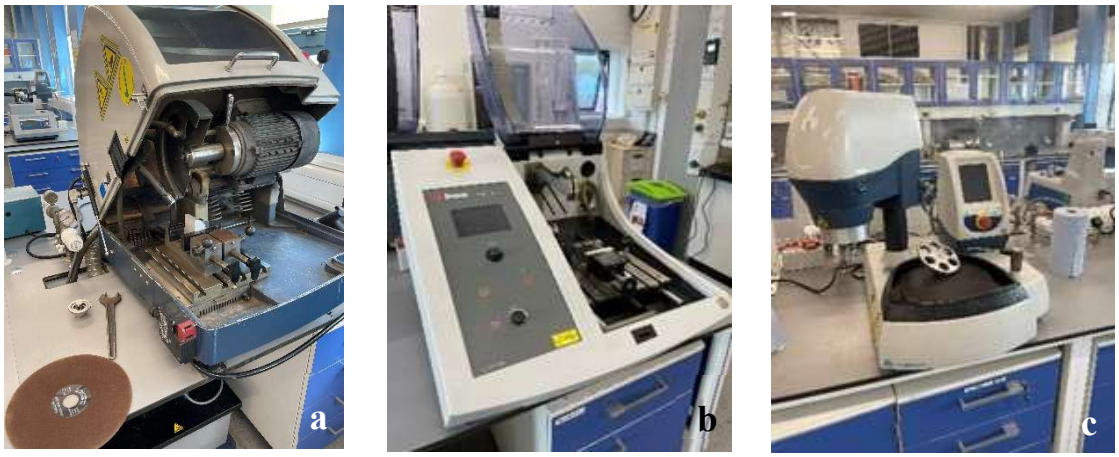

Figure 3-8 (a) The Buehler Abrasimet 250, (b) The Struers Secotom 50, (c) The Buehler Automet 250 Grinder-Polisher

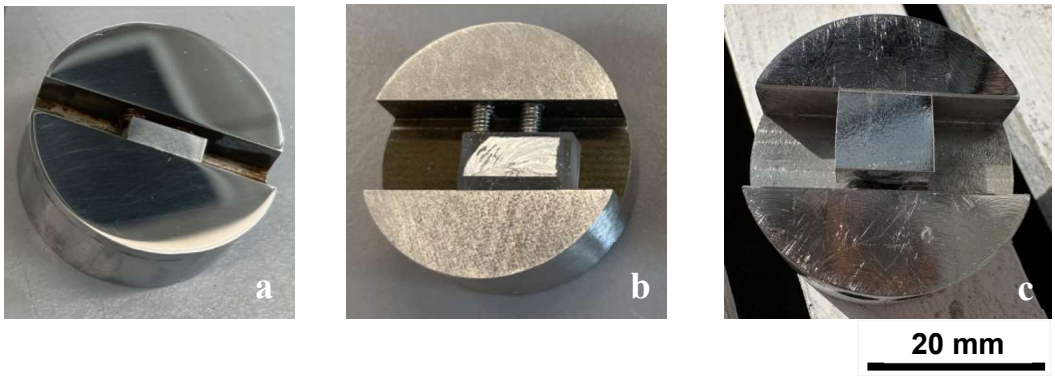

Figure 3-9 (a) The small gap sample holder, (b) (c) The large gap sample holder

For the EDS test samples, the same specimens were used from the homogenized ingots. The specimens were ground and polished again in the same way as the OM sample preparation. The only difference was that an extra colloidal silica suspension polishing process was carried out after the 0.25-micron polishing process. The Struers OP-S NonDry colloidal silica suspension was mixed with IPA at the ratio of 1:1 by volume. At least 15 minutes of OP-S polishing was required for this stage and the consumption of the mixed liquid was 20ml per 5 minutes. The lubrication for this process was still IPA. The sample was then ultrasonically cleaned for 5 minutes to remove any residual OP-S suspension. Then, EDS was performed on as-polished surface without etching.

There are some important points that need to be mentioned about sample preparation to achieve useable specimens for EBSD. During grinding and polishing, the force applied to the sample should not exceed 5N, because both Mg alloy and the epoxy

resin are soft such that a high load on the sample causes extra scratches and surface deformation. This force is much less than used for steel or other hard materials. When using the sample holder to prepare the sample, due to the heavy weight of the holder itself (stainless steel), the sample faced a much higher press force than that of the cold mounting specimen. However, an alternative way of cold mounting to prepare the samples was necessary, especially when a sample just needs OP-S polishing to remove the oxidized layer on the surface. The 12-hour curing time for the cold mounting was sometimes avoidable.

The time for etching the Mg alloys very much depended on the composition, e.g. the etching time for the Mg-0.5Ca (at%) alloy was less than 1 minute but the etching time for the Mg-0.1Ca-0.4Zn (at%) alloy could be more than 3 minutes. To ensure the sample was not over-etched, the time duration for each step of the etching process was short i.e. less than 30 seconds. Also, the sample needed to be checked under the OM after each step to check whether the etch was sufficient.

It is also worth noting that it was essential to take great care over the maintenance of the sample preparation equipment, the diamond suspension polishing cloth and the OP-S polishing cloth. Each cloth needed to be cleaned carefully after every usage, especially the OP-S polishing cloth. Otherwise, the remaining colloidal silica particles from the last time polishing could induce unwanted scratches on the surface of the sample.

For the EDS analysis, a mistake was made in the first-time sample preparation. The etching process was proceeded to the sample before the EDS test. This directly caused the consumption of the material which resulted in inaccurate test results (shown in Figures 3-10). Comparing Figure 3-10 and Figure 4-3 (b), it is clear to see that the proportion of the Ca in the etched sample is much lower than what it should be.

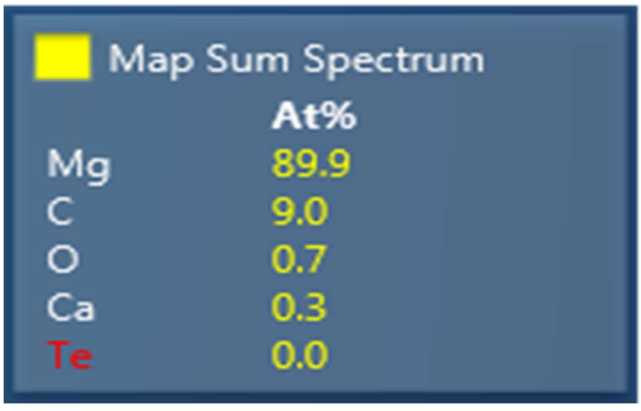

Figure 3-10 The map sum spectrum result of element proportion of the etched Mg-0.5Ca ingot

3.3 Channel die compression process [105]

Deformation of the Mg-alloys was undertaken using channel die compression. The exact procedure for compression evolved during the project based on experience gained in the first experiments. For the first batch of the alloys, the sample was compressed by the T-shape plunger in the channel die which restricts the deformation of the sample on its two sides i.e. the deformation of the sample can only happen in two directions. The assembly of the T-shape plunger and the channel die which was used for compressing the first batch samples is shown below in Figure 3-11. The material for making this channel die assembly was D2 tool steel. In this case, all the samples were first subject to a 10% size reduction. Then, half of the samples were subjected to another 10% size reduction in the same direction, and the other half were turned 90° followed by a 10% size reduction in the new direction. The one-direction (1D) compression and the two-direction (2D) compression were finished by these two processes, respectively. As a result, different strain paths were produced. The compression direction of two steps compression is shown below in Figure 3-12. The coordinates (RD, TD, ND) shown in Figure 3-12 , which indicates the direction of the specimens before they machined out from the as-rolled materials. The coordinate systems in all subsequent results (e.g. IPF maps and pole figures) are represented by these directions.

The test specimens were made from the first batch homogenized ingots. The Buehler Abrasimet 250 and the Struers Secotom 50 were used to cut the test specimens to size. The Abrasimet 250 was first used to finish the large-scale cutting followed by the Secotom 50 to carry out the high precision cutting. The size of the specimen was $15mm \times 10mm \times 4mm$. The thickness of the specimen was controlled to be as close as possible to 4mm, because 4mm was the width of the gap of the channel die. The closer the thickness of the specimen to the width of the channel die, the less deformation was induced in the width direction i.e. the real deformation was much closer to an ideal deformation which only takes place in the vertical direction and the transverse direction.

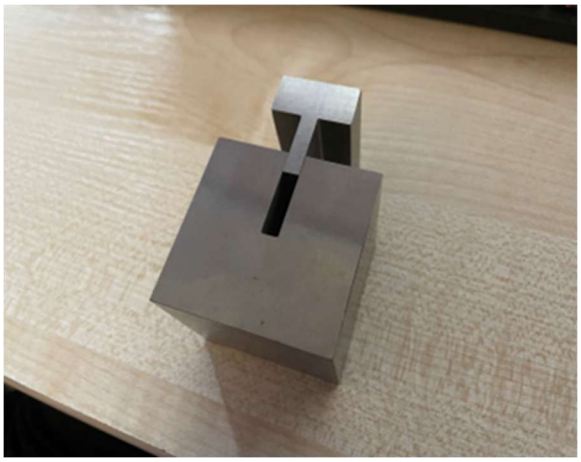

Figure 3-11 The channel die and the T-shape plunger

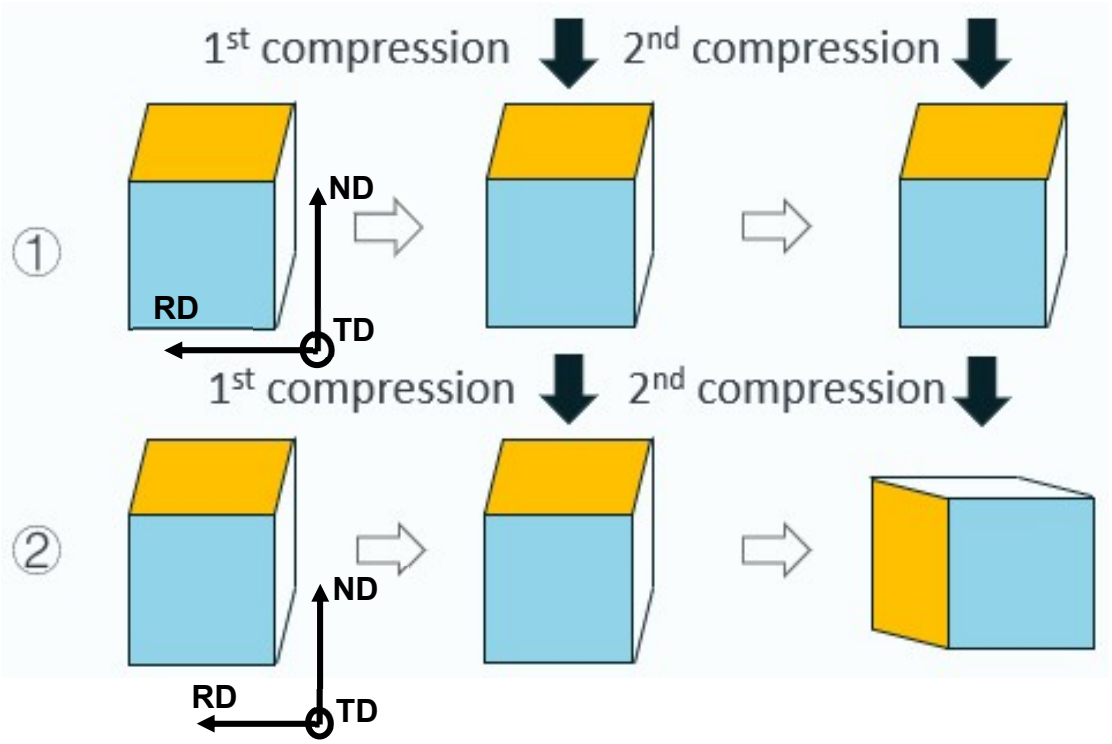

Figure 3-12 The compression direction to the specimens in the channel die compression: ① The one-direction compression, ② The two-direction compression; Blue surface: always contact with the side wall of the channel die, Yellow surface: compression surface of the 1st compression

Vaseline was applied as a lubricant around the inner surface of the channel die and the bottom surface of the T-shape plunger. Then, the specimen was placed at the bottom of the gap in the channel die and covered with the T-shape plunger above it. Next, the assembly was placed in the Hounsfield universal testing machine which can apply a maximum 75kN compressive load onto the plunger. The Hounsfield universal testing machine with the compression test kit before the start of the compression process is shown in Figure 3-13. The compression speed was set as 0.05mm per minute. The test end point (moving distance of the compression test head) was set as 1.5mm i.e. 10% size reduction of the sample. Then the second compression was carried out with the same speed in two different ways, as previously described. However, the second 10% size reduction was never conducted. Due to the defect in design of the channel die assembly and the shape of the test samples, the removal of the sample from the gap was very hard, rendering the test too difficult (which will be discussed in the following chapter). The readings of the force (N) and the compress distance (mm) were recorded automatically during the process.

Figure 3-13 (a) The Hounsfield universal testing machine,
(b) The compression test heads

For the second batch of hot rolled alloys, many changes were made to modify the channel die compression process. Firstly, the shape of the specimen was changed from the cuboid ($15mm \times 10mm \times 4mm$) to the cube ($10mm \times 10mm \times 10mm$). The regular shape of the specimen was considered not just much easier to be manufactured but also much easier to be simulated and analyzed in the simulation software (if needed). All the cubic specimens were manufactured from the hot rolled ingots by LAW Universal Grinding Ltd & Precision Engineering Services using wire-cutting process. Secondly, a new channel die assembly was designed by the author and manufactured (shown in Figure 3-14) by the same company. The material for making this new assembly was still D2 tool steel. The new channel die assembly was formed by five parts, the T-shape plunger, the left channel die, the right channel die, the plunger blocks and the screws. The separate two parts of the channel die was designed to disassemble after the compression via the vertical direction of the compression direction. Thus, the removal of the compressed specimen was free of direct contact on the specimen itself. The role of the two plunger blocks was to keep the T-shape plunger moving in the vertical direction. Screws were used to tighten the whole assembly during the compression. Also, the BN spray was used as the lubricant to replace the Vaseline during the compression process. In this case, all the samples were subjected to a 20% size reduction in the first compression. Then, half of the samples were subjected to another 15% size reduction in the same direction, and the other half were turned 90° followed by a 15% size reduction on the new direction.

In the channel die compression for the second batch of the specimens, the channel die assembly was first disassembled. The inner surface of the gap, the bottom of the T-shape plunger and the surface of the cubic specimen were coated with a thin layer of the BN (shown in Figure 3-15). Then, the specimen was placed onto the left part of the channel die followed by the assemble of the T-shape plunger on the top, right channel die, two die screws and the plunger blocks on the two sides. Next, the assembly was placed onto the ZwickRoell Z050 test frame (maximum 43kN compressive force) (shown in Figure 3-16) to conduct the two step compression processes mentioned above. The compression speed was still 0.050mm per minute. And the removal process of the specimen was to reverse the assemble process. The stress and strain were recorded automatically by the Zwick.

Figure 3-14 The new channel die

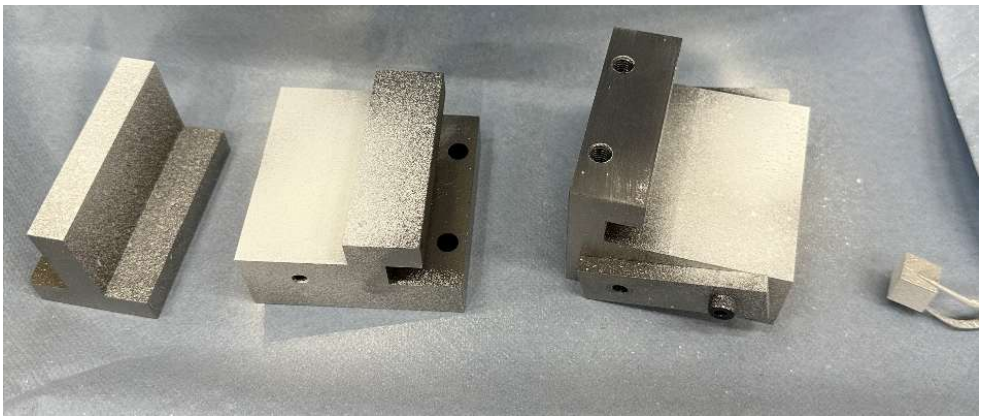

Figure 3-15 The disassembled channel die and specimen with BN layer

Figure 3-16 The ZwickRoell Z050 test frame

After finishing the compression process, all the specimens were cut from the middle along the direction of the gap. The specific marks were given to the specimens to identify the first compression direction and the second compression direction (shown in Figure 3-17). The same cold mounting sample grinding and polishing preparation process (including OP-S polishing) was conducted to all the compressed specimens. Due to the size limitations of the EBSD specimen on the JEOL 7900F (figure 3-18), the polished samples were manually cut out from the cold mount specimens by using hacksaw, followed by 5 minutes ultrasonic cleaning. For preparing an EBSD sample, the final preparation stage used the GATAN PECS II (fully automated argon ion polishing system) (shown in Figure 3-19). At a low glancing angle and accelerating voltage, it can polish samples rapidly giving a damage-free sample surface by using the Ar beam. The angle of the beam was set at 4° and the voltage was 5keV. The sample was polished for 1 hour. After finishing the surface processing on the GATAN PECS II, the compressed specimens were taken to the JEOL 7900F for the EBSD investigation.


Figure 3-17 The specimen with marks: O – first compression, Ø – second compression

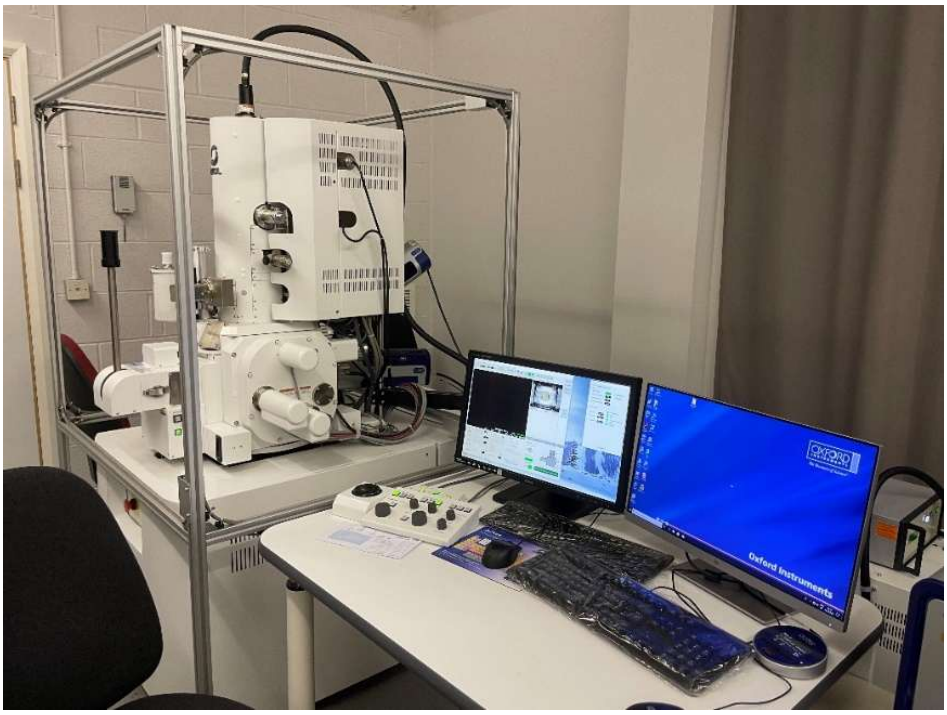

Figure 3-18 The JEOL 7900F scanning electron microscope

Figure 3-19 The GATAN PECS II fully automated argon ion polishing system

After the investigation of the crystallographic texture of the as-compressed samples, the annealing process for selected times (30s, then an additional time of 45s, 60s, 75s, 90s, 120s, 150s, 180s, 240s, 300s, 330s, 360s, 390s, 420s, 480s and 540s at 350℃) was conducted in turn on all the samples. In the following chapters, the annealing time will be presented in total annealing time i.e. 30s, 75s, 135s, 210s, 300s, 420s, 570s, 750s, 990s, 1290s, 1620s, 1980s, 2370s, 2790s, 3270s and 3810s. Between every annealing process, the same Ar ion beam milling surface preparation and EBSD investigation were undertaken at the same area (where the as-compressed specimen scanned) on each sample to make sure to track the site-specific microstructural changes as a function of the strain path. The annealing time was chosen to increase for about 30s or 60s after each annealing process to make sure the temperature of the specimens keeps increasing (till reach the target temperature 350℃). Which means after each annealing process, the microstructure evolution was pushed a step forward and the EBSD on the same site between each annealing process was able to track the variation of the microstructure. For the annealing, the samples were grouped into pairs of the same compositions to carry out the heat treatment i.e. the 1D compressed sample and the multiaxial compressed sample with the same composition were annealed together as a group. Samples were annealed in the tube furnace (Lenton 4701 tube furnace (shown in Figure 3-20)) at the heat treatment temperature (350 ℃) under the Ar inert gas atmosphere. The cooling method was water quench. The heating rate of the sample in the tube furnace was also measured by the thermocouple before the annealing process. The result is shown below in Figure 3-21.

Figure 3-20 The Lenton 4701 tube furnace

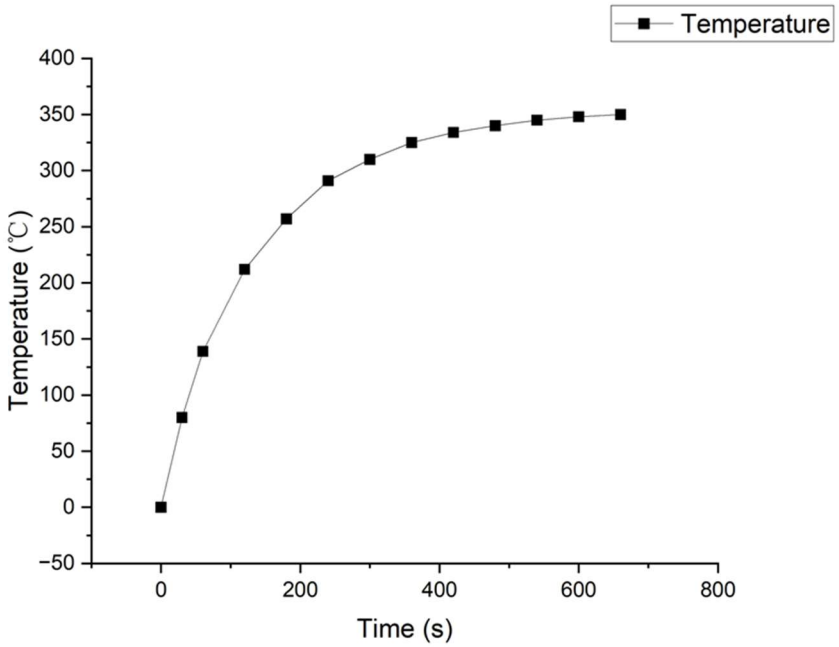

Figure 3-21 The temperature of the sample during the annealing process

3.4 SEM and EBSD characterization

The EBSD was the main technique for sample characterization throughout the whole study.

For the channel die compressed specimens, The EBSD was used to investigate crystallographic texture of the 1D compressed and the multiaxial compressed specimens on the JEOL 7900F. The prepared specimen was first mounted onto a sample stub by using silver paint. After 10 minutes of air dry, the stub was loaded onto the sample holder. Next, the sample holder was loaded into the transfer chamber followed by the vacuuming operation. When the gate of the transfer chamber opened, the specimen was transferred into the vacuum chamber. After adjusting the height of the specimen, the beam was turned on and the SEM image was used to adjust the focus. Then, the sample stage was tilted 4 times (20° each) to reach 70°. After each tilt operation, the sample stage was manually adjusted to make the target area in position. Before starting the EBSD scanning, a final focus was proceeded on the target area.

AZtec software was used to conduct EBSD scanning. After choosing the target element (Mg), the detector was moved in. Next, a SEM image was acquired and the EBSD pattern was optimized by changing the EBSD camera binning mode and exposure time and reacquiring background information. After considering the size of the characterized area and the scanning time cost, multi-frame synthesis EBSD was chosen as the characterizing method. Six EBSD maps with a magnification of 400 were montaged to one large EBSD map for the large area scanning. The accelerate voltage of the EBSD test were 20kV and the step size was $0.25\mu m$.

For the double truncated cone specimens, the process of EBSD investigation was the same as previously described.

3.5 Double truncated cone sample compression process [109]

In this compression process, a novel sample design (previously used in studies on titanium [109]) was used, called the double truncated cone sample (shown in Figure 3-22). This sample was designed to produce a wide range of strains and strain rates within a single sample after the compression process. The target shape of the compressed sample was a near-flat disc. Subsequent annealing was planned to allow the texture evolution to be investigated as a function of strain within one sample. Alloys were to be heat treated for various times to follow the recrystallisation process. Based on previous investigations of the Mg-Ca-Zn alloys, the heat treatment time and temperature were decided as following: 180s, 520s, 880s, 2110s, 3310s, and 6910s at 350 °C. Thus, the microstructural evolution was mapped as a function of strain and heat treatment time for each of the different alloys.

Figure 3-22 The double truncated cone sample [109]

Firstly, a piece of Mg alloy (Mg-6.8Zn-0.2Ca-0.4Ag) ingot left over from other experiments was used as the trial material to run the compression test, with the ingot machined by LAW Universal Grinding Ltd & Precision Engineering Services. Compression process was carried out on the Hounsfield universal testing machine. Vaseline was applied to the contact surfaces of the sample and the machine as the lubricant. The compression speed and the compression distance was set at 0.050mm per minute and 8mm, respectively. The compression of the Mg-6.8Zn-0.2Ca-0.4Ag double truncated cone samples was shown to be successful. Based on this success, this deformation approach was adopted and then the five ingots with different compositions were machined from the first batch of ingots accordingly. The same compression process as the Mg-6.8Zn-0.2Ca-0.4Ag samples was carried out on the new manufactured double truncated cone samples.

EBSD investigation was then carried out on the FEI Inspect F50 and JEOL 7900F. Firstly, the compressed samples were cut in the direction with the largest deformation

(shown in Figure 3-23). This is for acquiring as much information as possible about the deformation. Then, the sample was additionally cut into two pieces followed by another cut avoiding the centre line of the sample i.e. to avoid losing the information from the centre area in the cut (shown in Figure 3-24). The final dimensions of the sample were determined by the size of the specimen which could fit in the FEI Inspect F50 and JEOL 7900F. After the routine cold mounting, grinding and polishing (including OPS polishing) process, the Ar ion beam milling was carried out in the Gatan PECS II. However, unlike the channel die compressed samples, this process was carried out at a much lower beam angle (2°) combined with a much longer time (3-4 hours). Figure 3-25 shows the samples prepared for the EBSD test.

All the double truncated cone samples made from the first batch of ingots showed insufficient formability during the compression process with all the samples cracking in the middle of the compression process. Moreover, the deformation was not symmetrical about the sample even though the top surfaces of the sample were machined to be parallel and the dies were shown to be precisely aligned. The samples with the higher Ca proportion showed poorer formability compared to the low Ca-contained samples. This lack of symmetry made it impossible to judge the strain that the sample had received across its section. It also made it impossible to compare samples with different compositions. Thus, the following heat treatment of these samples was cancelled due to the obvious reason.

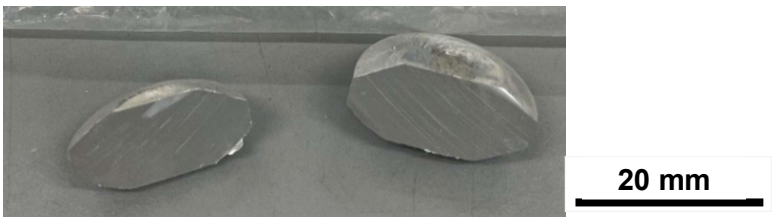

Figure 3-23 The cut Mg-0.1Ca-0.4Zn sample

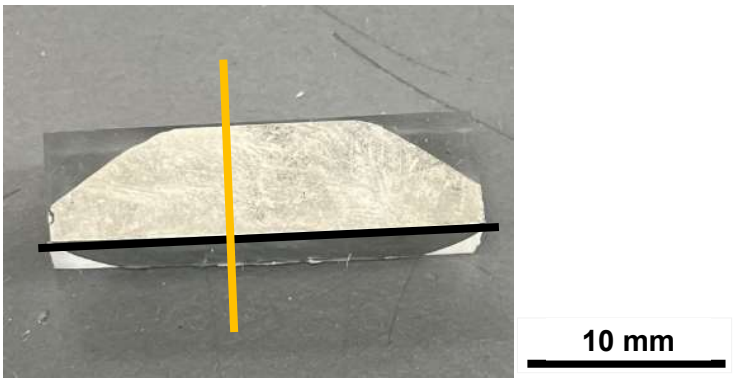

Figure 3-24 The further cut Mg-0.1Ca-0.4Zn sample (through black line) and the next cut (through yellow line)

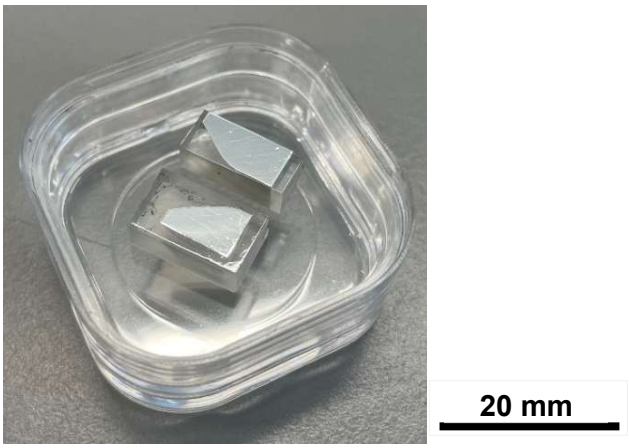

Figure 3-25 The prepared Mg-0.1Ca-0.4Zn sample for the EBSD test

4. Results

4.1 Ingots casting and hot rolling

The OM results of the first batch of as-cast ingots and the homogenized ingots are shown below in Figure 4-1 (a)-(e) and Figure 4-2 (a)-(e), respectively. It is clear that all the Mg alloys have a very large grain size, the average grain size of the as-cast and homogenized Mg-0.5Ca, Mg-0.4Ca-0.1Zn, Mg-0.2Ca-0.3Zn, Mg-0.1Ca-0.4Zn, Mg-0.5Zn ingot was 660μm, 625μm, 579μm, 601μm, 580μm and 657μm, 626μm, 585μm, 611μm, 587μm, respectively. Some grains were even over 1500μm. This larger than average grain size was likely to affect the formability of the samples [1]. Therefore, the deformation performance during the compression testing would not be as good as expected for these materials. However, comparing the grain size of the as-cast ingots and the homogenized ingots, there was no dramatic grain growth in the ingot after the heat treatment. The average grain size of the ingots increased from about 600μm before the homogenization to around 610μm after the homogenization.

In order to limit the number of experiments to a manageable level, the study with the second batch ingots was focused on three Mg alloys rather than the five alloys of the first batch. These were Mg-0.2Ca-0.3Zn, Mg-0.1Ca-0.4Zn and Mg-0.5Zn alloys. Figure 4-3 (a)-(c) and Figure 4-4 (a)-(c) give the OM results of the second batch of as-cast ingots and the homogenized ingots, respectively. The average grain size of the as-cast and homogenized Mg-0.2Ca-0.3Zn, Mg-0.1Ca-0.4Zn, Mg-0.5Zn ingot was 496μm, 459μm, 473μm and 527μm, 495μm, 524μm, respectively. The average grain size of the second batched ingots was much smaller (about 100μm in difference) compared to the first batch ingots. This was attributed to the faster cooling process in the second batch of casting. However, the grain size of the second batch of ingots was still considered too large to conduct the designed experiments. Therefore, hot rolling was chosen to carry out to further reduce the grain size. Figure 4-5 (a)-(c) show the OM results of the hot rolled ingots. The average grain size of the hot rolled Mg-0.2Ca-0.3Zn, Mg-0.1Ca-0.4Zn and Mg-0.5Zn ingot was 51μm, 45μm and 43μm, respectively. After the hot rolling, the average grain size of the ingots was significantly reduced from nearly 500μm to around 45μm which is closer to ideal. The grain shape of the hot rolled plates was also more uniform compared to the homogenized ingots.

There appeared to be a difference in the contrast in the optical microscopy images as a function of composition, with the higher the Ca content the greater the contrast range. The contrast obviously depends on the crystal orientation. The current results imply a greater range of crystal orientations the higher the Ca content, but of course, this is a subjective result.

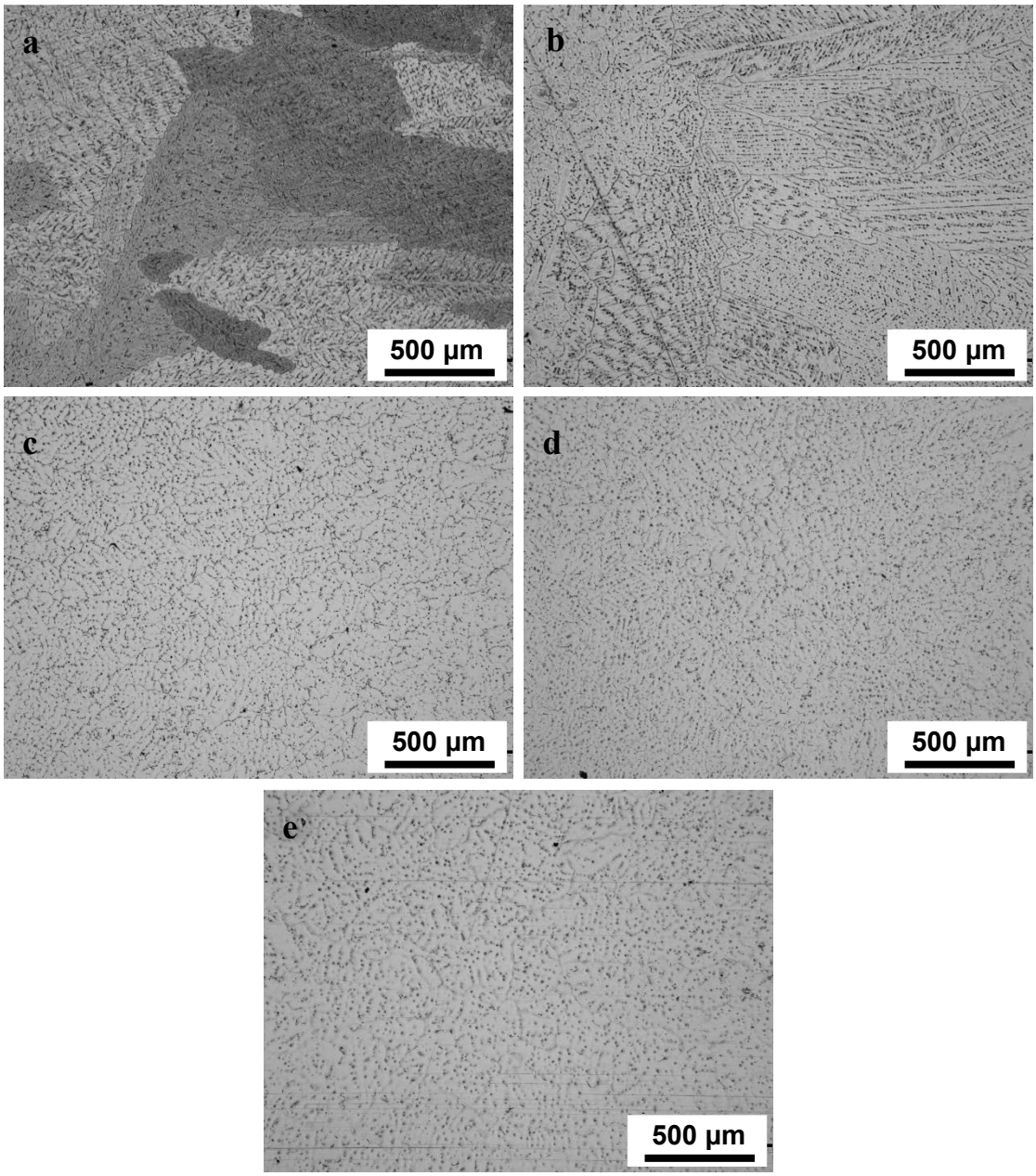

Figure 4-1 The OM images of the first batch of five as-cast Mg ingots: (a) Mg-0.5Ca, (b) Mg-0.4Ca-0.1Zn, (c) Mg-0.2Ca-0.3Zn, (d) Mg-0.1Ca-0.4Zn, (e) Mg-0.5Zn

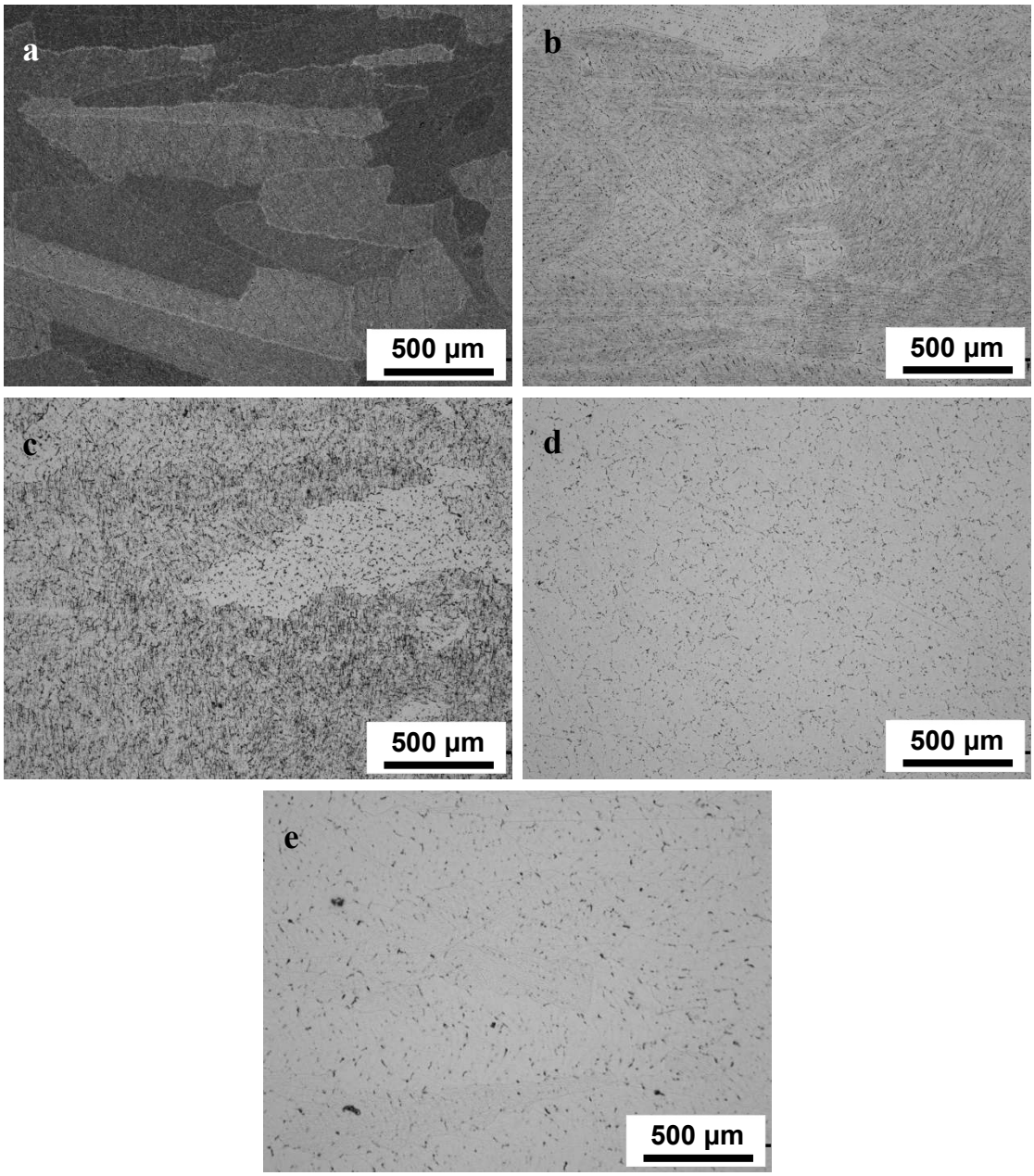

Figure 4-2 The OM images of the first batch of five homogenized Mg ingots: (a) Mg-0.5Ca, (b) Mg-0.4Ca-0.1Zn, (c) Mg-0.2Ca-0.3Zn, (d) Mg-0.1Ca-0.4Zn, (e) Mg-0.5Zn

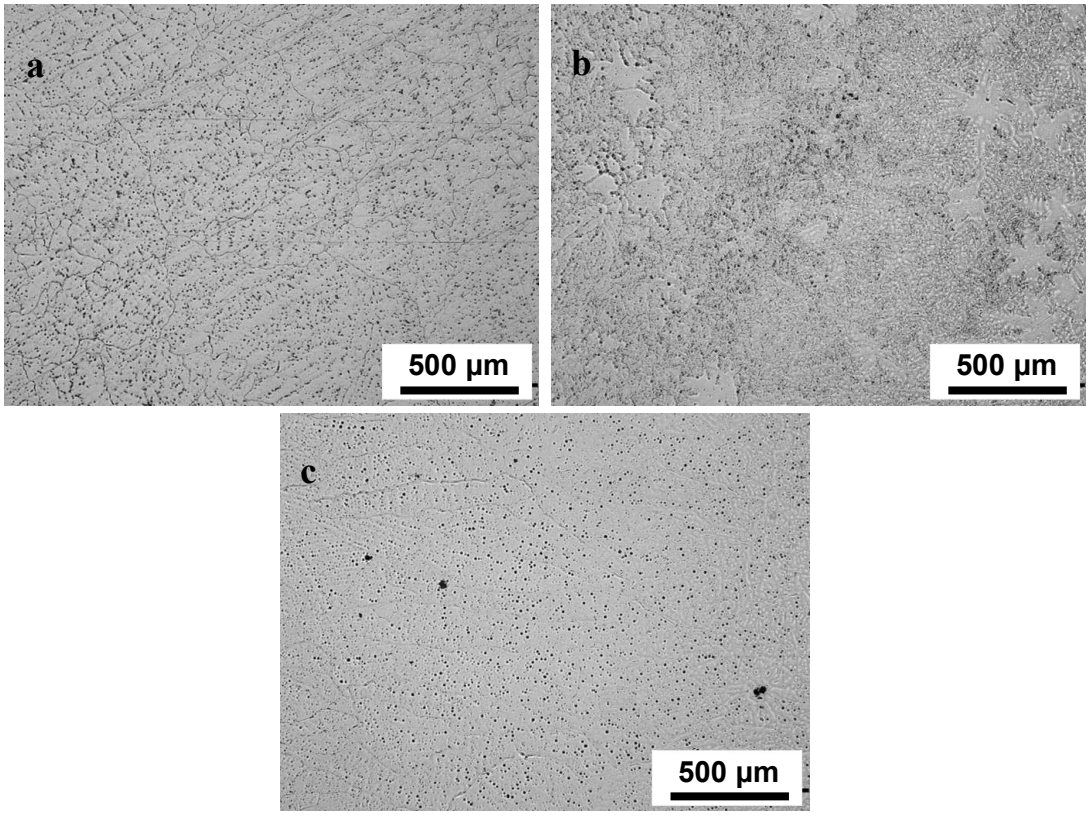

Figure 4-3 The OM images of the second batch of three as-cast Mg ingots: (a) Mg-0.2Ca-0.3Zn, (b) Mg-0.1Ca-0.4Zn, (c) Mg-0.5Zn

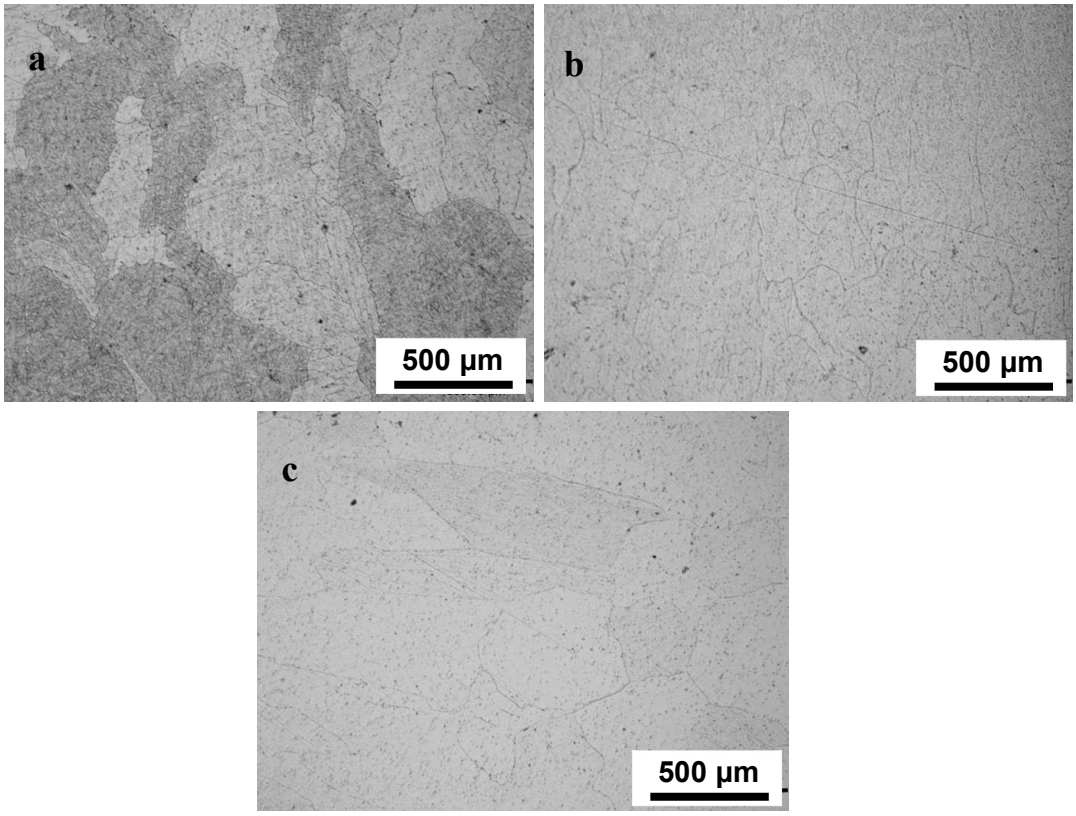

Figure 4-4 The OM images of the second batch of three homogenized Mg ingots: (a) Mg-0.2Ca-0.3Zn, (b) Mg-0.1Ca-0.4Zn, (c) Mg-0.5Zn

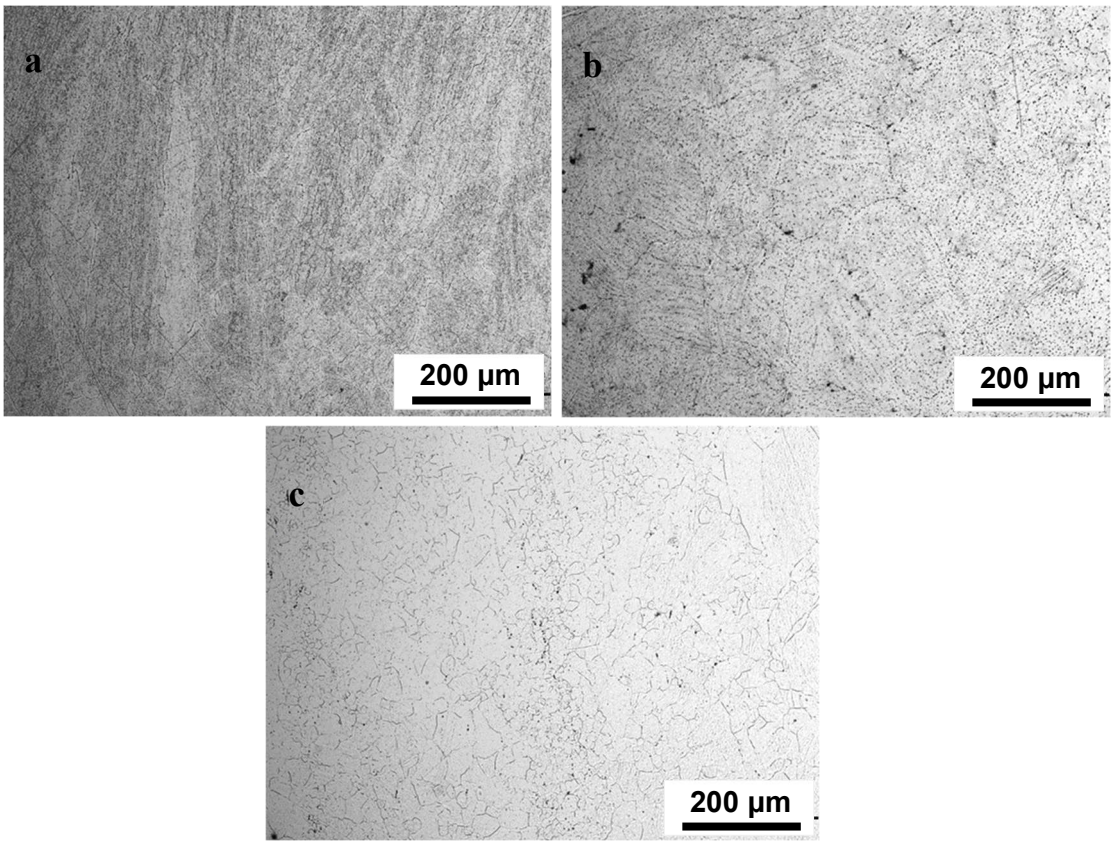

Figure 4-5 The OM images of the second batch of three as-rolled Mg ingots: (a) Mg-0.2Ca-0.3Zn, (b) Mg-0.1Ca-0.4Zn, (c) Mg-0.5Zn

Figures 4-6 to 4-10 give the SEM and EDX results of the first batch of homogenized ingots. Figure 4-6(b), 7(b), 8(b), 9(b) and 10(b) show the proportion (at%) of the alloying elements for each composition, which was close to the designed alloy content showing that the ingot casting procedure was successful. The backscattered images of five ingots indicated that there was obvious segregation of elements at the grain boundaries and within the grains in the Ca-containing ingots (shown in Figure 4-6(a), 7(a), 8(a), 9(a) and 10(a)). Only a few particles with bright contrast were found in the backscattered image of the Mg-0.5Zn (at%) ingots (Figure 4-10(a)), showing a quite uniform alloying element distribution.

Combining the backscattered images and the EDS Ca and Zn maps (Figure 4-6(c), 4-7(c, d), 4-8(c, d), 4-9(c, d), 4-10(c)) indicates that the Ca segregated at the grain boundaries and within the grains. Moreover, the number of segregating points increased with higher Ca content. The study of Nie [37] also observed this phenomenon. Comparing the obvious dendrite structure shown in the OM results of the first batch ingots and the phase diagram of Mg-Ca alloy (shown in Figure 4-15), it appeared that the alloy initially precipitates α dendrites during cooling. During the growth of the α dendrites, Ca becomes enriched in the liquid phase, resulting in changes to the liquid phase composition along the liquidus line in the phase diagram. Thus, the possibility to

form the second phase could be high with the further cooling of the ingot when considering the segregation of Ca in liquid phase and the higher Ca proportion in Mg-0.5Ca (at%) ingots. The Zn distribution appeared to be uniform in all cases. It is unlikely that Mg-Ca-Zn second phase particles formed as the Zn was too low.

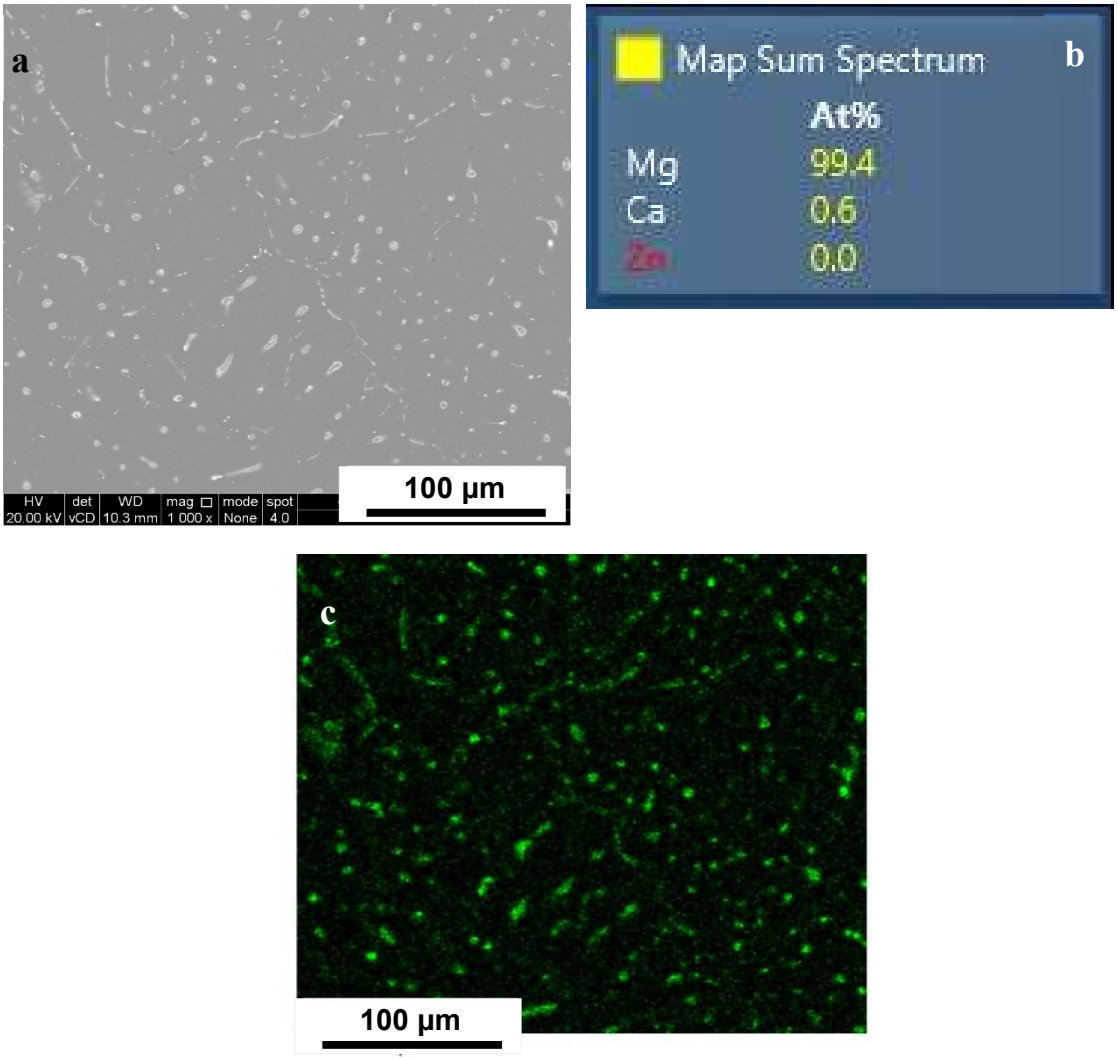

Figure 4-6 The SEM and EDX results (under BSE mode) of the Mg-0.5Ca ingot: (a) Back scattered image, (b) Map sum spectrum result of element proportion, (c) The distribution of Ca

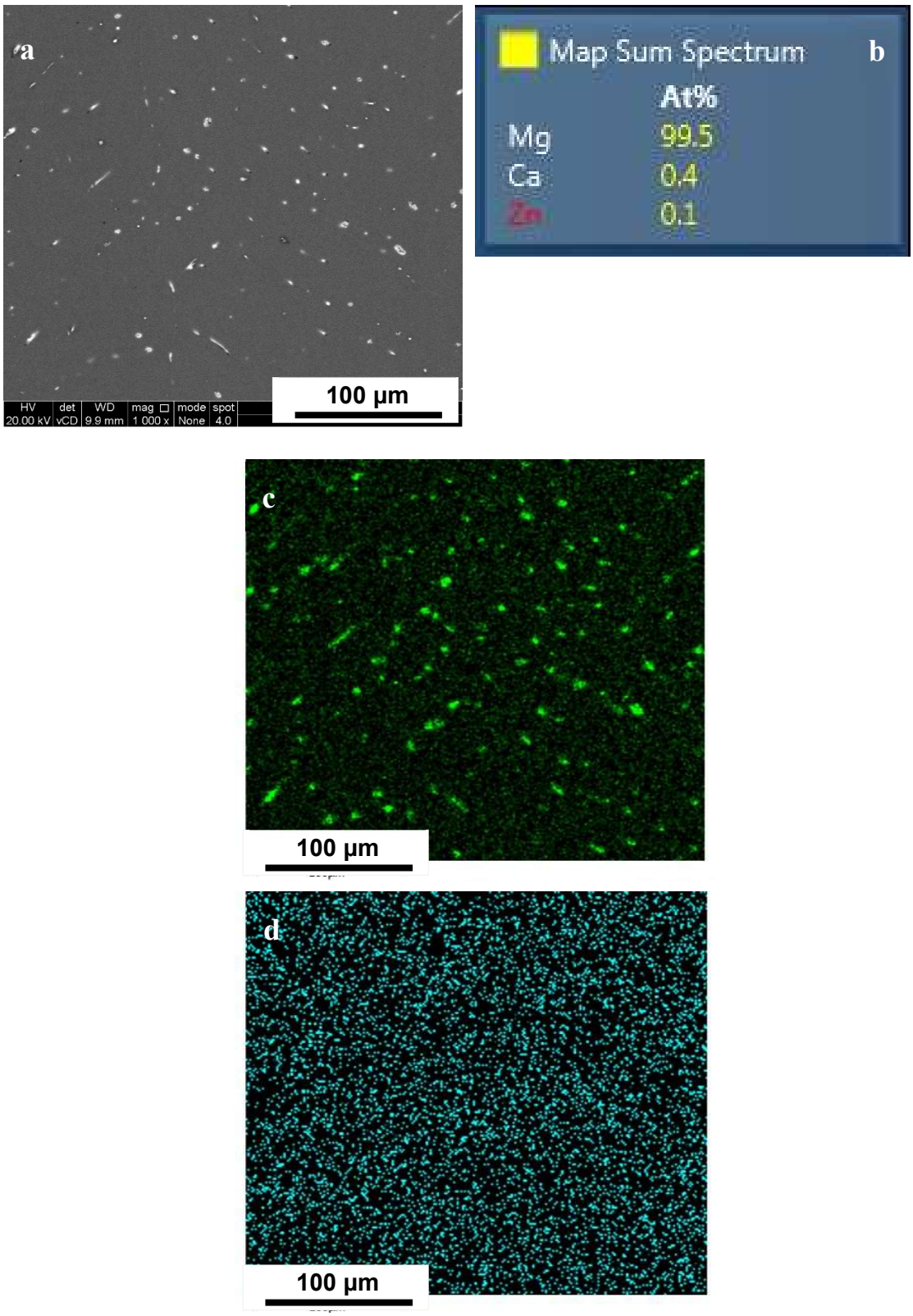

Figure 4-7 The SEM and EDX results (under BSE mode) of the Mg-0.4Ca-0.1Zn ingot: (a) Back scattered image, (b) Map sum spectrum result of element proportion, (c) The distribution of Ca, (d) The distribution of Zn

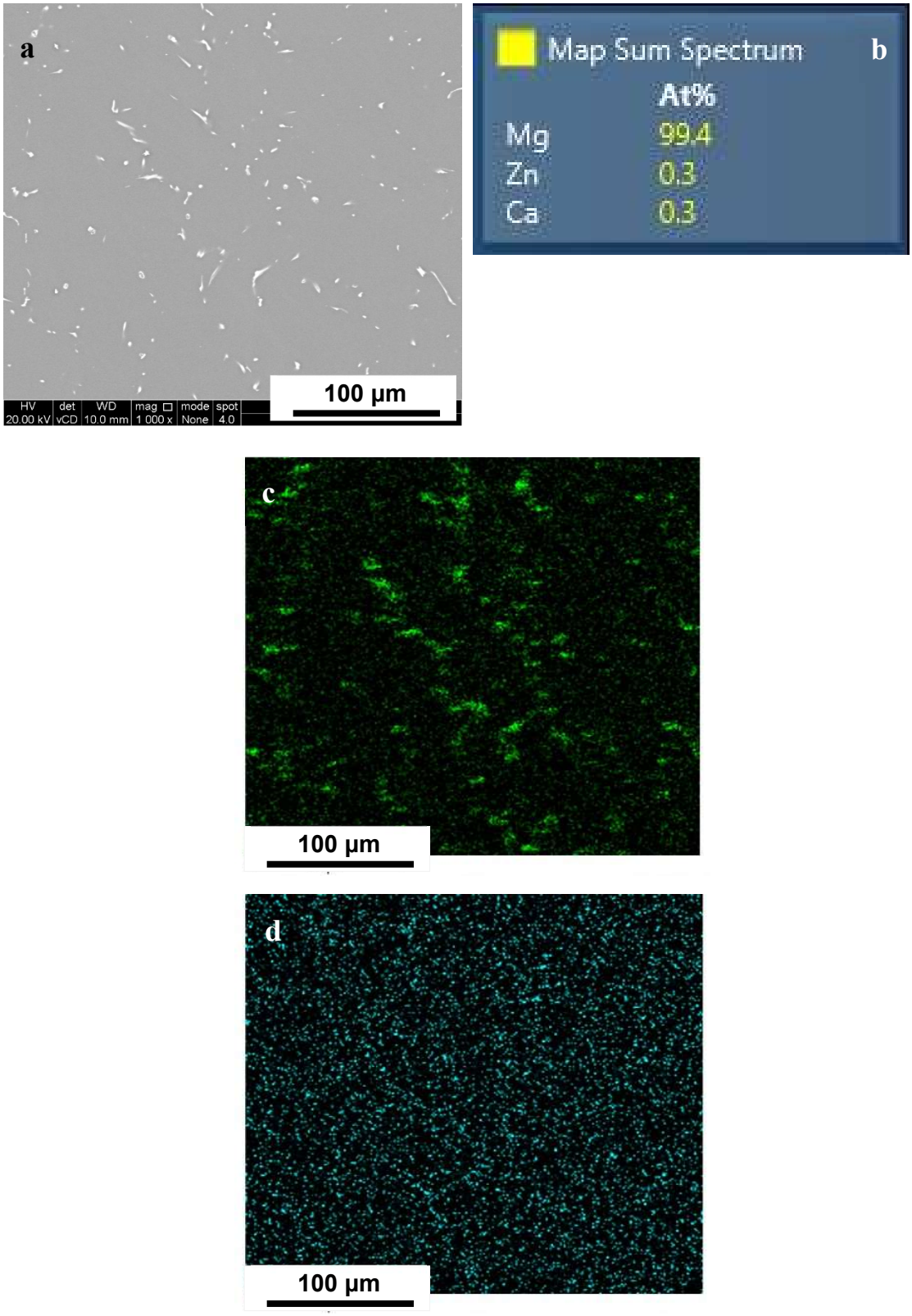

Figure 4-8 The SEM and EDX results (under BSE mode) of the Mg-0.2Ca-0.3Zn ingot: (a) Back scattered image, (b) Map sum spectrum result of element proportion, (c) The distribution of Ca, (d) The distribution of Zn

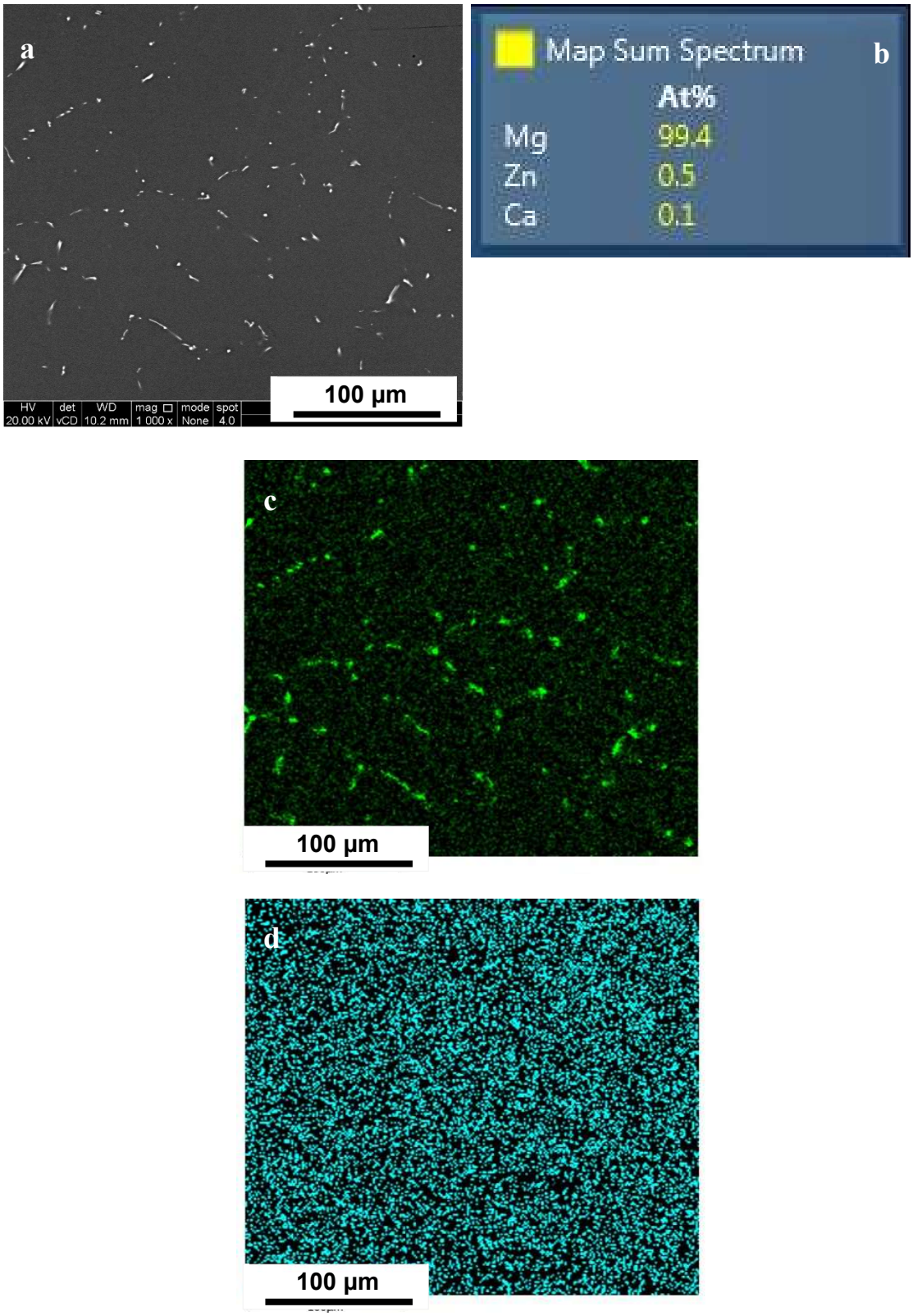

Figure 4-9 The SEM and EDX results (under BSE mode) of the Mg-0.1Ca-0.4Zn ingot: (a) Back scattered image, (b) Map sum spectrum result of element proportion, (c) The distribution of Ca, (d) The distribution of Zn

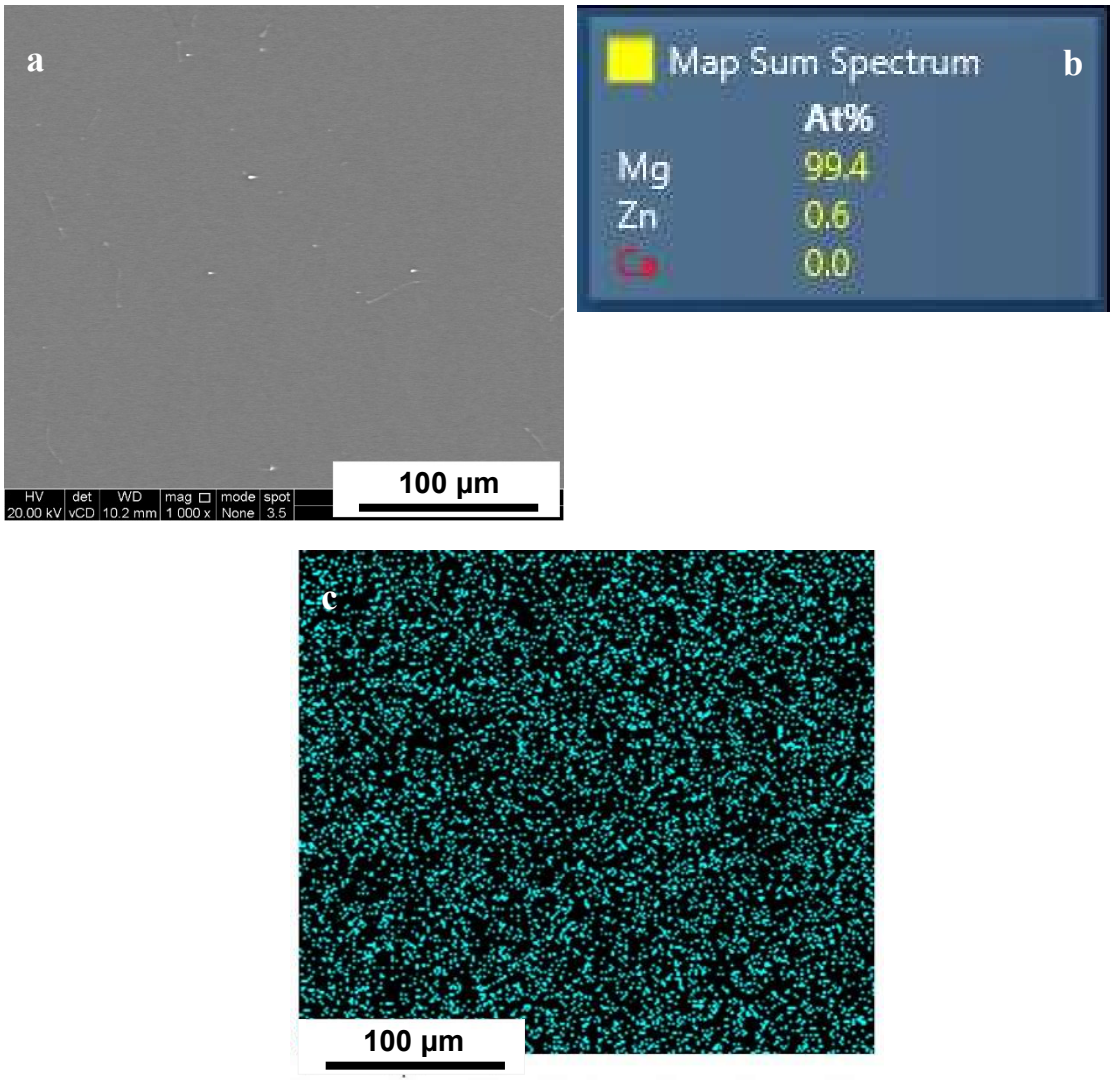

Figure 4-10 The SEM and EDX results (under BSE mode) of the Mg-0.5Zn ingot: (a) Back scattered image, (b) Map sum spectrum result of element proportion, (c) The distribution of Zn

Figures 4-11 to 4-13 shown below are the SEM and EDX test results of the second batch of the homogenized ingots. Figures 4-11(b), 4-12(b) and 4-13(b) show that the composition of these three ingots was as specified. The back scattered images (shown in Figure 4-11(a), 4-12(a) and 4-13(a)) of all three ingots present a very similar result of the element segregation to that of the first batch ingots. Also, the element distribution maps (Figure 4-11(c, d), 4-12(c, d), 4-13(c)) indicate that the segregation of Ca and the uniform distribution of Zn in the second batch ingots were the same as that in the first batch ingots.

The manufacture of two batches of ingots was therefore successful. Both batches of ingots reached the designed properties e.g. composition, grain size etc. These ingots were then used as the raw materials to produce all the experimental specimens.

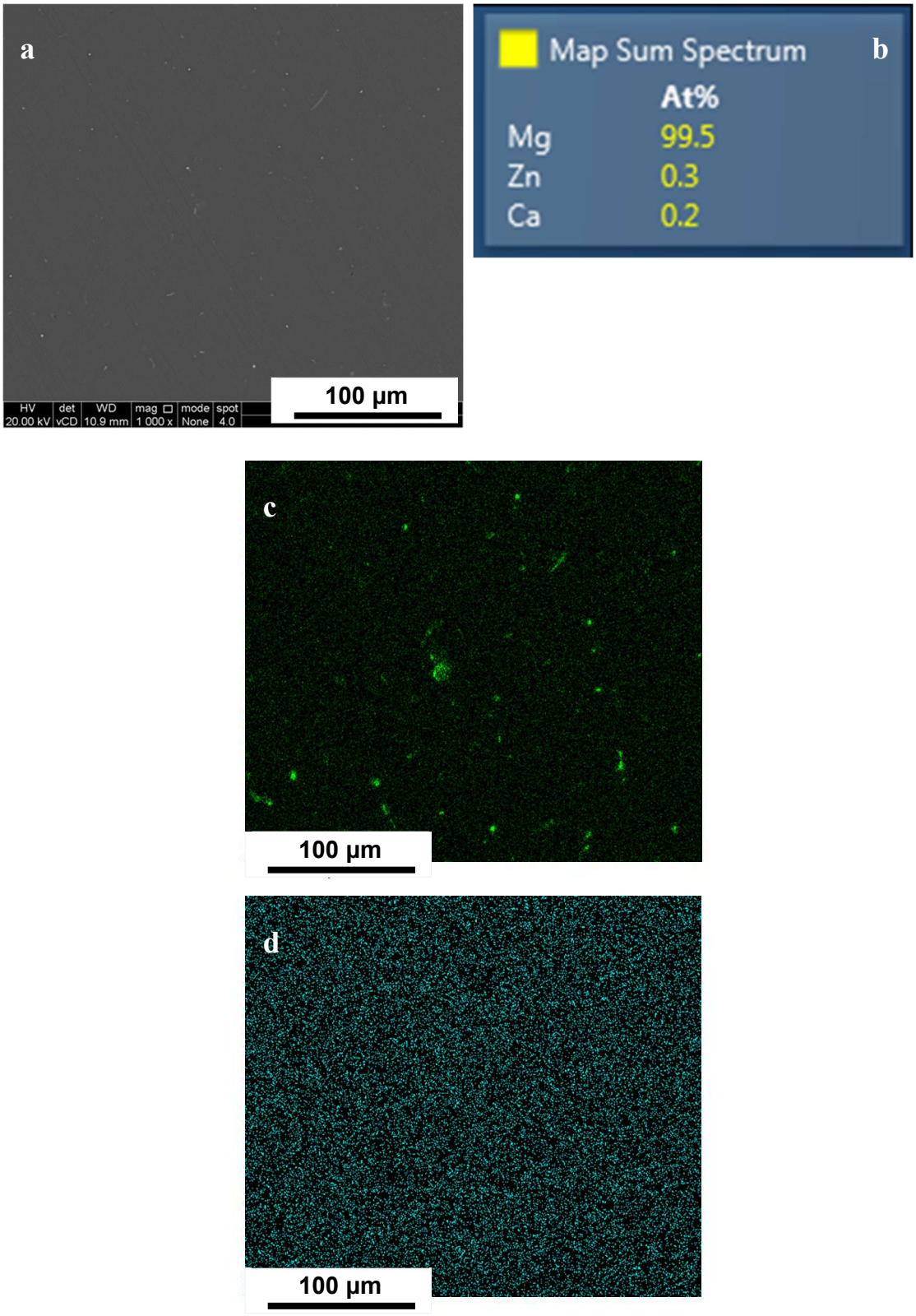

Figure 4-11 The SEM and EDX results (under BSE mode) of the second batch Mg-0.2Ca-0.3Zn ingot: (a) Back scattered image, (b) Map sum spectrum result of element proportion, (c) The distribution of Ca, (d) The distribution of Zn

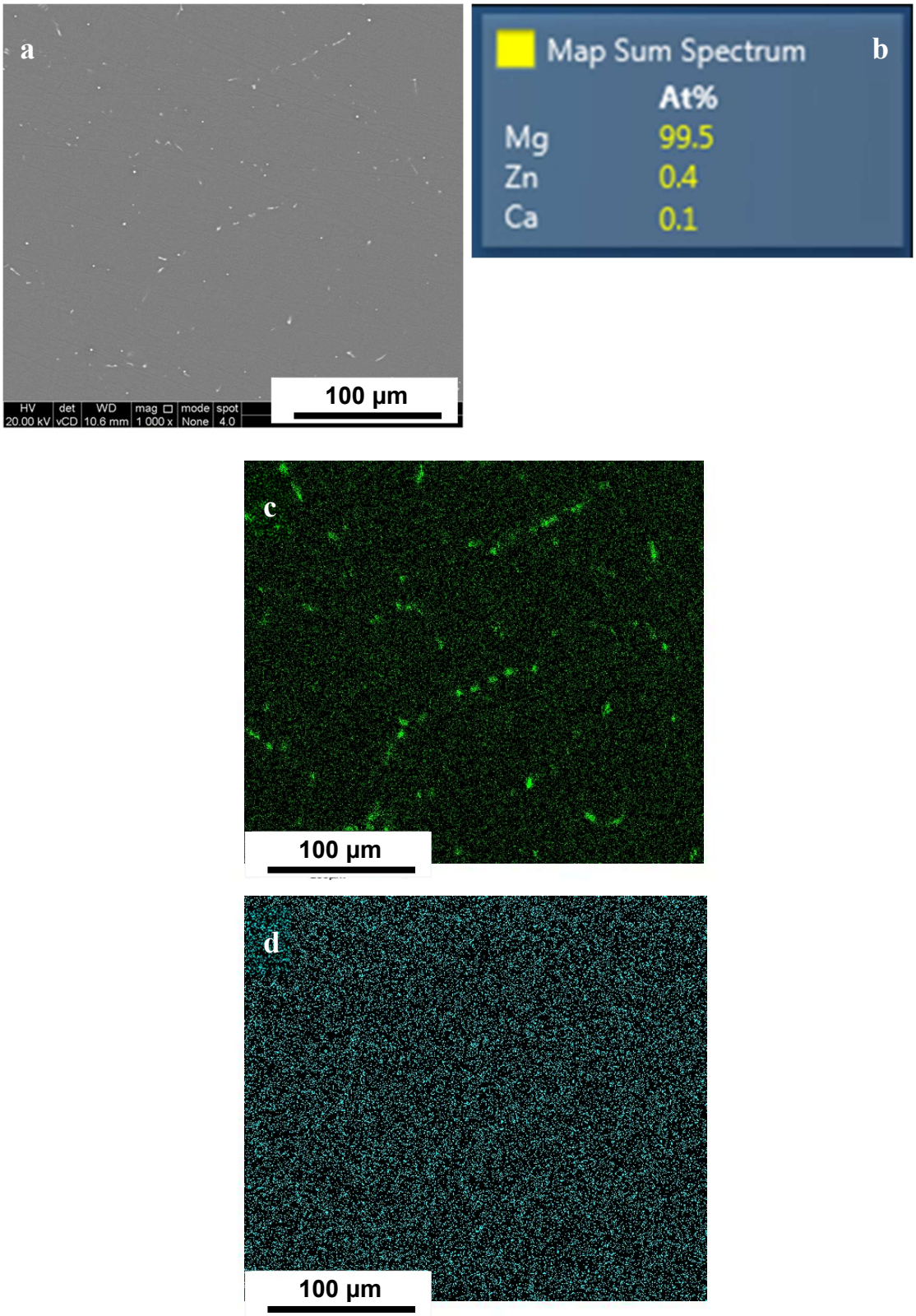

Figure 4-12 The SEM and EDX results (under BSE mode) of the second batch Mg-0.1Ca-0.4Zn ingot: (a) Back scattered image, (b) Map sum spectrum result of element proportion, (c) The distribution of Ca, (d) The distribution of Zn

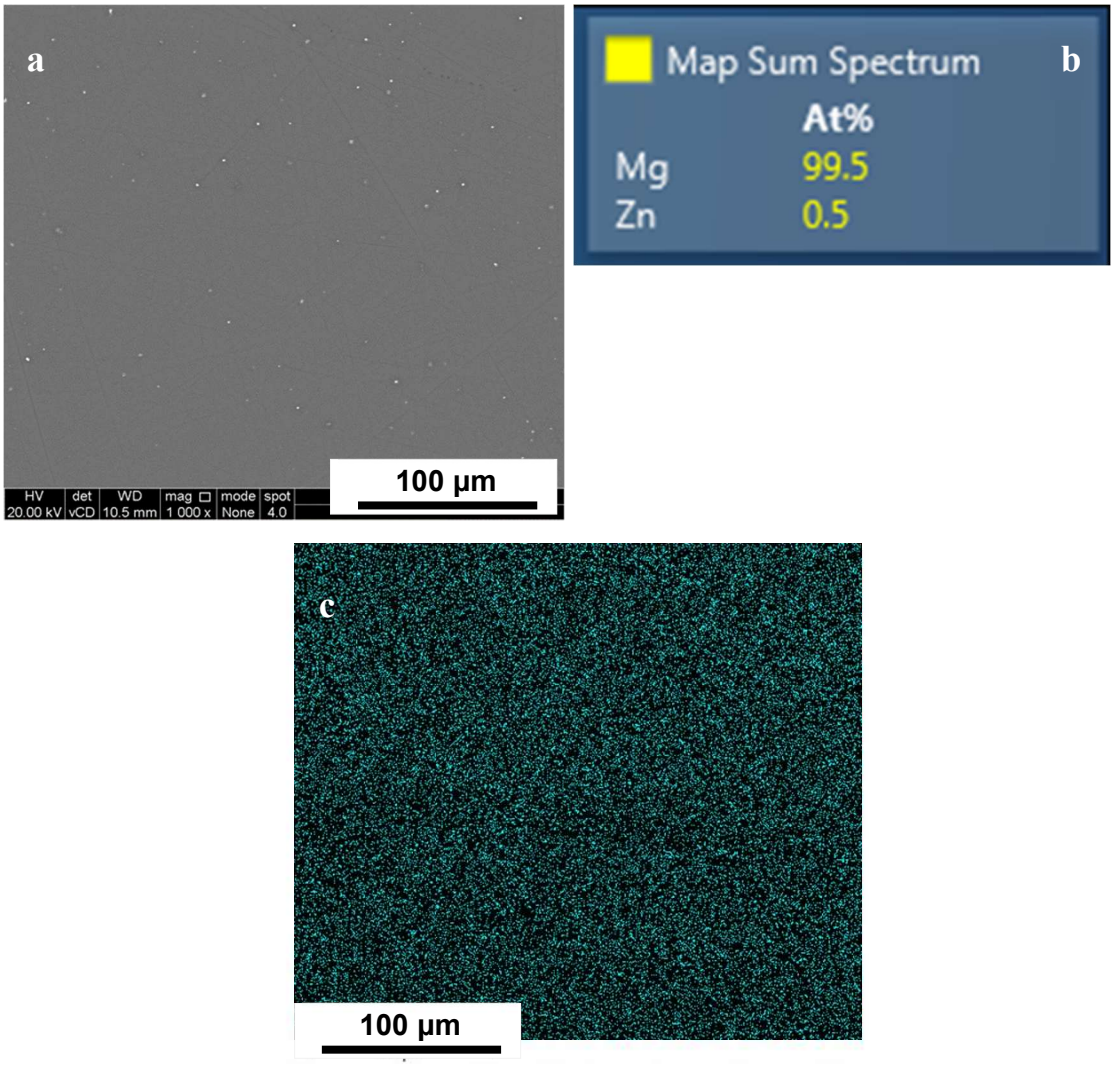

Figure 4-13 The SEM and EDX results (under BSE mode) of the second batch Mg-0.5Zn ingot: (a) Back scattered image, (b) Map sum spectrum result of element proportion, (c) The distribution of Zn

The grain orientation distribution of hot-rolled Mg-0.5Zn (at%) ingot is shown below in Figure 4-14. Due to the lack of experimental data and the same processing procedure, the pole figure of the hot-rolled Mg-0.5Zn (at%) ingot was used as the reference to present the grain orientation distribution of all three kinds of hot-rolled ingots.

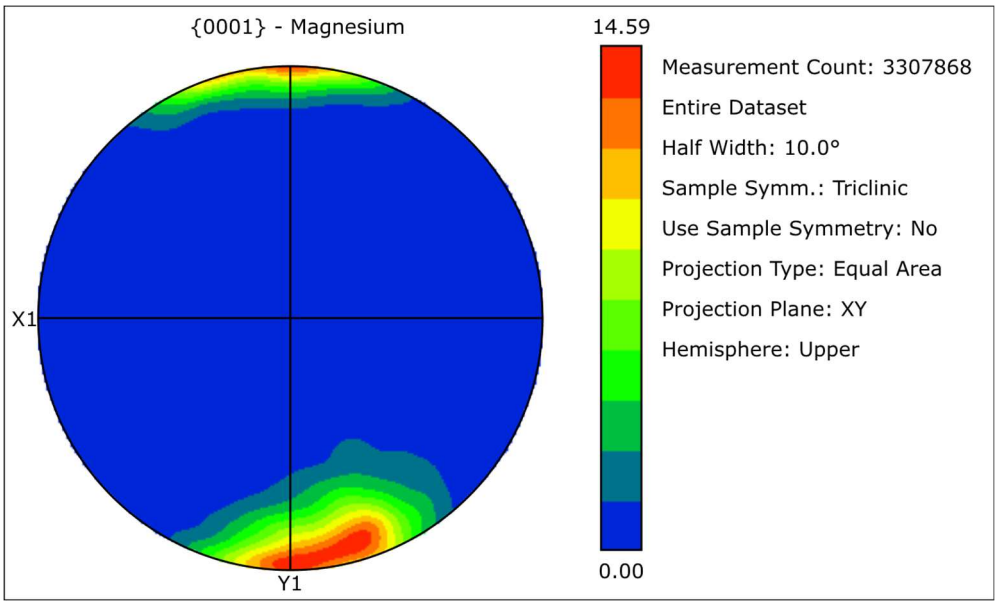

Figure 4-14 The pole figure of the hot-rolled Mg-0.5Zn (at%) ingot

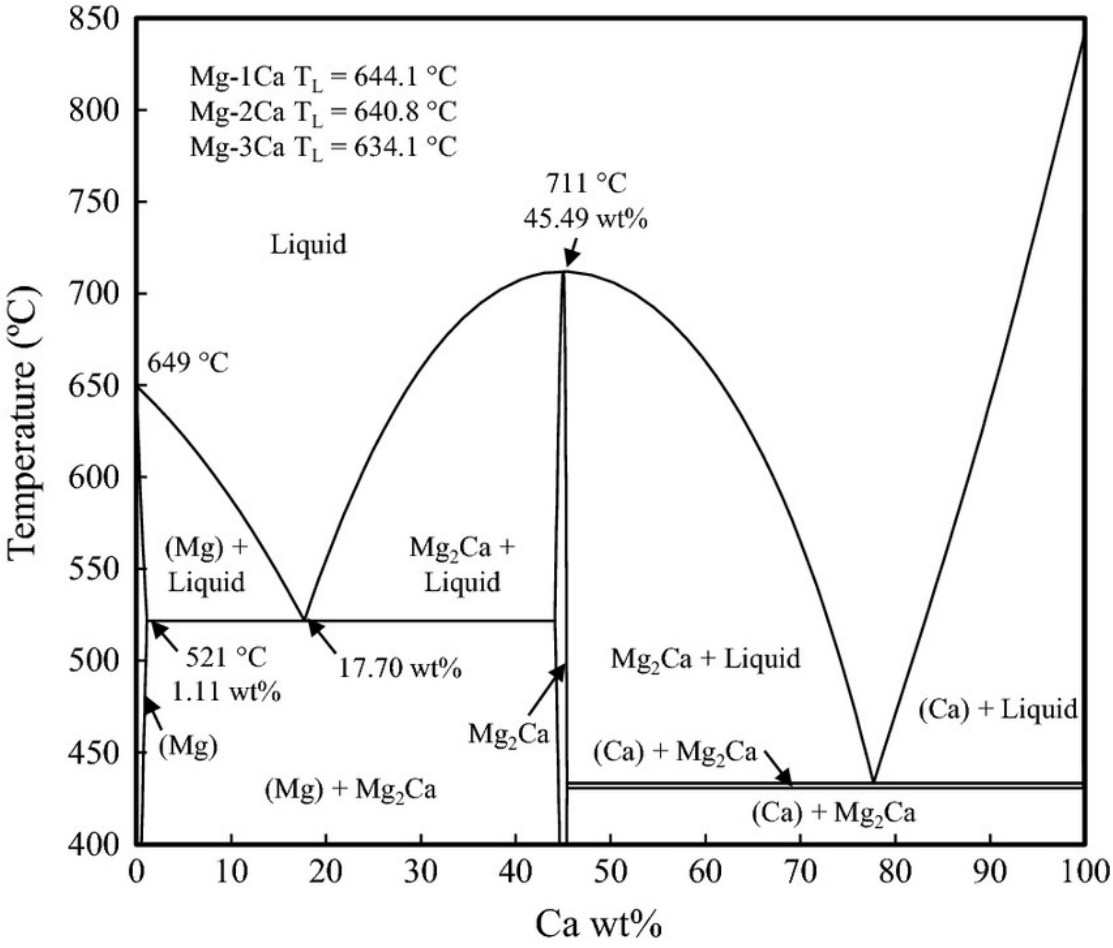

Figure 4-15 The phase diagram of Mg-Ca alloy [132]

4.2 Double truncated cone (DTC) sample compression experiment

4.2.1 The compression process of the DTC sample

Before using the actual study specimens to proceed with the compression process, to make sure the design of the experiment was feasible, some trial specimens made of the Mg-6.8Zn-0.2Ca-0.4Ag alloy were used to set up the experiment. Another reason for using these trial specimens was that the real experimental specimens were still in production at that time.

Figure 4-16 demonstrates the first compressed DTC trial sample. It is clear to see that the deformation of the sample was not uniform in the vertical direction. The shape of the sample showed a tilt after the compression i.e. the middle-right side of the sample was clearly much higher than the opposite side. This was because after the first compression trial, the surface of the compression heads (both upper head and bottom head) was found to have an uneven surface i.e. the test sample was not in a horizontal position when the process started. As a result, the direction of the applied stress was not in the vertical direction due to this potholed surface. Moreover, the first trial sample was compressed without applying any lubrication. The friction between the sample and the upper/lower compression head could be high during the compression process, particularly given that the stress kept increasing, the friction became greater which further caused the uneven deformation. The nonuniform deformation of the first trail sample was attributed to these two reasons.

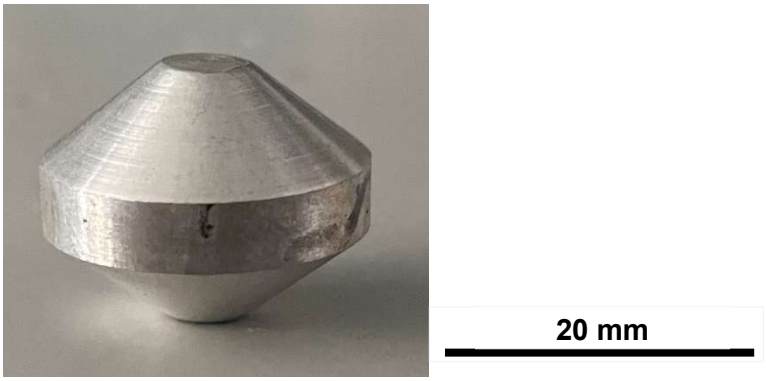

Figure 4-16 The compressed first trial sample of Mg-6.8Zn-0.2Ca-0.4Ag alloy

Based on the failure of the first trial sample compression process, two titanium (Ti) plates were used to cover the surface of the upper head and the bottom head. The assembly of the trial sample, Ti plates and test machine is shown in Figure 4-17 (a). The Ti plates improved the flatness and the parallelism of the two contact surfaces during the compression. In addition, Vaseline as a lubricant was applied to the upper/bottom contact surface of the sample and the contact area of the Ti plates. Figure 4-17 (b) shows the second trial sample after the compression. Figure 4-18(a) gives the

Force(N)-Compression Distance(mm) plot of this test, taken from the original data output from the Hounsfield universal test frame. Based on the result from the second trial compression process (Figure 4-17(b)), it was clear that the deformation in the vertical direction is still not uniform but much better than the result of the first trial sample. The total strain measured from the second trial sample was 29%. Before starting the next round of the trial compression process, a new reason which could cause poor formability was identified. The first two trial samples were manufactured directly from the as-cast Mg-6.8Zn-0.2Ca-0.4Ag ingot i.e. the homogenized trial sample could have a better compression performance. Thus, the last trial Mg-6.8Zn-0.2Ca-0.4Ag sample was homogenized at 290℃ for 8 hours before conducting the compression process.

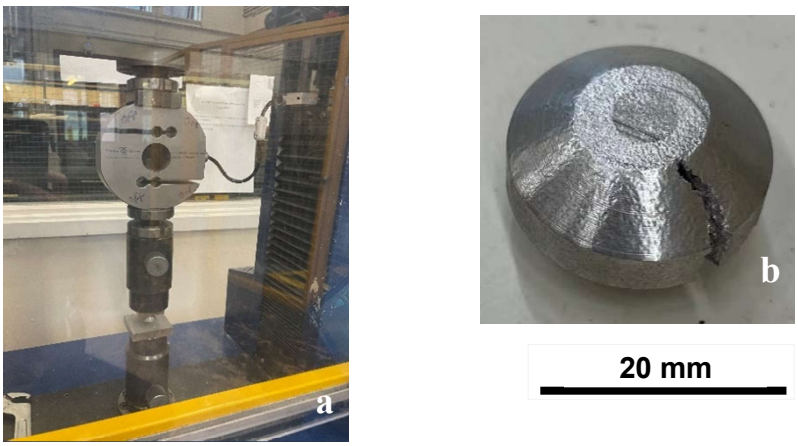

Figure 4-17 (a) The second compression process with two Ti plates
(b) The compressed second trial sample

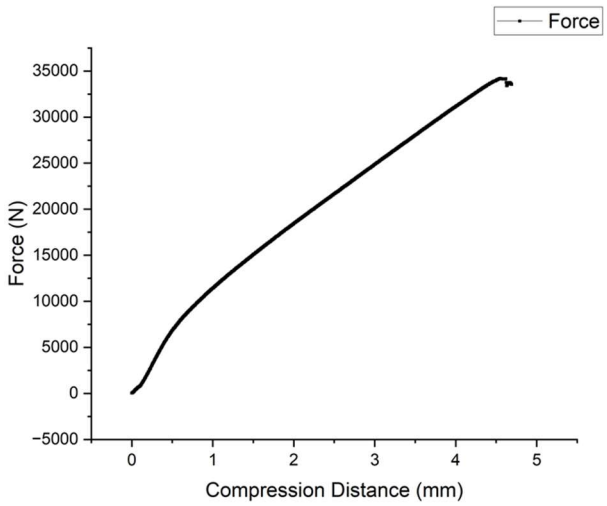

Figure 4-18 The force-compression distance curve of the second trial Mg-6.8Zn-0.2Ca-0.4Ag sample

For the last trial sample, the compression with the same process as the first two samples was carried out. The problem of the uneven surface of the compression heads was solved by re-machining the surface, which means that the Ti plates were no longer needed. Fewer moving parts were used in the experiment, which further improved the accuracy and reliability of the trial experiment. Meanwhile, the lubrication was also applied carefully to the sample and the contact surface of the two compression heads. The compression process was carried out four times on this sample. And the compression distance for each time was 3mm, 2mm, 3mm and 1.5mm, respectively. The experiment was stopped when the sample cracked. Figure 4-19 shows the third trial sample after the compression. The homogenized trial sample showed good formability compared to the first two samples. It had a maximum strain of about 60% which is believed can form a wide range of strains and strain rates within a single sample. And the deformation direction is also almost in the vertical direction.

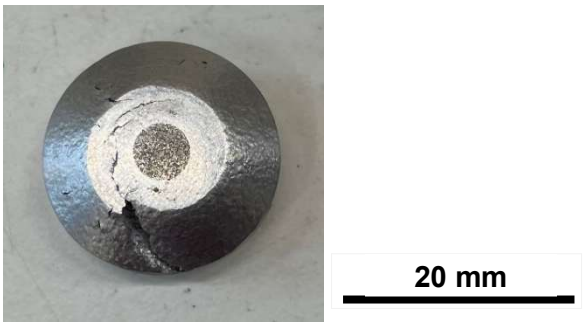

Figure 4-19 The third trial sample after the compression

After the trial compression, all the following specimens using the double truncated cone geometry were made from the first batch ingots. The large grain size in the ingots mentioned before clearly had a negative effect on the performance of the specimens during the compression process.

Figure 4-20 shows the force-compression distance curves of five samples with different compositions (Mg-0.5Ca, Mg-0.4Ca-0.1Zn, Mg-0.2Ca-0.3Zn, Mg-0.1Ca-0.4Zn and Mg0.5Zn (at%)). The DTC samples of Mg-0.5Ca, Mg-0.4Ca-0.1Zn and Mg-0.2Ca-0.3Zn (at%) were all found to crack at around 0.28 strain (4.5mm compress distance). The compression of the DTC samples made by Mg-0.1Ca-0.4Zn and Mg-0.5Zn (at%) alloy were stopped manually as there was no cracking until the deformation distance exceeded 5mm (0.32 strain). These tests were conducted with the same procedure, but clearly the results were very different. One reason was clearly the difference in composition. The Mg-6.8Zn-0.2Ca-0.4Ag alloy had better formability than the studied five alloys. Another reason was that the ingots cast in the Royce Institute had a very large grain size compared to that found in the purchased Mg-6.8Zn-0.2Ca-0.4Ag ingot (made by Luxfer MEL Technologies). Both the large grain size and the non-uniform grain size are clear disadvantages to the material formability [3].

Figure 4-21 shows the DTC samples after the compression process. The test results indicate that all the specimens have a uniform deformation in the vertical direction i.e. all the samples still showed tilt in the vertical direction but not as severe as the first trial sample. In contrast, all samples presented a preferred deformation orientation in the transverse direction giving a distinct asymmetry to the deformed sample. It is very clear that all the Ca-containing specimens had this "preferential orientated deformation". The top surface of all four Ca-contained specimens was no longer circular shape after compression. Thus, the strain and the strain rate varied in a non-symmetrical manner making comparison of one specimen with another very difficult. Only the Mg-0.5Zn specimen maintained a reasonably uniform deformation in the horizontal direction.

The non-uniform deformation of all the DTC specimens made the comparison of the samples with different compositions impossible as the strain and strain rate varied in an unpredictable manner throughout the sample. However, the DTC specimens were not completely useless. The compressed Mg-0.1Ca-0.4Zn (at%) DTC specimen was chosen to study the deformed microstructure at the low strain condition using EBSD. The reason for choosing this specimen was that it has an obvious non-uniform deformation (especially in one direction) i.e. it might contain more information on a single cross-section area, which was ideal for the EBSD investigation. Another reason was that it did not crack during the experiment. The impact of the crack on the EBSD result could be minimized by using this specimen.

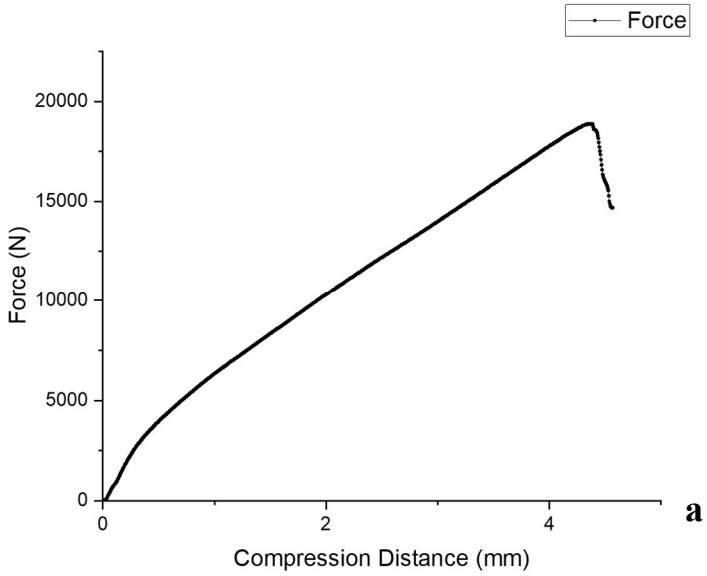

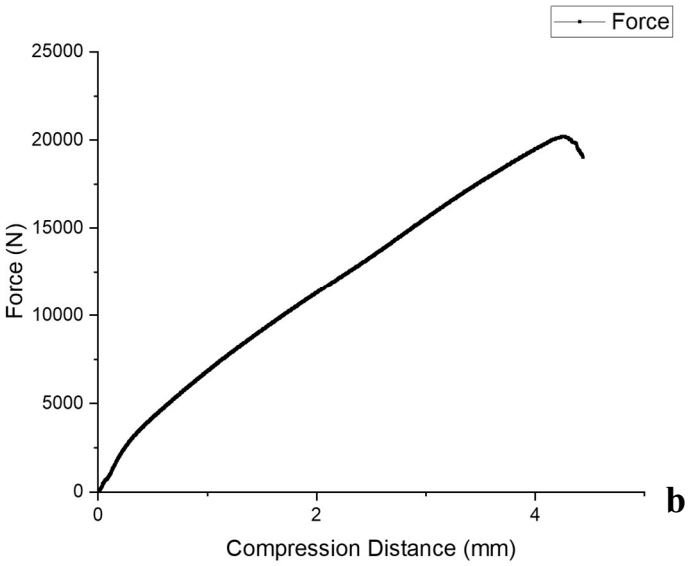
Force
25000
20000
15000
10000
5000
0
Force (N)
0
2
4
Compression Distance (mm)

b

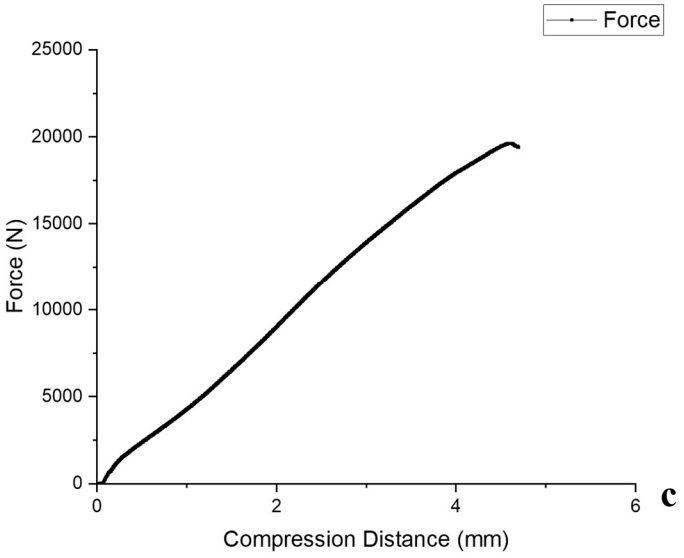
Force
25000
20000
15000
10000
5000
0
Force (N)
0
2
4
6
Compression Distance (mm)

c

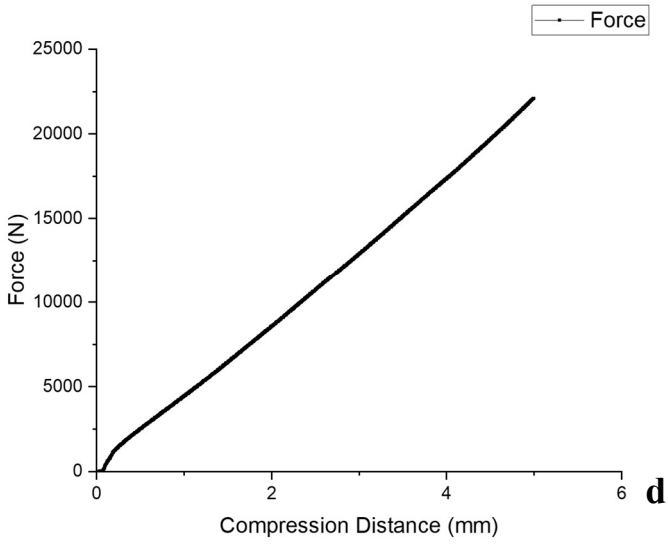
Force
25000
20000
15000
10000
5000
0
Force (N)
0
2
4
6
Compression Distance (mm)

d

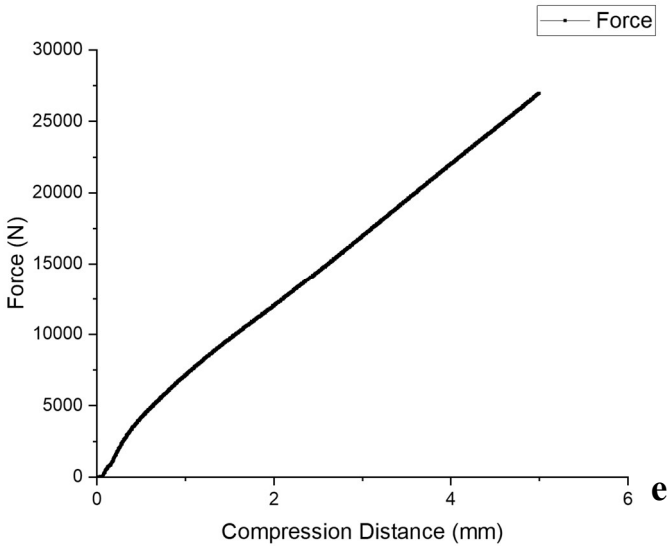

Figure 4-20 The force-compression distance curves of the (a) Mg-0.5Ca, (b) Mg-0.4Ca-0.1Zn, (c) Mg-0.2Ca-0.3Zn, (d) Mg-0.1Ca-0.4Zn, (e) Mg-0.5Zn alloy (at%)

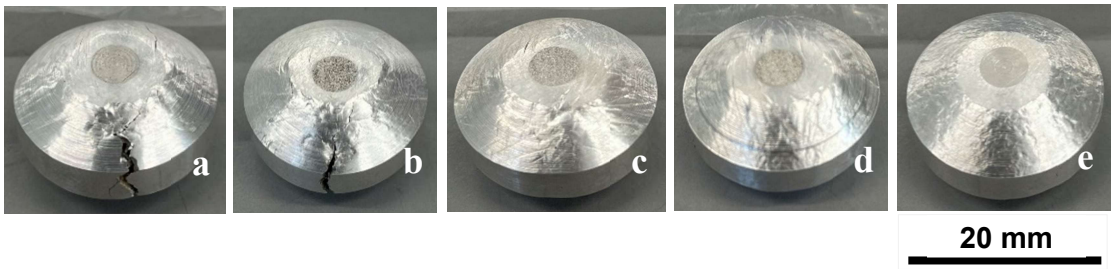

Figure 4-21 The compressed DTC samples of the (a) Mg-0.5Ca, (b) Mg-0.4Ca-0.1Zn, (c) Mg-0.2Ca-0.3Zn, (d) Mg-0.1Ca-0.4Zn, (e) Mg-0.5Zn alloy (at%)

4.2.2 The EBSD investigation of the DTC sample

The FEI Inspect F50 was initially used to conduct the EBSD investigation because at that time the JEOL 7900F was not available to use due to the COVID restriction policy. Figure 4-22 and Figure 4-23 show the two area EBSD results of Mg-0.1Ca-0.4Zn (at%) DTC sample using a step size of $1.5\mu m$, and a scan area of about 1.2mm $\times$ 1.2mm. Both maps covered an area of about ten large grains (larger than $500\mu m$). Due to this small scanning area and the large grain size, both Figure 4-22 and Figure 4-23 show very limited information about the microstructure of the sample.

However, the EBSD results still presented some useful information. Firstly, twins can be clearly seen in both Figures. The red, green and blue lines in the Figure 4-22 (b) and the Figure 4-23 (b) represent the boundaries of the tensile twins (<11-20> 86°), compressive twins (<11-20> 56°) and double twins (<11-20> 38°), respectively. For the first area, the tensile twin boundaries, the compressive twin boundaries and the double twin boundaries occupied 39.7%, 2.6% and 1.6% of the total boundaries,

respectively. For the second area, these three kinds of twin boundaries took 23.1%, 4.0% and 4.5% of the total boundaries, respectively. It was clear that the tensile twins were dominant in both areas of this deformed sample. Only a few compressive twins and double twins were found in both areas. A noticeable point is that according to the disorientation angle distribution chart of two areas (shown in Figure 4-22 (c) and Figure 4-23(c)), there was a quite strong peak at around 76° in both figures (especially in the second figure) which is not usually observed. In Figure 4-23(b), the morphology of the structure formed by these <11-20> 76° grain boundaries (shown in purple) indicated that these were twins. However, there was no resource or any report mentioning this twin mode with <11-20> 76°. The possible reason for this "new twin mode" was attributed to the poor sample preparation and the large scanning step size. The sample preparation at this stage was not good enough. Thus, many scratches and residual stress were left on the surface of the sample. Combined with the large scanning step size, this <11-20> 76° twin mode was considered as the error result of the <11-20> 86° tensile twin. Another noticeable point is that there was an obvious twin structure in the large green coloured grain in the middle of Figure 4-23 (a), but the boundaries were recognized as sub-grain boundaries. These twins with sub-grain boundaries were the twins that were being formed. Most of them were presumed to be tensile twins. It also explained the lower twin fraction in the second area. The reason for this was attributed to the location of the sample in the scanning area. The second area was much closer to the centre of the sample which had less deformation than that of the first area [109]. Thus, the kinetics of twin formation was lower than the first area.

Figure 4-22(d) and Figure 4-23(d) indicate that the Mg-0.1Ca-0.4Zn DTC sample had a very strong basal texture. The maximum pole intensity of the two areas in Figure 4-22 (d) is 20.6 and 45.6 in Figure 4-23 (d). However, for the same reason mentioned before, the large grains occupied the most area of the two EBSD maps, and the number of grains was not enough to be representative of the whole sample. Thus, the pole figure was not representative enough to be analysed and represent the whole sample.

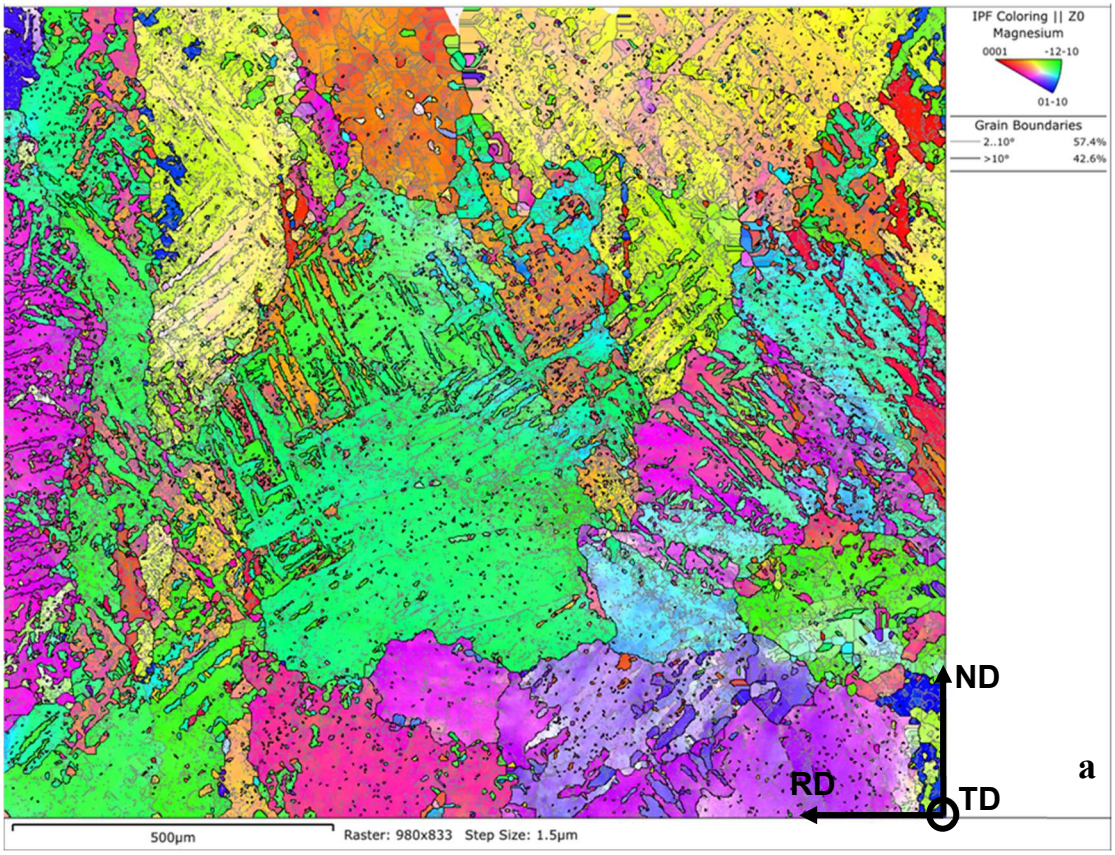
IPF Coloring || Z0
Magnesium
0001
-12-10
01-10
Grain Boundaries
2..10°
57.4%
>10°
42.6%
ND
RD
TD
a
500µm
Raster: 980x833 Step Size: 1.5µm

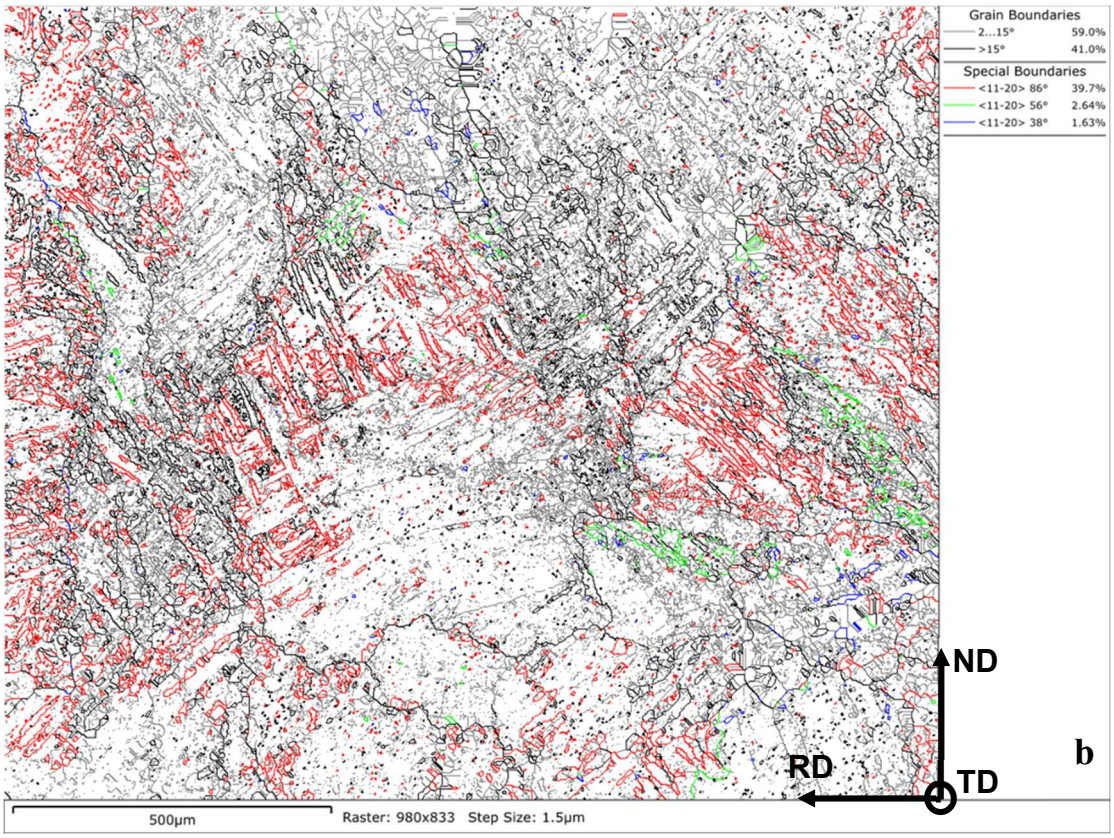
Grain Boundaries
2...15°
59.0%
>15°
41.0%
Special Boundaries
<11-20> 86°
39.7%
<11-20> 56°
2.64%
<11-20> 38°
1.63%
ND
RD
TD
b
500µm
Raster: 980x833 Step Size: 1.5µm

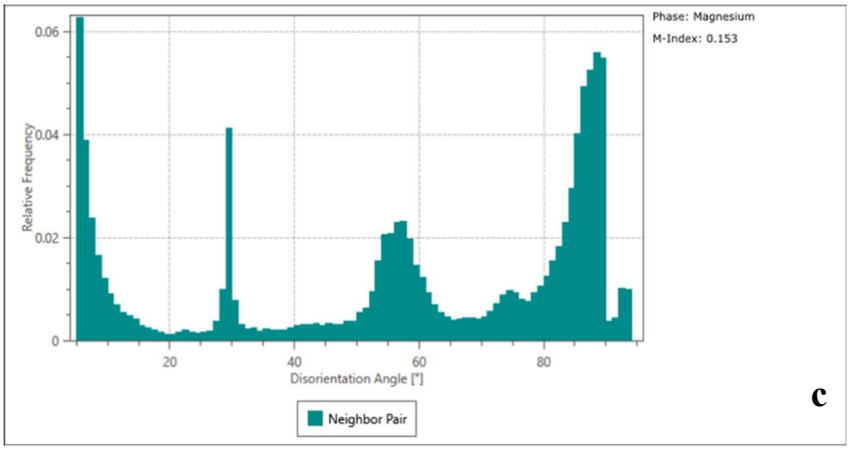

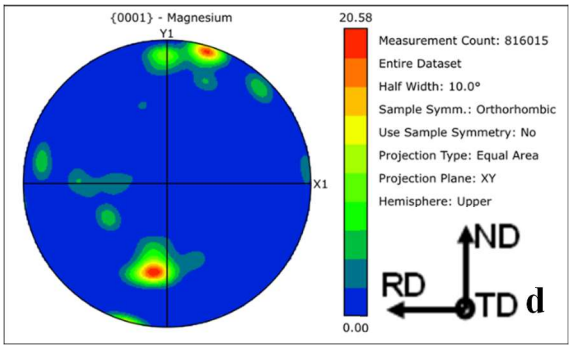

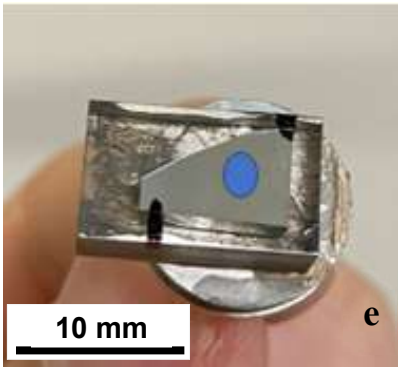

Figure 4-22 The first small areas EBSD result of the Mg-0.1Ca-0.4Zn sample: (a) The inverse pole figure (IPF) map and grain boundaries, (b) The grain boundaries and the special grain boundaries, (c) The disorientation angle distribution, (d) The pole figure, (e) Showing the area scanned

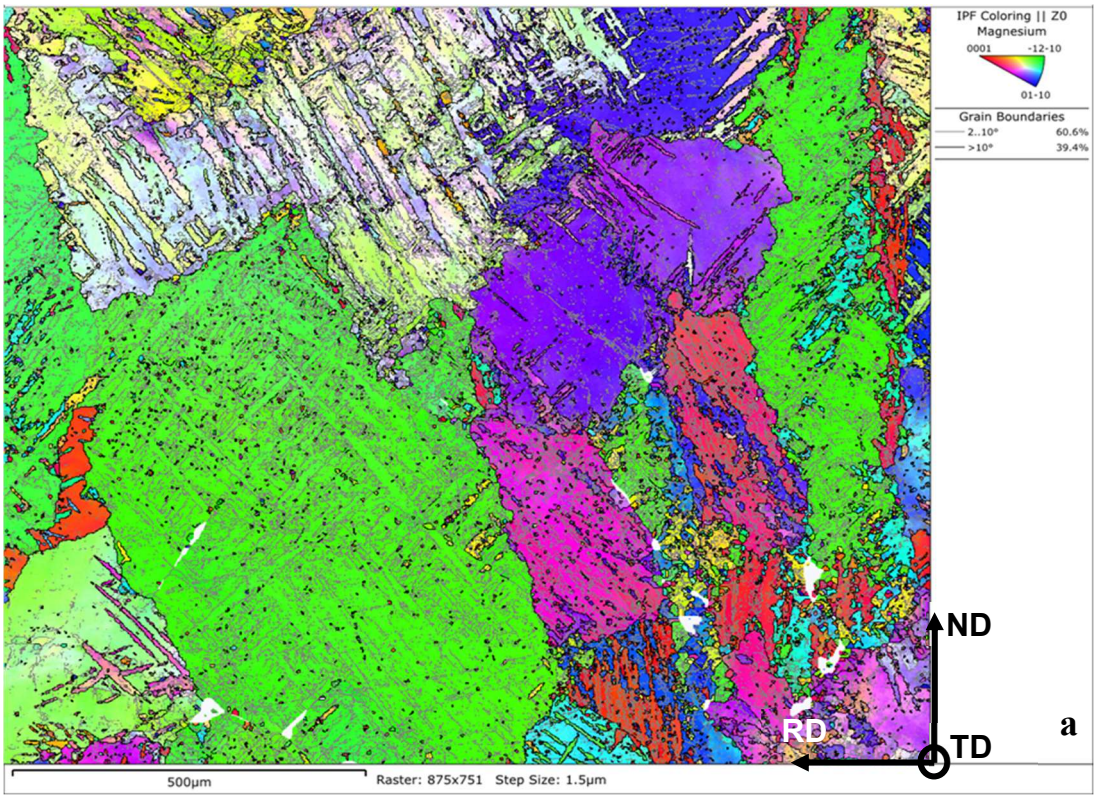

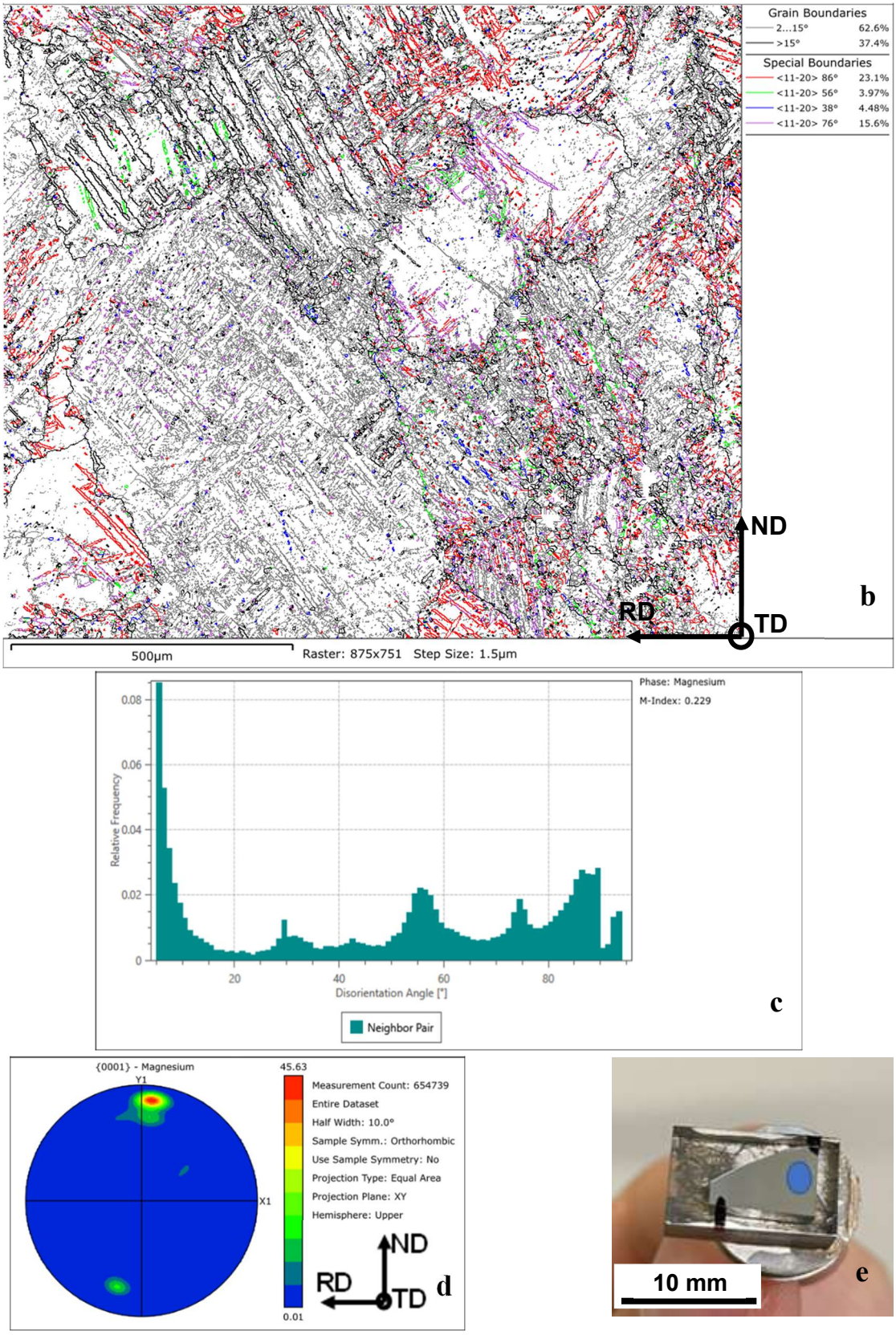

Figure 4-23 The second small areas EBSD result of the Mg-0.1Ca-0.4Zn sample: (a) The inverse pole figure (IPF) map and grain boundaries, (b) The grain boundaries and the special grain boundaries, (c) The disorientation angle distribution, (d) The pole figure, (e) Showing the area scanned

The FEI Inspect F50 had many limitations in performance e.g. the time for running the EBSD was much longer than that of the JEOL 7900F, which made it impossible to run a large-scale EBSD with fine step size. Moreover, the FEI Inspect F50 does not have the multipicture synthesis function, which the JEOL 7900F can do. Fortunately, after the EBSD investigation of the two areas mentioned above was finished, the JEOL 7900F became available to use. Therefore, the JEOL 7900F was used to conduct a large-area EBSD scanning (step size $1.5\mu m$) by using the multipicture synthesis function.

The other half of the compressed DTC Mg-0.1Ca-0.4Zn (at%) specimen after the cutting was used to prepare the new EBSD sample. To acquire a more reliable result, three different areas on the test sample were chosen which are shown in Figure 4-24 in three different colours. Figure 4-25 to Figure 4-27 show the multiple frame EBSD mapping of the areas marked by the blue, red and orange boxes in Figure(a) of each figure. As an overview, the number of twins was obviously large, with twins observed across the whole map in Figure 4-25(a), 4-26(a) and 4-27(a). Shear band structures were only largely observed in the red area (shown in Figure 4-26(a)). In Figure 4-25(b), Figure 4-26(b) and Figure 4-27(b), the tensile twin boundaries, the compressive twin boundaries and the double twin boundaries are highlighted in red, green and blue, respectively. Combining the grain boundary map with the disorientation angle distribution chart of each area (Figure 4-25(b, c), Figure 4-26(b, c) and Figure 4-27(b, c)), the tensile twins were found to be dominant, occupying 76.8% (blue area), 29.2% (red area) and 85% (orange area) of the boundaries. The compressive twin occupied 1.2% (blue area), 2.7% (red area) and 0.7% (orange area) of the boundaries, while the double twins occupied 2.1% (blue area), 3.1% (red area) and 0.7% (orange area). Although the tensile twins in all three areas were the main twin structure present, the proportion of the tensile twin boundaries in the red area was only 29.2%, which is much smaller than the other two areas (76.8% and 85%).

In the pole figures (Figure 4-25(d), Figure 4-26(d) and Figure 4-27(d)), the maximum pole intensity of the centre area was only 10.6 which is much lower than the maximum pole intensity of the left and the right area (20.5 and 15.4, respectively). Moreover, the pole figure of the centre area (Figure 4-26 (d)) indicates that the orientation distribution of the grains was much wider than that of the other two areas (Figure 4-24 (d) and Figure 4-25 (d)) i.e. the basal texture in the centre area was not as strong as that of the two corner areas.

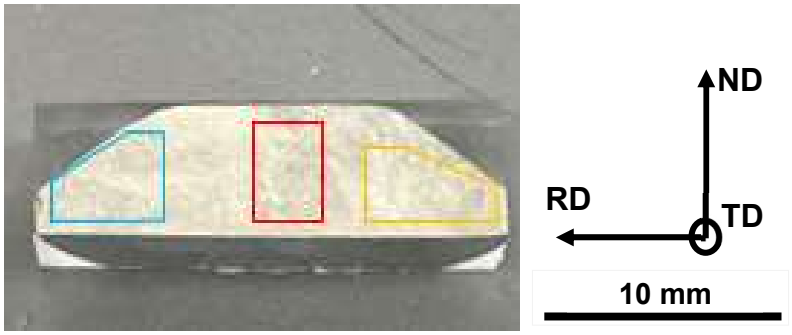

Figure 4-24 The three chosen areas of the large-scale scanning

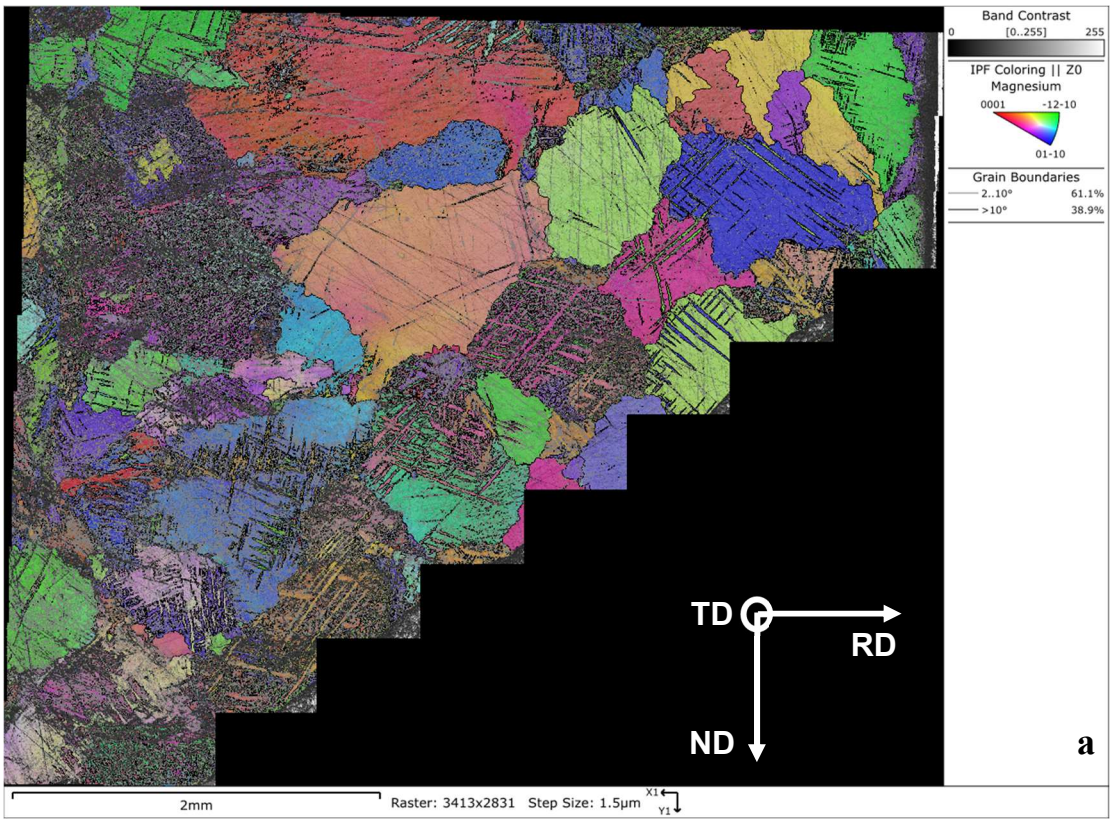

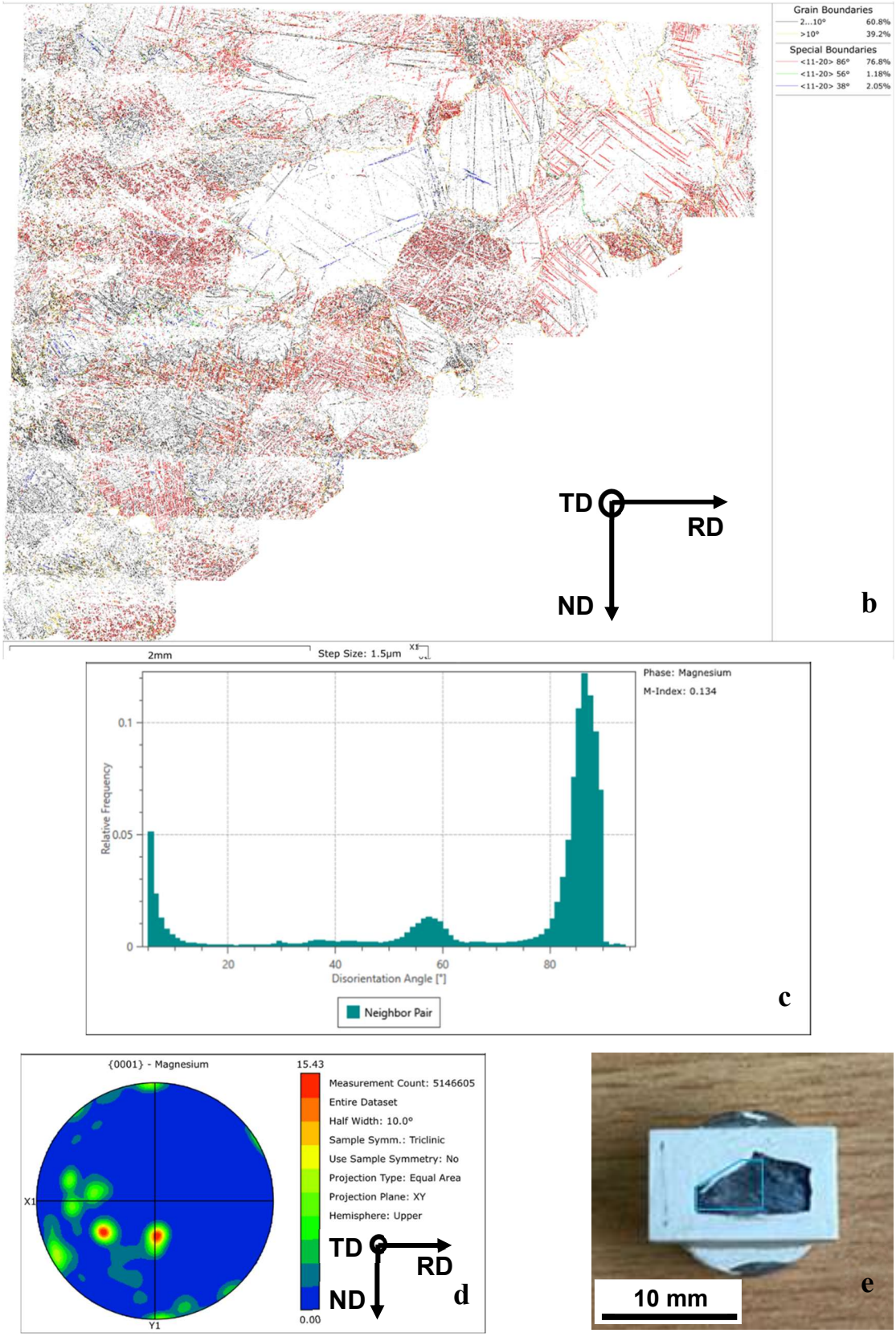

Figure 4-25 The blue area EBSD result of the Mg-0.1Ca-0.4Zn sample: (a) The inverse pole figure map, band contrast and grain boundaries, (b) The grain boundaries and the special grain boundaries, (c) The disorientation angle distribution, (d) The pole figure, (e) Showing the area scanned

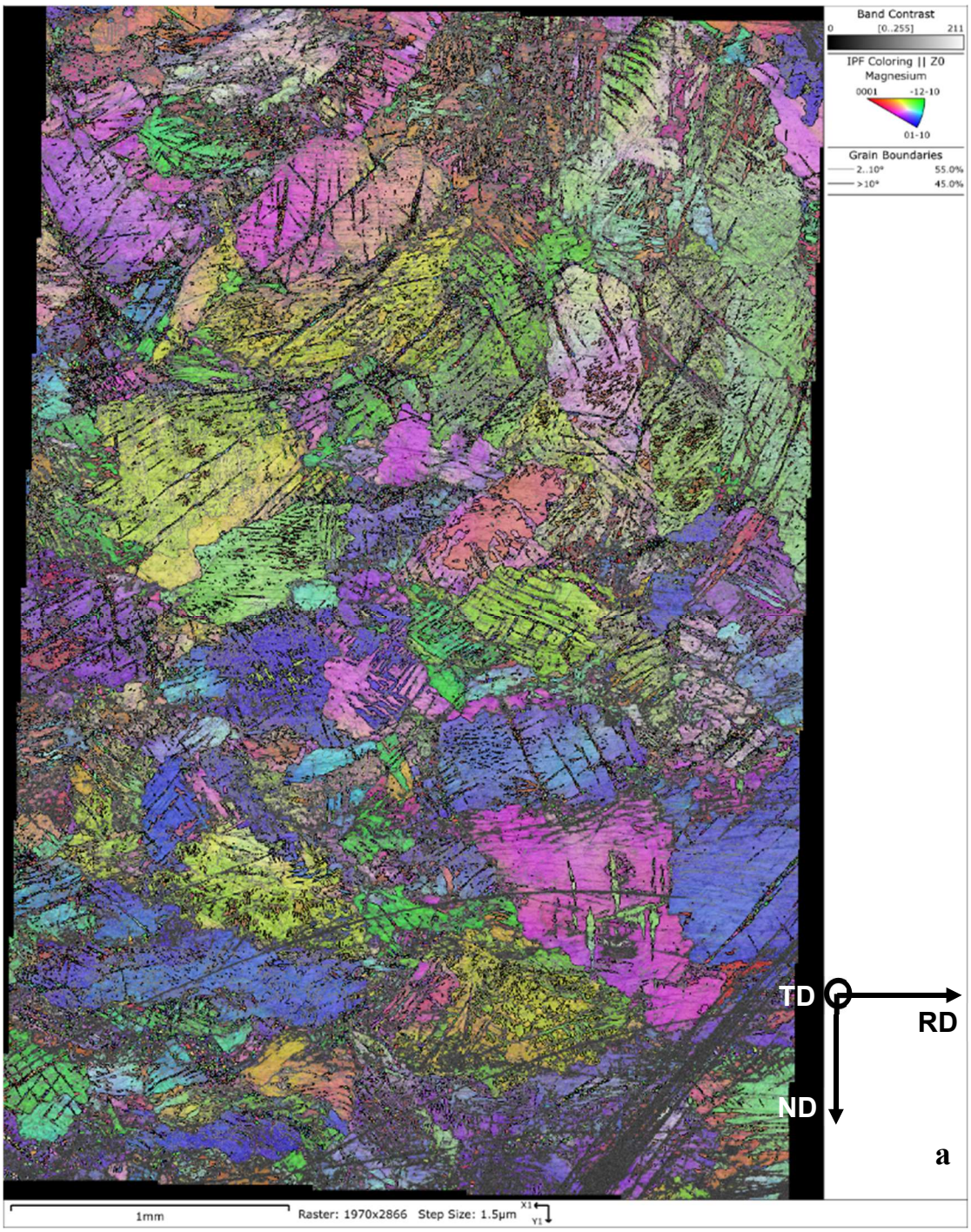
Band Contrast
0 [0..255] 211
IPF Coloring || Z0
Magnesium
0001 -12-10
01-10
Grain Boundaries
2..10° 55.0%
>10° 45.0%
TD
RD
ND
a
1mm
Raster: 1970x2866 Step Size: 1.5µm
X1
Y1

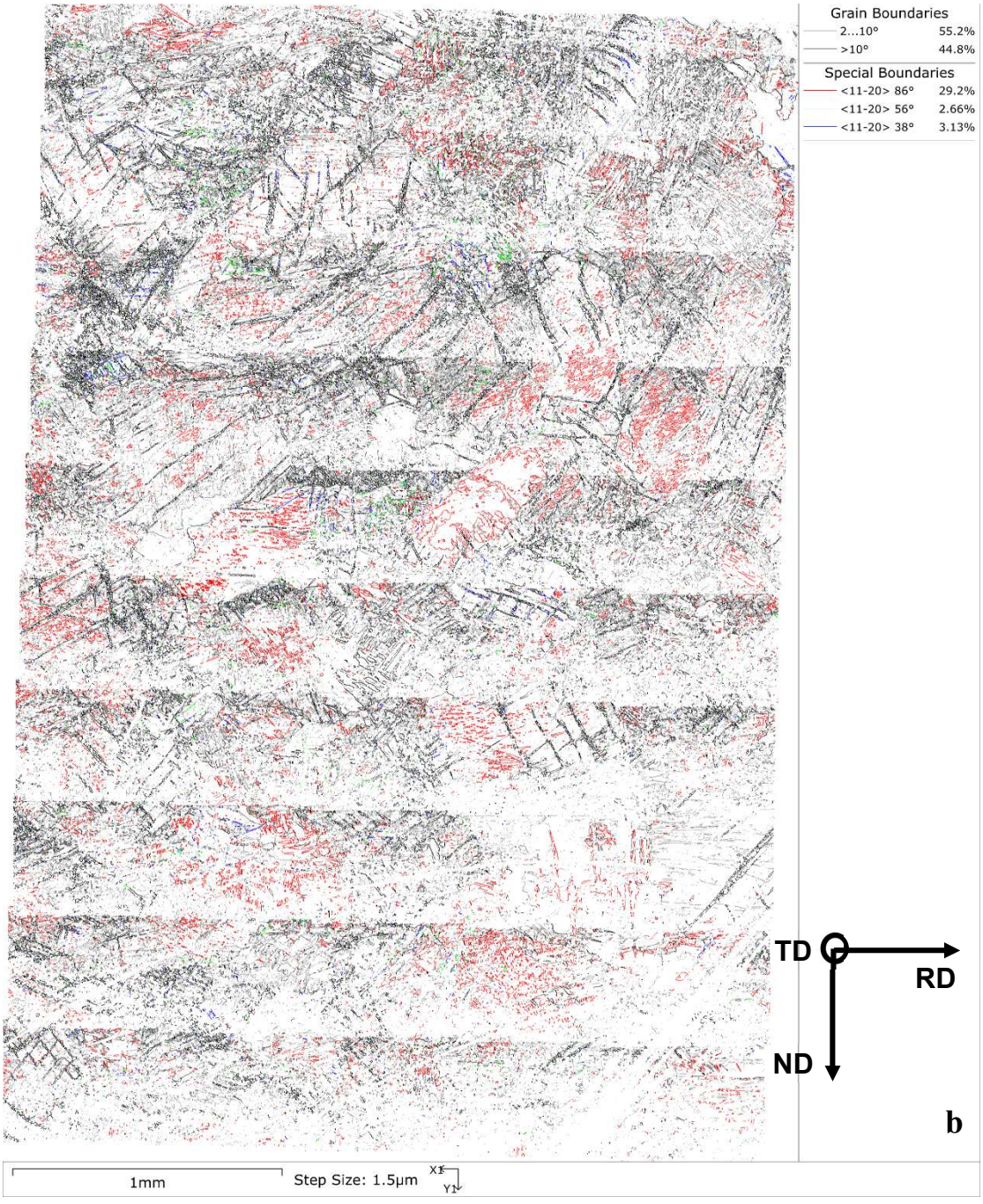
Grain Boundaries
2...10° 55.2%
>10° 44.8%
Special Boundaries
<11-20> 86° 29.2%
<11-20> 56° 2.66%
<11-20> 38° 3.13%
TD
RD
ND
b
1mm
Step Size: 1.5µm

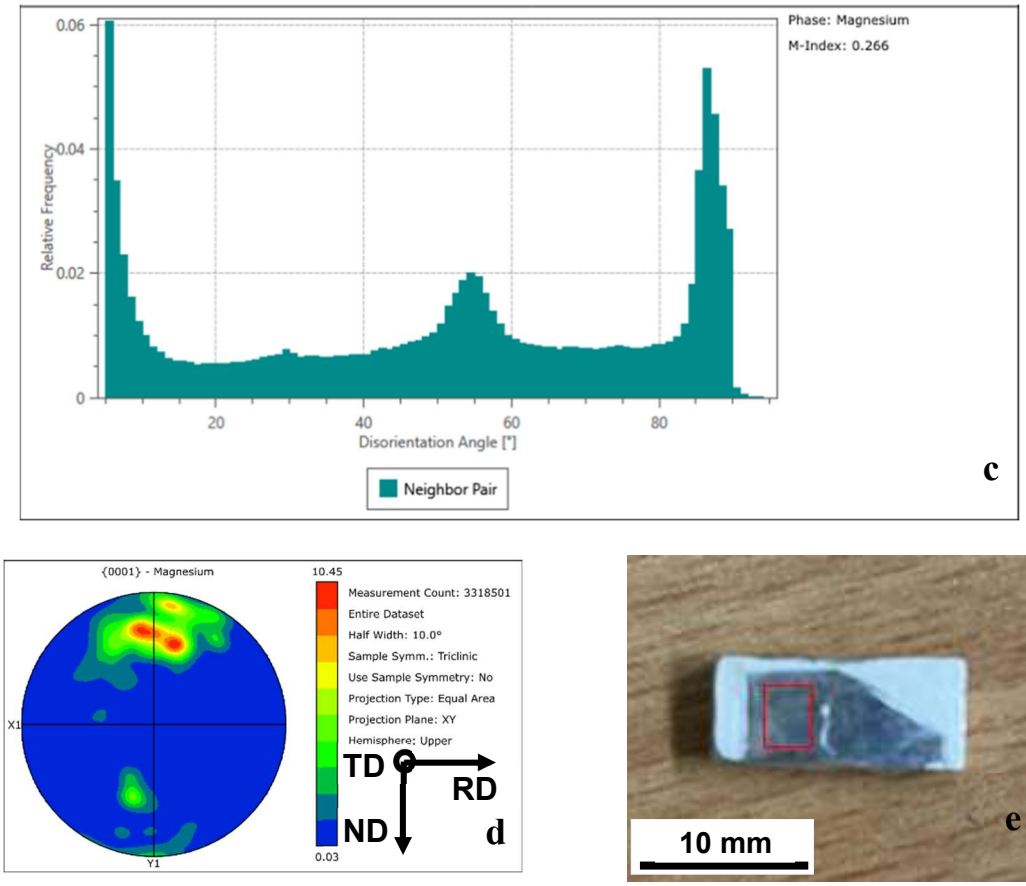

Figure 4-26 The red area EBSD result of the Mg-0.1Ca-0.4Zn sample: (a) The inverse pole figure map, band contrast and grain boundaries, (b) The grain boundaries and the special grain boundaries, (c) The disorientation angle distribution, (d) The pole figure, (e) Showing the area scanned

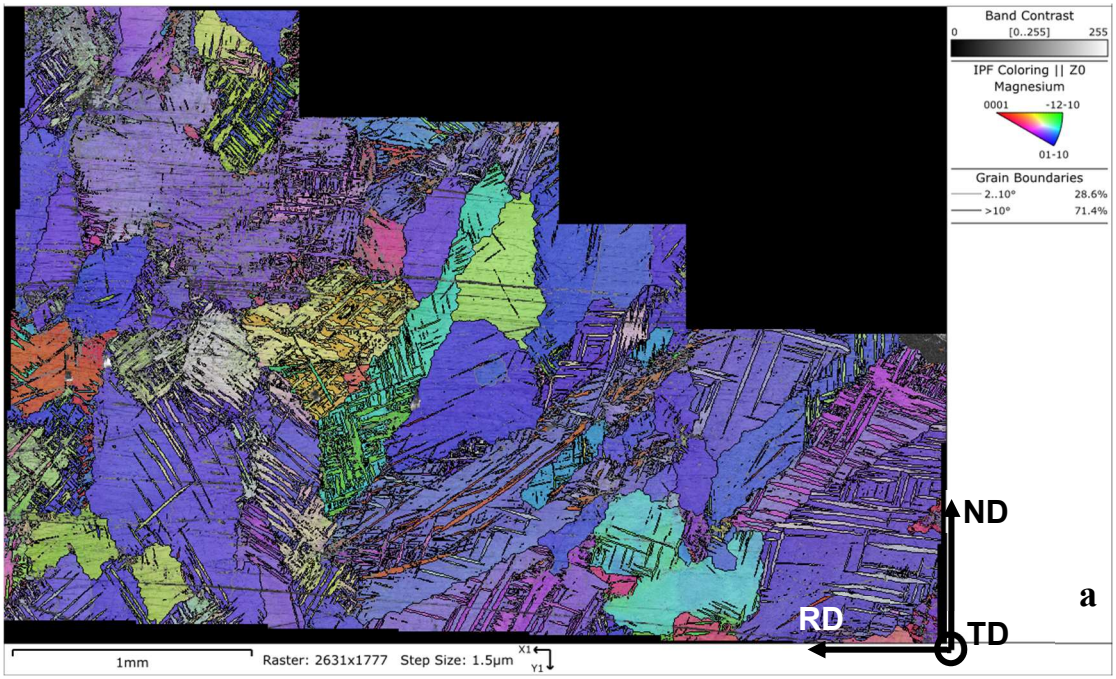

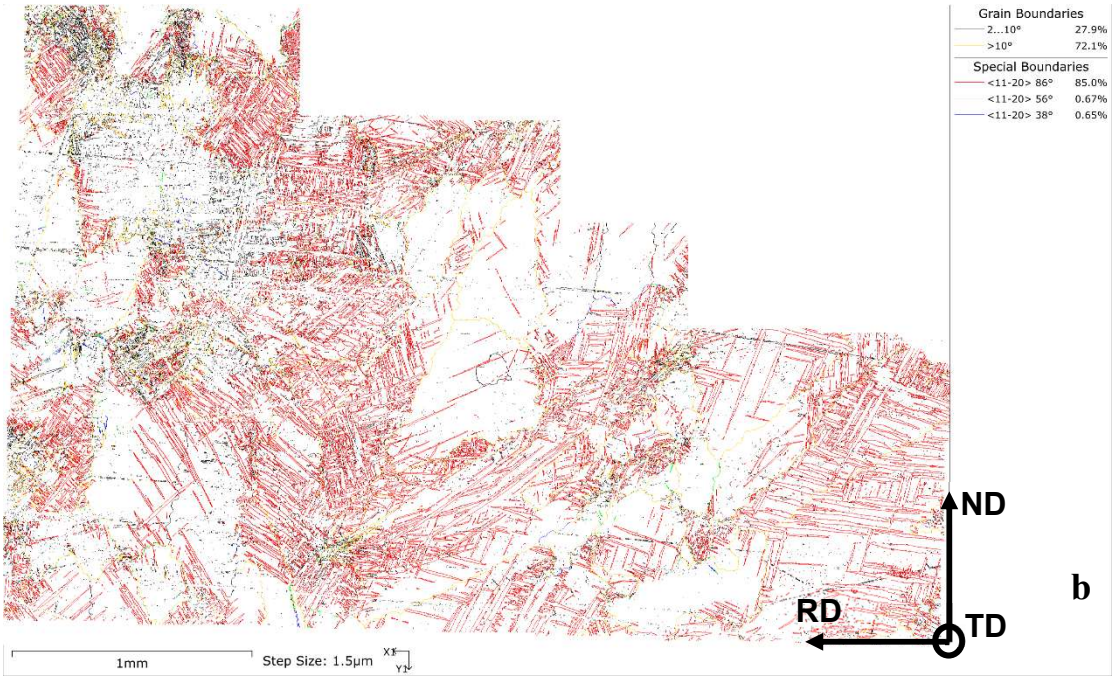

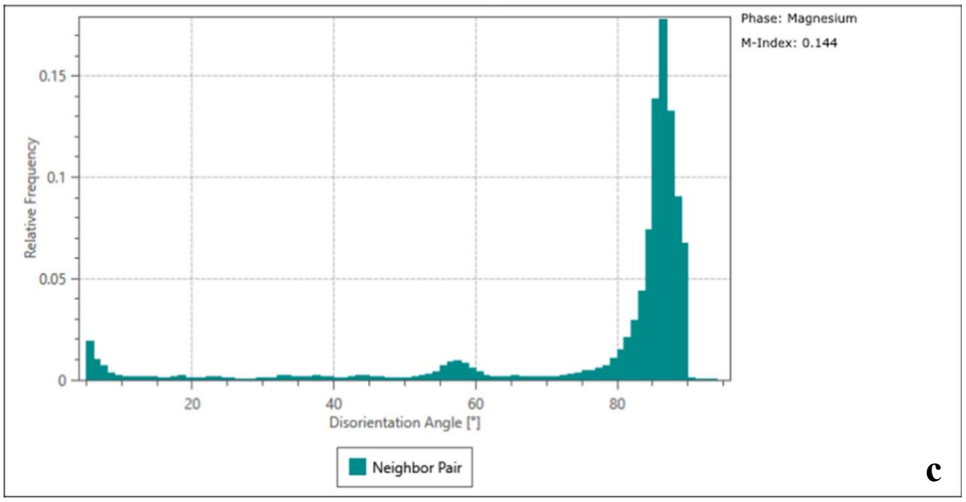

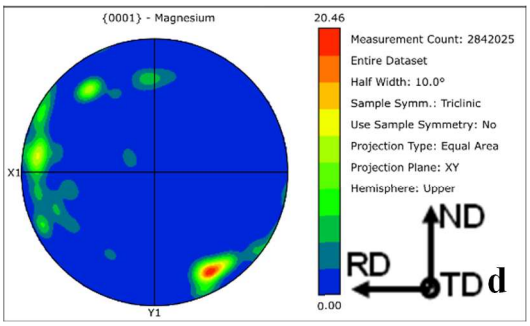

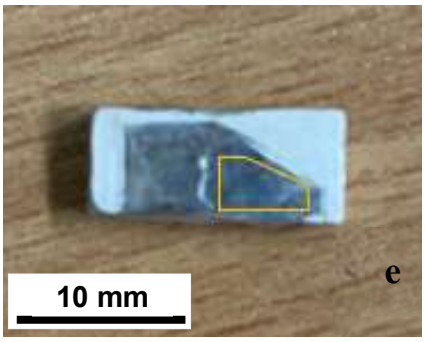

Figure 4-27 The yellow area EBSD result of the Mg-0.1Ca-0.4Zn sample: (a) The inverse pole figure map, band contrast and grain boundaries, (b) The grain boundaries and the special grain boundaries, (c) The disorientation angle distribution, (d) The pole figure, (e) Showing the area scanned

4.3 Channel die (CD) compression experiment

4.3.1 The CD compression using old channel die

The old channel is the channel die shown in Figure 3-11 which had an undetachable die body. For the CD compression using the old channel die parts, specimens used in this experiment were all made from the first batch ingots. The large original grain size of the ingots mentioned before did affect the performance of the specimens during the CD compression process which resulted in less-than-ideal results.

As with the DTC compression experiments, a trial test was conducted using the old channel die. The aim of this test was to find out the approximate compression deformation limit of this series of Mg alloys. The first trial specimen chosen was the Mg-0.2Ca-0.3Zn (at%) sample. The maximum compression distance was set as 5mm, and the velocity of the compression was 0.05mm per minute. Figure 4-28 gives the force(N)-compression distance(mm) plot of the compression, respectively. The force applied to the specimen is mapped as a function of the deformation distance. Based on Figure 4-28, it was clear that the specimen cracked when the deformation distance reached 2.2mm (about 0.15 strain).

After the compression, it was found that the specimen had cracked, and it was very hard to remove the cracked pieces from inside of the channel die. This was attributed to the expansion of the specimen in the width direction after the compression and the insufficient lubrication between the specimen and the channel die. The pieces had to be forcibly removed with a hammer. Figure 4-29 shows the cracked Mg-0.2Ca-0.3Zn (at%) specimen which was just removed from the channel die. The specimen showed quite large strain in the top 6mm area, but the rest of the specimen did not shown signs of deformation, which indicated highly non-uniform deformation. Moreover, the fractures occurred at 45° to the compression direction which is the maximum shear stress angle. The evidence of straining the top part of the specimen to failure while the lower part did not experience deformation indicated that the lubrication of the specimen was not good enough, with high friction between the specimen and the channel die preventing uniform material flow. Therefore, the 2.2mm compression moving distance could not be used as the reference for the maximum compression distance.

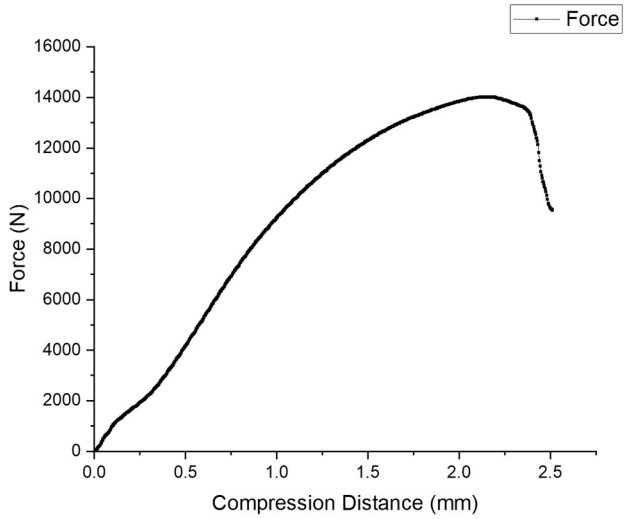

Figure 4-28 The force-compression distance curve of the Mg-0.2Ca-0.3Zn sample

Figure 4-29 The cracked Mg-0.2Ca-0.3Zn specimen after the compression

For the second trial compression, the Mg-0.5Zn (at%) sample was chosen as the trial specimen since this alloy presented the best formability and uniform deformation among all five kinds of alloy in the DTC compression tests.

Based on the experience from the first trial, Vaseline was used as a lubrication, applied to the inner surface of the channel die, the bottom surface of the T-shape plunger and the contact surface of the trial specimen. The second trial compression was designed in two steps. The maximum compression distance of each step was set as 2mm and each step was further divided into two operations to complete, each operation conducted 1mm compression. Figure 4-30 gives the force-compression distance curves of two compression operations of the first step compression. The results indicated that the 2mm displacement was not the deformation limit of the Mg-0.5Zn (at%) specimen.

In the first compression, the specimen did not crack. However, the second compression never proceeded because the specimen was again stuck to the die and could only be removed using a file and hammer. Although the specimen was not as firmly stuck to the die as the first experiment, there was still unwanted deformation in removing it, making the second compression pointless. Figure 4-31 shows the compressed Mg-0.5Zn (at%) specimen after being removed from the channel die, with the deformation from sample removal clear.

Inspection of the sample after removal showed an upper region with a very different morphology to the lower region, separated by a curved line. This suggests that, although the lubricant was applied evenly over the specimen, it did not remain in place in certain regions during the deformation. Therefore, the shape of the specimen and the size of the channel die were considered to be the source of this problem. Comparing the top/bottom surfaces and the forward/backward surfaces with the two-side surfaces (in contact with the channel die), the area of the side surface was much larger than that of the other surfaces. The large contact area of this surface inevitably led to differences in friction between this surface and the other surfaces which would inevitably lead to deformation asymmetry. Moreover, the shape of the specimen was also not ideal for the compression process. The compression direction was along the longer side of the sample. Both these factors would make studying strain path effects very difficult. When combined with the large grain size and alloying element segregation on the grain boundaries, this meant that the sample could become curved during the compression.

However, the idea of the channel die compression process was still good but a complete redesign of both the channel die and the specimen dimensions was required.

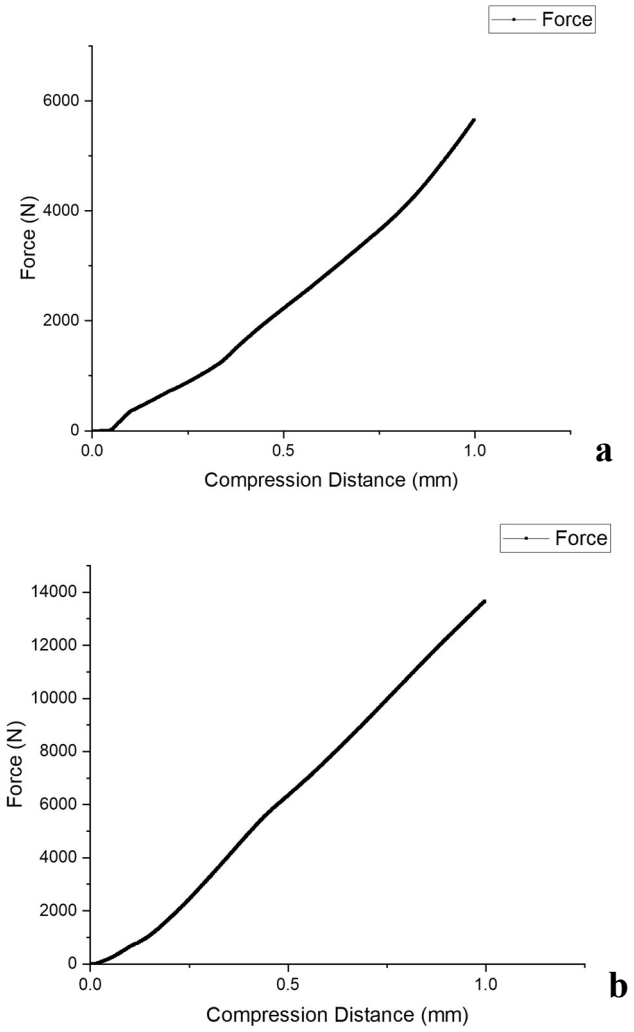

Figure 4-30 The force-compression distance curve of the Mg-0.5Zn alloy: (a) The first compression, (b) The second compression

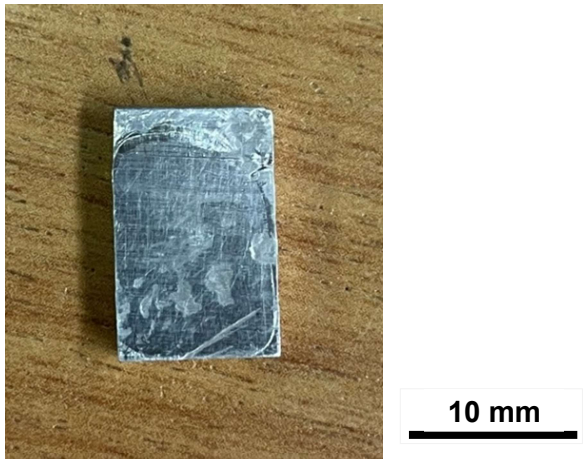

Figure 4-31 The Mg-0.5Zn specimen after the compression

Before the new channel die was manufactured, the Mg-0.5Zn (at%) CD trial sample was investigated using EBSD. The smaller section on top of the "dividing line" was chosen as the study area to investigate the microstructure by using the FEI Inspect F50. The reason for choosing this section was that it had a heavier deformation than the bottom part (based on the result of compressed Mg-0.2Ca-0.3Zn (at%) CD specimen).

The EBSD result is shown below in the Figure 4-32. Figure 4-32(a) which show extensive twinning, but no evidence of shear banding. Based on the special grain boundaries identification (shown in Figure 4-32(b)), the tensile twins (<11-20> 86°, red lines), the compressive twins (<11-20> 56°, green lines) and the double twins (<11-20> 38°, blue lines) occupied 65.1%, 0.3% and 0.4% in fraction of the total boundary area, respectively. As with the compressed double truncated cone samples, tensile twins dominated the twinning followed by the double twins and then compressive twins. Figure 4-32(c) presents a very strong pole intensity with a value of 51.7, indicating the strong texture of the sample, although there were only a few grains sampled, and the texture may well vary across the sample. The EBSD result of the channel die compressed Mg-0.5Zn (at%) sample confirmed that this die and specimen dimensions were of no use and a new die needed to be designed.

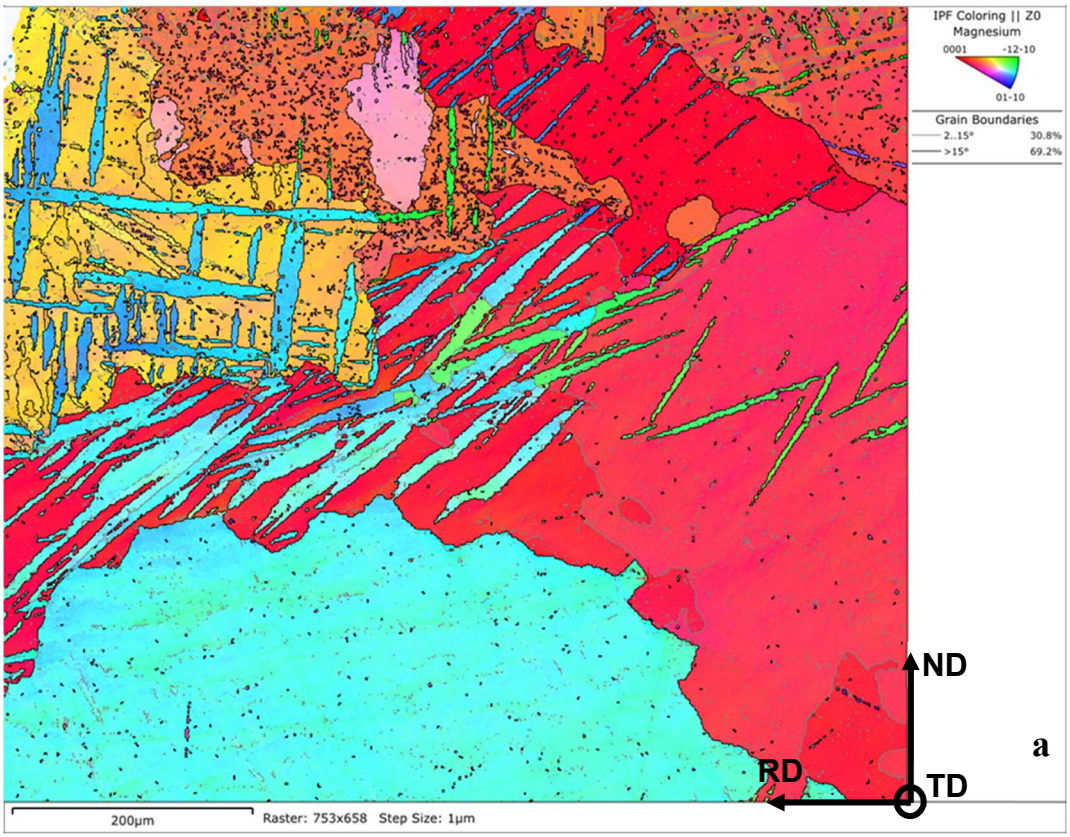

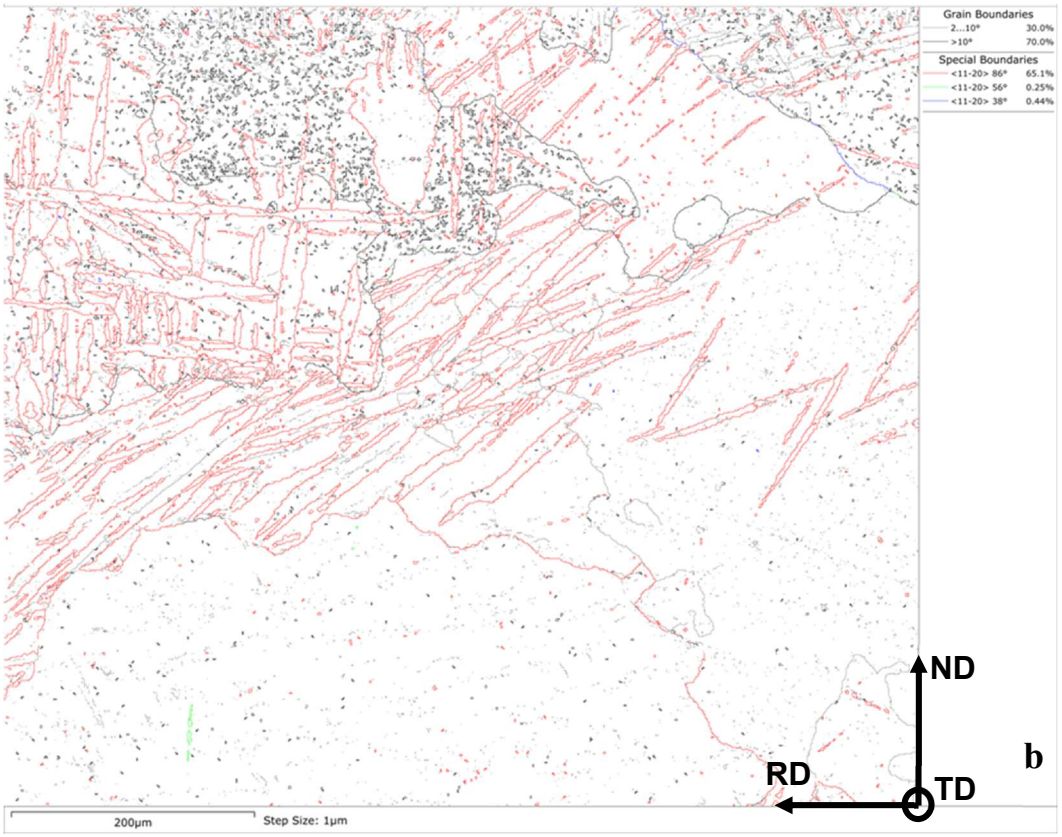

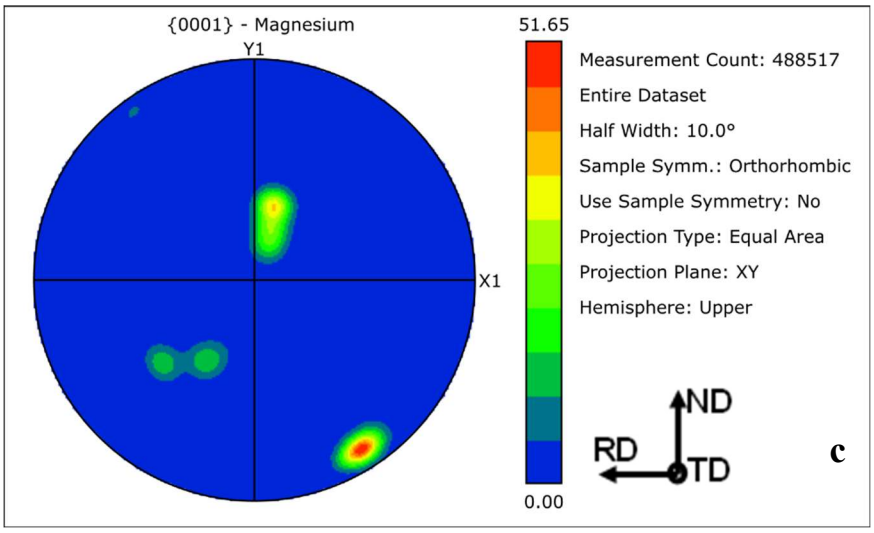

Figure 4-32 The EBSD result of the compressed Mg-0.5Zn: (a) The inverse pole figure map and grain boundaries, (b) The grain boundaries and the special grain boundaries, (c) The pole figure of the sample

4.3.2 The CD compression using new die mold

The new channel is the channel die shown in Figure 3-14 and 3-15 which had a detachable die body. The specimen was also redesigned (10mm cube in shape) for the

new channel die (shown in Figure 3-17). For the CD compression using the new channel die parts, specimens used in this experiment were all made from the second batch ingots. The smaller grain size of the ingots and the much finer grain size of the hot-rolled slabs gave the test specimens a better formability to complete the experiments.

The materials chosen to conduct these experiments were Mg-0.2Ca-0.3Zn, Mg-0.1Ca-0.4Zn and Mg-0.5Zn (at%) specimens. The CD compression experiment with the new die mould was conducted in two rounds in total. After a successful compression process (1D compression and 2D compression), the annealing results of the first-round experiment presented rapid recrystallization within the specimens i.e. after the first-time annealing, the specimens were almost fully recrystallized. Clearly, this was not useable since the study was to look at the nucleation and growth of recrystallisation and the resultant evolution of texture. Thus, the second-round experiment was conducted with the same materials, compression procedures and much shorter annealing time step, ensuring that nucleation and growth of recrystallisation and the resultant evolution of texture could be observed.

In the first round experiment, the heating rate of the specimen in the tube furnace was measured by the thermocouple before the annealing process (shown in Figure 3-21). The graph shows that the sample required more than 11 minutes of heating to reach the target heating temperature, which was much longer than expected. Based on this, the annealing process time with 180s, 360s, 540s, 720s, 900s,1080s and 1260s (as 180s, 540s, 1080s, 1800s, 2700s, 3780s and 5040s in total heat treatment time, respectively) was decided.

4.3.2.1 The first round of the channel die (CD) compression experiment

Figures 4-33 to 4-36 and Figures 4-37 to 4-40 present the EBSD results of the as-compressed state and annealed state of the Mg-0.1Ca-0.4Zn and Mg-0.5Zn (at%) specimens from the first-round experiment, respectively.

The results of two compressed Mg-0.1Ca-0.4Zn (at%) samples (shown in Figure 4-33(f) and Figure 4-34(f)) indicate that the average grain size of the 1D compressed specimen and 2D compressed specimen was $10.7\,\mu m$ and $8.7\,\mu m$, respectively. Although the average grain size of the two specimens was quite small, the grain size was not uniform. The large grains observed had a size exceeding $200\mu m$, while the fine grains showed a size smaller than $5\mu m$ in two specimens. In contrast, the compressed Mg-0.5Zn (at%) specimens exhibited a much better result regarding the uniform grain size (shown in Figure 4-35(f) and Figure 4-36(f)). The average grain size of the 1D compressed and the 2D compressed specimen was $19.6\mu m$ and $13.1\mu m$, respectively. The size of all the grains was similar. No extremely large or small grains were found. Additionally, a significant quantity of shear bands and fine twins were found in these

specimens (shown in Figure 4-33(c), Figure 4-34(c), Figure 4-35(c) and Figure 4-36(c)). Combining the figures of the IPF maps (Figure 4-33(a), Figure 4-34(a), Figure 4-35(a) and Figure 4-36(a)). The shear bands were mostly observed on the grain boundaries and occasionally were also found inside the large grains.

Figure 4-33(b), 4-34(b), 4-35(b) and 4-36(b) indicate that the distribution of the twins was uniform across the whole scanned area. No specific evidence of the irregular distribution of twins e.g. the twins concentrated in some locations or there were no twins at all in an area. The tensile twins (<11-20> 86°, highlighted in red) still dominated the twin type in all four samples which accounted for 47.4% and 46.2% in the 1D compressed and 2D compressed Mg-0.1Ca-0.4Zn (at%) specimens, respectively, and 64.6% and 59.7% in the 1D compressed and 2D compressed Mg-0.5Zn (at%) specimens, respectively. The fraction of compressive twins (<11-20> 56°, highlighted in green) in the 1D compressed and 2D compressed Mg-0.1Ca-0.4Zn (at%) specimens was 3.9% and 0.7%, respectively, while for the two Mg-0.5Zn (at%) specimens, it was 1.6% and 0.30%, respectively. The fraction of double twins (<11-20> 38°, blue lines) in the 1D compressed and 2D compressed Mg-0.1Ca-0.4Zn (at%) specimens were 8.00% and 2.6%, respectively, while in the 1D compressed and 2D compressed Mg-0.5Zn (at%) specimens were 2.8% and 0.7%, respectively.

Figure 4-34(d)(e), Figure 4-34(d)(e), Figure 4-35(d)(e) and Figure 4-36(d)(e) show the maximum pole intensity and the texture orientation of four compressed specimens. The Mg-0.1Ca-0.4Zn (at%) specimens showed a higher maximum pole intensity than the Mg-0.5Zn (at%), which were 19.3 to 11.9 (1D) and 10.2 to 7.9 (2D). Notably, all four specimens displayed a texture orientation aligned parallel to the direction of the final compression process, consistent with typical rolling textures.

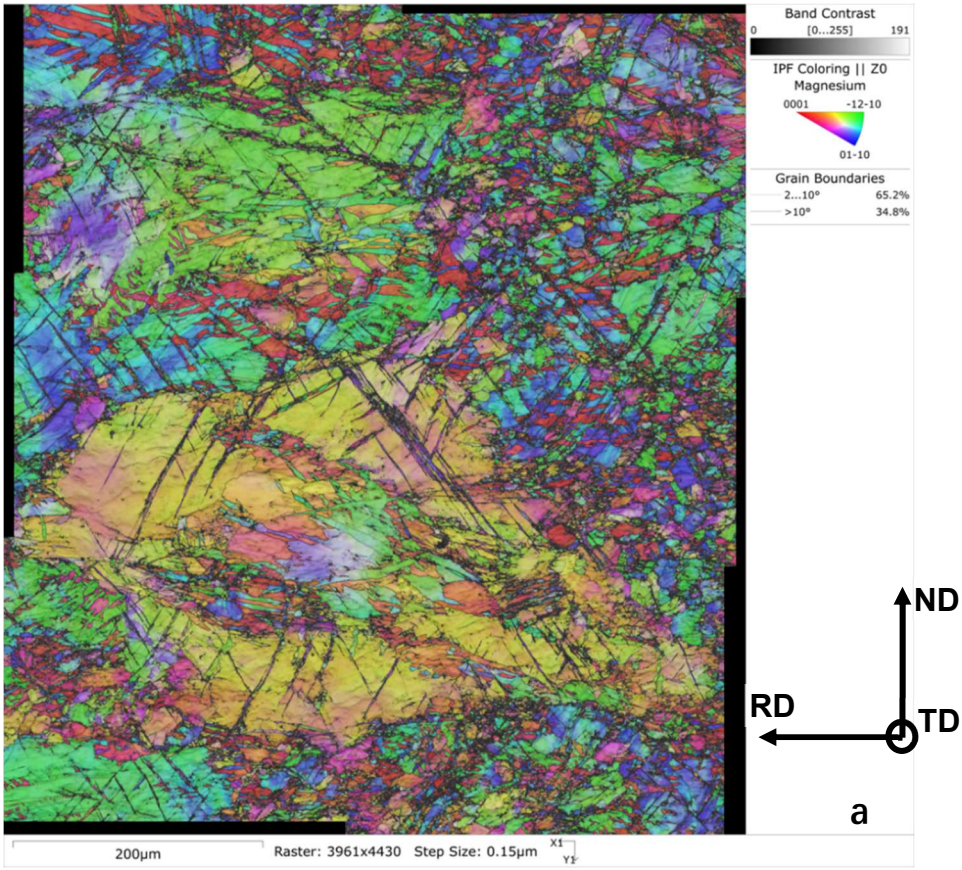
Band Contrast
0 [0...255] 191
IPF Coloring || Z0
Magnesium
0001 -12-10
01-10
Grain Boundaries
2...10° 65.2%
>10° 34.8%
ND
RD
TD
a
200µm
Raster: 3961x4430 Step Size: 0.15µm

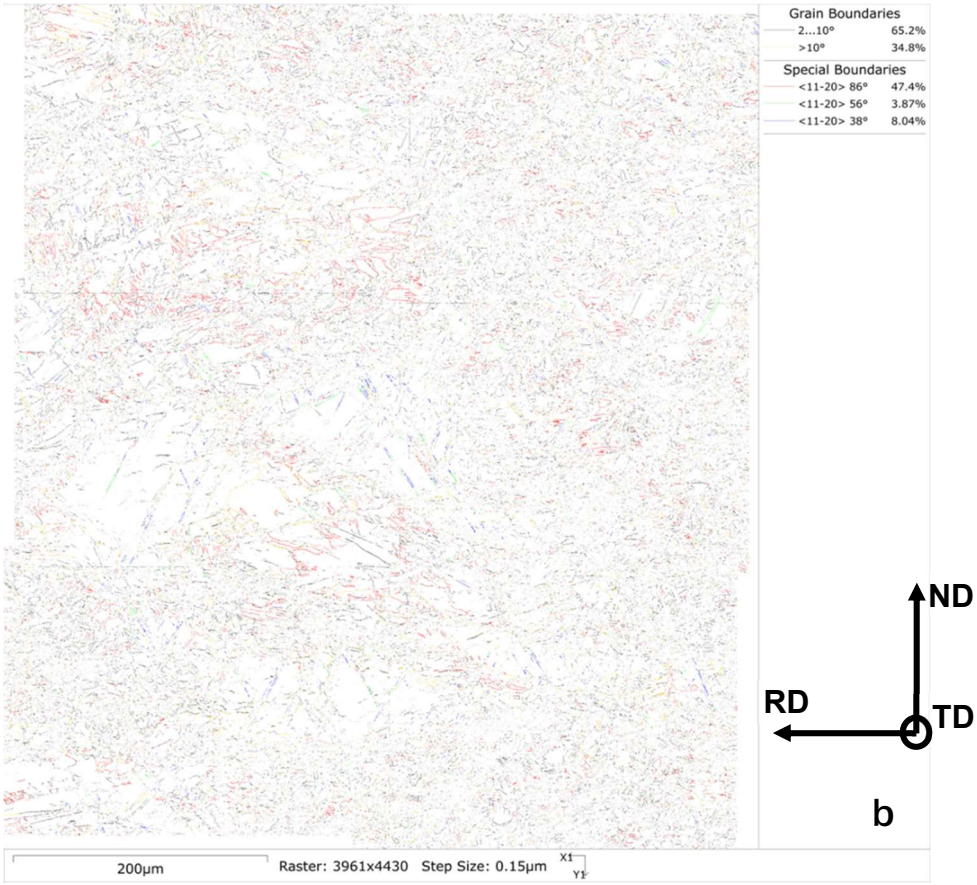
Grain Boundaries
2...10° 65.2%
>10° 34.8%
Special Boundaries
<11-20> 86° 47.4%
<11-20> 56° 3.87%
<11-20> 38° 8.04%
ND
RD
TD
b
200µm
Raster: 3961x4430 Step Size: 0.15µm

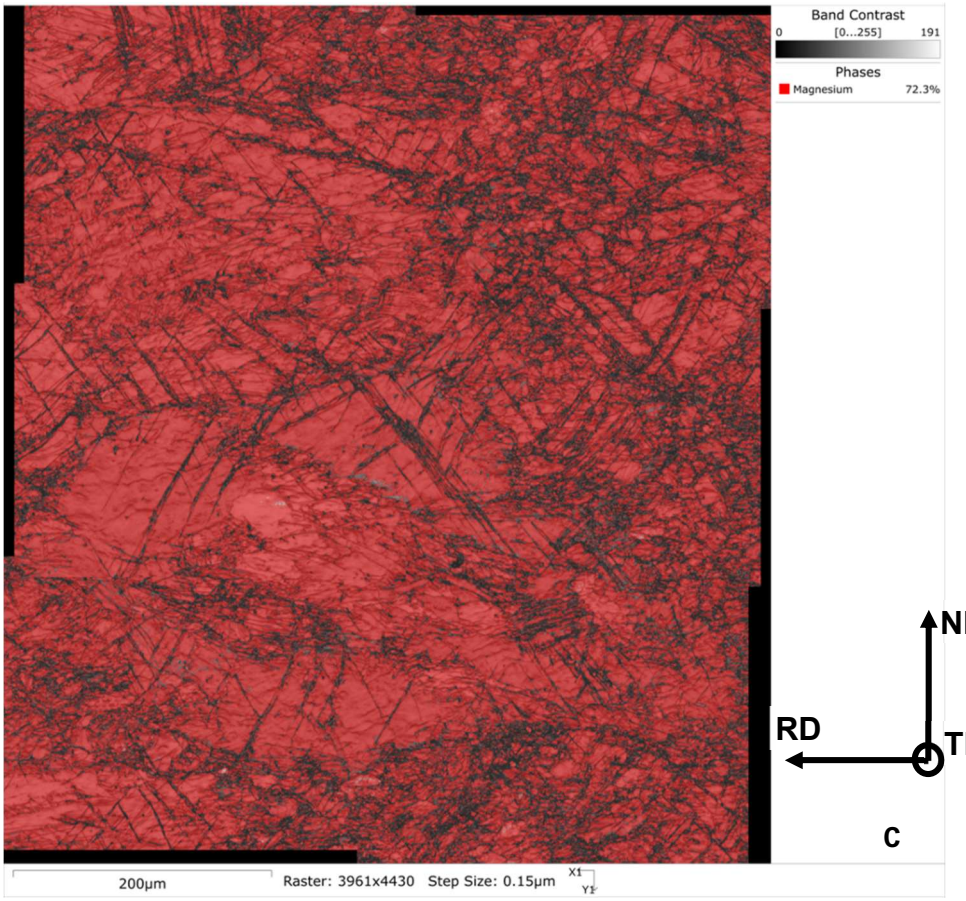
Band Contrast
0
[0...255]
191
Phases
Magnesium
72.3%
ND
RD
TD
c
200µm
Raster: 3961x4430
Step Size: 0.15µm
X1
Y1

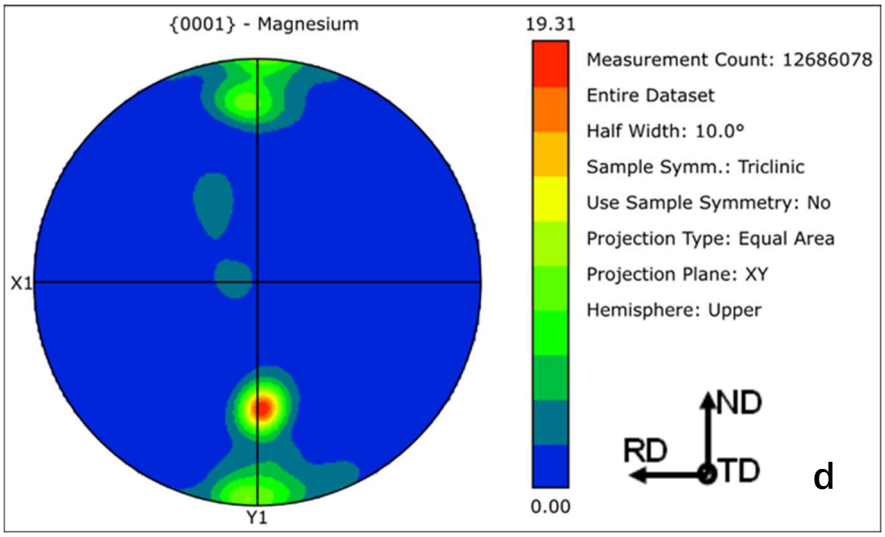
{0001} - Magnesium
19.31
0.00
Measurement Count: 12686078
Entire Dataset
Half Width: 10.0°
Sample Symm.: Triclinic
Use Sample Symmetry: No
Projection Type: Equal Area
Projection Plane: XY
Hemisphere: Upper
X1
Y1
ND
RD
TD
d

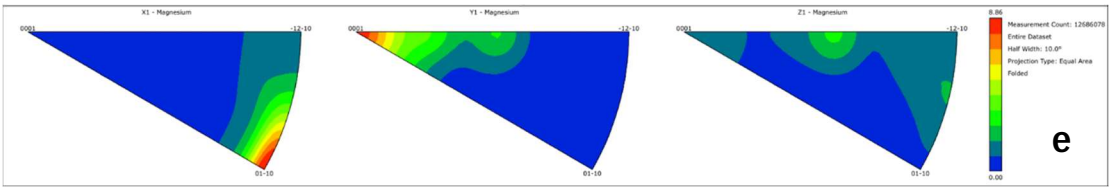
e

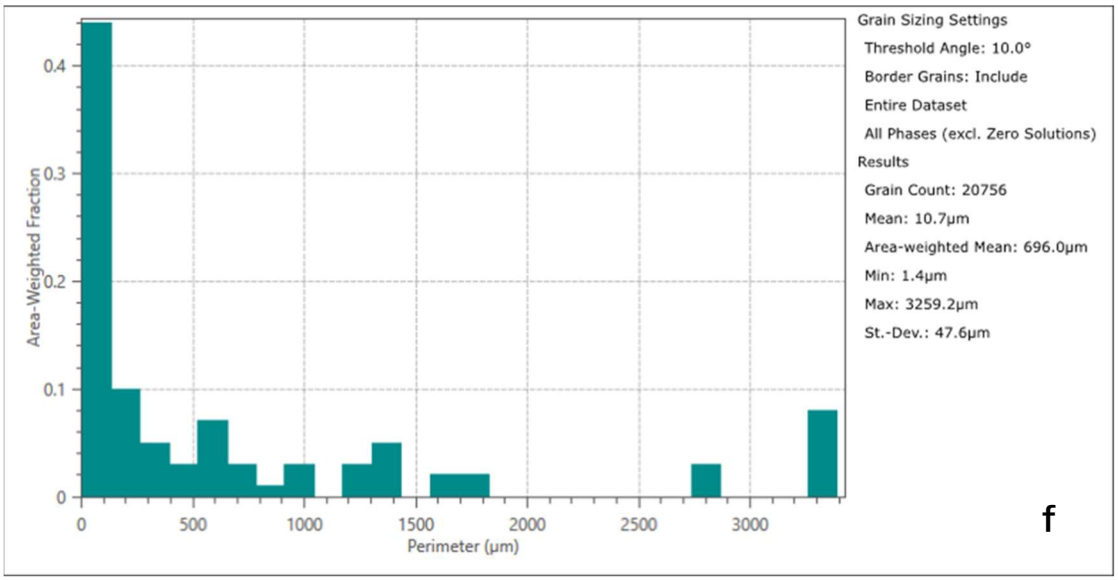

Figure 4-33 The EBSD result of the 1D compressed Mg-0.1Ca-0.4Zn specimen: (a) The inverse pole figure map and grain boundaries, (b) The grain boundaries and the special grain boundaries, (c) The band contrast and the phase analysis, (d) The pole figures, (e) The inverse pole figures, (f) Grain size distribution expressed as grain boundary perimeter

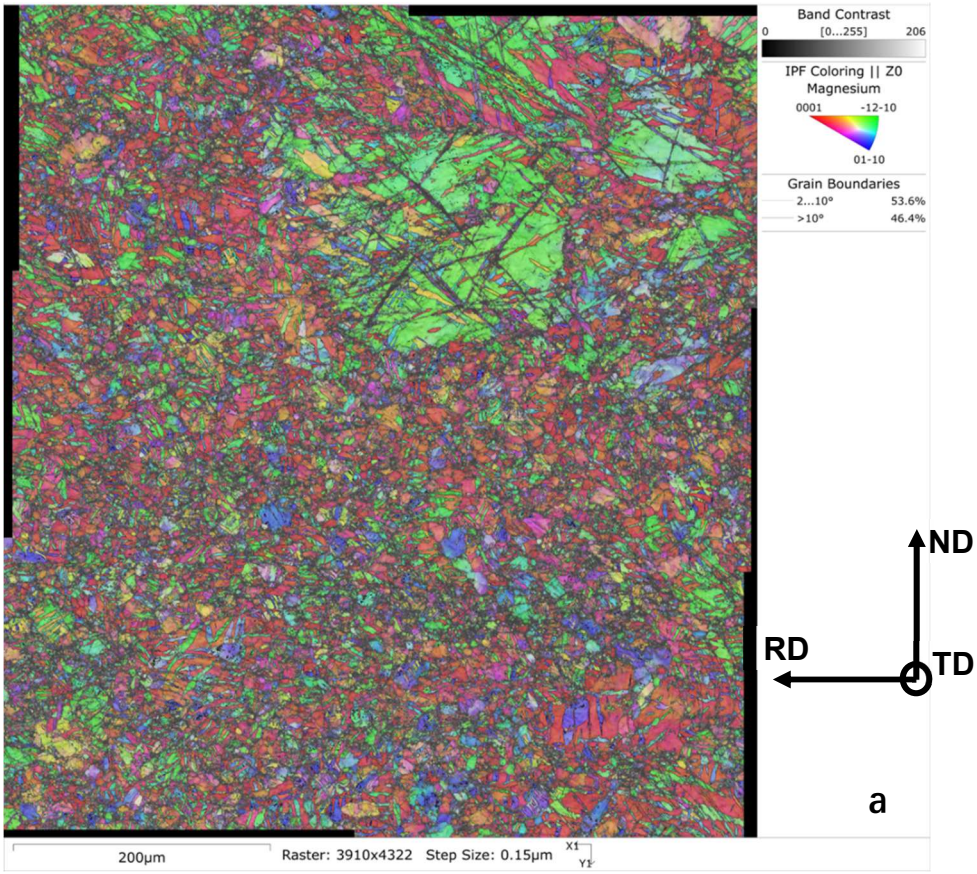

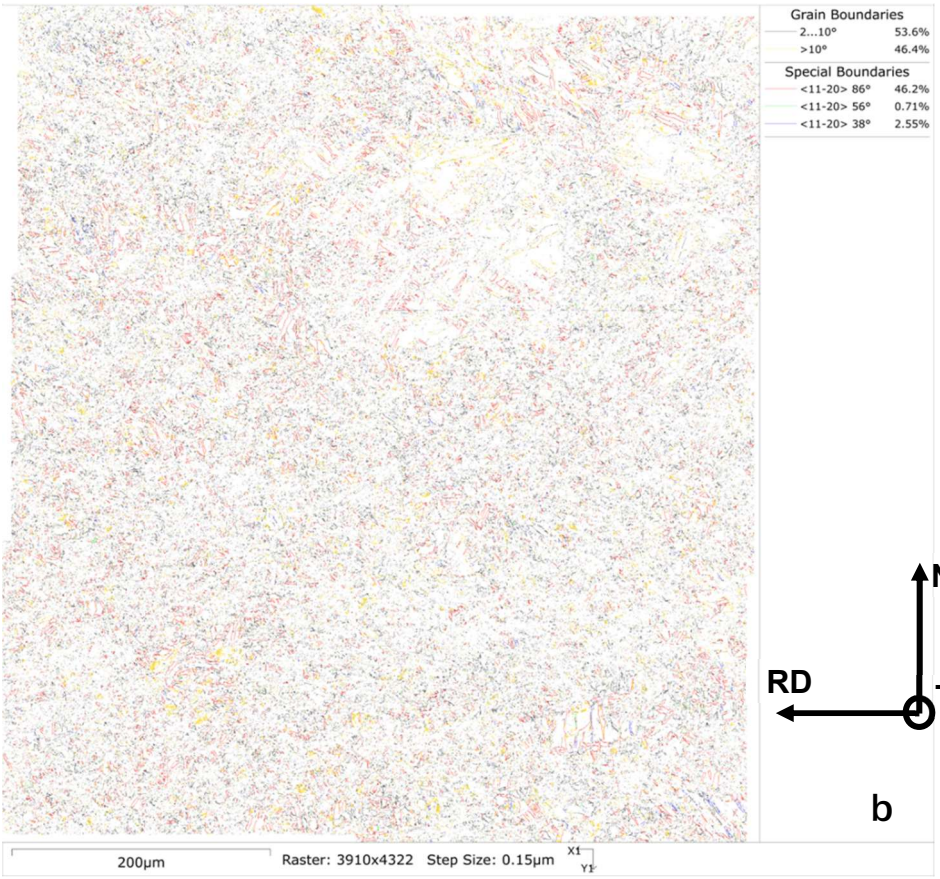
Grain Boundaries
2...10° 53.6%
>10° 46.4%
Special Boundaries
<11-20> 86° 46.2%
<11-20> 56° 0.71%
<11-20> 38° 2.55%
ND
RD
TD
b
200µm
Raster: 3910x4322 Step Size: 0.15µm
X1
Y1

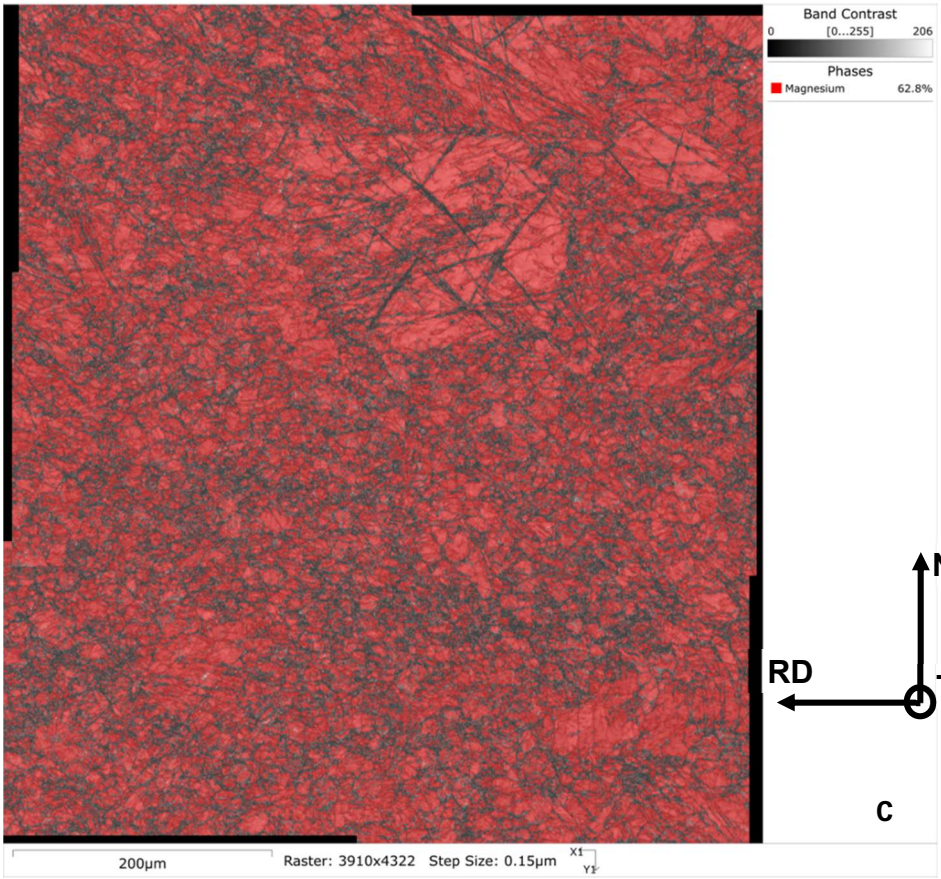
Band Contrast
0 [0...255] 206
Phases
Magnesium 62.8%
ND
RD
TD
c
200µm
Raster: 3910x4322 Step Size: 0.15µm
X1
Y1

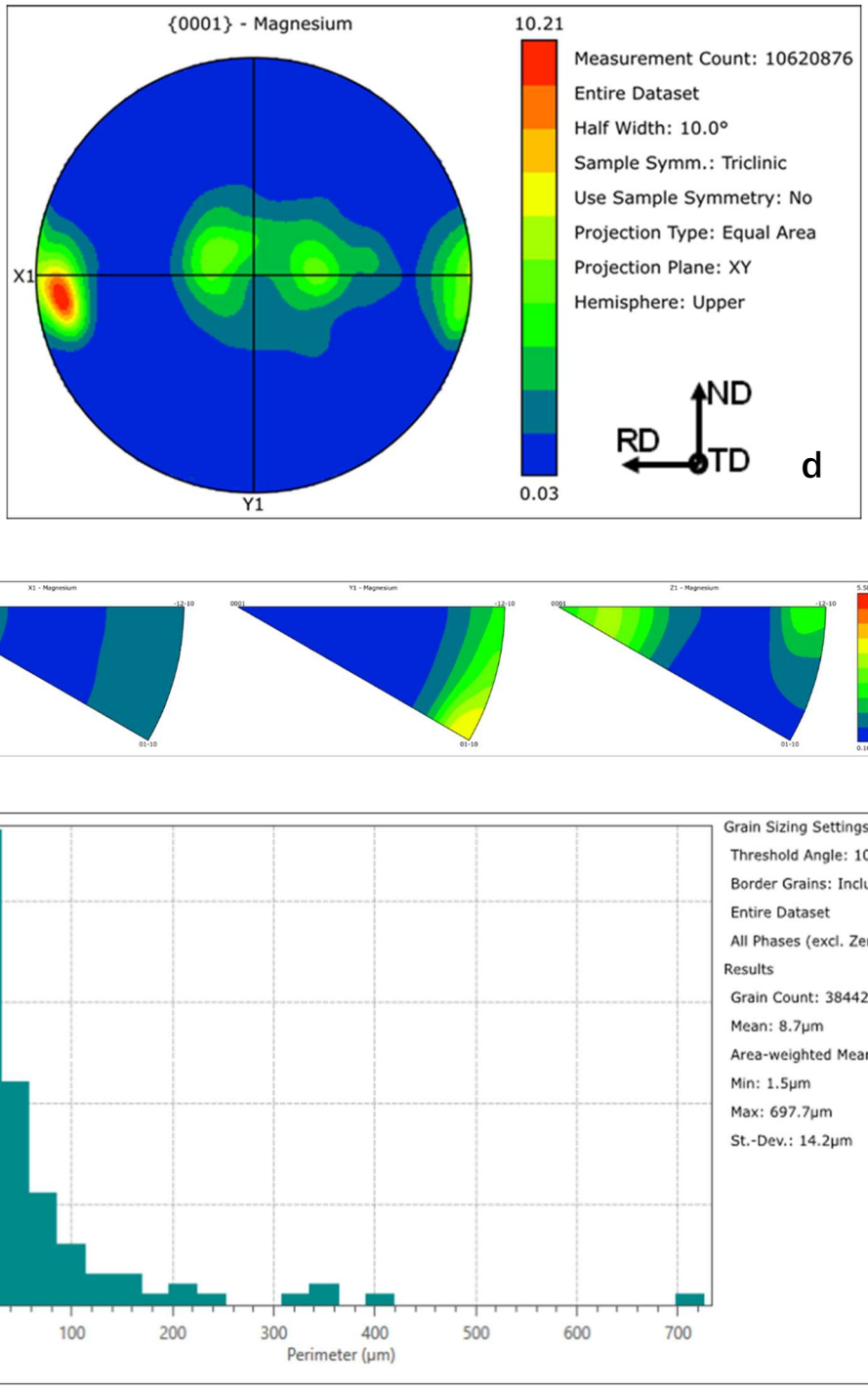

Figure 4-34 The EBSD result of the 2D compressed Mg-0.1Ca-0.4Zn specimen: (a) The inverse pole figure map and grain boundaries, (b) The grain boundaries and the special grain boundaries, (c) The band contrast and the phase analysis, (d) The pole figure, (e) The inverse pole figures, (f) Grain size distribution expressed as grain boundary perimeter

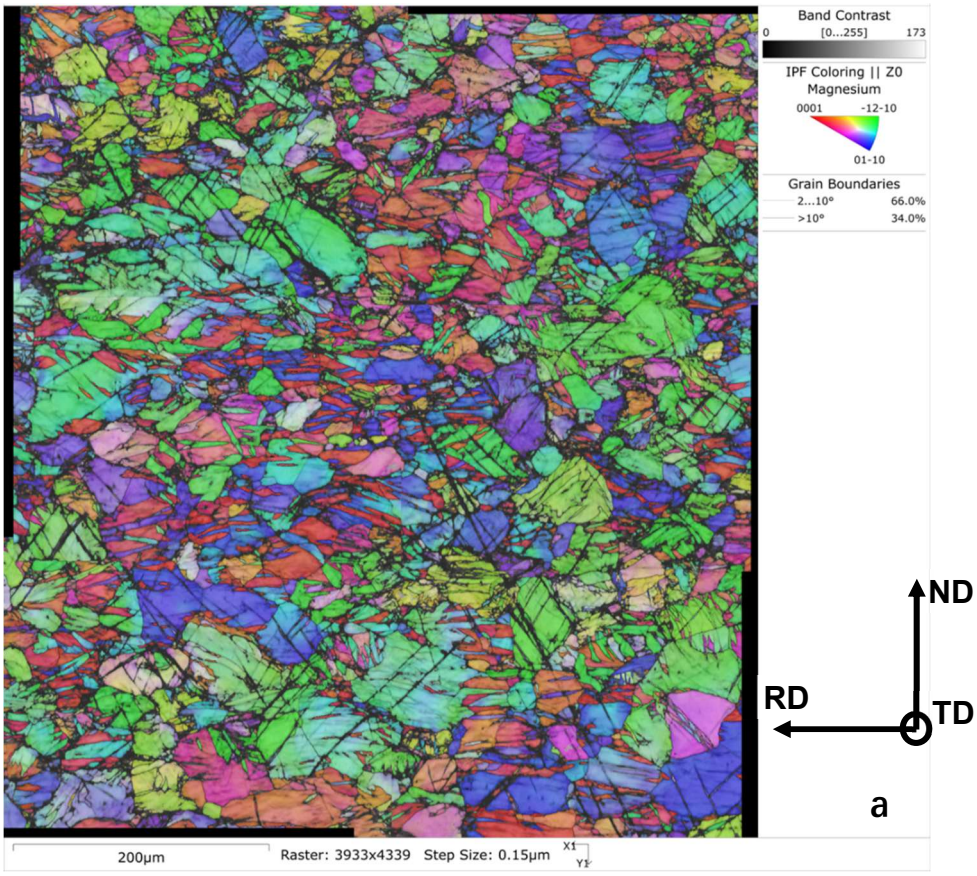
Band Contrast
0 [0...255] 173
IPF Coloring || Z0
Magnesium
0001 -12-10
01-10
Grain Boundaries
2...10° 66.0%
>10° 34.0%
ND
RD
TD
a
200µm
Raster: 3933x4339 Step Size: 0.15µm
X1
Y1

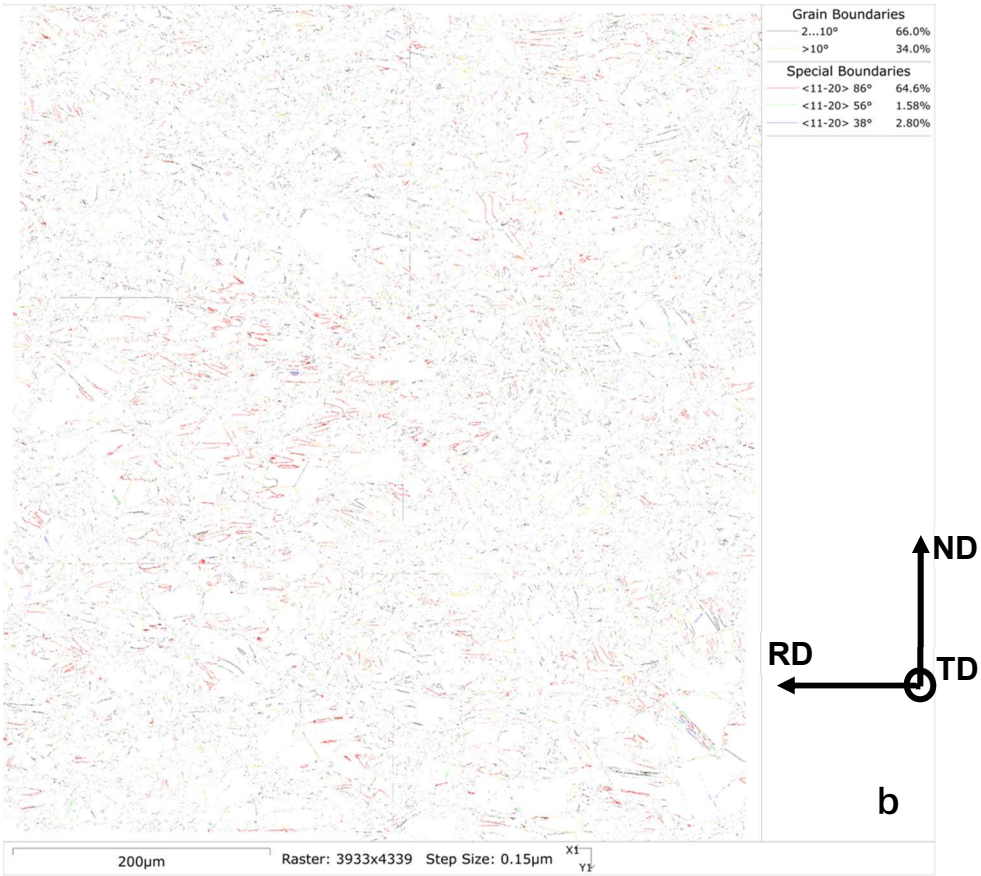
Grain Boundaries
2...10° 66.0%
>10° 34.0%
Special Boundaries
<11-20> 86° 64.6%
<11-20> 56° 1.58%
<11-20> 38° 2.80%
ND
RD
TD
b
200µm
Raster: 3933x4339 Step Size: 0.15µm
X1
Y1

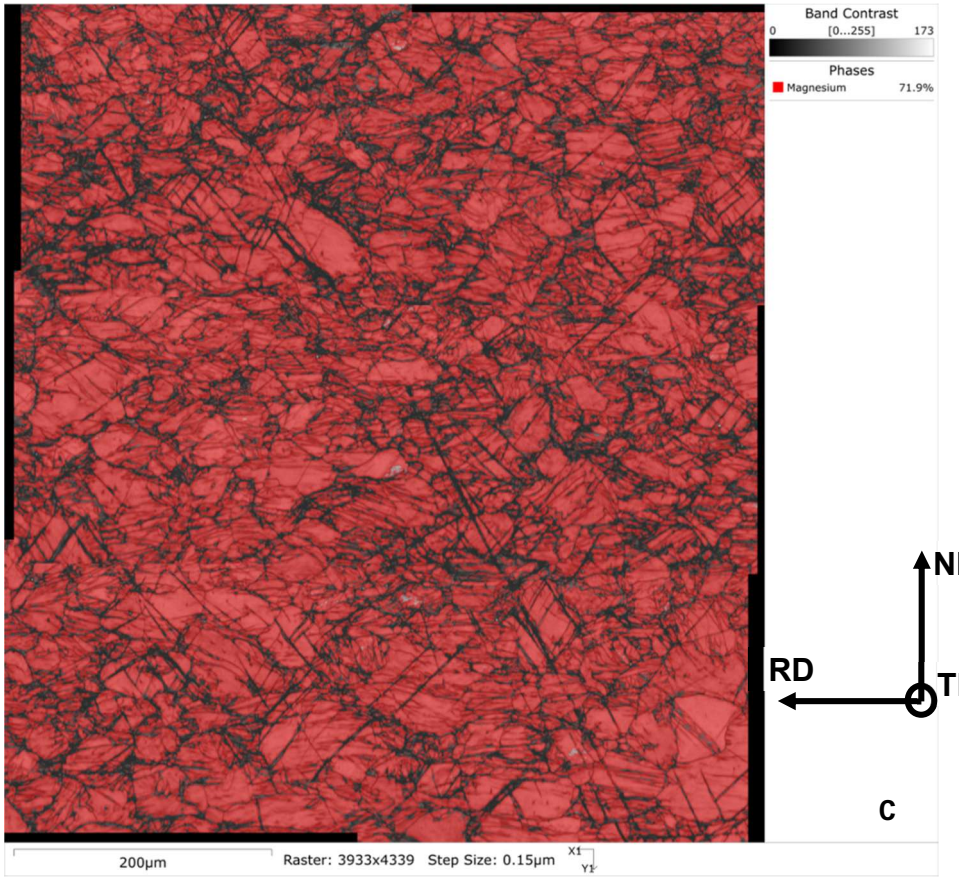
Band Contrast
0
[0...255]
173
Phases
Magnesium
71.9%
ND
RD
TD
c
200µm
Raster: 3933x4339
Step Size: 0.15µm
X1
Y1

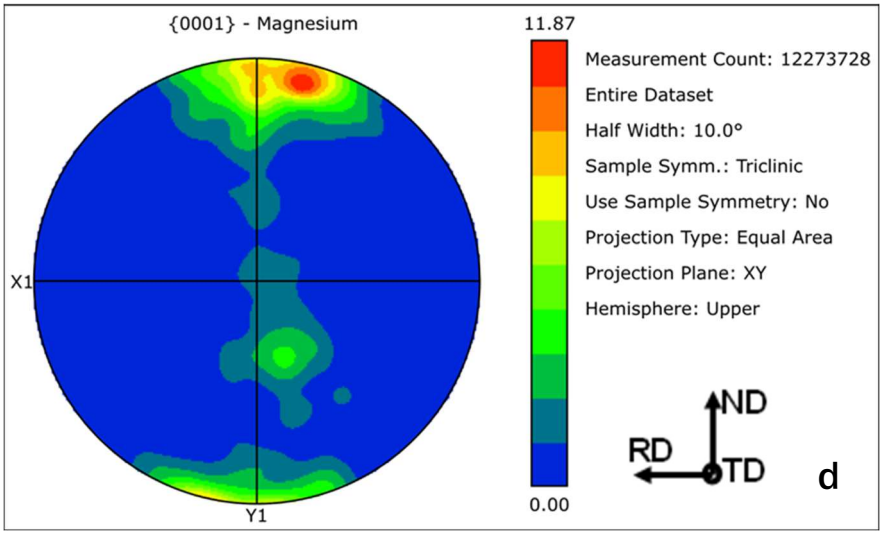
{0001} - Magnesium
11.87
0.00
Measurement Count: 12273728
Entire Dataset
Half Width: 10.0°
Sample Symm.: Triclinic
Use Sample Symmetry: No
Projection Type: Equal Area
Projection Plane: XY
Hemisphere: Upper
X1
Y1
ND
RD
TD
d

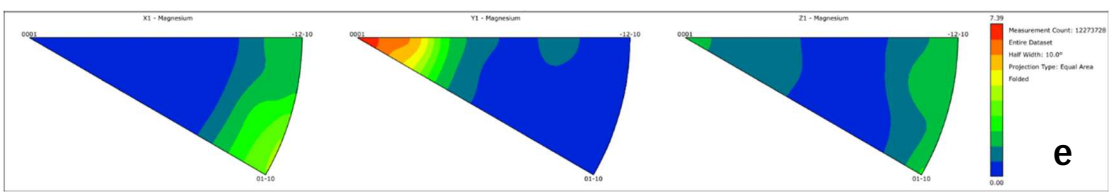
X1 - Magnesium
Y1 - Magnesium
Z1 - Magnesium
e

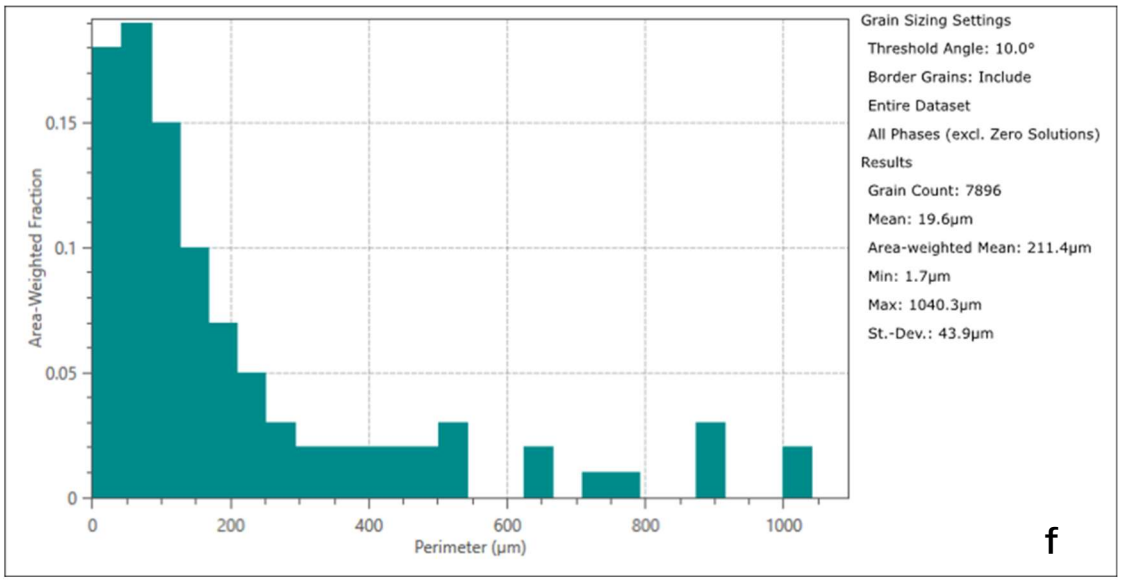

Figure 4-35 The EBSD result of the 1D compressed Mg-0.5Zn specimen: (a) The inverse pole figure map and grain boundaries, (b) The grain boundaries and the special grain boundaries, (c) The band contrast and the phase analysis, (d) The pole figure, (e) The inverse pole figures, (f) Grain size distribution expressed as grain boundary perimeter

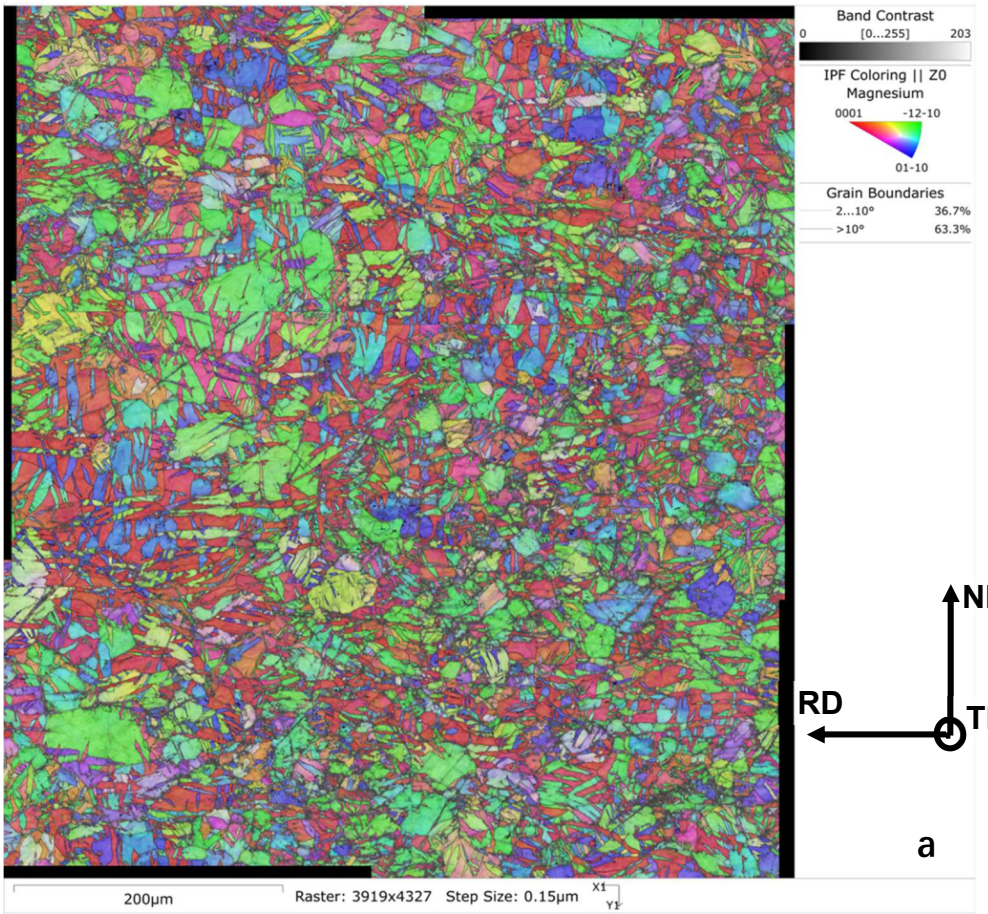

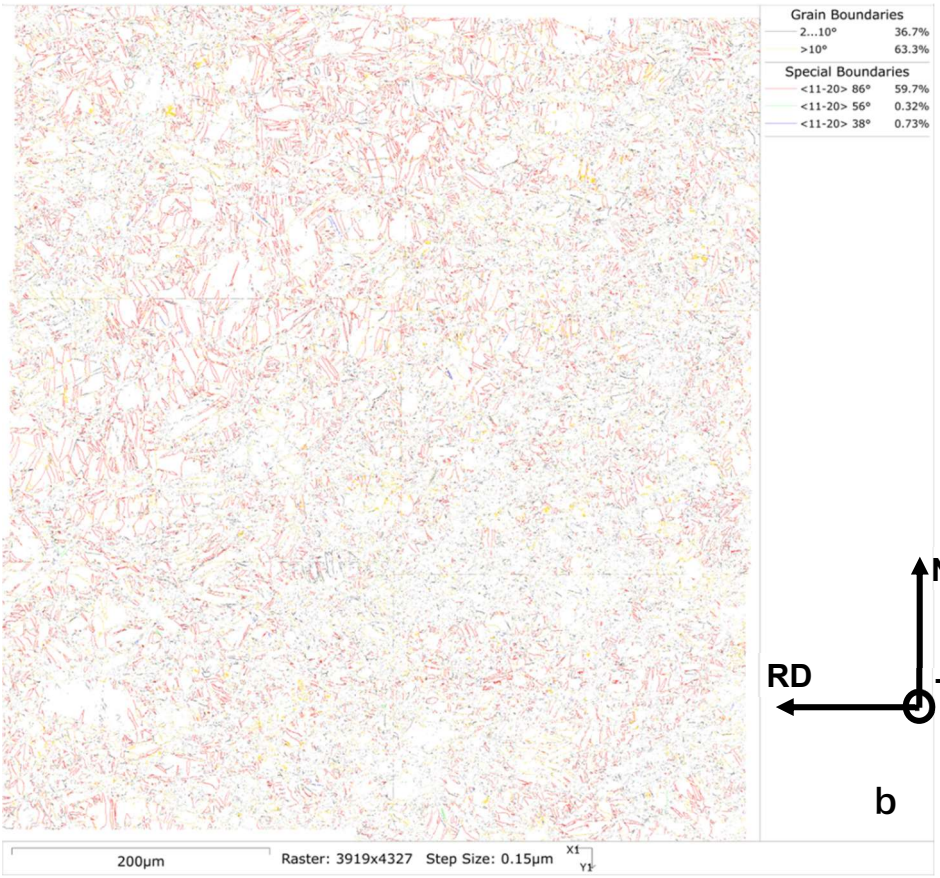
Grain Boundaries
2...10° 36.7%
>10° 63.3%
Special Boundaries
<11-20> 86° 59.7%
<11-20> 56° 0.32%
<11-20> 38° 0.73%
ND
RD
TD
b
200µm
Raster: 3919x4327 Step Size: 0.15µm
X1
Y1

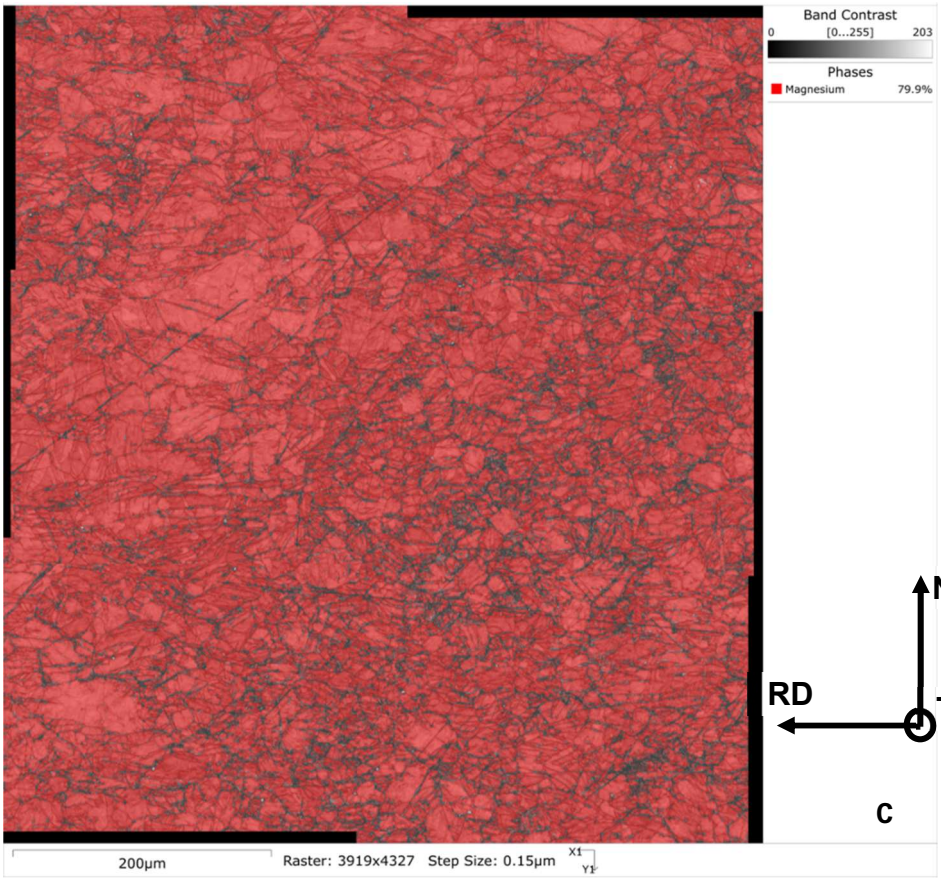
Band Contrast
0 [0...255] 203
Phases
Magnesium 79.9%
ND
RD
TD
c
200µm
Raster: 3919x4327 Step Size: 0.15µm
X1
Y1

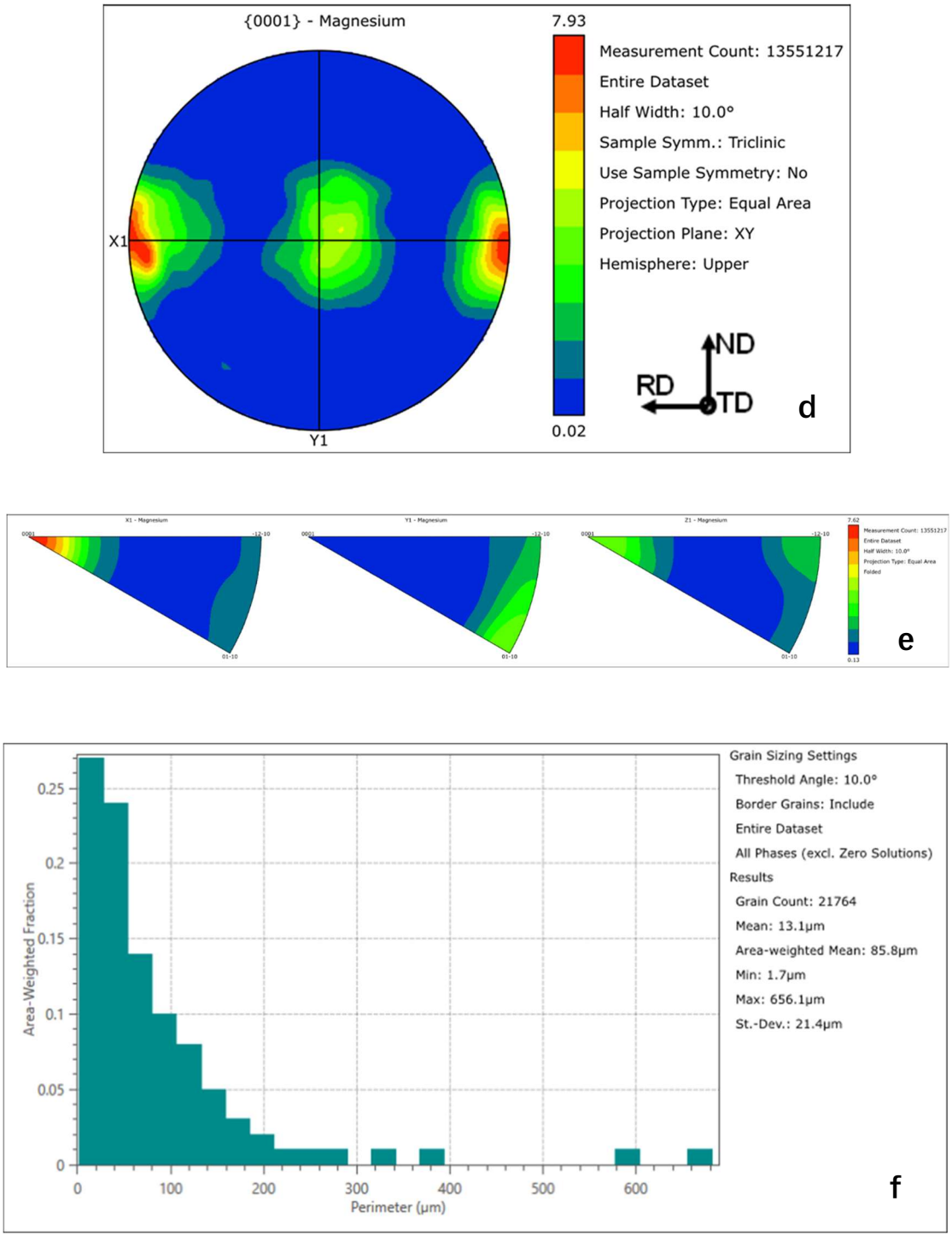

Figure 4-36 The EBSD result of the 2D compressed Mg-0.5Zn specimen: (a) The inverse pole figure map and grain boundaries, (b) The grain boundaries and the special grain boundaries, (c) The band contrast and the phase analysis, (d) The pole figure, (e) The inverse pole figures, (f) Grain size distribution expressed as grain boundary perimeter

Following the 180s annealing all specimens except the 1D compressed Mg-0.1Ca-0.4Zn (at%) sample exhibited an almost fully recrystallized microstructure, as shown in Figures 4-38, 4-39, and 4-40. According to Figure 4-34, the temperature of the samples after 180 seconds of annealing reached 257℃, which was significantly lower than the target process temperature (350℃). For the Mg-0.1Ca-0.4Zn (at%) specimen, a recrystallized structure (shown in Figure 4-37) was only achieved after an additional 360s of annealing, resulting in a total annealing time of 540s. The maximum temperature recorded during this extended annealing process was 325℃. As seen in Figure 4-37(a), recrystallization was strongly influenced by the non-uniform grain size. Two large grains, shown in green and yellow in Figure 4-33(a), persisted even after the extended annealing period, while the rest part of the sample exhibited a uniform recrystallized grain structure with an average grain size of $21\mu m$. The grain boundary analysis (Figures 4-37(b)) revealed unexpected results regarding boundary identification. The high-angle grain boundaries (shown in yellow) and the twin boundaries (shown in red) were identified as distributed within some recrystallized grains. Additionally, the pole figure (shown in Figure 4-37(d)(e)) show a reduction in maximum pole intensity from 19.3 to 10.6. The distribution of the grain orientation was diffused around the TD. However, the strongest point shown in the pole figure was still the same as that of the 1D compressed specimen.

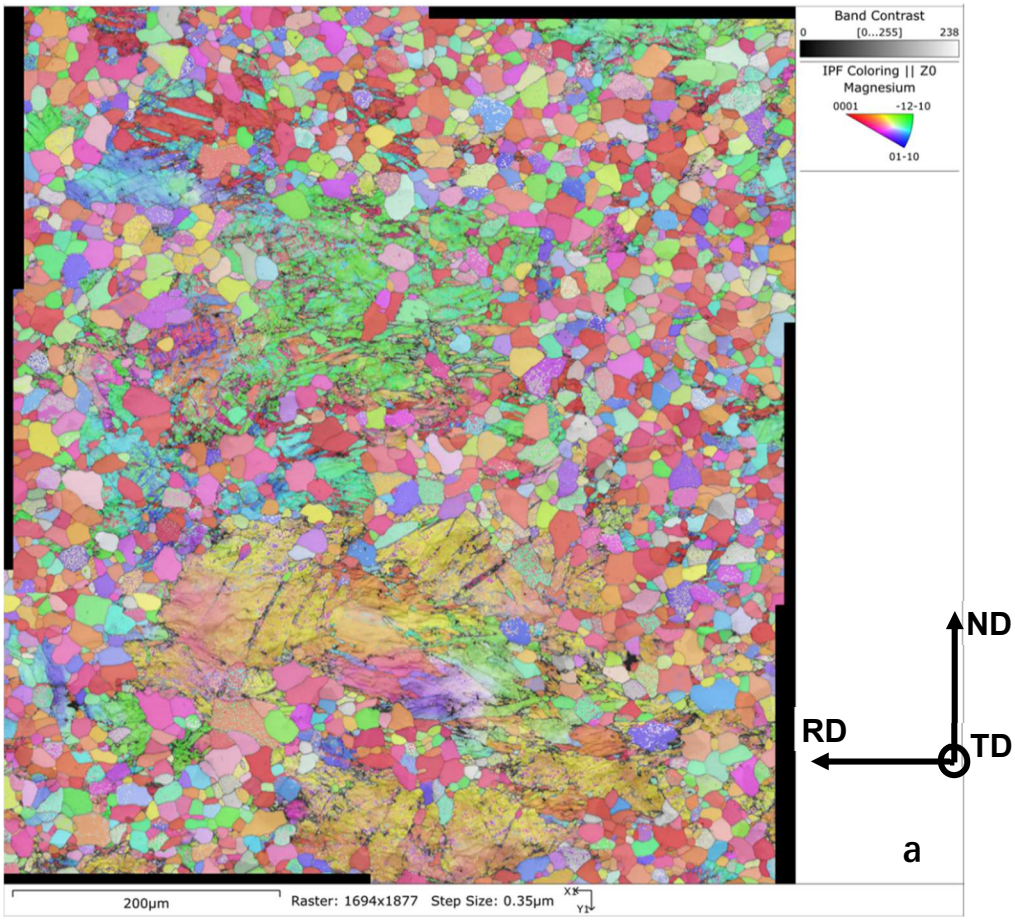

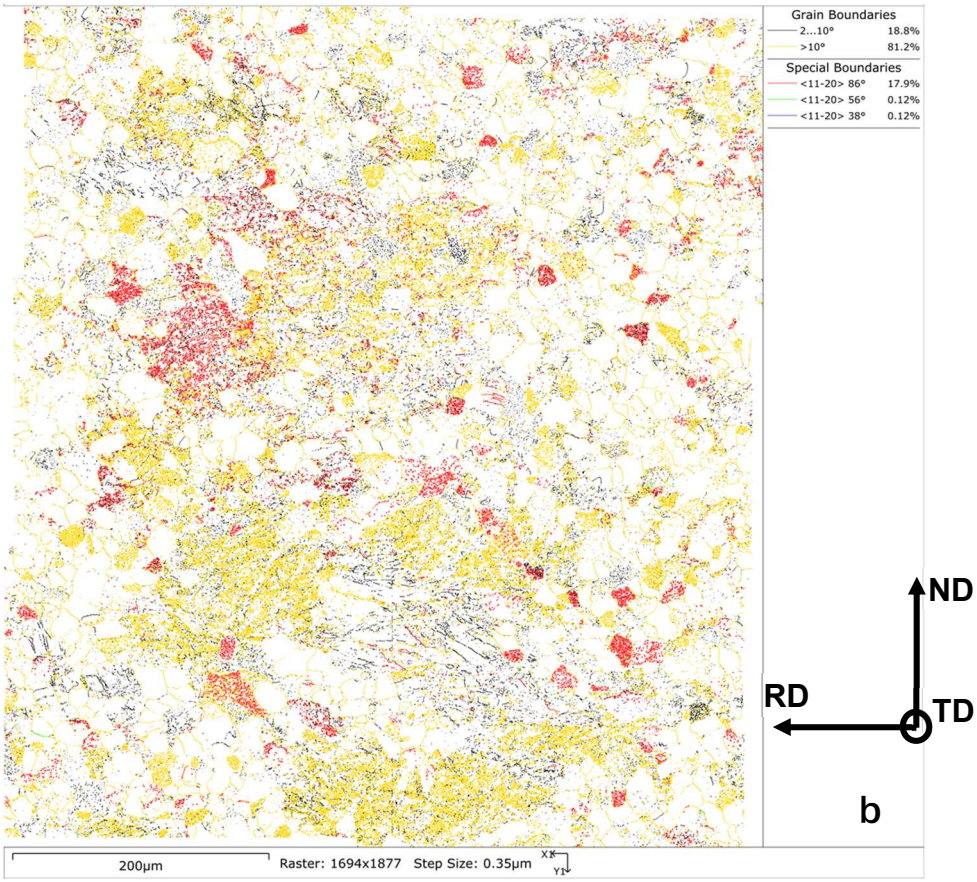
Grain Boundaries
2...10° 18.8%
>10° 81.2%
Special Boundaries
<11-20> 86° 17.9%
<11-20> 56° 0.12%
<11-20> 38° 0.12%
ND
RD
TD
b
200µm
Raster: 1694x1877 Step Size: 0.35µm

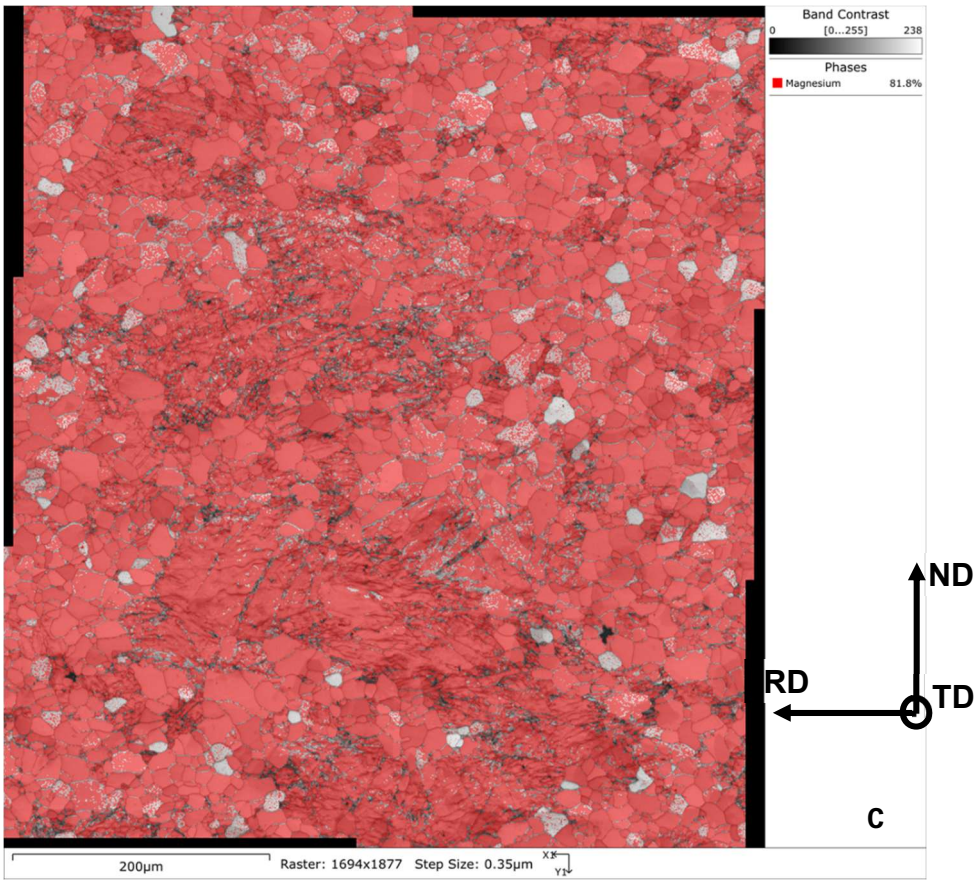
Band Contrast
0 [0...255] 238
Phases
Magnesium 81.8%
ND
RD
TD
c
200µm
Raster: 1694x1877 Step Size: 0.35µm

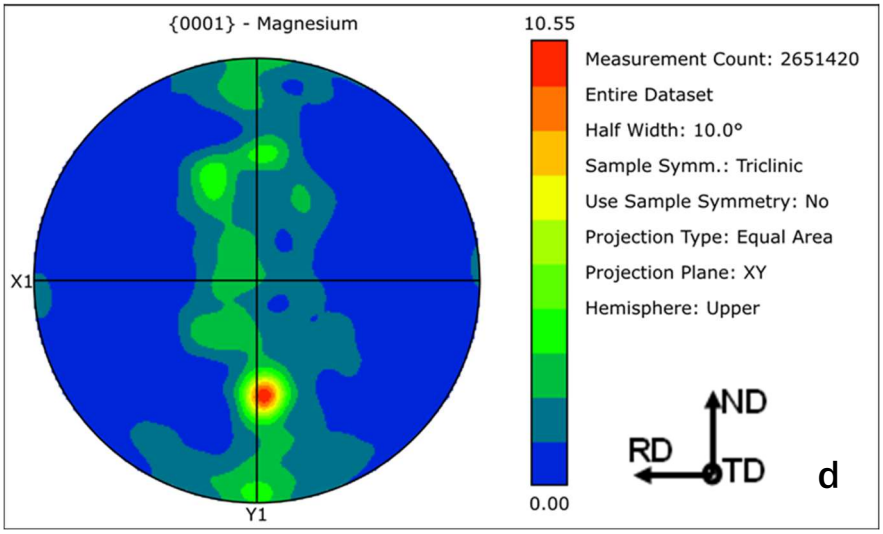

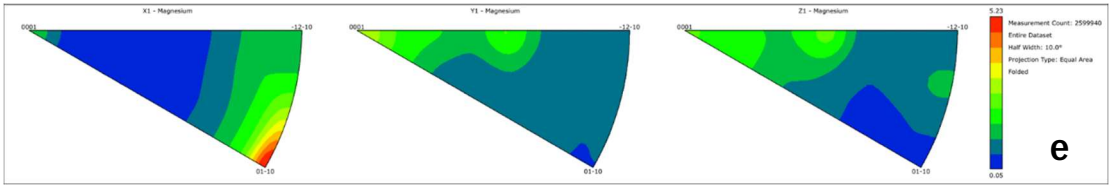

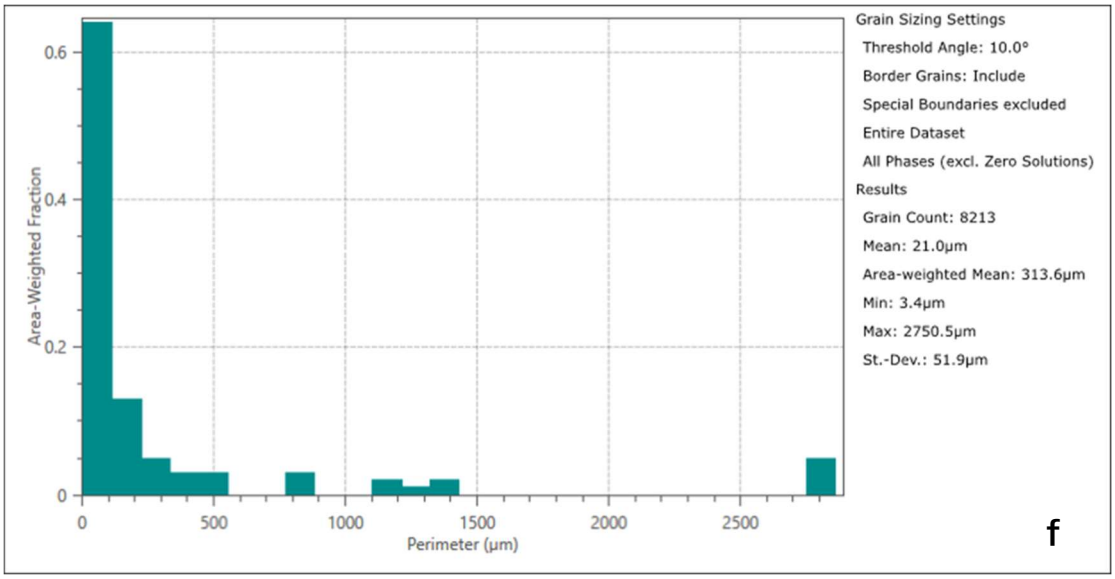

Figure 4-37 The EBSD result of the 1D compressed 540s annealed Mg-0.1Ca0.4Zn specimen: (a) The inverse pole figure map and grain boundaries, (b) The grain boundaries and the special grain boundaries, (c) The band contrast and the phase analysis, (d) The pole figure, (e) The inverse pole figures, (f) Grain size distribution expressed as grain boundary perimeter

Figure 4-38 presents results for the 2D compressed Mg-0.1Ca-0.4Zn (at%) specimen after the 180s annealing. An average recrystallized grain size of 22μm was noted (shown in Figure 4-38(f)), along with the persistence of large grains, such as the prominent grain (coloured green) in the top-center area (shown in Figure 4-38(a)). Boundary analysis (Figures 4-38(b)) confirms that the majority of the area was fully recrystallized. The fractions of tensile twins, compressive twins, and double twins were quantified as 8.2%, 0.4%, and 0.5%, respectively. Figure 4-38(d)(e) show that the maximum pole intensity of the specimen decreased to 6.1 following 180s of annealing. The grain orientation distribution exhibited a trend similar to that of the 1D compressed specimen, with recrystallized grains showing a tendency to diffuse around the transverse direction (TD). Furthermore, the strongest orientation signal remained the same as that of the compressed specimen.

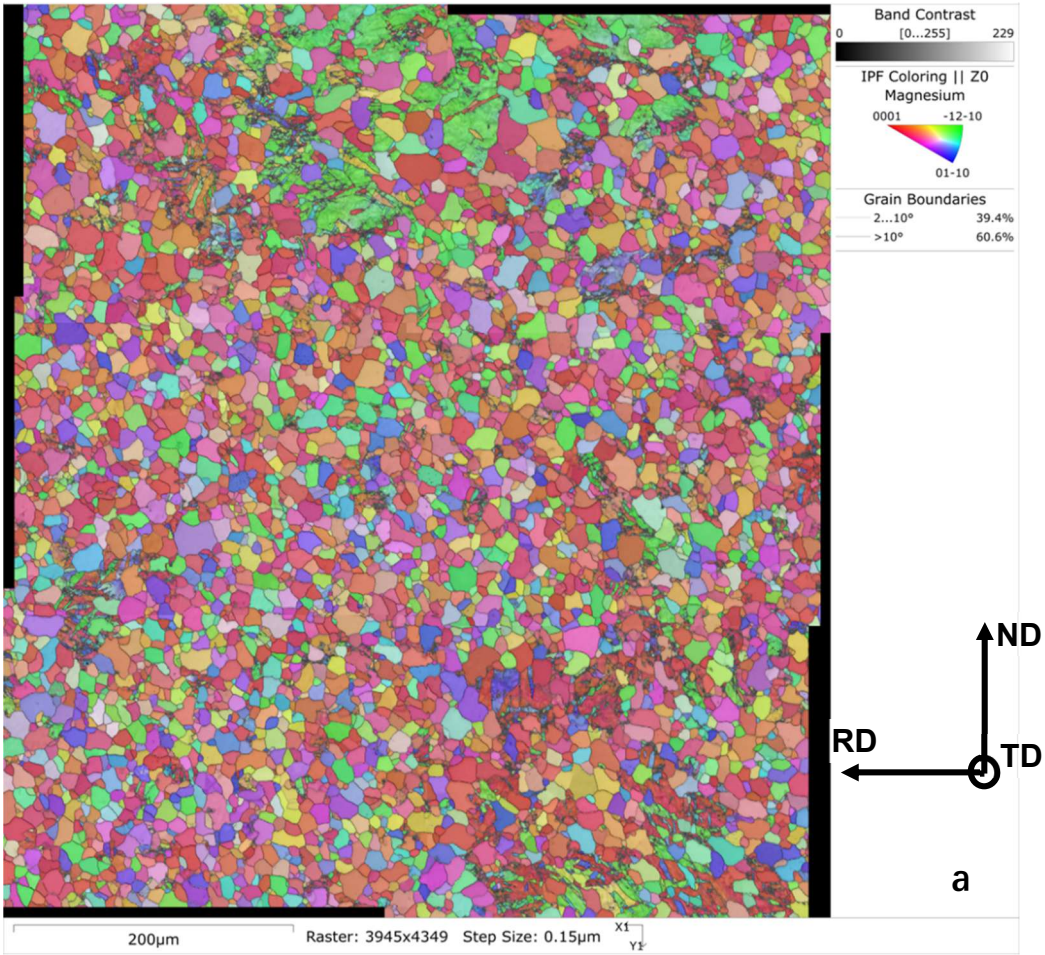

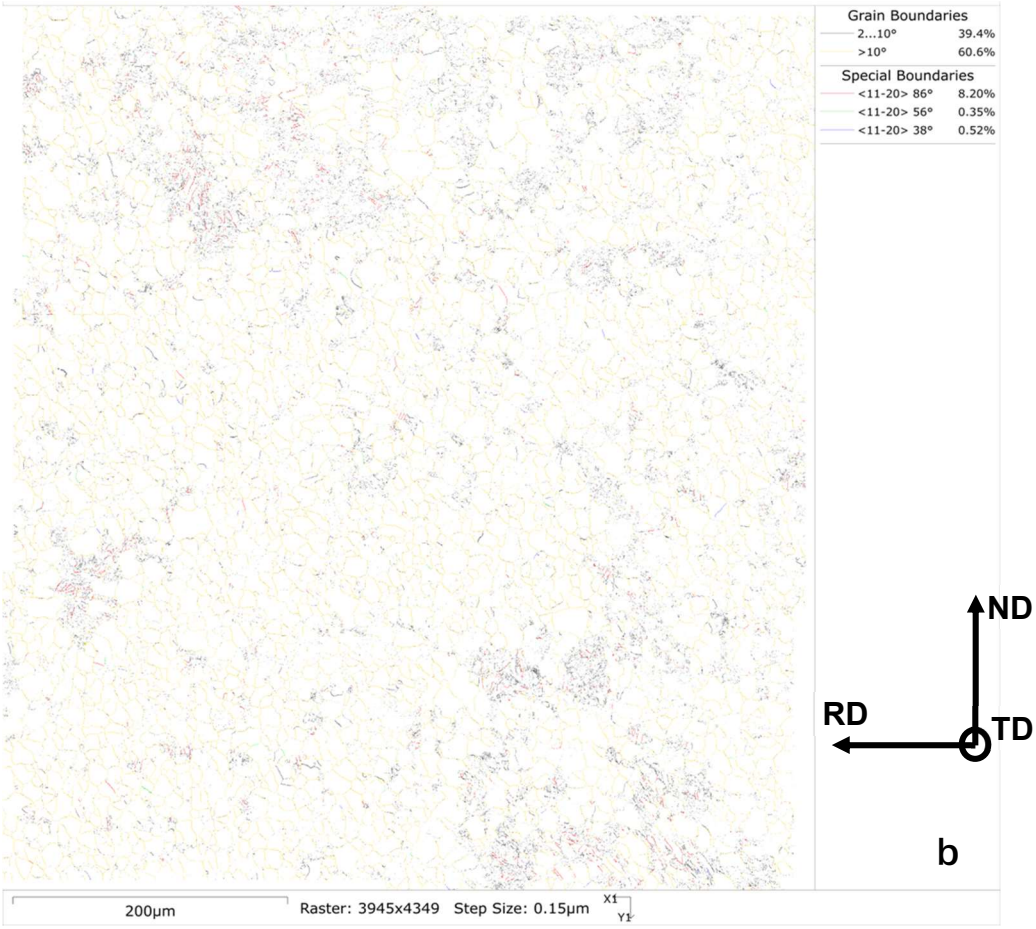
Grain Boundaries
2...10° 39.4%
>10° 60.6%
Special Boundaries
<11-20> 86° 8.20%
<11-20> 56° 0.35%
<11-20> 38° 0.52%
ND
RD
TD
b
200µm
Raster: 3945x4349 Step Size: 0.15µm

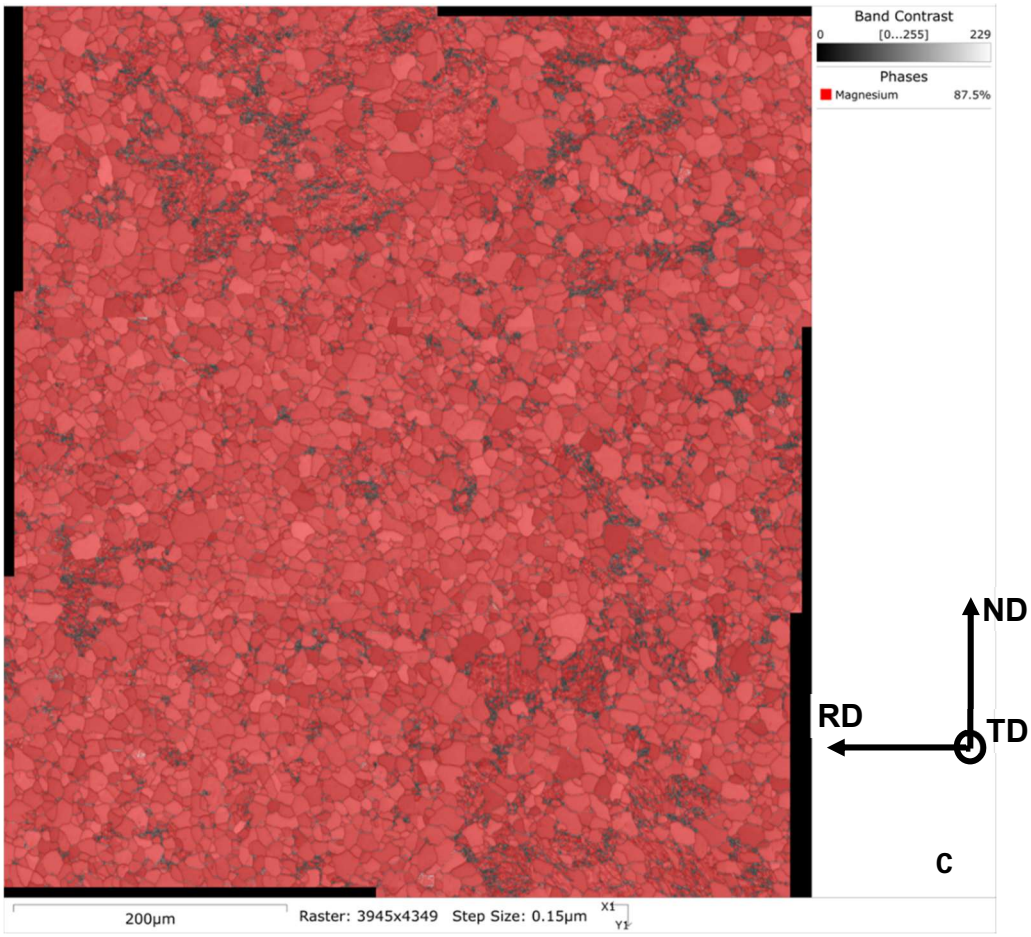
Band Contrast
0 [0...255] 229
Phases
Magnesium 87.5%
ND
RD
TD
c
200µm
Raster: 3945x4349 Step Size: 0.15µm

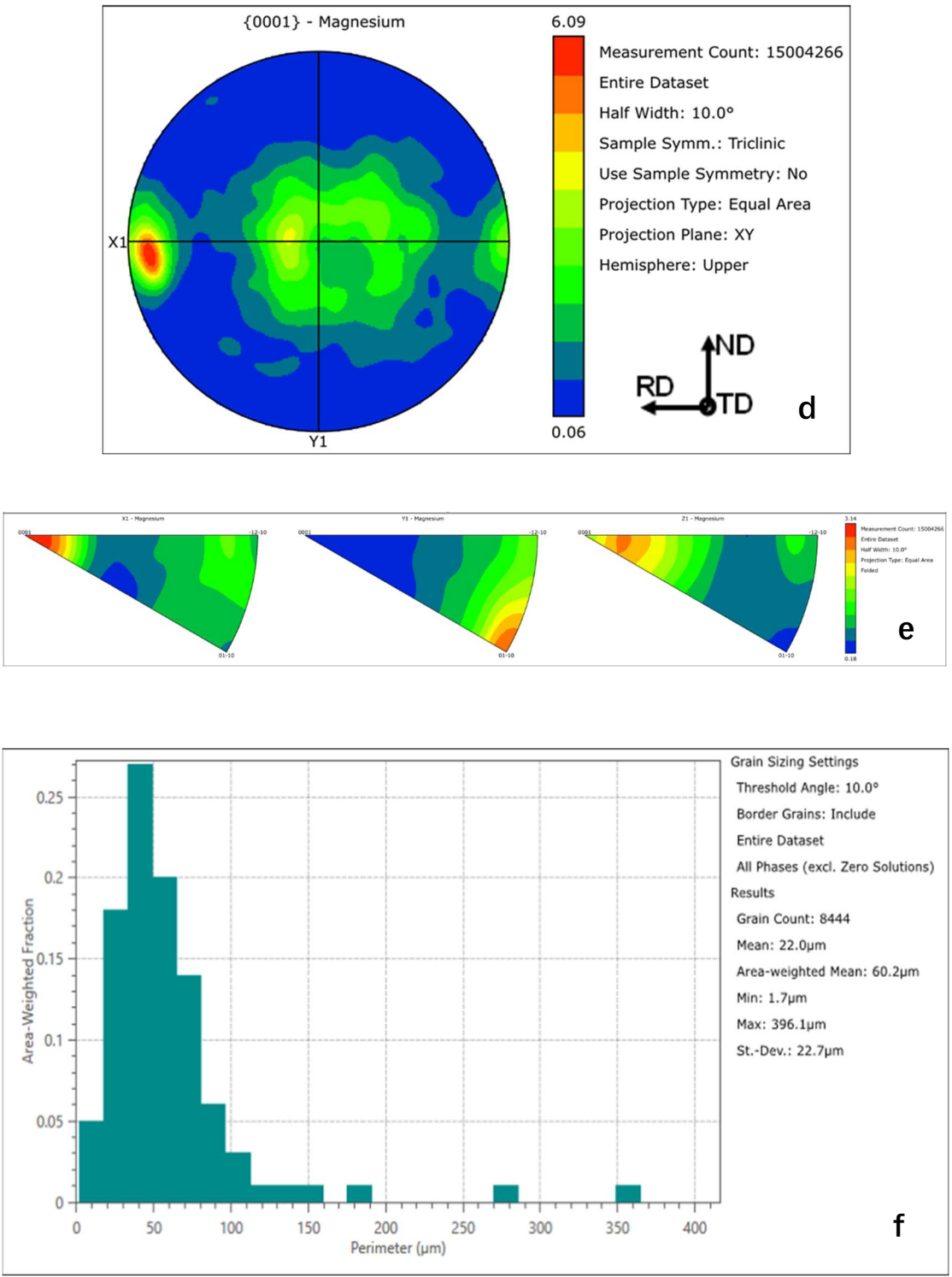

Figure 4-38 The EBSD result of the 2D compressed 180s annealed Mg-0.1Ca0.4Zn specimen: (a) The inverse pole figure map and grain boundaries, (b) The grain boundaries and the special grain boundaries, (c) The band contrast and the phase analysis, (d) The pole figure, (e) The inverse pole figures, (f) Grain size distribution expressed as grain boundary perimeter

For the Mg-0.5Zn specimens, both kinds of specimens showed a quite complete recrystallization structure in the IPF maps (shown in Figure 4-39(a) and Figure 4-40(a)). The average grain size of the annealed 1D and 2D compressed specimens was 83.4μm and 71.7μm, respectively (shown in Figure 4-39(f) and Figure 4-40(f)). The fractions of the tensile twins, compressive twins and double twins in the annealed 1D compressed Mg-0.5Zn (at%) specimen were reduced to 1.9%, 0.2% and 0.4%, respectively. For the 2D compressed Mg-0.5Zn (at%) specimen, these fractions were 5.0%, 0.1%, and 0.3%, respectively (shown in Figure 4-39(b) and Figure 4-40(b)). Figure 4-39(d)(e) indicate that the orientation distribution of the recrystallized grains in the 180s annealed 1D compressed Mg-0.5Zn (at%) sample was very similar to that of the Mg-0.1Ca-0.4Zn (at%) specimen. The grain orientation distributed on the ND-axis i.e. from ND to TD. The maximum value of the pole figure was 5.7. The pole figure of the recrystallized 2D compressed Mg-0.5Zn (at%) sample (shown in Figure 4-40(d)(e)) exhibited a typical basal texture with a maximum pole intensity of 9.3. The orientation distribution in this specimen was very different to the other three specimens which was concentrated in TD.

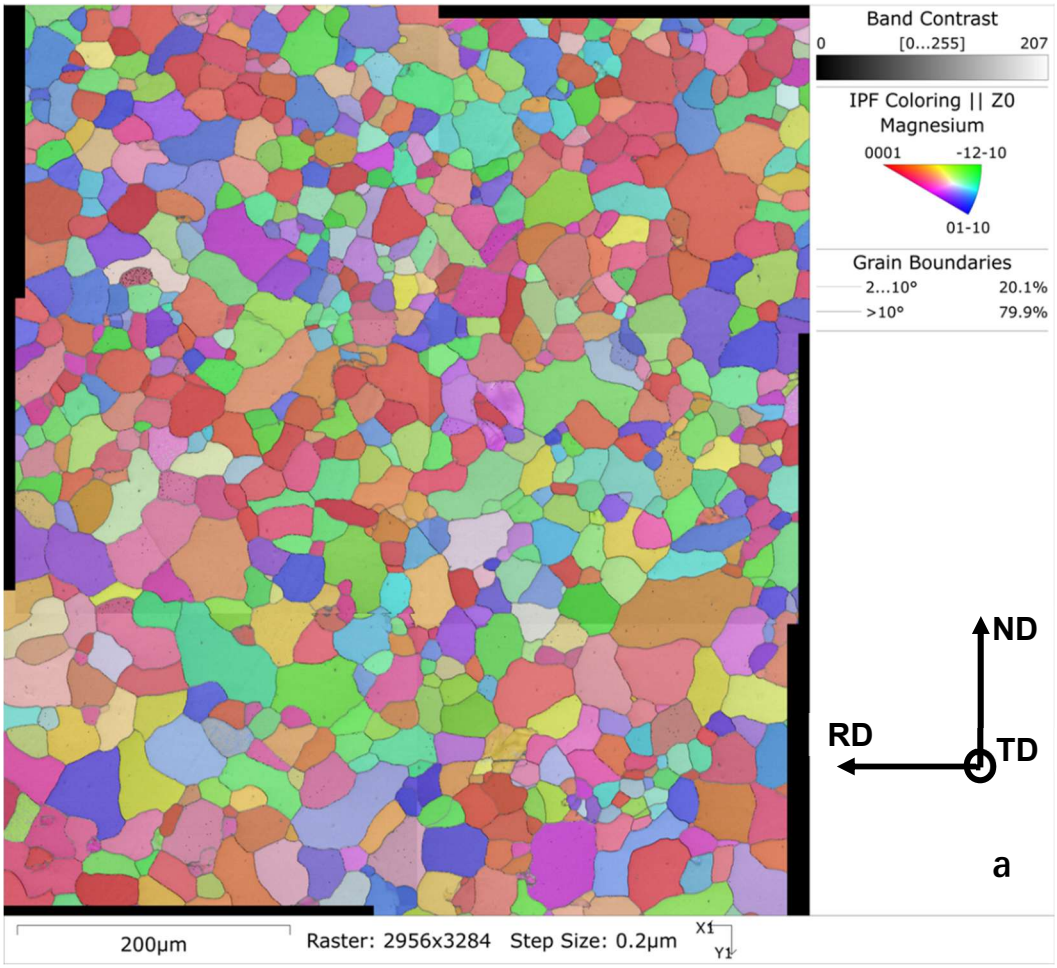

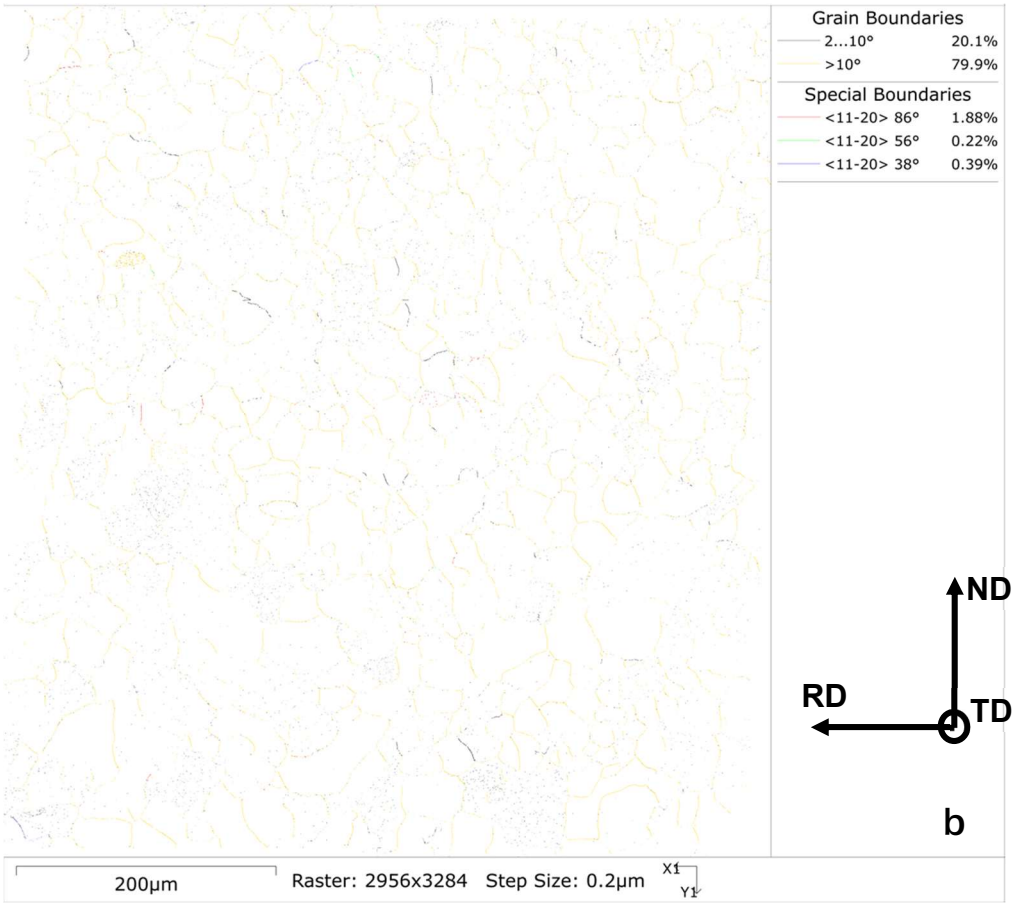
Grain Boundaries
2...10° 20.1%
>10° 79.9%
Special Boundaries
<11-20> 86° 1.88%
<11-20> 56° 0.22%
<11-20> 38° 0.39%
ND
RD
TD
b
200µm
Raster: 2956x3284 Step Size: 0.2µm
X1
Y1

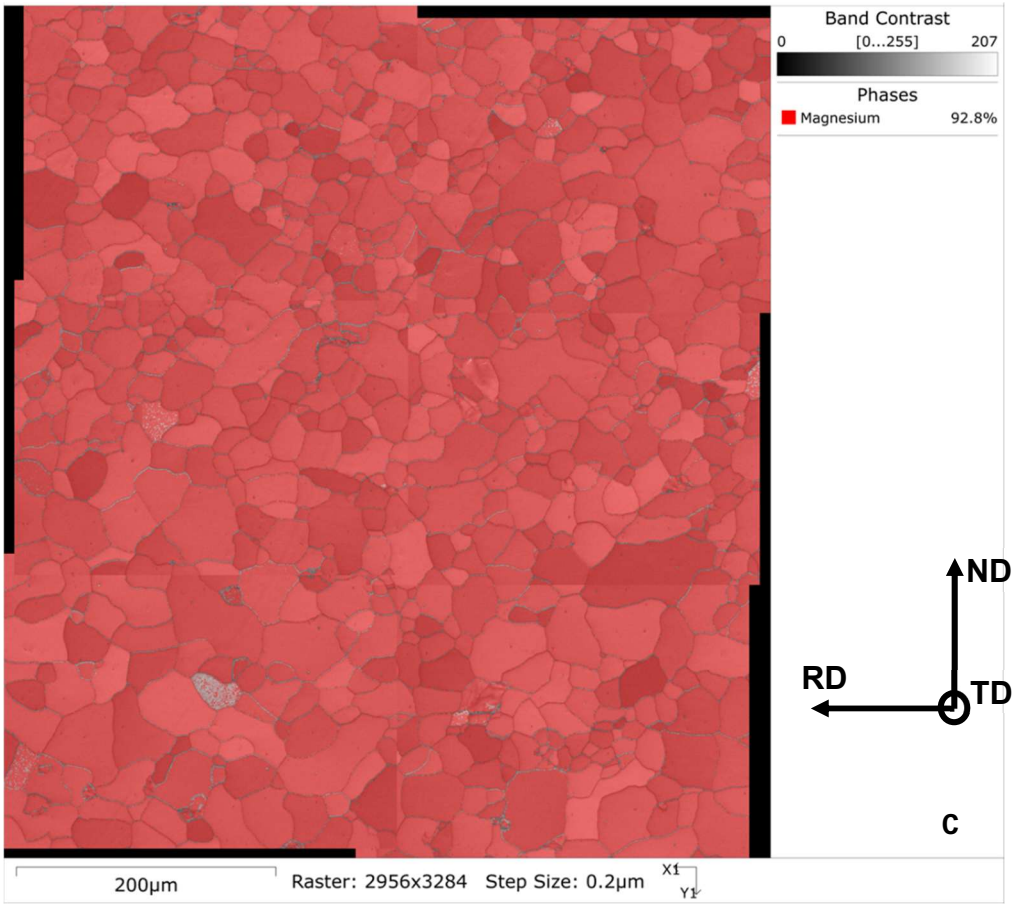
Band Contrast
0 [0...255] 207
Phases
Magnesium 92.8%
ND
RD
TD
c
200µm
Raster: 2956x3284 Step Size: 0.2µm
X1
Y1

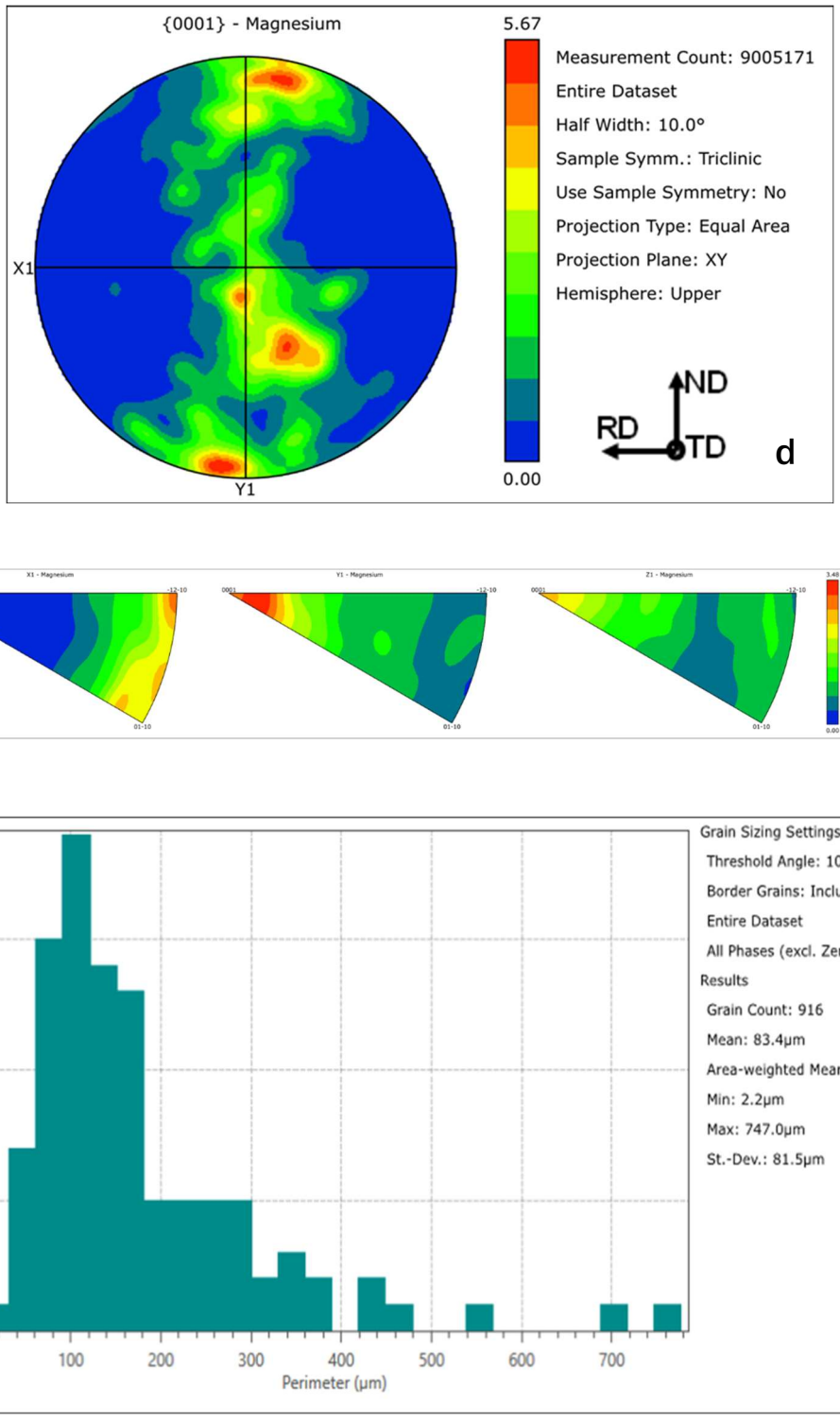

Figure 4-39 The EBSD result of the 1D compressed 180s annealed Mg-0.5Zn specimen: (a) The inverse pole figure map and grain boundaries, (b) The grain boundaries and the special grain boundaries, (c) The band contrast and the phase analysis, (d) The pole figure, (e) The inverse pole figures, (f) Grain size distribution expressed as grain boundary perimeter

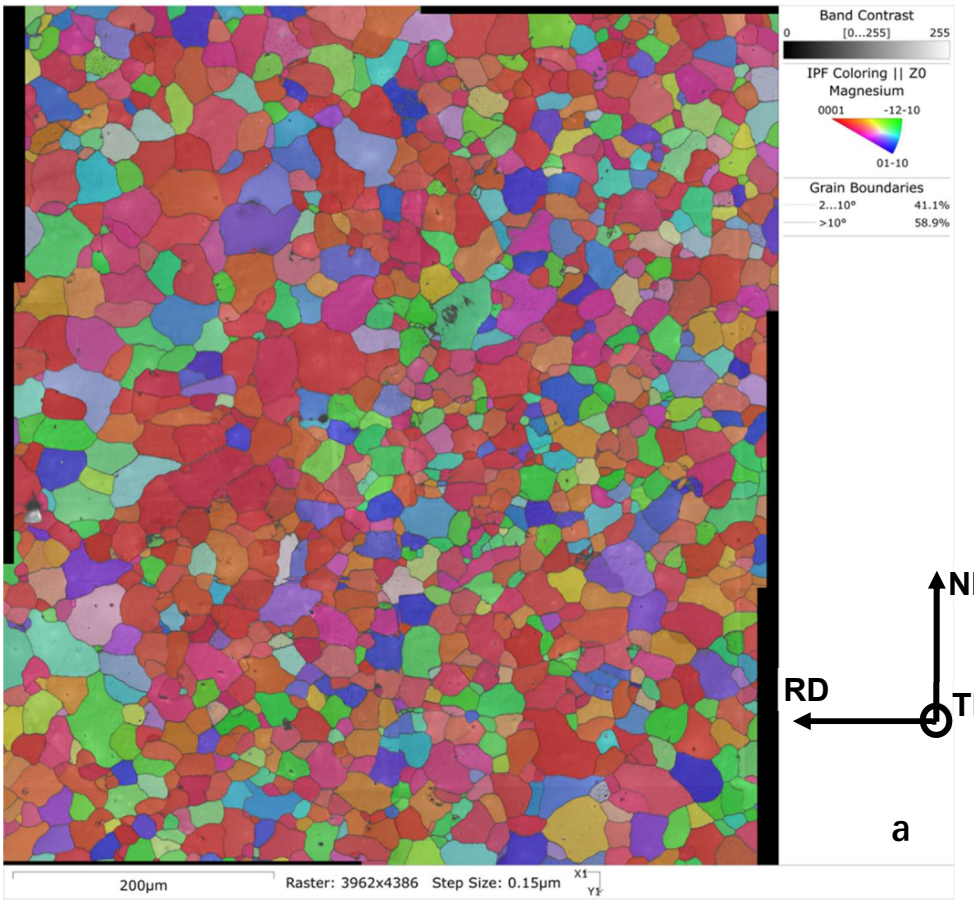
Band Contrast
0
[0...255]
255
IPF Coloring || Z0
Magnesium
0001
-12-10
01-10
Grain Boundaries
2...10°
41.1%
>10°
58.9%
ND
RD
TD
a
200µm
Raster: 3962x4386 Step Size: 0.15µm
X1
Y1

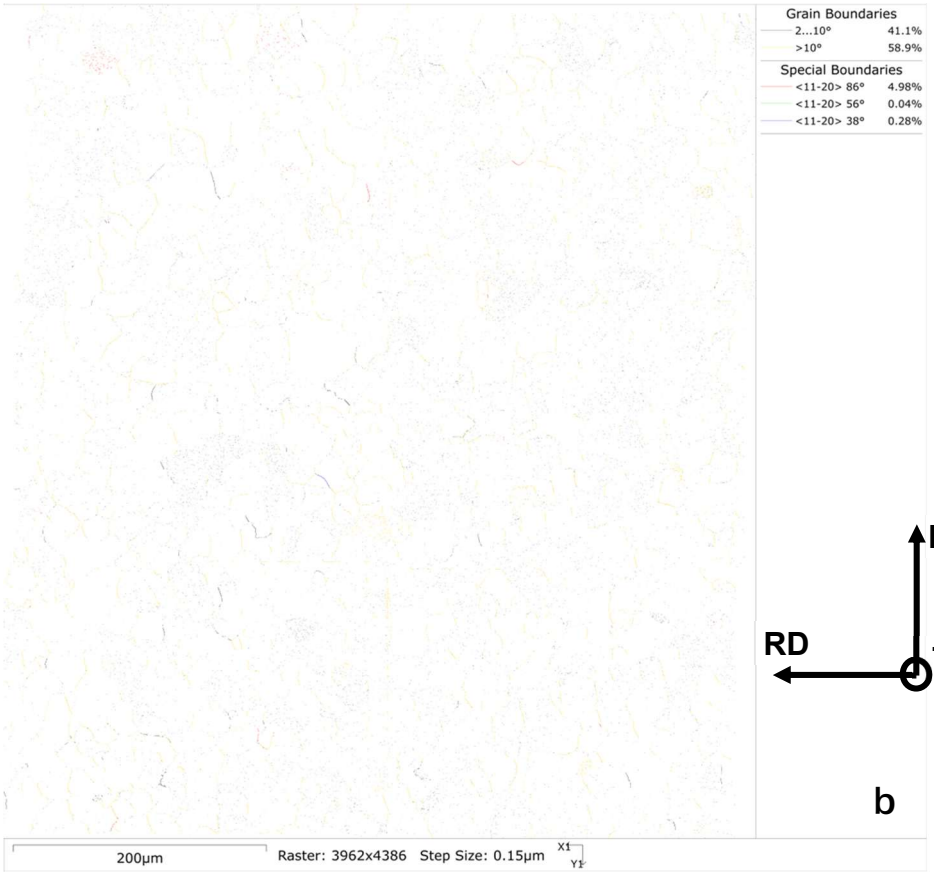
Grain Boundaries
2...10°
41.1%
>10°
58.9%
Special Boundaries
<11-20> 86°
4.98%
<11-20> 56°
0.04%
<11-20> 38°
0.28%
ND
RD
TD
b
200µm
Raster: 3962x4386 Step Size: 0.15µm
X1
Y1

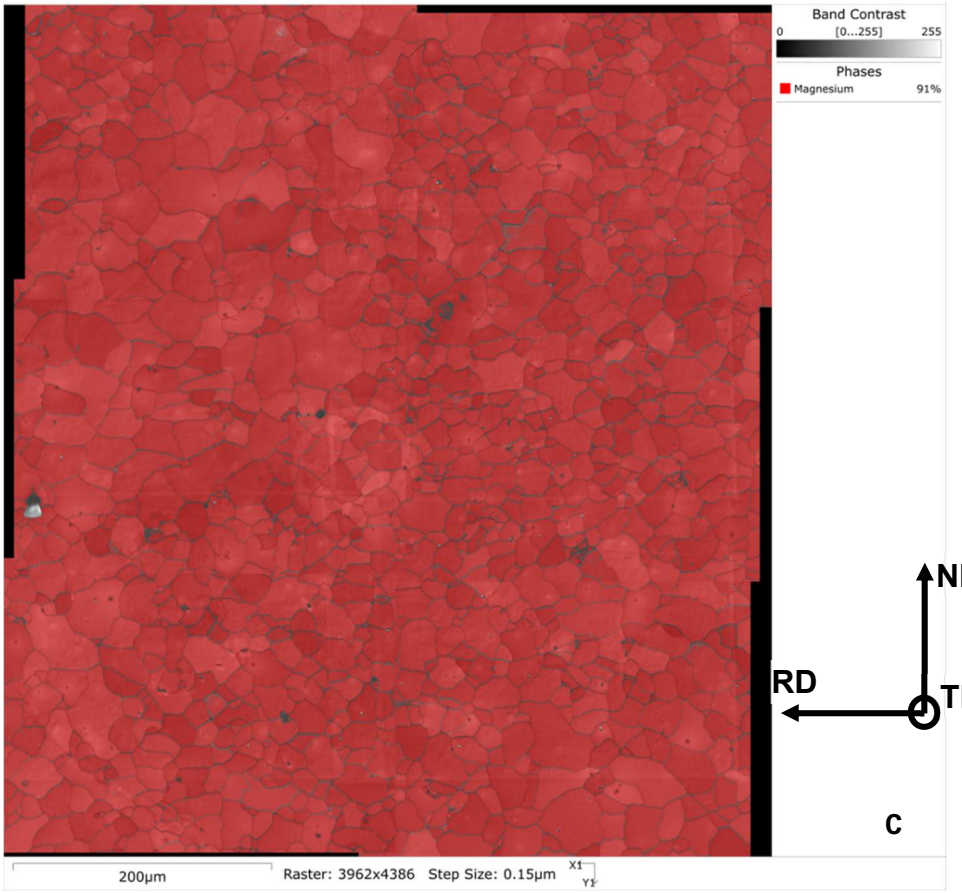
Band Contrast
0
[0...255]
255
Phases
Magnesium
91%
ND
RD
TD
c
200µm
Raster: 3962x4386
Step Size: 0.15µm
X1
Y1

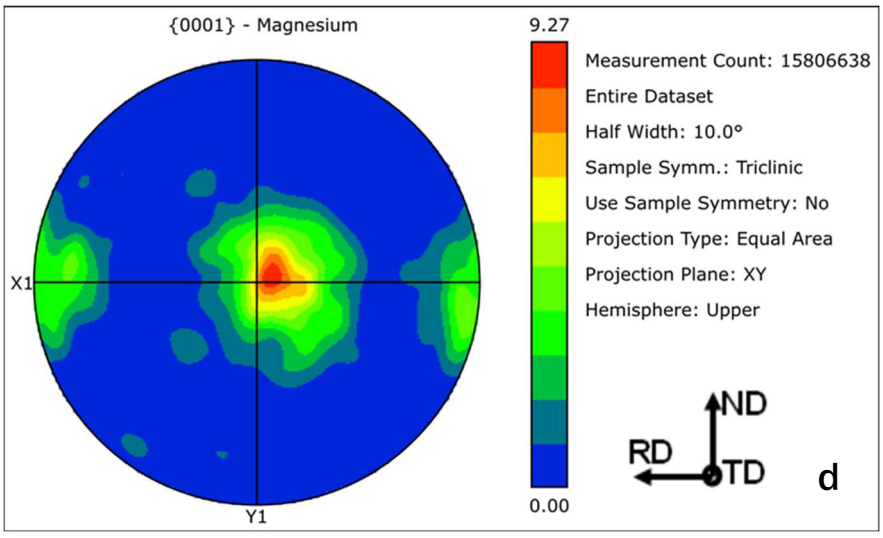
{0001} - Magnesium
9.27
0.00
Measurement Count: 15806638
Entire Dataset
Half Width: 10.0°
Sample Symm.: Triclinic
Use Sample Symmetry: No
Projection Type: Equal Area
Projection Plane: XY
Hemisphere: Upper
X1
Y1
ND
RD
TD
d

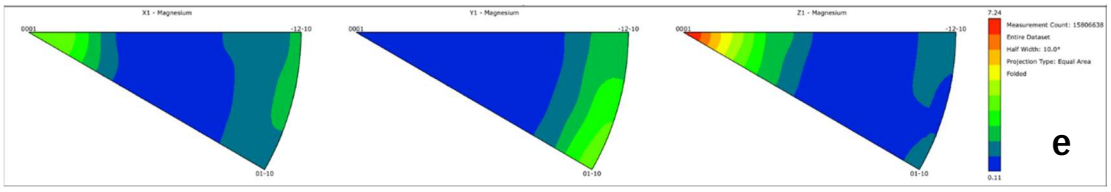
e

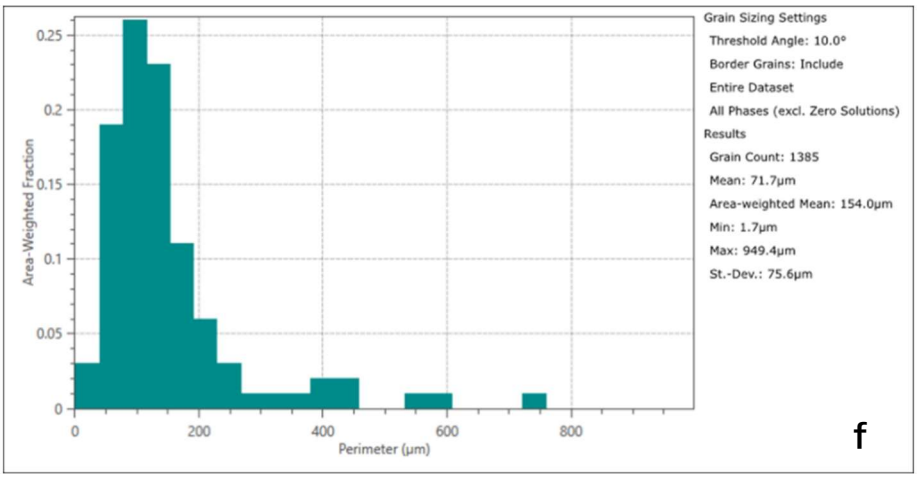

Figure 4-40 The EBSD result of the 2D compressed 180s annealed Mg-0.5Zn specimen: (a) The inverse pole figure map and grain boundaries, (b) The grain boundaries and the special grain boundaries, (c) The band contrast and the phase analysis, (d) The pole figure, (e) The inverse pole figures, (f) Grain size distribution expressed as grain boundary perimeter

4.3.2.2 The second round of the channel die (CD) compression experiment

In the second round of the experiment using second batch ingots, the annealing process time was adjusted to 30s, 45s, 60s, 75s, 90s 120s, 150s, 180s, 240s, 300s, 330s, 360s, 390s, 420s, 480s and 540s due to fast recrystallization of the samples (in total heat treatment time: 30s, 75s, 135s, 210s, 300s, 420s, 570s, 750s, 990s, 1290s, 1620s, 1980s, 2370s, 2790s, 3270s and 3810s). The reduced annealing time step allowed for detailed monitoring of texture evolution in all six specimens. Figures 4-41 to Figure 4-87 show the EBSD results of the 1D and 2D compressed Mg-0.2Ca-0.3Zn, Mg-0.1Ca-0.4Zn and Mg-0.5Zn (at%) specimens.

4.3.2.2.1 The one-direction (1D) compressed Mg-0.2Ca-0.3Zn (at%) specimen

Figure 4-41 to 4-50 show the EBSD results of the 1D compressed Mg-0.2Ca-0.3Zn (at%) specimen from the as-compressed state to the recrystallized state. The as-compressed specimen exhibited an uneven grain size (shown in Figure 4-41(a)). The large grain in the centre of the map had a size of over $500\mu m$, while the rest of the grains present a quite uniform size, averaging approximately $17.4\mu m$ (shown in Figure 4-41(g)). A significant number of shear bands (marked by white circles in Figure 4-41(c)) and fine twins were observed throughout the mapped area, occupying about 23% of the EBSD map (shown in Figure 4-41 (c)). The shear bands were found within the grains, across the grains and on the grain boundaries. Combining the result from Figure 4-41(b), the tensile twin boundaries accounted for 44.3% of the total boundary length and the compressive twin occupied 4.4% while the double twin boundary was 9.7%. Figure 4-41(e) and (f) indicated that the maximum pole intensity of this as-compressed

specimen was 27.3 and the grain orientation distribution was highly concentrated and predominantly aligned with the compression direction indicating the strong texture of the specimen.

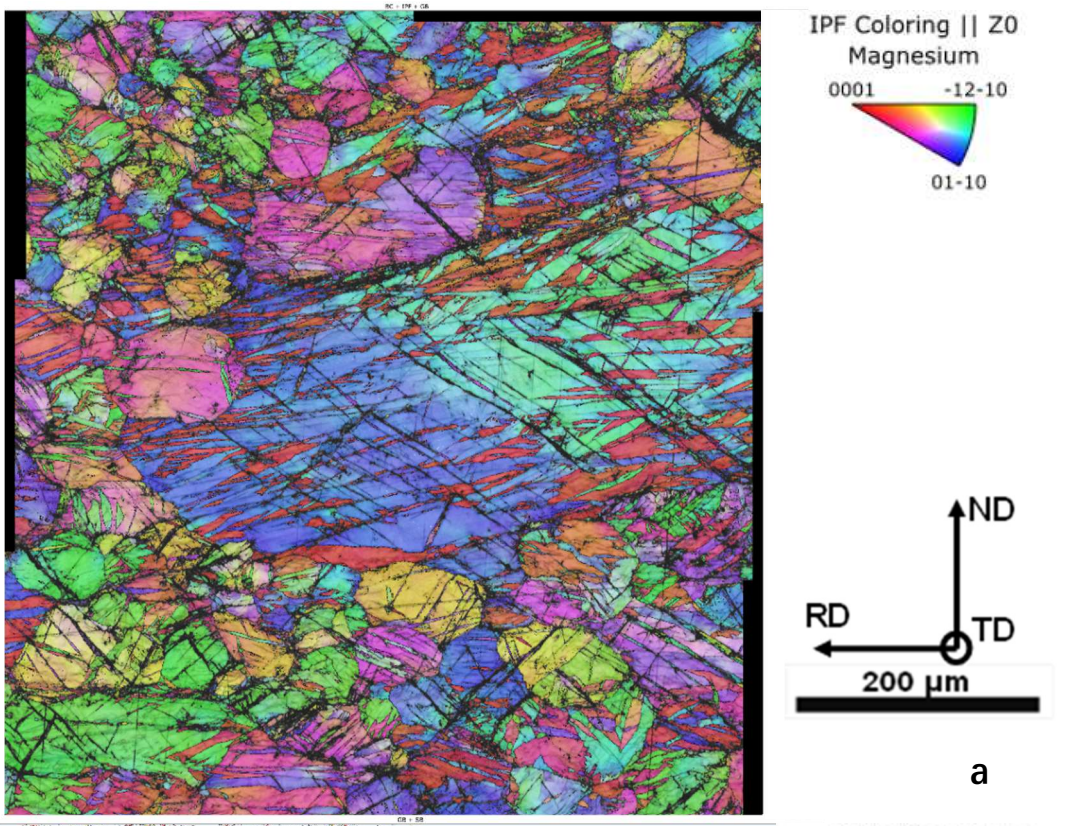

a

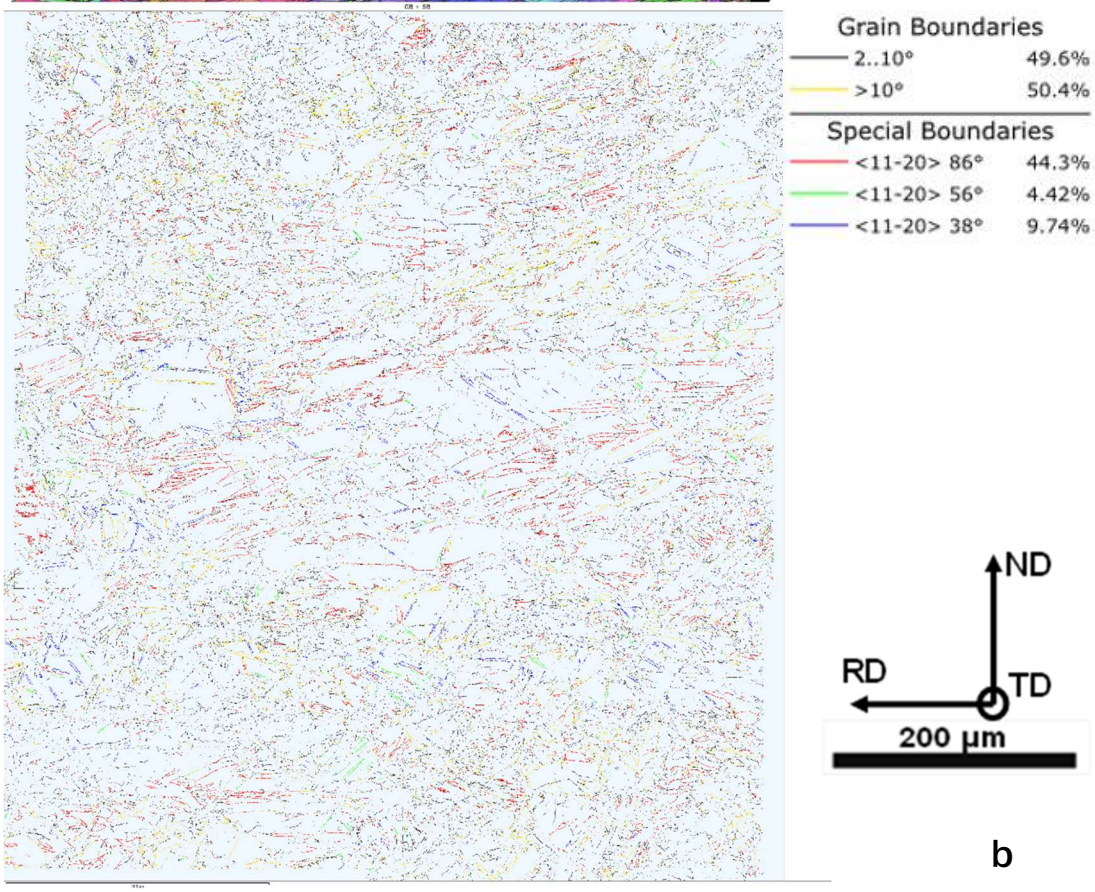

b

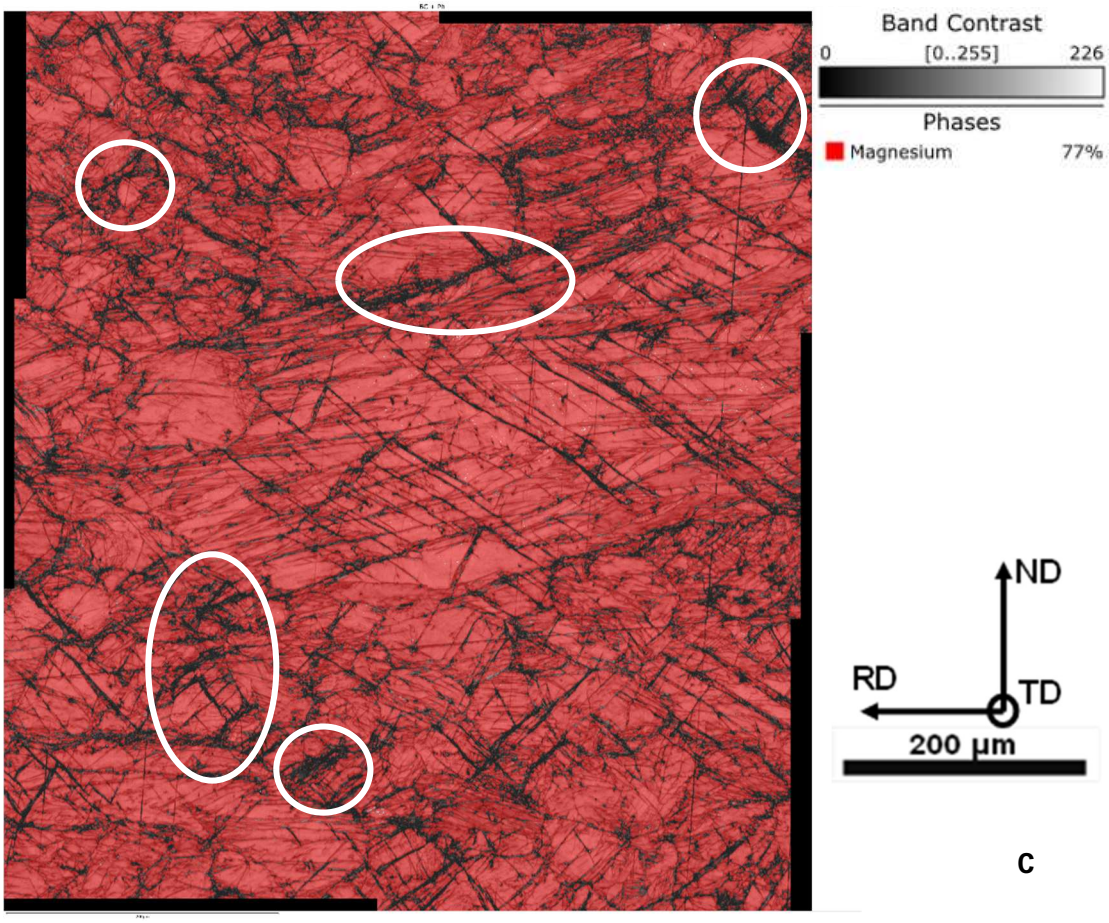
Band Contrast
0
[0..255]
226
Phases
Magnesium
77%
ND
RD
TD
200 µm

c

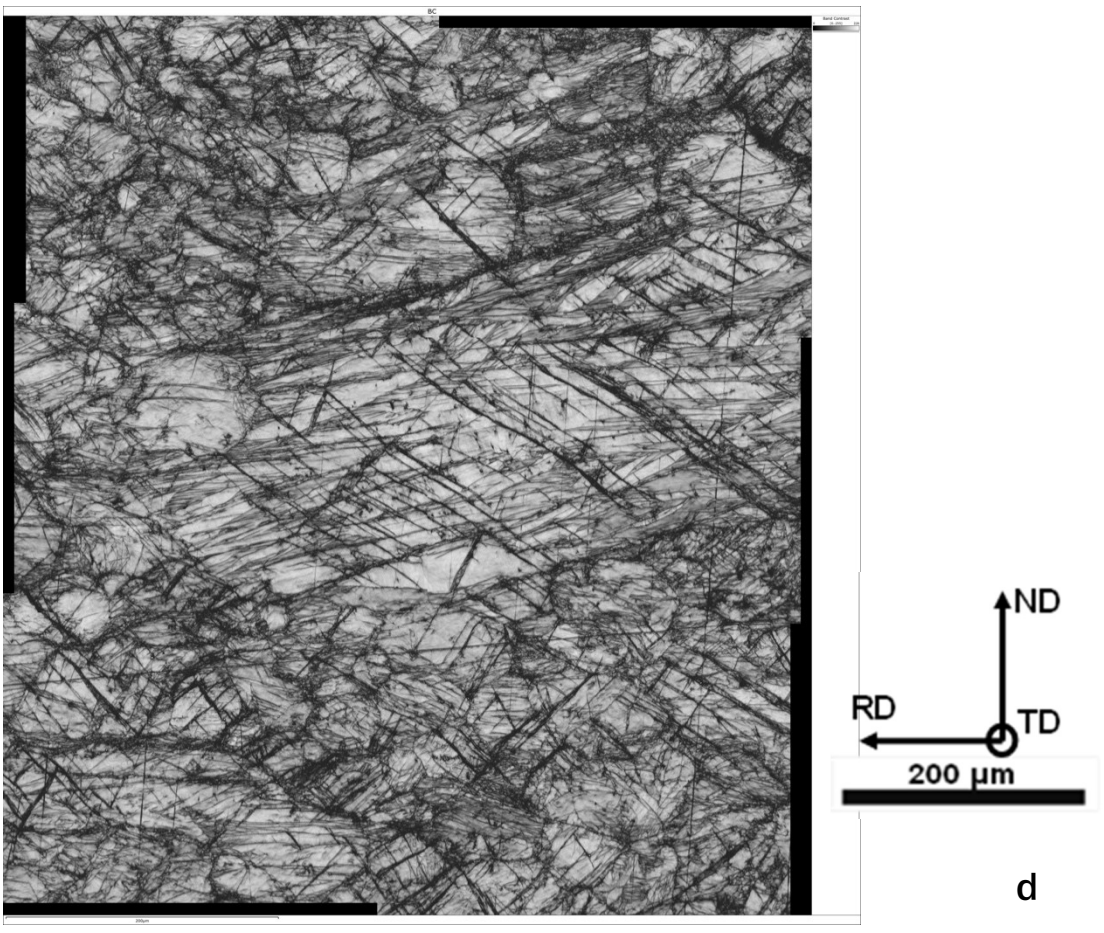
ND
RD
TD
200 µm

d

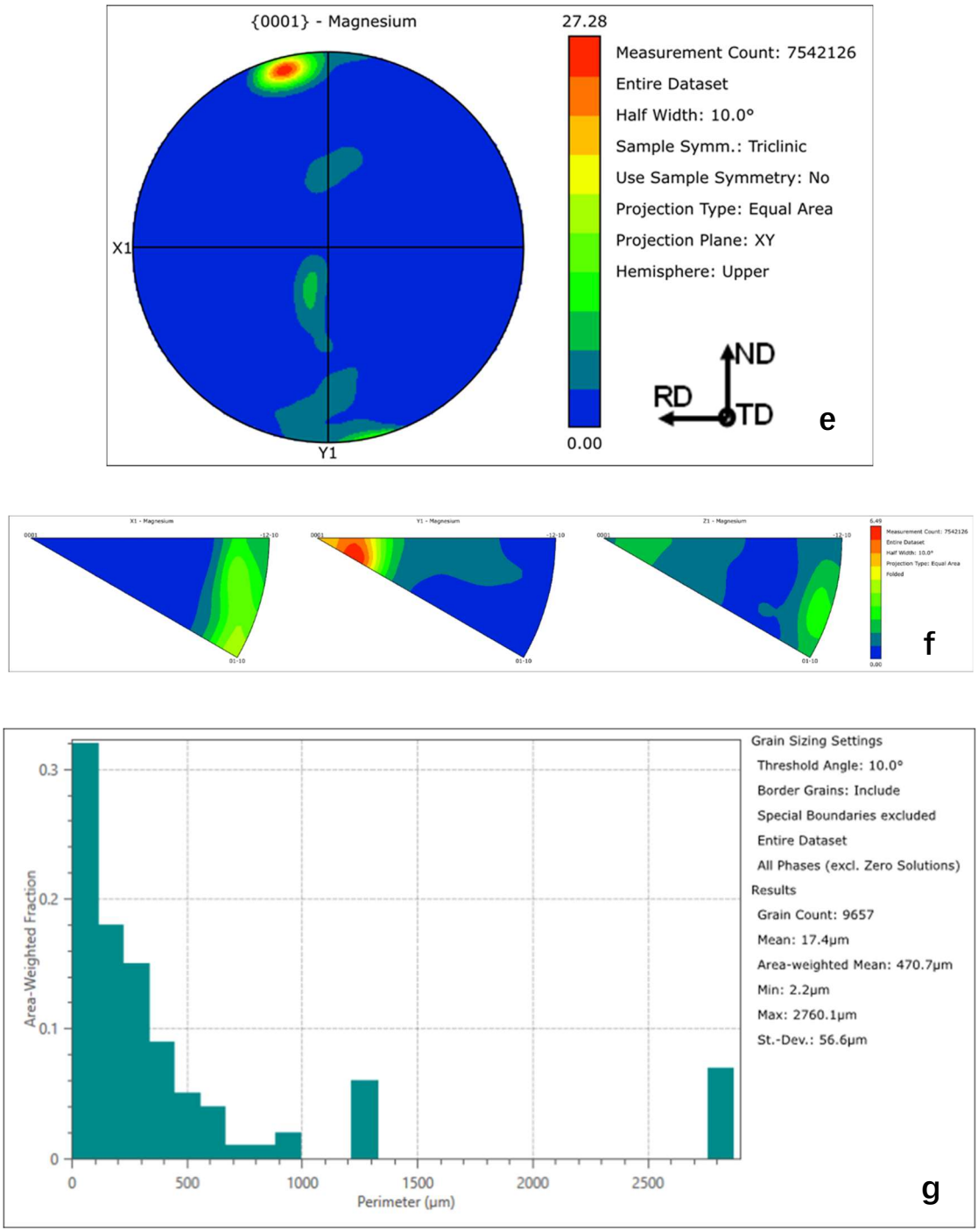

Figure 4-41 The EBSD result of the as-compressed 1D compressed Mg-0.2Ca-0.3Zn specimen: (a) The inverse pole figure map and grain boundaries, (b) The grain boundaries and the special grain boundaries, (c) The band contrast and the phase analysis, (d) The band contrast, (e) The pole figure, (f) The inverse pole figures, (g) Grain size distribution expressed as grain boundary perimeter

Before reaching the 1290s annealing time of the 1D compressed Mg-0.2Ca-0.3Zn (at%) specimen, no obvious recrystallization was found on the EBSD map. The results (shown in Figure 4-42) after the 990s annealing indicated that the specimen showed

recovery before the recrystallization started. At this stage, the temperature of the specimen was 291℃. Figure 4-42 (c) shows a slight decrease in the fraction of the non-indexed area from 23% to 22.6%. However, the non-indexed area on the EBSD map showed a large-scale reduction which could not match the 0.4% difference. This was attributed to the newly generated grey area on the EBSD map. This was the oxidized layer on the specimen surface. Thus, the real reduction of the non-indexed area should be higher than 0.4%. Figure 4-42 (b) indicates the changes in the fraction of the tensile twins, compressive twins and double twins from 44.3%, 4.4% and 9.7% to 42.1%, 3.8% and 7.7%, respectively. The morphology of the microstructure after 990s annealing did not show any difference compared to the as-compressed state. The average grain size ($17.6\mu m$) (Figure 4-42(g)) and the maximum pole intensity (27.9) (Figure 4-42(e)) only showed minor changes. With these changes, the increased fraction of low angle grain boundaries (shown in Figure 4-42(b)) suggests dislocation rearrangement into subgrain boundaries. This was the direct evidence that recovery had happened in the specimen. The EBSD results of the 30s, 45s, 60s, 75s, 90s, 120s, 150s and 180s annealing (30s, 75s, 135s, 210s, 300s, 420s, 570s and 750s heat treatment time in total, respectively) are presented in Appendix I and are not discussed further in the main text.

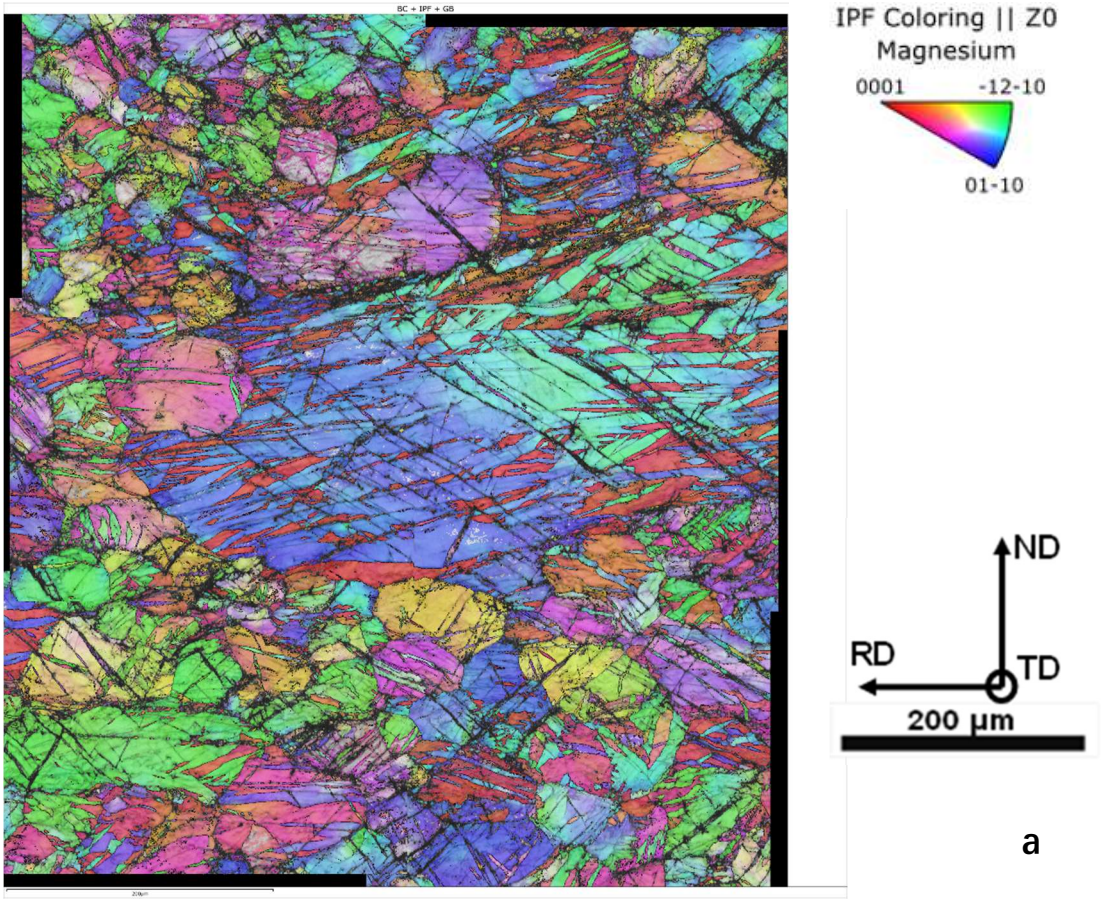

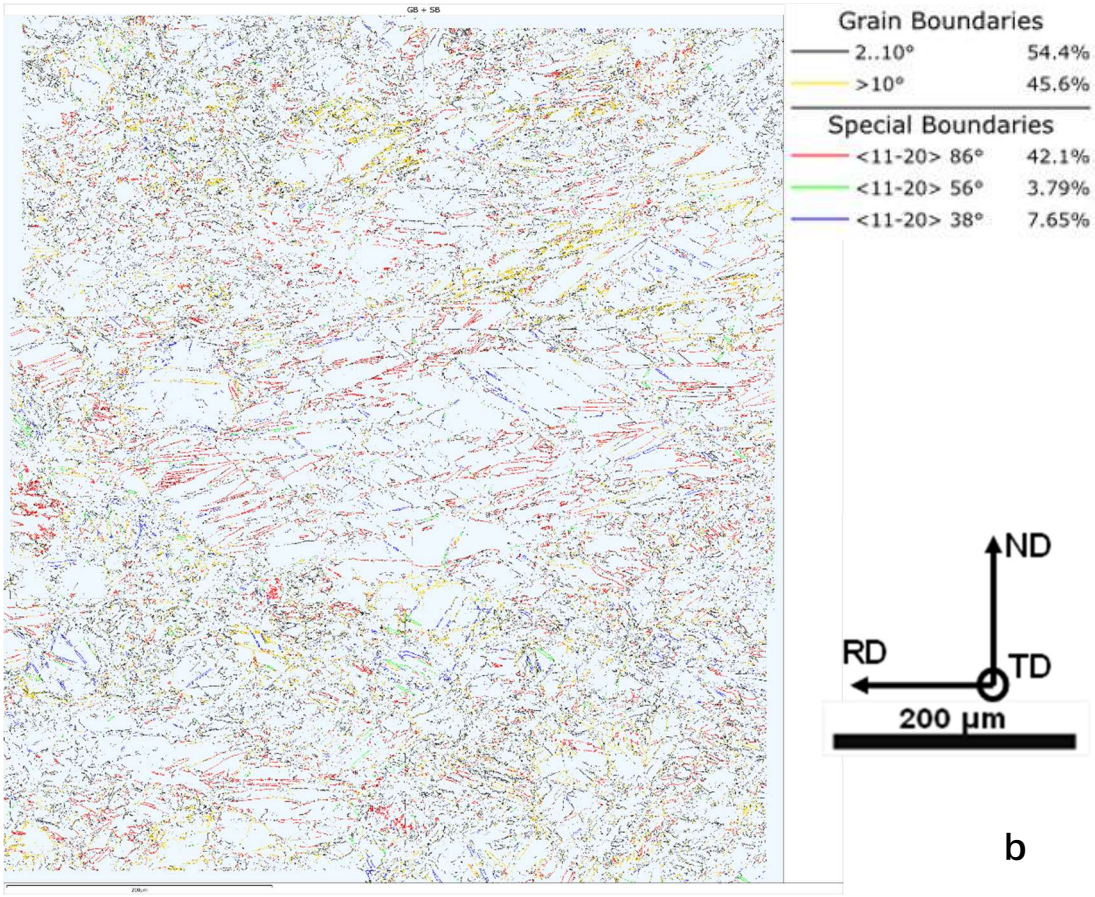
GB + SB
Grain Boundaries
2..10° 54.4%
>10° 45.6%
Special Boundaries
<11-20> 86° 42.1%
<11-20> 56° 3.79%
<11-20> 38° 7.65%
ND
RD
TD
200 µm

b

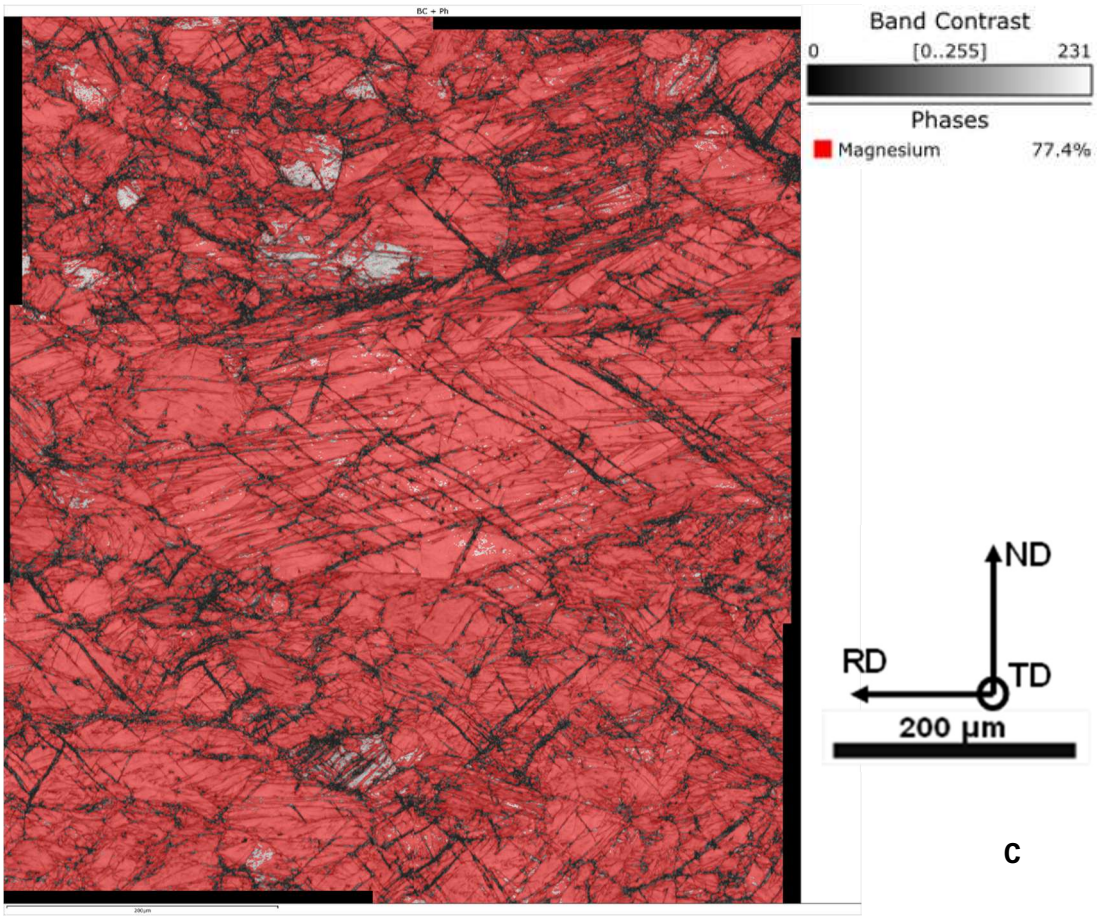
BC + Ph
Band Contrast
0 [0..255] 231
Phases
Magnesium 77.4%
ND
RD
TD
200 µm

c

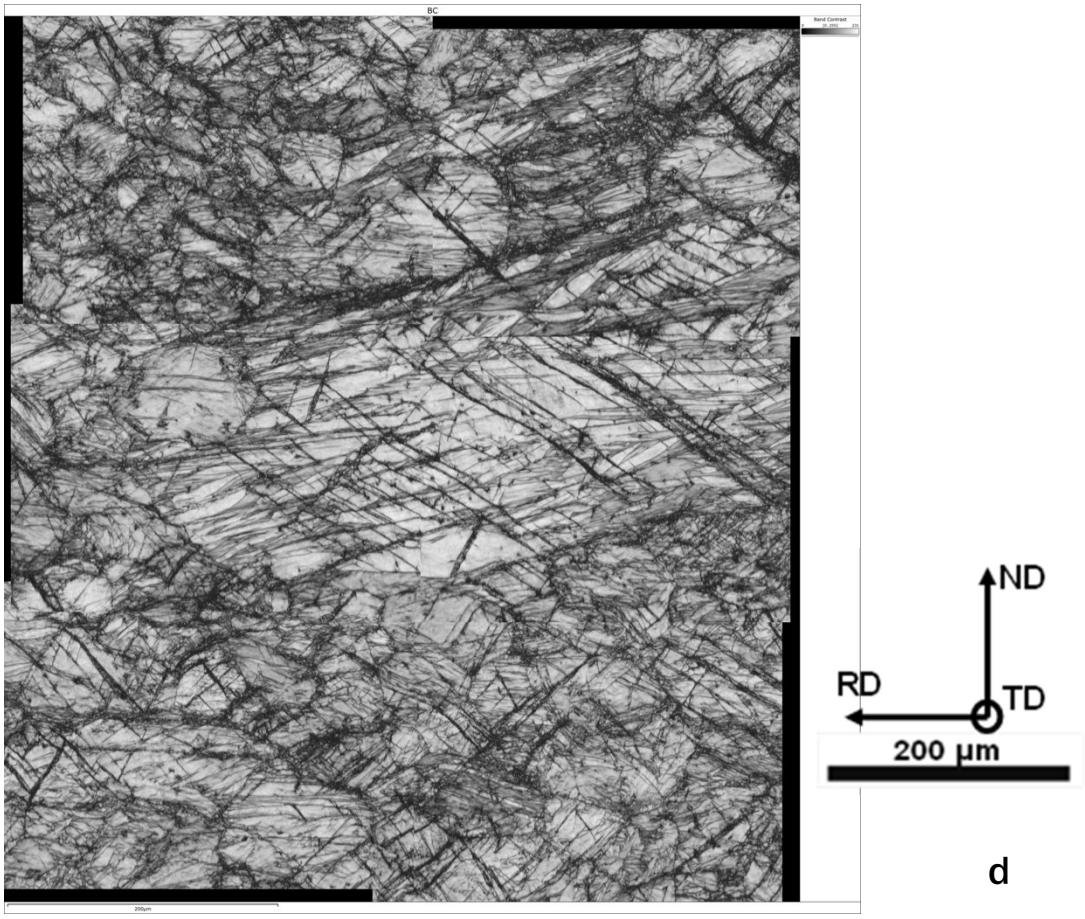
ND
RD
TD
200 µm

d

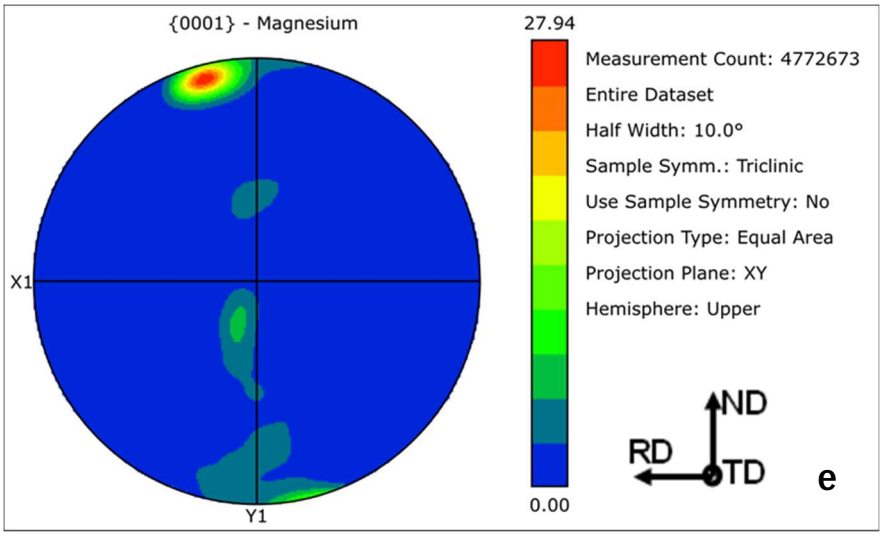
{0001} - Magnesium
27.94
0.00
X1
Y1
Measurement Count: 4772673
Entire Dataset
Half Width: 10.0°
Sample Symm.: Triclinic
Use Sample Symmetry: No
Projection Type: Equal Area
Projection Plane: XY
Hemisphere: Upper
ND
RD
TD

e

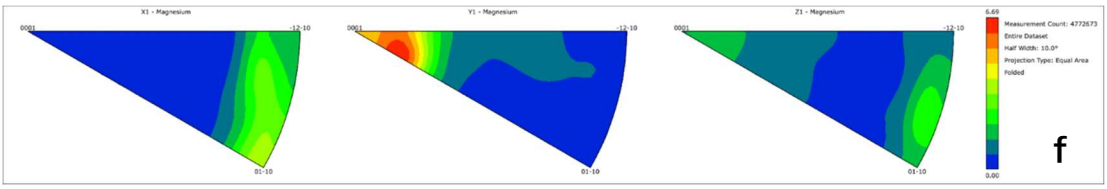

f

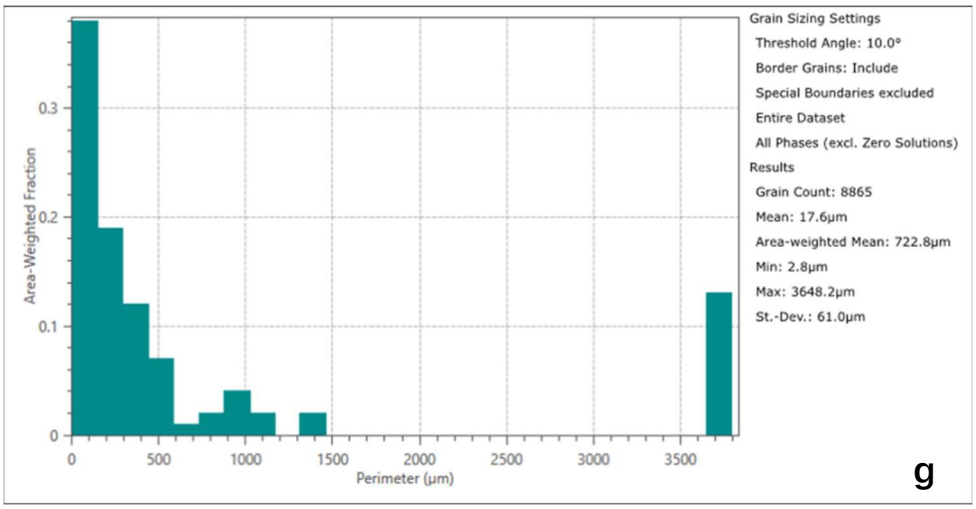

Figure 4-42 The EBSD result of the 990s annealed 1D compressed Mg-0.2Ca-0.3Zn specimen: (a) The inverse pole figure map and grain boundaries, (b) The grain boundaries and the special grain boundaries, (c) The band contrast and the phase analysis, (d) The band contrast, (e) The pole figure, (f) The inverse pole figures, (g) Grain size distribution expressed as grain boundary perimeter

Figure 4-43 shows the EBSD results of the same specimen after 1290s annealing at 310℃. The average grain size was 17.3μm (shown in Figure 4-43(g)). A notable number of recrystallized grains was observed throughout the whole mapped area (shown in Figure 4-43(a)). Meanwhile the non-indexed area was almost eliminated on the EBSD map. The nucleation site of recrystallized grains matched with where shear bands were observed on the previous EBSD map. The recrystallization of the specimen was found to start from the shear bands first at this stage. On the other hand, Figure 4-43(c) indicates that the fraction of the non-indexed area decreased from 22.6% (990s annealed) to 12.1% (1290s annealed). The remaining 12.1% non-indexed area almost consisted of the grey area (oxidized layer) mentioned above. The real area ratio of the non-indexed area was much lower than 12.1%. Figure 4-43(b) indicates that the number of twins did not change too much before and after the 1290s annealing. The boundary fraction of the tensile twins and double twins both reduced from 44.3% to 35.6% and 9.7% to 7.6, respectively. The compressive twins presented a slight increase in the value of the boundary fraction which was from 4.4% to 5.2%. Since the morphology and the fraction of the twins did not change significantly, there was no correlation between recrystallization and the twins at this stage. The pole figure and the inverse pole figure (IPF) of the annealed specimen (shown in Figure 4-43(e) and (f)) showed a predictable result. The maximum value of the pole figure was decreased from 27.9 to 24.5 after the specimen showed an obvious recrystallization. However, the grain orientation distribution shown in the pole figure did not present obvious differences. The large blue grain in the middle of the EBSD map had a high influence weight on the calculation of

the whole pole figure. Thus, the recrystallized grains might not be well reflected in the pole figure.

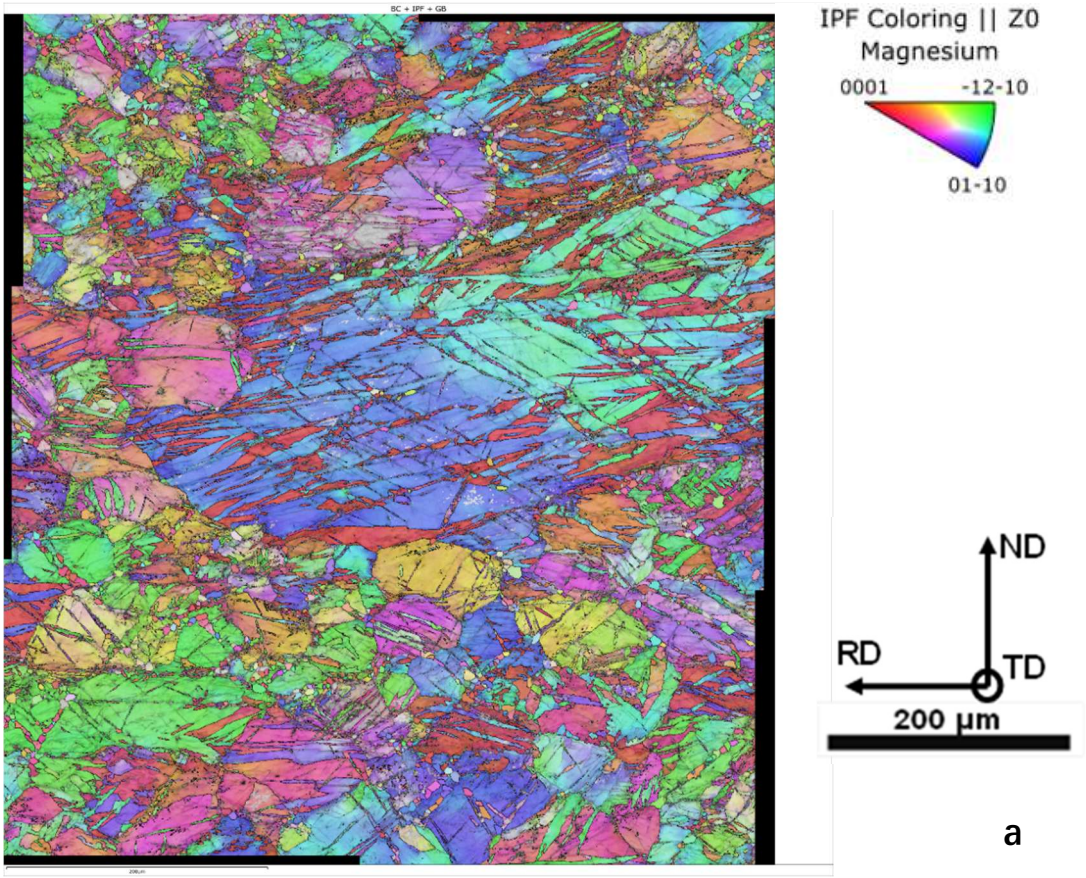

a

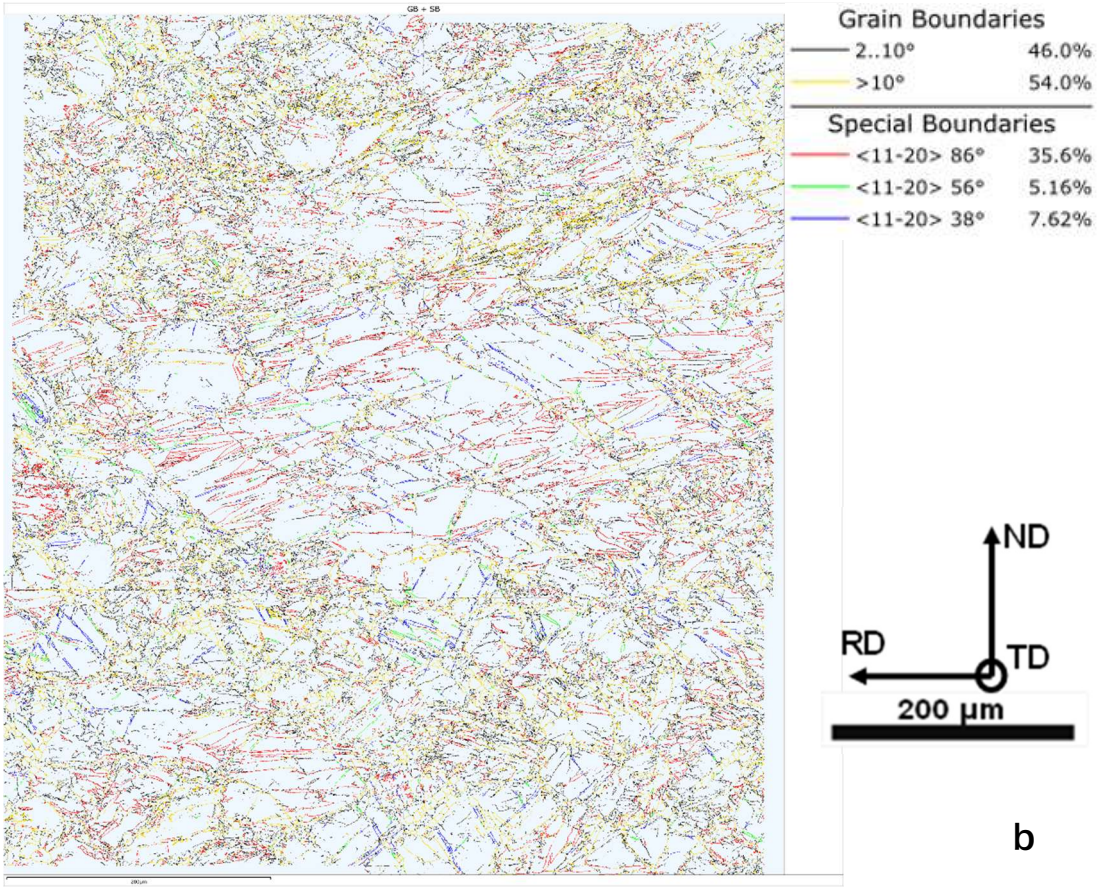

b

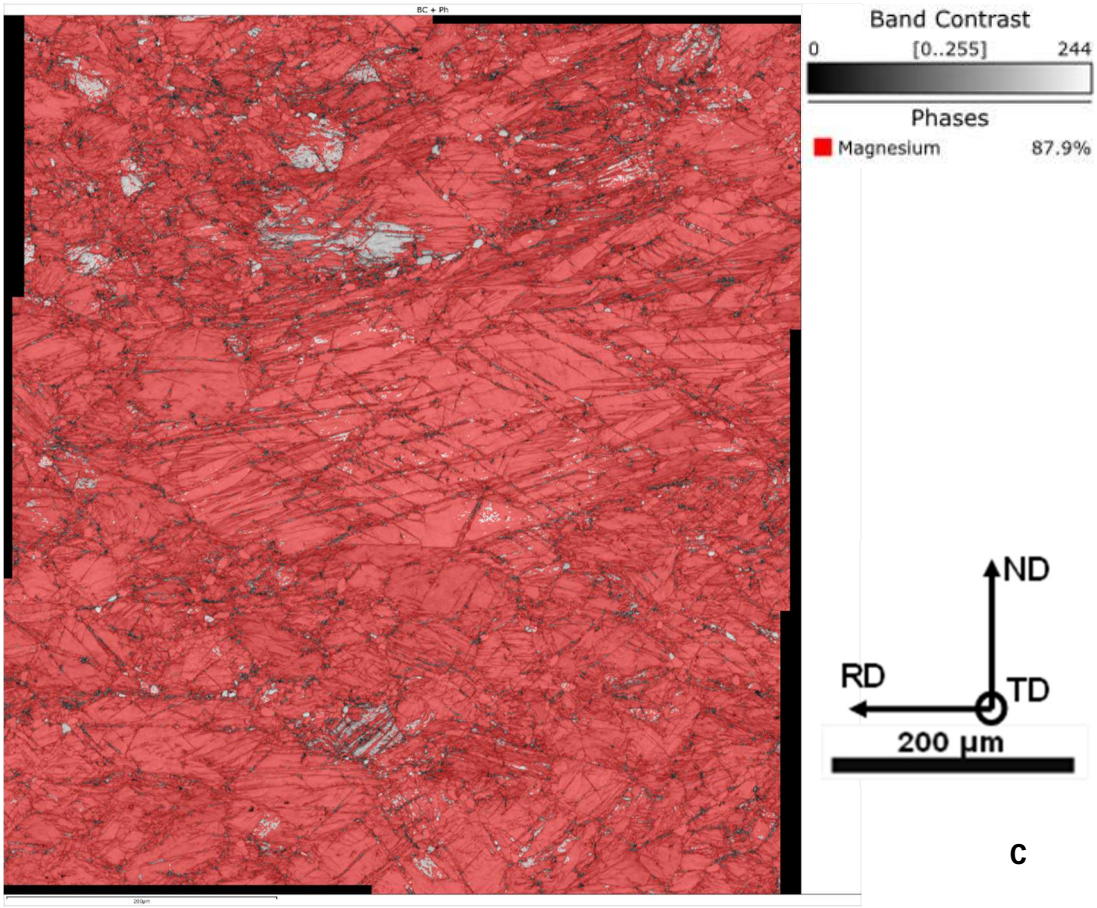
BC + Ph
Band Contrast
0
[0..255]
244
Phases
Magnesium
87.9%
ND
RD
TD
200 µm

c

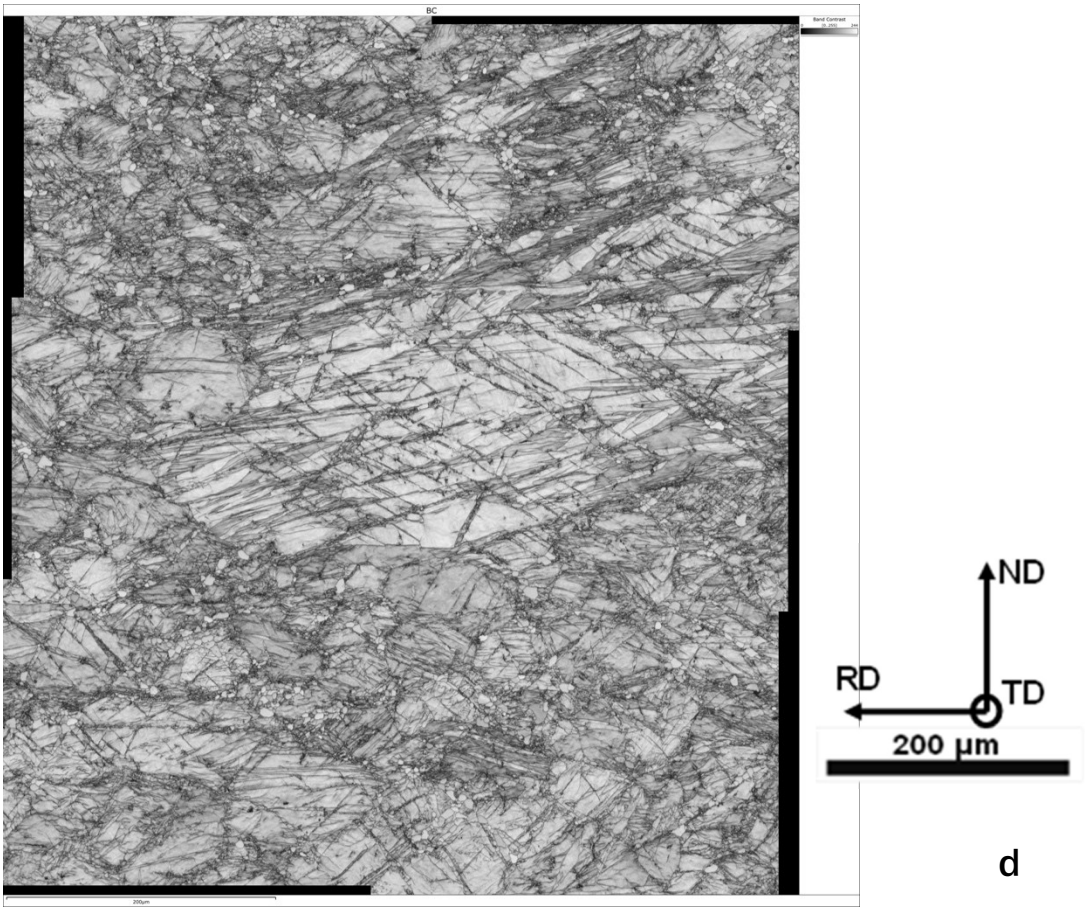
BC
ND
RD
TD
200 µm

d

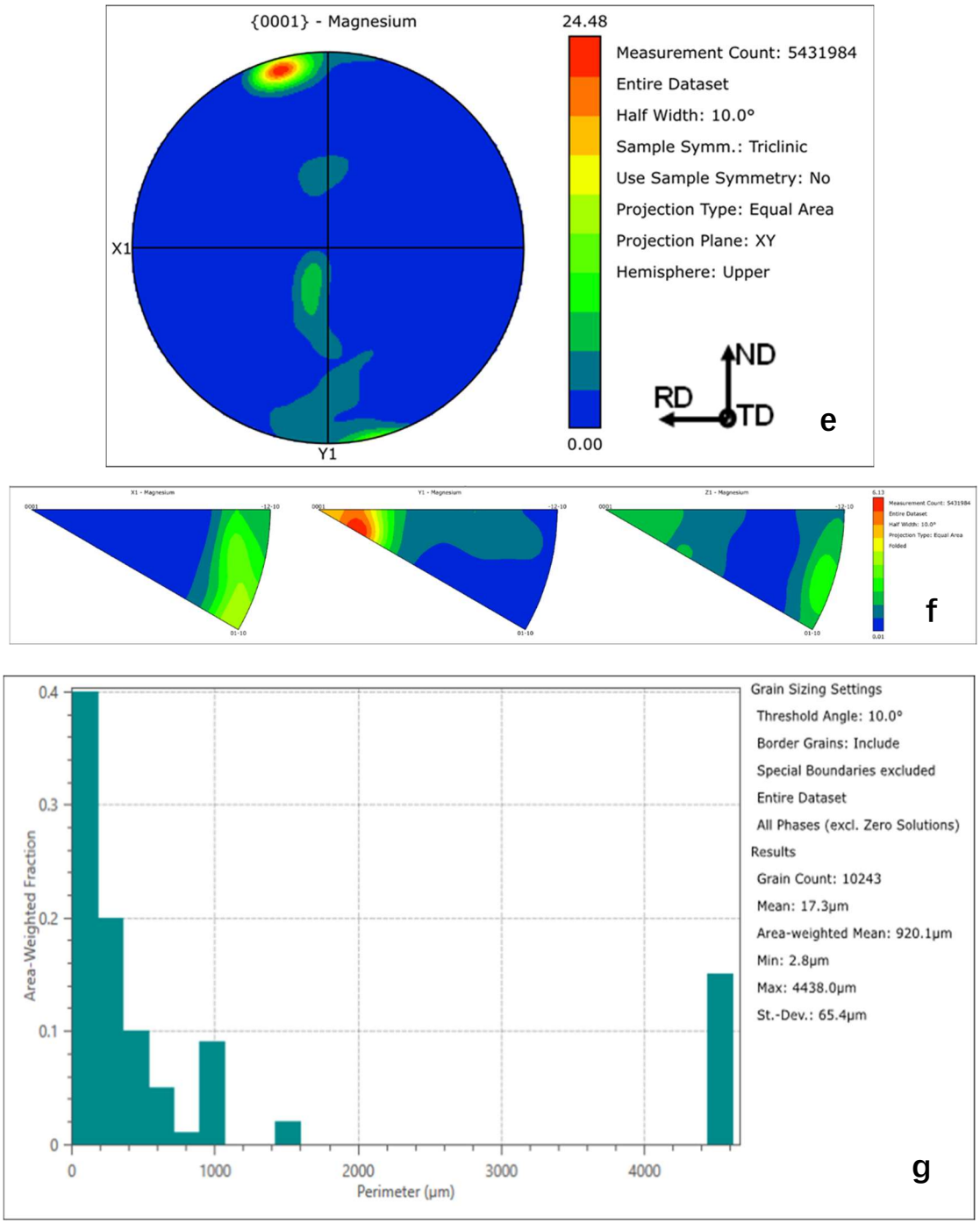

Figure 4-43 The EBSD result of the 1290s annealed 1D compressed Mg-0.2Ca-0.3Zn specimen: (a) The inverse pole figure map and grain boundaries, (b) The grain boundaries and the special grain boundaries, (c) The band contrast and the phase analysis, (d) The band contrast, (e) The pole figure, (f) The inverse pole figures, (g) Grain size distribution expressed as grain boundary perimeter

After an annealing for 1620s, the recrystallization became obvious and was easy to observe. The temperature of the specimen at that time point was 319℃. Figure 4-44 shows the EBSD results of the same specimen at that stage. From Figure 4-44(c), it was

clear that the shear bands, fine twins and the high residual stress areas had all disappeared. The recrystallization from the shear bands had finished and these new grains had started to grow (shown in Figure 4-44(a)). Meanwhile, the recrystallization nucleated in twins was observed. Figure 4-44(h) and (i) show the higher magnification images which were cropped from the large EBSD map marked in black rectangle. They show the nucleation of the recrystallized grains from the twins. Figure 4-44(b) shows that the boundary fractions of the tensile twins, compressive twins and double twins all showed a reduction from 35.6% to 28.3%, 5.2% to 3.7% and 7.6% to 5.1%, respectively. Meanwhile, the fraction of the high-angle grain boundary also presented notable change which increased from 54.0% (1290s in total annealing time) to 63.2% (1620s in total annealing time). The average grain size of the specimen was increased to $23\mu m$ (shown in Figure 4-44(g)). Figure 4-44(e) and (f) indicates that the maximum value of the pole figure also decreased from 24.5 to 22.4. However, the grain orientation distribution did not present any obvious changes in the pole figure. Only the peak close to the TD diffusing towards the normal direction (ND) showed an enhancement.

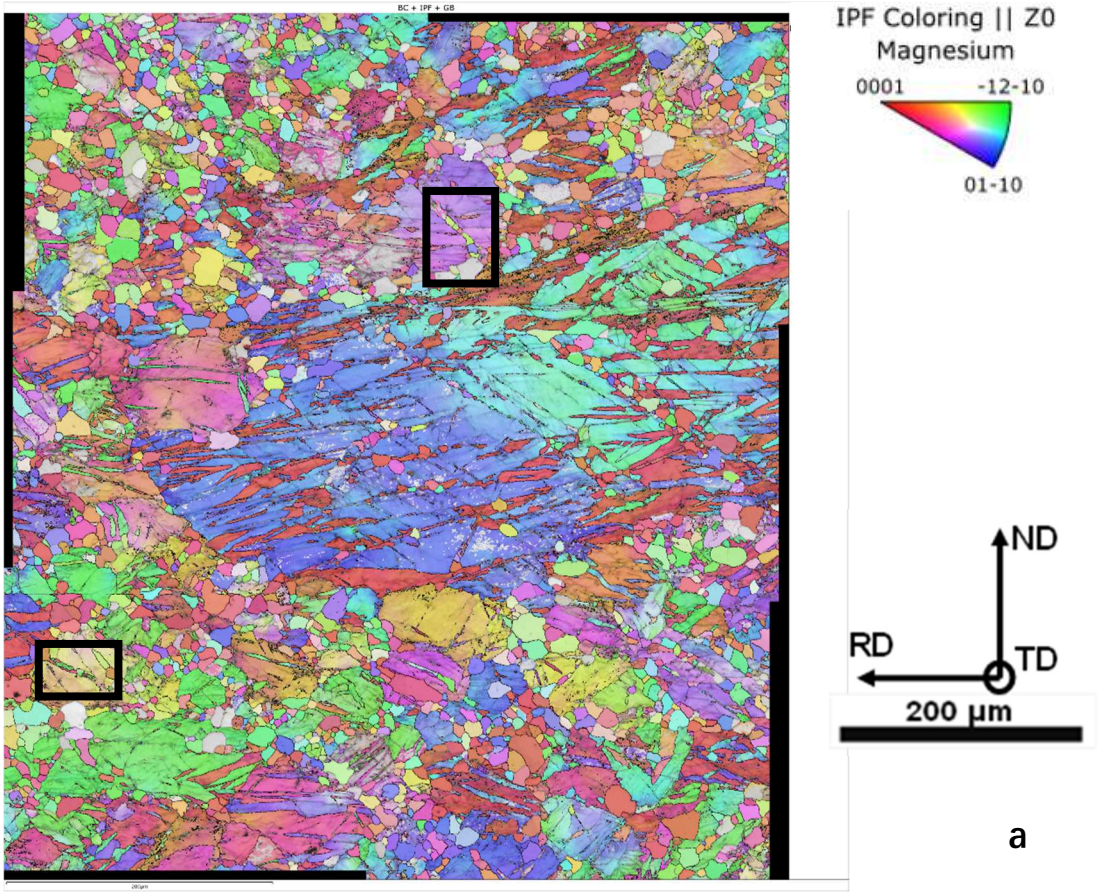

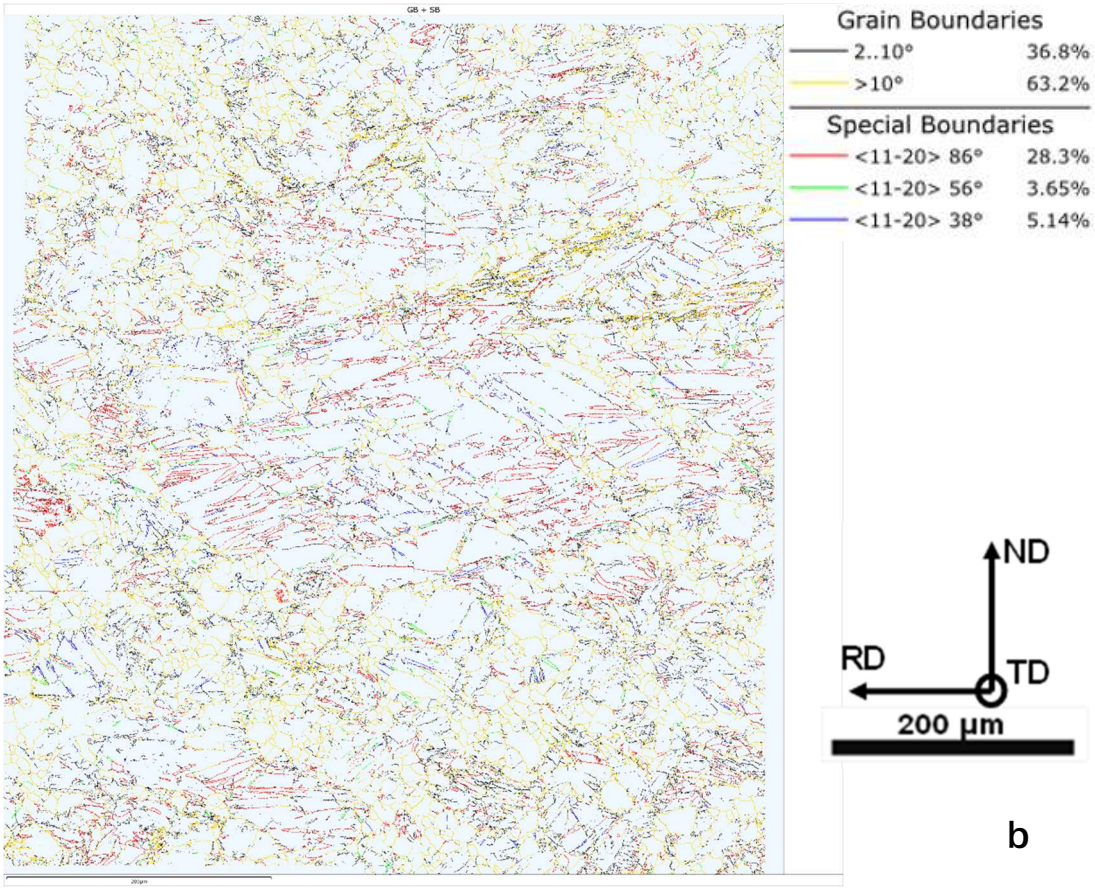
GB + SB
Grain Boundaries
2..10° 36.8%
>10° 63.2%
Special Boundaries
<11-20> 86° 28.3%
<11-20> 56° 3.65%
<11-20> 38° 5.14%
ND
RD
TD
200 µm

b

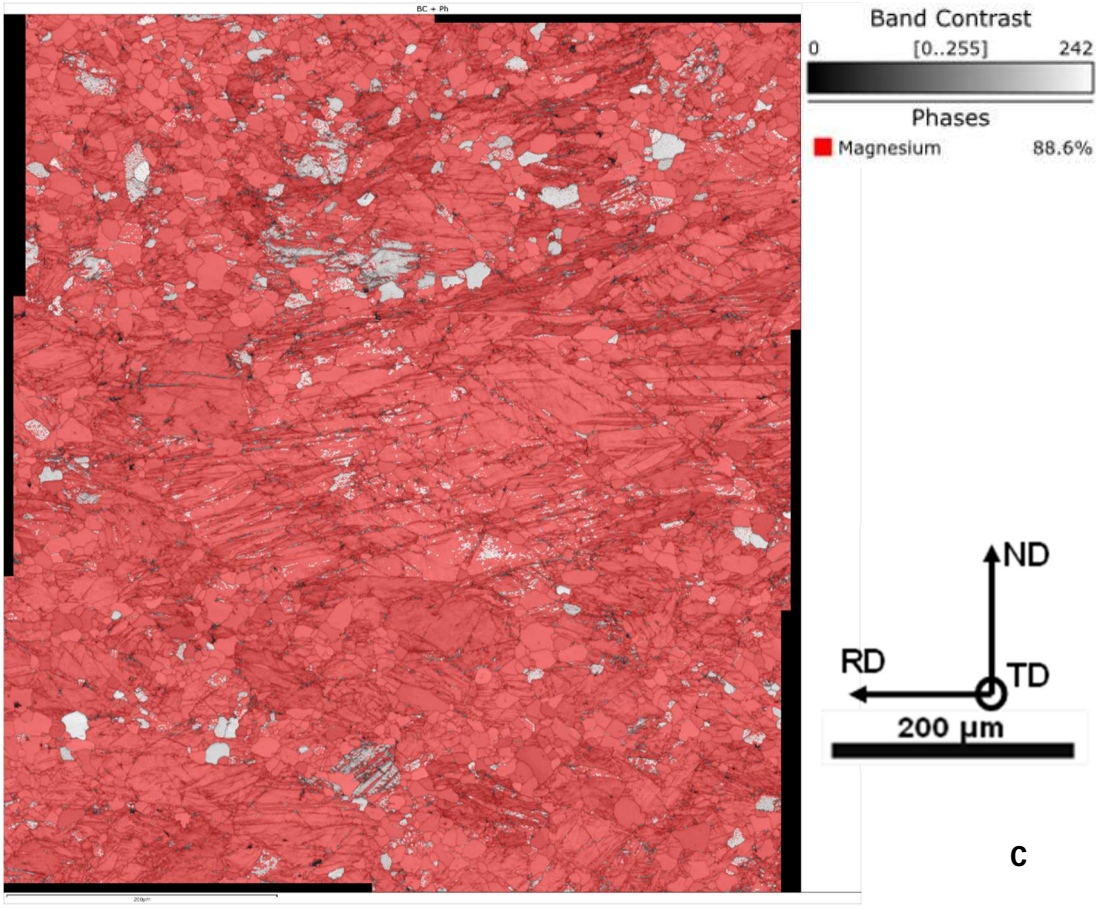
BC + Ph
Band Contrast
0 [0..255] 242
Phases
Magnesium 88.6%
ND
RD
TD
200 µm

c

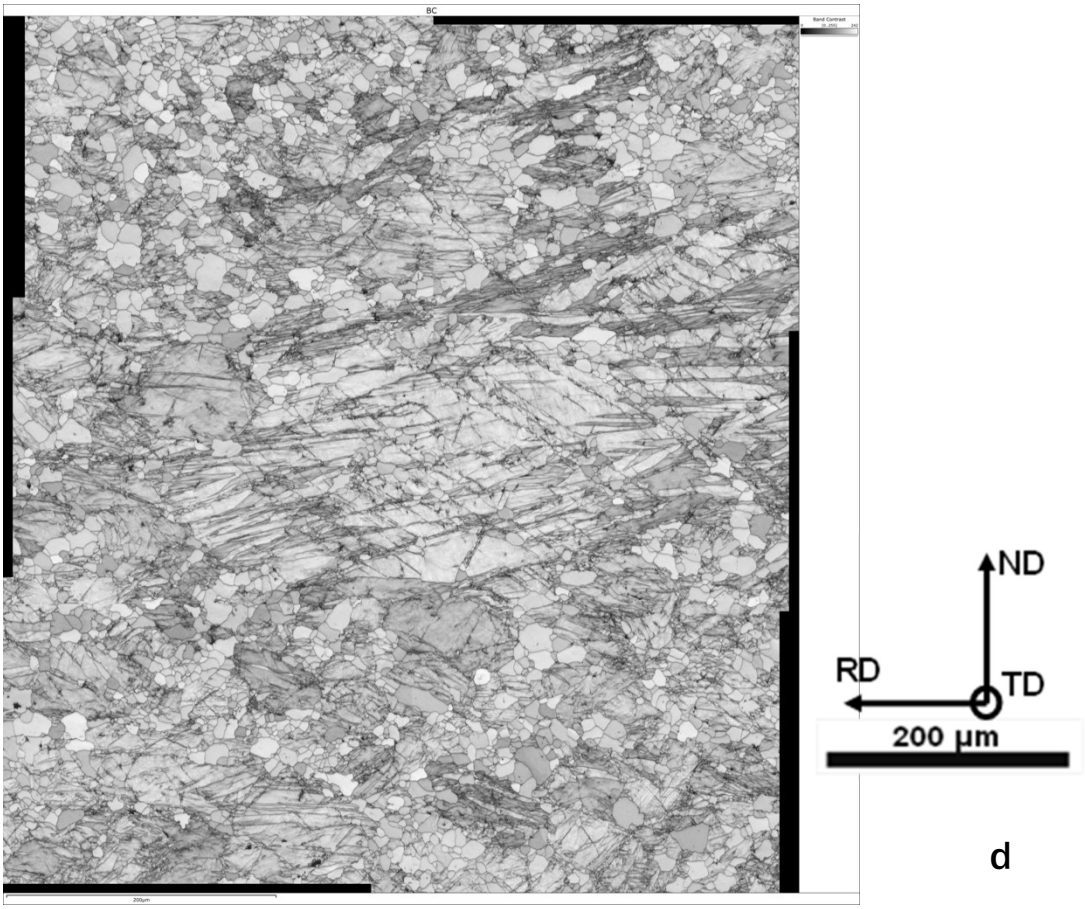
BC
ND
RD
TD
200 µm

d

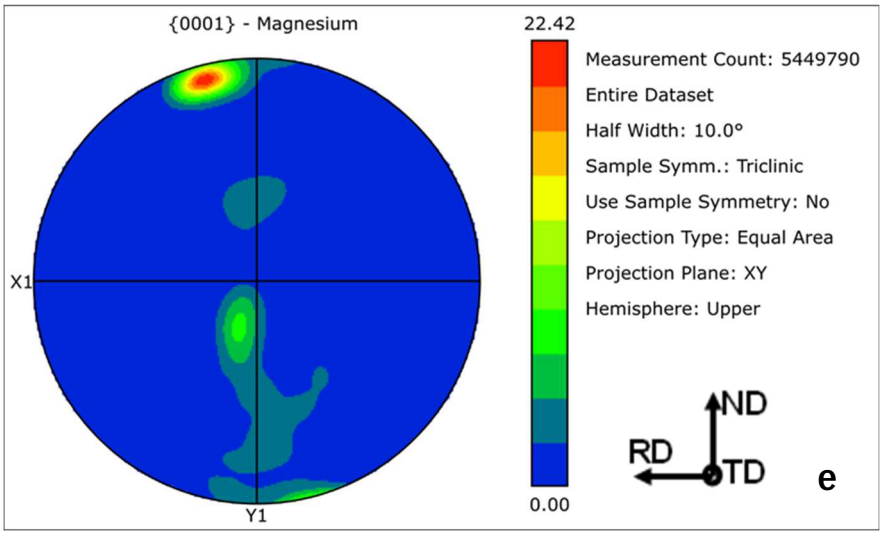
{0001} - Magnesium
22.42
0.00
Measurement Count: 5449790
Entire Dataset
Half Width: 10.0°
Sample Symm.: Triclinic
Use Sample Symmetry: No
Projection Type: Equal Area
Projection Plane: XY
Hemisphere: Upper
X1
Y1
ND
RD
TD

e

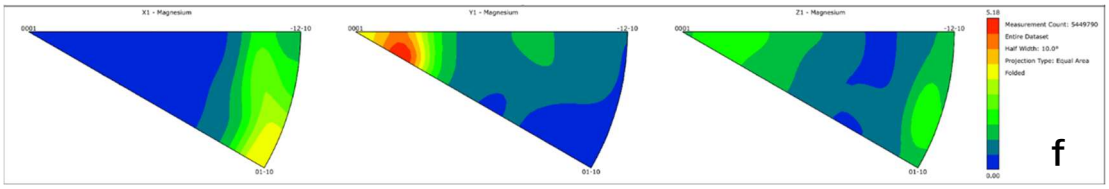
X1 - Magnesium
Y1 - Magnesium
Z1 - Magnesium

f

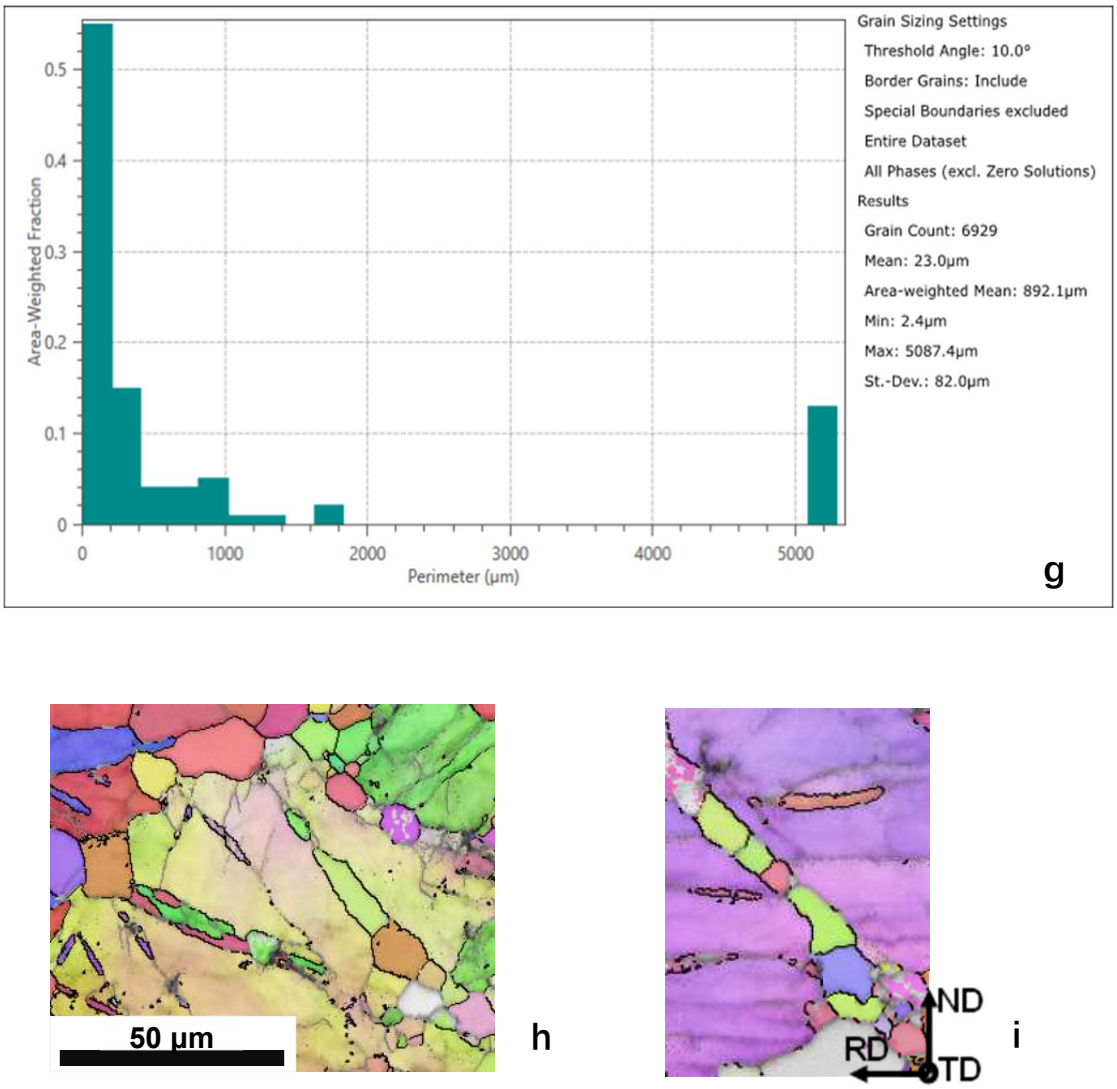

Figure 4-44 The EBSD result of the 1620s annealed 1D compressed Mg-0.2Ca-0.3Zn specimen: (a) The inverse pole figure map and grain boundaries, (b) The grain boundaries and the special grain boundaries, (c) The band contrast and the phase analysis, (d) The band contrast, (e) The pole figure, (f) The inverse pole figures, (g) Grain size distribution expressed as grain boundary perimeter , (h), (i) The grains nucleated from twins

Figure 4-45 shows the EBSD results of the same specimen after the 1980s annealing. The temperature of the specimen at that time point was 325℃. Unlike the early-stage annealing, the 30s increase in the annealing time did not bring a large change in temperature, which increased from 319℃ to 325℃. Thus, the EBSD results reflected that the changes between the two steps were small in the microstructure of the sample. The IPF map and the grain boundary figure (shown in Figure 4-45(a) and Figure 4-45(b), respectively) indicated that the recrystallization was still in progress. A few new grains were observed on the IPF map. The boundary fraction of the tensile twins, compressive twins and double twins all exhibited a decreasing trend, reducing

from 28.3% to 25.7%, 3.7% to 2.8% and 5.1% to 5.0%, respectively. Simultaneously, the boundary fraction of the low-angle grain boundary and the high-angle grain boundary presented corresponding changes, which decreased from 36.8% to 36.3% and increased from 63.2% to 63.7%, respectively. Moreover, the reduction of the maximum pole intensity was also observed (shown in Figure 4-45(e)). The value was reduced by 0.4 (from 22.4 to 22). However, the peak pole intensity area in the pole figure still showed no change. Also, no obvious difference was found in the rest of the area. The average grain size of the specimen showed a slight increase, which was 23.2 μm (shown in Figure 4-45(g)).

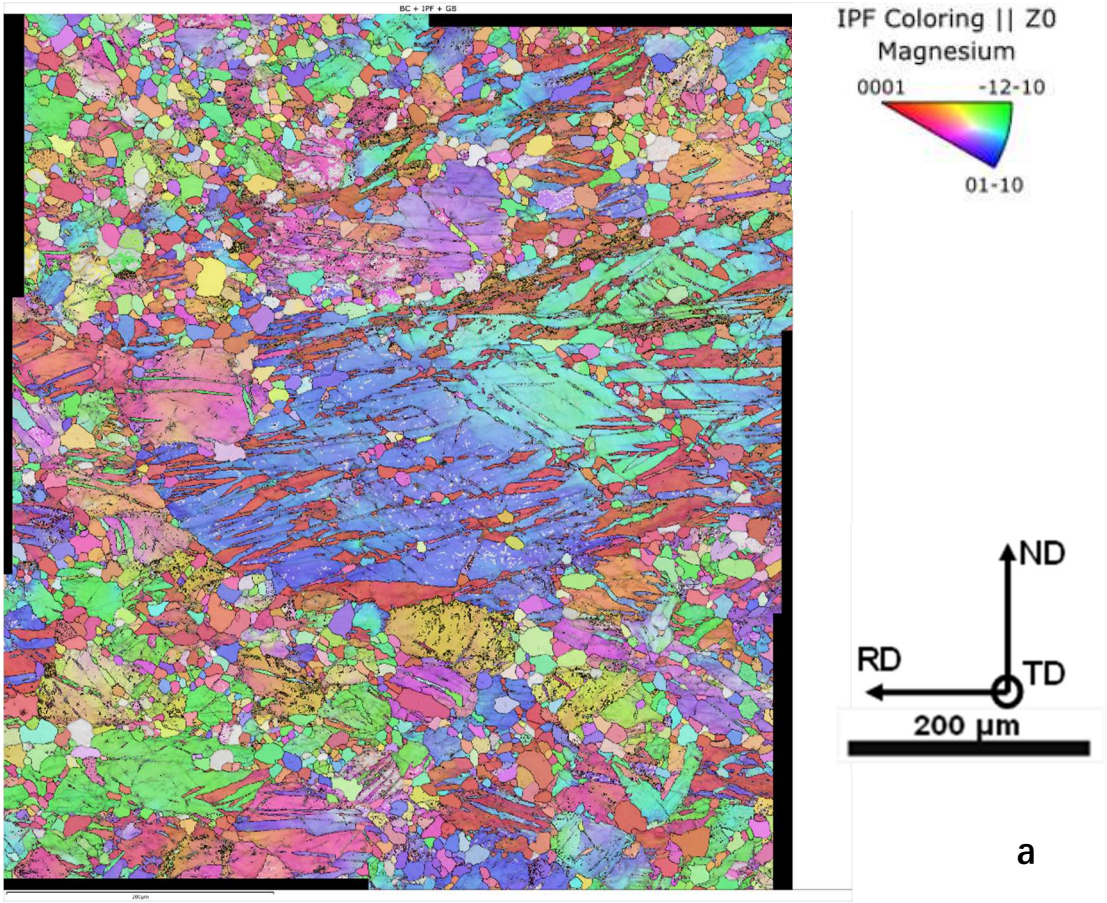

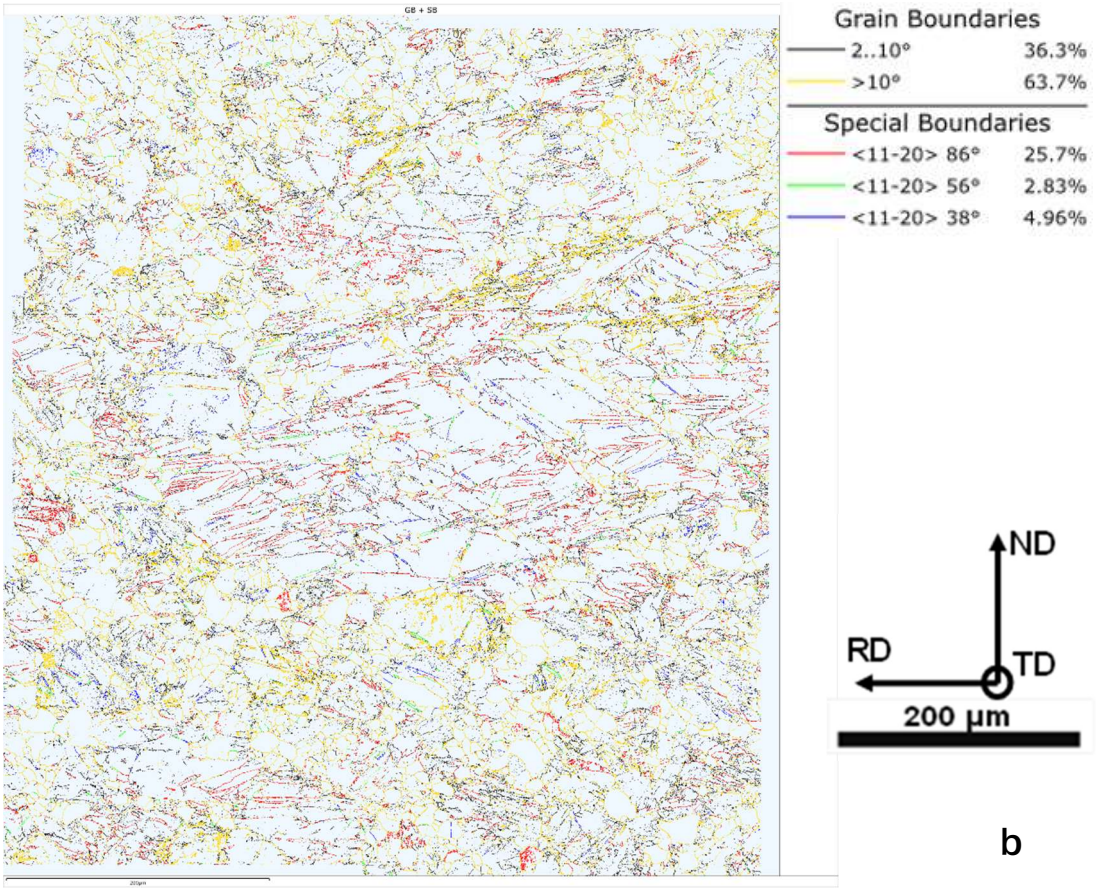
GB + SB
Grain Boundaries
2..10° 36.3%
>10° 63.7%
Special Boundaries
<11-20> 86° 25.7%
<11-20> 56° 2.83%
<11-20> 38° 4.96%
ND
RD
TD
200 µm

b

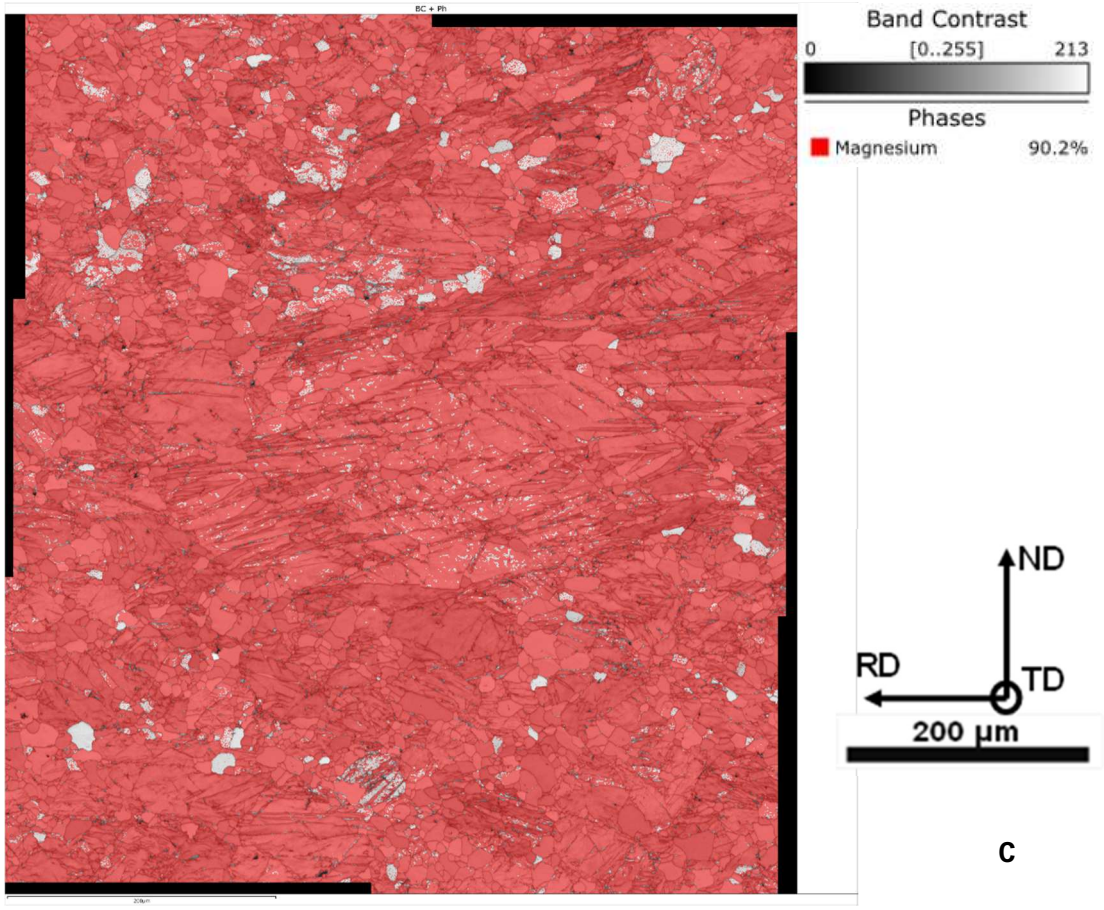
BC + Ph
Band Contrast
0 [0..255] 213
Phases
Magnesium 90.2%
ND
RD
TD
200 µm

c

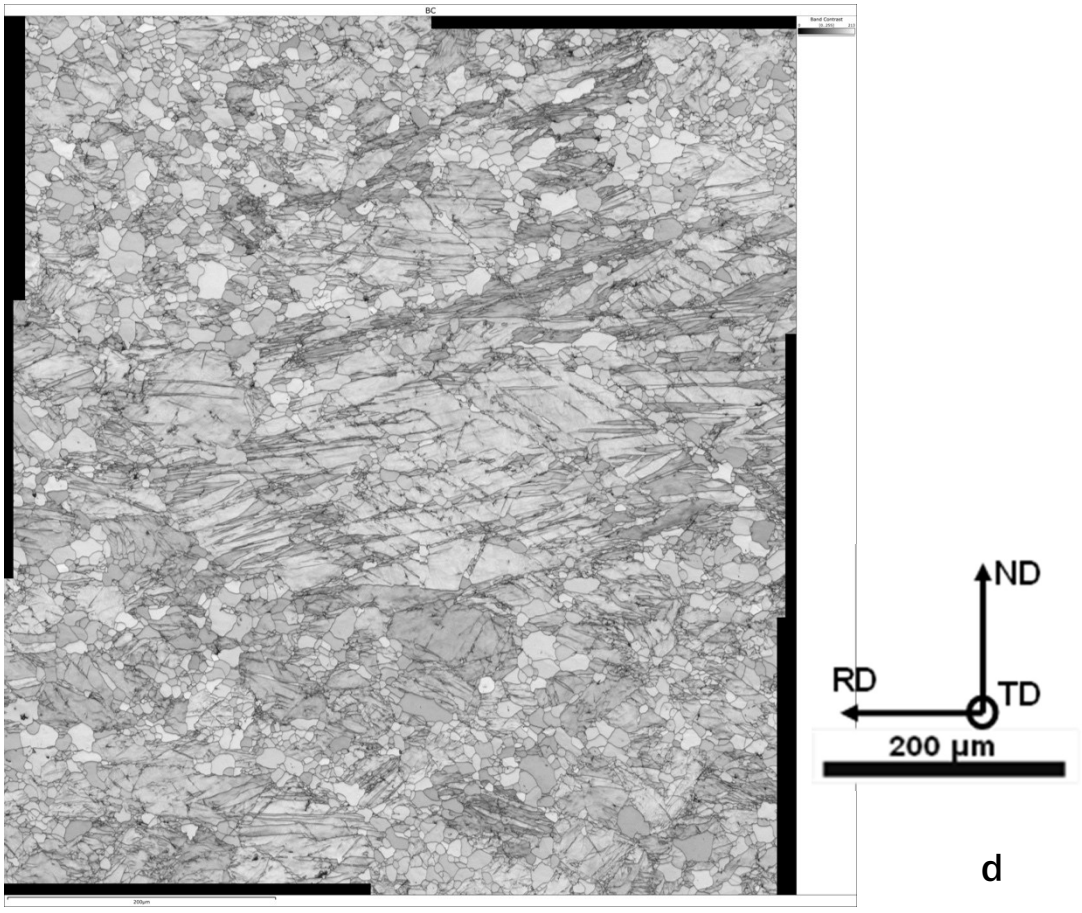
BC
ND
RD
TD
200 µm

d

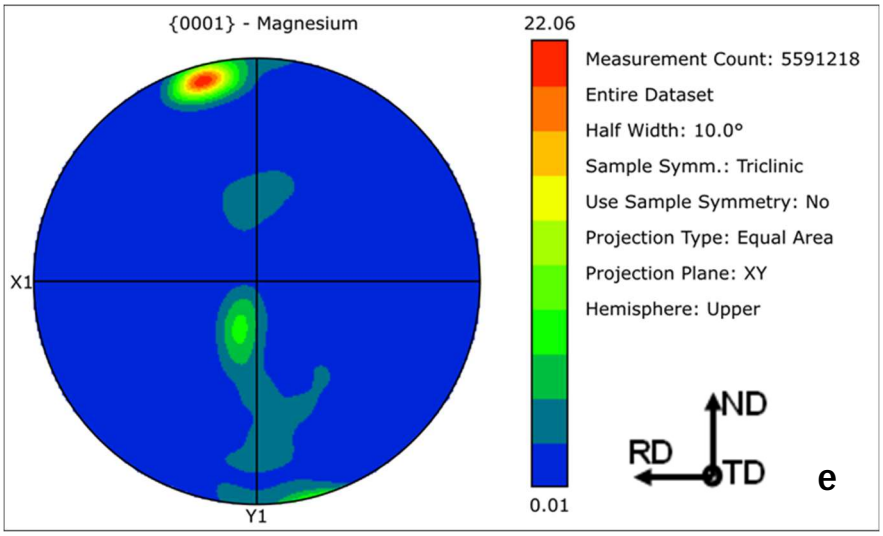
{0001} - Magnesium
22.06
0.01
Measurement Count: 5591218
Entire Dataset
Half Width: 10.0°
Sample Symm.: Triclinic
Use Sample Symmetry: No
Projection Type: Equal Area
Projection Plane: XY
Hemisphere: Upper
X1
Y1
ND
RD
TD

e

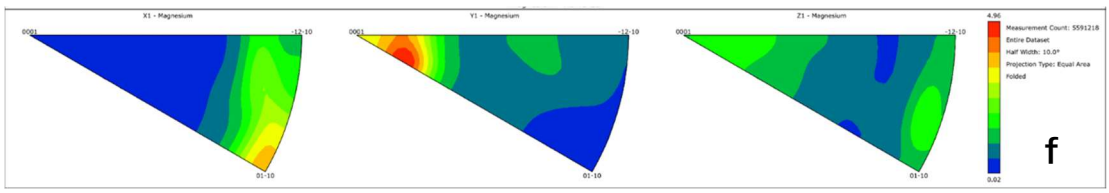
X1 - Magnesium
Y1 - Magnesium
Z1 - Magnesium
Measurement Count: 5591218
Entire Dataset
Half Width: 10.0°
Projection Type: Equal Area
Folded

f

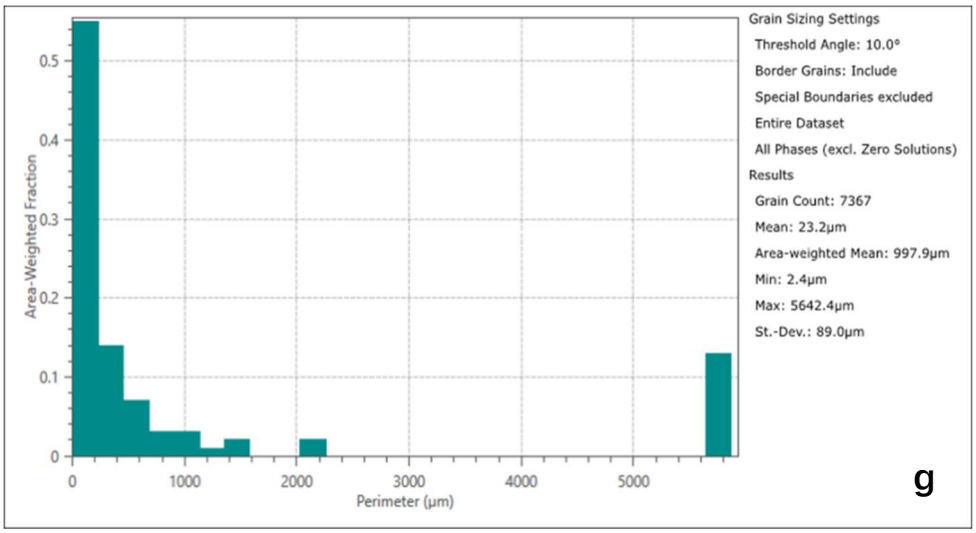

Figure 4-45 The EBSD result of the 1980s annealed 1D compressed Mg-0.2Ca-0.3Zn specimen: (a) The inverse pole figure map and grain boundaries, (b) The grain boundaries and the special grain boundaries, (c) The band contrast and the phase analysis, (d) The band contrast, (e) The pole figure, (f) The inverse pole figures, (g) Grain size distribution expressed as grain boundary perimeter

The EBSD result (shown in Figure 4-46) of the sample after the 2370s annealing indicated the slow kinetics of recrystallization at this stage. The highest temperature of the specimen during the annealing was 330℃. The IPF map (shown in Figure 4-46(a)) indicates that the grain growth was very limited in the recrystallized grains. Only a few grains were observed to grow in the IPF map. Simultaneously, the nucleation of new grains was observed but the quantity of new grains was very low. The average grain size exhibited a minor change which was slightly reduced from 23.2μm to 22.3μm (shown in Figure 4-46(g)). The changes of the boundary fraction also showed the slow evolution of the microstructure. Figure 4-46(b) shows the fluctuation of the value for different types of boundary fractions. The boundary fraction of the tensile twins, compressive twins and double twins changed from 25.7% to 26.7%, 2.8% to 2.7% and 5.0% to 4.5%, respectively. Meanwhile, the fraction of the low-angle grain boundary and the high-angle grain boundary was changed from 36.3% to 35.0% and from 63.7% to 65.0%, respectively. The increase in the boundary fraction of the tensile twins was affected by the extra area scanned in this step. This extra area contained a reasonable number of tensile twins at the bottom of the IPF map (marked in black rectangle in Figure 4-46(a)). For the grain orientation distribution, there was no obvious change in the pole figure and IPF compared to the last stage (shown in Figure 4-46(e) and (f)). The existence of the large grain was considered as a powerful signal source in the centre of the scanning area, which reduced the signal expression of the recrystallized grains in the pole figure. On the other hand, a higher reduction in maximum pole intensity was

found compared to the previous stage, decreasing from 22 to 20.6.

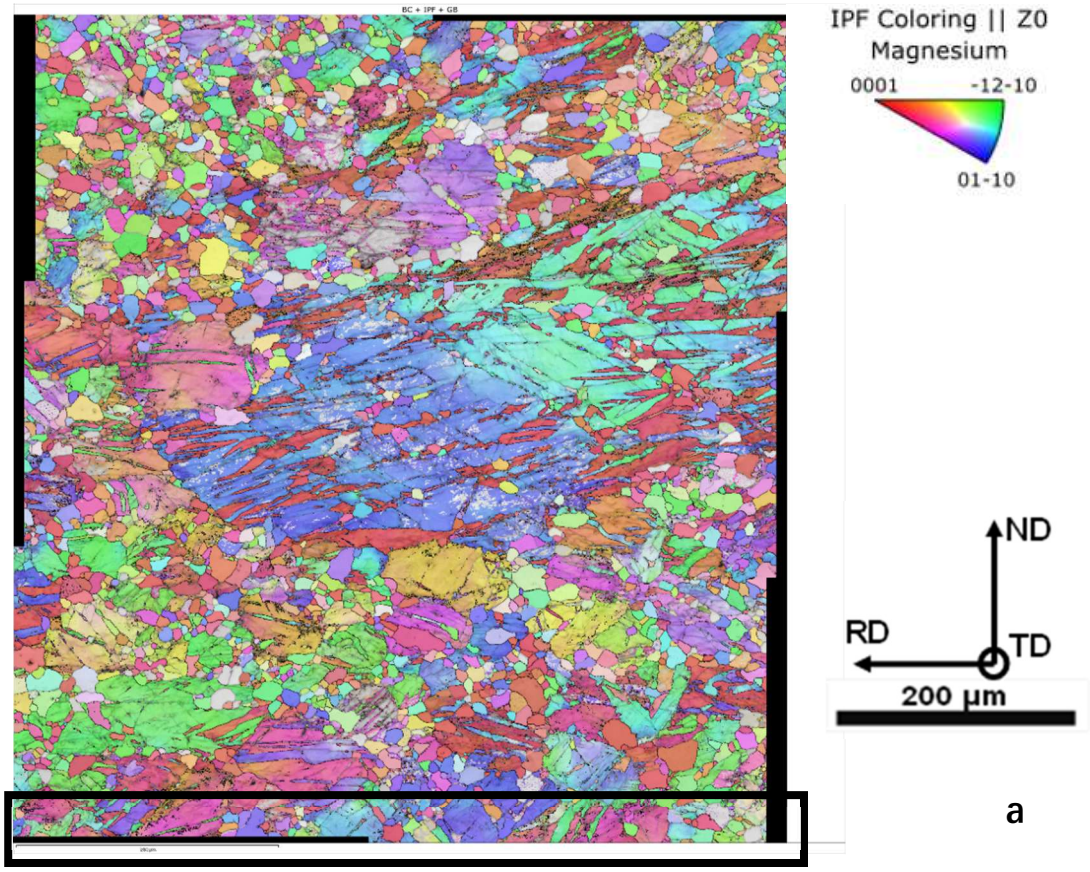

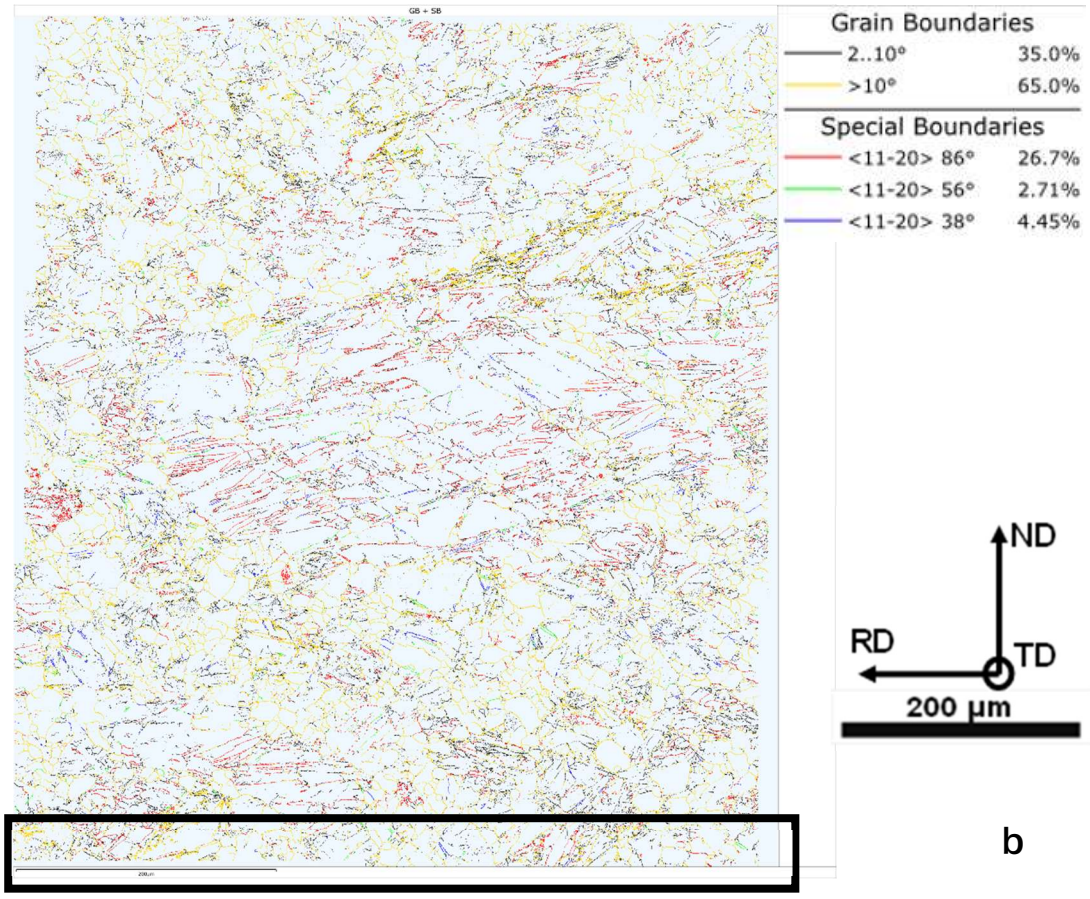

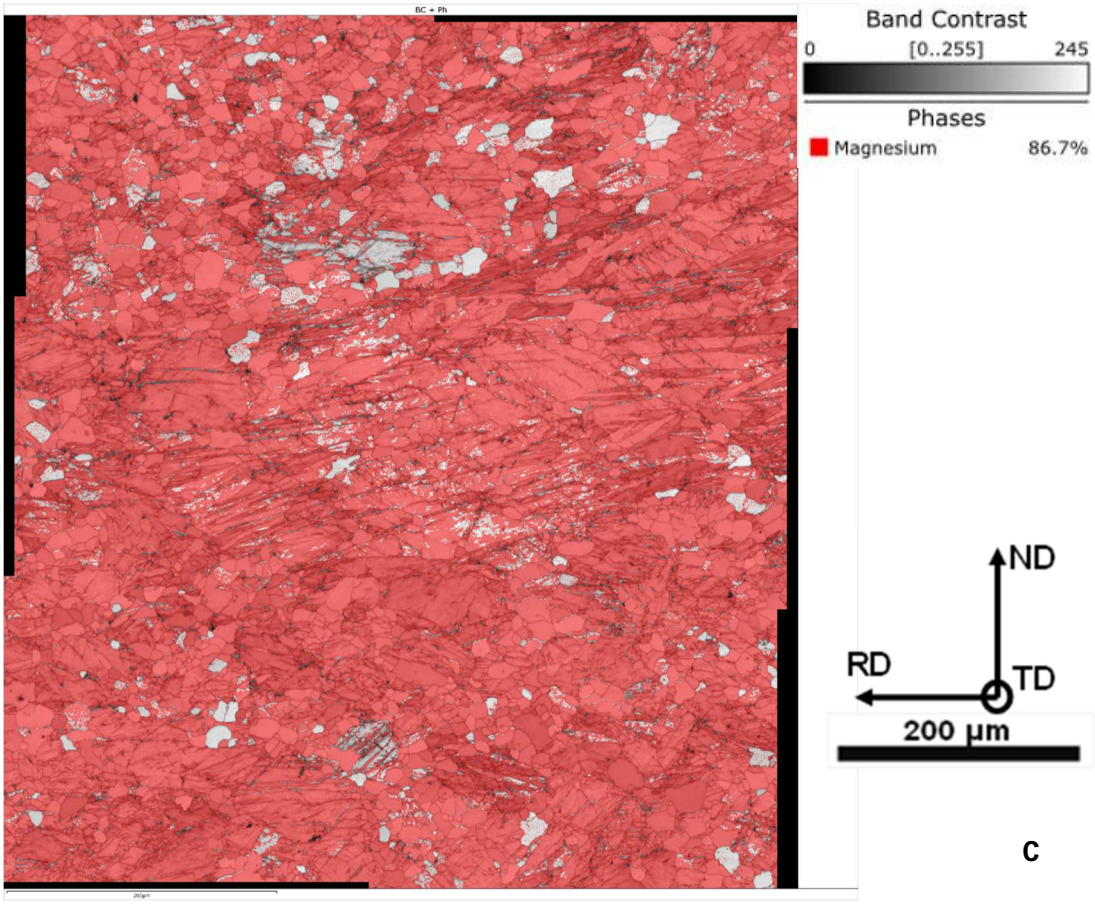
BC + Ph
Band Contrast
0
[0..255]
245
Phases
Magnesium
86.7%
ND
RD
TD
200 µm

c

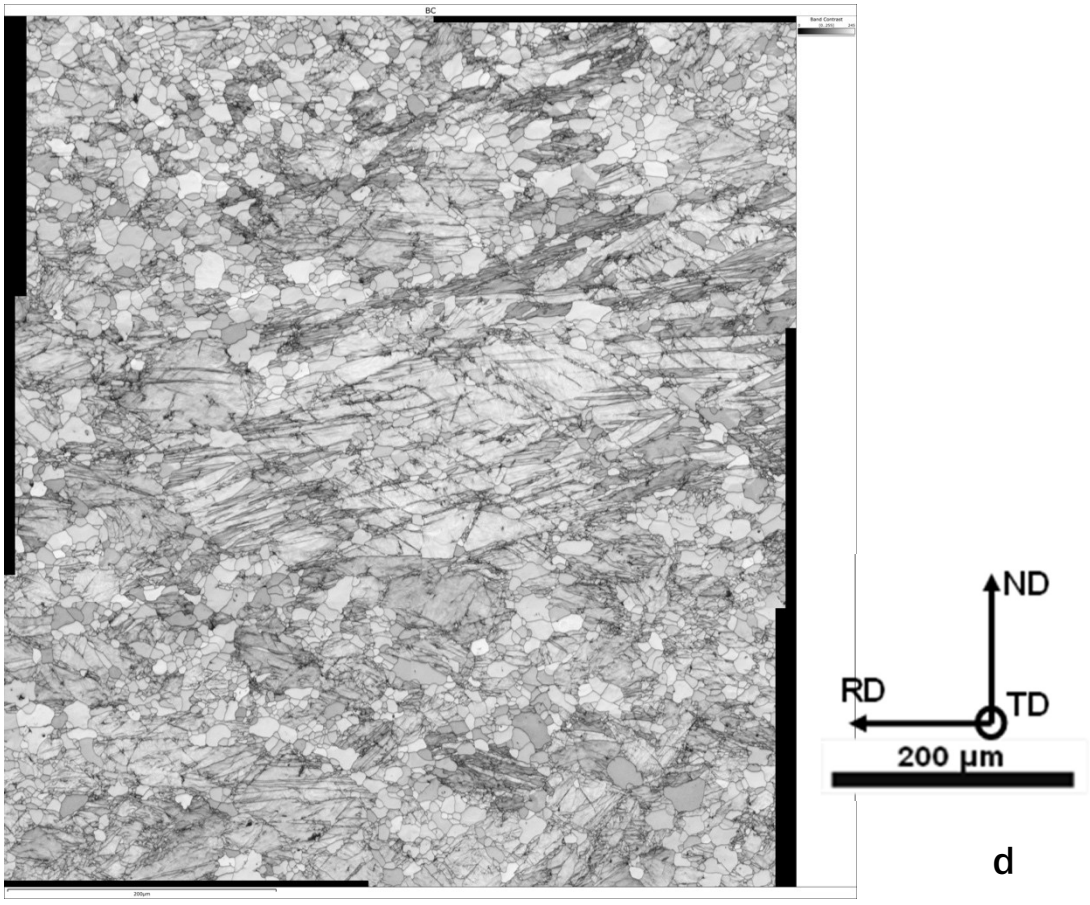
BC
ND
RD
TD
200 µm

d

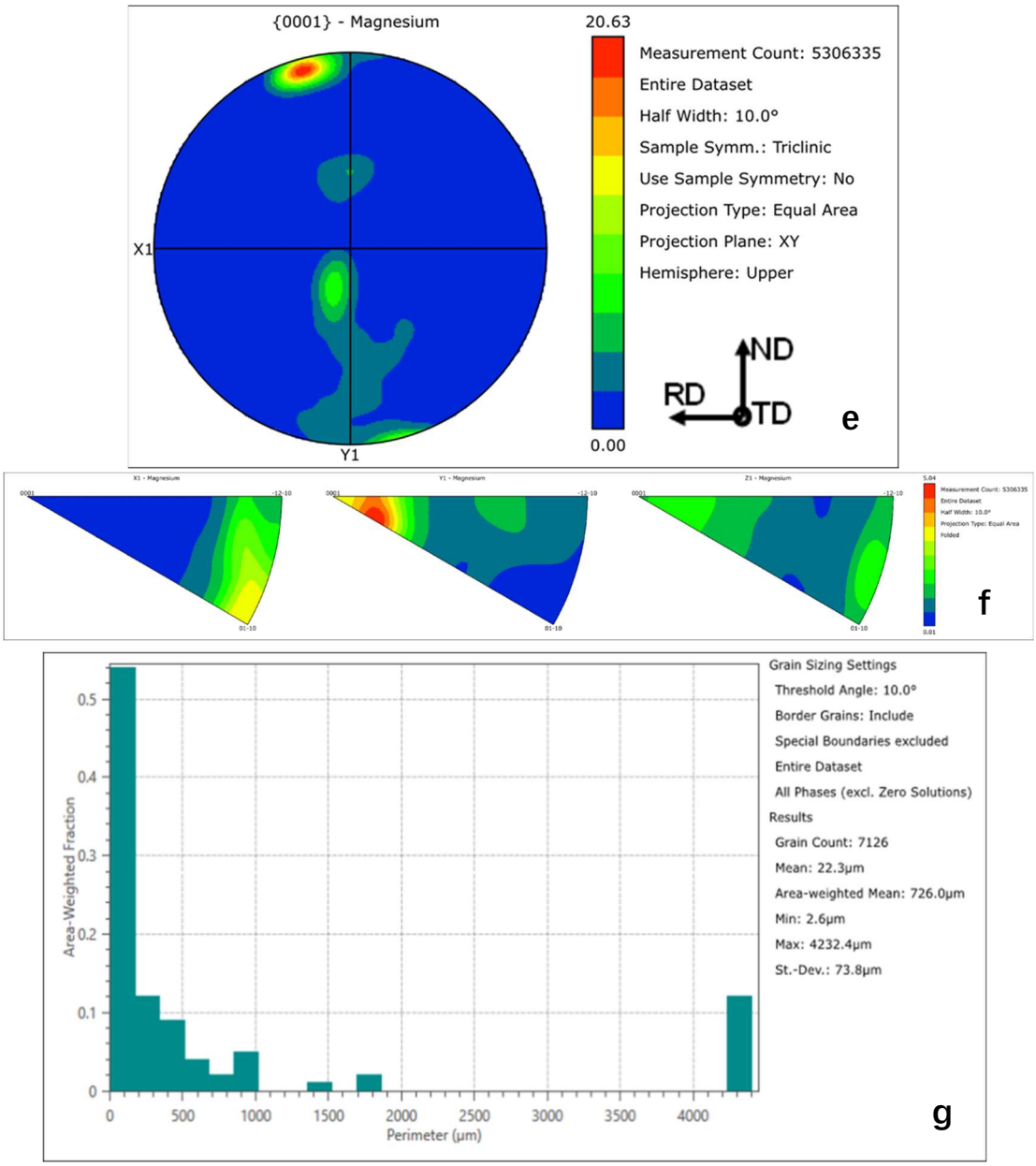

Figure 4-46 The EBSD result of the 2370s annealed 1D compressed Mg-0.2Ca-0.3Zn specimen: (a) The inverse pole figure map and grain boundaries, (b) The grain boundaries and the special grain boundaries, (c) The band contrast and the phase analysis, (d) The band contrast, (e) The pole figure, (f) The inverse pole figures, (g) Grain size distribution expressed as grain boundary perimeter

After the annealing for 2790s, obvious changes in the recrystallization were observed. The temperature of the specimen at that time point was 334℃. Figure 4-47(a) shows the IPF map of the scanning area. It was clear that the kinetics of recrystallization had made a large step forward i.e. dramatic grain growth of the recrystallized grains was found, and a large amount of the new recrystallized grains were observed throughout the whole mapping area. And the average grain size showed the corresponding change which was significantly increased from 22.3 μm to 28.1 μm

(shown in Figure 4-47(g)). Figure 4-47(b) presents the variation of the boundary fraction after this microstructure evolution. The boundary fraction of the tensile twins, compressive twins and double twins was changed from 26.7% to 18.1%, 2.7% to 2.7% and 4. 5% to 3.6%, respectively. Simultaneously, the fraction of the low-angle grain boundary and the high-angle grain boundary was changed from 35.0% to 24.9% and from 65.0% to 75.1%, respectively. The nucleation sites of the recrystallized grains were found mainly on the grain boundaries. Occasional new recrystallized grains were also found in the twins. The reduction of the fraction of the double twin boundaries was attributed to the new grain recrystallization. And the consumption of the twins by the growing recrystallized grains was observed across the scanning area. This was considered as the reason for the heavy reduction in the fraction value of the tensile twins (from 44.3% to 18.1% compared to the as-compressed state). As a result of the strong recrystallization, the pole figure and IPF also presented a corresponding change (shown in Figure 4-47(e) and (f)). The maximum value of the pole figure showed a significant reduction from 20.6 to 16.4. Moreover, although the position of the peak was still the same as the as-compressed state, the orientation of the recrystallized grains was able to be read in the pole figure at this stage. The new grains showed the direction which distributed along the bottom half of the ND-axis and meanwhile diffused around the weak peak close to the TD.

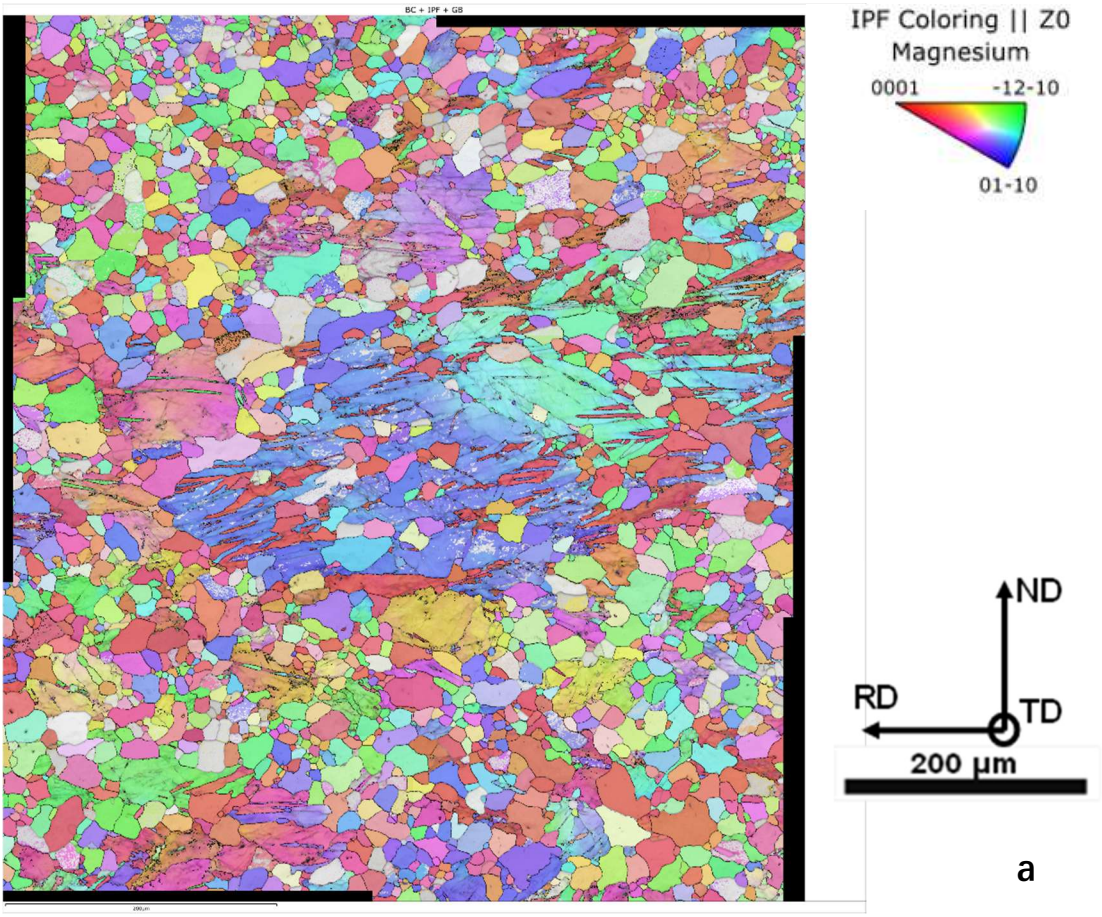

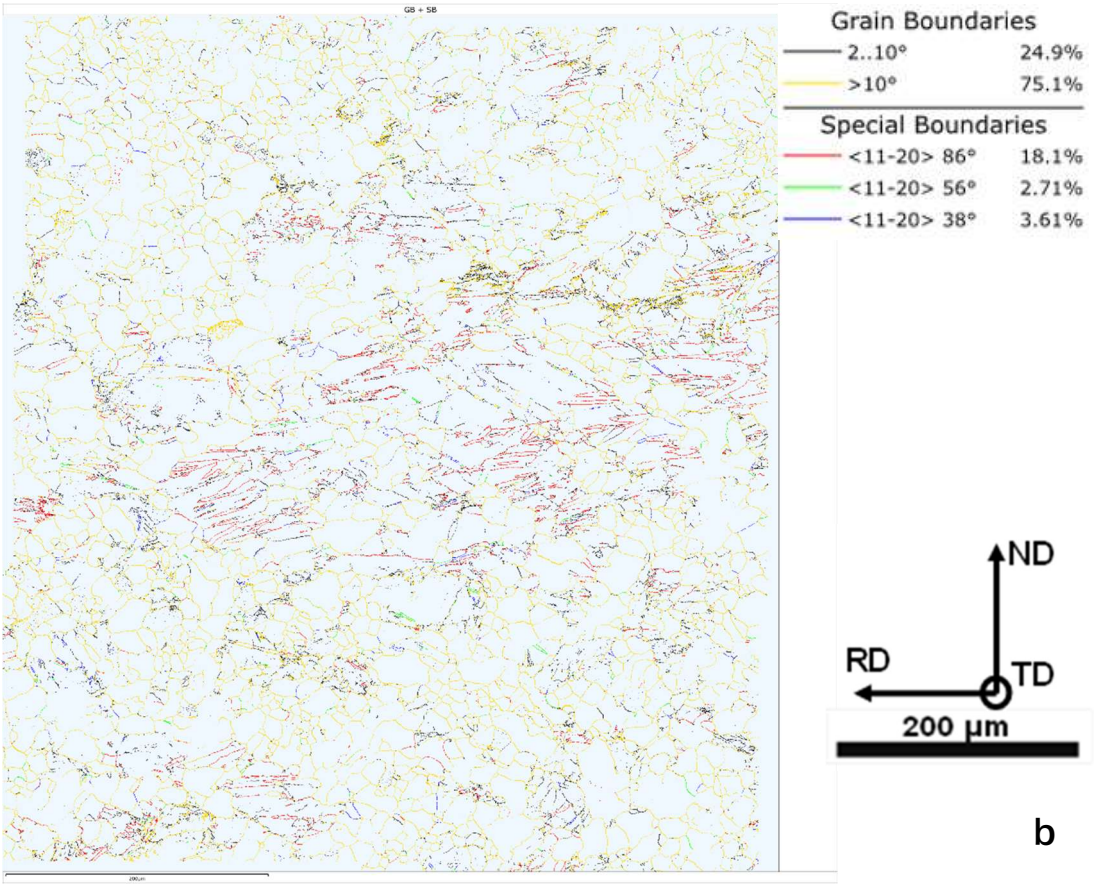
GB + SB
Grain Boundaries
2..10° 24.9%
>10° 75.1%
Special Boundaries
<11-20> 86° 18.1%
<11-20> 56° 2.71%
<11-20> 38° 3.61%
ND
RD
TD
200 µm

b

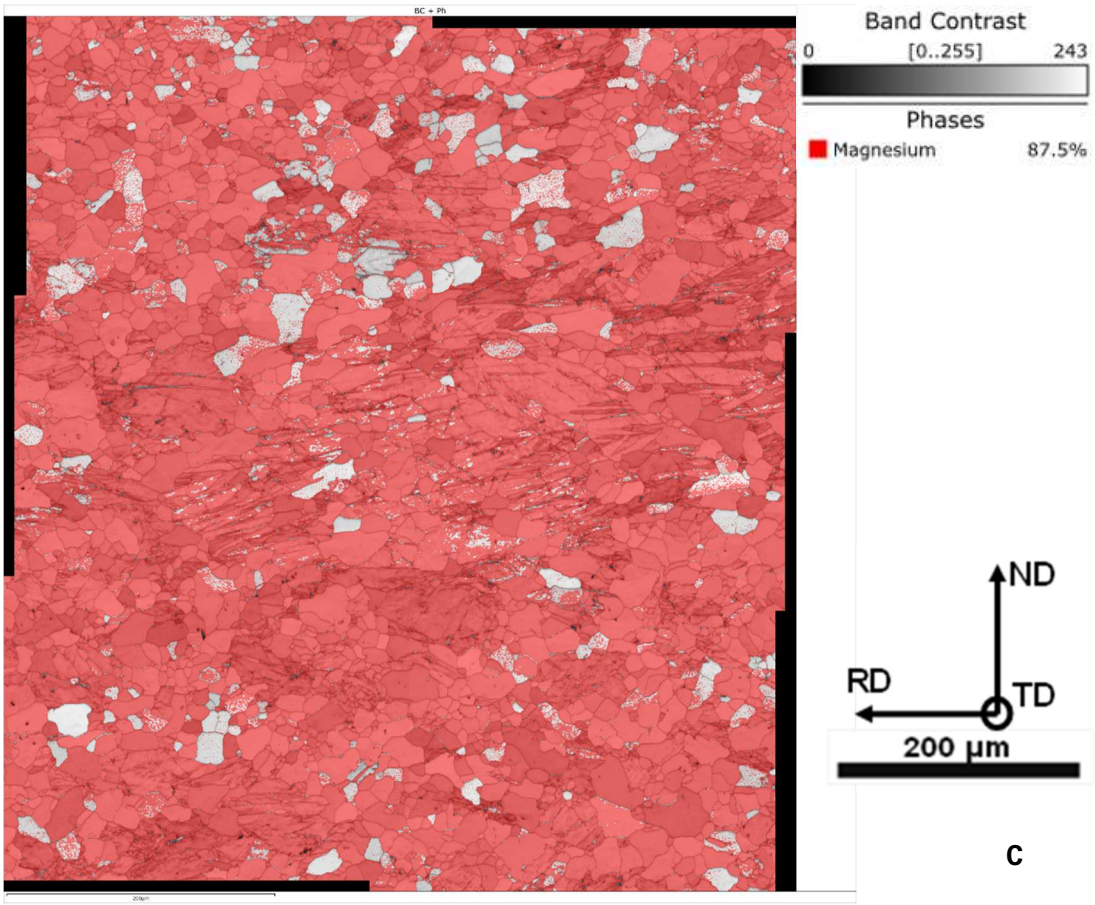
BC + Ph
Band Contrast
0 [0..255] 243
Phases
Magnesium 87.5%
ND
RD
TD
200 µm

c

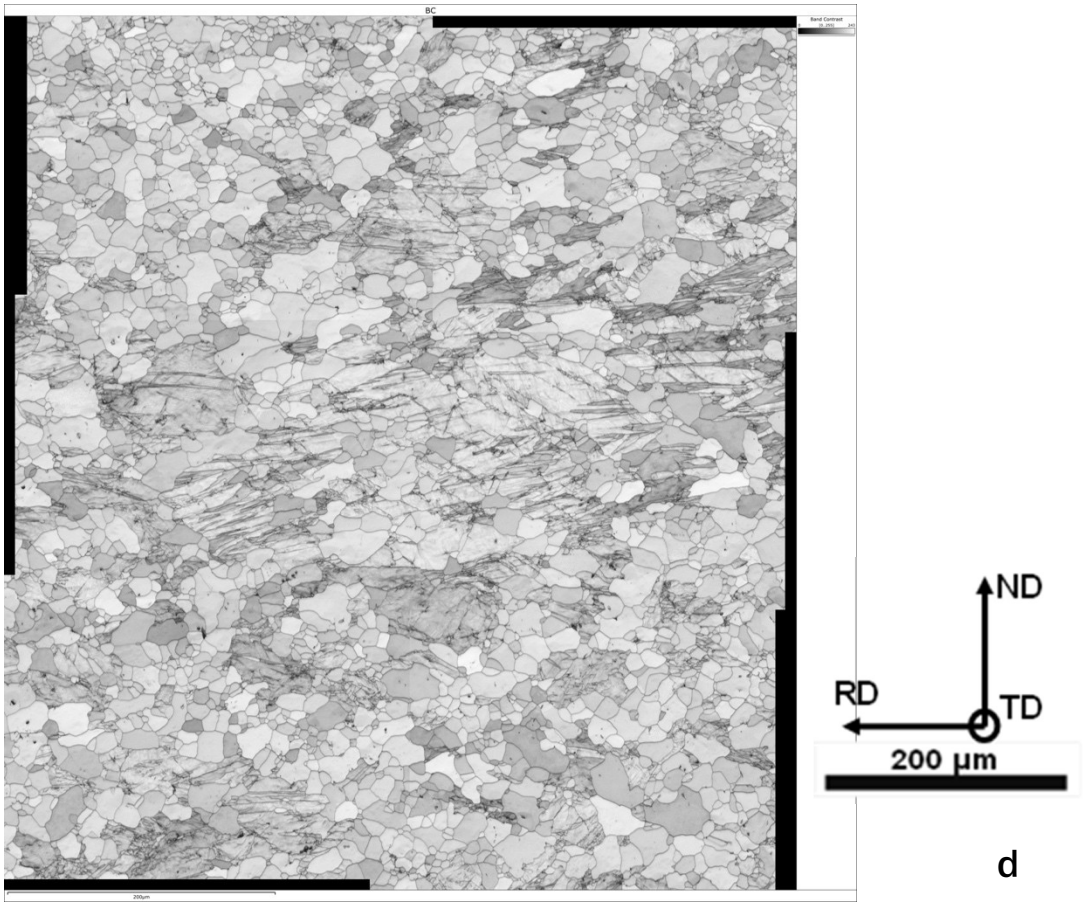
BC
ND
RD
TD
200 µm

d

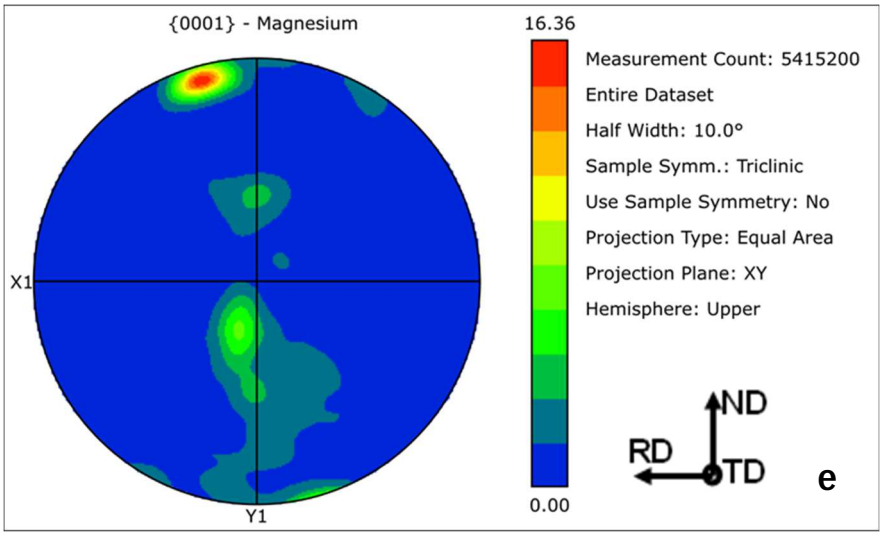
{0001} - Magnesium
16.36
Measurement Count: 5415200
Entire Dataset
Half Width: 10.0°
Sample Symm.: Triclinic
Use Sample Symmetry: No
Projection Type: Equal Area
Projection Plane: XY
Hemisphere: Upper
X1
Y1
0.00
ND
RD
TD

e

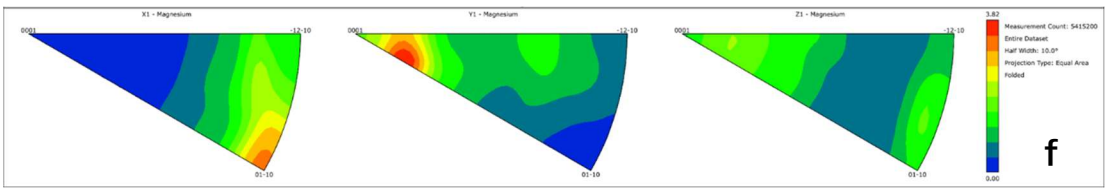
X1 - Magnesium
Y1 - Magnesium
Z1 - Magnesium
3.82
0.00

f

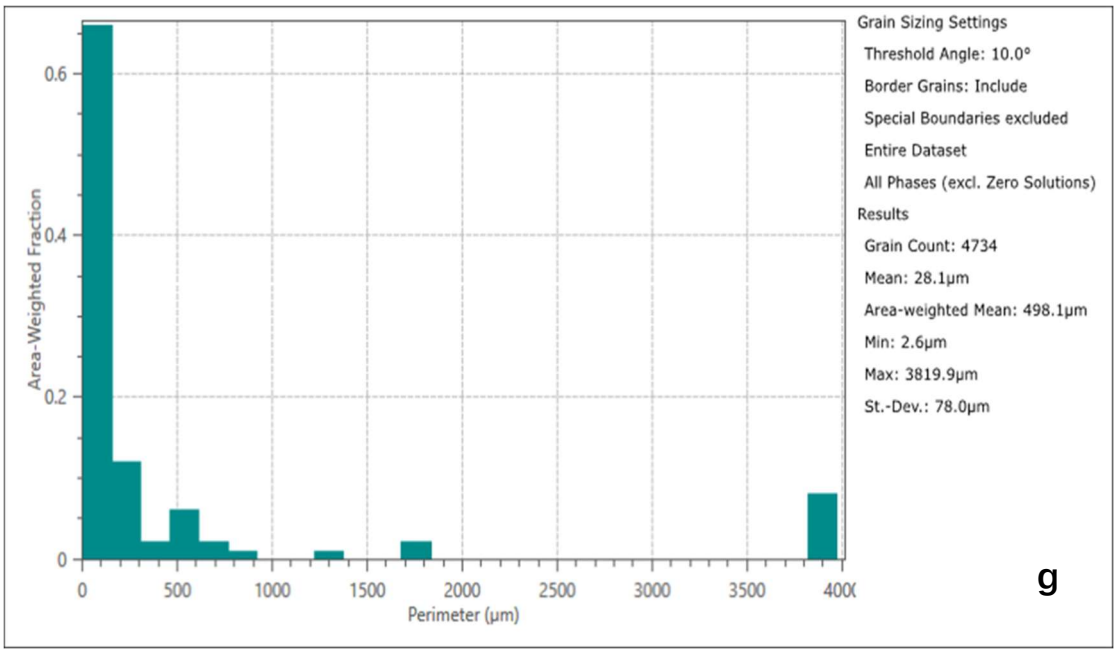

Figure 4-47 The EBSD result of the 2790s annealed 1D compressed Mg-0.2Ca-0.3Zn specimen: (a) The inverse pole figure map and grain boundaries, (b) The grain boundaries and the special grain boundaries, (c) The band contrast and the phase analysis, (d) The band contrast, (e) The pole figure, (f) The inverse pole figures, (g) Grain size distribution expressed as grain boundary perimeter

After a further increase in the annealing time by 60s i.e. after the 3270s annealing, the microstructure presented further changes in recrystallization. The temperature of the specimen at that time point was 340℃. The IPF map of the specimen (shown in Figure 4-48(a)) showed that the main variation of the microstructure was the grain growth during this longer annealing time. Only a very small number of new recrystallized grains were found in the scanning area. The average grain size of the specimen increased a little compared to the last stage, which was 28.5μm (shown in Figure 4-48(g)). The little changes in the microstructure were also reflected in the value of the boundary fraction. Figure 4-48(b) shows the boundary fraction of the tensile twins, compressive twins and double twins was changed from 18.1% to 17.6%, 2.7% to 2. 5% and 3.6% to 3.4%, respectively. Meanwhile, the fraction of the low-angle grain boundary and the high-angle grain boundary were changed from 24.9% to 23.8% and from 75.1% to 76.2%, respectively. Figure 4-48(e) indicates the reduction of the maximum value of the pole figure, which was from 16.4 to 15.2. The signal distributed along the ND-axis and the weak peak close to the TD were both found strengthened i.e. the weakened texture of the specimen was being formed.

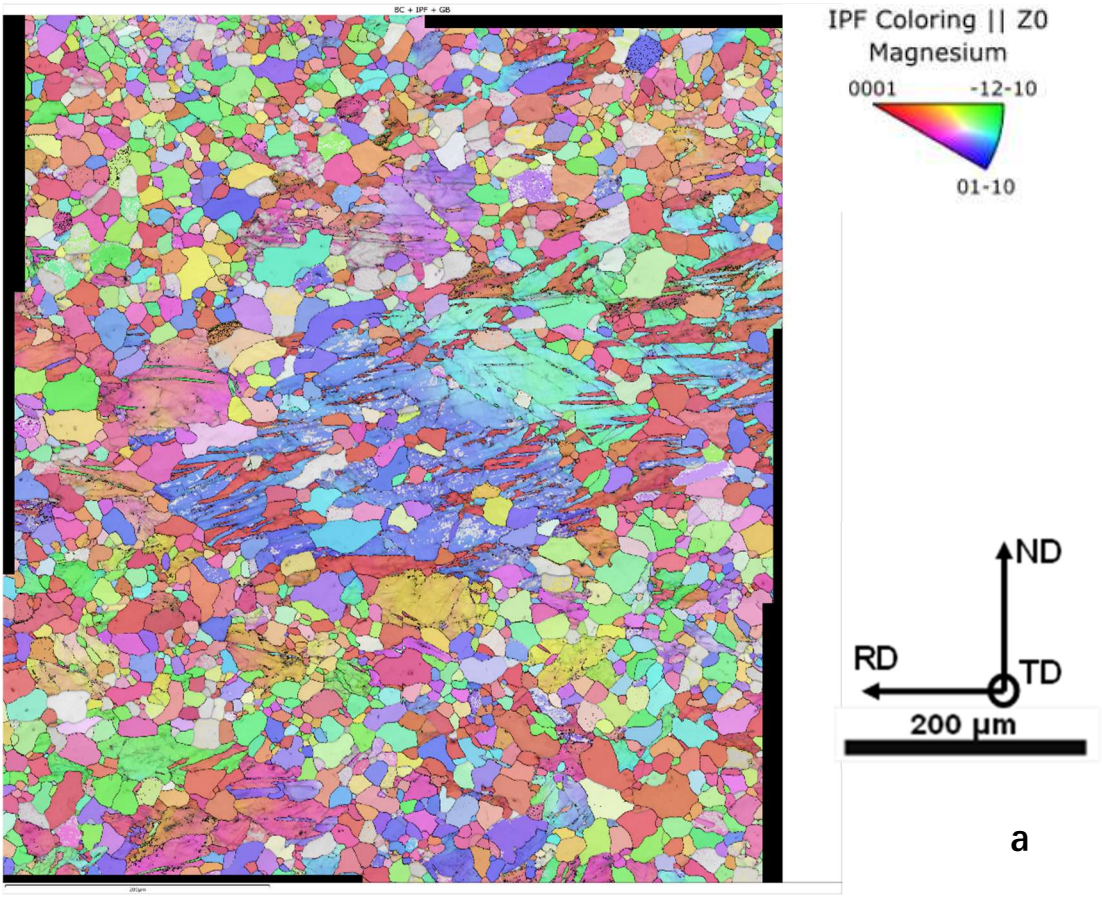
IPF Coloring || Z0
Magnesium
0001
-12-10
01-10
ND
RD
TD
200 µm

a

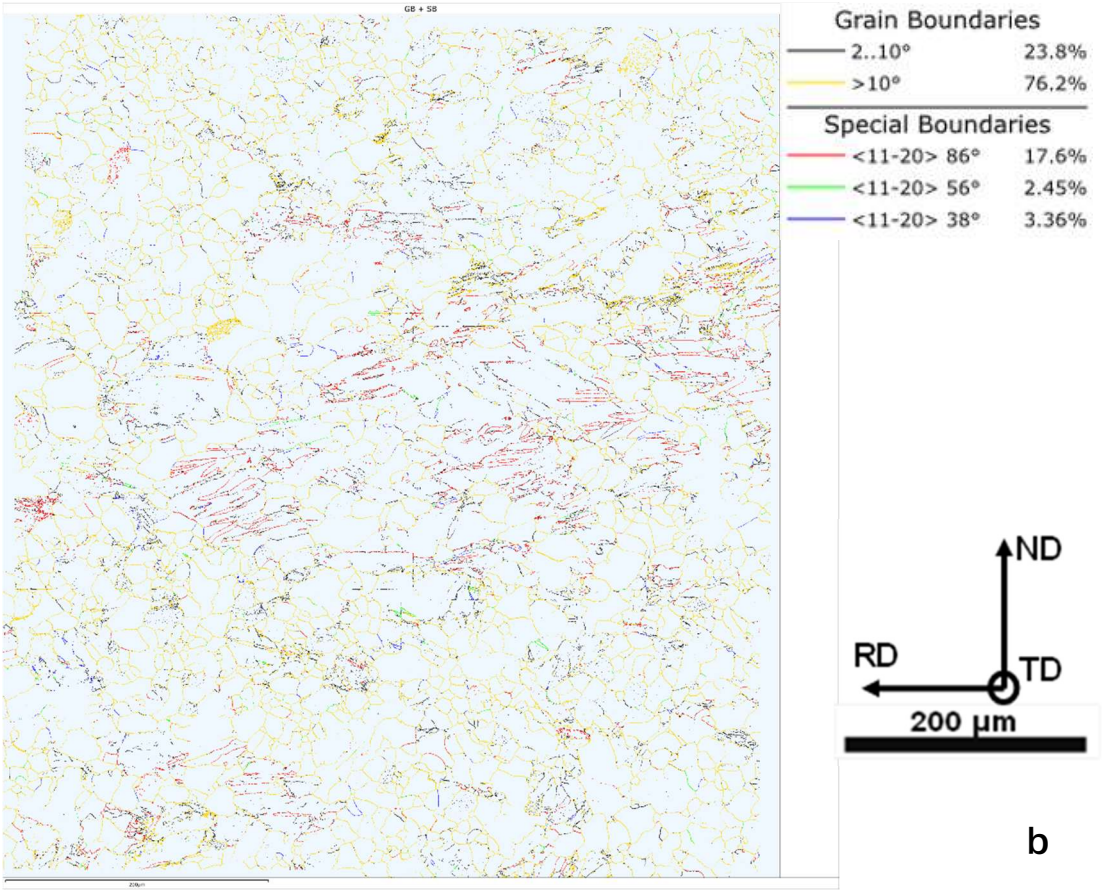
Grain Boundaries
2..10° 23.8%
>10° 76.2%
Special Boundaries
<11-20> 86° 17.6%
<11-20> 56° 2.45%
<11-20> 38° 3.36%
ND
RD
TD
200 µm

b

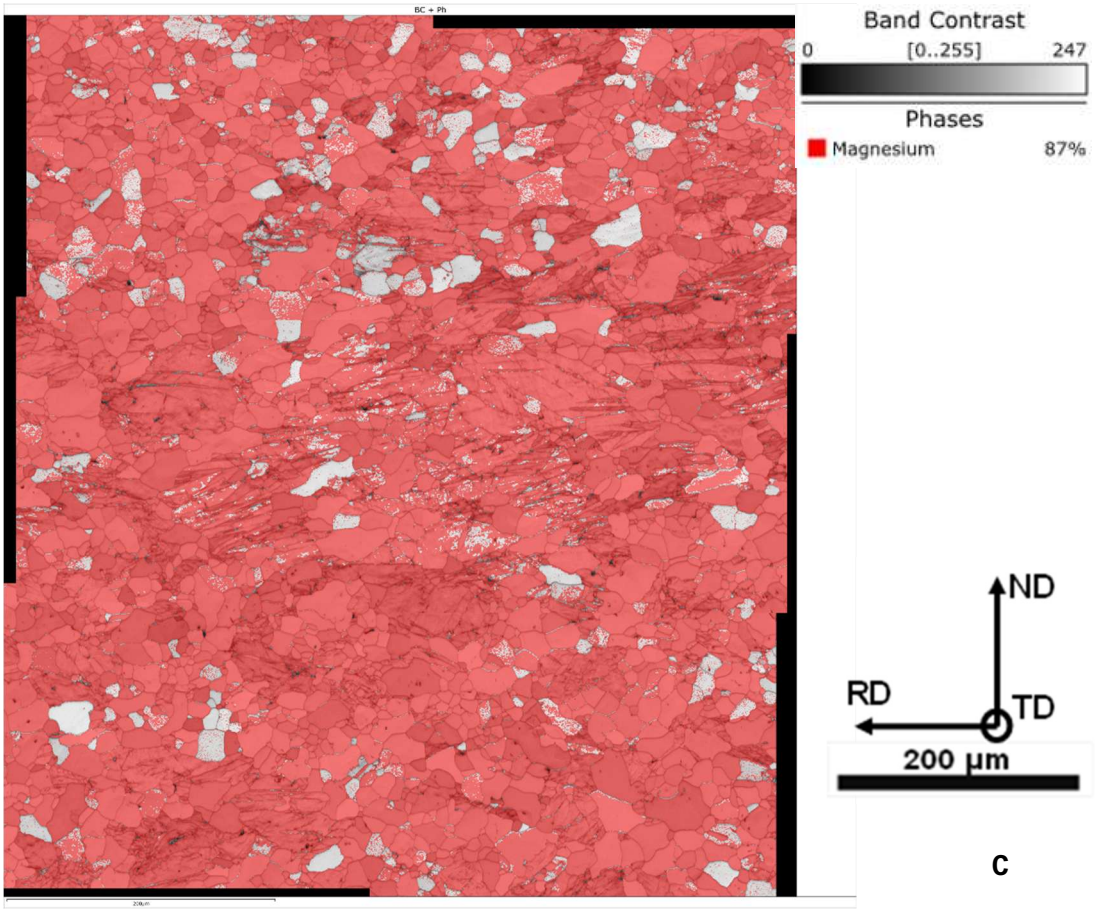
BC + Ph
Band Contrast
0
[0..255]
247
Phases
Magnesium
87%
ND
RD
TD
200 µm

c

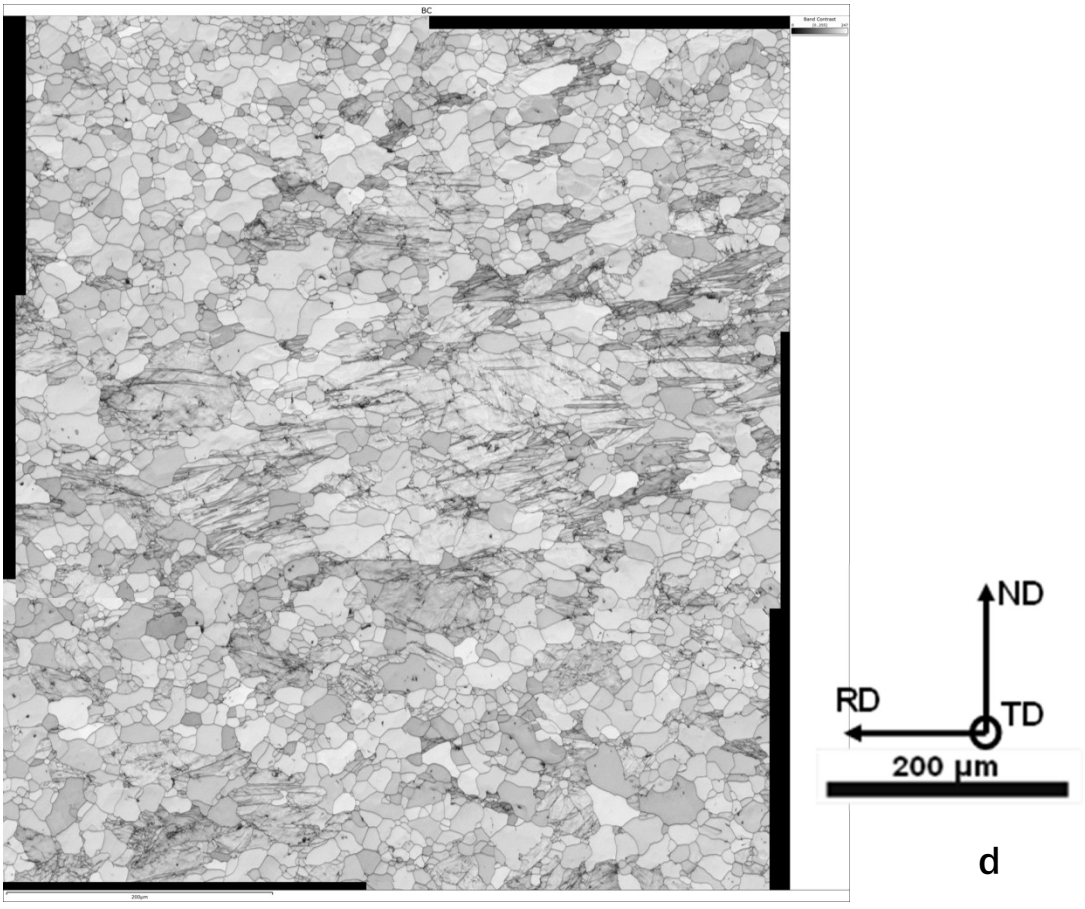
BC
ND
RD
TD
200 µm

d

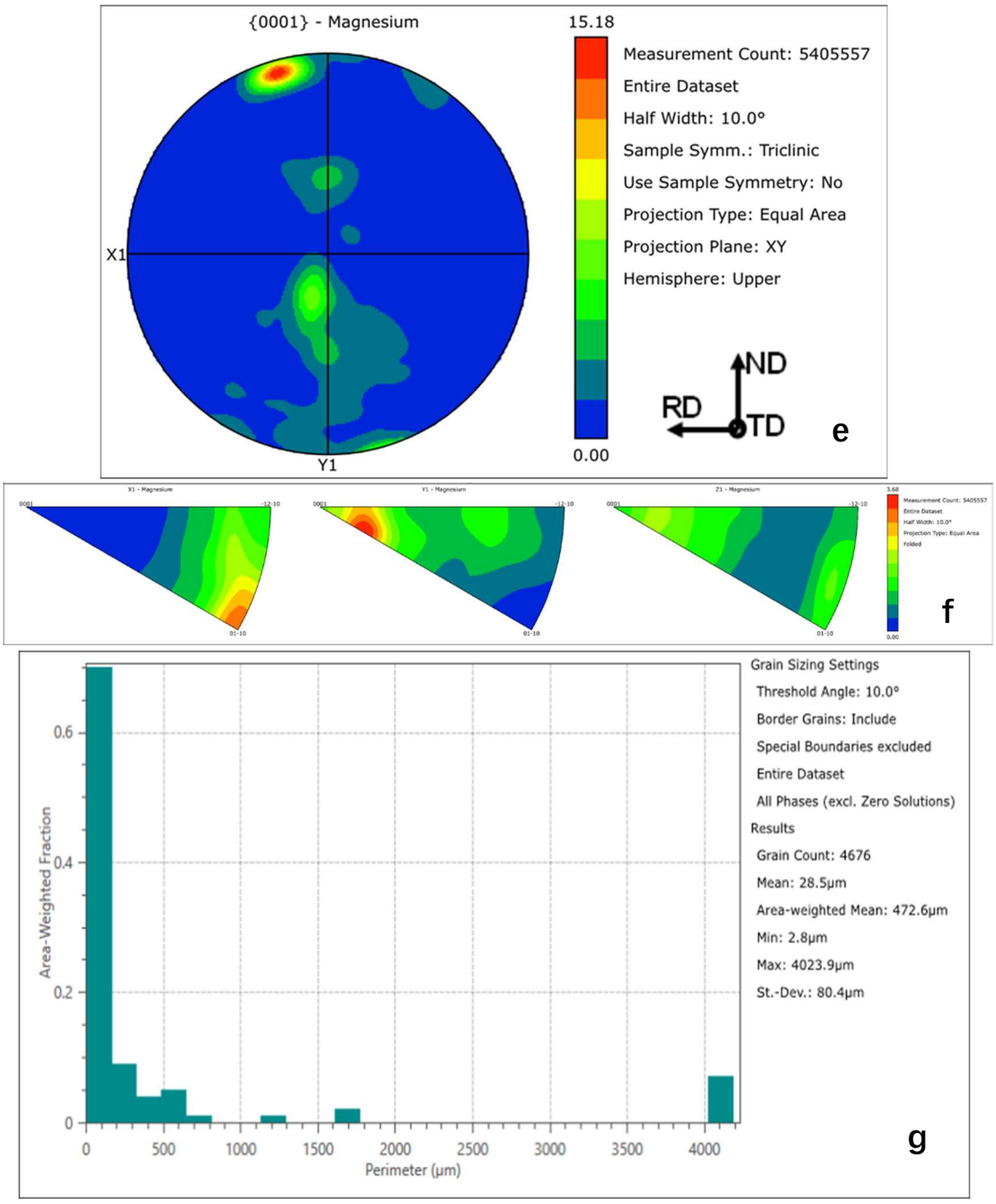

Figure 4-48 The EBSD result of the 3270s annealed 1D compressed Mg-0.2Ca-0.3Zn specimen: (a) The inverse pole figure map and grain boundaries, (b) The grain boundaries and the special grain boundaries, (c) The band contrast and the phase analysis, (d) The band contrast, (e) The pole figure, (f) The inverse pole figures, (g) Grain size distribution expressed as grain boundary perimeter

The last EBSD result of the 1D compressed Mg-0.2Ca-0.3Zn (at%) specimen (shown in Figure 4-49) was after 3810s annealing. The highest temperature of the specimen during annealing was 345℃. Figure 4-49(a) indicates that the 60s longer annealing and the 5℃ higher temperature were not enough to push the recrystallization a step forward in the specimen. Compared to the result from the last step, it was hard to

find differences based on the morphology of the grains in the IPF map. Only very few grains were found growing for about $1\mu m$. Except for the large grain in the centre of the scanning area, the top and the bottom region of the IPF map showed an almost fully recrystallized microstructure. The average grain size of the specimen was much smaller than the last stage, which was $20.2\mu m$ (shown in Figure 4-49(g)). This was attributed to the miss identified fine twins in the top left corner shown in red in Figure 4-49(b). The minor variation of the microstructure was also shown by the boundary fraction. Figure 4-49(b) shows the boundary fraction of the tensile twins, compressive twins and double twins all slightly decreased from 17.6% to 16.2%, 2. 5% to 2.2% and 3.4% to 2.9%, respectively. Meanwhile, the fraction of the low-angle grain boundary and the high-angle grain boundary were changed from 23.8% to 23.3% and 76.2% to 76.7%, respectively. A notable point was that the real fraction of the tensile twin boundary was supposed to be lower than 16.2%. The reason was attributed to misidentification within the grain located at the top-left of the scanning area (shown in Figure 4-49(b)), forming a “red grain”. For the grain orientation distribution, Figure 4-49(e) presents no obvious variation. A reduction of the maximum pole intensity was found, which was from 15.2 to 14.5. Meanwhile, the enhancement of the signal for the randomly distributed grains was also observed. The pole intensity of the weak peak close to the TD was found to increase to 6.7.

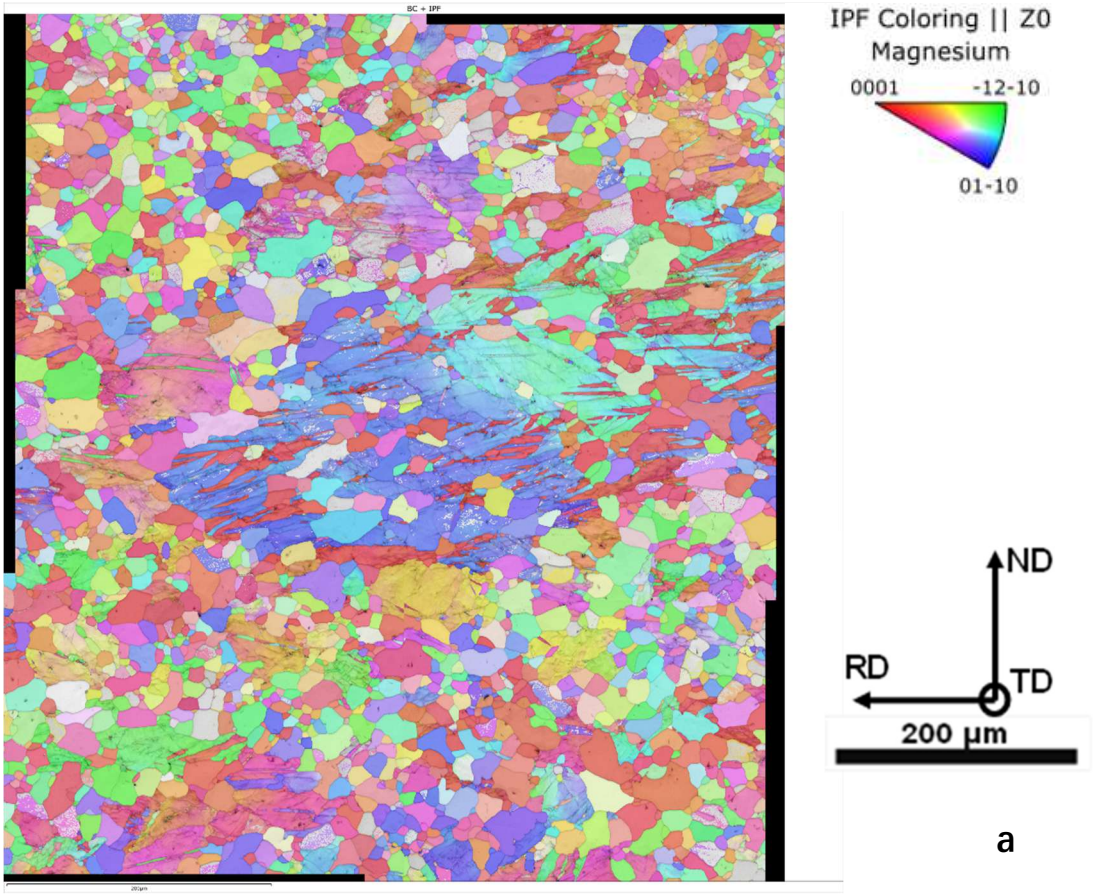

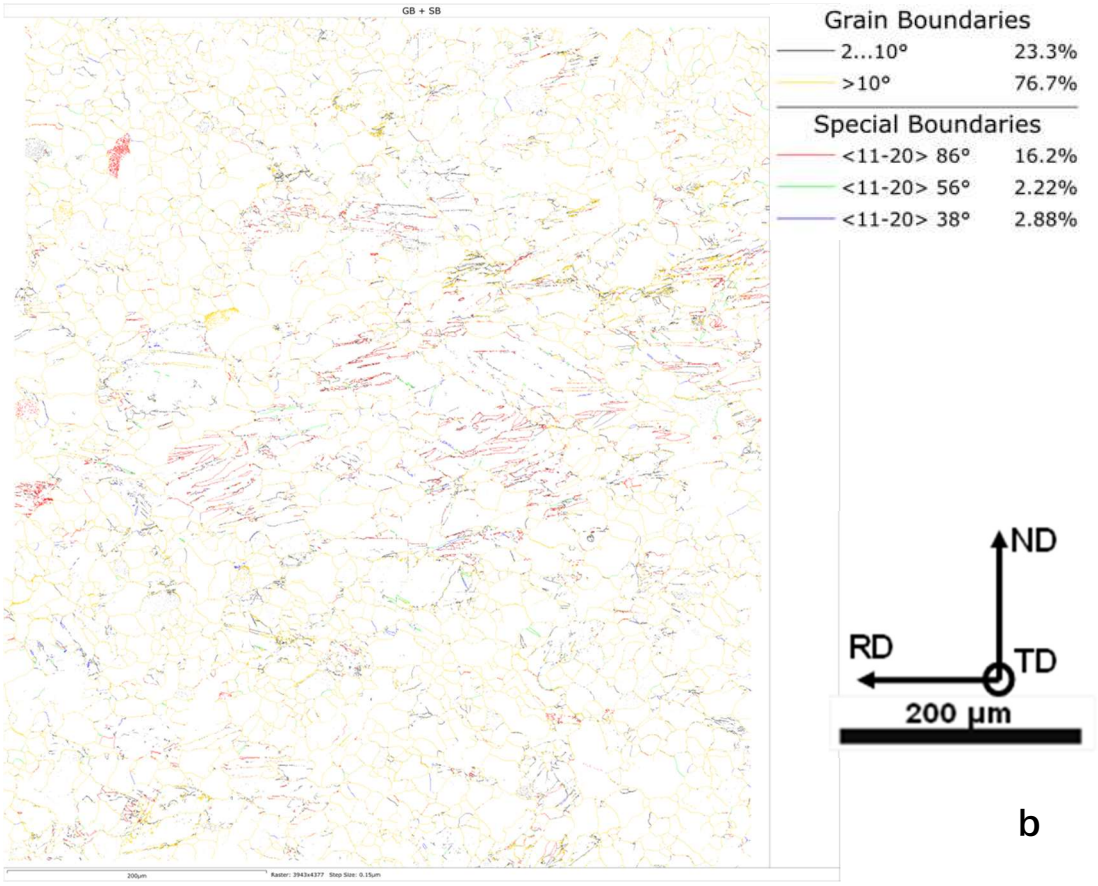
GB + SB
Grain Boundaries
2...10° 23.3%
>10° 76.7%
Special Boundaries
<11-20> 86° 16.2%
<11-20> 56° 2.22%
<11-20> 38° 2.88%
ND
RD
TD
200 µm

b

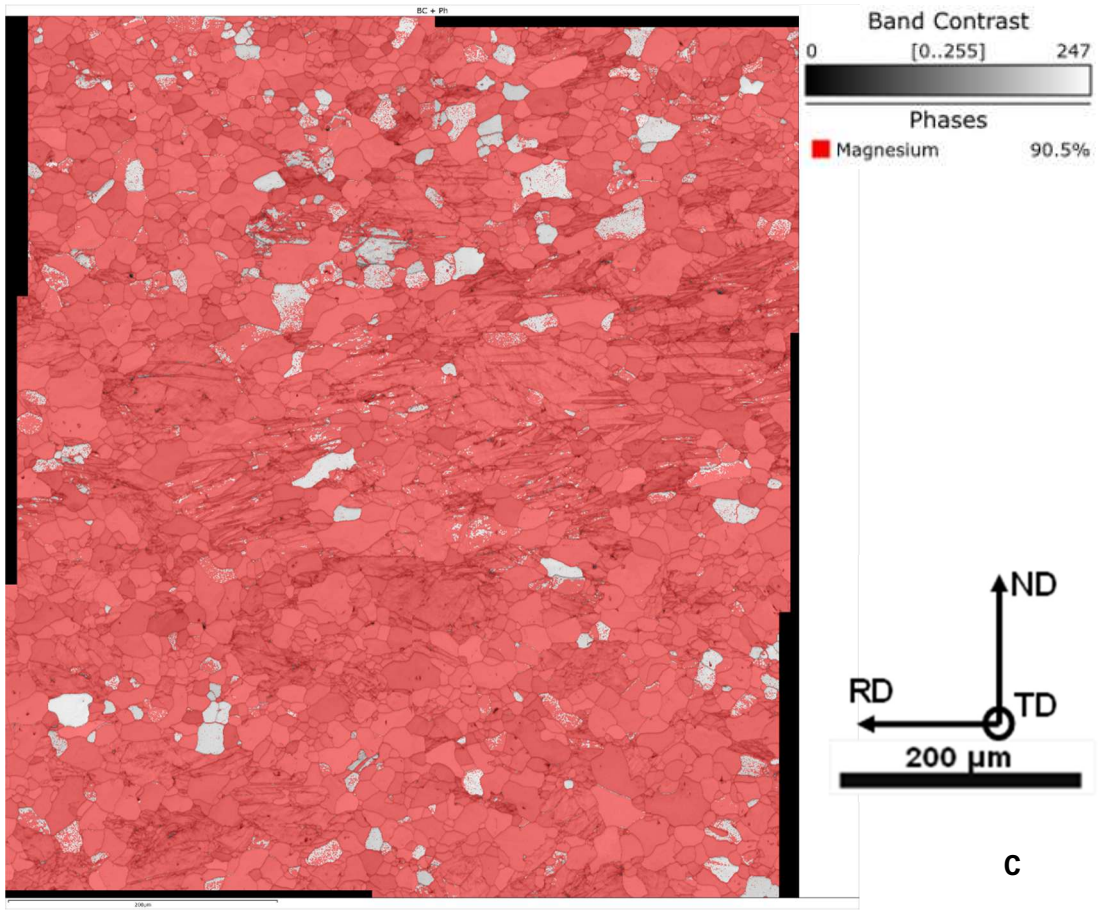
BC + Ph
Band Contrast
0 [0..255] 247
Phases
Magnesium 90.5%
ND
RD
TD
200 µm

c

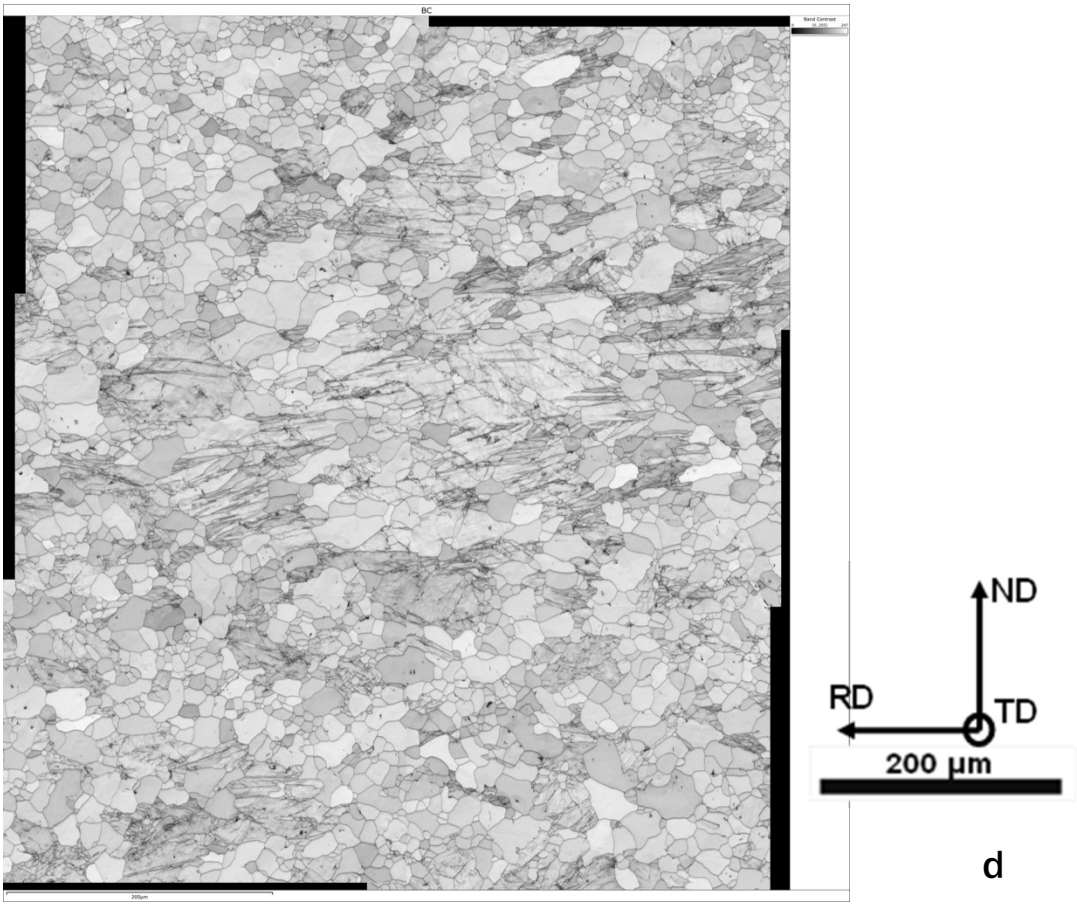
BC
ND
RD
TD
200 µm
d

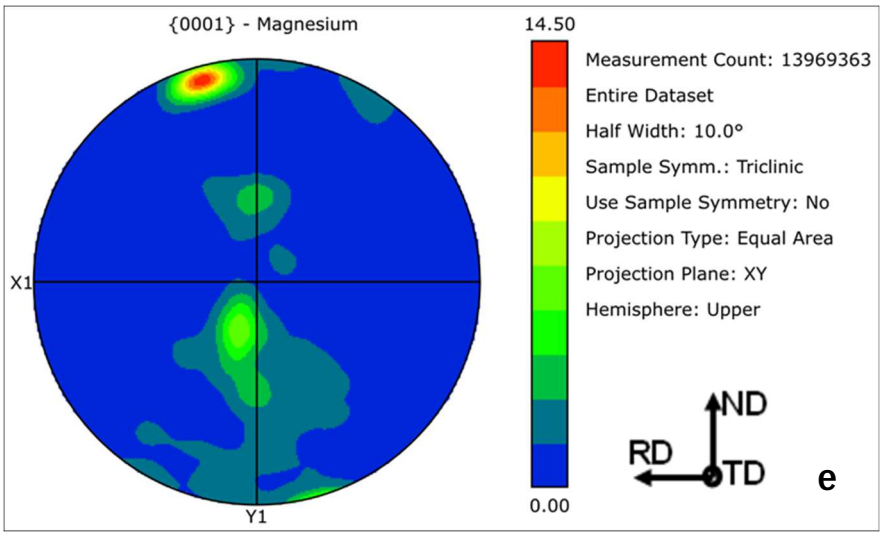
{0001} - Magnesium
14.50
0.00
Measurement Count: 13969363
Entire Dataset
Half Width: 10.0°
Sample Symm.: Triclinic
Use Sample Symmetry: No
Projection Type: Equal Area
Projection Plane: XY
Hemisphere: Upper
X1
Y1
ND
RD
TD
e

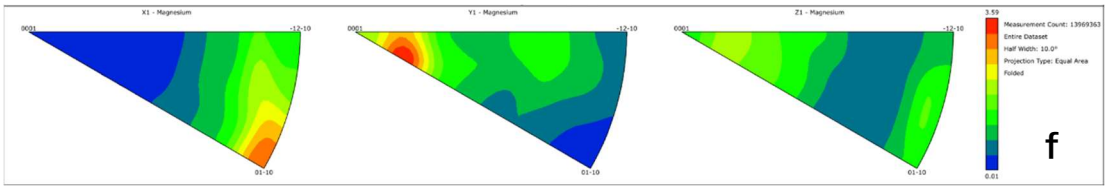
X1 - Magnesium
Y1 - Magnesium
Z1 - Magnesium
f

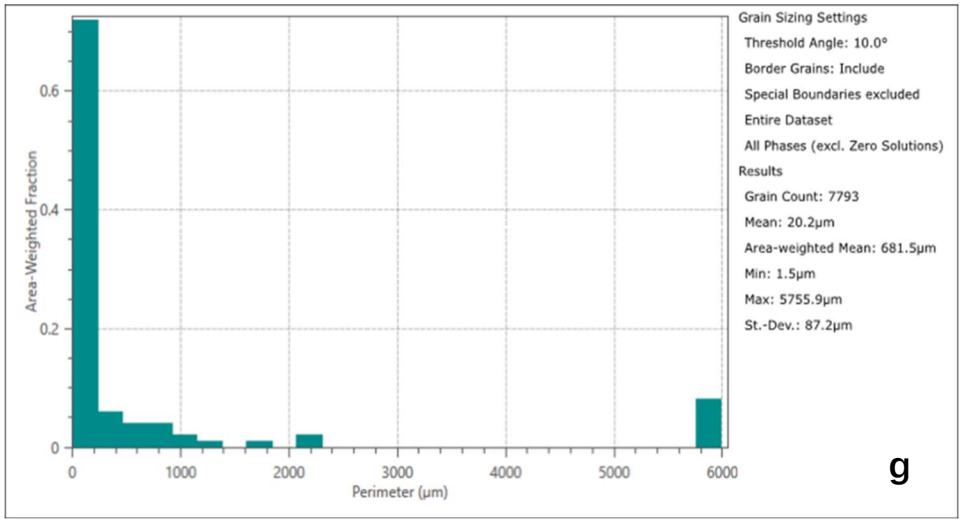

Figure 4-49 The EBSD result of the 3810s annealed 1D compressed Mg-0.2Ca-0.3Zn specimen: (a) The inverse pole figure map and grain boundaries, (b) The grain boundaries and the special grain boundaries, (c) The band contrast and the phase analysis, (d) The band contrast, (e) The pole figure, (f) The inverse pole figures, (g) Grain size distribution expressed as grain boundary perimeter

The fully recrystallized EBSD map of the 1D compressed Mg-0.2Ca-0.3Zn (at%) specimen could not be obtained due to the slow recrystallization of the large grain at the center of the scanning area. However, the rest of the scanned area exhibited a relatively high rate of recrystallization. Thus, the remaining area was used as the result of the nearly fully recrystallized specimen to be compared with other specimens. A subset of the same area without the large original grain was made from each group of EBSD results mentioned above and will be discussed in the next chapter. The EBSD subset shown below is for the 3810s annealed specimen (Figure 4-50). Figure 4-50(f) shows that the average grain size was reduced from $20.2\mu m$ to $19.1\mu m$. And the boundary fraction in the subset area is exhibited in Figure 4-50(b). The boundary fraction of the tensile twins, compressive twins and double twins was very different to the full map results, which all reduced from16.2% to 10.1%, 2.2% to 1.6% and 2.9% to 1.7%, respectively. Meanwhile, the fraction of the low-angle grain boundary and the high-angle grain boundary was 21.7% and 78.3%, respectively, indicating a higher fraction of recrystallization in this area. The most obvious difference was found in the pole figure and IPF (shown in Figure 4-50(d) and (e)). Compared to the very concentrated grain orientation distribution of the full map pole figure, the subset pole figure exhibited a much more random grain orientation distribution. The new grains showed a preferred orientation which was close to the TD (5° tilted from it). Another two weaker peaks were shown on the other side of the ND axis with similar tilt angle. The rest of the recrystallized grains had an orientation distributed between the ND and TD and diffused 5° to 30°. The position where the maximum pole intensity changed to

close the TD. The maximum value of the pole figure was significantly reduced from 14.5 to 5.0.

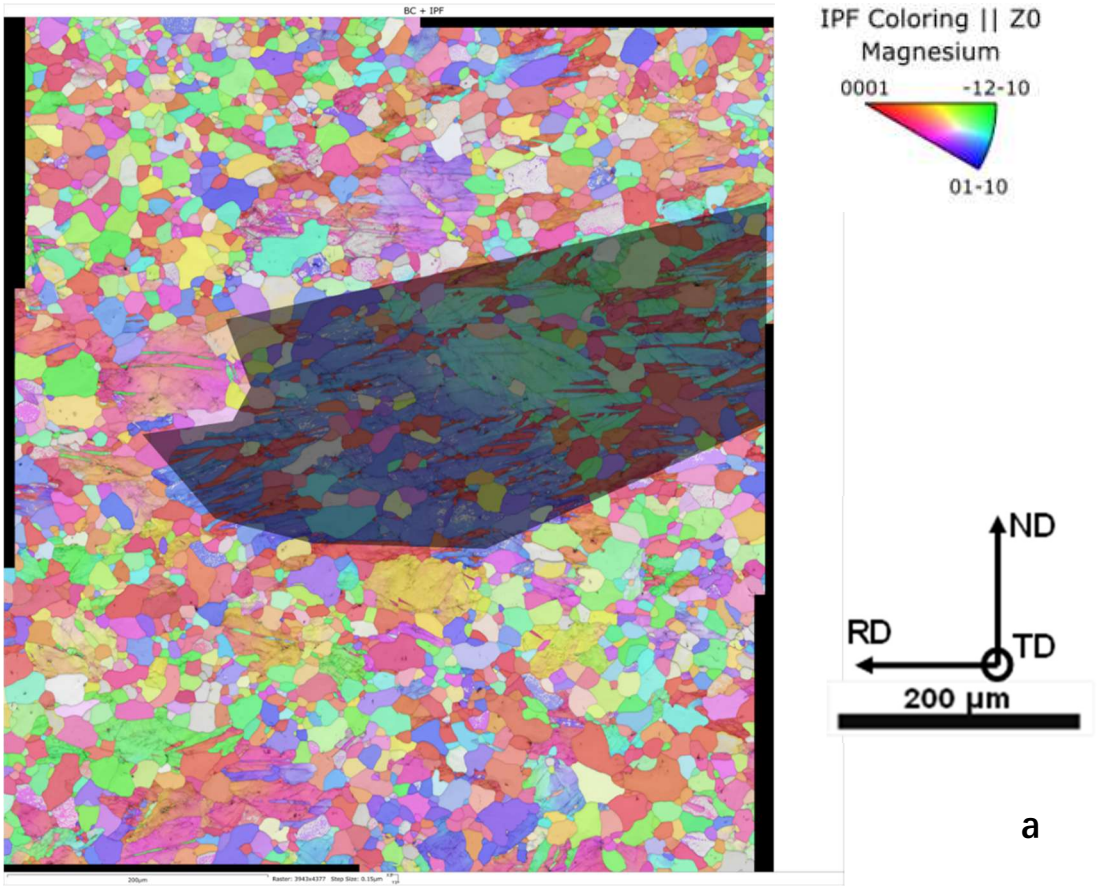

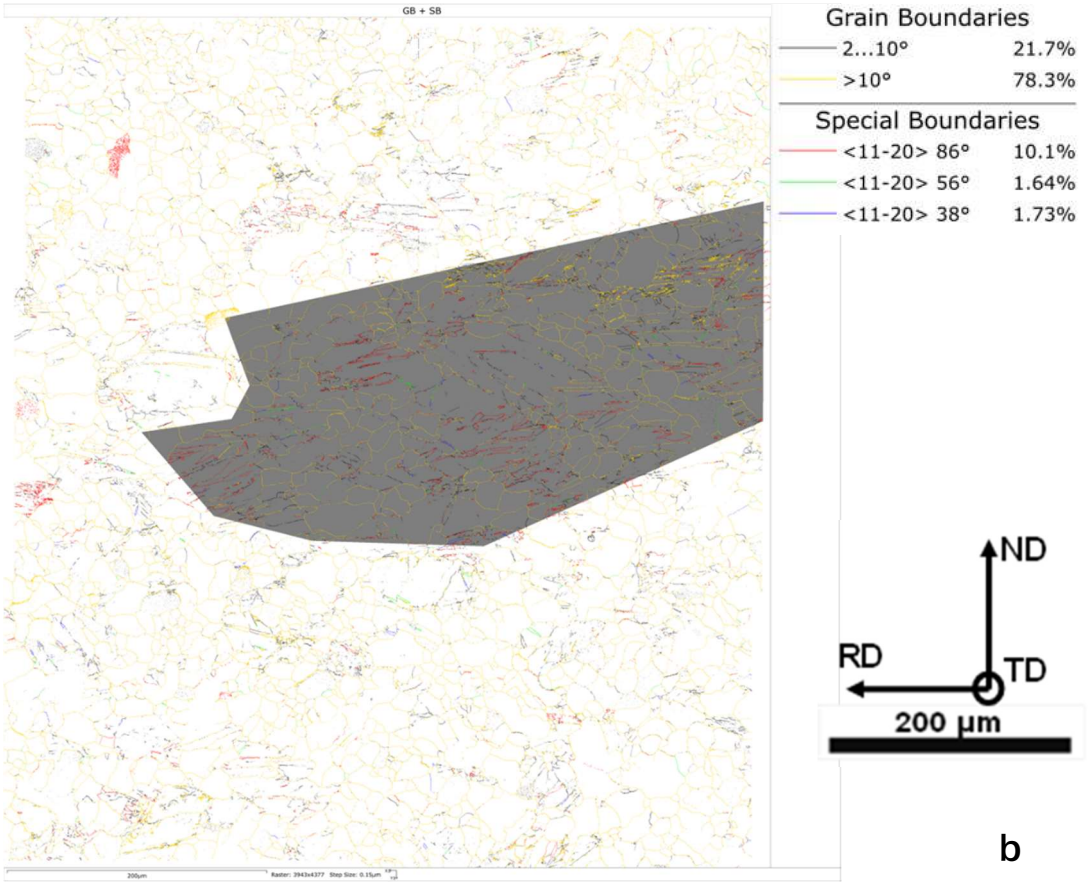

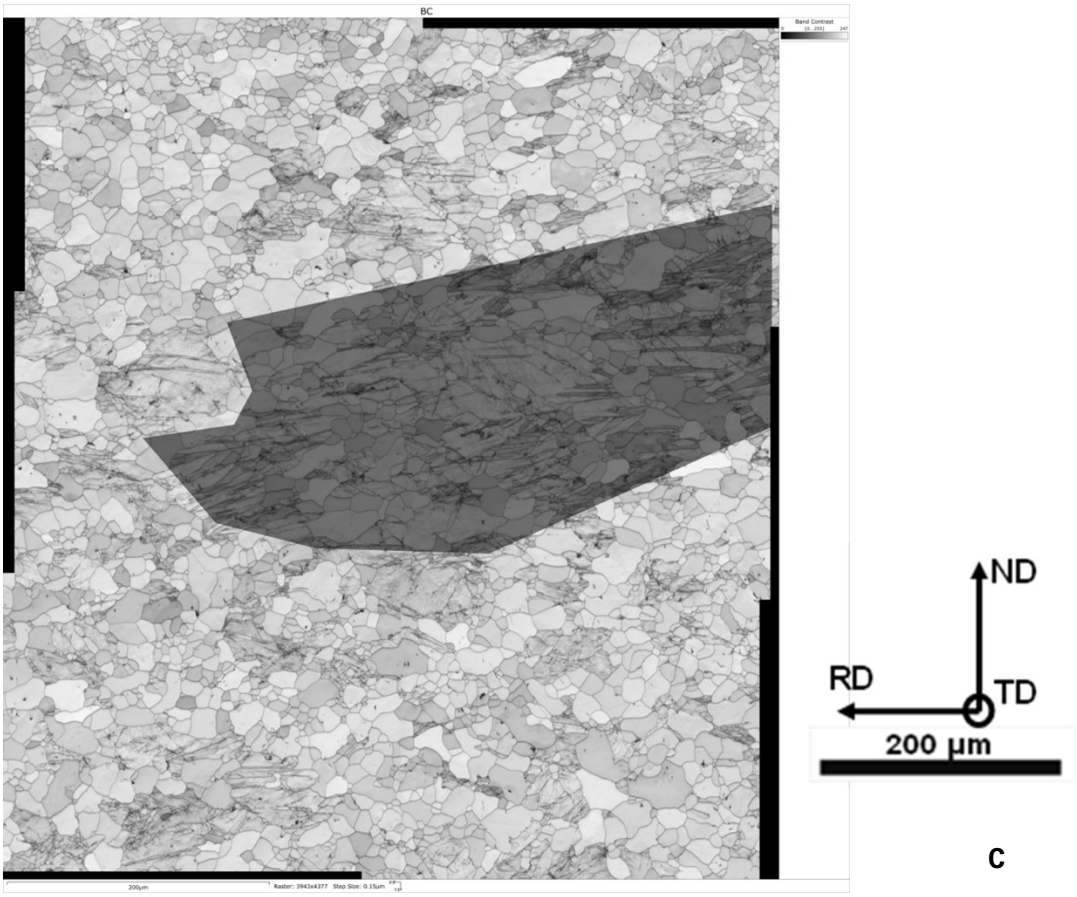
BC
Band Contrast
ND
RD
TD
200 µm
c

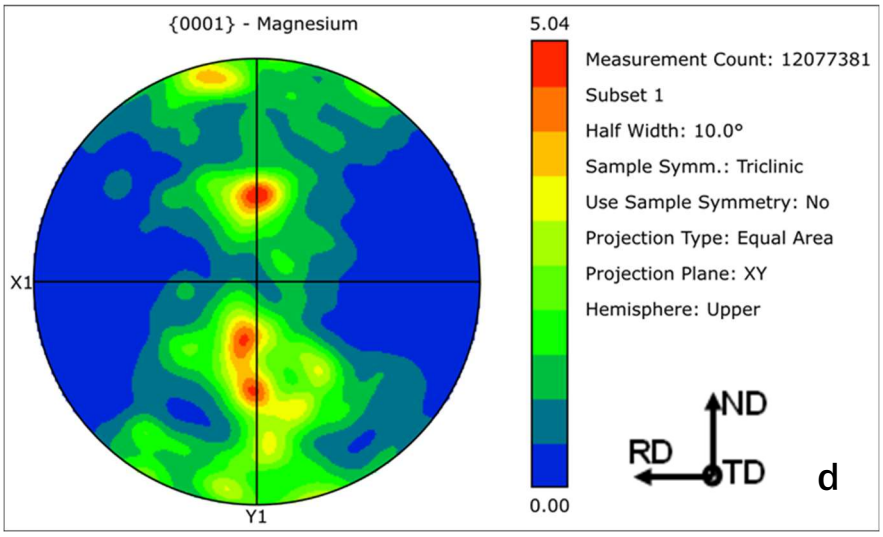
{0001} - Magnesium
5.04
0.00
Measurement Count: 12077381
Subset 1
Half Width: 10.0°
Sample Symm.: Triclinic
Use Sample Symmetry: No
Projection Type: Equal Area
Projection Plane: XY
Hemisphere: Upper
X1
Y1
ND
RD
TD
d

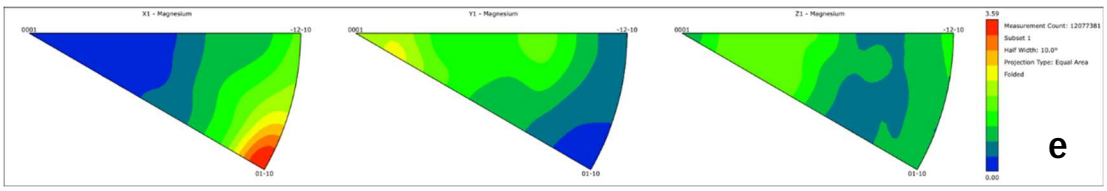
X1 - Magnesium
Y1 - Magnesium
Z1 - Magnesium
e

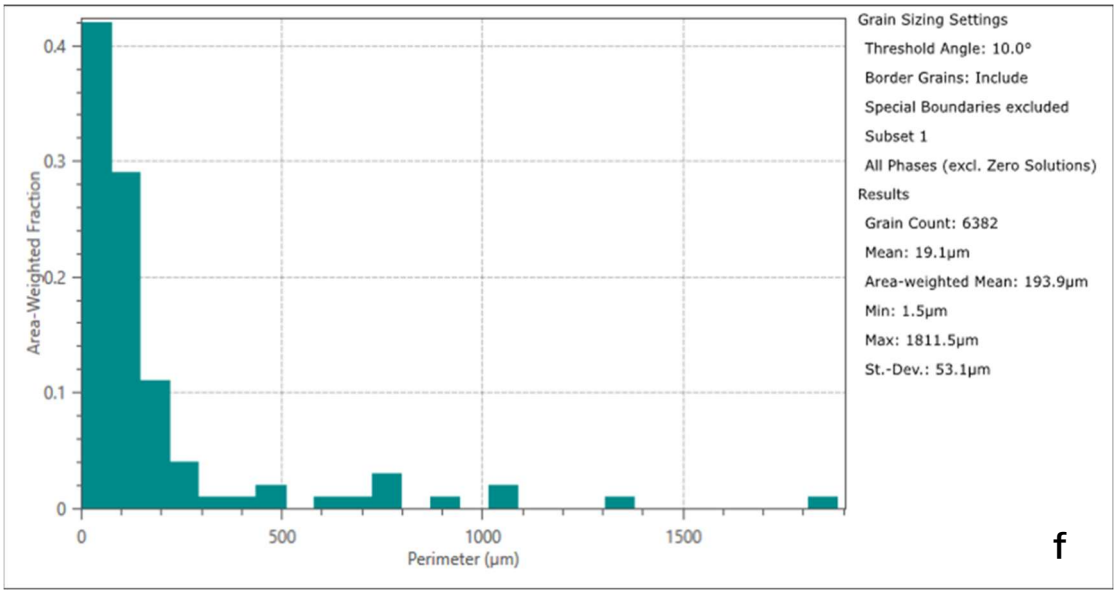

Figure 4-50 The EBSD result of the 3810s annealed 1D compressed Mg-0.2Ca-0.3Zn specimen without huge grain: (a) The inverse pole figure map and grain boundaries, (b) The grain boundaries and the special grain boundaries, (c) The band contrast, (d) The pole figure, (e) The inverse pole figures, (f) Grain size distribution expressed as grain boundary perimeter

4.3.2.2.2 The one-direction (1D) compressed Mg-0.1Ca-0.4Zn (at%) specimen

Figure 4-51 to 4-57 show the EBSD results of the 1D compressed Mg-0.1Ca-0.4Zn (at%) specimen from the as-compressed state to the recrystallized state. For the specimen before the annealing process, the grain size was not quite uniform (shown in Figure 4-51(a)). The largest grain had a size of about 160μm, while many small grains were as small as 3μm. The average grain size of the specimen was 14.7μm(shown in Figure 4-51(g)). From Figure 4-51(c) it was clear that the shear bands (marked by white circles) and the fine twins occupied approximately 28% of the area in the EBSD map. And the grain boundaries identification (shown in Figure 4-51(b)) indicated that the boundary fraction of the tensile twin, compressive twin and double twin was 39.5%, 3.4% and 8.4%, respectively. The pole figure and IPF (Figure 4-51(e) and (f)) of the specimen exhibited some differences compared to other specimens. Two prominent peaks were observed; both were found to locate near the ND indicating that the majority of the grains maintained an orientation parallel to the compression direction. The intensities of the two peaks were 9.4 and 8.6, respectively. Besides, a few grains aligned with the TD were also observed.

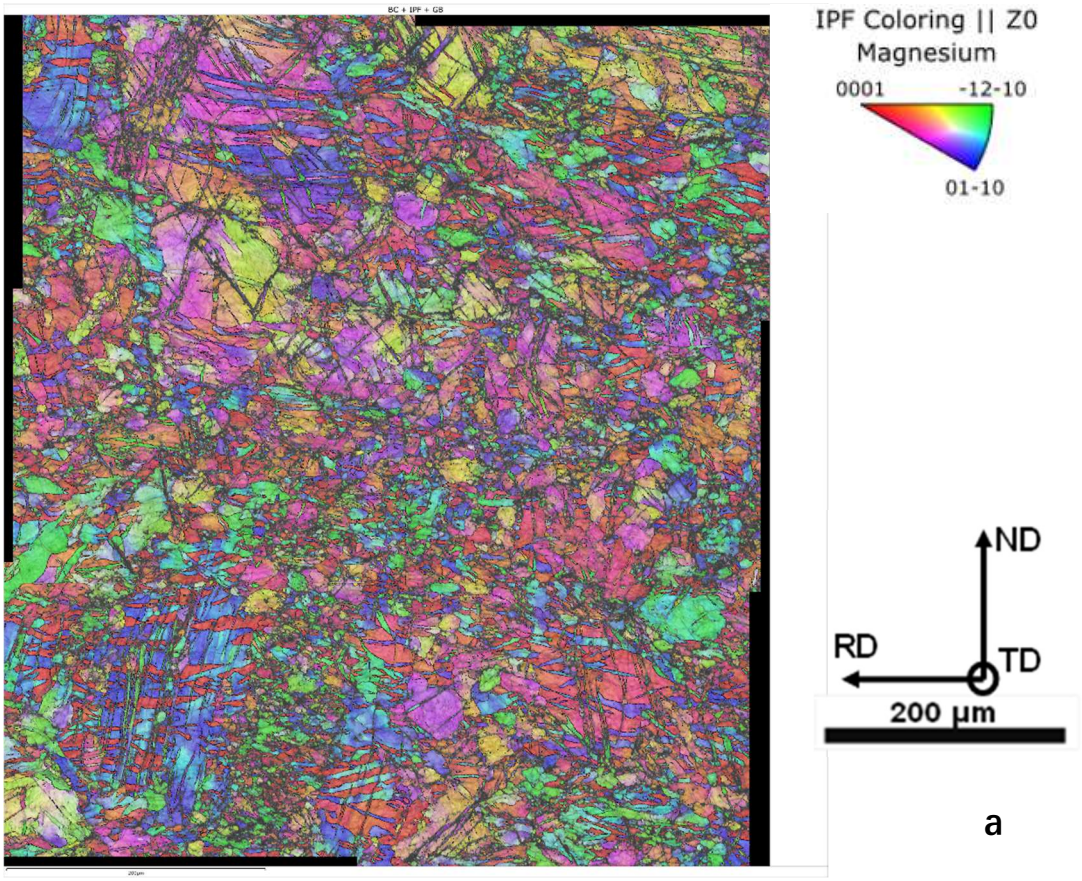
IPF Coloring || Z0
Magnesium
0001
-12-10
01-10
ND
RD
TD
200 µm

a

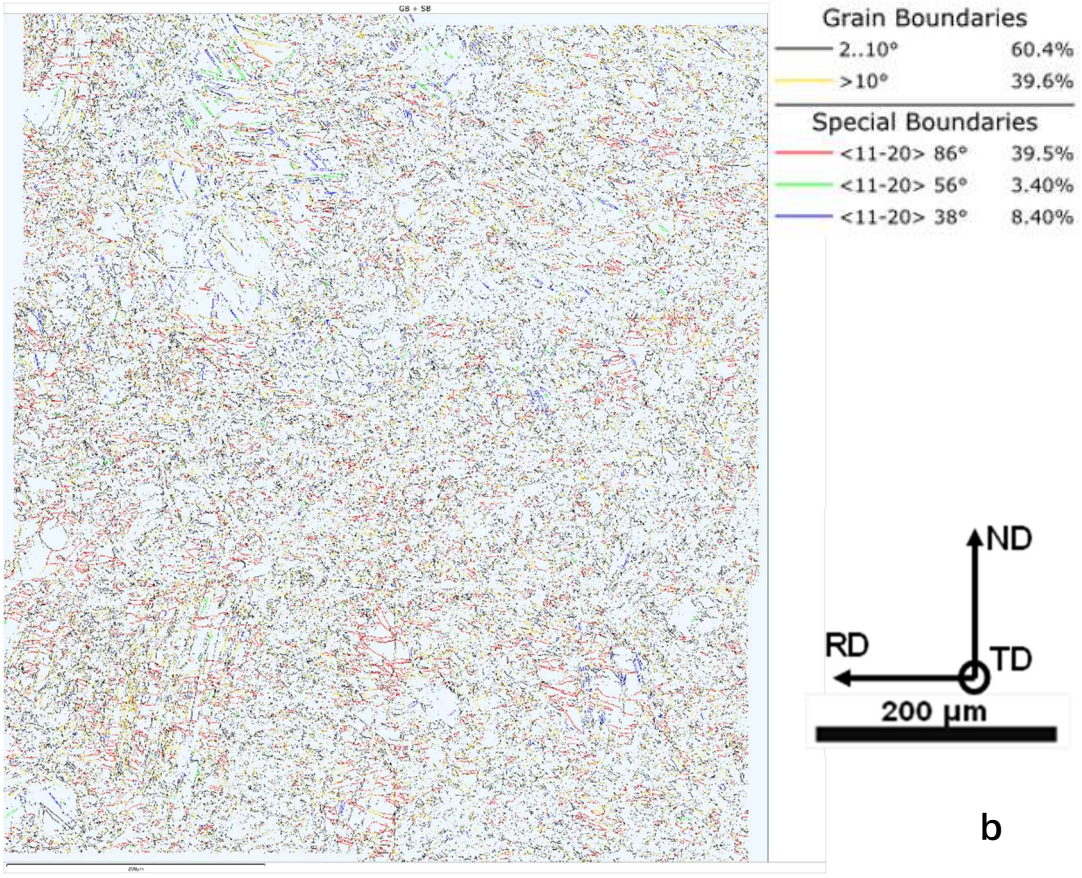
Grain Boundaries
2..10° 60.4%
>10° 39.6%
Special Boundaries
<11-20> 86° 39.5%
<11-20> 56° 3.40%
<11-20> 38° 8.40%
ND
RD
TD
200 µm

b

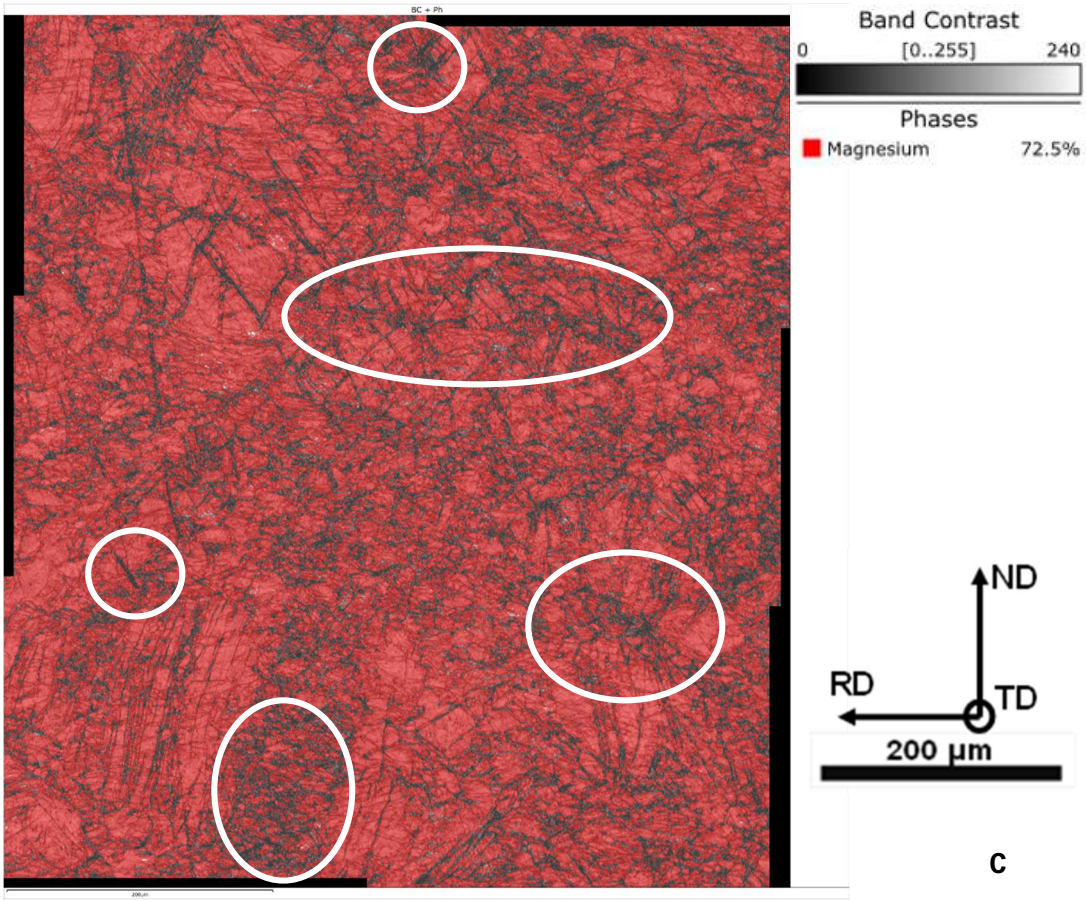
Band Contrast
0
[0..255]
240
Phases
Magnesium
72.5%
ND
RD
TD
200 µm

c

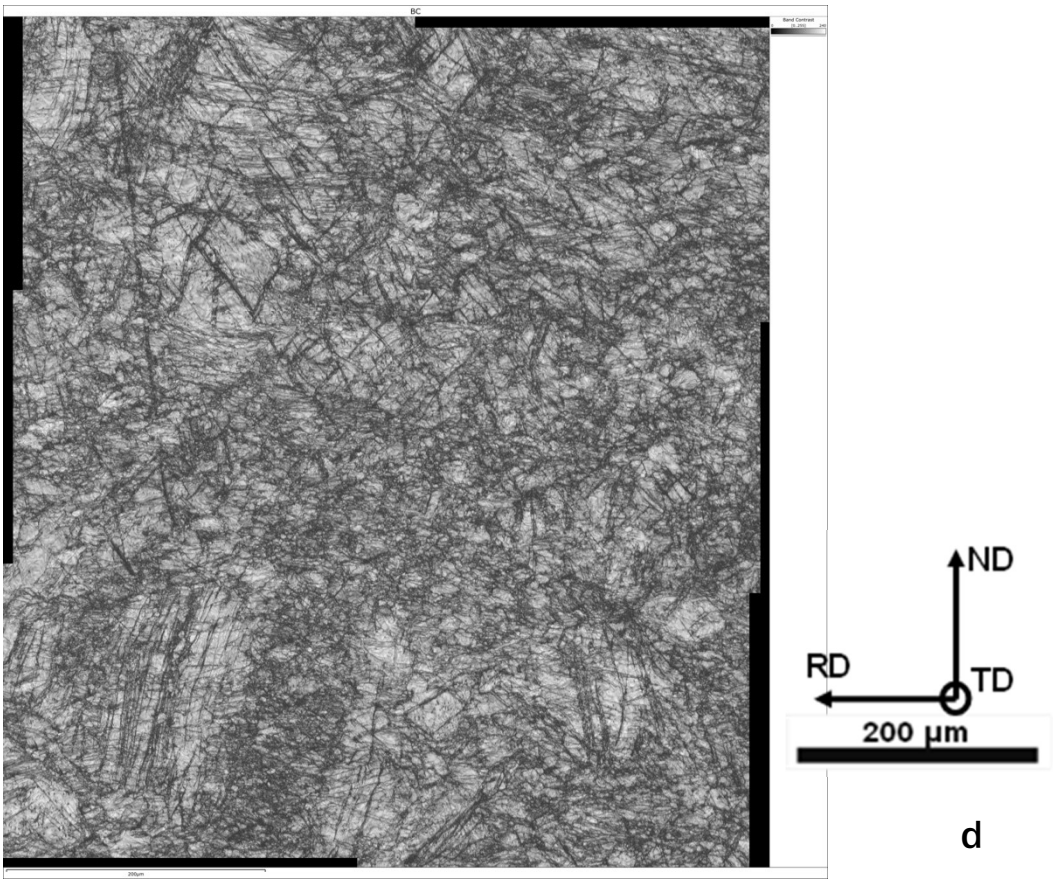
ND
RD
TD
200 µm

d

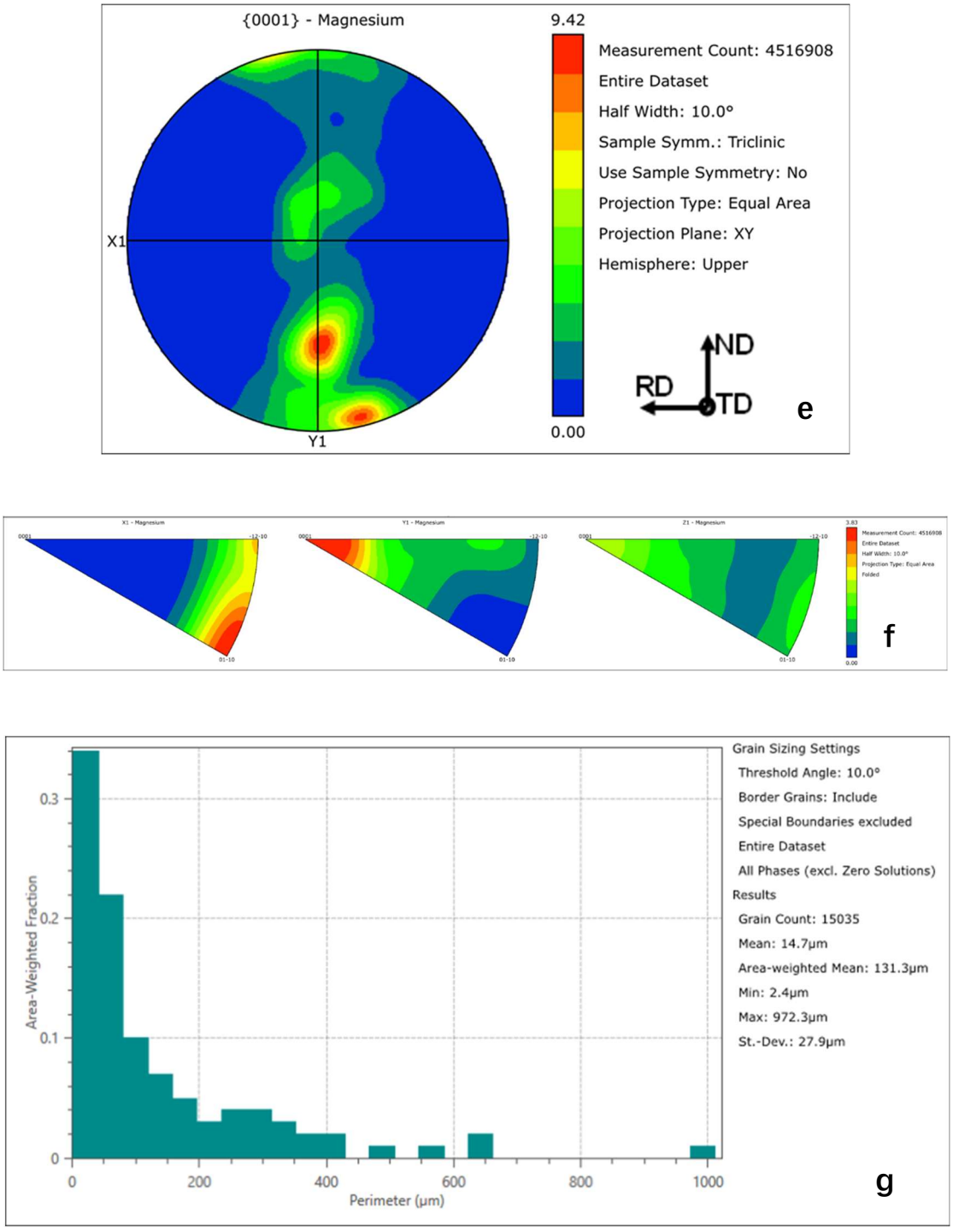

Figure 4-51 The EBSD result of the as-compressed 1D compressed Mg-0.1Ca-0.4Zn specimen: (a) The inverse pole figure map and grain boundaries, (b) The grain boundaries and the special grain boundaries, (c) The band contrast and the phase analysis, (d) The band contrast, (e) The pole figure, (f) The inverse pole figures, (g) Grain size distribution expressed as grain boundary perimeter

No obvious recrystallization was observed in the microstructure up to 420s in the 1D compressed Mg-0.1Ca-0.4Zn (at%) specimen. The results (shown in Figure 4-52)

after the 300s annealing indicated that the specimen had a recovery at that stage, while the temperature of the sample was 186℃. Figure 4-52(c) shows that the fraction of the non-indexed area was reduced from 27.5% to 19.2%. The boundary fraction of the tensile twins, compressive twins and double twins was changed from 39.5%, 3.4% and 8.4% to 36.0%, 3.8% and 8.9%, respectively. The maximum pole intensity was found to increase from 9.4 to 9.8. (shown in Figure 4-52(e)) Despite the changes mentioned above, the morphology of the microstructure did not show any difference in the IPF map (shown in Figure 4-52(a)). Meanwhile, Figure 4-52(g) indicates that the average grain size was 14.7μm which also remained unchanged. All the evidence indicated that the recovery happened in the specimen. The EBSD results of the 30s, 45s, 60s and 75s annealing (30s, 75s, 135s and 210s heat treatment time in total, respectively) are presented in Appendix I and are not discussed in the text.

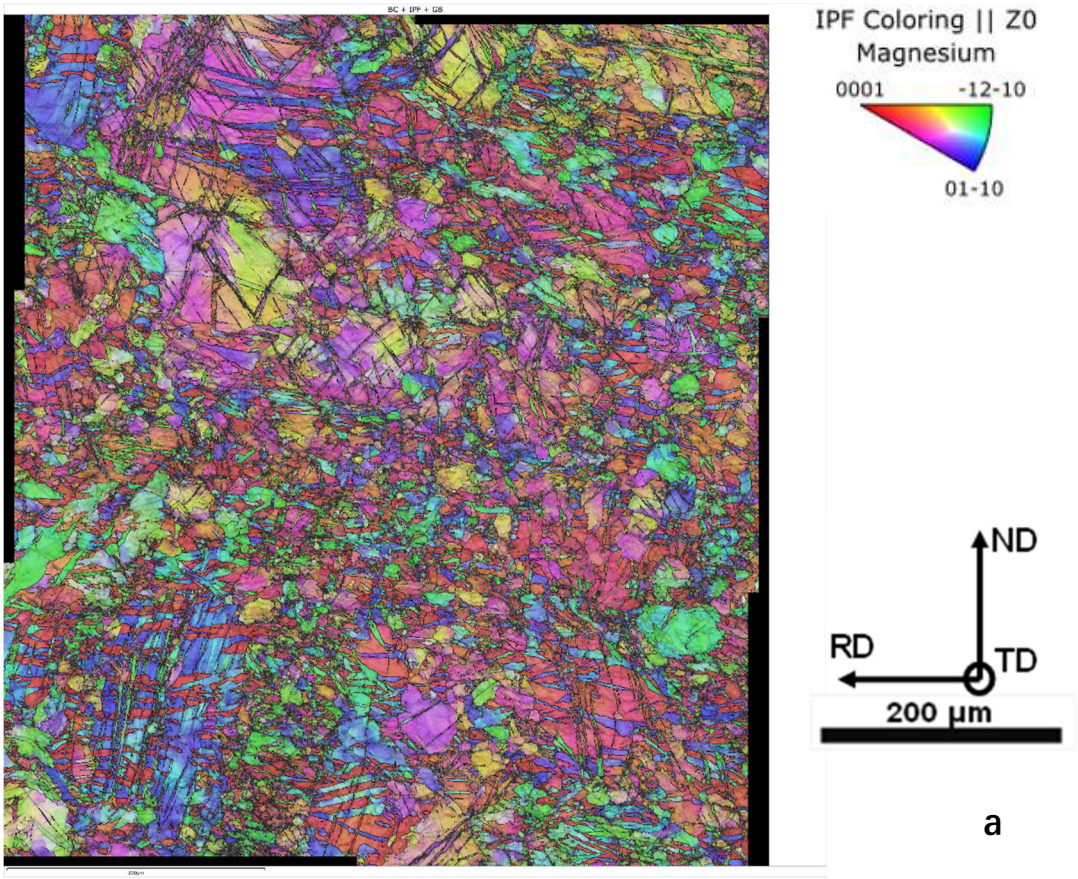

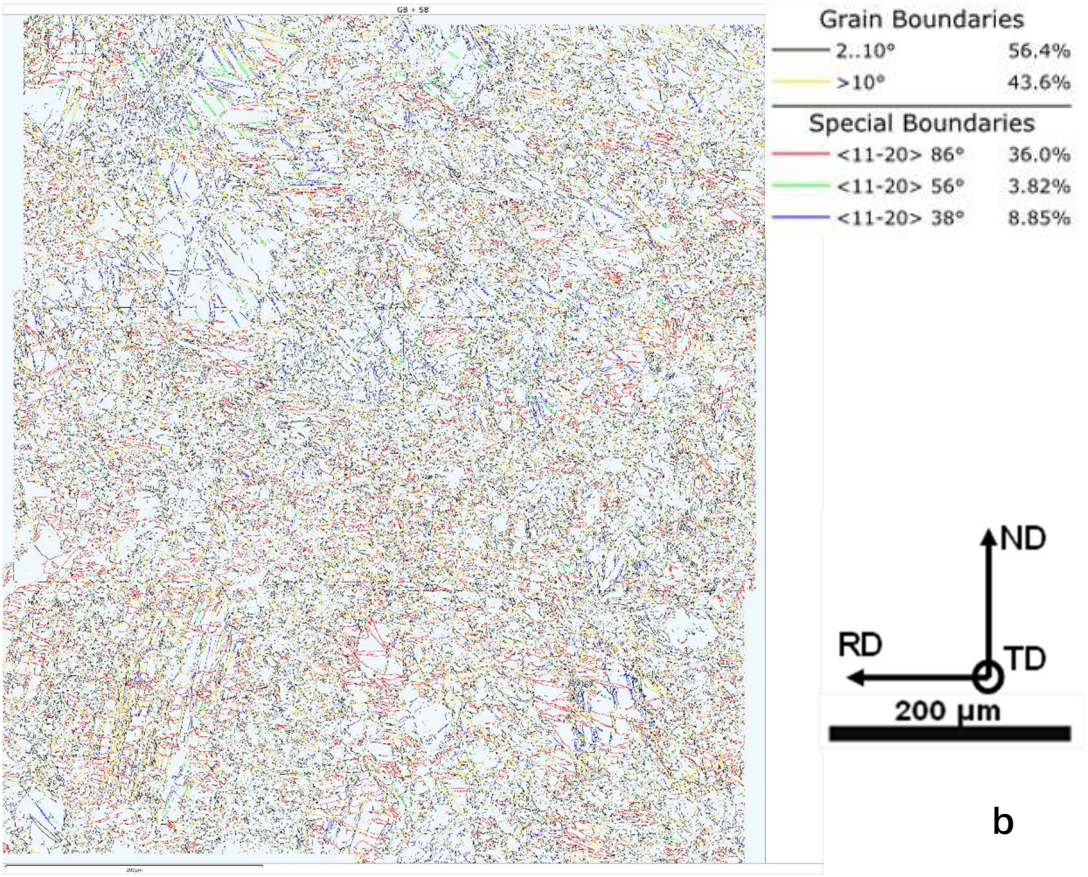
GB + SB
Grain Boundaries
2..10° 56.4%
>10° 43.6%
Special Boundaries
<11-20> 86° 36.0%
<11-20> 56° 3.82%
<11-20> 38° 8.85%
ND
RD
TD
200 µm

b

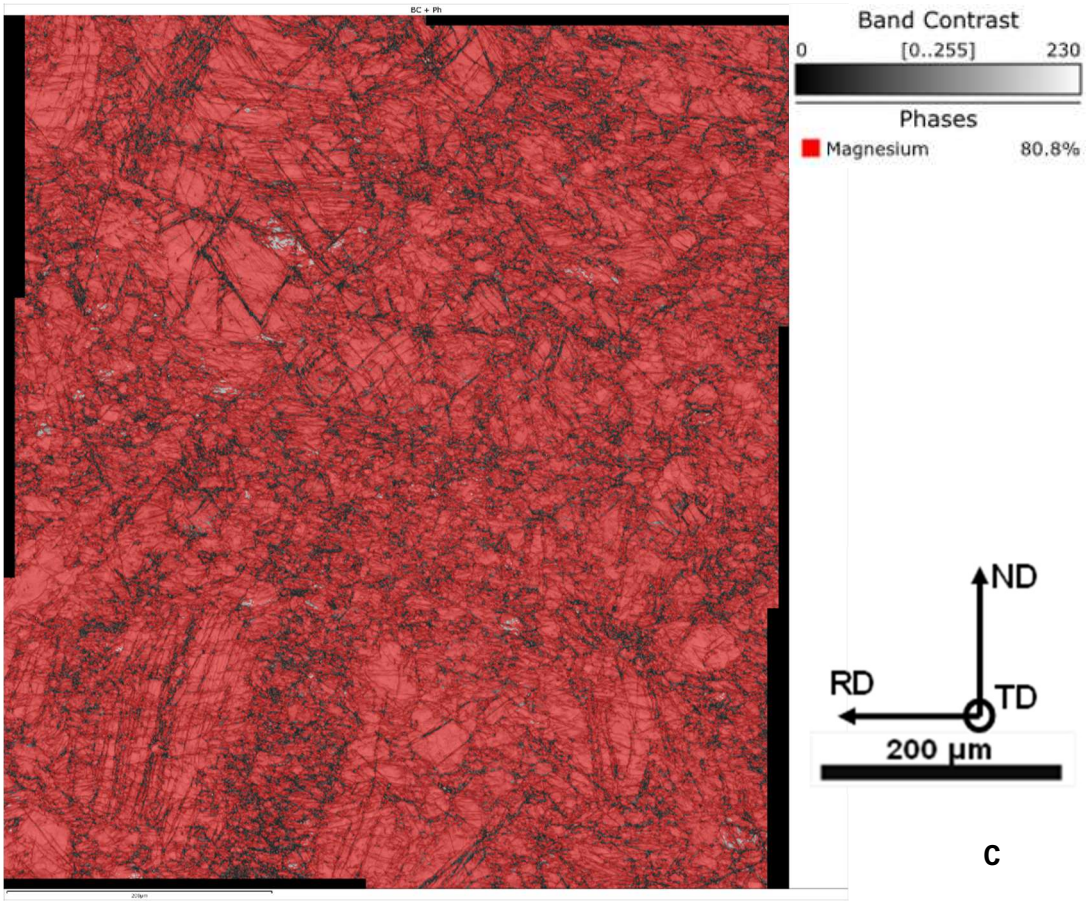
BC + Ph
Band Contrast
0 [0..255] 230
Phases
Magnesium 80.8%
ND
RD
TD
200 µm

c

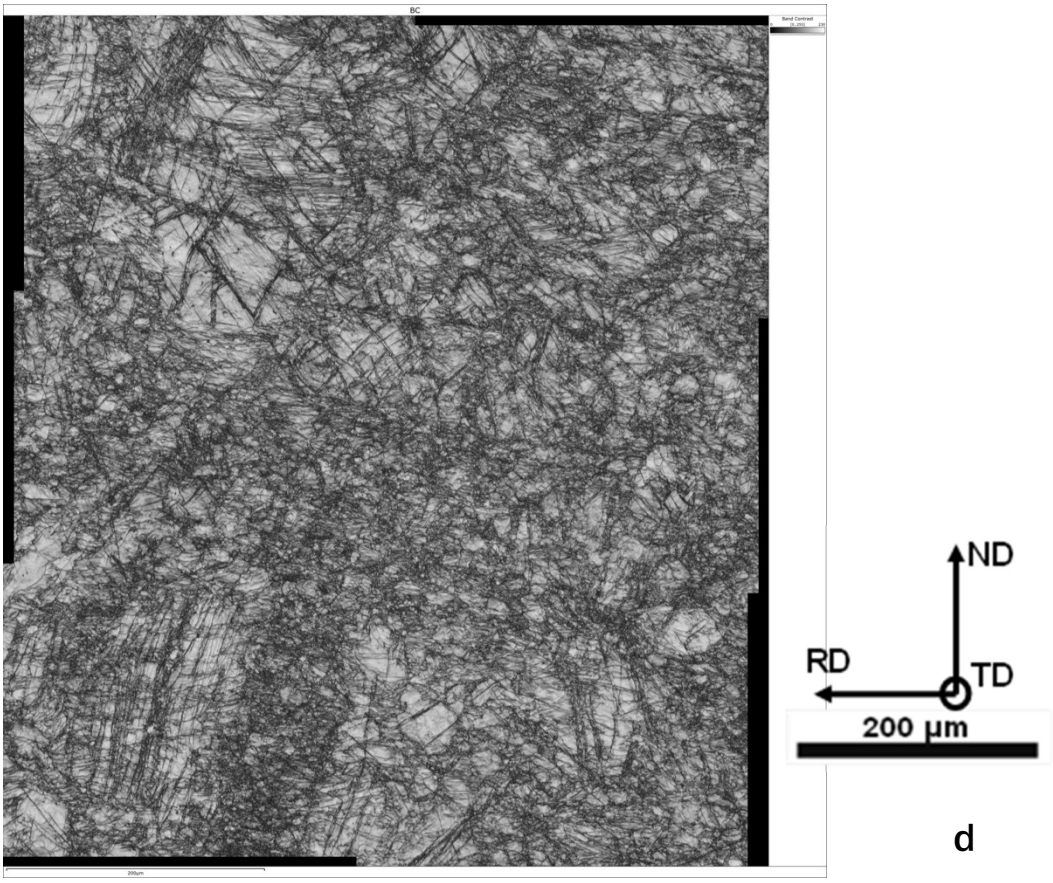
BC
ND
RD
TD
200 µm

d

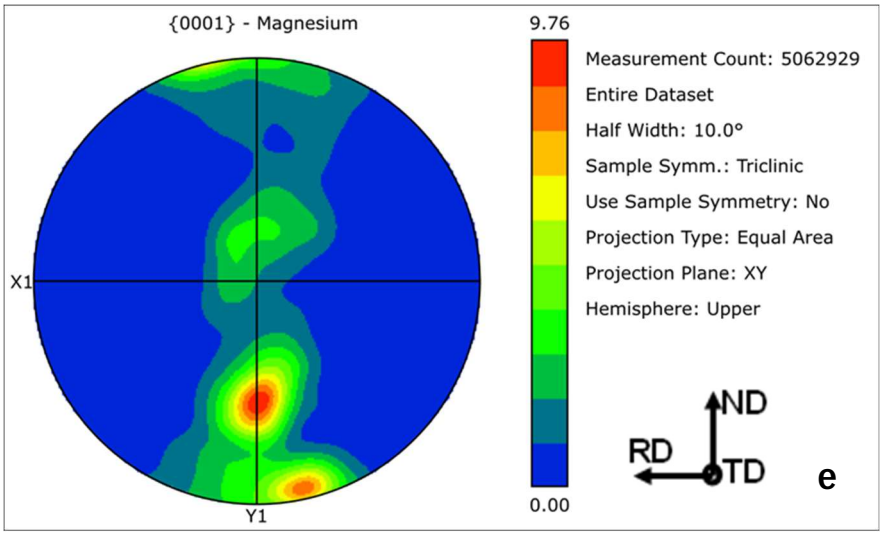
{0001} - Magnesium
9.76
0.00
Measurement Count: 5062929
Entire Dataset
Half Width: 10.0°
Sample Symm.: Triclinic
Use Sample Symmetry: No
Projection Type: Equal Area
Projection Plane: XY
Hemisphere: Upper
X1
Y1
ND
RD
TD

e

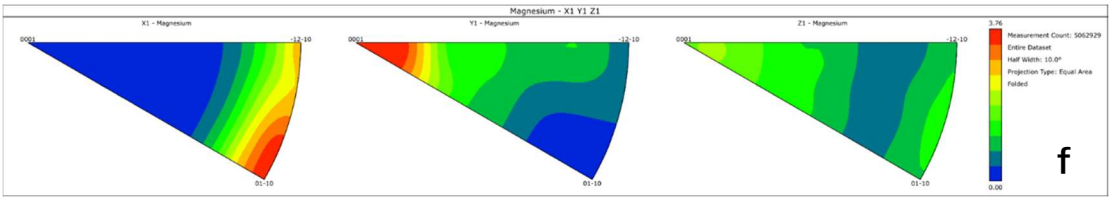
Magnesium - X1 Y1 Z1
X1 - Magnesium
Y1 - Magnesium
Z1 - Magnesium
Measurement Count: 5062929
Entire Dataset
Half Width: 10.0°
Projection Type: Equal Area
Folded

f

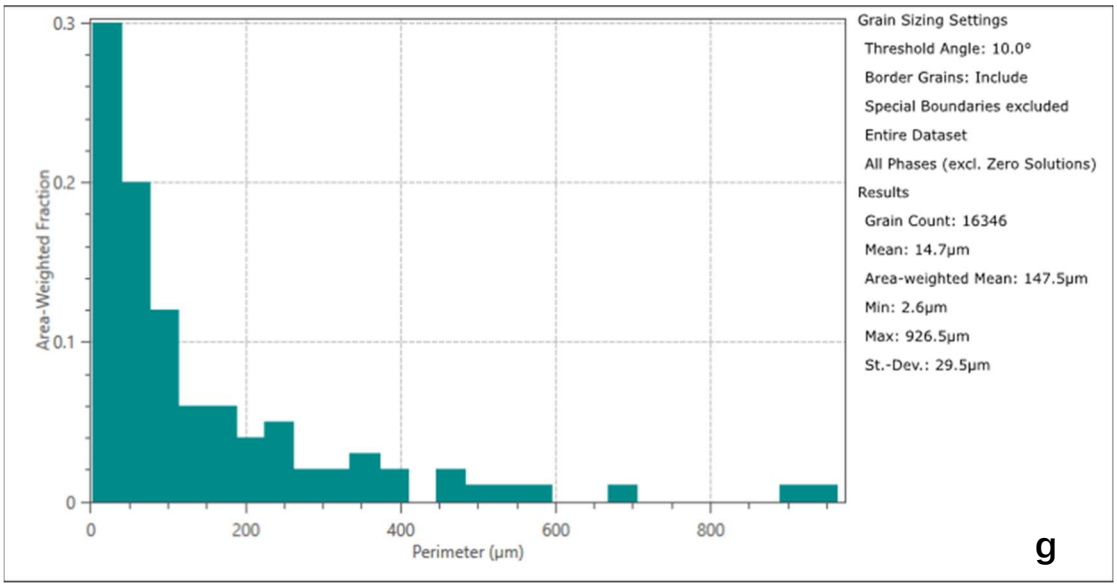

Figure 4-52 The EBSD result of the 300s annealed 1D compressed Mg-0.1Ca-0.4Zn specimen: (a) The inverse pole figure map and grain boundaries, (b) The grain boundaries and the special grain boundaries, (c) The band contrast and the phase analysis, (d) The band contrast, (e) The pole figure, (f) The inverse pole figures, (g) Grain size distribution expressed as grain boundary perimeter

Figure 4-53 shows the EBSD results of the same specimen after the 420s annealing process. Based on Figure 4-13, the temperature of the specimen at this stage was 212℃. The average grain size reduced from 14.7μm to 14.2μm (shown in Figure 4-53(g)). A significant number of the recrystallized grains were observed across the whole mapped area (shown in Figure 4-53(a)). Unlike other specimens, the fraction of the non-indexed area in the EBSD map increased slightly from 27.5% to 31.4%, as shown in Figure 4-53(c). However, this increase does not mean a rise in shear band formation or a failure in their transformation into recrystallized grains. Instead, it can be attributed to a lower indexing rate during the EBSD scan for this sample. Additionally, grey areas observed on the phase map may correspond to oxidized regions on the surface, which likely reduced the resolution of the EBSD results and influenced the area ratio calculations. Moreover, the nucleation sites of recrystallized grains remained consistent with the locations of shear bands observed in the previous EBSD map at this stage. Figure 4-53(b) indicates that the fraction of twin boundaries did not change significantly. The boundary fractions of the tensile twins, compressive twins and double twins were all slightly reduced from 39.5%, 3.4% and 8.4% (as compressed) to 37.5%, 2.7% and 7.1% (when recrystallization started), respectively. The pole figure and IPF of the annealed specimen (shown in Figure 4-53(e) and (f)) also showed a different reading compared

to other specimens. The maximum value of the pole figure increased a little bit which was from 9.4 to 9.8, after the specimen showed an obvious recrystallization. And the orientation distribution of the grains showed no difference after the recrystallization just started. The reason for this was also attributed to the lower resolution during the scanning process. After losing some information about the fine grains, the maximum value of the pole figure generated by the rest of the grains was shown to be higher than it should be.

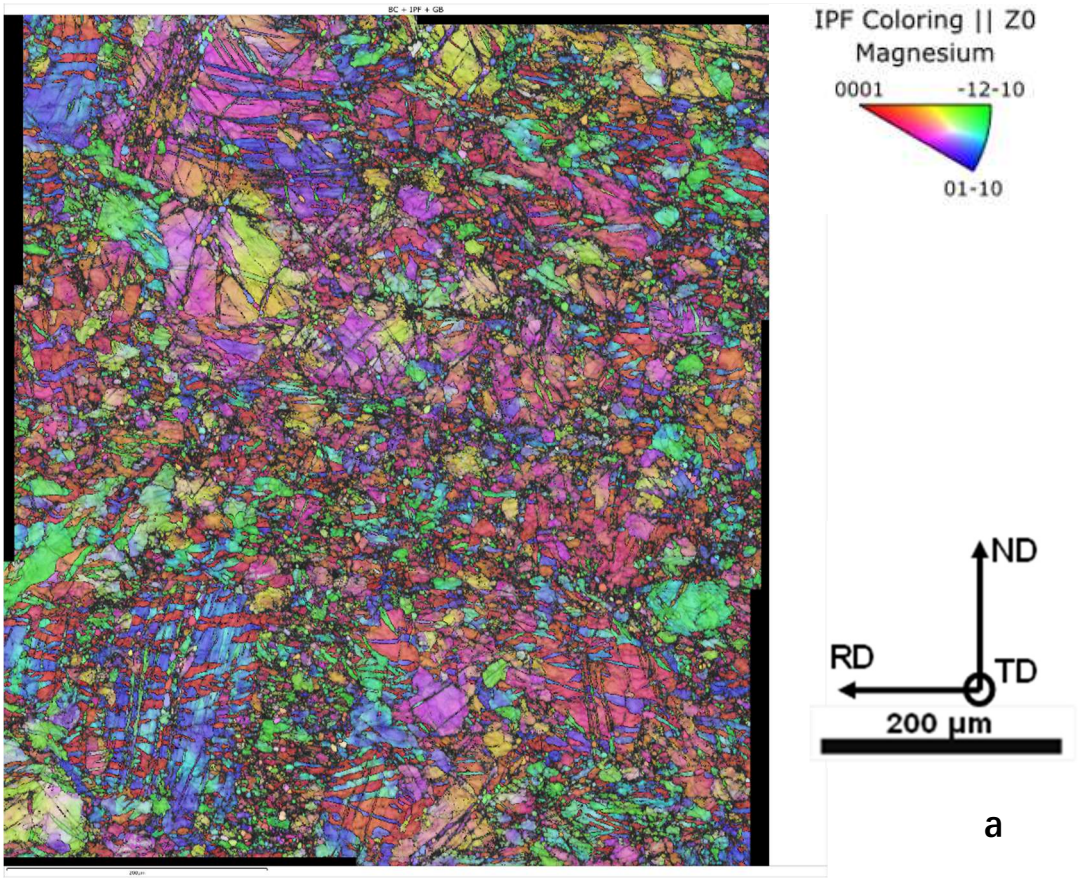

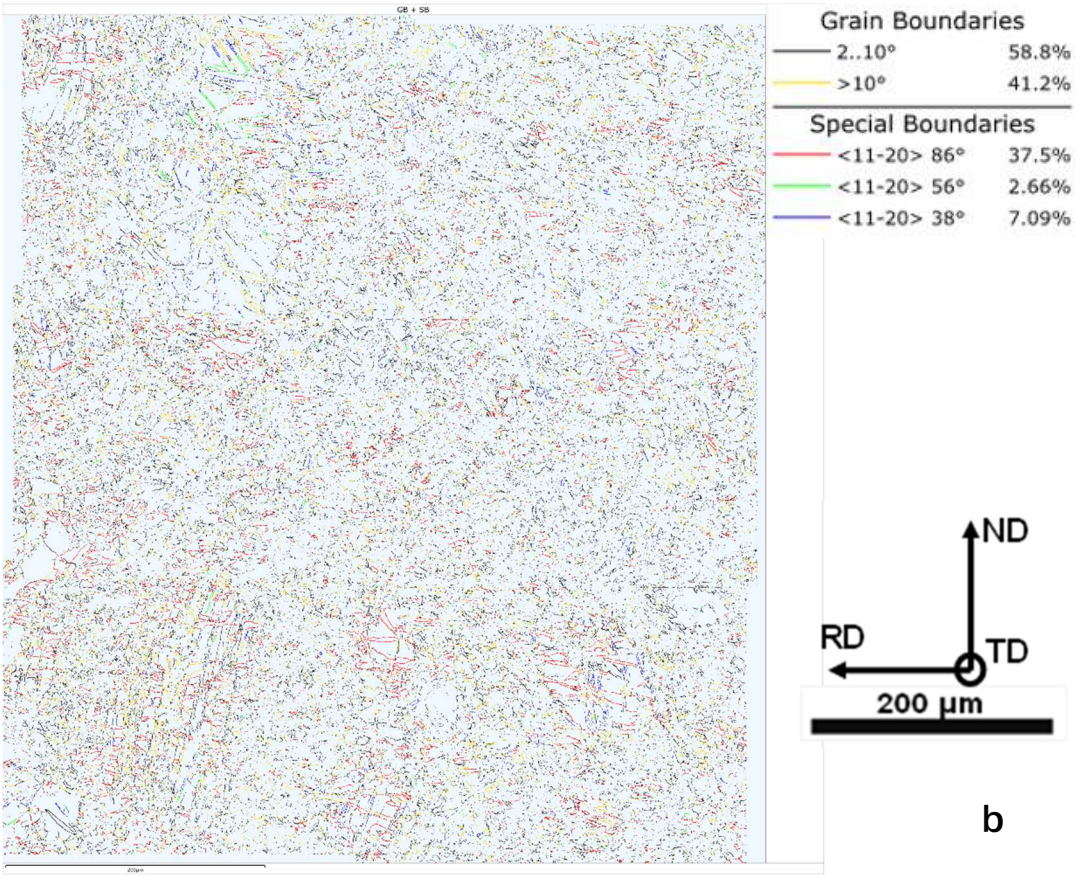
GB + SB
Grain Boundaries
2..10° 58.8%
>10° 41.2%
Special Boundaries
<11-20> 86° 37.5%
<11-20> 56° 2.66%
<11-20> 38° 7.09%
ND
RD
TD
200 µm

b

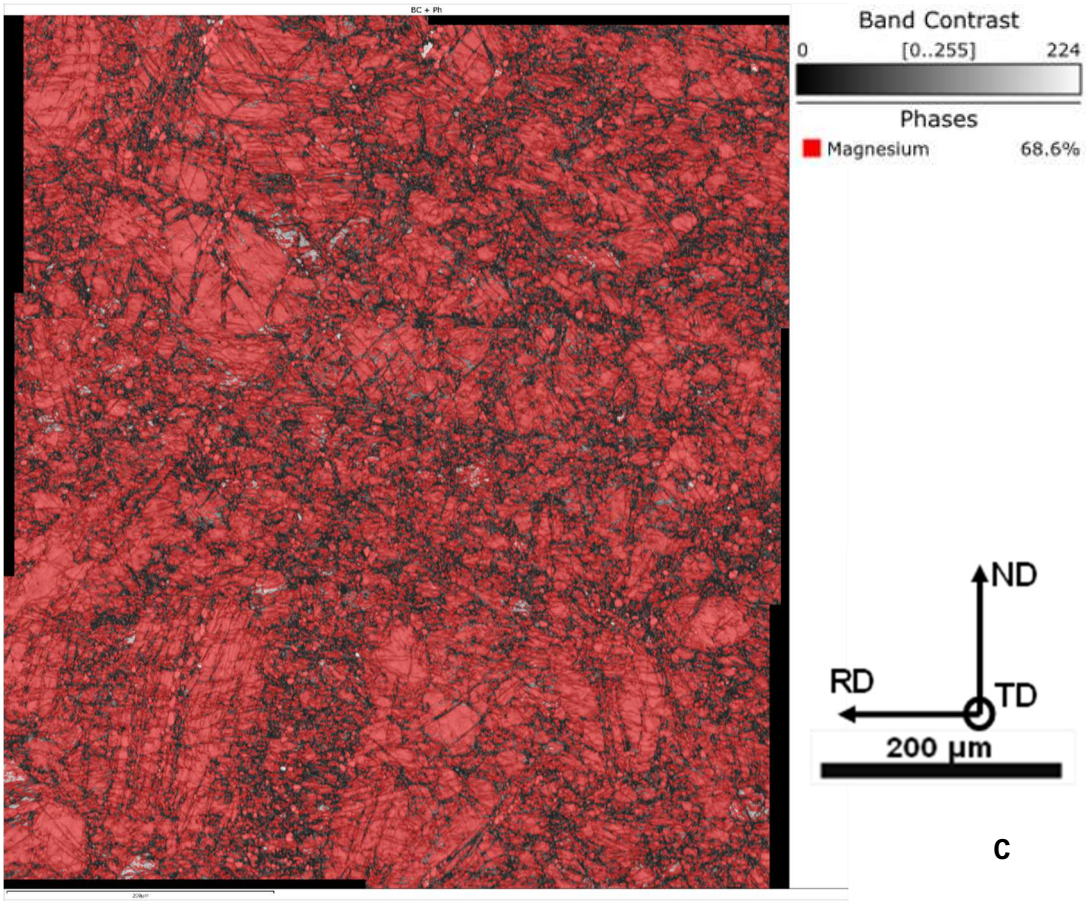
BC + Ph
Band Contrast
0 [0..255] 224
Phases
Magnesium 68.6%
ND
RD
TD
200 µm

c

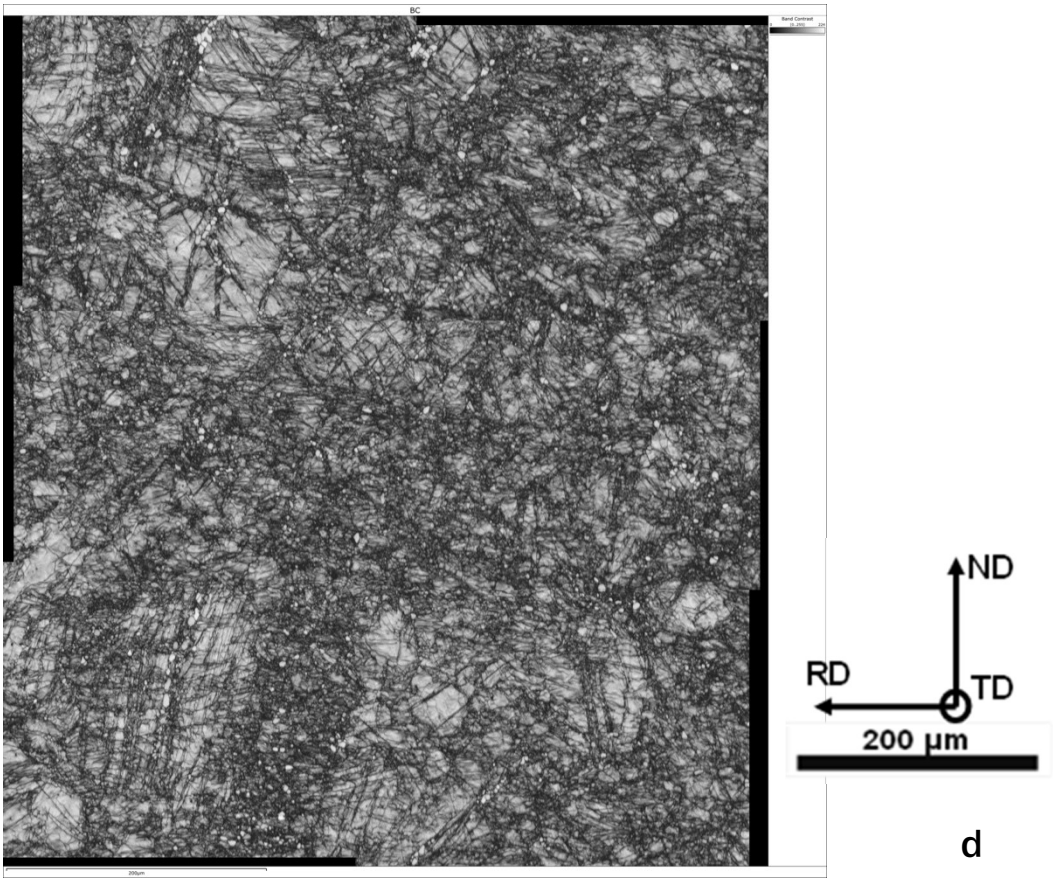
BC
ND
RD
TD
200 µm

d

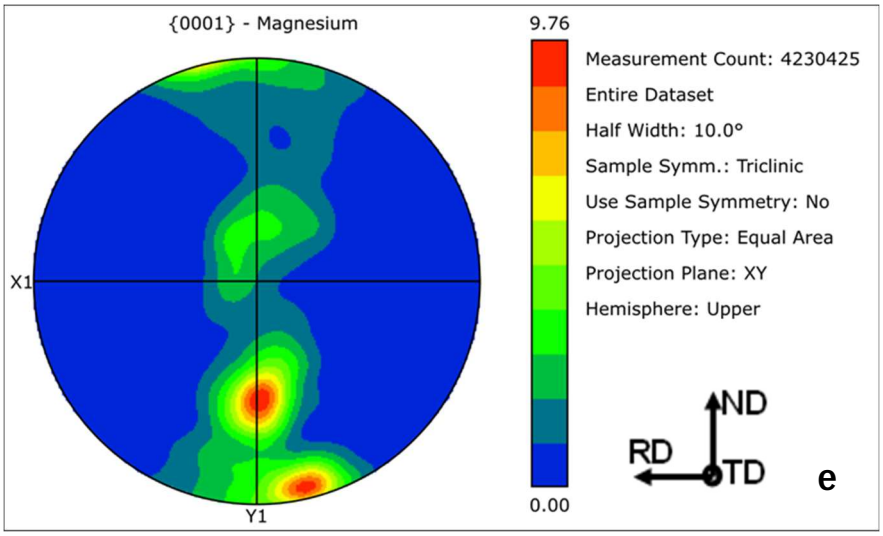
{0001} - Magnesium
9.76
0.00
Measurement Count: 4230425
Entire Dataset
Half Width: 10.0°
Sample Symm.: Triclinic
Use Sample Symmetry: No
Projection Type: Equal Area
Projection Plane: XY
Hemisphere: Upper
X1
Y1
ND
RD
TD

e

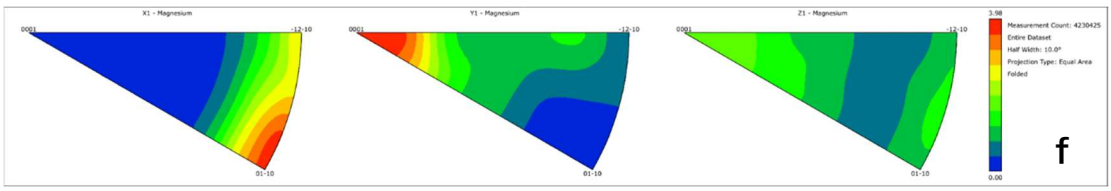
X1 - Magnesium
Y1 - Magnesium
Z1 - Magnesium

f

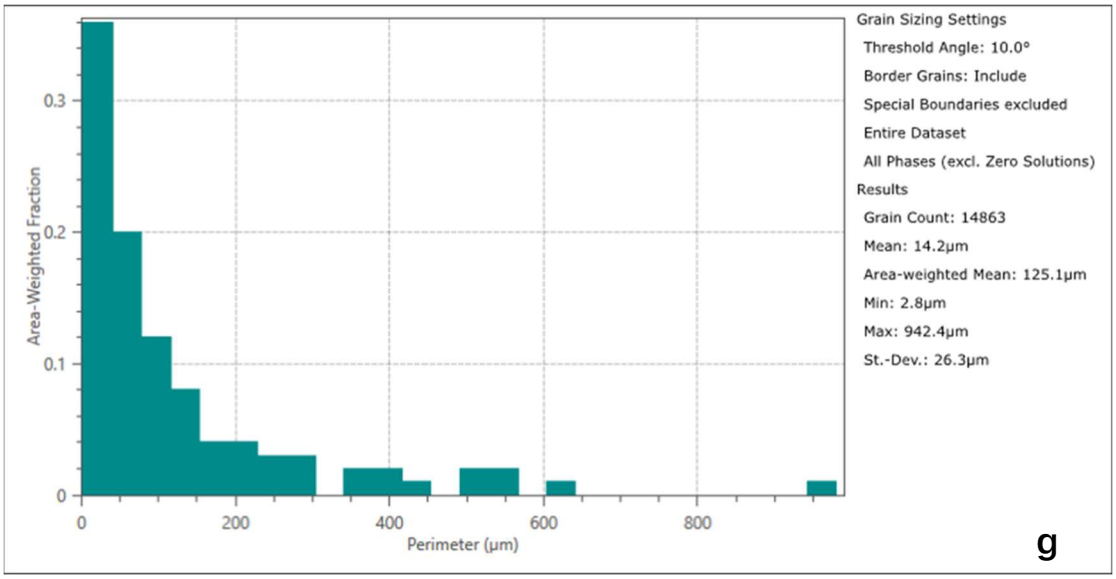

Figure 4-53 The EBSD result of the 420s annealed 1D compressed Mg-0.1Ca-0.4Zn specimen: (a) The inverse pole figure map and grain boundaries, (b) The grain boundaries and the special grain boundaries, (c) The band contrast and the phase analysis, (d) The band contrast, (e) The pole figure, (f) The inverse pole figures, (g) Grain size distribution expressed as grain boundary perimeter

When the annealing time increased another 30s i.e. after a total of 570s, the recrystallization stopped in the Mg-0.1Ca-0.4Zn (at%) specimen, in contrast to the Mg-0.2Ca-0.3Zn (at%) specimens. The temperature of the specimen at that time was 240℃. Figure 4-54 shows the EBSD results of the same specimen at that stage. In the same way as the Mg-0.2Ca-0.3Zn (at%) specimens after starting the recrystallization, the shear bands and the fine twinned areas almost disappeared (shown in Figure 4-54(c)). However, the non-indexed areas were not fully filled with the recrystallized grains like other specimens but were shown as the deformed grains. The recrystallization from the shear bands was almost finished but the new grains from the shear bands did not start to grow (shown in Figure 4-54(a)). Additionally, recrystallization nucleated in twins was not observed. Combining the information of the grain boundaries (shown in Figure 4-54(b)), the change in the fraction of three kinds of twins also showed this. The boundary fraction of the tensile twins, compressive twins and double twins was changed from 37.5% to 33.9%, 2.7% to 3.5% and 7.1% to 7.9%, respectively. Meanwhile, the fraction of the high-angle grain boundaries also presented a little increase from 41.2% (420s in total annealing time) to 45.9% (570s in total annealing time). The improvement of the resolution was responsible for this boundary fraction value fluctuation. The

average grain size of the specimen was quite similar to the last stage which was 14.6μm (shown in Figure 4-54(g)). Figure 4-54(e) indicates that the maximum value of the pole figure was close to that of the 420s annealed specimen. It just decreased from 9.8 to 9.4. Meanwhile, the grain orientation distribution did not present any changes between the two pole figures.

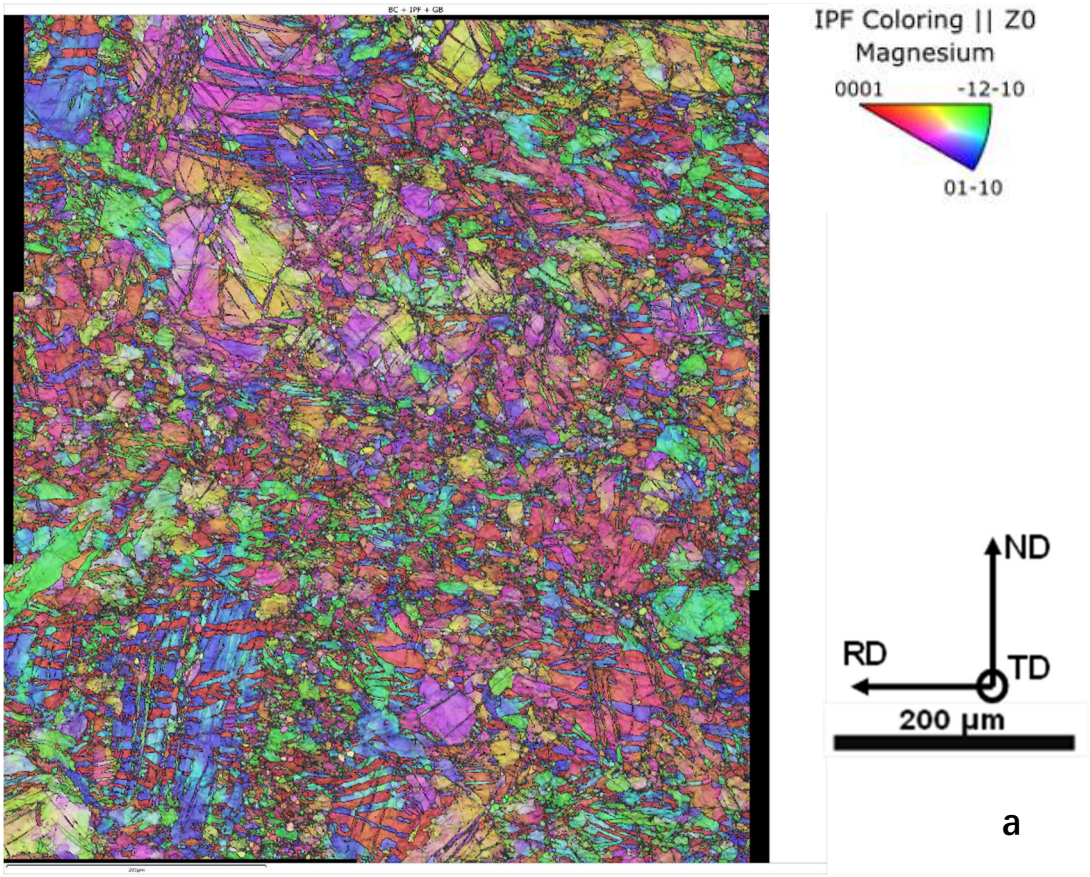

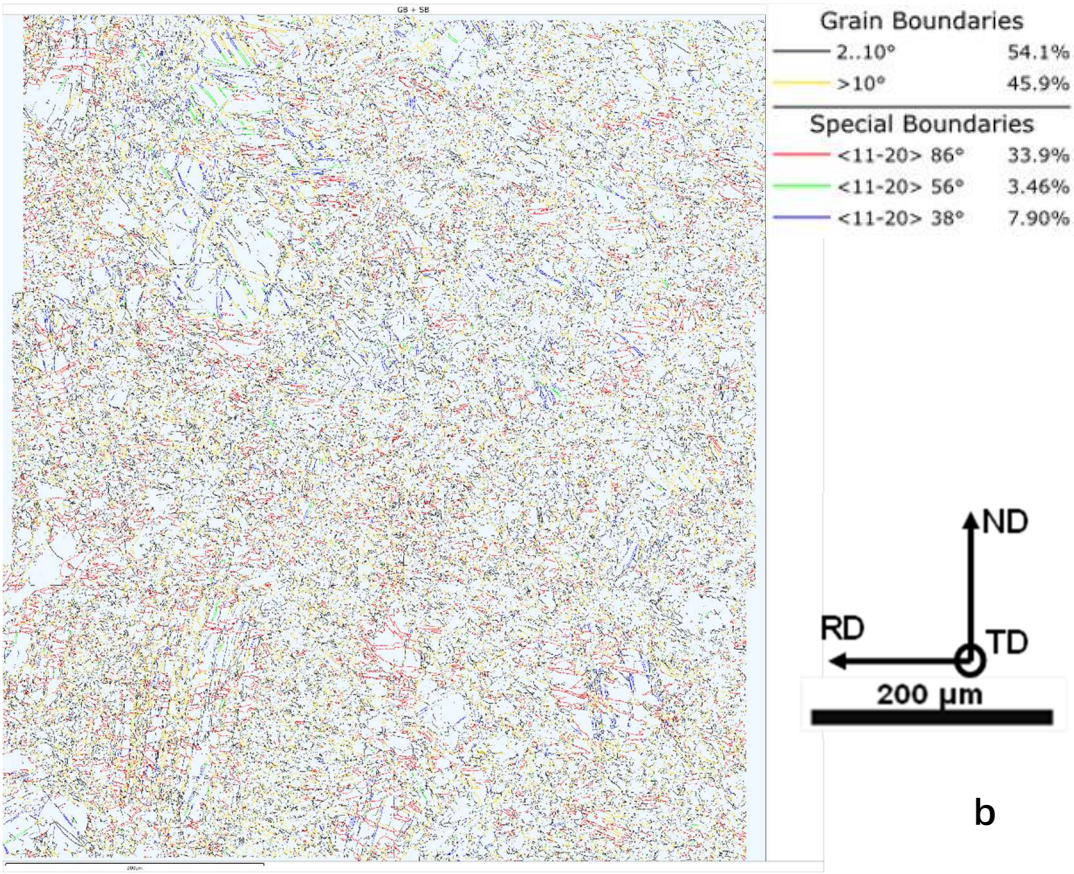
GS + SB
Grain Boundaries
2..10° 54.1%
>10° 45.9%
Special Boundaries
<11-20> 86° 33.9%
<11-20> 56° 3.46%
<11-20> 38° 7.90%
ND
RD
TD
200 µm

b

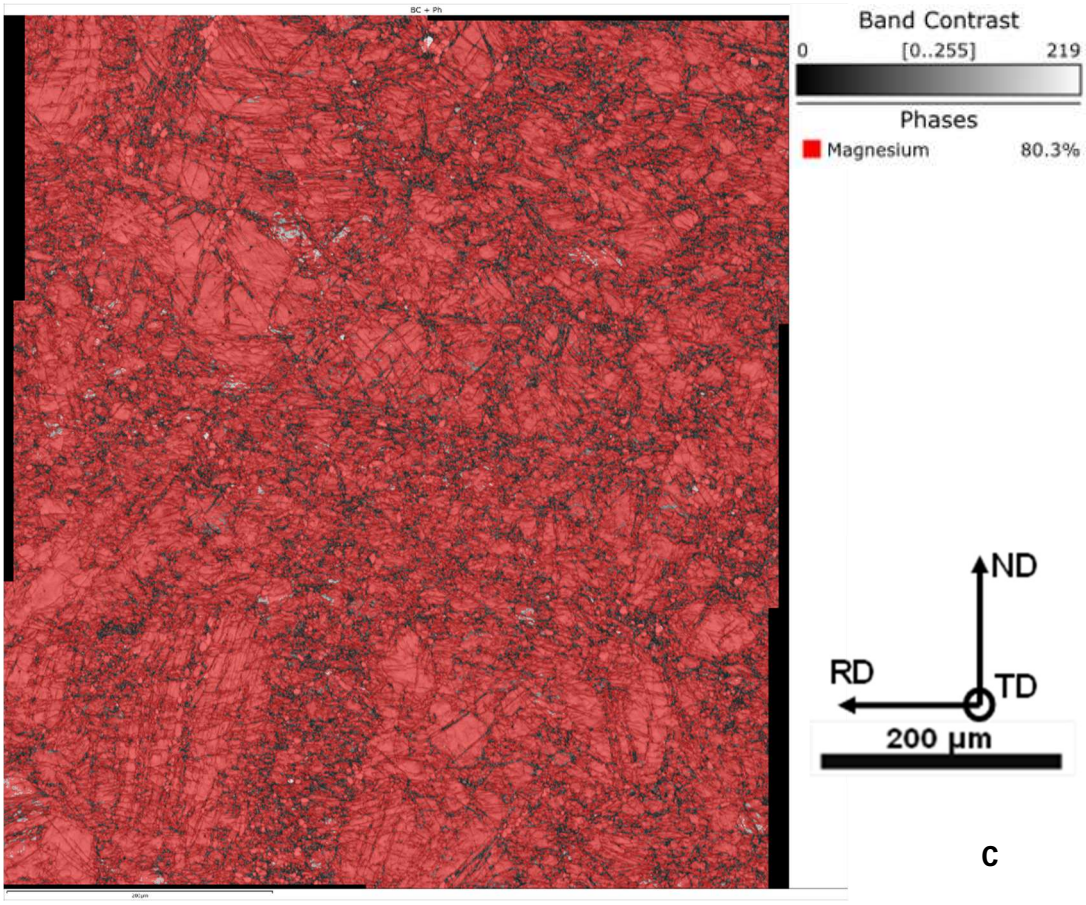
BC + Ph
Band Contrast
0 [0..255] 219
Phases
Magnesium 80.3%
ND
RD
TD
200 µm

c

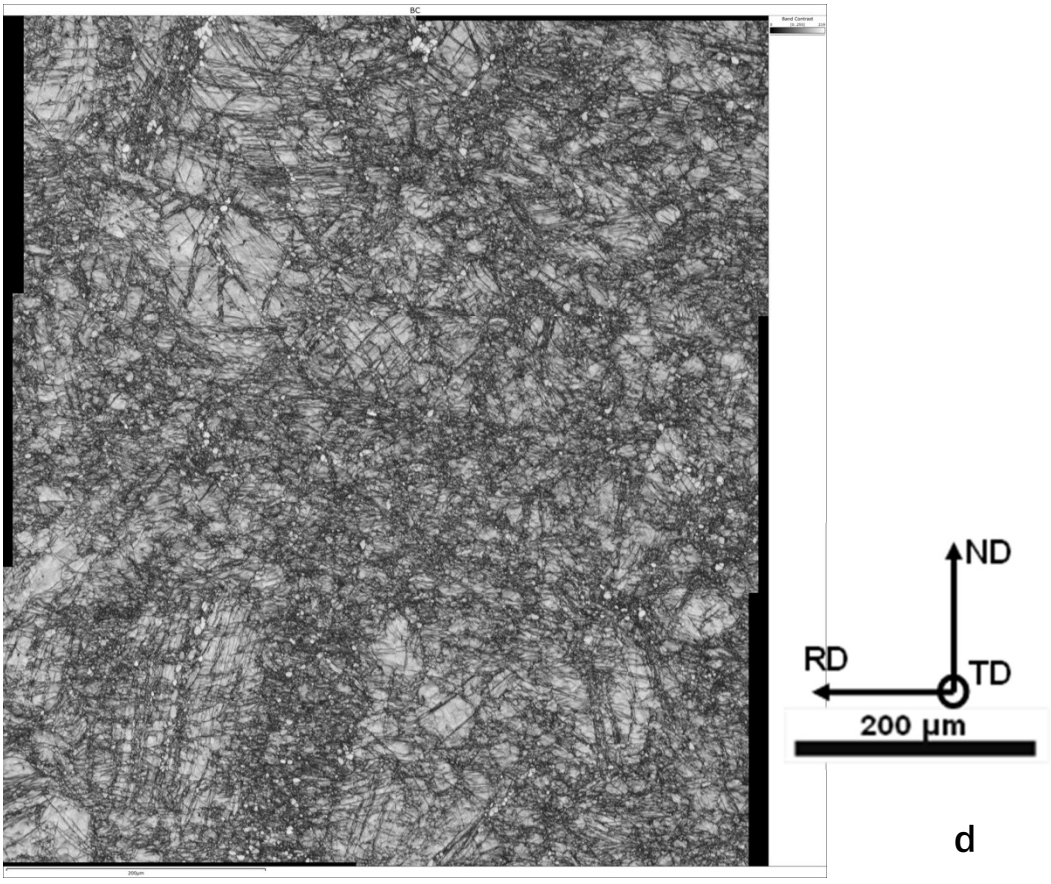
BC
ND
RD
TD
200 µm

d

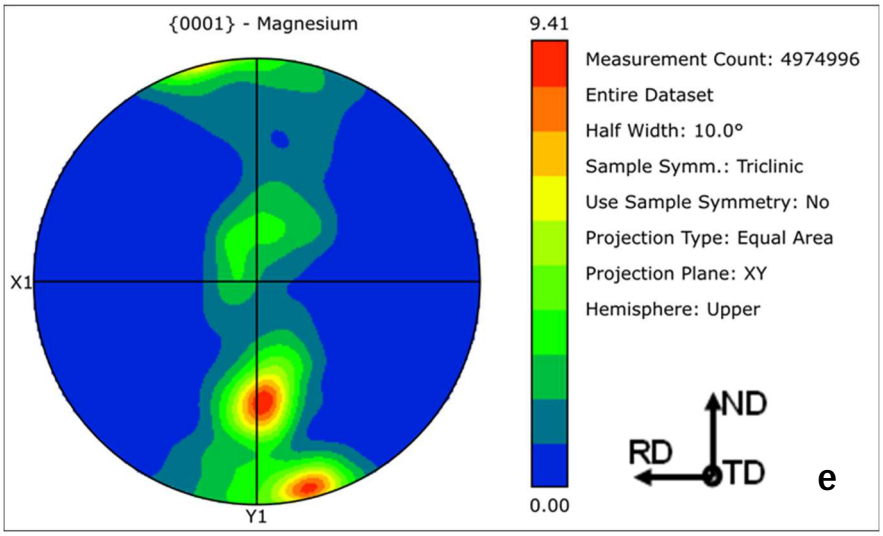
{0001} - Magnesium
9.41
0.00
X1
Y1
Measurement Count: 4974996
Entire Dataset
Half Width: 10.0°
Sample Symm.: Triclinic
Use Sample Symmetry: No
Projection Type: Equal Area
Projection Plane: XY
Hemisphere: Upper
ND
RD
TD

e

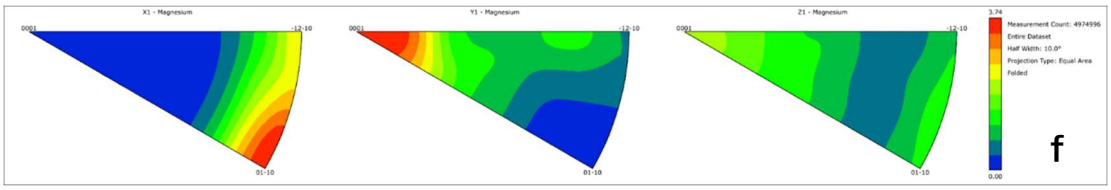
X1 - Magnesium
Y1 - Magnesium
Z1 - Magnesium
Measurement Count: 4974996
Entire Dataset
Half Width: 10.0°
Projection Type: Equal Area
Folded

f

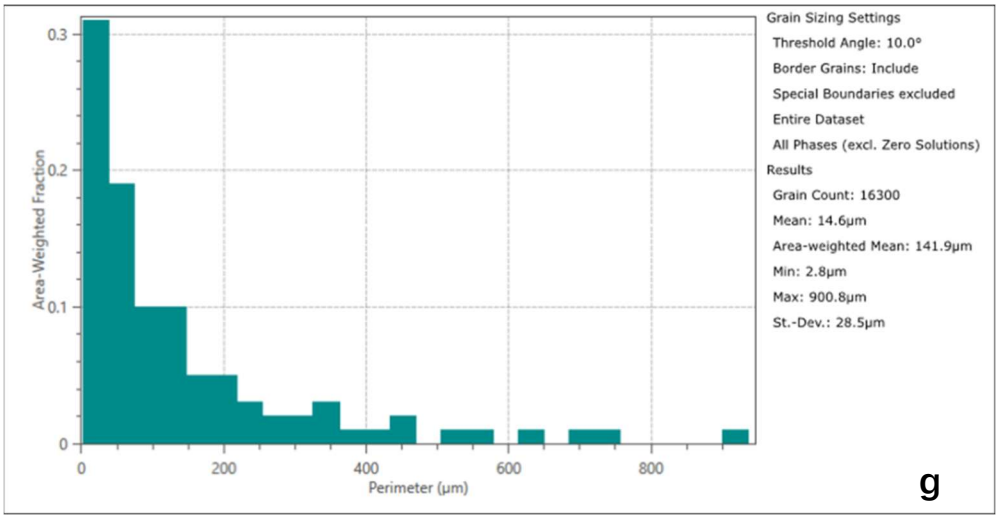

Figure 4-54 The EBSD result of the 570s annealed 1D compressed Mg-0.1Ca-0.4Zn specimen: (a) The inverse pole figure map and grain boundaries, (b) The grain boundaries and the special grain boundaries, (c) The band contrast and the phase analysis, (d) The band contrast, (e) The pole figure, (f) The inverse pole figures, (g) Grain size distribution expressed as grain boundary perimeter

The microstructural behavior of the 1D compressed Mg-0.1Ca-0.4Zn (at%) specimen after recrystallization initiation closely resembled that of the Mg-0.22Ca-0.23Zn (at%) specimen under similar conditions. Even after a 750s annealing, further recrystallization was not evident in the Mg-0.1Ca-0.4Zn (at%) specimen (shown in Figure 4-55). The temperature of the specimen at that time point was 257℃. For the same reason as the 1D compressed Mg-0.22Ca-0.23Zn (at%) specimen, the 30s increase of the annealing time did not bring a large difference in temperature (from 240℃ to 257℃). Thus, the IPF map (shown in Figure 4-55(a)) reflected that the changes of the microstructure between the two steps in the sample were small. The IPF map and the grain boundary figure (shown in Figure 4-54(b)) indicated that the recrystallization was not completely stopped but was still in progress. A few new grains were observed on the IPF map which were marked by the white circles. Figure 4-54(b) also shows that the boundary fraction of the tensile twins, compressive twins and double twins all exhibited a decreasing trend from 33.9% to 31.8%, 3.5% to 3.3% and 7.9% to 7.6%, respectively. Meanwhile, the boundary fraction of the low-angle grain boundary and the high-angle grain boundary presented corresponding changes, which decreased from 54.1% to 52.6% and increased from 45.9% to 47.4%, respectively. The reduction of the maximum pole intensity was also observed (shown in Figure 4-54(e)). The intensity was reduced by 0.1 (from 9.4 to 9.3). The two strong peaks in the pole figure remained almost unchanged. Only the direction of a few new grains showed a trend that tilted away from ND direction (marked by black circle). The average grain size of the specimen furtherly increased from 14.6μm to 15μm (shown in Figure 4-55(g)).

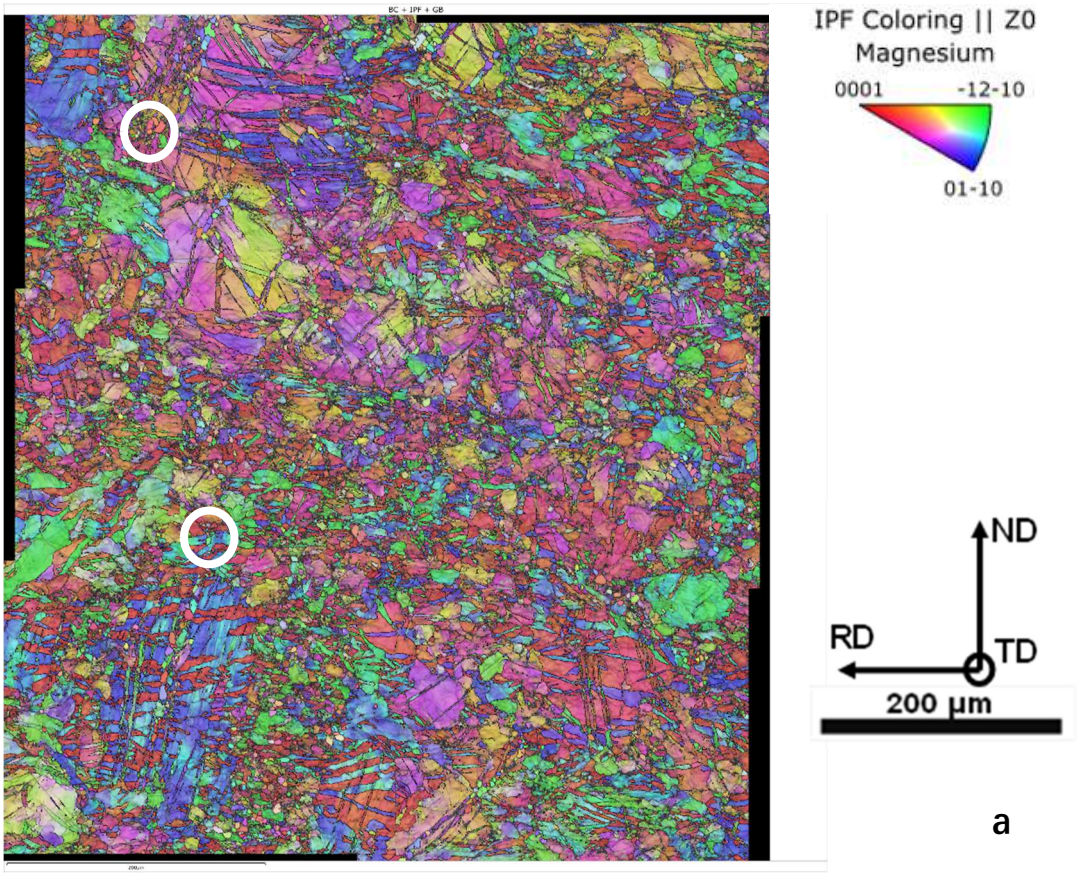
IPF Coloring || Z0
Magnesium
0001
-12-10
01-10
ND
RD
TD
200 µm

a

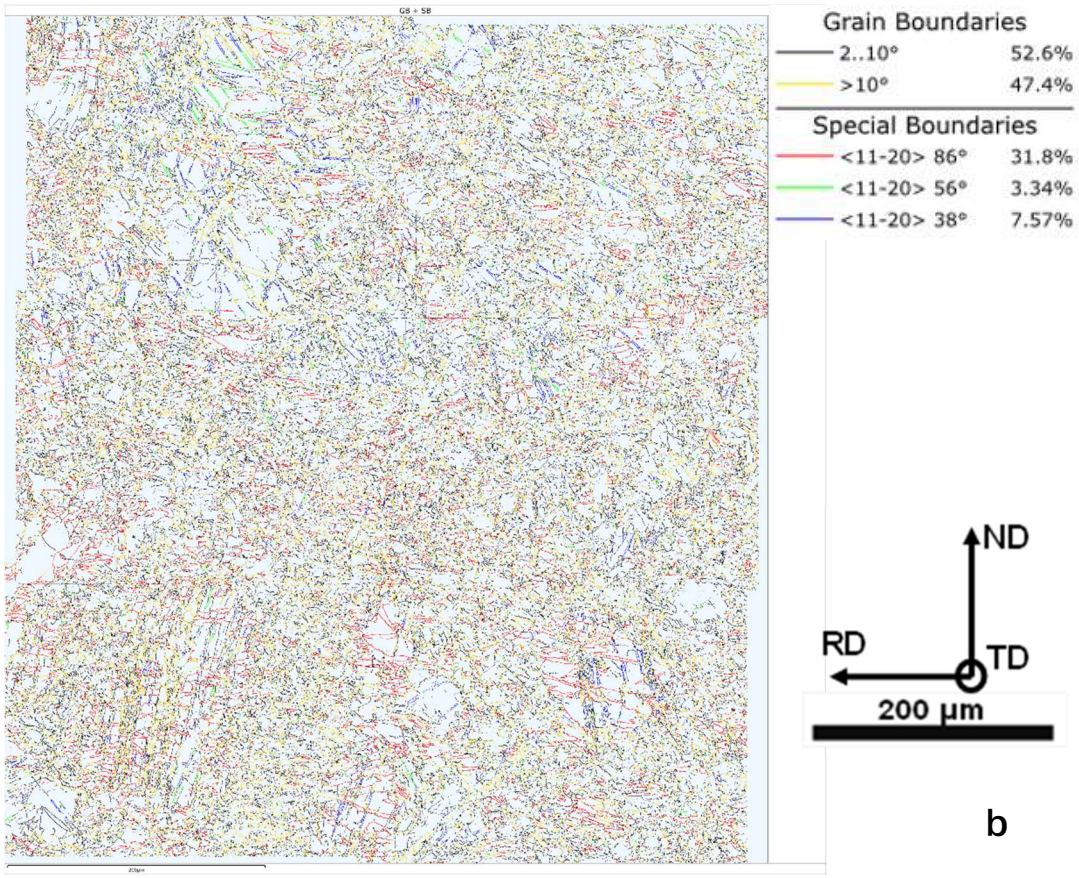
Grain Boundaries
2..10° 52.6%
>10° 47.4%
Special Boundaries
<11-20> 86° 31.8%
<11-20> 56° 3.34%
<11-20> 38° 7.57%
ND
RD
TD
200 µm

b

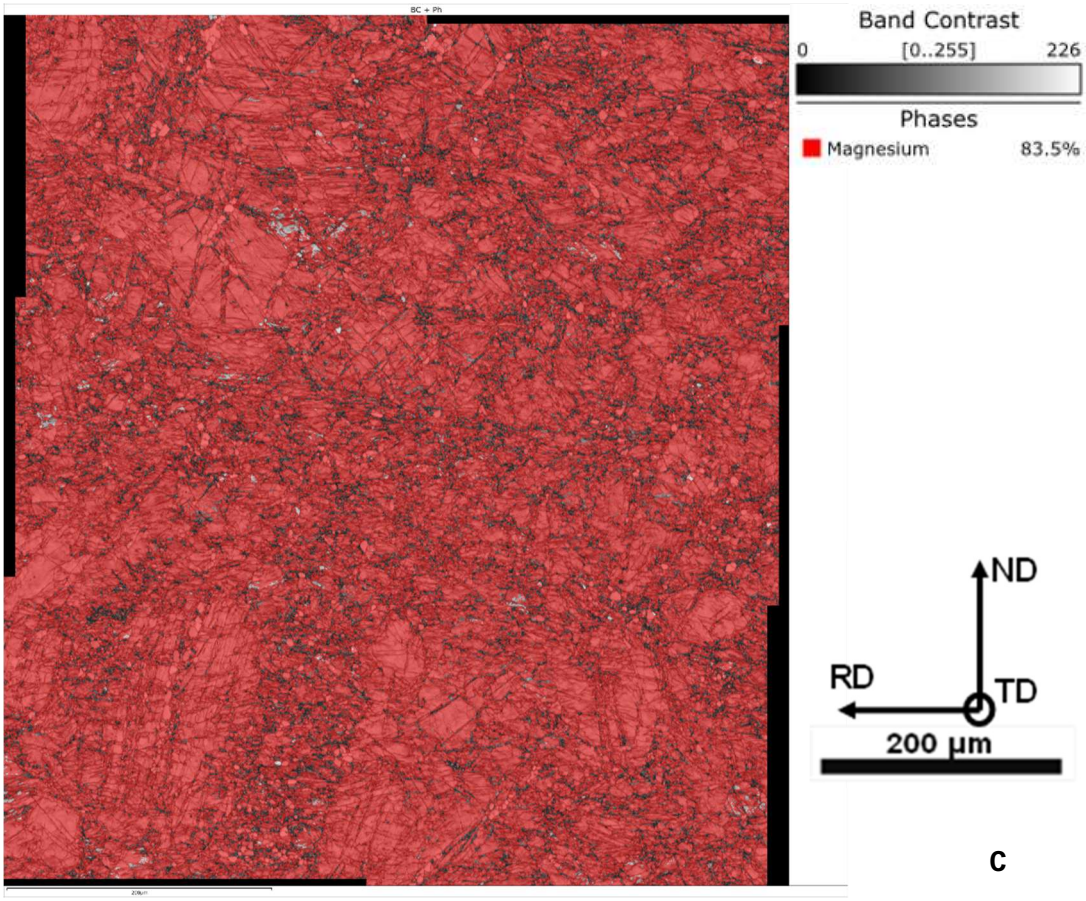
Band Contrast
0
[0..255]
226
Phases
Magnesium
83.5%
ND
RD
TD
200 µm

c

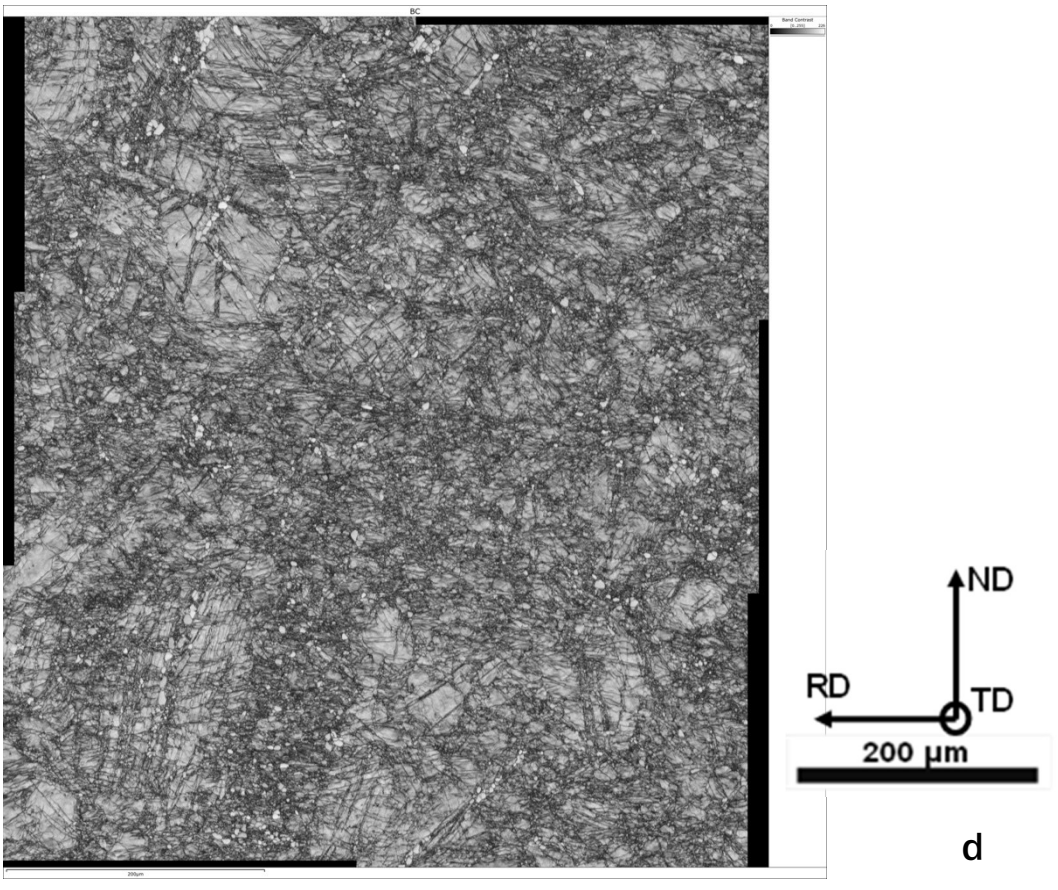
ND
RD
TD
200 µm

d

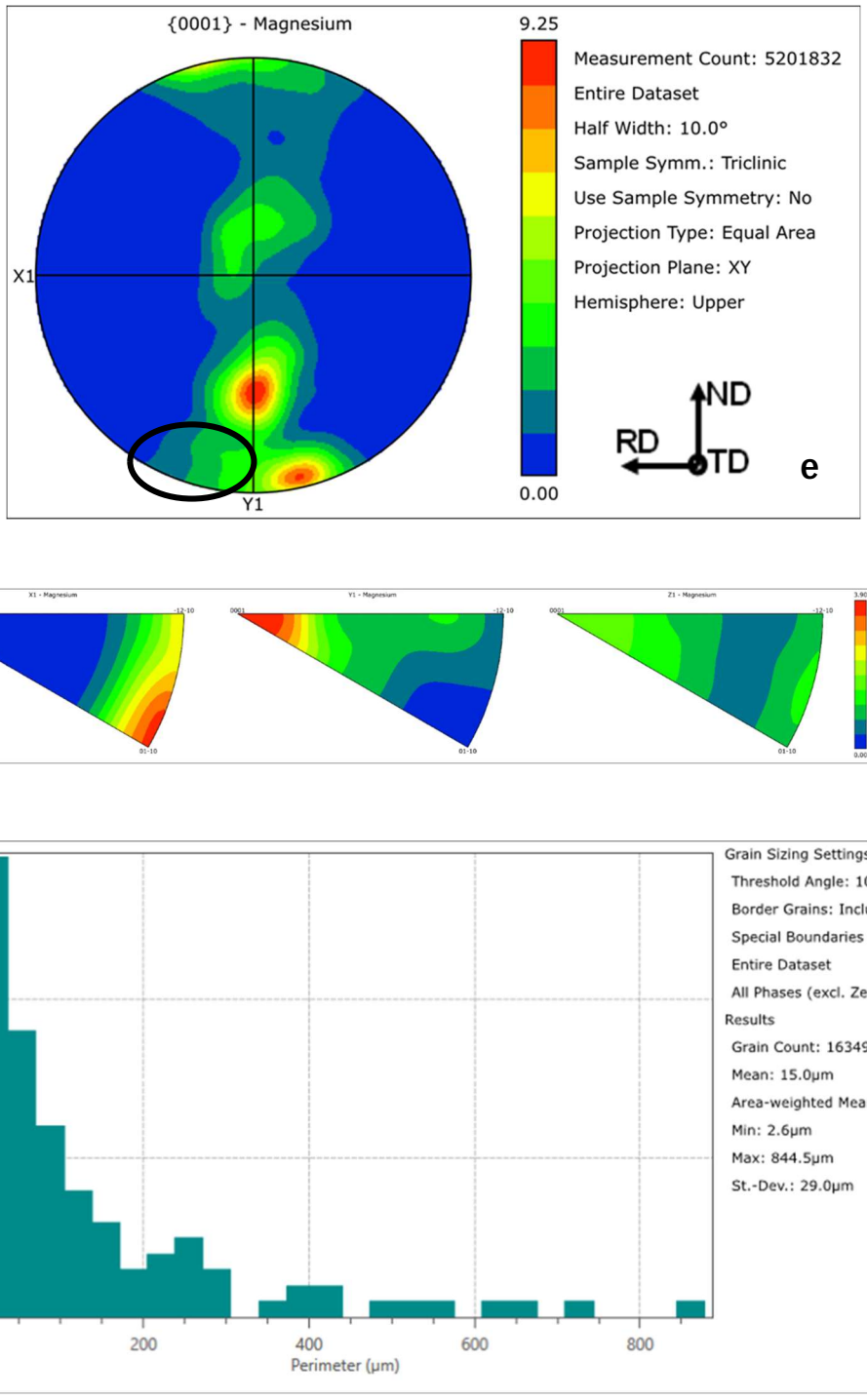

Figure 4-55 The EBSD result of the 750s annealed 1D compressed Mg-0.1Ca-0.4Zn specimen: (a) The inverse pole figure map and grain boundaries, (b) The grain boundaries and the special grain boundaries, (c) The band contrast and the phase analysis, (d) The band contrast, (e) The pole figure, (f) The inverse pole figures, (g) Grain size distribution expressed as grain boundary perimeter

After annealing for 990s, obvious changes of the recrystallization progress were observed (shown in Figure 4-56). The temperature of the specimen at that time point was 291℃. The IPF map (shown in Figure 4-56(a)) presented that not just the new

recrystallized grains from shear bands started to grow, but the nucleation from twins and the grain boundaries were also observed (marked by white circles in IPF map). The value of the average grain size showed the corresponding increase which was changed from $15\mu m$ to $16.4\mu m$ (shown in Figure 4-56(g)). The changes in the boundary fraction also matched the evolution of the microstructure. Figure 4-56(b) shows the variation of the value for the boundary fractions. The boundary fractions of the tensile twins, compressive twins and double twins were all reduced from 31.8% to 28.2%, 3.34% to 3.26% and 7.6% to 6.2%, respectively. Meanwhile, the fraction of the low-angle grain boundary and the high-angle grain boundary was changed from 52.6% to 49.9% and from 47.4% to 50.1%, respectively. On the other hand, as the recrystallization proceeded, the variation of the grain orientation distribution was observed in the pole figure and IPF (shown in Figure 4-56(e) and (f)). The extra signal which tilted 10° to the peak direction close to the ND and diffusely distributed was found in the pole figure. The maximum value of the pole figure was also found to be reduced by 0.6 (from 9.3 to 8.7).

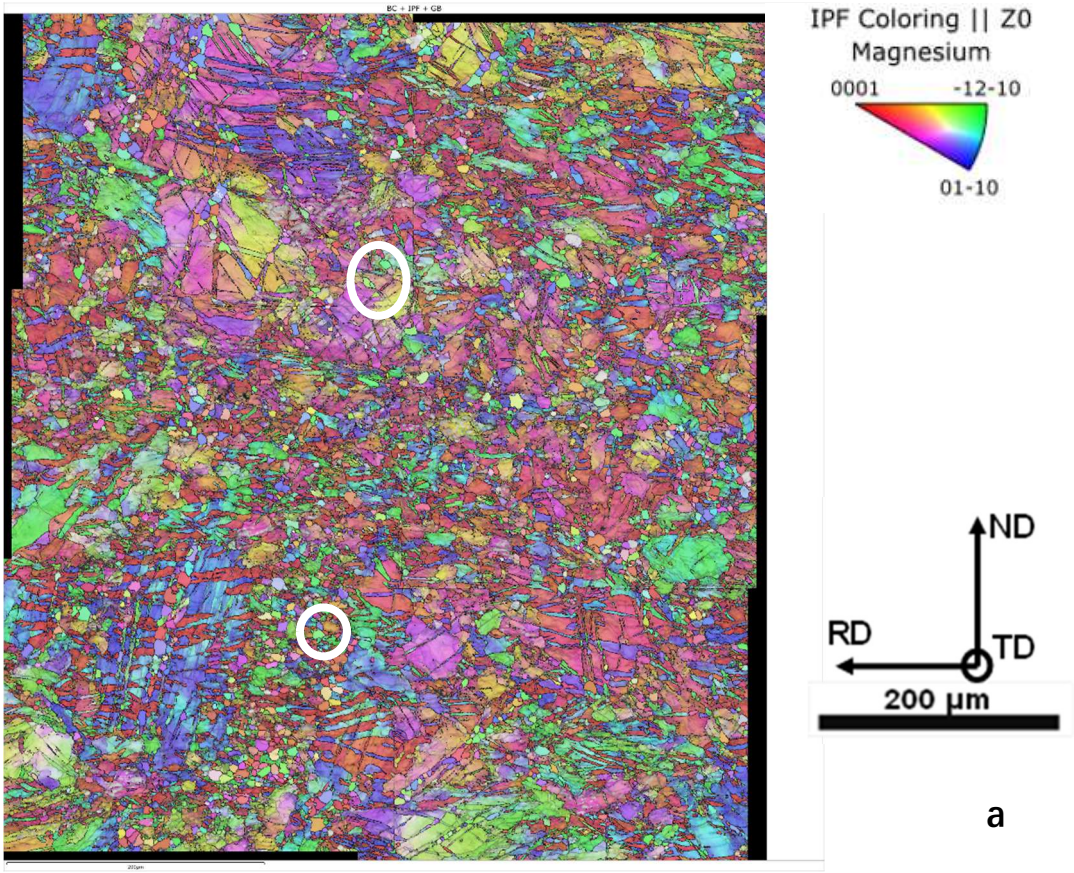

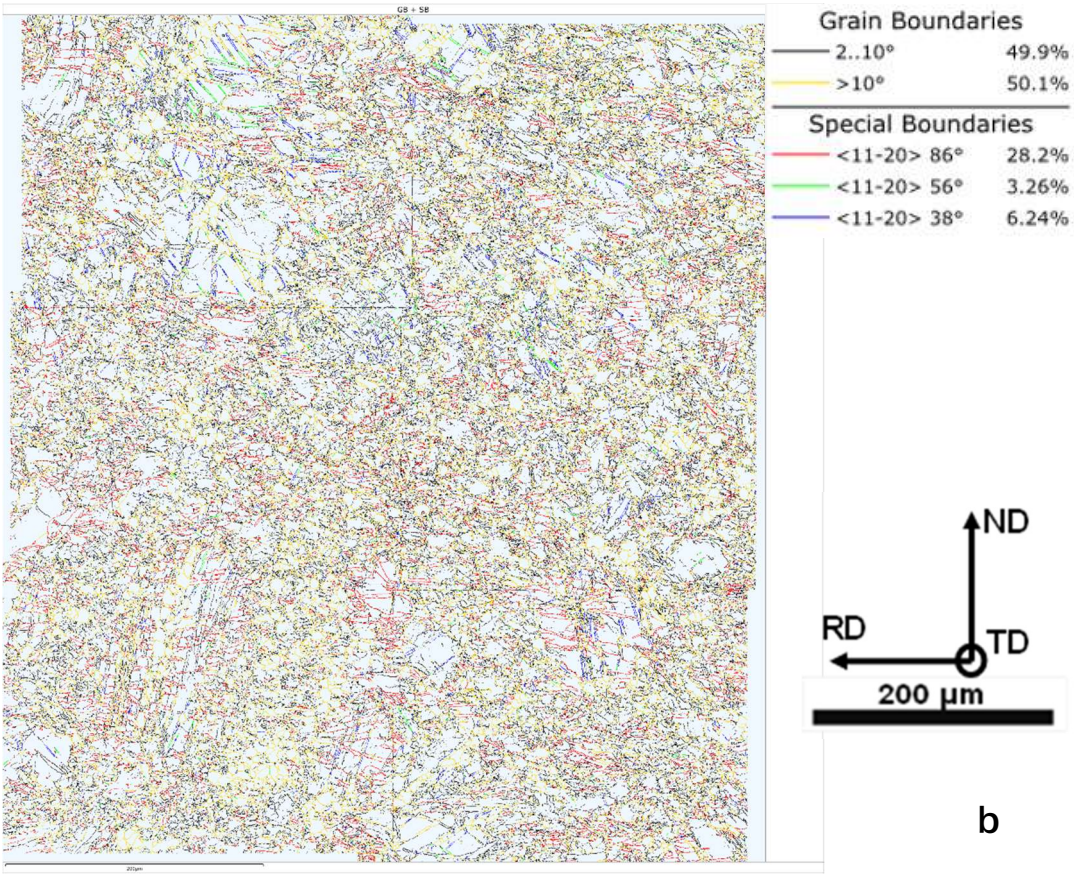
Grain Boundaries
2..10° 49.9%
>10° 50.1%
Special Boundaries
<11-20> 86° 28.2%
<11-20> 56° 3.26%
<11-20> 38° 6.24%
ND
RD
TD
200 µm

b

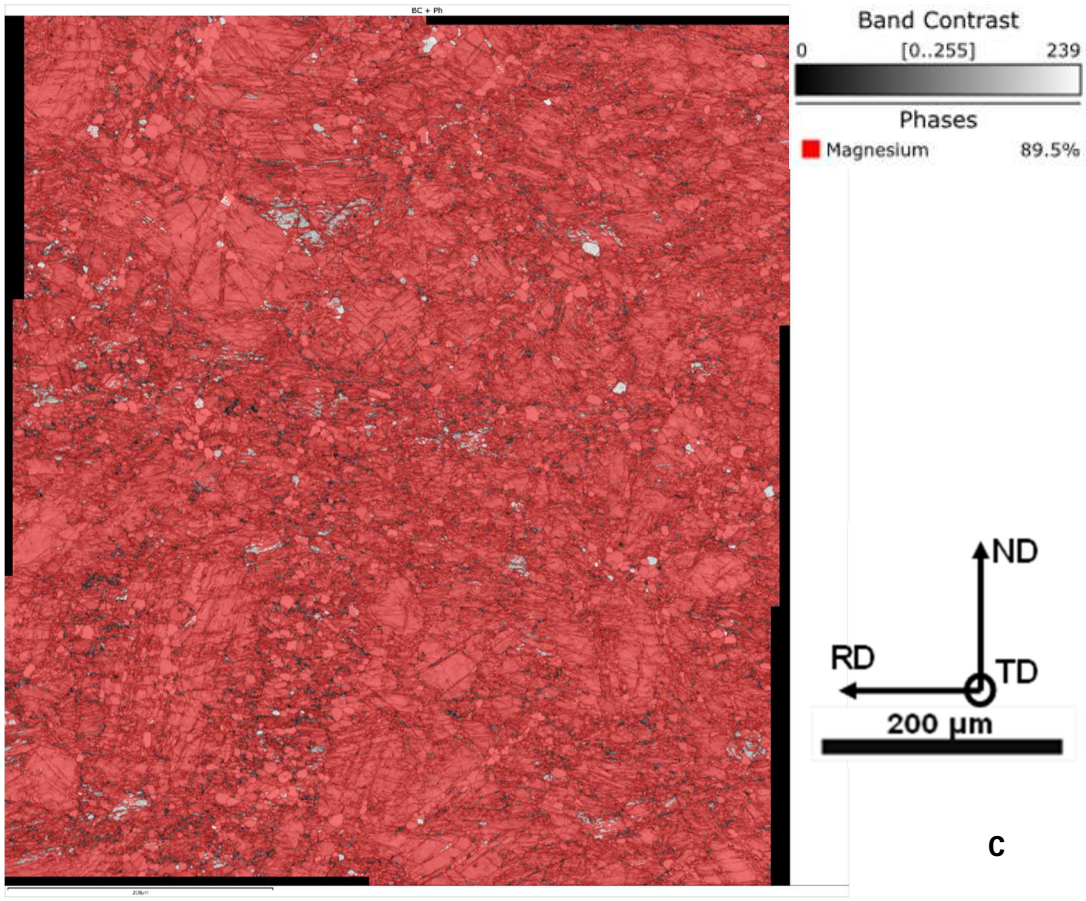
Band Contrast
0 [0..255] 239
Phases
Magnesium 89.5%
ND
RD
TD
200 µm

c

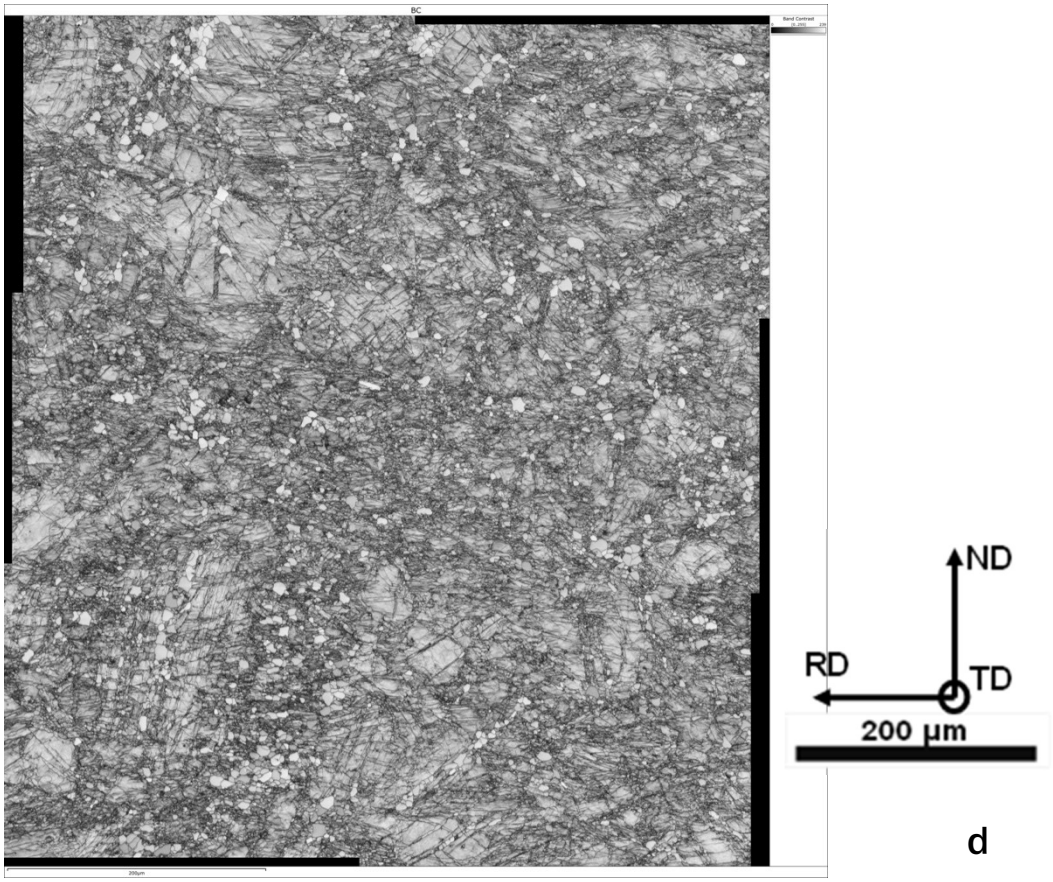
ND
RD
TD
200 µm
d

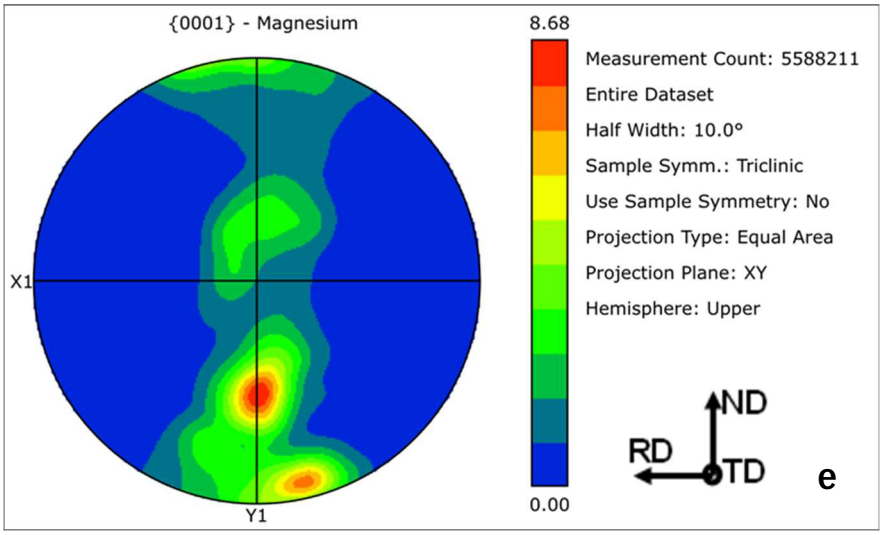
{0001} - Magnesium
8.68
0.00
X1
Y1
Measurement Count: 5588211
Entire Dataset
Half Width: 10.0°
Sample Symm.: Triclinic
Use Sample Symmetry: No
Projection Type: Equal Area
Projection Plane: XY
Hemisphere: Upper
ND
RD
TD
e

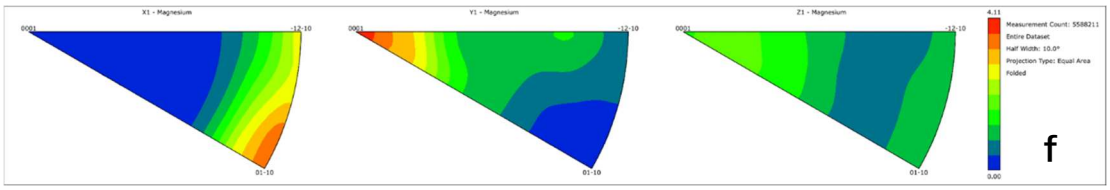
f

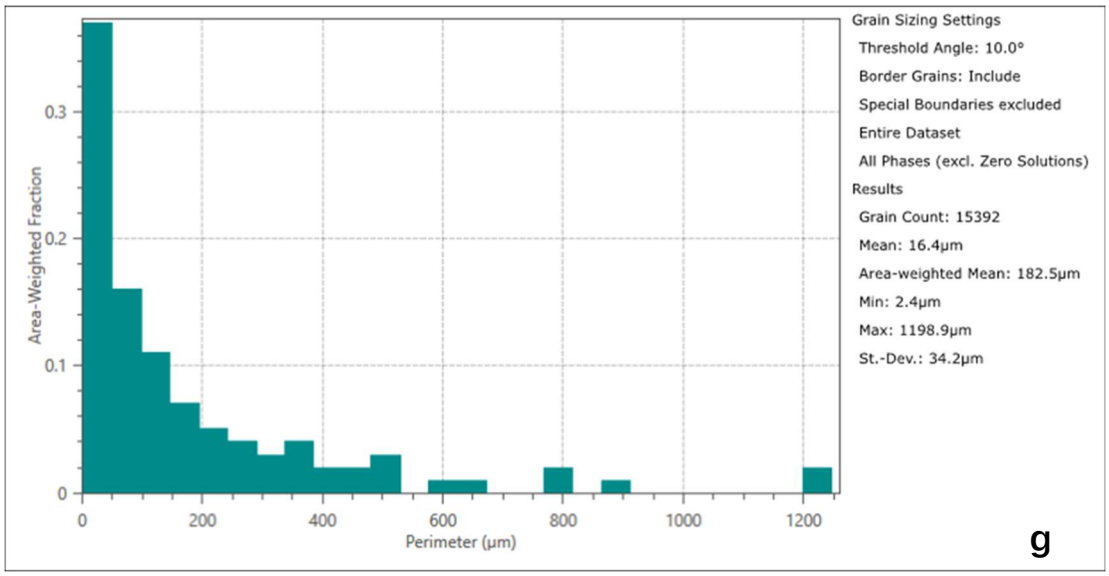

Figure 4-56 The EBSD result of the 990s annealed 1D compressed Mg-0.1Ca-0.4Zn specimen: (a) The inverse pole figure map and grain boundaries, (b) The grain boundaries and the special grain boundaries, (c) The band contrast and the phase analysis, (d) The band contrast, (e) The pole figure, (f) The inverse pole figures, (g) Grain size distribution expressed as grain boundary perimeter

The last EBSD result (shown in Figure 4-76) of the 1D compressed Mg-0.1Ca-0.4Zn (at%) specimen was after 1290s annealing. The highest temperature of the specimen during this annealing process was 310℃. After the 60s longer annealing and with the 21℃ difference in the highest temperature, the specimen showed an almost fully recrystallized microstructure in the IPF map (shown in Figure 4-57(a)). This indicated that the specimen experienced a rapid and complete recrystallization during annealing. Only a few original grains (part of) were found in the IPF map (marked with the white circles). The recrystallization specimen showed a much more uniform microstructure compared to that of the original ingot. The grain size ranged from 64μm to 3μm (shown in Figure 4-57(g)), while the average grain size was 29.8μm. In a similar manner to the 1D compressed Mg-0.2Ca-0.3Zn (at%) specimen, the non-indexed grains and the partially identified grains were found with different orientations in the IPF map (shown in Figure 4-57(a) and (c)). Additionally, recrystallized grains with orientations closer to the TD appeared darker in the band contrast map, as illustrated in Figure 4-57(d). The information about the grain boundaries (shown in Figure 4-57(b)) also presented a corresponding result after the full recrystallization. The boundary fraction of the tensile twins, compressive twins and double twins dramatically decreased from 28.2% to 3.7%, 3.3% to 0.6% and 6.2% to 0.3%, respectively. Meanwhile, after the recrystallization, the boundary fraction of the low-angle grain

boundary and the high-angle grain boundary was changed from 49.9% to 16.9% and 50.1% to 83.1%, respectively. The pole figure and IPF (shown in Figure 4-57(e) and (f)) also presented an obvious variation of the grain orientation distribution. The texture of the specimen was weakened after the recrystallization. The peak of the pole figure held its position (45° tilted from the TD), but the maximum intensity of the peak exhibited a reduction which was from 8.7 to 5.5. The second peak had vanished and the weak peak close to the TD became the second peak. The direction distribution of the recrystallized grains was found diffused around these peaks and meanwhile distributed along the ND-axis.

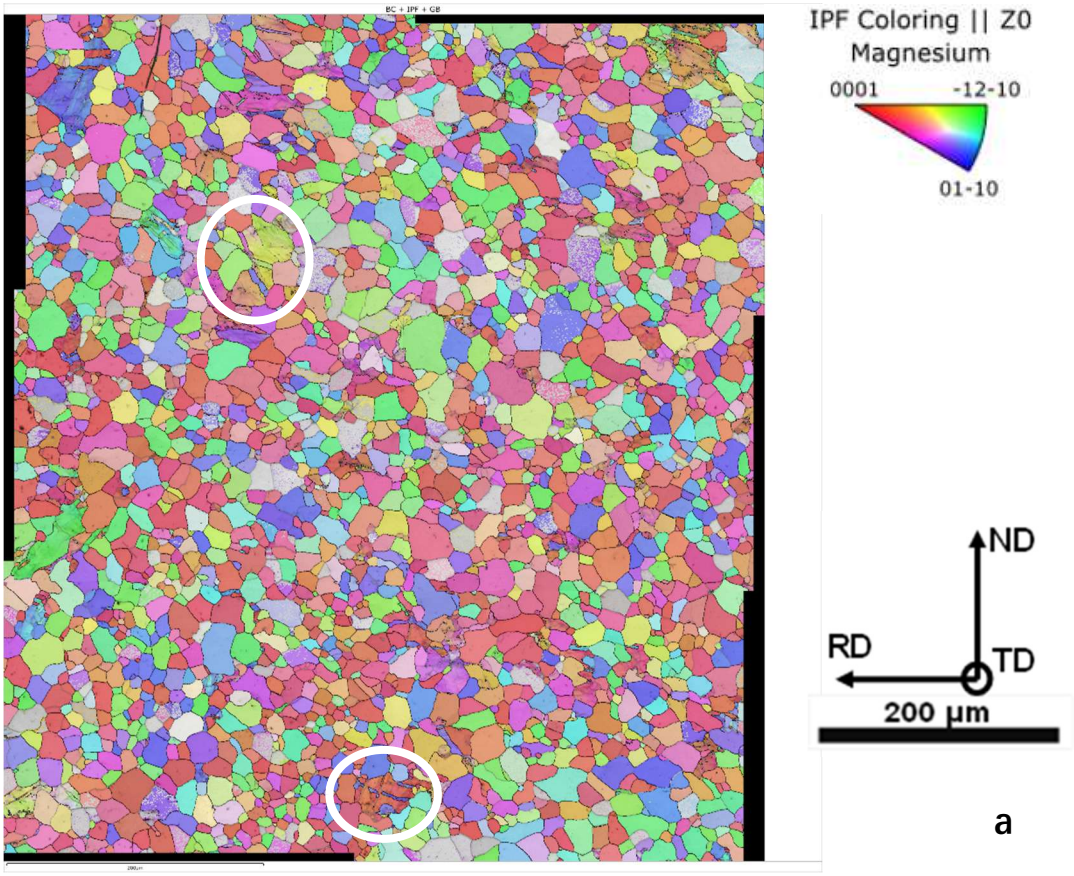

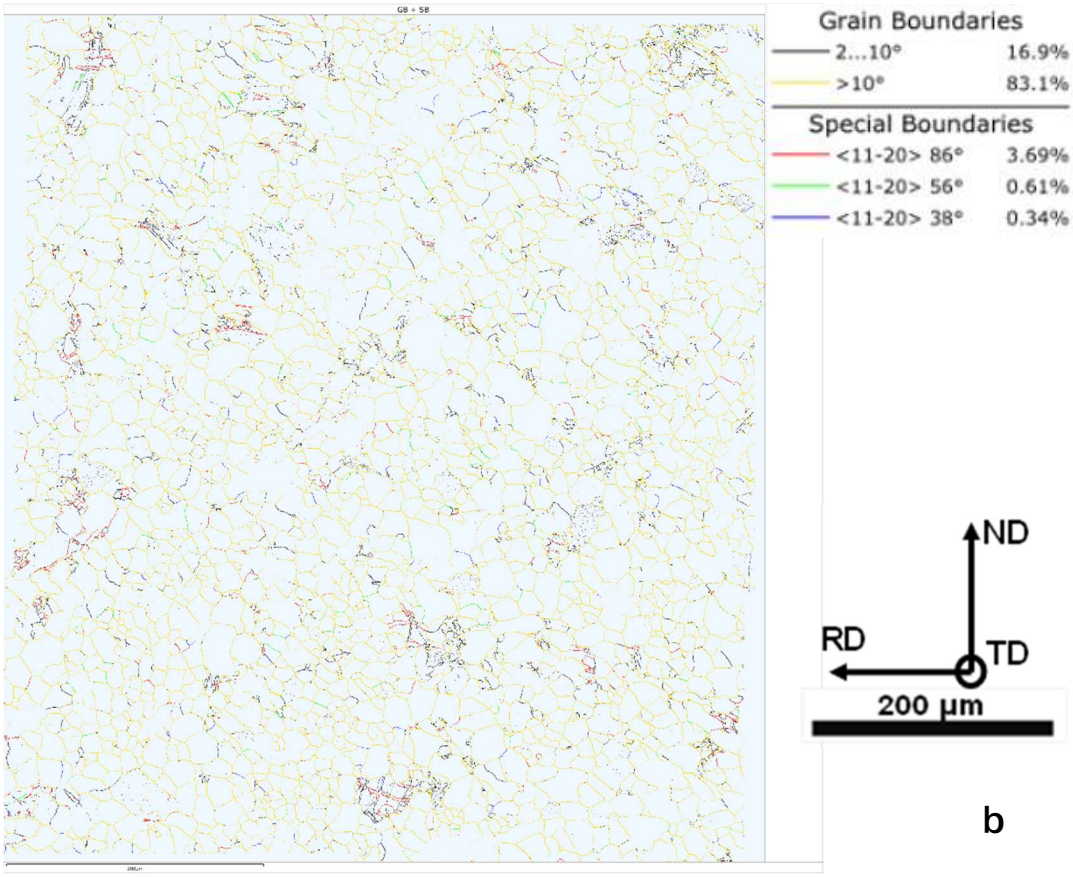
GB + SB
Grain Boundaries
2...10° 16.9%
>10° 83.1%
Special Boundaries
<11-20> 86° 3.69%
<11-20> 56° 0.61%
<11-20> 38° 0.34%
ND
RD
TD
200 µm

b

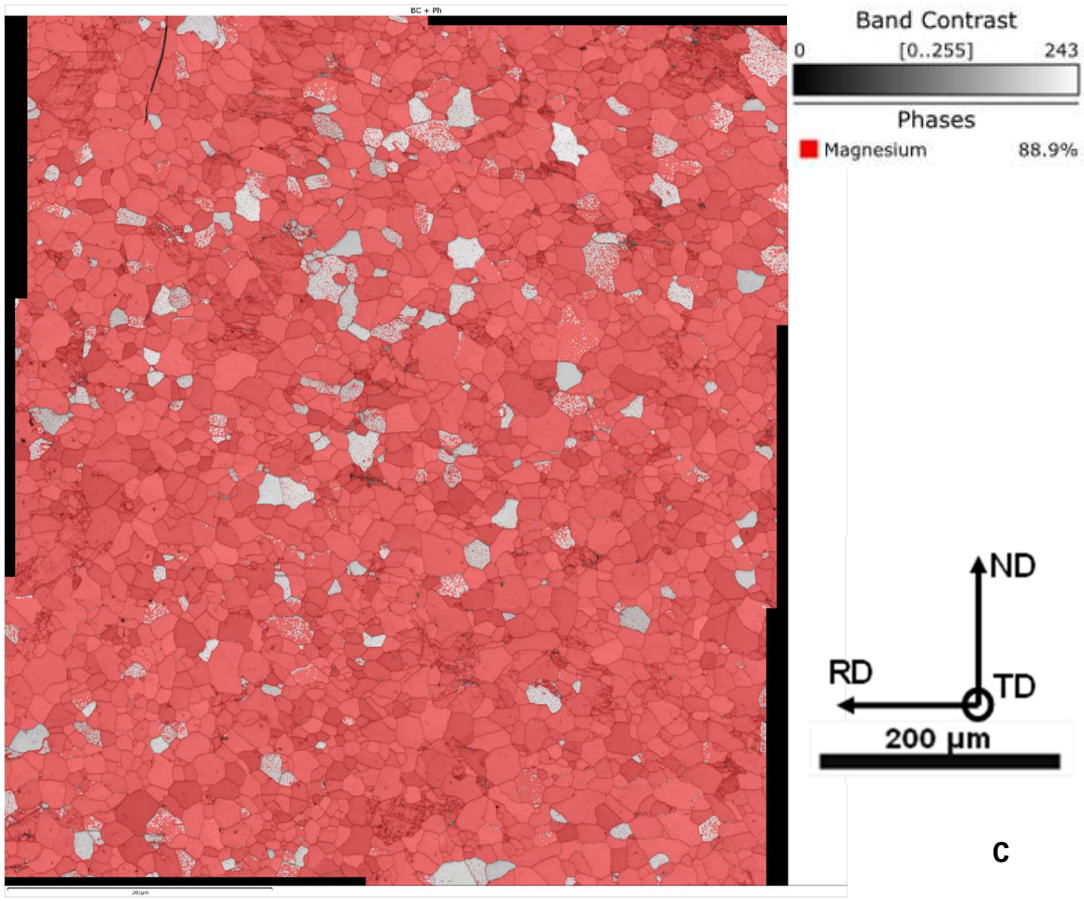
BC + Ph
Band Contrast
0 [0..255] 243
Phases
Magnesium 88.9%
ND
RD
TD
200 µm

c

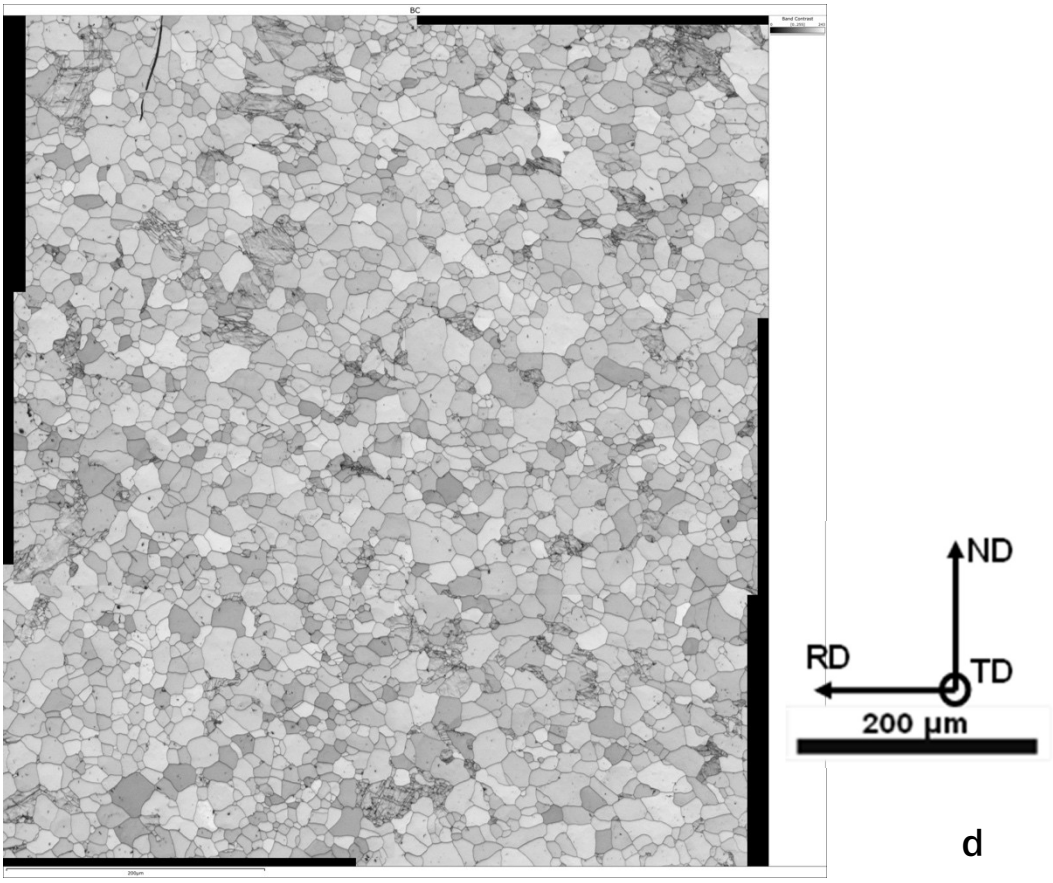
ND
RD
TD
200 µm

d

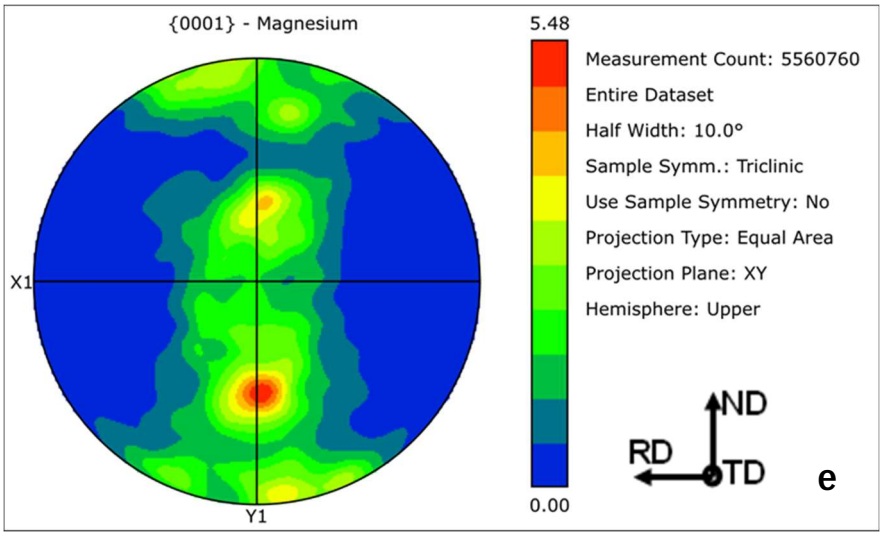
{0001} - Magnesium
5.48
0.00
X1
Y1
Measurement Count: 5560760
Entire Dataset
Half Width: 10.0°
Sample Symm.: Triclinic
Use Sample Symmetry: No
Projection Type: Equal Area
Projection Plane: XY
Hemisphere: Upper
ND
RD
TD

e

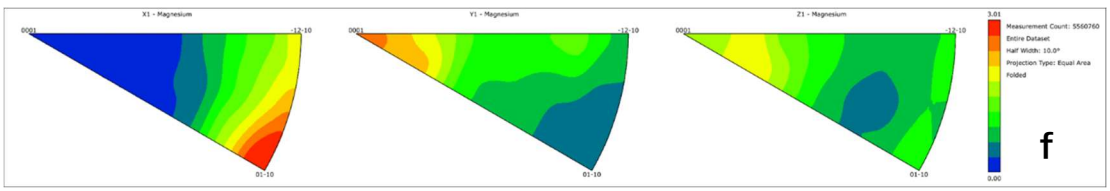

f

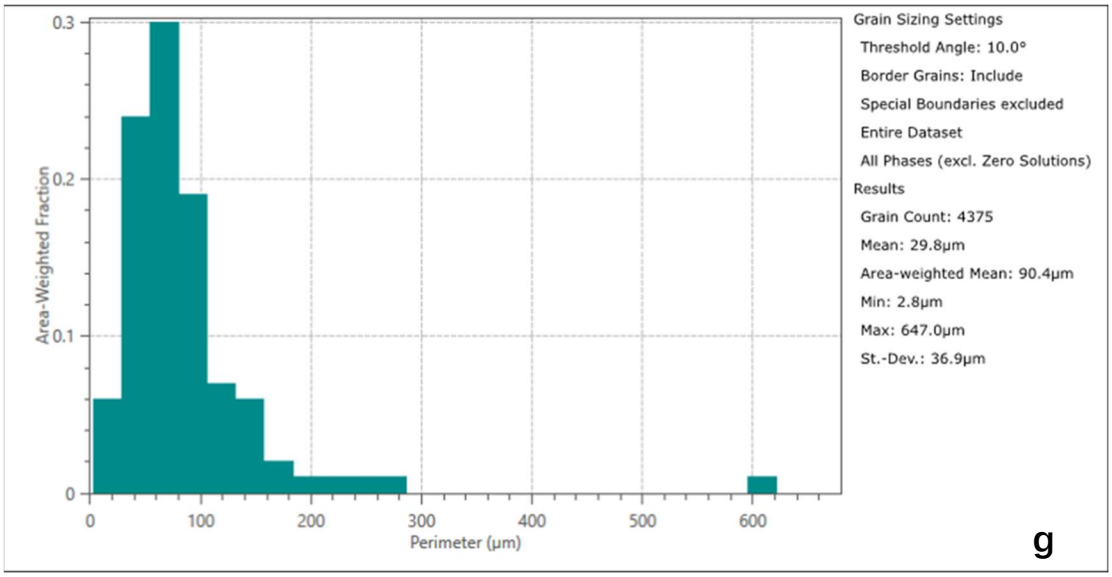

Figure 4-57 The EBSD result of the 1290s annealed 1D compressed Mg-0.1Ca-0.4Zn specimen: (a) The inverse pole figure map and grain boundaries, (b) The grain boundaries and the special grain boundaries, (c) The band contrast and the phase analysis, (d) The band contrast, (e) The pole figure, (f) The inverse pole figures, (g) Grain size distribution expressed as grain boundary perimeter

4.3.2.2.3 The one-direction (1D) compressed Mg-0.5Zn (at%) specimen

Figure 4-58 to 4-67 show the EBSD results of the 1D compressed Mg-0.5Zn (at%) specimen from the as-compressed state to the recrystallized state. The as-compressed specimen exhibited a quite uniform grain size distribution in the IPF map (shown in Figure 4-58(a)). Figure 4-58(g) indicates that the average grain size of the specimen was 23.3μm. The largest grain observed on the map had a size of approximate 75μm. Figure 4-58(c) indicates that about 20% of the area of the map was occupied by the shear bands (marked by white circles) and fine twins. On the other hand, Figure 4-58(b) gives information about the twins. The tensile twin still held the dominant position of all the twin types, 55.1% of the grain boundaries were identified as the tensile twin boundaries. The fraction of the compressive twin boundaries and the double twin boundaries was shown as 1.0% and 1.8%, respectively. The results of the pole figure and IPF (shown in Figure 4-58(e) and (f)) present a quite similar graph with the other 1D compressed specimens. Most of the grains showed a direction parallel to the compression direction. Only a few of the grains aligned with the TD. The maximum pole intensity shown in the figure was 11.6.

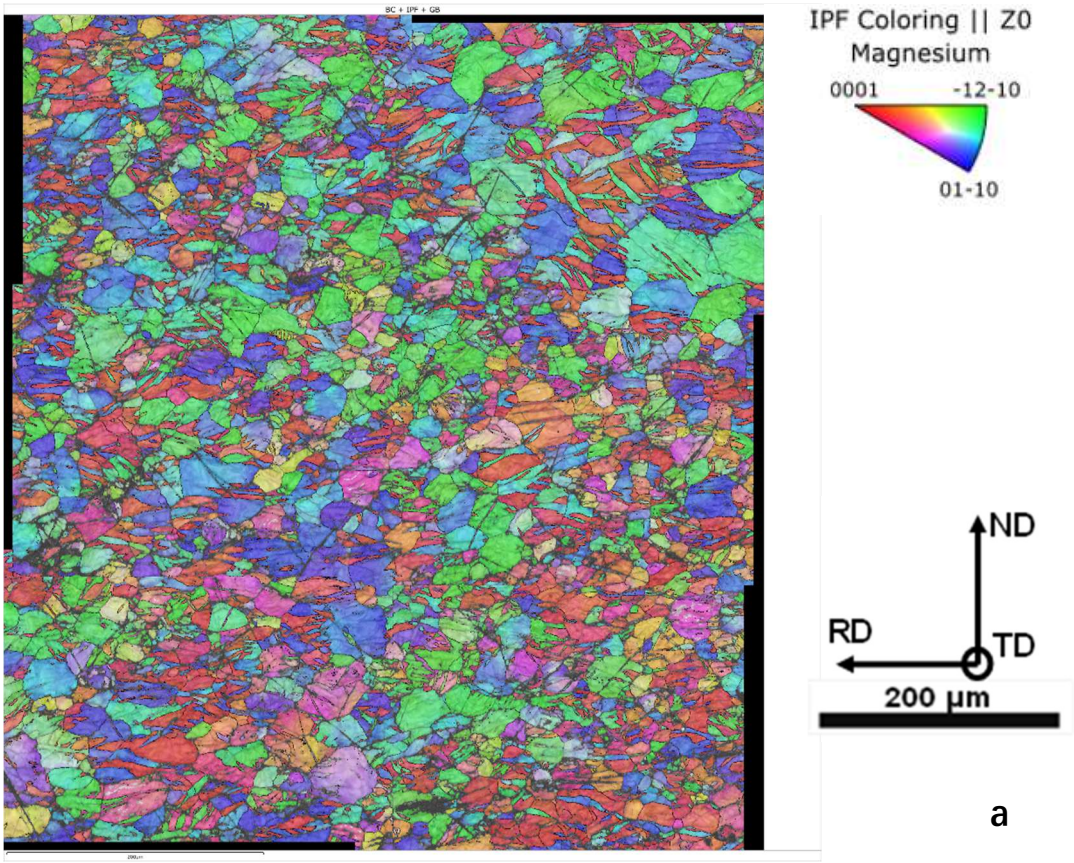
IPF Coloring || Z0
Magnesium
0001
-12-10
01-10
ND
RD
TD
200 µm

a

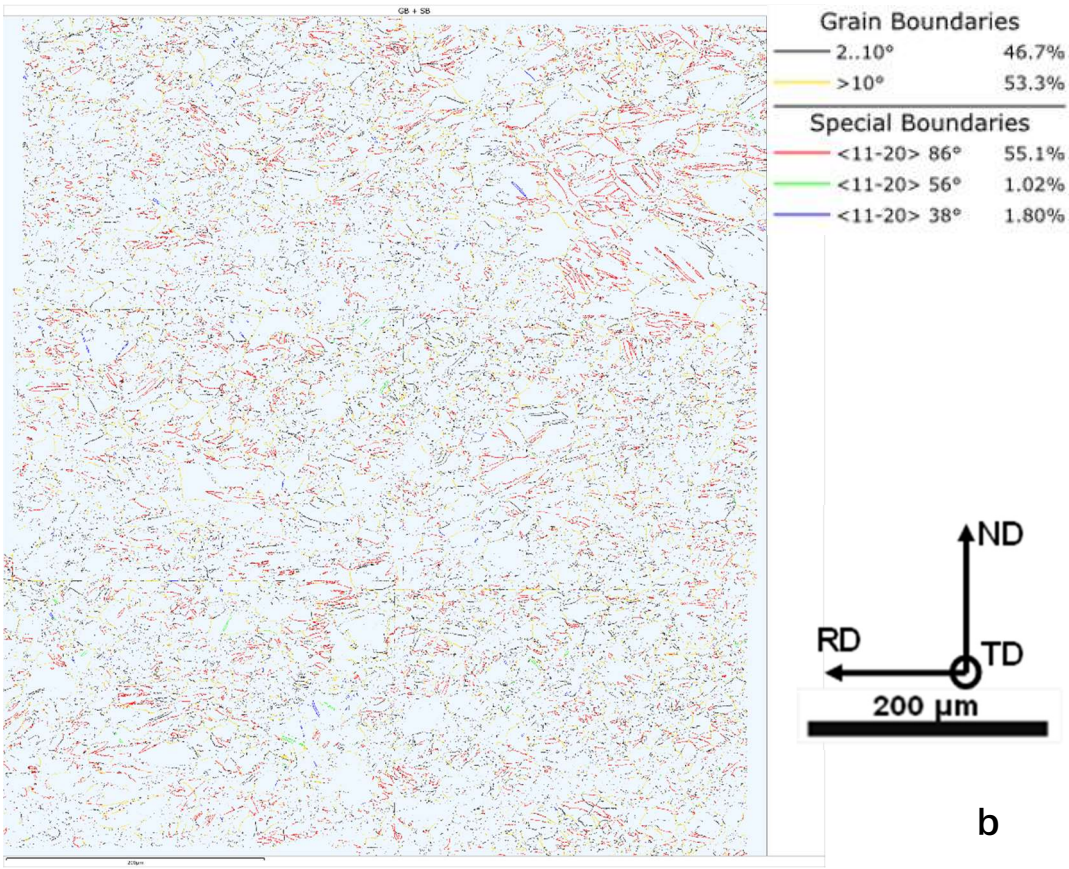
Grain Boundaries
2..10° 46.7%
>10° 53.3%
Special Boundaries
<11-20> 86° 55.1%
<11-20> 56° 1.02%
<11-20> 38° 1.80%
ND
RD
TD
200 µm

b

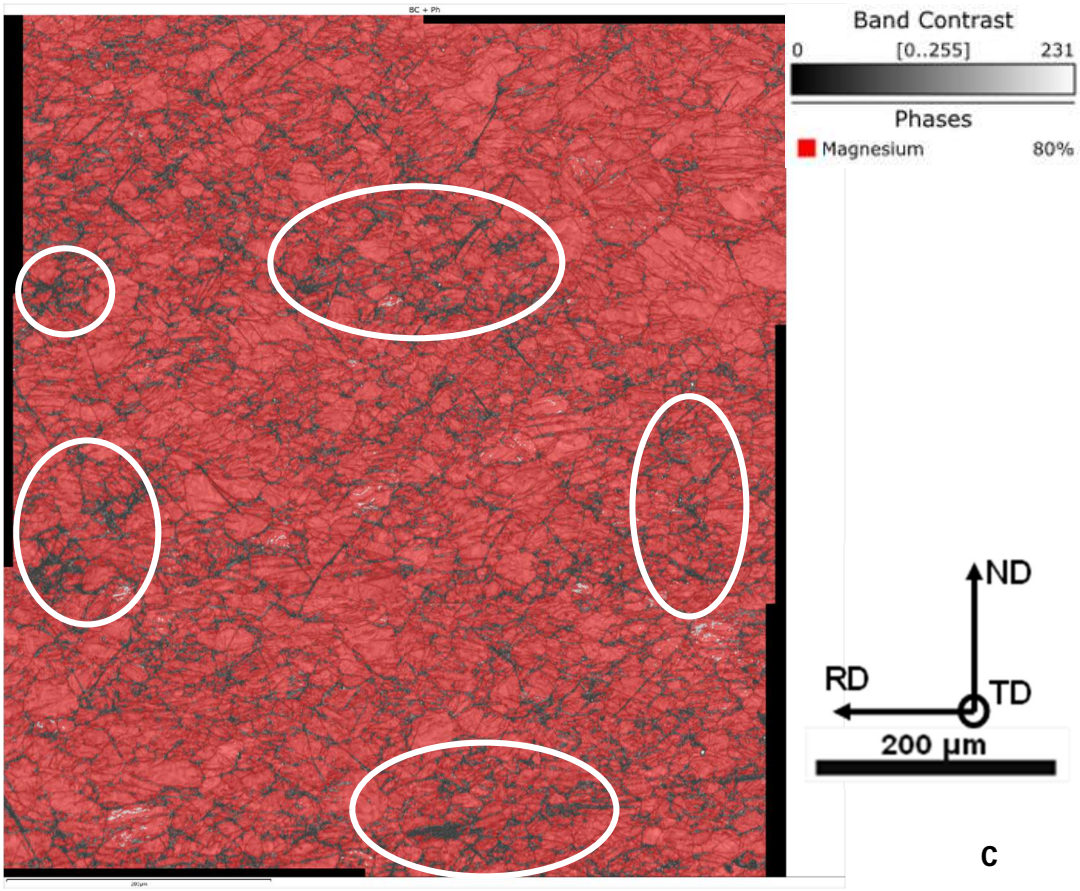
Band Contrast
0
[0..255]
231
Phases
Magnesium
80%
ND
RD
TD
200 µm

c

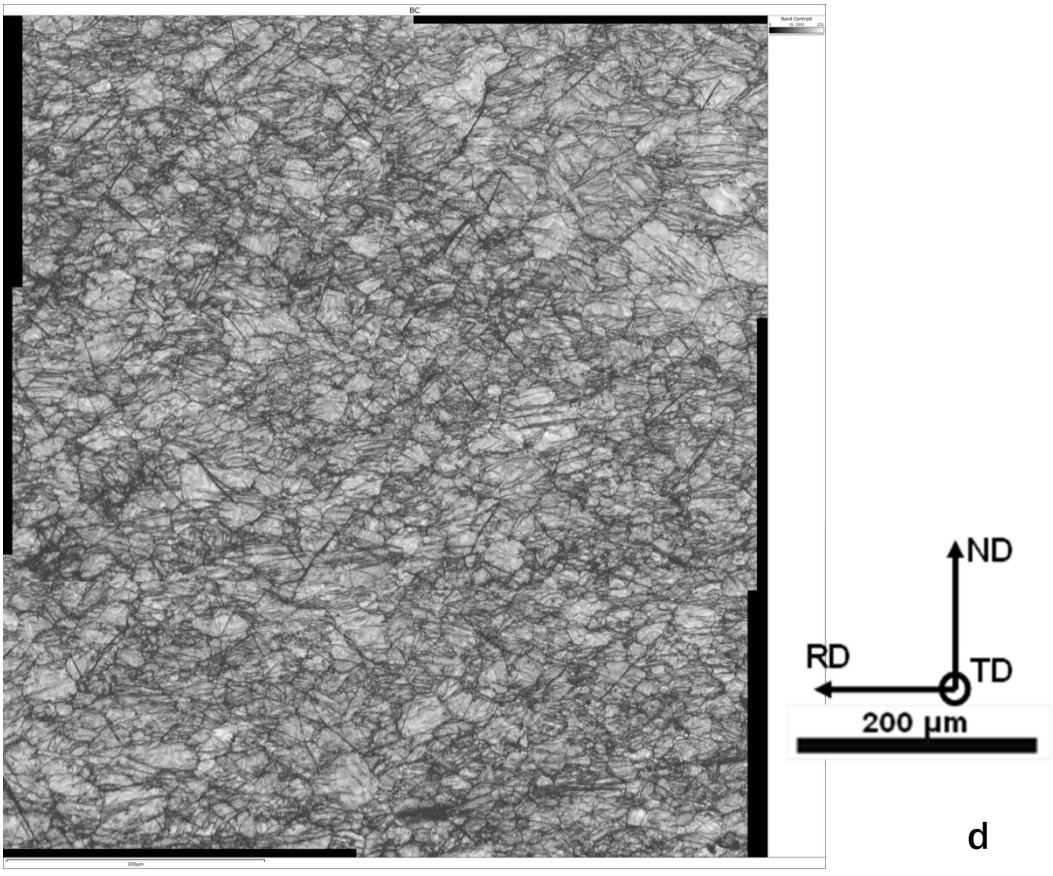
ND
RD
TD
200 µm

d

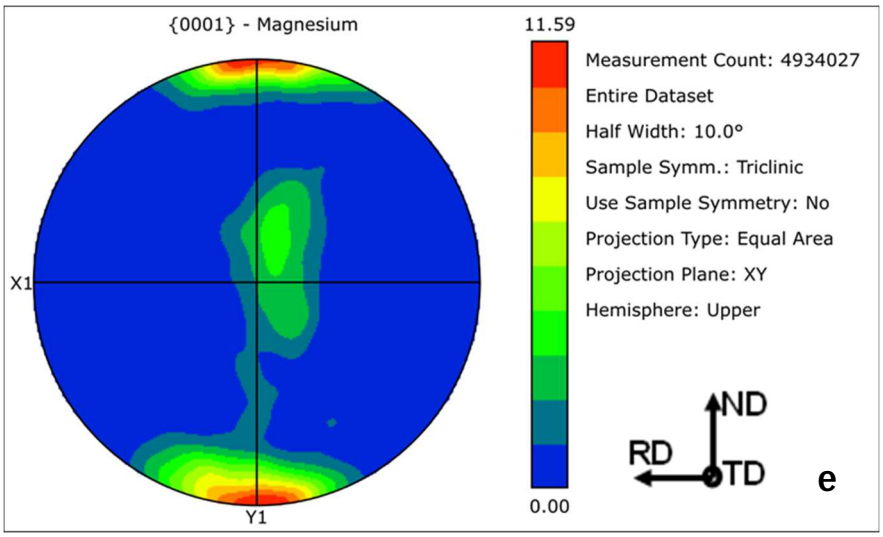

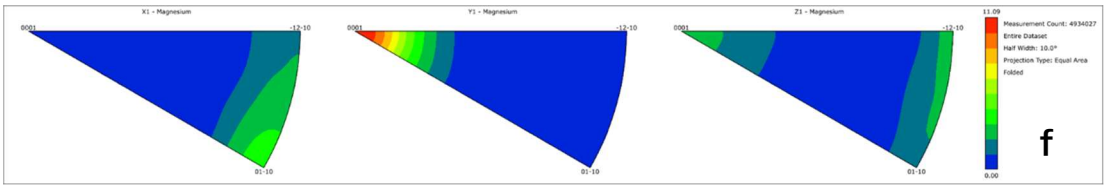

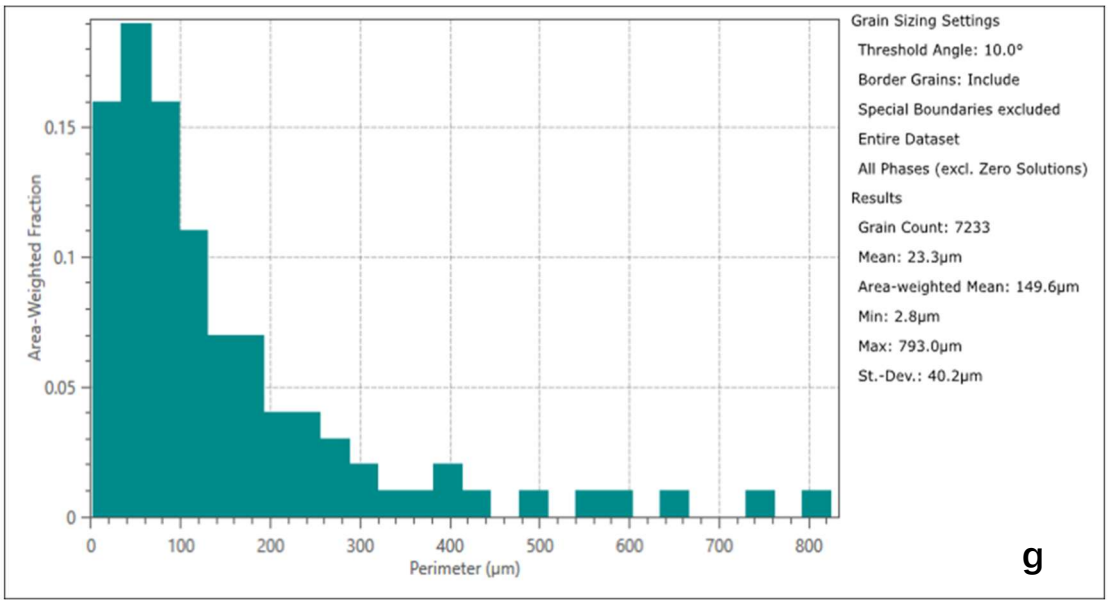

Figure 4-58 The EBSD result of the as-compressed 1D compressed Mg-0.5Zn specimen: (a) The inverse pole figure map and grain boundaries, (b) The grain boundaries and the special grain boundaries, (c) The band contrast and the phase analysis, (d) The band contrast, (e) The pole figure, (f) The inverse pole figures, (g) Grain size distribution expressed as grain boundary perimeter

Figure 4-59 shows the EBSD results of the same specimen after annealing for 30s. Combining the information from Figure 4-59(a) and Figure 4-59(b), it was very clear that the recrystallization was already started when the sample temperature reached 80℃.

At this stage, the average grain size increased slightly to 23.7μm (shown in Figure 4-59(g)). Figure 4-59(c) indicates that the fraction of the non-indexed area on the map was reduced from 20.0% to 9.8%. Notably, most of the recrystallized grains were observed at the previous shear bands position. This suggested that apart from the very few recovery areas, the reduction in non-indexed regions was primarily due to the transformation of shear bands into recrystallized grains. Figure 4-59(b) provides information about the twins after the recrystallization started in the specimen. The boundary fraction of the tensile twin boundaries was shown reduced from 55.1% to 45.2%. However, a comparison of Figure 4-58(b) and Figure 4-59(b) reveals that the absolute quantity of tensile twins did not decrease—in fact, it slightly increased. The reason for this was attributed to the generation of the recrystallized grains causing an increase in the total grain boundaries. Meanwhile, the morphology of the tensile twins did not show obvious differences compared to the previous stage, with the fraction of the compressive twin boundaries and double twin boundaries almost the same as the as-compressed state, which was 1.1% and 1.8%, respectively. The pole figures of the 30s annealed specimen (shown in Figure 4-59(e) and (f)) did not show much difference compared to the as-compressed state. The maximum pole intensity reduced from 11.6 to 10.5. There were no obvious changes in the grain orientation distribution.

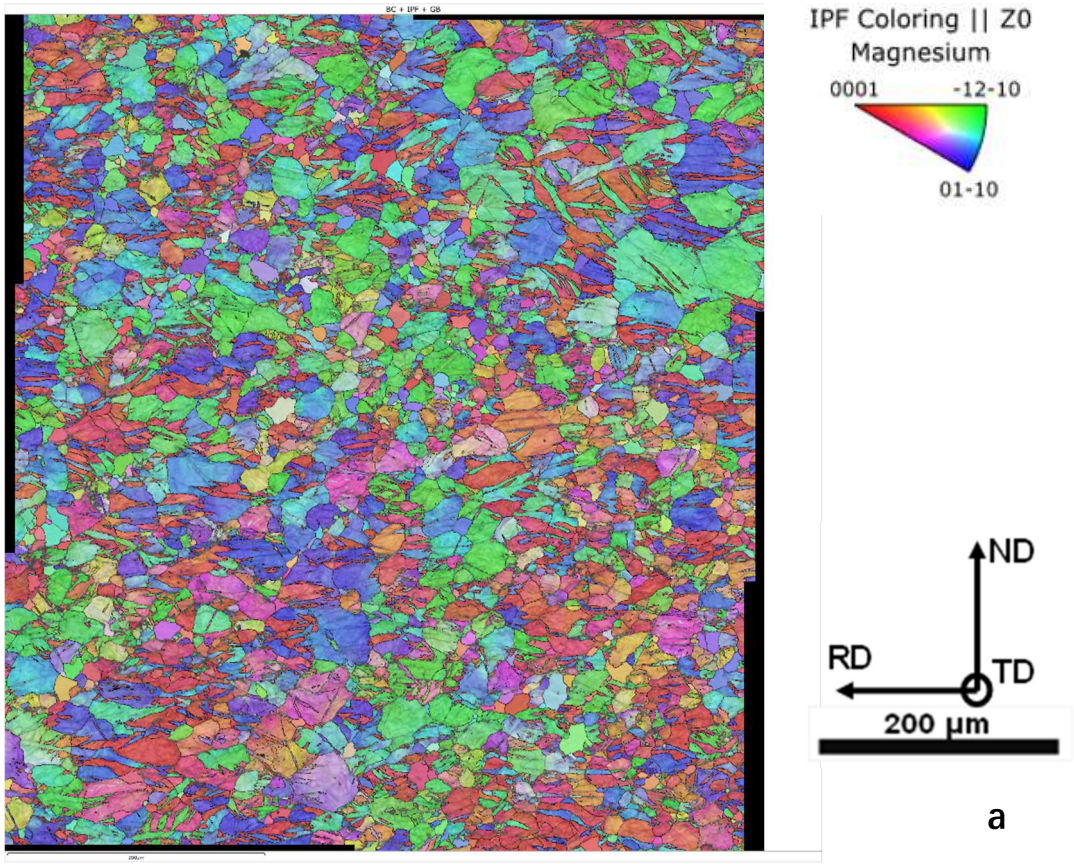

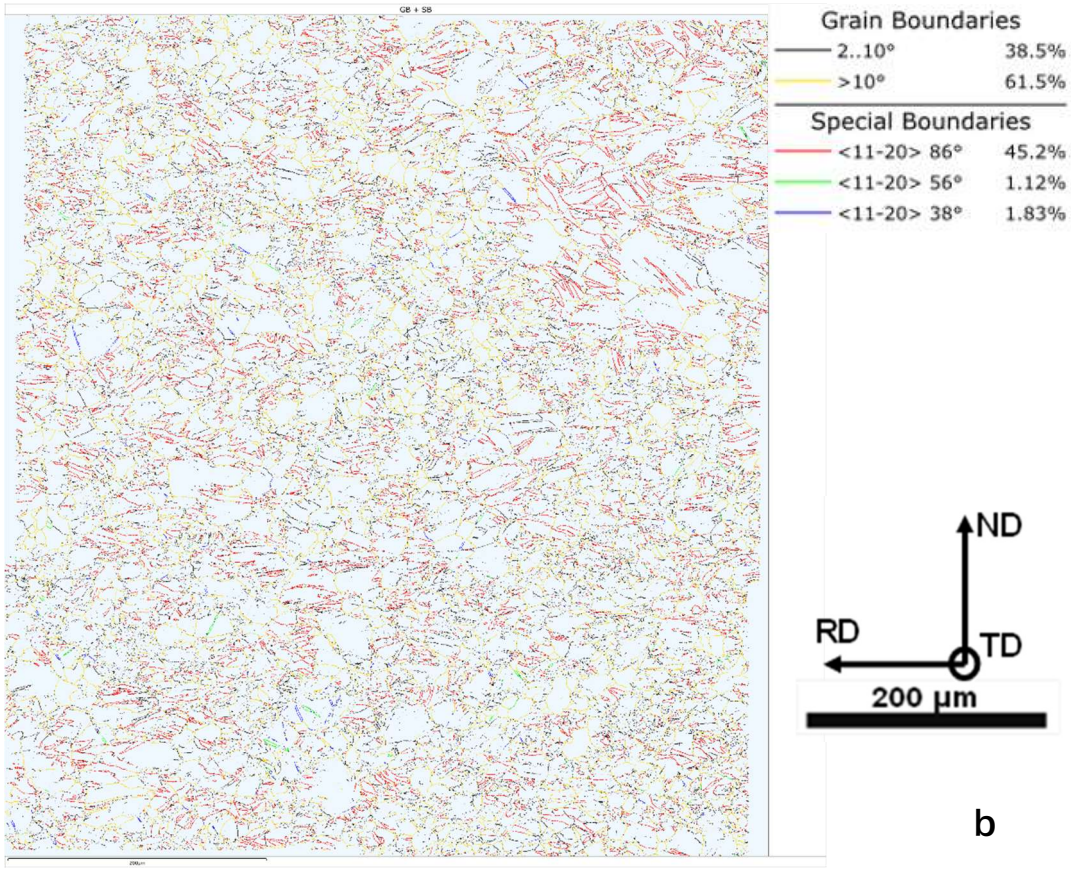
GB + SB
Grain Boundaries
2..10° 38.5%
>10° 61.5%
Special Boundaries
<11-20> 86° 45.2%
<11-20> 56° 1.12%
<11-20> 38° 1.83%
ND
RD
TD
200 µm

b

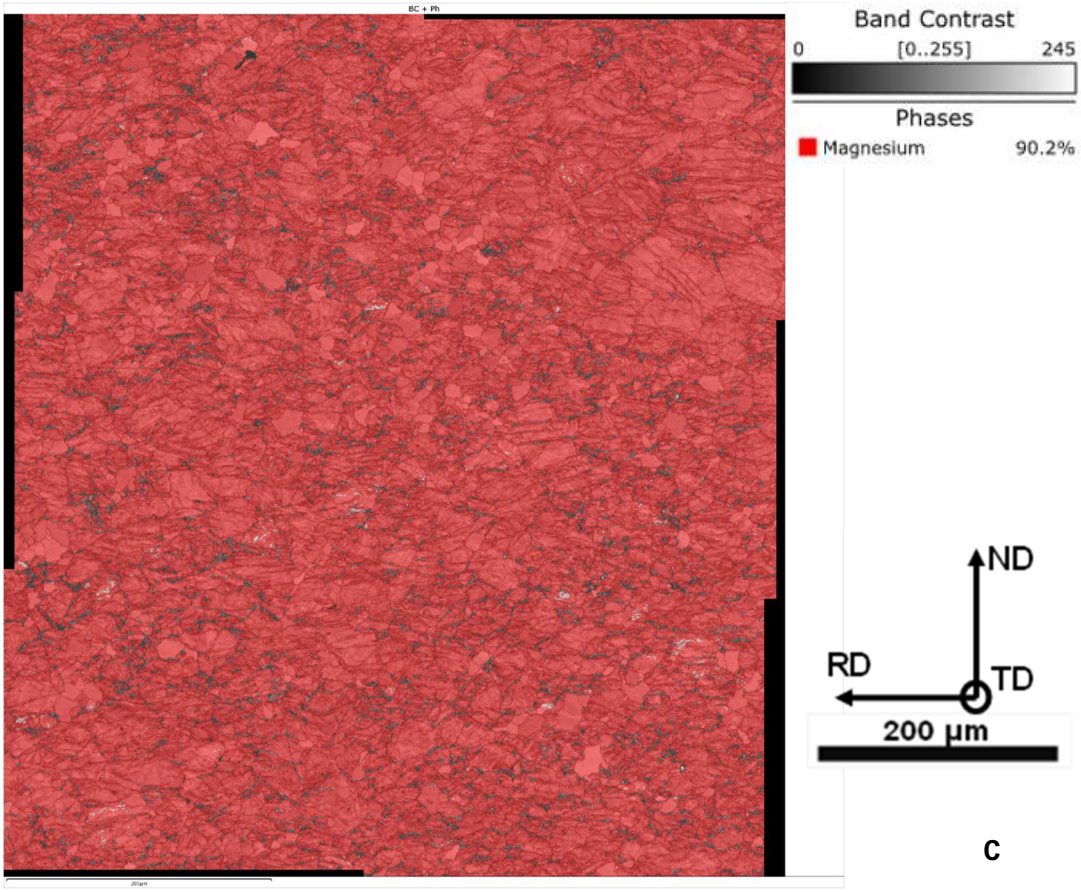
BC + Ph
Band Contrast
0 [0..255] 245
Phases
Magnesium 90.2%
ND
RD
TD
200 µm

c

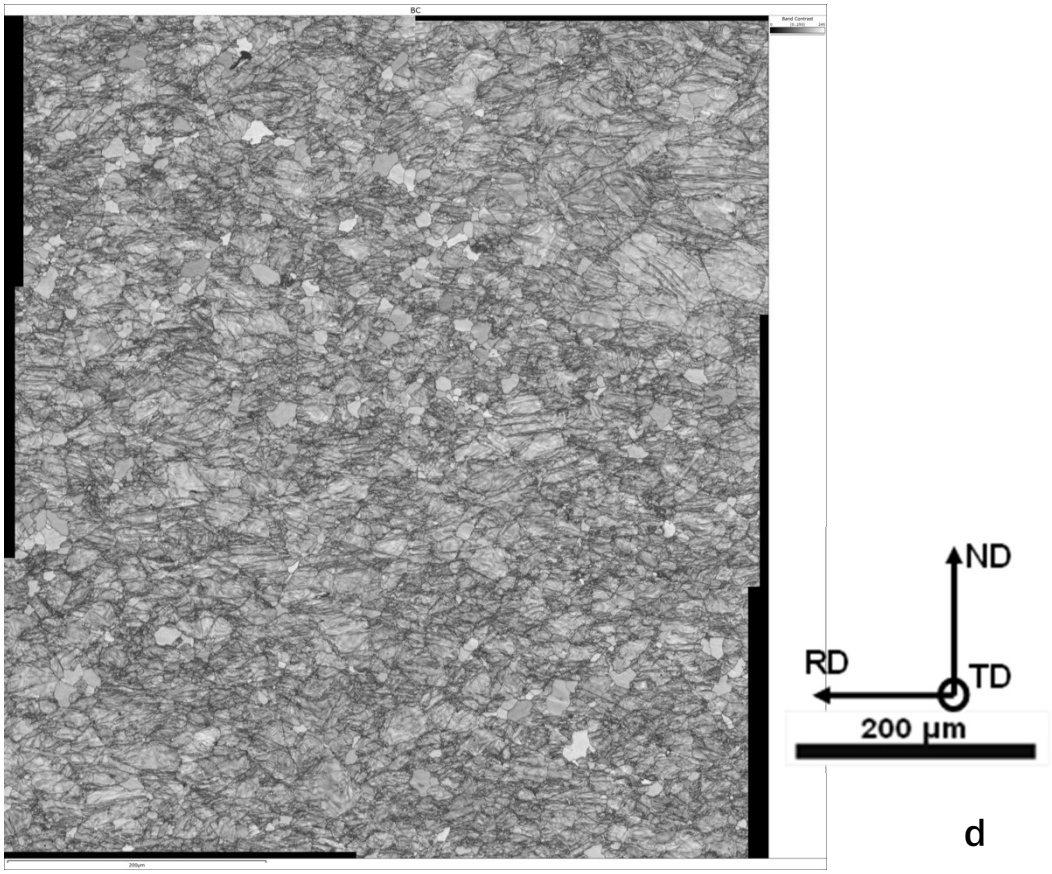
BC
ND
RD
TD
200 µm
d

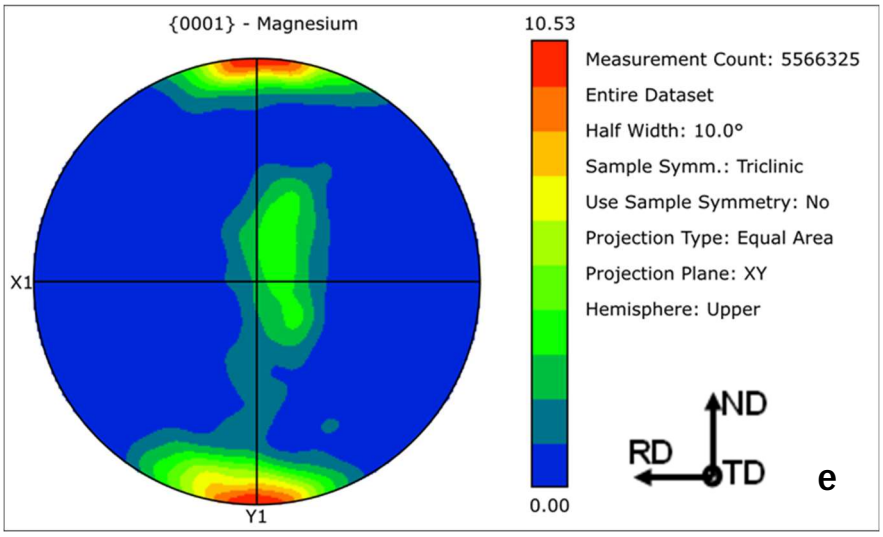
{0001} - Magnesium
10.53
Measurement Count: 5566325
Entire Dataset
Half Width: 10.0°
Sample Symm.: Triclinic
Use Sample Symmetry: No
Projection Type: Equal Area
Projection Plane: XY
Hemisphere: Upper
X1
Y1
0.00
ND
RD
TD
e

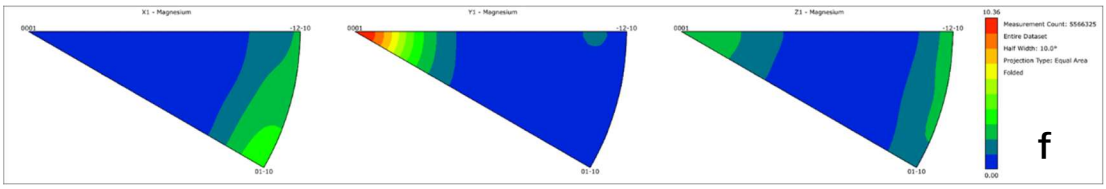
f

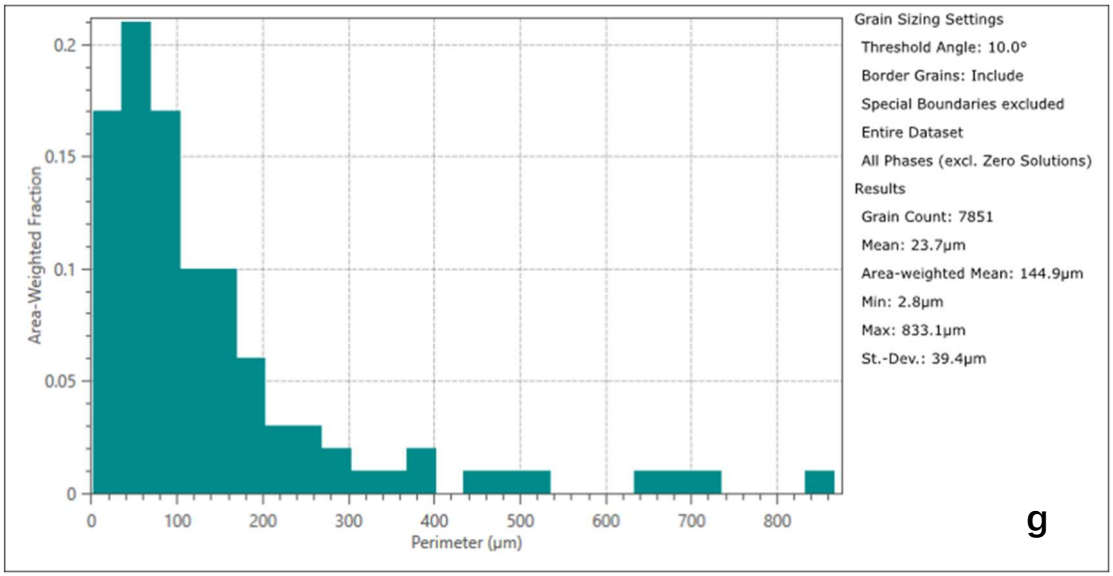

Figure 4-59 The EBSD result of the 30s annealed 1D compressed Mg-0.5Zn specimen: (a) The inverse pole figure map and grain boundaries, (b) The grain boundaries and the special grain boundaries, (c) The band contrast and the phase analysis, (d) The band contrast, (e) The pole figure, (f) The inverse pole figures, (g) Grain size distribution expressed as grain boundary perimeter

Figure 4-60 presents the further microstructure changes of the same sample after a further 75s annealing. The temperature of the specimen before the water quench was 110℃. From Figure 4-60(a), it was clear that the recrystallization in the specimen continued and became apparent i.e. the existing recrystallized grains started to grow, and the new recrystallized grains were also observed. The new recrystallized grains were mainly found nucleated on the grain boundaries rather than twins. The fraction of the twin boundaries also showed that the twins were not yet recrystallized. Figure 4-60(b) shows the boundary fraction of the tensile twins, compressive twins and double twins were 42.6%, 1.08% and 1.76%, respectively. Compared to the 30s annealed sample, the differences in the twin boundary fraction were only 2.6%, 0.04% and 0.07%, respectively. Moreover, the decrease in the low-angle grain boundary fraction (from 38.5% to 33.1%) and the increase in the high-angle grain boundary fraction (from 61.5% to 66.9%) also showed that the recrystallization was occurring, but not in the twins. The average grain size showed obvious change, which was increased to $26\mu m$ (shown in Figure 4-60(g)). Also, Figure 4-60(e) and (f) show some changes in the pole figure and IPF. The maximum value of the pole figure slightly reduced from 10.5 to 10.2. And the grains with the orientation parallel to the TD were found to have increased slightly. Also, some new signals were found distributed along the ND-axis.

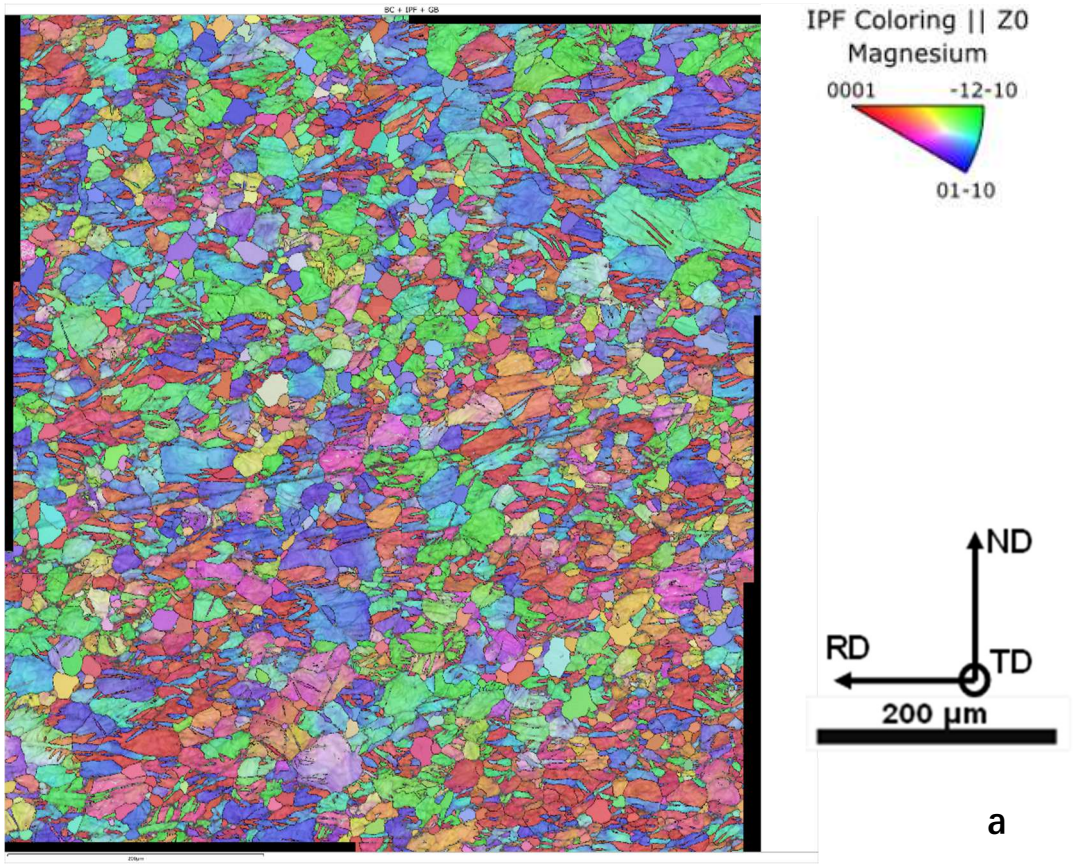
IPF Coloring || Z0
Magnesium
0001
-12-10
01-10
ND
RD
TD
200 µm

a

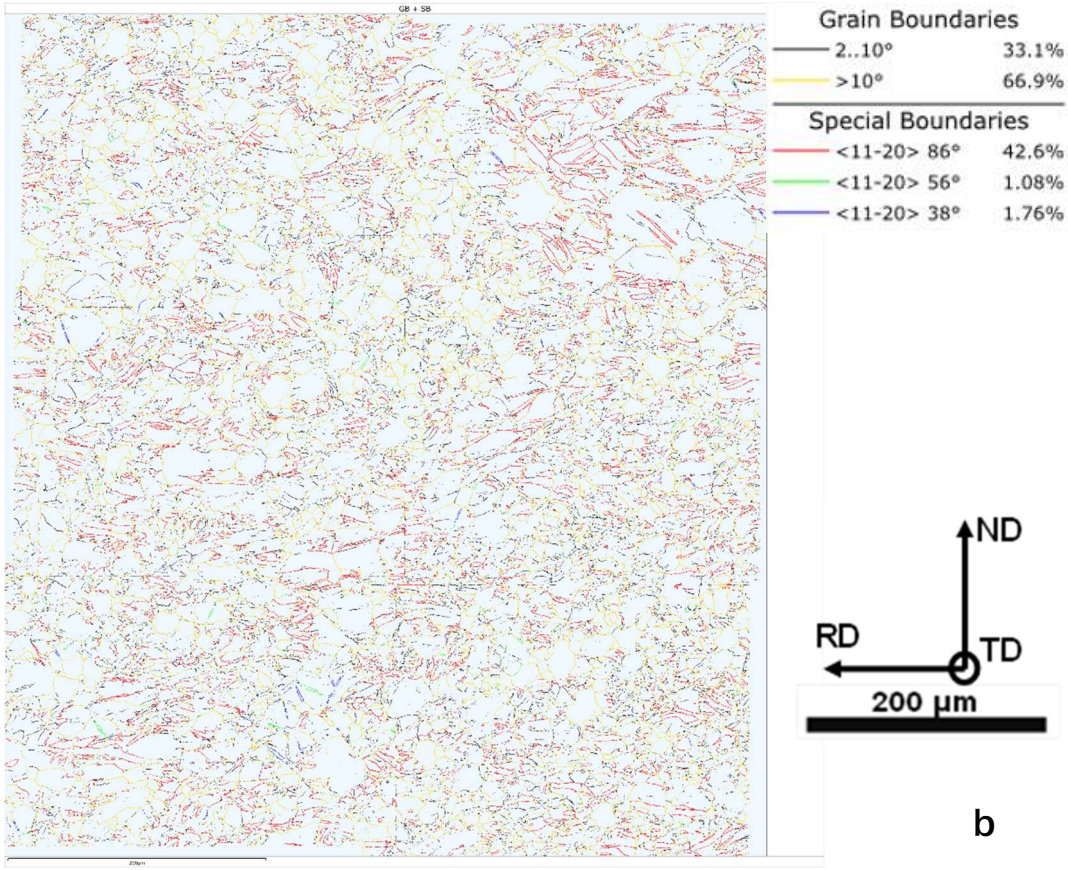
Grain Boundaries
2..10° 33.1%
>10° 66.9%
Special Boundaries
<11-20> 86° 42.6%
<11-20> 56° 1.08%
<11-20> 38° 1.76%
ND
RD
TD
200 µm

b

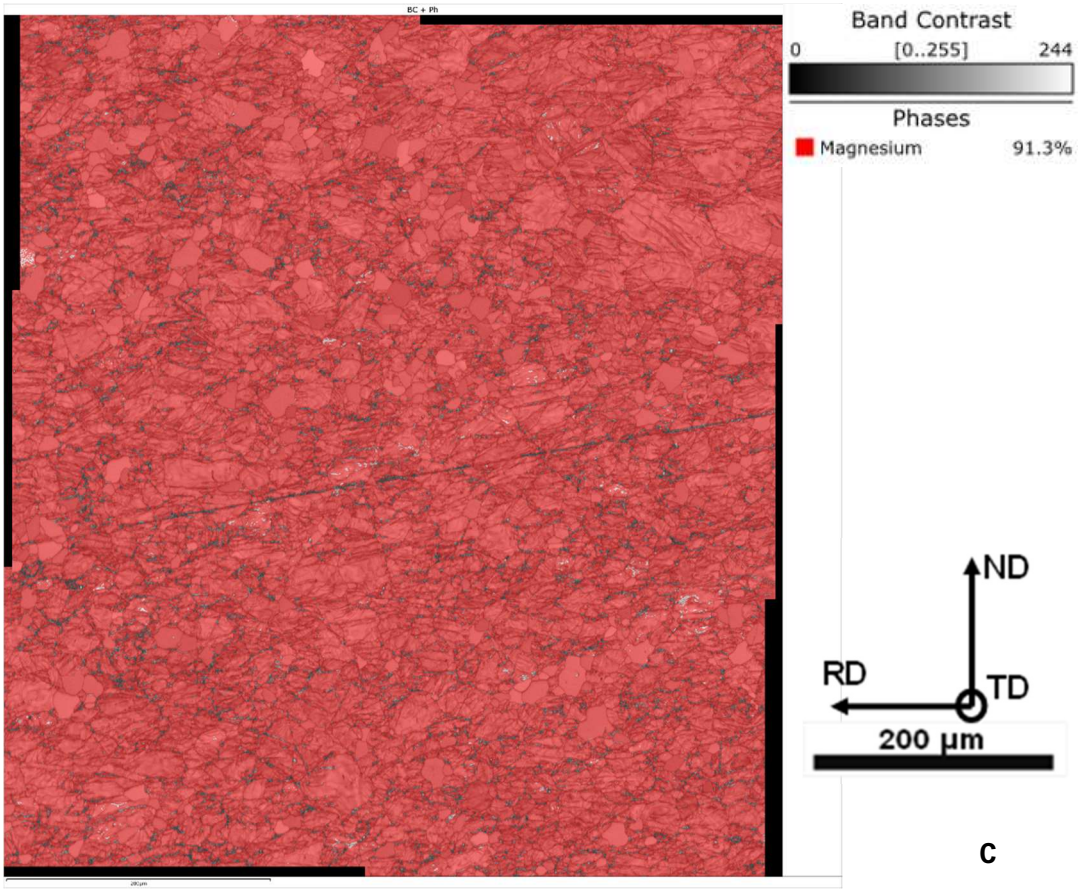
BC + Ph
Band Contrast
0
[0..255]
244
Phases
Magnesium
91.3%
ND
RD
TD
200 µm

c

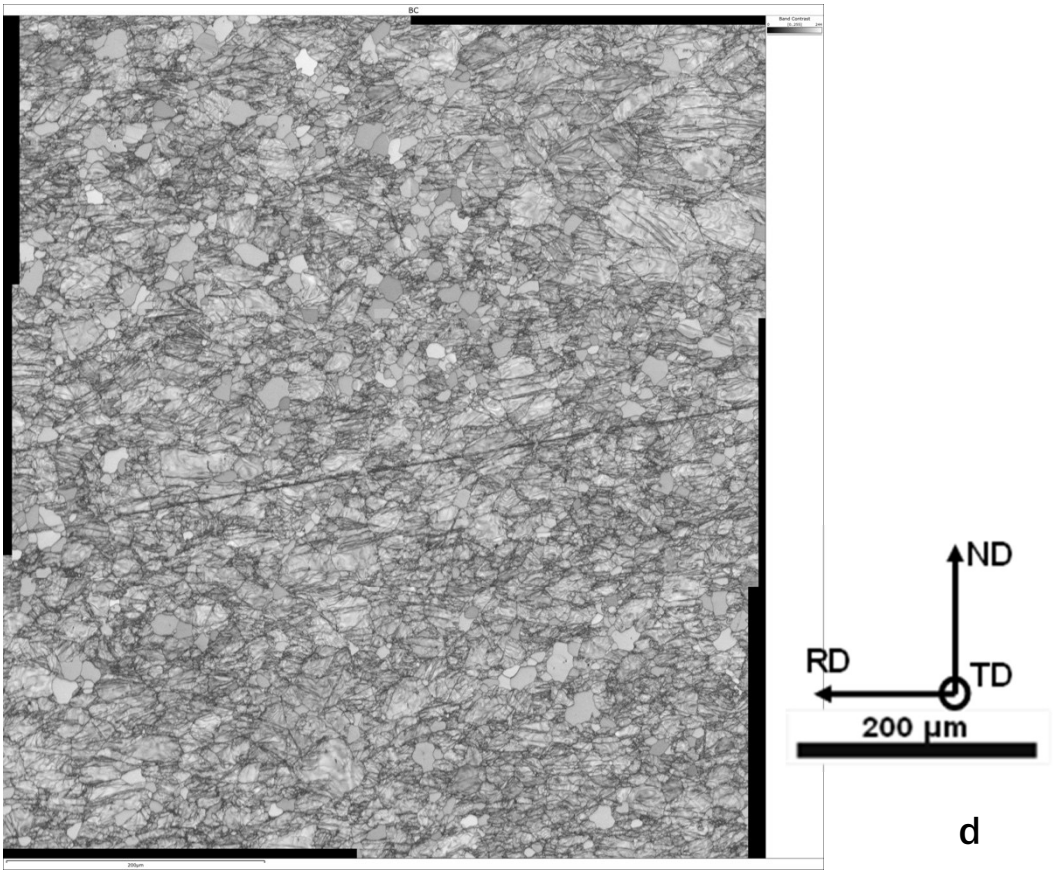
BC
ND
RD
TD
200 µm

d

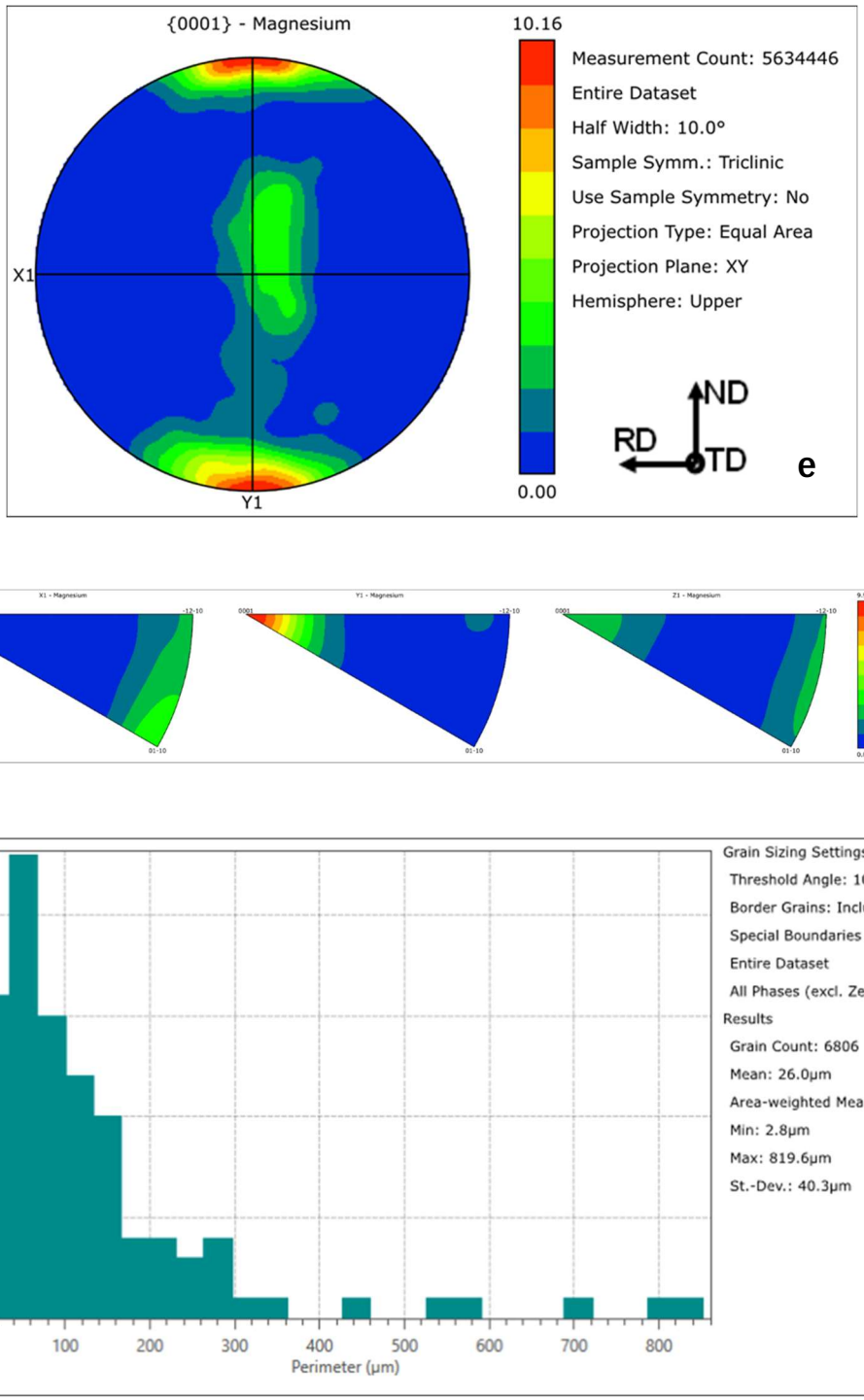

Figure 4-60 The EBSD result of the 75s annealed 1D compressed Mg-0.5Zn specimen: (a) The inverse pole figure map and grain boundaries, (b) The grain boundaries and the special grain boundaries, (c) The band contrast and the phase analysis, (d) The band contrast, (e) The pole figure, (f) The inverse pole figures, (g) Grain size distribution expressed as grain boundary perimeter

After an additional 15s anneal, resulting in a total annealing time of 135s, the microstructure of the specimen exhibited minor changes. The temperature of the

specimen at that time point was 139℃. Figure 4-61 shows the EBSD results of the specimen at that stage. The IPF map of the specimen (shown in Figure 4-61(a)) indicated that almost no change was observed in the morphology of the microstructure. The average grain size showed a decrease from $26\mu m$ to $25.4\mu m$ (shown in Figure 4-61(g)). A similar numerical fluctuation was also found in the boundary fraction of twins (shown in figure 4-61(b)), the boundary fraction of tensile twins, compressive twins and double twins was 43.7%, 1.1% and 1.8%, respectively. The differences of each value were lower than 1.0% compared to the 75s annealed specimen. Figure 4-61(b) also shows that the boundary fraction of the low-angle grain boundary and the high-angle grain boundary was 33.2% and 66.8%, respectively. Both values were only 0.1% different from the last step. Due to the rapid recrystallization (found after only 30s annealing process) in the specimen, the microstructure was expected to recrystallize in a very short time e.g. from 30s anneal (80℃) to 60s anneal (139℃) the evolution of the microstructure was expected to be continuous. However, the specimen at this stage did not show significant changes. The only evidence that the microstructure evolution did not stop was from the pole figure (shown in Figure 4-61(e)). Although the grain orientation distribution in the pole figure did not present any obvious difference, the maximum pole intensity showed a decrease from 10.2 to 9.9.

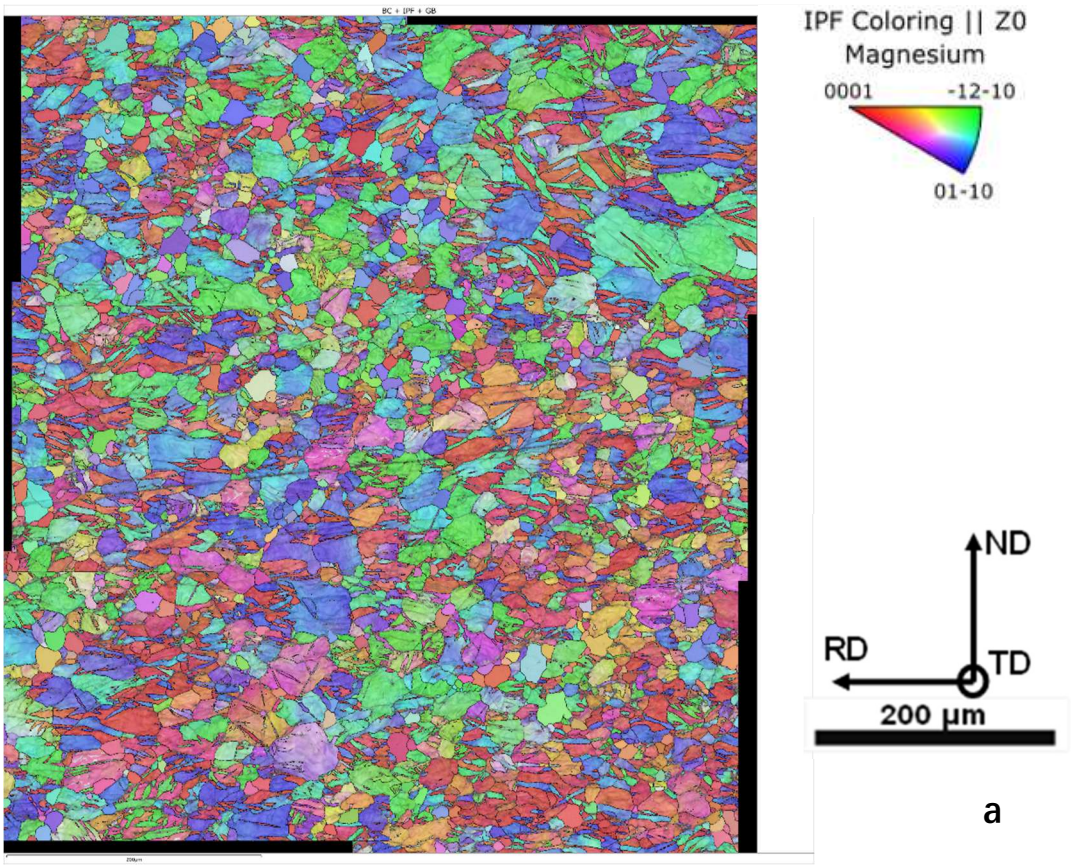

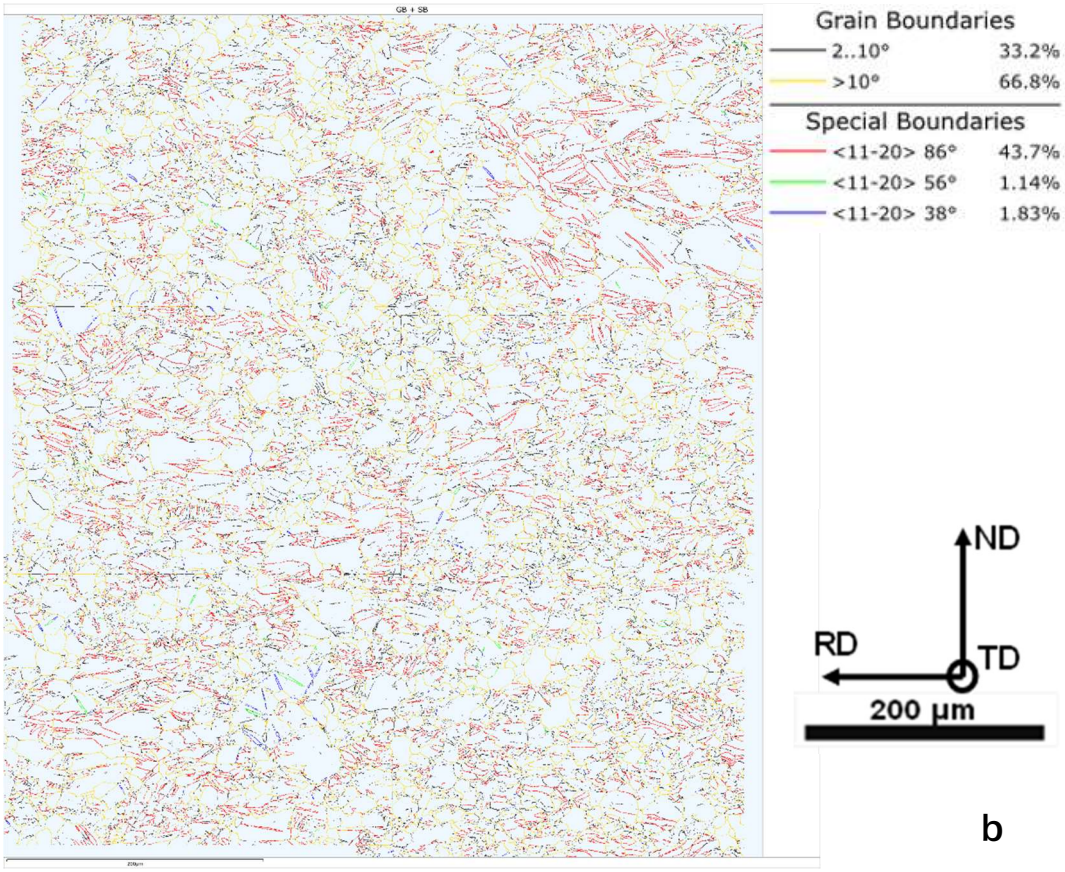
GB + SB
Grain Boundaries
2..10° 33.2%
>10° 66.8%
Special Boundaries
<11-20> 86° 43.7%
<11-20> 56° 1.14%
<11-20> 38° 1.83%
ND
RD
TD
200 µm

b

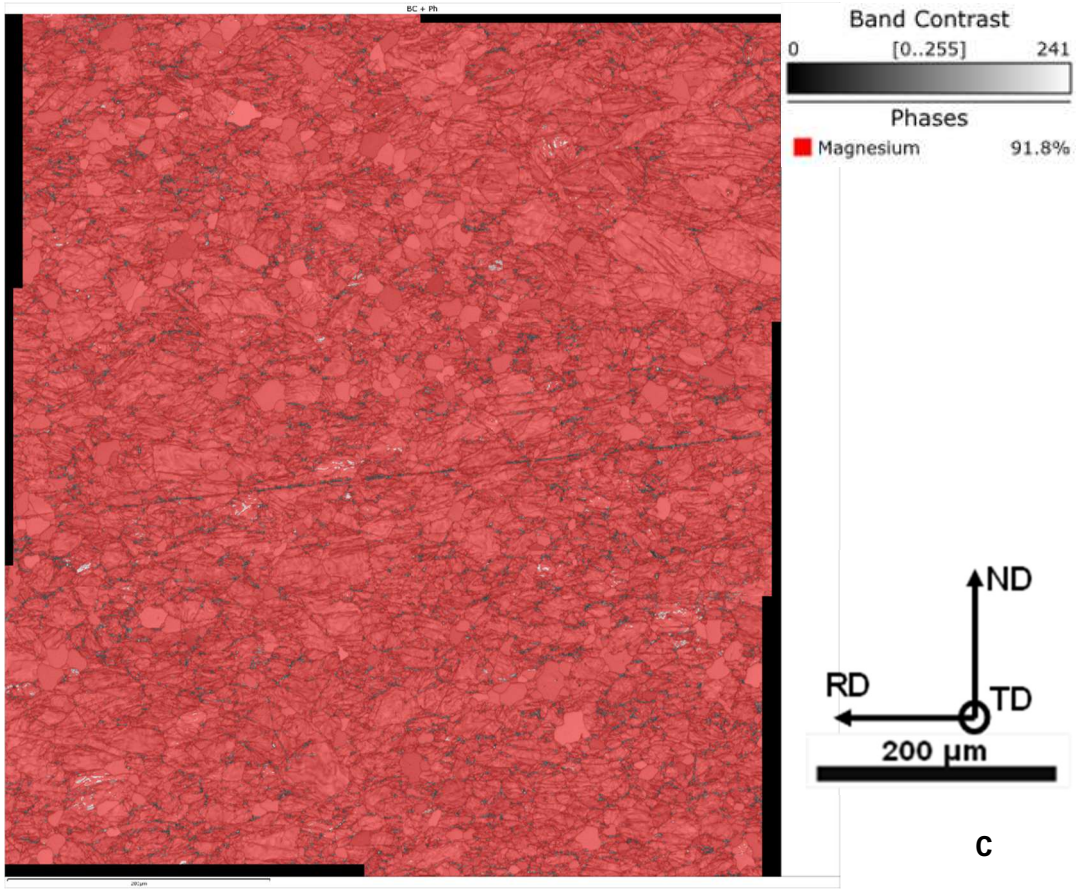
BC + Ph
Band Contrast
0 [0..255] 241
Phases
Magnesium 91.8%
ND
RD
TD
200 µm

c

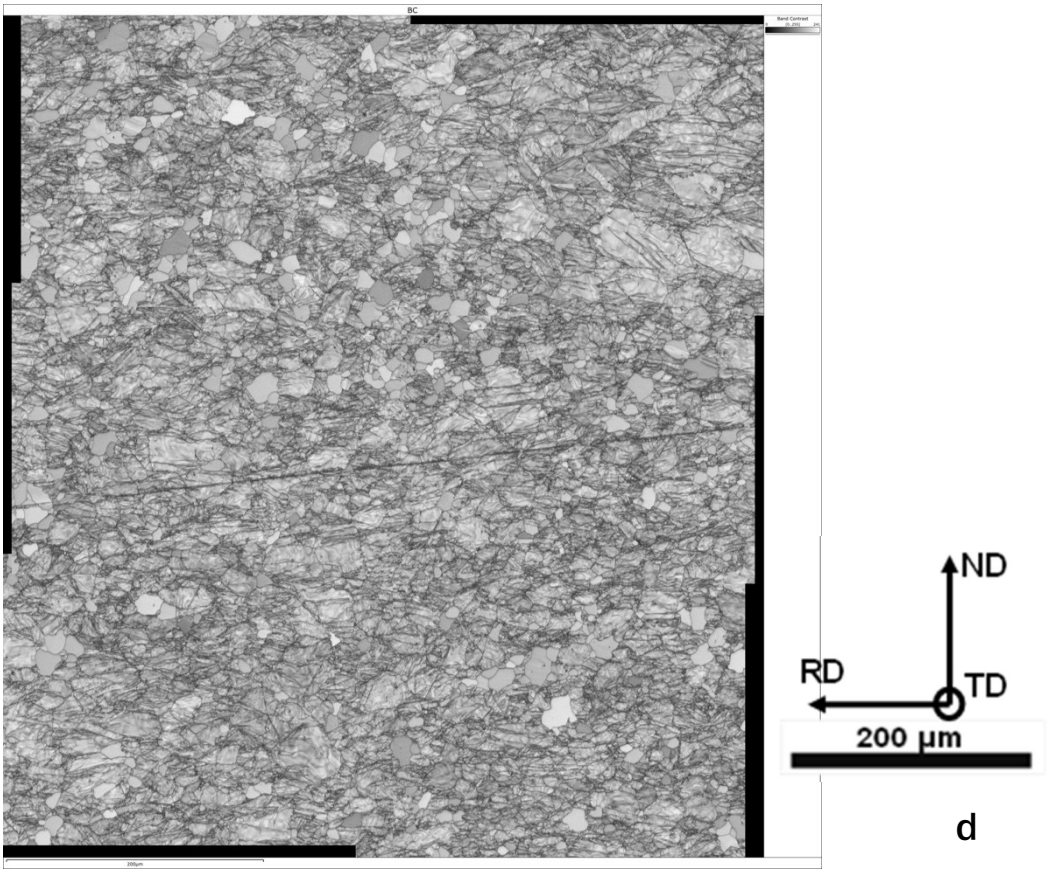
BC
ND
RD
TD
200 µm

d

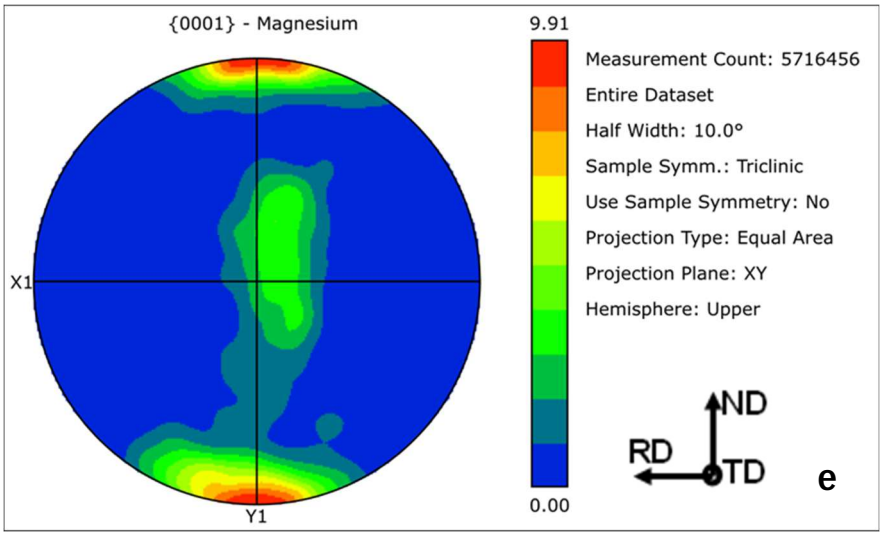
{0001} - Magnesium
9.91
0.00
X1
Y1
Measurement Count: 5716456
Entire Dataset
Half Width: 10.0°
Sample Symm.: Triclinic
Use Sample Symmetry: No
Projection Type: Equal Area
Projection Plane: XY
Hemisphere: Upper
ND
RD
TD

e

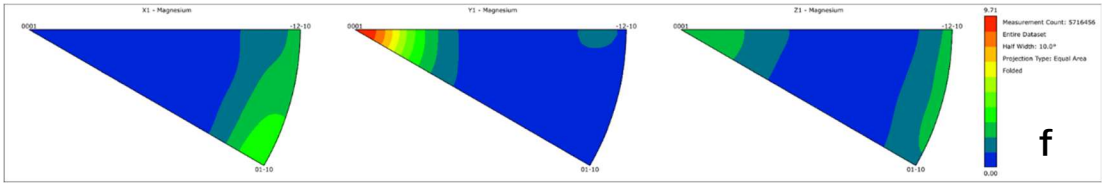
X1 - Magnesium
Y1 - Magnesium
Z1 - Magnesium
0001
-12-10
01-10
9.71
0.00
Measurement Count: 5716456
Entire Dataset
Half Width: 10.0°
Projection Type: Equal Area
Folded

f

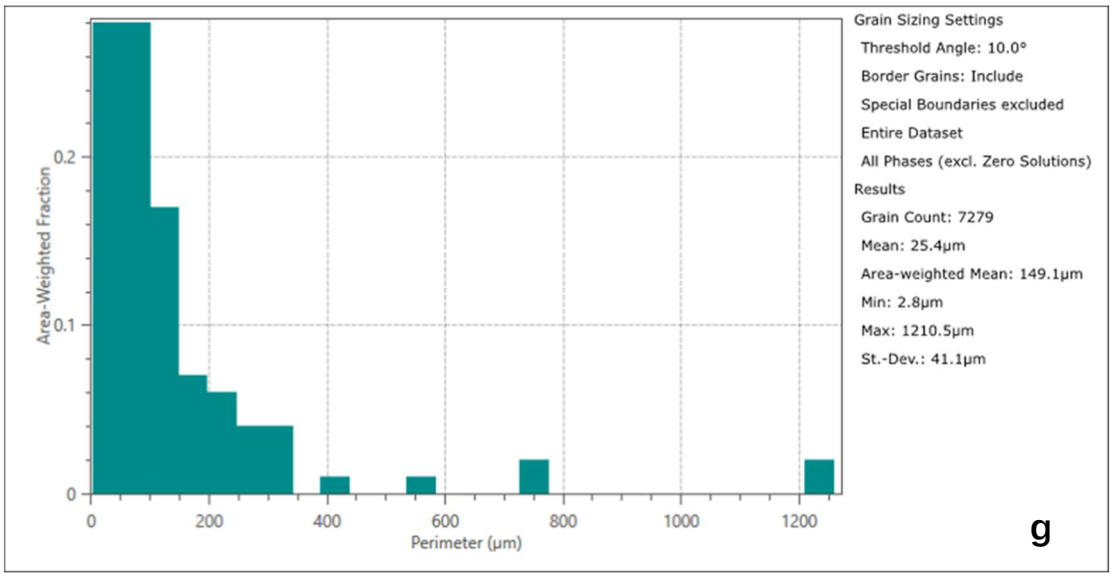

Figure 4-61 The EBSD result of the 135s annealed 1D compressed Mg-0.5Zn specimen: (a) The inverse pole figure map and grain boundaries, (b) The grain boundaries and the special grain boundaries, (c) The band contrast and the phase analysis, (d) The band contrast, (e) The pole figure, (f) The inverse pole figures, (g) Grain size distribution expressed as grain boundary perimeter

Figure 4-62 shows the EBSD results of the same specimen after annealing for 210s. The highest temperature of the specimen during this stage was 165℃. The IPF map (shown in Figure 4-62(a)) indicated that the 15s increase in the annealing time (highest temperature from 139℃ to 165℃) did not bring any obvious difference to the microstructure. The grain growth of the recrystallized grains was very limited and only a few nucleated grains was observed. The slightly increase in average grain size (from 25.4μm to 25.5μm) was probably not statistically significant, showing the limited variation of the microstructure (shown in Figure 4-62(g)). Comparing the average grain size to that of the 75s annealed specimen, the average grain size was the same. Figure 4-62(b) indicates the minor change of the boundary fraction under the slow progress of the recrystallization. The boundary fraction of the tensile twins, compressive twins and double twins was changed from 43.7% to 43.6%, 1.1% to 1.4% and 1.8% to 1.9%, respectively. Meanwhile, the fraction of the low-angle grain boundary and the high-angle grain boundary was changed from 33.2% to 28.2% and from 66.8% to 71.8%, respectively. Compared to the stable value of the twin boundary fractions, the 5.0% changes in the fraction of the low-angle grain boundary and the high-angle grain boundary were much more obvious. The reason for this was attributed to the reduction of the miss-identification of the scanning frame edges. Less scanning frame edges were identified as the low-angle grain boundaries caused the decrease of the fraction of the

low-angle grain boundary. On the other hand, due to the slow recrystallization progress, no dramatic changes were observed in the pole figure and IPF (shown in Figure 4-62(e) and (f)). The maximum pole intensity did not decrease too much which was from 9.9 to 9.7 (only 0.2 in difference). Meanwhile, only a little difference of the grain orientation distribution was found in the pole figure. The signal of the grain orientations which was close to the TD was found enhanced. The pole intensity of this area increased from 4.5 to 4.7, which means the new grains which had an orientation similar to the TD were increased.

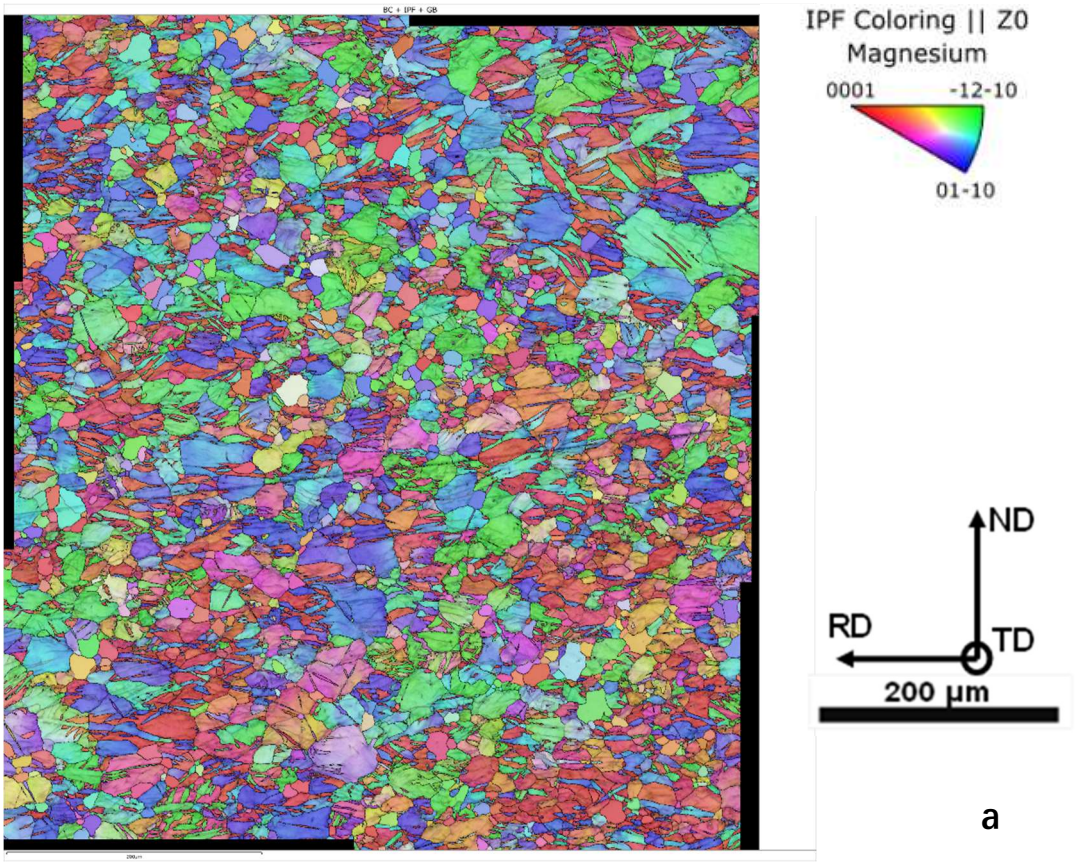

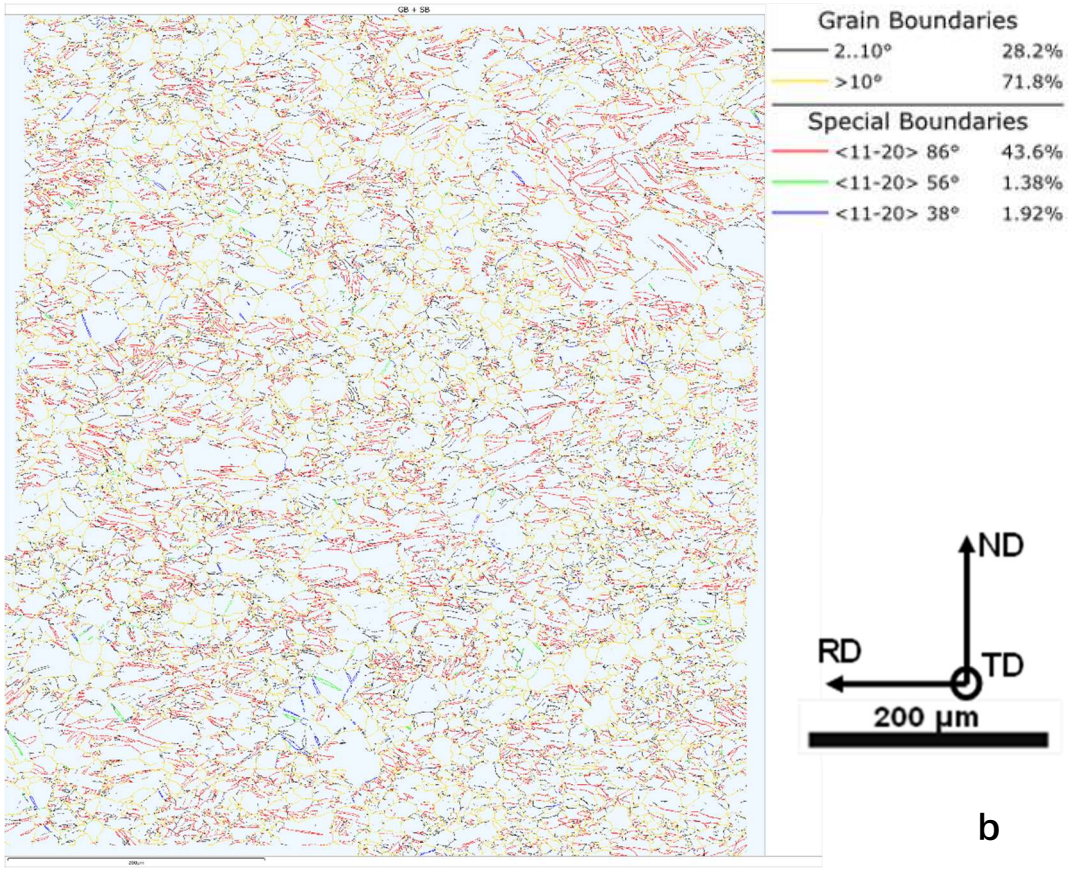
GB + SB
Grain Boundaries
2..10° 28.2%
>10° 71.8%
Special Boundaries
<11-20> 86° 43.6%
<11-20> 56° 1.38%
<11-20> 38° 1.92%
ND
RD
TD
200 µm

b

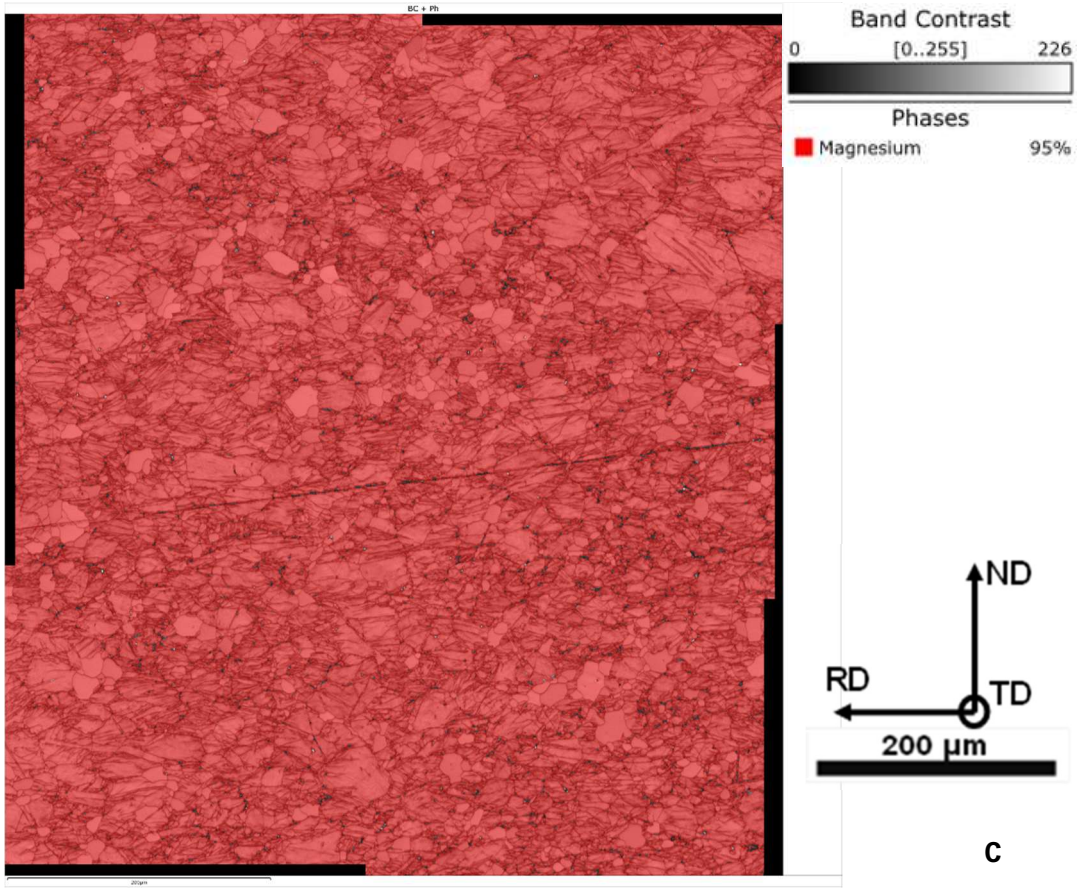
BC + Ph
Band Contrast
0 [0..255] 226
Phases
Magnesium 95%
ND
RD
TD
200 µm

c

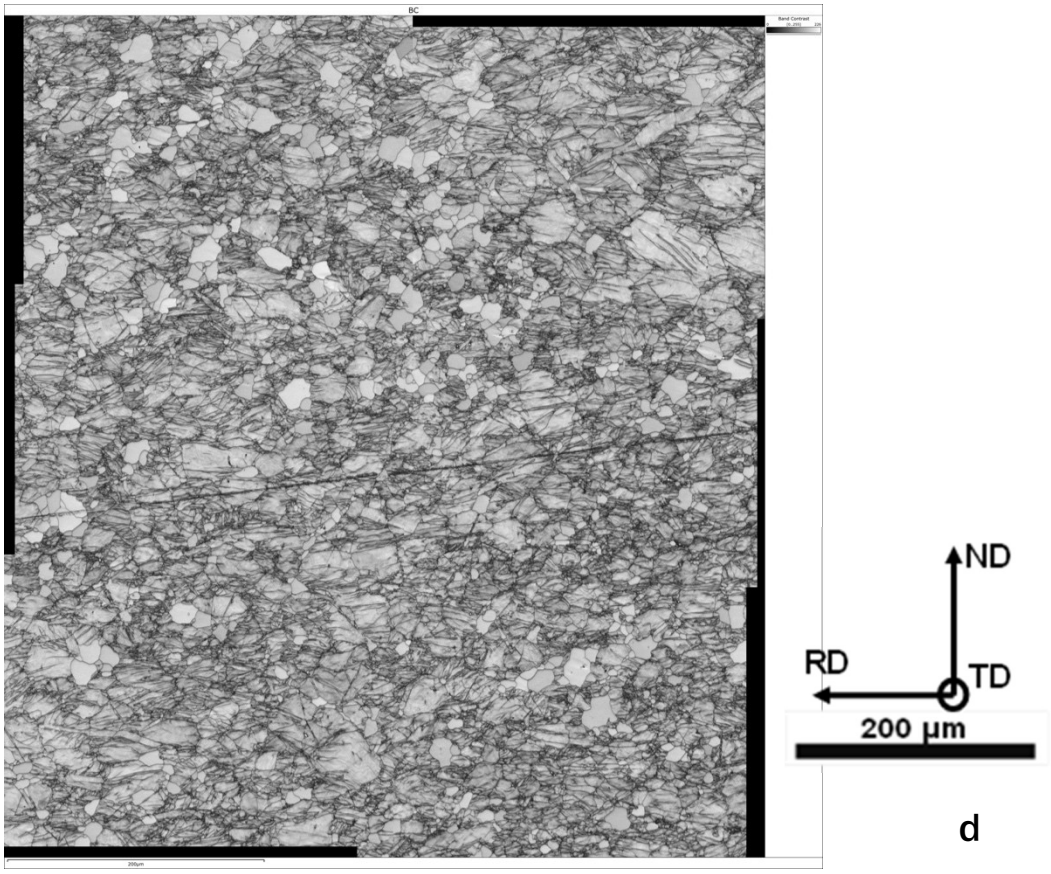
ND
RD
TD
200 µm

d

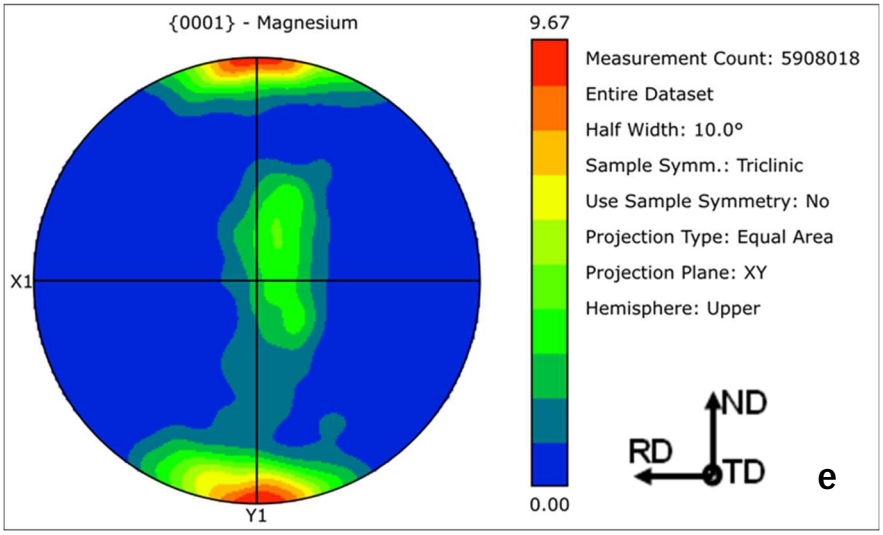
{0001} - Magnesium
9.67
0.00
X1
Y1
Measurement Count: 5908018
Entire Dataset
Half Width: 10.0°
Sample Symm.: Triclinic
Use Sample Symmetry: No
Projection Type: Equal Area
Projection Plane: XY
Hemisphere: Upper
ND
RD
TD

e

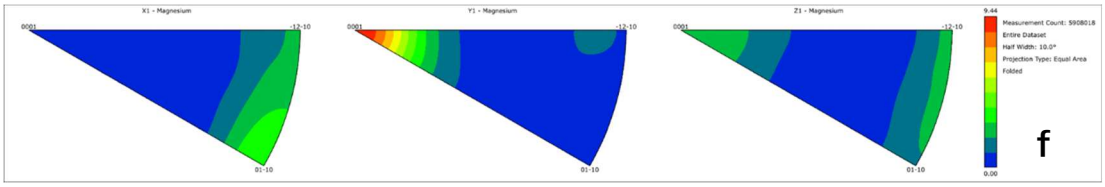

f

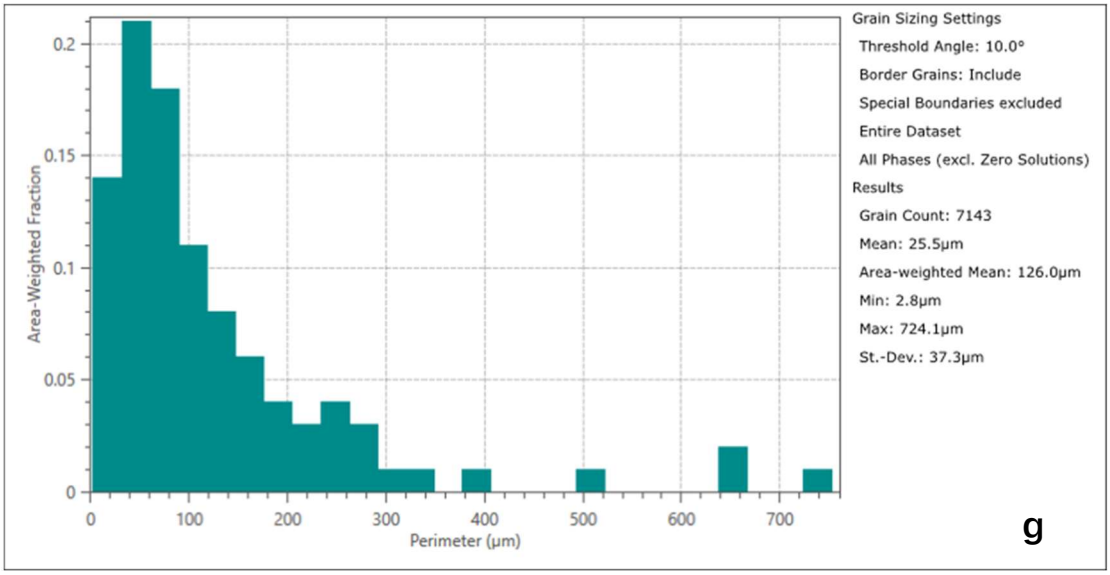

Figure 4-62 The EBSD result of the 210s annealed 1D compressed Mg-0.5Zn specimen: (a) The inverse pole figure map and grain boundaries, (b) The grain boundaries and the special grain boundaries, (c) The band contrast and the phase analysis, (d) The band contrast, (e) The pole figure, (f) The inverse pole figures, (g) Grain size distribution expressed as grain boundary perimeter

When the annealing process time of the sample increased another 15s i.e. a further 300s anneal, the progress in recrystallization was still slow. The temperature of the sample before the water quench was 186℃. Figure 4-63 shows the EBSD results of the specimen. The IPF map (shown in Figure 4-63(a)) indicated that the microstructure of the sample almost showed no change in morphology. Moreover, the index rate of the sample in this round of EBSD scanning was a little bit lower than before. Thus, the quality of the map was not as good as that of the 310s annealed specimen. The fraction of the phase identification of the Mg also showed this (shown in Figure 4-63(c)), which was reduced from 95.0% to 92.2%. The surface oxidation was the reason for this reduction. Although the quality of the image was lower than in the last step, the non-indexed areas were mainly shown within the grains i.e. the information of the grain boundaries was not affected. The boundary fractions of the twins also proved minor changes of the microstructure. Figure 4-63(b) indicates that the boundary fraction of the tensile twins, compressive twins and double twins at this stage was 43.5%, 1.19% and 1.75%, respectively. The difference in the boundary fraction of three kinds of twins to the last stage was 0.00%, 0.19% and 0.17%, respectively. However, a quite obvious change was in the fraction of the low-angle grain boundary and the high-angle grain boundary were found (from 28.2% to 33.0% and from 71.8% to 67.0%, respectively). The miss-identification of the scanning frame edge (identified as the low-angle grain

boundaries) was considered responsible for these changes. Based on this information, it was clear that no recrystallization had occurred in the twins at this stage. And the average grain size of the specimen decreased compared to the last stage which was from 25.5μm to 24.7μm (shown in Figure 4-63(g)). The average grain size was the same value as the 135s annealed specimen. On the other hand, for the same reason (less identified area), the maximum pole intensity did not decrease as in other samples but increased a little bit from 9.7 to 10 (shown in Figure 4-63(e)). Meanwhile, only very small changes of the grain orientation distribution were found in the pole figure. The grains with a TD-like orientation were found increasing (marked by black circles).

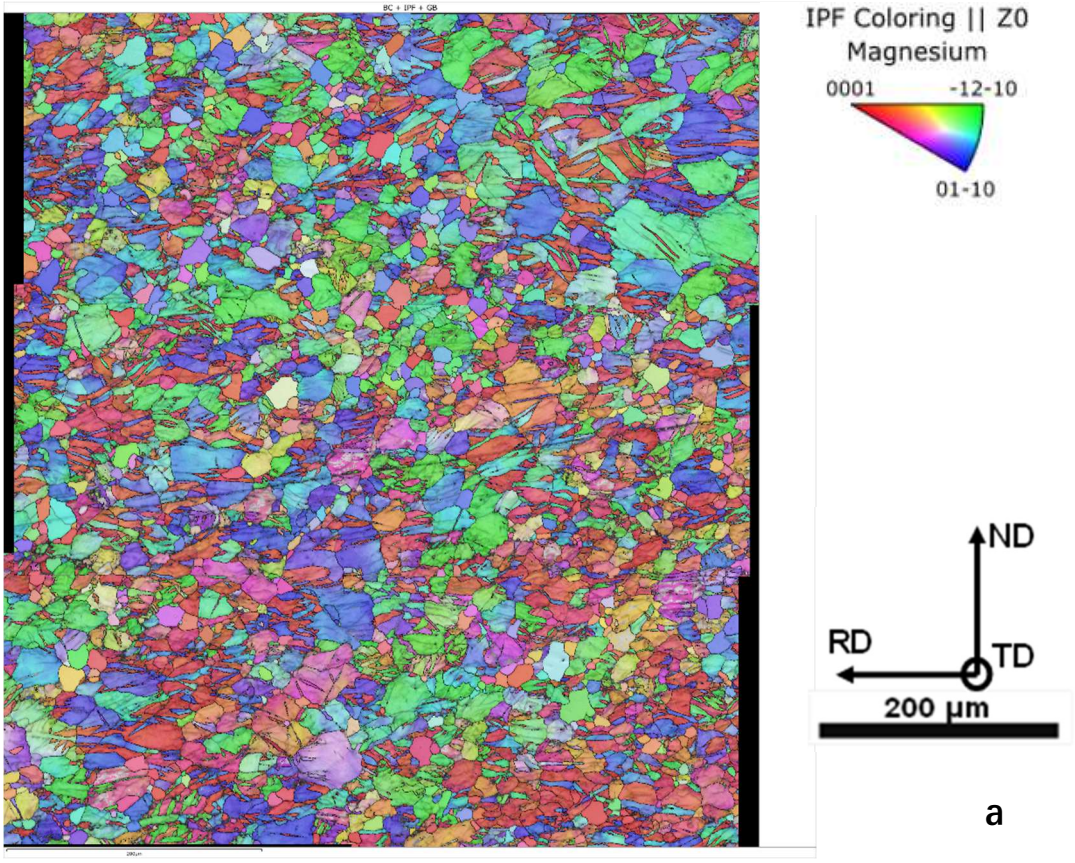

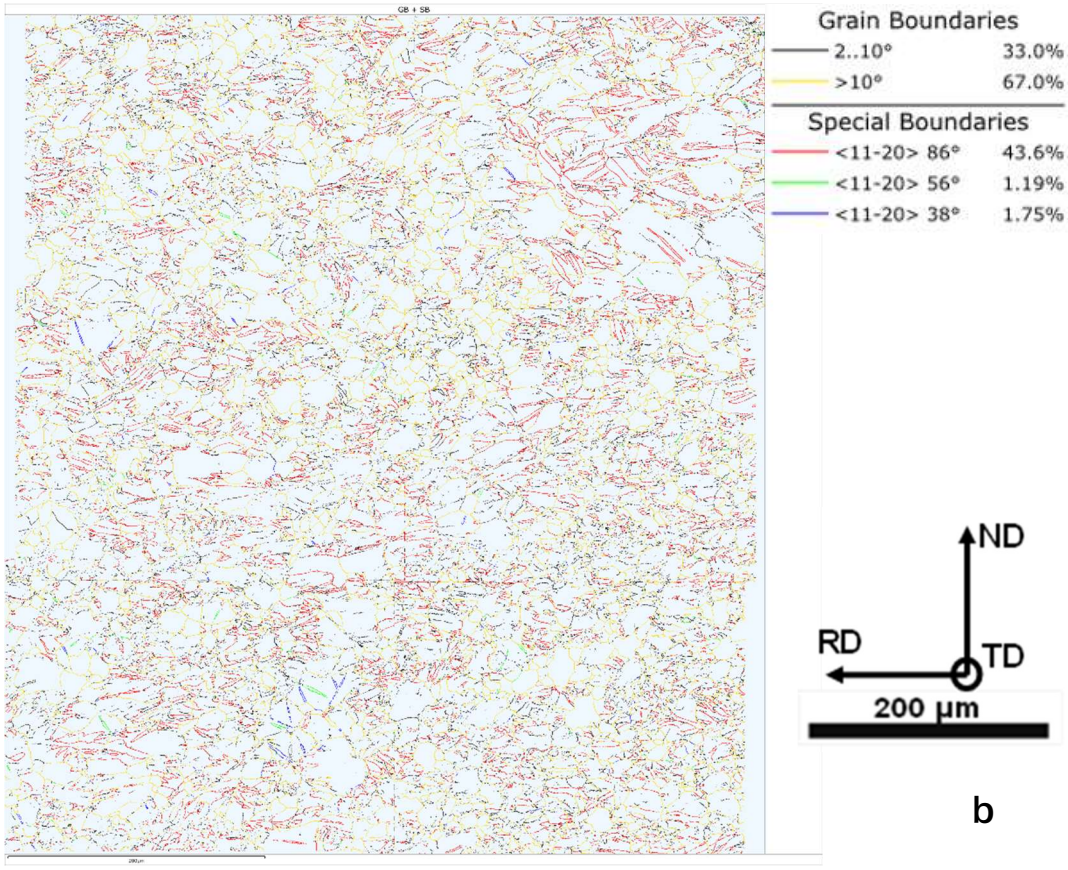
GB + SB
Grain Boundaries
2..10° 33.0%
>10° 67.0%
Special Boundaries
<11-20> 86° 43.6%
<11-20> 56° 1.19%
<11-20> 38° 1.75%
ND
RD
TD
200 µm

b

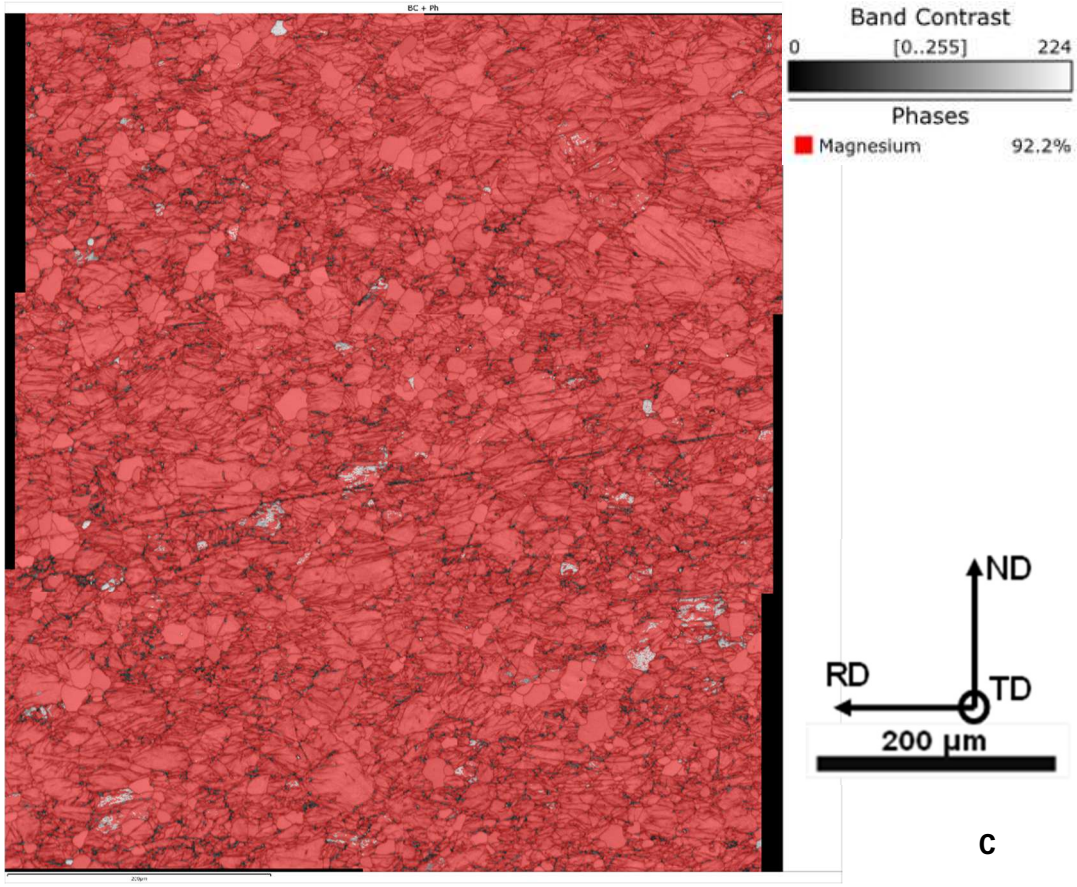
BC + Ph
Band Contrast
0 [0..255] 224
Phases
Magnesium 92.2%
ND
RD
TD
200 µm

c

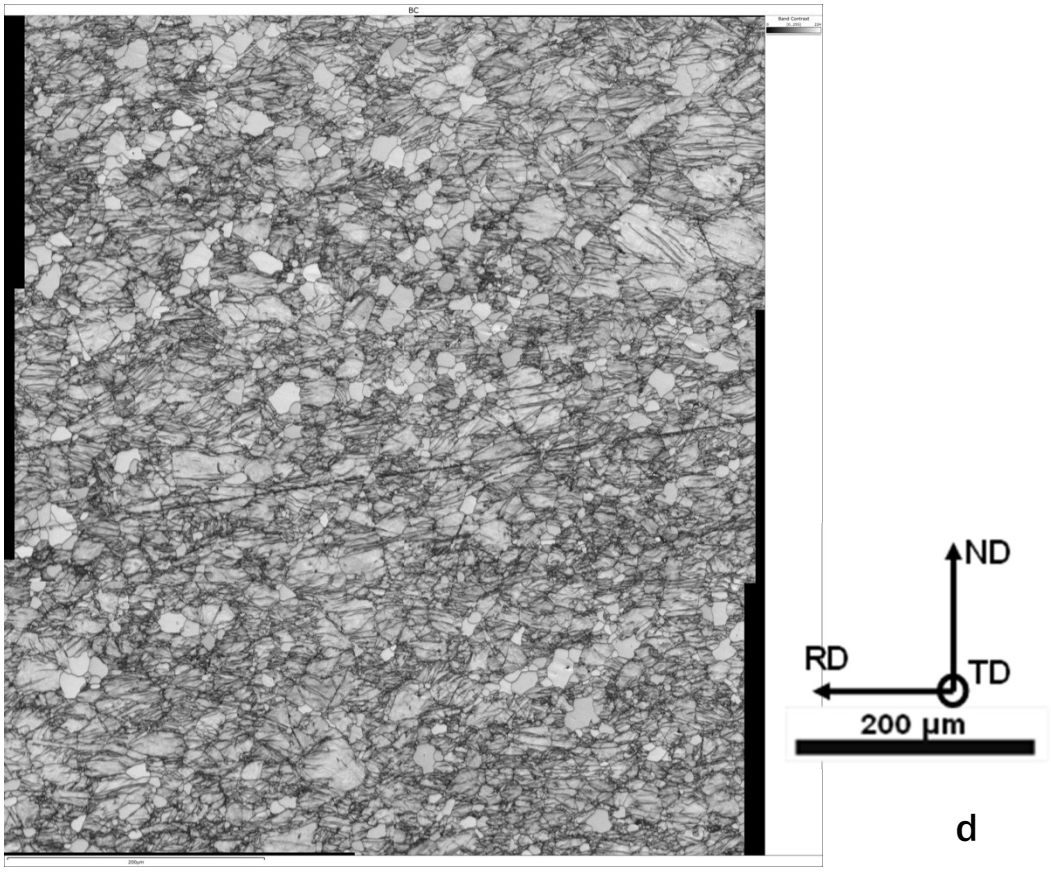
ND
RD
TD
200 µm

d

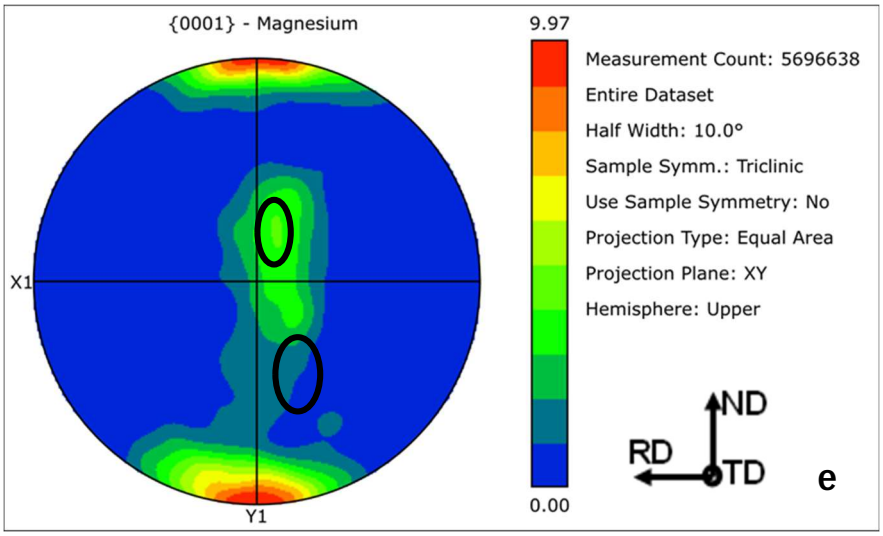
{0001} - Magnesium
9.97
0.00
X1
Y1
Measurement Count: 5696638
Entire Dataset
Half Width: 10.0°
Sample Symm.: Triclinic
Use Sample Symmetry: No
Projection Type: Equal Area
Projection Plane: XY
Hemisphere: Upper
ND
RD
TD

e

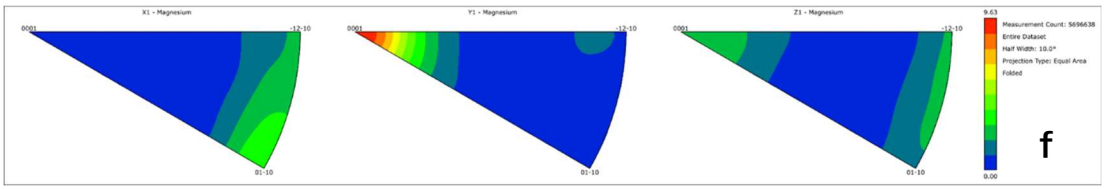

f

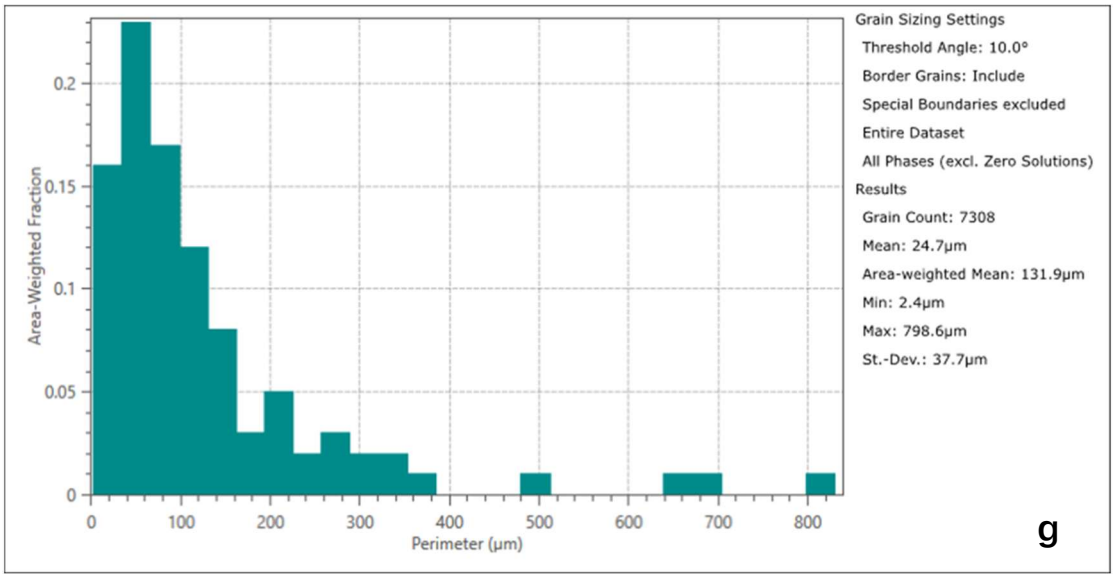

Figure 4-63 The EBSD result of the 300s annealed 1D compressed Mg-0.5Zn specimen: (a) The inverse pole figure map and grain boundaries, (b) The grain boundaries and the special grain boundaries, (c) The band contrast and the phase analysis, (d) The band contrast, (e) The pole figure, (f) The inverse pole figures, (g) Grain size distribution expressed as grain boundary perimeter

Figure 4-64 shows the EBSD results of the same specimen after annealing for 420s. The highest temperature of the specimen during this stage was 212℃. The IPF map (shown in Figure 4-64(a)) indicated that the 30s increase of the annealing time (highest temperature from 186℃ to 212℃) still did not bring any obvious difference to the microstructure. The grain growth of the recrystallized grains was very limited, and no nucleation of grains was observed. The almost unchanged average grain size ($24.8\mu m$) at this stage also reflected the limited variation of the microstructure (shown in Figure 4-64(g)). Figure 4-64(b) indicates the minor change of the boundary fraction, the boundary fraction of the tensile twins, compressive twins and double twins were all found to show no statistical difference from 43.6% to 43.7%, 1.2% to 1.3% and 1.8% to 1.9%, respectively. Meanwhile, the fraction of the low-angle grain boundary and the high-angle grain boundary was changed from 33.0% to 31.7% and from 67.0% to 68.3%, respectively. The increase of the boundary fraction of all three kinds of twins was never observed with the recrystallization progress. The reason for this was attributed to the extra scanned area which was included during this round of EBSD investigation. The extra scanned area at the bottom of the EBSD map (marked with black rectangle in Figure 4-64(a)) showed a reasonable number of tensile twins, compressive twins and double twins, which caused the increase in the value of the corresponding boundary fraction. Additionally, with the change in the boundary

fraction of the twins, the changes in the boundary fraction of the low-angle grain boundary and the high-angle grain boundary were very typical. The grain growth and the nucleation of the recrystallized grains did cause the increase of the high-angle grain boundary and the decrease of the low-angle grain boundaries. On the other hand, due to the slow recrystallization progress, the maximum pole intensity did not decrease too much which was from 10 to 9.8 (shown in Figure 4-64(e)). Also, it was very hard to find the obvious difference of the grain orientation distribution between the two steps in the pole figure and IPF. The only notable point was that due to the extra area was scanned in this stage, the information from the pole figure could show some abnormal changes when compared to the pole figure of the next stage.

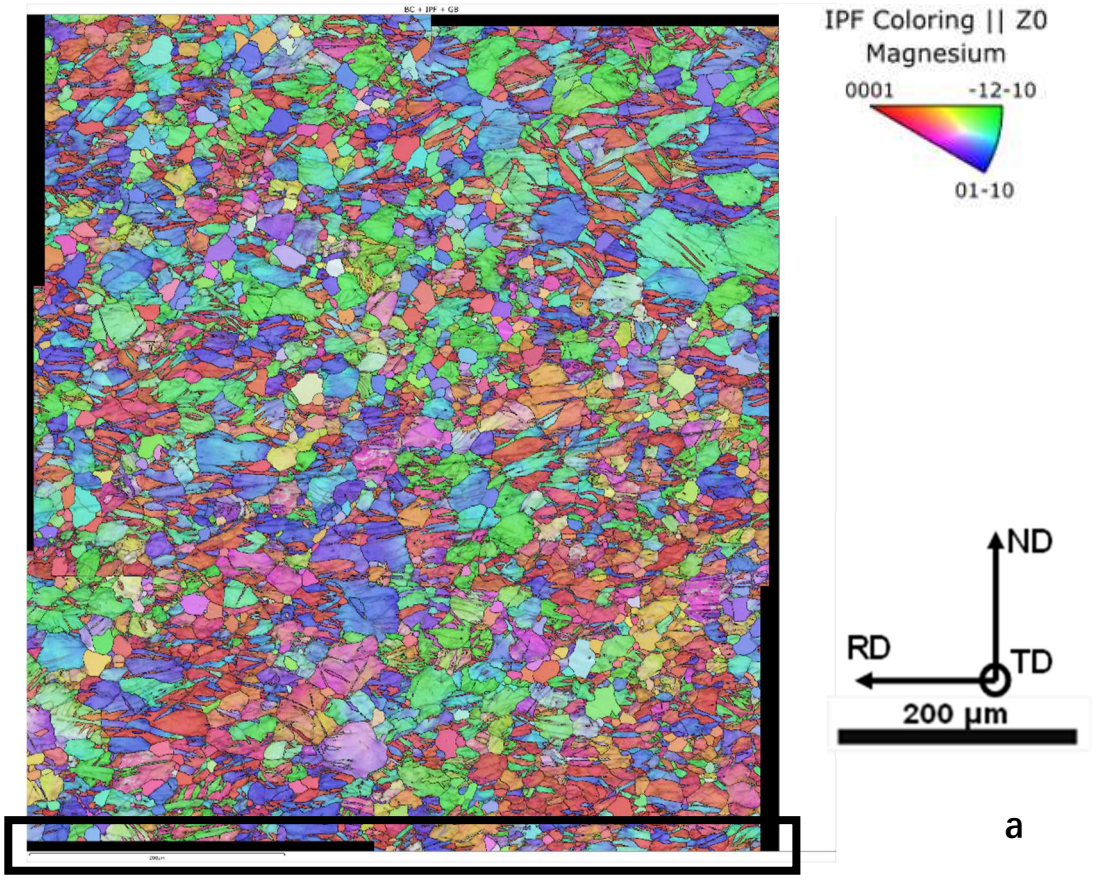

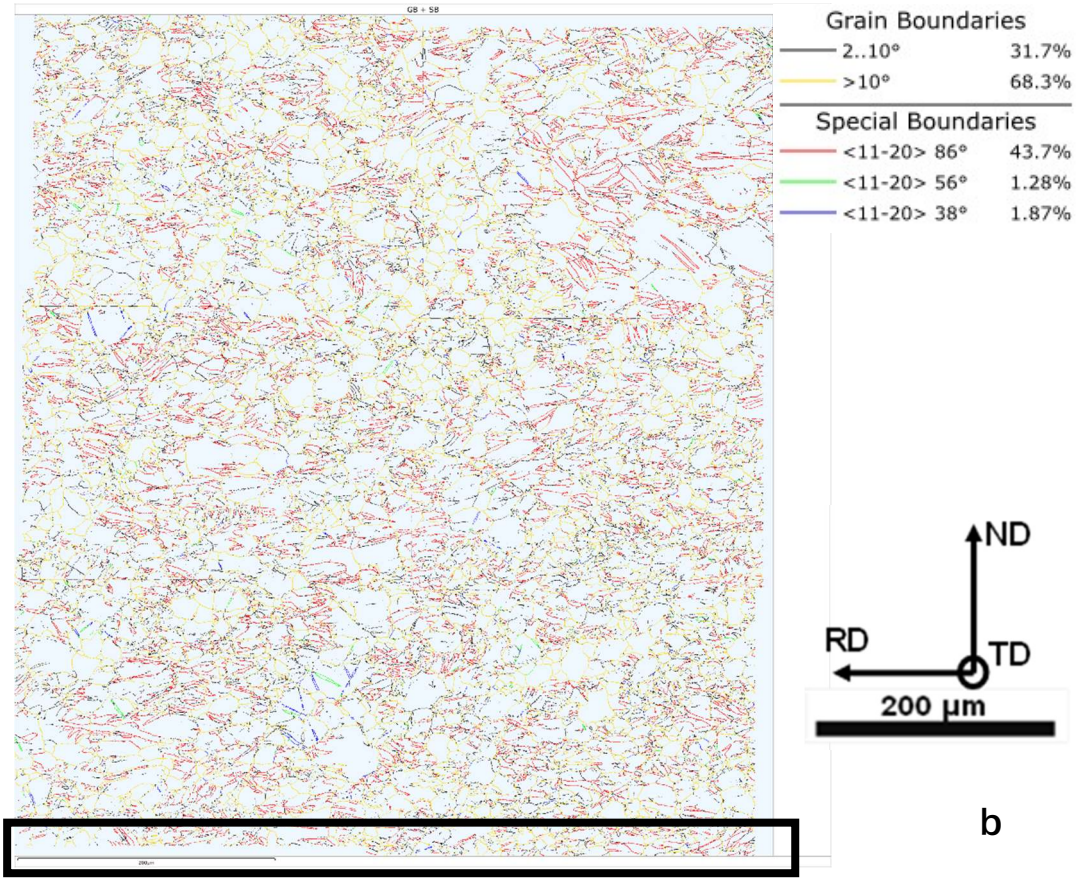
GB + SB
Grain Boundaries
2..10° 31.7%
>10° 68.3%
Special Boundaries
<11-20> 86° 43.7%
<11-20> 56° 1.28%
<11-20> 38° 1.87%
ND
RD
TD
200 µm

b

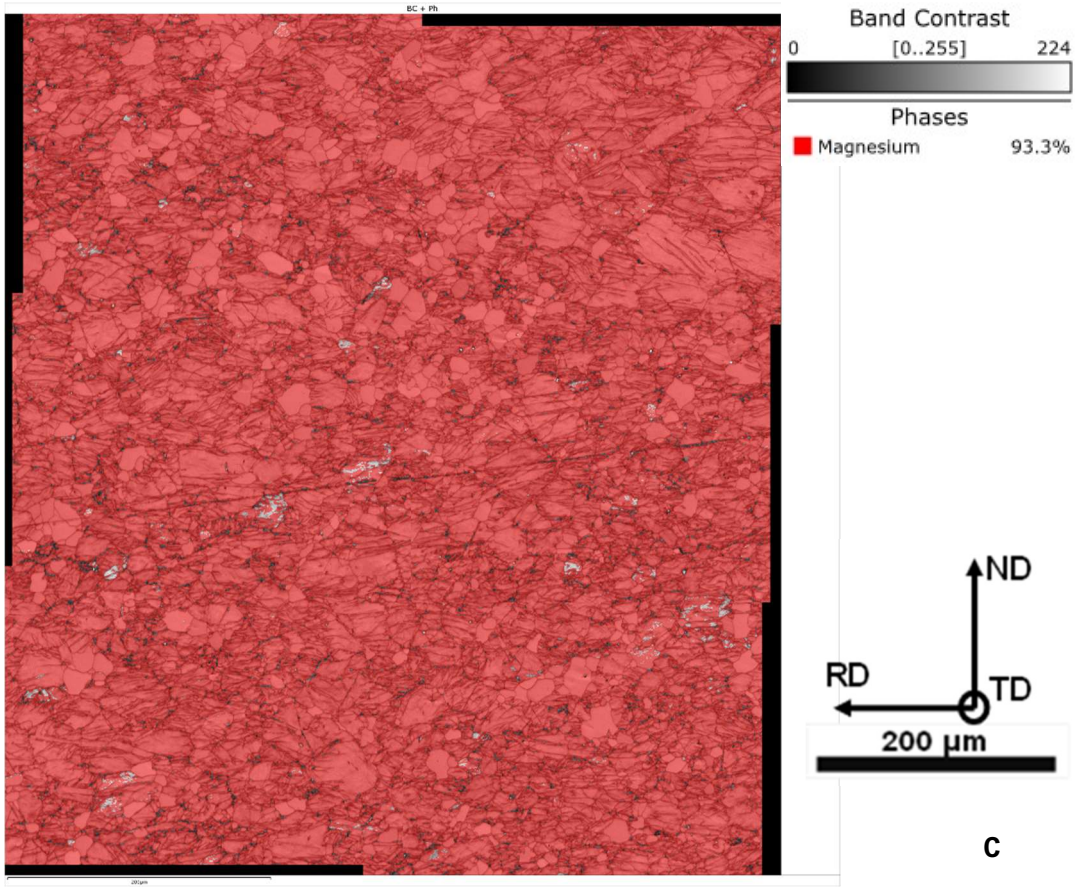
BC + Ph
Band Contrast
0 [0..255] 224
Phases
Magnesium 93.3%
ND
RD
TD
200 µm

c

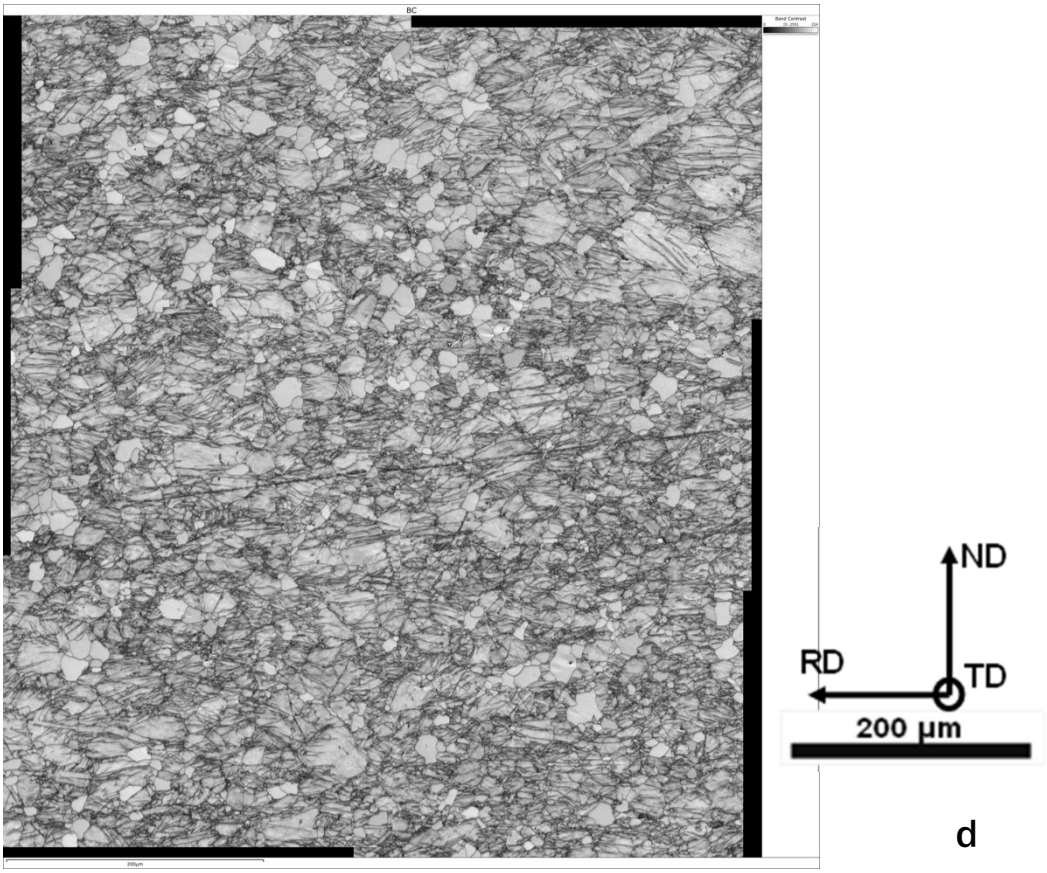
BC
ND
RD
TD
200 µm

d

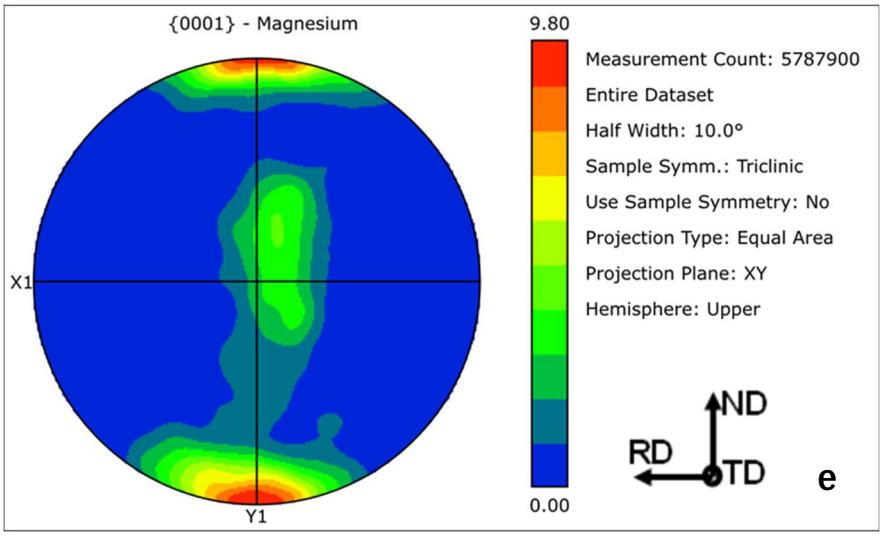
{0001} - Magnesium
X1
Y1
9.80
0.00
Measurement Count: 5787900
Entire Dataset
Half Width: 10.0°
Sample Symm.: Triclinic
Use Sample Symmetry: No
Projection Type: Equal Area
Projection Plane: XY
Hemisphere: Upper
ND
RD
TD

e

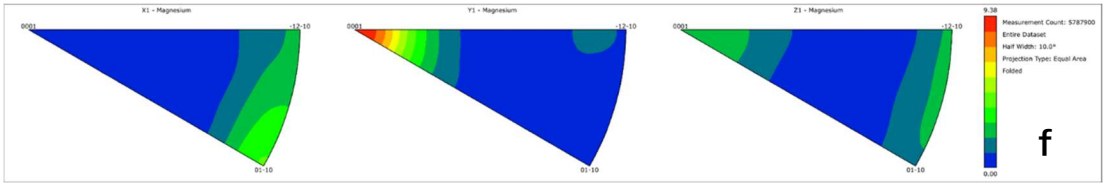
X1 - Magnesium
Y1 - Magnesium
Z1 - Magnesium
Measurement Count: 5787900
Entire Dataset
Half Width: 10.0°
Projection Type: Equal Area
Folded

f

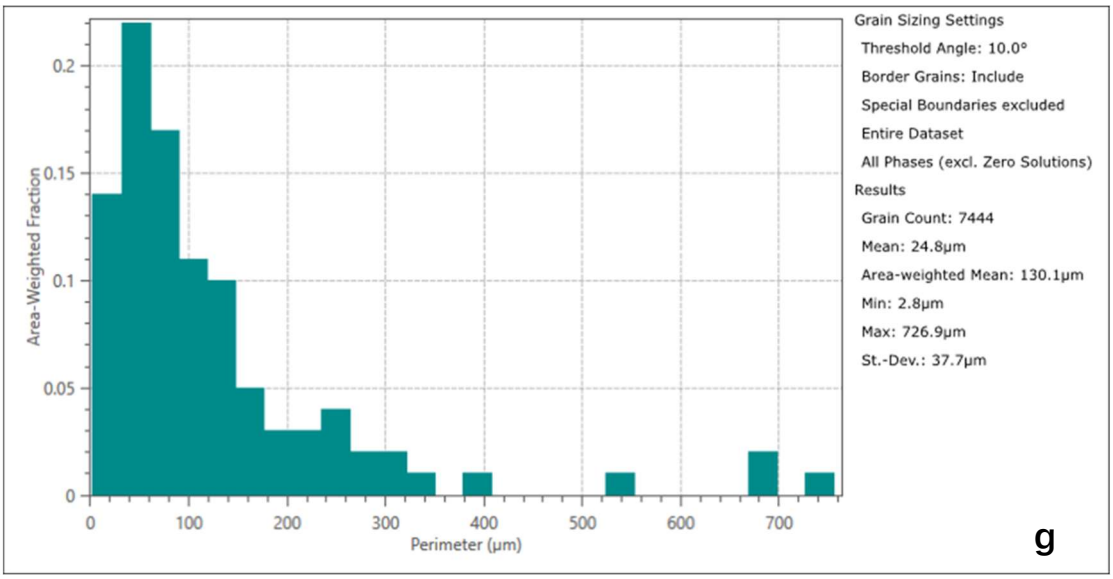

Figure 4-64 The EBSD result of the 420s annealed 1D compressed Mg-0.5Zn specimen: (a) The inverse pole figure map and grain boundaries, (b) The grain boundaries and the special grain boundaries, (c) The band contrast and the phase analysis, (d) The band contrast, (e) The pole figure, (f) The inverse pole figures, (g) Grain size distribution expressed as grain boundary perimeter

After annealing for another 30s i.e. a 570s total annealing time, the microstructure presented further changes about recrystallization. The temperature of the specimen at that time point was 240℃. Figure 4-65 shows the EBSD results of the specimen at that stage. The IPF map of the specimen (shown in Figure 4-65(a)) indicated the obvious grain growth (about 1-5μm growth in size) of the recrystallized grains and the grain nucleation across the whole scanning area. The new recrystallized grains were mainly found nucleated on the grain boundaries rather than twins. The fraction value of the twin boundaries also showed that the twins were not yet involved in the recrystallization. Figure 4-65(b) shows the boundary fraction of the tensile twins, compressive twins and double twins which were 41.8%, 1.3% and 1.8%, respectively. Compared to the 120s annealed sample, the difference of three kinds of twin boundary fraction was only 1.9%, 0.01% and 0.07%, respectively. Moreover, the decrease of the low-angle grain boundary fraction (from 31.7% to 31.0%) and the increase of the high-angle grain boundary fraction (from 68.3% to 69.0%) also showed that recrystallization occurred but not to a very large scale at that time point. The average grain size at this stage slightly increased which was from 24.8μm to 25μm (shown in Figure 4-65(g)). Compared to the pole figure and IPF of the last stage, the pole figures of the 570s annealed specimen (shown in Figure 4-65(e) and (f)) showed no obvious difference in

the grain orientation distribution. However, the maximum value of the pole figure only increased by 0.1 to 9.9 at this stage. For the same reason mentioned for the 420s annealed specimen, the increase of the maximum pole intensity between these two stages was not statistically significant. When comparing the maximum pole intensity of the sample annealed for 300 seconds to that of this stage, the reduction from 10 to 9.9 was also not statistically significant.

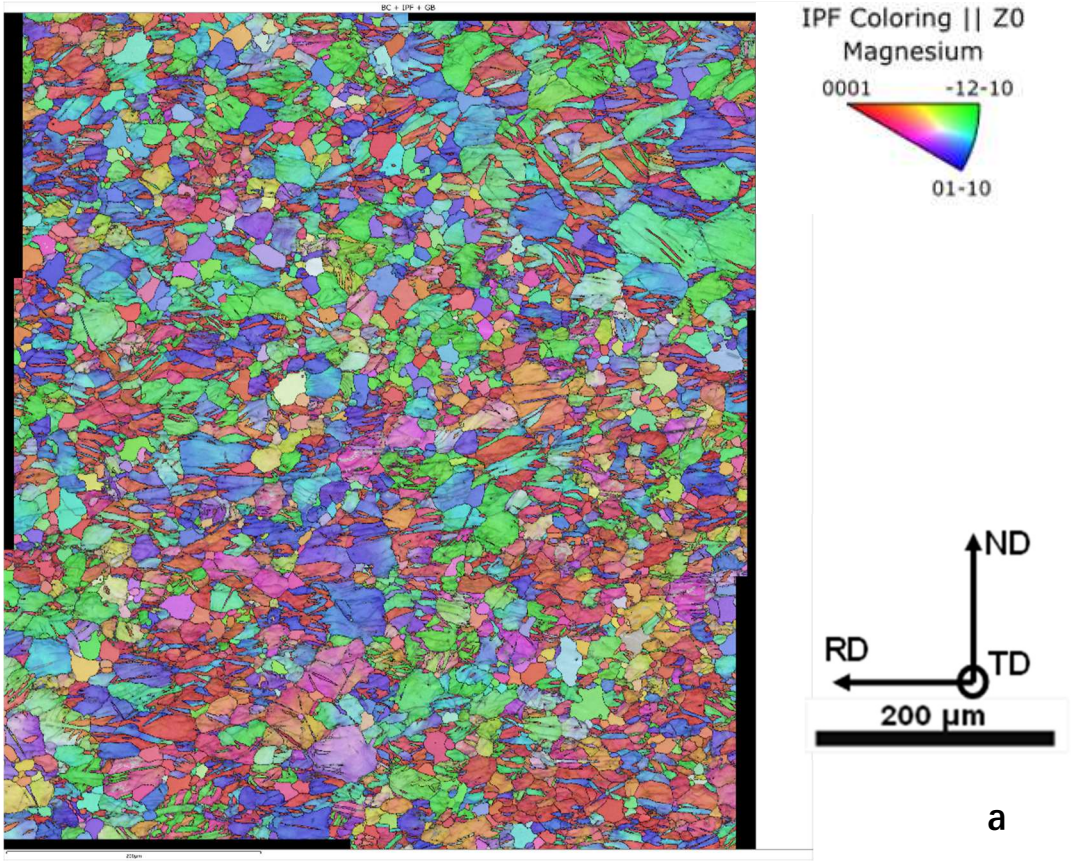

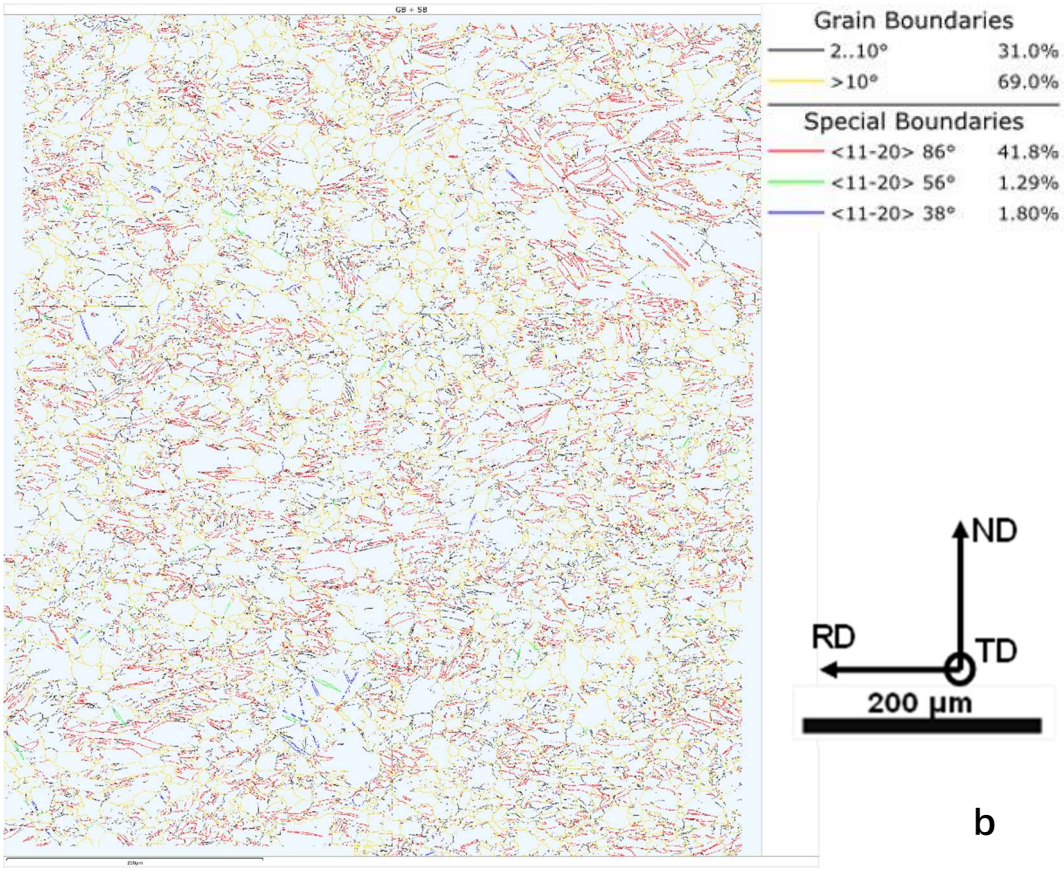
GB + SB
Grain Boundaries
2..10° 31.0%
>10° 69.0%
Special Boundaries
<11-20> 86° 41.8%
<11-20> 56° 1.29%
<11-20> 38° 1.80%
ND
RD
TD
200 µm

b

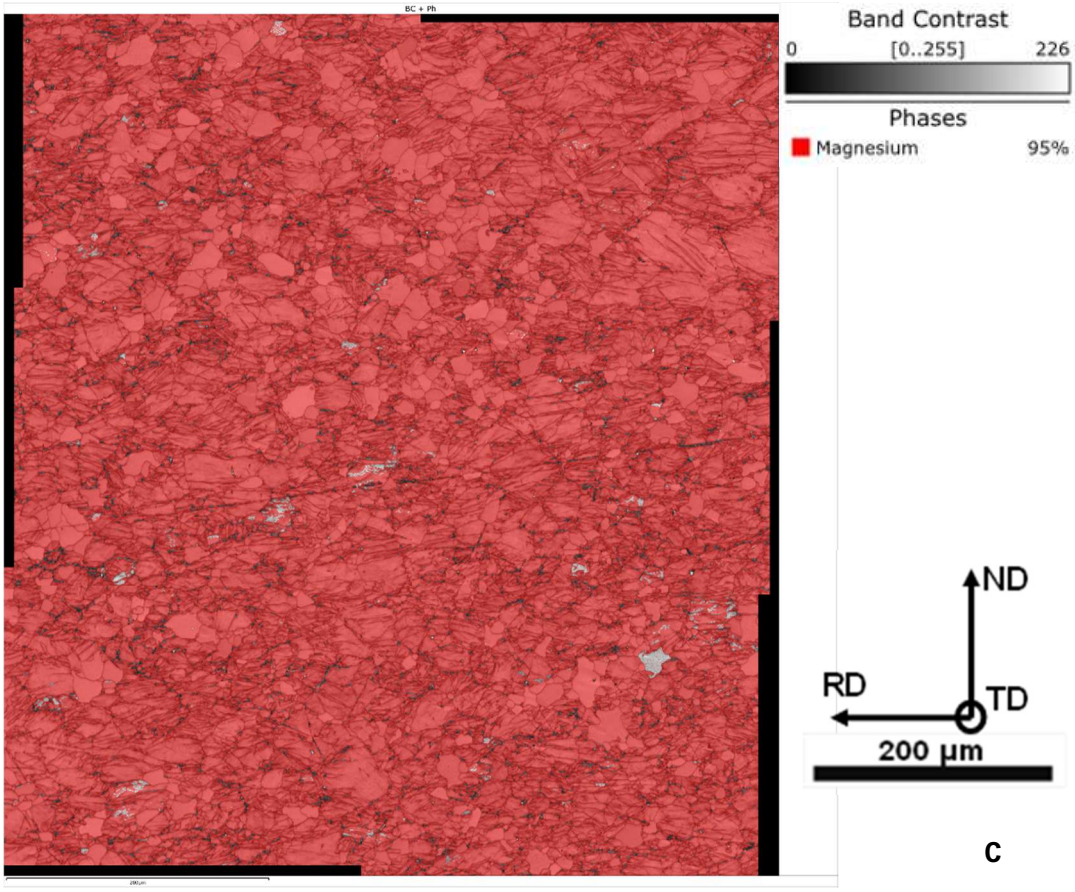
BC + Ph
Band Contrast
0 [0..255] 226
Phases
Magnesium 95%
ND
RD
TD
200 µm

c

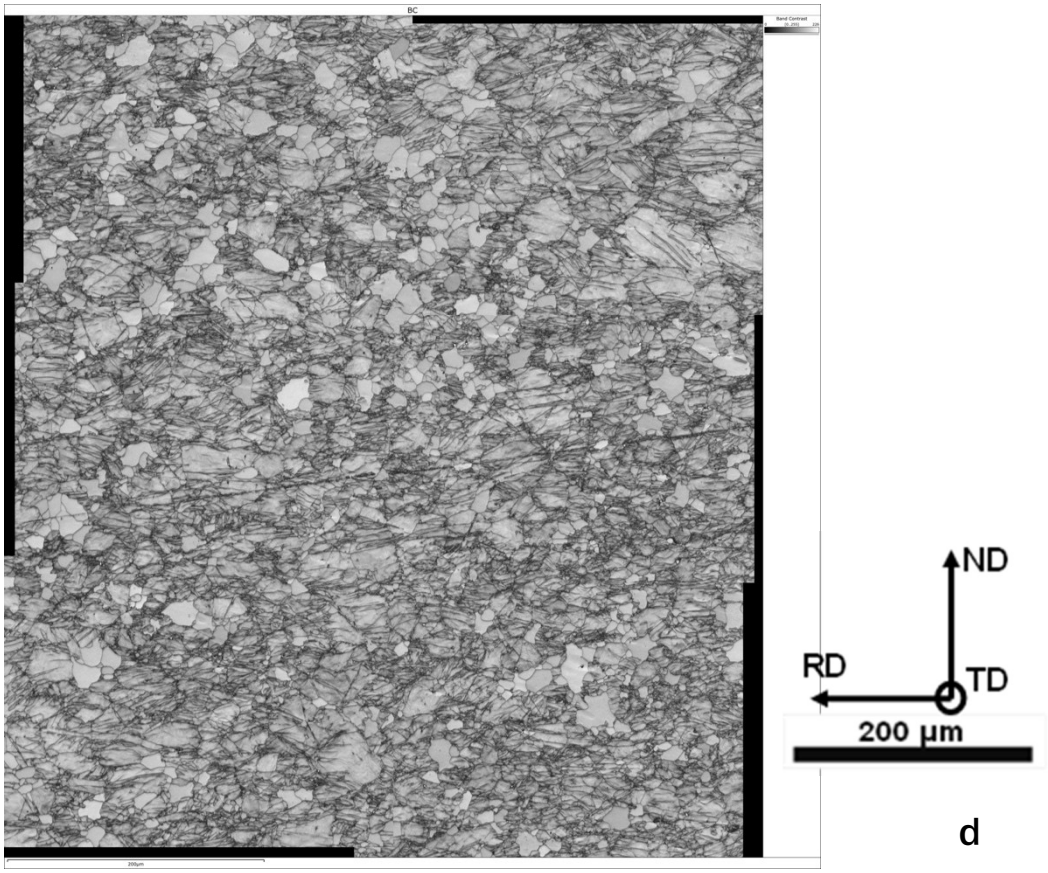
BC
ND
RD
TD
200 µm
d

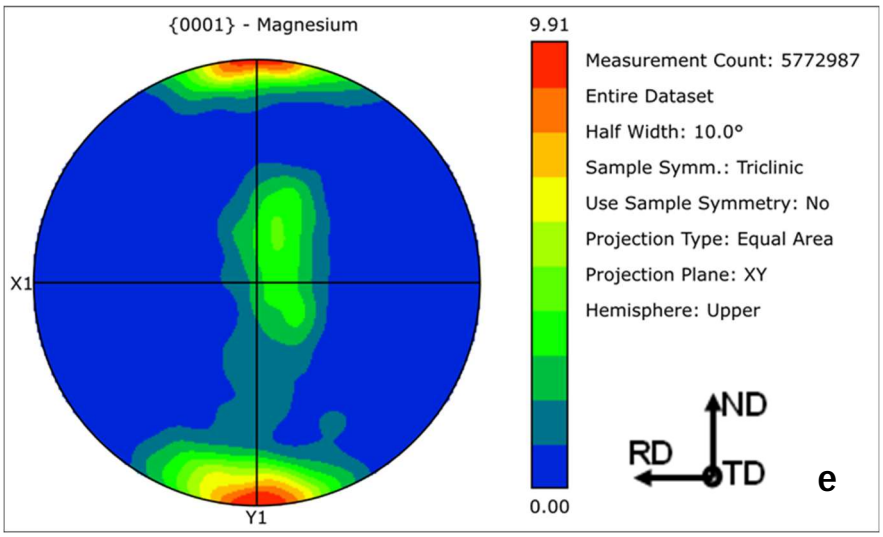
{0001} - Magnesium
9.91
0.00
X1
Y1
Measurement Count: 5772987
Entire Dataset
Half Width: 10.0°
Sample Symm.: Triclinic
Use Sample Symmetry: No
Projection Type: Equal Area
Projection Plane: XY
Hemisphere: Upper
ND
RD
TD
e

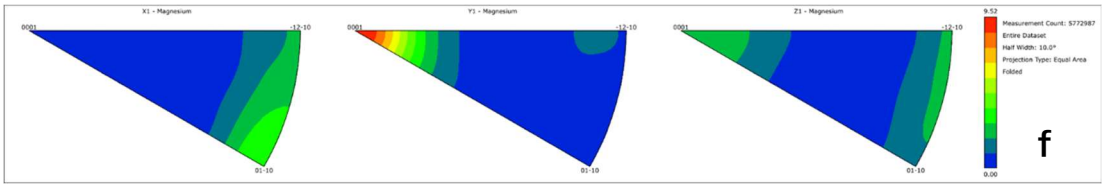
f

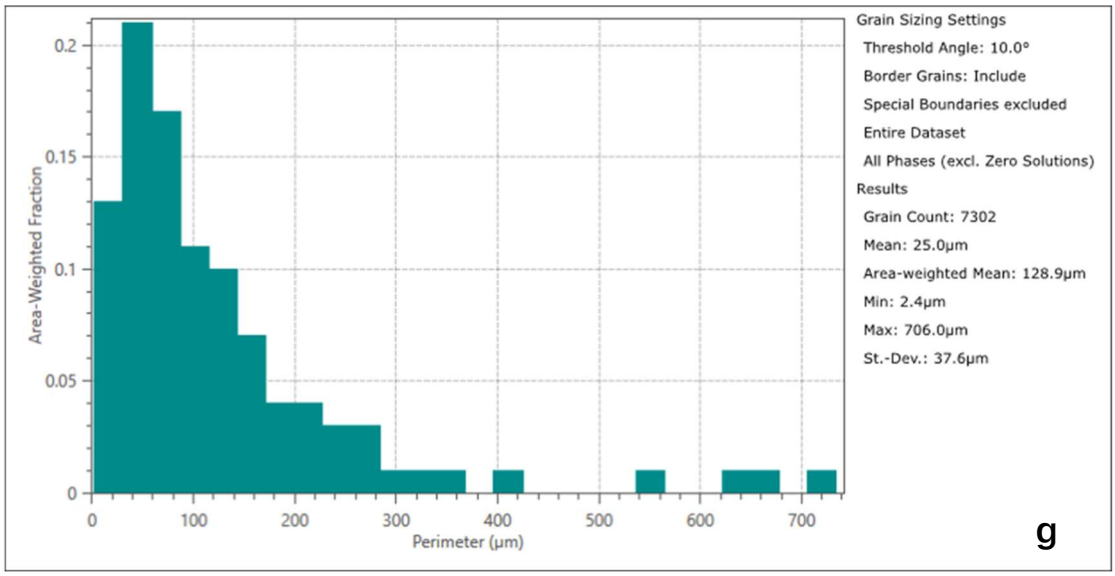

Figure 4-65 The EBSD result of the 570s annealed 1D compressed Mg-0.5Zn specimen: (a) The inverse pole figure map and grain boundaries, (b) The grain boundaries and the special grain boundaries, (c) The band contrast and the phase analysis, (d) The band contrast, (e) The pole figure, (f) The inverse pole figures, (g) Grain size distribution expressed as grain boundary perimeter

Figure 4-66 shows the EBSD results of the same specimen after annealing for 750s. The temperature of the specimen at that time point was 257℃. In contrast to the previous stage, with only a 30s longer annealing process and a 17℃ temperature difference, the microstructure of this 1D compressed specimen showed extensive recrystallisation. The IPF map (shown in Figure 4-66(a)) indicated that the specimen experienced rapid grain growth during the annealing process. Across the whole map, not just the existing recrystallized grains showed obvious grain growth (e.g. from around $10\mu m$ to about $40\mu m$) but also many rapid-growing new recrystallized grains were found (e.g. from $0\mu m$ to about $20\mu m$). The white circles in Figure 4-66(a) mark some of the areas where such rapid growth was observed. The average grain size of the specimen also increased from $25\mu m$ to $29.8\mu m$ (shown in Figure 4-66(g)). Similar to the other test specimens, the fast-growing recrystallized grains were not just from shear bands but also from twins. The changes of the twin boundary fractions also reflected the progress of the recrystallization. Figure 4-66(b) indicates that the boundary fraction of the tensile twins, compressive twins and double twins all decreased from 41.8% to 28.2%, 1.3% to 1.2% and 1.9% to 1.8%, respectively. Meanwhile, the fraction of the low-angle grain boundary and the high-angle grain boundary were correspondingly changed from 31.0% to 24.1% and from 69.0% to 75.9%, respectively. Compared to the dramatic variation shown on the IPF map, the changes were not that obvious in the

pole figure and IPF (shown in Figure 4-66(e) and (f)). Due to the recrystallization and the grain growth started to happen throughout the entire scanned area, the orientation distribution of the recrystallized grains (weak peak close to the TD) was found to start to expand along the ND-axis. More signals were found distributed between the old peak and the TD along the ND-axis. As a result of the recrystallization progress, the maximum value of the pole figure was reduced from 9.9 to 9.3.

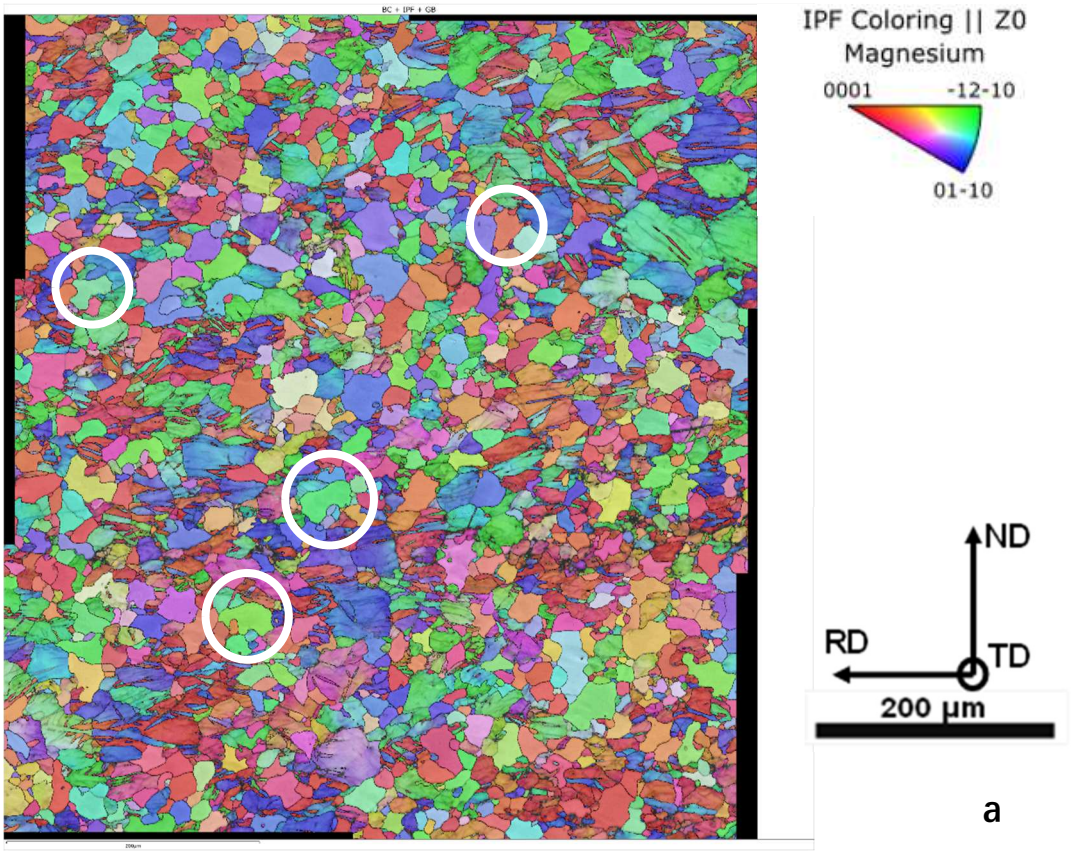

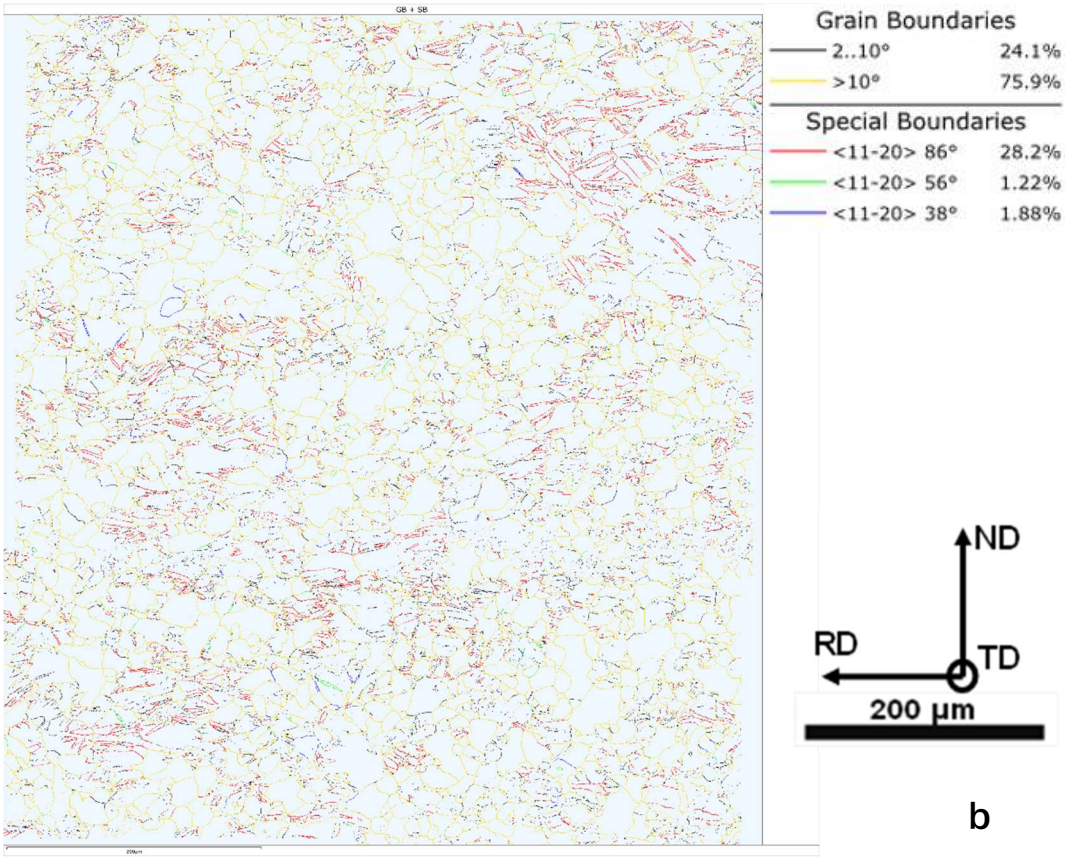
GB + SB
Grain Boundaries
2..10° 24.1%
>10° 75.9%
Special Boundaries
<11-20> 86° 28.2%
<11-20> 56° 1.22%
<11-20> 38° 1.88%
ND
RD
TD
200 µm

b

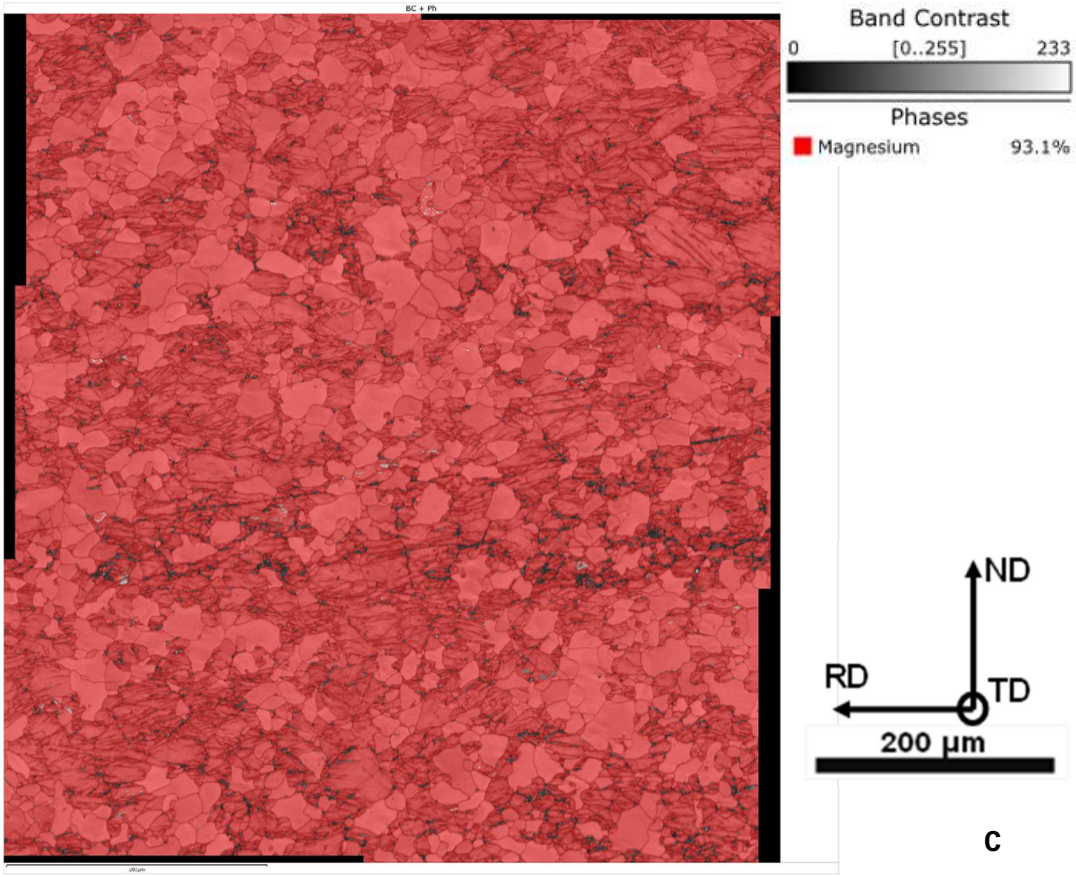
BC + Ph
Band Contrast
0 [0..255] 233
Phases
Magnesium 93.1%
ND
RD
TD
200 µm

c

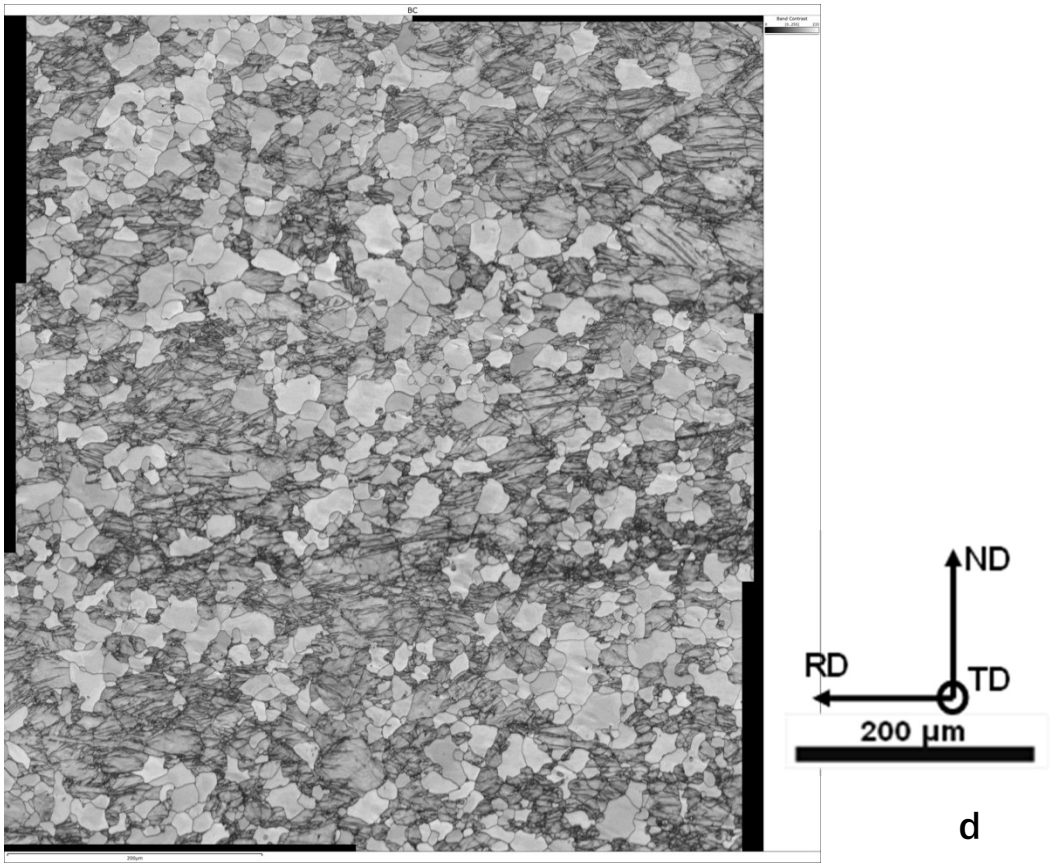
BC
ND
RD
TD
200 µm

d

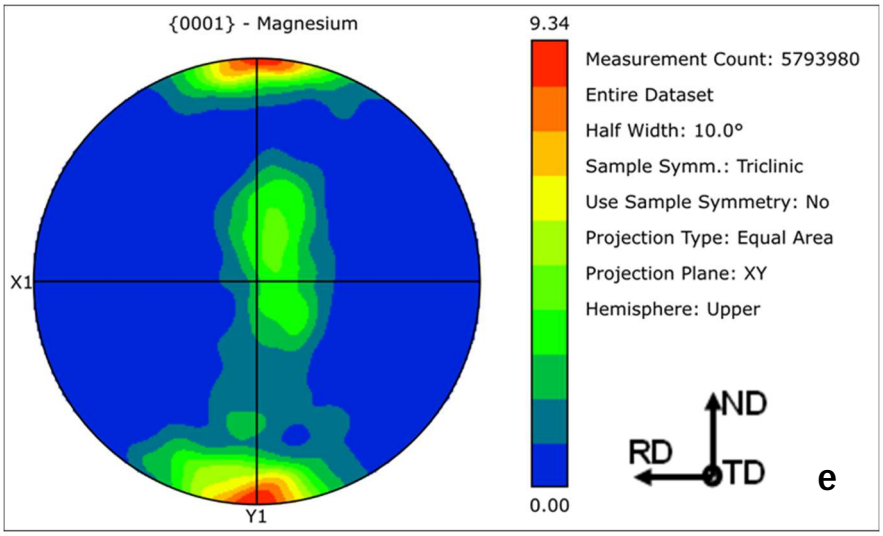
{0001} - Magnesium
9.34
0.00
Measurement Count: 5793980
Entire Dataset
Half Width: 10.0°
Sample Symm.: Triclinic
Use Sample Symmetry: No
Projection Type: Equal Area
Projection Plane: XY
Hemisphere: Upper
X1
Y1
ND
RD
TD

e

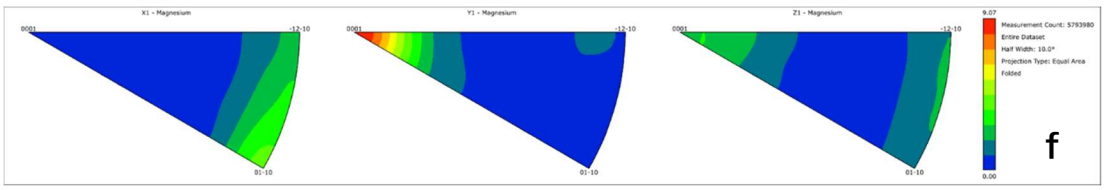
X1 - Magnesium
Y1 - Magnesium
Z1 - Magnesium
9.07
0.00
Measurement Count: 5793980
Entire Dataset
Half Width: 10.0°
Projection Type: Equal Area
Folded

f

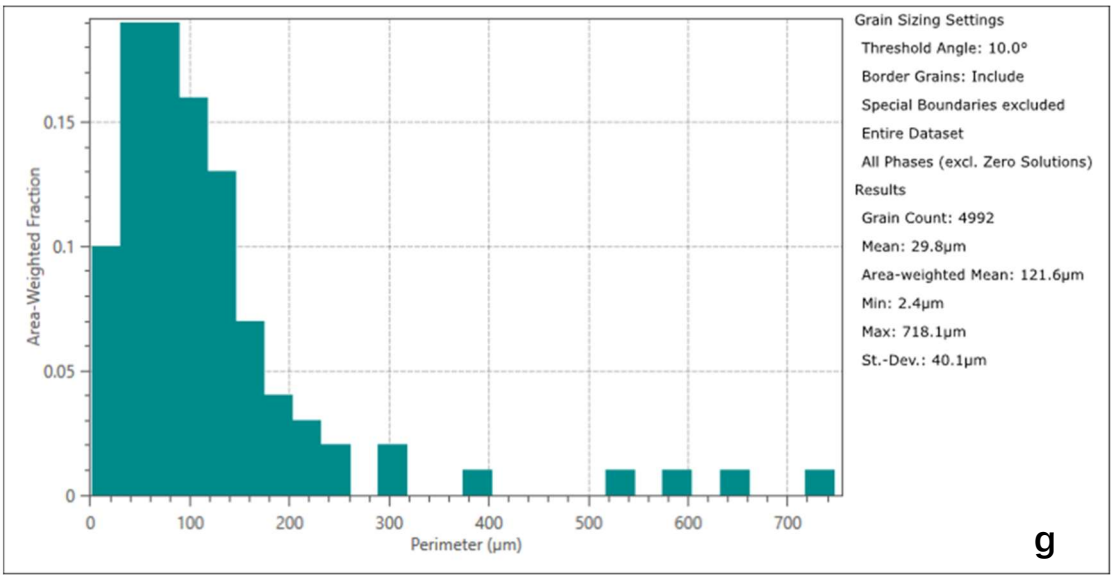

Figure 4-66 The EBSD result of the 750s annealed 1D compressed Mg-0.5Zn specimen: (a) The inverse pole figure map and grain boundaries, (b) The grain boundaries and the special grain boundaries, (c) The band contrast and the phase analysis, (d) The band contrast, (e) The pole figure, (f) The inverse pole figures, (g) Grain size distribution expressed as grain boundary perimeter

The last EBSD result of the 1D compressed Mg-0.5Zn (at%) specimen (shown in Figure 4-67) was from the 990s annealing. The highest temperature of the specimen during the annealing process was 291℃. Very similar to the Mg-0.1Ca-0.4Zn (at%) specimen, the 60s longer annealing process and the 34℃ higher temperature gave the specimen enough energy to continue the recrystallization. The morphology of the grains in the IPF map (shown in Figure 4-67(a)) was completely different to that of the previous stage i.e. except for the very small area close to the top of the IPF map (marked with the white circle in Figure 4-67(a)), the rest of the area showed a fully recrystallized microstructure. The average grain size of the specimen was also very different compared to the previous stage, which was changed from 29.8μm to 50.6μm (shown in Figure 4-67(g)). The grains exhibited a quite uniform size compared to the specimen before the compression process. The largest grain and the smallest grain had a grain size of 64.7μm and 1μm, respectively. Meanwhile, the recrystallized grains which had a direction closer to the TD showed darker on the band contrast map (shown in Figure 4-67(d)). Only a few partially identified and non-indexed grains were found in the IPF map. The significant variation of the microstructure was also reflected in the value of the boundary fraction. Figure 4-67(b) shows the boundary fraction of the tensile twins, compressive twins and double twins significantly reduced from 28.2% to 3.5%, 1.2% to 0.2% and 1.9% to 0.2%, respectively. Meanwhile, the fraction of the low-angle grain

boundary and the high-angle grain boundary was changed from 24.1% to 11.3% and from 75.9% to 88.7%, respectively. For the pole figure of the recrystallized specimen, Figure 4-67(e) presents the obvious reduction of the maximum pole intensity from the previous stage (from 9.3 to 6.7). Meanwhile, an increasing number of random distributed grains were also observed. The pole intensity of the weak peak close to the TD was found to increase to 4.7. The orientation distribution of new grains (the weak peaks around the TD) showed a more dispersed distribution compared to the last stage. However, the maximum pole intensity was still found in the compression direction. The grain orientation distribution of the recrystallized specimen was not dispersed wide enough to show a weakened texture. The grain orientations were mainly distributed along the ND-axis of the pole figure. And most of the recrystallized grains had direction which tilted 10° to 45° from the TD.

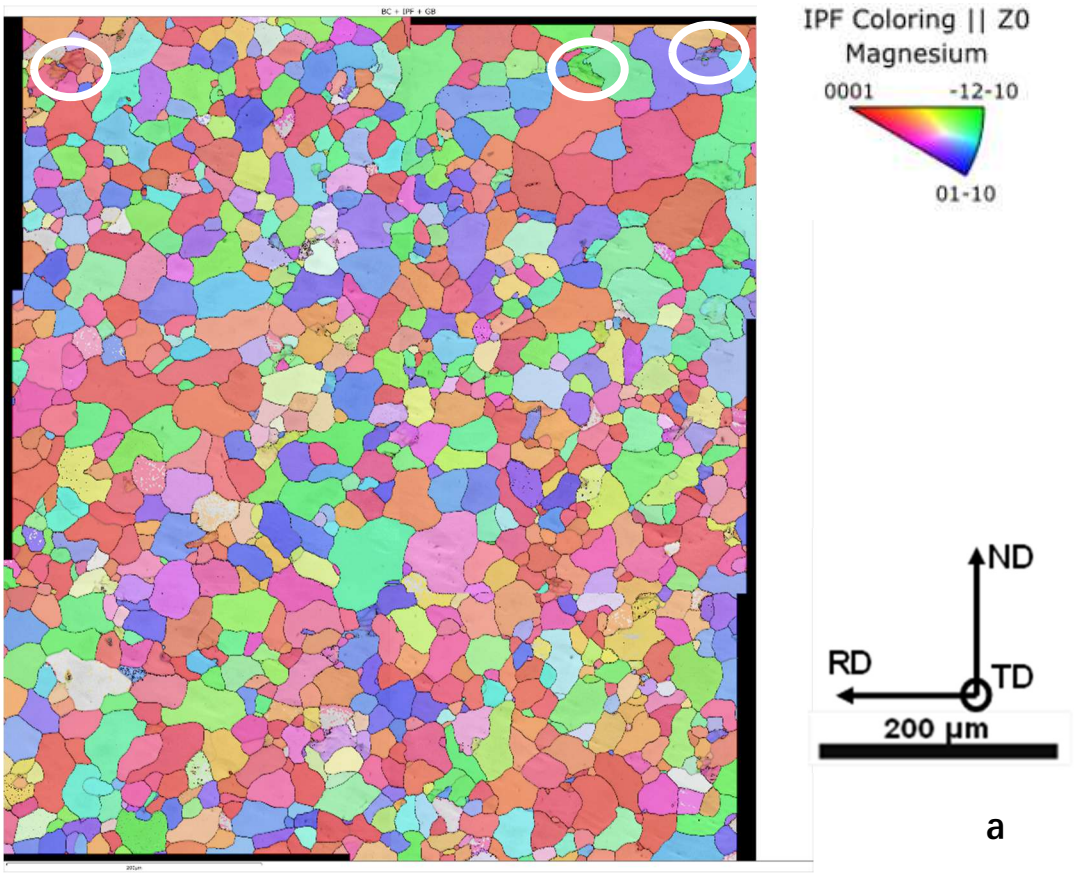

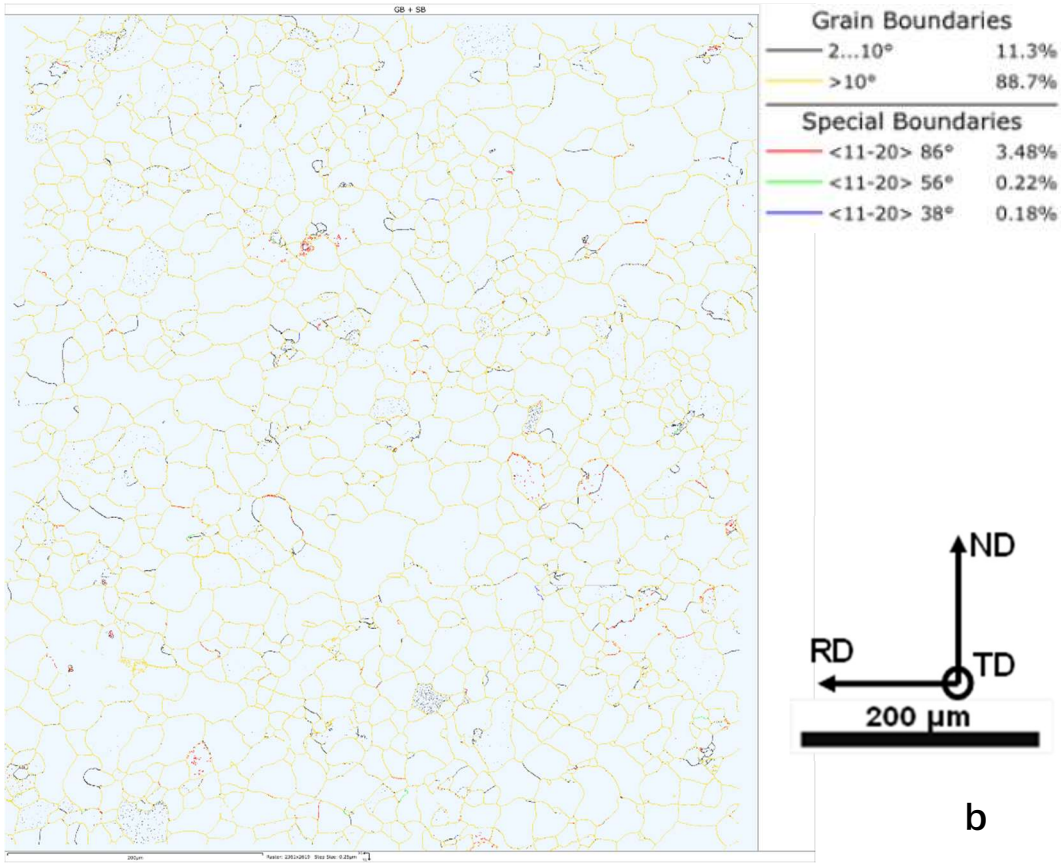
GB + SB
Grain Boundaries
2...10° 11.3%
>10° 88.7%
Special Boundaries
<11-20> 86° 3.48%
<11-20> 56° 0.22%
<11-20> 38° 0.18%
ND
RD
TD
200 µm

b

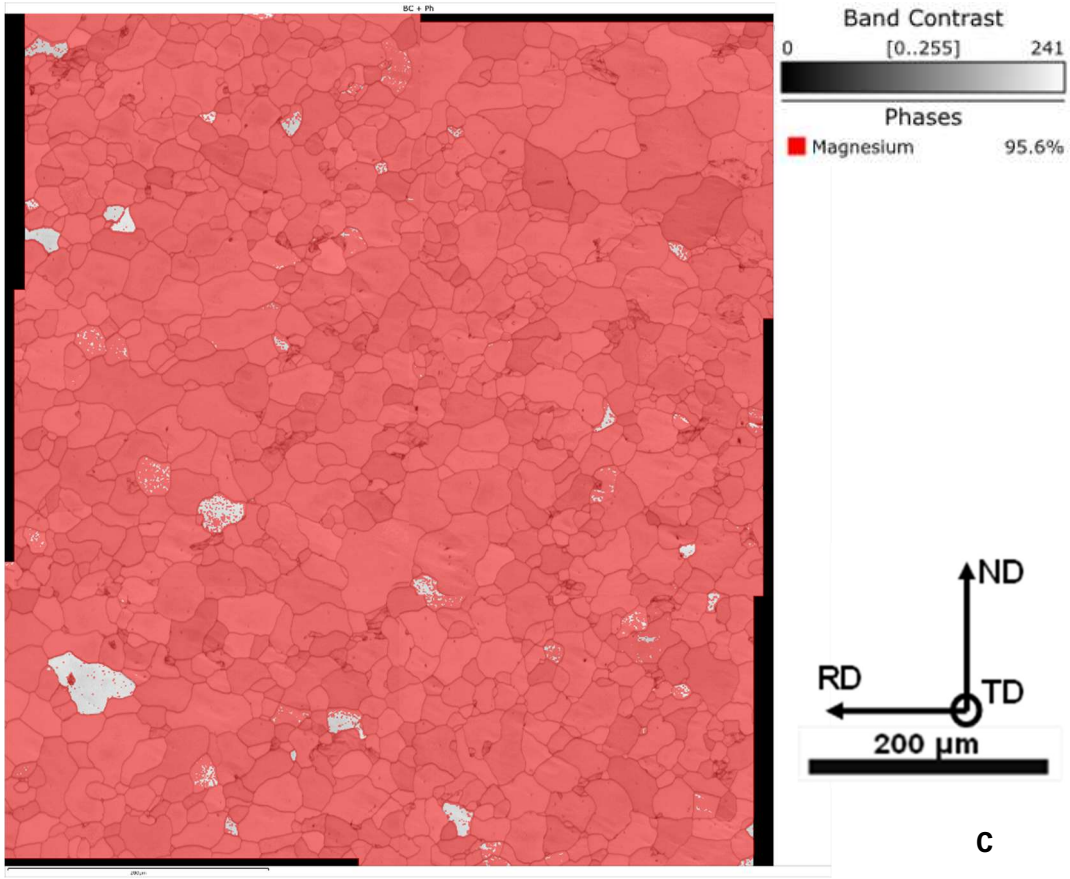
BC + Ph
Band Contrast
0 [0..255] 241
Phases
Magnesium 95.6%
ND
RD
TD
200 µm

c

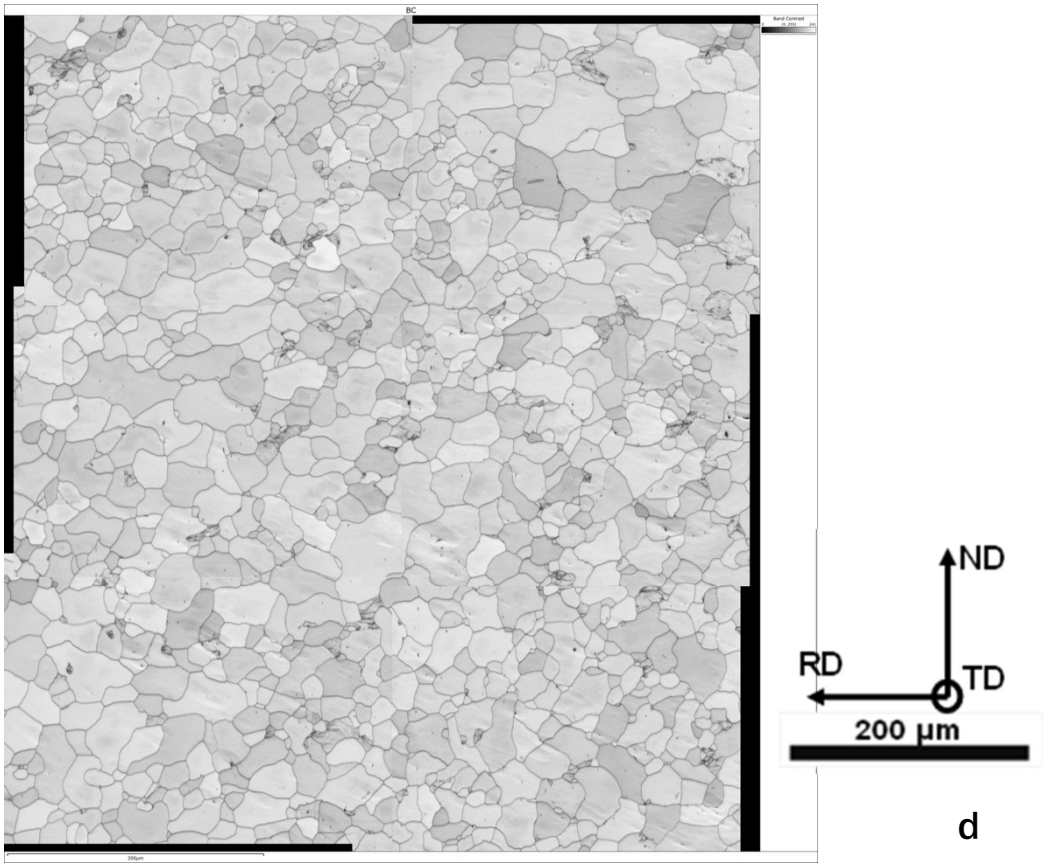
BC
ND
RD
TD
200 µm

d

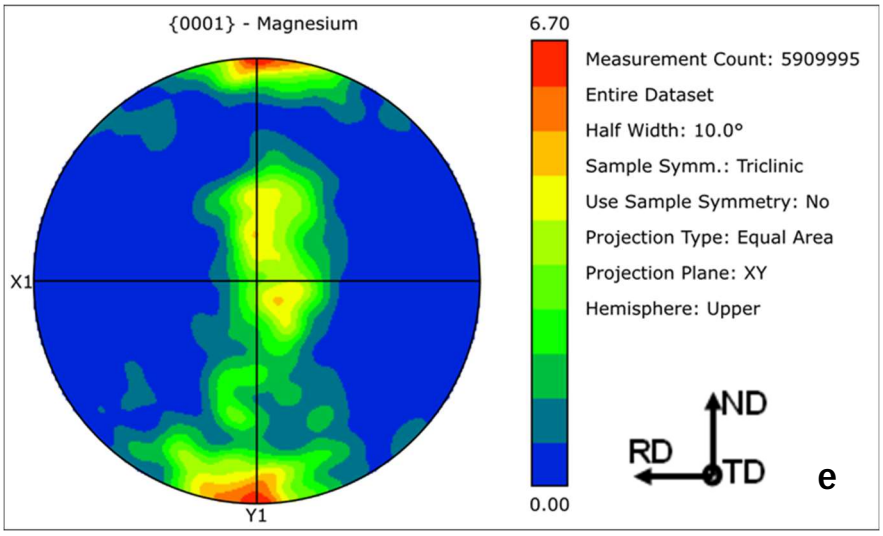
{0001} - Magnesium
6.70
0.00
Measurement Count: 5909995
Entire Dataset
Half Width: 10.0°
Sample Symm.: Triclinic
Use Sample Symmetry: No
Projection Type: Equal Area
Projection Plane: XY
Hemisphere: Upper
X1
Y1
ND
RD
TD

e

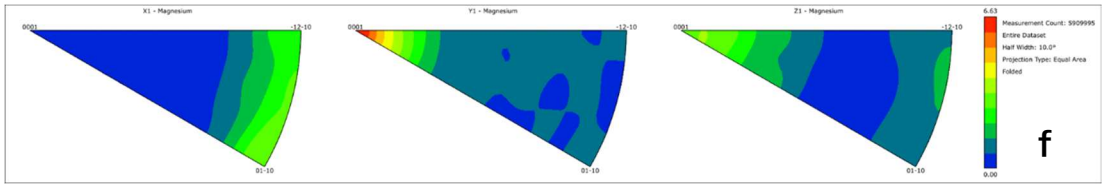
X1 - Magnesium
Y1 - Magnesium
Z1 - Magnesium
0001
-12-10
01-10
6.63
0.00
Measurement Count: 5909995
Entire Dataset
Half Width: 10.0°
Projection Type: Equal Area
Folded

f

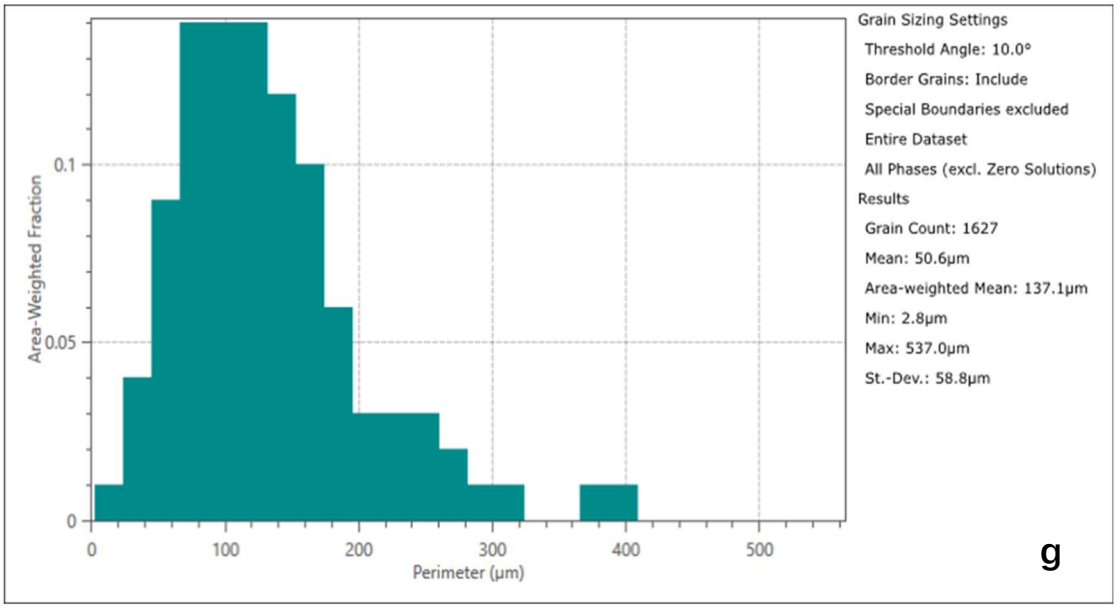

Figure 4-67 The EBSD result of the 990s annealed 1D compressed Mg-0.5Zn specimen: (a) The inverse pole figure map and grain boundaries, (b) The grain boundaries and the special grain boundaries, (c) The band contrast and the phase analysis, (d) The band contrast, (e) The pole figure, (f) The inverse pole figures, (g) Grain size distribution expressed as grain boundary perimeter

4.3.2.2.4 The two-direction (2D) compressed Mg-0.2Ca-0.3Zn (at%) specimen

Figure 4-68 to 4-74 show the EBSD results of the 2D compressed Mg-0.2Ca-0.3Zn (at%) specimen from the as-compressed state to the recrystallized state. The grain size was quite uniform with an average size of 12.7μm in the as-compressed specimen (shown in Figure 4-68(g)). As with the 1D compressed Mg-0.2Ca-0.3Zn (at%) specimen, a significant amount of shear banding and fine twins were observed throughout the whole area. Figure 4-68(c) shows that about 19.3% of the whole map was taken by the shear bands (marked by white circles) and the fine twins. Figure 4-68 (b) indicates that the boundary fraction of the tensile twins, compressive twins and double twins was 64.9%, 1.3% and 1.9%, respectively. The pole figure and IPF (Figure 4-68 (e) and (f)) showed that most of the grains had a direction parallel to the RD i.e. the direction of the second compression to the specimen. The maximum pole intensity was also found in this direction with the value of 7.6. Only a few grains showed an orientation scattering around the TD.

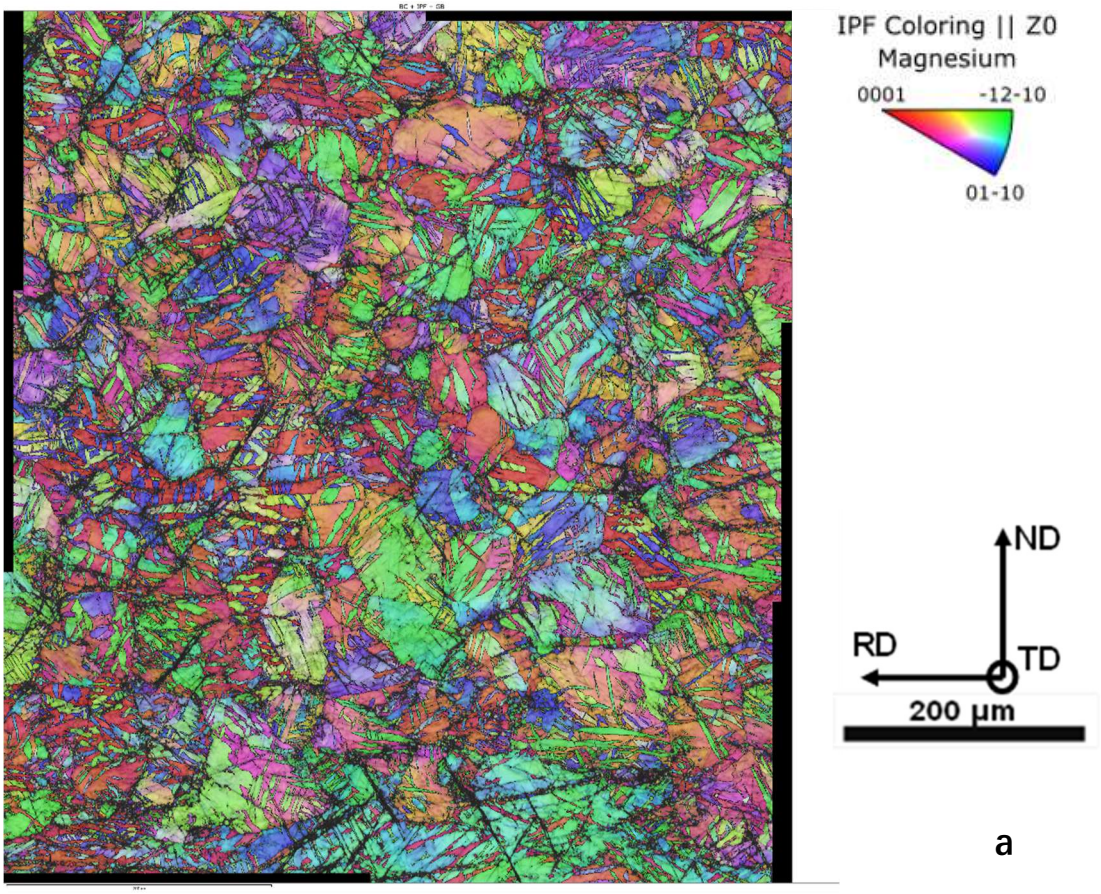
IPF Coloring || Z0
Magnesium
0001
-12-10
01-10
ND
RD
TD
200 µm

a

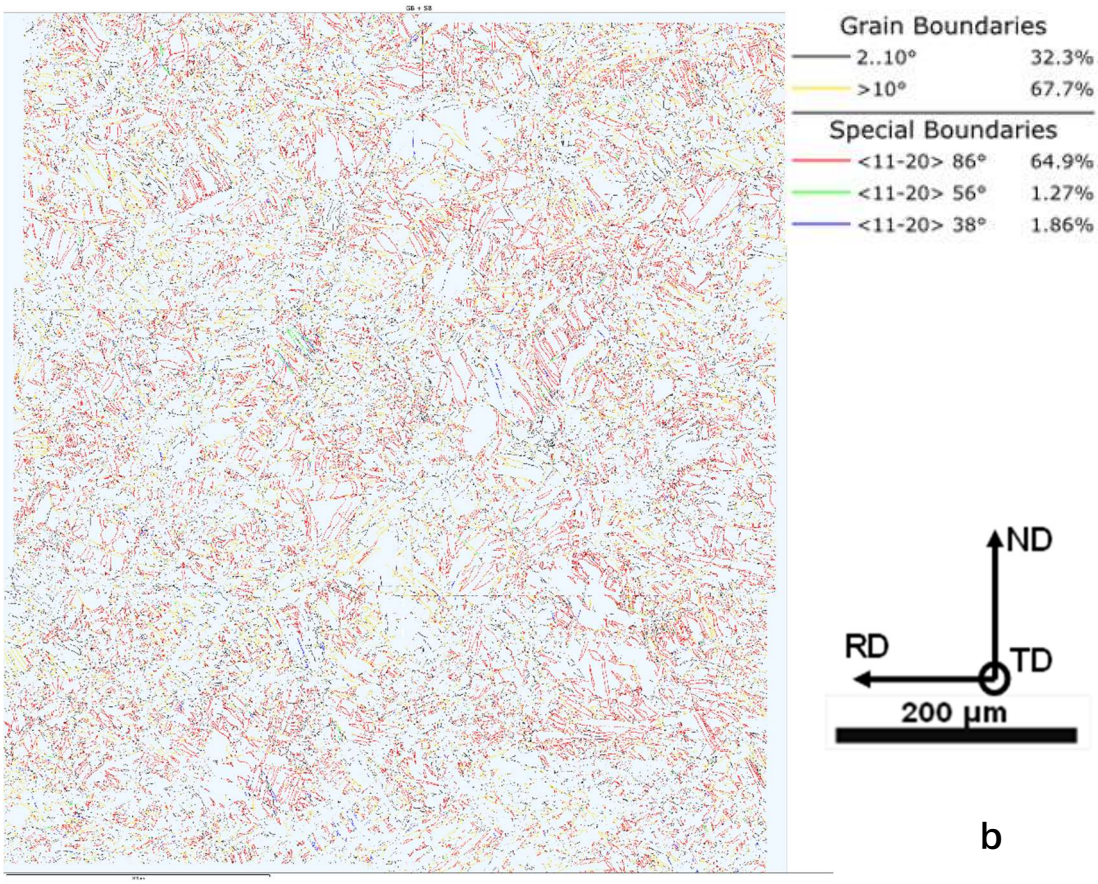
Grain Boundaries
2..10° 32.3%
>10° 67.7%
Special Boundaries
<11-20> 86° 64.9%
<11-20> 56° 1.27%
<11-20> 38° 1.86%
ND
RD
TD
200 µm

b

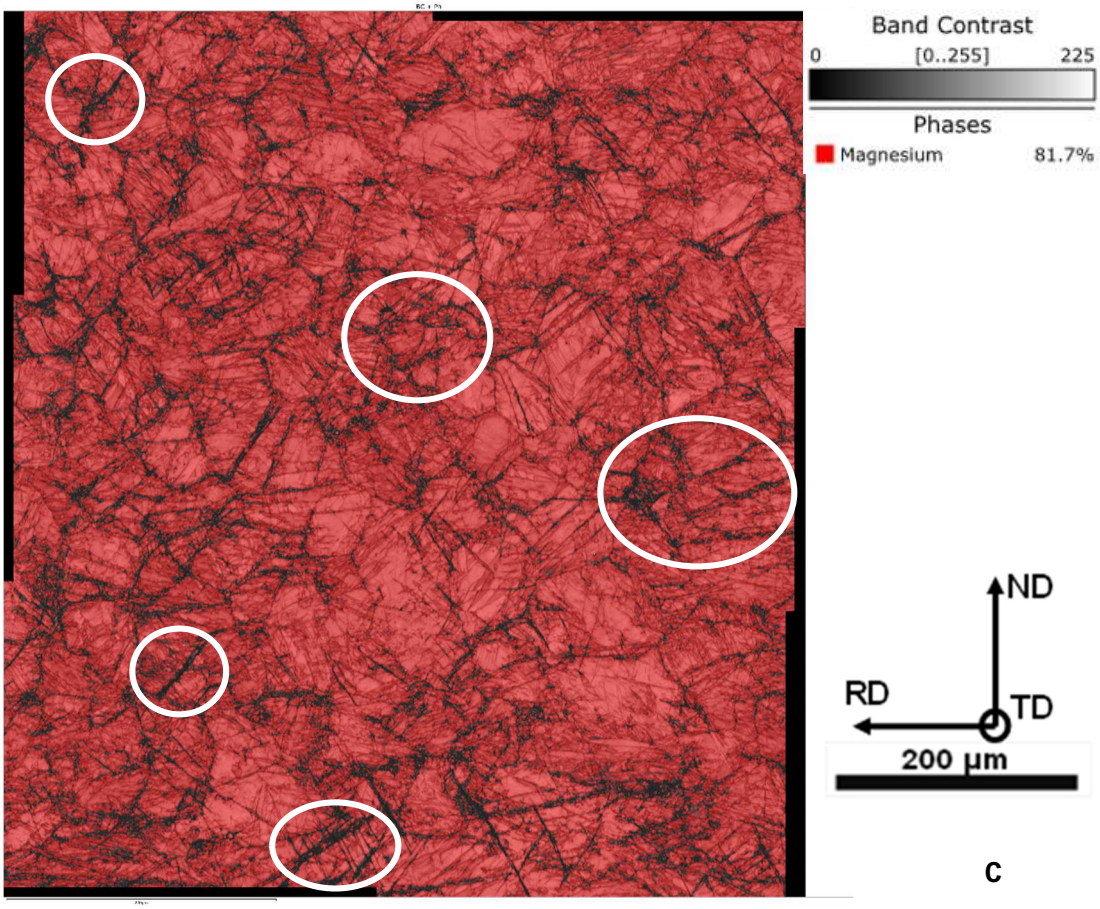
Band Contrast
0
[0..255]
225
Phases
Magnesium
81.7%
ND
RD
TD
200 µm

c

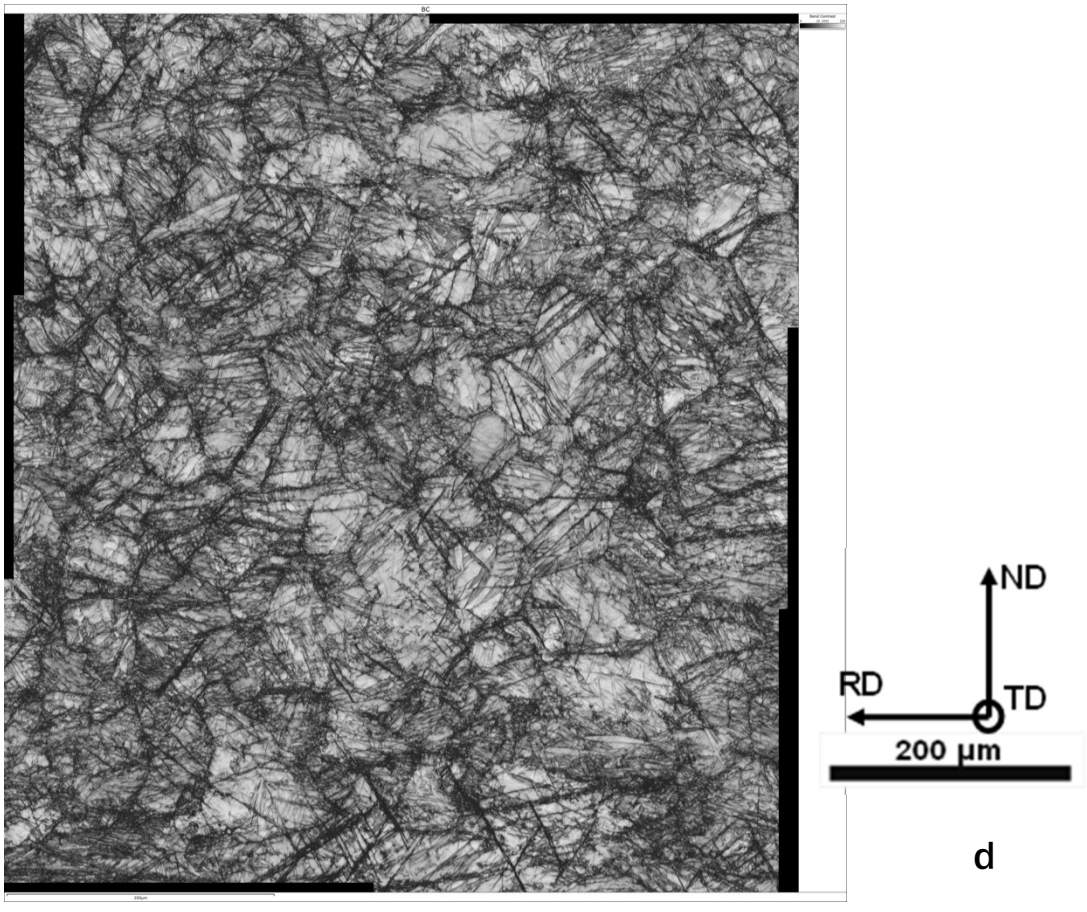
ND
RD
TD
200 µm

d

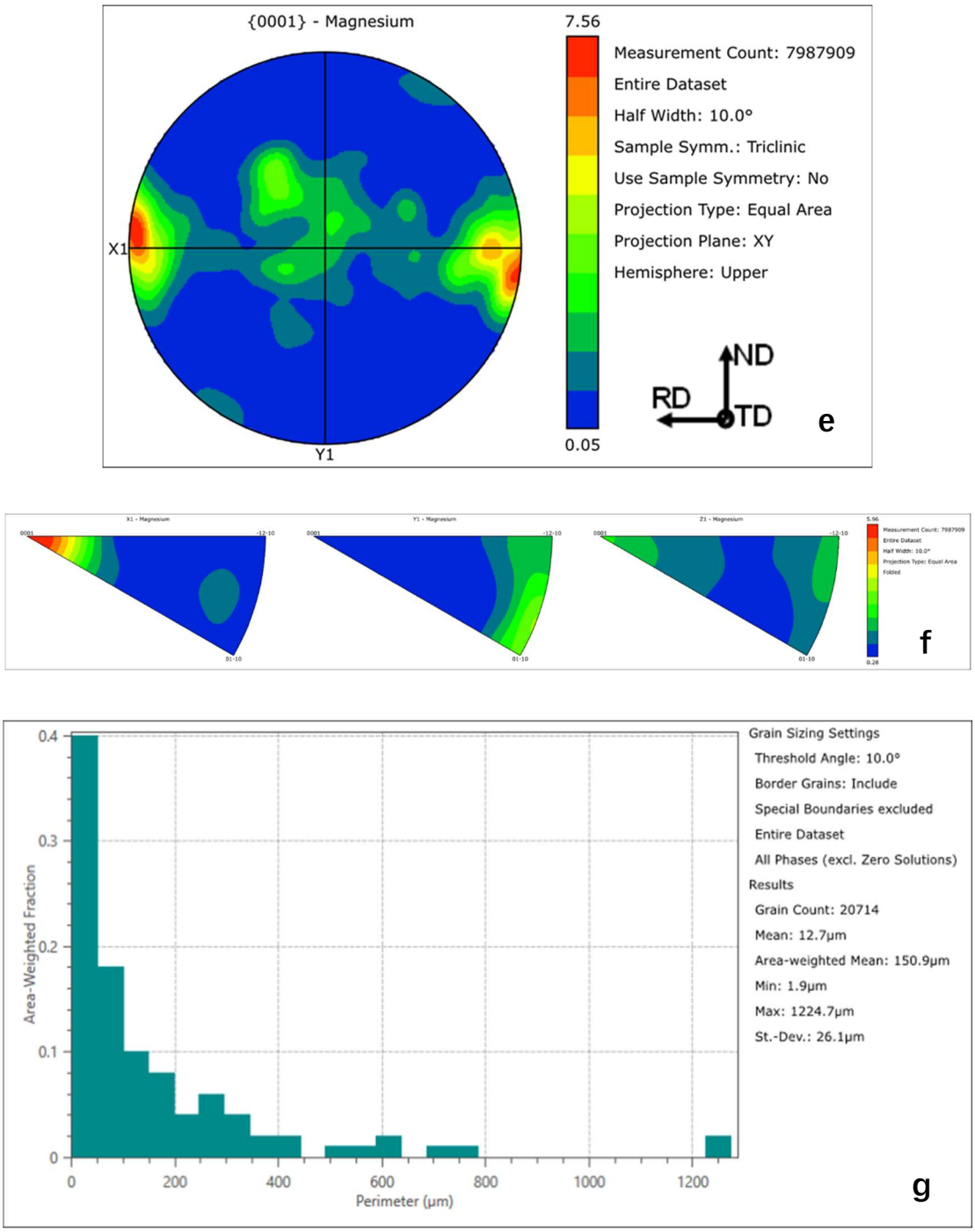

Figure 4-68 The EBSD result of the as-compressed 2D compressed Mg-0.2Ca-0.3Zn specimen: (a) The inverse pole figure map and grain boundaries, (b) The grain boundaries and the special grain boundaries, (c) The band contrast and the phase analysis, (d) The band contrast, (e) The pole figure, (f) The inverse pole figures, (g) Grain size distribution expressed as grain boundary perimeter

In a similar manner to the 1D compressed Mg-0.2Ca-0.3Zn (at%) specimen, the 2D compressed specimen showed the recrystallized structure after 1290s annealing. At a shorter annealing time, the EBSD results of the 990s annealed specimen indicated that

recovery had occurred (shown in Figure 4-69(a) and (c)). The temperature of the specimen at that time was 291℃. Figure 4-69(c) also shows the grey area (oxidized area) in the EBSD map (same as the 1D compressed specimen). Although the reduction of the non-indexed region was also observed, the fraction of the non-indexed area increased from 18.3% (before annealing) to 27.8% (after 990s annealing). The oxidized area was obviously responsible for this abnormal increase. In the 990s annealed specimen, Figure 4-69(b) presents that the boundary fraction of three types of twins was 49.4%, 0.7% and 1.9%, respectively. The reduction in the fraction of the tensile twins was considered to be a result of the signal losses from the oxidized area (grey area). The maximum value of the pole figure at this stage was 7.9 (shown in Figure 4-69(e)), which was 0.3 higher than that of the as-compressed specimen. For the grain orientation distribution, an enhancement of the signal close to the TD was observed. The average grain size of the specimen at this stage was 13.8μm. The EBSD results of the 30s, 45s, 60s, 75s, 90s, 120s, 150s and 180s annealing (30s, 75s, 135s, 210s, 300s, 420s, 570s and 750s heat treatment time in total, respectively) are presented in Appendix I and are not discussed further in the text.

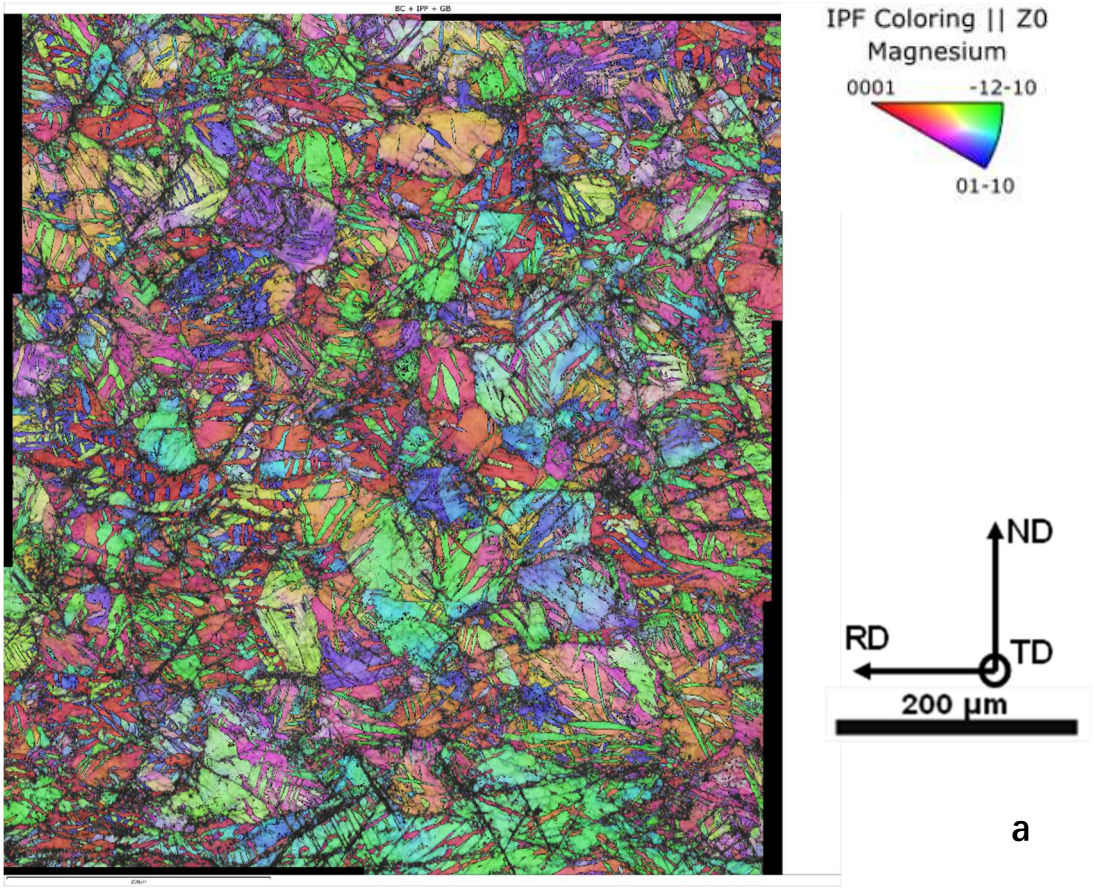

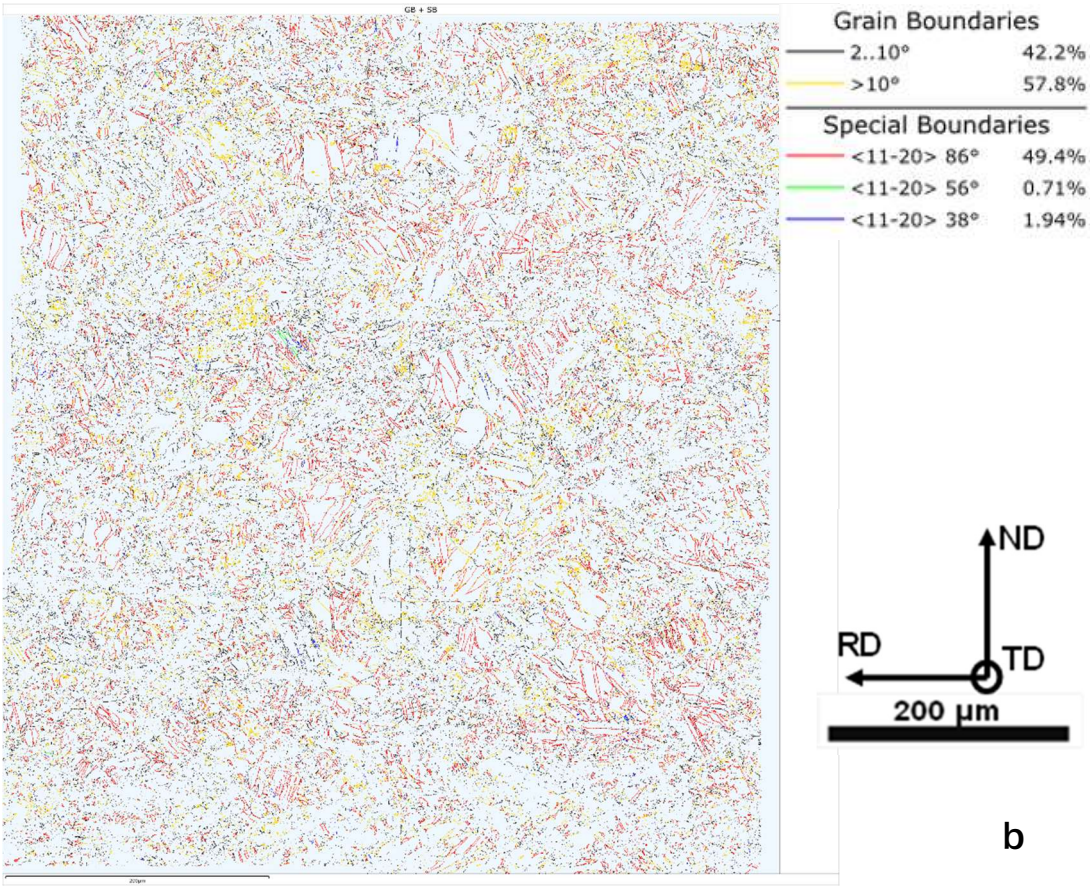
GB + SB
Grain Boundaries
2..10° 42.2%
>10° 57.8%
Special Boundaries
<11-20> 86° 49.4%
<11-20> 56° 0.71%
<11-20> 38° 1.94%
ND
RD
TD
200 µm

b

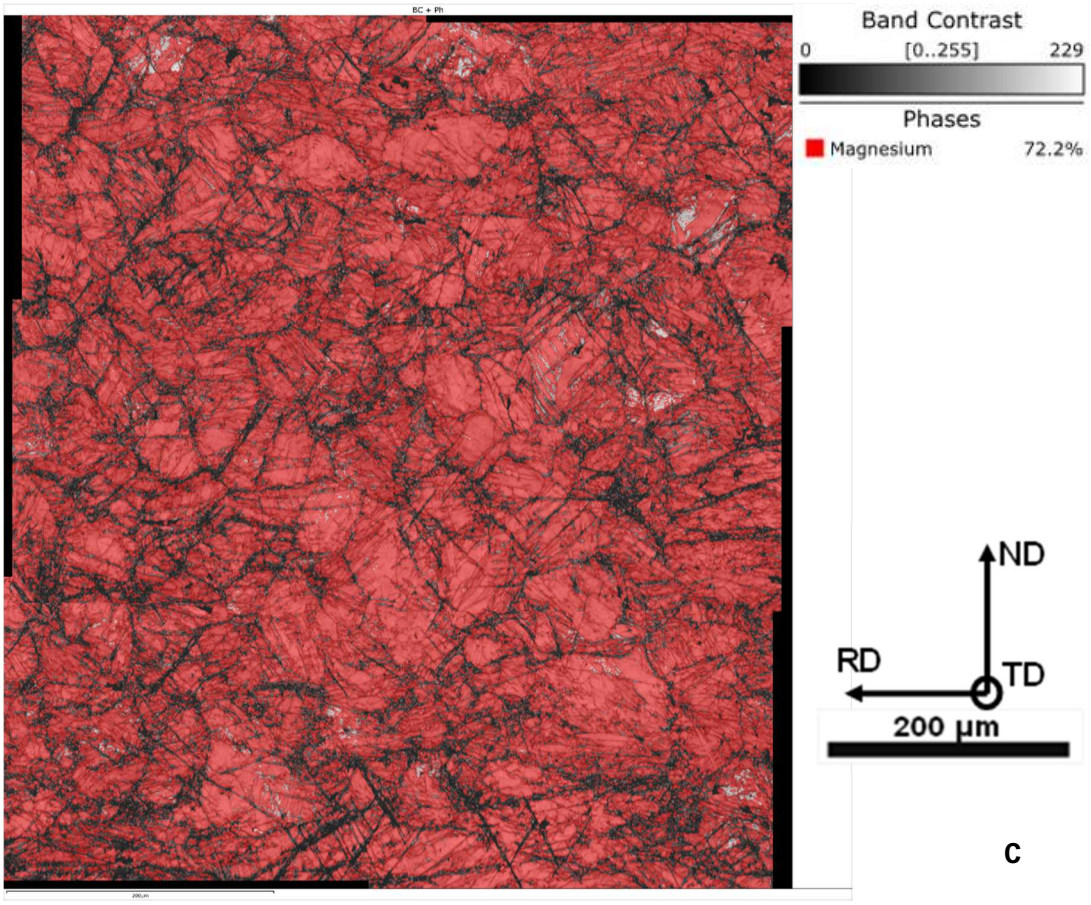
BC + Ph
Band Contrast
0 [0..255] 229
Phases
Magnesium 72.2%
ND
RD
TD
200 µm

c

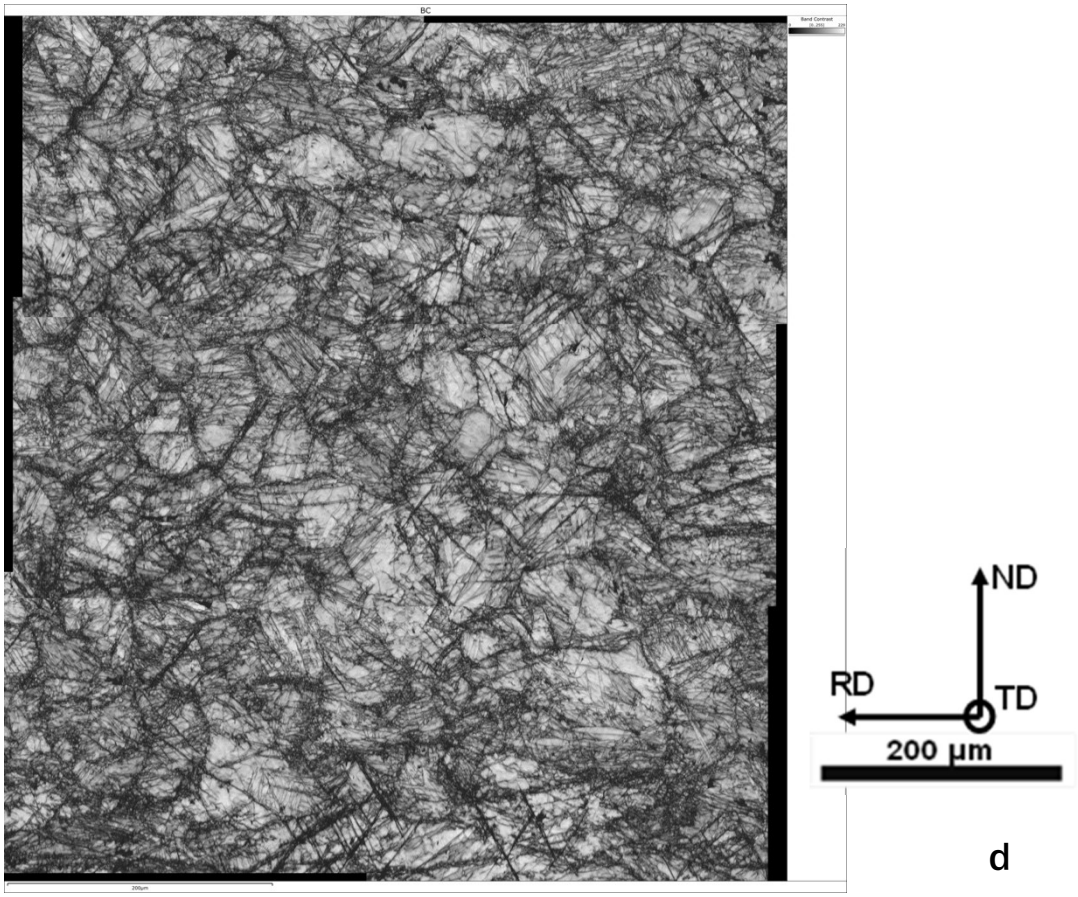
BC
ND
RD
TD
200 µm
d

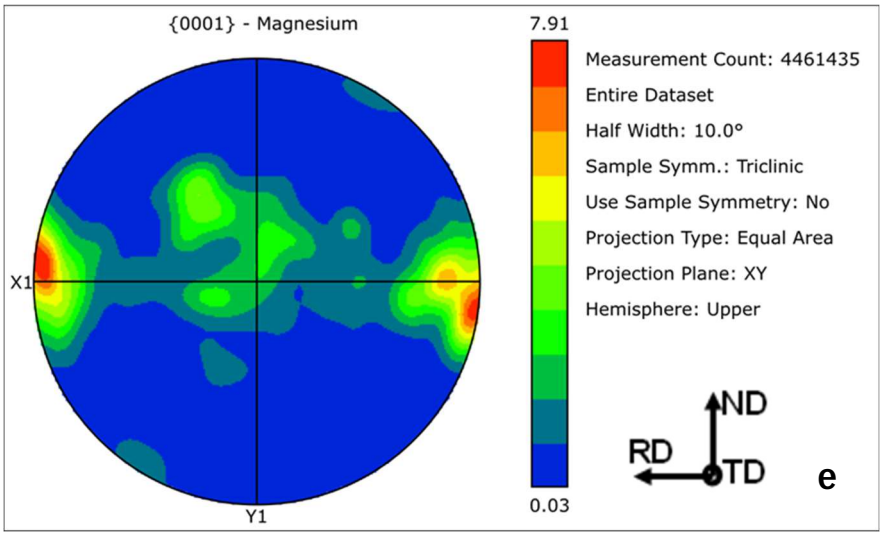
{0001} - Magnesium
7.91
0.03
Measurement Count: 4461435
Entire Dataset
Half Width: 10.0°
Sample Symm.: Triclinic
Use Sample Symmetry: No
Projection Type: Equal Area
Projection Plane: XY
Hemisphere: Upper
X1
Y1
ND
RD
TD
e

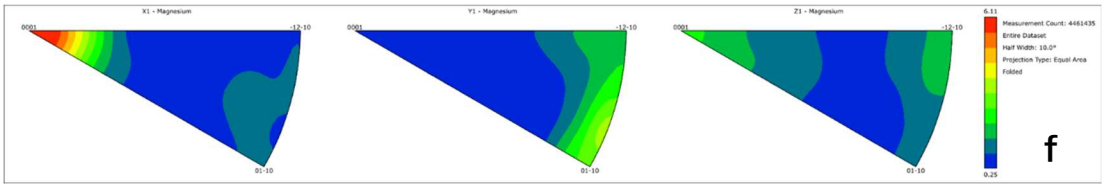
X1 - Magnesium
Y1 - Magnesium
Z1 - Magnesium
f

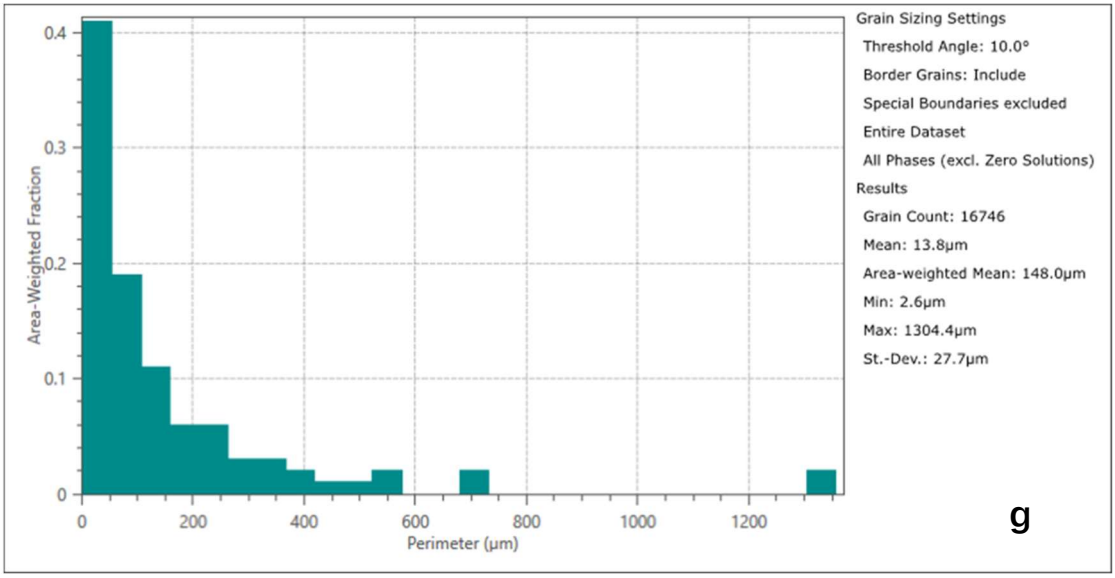

Figure 4-69 The EBSD result of the 990s annealed 2D compressed Mg-0.2Ca-0.3Zn specimen: (a) The inverse pole figure map and grain boundaries, (b) The grain boundaries and the special grain boundaries, (c) The band contrast and the phase analysis, (d) The band contrast, (e) The pole figure, (f) The inverse pole figures, (g) Grain size distribution expressed as grain boundary perimeter

Figure 4-70 shows the EBSD results of the same specimen after annealing for 1290s. The temperature of the specimen at this stage was 310℃. The average grain size of the specimen was $14\mu m$ (shown in Figure 4-70(g)). Only a small number of recrystallized grains were found inside the shear bands (shown in Figure 4-70(a)), which means that the 2D compressed specimen had a later recrystallization starting point than that of the 1D compressed specimen. Combining the information from Figure 4-70 (c), the non-indexed area of the map was even further increased from 27.8% to 28.1%. Considering the recrystallization was found within the shear bands and the existence of grey areas (oxidized layer), the abnormal increase of non-indexed area fraction was attributed to the increase of the oxidized layer. After the specimen started recrystallization, the result from Figure 4-70(b) presents a trend which the boundary fraction of the tensile twins, compressive twins and double twins all decreased from 49.4% to 43.7%, 0.7% to 0.6% and 1.94% to 1.92%, respectively. On the other hand, Figure 4-70(e) shows that the maximum pole intensity was reduced from 7.9 to 6.9. The diffusion areas of two peaks along the RD did not show obvious changes. However, the grains with a similar direction to the TD (meanwhile diffused along ND) showed a significant increase.

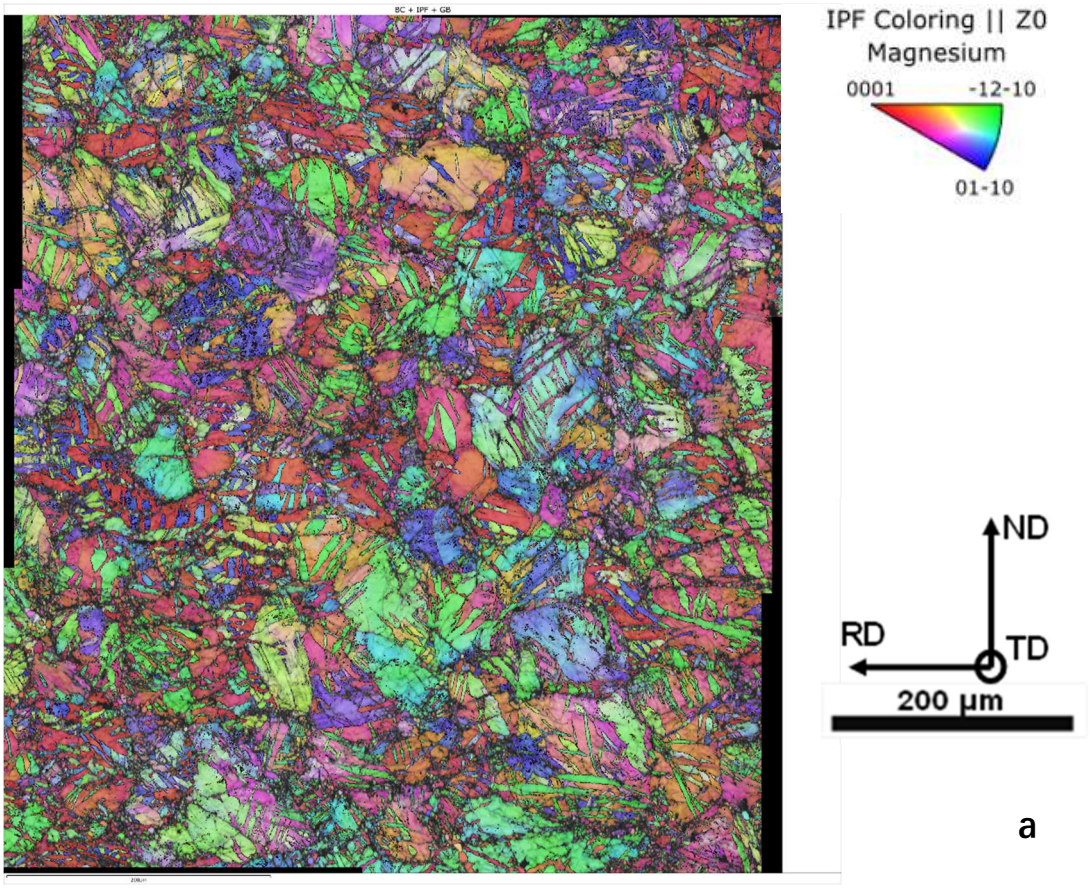
IPF Coloring || Z0
Magnesium
0001
-12-10
01-10
ND
RD
TD
200 µm

a

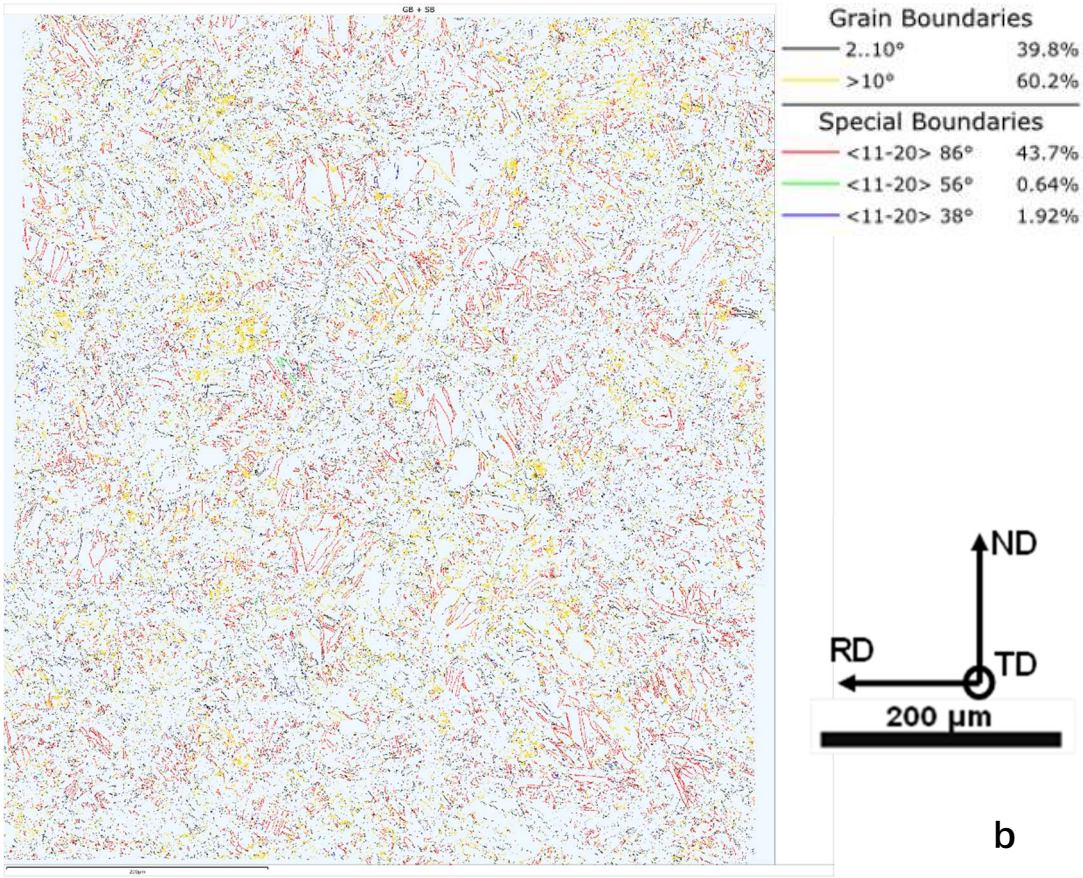
Grain Boundaries
2..10° 39.8%
>10° 60.2%
Special Boundaries
<11-20> 86° 43.7%
<11-20> 56° 0.64%
<11-20> 38° 1.92%
ND
RD
TD
200 µm

b

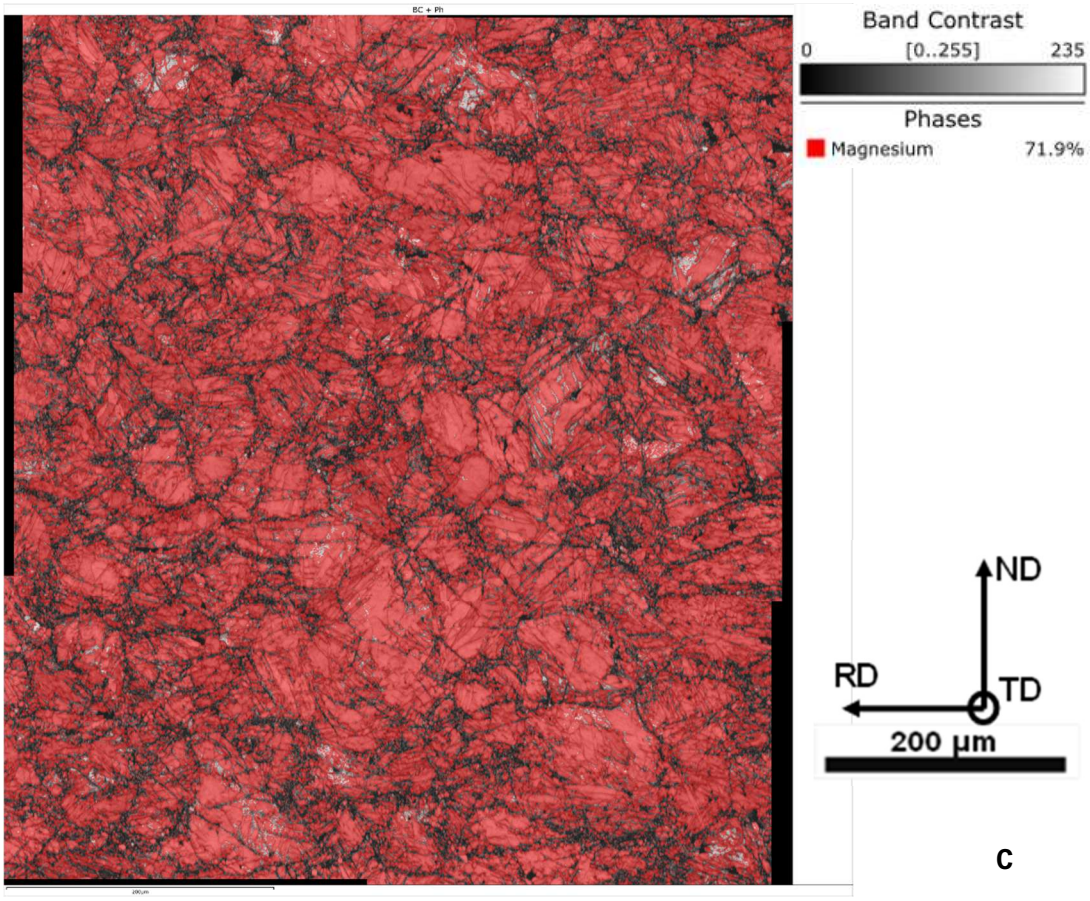
BC + Ph
Band Contrast
0
[0..255]
235
Phases
Magnesium
71.9%
ND
RD
TD
200 µm

c

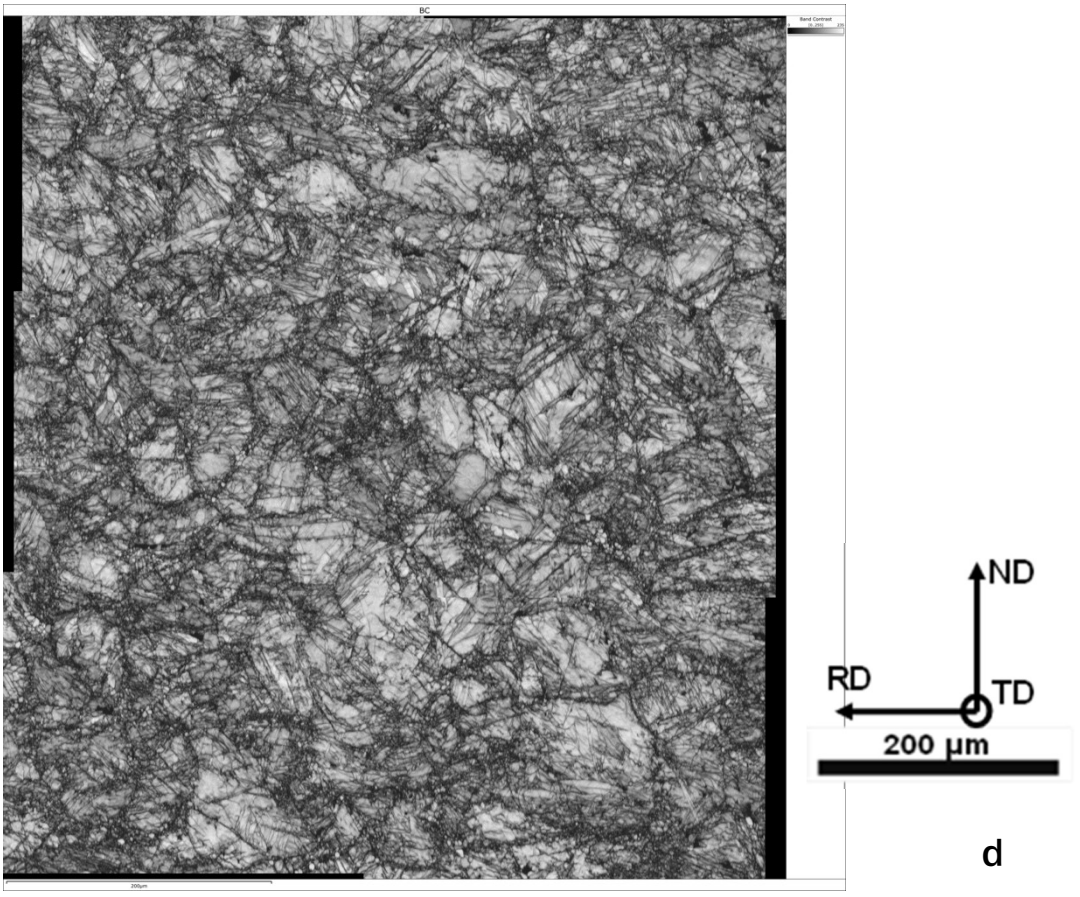
BC
ND
RD
TD
200 µm

d

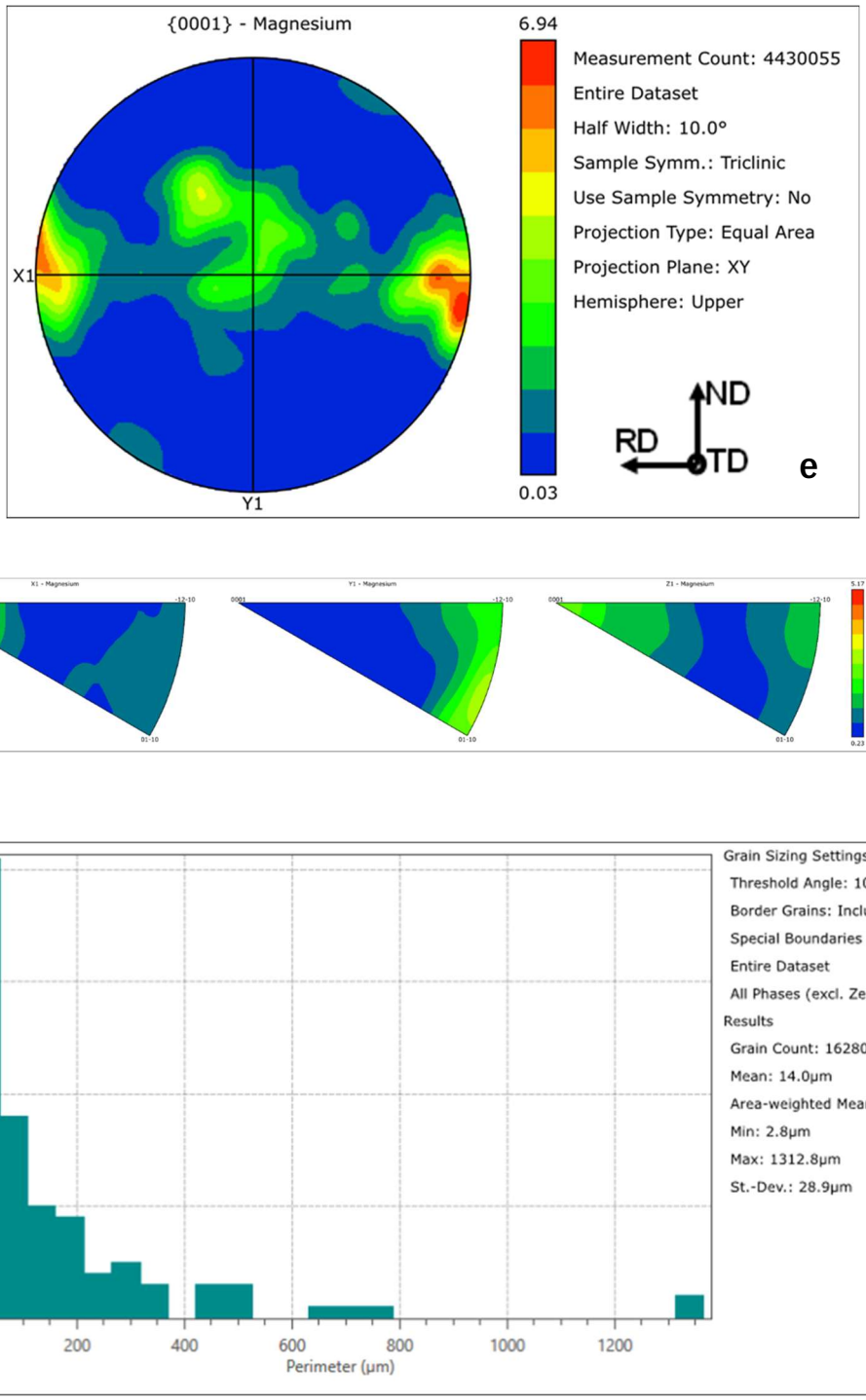

Figure 4-70 The EBSD result of the 1290s annealed 2D compressed Mg-0.2Ca-0.3Zn specimen: (a) The inverse pole figure map and grain boundaries, (b) The grain boundaries and the special grain boundaries, (c) The band contrast and the phase analysis, (d) The band contrast, (e) The pole figure, (f) The inverse pole figures, (g) Grain size distribution expressed as grain boundary perimeter

Recrystallization in the specimen continued and became apparent when the annealing time came to 1620s. The temperature of the specimen was the same as the 1D compressed sample which was 319℃. Figure 4-71 shows quite similar changes in

EBSD results of the 2D compressed specimen to that of the 1D compressed specimen. From Figure 4-71(c) it was clear that the recrystallisation had consumed all the shear bands. The shear bands were all replaced by the recrystallized grains, while the new grains which were found in the last EBSD map (1290s annealing) started to grow (shown in Figure 4-71(a)). Unlike the 1D compressed specimen, the recrystallization based on twins was not observed at this stage. Based on the information of the grain boundaries (shown in Figure 4-71(b)), the number of three kinds of twins remained stable. The boundary fraction of the tensile twins, compressive twins and double twins showed a little fluctuation from 43.7% to 43.4%, 0.6% to 1.3% and 1.9% to 2.3%, respectively. The increase of the boundary fraction was attributed to the recovery and the following improvement of the resolution. Due to the start of the recrystallization, the fraction of the high-angle grain boundaries increased from 60.2% (1290s annealed) to 67.2% (1620s annealed). The average grain size of the specimen increased to 16.8μm (shown in Figure 4-71(g)). Figure 4-71(e) indicates that the maximum pole intensity decreased from 6.9 to 6.1. However, the grain orientation distribution shown in the pole figure and IPF did not present an obvious change. Only the weak peak close to the TD tilted about 30° showed an enhancement.

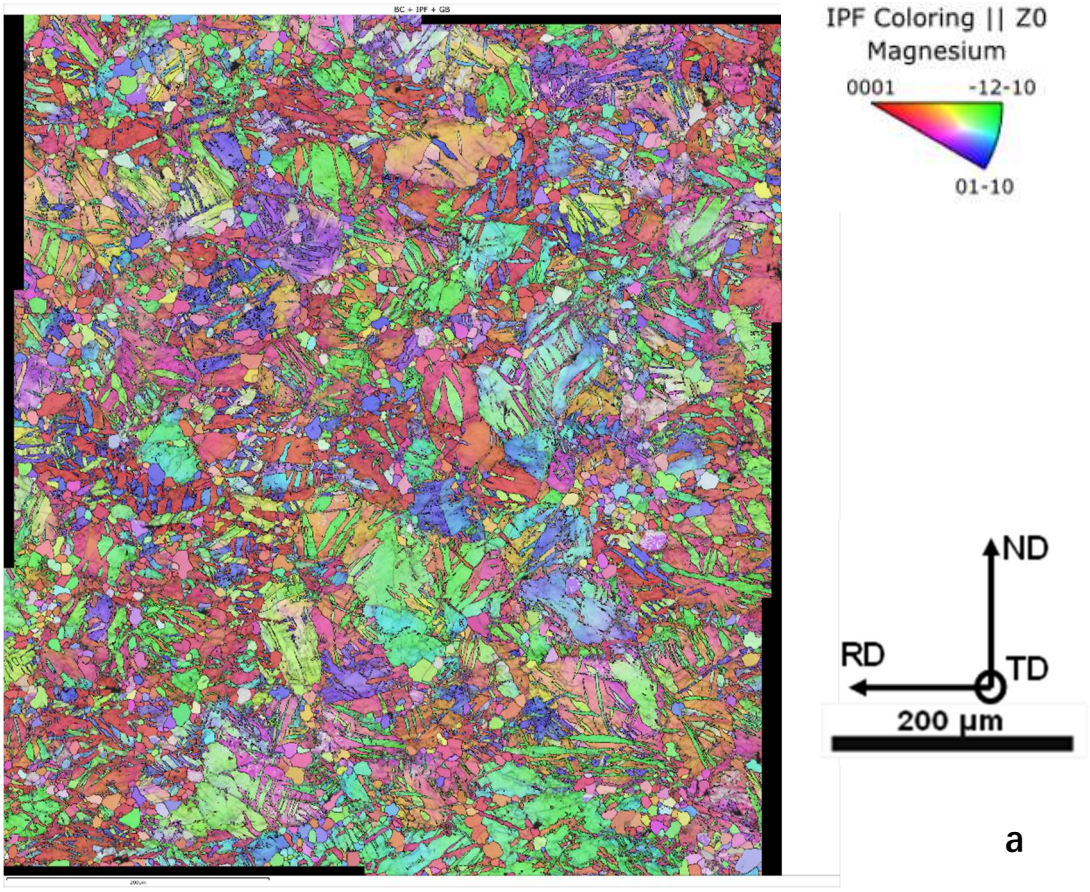

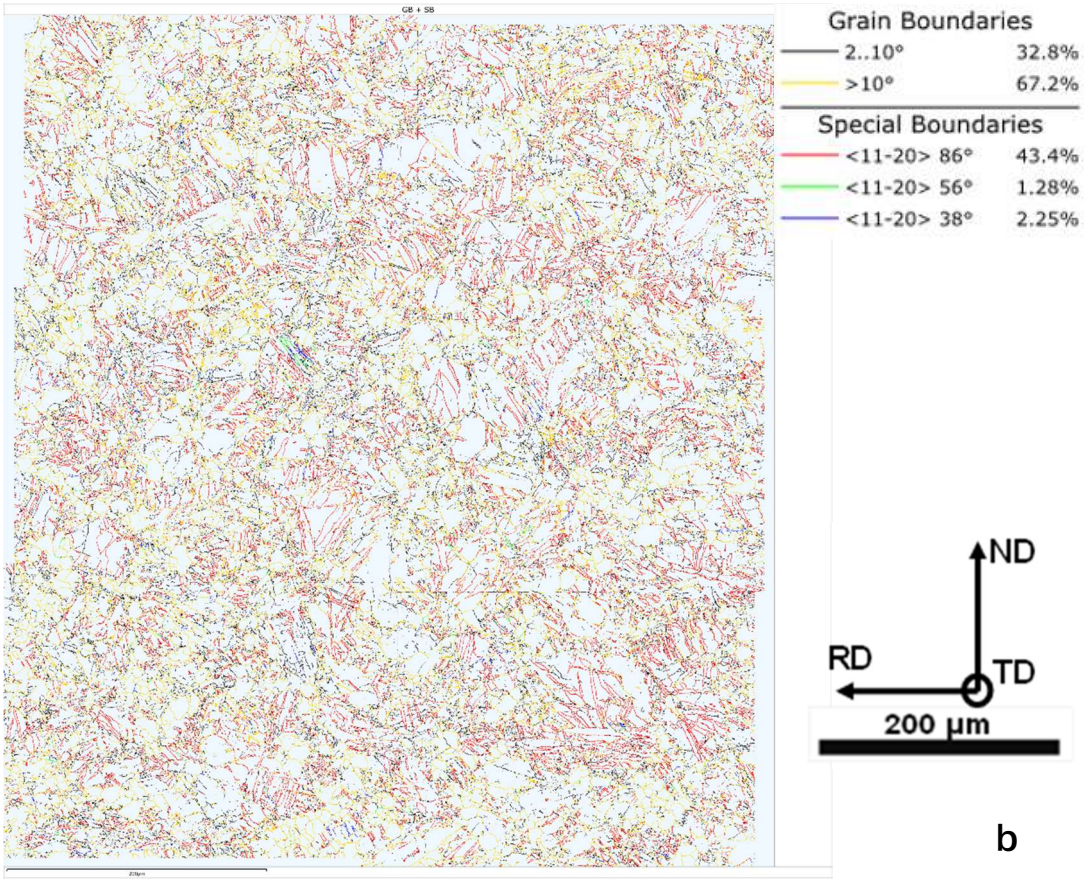
GB + SB
Grain Boundaries
2..10° 32.8%
>10° 67.2%
Special Boundaries
<11-20> 86° 43.4%
<11-20> 56° 1.28%
<11-20> 38° 2.25%
ND
RD
TD
200 µm

b

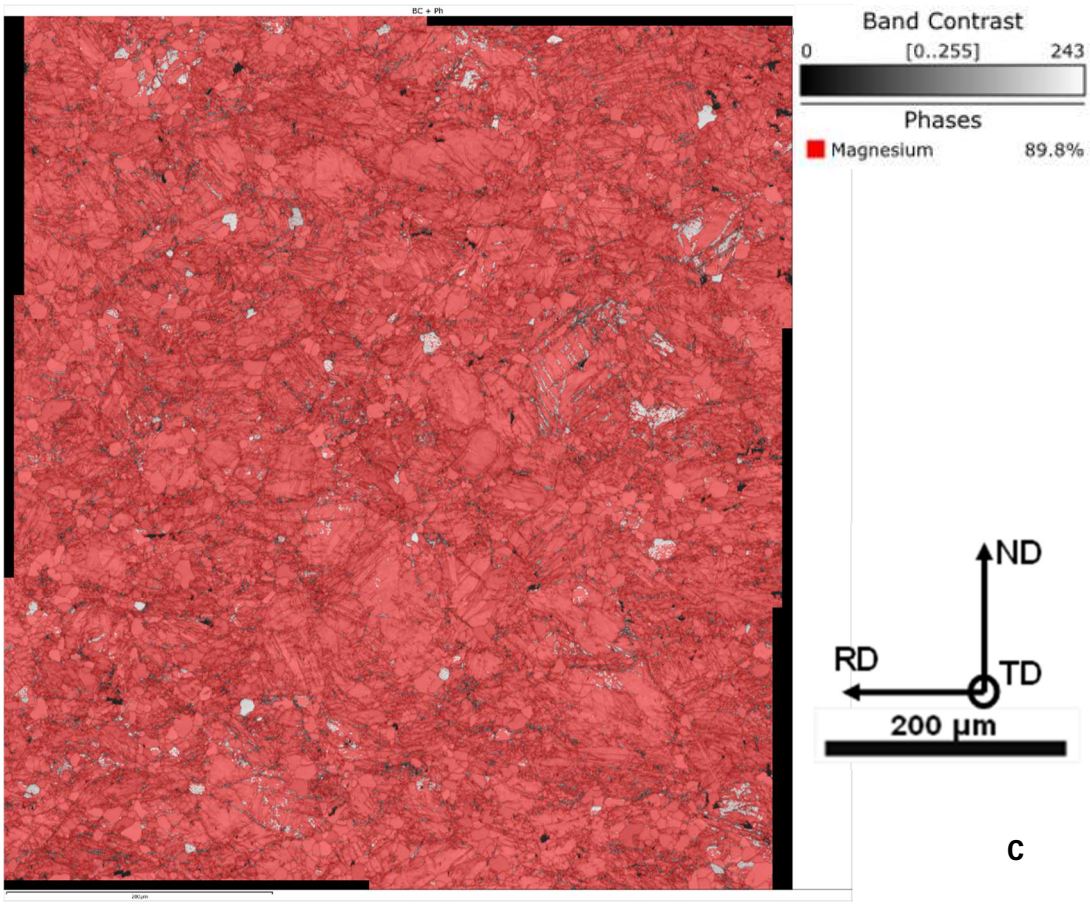
BC + Ph
Band Contrast
0 [0..255] 243
Phases
Magnesium 89.8%
ND
RD
TD
200 µm

c

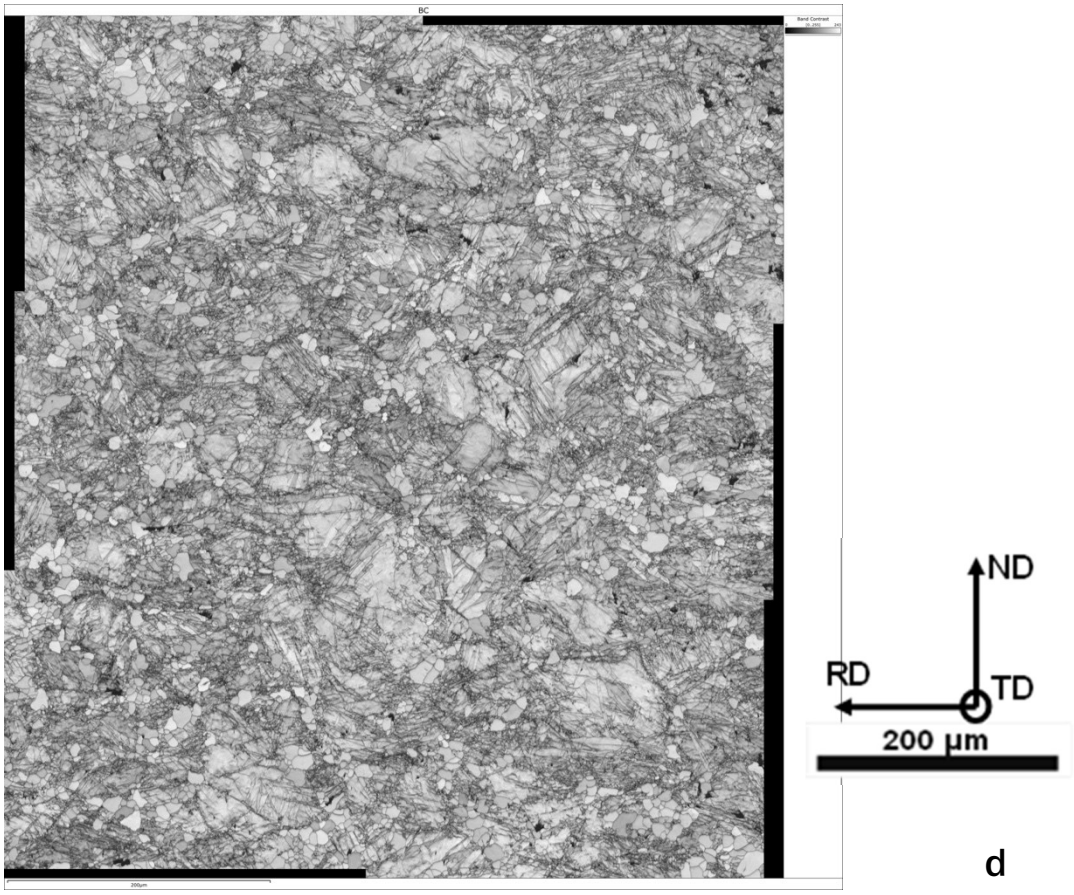
BC
ND
RD
TD
200 µm

d

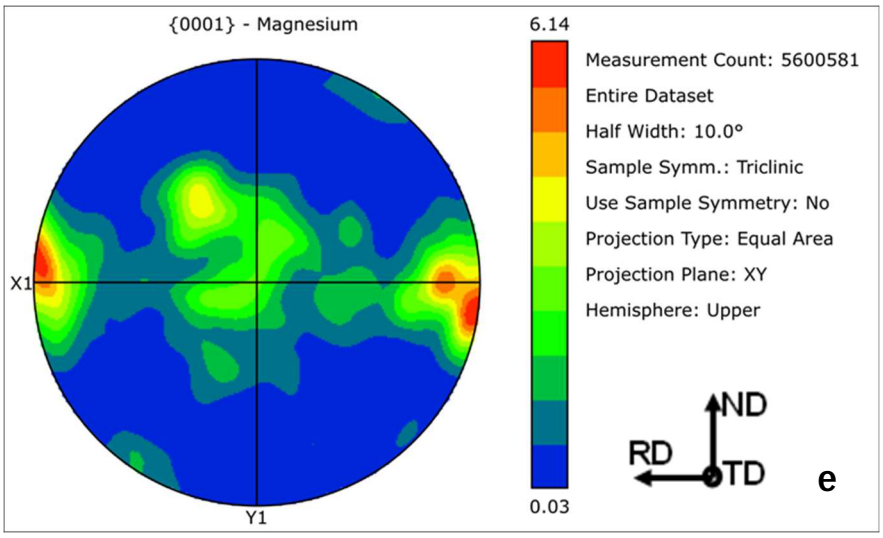
{0001} - Magnesium
6.14
0.03
Measurement Count: 5600581
Entire Dataset
Half Width: 10.0°
Sample Symm.: Triclinic
Use Sample Symmetry: No
Projection Type: Equal Area
Projection Plane: XY
Hemisphere: Upper
X1
Y1
ND
RD
TD

e

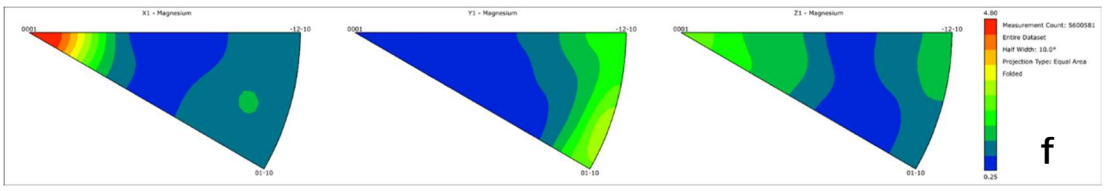
X1 - Magnesium
Y1 - Magnesium
Z1 - Magnesium
Measurement Count: 5600581
Entire Dataset
Half Width: 10.0°
Projection Type: Equal Area
Folded

f

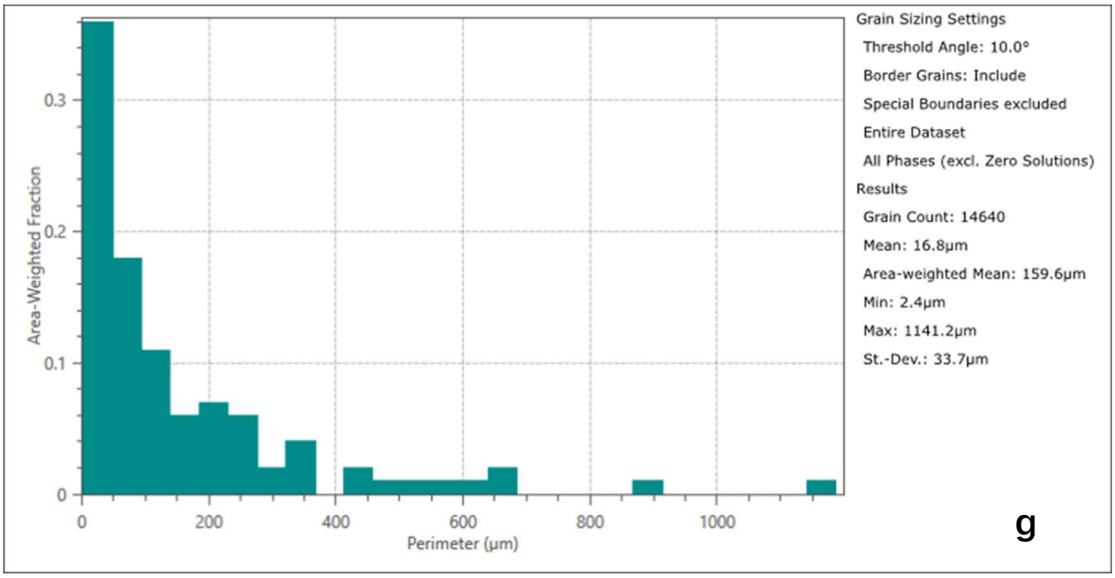

Figure 4-71 The EBSD result of the 1620s annealed 2D compressed Mg-0.2Ca-0.3Zn specimen: (a) The inverse pole figure map and grain boundaries, (b) The grain boundaries and the special grain boundaries, (c) The band contrast and the phase analysis, (d) The band contrast, (e) The pole figure, (f) The inverse pole figures, (g) Grain size distribution expressed as grain boundary perimeter

Figure 4-72 shows the EBSD results of the same specimen after 980s annealing. The temperature of the specimen at that time point was 325℃. With only 30s longer annealing and 6℃ temperature difference, the microstructure of the 2D compressed specimen exhibited obvious evolution which was very different to the 1D compressed specimen at this stage. The IPF map indicated that (shown in Figure 4-72(a)) the specimen experienced rapid grain growth during the annealing. Across the whole map, not just the existing recrystallized grains showed obvious grain growth (e.g. from around $10\mu m$ to about $40\mu m$) but also many rapid-growth new recrystallized grains were found (e.g. from $0\mu m$ to about $20\mu m$). The white circles in Figure 4-72(a) marked some of the areas which had such rapid-growth grains. At this stage, the fast-growing recrystallized grains were not just from shear bands but also from twins. The average grain size of the specimen also slightly increased from $16.8\mu m$ to $18.8\mu m$ (shown in Figure 4-72(g)). The changes in the twin boundary fractions also reflected microstructure evolution. Figure 4-72(b) shows that the boundary fraction of the tensile twins, compressive twins and double twins all decreased from 43.4% to 24.1%, 1.3% to 0.9% and 2.3% to 2.1%, respectively. For the low-angle grain boundaries and the high-angle grain boundaries, it is worth noting that the grain boundary identification was affected by the oxidized layer i.e. the irregular accumulated high-angle grain boundaries in the map (shown in yellow in Figure 4-72(b)). The most significant change

was from the pole figure and IPF (shown in Figure 4-72(e) and (f)). Due to recrystallization and the grain growth happening throughout the entire scanned area, the texture started to show a "weakened RE-texture" in the pole figure i.e. the grain orientation started to show a random-like distribution. The value of the maximum pole intensity also showed a notable reduction from 6.1 to 4.2. Another notable point of the changes in the pole figure was that the grain orientation distribution was not completely random but had a range which diffused about 30° around the TD. The intensity of the weak peak which was mentioned before close to the TD was further enhanced from 3.7 to 4.1.

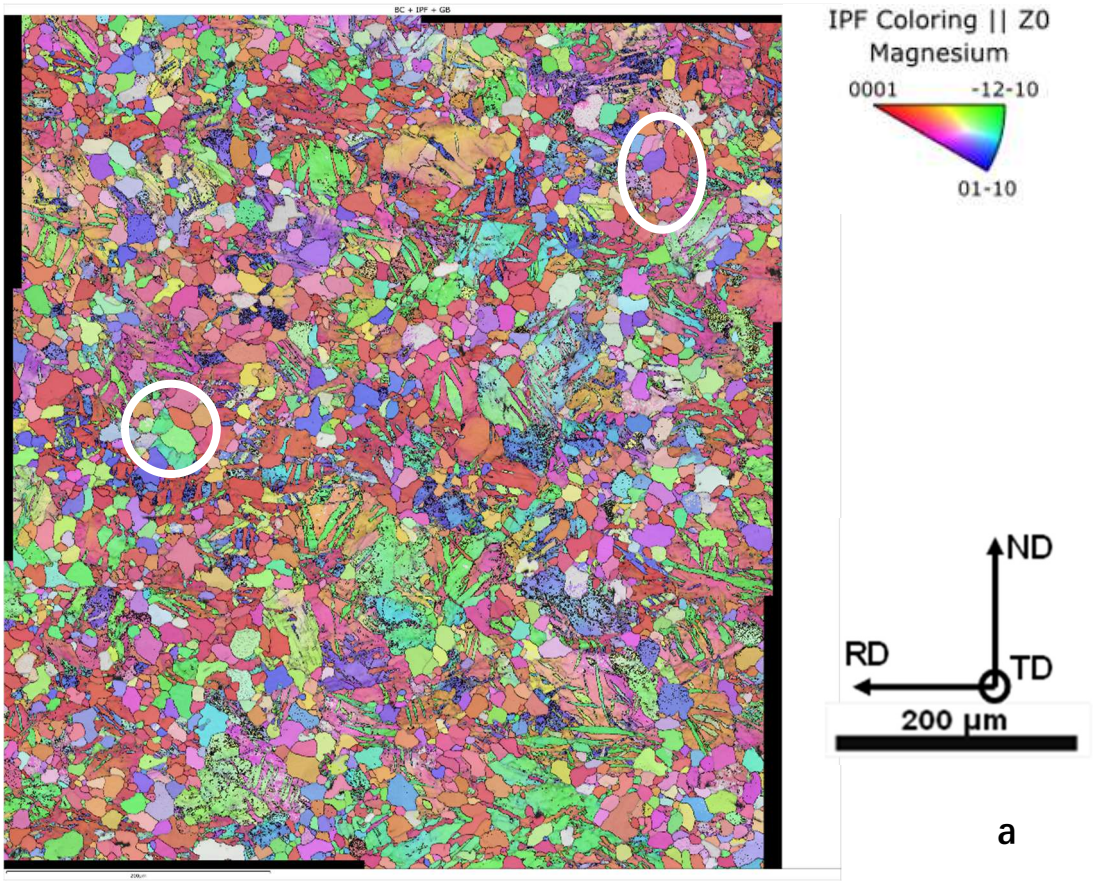

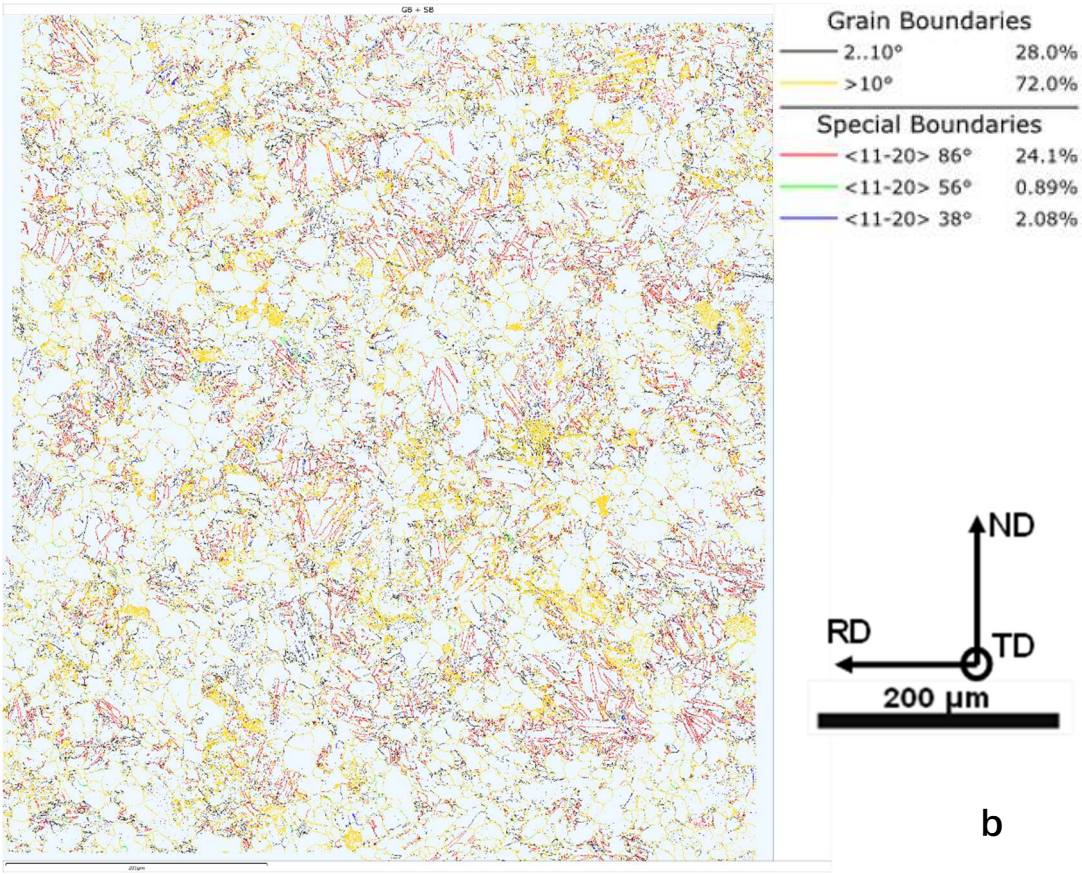
GB + SB
Grain Boundaries
2..10° 28.0%
>10° 72.0%
Special Boundaries
<11-20> 86° 24.1%
<11-20> 56° 0.89%
<11-20> 38° 2.08%
ND
RD
TD
200 µm

b

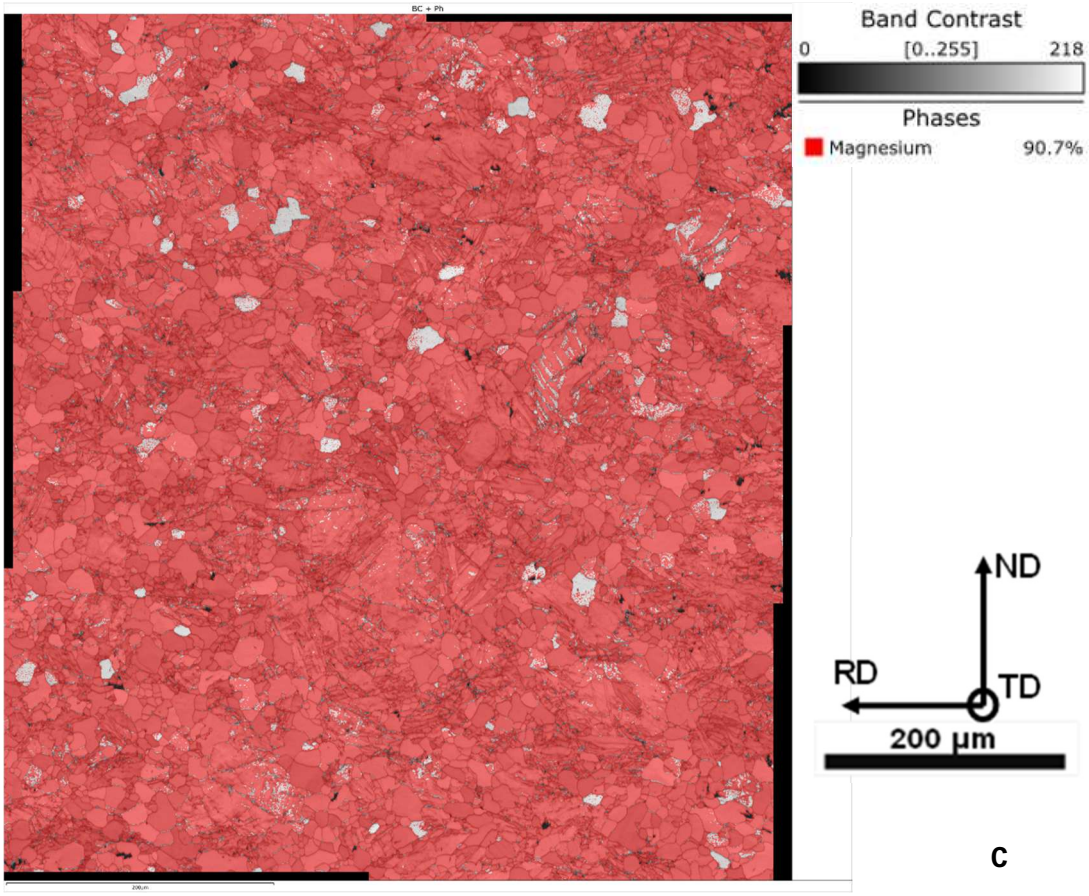
BC + Ph
Band Contrast
0 [0..255] 218
Phases
Magnesium 90.7%
ND
RD
TD
200 µm

c

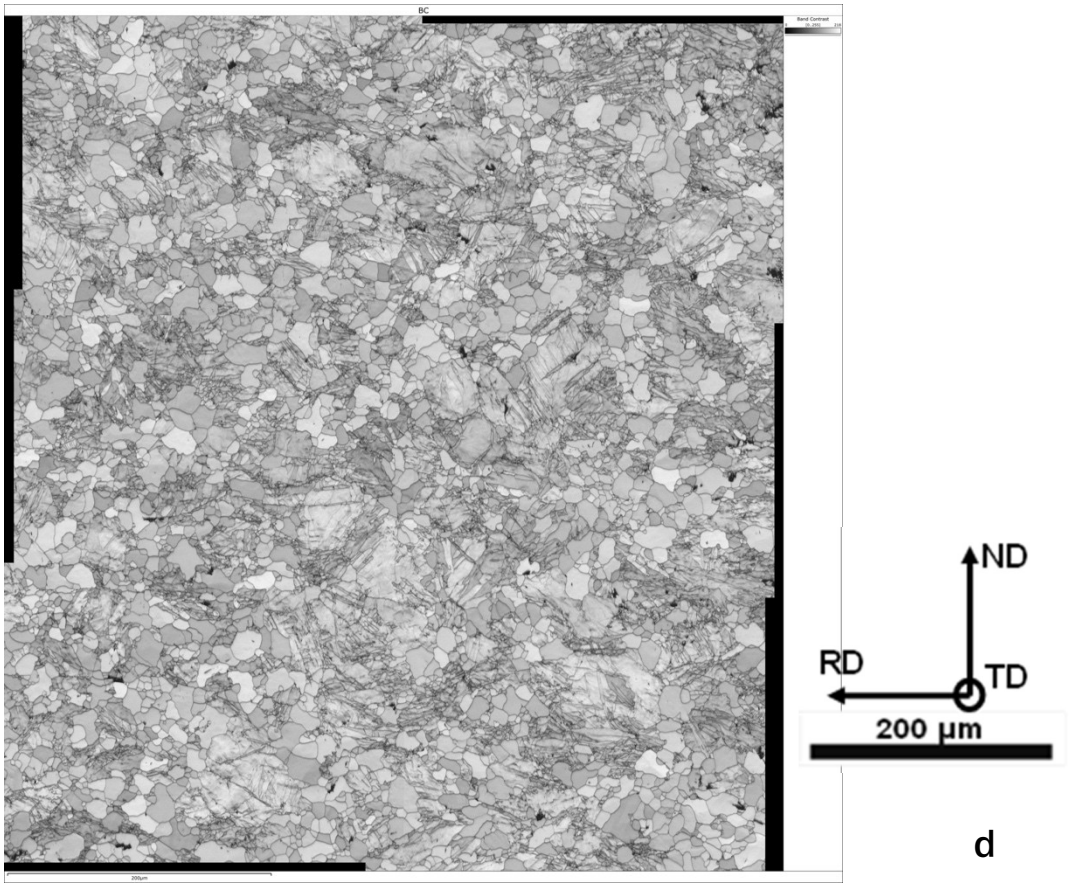
ND
RD
TD
200 µm

d

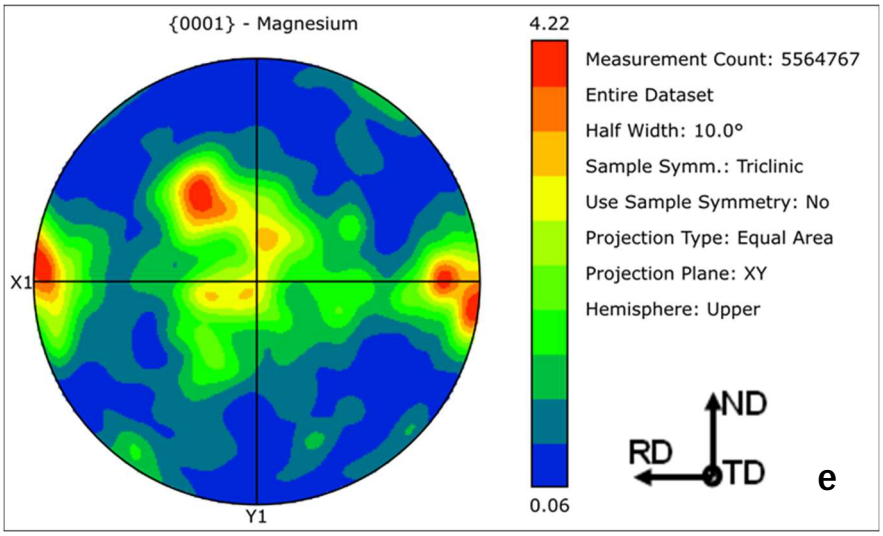
{0001} - Magnesium
4.22
0.06
Measurement Count: 5564767
Entire Dataset
Half Width: 10.0°
Sample Symm.: Triclinic
Use Sample Symmetry: No
Projection Type: Equal Area
Projection Plane: XY
Hemisphere: Upper
X1
Y1
ND
RD
TD

e

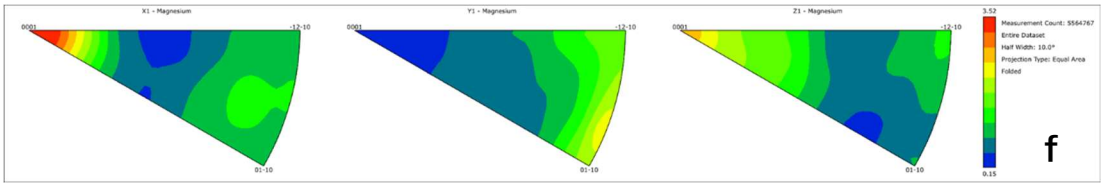

f

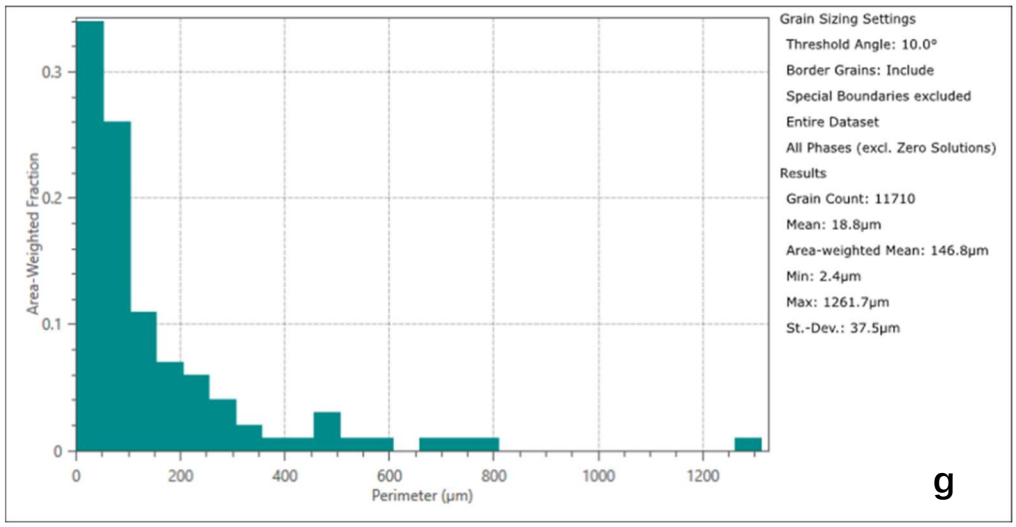

Figure 4-72 The EBSD result of the 1980s annealed 2D compressed Mg-0.2Ca-0.3Zn specimen: (a) The inverse pole figure map and grain boundaries, (b) The grain boundaries and the special grain boundaries, (c) The band contrast and the phase analysis, (d) The band contrast, (e) The pole figure, (f) The inverse pole figures, (g) Grain size distribution expressed as grain boundary perimeter

After 2370s annealing, the EBSD results (shown in Figure 4-73) of the sample indicates that the recrystallization was still slow at this stage. The highest temperature of the specimen during the annealing process was 330℃. The information from Figure 4-73(a) indicates that the grain growth of the recrystallized grains was very limited, which was only observed on a few grains. And the nucleation of new grains was hard to find. The value of the average grain size showed the corresponding change which increased from 18.8μm to 21.3μm (shown in Figure 4-73(g)). The changes in the boundary fraction also proved that the evolution of the microstructure was slow. Figure 4-73(b) shows the fluctuation of the value for the boundary fractions. The boundary fraction of the tensile twins, compressive twins and double twins was changed from 24.1% to 35.0%, 0. 9% to 1.2% and 2.08% to 2.10%, respectively. Simultaneously, the fractions of the low-angle grain boundary and the high-angle grain boundary were changed from 28.0% to 27.6% and from 72.0% to 72.4%, respectively. The dramatic increase in the value of the tensile twins was affected by the reduction of the miss-identification. The EBSD results of the last stage contained the information from the oxidized layer on the specimen surface. And the EBSD results of the specimen at this stage were more accurate. For the grain orientation distribution, changes were found compared to the last stage in the pole figure and IPF (shown in Figure 4-73(e) and (f)). A much higher maximum pole intensity than the last stage was found, which increased from 4.2 to 4.6. Meanwhile, the reduction of the intensity of the weak peak close to the TD was also observed. Considering the influence of the oxidized layer in the previous stage, a higher number of grains were identified, and fewer miss-identifications were

made in this stage. The unusual variation shown in the pole figure was acceptable.

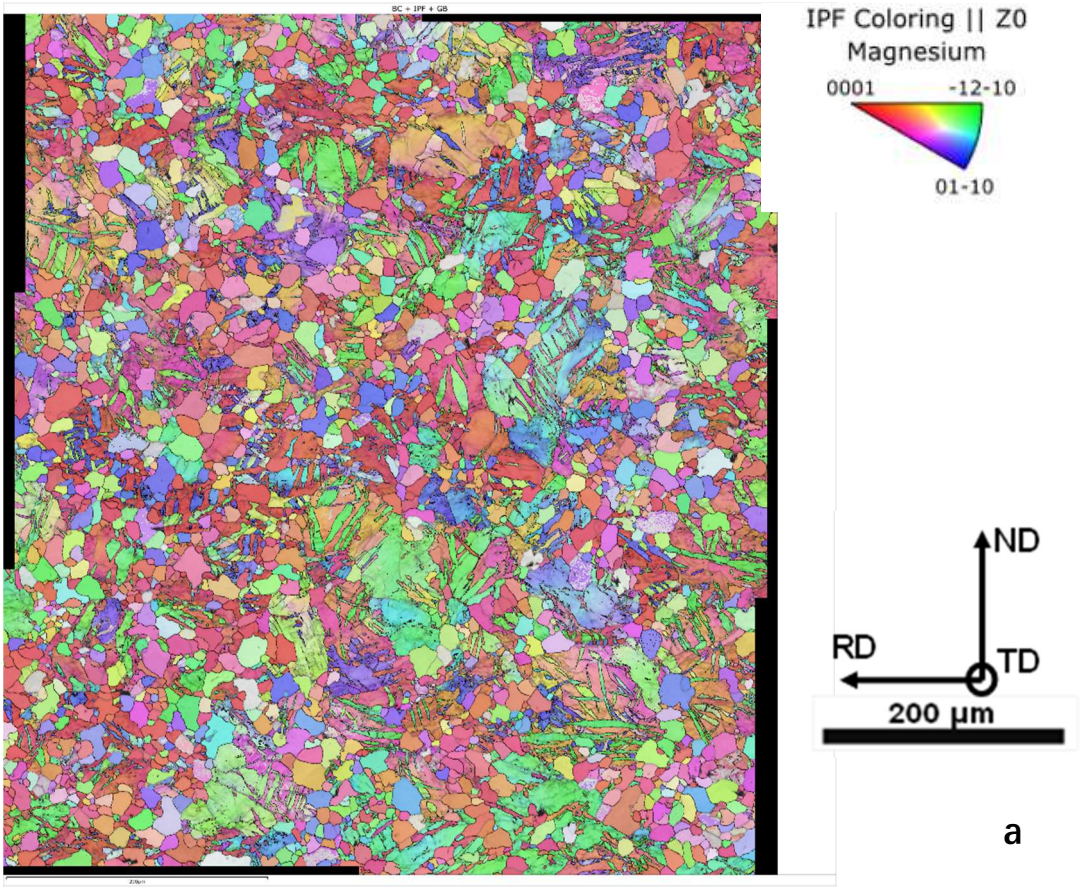

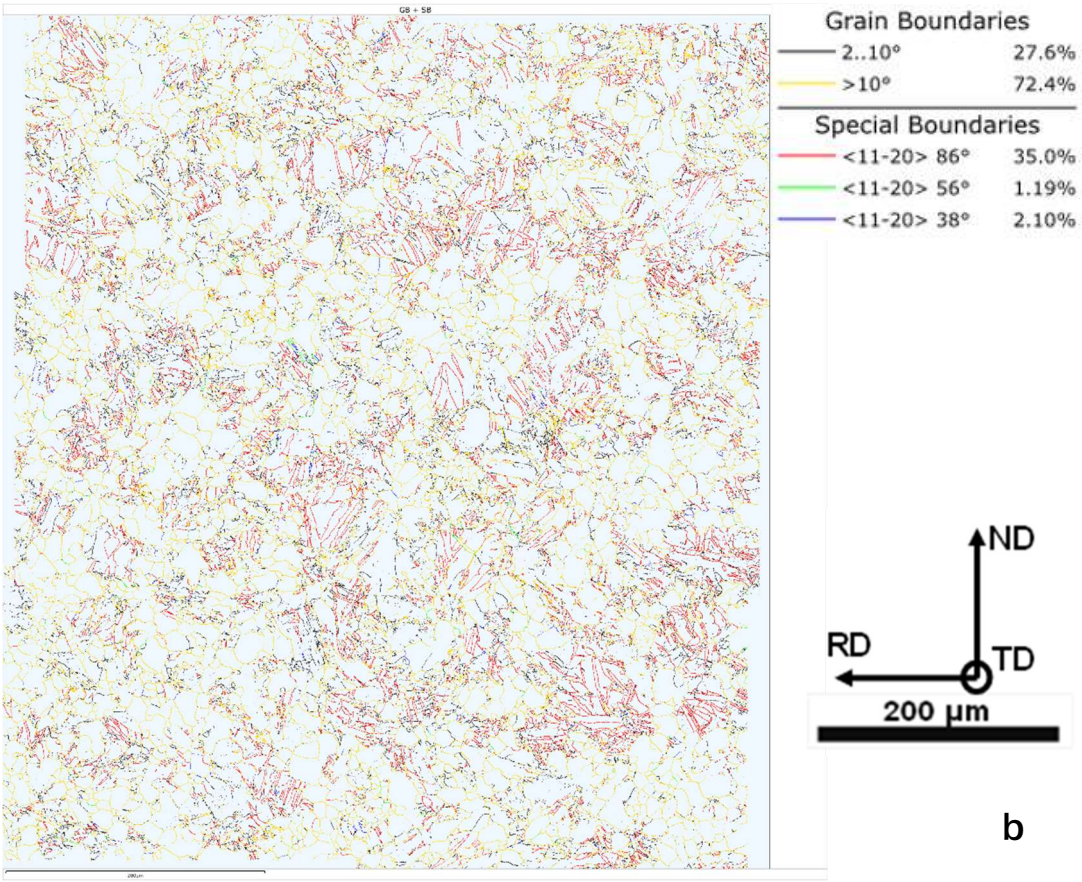

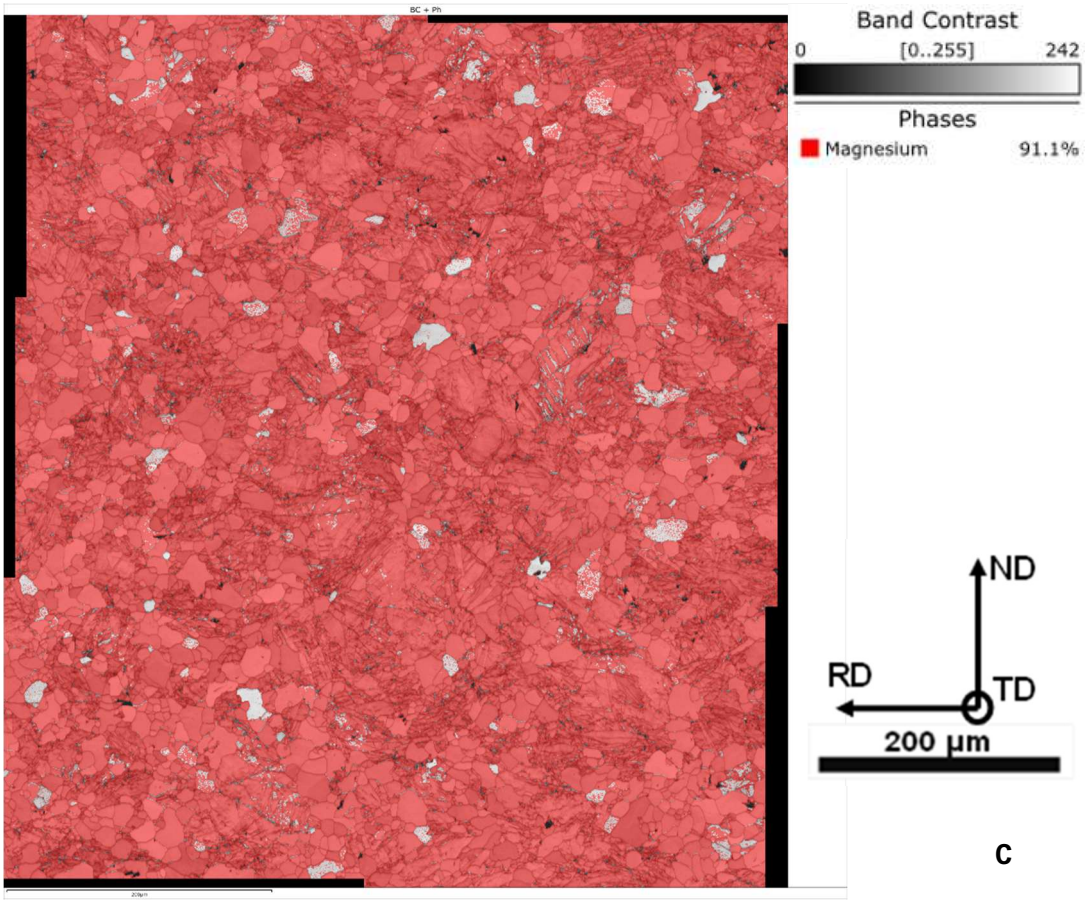
BC + Ph
Band Contrast
0
[0..255]
242
Phases
Magnesium
91.1%
ND
RD
TD
200 µm

c

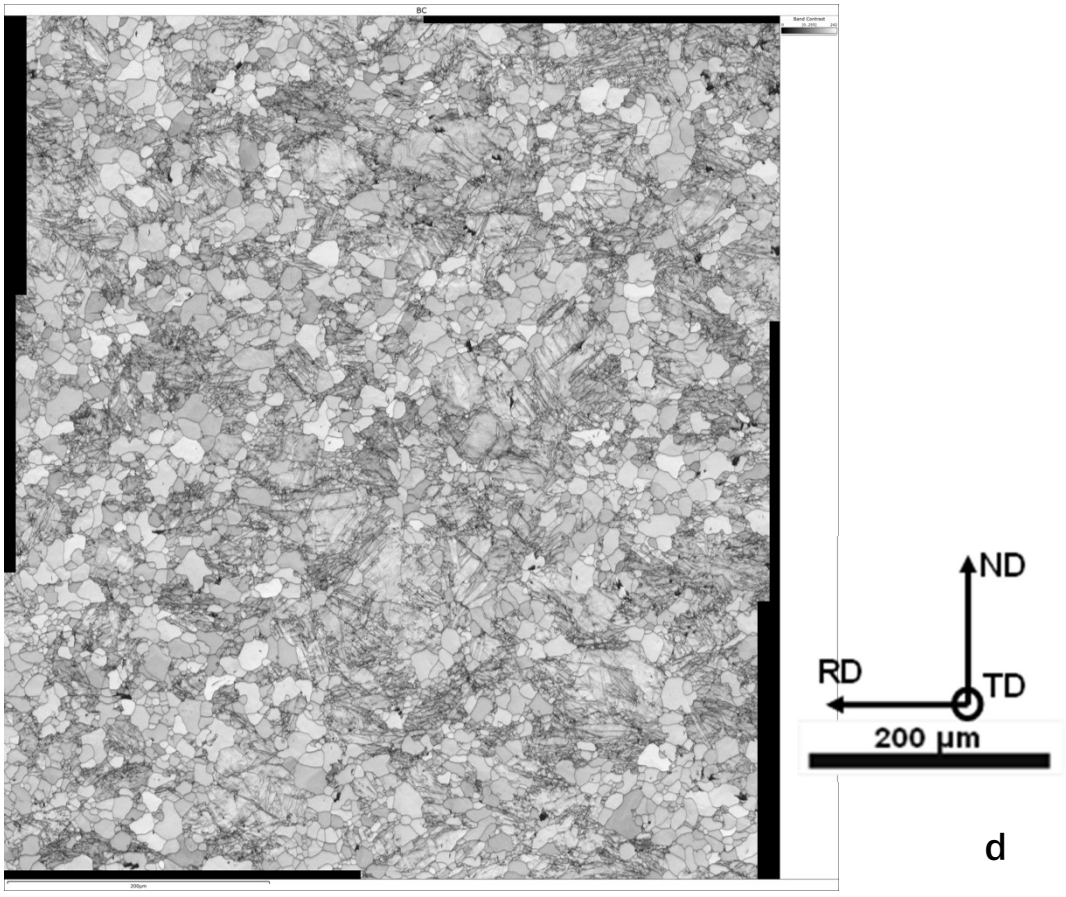
BC
ND
RD
TD
200 µm

d

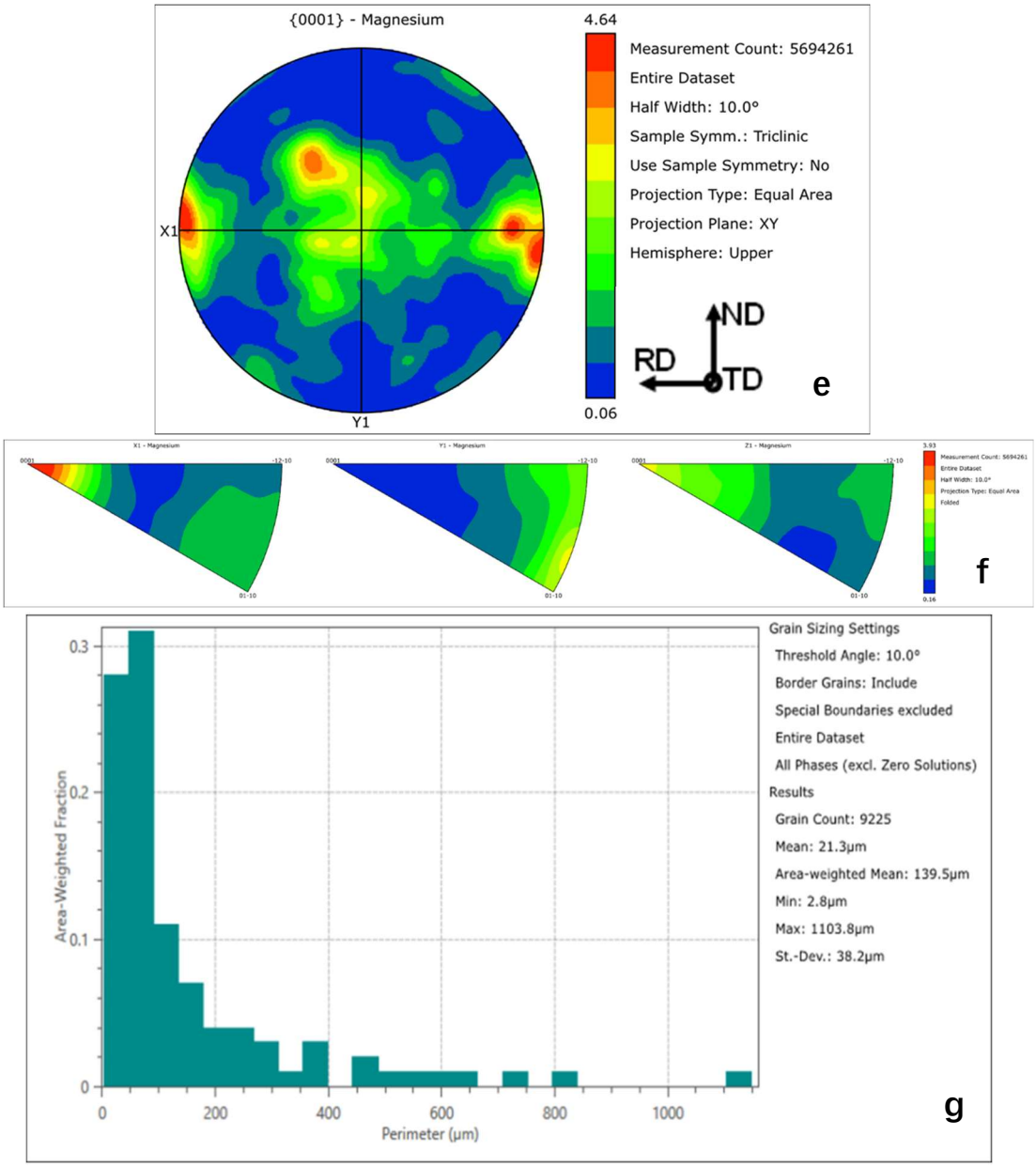

Figure 4-73 The EBSD result of the 2370s annealed 2D compressed Mg-0.2Ca-0.3Zn specimen: (a) The inverse pole figure map and grain boundaries, (b) The grain boundaries and the special grain boundaries, (c) The band contrast and the phase analysis, (d) The band contrast, (e) The pole figure, (f) The inverse pole figures, (g) Grain size distribution expressed as grain boundary perimeter

After annealing for 2790s, obvious changes were observed during the recrystallization from the EBSD results (shown in Figure 4-74). And this was the last group of the EBSD results for the 2D compressed Mg-0.2Ca-0.3Zn (at%) specimen. The temperature of the specimen at that time point was 334℃. Figure 4-74(a) shows the IPF map of the scanned area. It was very clear that the specimen experienced fast recrystallization during the last annealing time. The difference of the annealing time between the two steps was just 30s longer annealing and 4℃ higher of the temperature.

Almost the whole scanning section showed a recrystallized structure. Only a few original grains were found in the IPF map (marked with the white circles). The recrystallization specimen showed a much more uniform microstructure compared to that of the original ingot. Figure 4-74(g) shows that the average grain size of the specimen was 35.1μm. Combining Figure 4-74(a), (c) and (d), it was found that the non-indexed grains or partially identified grains had different colour i.e. the direction of these grains was quite random. The other point is that the darker the recrystallized grains shown on the band contrast map, the closer the direction of the grains to the TD are. The information about the grain boundaries (shown in Figure 4-74(b)) also presented a corresponding result after the recrystallization. The boundary fraction of the tensile twins, compressive twins and double twins dramatically decreased from 35.0% to 5.0%, 1.2% to 0.2% and 2.1% to 0.1%, respectively. Meanwhile, following the recrystallization, the boundary fraction of the low-angle grain boundary decreased from 27.6% to 11.3%, while that of the high-angle grain boundary increased from 72.4% to 88.7%. The pole figure and IPF (shown in Figure 4-74(e) and (f)) also presented a significant result of the grain orientation distribution. A very random distributed grain orientations were shown in the pole figure. The directions of the recrystallized grains were found diffusing around the TD with a quite large angle (about 45°). The original peaks on the two sides of the RD had almost vanished. And the direction of the new peak was changed to the TD in the pole figure. The maximum value of the pole figure showed a further reduction which reached 3.4.

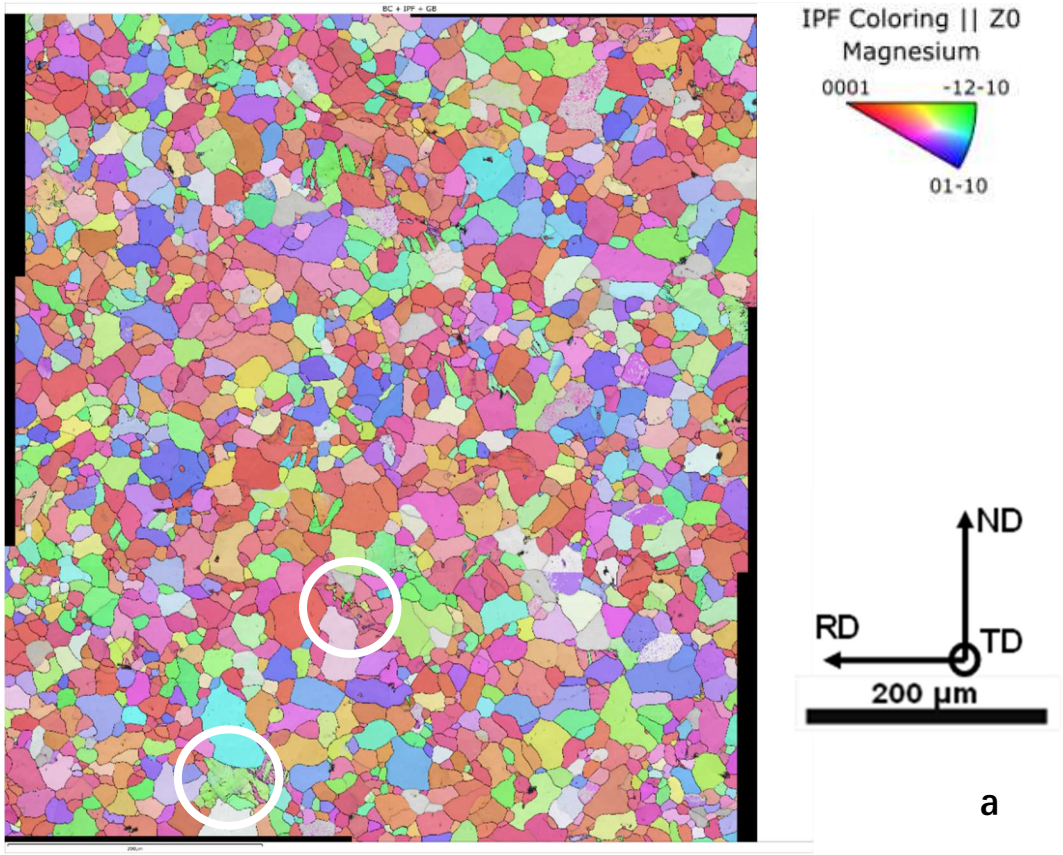

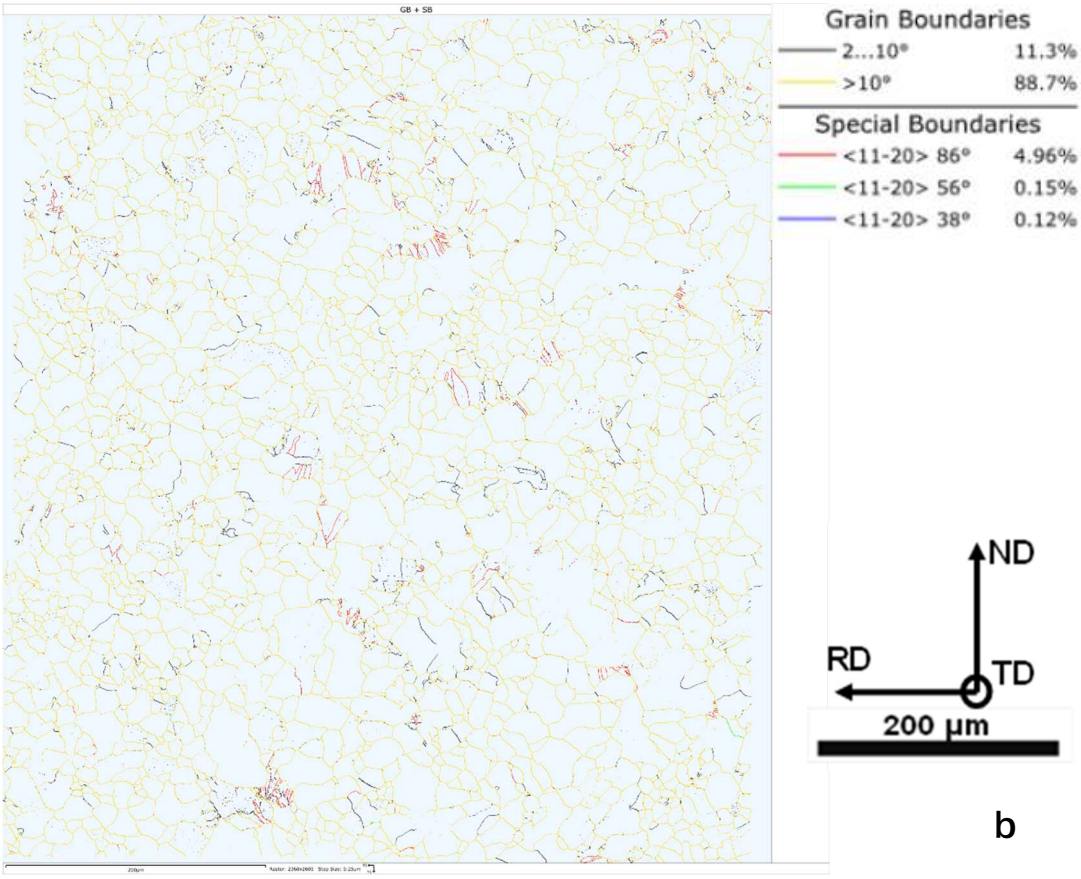
GB + SB
Grain Boundaries
2...10° 11.3%
>10° 88.7%
Special Boundaries
<11-20> 86° 4.96%
<11-20> 56° 0.15%
<11-20> 38° 0.12%
ND
RD
TD
200 µm

b

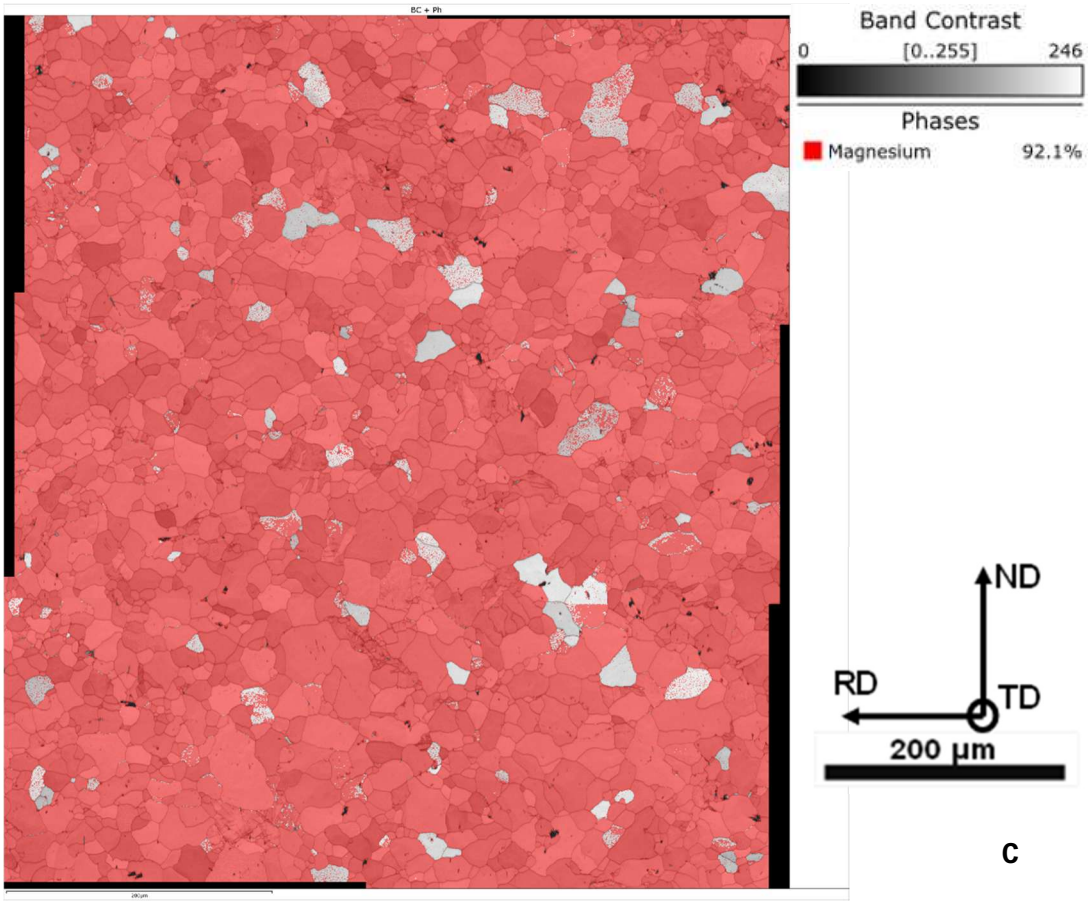
BC + Ph
Band Contrast
0 [0..255] 246
Phases
Magnesium 92.1%
ND
RD
TD
200 µm

c

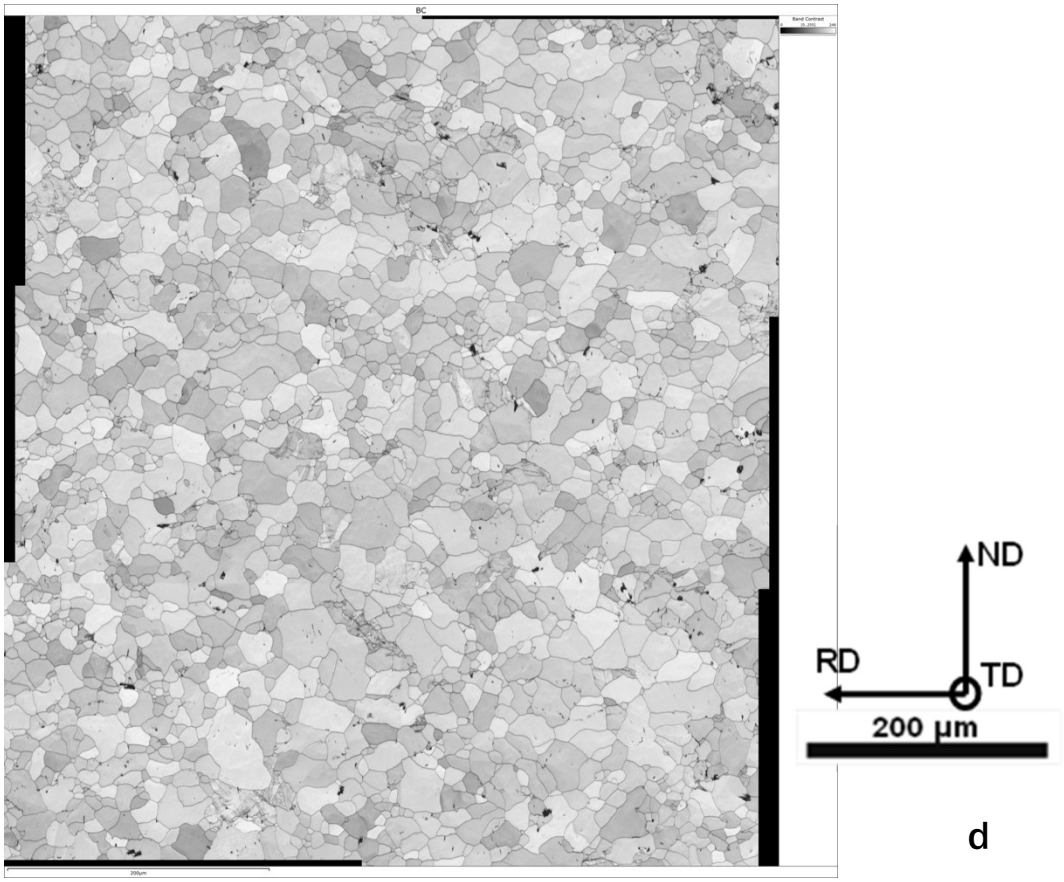
BC
ND
RD
TD
200 µm

d

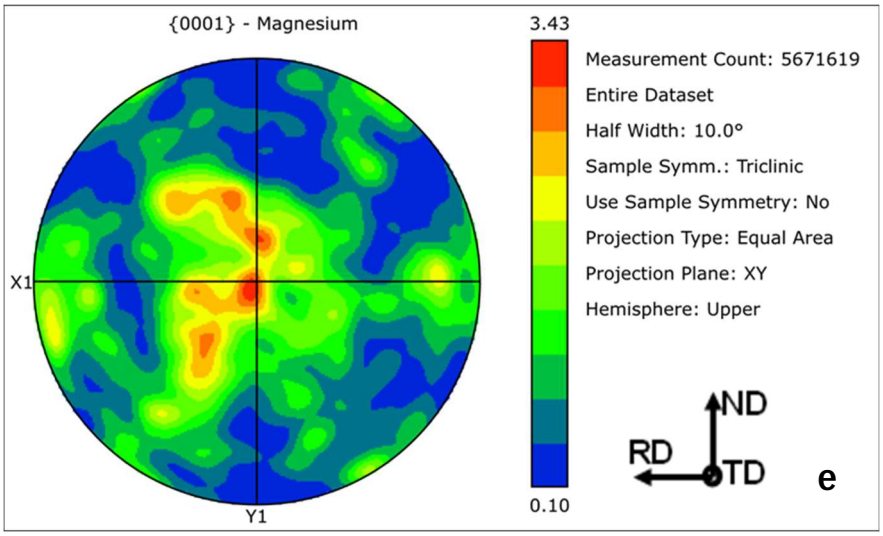
{0001} - Magnesium
3.43
0.10
Measurement Count: 5671619
Entire Dataset
Half Width: 10.0°
Sample Symm.: Triclinic
Use Sample Symmetry: No
Projection Type: Equal Area
Projection Plane: XY
Hemisphere: Upper
X1
Y1
ND
RD
TD

e

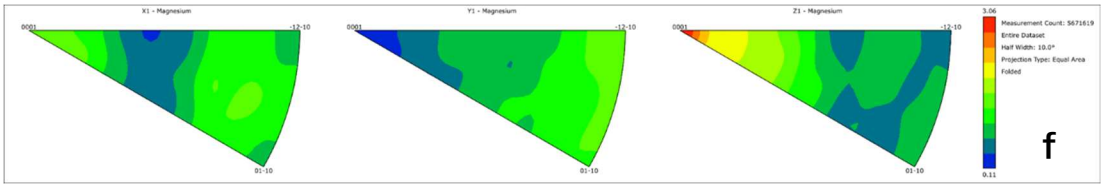
X1 - Magnesium
Y1 - Magnesium
Z1 - Magnesium
0001
-12-10
01-10
3.06
0.11
Measurement Count: 5671619
Entire Dataset
Half Width: 10.0°
Projection Type: Equal Area
Folded

f

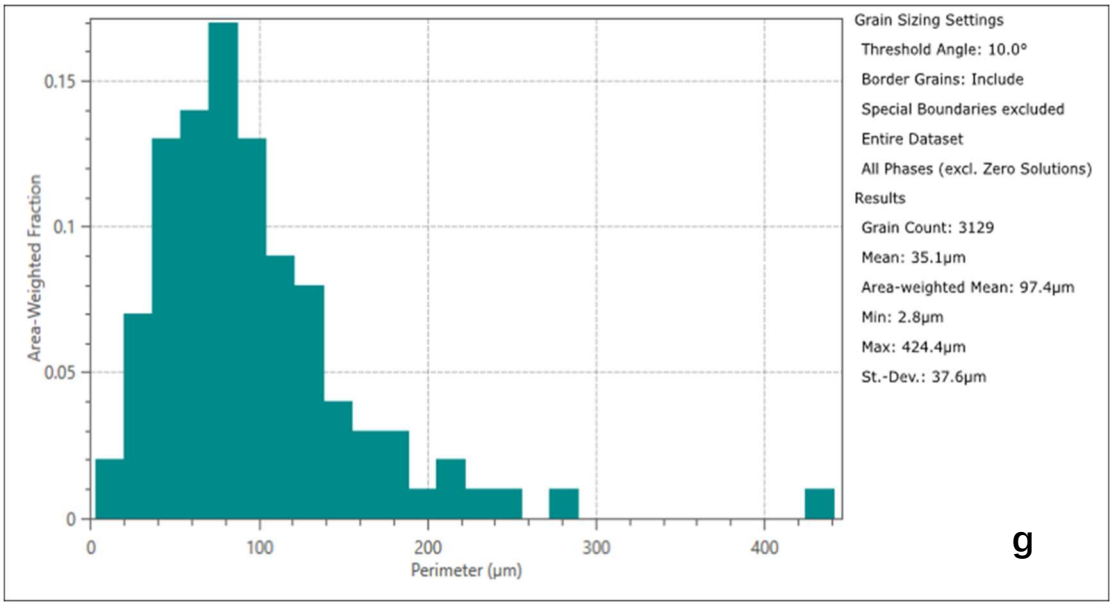

Figure 4-74 The EBSD result of the 2790s annealed 2D compressed Mg-0.2Ca-0.3Zn specimen: (a) The inverse pole figure map and grain boundaries, (b) The grain boundaries and the special grain boundaries, (c) The band contrast and the phase analysis, (d) The band contrast, (e) The pole figure, (f) The inverse pole figures, (g) Grain size distribution expressed as grain boundary perimeter

4.3.2.2.5 The two-direction (2D) compressed Mg-0.1Ca-0.4Zn (at%) specimen

Figures 4-75 to 4-81 show the EBSD results of the 2D compressed Mg-0.1Ca-0.4Zn (at%) specimen from the as-compressed state to the recrystallized state. The as-compressed specimen presented a similar grain morphology as that of the 1D compressed specimen (shown in Figure 4-75(a)) i.e. the size difference between the grains was large. The largest grain had a size of about $100\mu m$ at the bottom of the map, while many small grains were smaller than $3\mu m$ in the top right corner. Figure 4-75(g) indicates that the average grain size of the sample was $11.4\mu m$. The fraction of the shear bands (marked by white circles in Figure 4-75(c)) and fine twins was hard to quantify due to the high density of the non-indexed region in the top right corner of the map (shown in Figure 4-75(c)). However, in the bottom half of the map, the fraction of the shear bands and fine twins was calculated as ~24%. Figure 4-75(b) shows that the boundary fraction of the tensile twin, compressive twin and double twin was 50.3%, 2.2% and 4.2%, respectively. The pole figure of the specimen (Figure 4-75(e) and (f)) showed a typical rolling texture orientation which was aligned with the RD i.e. the orientation of the grains was parallel to the second compression direction of the specimen. Additionally, a few very weak signals were also found diffusing around the TD. The maximum value of the pole figure was 14.

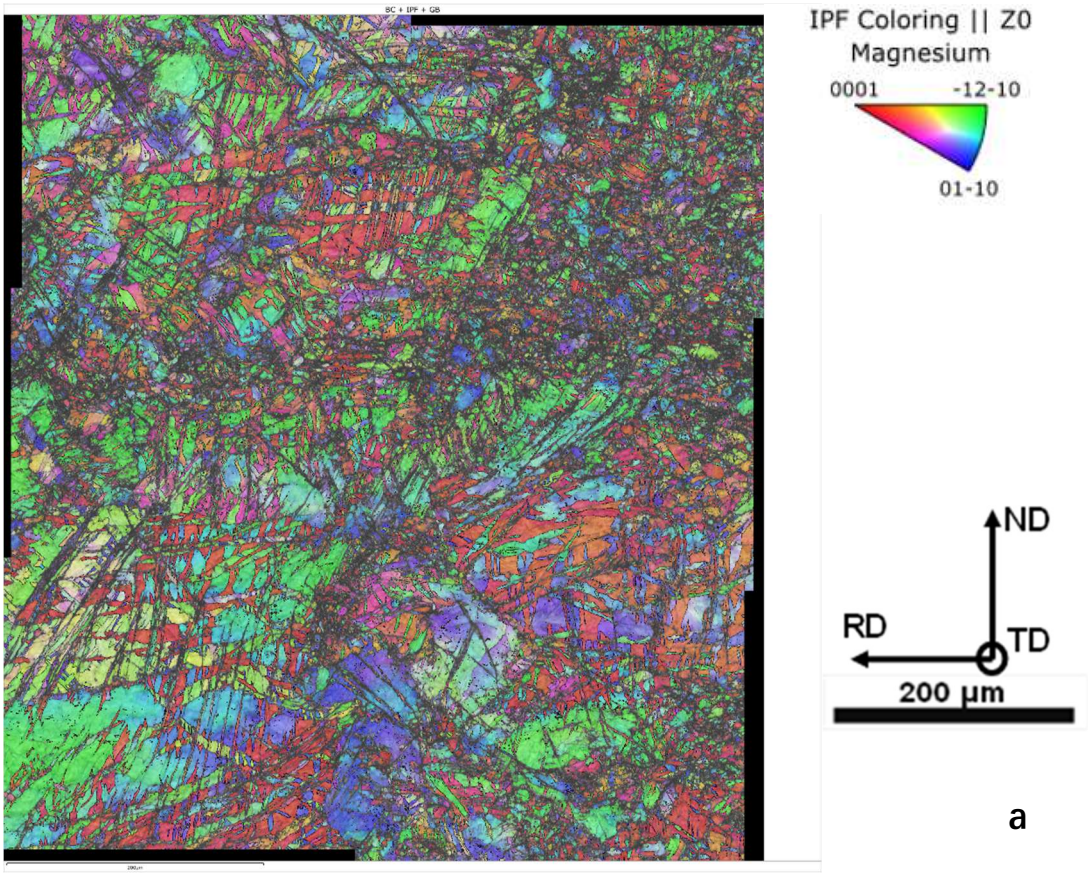
IPF Coloring || Z0
Magnesium
0001
-12-10
01-10
ND
RD
TD
200 µm

a

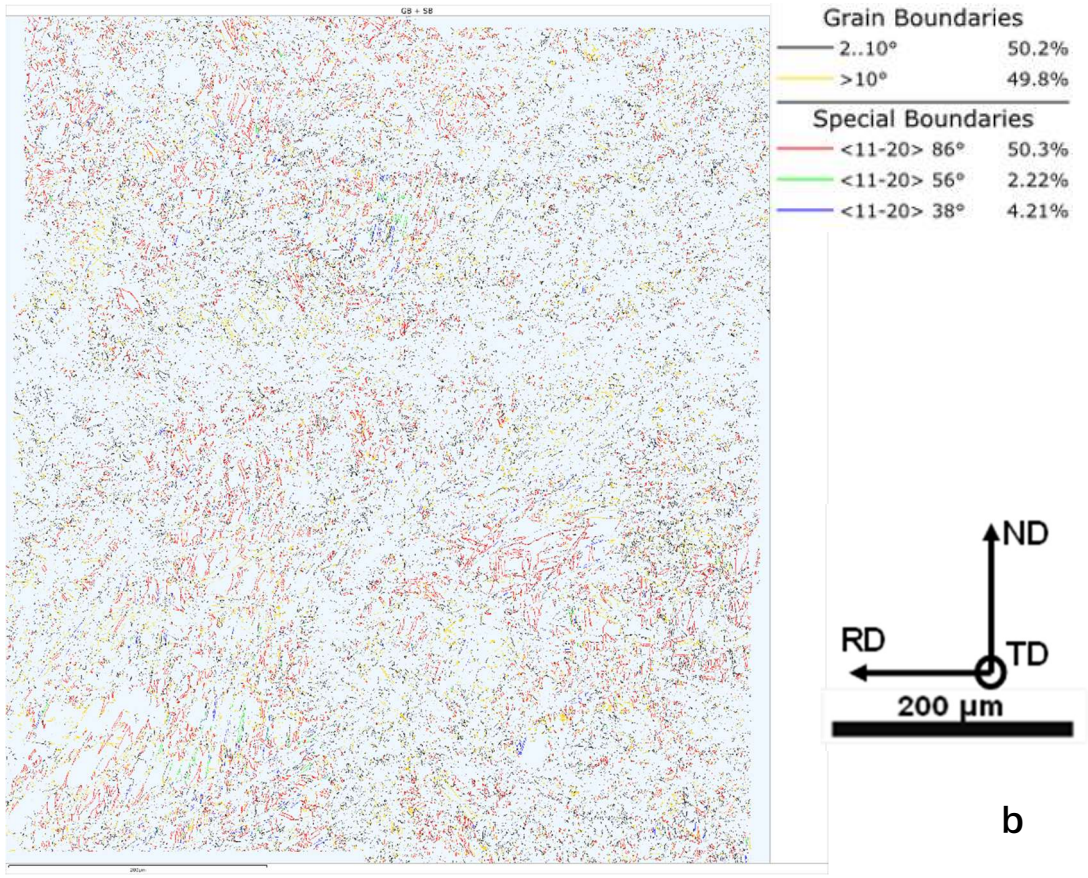
Grain Boundaries
2..10° 50.2%
>10° 49.8%
Special Boundaries
<11-20> 86° 50.3%
<11-20> 56° 2.22%
<11-20> 38° 4.21%
ND
RD
TD
200 µm

b

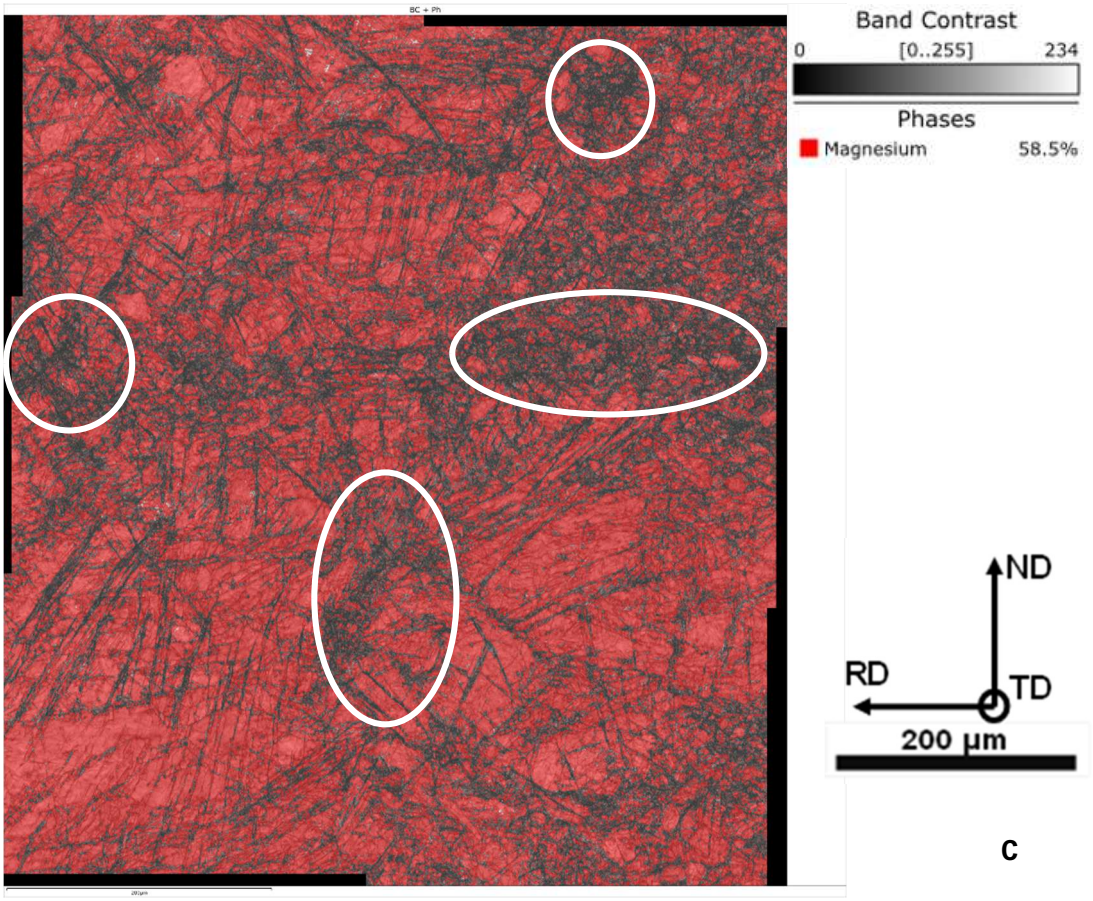
Band Contrast
0
[0..255]
234
Phases
Magnesium
58.5%
ND
RD
TD
200 µm

c

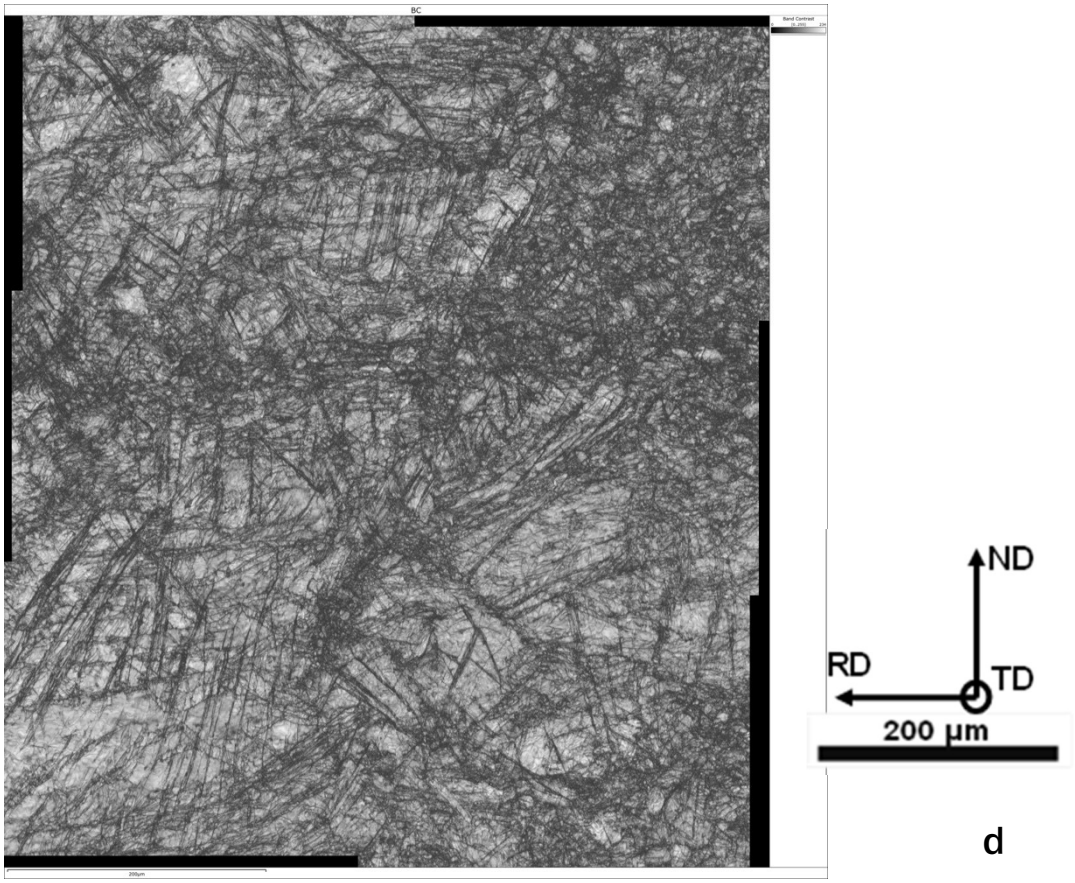
ND
RD
TD
200 µm

d

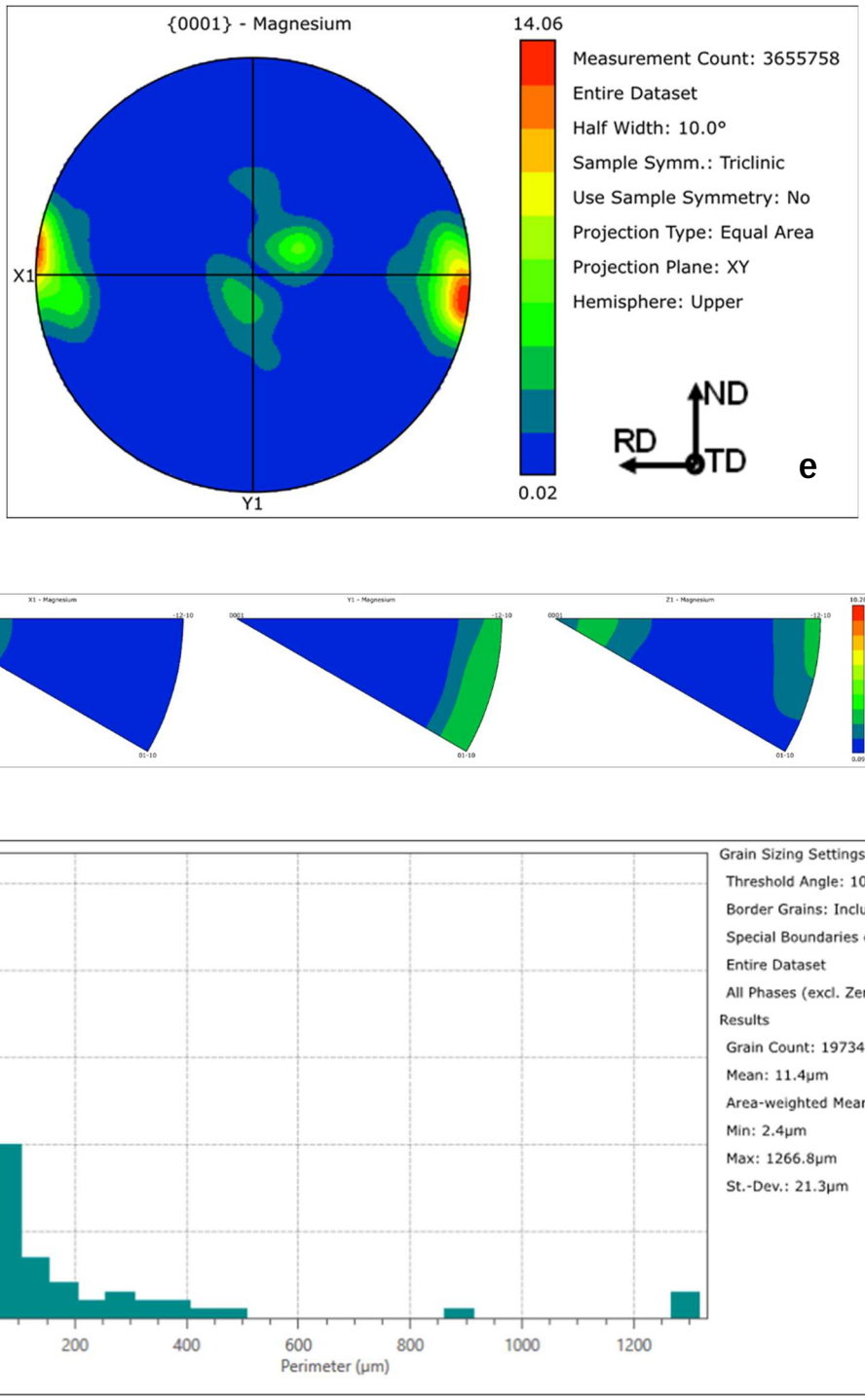

Figure 4-75 The EBSD result of the as-compressed 2D compressed Mg-0.1Ca-0.4Zn specimen: (a) The inverse pole figure map and grain boundaries, (b) The grain boundaries and the special grain boundaries, (c) The band contrast and the phase analysis, (d) The band contrast, (e) The pole figure, (f) The inverse pole figures, (g) Grain size distribution expressed as grain boundary perimeter

In a similar way to the 1D compressed Mg-0.1Ca-0.4Zn (at%) specimen, the 2D compressed specimen showed a recrystallized structure after the 420s annealing. Before 420s, the EBSD results indicated that the recovery happened in the 300s annealed

specimen (shown in Figure 4-76). The temperature of the sample was 186℃ at that stage. Figure 4-76(c) indicates that the fraction of the non-indexed area was dramatically reduced from 41.5% (before annealing) to 29.4% (after 300s annealing). The resolution of the image became better, and the fraction of the twins almost remained the same. Figure 4-76(b) shows that the boundary fraction of the tensile twins, compressive twins and double twins was 50.6%, 2.6% and 5.0%, respectively. Additionally, the average grain size of the specimen also showed limited change from $11.4\mu m$ to $11.2\mu m$ (shown in Figure 4-76(g)). The maximum value of the pole figure at this stage was 12.3 (shown in Figure 4-76(e)), which was 1.7 lower than that of the as-compressed specimen. The grain orientation distribution also did not show any obvious change. All the points mentioned above suggested that the recovery happened in the specimen at this stage. The EBSD results of the 30s, 45s, 60s and 75s annealing (30s, 75s, 135s and 210s heat treatment time in total, respectively) are put in Appendix I and are not discussed in text.

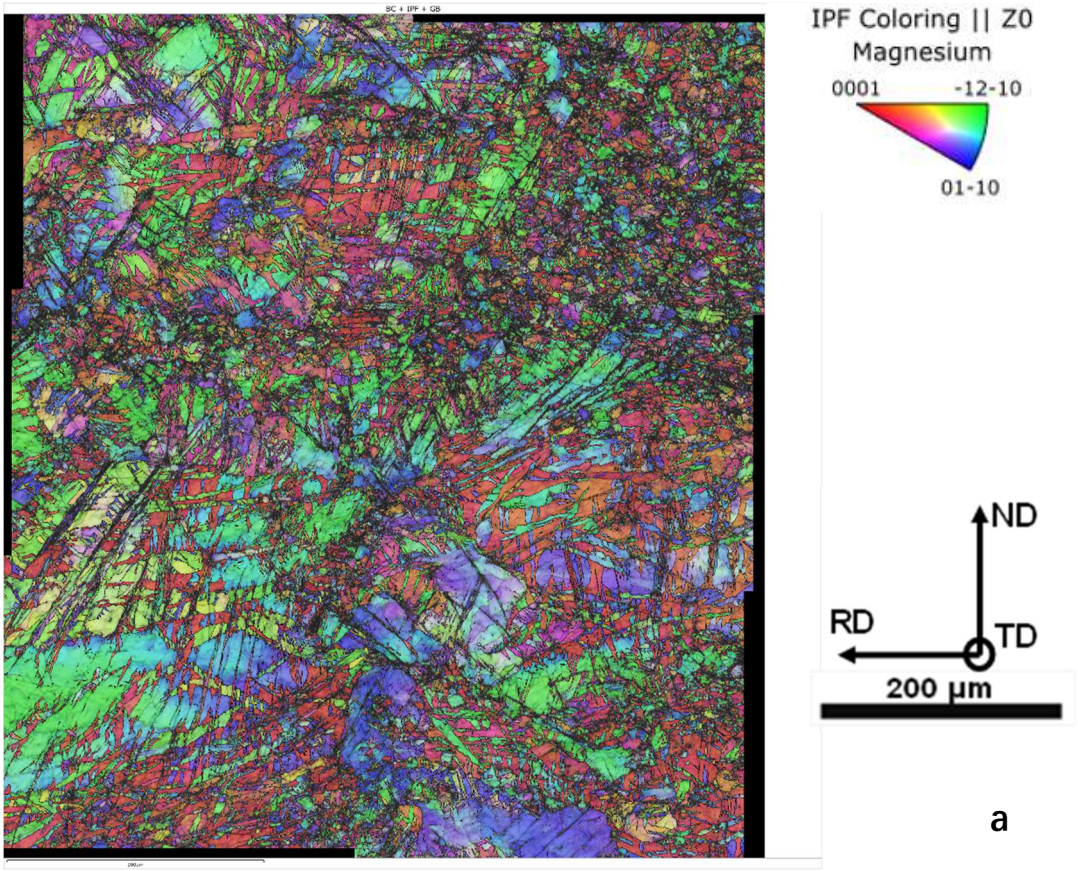

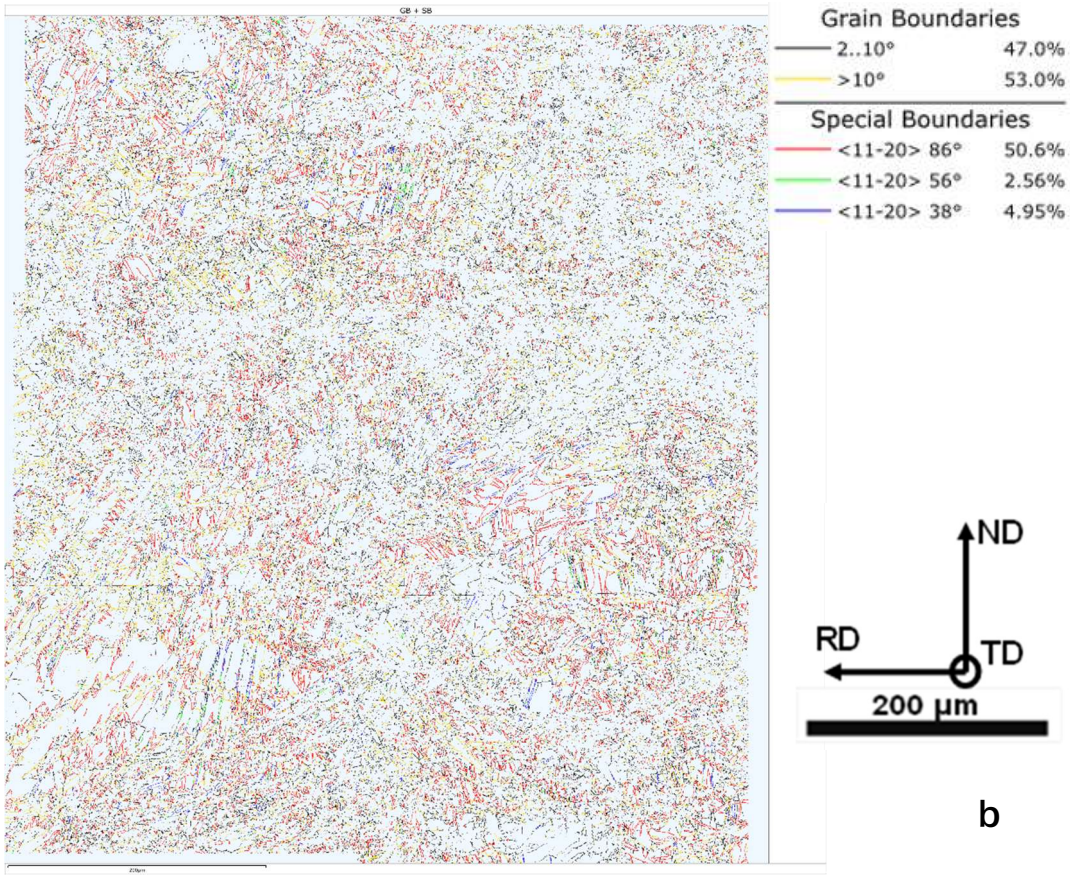
GB + SB
Grain Boundaries
2..10° 47.0%
>10° 53.0%
Special Boundaries
<11-20> 86° 50.6%
<11-20> 56° 2.56%
<11-20> 38° 4.95%
ND
RD
TD
200 µm

b

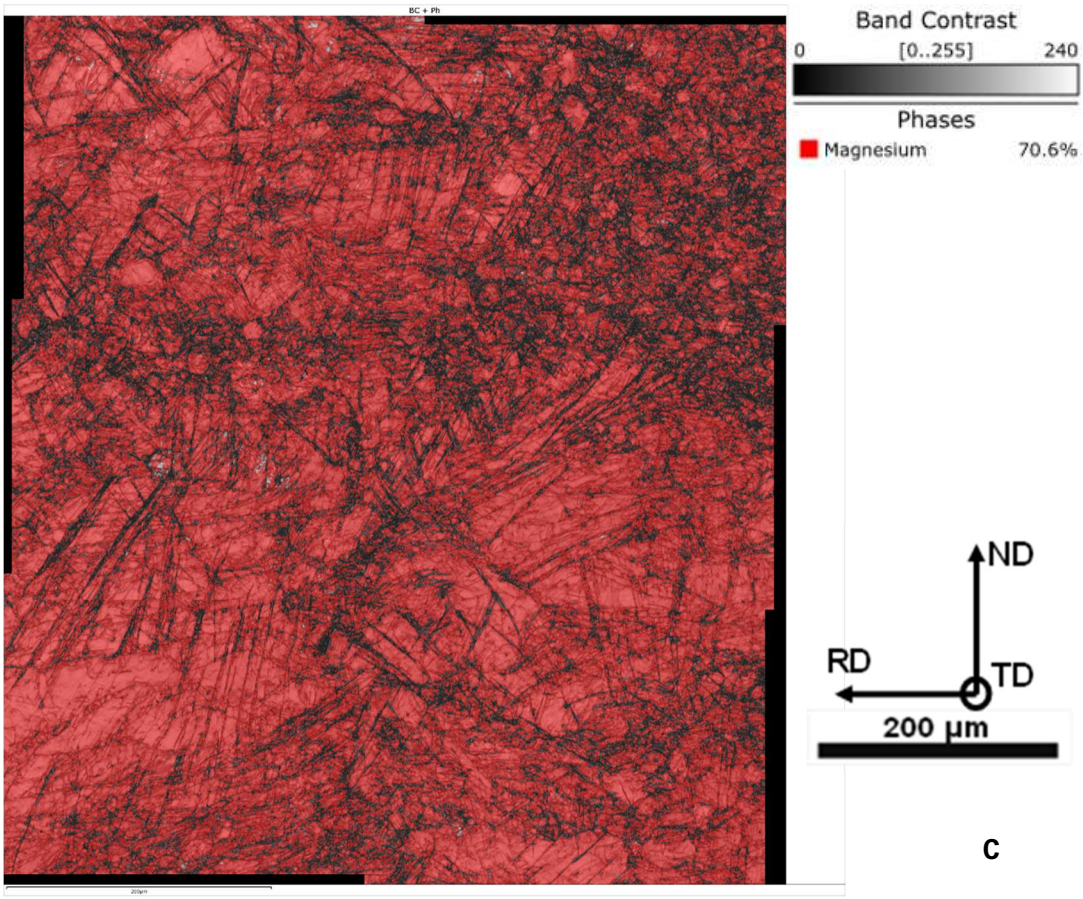
BC + Ph
Band Contrast
0 [0..255] 240
Phases
Magnesium 70.6%
ND
RD
TD
200 µm

c

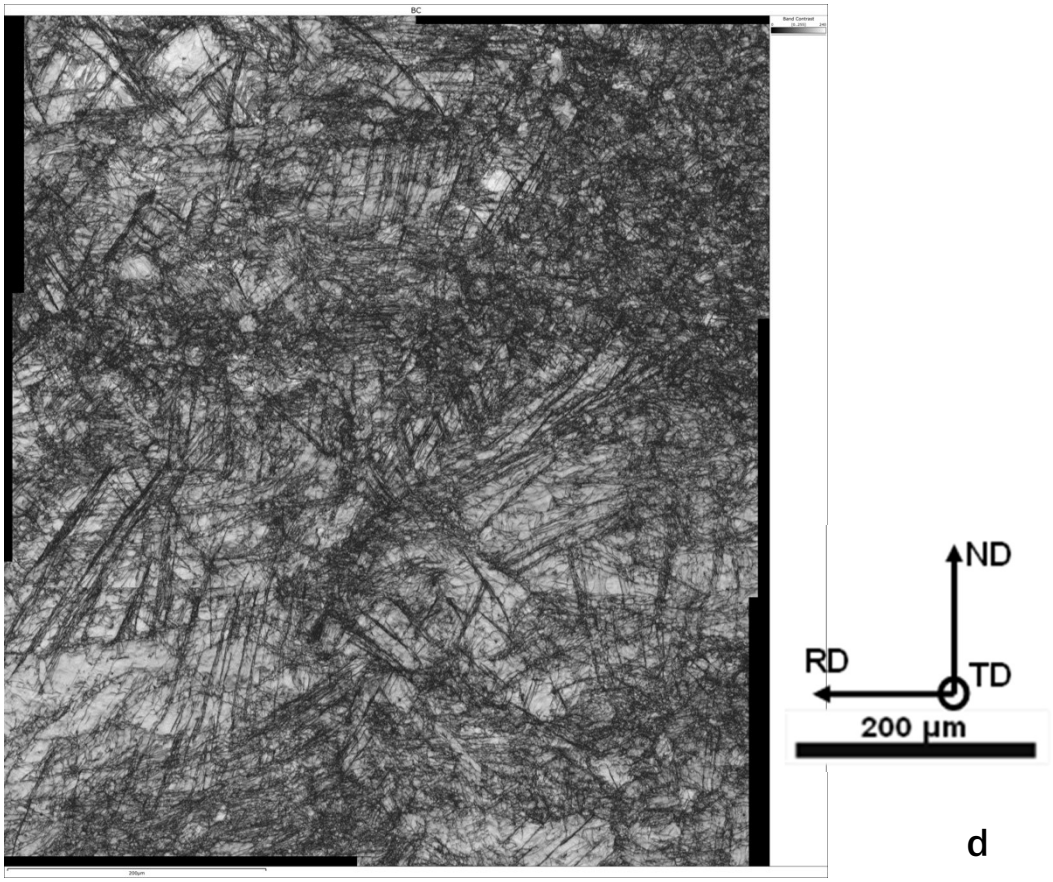
ND
RD
TD
200 µm

d

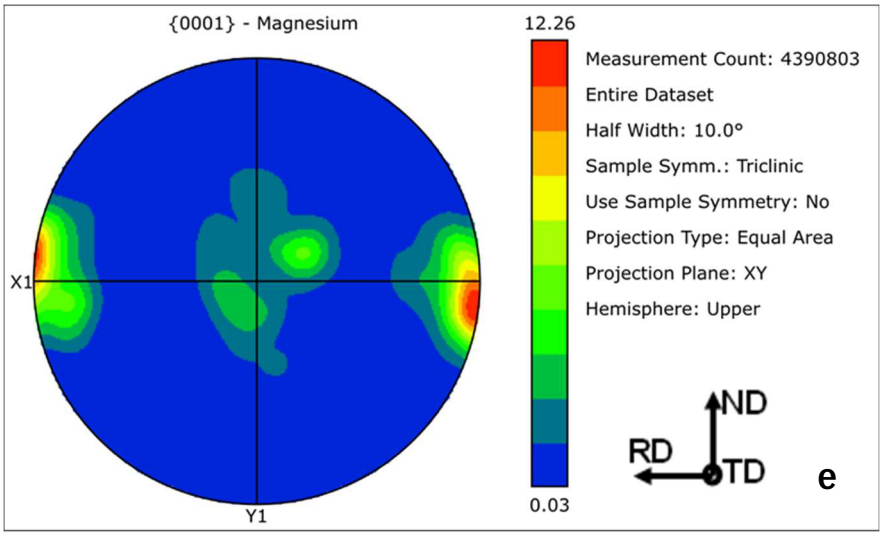
{0001} - Magnesium
12.26
0.03
Measurement Count: 4390803
Entire Dataset
Half Width: 10.0°
Sample Symm.: Triclinic
Use Sample Symmetry: No
Projection Type: Equal Area
Projection Plane: XY
Hemisphere: Upper
X1
Y1
ND
RD
TD

e

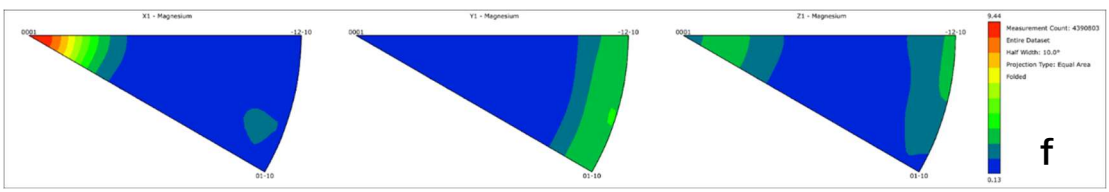

f

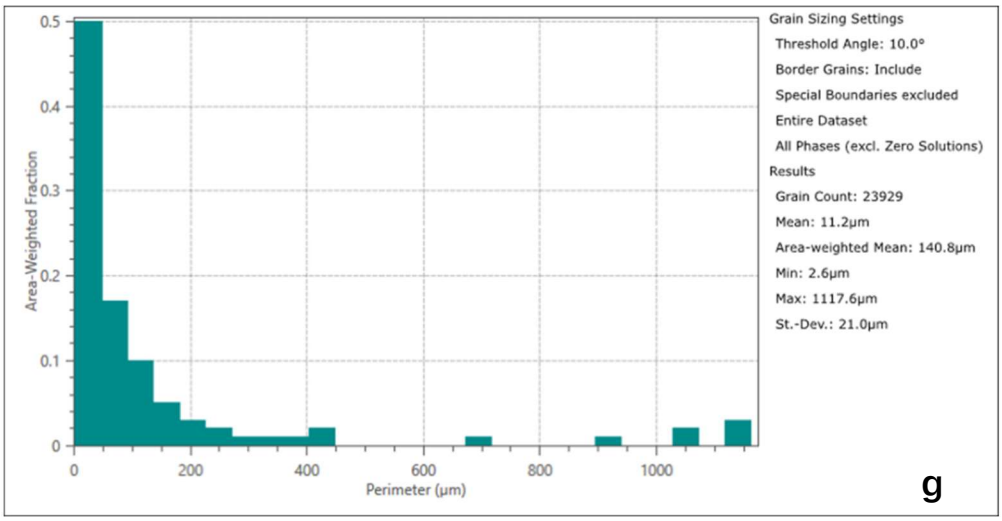

Figure 4-76 The EBSD result of the 300s annealed 2D compressed Mg-0.1Ca-0.4Zn specimen: (a) The inverse pole figure map and grain boundaries, (b) The grain boundaries and the special grain boundaries, (c) The band contrast and the phase analysis, (d) The band contrast, (e) The pole figure, (f) The inverse pole figures, (g) Grain size distribution expressed as grain boundary perimeter

Figure 4-77 shows the EBSD results of the same specimen after annealing for 420s. In the same way as the 1D compressed sample, the temperature of the specimen at this stage was 212℃. The average grain size increased slightly to 11.5μm (shown in Figure 4-77(g)). Figure 4-77(a) and 4-77(b) show that a large number of recrystallized grains were generated at this stage. Figure 4-77(c) indicates that the non-indexed area fraction was further reduced from 29.4% to 22.4%, especially in the top right corner area, the recrystallized grains almost fully filled the gap between the existing grains. Meanwhile, a lot of recrystallized grains were also found in the shear bands across the whole map. For the twins, the information from Figure 4-77(b) shows that the boundary fraction of the twin boundaries only changed a little bit while the recrystallization started. The boundary fraction of the tensile twin, compressive twin and double twin was changed from 50.3% to 42.4%, 2.2% to 2.7% and 4.2% to 5.0%, respectively. The small changes in the number of the twins indicated that the twins were not involved in the recrystallization process at this time i.e. The prior recrystallization in the shear bands at the early stage of the annealing process in this specimen was the same as other specimens. On the other hand, due to the recrystallization in the sample, the difference in the pole figures was quite notable (shown in Figure 4-77(e) and (f)). The maximum pole intensity was reduced by 2.1 compared to the as-compressed state (from 14 to 11.9). At this stage, an enlargement of grain orientation deviation from the “peak direction” was observed. Meanwhile, the direction distribution of the recrystallized grains was found to be not completely random but still showed a trend i.e. the orientation of the new grains was found mainly distributed around the TD and diffuse along the ND-axis.

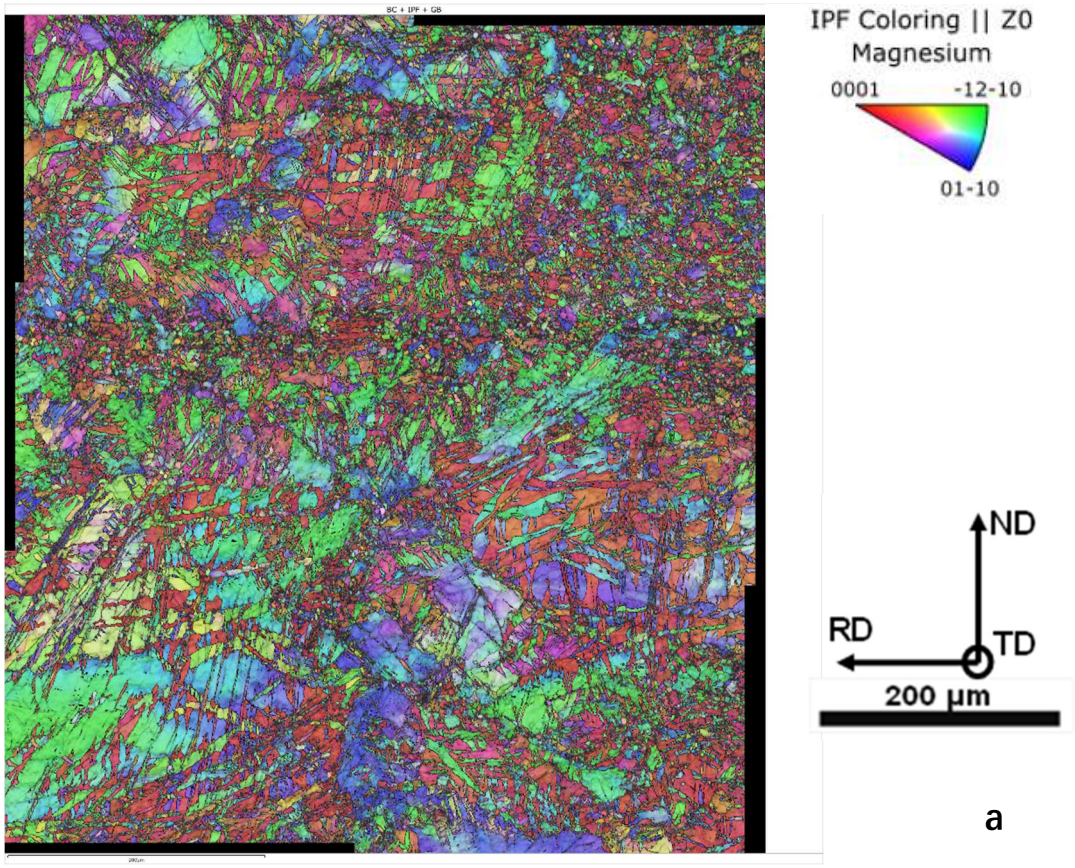
IPF Coloring || Z0
Magnesium
0001
-12-10
01-10
ND
RD
TD
200 µm

a

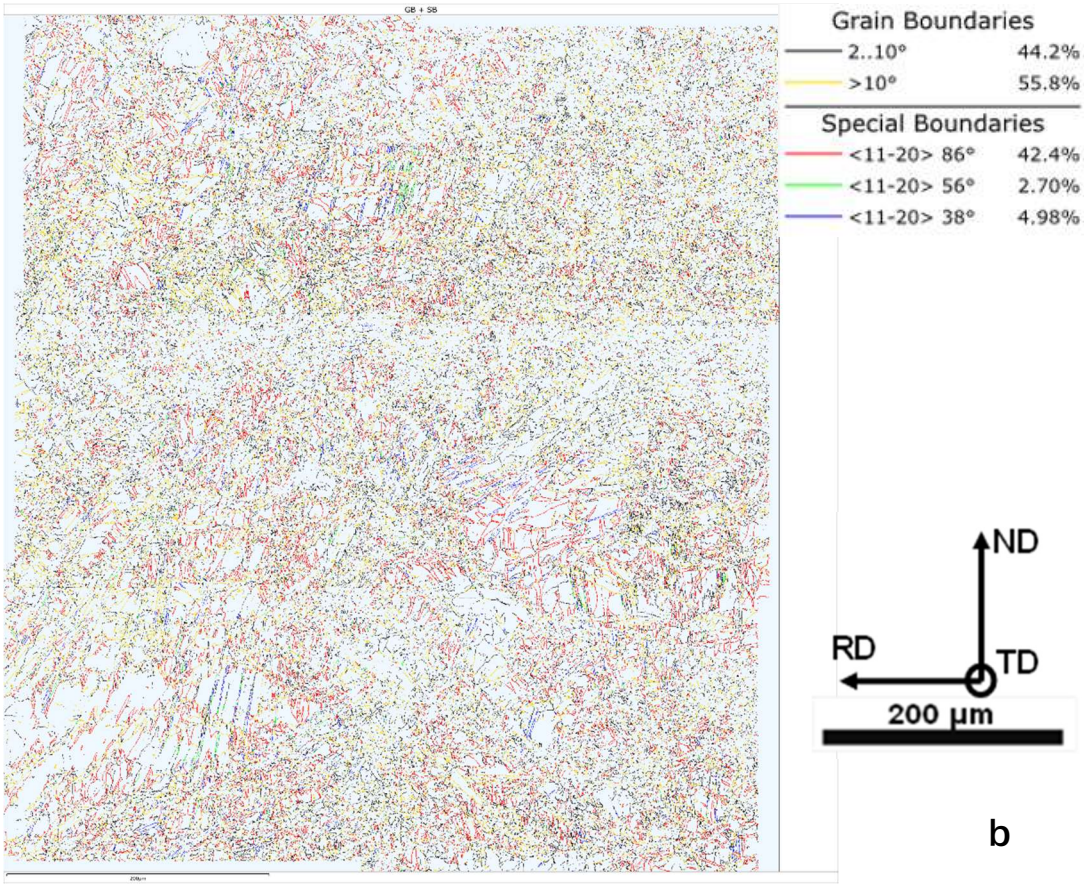
Grain Boundaries
2..10° 44.2%
>10° 55.8%
Special Boundaries
<11-20> 86° 42.4%
<11-20> 56° 2.70%
<11-20> 38° 4.98%
ND
RD
TD
200 µm

b

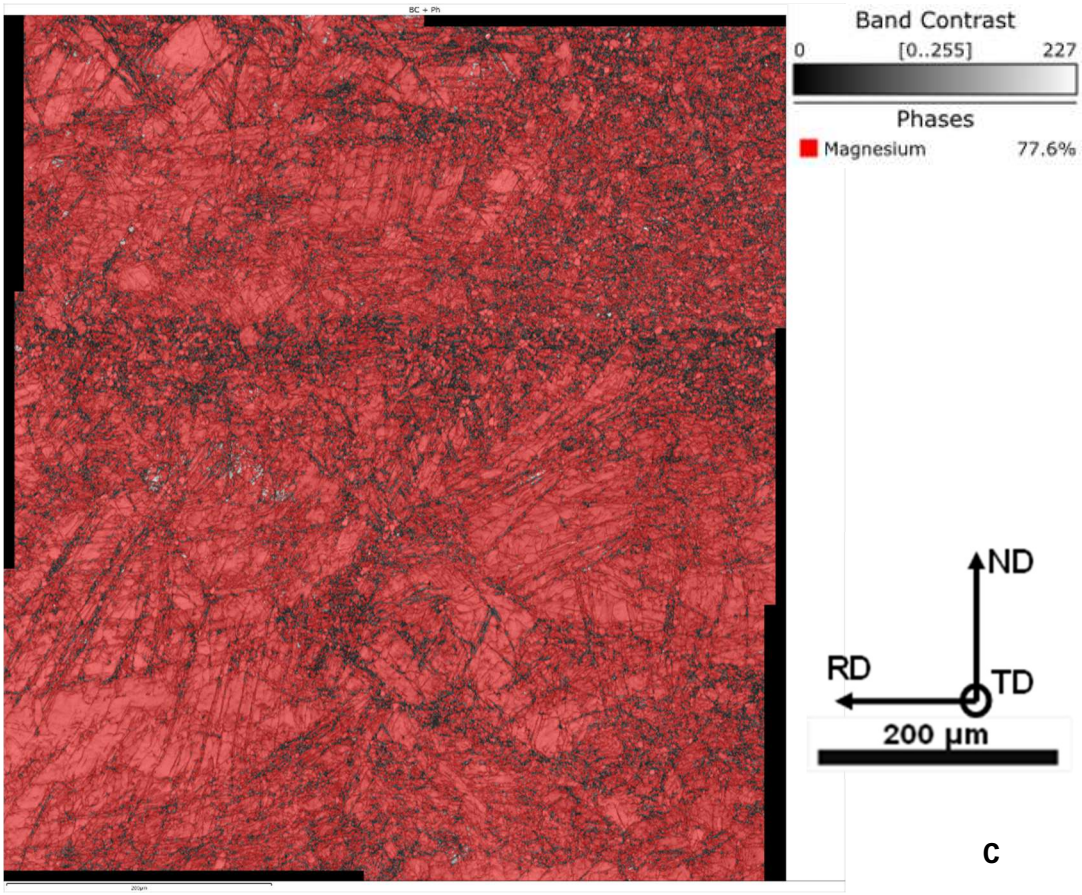
Band Contrast
0
[0..255]
227
Phases
Magnesium
77.6%
ND
RD
TD
200 µm

c

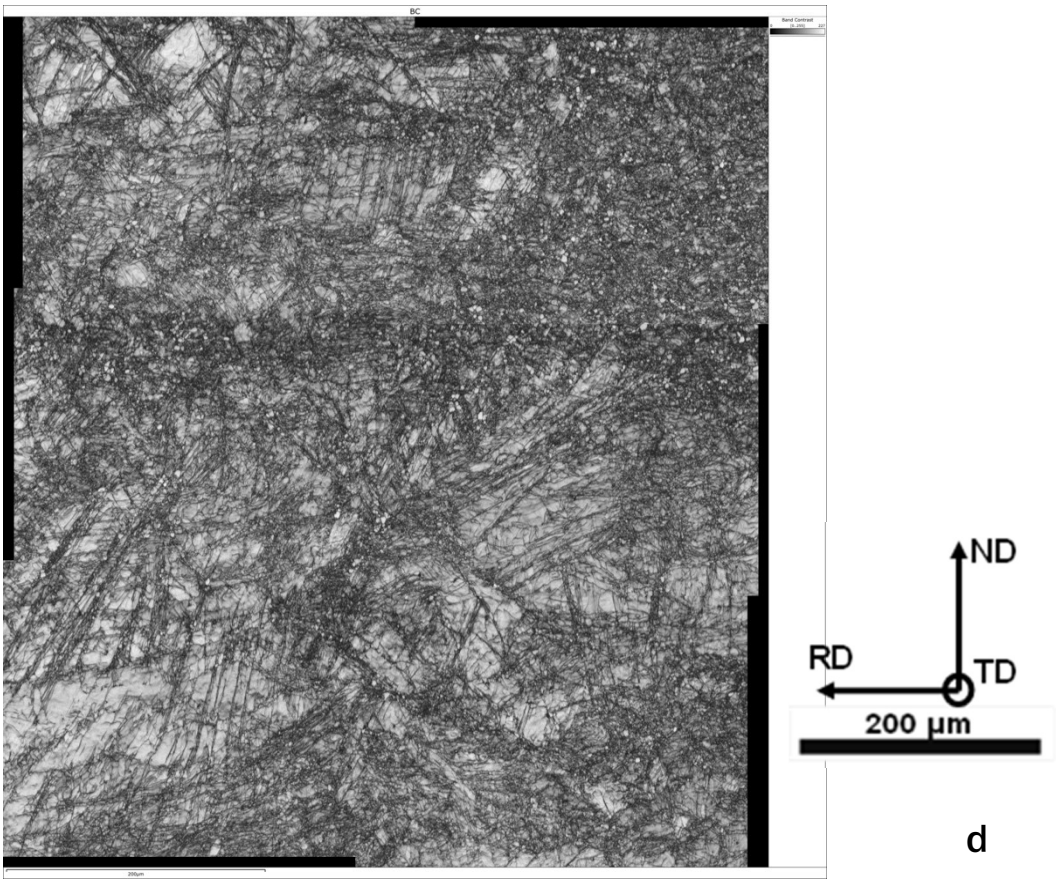
ND
RD
TD
200 µm

d

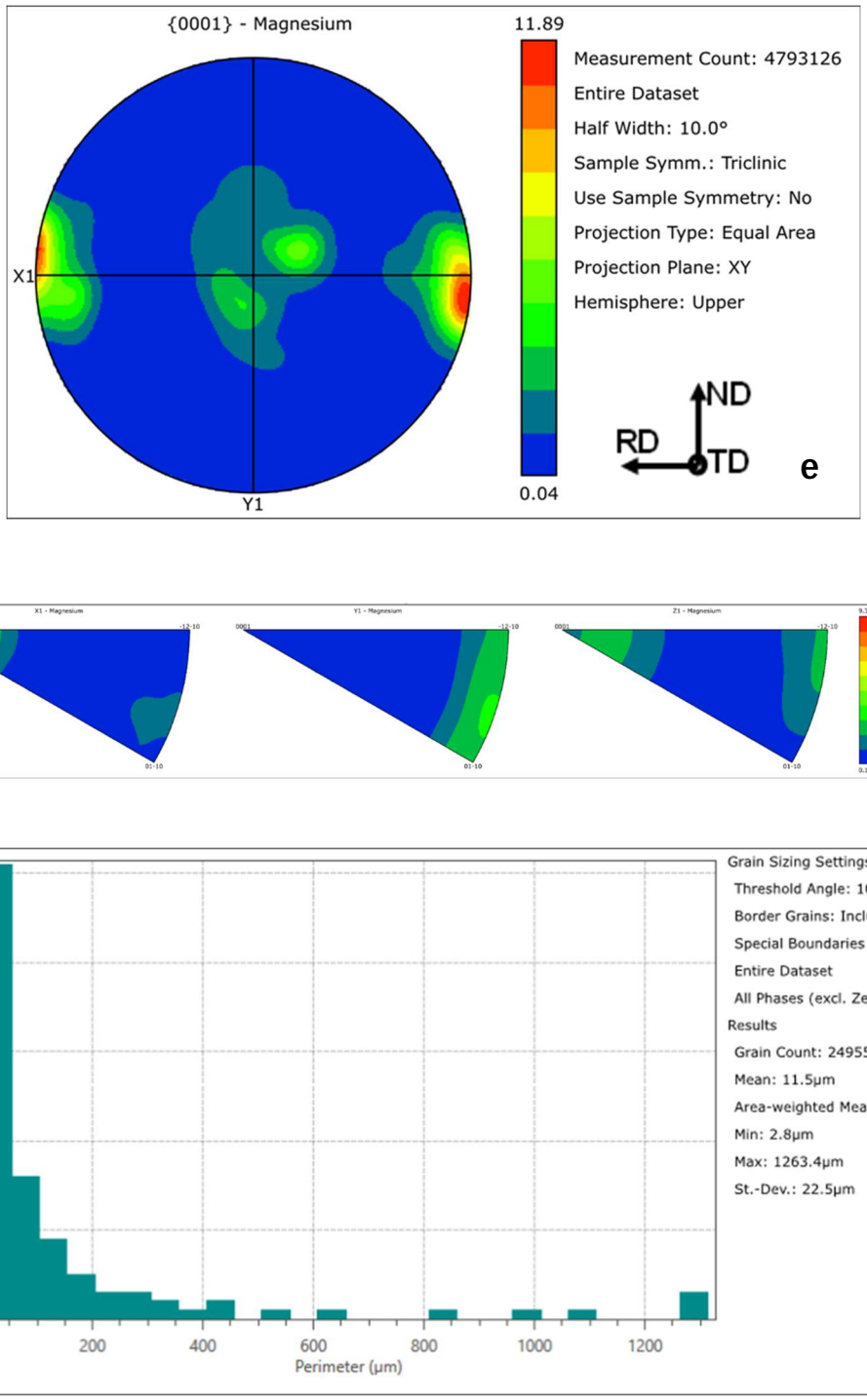

Figure 4-77 The EBSD result of the 420s annealed 2D compressed Mg-0.1Ca-0.4Zn specimen: (a) The inverse pole figure map and grain boundaries, (b) The grain boundaries and the special grain boundaries, (c) The band contrast and the phase analysis, (d) The band contrast, (e) The pole figure, (f) The inverse pole figures, (g) Grain size distribution expressed as grain boundary perimeter

In a similar manner to the 1D compressed Mg-0.1Ca-0.4Zn (at%) specimen, the 2D compressed specimen did not show further recrystallization after 570s annealing. The temperature of the sample before the water quench was 240℃. Figure 4-78 shows

the EBSD results of the specimen. The IPF map (shown in Figure 4-78(a)) indicated that the microstructure of the sample almost showed no change in morphology. Moreover, the index rate of the sample in this round of EBSD scanning was a little bit lower than before. Thus, the quality of the map was not as good as that of the 420s annealed specimen. The fraction of the identified area also showed this (shown in Figure 4-78(c)) as it was reduced from 77.6% to 71.4%. Due to the reduction of the image quality, the progress of the recovery could not be accurately judged. The twin fraction did not appreciably change. Figure 4-78(b) shows that the boundary fraction of the tensile twins, compressive twins and double twins at this stage was 43.4%, 2.4% and 4.4%, respectively. The difference in the boundary fraction of three kinds of twins to the last stage was 1.00%, 0.3% and 0.6%, respectively, which is within experimental error. Thus, no recrystallization had occurred in the twins at this stage. And the average grain size of the specimen was even smaller than the last stage which was 11.3μm (shown in Figure 4-78(g)). On the other hand, due to the low indexing rate, the maximum pole intensity did not decrease as observed in other samples but increased from 11.9 to 12.3, as shown in Figure 4-78(e). Furthermore, no changes in grain orientation distribution were observed in the pole figure and IPF.

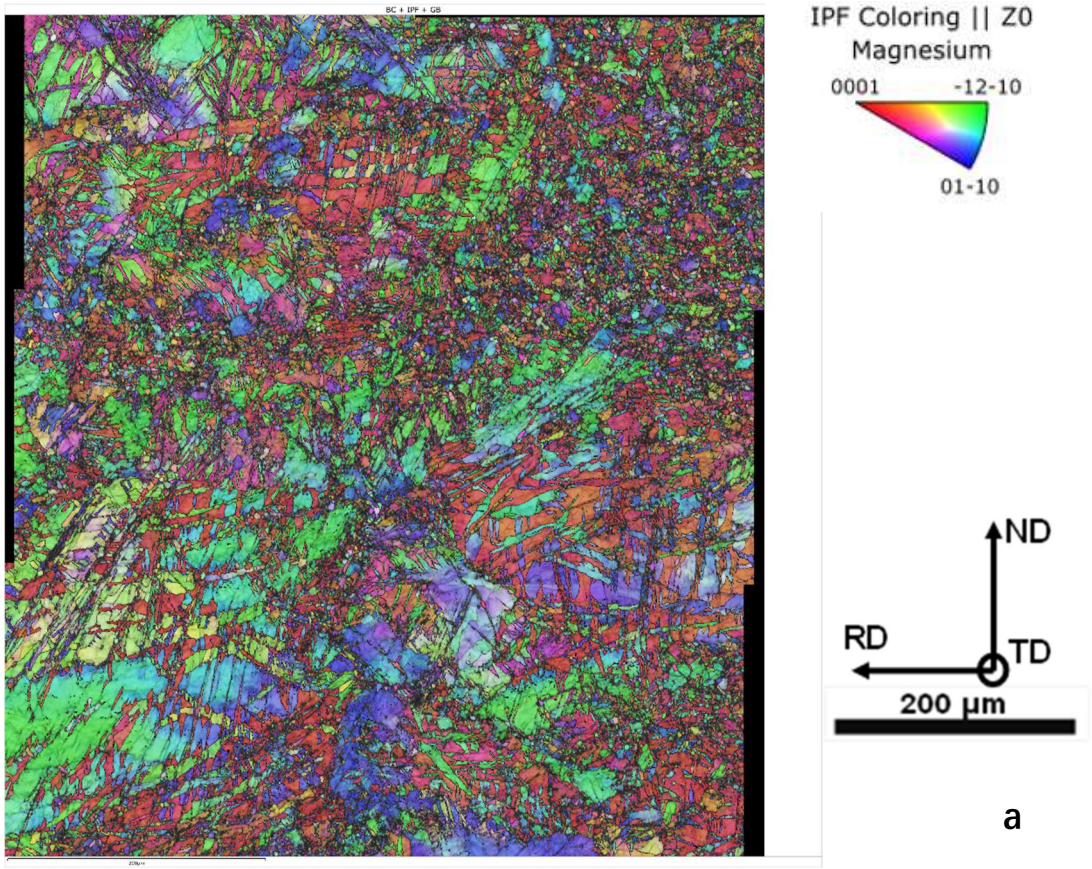

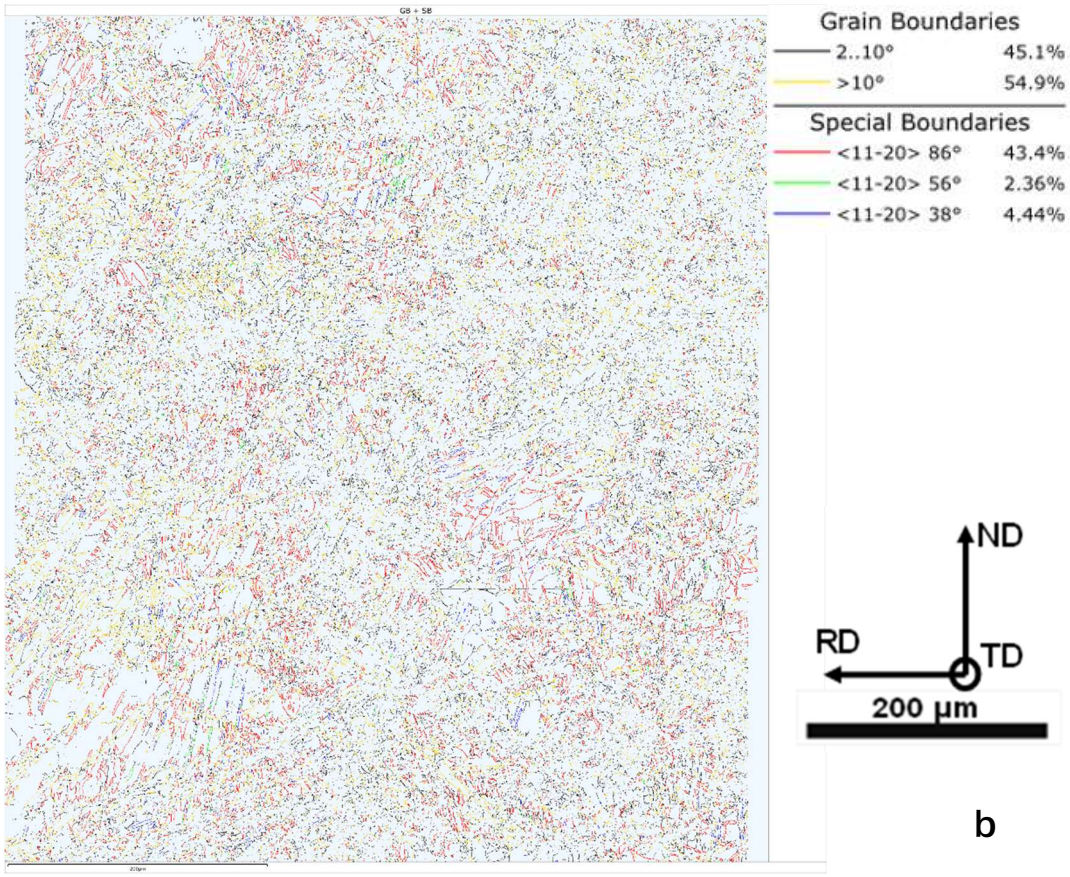
Grain Boundaries
2..10° 45.1%
>10° 54.9%
Special Boundaries
<11-20> 86° 43.4%
<11-20> 56° 2.36%
<11-20> 38° 4.44%
ND
RD
TD
200 µm

b

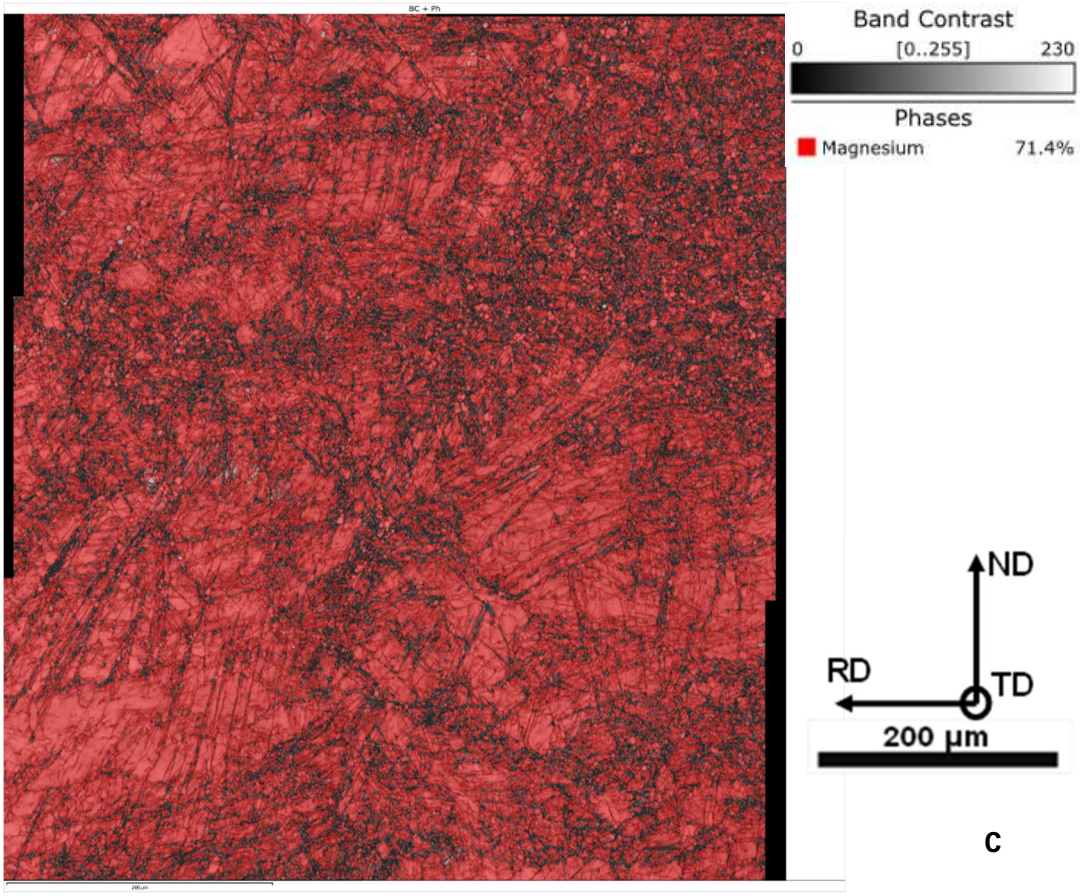
Band Contrast
0 [0..255] 230
Phases
Magnesium 71.4%
ND
RD
TD
200 µm

c

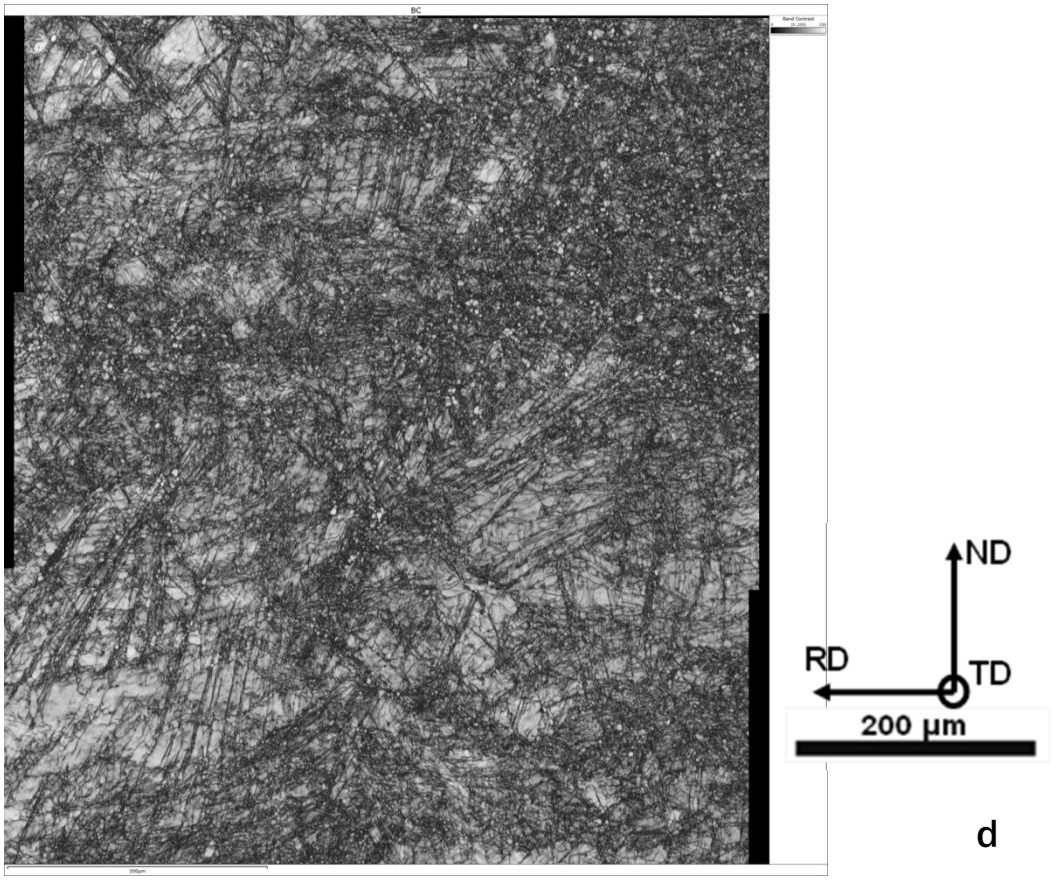
BC
ND
RD
TD
200 µm

d

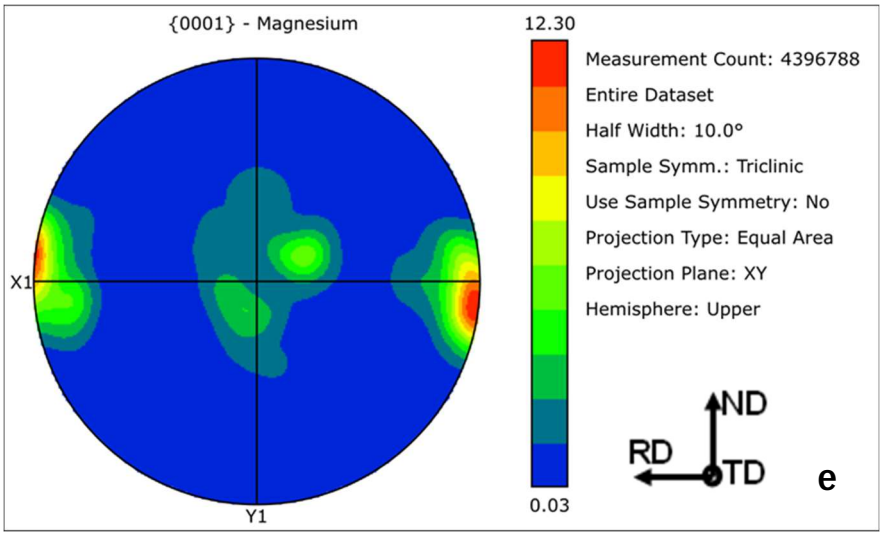
{0001} - Magnesium
12.30
0.03
Measurement Count: 4396788
Entire Dataset
Half Width: 10.0°
Sample Symm.: Triclinic
Use Sample Symmetry: No
Projection Type: Equal Area
Projection Plane: XY
Hemisphere: Upper
X1
Y1
ND
RD
TD

e

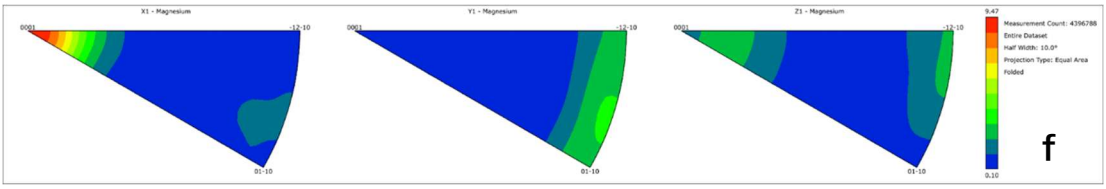
X1 - Magnesium
Y1 - Magnesium
Z1 - Magnesium
Measurement Count: 4396788
Entire Dataset
Half Width: 10.0°
Projection Type: Equal Area
Folded

f

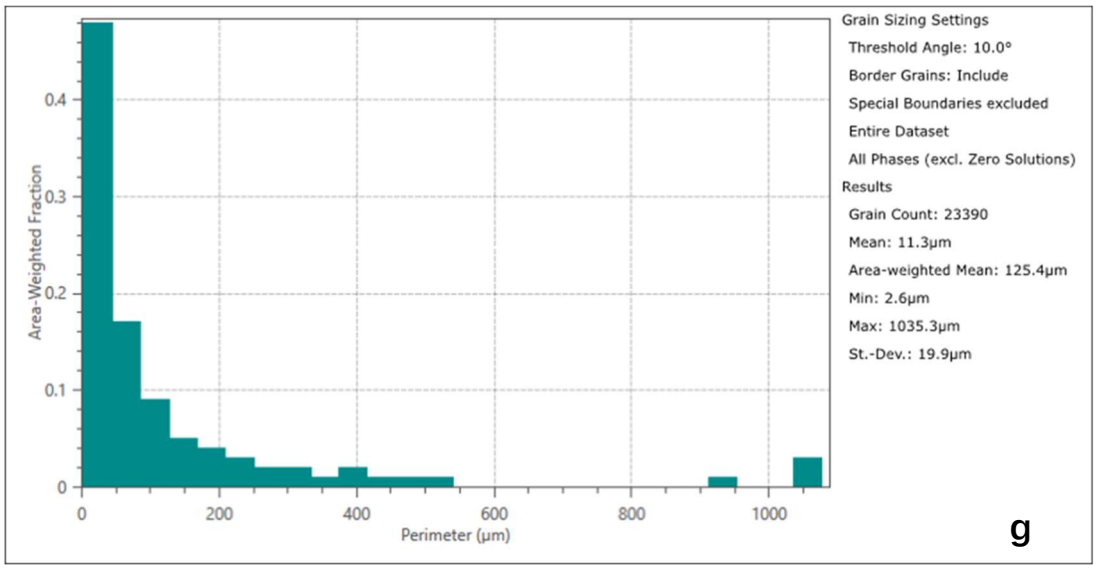

Figure 4-78 The EBSD result of the 570s annealed 2D compressed Mg-0.1Ca-0.4Zn specimen: (a) The inverse pole figure map and grain boundaries, (b) The grain boundaries and the special grain boundaries, (c) The band contrast and the phase analysis, (d) The band contrast, (e) The pole figure, (f) The inverse pole figures, (g) Grain size distribution expressed as grain boundary perimeter

Figure 4-79 presents further microstructure evolution of the same sample after annealing for 750s. The temperature of the specimen at this time point was 257℃. From Figure 4-79(a), it was clear that the recrystallization in the specimen continued. The grain growth of the existing recrystallized grains was found across the scanned area. However, the size of these grains did not change too much, which was just 3-5μm growth. The increase in average grain size from 11.3 μm to 11.7 μm was not statistically significant (shown in Figure 4-79(g)). On the other hand, the nucleation of new recrystallized grains was also observed on the grain boundaries. There was no evidence that the twins were involved in the recrystallization progress at this time point as the twin boundary fraction did not change in a statistically significant way. Figure 4-79(b) shows that the boundary fraction of the tensile twins, compressive twins and double twins changed from 43.4% to 40.6%, 2.4% to 2.5% and 4.4% to 4.6%, respectively. The boundary fraction of the low-angle grain boundary and the high-angle grain boundary was changed from 45.1% to 43.5% and 54.9% to 56.5%, respectively. The decrease of the low-angle grain boundaries and the increase of the high-angle grain boundaries, while small, indicated that the recrystallization was still in progress. Moreover, the changes from the pole figure and IPF (shown in Figure 4-79(e) and (f)) also provided some useful information. Although no obvious grain growth was found, the maximum value of the pole figure showed a 0.5 reduction (from 12.3 to 11.8). Meanwhile, the weak peak which was close to the TD above the RD-axis was found expanding towards the TD.

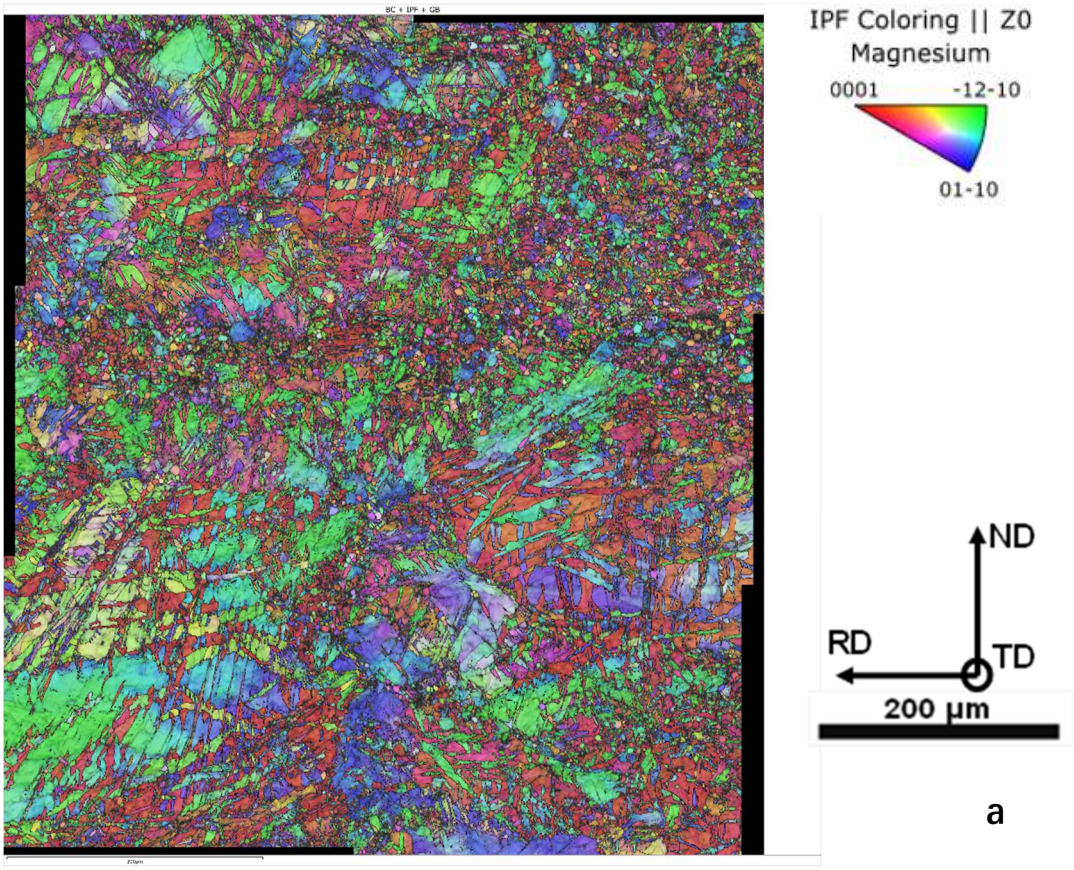
IPF Coloring || Z0
Magnesium
0001
-12-10
01-10
ND
RD
TD
200 µm

a

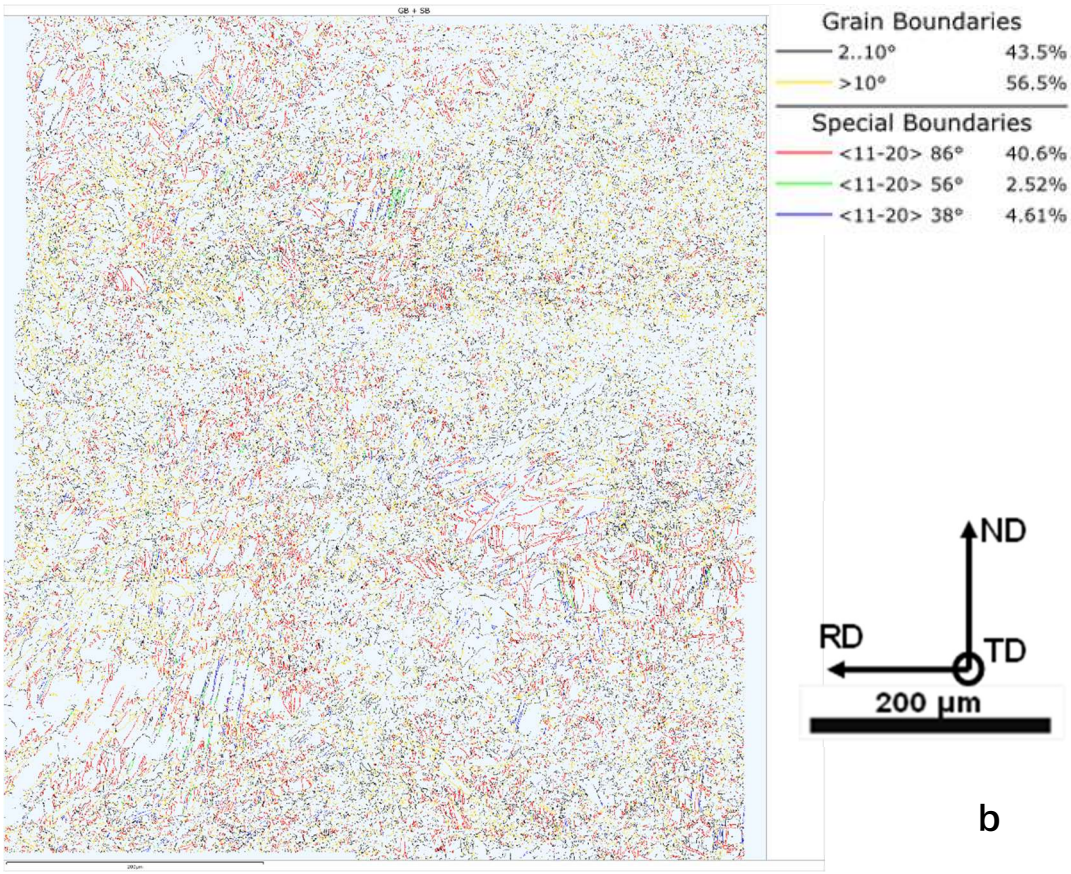
Grain Boundaries
2..10° 43.5%
>10° 56.5%
Special Boundaries
<11-20> 86° 40.6%
<11-20> 56° 2.52%
<11-20> 38° 4.61%
ND
RD
TD
200 µm

b

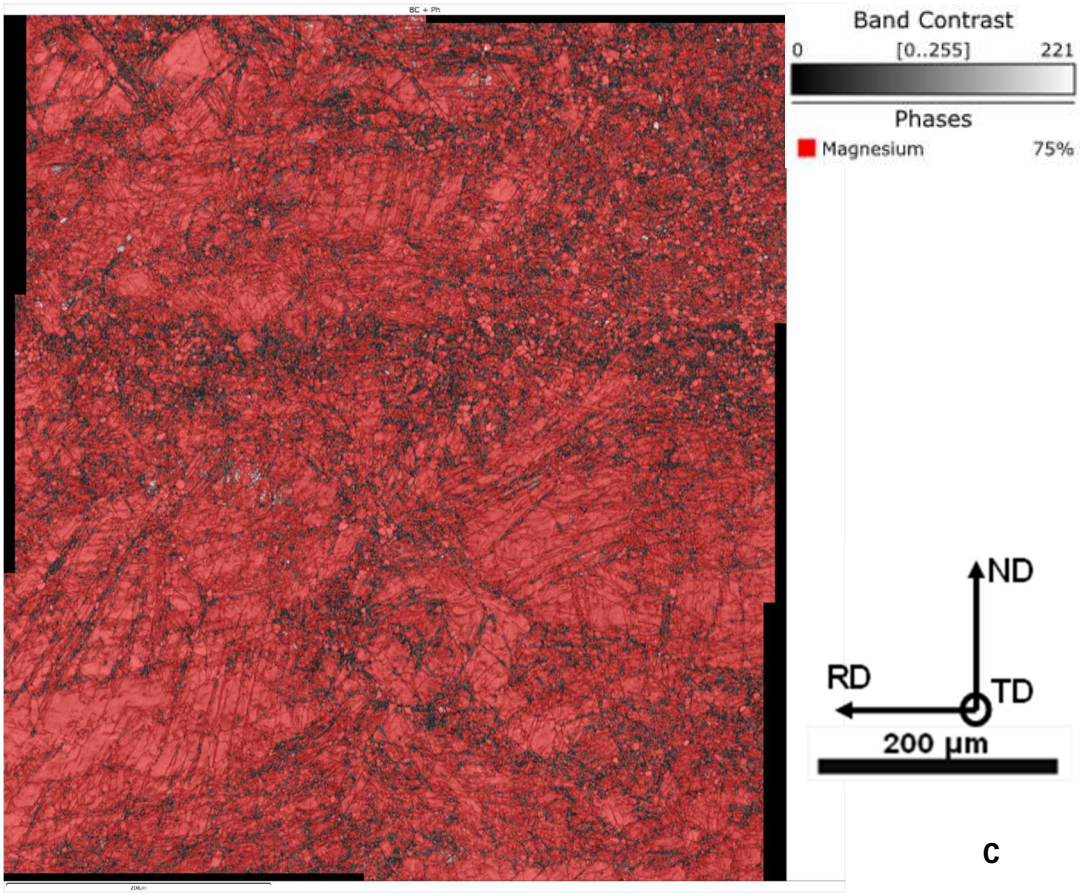
Band Contrast
0
[0..255]
221
Phases
Magnesium
75%
ND
RD
TD
200 µm

c

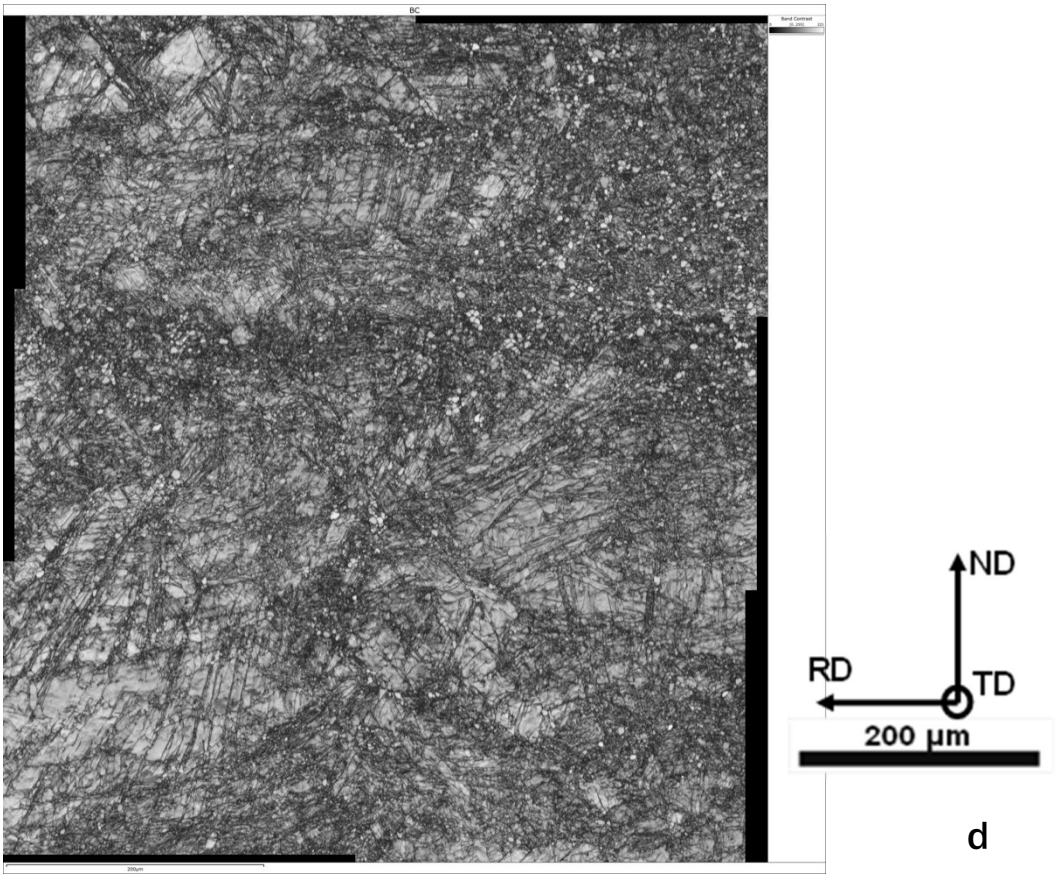
ND
RD
TD
200 µm

d

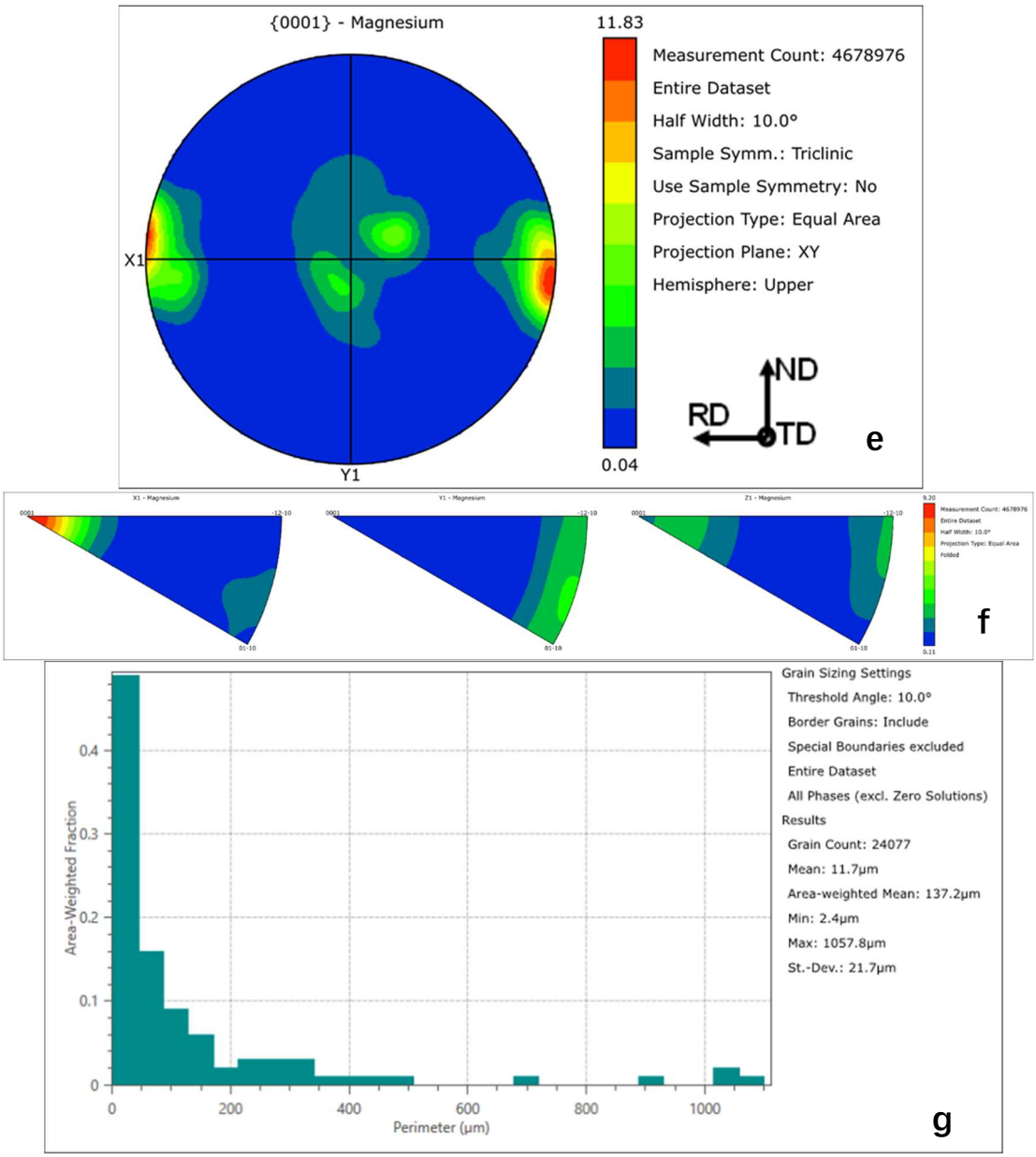

Figure 4-79 The EBSD result of the 750s annealed 2D compressed Mg-0.1Ca-0.4Zn specimen: (a) The inverse pole figure map and grain boundaries, (b) The grain boundaries and the special grain boundaries, (c) The band contrast and the phase analysis, (d) The band contrast, (e) The pole figure, (f) The inverse pole figures, (g) Grain size distribution expressed as grain boundary perimeter

Figure 4-80 shows the EBSD results of the same specimen after annealing for 990s. The highest temperature of the specimen during this stage was 291℃. The IPF map (shown in Figure 4-80(a)) indicated that the 60s increase in annealing time (highest temperature from 257℃ to 291℃) did not bring a significant difference to the microstructure. The grain growth of the recrystallized grains was very limited and only a few nucleation events were observed. The slight change in average grain size ($11.8\mu m$) also reflected the limited variation of the microstructure at this stage (shown in Figure

4-80(g)). Figure 4-80(b) indicates the minor change of the boundary fraction under the slow progress of the recrystallization. The boundary fraction of the tensile twins, compressive twins and double twins was changed from 40.6% to 34.7%, 2.5% to 2.3% and 4.6% to 4.3%, respectively. Meanwhile, the fraction of the low-angle grain boundary and the high-angle grain boundary was changed from 43.5% to 43.4% and from 56.5% to 56.6%, respectively. Compared to the fraction variation of the compressive twins and double twins, the 5.9% reduction of the tensile twins was quite high. The reason for this was attributed to the grain growth of the recrystallized grains. Some of the tensile twins were consumed during the grain growth stage. Additionally, with the change of the boundary fraction of the tensile twins, the boundary fraction of the low-angle grain boundary and the high-angle grain boundary was very stable. The grain growth and the nucleation of the recrystallized grains resulted in an increase in the high-angle grain boundary fraction. However, due to the improvement of the resolution, more low-angle grain boundaries were shown on the EBSD map. Thus, the unchanged value of this boundary fraction was shown. On the other hand, due to the slow recrystallization progress, the maximum pole intensity did not decrease too much which was from 11.8 to 11.4 (shown in Figure 4-80(e)). Also, only a little difference in the grain orientation distribution was found in the pole figure and IPF. The two sets of signals which were close to the TD were both found enlarged i.e. the new grains which had the orientation similar to the TD were increasing.

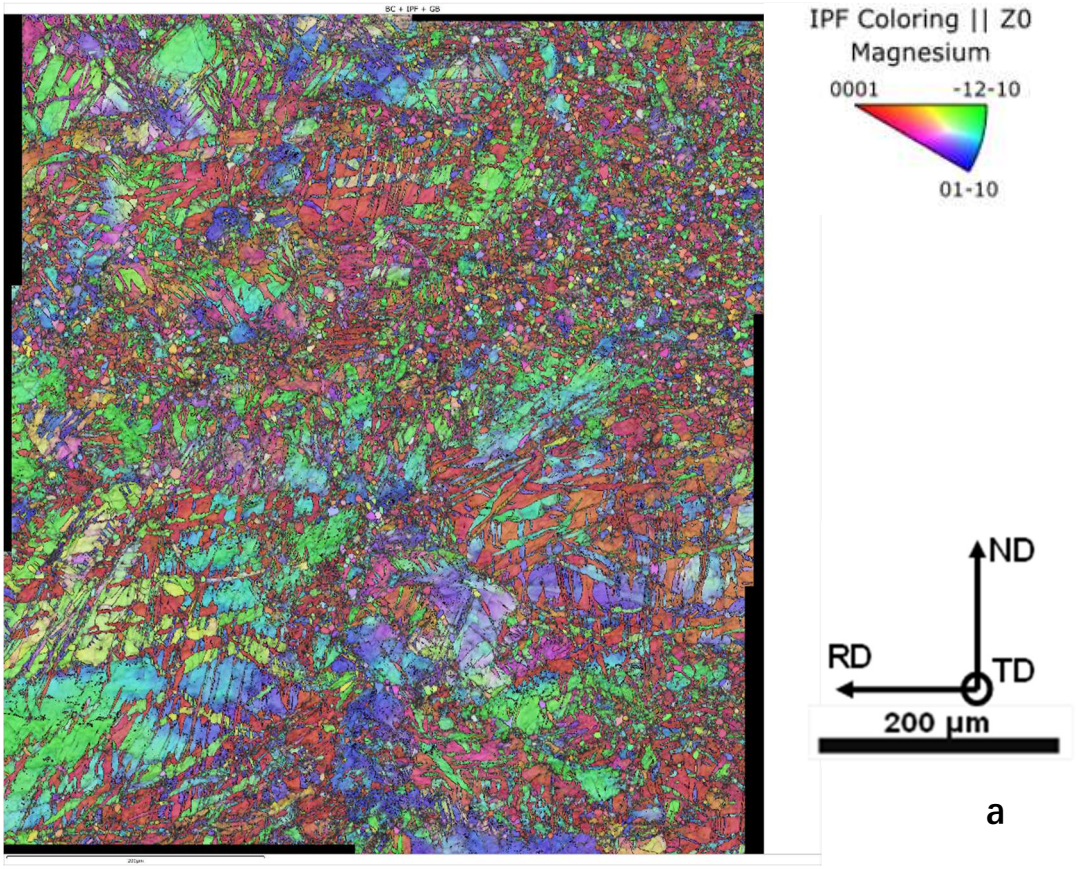

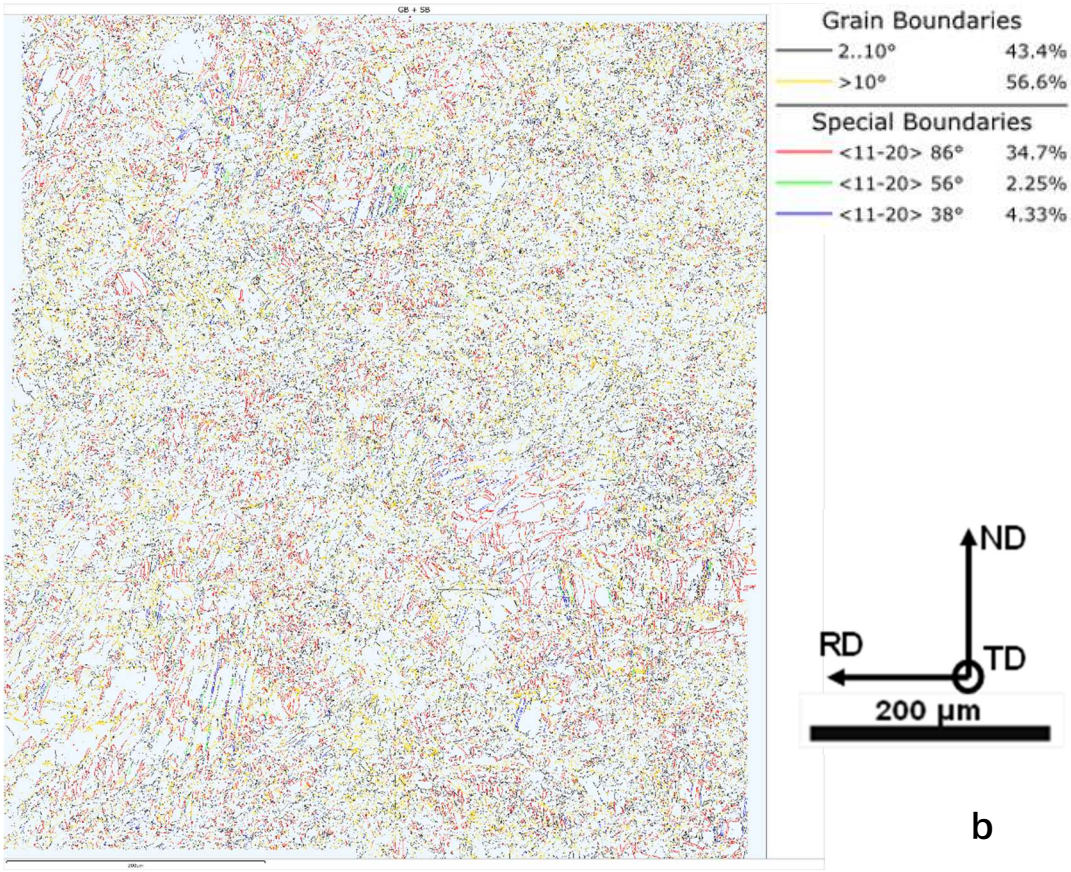
Grain Boundaries
2..10° 43.4%
>10° 56.6%
Special Boundaries
<11-20> 86° 34.7%
<11-20> 56° 2.25%
<11-20> 38° 4.33%
ND
RD
TD
200 µm

b

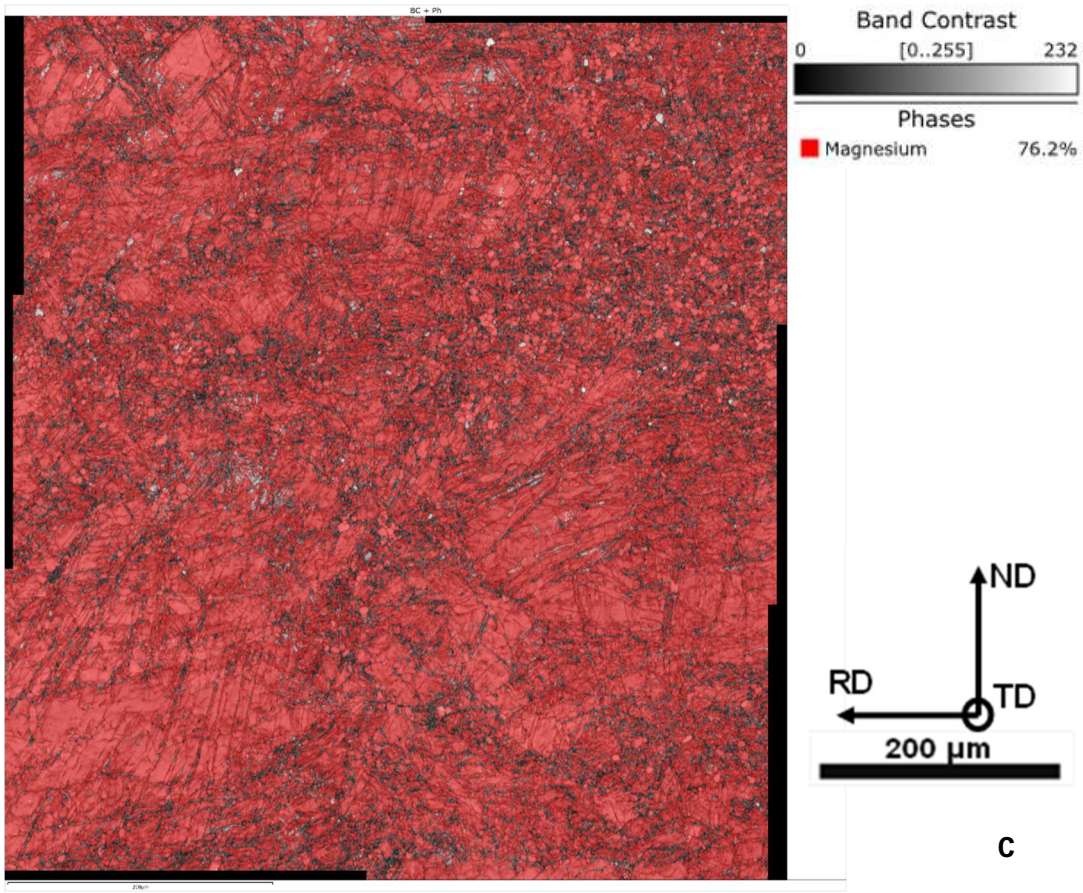
Band Contrast
0 [0..255] 232
Phases
Magnesium 76.2%
ND
RD
TD
200 µm

c

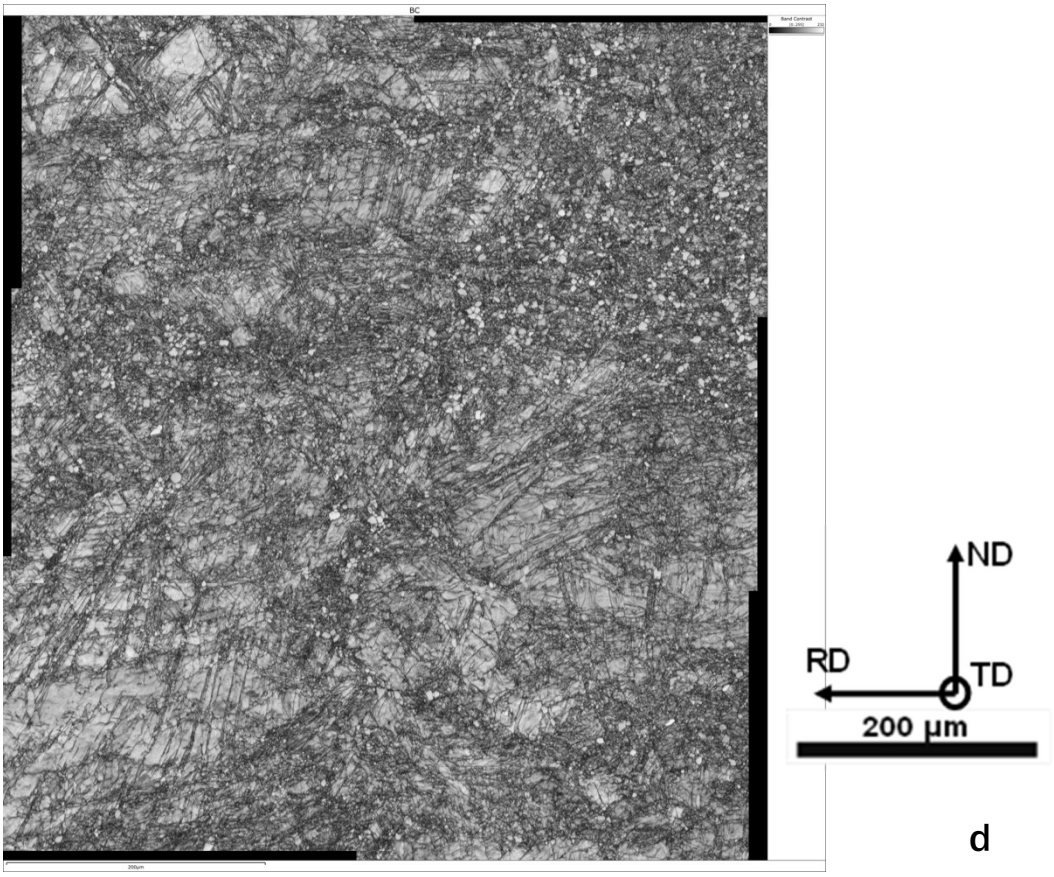
ND
RD
TD
200 µm
d

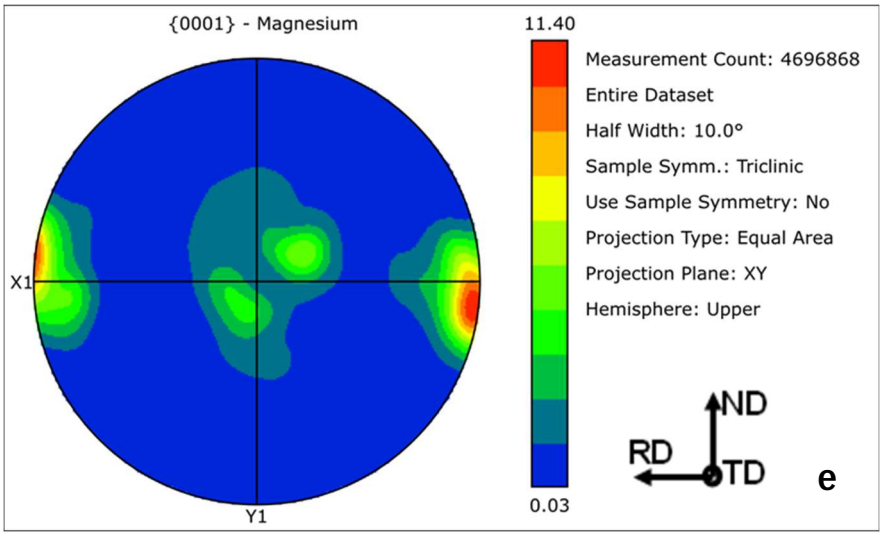
{0001} - Magnesium
11.40
0.03
Measurement Count: 4696868
Entire Dataset
Half Width: 10.0°
Sample Symm.: Triclinic
Use Sample Symmetry: No
Projection Type: Equal Area
Projection Plane: XY
Hemisphere: Upper
X1
Y1
ND
RD
TD
e

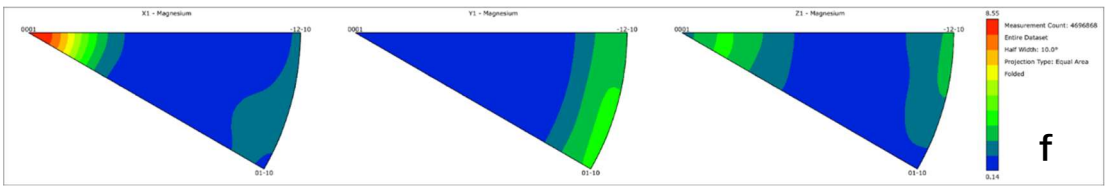
X1 - Magnesium
Y1 - Magnesium
Z1 - Magnesium
f

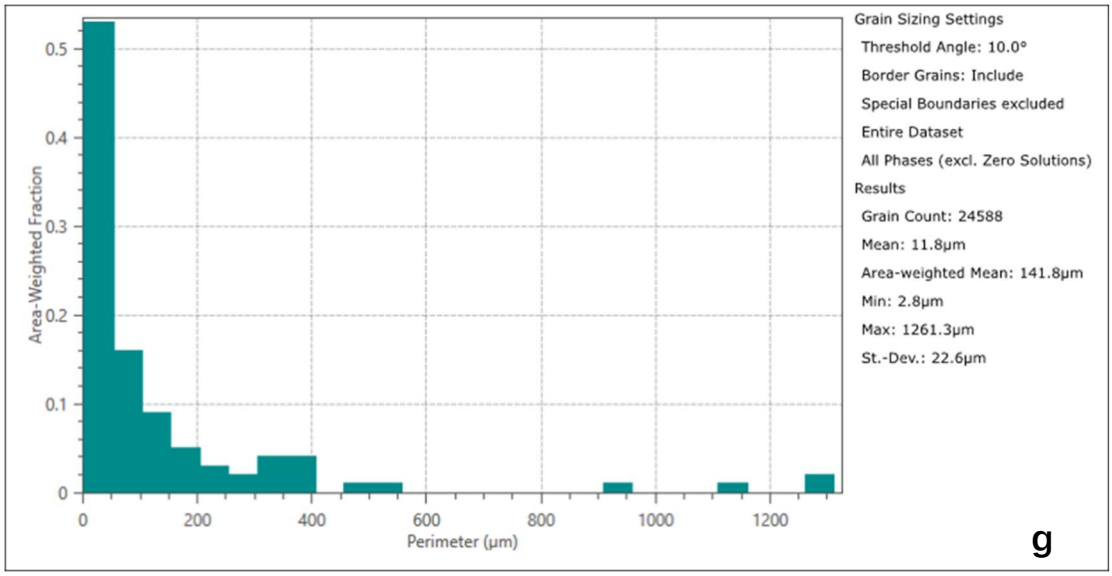

Figure 4-80 The EBSD result of the 990s annealed 2D compressed Mg-0.1Ca-0.4Zn specimen: (a) The inverse pole figure map and grain boundaries, (b) The grain boundaries and the special grain boundaries, (c) The band contrast and the phase analysis, (d) The band contrast, (e) The pole figure, (f) The inverse pole figures, (g) Grain size distribution expressed as grain boundary perimeter

The last EBSD result (shown in Figure 4-81) of the 2D compressed Mg-0.1Ca-0.4Zn (at%) specimen was from annealing for 1290s. The highest temperature of the specimen during the annealing process was 310℃. Very similar to the 1D compressed Mg-0.1Ca-0.4Zn (at%) specimen, the IPF map (shown in Figure 4-81(a)) showed that the specimen experienced a rapid and complete recrystallization during the last annealing time. With the same 60s longer annealing process and the 21℃ difference in the highest temperature, the microstructure exhibited an even higher degree of recrystallization completion than that of the 1D compressed Mg-0.1Ca-0.4Zn (at%) specimen. Significantly fewer original grains were observed in the specimen, with these grains confined to the bottom half of the IPF map (marked with the white circles). The recrystallization specimen showed a much more uniform microstructure compared to that of the original ingot. Figure 4-81(g) shows that the grain size varied between 78μm and 3μm, with an average grain size of 32.7μm. Additionally, the non-indexed grains and the partially identified grains were also found with different colour in the IPF map (shown in Figure 4-81(c) and (a)). The recrystallized grain which had the direction closer to the TD showed darker was also observed in the band contrast map (shown in Figure 4-81(d)). Figure 4-81(b) shows the boundary fraction of the tensile twins, compressive twins and double twins were all significantly reduced from 34.7% to 3.8%, 2.3% to 0.4% and 4.3% to 0.5%, respectively. Meanwhile, the fraction of the low-angle

grain boundary and the high-angle grain boundary was changed from 43.4% to 13.3% and from 56.6% to 86.7%, respectively. The dramatic changes of the boundary fraction in the 2D compressed Mg-0.1Ca-0.4Zn (at%) specimen were similar to that of other test specimens. An obvious variation of the grain orientation distribution was observed in the pole figure and IPF results (shown in Figure 4-81(e) and (f)). It showed that the texture of the specimen was largely weakened. The grain orientation distribution of the recrystallized 2D compressed specimen was very similar to that of the recrystallized 1D compressed specimen. The peak of the pole figure was found to hold its position (aligned to the RD). And the maximum intensity of the peak exhibited a reduction which was from 11.4 to 4.7. The distribution of the recrystallized grains orientation was found to be diffused around the weak peaks which were close to the TD mentioned before and meanwhile the orientation distribution of the recrystallized grains was found also distributed along the RD-axis. The orientation distribution of the recrystallized specimen showed a trend that the direction of the new grains was mainly distributed between the TD and the compression direction. Meanwhile, the concentration of the orientation distribution close to the TD was also found.

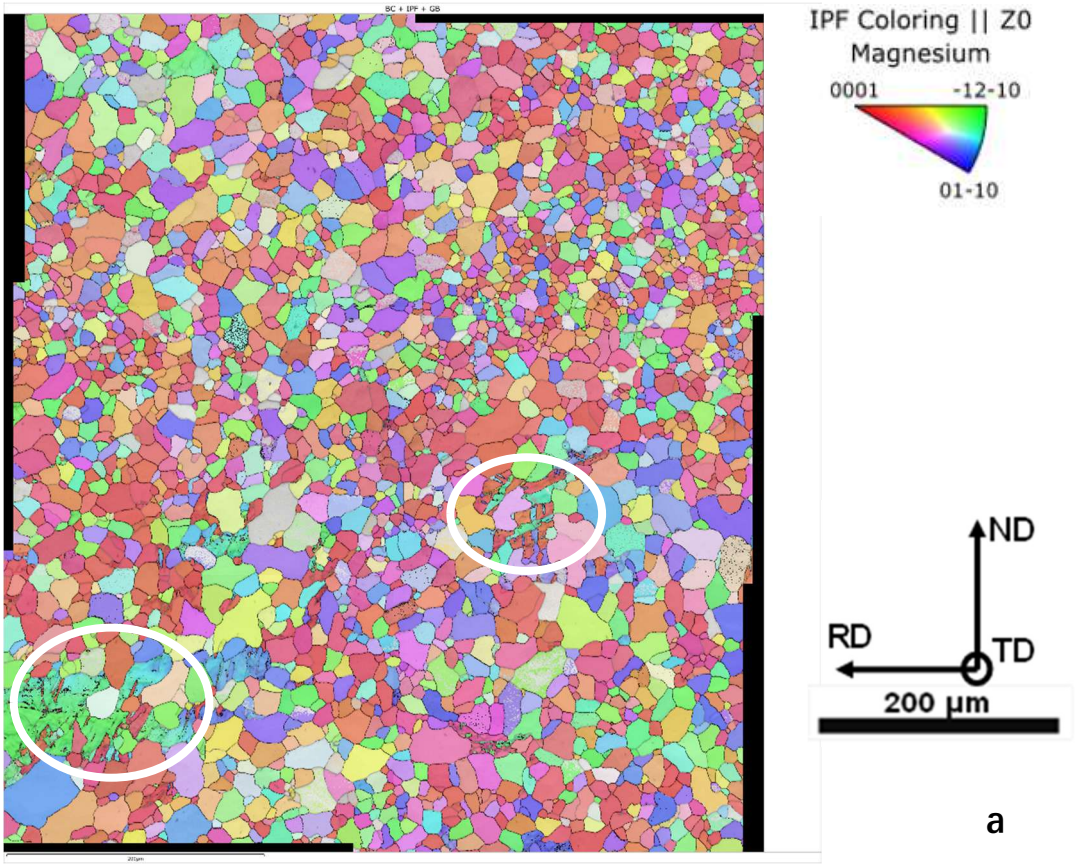

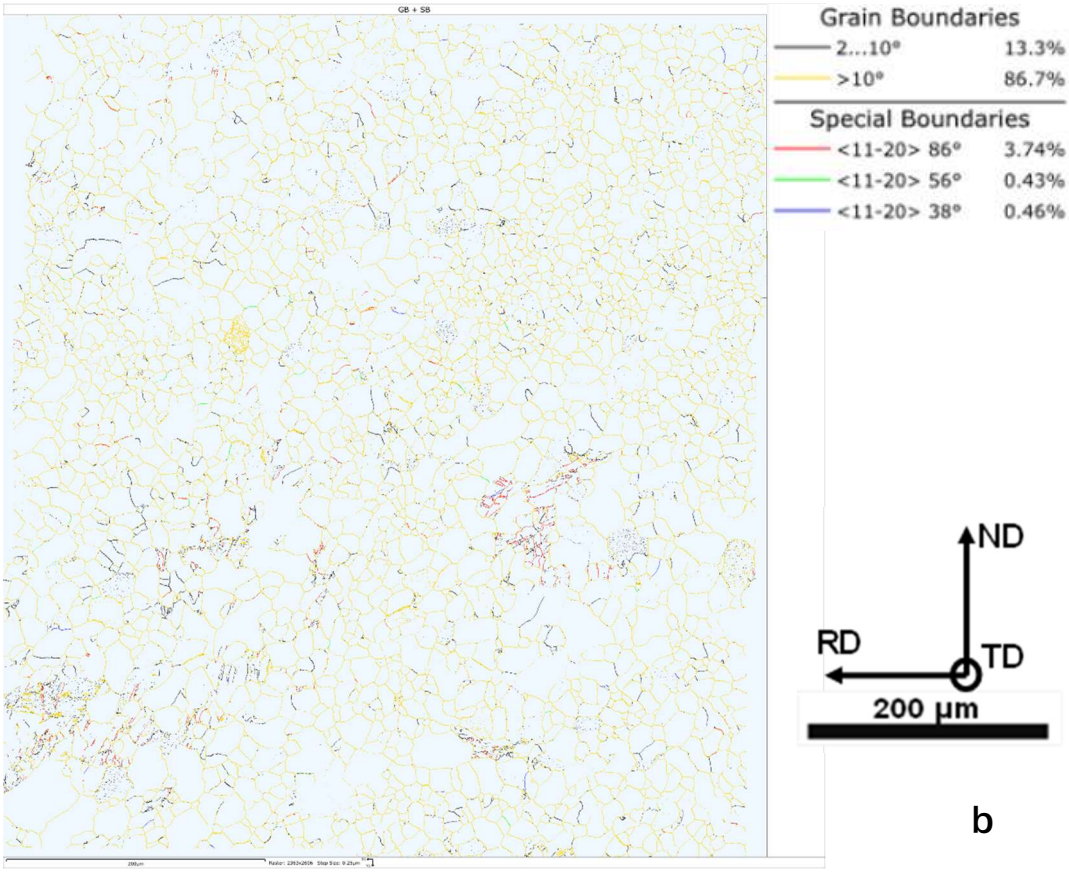
GB + SB
Grain Boundaries
2...10° 13.3%
>10° 86.7%
Special Boundaries
<11-20> 86° 3.74%
<11-20> 56° 0.43%
<11-20> 38° 0.46%
ND
RD
TD
200 µm

b

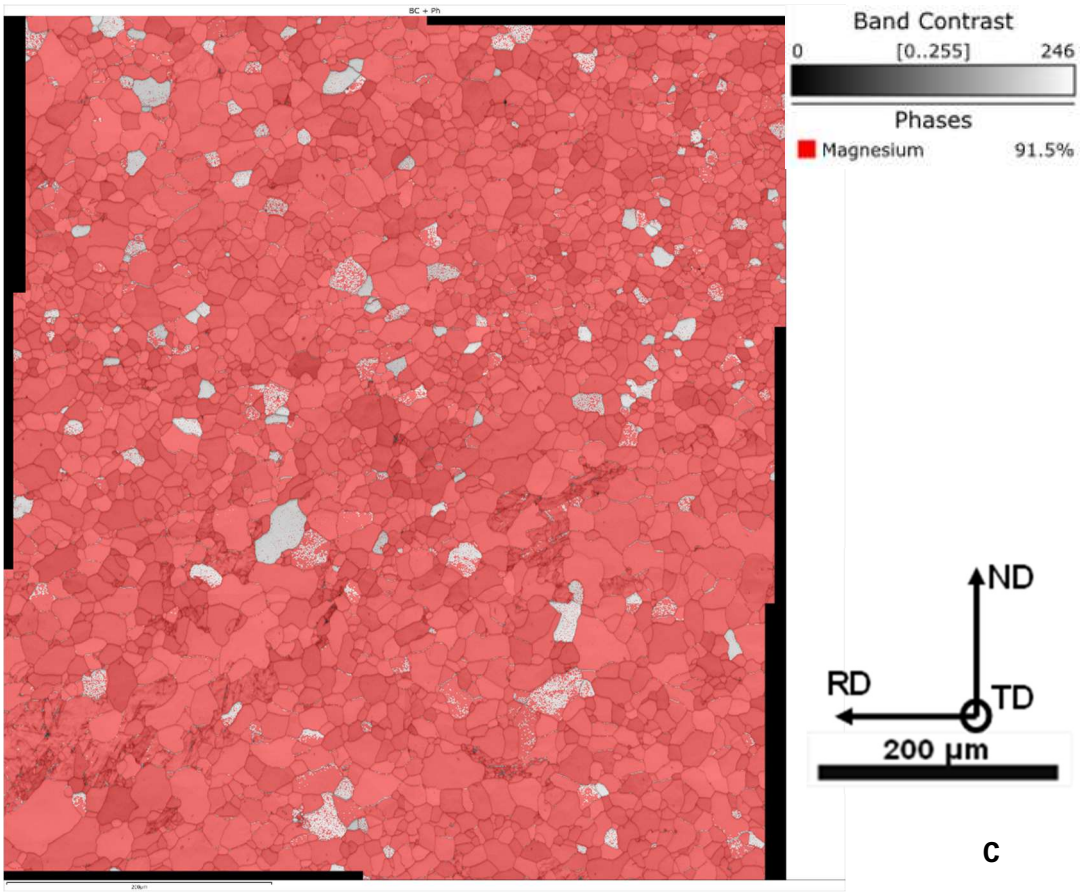
BC + Ph
Band Contrast
0 [0..255] 246
Phases
Magnesium 91.5%
ND
RD
TD
200 µm

c

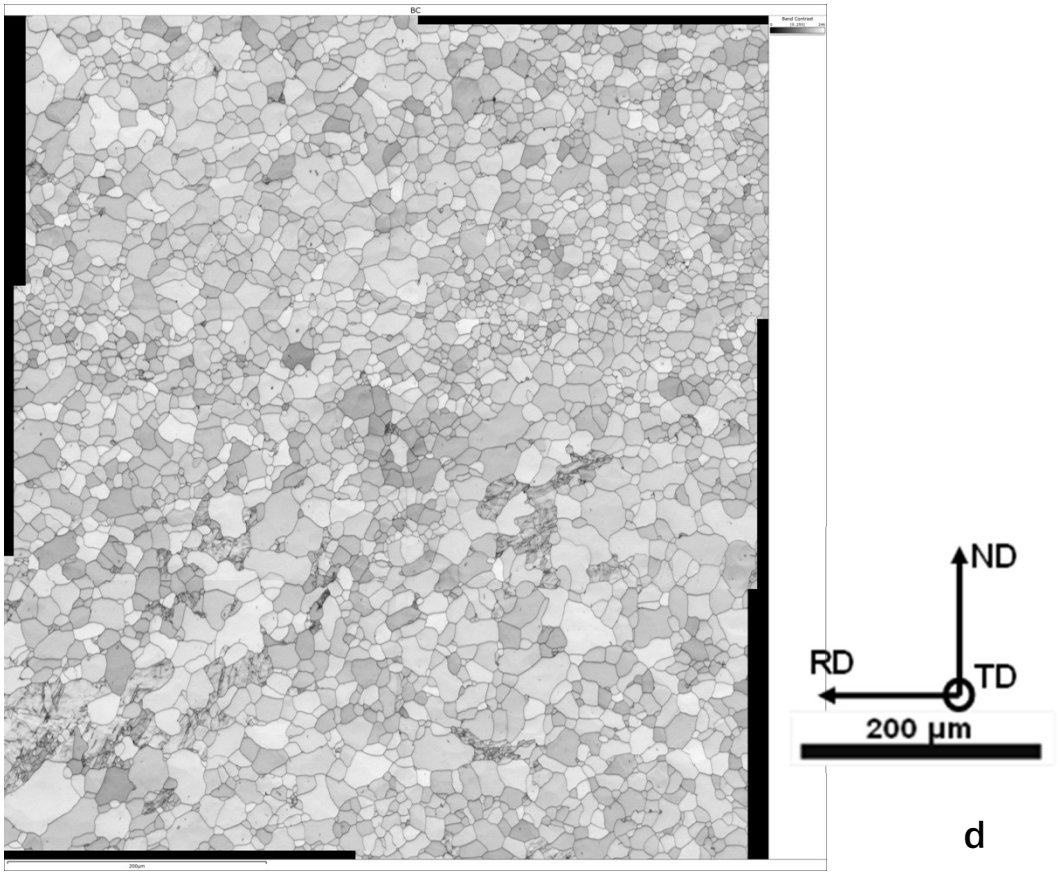
BC
ND
RD
TD
200 µm

d

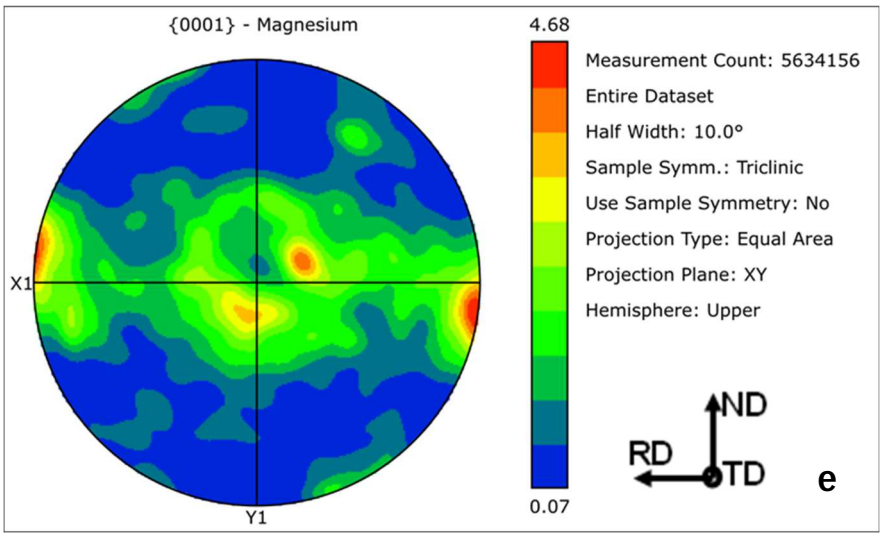
{0001} - Magnesium
4.68
0.07
Measurement Count: 5634156
Entire Dataset
Half Width: 10.0°
Sample Symm.: Triclinic
Use Sample Symmetry: No
Projection Type: Equal Area
Projection Plane: XY
Hemisphere: Upper
X1
Y1
ND
RD
TD

e

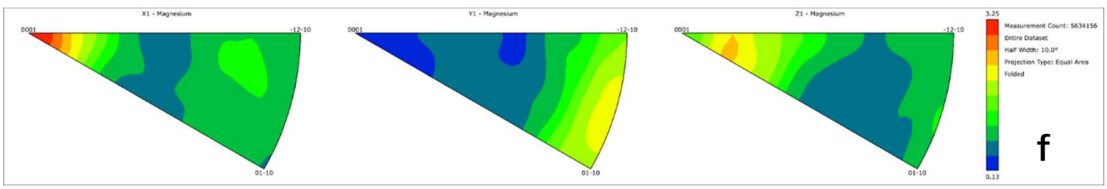
X1 - Magnesium
Y1 - Magnesium
Z1 - Magnesium
Measurement Count: 5634156
Entire Dataset
Half Width: 10.0°
Projection Type: Equal Area
Folded

f

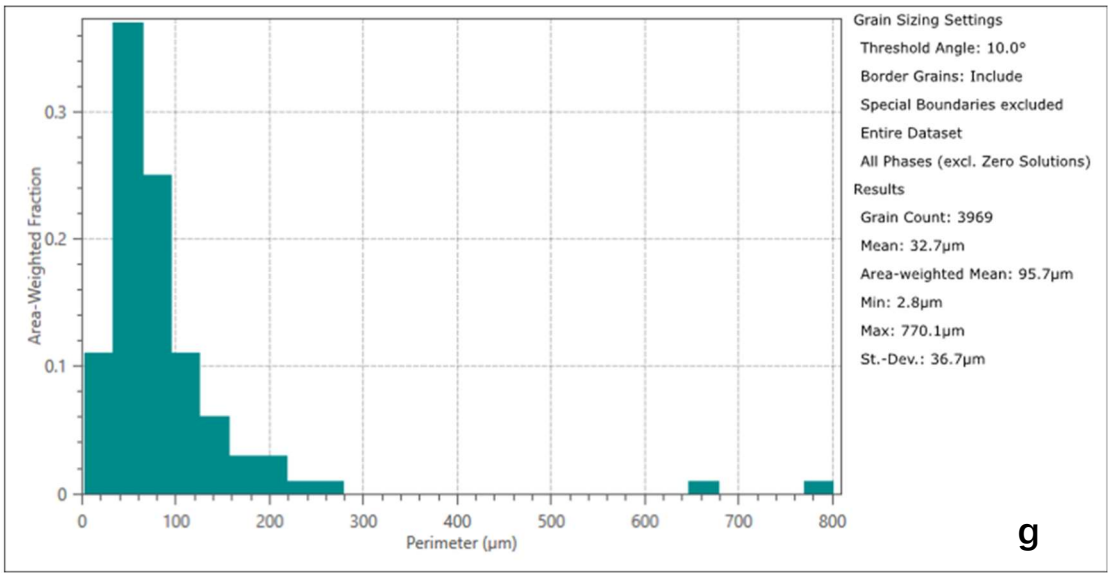

Figure 4-81 The EBSD result of the 1290s annealed 2D compressed Mg-0.1Ca-0.4Zn specimen: (a) The inverse pole figure map and grain boundaries, (b) The grain boundaries and the special grain boundaries, (c) The band contrast and the phase analysis, (d) The band contrast, (e) The pole figure, (f) The inverse pole figures, (g) Grain size distribution expressed as grain boundary perimeter

4.3.2.2.6 The two-direction (2D) compressed Mg-0.5Zn (at%) specimen

Figure 4-82 to 4-87 show the EBSD results of the 2D compressed Mg-0.5Zn (at%) specimen from the as-compressed state to the recrystallized state. For the specimen before annealing, the 2D compressed specimen showed a uniform microstructure like the 1D compressed specimen (shown in Figure 4-82(a)). Figure 4-82(g) shows that the average grain size of the specimen was 15.3μm. The largest grain on the map had a grain size of about 80μm. Figure 4-82(c) indicates that a considerable amount of shear bands (marked by white circles) and fine twins existed in the specimen occupying 24.4% of the scanned area. For the twin boundary fractions, Figure 4-82(b) shows that 55.2% of the grain boundaries were identified as the tensile twin boundaries. The fraction of the compressive twin boundaries and double twin boundaries were much less than the tensile twin boundaries with 0.3% and 0.9%, respectively. The result of the pole figure (shown in Figure 4-82(e) and (f)) showed a slightly different grain orientation distribution in the 2D compressed Mg-0.5Zn (at%) specimen. The main direction of the texture was still along the RD i.e. the direction of the second compression. However, another weak peak was observed close to the TD. It indicated that a notable number of grains were in this direction. The maximum pole intensity of the pole figure was 9.5. And the pole intensity of the weaker peak was 6.3.

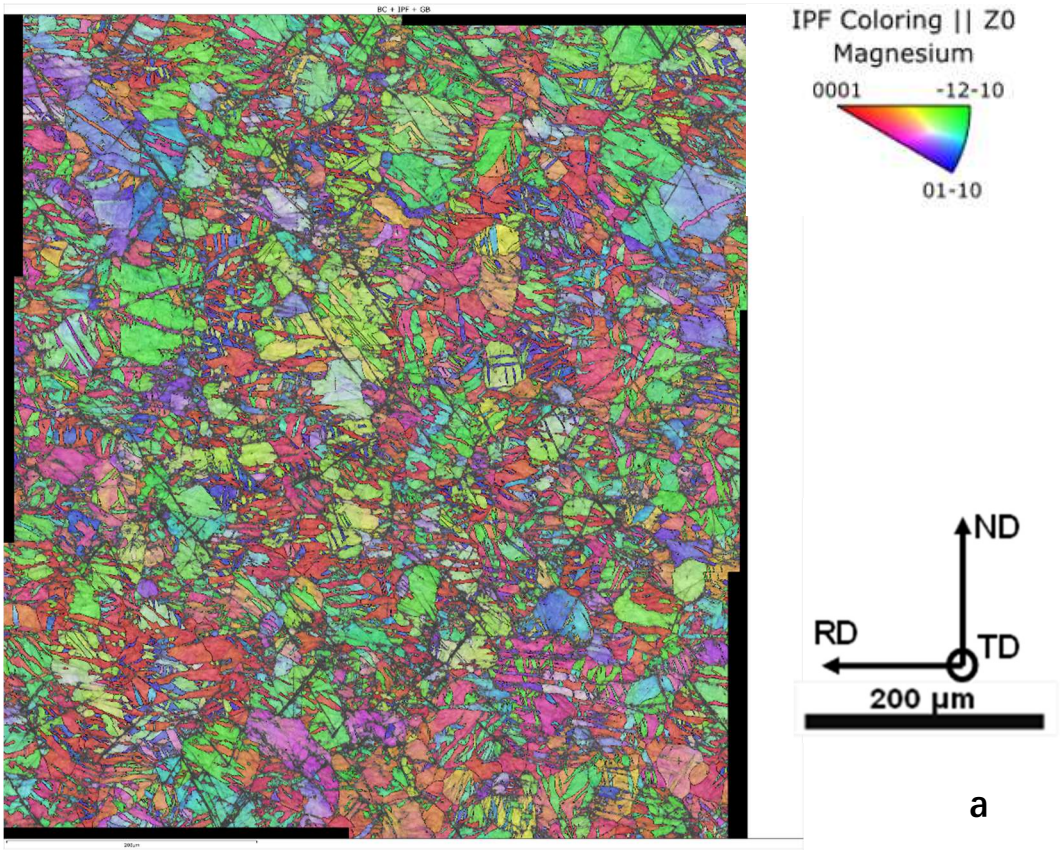
IPF Coloring || Z0
Magnesium
0001
-12-10
01-10
ND
RD
TD
200 µm

a

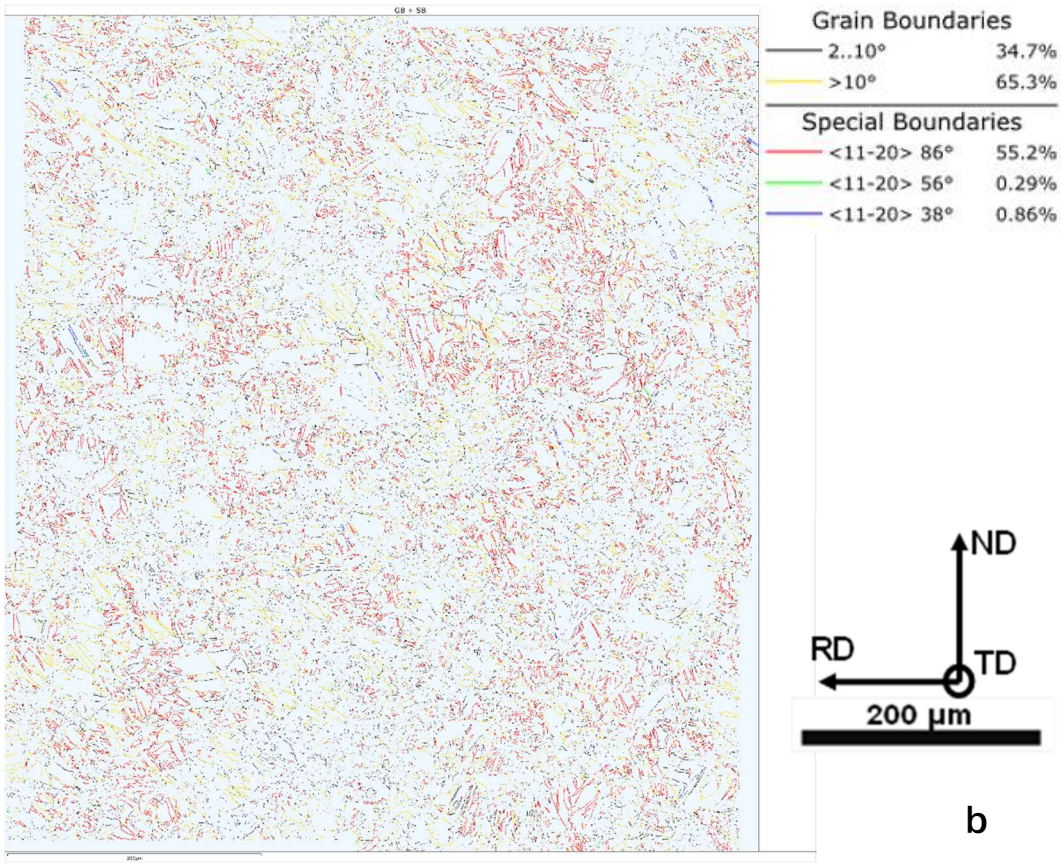
Grain Boundaries
2..10° 34.7%
>10° 65.3%
Special Boundaries
<11-20> 86° 55.2%
<11-20> 56° 0.29%
<11-20> 38° 0.86%
ND
RD
TD
200 µm

b

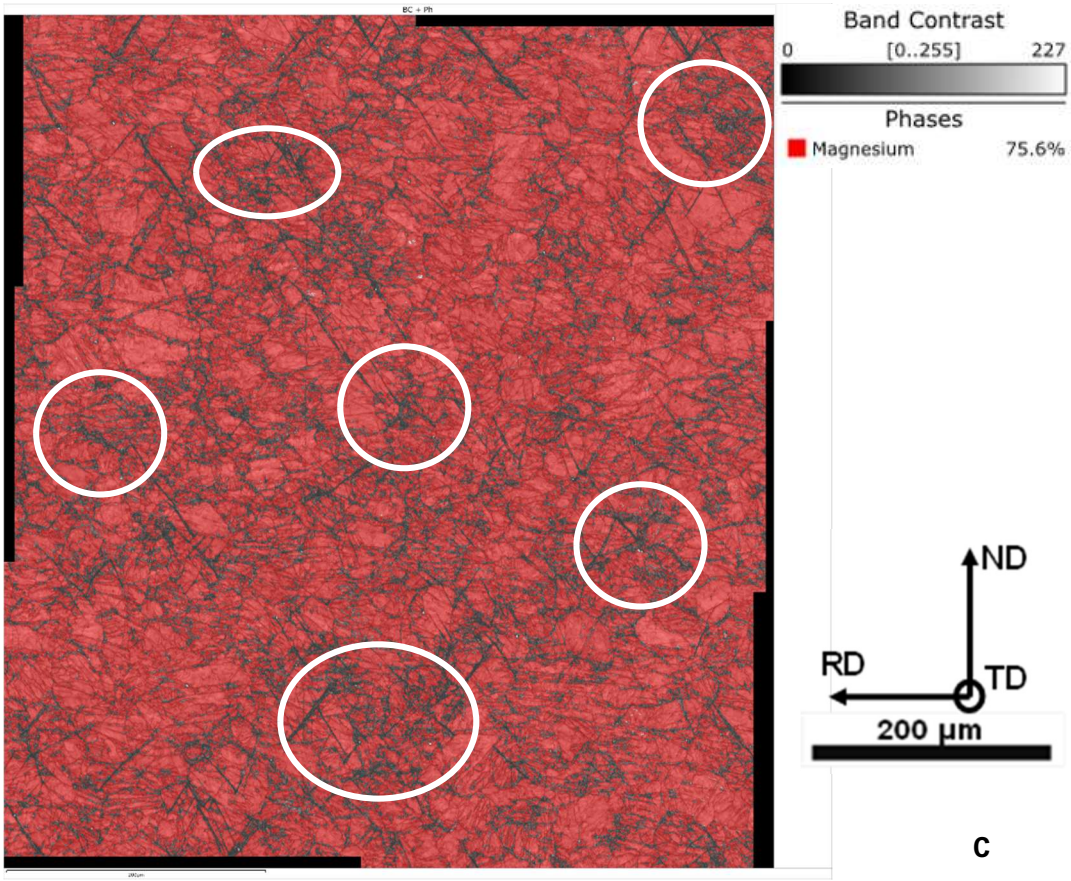
Band Contrast
0
[0..255]
227
Phases
Magnesium
75.6%
ND
RD
TD
200 µm

c

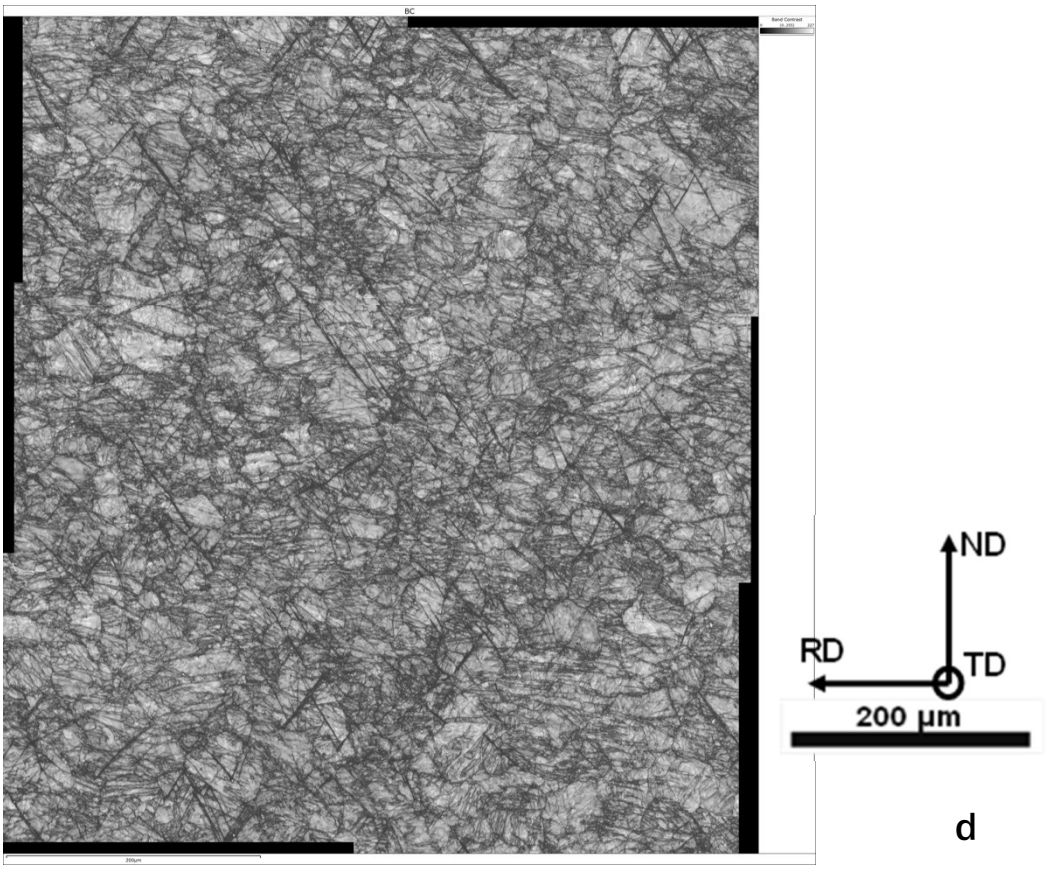
ND
RD
TD
200 µm

d

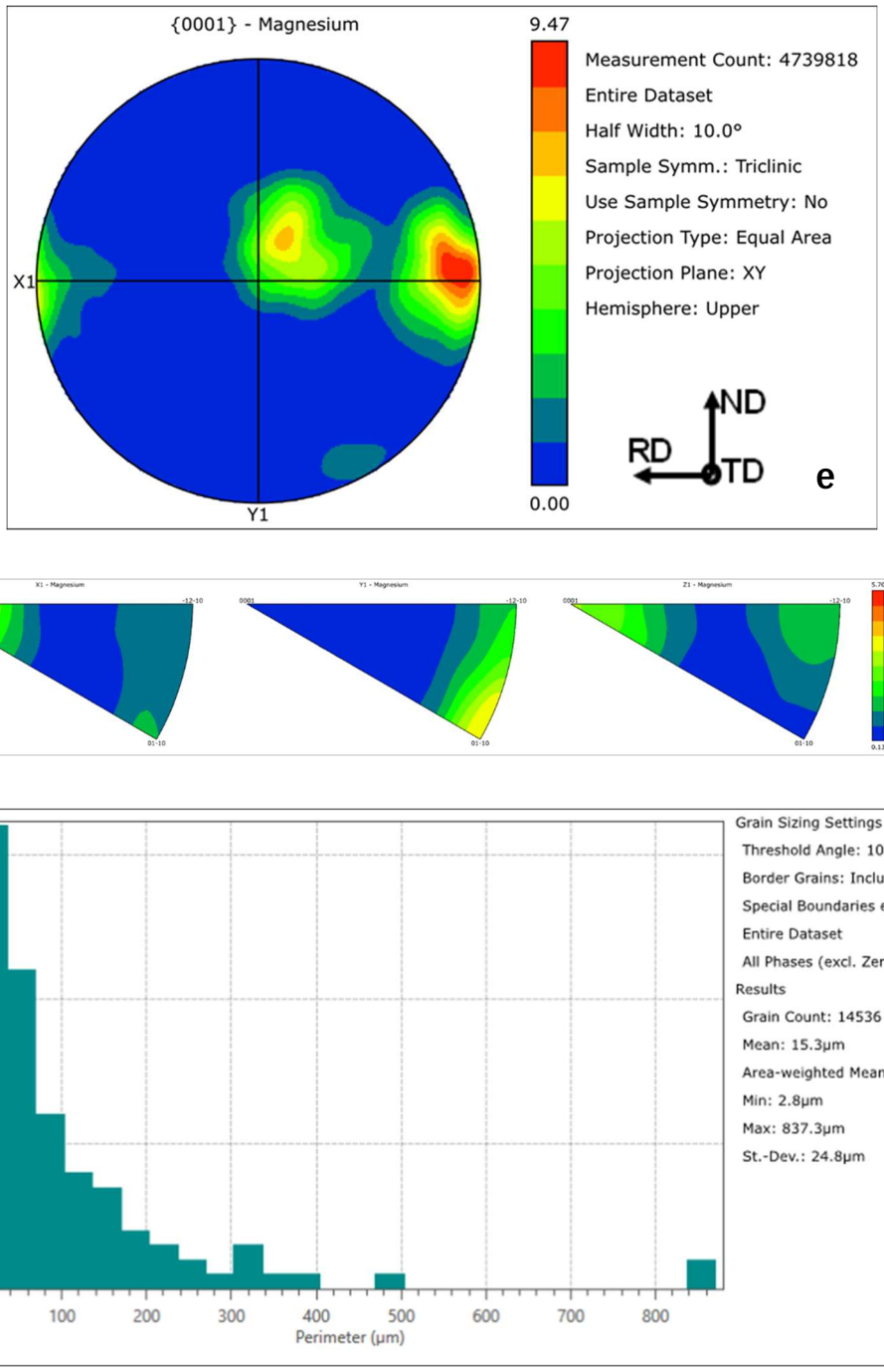

Figure 4-82 The EBSD result of the as-compressed 2D compressed Mg-0.5Zn specimen: (a) The inverse pole figure map and grain boundaries, (b) The grain boundaries and the special grain boundaries, (c) The band contrast and the phase analysis, (d) The band contrast, (e) The pole figure, (f) The inverse pole figures, (g) Grain size distribution expressed as grain boundary perimeter

No obvious change was observed in the microstructure, including no evidence of recovery, was found for an annealing time of 210s in the 2D compressed Mg-0.5Zn (at%) specimen. The EBSD results of the 30s, 45s and 60s annealing (30s, 75s and 135s heat treatment time in total, respectively) are presented in Appendix I and are not

discussed in the text.

Figure 4-83 shows the EBSD results of the same specimen after annealing for 210s. The temperature of the specimen at this stage was 165℃ (based on Figure 4-13). The IPF map showed that the 2D compressed specimen was just starting recrystallization (shown in Figure 4-83(a)). The average grain size ($15.4\mu m$) at this stage was almost not changed (shown in Figure 4-83(g)). As with the other specimens, a large number of recrystallized grains were found inside the shear bands and fine twinned area. Figure 4-83(c) indicates that the non-indexed area of the map was found to reduce from 24.4% to 12%. Given the limited recovery regions identified in the specimen, the 12.4% reduction in the unknown region was attributed to the reduction of shear bands, which transformed into recrystallized grains. The result from Figure 4-83(b) presents quite a similar trend as the other boundaries, in which the boundary fraction of the tensile twins decreased from 55.2% to 49.1% after the specimen started recrystallization while the fraction of the compressive twins and the double twins increased from 0.3% to 0.4% and from 0.9% to 1.2%, respectively. On the other hand, Figure 4-83(e) shows that the maximum pole intensity reduced from 9.5 to 8.7. The diffusion areas of two peaks in the pole figure did not show obvious change i.e. there were not many changes in grain orientation. A notable point was that the pole intensity of the weaker peak slightly increased from 6.3 to 6.7.

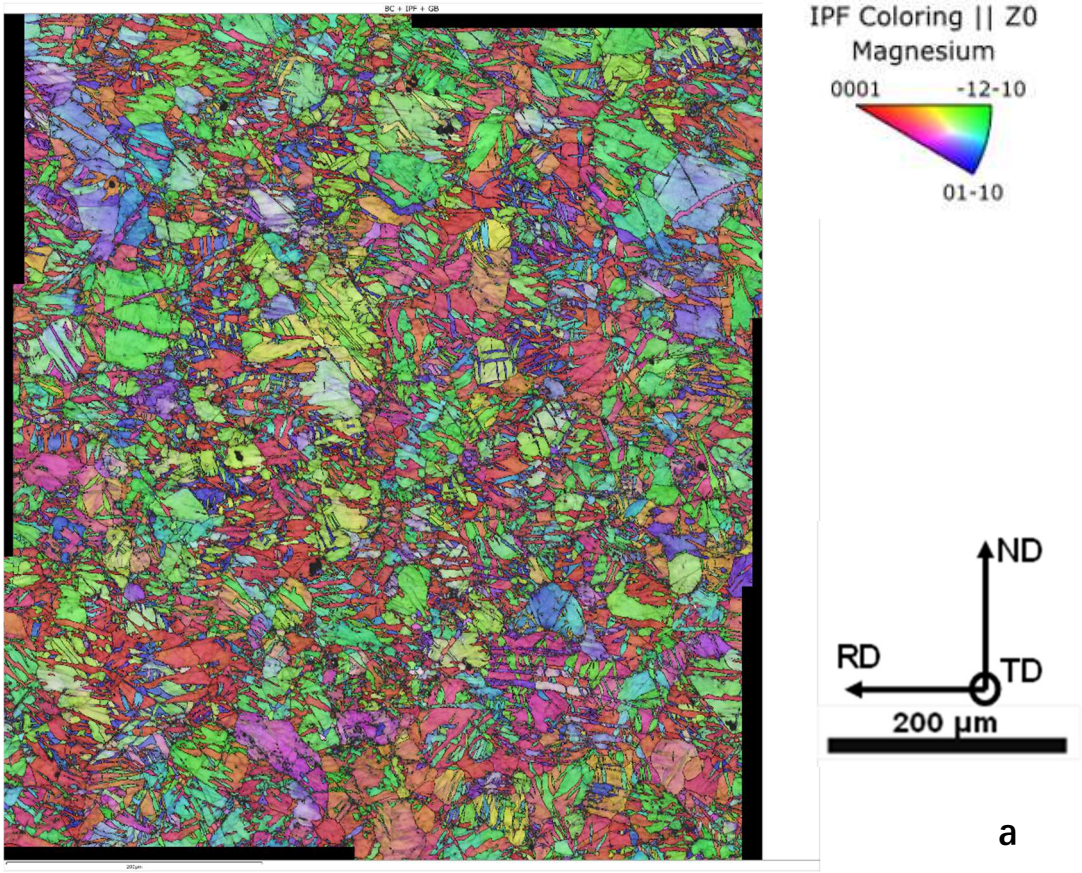

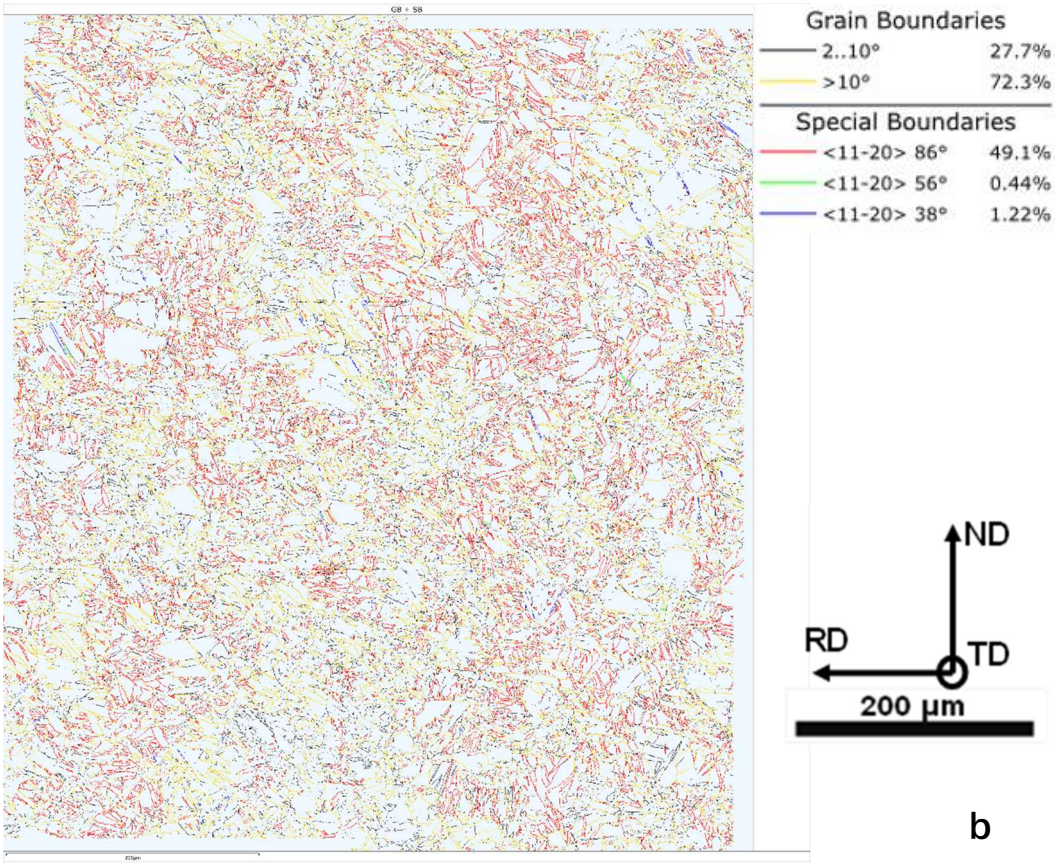
GB + SB
Grain Boundaries
2..10° 27.7%
>10° 72.3%
Special Boundaries
<11-20> 86° 49.1%
<11-20> 56° 0.44%
<11-20> 38° 1.22%
ND
RD
TD
200 µm

b

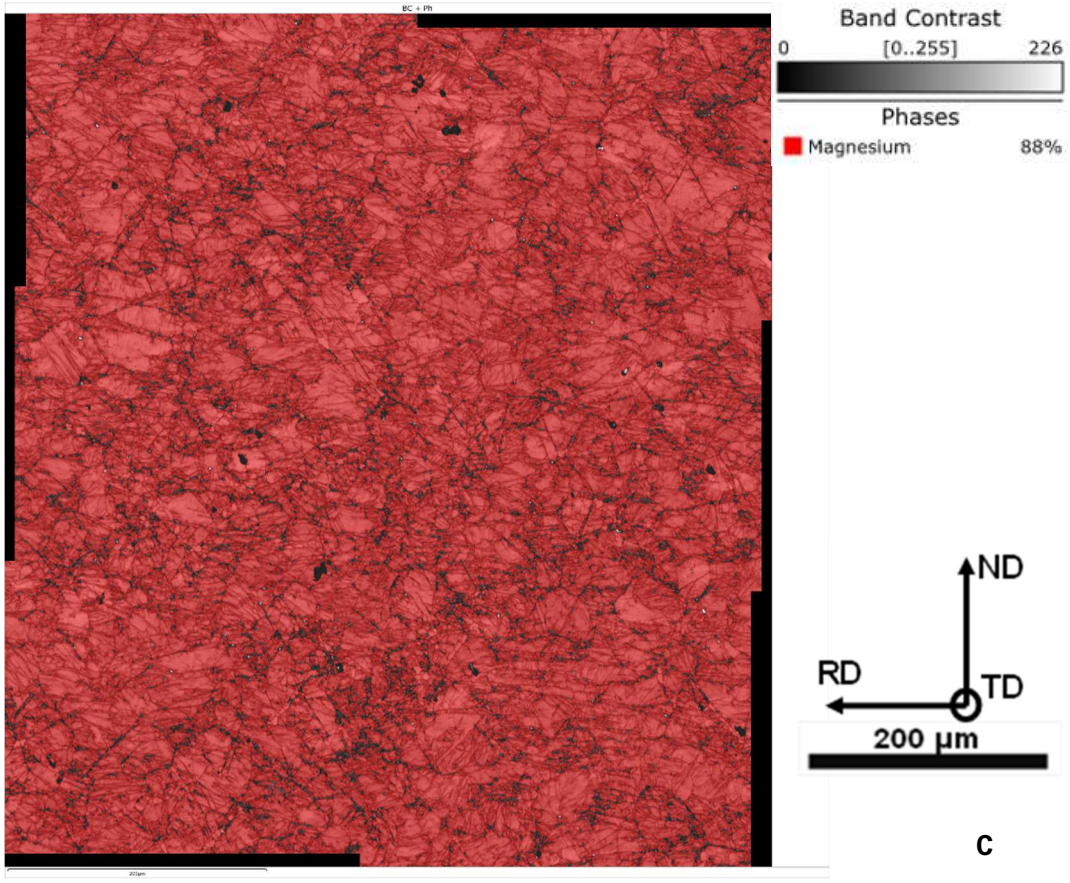
BC + Ph
Band Contrast
0 [0..255] 226
Phases
Magnesium 88%
ND
RD
TD
200 µm

c

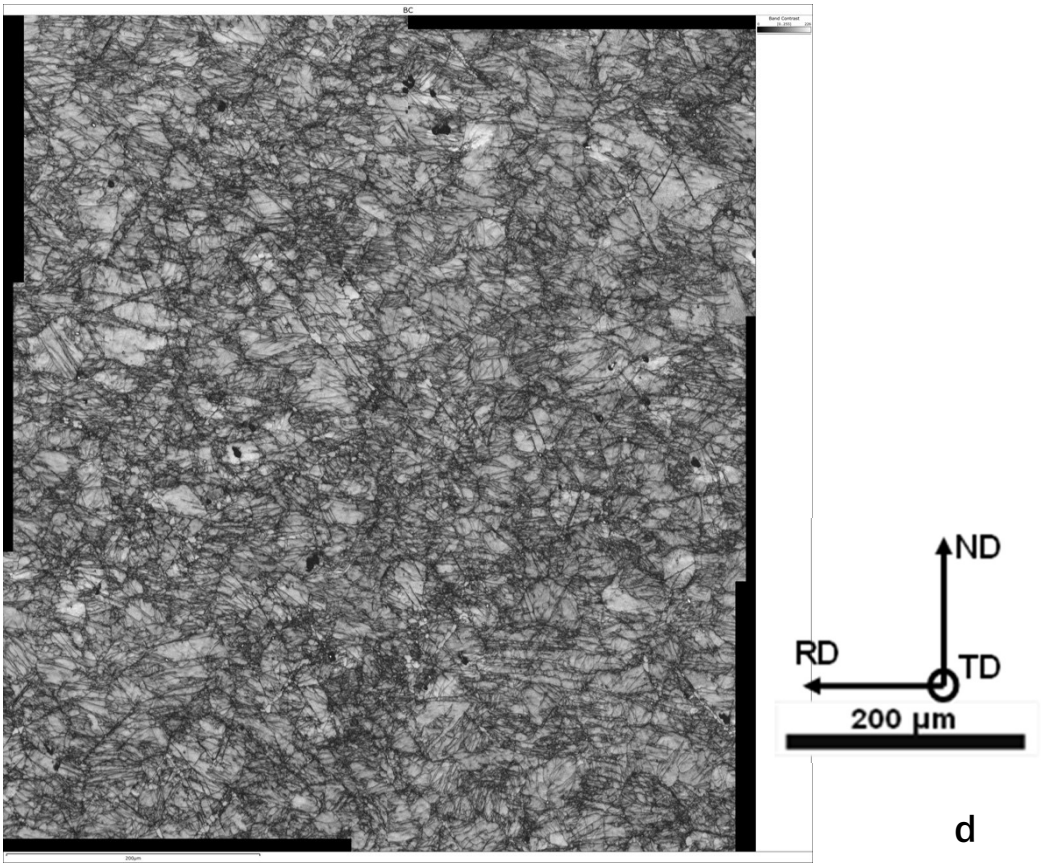
ND
RD
TD
200 µm

d

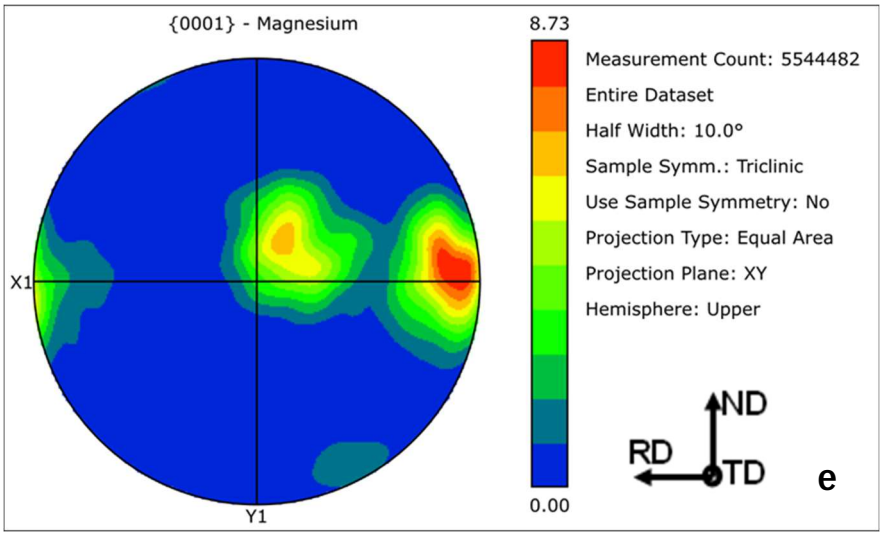
{0001} - Magnesium
8.73
0.00
Measurement Count: 5544482
Entire Dataset
Half Width: 10.0°
Sample Symm.: Triclinic
Use Sample Symmetry: No
Projection Type: Equal Area
Projection Plane: XY
Hemisphere: Upper
X1
Y1
ND
RD
TD

e

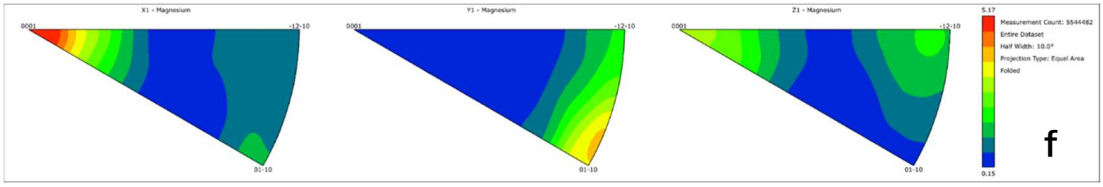

f

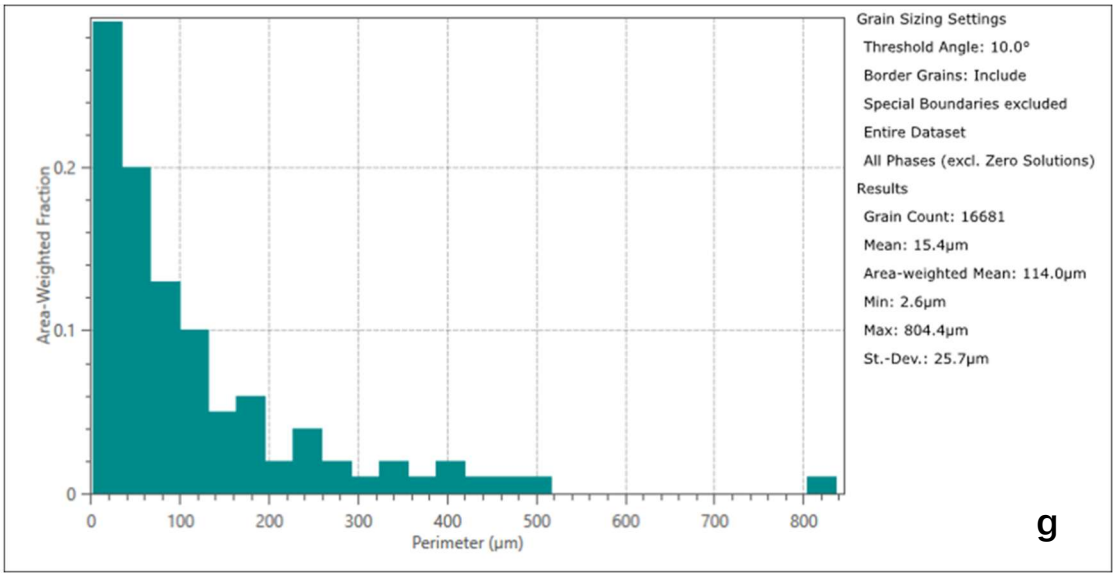

Figure 4-83 The EBSD result of the 210s annealed 2D compressed Mg-0.5Zn specimen: (a) The inverse pole figure map and grain boundaries, (b) The grain boundaries and the special grain boundaries, (c) The band contrast and the phase analysis, (d) The band contrast, (e) The pole figure, (f) The inverse pole figures, (g) Grain size distribution expressed as grain boundary perimeter

A further 15s anneal, i.e. after a total of 300s annealing, the recrystallization became obvious and was easy to observe. The temperature of the specimen at that time point was 186℃. Figure 4-84 shows the EBSD results of the same specimen at that stage. From Figure 4-84(a), it was clear that the scanning quality was not as good as last time. The fraction of the identified area was reduced from 88.0% to 76.1%. Thus, the readings from this stage might show some abnormal increase (or decrease). However, the growth of the existing recrystallized grains and the newly generated grains were still able to be observed (shown in Figure 4-84(a)). The recrystallization from the shear bands was almost finished (shown in Figure 4-84(c)) and the new grains from the shear bands started to grow. Meanwhile, the recrystallization based on twins was also observed. Figure 4-84(h) and (i) show the zoomed image which was cropped from the large EBSD map marked by the black rectangle. It shows the nucleation of the recrystallized grains from the twins. The changes in the twin boundary fractions also reflected the recrystallization. Figure 4-84(b) shows that the boundary fraction of the tensile twins, compressive twins and double twins all reduced from 49.1% to 44.9%, 0.44% to 0.40% and 1.2% to 0.8%, respectively. However, the fraction of the low-angle grain boundary and the high-angle grain boundary did not change as they should be, which the low-angle grain boundary increased from 27.7% to 31.6% and the high-angle grain boundary reduced from 72.3% to 68.4%. The reason for this abnormal change

was already mentioned above i.e. the lower index rate during the scanning caused the loss of the boundary information. The average grain size of the specimen was 16.7μm (shown in Figure 4-84(g)). Due to the low scanning quality, Figure 4-84(e) indicates that the maximum value of the pole figure was increased rather than decreased from 8.7 to 9. Meanwhile, the weak peak close to the TD along with the ND mentioned before showed a further enhancement, in which the pole intensity increased from 6.7 to 7.5.

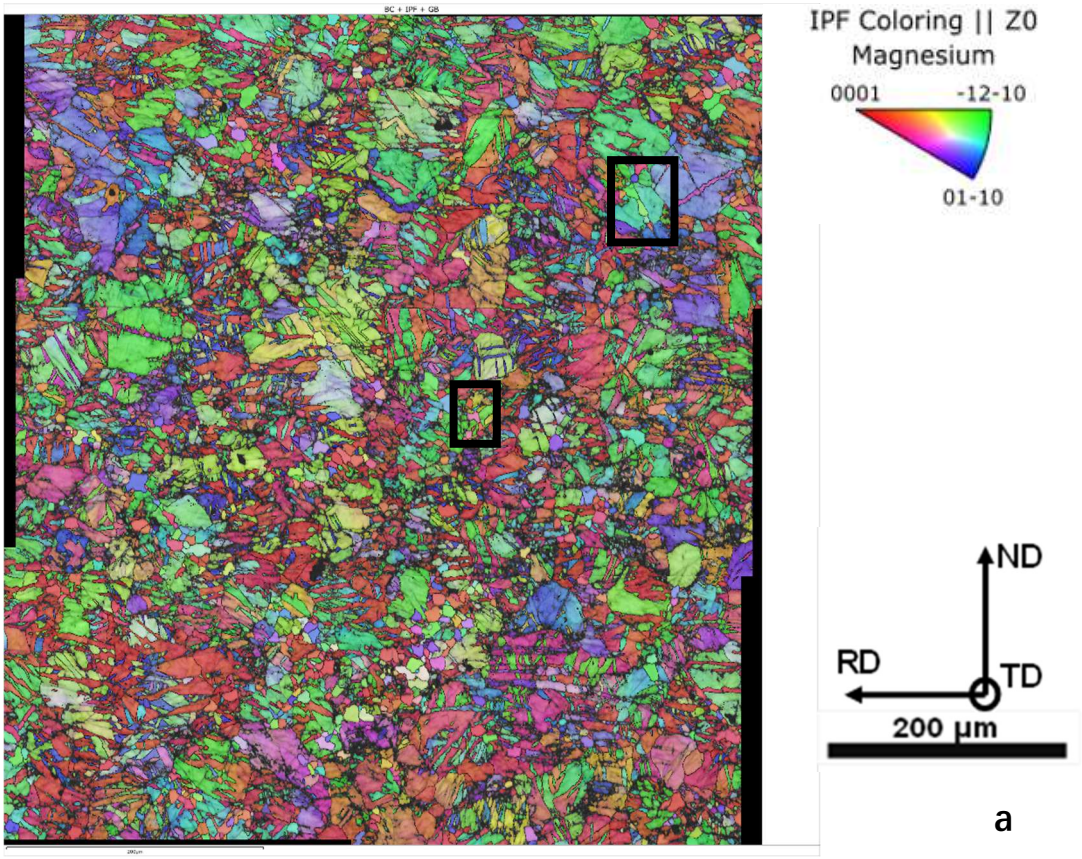

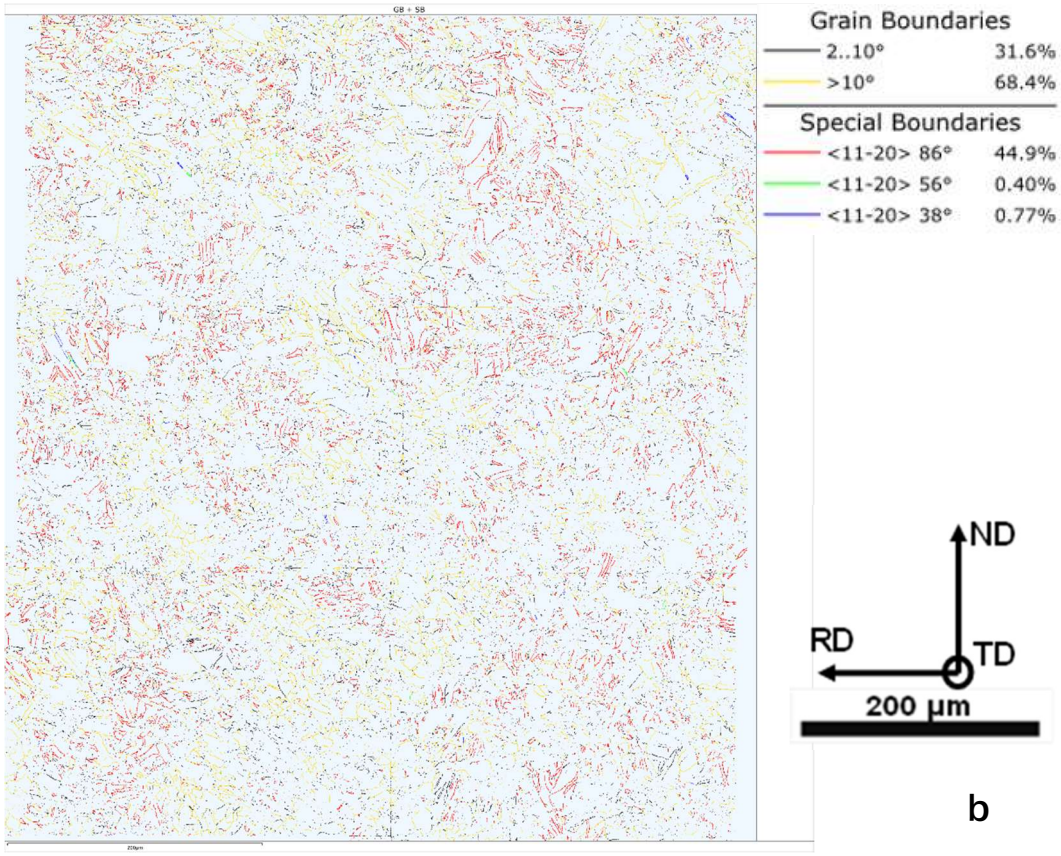
GB + SB
Grain Boundaries
2..10° 31.6%
>10° 68.4%
Special Boundaries
<11-20> 86° 44.9%
<11-20> 56° 0.40%
<11-20> 38° 0.77%
ND
RD
TD
200 µm

b

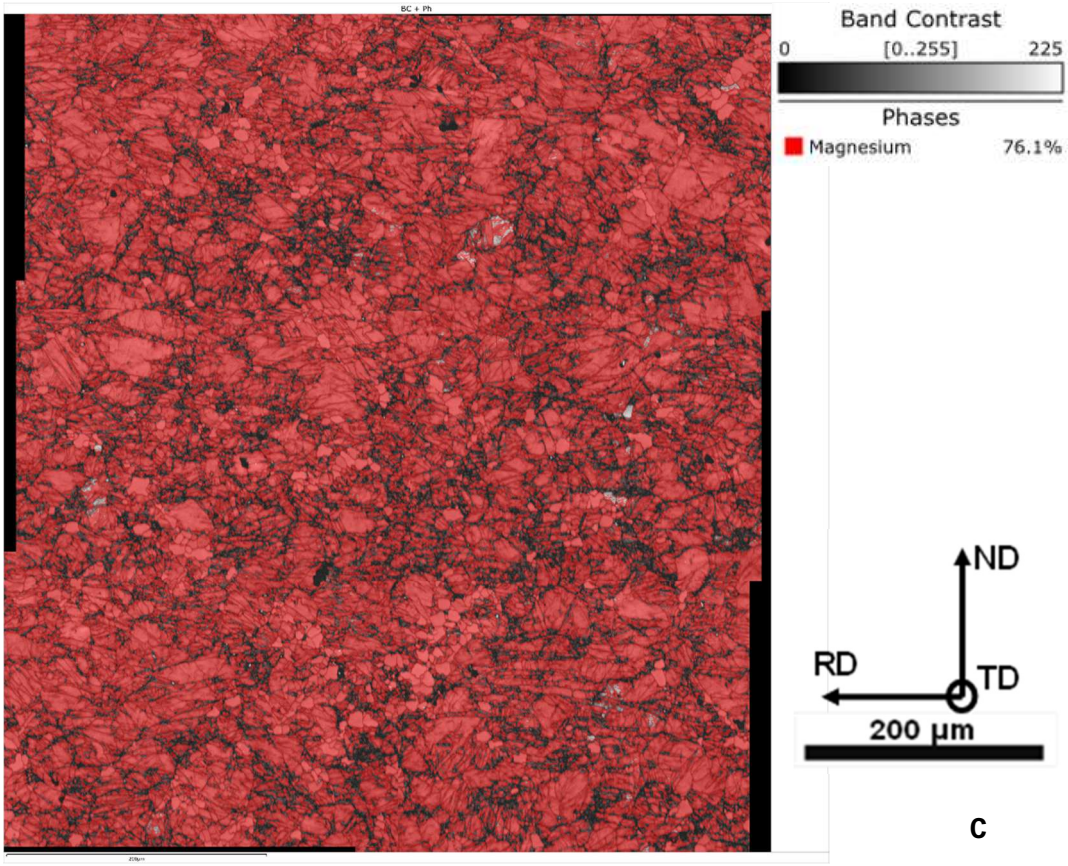
BC + Ph
Band Contrast
0 [0..255] 225
Phases
Magnesium 76.1%
ND
RD
TD
200 µm

c

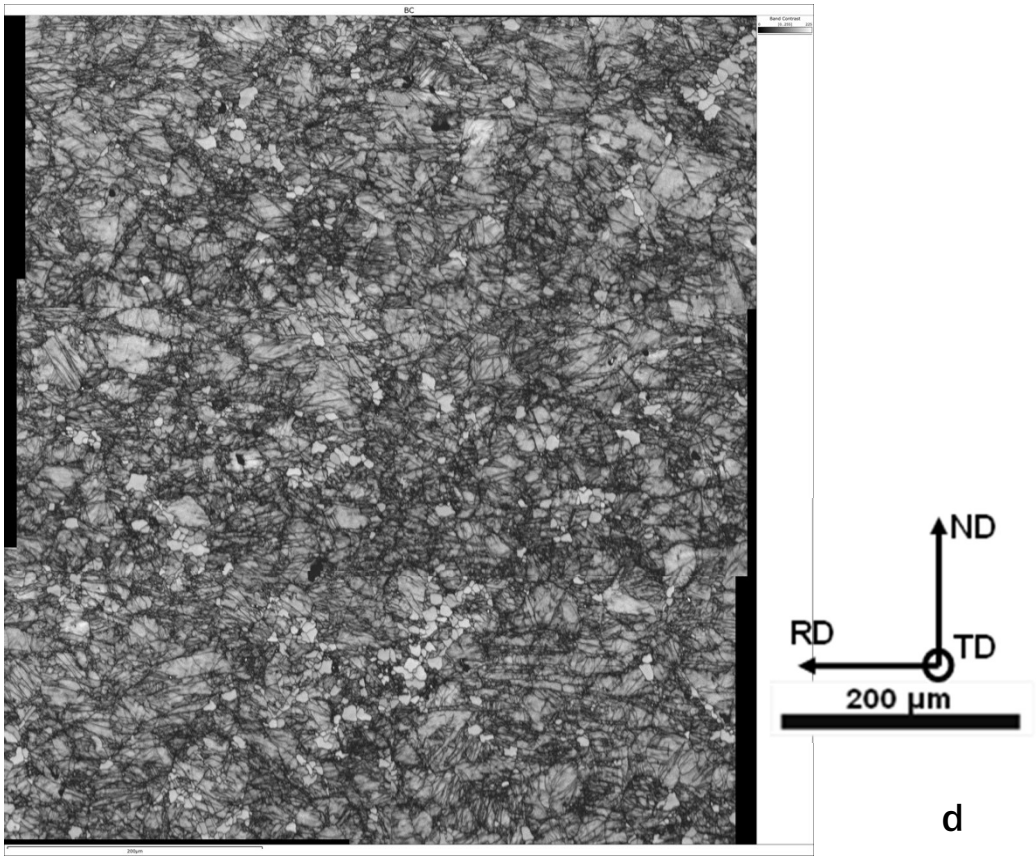
BC
ND
RD
TD
200 µm

d

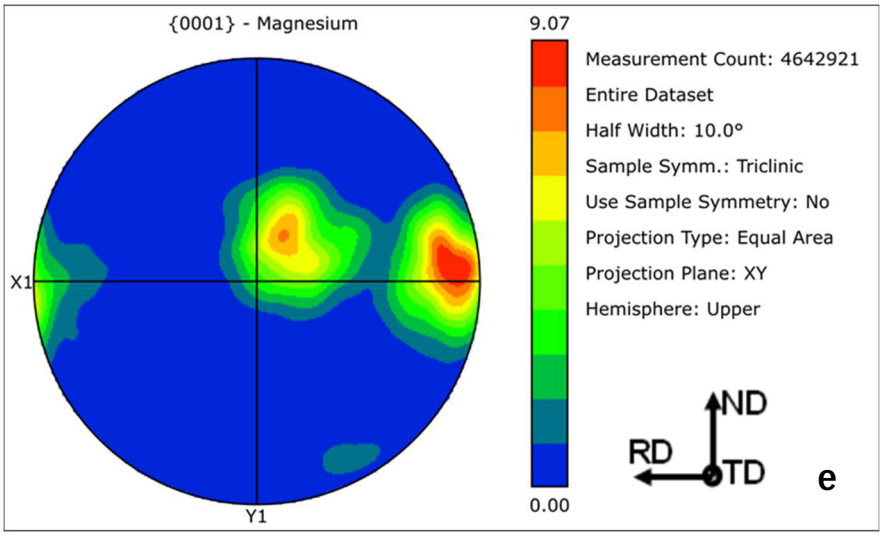
{0001} - Magnesium
9.07
0.00
Measurement Count: 4642921
Entire Dataset
Half Width: 10.0°
Sample Symm.: Triclinic
Use Sample Symmetry: No
Projection Type: Equal Area
Projection Plane: XY
Hemisphere: Upper
X1
Y1
ND
RD
TD

e

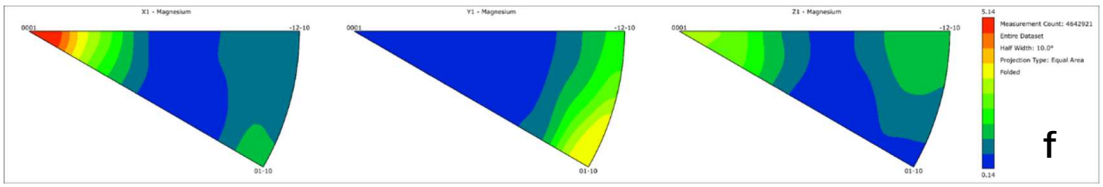
X1 - Magnesium
Y1 - Magnesium
Z1 - Magnesium
5.14
0.14
Measurement Count: 4642921
Entire Dataset
Half Width: 10.0°
Projection Type: Equal Area
Folded

f

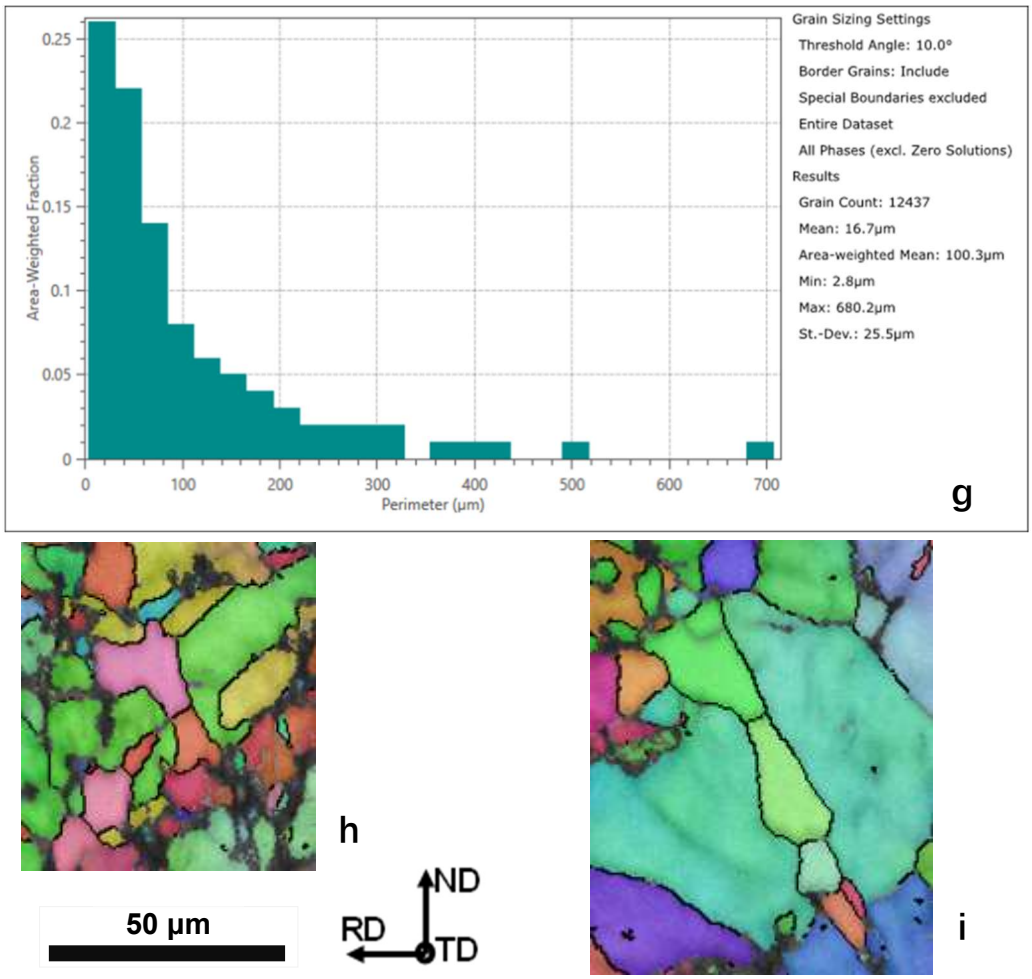

Figure 4-84 The EBSD result of the 300s annealed 2D compressed Mg-0.5Zn specimen: (a) The inverse pole figure map and grain boundaries, (b) The grain boundaries and the special grain boundaries, (c) The band contrast and the phase analysis, (d) The band contrast, (e) The pole figure, (f) The inverse pole figures, (g) Grain size distribution expressed as grain boundary perimeter, (h) and (i) The grain nucleated from twins

Figure 4-85 presents the microstructure after a total annealing time of 420s. The temperature of the specimen at that time point was 212℃. From Figure 4-85(a), it was clear that the recrystallization continued during the 30s increased annealing time. The grain growth and the recrystallized grain nucleation were observed across the whole scanned area. The average grain size at this stage was 16μm (shown in Figure 4-85(g)), which was smaller than that of the last step. It also showed that a large number of new grains were generated. However, all the new recrystallized grains were found to have nucleated at the grain boundaries. Except for the recrystallized grains mentioned in the last stage, no more new recrystallized grains were found related to twins. Meanwhile, the size of all these twin-related new grains was found to be almost the same as in the last stage i.e. the recrystallized grains which were found to grow were all nucleated

from the grain boundaries. Figure 4-85(b) presents the boundary fraction of the tensile twins, compressive twins and double twins and it shows that the boundary fraction of twins did not change very much. The boundary fraction of three kinds of twins changed from 44.9% to 41.6%, 0.40% to 0.43% and 0.77% to 0.83%, respectively. The boundary fraction of the low-angle grain boundaries and high-angle grain boundaries exhibited an increase and a decrease from 31.6% to 34.0% and 68.4% to 66.0%, respectively. The abnormal changes of the low-angle grain boundaries and high-angle grain boundaries were attributed to the error of the boundary identification. The EBSD map was montaged by six small frames. The edge of the frames was identified as the low-angle grain boundaries causing the irregular change of the fraction value. For the grain orientation distribution, the pole figure and IPF of this stage showed some different results compared to other kinds of specimens. Figure 4-85(e) and (f) indicate that the orientation of the new grains did not show a random distribution in the pole figure but showed a more concentrated distribution diffused around the weak peak mentioned before. The orientation of the weak peak was very close to the TD and the weak peak formed by the recrystallized grains had become stronger than the previous stage. The pole intensity of the weak peak increased from 7.5 to 8. The orientation distribution of the recrystallized grains was found to show a trend to change to the basal texture orientation distribution. Meanwhile, the maximum value of the pole figure increased a little from 9 to 9.2.

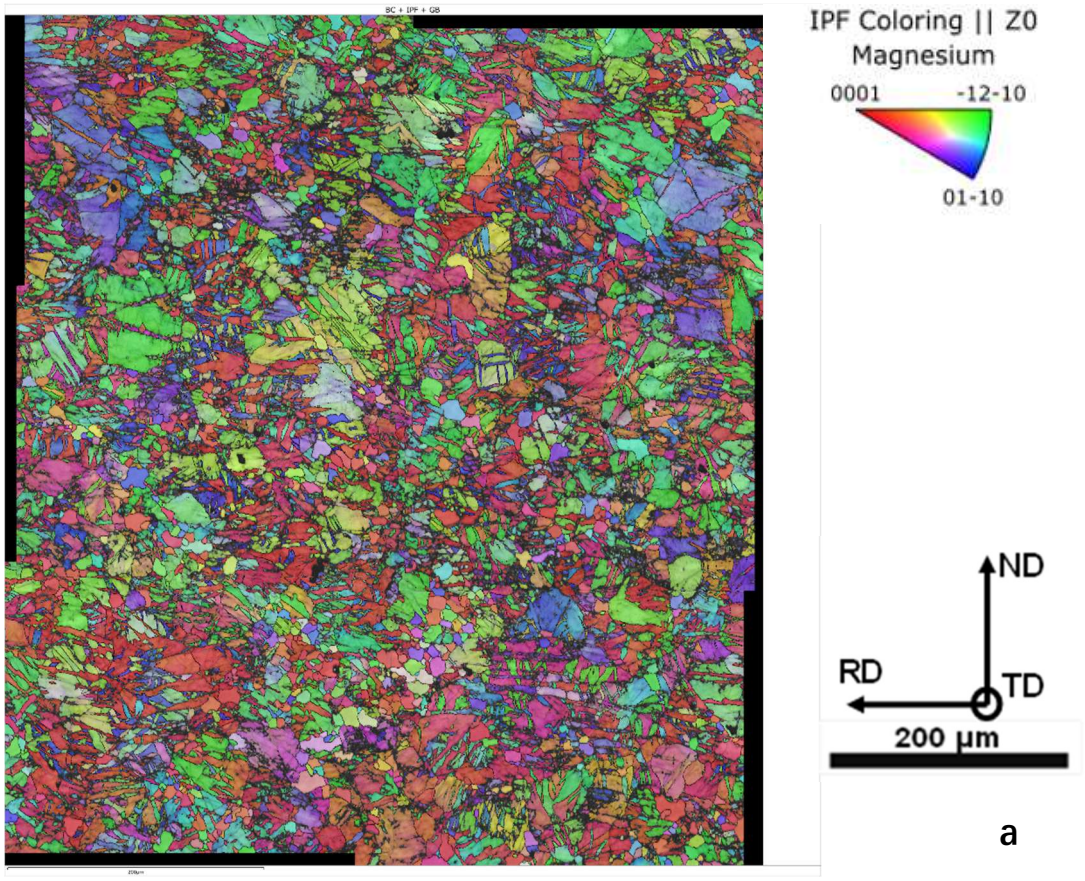

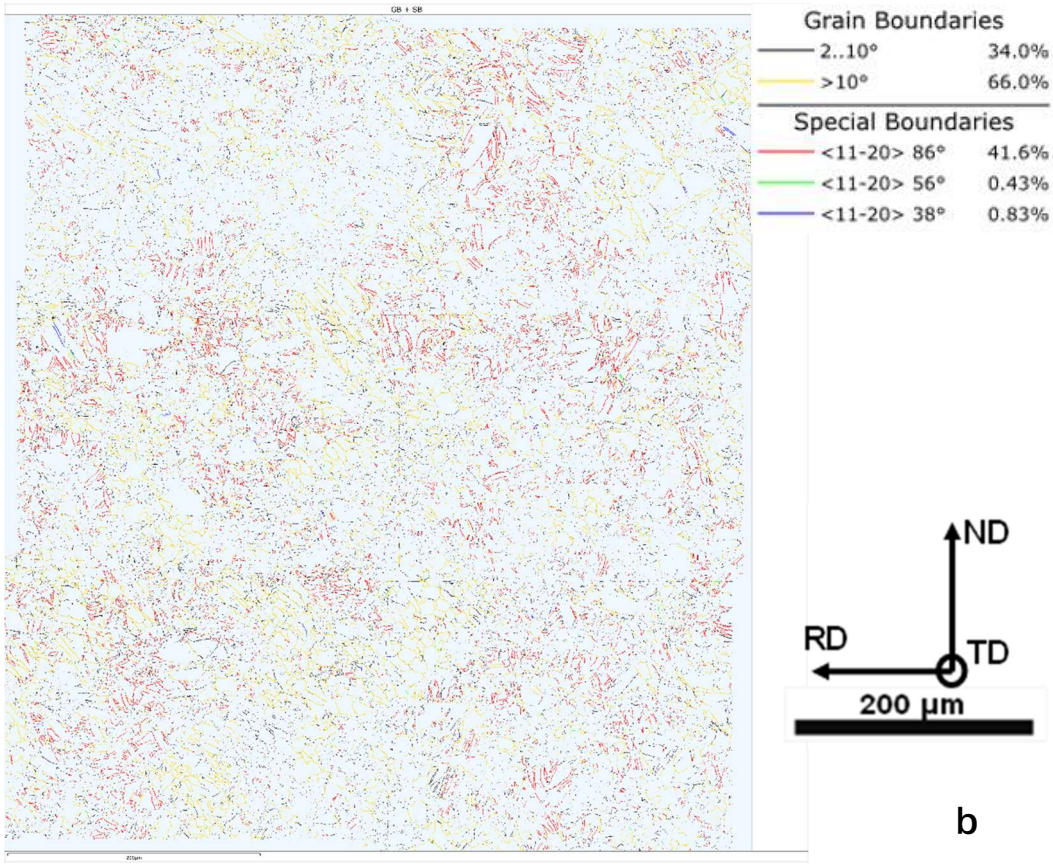
GB + SB
Grain Boundaries
2..10° 34.0%
>10° 66.0%
Special Boundaries
<11-20> 86° 41.6%
<11-20> 56° 0.43%
<11-20> 38° 0.83%
ND
RD
TD
200 µm

b

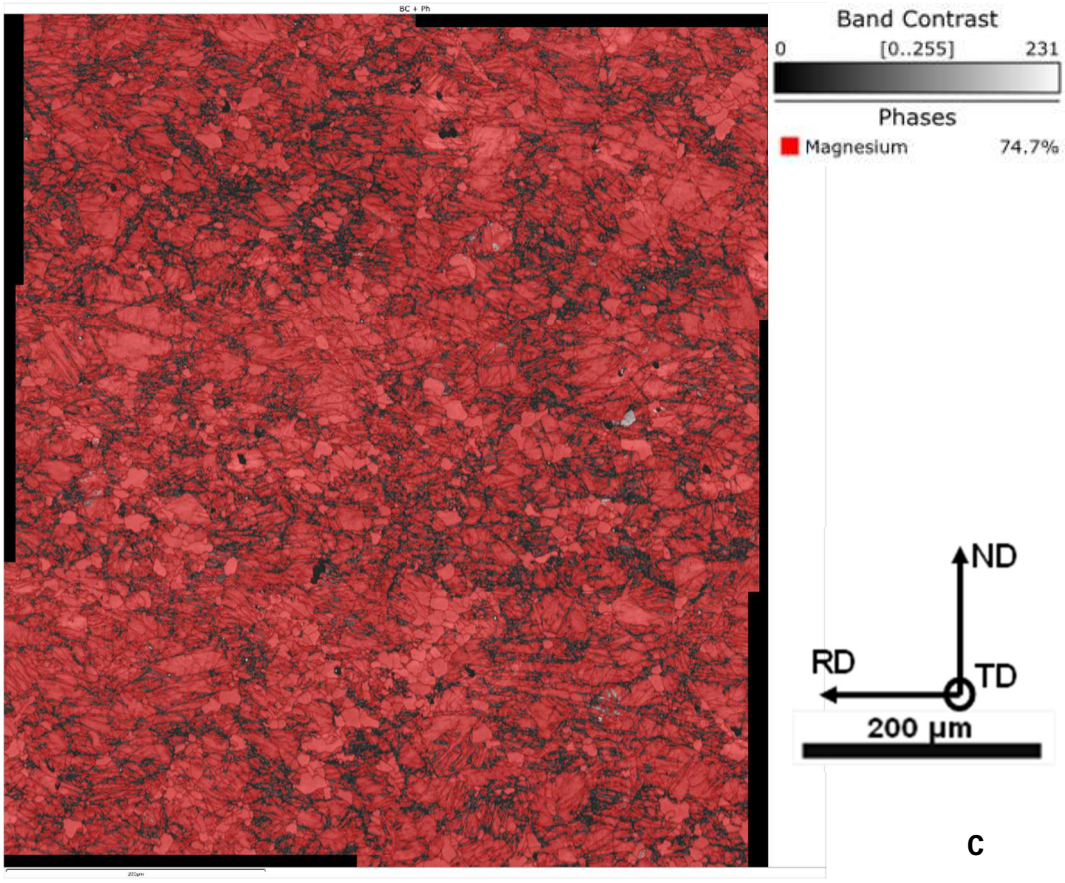
BC + Ph
Band Contrast
0 [0..255] 231
Phases
Magnesium 74.7%
ND
RD
TD
200 µm

c

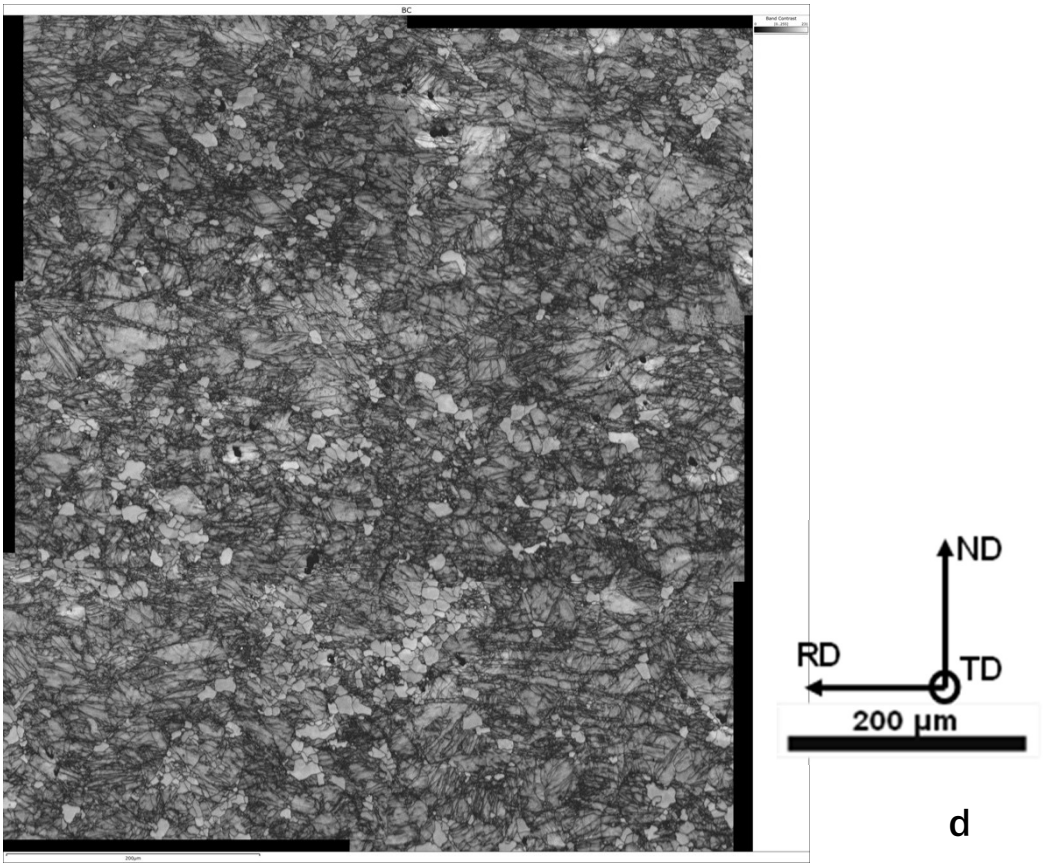
BC
ND
RD
TD
200 µm

d

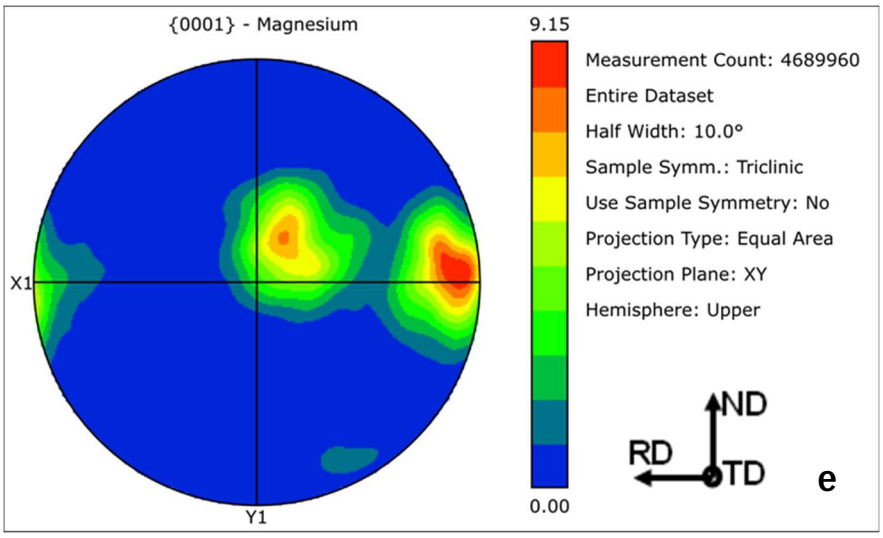
{0001} - Magnesium
9.15
0.00
Measurement Count: 4689960
Entire Dataset
Half Width: 10.0°
Sample Symm.: Triclinic
Use Sample Symmetry: No
Projection Type: Equal Area
Projection Plane: XY
Hemisphere: Upper
X1
Y1
ND
RD
TD

e

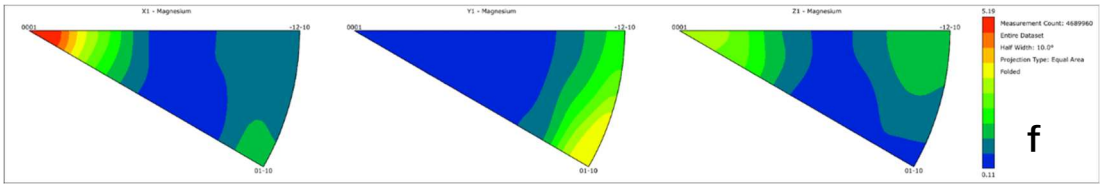

f

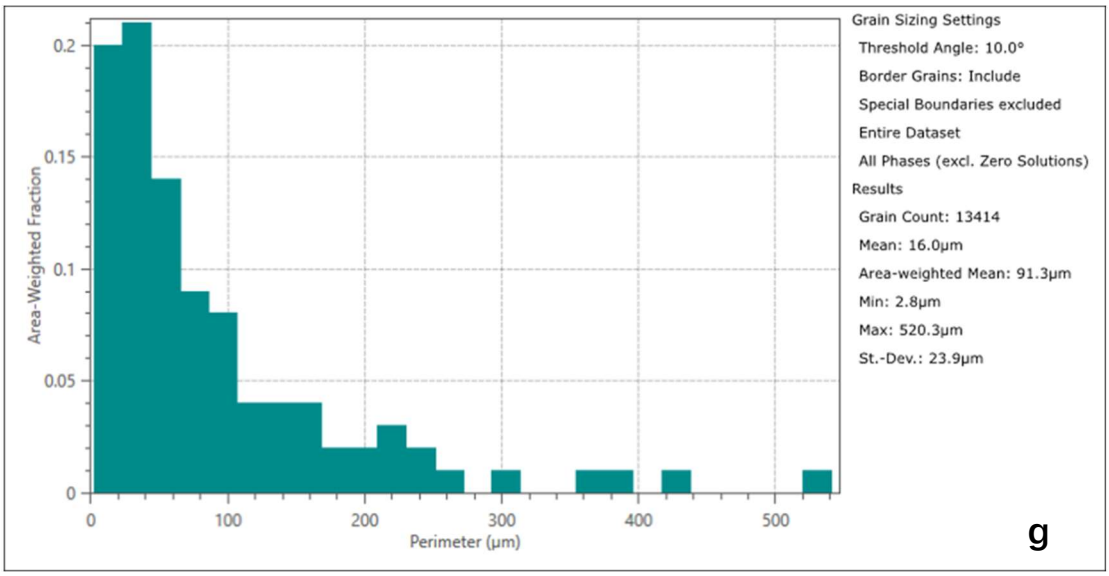

Figure 4-85 The EBSD result of the 420s annealed 2D compressed Mg-0.5Zn specimen: (a) The inverse pole figure map and grain boundaries, (b) The grain boundaries and the special grain boundaries, (c) The band contrast and the phase analysis, (d) The band contrast, (e) The pole figure, (f) The inverse pole figures, (g) Grain size distribution expressed as grain boundary perimeter

Figure 4-86 shows the EBSD results of the same specimen after annealing for 570s. The temperature of the specimen at that time point was 240℃. In contrast to the previous stage, with only a 30s longer annealing and a 28℃ temperature difference, the microstructure of this 1D compressed specimen showed obvious variation. The IPF map (shown in Figure 4-86(a)) indicated that the specimen experienced rapid grain growth during the annealing process. Very similar to the rapid recrystallization in other specimens, not just the existing recrystallized grains showed obvious grain growth (e.g. from around $10\mu m$ to about $50\mu m$) but also many rapid growth new recrystallized grains were found (e.g. from $0\mu m$ to about $40\mu m$) across the whole map. The white circles in Figure 4-86(a) mark some of the areas which had such rapid-growth grains. The average grain size of the specimen increased from $16\mu m$ to $20.7\mu m$ (shown in Figure 4-86(g)). These fast-growing recrystallized grains were found not just from shear bands but also from grain boundaries. The recrystallized grains from twins exhibited limited grain growth compared to the other recrystallized grains. On the other hand, the consumption of twins (especially tensile twins) was observed. The changes in the twin boundary fractions were the evidence for proving this. Figure 4-86(b) indicates that the boundary fraction of the tensile twins, compressive twins and double twins changed from 41.9% to 33.4%, 0.4% to 0.7% and 0.8% to 1.1%, respectively. Meanwhile, the fraction of the low-angle grain boundary and the high-angle grain

boundary showed a corresponding change from 34.0% to 22.1% and from 66.0% to 77.9%, respectively. With the progress of the recrystallization, the increase in the boundary fraction of the compressive twins and double twins was not normal. The reason for this was attributed to the improvement of the scanning quality. More details of the grain boundaries were shown on the map (Figure 4-86(b)) than in the previous stage. Compared to the dramatic variation shown in the IPF map, the changes were not that significant in the pole figure and IPF (shown in Figure 4-86(e) and (f)). The general grain orientation distribution was almost the same compared to the previous stage shown in the pole figure. The direction of the grains did not further spread out but concentrated in this range i.e. a weakened texture was not shown. As a result, the pole intensity of the recrystallized grains (weak peak close to the TD mentioned in the last step) was found to increase from 8.0 to 9.4, which became the strongest peak in the pole figure. The pole intensity of the previous strongest peak was now reduced from 9.2 to 8.5. Compared to the maximum value of the pole figure from the previous stage, it was found to increase by 0.2 (from 9.2 to 9.4) rather than decrease as the other specimens.

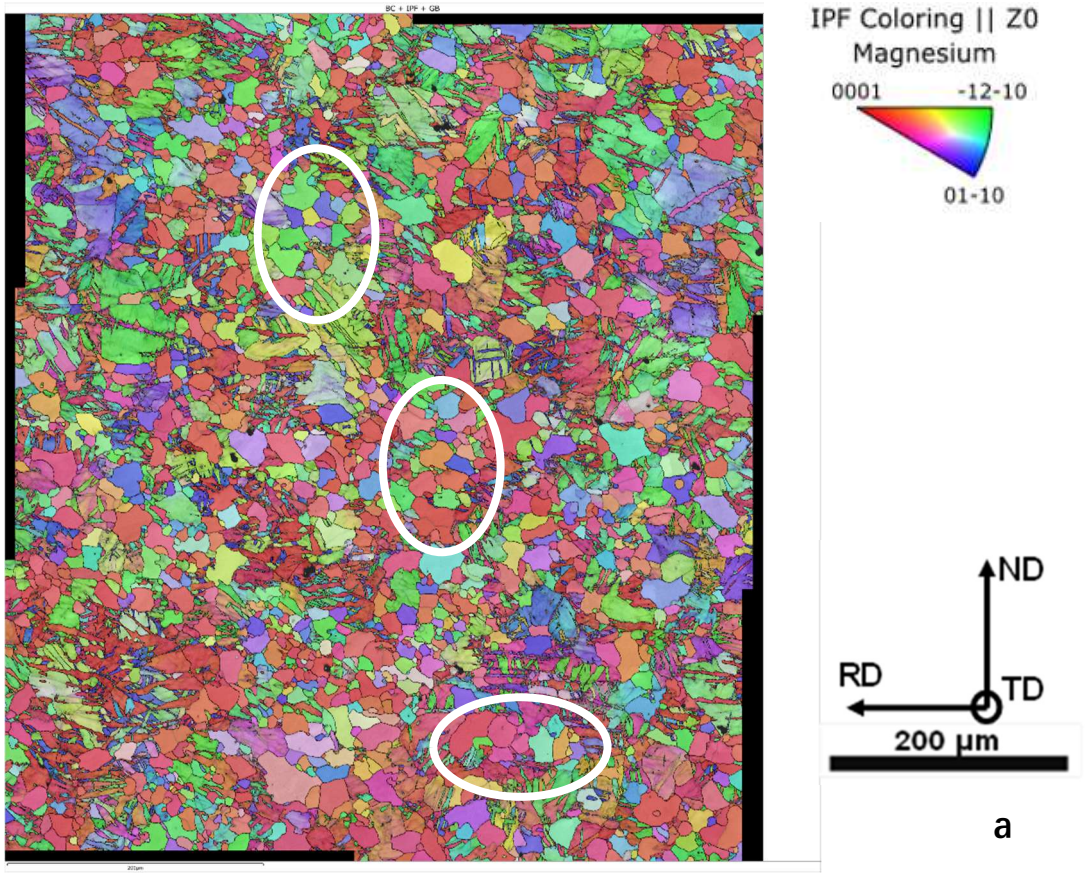

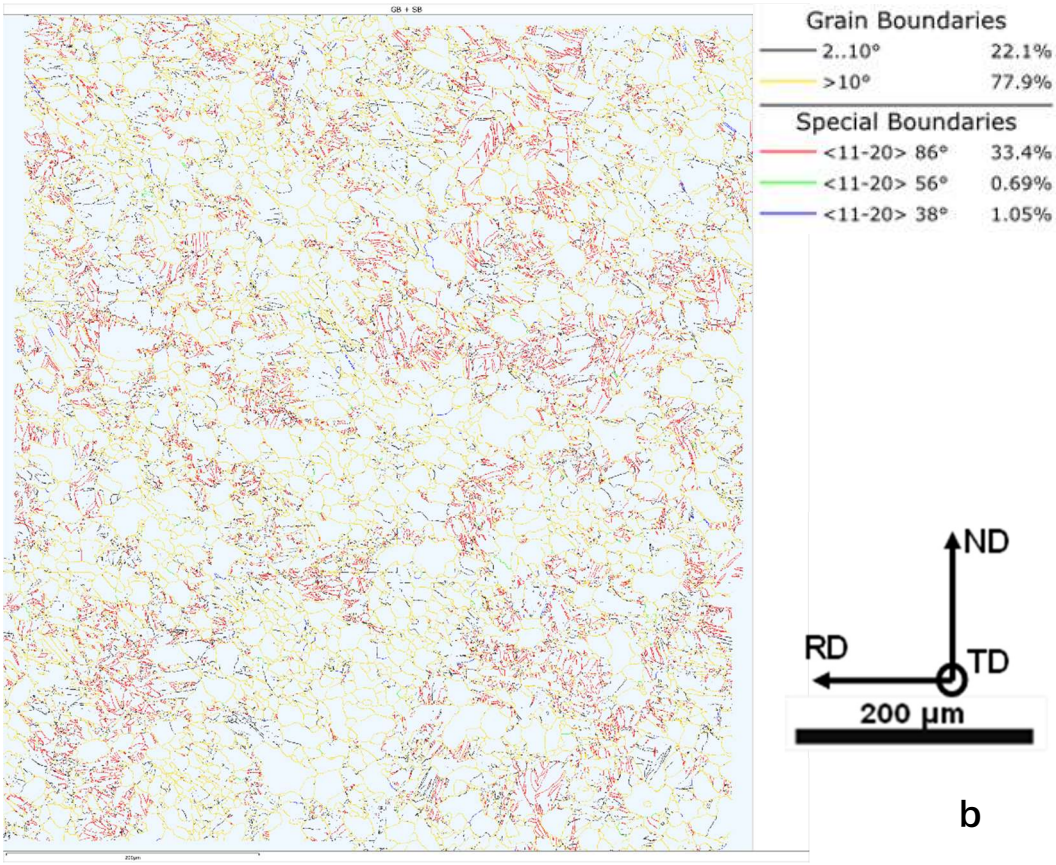
GB + SB
Grain Boundaries
2..10° 22.1%
>10° 77.9%
Special Boundaries
<11-20> 86° 33.4%
<11-20> 56° 0.69%
<11-20> 38° 1.05%
ND
RD
TD
200 µm

b

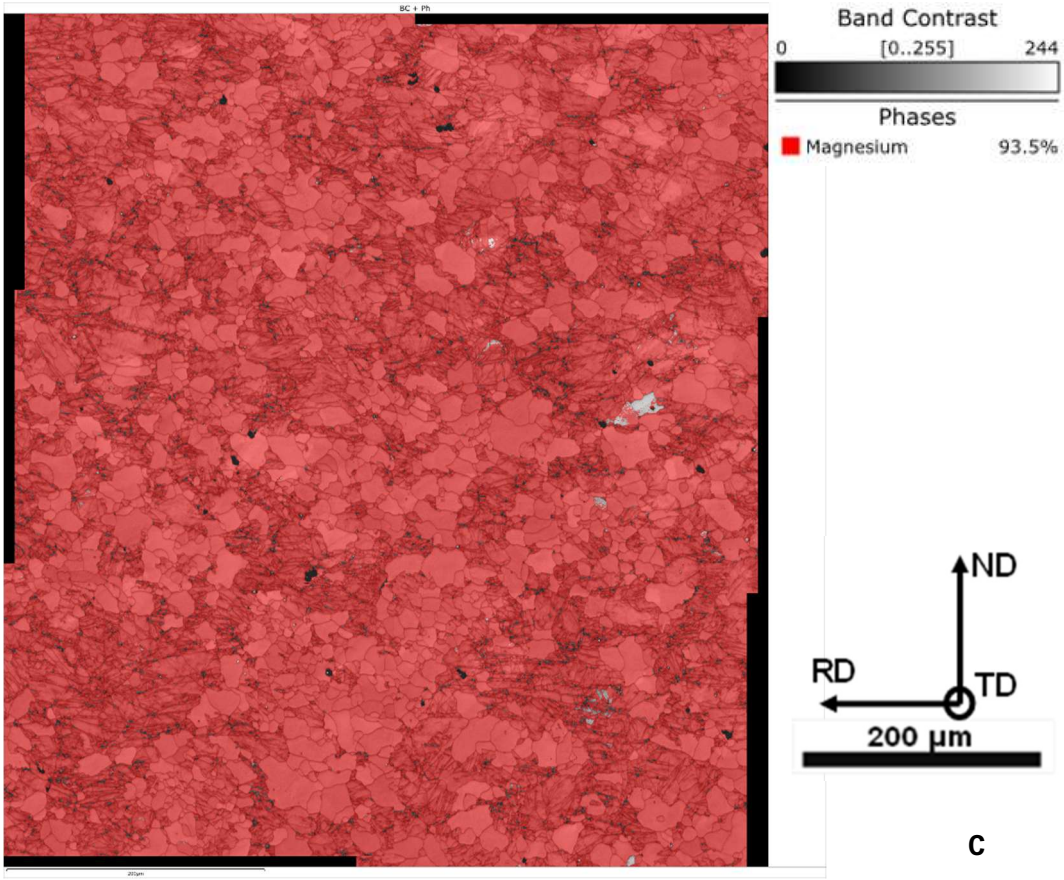
BC + Ph
Band Contrast
0 [0..255] 244
Phases
Magnesium 93.5%
ND
RD
TD
200 µm

c

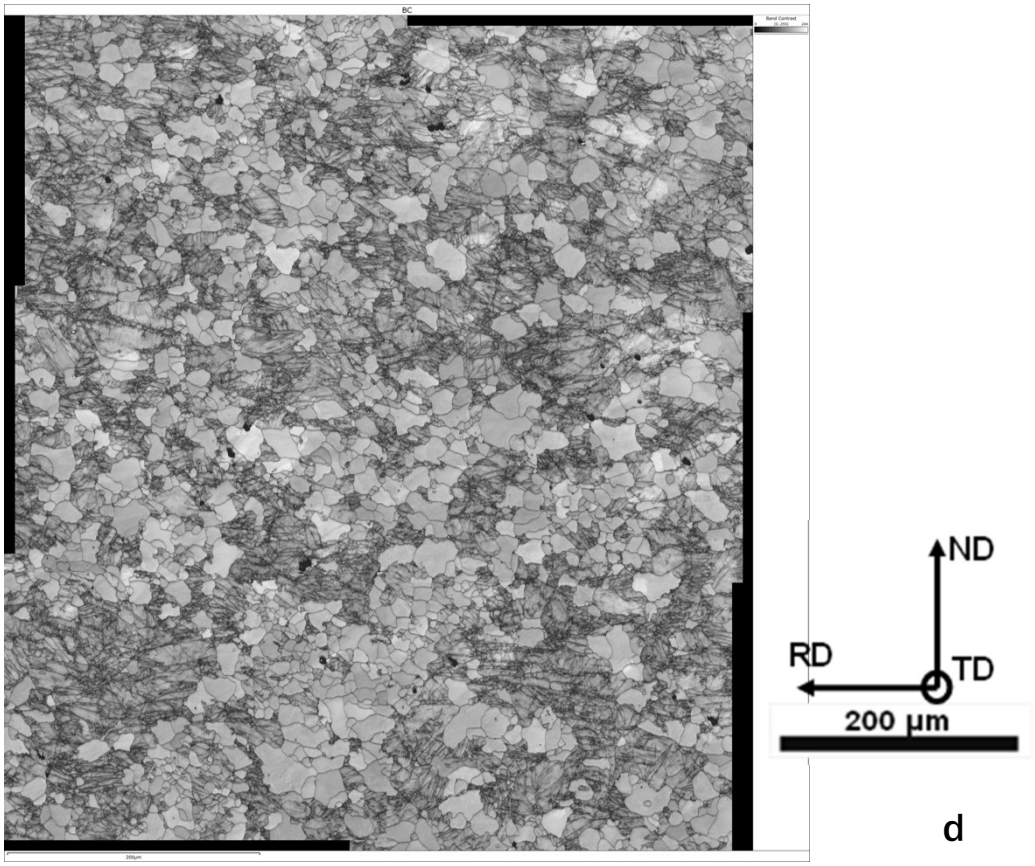
ND
RD
TD
200 µm

d

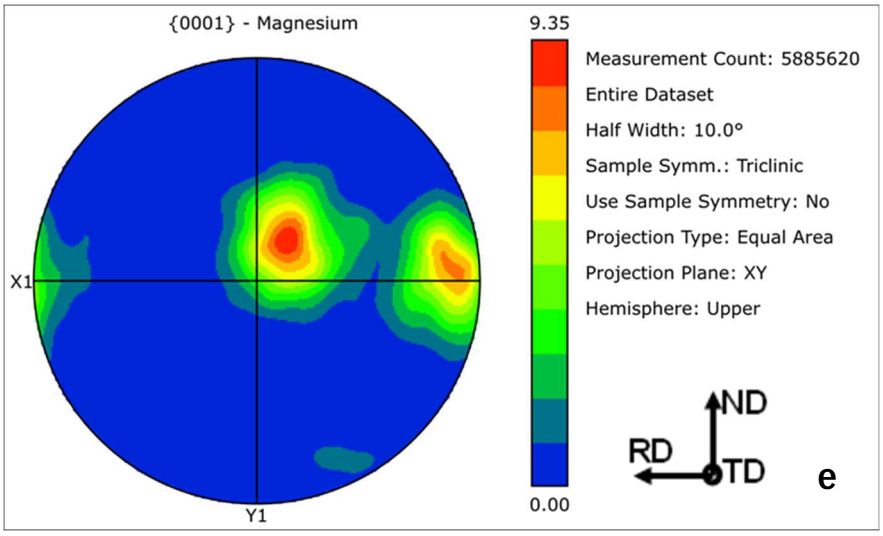
{0001} - Magnesium
9.35
0.00
X1
Y1
Measurement Count: 5885620
Entire Dataset
Half Width: 10.0°
Sample Symm.: Triclinic
Use Sample Symmetry: No
Projection Type: Equal Area
Projection Plane: XY
Hemisphere: Upper
ND
RD
TD

e

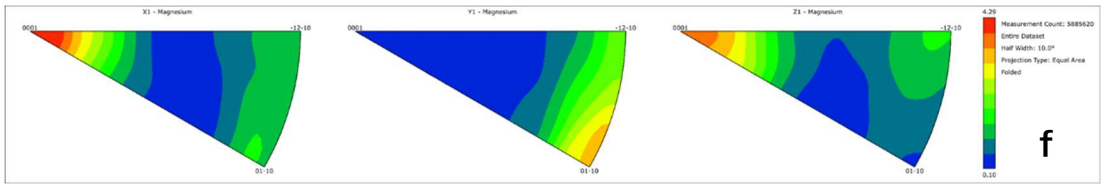

f

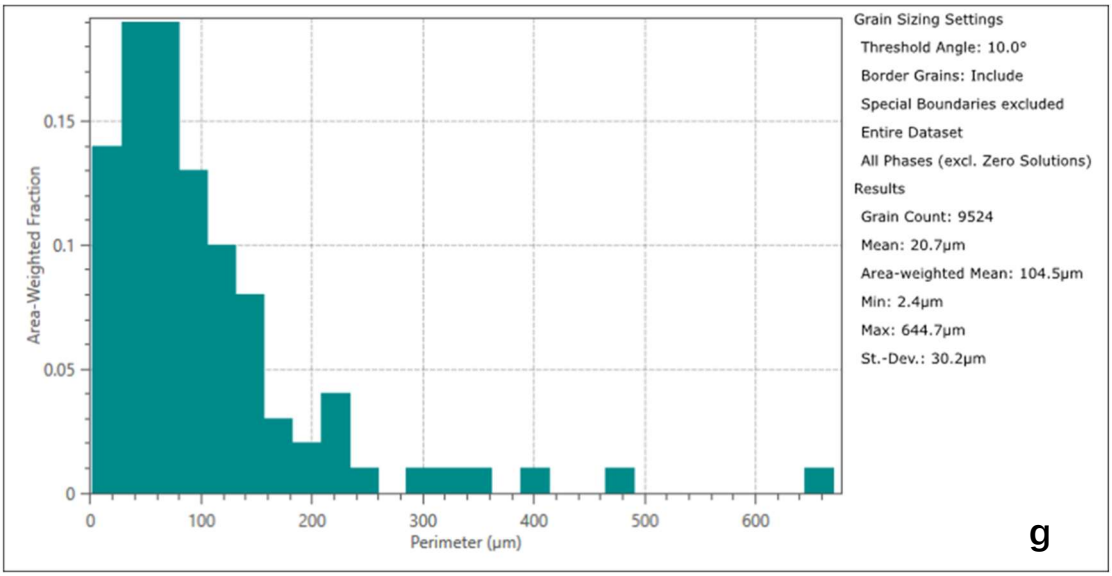

Figure 4-86 The EBSD result of the 570s annealed 2D compressed Mg-0.5Zn specimen: (a) The inverse pole figure map and grain boundaries, (b) The grain boundaries and the special grain boundaries, (c) The band contrast and the phase analysis, (d) The band contrast, (e) The pole figure, (f) The inverse pole figures, (g) Grain size distribution expressed as grain boundary perimeter

When the annealing time increased to 750s, a fully recrystallized microstructure was observed from the EBSD results (shown in Figure 4-87). This was the last group of the EBSD results for the 2D compressed Mg-0.5Zn (at%) specimen. The temperature of the specimen at that time point was 257℃. Figure 4-87(a) presents the IPF map of the scanned area, clearly showing that the specimen underwent further rapid recrystallization during the final annealing stage. This progression occurred with only a 30s increase in annealing time and a 17℃ rise in temperature between the two stages. Similar to the 1D compressed Mg-0.5Zn (at%) specimen, the morphology of the grains on the IPF map was completely different to that of the last stage i.e. except a few of the original grains on the IPF map (marked with the white circles in Figure 4-87(a), the rest of the area showed a fully recrystallized microstructure. As a result, the average grain size of the specimen also exhibited a dramatic difference, which changed from 20.7μm to 38.6μm (shown in Figure 4-87(g). The grains did not show a very uniform size compared to the 1D compressed specimen. The largest grain and the smallest grain had a grain size of 61μm and 1μm, respectively. Meanwhile, the recrystallized grain which had a direction closer to the TD showed darker in the band contrast map (shown in Figure 4-87(d)) was also observed. Meanwhile, much fewer partially identified/non-indexed grains were found compared to other specimens on the IPF map. The dramatic variation of the microstructure was also reflected in the value of the boundary fraction.

Figure 4-87(b) shows the boundary fraction of the tensile twins, compressive twins and double twins significantly reduced from 33.4% to 5.8%, 0.7% to 0.2% and 1.1% to 0.3%, respectively. Meanwhile, the fraction of the low-angle grain boundary and the high-angle grain boundary changed from 22.1% to 13.0% and from 77.9% to 87.0%, respectively. On the other hand, for the pole figures of the recrystallized specimen, very similar results (shown in Figure 4-87(e) and (f)) were shown compared to the recrystallized Mg-0.5Zn specimen in the first-round experiment (shown in Figure 4-40(d) and (e)). The 2D compressed Mg-0.5Zn specimen presented a very different pole figure compared to all the other specimens. Firstly, the maximum value of the pole figure further increased, which was from 9.4 to 11.6. The peak of the pole figure was only 10° tilted from the TD. Secondly, the grain orientation distribution of the recrystallized specimen was concentrated. The orientation distribution of the recrystallized grains exhibited a diffusion of approximately 30° around the peak orientation. When combined with the peak orientation, the recrystallized specimen displayed a characteristic basal texture typical of Mg alloys. Furthermore, the only notable similarity between the 2D compressed Mg-0.5Zn (at%) specimen and other specimens was the weakening of the original peak intensity, which decreased from 8.5 to 4.8.

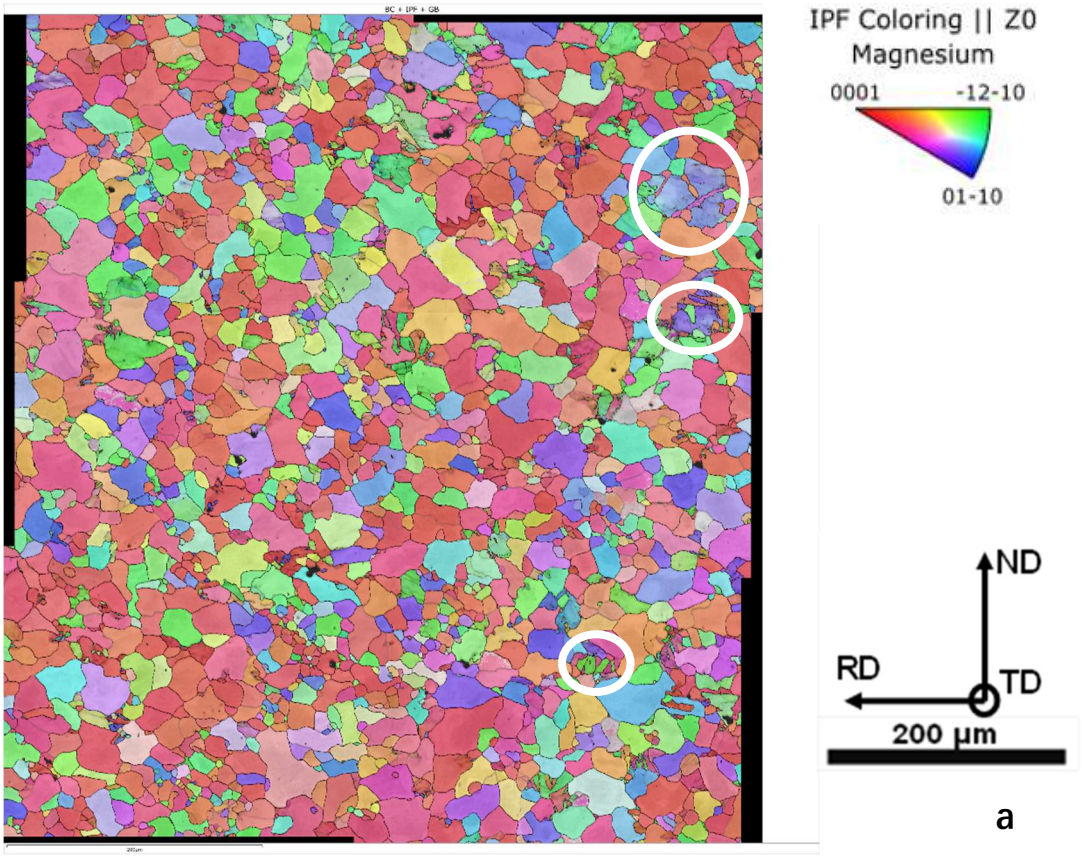

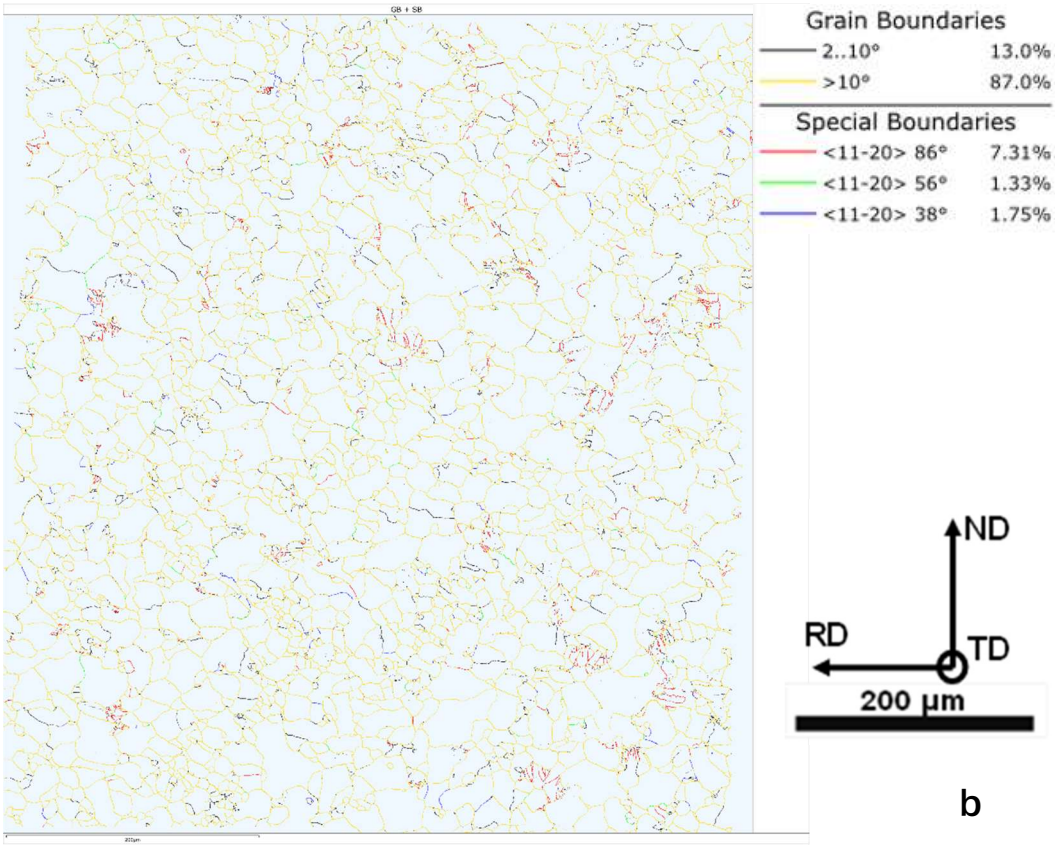
GB + SB
Grain Boundaries
2..10° 13.0%
>10° 87.0%
Special Boundaries
<11-20> 86° 7.31%
<11-20> 56° 1.33%
<11-20> 38° 1.75%
ND
RD
TD
200 µm

b

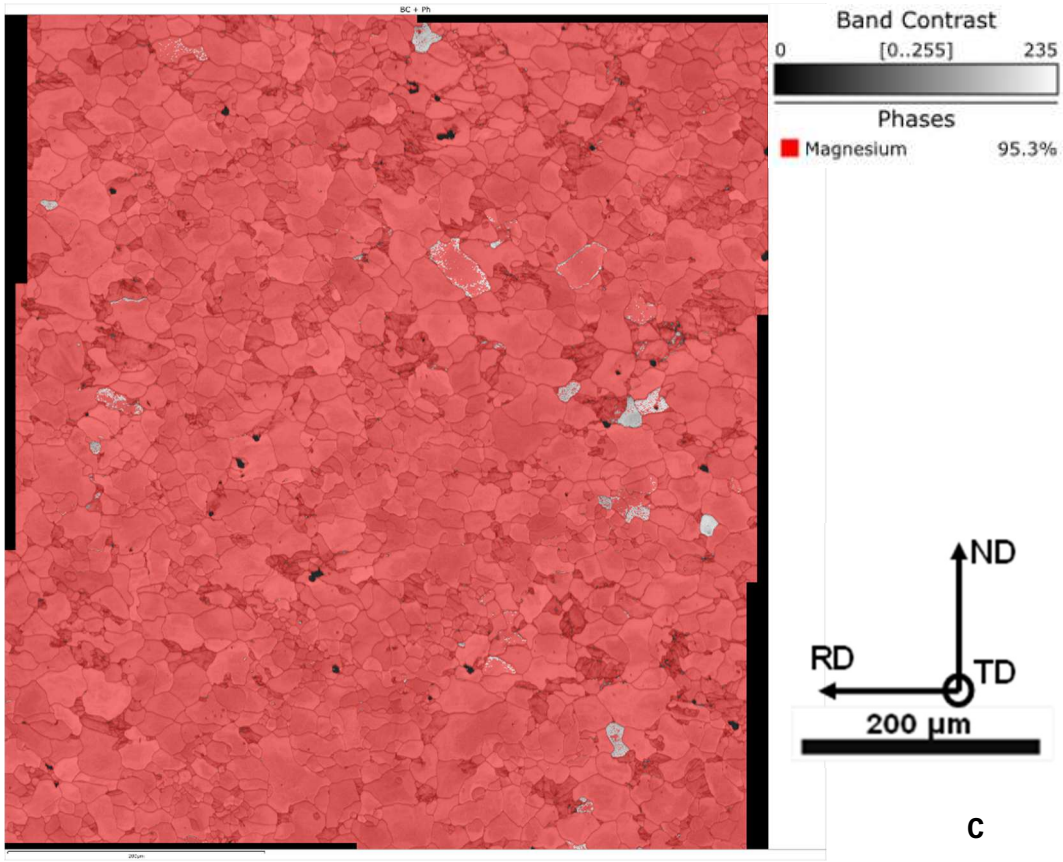
BC + Ph
Band Contrast
0 [0..255] 235
Phases
Magnesium 95.3%
ND
RD
TD
200 µm

c

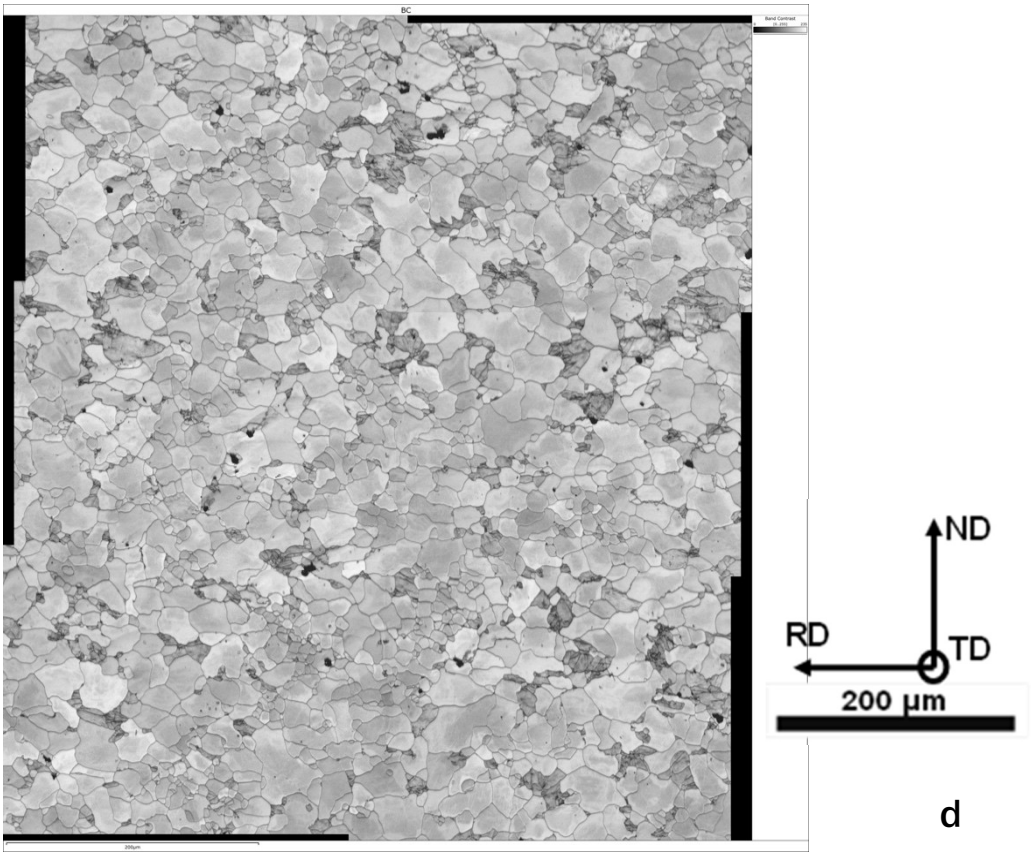
BC
ND
RD
TD
200 µm

d

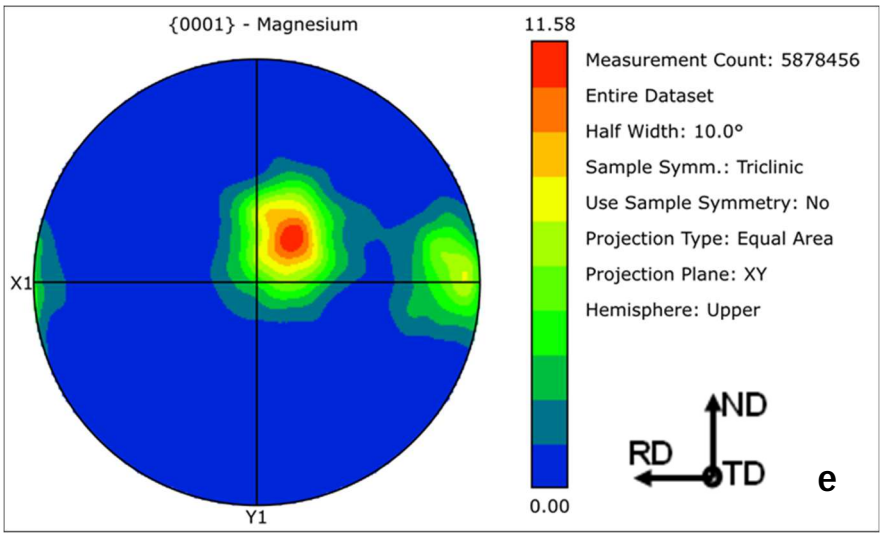
{0001} - Magnesium
11.58
0.00
Measurement Count: 5878456
Entire Dataset
Half Width: 10.0°
Sample Symm.: Triclinic
Use Sample Symmetry: No
Projection Type: Equal Area
Projection Plane: XY
Hemisphere: Upper
X1
Y1
ND
RD
TD

e

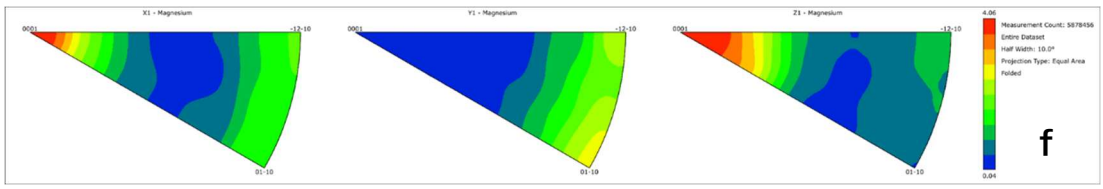
X1 - Magnesium
Y1 - Magnesium
Z1 - Magnesium
Measurement Count: 5878456
Entire Dataset
Half Width: 10.0°
Projection Type: Equal Area
Folded

f

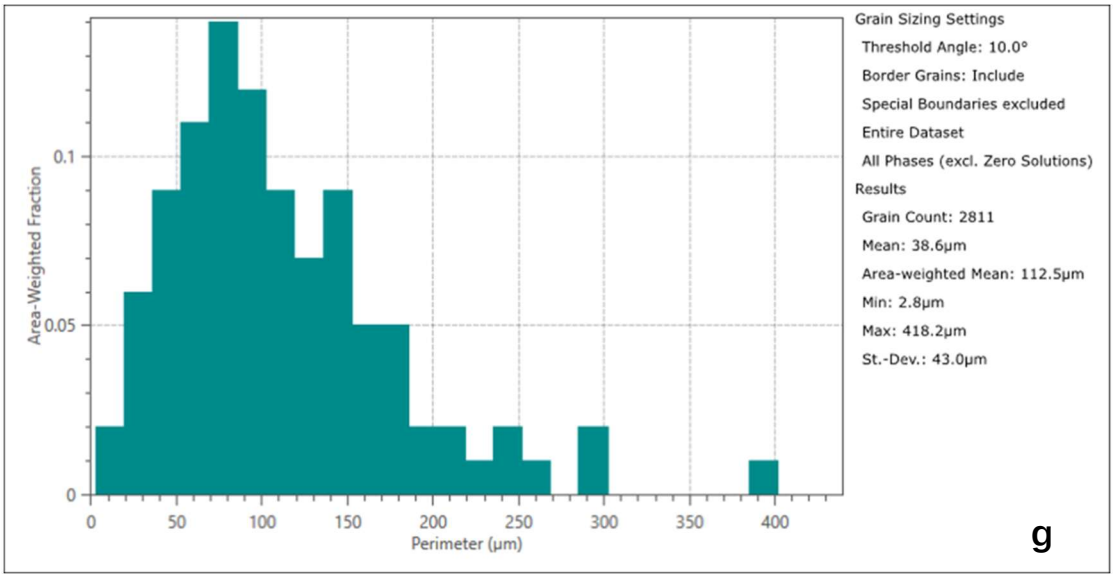

Figure 4-87 The EBSD result of the 750s annealed 2D compressed Mg-0.5Zn specimen: (a) The inverse pole figure map and grain boundaries, (b) The grain boundaries and the special grain boundaries, (c) The band contrast and the phase analysis, (d) The band contrast, (e) The pole figure, (f) The inverse pole figures, (g) Grain size distribution expressed as grain boundary perimeter

5. Discussion

5.1 The double truncated cone (DTC) specimen experiments

In the Ca-containing DTC samples, the reason for the non-uniform deformation and cracking at the early stage of the deformation was attributed to the large grain size [1, 3]. The deformation of coarse grains is not as uniform as the fine grains, which makes it easier to produce stress concentrations leading to cracking. Because the deformation was not uniform, the strain difference between the grains and the grain boundaries was larger than that of the fine grains. Thus, the probability of sample cracking due to the stress concentration caused by the uneven deformation was relatively higher. The possible existence of second phase particles (in Mg-0.5Ca and Mg-0.4Ca-0.1Zn) on the grain boundaries played a similar role during deformation. They led to uneven deformation and promoted the accumulation of dislocations, which was also the cause of cracking. The higher the Ca content, the greater the fraction of second phase particles, which were not just distributed on the grain boundaries but also inside the grains, which will have further reduced the formability of the sample.

The EBSD results from the DTC sample (shown in Figure 4-26) showed the reason for the difference in the tensile twin fraction between the centre area and the corner areas, which was attributed to higher strain in the centre area, which also resulted in unexpected recrystallization. More shear bands and fewer twins were found in the high-strain area (top part of the map in Figure 4-26(a)). In contrast, the fraction of twins in the bottom part of the map was higher. In the centre area of the DTC sample, which had the highest strain (shown in Figure 4-28 [109]) shear bands often formed, with fewer twins, consistent with the high local strain. Surprisingly, many recrystallized structures were found across the high strain area, evident on higher magnification examination of the centre area (shown in Figure 5-1). Most of the recrystallization occurred inside the shear bands, which was similar to the results of CD compressed specimens. However, there was still a considerable amount of the recrystallization grains generated inside the twins. Therefore, many twin boundaries were transformed to recrystallized grain boundaries i.e. the high-angle grain boundaries. This further reduced the fraction of twin boundaries.

The unexpected recrystallization also explained the slightly weakened texture found in the centre area (shown in Figure 4-26(d)). The newly recrystallized grains had much more random orientations compared to the original grains. This resulted in the reduction of the maximum pole intensity and the spread of the orientations as shown in the pole figure. Fortunately, the recrystallization process had only just started, allowing the structure of the shear bands and the twins to still be seen.

The unexpected recrystallization was considered to be triggered by the ion beam polishing that was used to improve surface quality to allow satisfactory EBSD images. The normal processing time of a sample on PECS II was 15-30 minutes. However, for the test Mg-0.1Ca-0.4Zn DTC sample, an 8-hour long-time polishing was conducted. This was due to the large scan area which requires a very low beam angle to cover the area. To make sure the scan area was fully polished, the polishing time of 8 hours was used. However, when the ion beam hit the surface of the sample, it generated heat and this probably was enough to initiate recrystallisation.

As for the two corner areas, although the strain was lower in these areas, it was still sufficient to generate an abundant amount of twinning. Just like the bottom section of the centre area EBSD map, the tensile twins, compressive twins and double twins had all formed at this early deformation stage. Moreover, combining the results from the corner areas and centre area, it is clear that at lower strains deformation through twinning occurred preferentially to the formation of shear bands.

Unfortunately, there was no absolute correlation between the simulated strain distribution inside the double truncated cone sample (Figure 4-28) [109] and the occurrence of twinning or shear banding in the large-scale EBSD map, due to the nonuniform deformation. Similarly, there was no correlation between the strain rate and the twinning or shear banding.

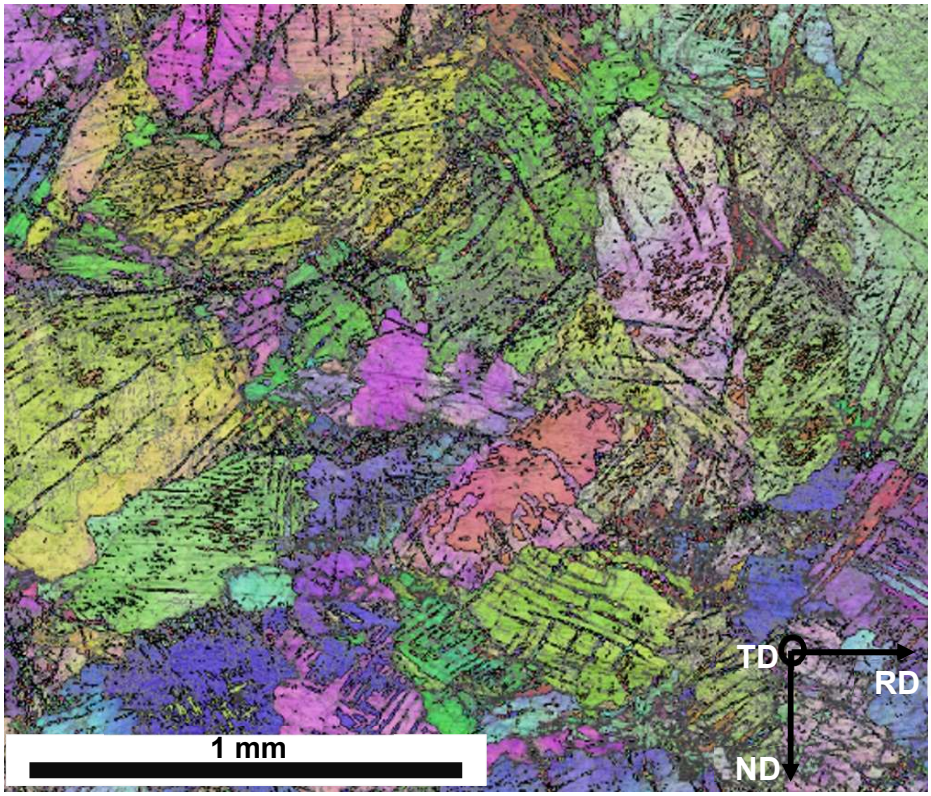

Figure 5-1 The zoomed EBSD map of the centre area (blue box)

5.2 For different compositions in the channel die (CD) compression experiment

When analyzing the relationship between the different strain paths and the microstructure evolution, many differences were observed between specimens with different compositions e.g. the increasing annealing time to complete the recrystallization and weaker texture accompanied by the increasing Ca proportion and the strong texture shown in the Mg-0.5Zn (at%) specimen etc. Thus, it is necessary to discuss the relationship between the alloying elements and these differences.

5.2.1 The one-direction compressed specimens

In the 1D compressed specimens, the differences between the three kinds of specimens was first shown in the as-compressed stage. Figure 5-2(a) to (c) indicate the boundary fractions of the compressive twins and the double twins in three specimens, which were 4.5% and 10.1% (Mg-0.2Ca-0.3Zn at%), 3.4% and 8.4% (Mg-0.1Ca-0.4Zn at%) and 1.0% and 1.8% (Mg-0.5Zn at%), respectively. The boundary fraction of the compressive twins and the double twins showed a decreasing trend when the Ca addition reduced in three specimens. Similar results were also reported in other publications [15]. The increase in Ca content led to more compressive twins and double twins. However, the reason for this was not mentioned in the literature.

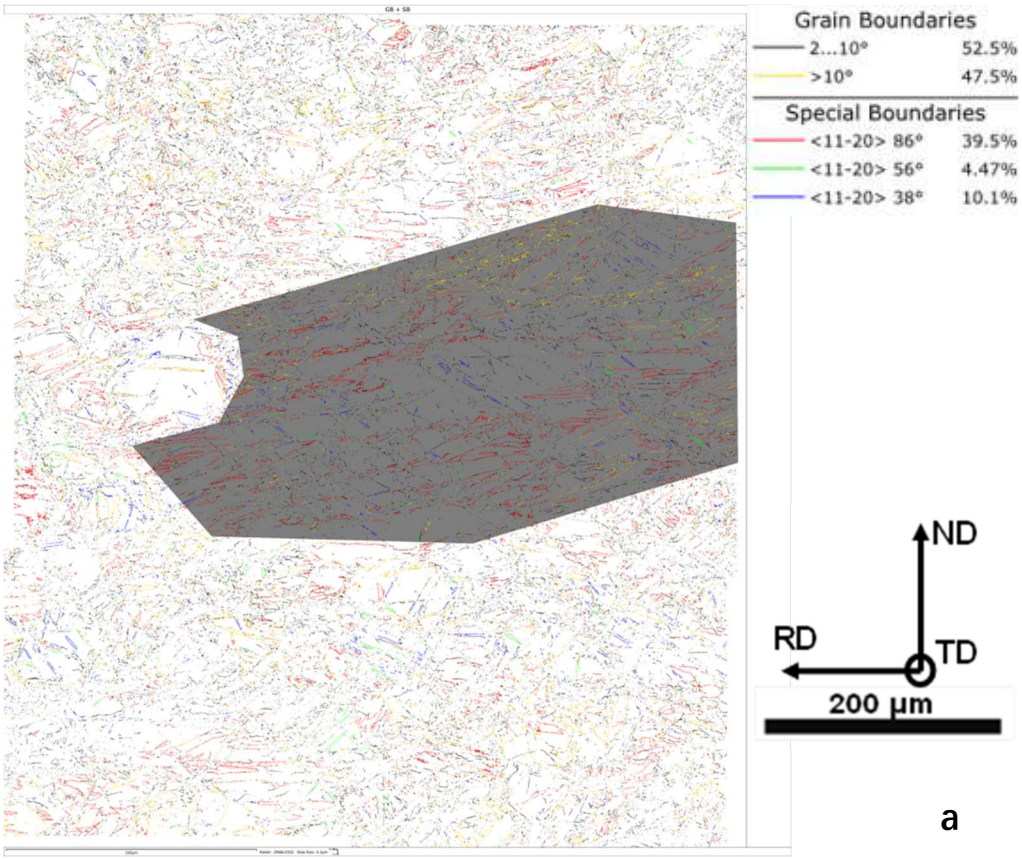

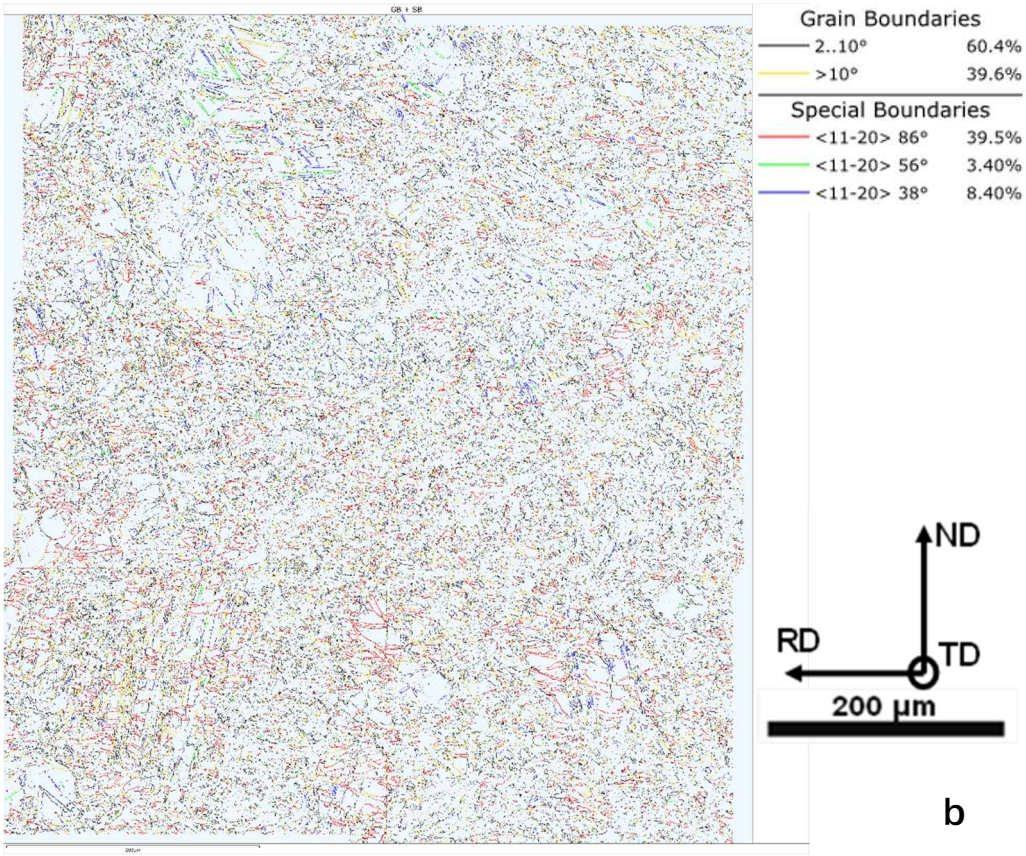

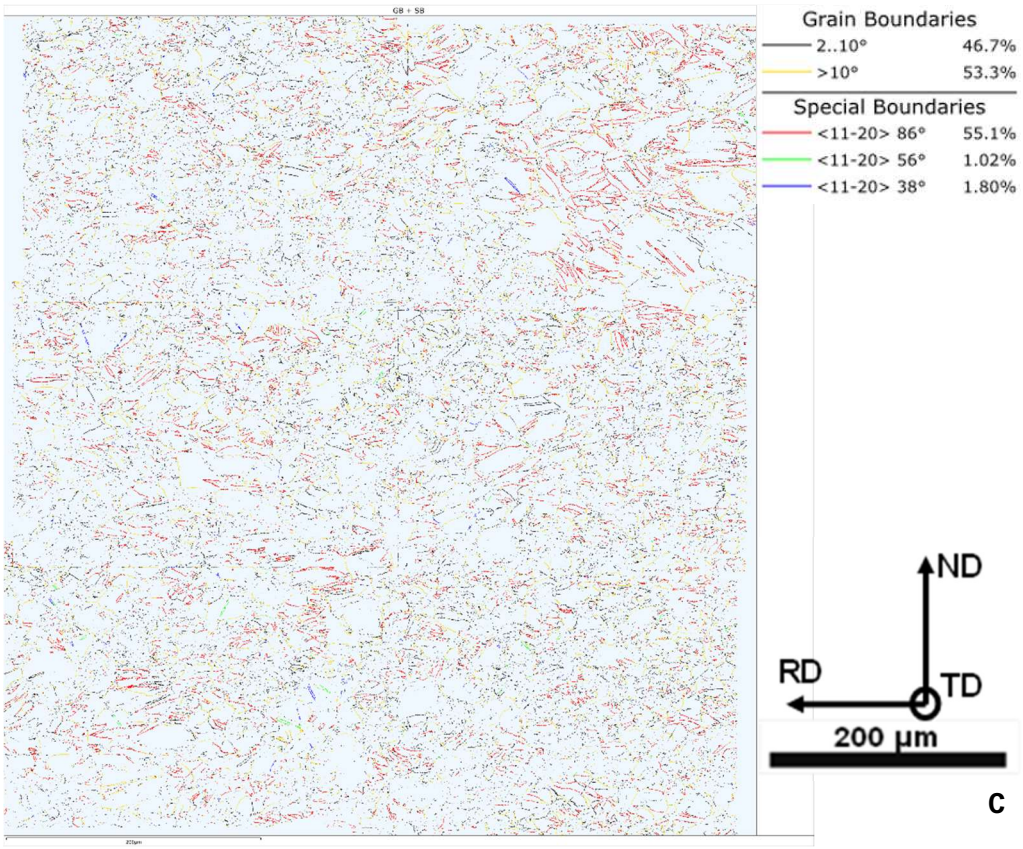

Figure 5-2 The boundary fractions of the as-compressed 1D compressed specimens (at%): (a) Mg-0.2Ca-0.3Zn, (b) Mg-0.1Ca-0.4Zn, (c) Mg-0.5Zn

It was clear that the recrystallization kinetics were different in the three specimens. In the Mg-0.2Ca-0.3Zn (at%) specimen, the recrystallization was observed after the 1290s annealing, while in the Mg-0.1Ca-0.4Zn and the Mg-0.5Zn (at%) specimen was after 420s and 30s annealing, respectively. The end time of the recrystallization in the Mg-0.2Ca-0.3Zn, Mg-0.1Ca-0.4Zn and the Mg-0.5Zn (at%) specimen was 3810s, 1290s and 990s, respectively. Figure 5-3(a) to (d) show the EDX results of the Ca distribution before and after annealing in Mg-0.2Ca-0.3Zn and Mg-0.1Ca-0.4Zn (at%) specimen. It was clear that the Ca addition was not just dissolved in the matrix but also segregated to the grain boundaries. The higher the Ca content, the more Ca segregated to the grain boundaries. The interaction between trace solute atoms and dislocations and grain boundaries would hinder the glide and climb of dislocations and also block the migration of grain boundaries [73], thereby hindering the nucleation and growth of recrystallization. Thus, the Ca addition was believed to be the reason for the slower recrystallization in the Ca-contained specimens.

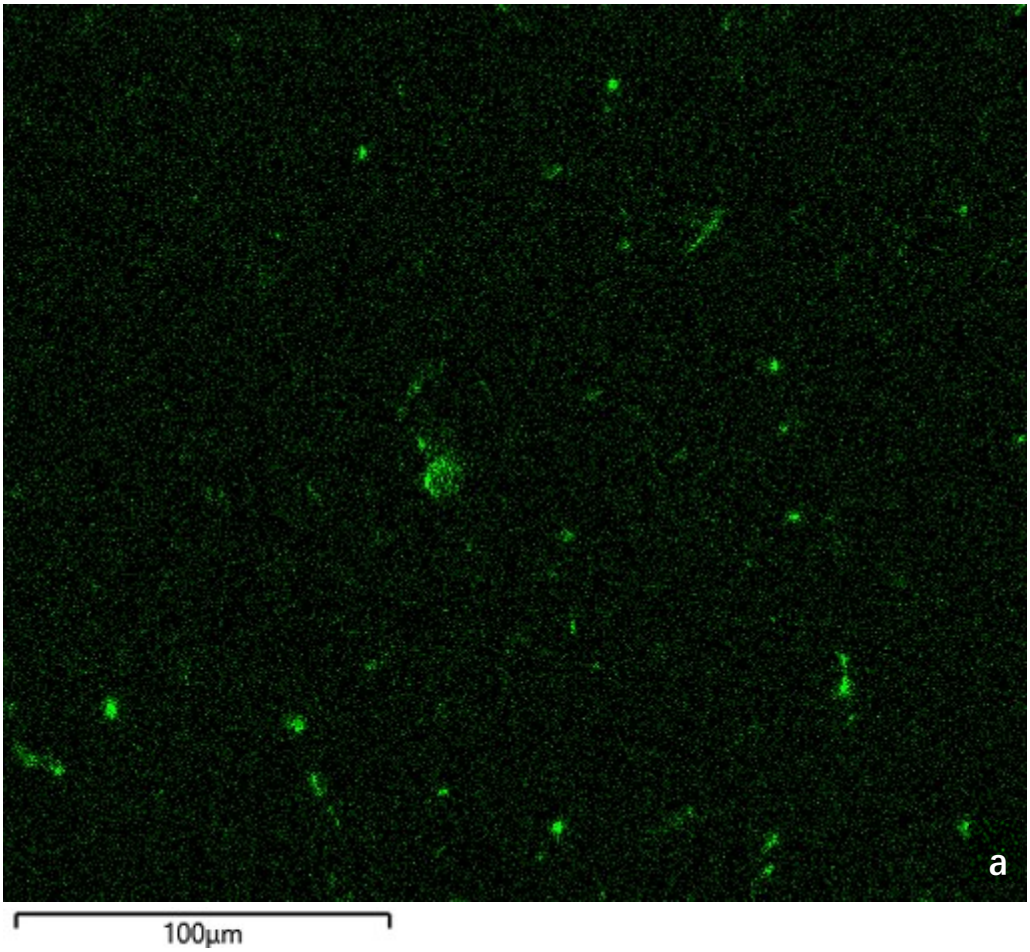

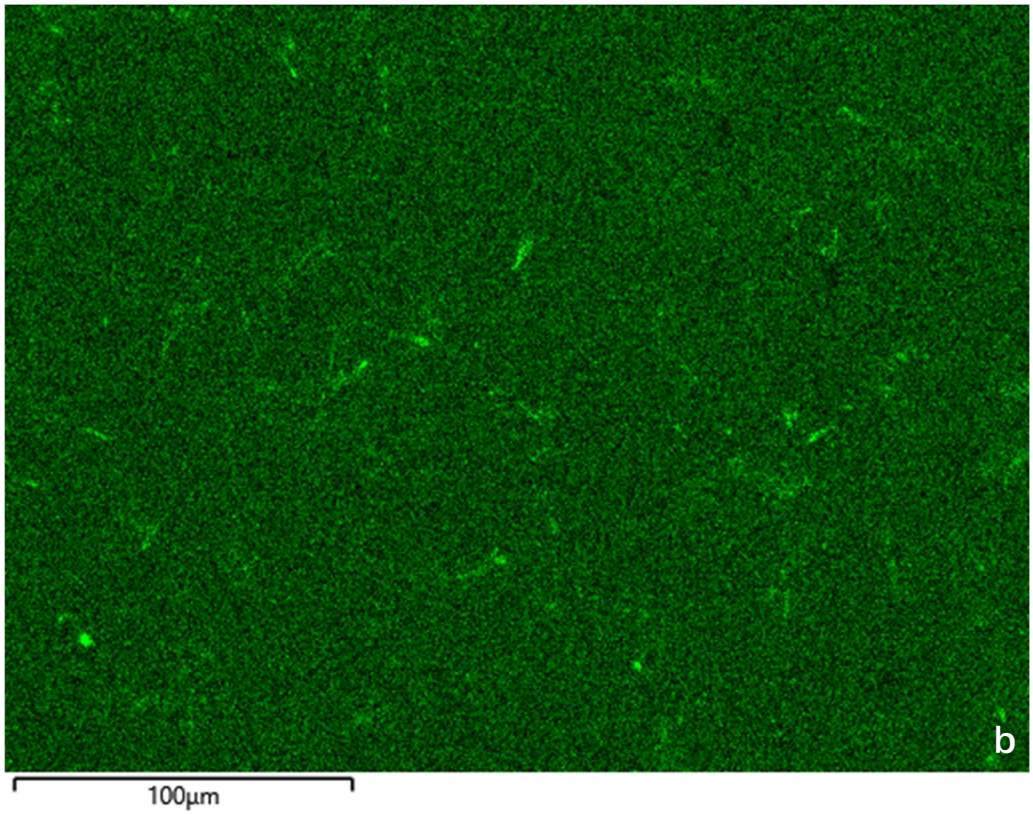
b
100µm

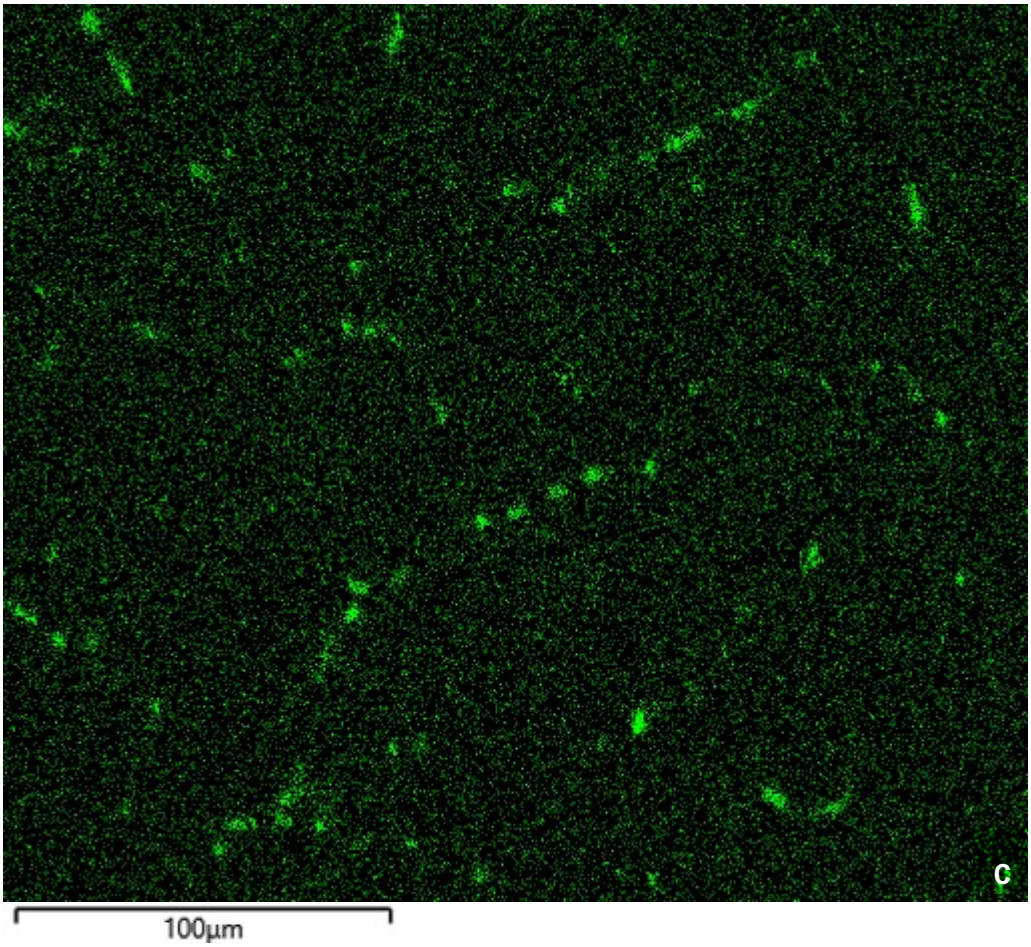
c
100µm

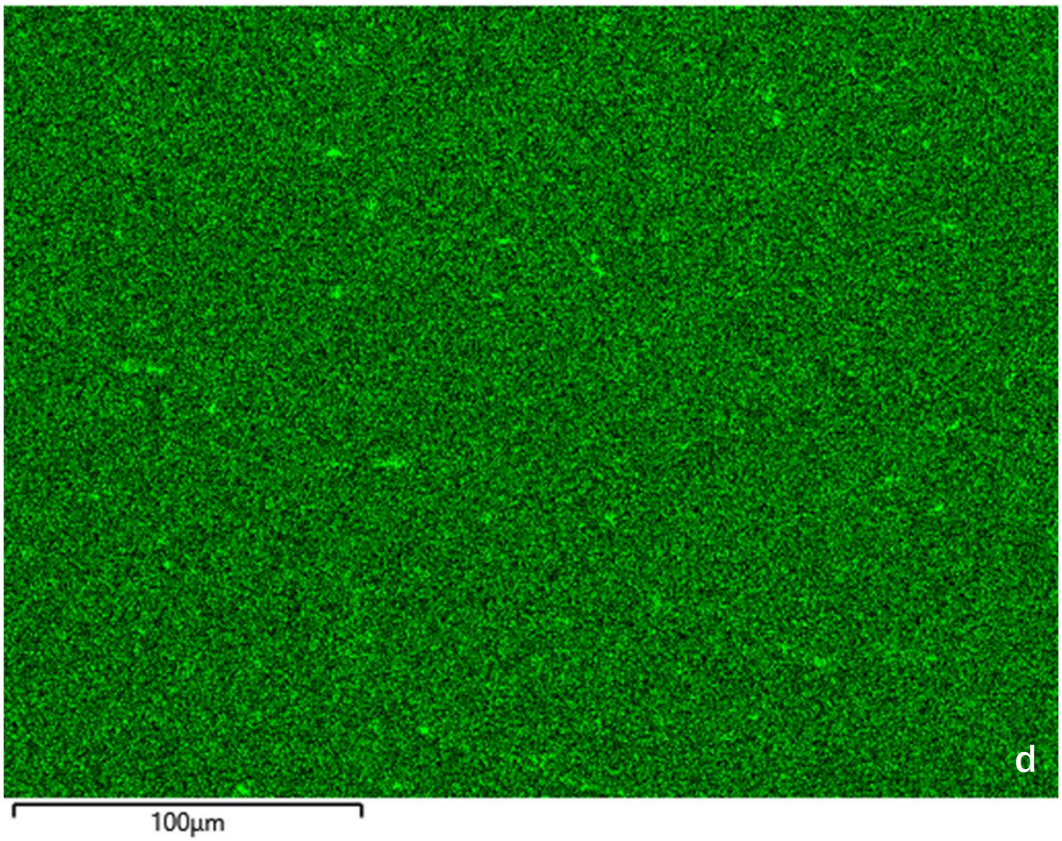

Figure 5-3 The distribution of Ca in the specimens: (a) Mg-0.2Ca-0.3Zn (at%) before annealing, (b) Mg-0.2Ca-0.3Zn (at%) after annealing, (c) Mg-0.1Ca-0.4Zn (at%) before annealing, (d) Mg-0.1Ca-0.4Zn (at%) after annealing

An increase in Ca content led to a weakening of the texture in the fully recrystallized condition. Figure 5-4(a) to (c) show the maximum pole intensity of Mg-0.2Ca-0.3Zn, Mg-0.1Ca-0.4Zn and Mg-0.5Zn (at%) specimen of 5, 5.5 and 6.7, respectively. Meanwhile, the grain orientation distribution in the Mg-0.2Ca-0.3Zn (at%) specimen showed as the most widely scattered distribution. With the decrease in the Ca proportion, the grain orientation distribution became more and more concentrated. No second phase was detected in the low Ca and Zn content specimens. Thus, the texture weakening mechanism from second phase particles (PSN) was not considered in the present experiment. Rather it was believed to be associated with solute drag resulting from the segregated Ca on the grain boundaries, and the dissolved Ca in the matrix which reduced the stacking fault energy (SFE), which has also been reported by Guan, Nakata and other researchers [34, 35, 57, 73].

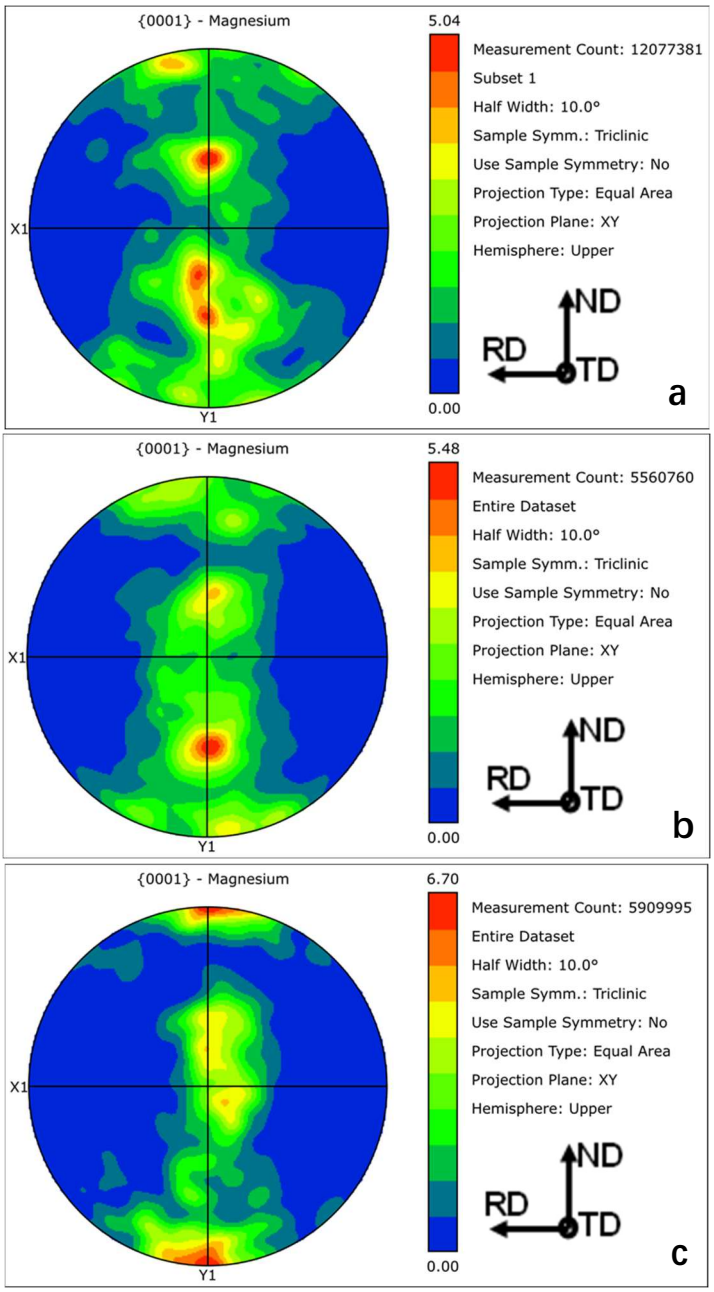

Figure 5-4 The pole figures of the recrystallized 1D compressed specimens: (a) Mg-0.2Ca-0.3Zn (at%), (b) Mg-0.1Ca-0.4Zn (at%), (c) Mg-0.5Zn (at%)

5.2.2 The two-direction compressed specimens

In the 2D compressed specimens, the difference among the three compositions was very similar to the 1D compressed specimens in the as-compressed stage. Figure 5-5(a) to (c) indicate the boundary fractions of the compressive twins and the double twins in the three specimens, which were 2.2% and 4.2% (Mg-0.2Ca-0.3Zn at%), 1.3% and 1.9% (Mg-0.1Ca-0.4Zn at%) and 0.3% and 0.9% (Mg-0.5Zn at%), respectively. The strain path did not change the role of the Ca addition, the specimen with higher Ca proportion showed more compressive twins and double twins in the as-compressed stage.

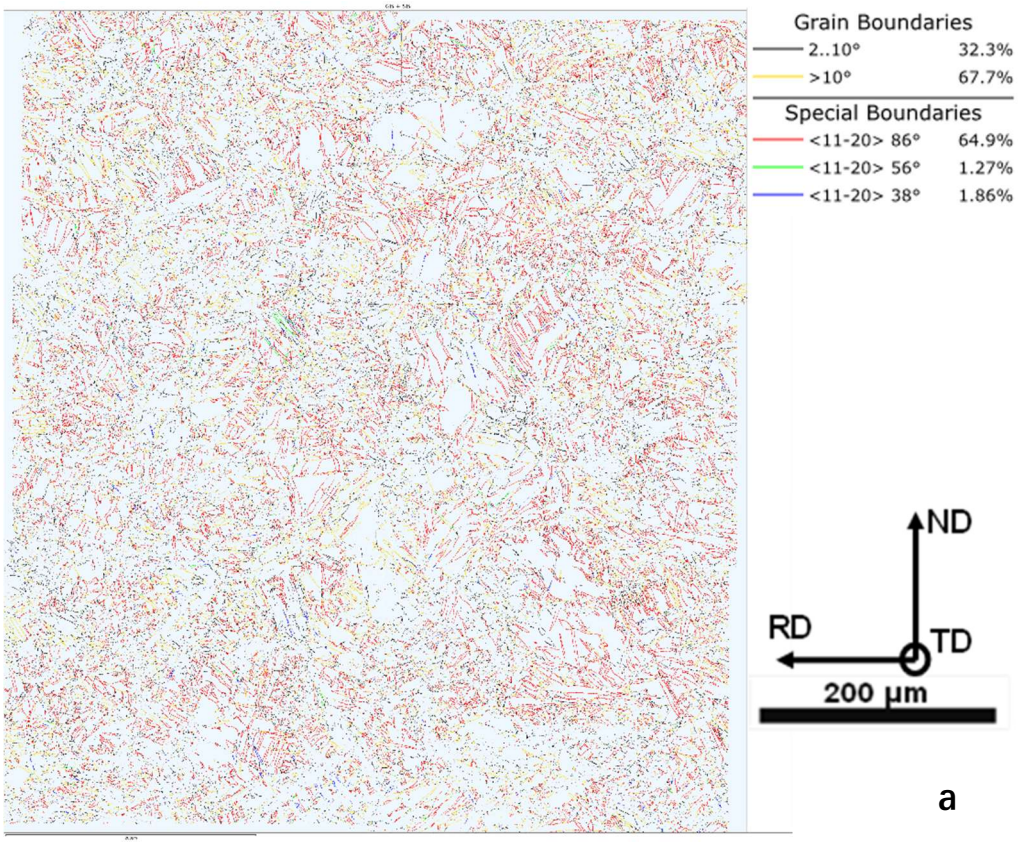
Grain Boundaries
2..10° 32.3%
>10° 67.7%
Special Boundaries
<11-20> 86° 64.9%
<11-20> 56° 1.27%
<11-20> 38° 1.86%
ND
RD
TD
200 µm

a

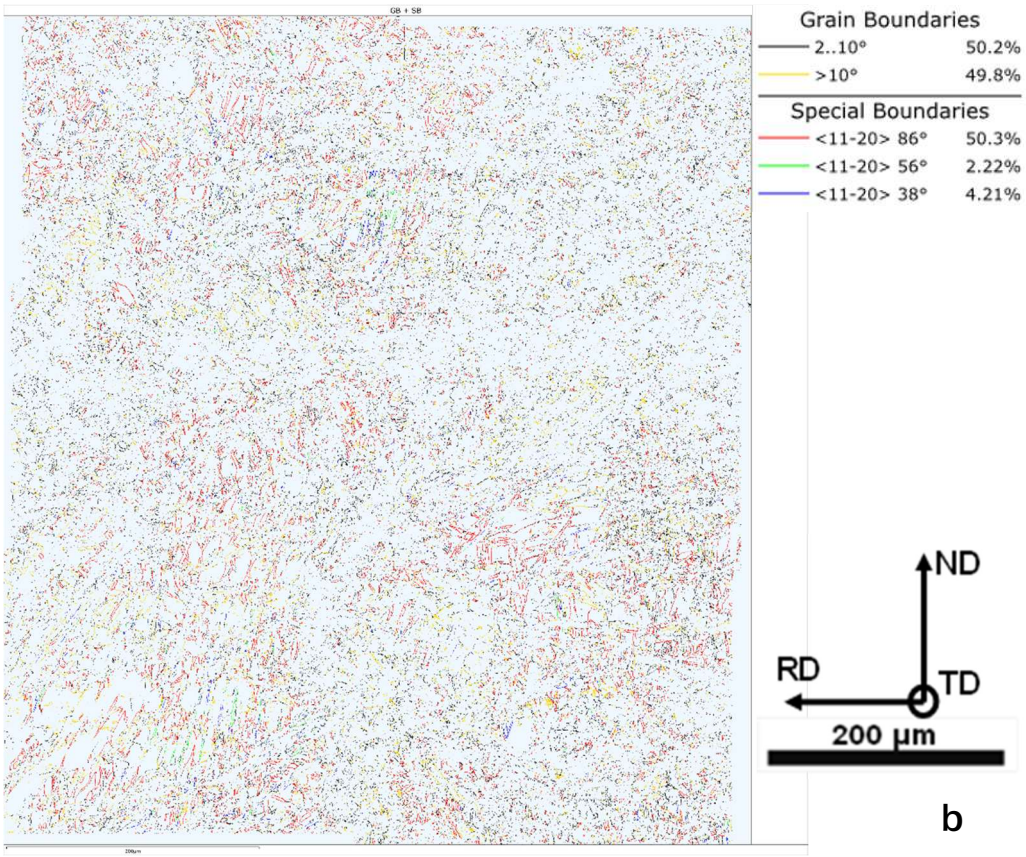
GB + SB
Grain Boundaries
2..10° 50.2%
>10° 49.8%
Special Boundaries
<11-20> 86° 50.3%
<11-20> 56° 2.22%
<11-20> 38° 4.21%
ND
RD
TD
200 µm

b

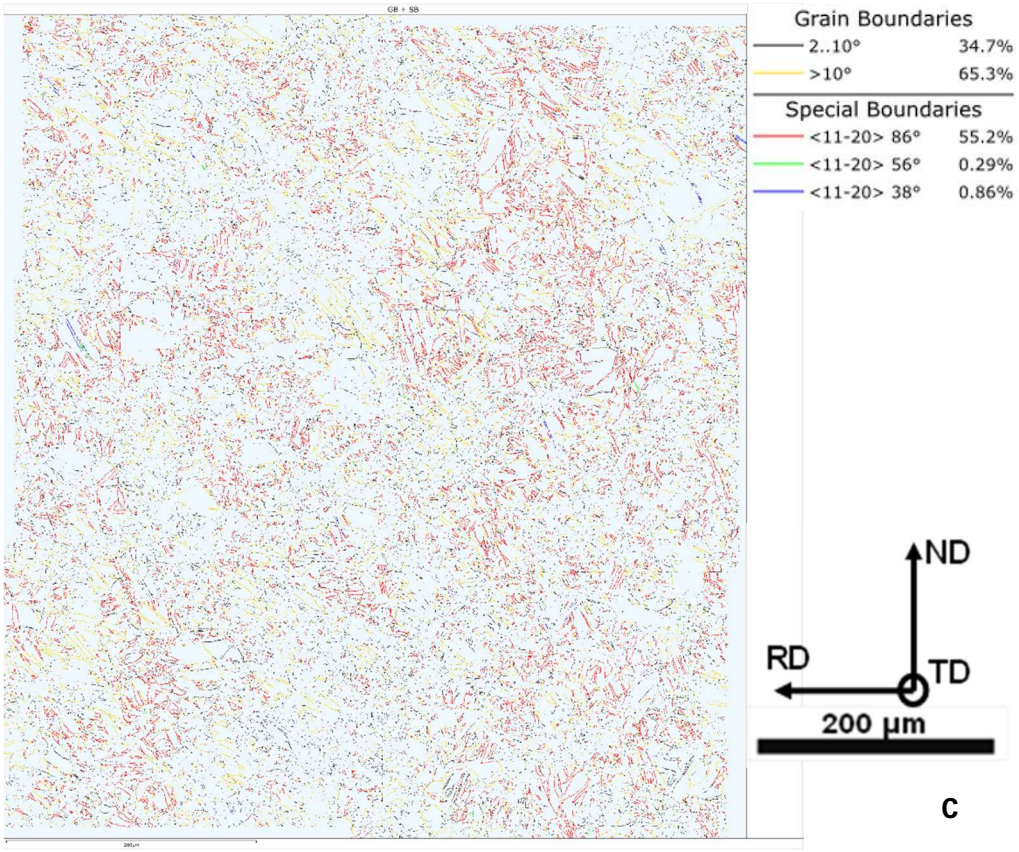

Figure 5-5 The boundary fractions of the as-compressed 2D compressed specimens (at%): (a) Mg-0.2Ca-0.3Zn, (b) Mg-0.1Ca-0.4Zn, (c) Mg-0.5Zn

Composition also affected the kinetics of recrystallization in the Mg-0.2Ca-0.3Zn (at%) specimen; recrystallization was observed after the 1290s, while in the Mg-0.1Ca-0.4Zn and the Mg-0.5Zn (at%) specimen was after 420s and 210s, respectively. The end time of the recrystallization in Mg-0.2Ca-0.3Zn, Mg-0.1Ca-0.4Zn and the Mg-0.5Zn (at%) specimen was 2790s, 1290s and 750s, respectively. Although the time points of the recrystallization were not the same as the 1D compressed specimens, the 2D compressed specimen with higher Ca proportion still showed a longer time to the start and finish of this recrystallization. The reasons for this are the same as in the 1D compressed specimens.

In a similar manner to the 1D compressed specimens, a trend of texture weakening accompanied by the increase of the Ca proportion was observed after the microstructure became almost fully recrystallized in the 2D compressed specimens. Figure 5-6(a) to (c) show that the maximum pole intensity of Mg-0.2Ca-0.3Zn, Mg-0.1Ca-0.4Zn and Mg-0.5Zn (at%) specimen was 3.4, 4.7 and 11.6, respectively. The Mg-0.2Ca-0.3Zn (at%) specimen showed the weakest texture among three specimens, followed by the Mg-0.1Ca-0.4Zn and Mg-0.5Zn (at%) specimen. The reason for the weakened texture in the 2D compressed specimens was the same as in the 1D compressed specimens.

Additionally, a notable point of the 2D compressed Mg-0.5Zn (at%) specimen was that the prior nucleation of the grains with the TD orientation. Unlike the 1D compressed specimens, the nucleation sites for recrystallisation in the 2D compressed specimen did not include twins, rather, shear bands and grain boundaries became the main nucleation sites. Recrystallized grains from the shear bands and grain boundaries generally showed a TD-orientated direction rather than a random orientation in the 2D compressed Mg-0.5Zn (at%) specimen (shown in Figure 5-7(a) and (b)). With the progress of the recrystallization, these TD-orientated grains dominated the new microstructure, resulting in a very typical basal texture in the specimen. Combining the EDX result of the Mg-0.5Zn (at%) specimen (shown in Figure 5-8), it was obvious that the lean Zn addition was dissolved in the matrix. Without the Ca addition, there was no segregation on the grain boundaries and also no larger size atom substitution in the matrix, making the Mg-Zn lean alloy showed a much closer lattice structure to the pure Mg. Thus, it was easy to form the strong basal texture as the pure Mg.

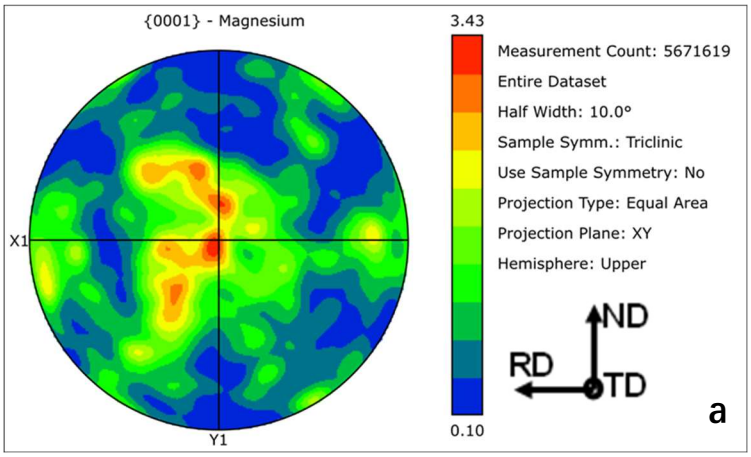

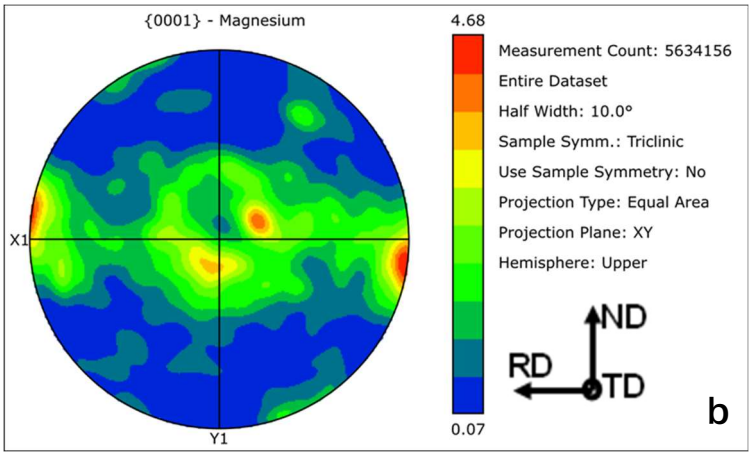

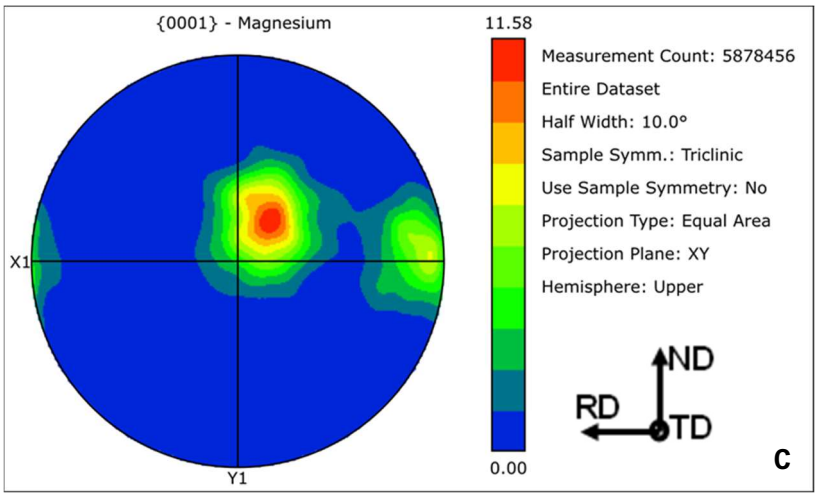

Figure 5-6 The pole figures of the recrystallized 2D compressed specimens: (a) Mg-0.2Ca-0.3Zn (at%), (b) Mg-0.1Ca-0.4Zn (at%), (c) Mg-0.5Zn (at%)

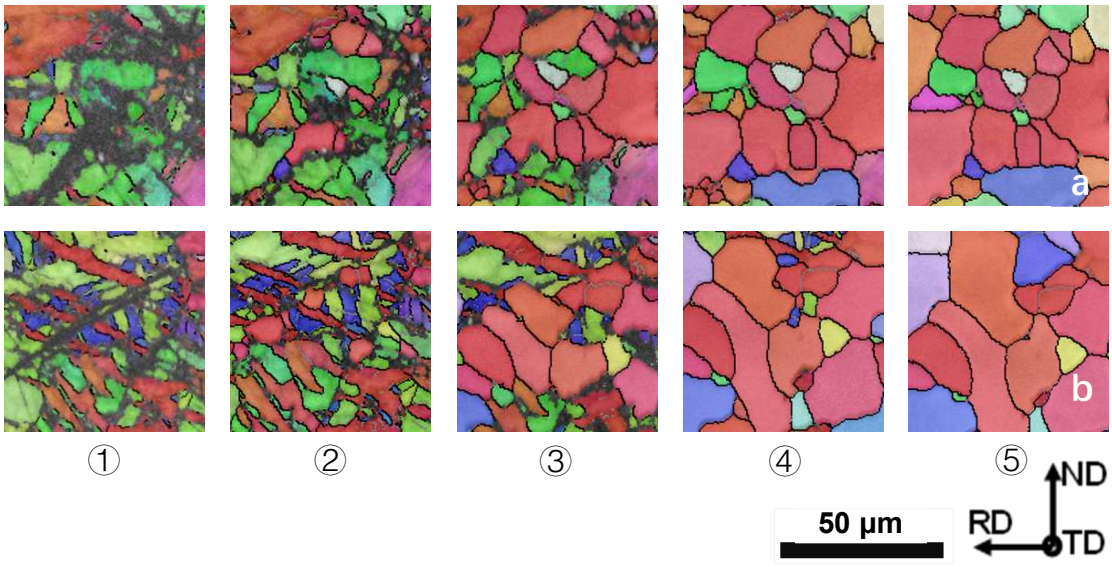

Figure 5-7 The TD-orientated recrystallized grains in the 2D compressed Mg-0.5Zn (at%) specimens: (a) site 1: ①0s, ②210s, ③420s, ④570s and ⑤750s (b) site 2: ①0s, ②210s, ③420s, ④570s and ⑤750s

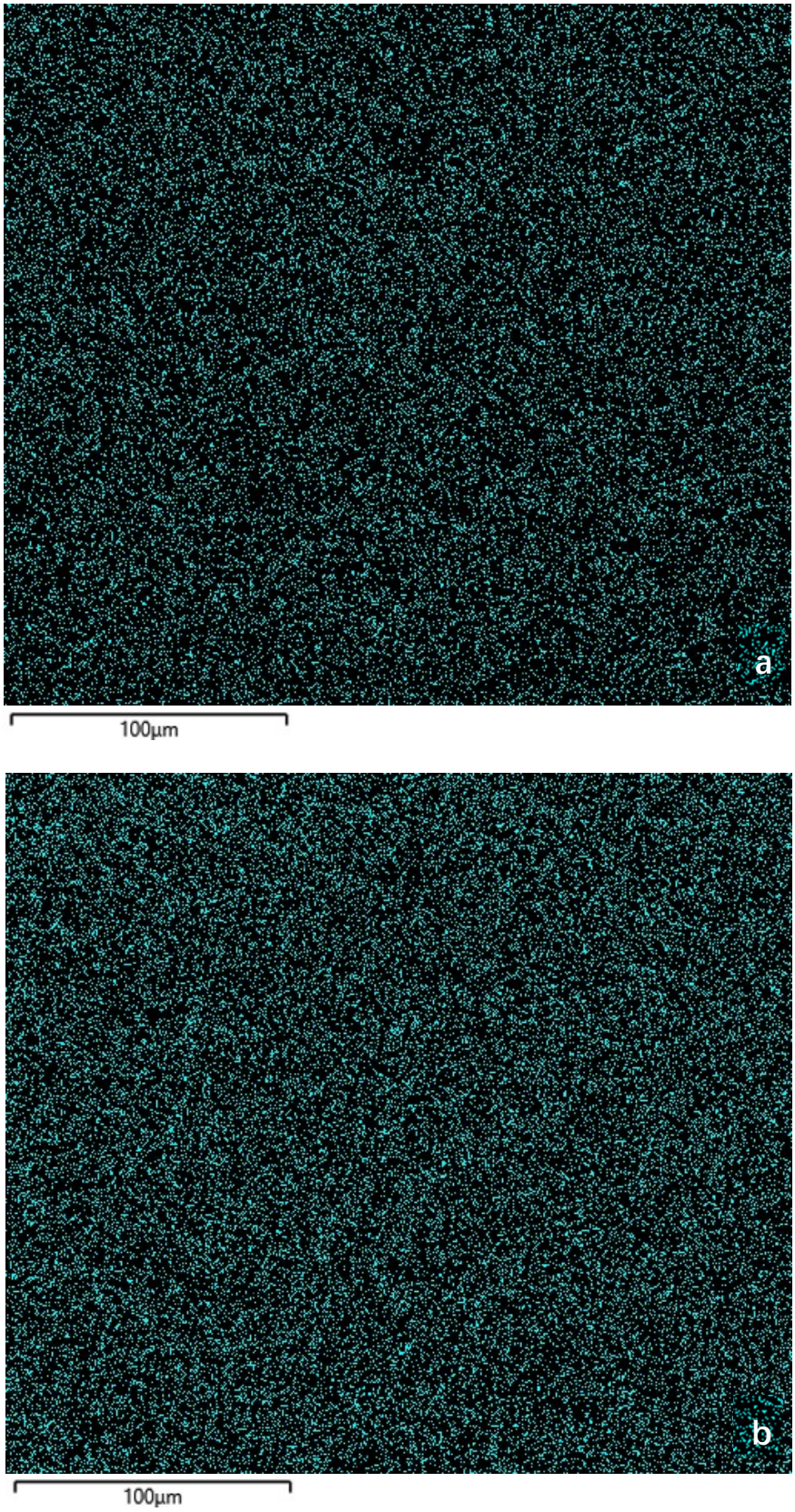

Figure 5-8 The distribution of Zn in the specimens: (a) Mg-0.5Zn (at%) before annealing, (b) Mg-0.5Zn (at%) after annealing (fully recrystallized)

5.3 For different strain paths in the channel die (CD) compression experiment

Given the repetitive nature of the process and outcomes between the first-round and second-round new CD compression experiments, this part of the discussion will primarily focus on the results from the second-round CD compression experiment.

5.3.1 Mg-0.2Ca-0.3Zn (at%) specimens

The charts shown below in Figure 5-9 present the variation of the grain boundaries, twin boundaries and maximum pole intensity of the 1D/2D Mg-0.2Ca-0.3Zn(at%) specimens during the annealing process, which will be discussed in the following chapters.

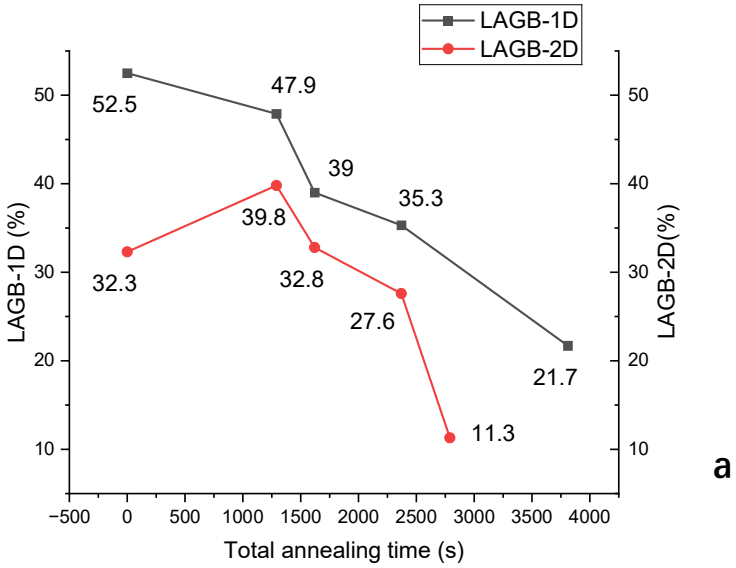

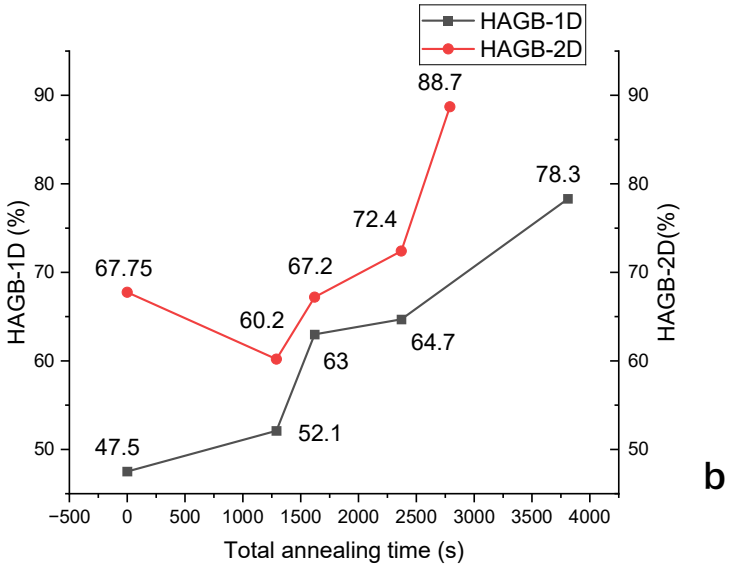

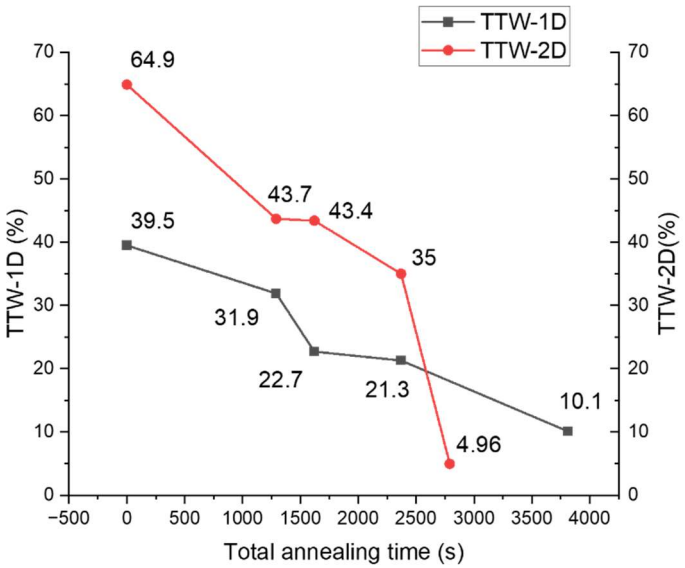
TTW-1D
TTW-2D
64.9
43.7
43.4
35
39.5
31.9
22.7
21.3
10.1
4.96
TTW-1D (%)
TTW-2D(%)
Total annealing time (s)

c

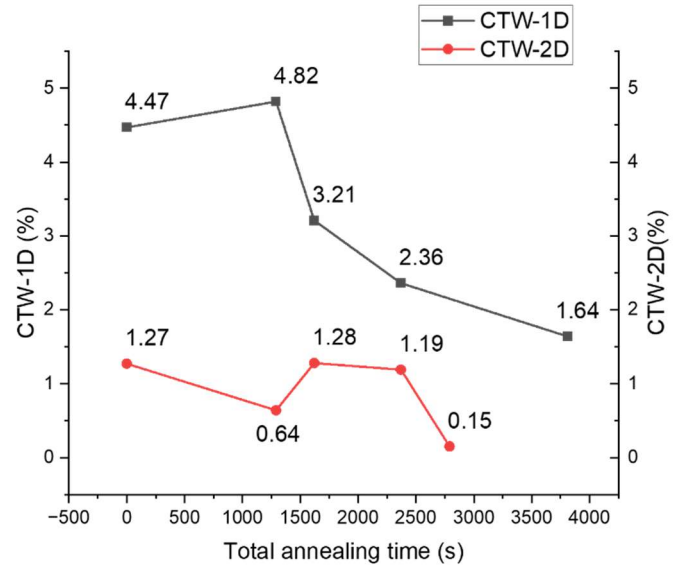
CTW-1D
CTW-2D
4.47
4.82
3.21
2.36
1.64
1.27
1.28
1.19
0.64
0.15
CTW-1D (%)
CTW-2D(%)
Total annealing time (s)

d

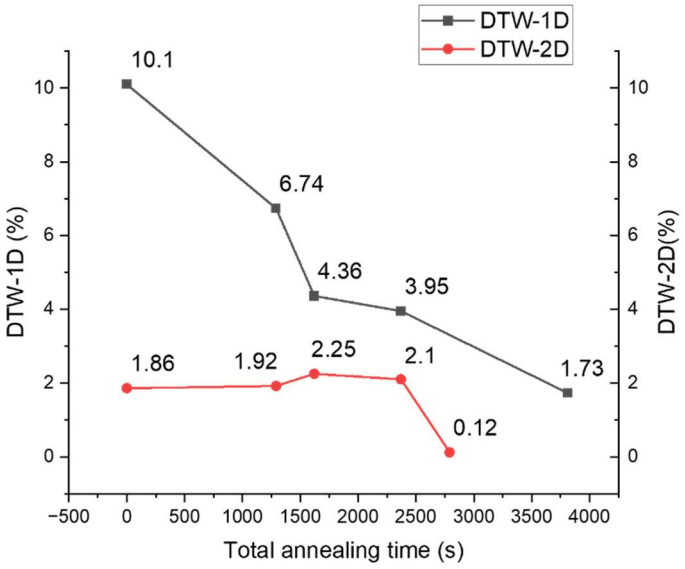
DTW-1D
DTW-2D
10.1
6.74
4.36
3.95
1.73
1.86
1.92
2.25
2.1
0.12
DTW-1D (%)
DTW-2D(%)
Total annealing time (s)

e

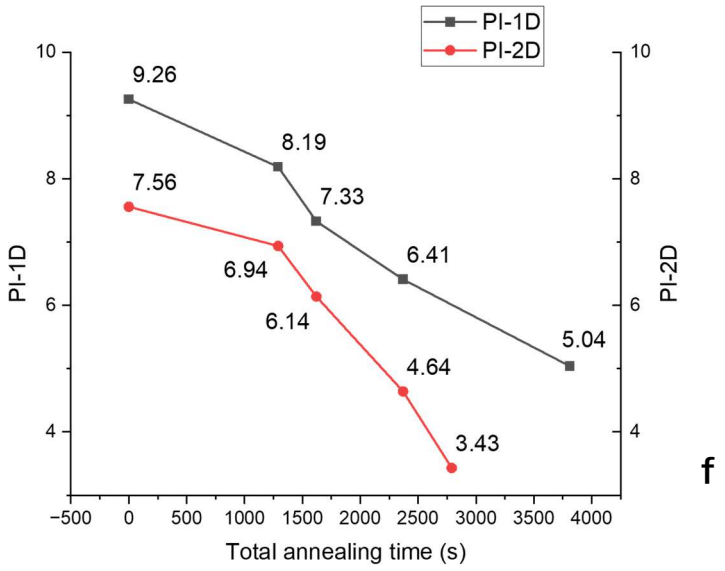

Figure 5-9 The variation in the 1D/2D compressed Mg-0.2Ca-0.3Zn (at%) during annealing: (a) low angle grain boundary (LAGB), (b) high angle grain boundary (HAGB), (c) tensile twin (TTW) boundary, (d) compressive twin (CTW) boundary, (e) double twin (DTW) boundary, (f) maximum pole intensity (PI)

5.3.1.1 Mg-0.2Ca-0.3Zn (at%) specimens after compression

The Mg-0.2Ca-0.3Zn (at%) specimens had the highest Ca addition in all three test alloys. The grain size of the Mg-0.2Ca-0.3Zn (at%) ingot was not as uniform as the other two compositions. The 1D compressed Mg-0.2Ca-0.3Zn (at%) specimen showed a very large grain in the centre of the IPF map (shown in Figure 4-41(a)). To get a more objective comparison, the IPF maps with and without the large grain in the centre (shown in Figure 5-10) were both made a comparison to the IPF map of the 2D compressed specimen (shown in Figure 4-68(a)).

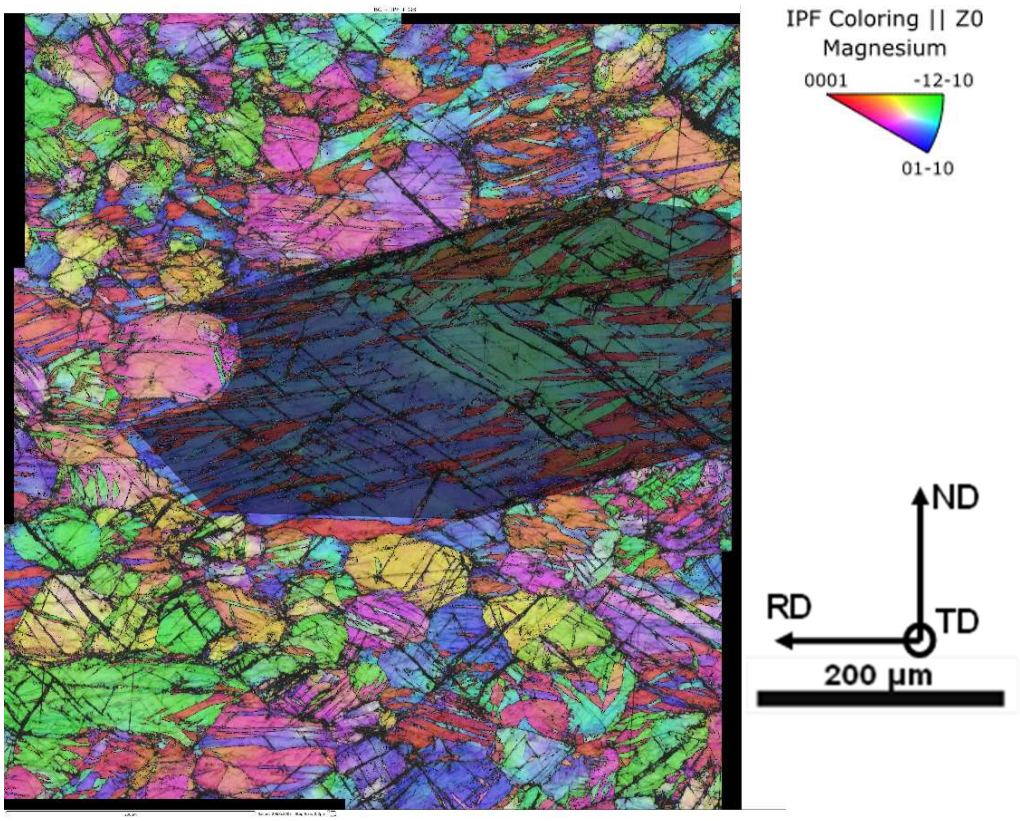

Figure 5-10 The IPF map of the as-compressed 1D compressed Mg-0.2Ca-0.3Zn (at%) specimen without large grain in the centre

In the as-compressed state, both 1D compressed (shown in Figure 4-41(c)) and 2D compressed specimens (shown in Figure 4-68(c)) showed a considerable non-indexed area which occupied 23% and 18.3% of the total scan area, respectively. The non-indexed area in the two specimens was considered to consist of shear bands and non-indexed fine twins. Based on the morphology of the non-indexed area, part of the non-indexed sections in the 1D compressed specimen were identified as twins but the proportion was considered lower than the shear bands. In the 2D compressed specimen, most of the non-indexed areas were identified as shear bands rather than twins. A noticeable point of the as-compressed 1D compressed specimen was that a few scratches were also included in the 23% non-indexed area. Thus, the real non-indexed area of the 1D compressed specimen excluding the scratches was about 21%. The large grain in the centre had a large amount of non-indexed area within it; by excluding the large grain, the fraction of the non-indexed area in the remainder, which was generally of uniform grain size was about 17%. However, due to the limitation of the software, the large grain-excluded non-indexed area fraction could not be calculated. The fraction of the identified area was still shown as 77% (shown in Figure 5-11).

The non indexed area was believed to be due to a deformed structure that EBSD could not resolve, which is believed to arise from shear bands. The higher fraction of the non-indexed area and the lower fraction of twins in the as-compressed 2D compressed specimen indicated that it contained more shear bands than the 1D compressed specimen at this stage.

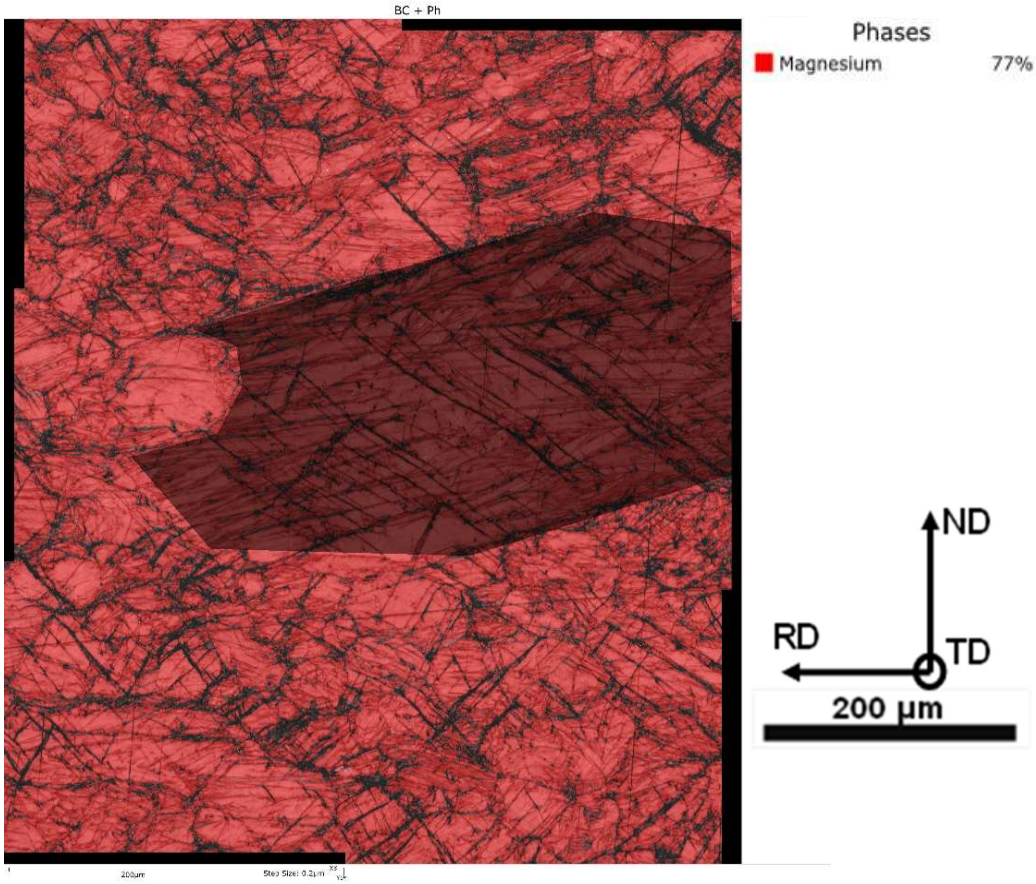

Figure 5-11 The phase map of the as-compressed 1D compressed Mg-0.2Ca-0.3Zn (at%) specimen without large grain in the centre

The number of twin types was also different in the 1D and 2D specimens. From Figure 4-41(b), Figure 4-68(b) and Figure 5-9(c)-(e), it was clear that the 1D compressed specimen had a much lower tensile twin boundary fraction (44.3%) than that of the 2D compressed specimen (64.9%). However, there was a higher boundary fraction of both compressive twins (4.42%) and double twins (9.74%) in 1D compressed specimen compared to 1.27% (compressive twins) and 1.86% (double twins) of the total boundary in the 2D compressed specimen. Even in the 1D compressed specimen where the large grain in the centre was excluded (shown in Figure 5-4), the boundary fraction of the tensile twins, compressive twins and double twins was 39.5%, 4.47% and 10.1%, respectively. The lower quantity of tensile twins and the higher quantity of compressive twins and double twins in the 1D compressed specimen compared to the 2D compressed specimen were still obvious. The reason for this

difference was attributed to the hcp structure of the Mg alloy and the compression direction of the specimens. All the cube specimens were made from hot-rolled ingots. This means that all the cube specimens had the same grain orientation distribution before the compression process. During the compression, the first compression direction of all the specimens was along the ND. This means that after the first compression, all specimens had a grain orientation distribution along the ND i.e. the c axis of most of their grains was parallel to ND [54]. For the 1D compressed and 2D compressed specimens, the direction of the second compression was parallel to the ND and rolling direction (RD), respectively. For the second compression, the 1D compressed specimen experienced the compression state of the c axis (on the hard orientation), which facilitated the formation of compressive twins and double twins. The formation of the tensile twins was not preferred at this stage. The second compression of the 2D compressed specimen was quite different. The compression direction along the RD of the specimen brought a deformation which was normal to the c axis of the grains i.e. the soft orientation of the specimen. Thus, the c axis of the grains was at an extension state during the second compression. As a result, the extension on the c axis of grains facilitated the formation of the tensile twins. In contrast, the formation of the compression twins and double twins was not preferred at this stage. Thus, for the 1D compressed Mg-0.2Ca-0.3Zn (at%) specimen, the ND direction compression suppressed the formation of the tensile twins but supported the formation of compressive twins and double twins, resulting in a greater fraction of compressive twins and double twins. The 2D compressed Mg-0.2Ca-0.3Zn (at%) specimen had the same first compression. However, the second RD compression was more conducive to the formation of tensile twins, which led to the increase in the number of tensile twins. Another noticeable point was that for both 1D compressed and 2D compressed specimens, although the generation of the tensile twins under ND direction compression was theoretically unfavorable, due to the easier generation of tensile twins than other twins [64] (which is also shown in the compressed DTC specimens), the tensile twins still dominated the twin type in both specimens with 39.5% and 64.9%, respectively (shown in Figure 5-9(c)-(e), Figure 5-12 and Figure 4-68(b)).

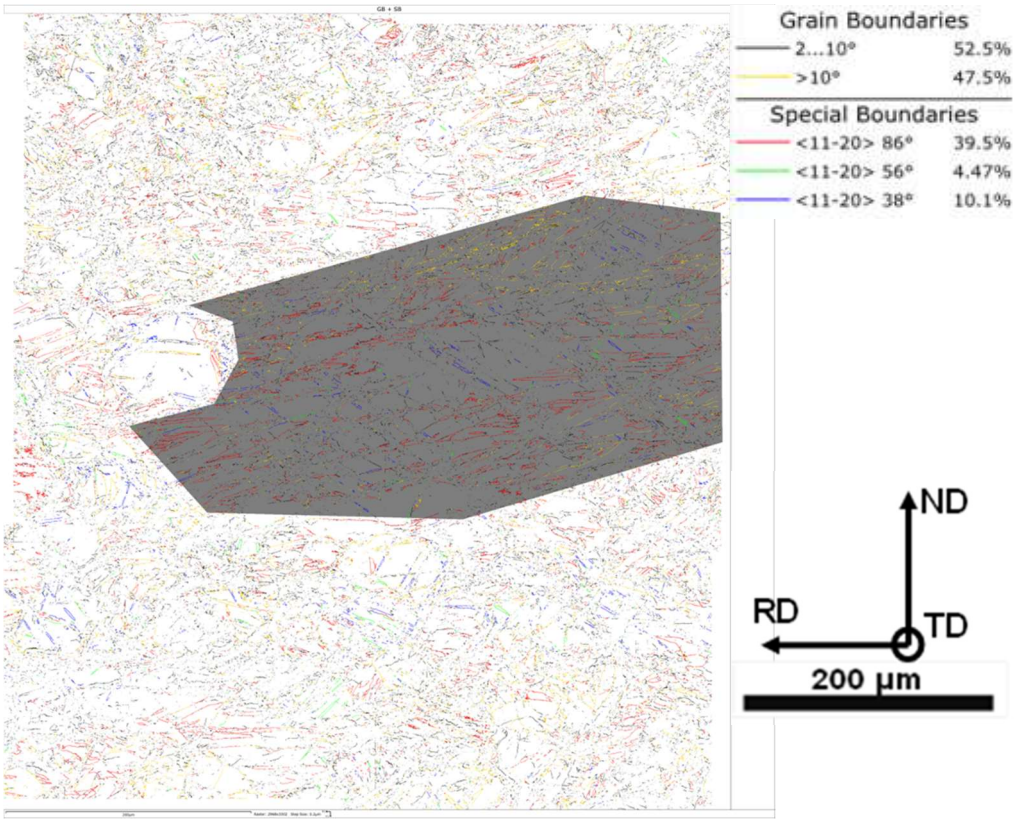

Figure 5-12 The boundary fractions of the as-compressed 1D compressed Mg-0.2Ca-0.3Zn (at%) specimen without the large grain in the centre

In addition to the differences in the shear bands and twins, the grain orientation distribution of the two strain paths was also different. First of all, considering that the OM results of the as-rolled samples reveal that the majority of grains are newly formed through the rolling (with the new grain size (Figure 4-5) being significantly smaller than the as-cast grain size (Figure 4-4)), and that the textures of the two kinds compressed samples exhibit substantial differences, the possibility of a strong correlation between the texture of the compressed samples and the as-rolled microstructure is therefore ruled out. The texture after compression deformation should be attributed solely to the compression process. The pole figure of the 1D compressed Mg-0.2Ca-0.3Zn (at%) specimen (shown in Figure 4-41(e)) showed that the as-compressed specimen had a very strong texture. The maximum pole intensity at this time point was 27.3 (shown in Figure 5-9(f)). Almost all the grains had an orientation which just 10° tilted from the ND shown in the pole figure. However, due to the existence of the large grain in the centre of the scan area, the results of the pole figure were biased by the large grain. After excluding the large grain, a very different pole figure was found (shown in Figure 5-13). The maximum pole intensity was reduced from 27.3 to 9.3. The grain orientation distribution was not as focused as before.

Although most of the grains still showed the same orientation as the old pole figure (10° tilted from the ND), some grains were found to have a direction close to the TD which was 20°-30° tilted from the TD. The pole figure of the 2D compressed Mg-0.2Ca-0.3Zn (at%) specimen (shown in Figure 4-68(e) and Figure 5-9(f)) showed a very different grain orientation distribution compared to that of the 1D compressed specimen. The maximum intensity of the pole figure was lower than that of the 1D compressed specimen which was only 7.6. And the preferred orientation of the as-compressed specimen was almost parallel to the RD. In addition, a similar grain orientation distributed close to the TD as the 1D compressed specimen was found. The difference was that these grains in the 2D compressed specimen showed a more concentrated distribution diffusing about the TD. The generation of these TD-orientated grains could be caused by the deformation on the TD. Although the size of the channel die and the cube specimens was supposed to be perfectly matched, there was still the possibility of the existence of a gap between the specimen and the channel die. Even the smallest gap was still able to leave a space for the specimen to deform a small amount in the TD. Overall, the reason for this 90° difference in the grain orientation between two specimens was attributed to the compression direction. The channel die compression restricted the deformation in the TD. Thus, the deformation only happened in the RD-ND plane. It caused the easier formation of the as-rolled grain orientation distribution i.e. the deformed grains had a parallel orientation to the compression direction.

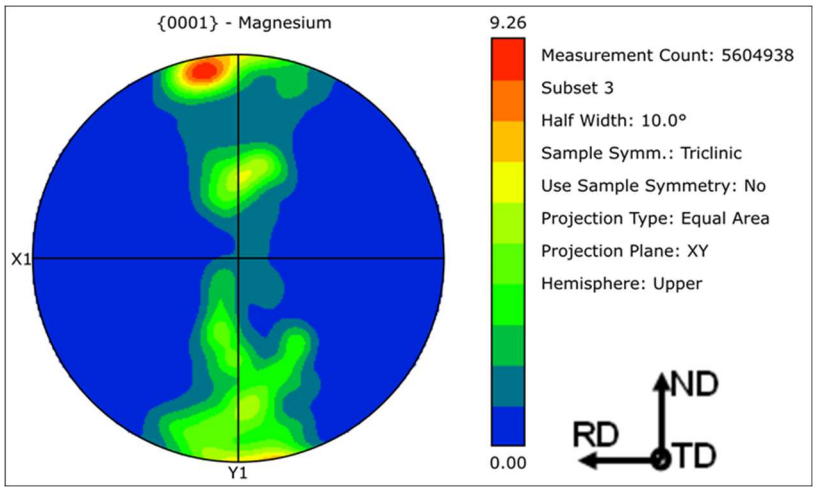

Figure 5-13 The pole figures of the as-compressed 1D compressed Mg-0.2Ca-0.3Zn (at%) specimen without large grain in the centre

At the as-compressed stage of the Mg-0.2Ca-0.3Zn (at%) specimens, it was clear that the different strain paths brought very different as-compressed microstructures to the specimens. The 1D compressed Mg-0.2Ca-0.3Zn (at%) specimen had fewer shear bands and tensile twins but more compressive twins and double twins than that of the

2D compressed Mg-0.2Ca-0.3Zn (at%) specimen. The grain orientation distribution of the two kinds of specimens presented a trend that most of the grains had the same orientation in the direction of the last compression. The influence of the different strain paths on the specimens was already shown at the as-compressed stage.

5.3.1.2 The recrystallization of Mg-0.2Ca-0.3Zn (at%) specimens

After the 1D and 2D compressions, 350℃ annealing was conducted on the specimens. Both specimens were found to start to recrystallize after the 1290s annealing. However, when comparing the phase map of two specimens (shown in Figure 4-43(c) and 4-70(c)), it was clear that the non-indexed region of the 1D compressed specimen was dramatically reduced from about 21% to 12.1%. After removing the large grain in the centre of the scanned area, the fraction of the non-indexed area was constant at 12.1%. On the other hand, although the microstructure of the 2D compressed specimen was found to recrystallize, the area of the non-indexed region did not change greatly. It showed a small reduction in the area fraction from 18.3% to 18.1%. Meanwhile, with the reduction of the non-indexed region in the 1D compressed specimen, the recrystallized grains were extensively found in these positions (shown in Figure 5-14 (a)). However, not all the new grains were from the non-indexed area, a few recrystallized grains were also found from the twins (shown in Figure 5-14 (b)). As for the 2D compressed specimen, almost all the recrystallized grains were found in the previous non-indexed area (shown in Figure 5-15). It was very hard to find the grains which had nucleated from the grain boundary or twins. In short, the non-indexed shear bands and fine twins had almost vanished and were replaced by the recrystallized grains in the 1D compressed specimen. In contrast, the large non-indexed region still remained in the 2D compressed specimen, indicating there was no recrystallisation in that area. At this time, recrystallization from the grain boundaries was already observed in the 1D compressed specimen, but this was not observed in the 2D compressed specimen. These differences suggested that the recrystallization in two specimens was not the same i.e. the recrystallization in the 1D compressed specimen started earlier than that of the 2D compressed specimen.

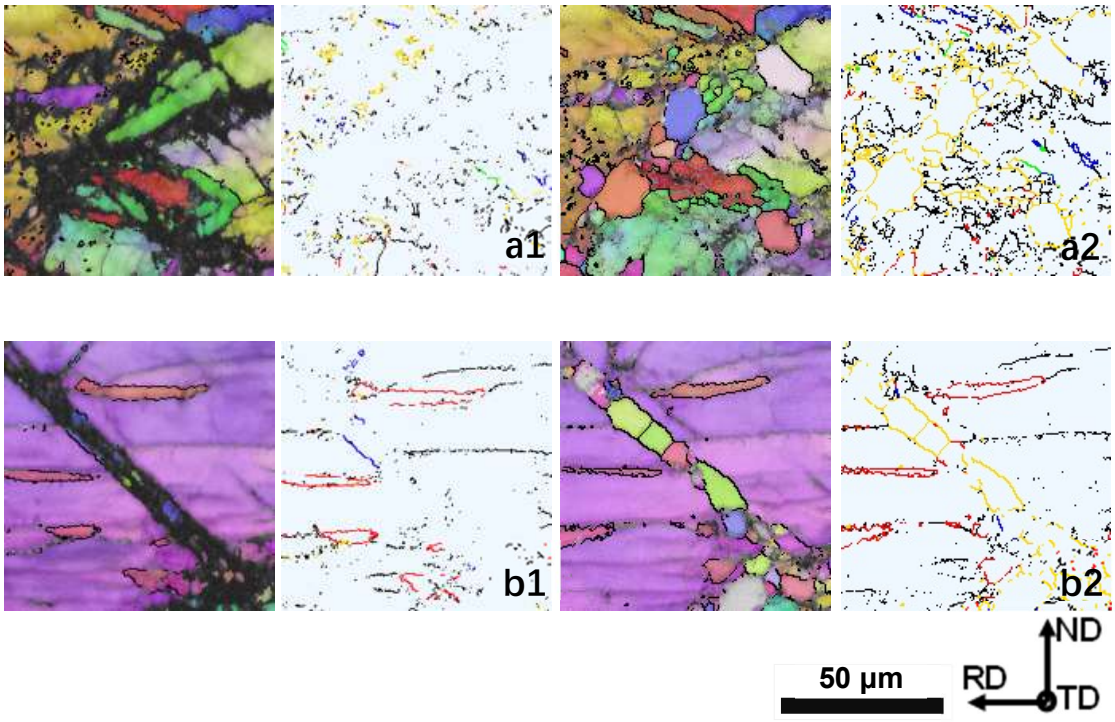

Figure 5-14 The nucleation sites in the 1290s annealed 1D compressed Mg-0.2Ca-0.3Zn (at%) specimen: (a1) (a2) from shear bands, (b1) (b2) from twins

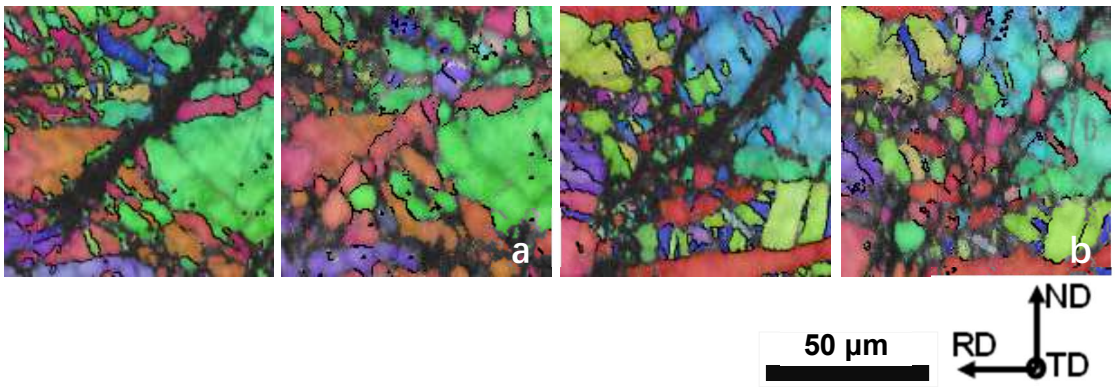

Figure 5-15 The nucleation sites in the 1290s annealed 2D compressed Mg-0.2Ca-0.3Zn (at%) specimen: (a) site 1, (b) site 2

Compared to the obvious changes in the non-indexed areas, the quantity of high angle grain boundaries, and the three twin types did not show a dramatic variation in the two strain paths (shown in Figure 5-9(a)-(e)). Figure 4-43(b), Figure 5-9(b)-(e) and Figure 5-16 show the boundary fractions of the high angle grain boundaries, tensile twins, compressive twins and double twins in 1D compressed Mg-0.2Ca-0.3Zn (at%) specimen were 54.0%, 35.6%, 5.2% and 7.6%, respectively. After removing the large grain in the centre of the 1D compressed specimen, the boundary fraction of the high

angle grain boundaries, the tensile twins, compressive twins and double twins was 52.1%, 31.9%, 4.8% and 6.7%, respectively. The boundary fraction of the high angle grain boundaries, the tensile twins, compressive twins and double twins in the 2D compressed specimen was 60.2%, 43.7%, 0.64% and 1.92%, respectively (shown in Figure 5-9(b)-(e)). Except for the fraction of tensile twins in both compressed specimens, the high angle grain boundaries and all the other twin boundary fraction values changes that are probably not statistically significant. The recrystallization at this stage did not result in many changes in the boundaries. The decrease in the tensile twin boundary fraction of both specimens was attributed to the consumption of the tensile twins during the recrystallization. However, no nucleation from tensile twins was observed. Nucleation from tensile twins is difficult because of the easy migration of the twin plane, resulting in the hard accumulation of the strain energy, which prevented the formation of the required heterogeneous strain region required to nucleate recrystallisation [57, 64]. Thus, the reduction of the tensile twins was not caused by the nucleation of recrystallisation within them but by the consumption of the recrystallized grains.

A noticeable point of the 2D compressed specimen was the dramatic reduction in the fraction tensile twins. The boundary fraction of the tensile twins in the 1D compressed specimen was shown to decrease by 7.6%, while in the 2D compressed specimen it decreased by 21.2%. This dramatic reduction was not completely caused by the consumption of recrystallization, let alone the recrystallization in 2D compressed specimen was just started. Combining Figure 4-69(b) and Figure 4-70(b), it was easy to see that many of the twins had stayed the same, but the boundaries of these twins were identified as the high angle grain boundaries rather than tensile twin boundary. As mentioned before, this was probably a result of the low EBSD index rate of the Mg alloy. Thus, the real boundary fraction of the tensile twins in the 2D compressed specimen was almost certainly much higher than 43.7%.

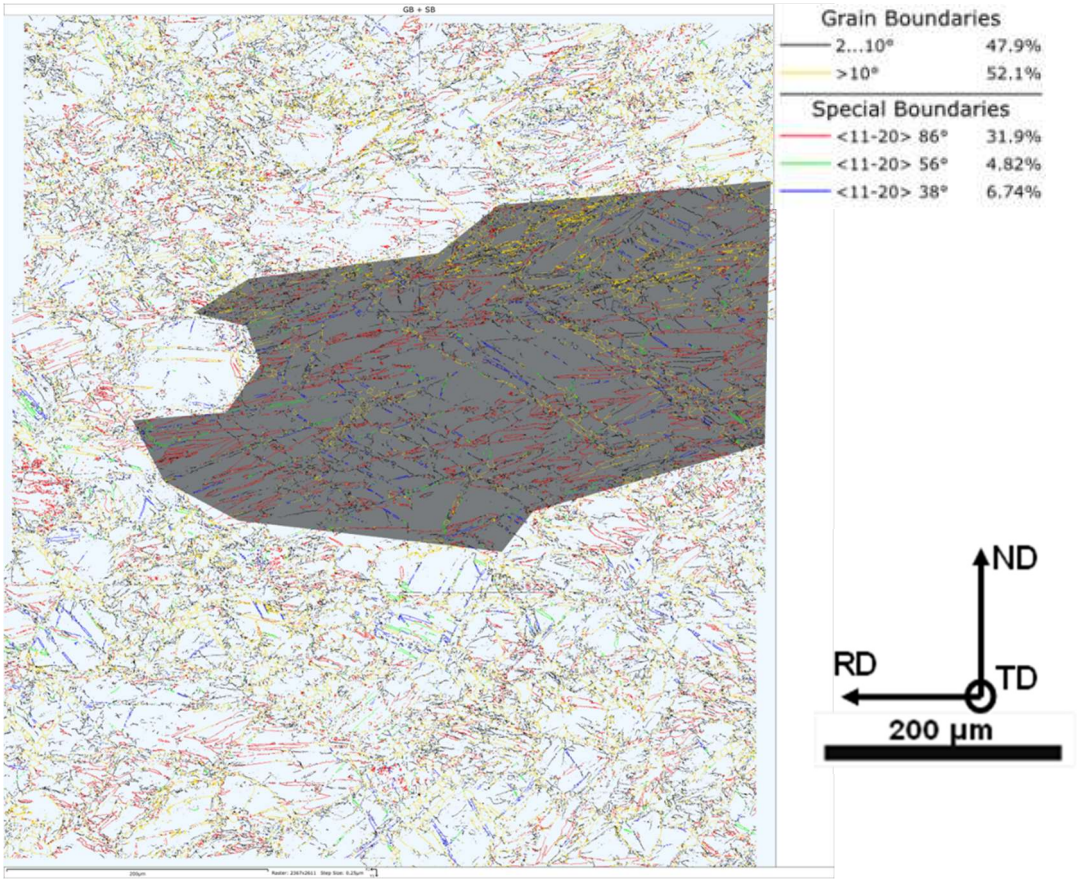

Figure 5-16 The boundary fractions of the 1290s annealed 1D compressed Mg-0.2Ca-0.3Zn (at%) specimen: (a) original, (b) without large grain in the centre

The texture evolution was followed for both strain path specimens using the pole figure derived from the EBSD data. The pole figure (shown in Figure 4-43(e)) of the whole scan area of the 1D compressed specimen indicated that the maximum pole intensity was reduced by 2.8 (to 24.5), but there was no detectable difference in the grain orientation distribution. After excluding the large grain in the centre (shown in Figure 5-17), the maximum pole intensity decreased from 9.7 to 8.2. For the 2D compressed specimen, the maximum value of the pole figure was also found to decrease from 7.6 to 6.9 (shown in Figure 4-70(e)). The reduction in the maximum pole intensity was due to the recrystallization. The 1D compressed specimen still showed a stronger texture than that of the 2D compressed specimen. Also, because the recrystallization had just started at this stage, the changes in the maximum pole intensity in two specimens did not give any other information. However, the grain orientation distribution of the two specimens showed some changes. The pole figure of the 1D compressed specimen excluding the large grain showed that the signal scattering around the TD was increased i.e. at this stage, most of the recrystallized grains had a direction close to the TD. Meanwhile, the same result was also observed in the 2D compressed specimen. The previously observed signals scattered around the TD were enhanced at

this stage. Combining the recrystallization of the specimen, the recrystallized grains in the 2D compressed specimen had a similar TD direction to that of the 1D compressed specimen.

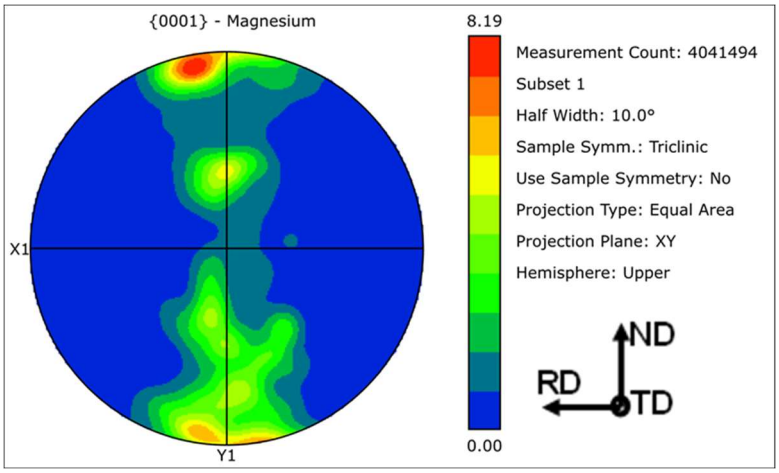

Figure 5-17 The pole figures of the 1290s annealed 1D compressed Mg-0.2Ca-0.3Zn (at%) specimen without large grain in the centre

Because the recrystallization of the two specimens was in the early stages, only a little information was acquired. At this stage, the only difference between the two Mg-0.2Ca-0.3Zn (at%) specimens was that recrystallisation started earlier in the 1D compressed specimen compared to the 2D compressed specimen.

With increased annealing time, the recrystallization behaviour of the Mg-0.2Ca-0.3Zn (at%) specimens became obvious and was easily observed across the whole scan area. The EBSD results of two specimens after the 1620s and 2370s at 350℃ were chosen as the examples to be discussed. The 1620s annealed and 2370s annealed IPF maps of the two specimens (shown in Figure 5-18(a) to (d)) showed obvious grain growth and recrystallized grain nucleation in both specimens with the progression of the annealing. For the 1D compressed specimen, between the 1290s and 1620s annealing, the microstructure evolution was found to consist of the grain growth of the existing recrystallized grains and the grain nucleation from the twins and the grain boundaries. After 2370s, grain growth of the existing recrystallized grains dominated the microstructure evolution of the 1D compressed specimen and only a few new grains were found at this stage. A noticeable point of the growth of recrystallized grains from the twins was that during 1290s to 2370s annealing, the variation of these grains was very limited (almost no changes) while the other recrystallized twins presented an obvious difference in size (from about $2\mu m$ to about $9\mu m$).

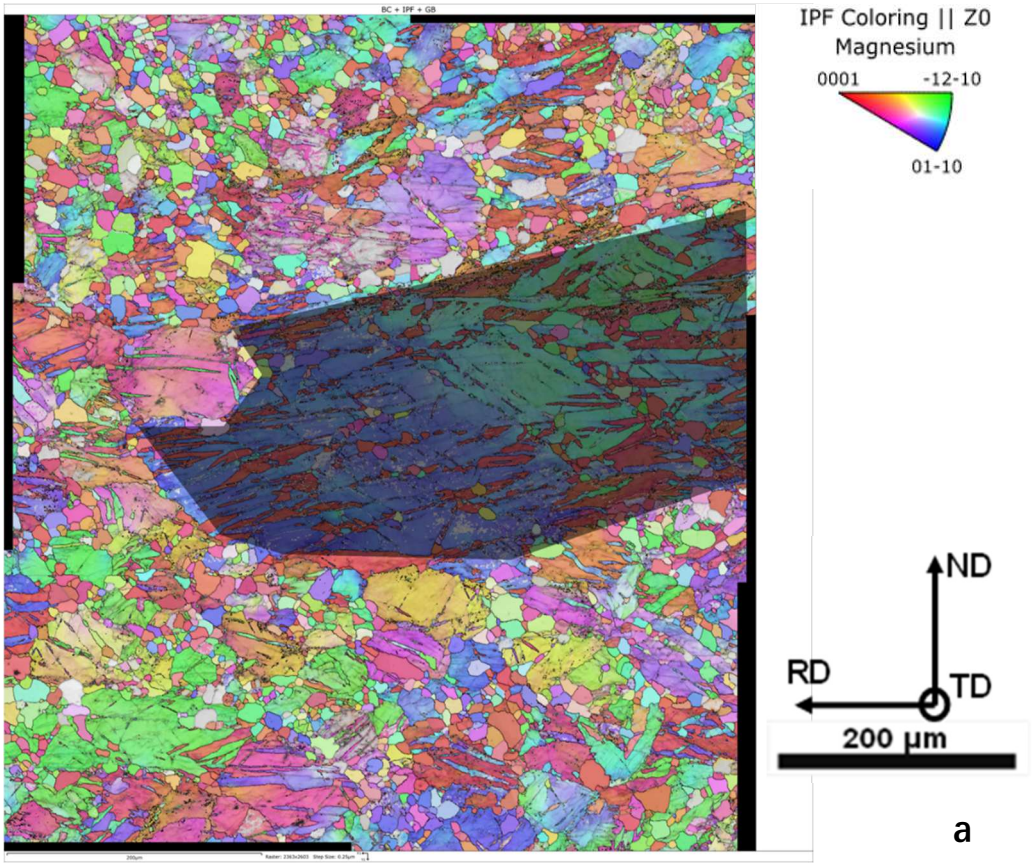
IPF Coloring || Z0
Magnesium
0001
-12-10
01-10
ND
RD
TD
200 µm

a

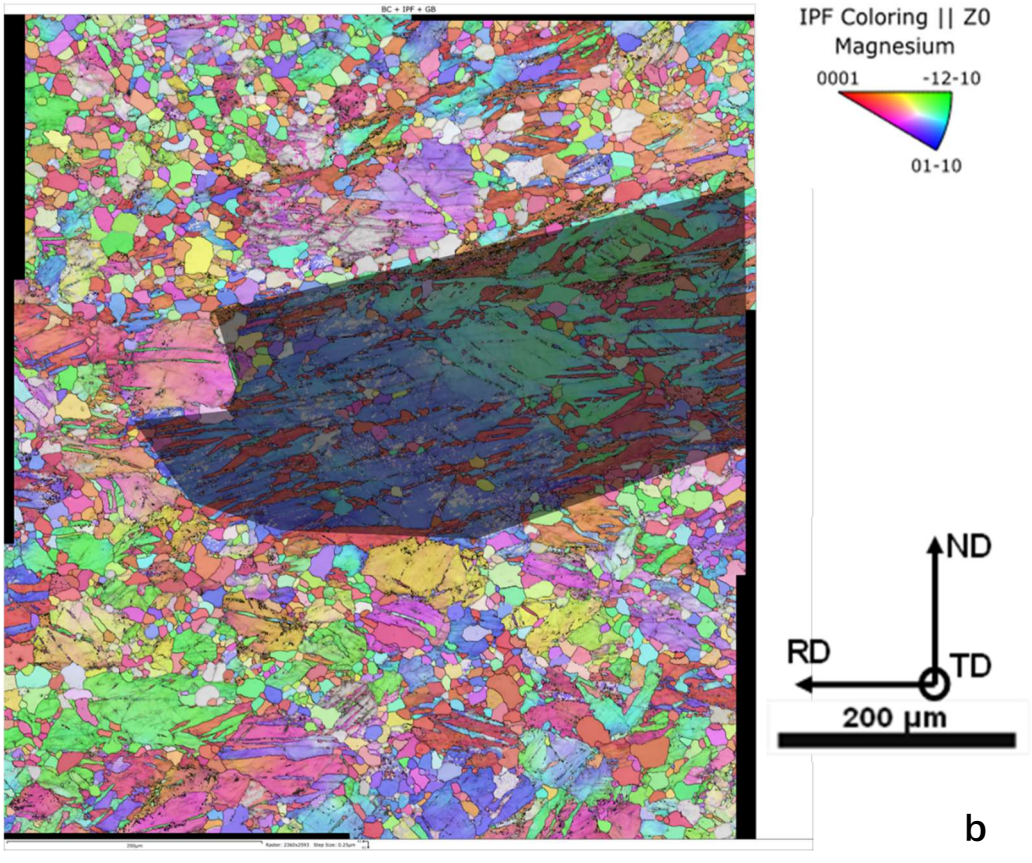
IPF Coloring || Z0
Magnesium
0001
-12-10
01-10
ND
RD
TD
200 µm

b

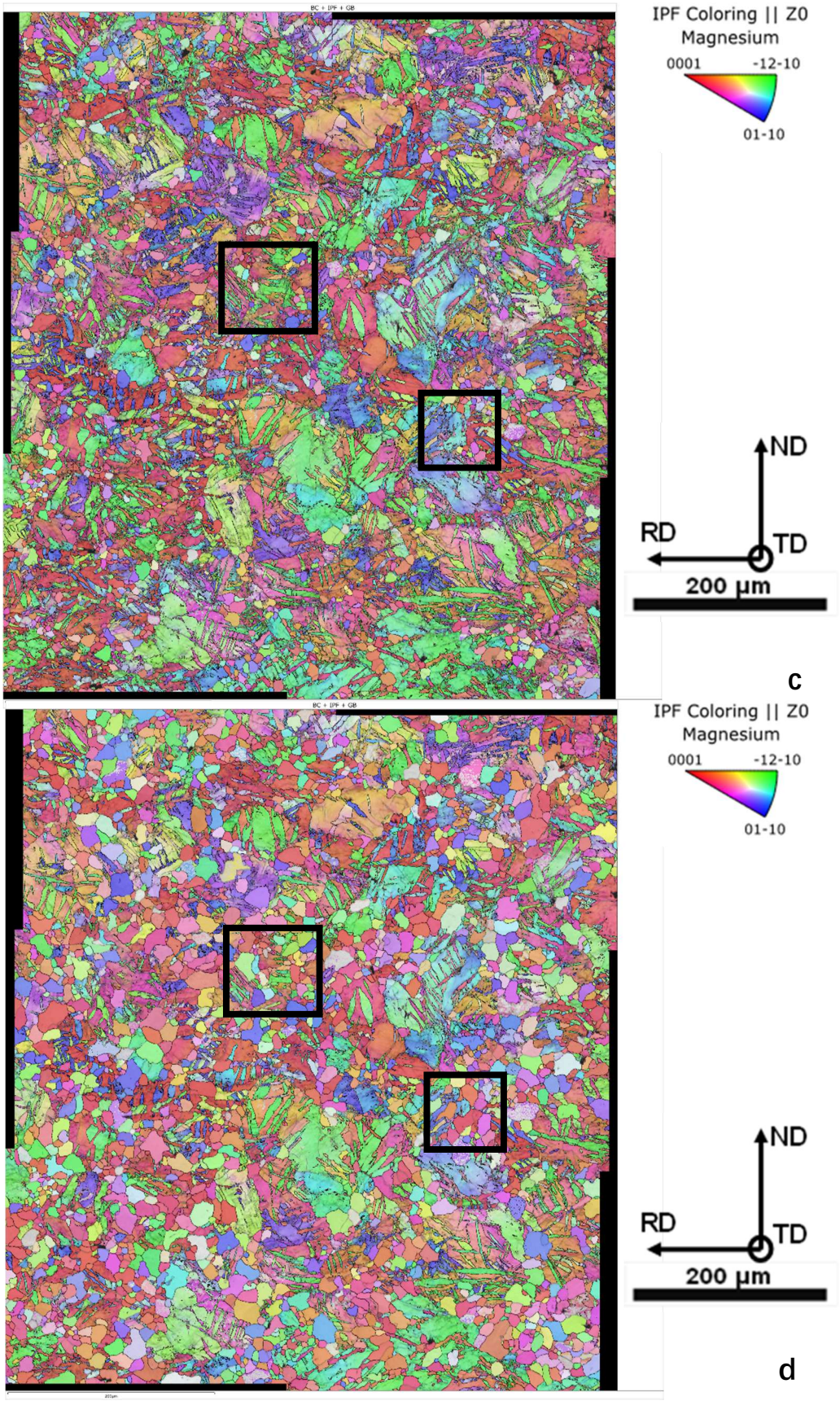

Figure 5-18 The IPF maps of the Mg-0.2Ca-0.3Zn (at%) specimen: (a) 1D compressed 1620s annealed, (b) 1D compressed 2370s annealed, (c) 2D compressed 1620s annealed, (d) 2D compressed 2370s annealed

Compared to the 1D compressed specimen, the 2D compressed specimen showed quite a different microstructural evolution. Between 1290s and 1620s, grain nucleation dominated the microstructure evolution in the 2D compressed specimen. Most of these new grains were found to have come from the previous non-indexed area, with the remainder found at the grain boundaries. However, no recrystallisation nucleated from the twins. Meanwhile, the growth of the existing recrystallized grains was very limited (about 1-3μm difference in size). After annealing the 2D compressed specimen for 2370s, not just the grain growth of the existing recrystallized grains was observed but also the nucleation of new grains was found (shown in Figure 5-19(a) and (b)). The original positions of two sites are marked by black rectangle in Figure 5-18(c) and (d). Compared to the grains in the 1D compressed specimen, the grains in the 2D compressed specimen for 2370s showed a similar average grain size (22.3μm to 21.3μm). Figures 5-20(a) and (b) show that after excluding the large grain in the centre of the 1D compressed specimen, the 2D compressed specimen also showed a larger recrystallized area fraction (about 36%) than that of the 1D compressed specimen (about 22%). The result of the average recrystallized grain size and the area fraction of the recrystallized grains in two specimens suggested that the speed of recrystallization in the 2D compressed specimen was faster than that of the 1D compressed specimen at this stage.

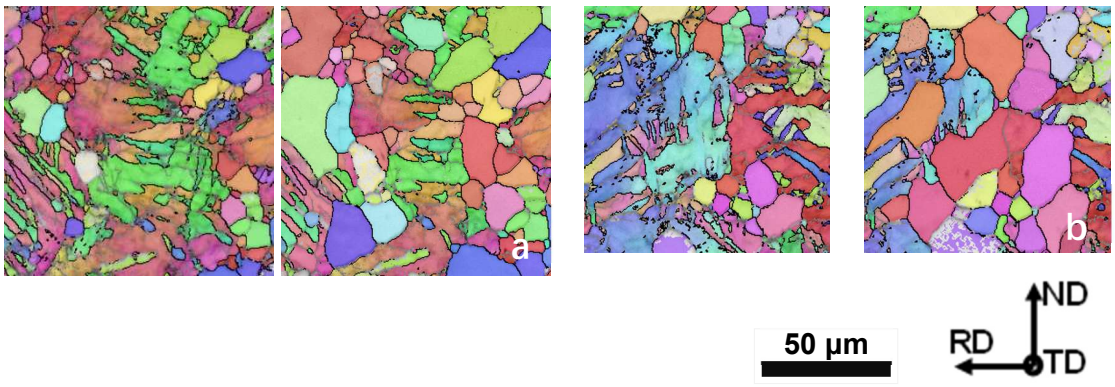

Figure 5-19 The nucleation and the grain growth in the 2D compressed Mg-0.2Ca-0.3Zn (at%) specimen during 1620s to 2370s annealing: (a) site 1, (b) site 2

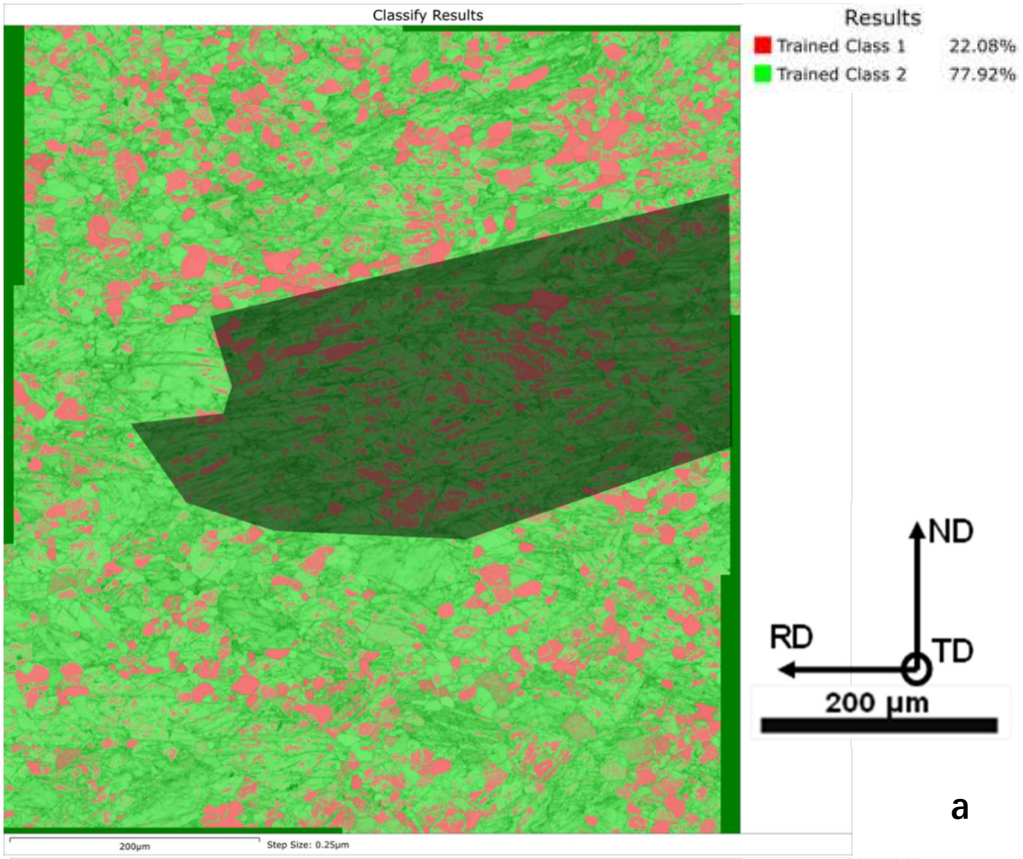

Figure 5-20 The classified results of the recrystallized grains (red) and unrecrystallized grains (green) in the Mg-0.2Ca-0.3Zn (at%) specimens after 2370s annealing: (a) 1D compressed, (b) 2D compressed

As one of the important roles in the deformation and recrystallization of Mg alloys is the changes to the twins in both strain path specimens was observed during the 1290s to 2370s annealing. Figure 5-9(c)-(e) show the grain boundary information of the 1D compressed and 2D compressed Mg-0.2Ca-0.3Zn (at%) specimens. For a more accurate result of the 1D compressed specimen, the large grain in the centre was also excluded and the new results were used in the discussion. For the 1D compressed specimen after 1620s annealing, the boundary fractions of the tensile twins, compressive twins and double twins decreased from 31.9% to 22.7%, 4.8% to 3.2% and 6.7% to 4.4%, respectively. After 2370s, the boundary fractions of the tensile twins, compressive twins and double twins further reduced to 21.3%, 2.4% and 4.0%, respectively. Meanwhile, with the recrystallization progressing, the fraction of the low angle grain boundary and high angle grain boundary also showed corresponding changes i.e. the fraction of the low angle grain boundary was reduced from 46% (1290s) to 37% (1620s) and then reached 35.3% (2370s). The fraction of the high angle grain boundary was found to increase from 54.0% (1290s) to 63.0% (1620s) and then reached 64.7% (2370s).

For the 2D compressed specimen at the same time point (1620s), the boundary fraction of tensile, compressive and double twins showed changes from 43.7% to 43.4%, 0.6% to 1.3% and 1.9% to 2.3%, respectively (Figure 5-9(c)-(e)). The small reduction in tensile twin fraction and the increase in compressive twin and double twin fraction were related to the low index rate of the 1290s annealed specimen EBSD result. All three values of the twin boundary fractions in the 1290s annealed specimen were lower than it supposed to be. The results from the 2370s annealed 2D compressed specimen (Figure 5-9(c)-(e)) showed more regular changes. The boundary fraction of the tensile, compressive and double twins reduced to 35.0%, 1.2% and 2.1%, respectively. Meanwhile, as with the 1D compressed specimen, the fraction of the low angle grain boundary and high angle grain boundary in the 2D compressed specimen also showed corresponding variation, i.e. the fraction of the low angle grain boundary was reduced from 39.8% (1290s) to 32.8% (1620s) and then reached 27.6% (2370s). The fraction of the high angle grain boundary increased from 60.2% (1290s) to 67.2% (1620s) and then reached 72.4%(2370s).

It was clear that the 2D compressed specimen exhibited fewer low angle grain boundaries and more high angle grain boundaries than the 1D compressed specimen. This suggested that the 2D compressed specimen had more recrystallized grains or the area of recrystallized grains was much larger than that of the 1D compressed specimen i.e. the 2D compressed specimen had higher degree of recrystallization. Combined with the results from Figure 5-9 and Figure 5-19, it further showed that the 2D compressed specimen had faster recrystallization kinetics than the 1D compressed specimen. The

grain boundary energy is related to the orientation difference of adjacent grains. The interface energy of low angle grain boundary is low. So, the driving force of interface movement is low, resulting in a slow grain boundary rate. However, the mobility of the high angle grain boundary with higher grain boundary energy is higher. Thus, the higher fraction of high angle grain boundary in the 2D compressed specimen could result in faster recrystallized grain growth kinetics than in the 1D compressed specimen. In addition, the 2D compressed specimen retained a higher fraction of tensile twins compared to the 1D compressed specimen. Normally, the low interface energy (0.01-0.03 J/m²) of tensile twin will significantly hinder the grain growth during the recrystallization process [133]. However, the consumption of the tensile twins may also promote grain growth in 2D specimens when having enough nucleation site [133, 134]. Therefore, it would be expected that the 2D compressed Mg-0.2Ca-0.3Zn (at%) specimen would finish recrystallization earlier than the 1D compressed Mg-0.2Ca-0.3Zn (at%) specimen.

The variation of the grain orientation distribution was also discussed between two the specimens annealed from 1290s to 2370s. It was hard to find a difference in grain orientation in the 1D compressed specimen with the large grain in the centre (shown in Figure 4-44(e) and Figure 4-46(e)). Only the maximum pole intensity showed an obvious reduction from 24.5 (1290s) to 23.7 (1620s) and reached 20.6 (2370s). After excluding the large grain area, the variation of the grain orientation distribution of the 1D compressed specimen is shown in Figure 5-21. A continuous weakening of the peak intensity was observed between 1290s and 2370s annealing. The maximum value of the pole figure reduced from 8.2 (1290s) to 7.3 (1620s) and then reached 6.4 (2370s). At the same time, the signal distributed along the ND was enhanced i.e. more grains with a direction distributed between TD and ND were detected. Moreover, rather than a random grain orientation from TD to ND, the scattering concentrated 20°-30° around the TD-ND plane with increasing recrystallization. Figure 4-71(e) and Figure 4-73(e) show the pole figure of the 2D compressed specimen under the same time point as the 1D compressed specimen. In a similar manner to the 1D compressed specimen, a continuous weakening of the peak intensity was also observed. The maximum value of the pole figure was shown to reduce from 6.9 (1290s) to 6.1 (1620s) and then reached 4.6 (2370s). Also, the variation of the grain orientation distribution was quite similar to that of the 1D compressed specimen. An increasing number of recrystallized grains with random orientation were found. The direction of the recrystallized grains distributed along the TD-RD plane but scattered wider from the RD axis (20°-40°) than that of the 1D compressed specimen during the annealing. It was clear that the 2D compressed specimen always had a lower maximum pole intensity from 1290s to 2370s. In addition, both specimens showed a grain orientation distribution related to the last compression

direction i.e. the 1D compressed specimen had a TD-ND distributed grain orientations and 2D compressed specimen had a TD-RD distributed grain orientations. However, the 2D compressed specimen had a much more dispersed grain orientation distribution than the 1D compressed specimen at these stages i.e. the 2D compressed specimen had a weaker texture than the 1D compressed specimen.

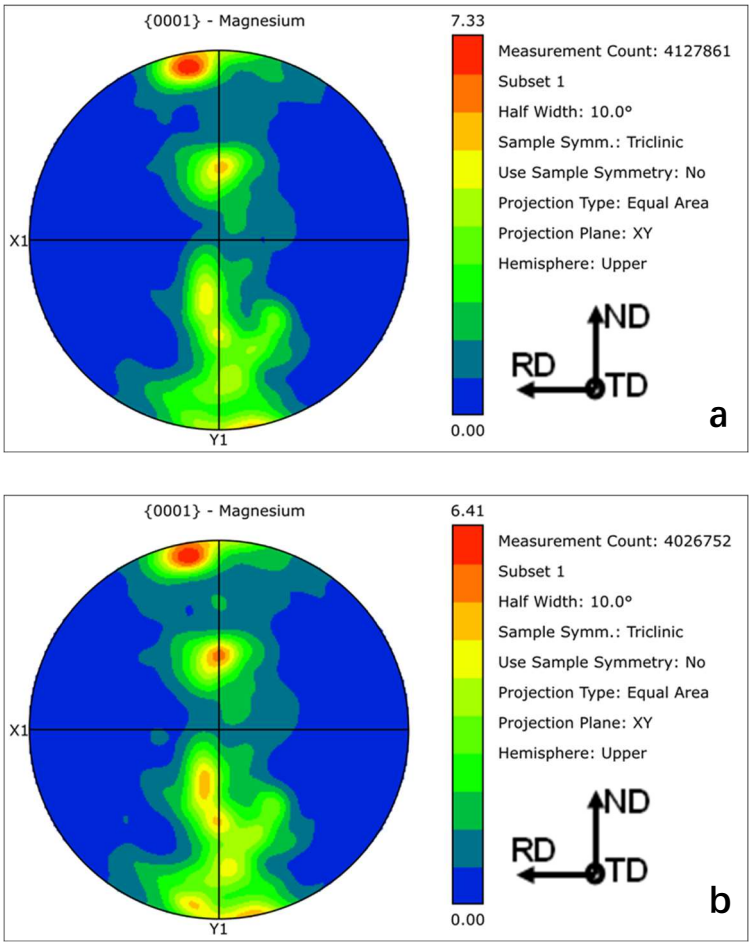

Figure 5-21 The pole figures of the 1D compressed Mg-0.2Ca-0.3Zn (at%) specimen without large grain: (a) 1620s annealed, (b) 2370s annealed

The large-scale recrystallized microstructure was observed in the IPF map in 1D compressed specimen (excluding the large grain) after 3810s annealing (shown in Figure 4-50(a)), while a fully recrystallized microstructure was observed in 2D compressed specimen after 2790s annealing (shown in Figure 4-74(a)). The IPF maps also indicate that the two specimens showed a similar microstructure evolution in the last annealing stage. Further growth of the existing recrystallized grains and the nucleation of the new grains were the reasons for the formation of the final microstructures in both specimens. Figure 4-50(f) and Figure 4-74(g) show the average grain size of the 1D compressed specimen and the 2D compressed specimen as 19.1μm and 35.1μm, respectively. The much larger average grain size in the 2D compressed

specimen indicated that a higher number of recrystallized grains entered the grain growth stage compared to the 1D compressed specimen. Figure 4-50(b) and Figure 4-74(b) indicate the final boundary fractions of the two strain path specimens. In the 1D compressed specimen, the fractions of the low angle grain boundary, high angle grain boundary, tensile twins, compressive twins and double twins were 21.7%, 78.3%, 10.1%, 1.6% and 1.7%, respectively, while the fractions in 2D compressed specimen were 11.3%, 88.7%, 5.0%, 0.2% and 0.1%, respectively. In the 2D compressed specimen, the lower twin boundary fractions and higher high angle grain boundary fraction indicated that it had more extensive recrystallization than the 1D compressed specimen. Compared to the 1D compressed specimen, the 2D compressed specimen had larger average grain size, lower twin boundary fractions and higher high angle grain boundary fraction. It was very clear that the 2D compressed specimen finished the recrystallization earlier than the 1D compressed specimen.

Both the 1D compressed specimen and the 2D compressed specimen showed a weakened texture in Figure 4-50(d) and Figure 4-74(e), respectively, after annealing. The 1D compressed specimen showed a higher maximum pole intensity (5) than that of the 2D compressed specimen (3.4). Also, a wider scattered grain orientation distribution was found in the 2D compressed specimen. The grain orientation distribution of the 1D compressed specimen still showed a trend that scattered around the ND-axis i.e. the TD-ND plane. However, the grain orientation distribution of the 2D compressed specimen showed a typical “Rare Earth like” structure i.e. a well-spread random distributed grain orientation distribution. The reason for this difference is discussed as follows. In the 1D compressed specimens, the recrystallized grains originating from the twins showed limited growth compared to the recrystallized grains from shear bands and grain boundaries. In the 2D compressed sample, the recrystallized grains were almost entirely from shear bands and grain boundaries, which are very important sources of the random orientated grains [135]. Considering the higher fraction of the shear bands and double twins in the 1D compressed specimen, the reason for the weaker texture in the 2D compressed specimen was attributed to its higher fraction of tensile twins. The recrystallization from the shear bands and double twins was found in the very early stage of the annealing, promoting a random orientation at the start. In the 2D compressed specimen, the higher fraction of tensile twins did not hinder the growth of the recrystallized grains but helped these random orientated grains to grow by being consumed (shown in Figure 5-22), which the similar result was reported by Ye et al. [133] and I. Basu and T. Al-Samman [134]. Meanwhile, the random orientated grains in 1D specimen showed a limited growth or they were even consumed by other grains throughout the whole annealing process (shown in Figure 5-23). Thus, more random orientated grains with larger size were preserved to the end of the

recrystallization in the 2D compressed specimen. Thus, the 2D compressed specimen showed a weaker texture compared to the 1D compressed specimen.

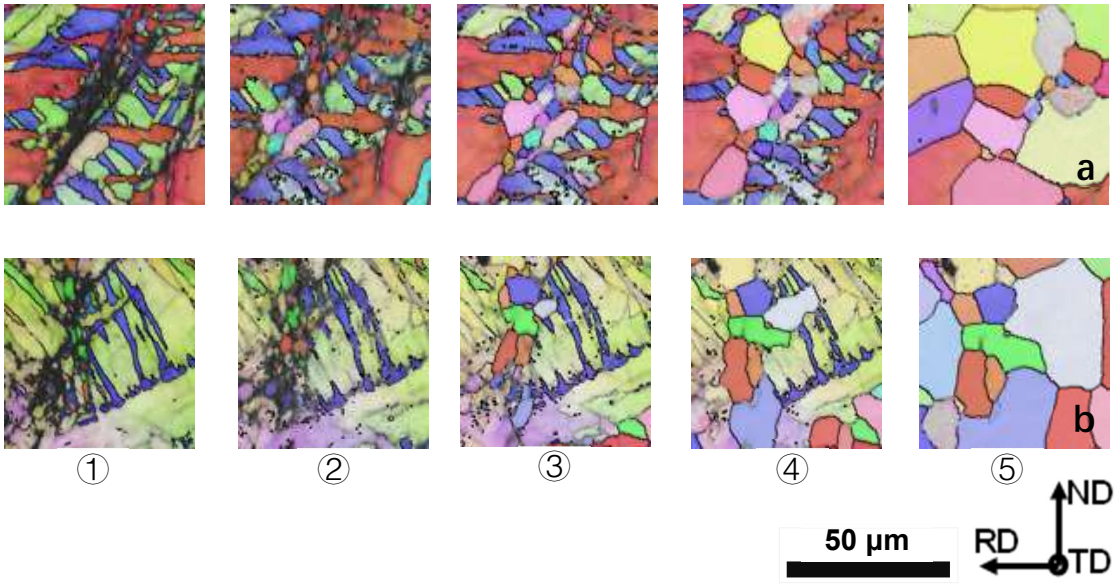

Figure 5-22 The recrystallization in the 2D compressed Mg-0.2Ca-0.3Zn (at%) specimen: (a) site 1 after ①0s ②1290s ③1620s ④2370s ⑤2790s annealing (b) site 2 after ①0s ②1290s ③1620s ④2370s ⑤2790s annealing

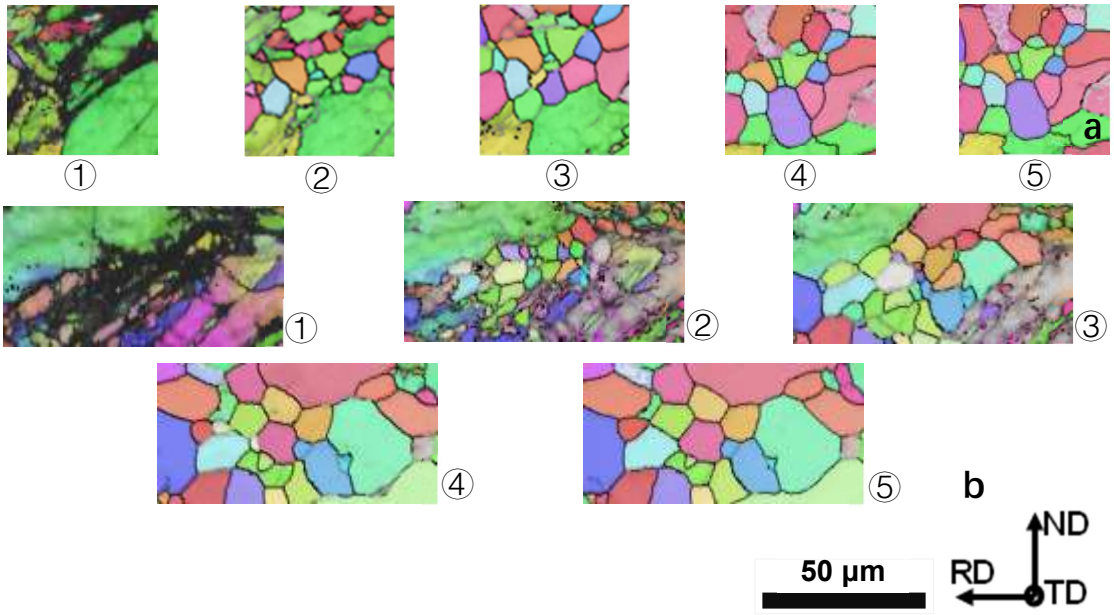

Figure 5-23 The recrystallization in the 1D compressed Mg-0.2Ca-0.3Zn (at%) specimen: (a) site 1 after ①0s ②1290s ③2370s ④2790s ⑤3810s, (b) site 2 after ①0s ②1290s ③2370s ④2790s ⑤3810s

5.3.2 Mg-0.1Ca-0.4Zn (at%) specimens

The charts shown below in Figure 5-24 present the variation of the grain boundaries, twin boundaries and maximum pole intensity of the 1D/2D Mg-0.1Ca-0.4Zn(at%) specimens during the annealing process, which will be discussed in the following chapters.

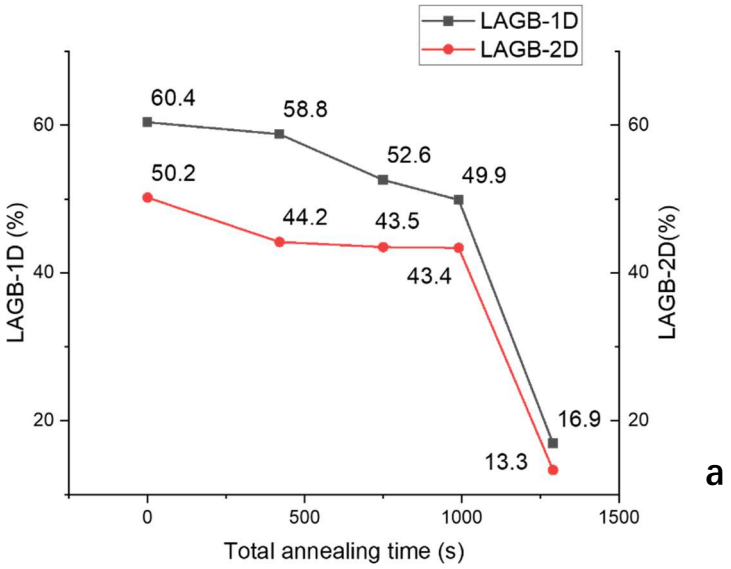

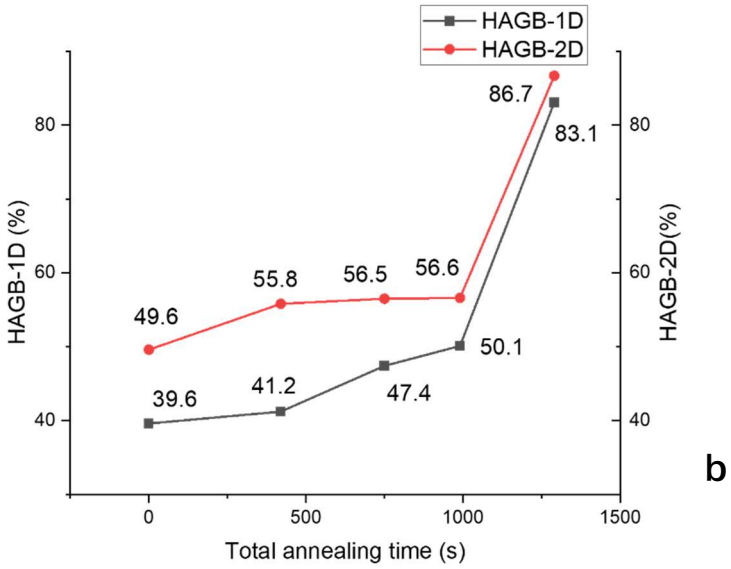

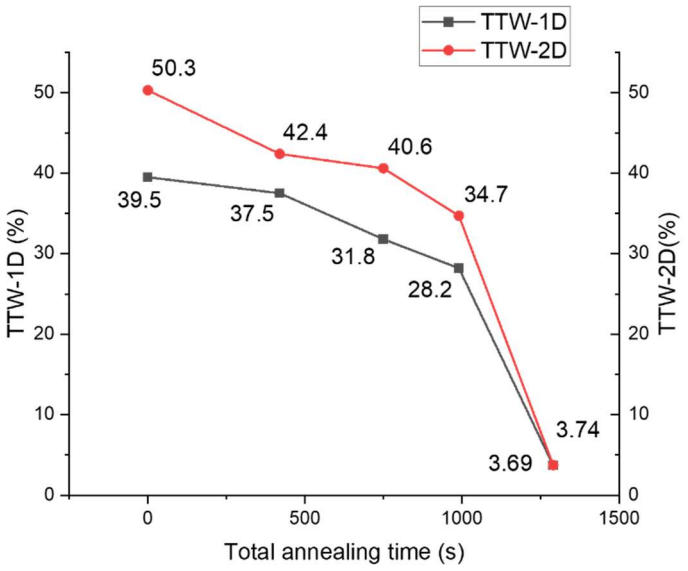
TTW-1D
TTW-2D
50.3
42.4
40.6
34.7
39.5
37.5
31.8
28.2
3.74
3.69
TTW-1D (%)
TTW-2D(%)
Total annealing time (s)

c

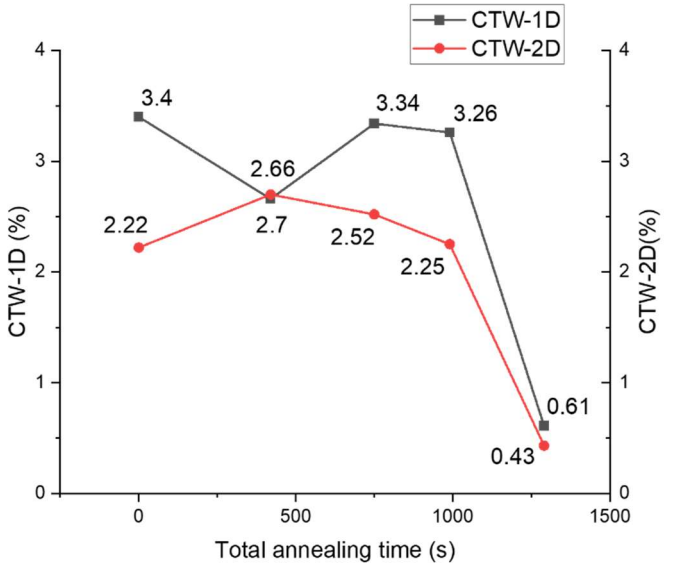
CTW-1D
CTW-2D
3.4
3.34
3.26
2.66
2.22
2.7
2.52
2.25
0.61
0.43
CTW-1D (%)
CTW-2D(%)
Total annealing time (s)

d

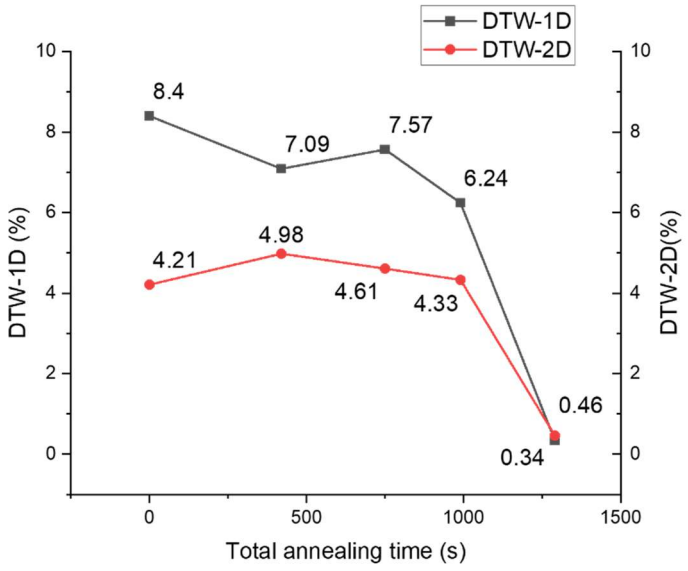
DTW-1D
DTW-2D
8.4
7.09
7.57
6.24
4.21
4.98
4.61
4.33
0.46
0.34
DTW-1D (%)
DTW-2D(%)
Total annealing time (s)

e

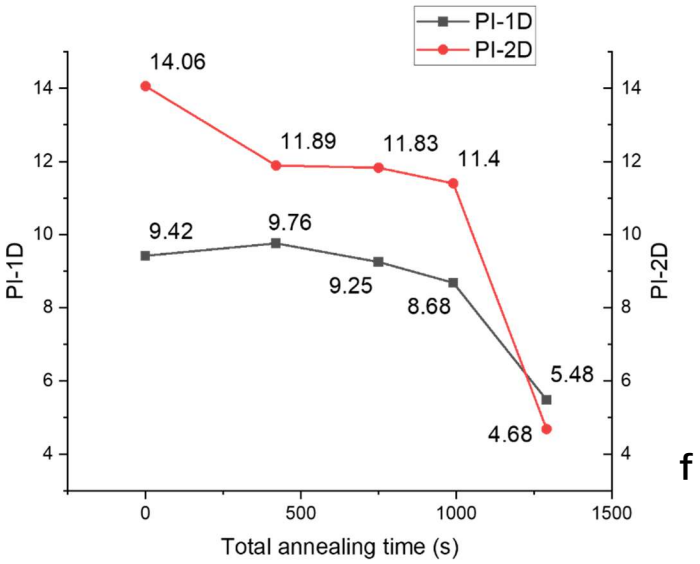

Figure 5-24 The variation in the 1D/2D compressed Mg-0.1Ca-0.4Zn (at%) during annealing: (a) low angle grain boundary (LAGB), (b) high angle grain boundary (HAGB), (c) tensile twin (TTW) boundary, (d) compressive twin (CTW) boundary, (e) double twin (DTW) boundary, (f) maximum pole intensity (PI)

5.3.2.1 Mg-0.1Ca-0.4Zn (at%) specimens after compression

At the as-compressed stage of the Mg-0.1Ca-0.4Zn (at%) specimens, both 1D compressed (shown in Figure 4-51(c)) and 2D compressed specimens (shown in Figure 4-75(c)) showed a considerable non-indexed area in EBSD maps which occupied 27.5% and 41.5% of the total scan area, respectively. The non-indexed area in the two specimens was considered to consist of shear bands and fine twins. In a similar manner to the Mg-0.2Ca-0.3Zn (at%) specimens, most of the non-indexed sections in both specimens were identified as shear bands rather than twins. This was particularly the case for the 2D compressed specimen where 41.5% of the scan area was not indexed, and based on morphology, the twins in the non-indexed area only occupied a quite low fraction of this 41.5% area i.e. the shear bands dominated the non-indexed region (especially on the top right corner of the scan area). The 1D compressed specimen showed fewer shear bands but more twins in the non-indexed area compared to the 2D compressed specimen after the compression (shown in Figure 4-51(c) and Figure 4-75(c)).

A very similar result was observed for the twin distribution as found in the Mg-0.2Ca-0.3Zn (at%) specimens. The 1D compressed Mg-0.1Ca-0.4Zn (at%) specimen had fewer tensile twins (39.5%) but more compression twins (3.4%) and double twins (8.4%) compared to that of the 2D compressed specimen (50.3%, 2.2% and 4.2%, respectively) (shown in Figure 5-24(c)-(e)). The reason for this result was the same as the Mg-0.2Ca-0.3Zn (at%) specimens mentioned before. The different compression

directions from the hard orientation and the soft orientation brought different kinds of twins to the advantageous position for forming during the deformation.

The results from the pole figures of the two strain paths (shown in Figure 4-51(e) and Figure 4-75(e)) show their different grain orientation distributions. The 1D compressed specimen had a maximum value of 9.4 in the pole figure which was much lower than that of the 2D compressed specimen (14.1). However, due to the existence of the second peak with a pole intensity of 9.0 shown in the pole figure of the 1D compressed specimen and the angle difference between the two peaks was less than 30°, the texture of the 1D compressed specimen was considered stronger than the texture of the 2D compressed specimen. The two peaks were both close to the ND and tilted about 30° from it. In addition to the double peaks mentioned above, the as-compressed grains of the 1D compressed specimen were also found to have a direction diffuse around the TD (tilted 10°-20°). On the other hand, most of the grains in the 2D compressed specimen showed an orientation parallel to the RD. Compared to the 1D compressed specimen, only a few grain orientations were found diffuse around the TD. The reason for this difference was already mentioned in the discussion of the as-compressed Mg-0.2Ca-0.3Zn (at%) specimens.

The microstructure of the as-compressed 1D and 2D Mg-0.1Ca-0.4Zn (at%) specimens showed many differences caused by the different strain paths such as the shear bands, twins and grain orientation distributions etc. The 1D compressed specimen showed fewer shear bands and tensile twins but more compressive twins and double twins. The different textures found between the two strain paths of the Mg-0.1Ca-0.4Zn (at%) specimens is consistent with the differences found in the as-compressed Mg-0.2Ca-0.3Zn (at%) specimens, suggesting that the texture differences were a true reflection of the differences in the strain path.

5.3.2.2 The recrystallization of Mg-0.1Ca-0.4Zn (at%) specimens

During annealing, the recrystallization structure was found in the two specimens after the 420s annealing at 350℃. The phase map of the two specimens (shown in Figure 4-53(c) and Figure 4-77(c)) showed the changes in the non-indexed area. Although the specimen was found to start recrystallization, the 1D compressed specimen showed a higher non-indexed area fraction which increased from 27.5% to 31.4%. The reason for this was attributed to the unstable index rate of the Mg alloys in the EBSD. The EBSD map resolution of the 420s annealed 1D compressed specimen was not as good as the as-compressed stage. However, the recrystallization from the shear bands, twins and grain boundaries was clear enough to see in the IPF map (shown in Figure 4-53(a)). On the other hand, the 2D compressed specimen presented a dramatic variation in the non-indexed area. The area fraction of the non-indexed area reduced from 41.5% to 22.4%.

Unlike the 1D compressed specimen, the recrystallized grains in the 2D compressed specimen were rarely found originating from the grain boundaries or twins that were large enough to be indexed in EBSD (shown in Figure 4-77(a)). Almost all the recrystallized grains were found from the previous non-indexed region i.e. the shear bands and fine twins. And this also was the reason why the non-indexed area dramatically reduced in the 2D compressed specimen. When comparing the recrystallized grains in the different strain paths, the recrystallized grains in the 1D compressed specimen were found to be larger than the recrystallized grains in the 2D compressed specimen. If the grain boundary velocity in the two specimens was similar, then the larger recrystallized grains in the 1D compressed specimen were the result of the earlier recrystallization. However, it was very hard to measure the grain boundary velocity in the specimens at this stage.

At the start of the recrystallization, the grain boundaries in the two strain path specimens showed similar changes. The fraction of the high angle grain boundaries in both 1D and 2D compressed specimens increased from 39.6% to 41.2% and 49.8% to 55.8%, respectively (shown in Figure 5-24(a) and (b)). However, some boundary information was missing because of the non-indexed areas, particularly for the 1D compressed specimen, suggesting a higher than 41.2% fraction of high angle boundaries. The changes in compressive twins and double twins were not obvious, with a statistically not significant reduction of the tensile twin boundary fraction in the 1D specimen (from 39.5% to 37.5%) and a more significant reduction in the 2D specimen (from 50.3% to 42.4%).

The variation in the pole figures of the two strain paths (shown in Figure 4-53(e) and Figure 4-77(e)) was small, and consistent with the changes in the boundaries. Due to the lower EBSD scanning quality, the 420s annealing 1D compressed specimen showed a higher non-indexed area fraction than that of the as-compressed stage. The maximum pole intensity of the 1D specimen showed a change from 9.4 to 9.8 and the intensity of the second peak also increased from 9.0 to 9.2, neither of which are statistically significant. In contrast, the 2D specimen exhibited a more significant drop in the maximum pole intensity from 14.1 to 11.9. In a similar manner to the Mg-0.2Ca-0.3Zn (at%) specimens, at the beginning of the recrystallization, the 1D compressed Mg-0.1Ca-0.4Zn (at%) specimen still presented a weaker texture than that of the 2D compressed Mg-0.1Ca-0.4Zn (at%) specimen. Although the changes in the maximum pole intensity in the 1D compressed specimen was small, an increase in the number of TD-orientated grains was observed. The same result was also observed in the pole figure of the 420s annealed 2D compressed specimen. Thus, at the start of the recrystallization, the recrystallized grains in both Mg-0.1Ca-0.4Zn (at%) specimens showed a trend that orientated towards the TD.

No obvious difference was found in the starting point of recrystallization between the two strain paths for the Mg-0.1Ca-0.4Zn (at%) specimens. The only noticeable difference was that the recrystallized grains were larger than that of the 2D compressed specimen in the 1D compressed specimen. This could be evidence of the earlier recrystallization in the 1D compressed specimen.

With the increase in annealing time, the recrystallization behaviour of the Mg-0.1Ca-0.4Zn (at%) specimens was observed across the whole scan area. The EBSD results of the two specimens after the 750s and 990s at 350℃ were chosen as examples to be discussed. The 750s annealed and the 990s annealed IPF maps of two specimens (shown in Figure 4-55, 4-56 and Figure 4-79, 4-80) showed that grain growth and grain nucleation in both specimens progressed with annealing. For the 1D compressed specimen between 420s and 750s annealing (shown in Figure 5-25(a)), the microstructure evolution was found to consist of the grain growth of the existing recrystallized grains and grain nucleation from the twins and grain boundaries. By 990s (shown in Figure 5-25(b)), grain growth of the existing recrystallized grains and grain nucleation from the twins and the grain boundaries were still observed. A notable point of the growth of recrystallized grains from the twins was that during the 420s to 990s annealing, the variation of these grains was very limited which was just 2-3 μm increase in size (shown in Figure 5-26(a)), while Figure 5-26(b) indicates that other recrystallized twins (e.g. nucleating from the grain boundaries) presented an obvious difference in size (from 0μm to about 15μm). The example areas are marked by black rectangles in the figures.

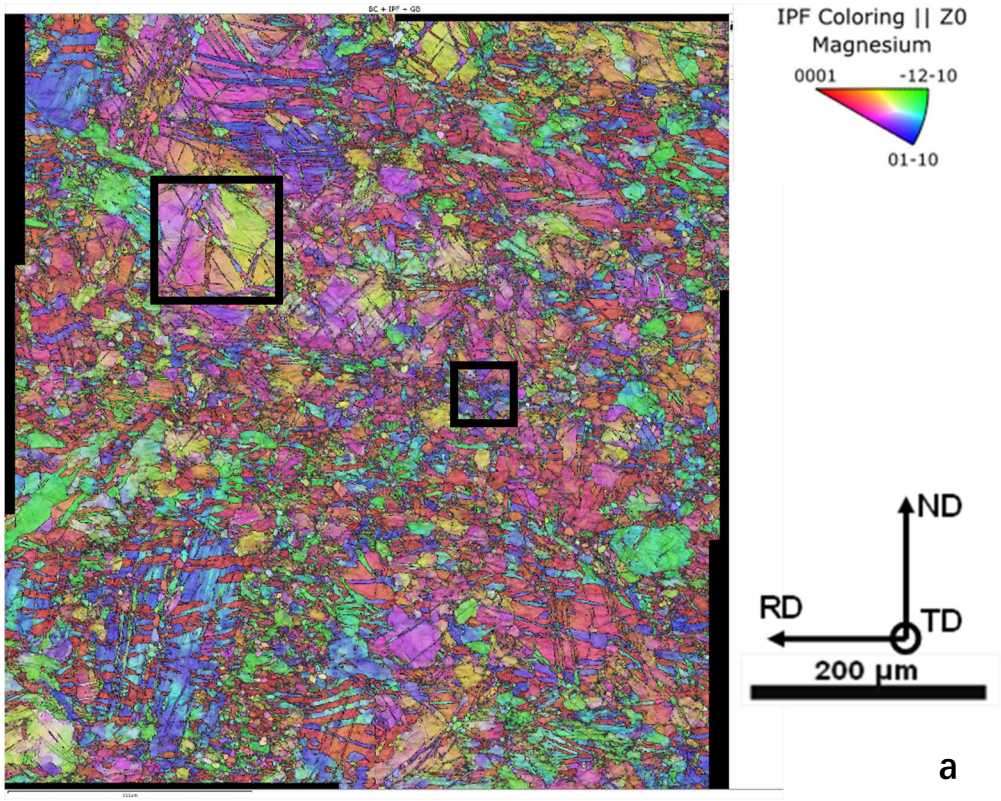

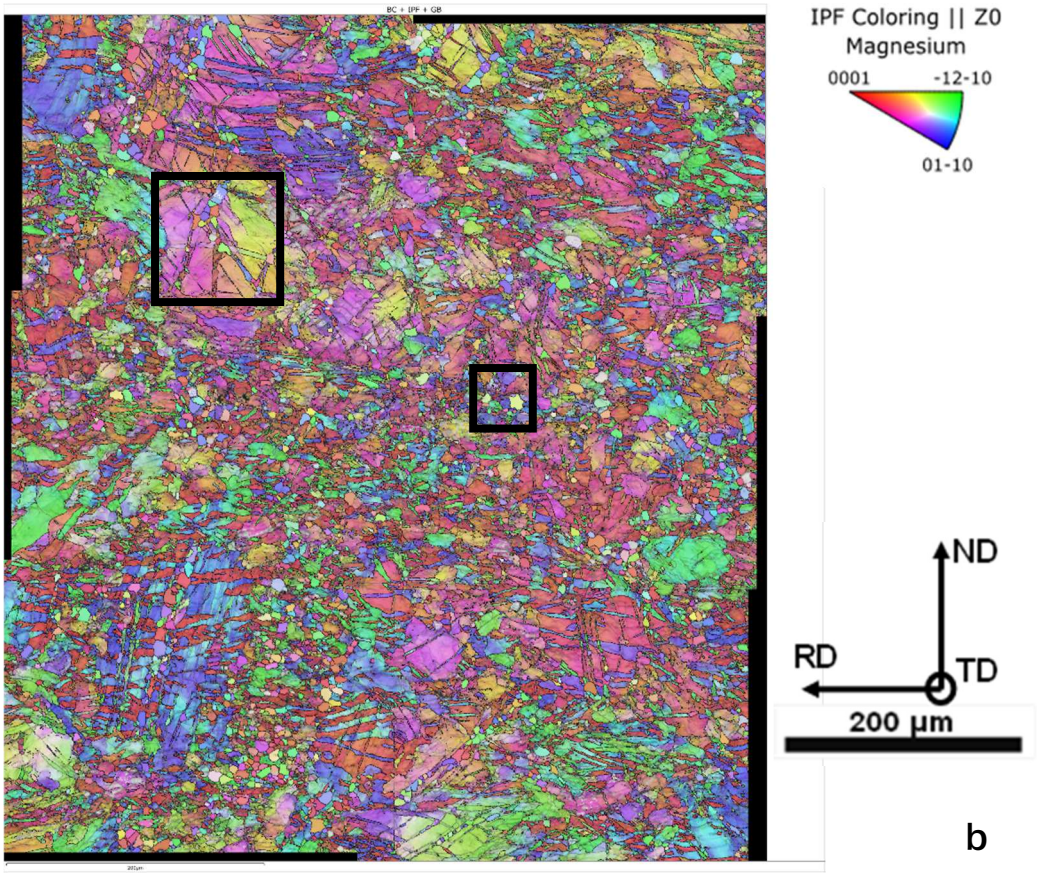

Figure 5-25 The IPF maps of the Mg-0.1Ca-0.4Zn (at%) specimen: (a) 1D compressed 750s annealed, (b) 1D compressed 990s annealed

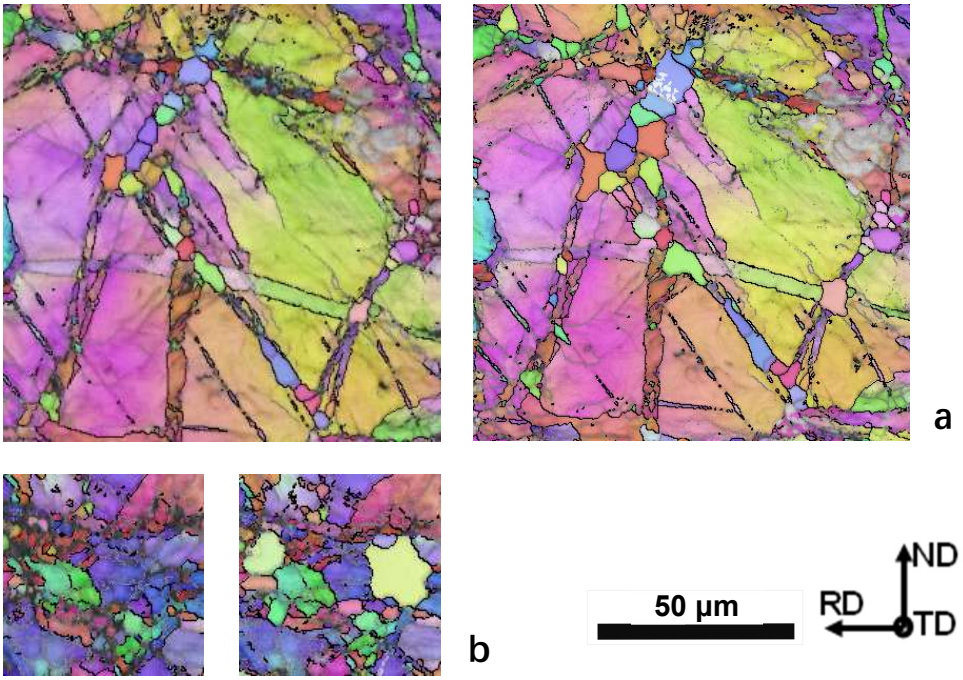

Figure 5-26 The nucleation and the grain growth in the 1D compressed Mg-0.1Ca-0.4Zn (at%) specimen during 750s to 990s annealing: (a) from twins, (b) from grain boundary

Compared to the 1D compressed specimen, the 2D compressed specimen showed quite different microstructural evolution. First of all, the scale of the recrystallization in 2D compressed specimen was much smaller than the 1D compressed specimen. Figure 5-27(a) and (b) indicate the area fraction of the recrystallized grains in two specimens after 990s annealing. The recrystallized grains occupied about 11% and about 5% of the EBSD mapping area of the 1D compressed and 2D compressed specimen, respectively. Although both grain growth and recrystallized grain nucleation were also observed in the 2D compressed specimen during the annealing, the size of these grains was much smaller than that of the 1D compressed specimen. The largest recrystallized grain in the 2D compressed specimen after the 990s annealing was $5\mu m$ which was much smaller than the $15\mu m$ of the 1D compressed specimen. Meanwhile, the IPF map of the 990s annealed 2D compressed specimen indicated that there was still a few non-indexed regions remaining i.e. there were still many potential nucleation sites across the whole specimen. Compared to the 990s annealed 1D compressed specimen, the recrystallization of the 2D compressed specimen was obviously one step later i.e. at least no non-indexed region was found in the 1D compressed specimen. This suggested that the 2D compressed specimen was still in the early stage of recrystallization after the 990s annealing. The larger recrystallized area in the 1D compressed specimen could be the result of the early recrystallization within it.

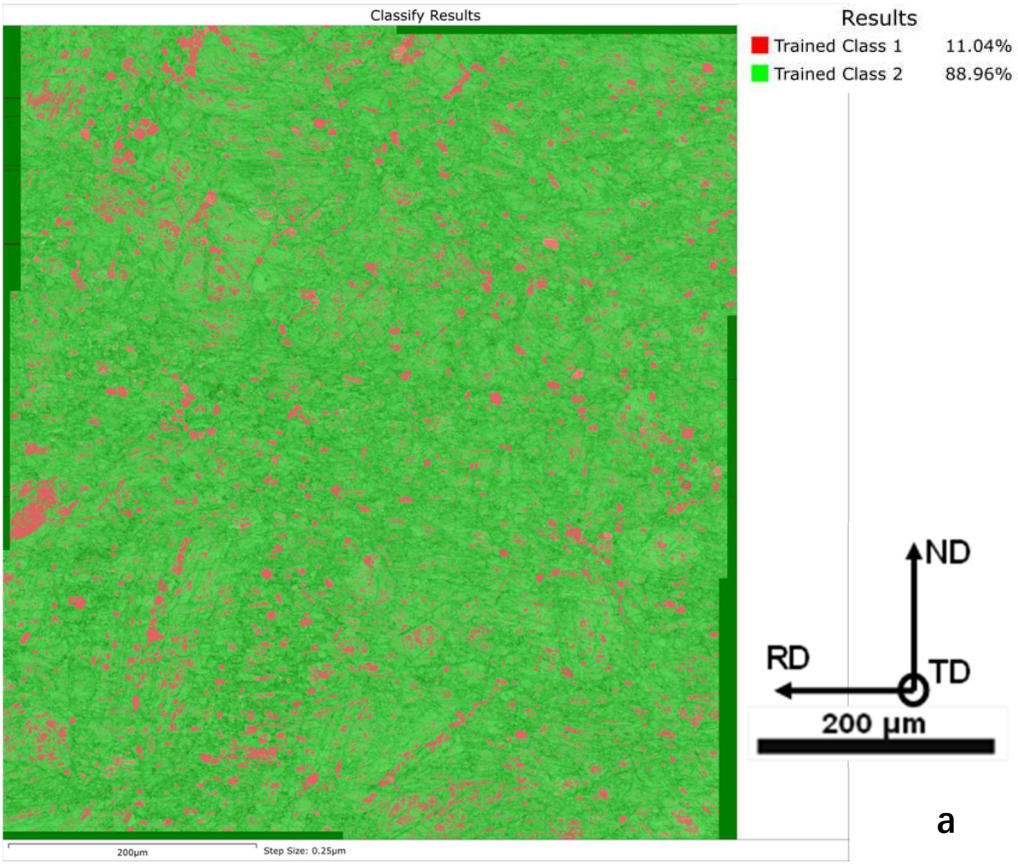

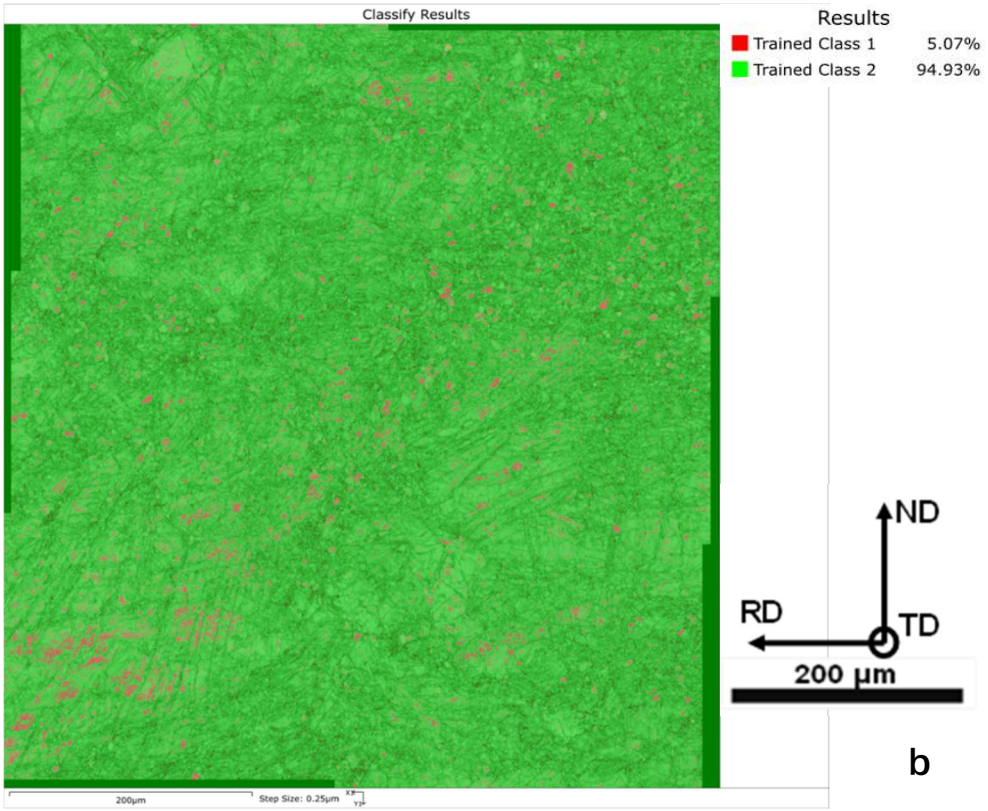

Figure 5-27 The classified results of the recrystallized grains (red) and unrecrystallized grains (green) in the Mg-0.1Ca-0.4Zn (at%) specimens after 990s annealing: (a) 1D compressed, (b) 2D compressed

Changes in the twins in the two specimens during the 420s to 990s annealing were also observed. Figure 5-24(a)-(e) show the grain boundary information of the 1D compressed and 2D compressed Mg-0.1Ca-0.4Zn (at%) specimens. For the 1D compressed specimen, after annealing for 750s, the boundary fractions of the tensile twins decreased from 37.5% to 31.8%. The boundary fraction of the compressive twins and the double twins was found to increase from 2.7% to 3.3% and 7.1% to 7.6%, respectively. The increase in the fraction of the compressive twins and the double twins was related to the low EBSD index rate of the 420s annealed specimen. Both values of the boundary fractions of compressive twins and double twins in the 420s annealed specimen were lower than expected. The results from the 990s annealed 1D compressed specimen showed more regular changes. After annealing for 990s, the boundary fractions of the tensile twins, compressive twins and double twins all reduced to 28.2%, 3.3% and 6.2%, respectively. Meanwhile, with the recrystallization progressing, the fraction of the low angle grain boundary and high angle grain boundary also showed corresponding variation i.e. the fraction of the low angle grain boundary was reduced from 58.8% (420s) to 52.6% (750s) and then reached 49.9% (990s). The fraction of the high angle grain boundary increased from 41.2% (420s) to 47.4% (750s) and then reached 50.1%(990s).

For the 2D compressed specimen at the same time point (750s) (shown in Figure 5-24(a)-(e)), the boundary fraction of tensile twins, compressive twins and double twins showed changes from 42.4% to 40.6%, 2.7% to 2.5% and 5.0% to 4.6%, respectively. After 990s, the boundary fraction of the tensile twins, compressive twins and double twins further reduced to 34.7%, 2.3% and 4.3%, respectively (shown in Figure 5-24(a)-(e)). Meanwhile, like the 1D compressed specimen, the fraction of the low angle grain boundaries and high angle grain boundaries in the 2D compressed specimen also showed corresponding variation i.e. the fraction of the low angle grain boundary was reduced from 44.2% (420s) to 43.5% (750s) and then reached 43.4% (990s). The fraction of the high angle grain boundary increased from 55.8% (420s) to 56.5% (750s) and then reached 56.6%(990s).

Based on the boundary information of the two specimens, it was clear that during annealing for 420s to 990s, the recrystallization progress of the 2D compressed specimen was slow and lagged behind that of the 1D compressed specimen. The difference of the high angle boundary fraction of the 2D compressed specimen (0.8%) was also much smaller than that of the 1D compressed specimen (8.9%). Also, the differences in the fraction of compressive twins and double twins in the 2D compressed specimen were not as much as found in the 1D compressed specimen. Before recrystallisation started to progress quickly in the Mg-0.1Ca-0.4Zn (at%) specimens, the 1D compressed specimen had more grains nucleated which then started to grow than that of the 2D compressed specimen. Combined with the results from the IPF maps, the smaller area fraction of recrystallized grains in the 2D compressed specimen was caused by its late recrystallization. Another notable point was that the inaccurate fraction of the compressive twins and the double twins in the 2D compressed specimen, this was attributed to the missing boundary information caused by the low index rate during the EBSD scanning. Many boundaries of the original grains and the recrystallized grains were not identified and therefore not shown on the map. Thus, the real boundary fraction of the compressive twins and the double twins was probably lower than it showed.

For the 1D compressed specimen (shown in Figure 4-55(e) and 4-56(e)), only a few differences were observed during 420s to 990s for both strain paths. The maximum intensity of the pole figure showed a reduction from 9.8 (420s) to 9.3 (750s) and reached 8.7 (990s) (shown in Figure 5-24(f)). Recrystallization resulted in an increasing number of new orientations between TD and ND, especially the grains with an orientation close to the ND and tilted 20°from the direction of the peak signal. The grains with an orientation close to the TD were also found to increase slightly. Figure 4-79(e) and 4-80(e) give pole figures of the 2D compressed specimen at the same time point as the 1D compressed specimen. In a similar way to the 1D compressed specimen, a

continuous weakening of the peak signal was also observed. Although the changes brought by recrystallization were not obvious, the maximum intensity of the pole figure was shown to reduce from 11.9 (420s) to 11.8 (750s) and then reached 11.4 (990s) in Figure 5-24(f). Compared to the changes in the pole figure of the 1D compressed specimen, the differences shown in the 2D compressed specimen were not statistically significant. Only the signal scattered around the TD showed a limited enhancement i.e. the number of grains with the orientation close to TD slightly increased. Thus, the progress of the 1D compressed specimen and the 2D compressed specimen was not at the same level and the 1D compressed specimen showed earlier recrystallization than the 2D compressed specimen.

After 1290s, both of the 1D compressed and 2D compressed Mg-0.1Ca-0.4Zn (at%) specimens showed almost fully recrystallization in the IPF map, Figures 5-28(a) and (b), respectively. Only a few grains could be tracked from the existing recrystallized grains in both specimens (marked by white circles in the IPF maps). The origin of most of the recrystallized grains was hard to trace due to the extremely rapid recrystallization. The grain sizes of the recrystallized grains were quite uniform in both strain path specimens. The average grain size of the 1D compressed specimen and 2D compressed specimen was 29.8μm and 32.7μm, respectively (shown in Figure 4-57(g) and 4-81(g)). In a similar manner to the Mg-0.2Ca-0.3Zn (at%) specimens, a larger average grain size was found in the 2D compressed specimen. The difference in boundary fractions was not obvious. In the 1D compressed specimen, the fractions of the low angle grain boundary, high angle grain boundary, tensile twins, compressive twins and double twins were 16.9%, 83.1%, 3.7%, 0.6% and 0.3%, respectively, while the fractions in 2D compressed specimen were 13.3%, 86.7%, 3.7%, 0.43% and 0.5%, respectively (shown in Figure 5-24(a)-(e)). Except the fraction of high angle grain boundary was 3% higher in the 2D compressed specimen, the fraction of twin boundaries was almost the same in the two strain path specimens. Figure 4-57(e), 4-81(e) and Figure 5-24(f) present the pole figure of the 1D compressed and the 2D compressed specimen, respectively. Due to the rapid recrystallization, a dramatic reduction in maximum pole figure was observed in the 1D compressed specimen (8.7 to 5.5) and 2D compressed specimen (from 11.4 to 4.7). Although both specimens showed a scattered grain orientation distribution, the 2D compressed specimen showed a more than 40° tilted angle from the RD-TD plane compared to the 30° tilted from the ND-TD plane in the 1D compressed specimen. It was obvious that the variation of the grain orientation distribution was more significant in the 2D compressed specimen, and also the 2D compressed specimen had a weaker texture than the 1D compressed specimen.

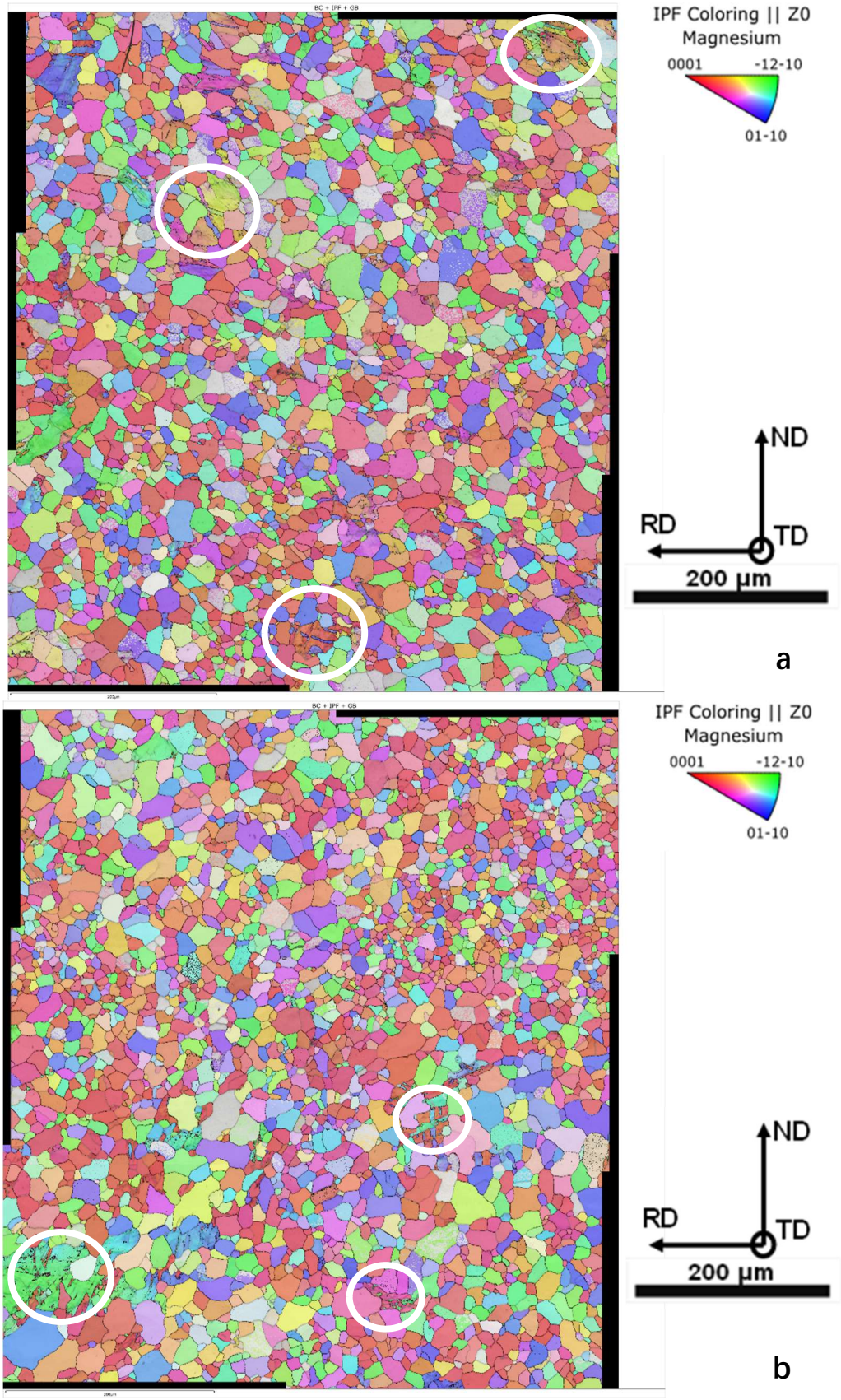

Figure 5-28 The IPF maps of the 1290s annealed Mg-0.1Ca-0.4Zn (at%) specimens: (a) 1D compressed, (b) 2D compressed

The recrystallization in the 2D compressed specimen had already surpassed that of the 1D compressed specimen at this time point and recrystallization had shifted from nucleation to grain growth in the 2D compressed specimen. The reason for the faster recrystallization in 2D compressed specimen was considered the same as in the Mg-0.2Ca-0.3Zn (at%) specimens. As with the Mg-0.2Ca-0.3Zn (at%) specimens, a weaker texture was also found in the 2D compressed specimen. Although the rapid recrystallization was not monitored in both specimens, the role that tensile twins played in the texture weakening was believed to be the same as in the Mg-0.2Ca-0.3Zn (at%) specimens. Also, the 2D compressed Mg-0.1Ca-0.4Zn (at%) specimen had a much higher fraction of shear bands and fine twins, which could bring a larger number of random orientated recrystallized grains.

5.3.3 Mg-0.5Zn (at%) specimens

The charts shown below in Figure 5-29 present the variation of the grain boundaries, twin boundaries and maximum pole intensity of the 1D/2D Mg-0.5Zn(at%) specimens during the annealing process, which will be discussed in the following sections.

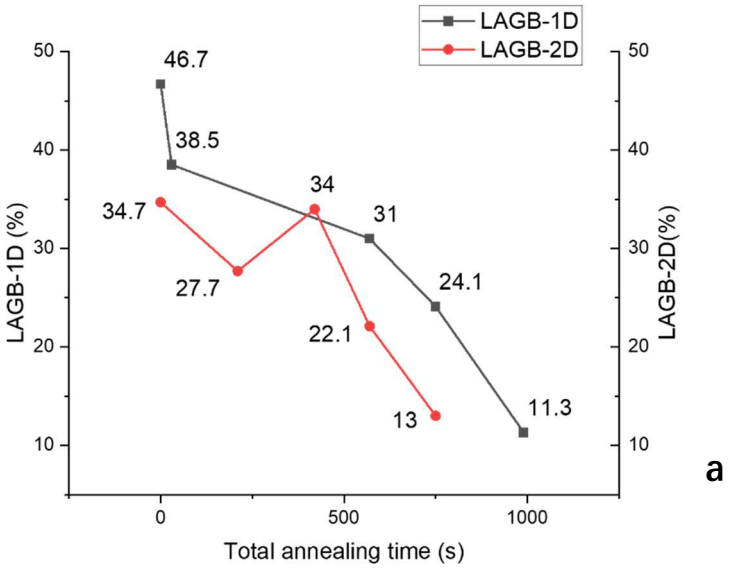

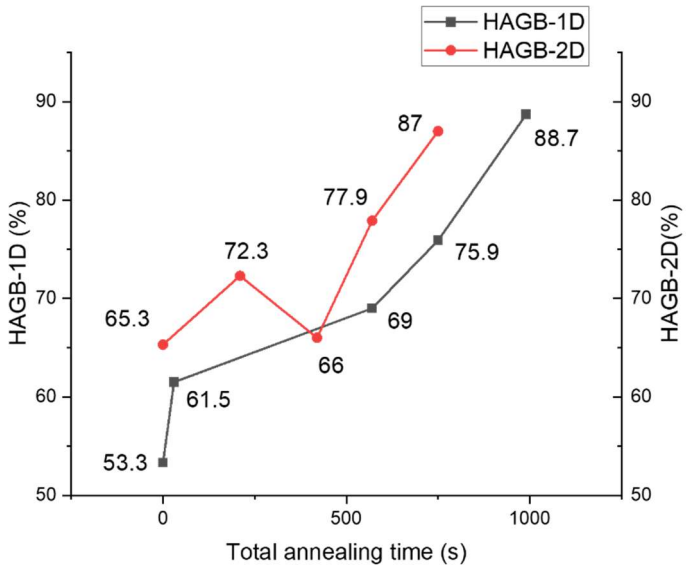
HAGB-1D
HAGB-2D
HAGB-1D (%)
HAGB-2D(%)
Total annealing time (s)
53.3
61.5
69
75.9
88.7
65.3
72.3
66
77.9
87

b

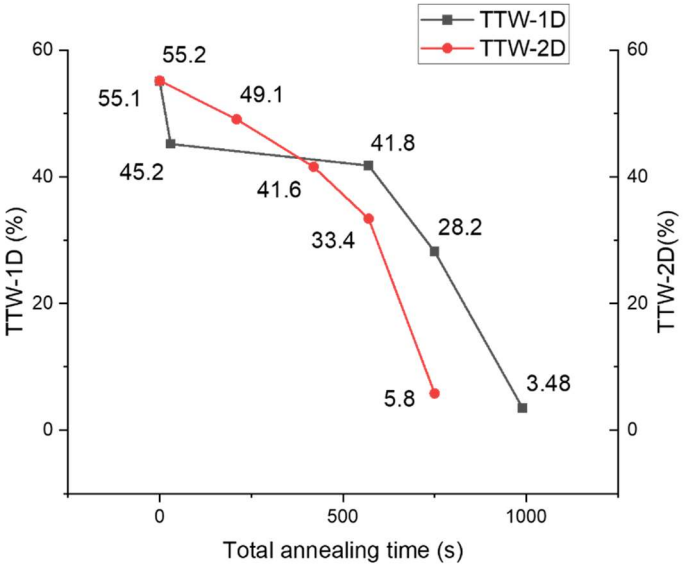
TTW-1D
TTW-2D
TTW-1D (%)
TTW-2D(%)
Total annealing time (s)
55.1
45.2
41.8
28.2
3.48
55.2
49.1
41.6
33.4
5.8

c

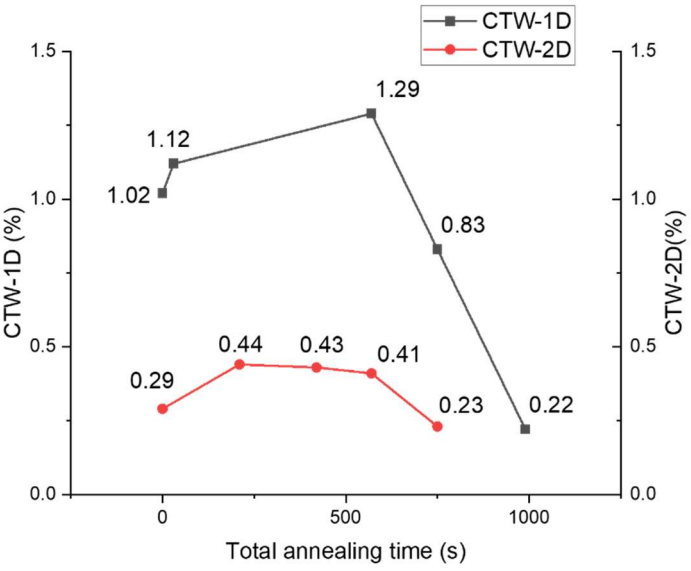
CTW-1D
CTW-2D
CTW-1D (%)
CTW-2D(%)
Total annealing time (s)
1.02
1.12
1.29
0.83
0.22
0.29
0.44
0.43
0.41
0.23

d

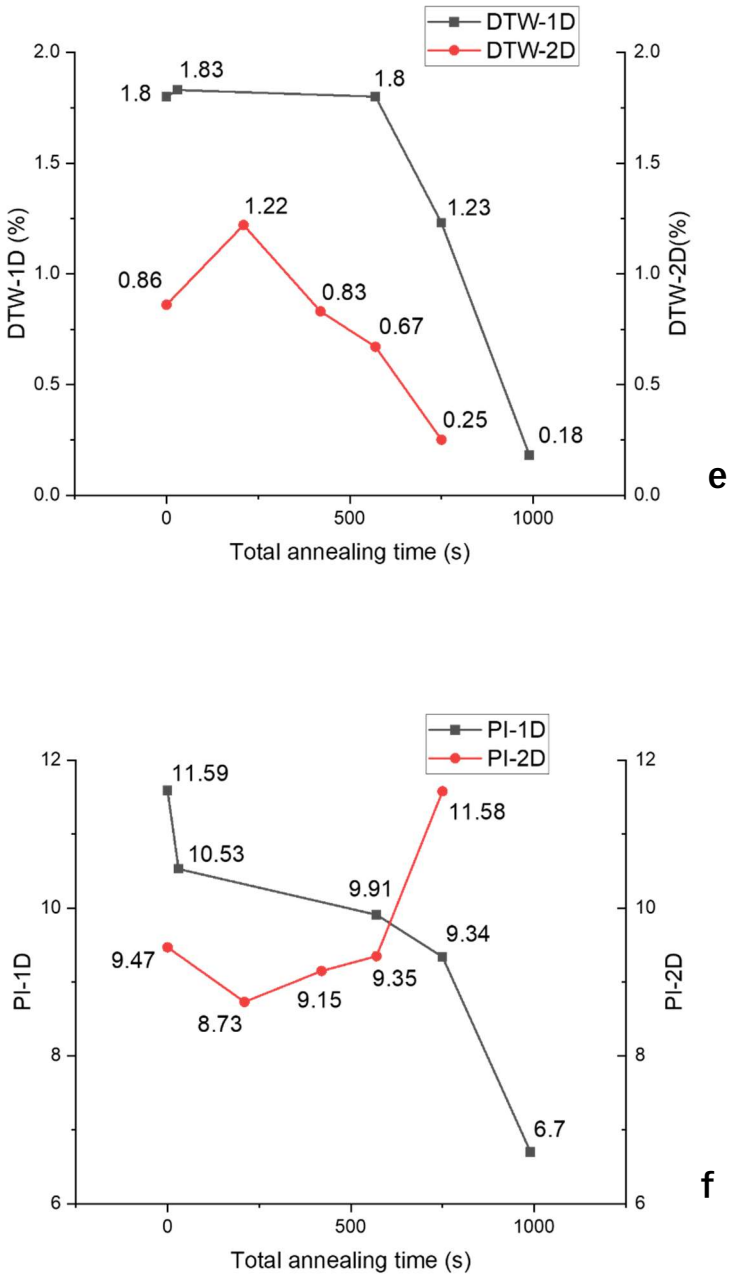

Figure 5-29 The variation in the 1D/2D compressed Mg-0.5Zn (at%) during annealing: (a) low angle grain boundary (LAGB), (b) high angle grain boundary (HAGB), (c) tensile twin (TTW) boundary, (d) compressive twin (CTW) boundary, (e) double twin (DTW) boundary, (f) maximum pole intensity (PI)

5.3.3.1 Mg-0.5Zn (at%) specimens after compression

The Mg-0.5Zn (at%) specimens were the only samples without Ca addition and were included as a base point. After the 1D compression and 2D compression, the Mg-0.5Zn (at%) specimens showed extensive non-indexed regions in the EBSD results. Figure 4-

58(c) and 4-82(c) indicate that the area fraction of the non-indexed region in the 1D compressed specimen and the 2D compressed specimen was 20% and 24%, respectively. The non-indexed regions were considered to consist of shear bands and fine twins, with the morphology suggesting that the shear bands were the main component. The existence of twins in these areas was also confirmed by the morphology and the twin boundaries analysis. The 1D compressed specimen showed a smaller number of shear bands and twins in the non-indexed regions than that of the 2D compressed specimen (shown in Figure 4-58(c) and 4-82(c)).

The difference between the 1D compressed specimen and the 2D compressed specimen was not only in the amount of shear bands, but also the number of the different kinds of twins. Based on the twin boundaries fraction of the two strain paths (shown in Figure 5-29(a)-(e)), the boundary fraction of tensile twins in 1D compressed specimen and 2D compressed specimen was very close, 55.1% and 55.2%, respectively. The higher boundary fraction of the compressive twins (1.0%) and double twins (1.8%) was found in the 1D compressed specimen. However, the boundary fraction of compressive twins (0.3%) and double twins (0.9%) in the 2D compressed specimen did not show a large difference compared to that of the 1D compressed specimen. The reason for this was attributed to the existence of the extra twins. In the 2D compressed specimen, there were some grains with typical twin morphology but not belonging to any of the tensile twins, compressive twins or double twins (marked in black circle in Figure 5-30). Meanwhile, these structures were not found in the 1D compressed specimen. After further investigation, the boundary of these “twins” was found to deviate about 20° from the typical tensile twin boundaries (<11-20> 86°). Thus, these “twins” were still treated as tensile twins for analysis. The final boundary fraction of the tensile twins in the 2D compressed specimen was 72.3%. As a result, the 2D compressed specimen showed an obviously larger number of tensile twins and a fewer number of compressive twins and double twins. The reason for this result was the same as the Mg-0.2Ca-0.3Zn (at%) specimens mentioned before.

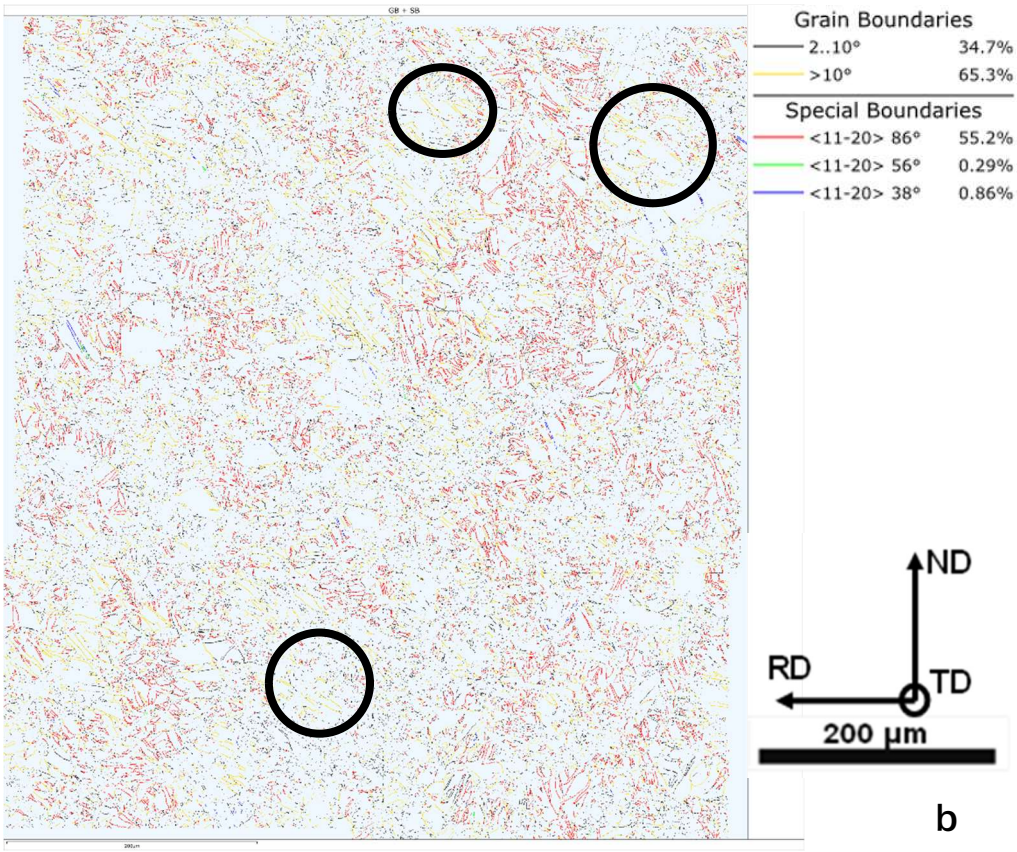

Figure 5-30 The boundary fractions of the as-compressed 2D Mg-0.5Zn (at%) specimen

Except for the shear bands and twins, the grain orientation distribution of the two strain paths of the Mg-0.5Zn specimens was also found to be different (shown in Figure 4-58(e) and 4-82(e)). The 1D compressed specimen had a maximum pole figure intensity of 11.6 which was higher than the maximum pole intensity (14.1) of the 2D compressed specimen. Figure 4-58(e) and 4-82(e) also indicate that both the 1D compressed specimen and the 2D compressed specimen had the as-rolled grain orientation i.e. the orientation of most of the grains of the 1D compressed specimen was parallel to the ND and the orientation of most of the grains of the 2D compressed specimen was parallel to the RD. In addition, a few grains of both kinds of specimens showed a concentrated direction distribution close to the TD. The 2D compressed specimen had more grains with this TD-parallel orientation than that of the 1D compressed specimen. Also, the direction of the grains with a similar TD orientation was more widely scattered in the 2D compressed specimen. The reason for this difference was already mentioned in the discussion of the as-compressed Mg-0.2Ca-0.3Zn (at%) specimens.

The 1D compression resulted in fewer shear bands and tensile twins but more compressive twins and double twins. A weaker texture and a different grain orientation

distribution were also found in the 2D compressed specimen. These differences induced by the strain path provided the original information of the specimens before the annealing. The following discussion will focus on the recrystallization behaviour of 1D/2D compressed Mg-0.5Zn (at%) specimens during the annealing.

5.3.3.2 The recrystallization of Mg-0.5Zn (at%) specimens

Unlike the other two groups of Ca-contained specimens, very obvious differences of the recrystallization starting point was found between the Mg-0.5Zn (at%) 1D compressed and 2D compressed specimens. The recrystallization structure was found after the 30s 350℃ annealing in the IPF map of the 1D compressed specimen (shown in Figure 4-59(a)), while the recrystallization structure was found after the 210s 350℃ annealing in the IPF map of the 2D compressed specimen (shown in Figure 4-83(a)). The 1D compressed specimen showed much earlier recrystallization behaviour than the 2D compressed specimen. This was also the first direct evidence of the earlier recrystallization in 1D compressed specimens. As the recrystallization progressed the non-indexed region in both Mg-0.5Zn (at%) strain path specimens reduced. The area fraction of the non-indexed region in the 1D compressed specimen (shown in Figure 4-59(c)) and the 2D compressed specimen (shown in Figure 4-83(c)) decreased from 20% to 10.8% and from 24.4% to 12%, respectively. The fraction reduction of the non-indexed region in both specimens was about 10%, which was a statistically significant value. Combining the IPF maps of the two specimens, the 10% reduction in non-indexed region was almost all replaced by recrystallized grains. Unlike the recrystallization in Ca-contained specimens, the nucleation from the double twins was observed in both Mg-0.5Zn (at%) specimens i.e. the recrystallization in Mg-0.5Zn (at%) specimens was very fast. In a very short time, not just the non-indexed region was no longer present but also the twins started to recrystallize. Moreover, the recrystallized grain size was larger in the 1D compressed specimen compared to the 2D compressed specimen. This indicated that the recrystallization in the 1D compressed specimen was not just starting earlier than the 2D compressed specimen but also progressing faster at this stage.

Figure 5-29(a)-(e) show the boundary information after recrystallization had started for each strain path. The different strain paths in the Mg-0.5Zn (at%) specimens showed an obvious difference in the fraction of the high angle grain boundaries; they increased from 53.3% to 61.5% in the 1D compressed specimen and from 65.3% to 72.3%, in the 2D compressed specimen. Clearly, the increasing number of recrystallized grains resulted in more high angle grain boundaries. Compared to the obvious changes in the non-indexed areas, the number of twins in the two specimens did not show a dramatic difference, except the tensile twins. The boundary fraction of the tensile twins,

compressive twins and double twins in 1D compressed 30s annealed Mg-0.5Zn (at%) specimen was 45.2%, 1.1% and 1.8%, respectively. The boundary fraction of the tensile twins, compressive twins and double twins in 2D compressed 210s annealed specimen was 49.1%, 0.4% and 1.2%, respectively. Except for the fraction of tensile twins of both compressed specimens, all the other twin boundary fraction values showed a slight increase i.e. considering the improvement of the EBSD index rate with the recovery of the specimens, the minor fluctuation of the boundary fraction value was treated as no change. Besides, with the recrystallization from the double twins observed in both specimens, the increase of the boundary fraction of the compressive twins and the double twins in both specimens further showed that recrystallization was occurring at a very early stage. The compressive twins and double twins did not particularly participate in the recrystallization. On the other hand, the decrease in the boundary fraction of the tensile twins (by 9.9% and 6.1% in the 1D compressed and 2D compressed specimens) was attributed to the consumption of the tensile twins during the recrystallization. In the Mg-0.5Zn (at%) specimens, the variation of twins did not show an obvious difference between the two kinds of strain paths at the early stage of the recrystallization.

The limited variation in the pole figures were observed (shown in Figure 4-59(e) and 4-83(e)) while the onset of the recrystallization of the two Mg-0.5Zn (at%) specimens. With the recrystallization progressing in the 30s annealed 1D compressed specimen, the maximum value of the pole figure reduced from 11.6 to 10.5, while the maximum pole intensity of the 210s annealed 2D compressed specimen reduced from 9.5 to 8.7 (shown in Figure 5-29(f)). The 1D compressed specimen showed a stronger texture than that of the 2D compressed specimen again at the beginning of the recrystallization. For the grain orientation distribution, no obvious changes were found in the pole figures of the two specimens. Only the intensity of the signal scattering around the TD was found to have increased by 0.2-0.5 in both specimens i.e. both the 1D compressed specimen and the 2D compressed specimen had more TD-orientated recrystallized grains.

For the early-stage recrystallized Mg-0.5Zn (at%) specimens, no obvious difference in microstructural evolution was found between the two strain paths. The only difference was that the 1D compressed specimen showed earlier recrystallization (30s annealing) and a larger recrystallized grain size than the 2D compressed specimen (210s annealing). The reason for the later recrystallization in the 2D compressed specimen was considered to be the result of the much higher fraction of tensile twins, which did not provide nucleation sites. This is because the twin plane easily migrates causing the hard accumulation of the strain energy, which made it hard to form the non-uniform strain region to nucleate grains [57, 64].

With the increase in annealing time, the recrystallization behaviour of the Mg-0.5Zn (at%) specimens could be observed across the whole scan area. Due to the different starting time of detectable recrystallization, the EBSD results as a function of the different strain paths will be considered for the same proportion of recrystallization and therefore different annealing times (570s and 750s 350℃ for the 1D compressed specimen, and 420s and 570s 350℃ for the 2D specimen). The IPF maps in four different time points of two specimens (shown in Figure 5-31(a) to (d)) show the grain growth and grain nucleation as a function of annealing time. For the 1D compressed specimen, between the 30s annealing and the 570s annealing, the microstructure evolution was found to consist of the grain growth of the existing recrystallized grains and new grain nucleation from the grain boundaries. After 750s, grain growth of the existing recrystallized grains and grain nucleation from the twins and the grain boundaries were still observed. However, grain growth of those grains that had nucleated in the twins was very limited, with these grains typically increasing by just 2-3μm. In contrast, recrystallized grains nucleating from the grain boundaries increased far more, approximately from 4μm to about 20 μm. The example sites are marked by black rectangles in Figure 5-31(a) and (b) and shown below in Figure 5-32.

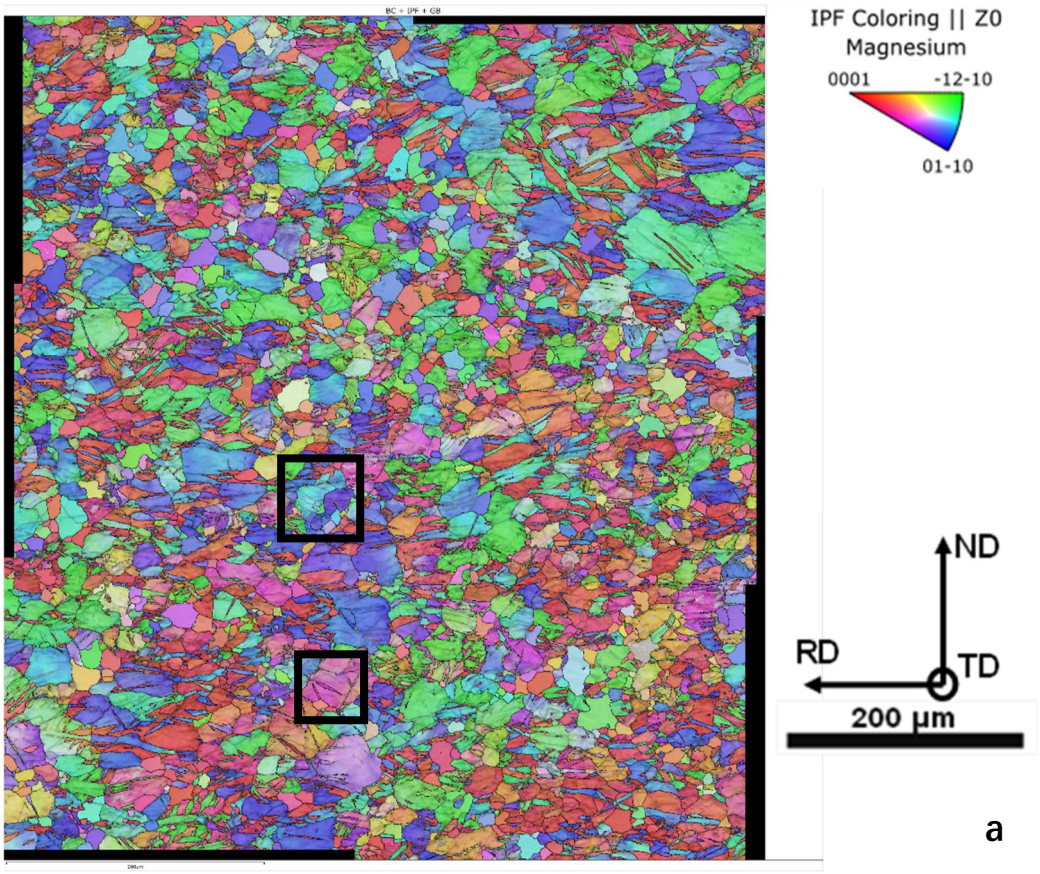

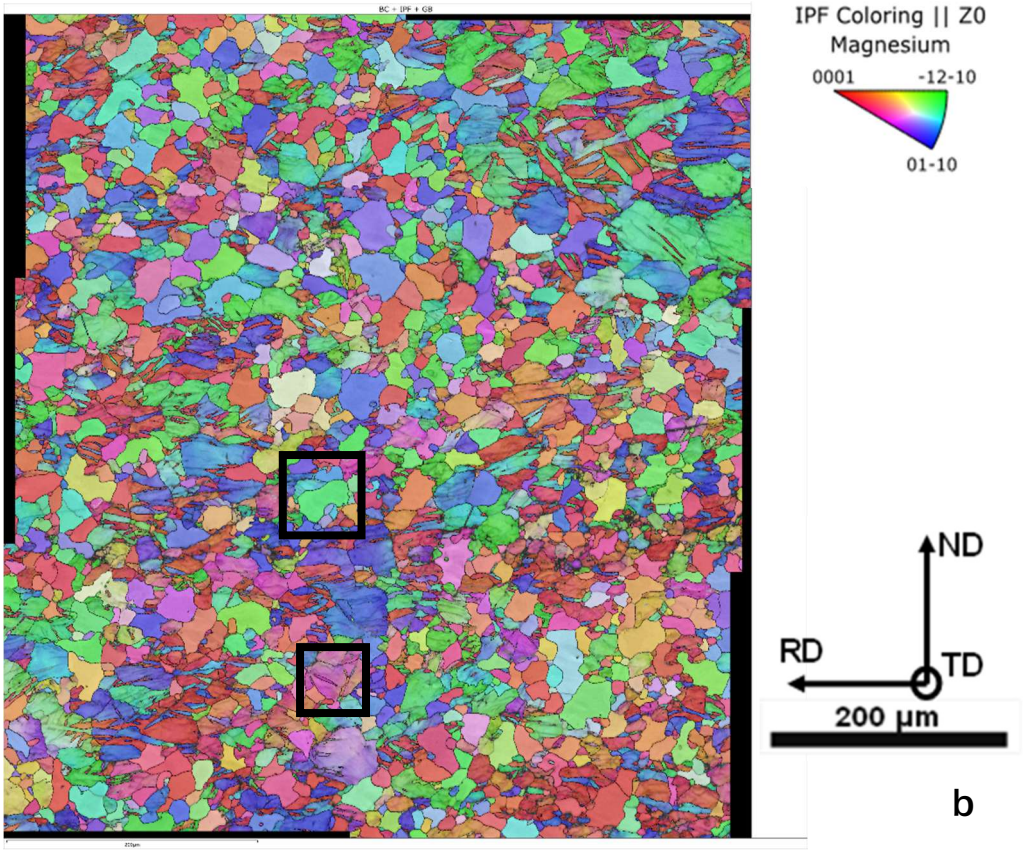
IPF Coloring || Z0
Magnesium
0001
-12-10
01-10
ND
RD
TD
200 µm

b

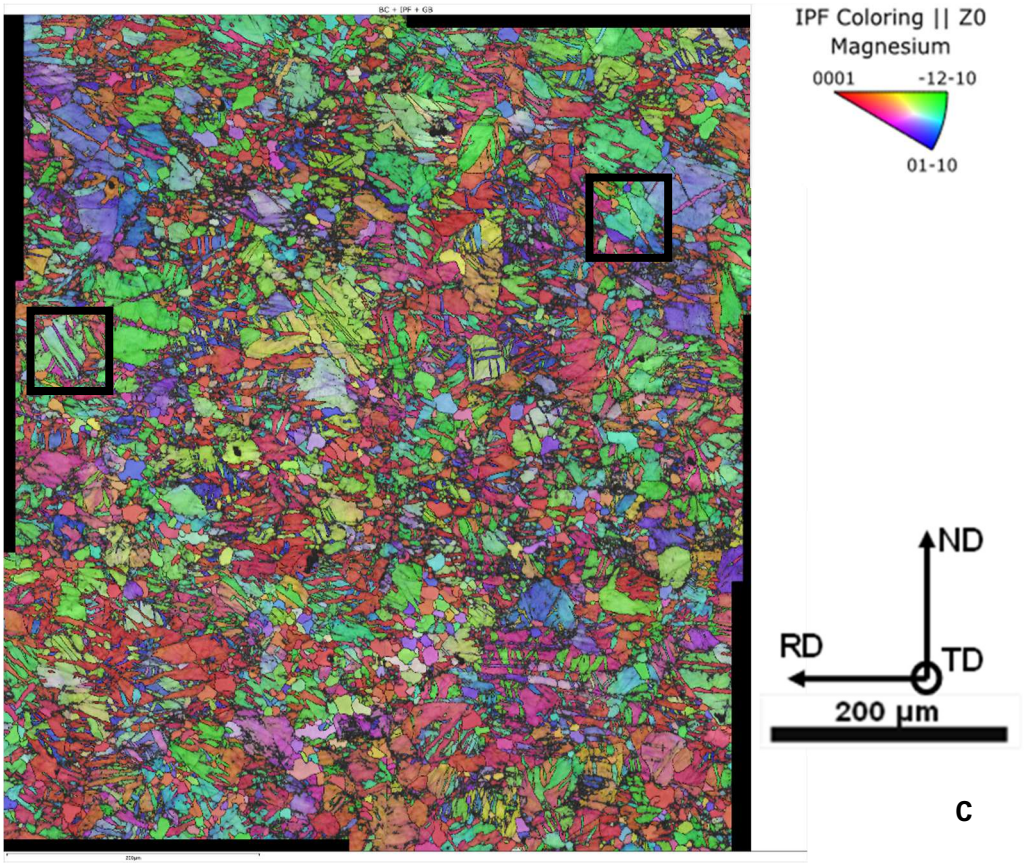
IPF Coloring || Z0
Magnesium
0001
-12-10
01-10
ND
RD
TD
200 µm

c

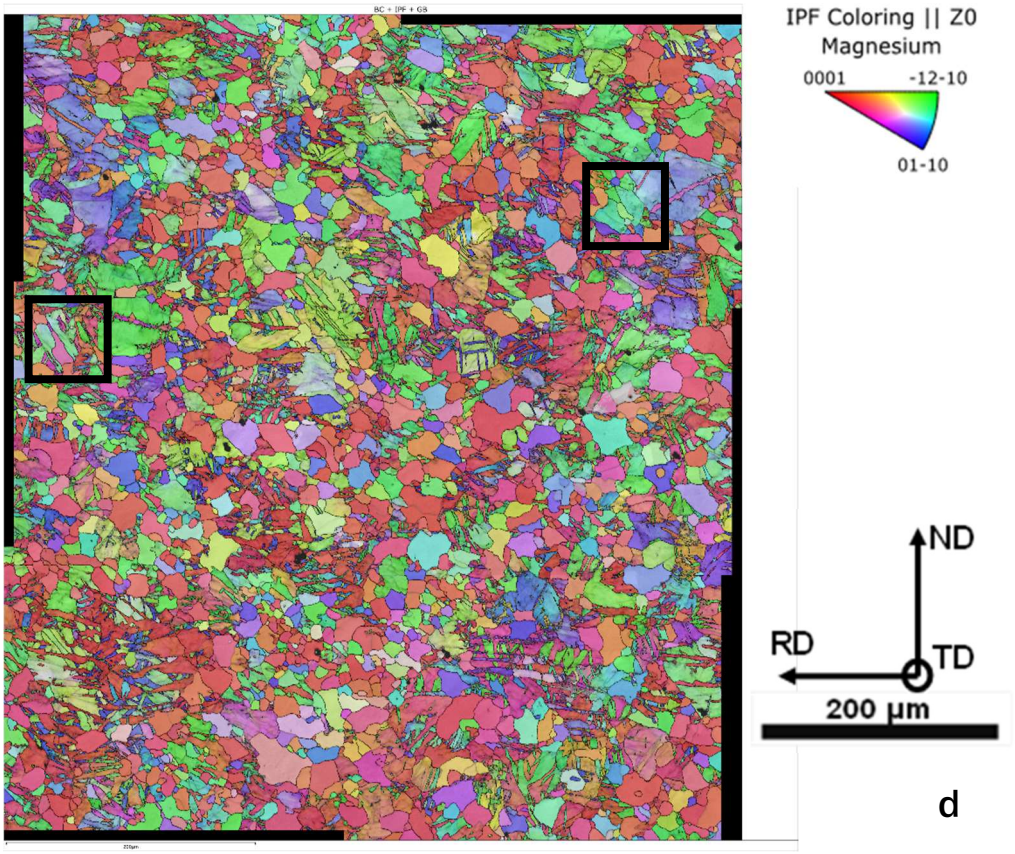

Figure 5-31 The IPF maps of the Mg-0.5Zn (at%) specimen: (a) 1D compressed 570s annealed, (b) 1D compressed 750s annealed, (c) 2D compressed 420s annealed, (d) 2D compressed 570s annealed

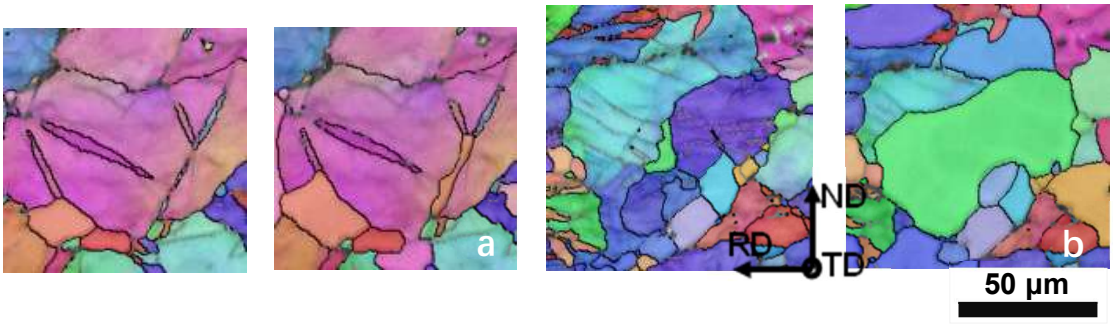

Figure 5-32 The nucleation and the grain growth in the 1D compressed Mg-0.5Zn (at%) specimen during 570s to 750s annealing: (a) from twins, (b) from grain boundary

The 2D compressed specimen showed a very similar microstructure evolution in the different time points compared to the 1D compressed specimen. Between 210s and 420s, the microstructure evolution was found to consist of the grain growth of the existing recrystallized grains and recrystallized grain nucleation from the grain boundaries (shown in Figure 5-31(c)). After 570s, grain growth of the existing recrystallized grains and grain nucleation from the twins and the grain boundaries were

also observed (shown in Figure 5-31(d)). The same limited growth of the recrystallized grains from the twins was observed in the 2D compressed specimen as well (shown in Figure 5-33). The example sites are marked by black rectangles in Figure 5-31(c) and (d). It was clear that recrystallization started earlier in the 1D compressed specimen (from 30s annealing) than in the 2D compressed specimen (from 210s annealing). However, the subsequent recrystallization kinetics in the 1D compressed specimen was much slower than in the 2D compressed specimen. Figure 5-34 indicates the area fraction of the recrystallized grains in 1D compressed specimen after the 750s annealing was about 26% while the 2D compressed specimen had about 33% of the recrystallized grains after 570s annealing.

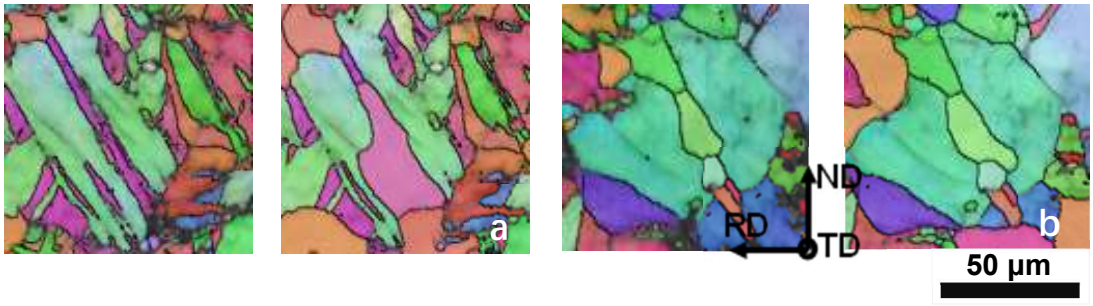

Figure 5-33 The limited grain growth of recrystallized grains from twins in the 2D compressed Mg-0.5Zn (at%) specimen during 420s to 570s annealing:
(a) site 1, (b) site 2

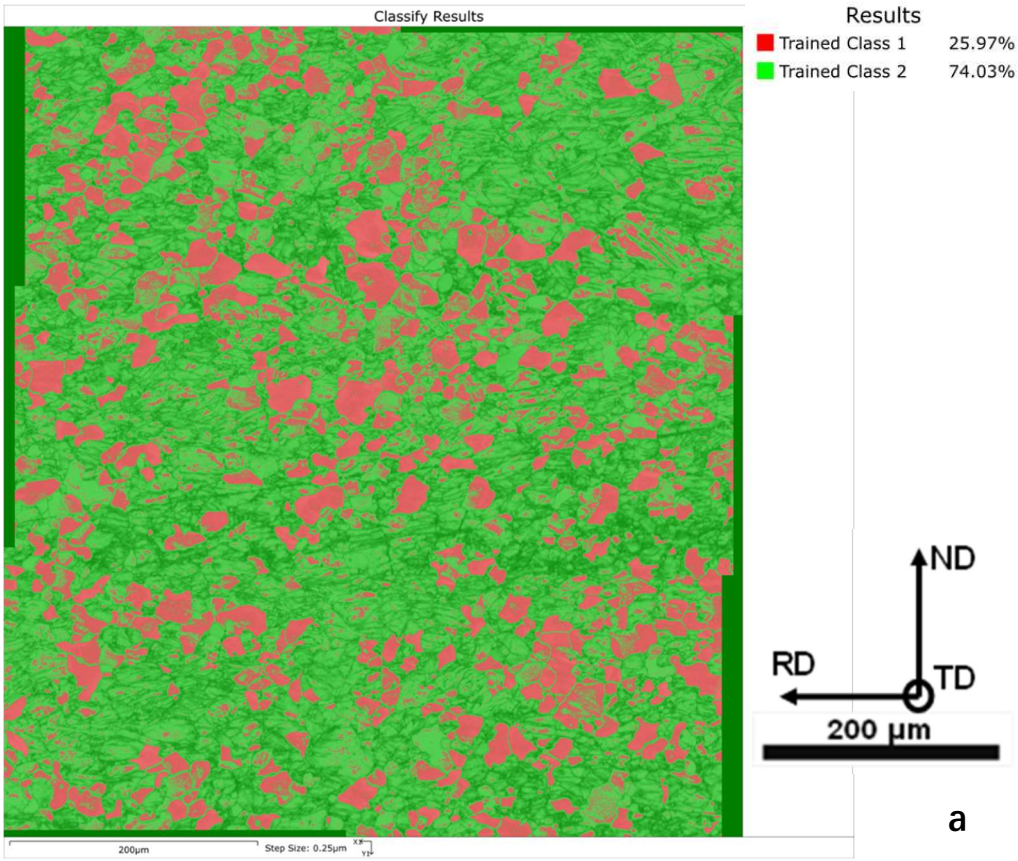

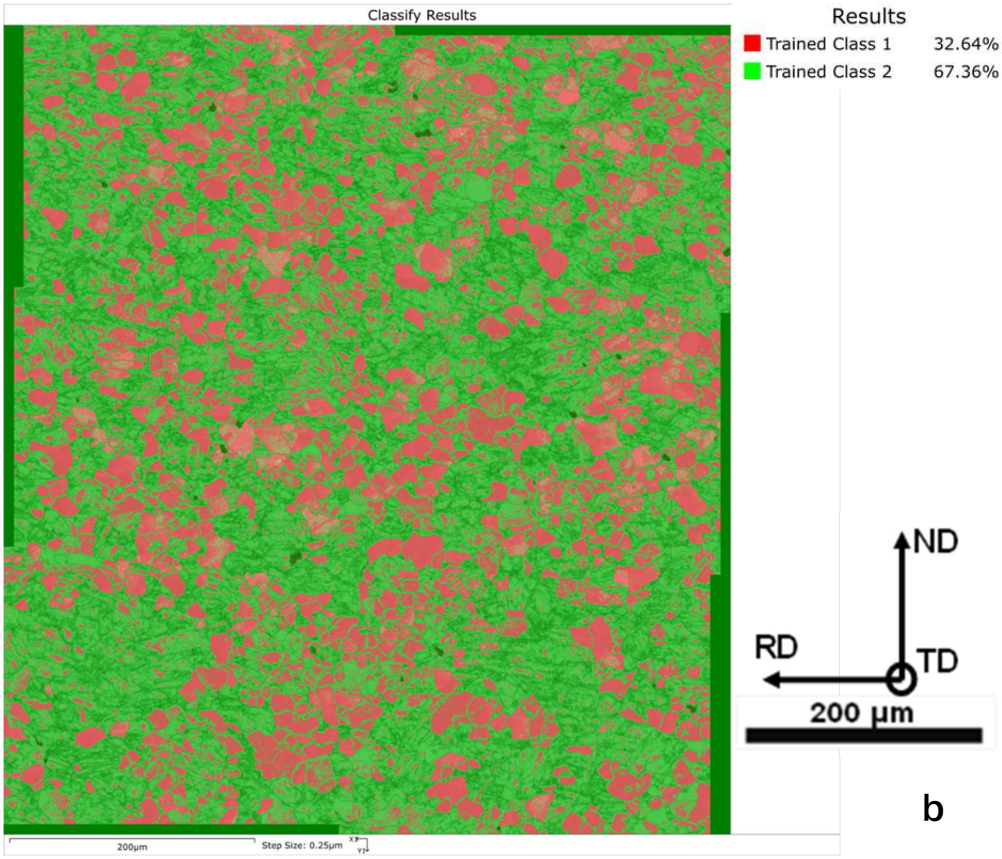

Figure 5-34 The classified results of the recrystallized grains (red) and unrecrystallized grains (green) in the Mg-0.5Zn (at%) specimens: (a) 1D compressed 750s annealed, (b) 2D compressed 570s annealed

As one of the important roles in the deformation and recrystallization of Mg alloys, the changes in the twins as a function of strain path during the annealing were also compared. Figure 5-29(a)-(e) show the grain boundary information of the 1D compressed and 2D compressed Mg-05Zn (at%) specimens at different times. For the 1D compressed specimen, after 570s, the boundary fraction of the tensile twins decreased a small amount from 45.2% to 41.8% while the double twins from 1.83% to 1.8%, respectively. The compressive twin boundary fraction was found to increase marginally from 1.1% to 1.3%, but the low index rate of the EBSD in the 30s annealed specimen must be considered when putting these values in context. The values of the boundary fractions of both compressive twins and double twins were lower than expected.

The results from the 750s annealed 1D compressed specimen showed more regular changes. After the 750s, the boundary fractions of the tensile twins, compressive twins and double twins all reduced to 28.2%, 0.8% and 1.2%, respectively. Meanwhile, the fraction of the low angle grain boundary and high angle grain boundary also showed a corresponding variation i.e. the fraction of the low angle grain boundary was reduced from 38.5% (30s) to 31% (570s) and then reached 24.1% (750s). The fraction of the

high angle grain boundary increased from 61.5% (30s) to 69% (570s) and then reached 75.9%(750s).

For the 2D compressed specimen at the same stage (420s), the boundary fraction of tensile twins, compressive twins and double twins showed a decrease from 49.1% to 41.6%, 0.44% to 0.43% and 1.2% to 0.8%, respectively (Figure 5-29(c)-(e)). After the 570s, the boundary fraction of the tensile twins, compressive twins and double twins furtherly reduced to 33.4%, 0.41% and 0.67%, respectively (Figure 5-29(c)-(e)). Meanwhile, like the 1D compressed specimen, the fraction of the low and high angle grain boundaries showed a corresponding variation i.e. the fraction of the low angle grain boundary was reduced from 27.7% (210s) to 22.1% (570s), while the fraction of the high angle grain boundaries increased from 72.3% (210s) to 77.9%(570s). Although the changes in the high angle grain boundaries of the 2D compressed specimen was small (5.6%), the reduction in boundary fraction of the tensile twins (15.7%) indicated that a quite reasonable fraction of the boundaries of the tensile twins were recrystallized. The area fraction of the recrystallized grains in the 750s annealed 1D compressed specimen and the 570s annealed 2D compressed specimen was 26% and 33%, respectively (shown in Figure 5-34(a) and (b)). This further demonstrated that the 2D compressed specimen had recrystallized faster.

For the grain orientation distribution of 1D compressed and 2D compressed specimen during annealing at 30s to 750s and 210s to 570s, respectively, some different results were observed. Figure 4-65(e) and 4-66(e) show the pole figures of the 1D compressed specimen, Figure 4-85(e) and 4-86(e) show the pole figures of the 2D compressed specimen. As recrystallization progressed, the 1D compressed specimens did not show a very obvious scattered grain orientation distribution. Only a few new grains with a direction between the TD and ND were found. Meanwhile, most of the new grains showed a similar orientation to each other which was scattered around a direction close to the TD. The maximum pole intensity of the specimen showed a continuous reduction from 10.5 (30s) to 9.9 (570s) and reached 9.3 (750s) (shown in Figure 5-29(f)). The grain orientation distribution of the 2D compressed specimen showed different variations. With the progress of recrystallization, the intensity of the second peak in the pole Figure was found to continuously increase i.e. the orientation of the new grains was almost the same. There was no trend for the newly generated random orientated grains. The maximum pole intensity of the specimen showed a continuous increase from 8.7 (210s) to 9.2 (420s) and reached 9.4 (570s) (shown in Figure 5-29(f)).

For the grain orientation distribution, no clear difference was found in the specimens between the 1D compression and the 2D compression. Both specimens showed an enhanced TD-orientated grain orientation distribution.

The fully recrystallized microstructure was observed in the IPF map of the 1D compressed specimen after 990s (shown in Figure 4-67(a)), while a fully recrystallized microstructure was observed in the IPF map of the 2D compressed specimen after 750s (shown in Figure 4-87(a)). The IPF maps indicate that the two specimens showed a similar microstructure evolution in the last stages of annealing. The further growth of the existing recrystallized grains and the nucleation of the new grains were the reasons for the formation of the final microstructures in both specimens. Figure 4-67(g) and 4-87(g) show the average grain size of the 1D compressed specimen and the 2D compressed specimen as 50.6μm and 38.6μm, respectively. The grain boundaries and twin boundaries also showed corresponding changes. Figure 5-29(a)-(e) show the fractions of the low angle grain boundaries, high angle grain boundaries, tensile twins, compressive twins and double twins in the 1D compressed specimen were 11.3%, 88.7%, 3.5%, 0.2% and 0.2%, respectively, while the fractions in the 2D compressed specimen were 13%, 87%, 5.8%, 0.2% and 0.3%, respectively. Although in the 2D compressed specimen the average grain size was larger, the fraction of the high angle grain boundary was lower and more twins compared to the 1D compressed specimen, the time for the 2D compressed specimen to reach this point was much shorter than that of the 1D compressed specimen. The abundant number of tensile twins in the 2D compressed specimen was believed to play an important role in this. A similar result was found for the evolution of the recrystallized grains from in the 1D compressed and 2D compressed Mg-0.5Zn (at%) specimens, a similar result as the Mg-0.2Ca-0.3Zn (at%) specimens. The reason for the faster recrystallization in the 2D compressed Mg-0.5Zn (at%) specimen was considered the same as other specimens.

For the grain orientation distribution, the 1D compressed specimen (shown in Figure 4-67(e)) and the 2D compressed specimen (shown in Figure 4-87(e)) showed different variations. In the 1D compressed specimen, the orientation of the recrystallized grains showed limited scattering along the ND-axis. The maximum pole intensity was reduced from 9.3 to 6.7 (shown in Figure 5-29(f)). In the 2D compressed specimen, no spread grain orientation was found. A very strong TD-orientated texture was observed. The maximum pole intensity further increased from 9.4 to 11.6 (shown in Figure 5-29(f)). The abnormal texture variation in the 2D compressed specimen was related to the absence of Ca rather than the effect of different strain paths. The details are discussed in the next part. The tensile twins supported grain growth was also observed in the 2D compressed Mg-0.5Zn (at%) specimen shown below in Figure 5-35. This indicates that the texture weakening effect of the tensile twins brought by the 2D compression is also related to the composition of the alloy.

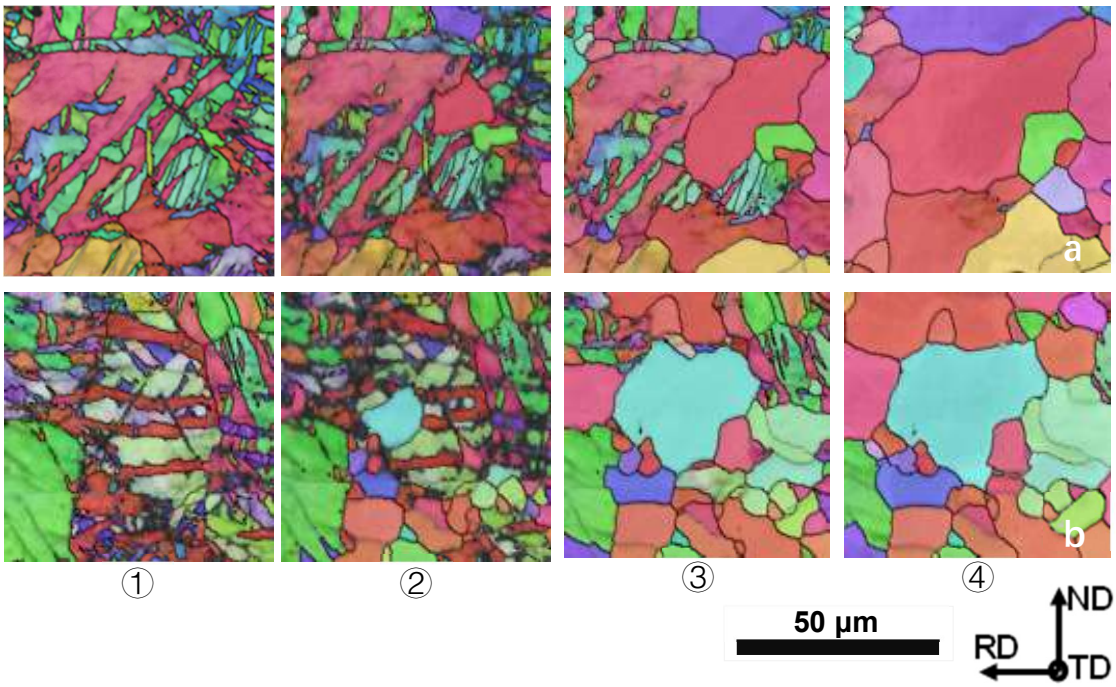

Figure 5-35 The tensile twins related grain growth in the 2D compressed Mg-0.5Zn (at%) specimen: (a) site 1: ①0s, ②75s, ③570s and ④750s (b) site 2: ①0s, ②75s, ③570s and ④750s

For all the 1D and 2D compressed specimens, recrystallization was found to start earlier in the 1D compressed specimens. The reason for this was attributed to the higher deformation energy brought by the 1D compression. The only difference between these two kinds of specimens was the compression method. Although the deformation of the specimens was the same for two compressions (20% and 15%), the 1D deformation resulted in stress concentration in one direction due to the stress acting mainly in that direction. Considering the reversibility of the deformation i.e. dislocations can move irreversibly or can move reversibly-i.e. back on themselves, for the 1D compressed specimens there will not be any reversible deformation. For the 2D compressed specimens there may be some. The stress distribution of the 2D compressed specimen was more uniform in both directions and the deformation was also relatively uniform. Using the higher deformation energy storage as the driving force made it easier to start recrystallization. As a result, earlier recrystallization was observed in all 1D compressed specimens. Not like Li's [89] and Du's [88] study, the 2D compressed specimen showed more shear bands and twins than the 1D compressed specimen after the compression. The 1D compression was quite similar to their unidirectional rolling (UR) but 2D compression was very different to their cross-rolling (CR) i.e. the second compression direction was completely different.

Once recrystallization had been initiated, faster recrystallization was observed in all 2D compressed specimens, with complete recrystallization finishing earlier. The

main reason for this was attributed to the higher fraction of the tensile twins in the 2D compression specimens. At the start of the recrystallization, the higher fraction of the tensile twins was unfavorable for the nucleation in the 2D compressed specimens. However, the high fraction of shear bands (even a higher fraction in Mg-0.1Ca-0.4Zn and Mg-0.5Zn (at%)) compensated for the deficiency of nucleation sites in the 2D compressed specimens. During rapid recrystallization, the tensile twin boundary was easily consumed by grain growth. The growth of the recrystallized grains in the 2D compressed specimens was obviously easier than that of the 1D compressed specimens due to their higher fraction of tensile twins. Additionally, the limited growth of the recrystallized grains from the double twins were observed in the 1D compressed specimens, while the recrystallized grains in the 2D compressed specimens were from shear bands and grain boundaries, which did not have such problem. As a result, the grain growth in the 2D compressed specimens was also more uniform than the 1D compressed specimens. With the faster kinetics and the more uniform growth of the recrystallized grains, the 2D compressed specimens finished recrystallization earlier.

After recrystallization was complete, all the Ca-contained 2D compressed specimens showed a wider scattered grain orientation distribution compared to the 1D compressed specimens i.e. the 2D compressed specimens had a weaker texture than the 1D compressed specimens. The high fraction of the tensile twins in the 2D compressed specimens again played an important role. The random orientated grains from the shear bands grew by consuming the abundant tensile twins and were preserved during recrystallization. In combination with the recrystallized grains from grain boundaries, the Ca-contained 2D compressed specimens showed a weaker texture compared to the 1D compressed specimens. Although the Mg-0.5Zn (at%) specimens did not show such weakened texture after the annealing, the recrystallized grains from the shear bands were preserved by consuming tensile twins. The random orientated grains were considered to be dependent on the alloy composition. With the higher Ca content, the weaker texture was observed in the specimen. The unfavorable role of tensile twins as the nucleation site was reported by many researchers [39, 54-57, 59, 73]. However, the other roles of tensile twins in the recrystallization process have rarely been reported. The high fraction of tensile twins can not just accelerate recrystallization and help to form a uniform microstructure but also can preserve the random orientated grains by sacrificing themself.

For the 1D and 2D channel die compression, the process method is not just simulating the rolling condition (thickness reduction and longitude elongation) but also simulating a multidirectional deformation e.g. progressive die process etc., which also have rarely been reported in Mg area.

5.4 Other discussion

The recrystallized grains with TD orientation showed a darker colour in band contrast (BC) (shown in Figure (d) of 4-49, 4-74, 4-57, 4-81, 4-67 and 4-87). The reason for this was attributed to the affection of the grain orientation to the EBSD pattern quality. Claves and Deal [136] reported that with the rotation of the material, the EBSD pattern quality showed periodic fluctuations. The most direct reflection of pattern quality is the difference of the brightness of images in BC i.e. the better the pattern quality, the brighter the image. Thus, TD orientation was hypothesized as the poor pattern quality orientation of the used experimental material, causing the brightness difference of the recrystallized grains on the BC map.

For the oxidized grains depicted in the phase maps (in grey), since these grains exhibited a variety of orientations (as shown in the IPF maps) with no discernible trend correlating oxidation to specific orientations, the loss of information from this group of grains is unlikely to impact the accuracy of the final results. Additionally, the highest proportion of oxidized grains was 11% in the 1290s annealed 1D compressed Mg-0.1Ca-0.4Zn specimen (shown in Figure 4-57(c)). The remaining 89% of the scanned area provides sufficient data for reliable analysis. Consequently, the EBSD results, despite containing oxidized grains, remain valid for use.

6. Conclusions

6.1 For double truncated cone (DTC) compression experiment

The conclusion for the whole double truncated cone compression experiments was that it was very difficult to generate strains and strain rates that were predictable in a single sample and varied from sample to sample, particularly with these large grain sized materials. Considering the time limit of the PhD study and the disappointing results from the DTC approach, the DTC specimen compression study was suspended after finishing the EBSD investigation on compressed Mg-0.1Ca-0.4Zn (at%) DTC specimen.

6.2 For different compositions in the channel die (CD) compression experiment

The study highlights the significant influence of alloying elements, specifically calcium (Ca) and zinc (Zn), on the microstructure evolution and texture development in magnesium alloys under varying strain paths and annealing processes. The addition of Ca resulted in a pronounced increase in twin boundary fractions and a slower recrystallization process due to solute drag and grain boundary segregation. The observed differences in recrystallization rates and texture weakening were consistent across both 1D and 2D compression scenarios, with higher Ca content contributing to more dispersed grain orientation and reduced stacking fault energy.

The Mg-0.5Zn specimen, devoid of Ca, displayed distinct behaviour, forming a strong basal texture due to the absence of significant solute segregation and lattice distortion, thereby resembling the behavior of pure magnesium. These findings underline the critical role of alloy composition in tailoring the mechanical properties and microstructural features of magnesium alloys, providing valuable insights for the design and optimization of lightweight materials for various applications. Further investigations into the interplay between alloying elements, strain paths, and thermal treatments are essential to fully harness these effects for industrial applications.

6.3 For different strain paths in the channel die (CD) compression experiment

The recrystallization behavior of 1D and 2D compressed specimens revealed distinct differences driven by their respective deformation modes. Recrystallization initiated earlier in 1D compressed specimens due to higher deformation energy and stress concentration in a single direction, acting as a strong driving force. In contrast, 2D compressed specimens exhibited a more uniform stress and deformation distribution,

resulting in a delayed recrystallization onset. However, 2D compressed specimens exhibited faster and more uniform recrystallized grain growth, attributed to their higher fraction of tensile twins and the additional nucleation sites provided by shear bands and grain boundaries.

With different strain paths, the 2D compressed specimens showed more shear bands and tensile twins, but less compressive twins and double twins compared to the 1D compressed specimens. The higher fraction of tensile twins was mainly caused by the second compression in the 2D compression process. The compression direction was vertical to the c axis of most of the grains, causing tension to generate more tensile twins in the 2D compressed specimen. These tensile twins were easy to consume in the grain growth of all recrystallized grains e.g. nucleate from shear bands, grain boundaries and twins, resulting in a faster uniform recrystallization. On the other hand, although the 1D compressed specimens had more compressive twins and double twins and they did generate random orientated grains, the growth of these grains was found to be very limited, especially for those without tensile twins nearby. It directly caused uneven grain growth in the 1D compressed specimen. With fewer tensile twins, the recrystallization also showed a slower progression in the 1D compressed specimens.

Furthermore, 2D compressed specimens showed weaker texture after annealing, especially in Ca-containing alloys, due to the random orientation of grains derived from shear bands and tensile twin consumption during recrystallization. The role of alloy composition, particularly the Ca content, was critical in influencing texture weakening. The 2D specimens had better isotropy i.e. better formability, while the 1D specimens showed strong anisotropy. The different strain paths obviously affect the performance of the Mg alloys. Thus, it is possible for people to acquire the desired materials properties by controlling the strain path. These findings provide insights into how compression methods and material composition affect recrystallization dynamics and final microstructure, offering valuable guidance for tailoring materials with desired grain structures and textures, especially for the rolling processed and progressive punching processed Mg products.

7. Future work

For getting a better EBSD result i.e. less scratches on the sample surface, the electropolishing could be an alternative way compared to the currently used polishing method. When in the current polishing process, the Mg alloy was too soft compared to steels, Ti alloys etc., so it was very likely to induce scratches on the surface of the specimen. To make a non-scratch Mg sample, it normally takes 3-4 times extra polishing time than preparing a steel sample. The electropolishing is free of mechanical movement, and the electrochemical process that removes material from the metallic workpiece generate zero scratches on the sample surface, which would be the ideal preparation process for the Mg specimens.

For the test Mg-Ca-Zn lean alloys, it is not 100% sure that the second phase does not exist. Thus, a TEM investigation needs to be employed to understand the status of the second phase in these experimental materials.

The unfinished study about strain and texture evolution is worth continuing. The relationship between different strain and texture evolution can help to further understand the influence of the different strain paths to the texture evolution. The double truncated cone specimen is ideal for this experiment. Generating different strain and strain rate within one specimen with one compression is very attractive. The uniform deformation of the double truncated cone specimen is the main problem that needs to be solved. The self-cast material cannot meet this need of the experiment. Improving the quality (uniform and fine grain size) of the test specimen is necessary.

In the channel die compression experiments, the Mg-0.5Ca and Mg-0.4Ca-0.1Zn (at%) specimens were not investigated. The texture evolution under different strain paths in Mg-Ca-Zn lean alloys needs more investigations, especially for the Mg-Ca-Zn lean alloys with higher Ca proportion and without Zn content. By doing this, it is possible to have a further understanding of the influence of different Ca/Zn ratio to the texture evolution/weakening.

Analyzing data by using machine learning has become a very popular topic these days. The use of this technique in tracking the grains during the recrystallization process would be powerful. There are many different nucleation sites for the recrystallized grains in this study. In the research group of Dr. D Guan (University of Southampton), it is now possible to use machine learning to track the grains in a small area. When this tool can track a wider range of grains, it will greatly help to further understand the recrystallization mechanism of magnesium alloys e.g. where the new grains nucleate, do they survive after the recrystallization etc.

Based on the existing studies, it is also worthwhile investigating the performance of other commercial Mg alloys, such as WE43, the AZ series, and the AS series etc.

under the same channel die compression. This investigation could provide deeper insights into how different alloying elements influence the outcomes under different strain paths. Furthermore, research involving these commercial Mg alloys could serve as a valuable reference for studying industrial processes such as multi-pass cross rolling or progressive die punching of Mg alloys.

8. References

[1] M. Gupta and N.M.L. Sharon, *Magnesium, magnesium alloys, and magnesium composites [electronic resource]: a guide*, New York: John Wiley & Sons, 2011.

[2] K. U. Kainer, *Magnesium – Alloys and Technology [electronic resource]*, John Wiley & Sons, 2003.

[3] H. E. Friedrich and B. L. Mordike, *Magnesium Technology: Metallurgy, Design Data, Applications*, 1st ed. Berlin, Heidelberg: Springer Berlin / Heidelberg, 2005.

[4] G. Cao, J. Kobliska, H. Konishi, X. Li, "Tensile Properties and Microstructure of SiC Nanoparticle–Reinforced Mg-4Zn Alloy Fabricated by Ultrasonic Cavitation–Based Solidification Processing," *Metallurgical and Materials Transactions. A, Physical Metallurgy and Materials Science*, 2008, **39(4)**, 880-886.

[5] H. Friedrich and S. Schumann, "Research for a 'New Age of Magnesium' in the Automotive Industry," *Journal of Materials Processing Technology*, 2001, **117**, 276–281.

[6] M.R. Barnett, "A Practical Condition for Migration Dynamic Recrystallization," *Acta Materialia*, 2007, **55**, 3271–3278.

[7] E.A. Ball and P.B. Prangnell, "Tensile-Compressive Yield Asymmetries in High Strength Wrought Magnesium Alloys," *Scripta Metallurgica Et Materiala*, 1994, **31**, 111–116.

[8] T. Al-Samman and X. Li, "Sheet Texture Modification in Magnesium-Based Alloys by Selective RE Alloying," *Materials Science & Engineering A*, 2011, **528**, 3809–3822.

[9] I. Basu, T. Al-Samman and G. Gottstein, "Shear Band-Related Recrystallization and Grain Growth in Two Rolled Magnesium-RE Alloys," *Materials Science and Engineering A-Structural Materials Properties Microst*, 2013, **579**, 50–56.

[10] N. Stanford and M. Barnett, "Effect of Composition on the Texture and Deformation Behaviour of Wrought Mg Alloys," *Scripta Materialia*, 2008, **58**, 179–182.

[11] B. Beausir, S. Suwas, L.S. Tóth, K.W. Neale and J-J. Fundenberger, "Analysis of Texture Evolution in Magnesium during Equal Channel Angular Extrusion," *Acta Materialia*, 2008, **56**, 200–214.

[12] N. Stanford, "The effect of calcium on the texture, microstructure and mechanical properties of extruded Mg-Mn-Ca alloys," *Materials Science & Engineering A*, 2010, **528**, 314–322.

[13] S. W. Xu, K. Oh-ishi, S. Kamado, F. Uchida, T. Homma and K. Hono, "High-strength extruded Mg–Al–Ca–Mn alloy," *Scripta Materialia*, 2011, **65(3)**, 269–272.

[14] J. G. Mezoff, “Magnesium for Automobiles, In Perspective,” *SAE Transactions*, 1980, **89**, 1617-1630.

[15] R. Miranda, “Advances in wrought magnesium alloys, International journal of environmental studies,” *Routledge*, 2013, **70(2)**, 336–336.

[16] J. F. Nie, K. S. Shin, and Z. R. Zeng, “Microstructure, Deformation, and Property of Wrought Magnesium Alloys,” *Metallurgical and materials transactions. A, Physical metallurgy and materials science*, 2020, **51(12)**, 6045–6109.

[17] W. Jin, B. Wu, L. Zhang, J. Wang, C. Esling, and M.-J. Philippe, “Understanding the basal texture initiation in a randomly-oriented AZ31B alloy during cold-rolling,” *Journal of magnesium and alloys*, 2024, **12(10)**, 4311–4333.

[18] M.T Pérez-Prado and O.A Ruano, “Texture evolution during grain growth in annealed MG AZ61 alloy”, *Scripta Materialia*, 2003, **48(1)**, 59-64.

[19] S. R. Agnew, P. Mehrotra, T. M. Lillo, G. M. Stoica, and P. K. Liaw, “Texture evolution of five wrought magnesium alloys during route A equal channel angular extrusion: Experiments and simulations,” *Acta materialia*, 2005, **53(11)**, 3135–3146.

[20] L. Wang, E. Mostaed, X. Cao, G. Huang, A. Fabrizi, F. Bonollo, C. Chi and M. Vedani, “Effects of texture and grain size on mechanical properties of AZ80 magnesium alloys at lower temperatures”, *Materials & Design*, 2016, **89**, 1-8.

[21] I.H. Jung, M. Sanjari, J. Kim, S. Yue, “Role of RE in the deformation and recrystallisation of Mg alloy and a new alloy design concept for Mg–RE alloys,” *Scripta Materialia*, 2015, **102**, 1–6.

[22] S. Sandlöbes, S. Zaefferer, I. Schestakow, S. Yi, and R. Gonzalez-Martinez, “On the role of non-basal deformation mechanisms for the ductility of Mg and Mg–Y alloys,” *Acta materialia*, 2011, **59(2)**, 429–439.

[23] S. Sandlöbes *et al.*, “The relation between ductility and stacking fault energies in Mg and Mg–Y alloys,” *Acta materialia*, 2012, **60(6–7)**, 3011–3021.

[24] R. K. Mishra, A. Brahme, R. K. Sabat, L. Jin, and K. Inal, “Twinning and texture randomization in Mg and Mg-Ce alloys,” *International journal of plasticity*, 2019, **117**, 157–172.

[25] B. Z. Sun *et al.*, “Rotational and translational domains of beta precipitate in aged binary Mg−Ce alloys,” *Journal of magnesium and alloys*, 2021, **9(3)**, 1039–1056.

[26] E. L. S. Solomon, A. R. Natarajan, A. M. Roy, V. Sundararaghavan, A. Van der Ven, and E. A. Marquis, “Stability and strain-driven evolution of β′ precipitate in Mg-Y alloys,” *Acta materialia*, 2019, **166(C)**, 148–157.

[27] D. Qiu, M.-X. Zhang, J. A. Taylor, and P. M. Kelly, “A new approach to designing a grain refiner for Mg casting alloys and its use in Mg–Y-based alloys,” *Acta materialia*, 2009, **57(10)**, 3052–3059.

[28] K. Yaddanapudi *et al.*, “Accommodation and formation of {-1012} twins in Mg-Y alloys,” *Acta materialia*, 2021, **204**, 116514.

[29] B. Zhang, L. Geng, L. Huang, X. Zhang and C. Dong, “Enhanced Mechanical Properties in Fine-Grained Mg-1.0Zn-0.5Ca Alloys Prepared by Extrusion at Different Temperatures,” *Scripta Materialia*, 2010, **63**, 1024–1027.

[30] Y. Chino, T. Ueda, Y. Otomatsu, K. Sassa, X. Huang, K. Suzuki and M. Mabuchi, “Effects of Ca on Tensile Properties and Stretch Formability at Room Temperature in Mg-Zn and Mg-Al Alloys,” *Materials Transactions*, 2011, **52**, 1477–1482.

[31] Z. Zeng, M. Bian, S. Xu, C.H.J. Davies, N. Birbilis and J. Nie, “Texture Evolution during Cold Rolling of Dilute Mg Alloys,” *Scripta Materialia*, 2015, **108**, 6–10.

[32] M. Z. Bian, T. T. Sasaki, T. Nakata, S. Kamado, and K. Hono, “Effects of rolling conditions on the microstructure and mechanical properties in a Mg–Al–Ca–Mn–Zn alloy sheet,” *Materials science & engineering. A, Structural materials : properties, microstructure and processing*, 2018, **730**, 147–154.

[33] K. Kim, D. Han, and K. Kim, “Effect of Ca concentration on Microstructure formation behaviors in AZ61 magnesium alloy,” *Journal of physics. Conference series*, 2019, **1270(1)**, 12044.

[34] I. A. F. Rabbi, M. M. A. Shawon, and H. M. M. A. Rashed, “Effects of Ca Addition on Microstructure and Hot Deformation of AZ61 Magnesium Alloy,” *IOP conference series. Materials Science and Engineering*, 2018, **438(1)**, 12009.

[35] H. Takabayashi and T. Shimizu, “Effects of Heat Treatment and Calcium Addition on Hot-Workability of Cast AZ61 Alloy,” *DENKI-SEIKO*, 2006, **77(2)**, 123–132.

[36] M. Yuasa, X. Huang, K. Suzuki, N. Saito, and Y. Chino, “Effects of Solution Treatment on Corrosion Properties of Mg–6 mass%Al–1 mass%Zn–2 mass%Ca (AZX612) and Mg–6 mass%Al–1 mass%Zn (AZ61) Alloys,” *MATERIALS TRANSACTIONS*, 2018, **59(7)**, 1173–1179.

[37] T. S. ASHOKAN, S. SWAMYNATHAN, and S. SELVARANGAN, “Investigation of Mechanical Properties of Biodegradable AZ31 Magnesium Alloys with Calcium Addition,” *Medžiagotyra*, 2025.

[38] J. Bohlen, J. Wendt, M. Nienaber, K. U. Kainer, L. Stutz, D. Letzig, “Calcium and zirconium as texture modifiers during rolling and annealing of magnesium–zinc alloys,” *Materials Characterization*, 2015, **101**, 144–152.

[39] H. Ding, X. Shi, Y. Wang, G. Cheng and S. Kamado, “Texture Weakening and Ductility Variation of Mg–2Zn Alloy with CA or RE Addition,” *Materials Science & Engineering A*, 2015, **645**, 196–204.

[40] Y. Du, X. Qiao, M. Zheng, D. Wang, K. Wu, I.S. Golovin, “Effect of microalloying with Ca on the microstructure and mechanical properties of Mg-6 mass%Zn alloys,” *Materials & Design*, 2016, **98**, 285–293.

[41] M. Jiang, C. Xu, T. Nakata, H. Yan, R. Chen, S. Kamado, "Development of dilute Mg–Zn–Ca–Mn alloy with high performance via extrusion," *Journal of Alloys and Compounds*, 2016, **668**, 13–21.

[42] Z. Zeng, Y. Zhu, S. Xu, M. Bian, C.H.J. Davies, N. Birbilis and J. Nie, "Texture Evolution during Static Recrystallization of Cold-Rolled Magnesium Alloys," *Acta materialia*, 2016, **105**, 479–494.

[43] J. Wang, Y. Chen, Z. Chen, J. Llorca and X. Zeng, "Deformation mechanisms of Mg-Ca-Zn alloys studied by means of micropillar compression tests," *Acta materialia*, 2021, **217**, 117151.

[44] T. Nakata, C. Xu, K. Suzawa, K. Yoshida, N. Kawabe, S. kamado, "Enhancing mechanical properties of rolled Mg-Al-Ca-Mn alloy sheet by Zn addition," *Materials Science & Engineering. A, Structural Materials: Properties, Microstructure and Processing*, 2018, **737**, 223–229.

[45] A. Incesu and A. Gungor, "Mechanical properties and biodegradability of Mg–Zn–Ca alloys: homogenisation heat treatment and hot rolling," *Journal of Materials Science. Materials in Medicine*, 2020, **31(12)**, 123–123.

[46] K. Nie, Z. Zhu, P. Munroe, K. Deng, J. Han, "The effect of Zn/Ca ratio on the microstructure, texture and mechanical properties of dilute Mg-Zn-Ca-Mn alloys that exhibit superior strength," *Journal of Materials Science*, 2020, **55(8)**, 3588–3604.

[47] G. Wang, G. Huang, Y. Huang, C. Zheng, B. Jiang, A. Tang, F. Pan, "Achieving High Ductility in Hot-Rolled Mg-xZn-0.2Ca-0.2Ce Sheet by Zn Addition," *JOM (1989)*, 2020, **72(4)**, 1607–1618.

[48] M. Zhou, X. Huang, Y. Morisada, H. Fujii, Y. Chino, "Effects of Ca and Sr additions on microstructure, mechanical properties, and ignition temperature of hot-rolled Mg–Zn alloy," *Materials Science & Engineering. A, Structural Materials: Properties, Microstructure and Processing*, 2020, **769**, 138474.

[49] J.B. Go, J.U. Lee, B.G. Moon, J.H. Yoon, S.H. Park, "Improvement in Mechanical Properties of Rolled AZ31 Alloy Through Combined Addition of Ca and Gd," *Metals and Materials International*, 2020, **26(12)**, 1779–1785.

[50] K. Oh-Ishi, R. Watanabe, C. L. Mendis and K. Hono, "Age-hardening response of Mg—0.3 at.%Ca alloys with different Zn contents," *Materials science & engineering. A, Structural materials: properties, microstructure and processing*, 2009, **526(1-2)**, 177–184.

[51] Z.H. Li, T.T. Sasaki, A. Uedono and K. Hono, "Role of Zn on the rapid age-hardening in Mg-Ca-Zn alloys," *Scripta Materialia*, 2022, **216**, 114735.

[52] T. Nakata *et al.*, "Strong and ductile age-hardening Mg-Al-Ca-Mn alloy that can be extruded as fast as aluminum alloys," *Acta materialia*, 2017, **130**, 261–270.

[53] S. Du, K. Yang, M. Li, J. Li, Y. Ren, Q. Huang, H. Pan and G. Qin, “Achieving high strength above 400 MPa in conventionally extruded Mg-Ca-Zn ternary alloys,” *Science China. Technological Sciences*, 2022, **65(3)**, 519–528.

[54] H. Pan, C. Yang, Y. Yang, Y. Dai, D. Zhou, L. Chai, Q. Huang, Q. Yang, S. Liu, Y. Ren and G. Qin, “Ultra-fine grain size and exceptionally high strength in dilute Mg–Ca alloys achieved by conventional one-step extrusion,” *Materials Letters*, 2019, **237**, 65–68.

[55] J. Hofstetter *et al.*, “High-Strength Low-Alloy (HSLA) Mg–Zn–Ca Alloys with Excellent Biodegradation Performance,” *JOM (1989)*, 2014, **66(4)**, pp. 566–572.

[56] C.L. Mendis, K. Oh-ishi, Y. Kawamura, T. Honma, S. Kamado, and K. Hono, “Precipitation-hardenable Mg–2.4Zn–0.1Ag–0.1Ca–0.16Zr (at.%) wrought magnesium alloy,” *Acta materialia*, 2009, **57(3)**, pp. 749–760.

[57] K. Yamagishi, K. Onyam, Y. Ogawa, D. Ando and Y.Sutou, “Abnormal grain growth through cyclic heat treatment in a Mg-Sc alloy,” *Journal of Alloys and Compounds*, 2023, **938**, 168415.

[58] R.C. Zeng, L. Sun, Y.F. Zheng, H.Z. Cui and E.H. Han, “Corrosion and characterisation of dual phase Mg-Li-Ca alloy in Hank’s solution: The influence of microstructural features,” *Corrosion Science*, 2014, **79(feb.)**, 69-82.

[59] R.C. Zeng, W.C. Qi, H.Z. Cui, F. Zhang and E.H. Han, “In vitro corrosion of as-extruded Mg-Ca alloys-The influence of Ca concentration,” *Corrosion Science*, 2015, **96(jul.)**, 23-31.

[60] Zander, Daniela, Zumdick and A. Naemi, “Influence of Ca and Zn on the microstructure and corrosion of biodegradable Mg-Ca-Zn alloys,” *Corrosion Science: The Journal on Environmental Degradation of Materials and its Control*, 2015.

[61] E. A. Lukyanova *et al.*, “Structure and Mechanical and Corrosion Properties of a Magnesium Mg–Y–Nd–Zr Alloy after High Pressure Torsion,” *Russian metallurgy Metally*, 2017, **2017(11)**, 912–921.

[62] B. Zhang, Y. Wang, L. Geng and C. Lu, “Effects of Calcium on Texture and Mechanical Properties of Hot-Extruded Mg–Zn–Ca Alloys,” *Materials Science & Engineering A*, 2012, **539**, 56–60.

[63] X. Wang and D. Guan, “The evolution of coarse grains and its effects on weakened basal texture during annealing of a cold-rolled magnesium AZ31B alloy,” *Journal of magnesium and alloys*, 2022, **10(5)**, 1235-741.

[64] H. Nakano, M. Yuasa, Y. Chino, M. Mabuchi, “{10-12} twins in the rolled Mg-Zn-Ca alloy with high formability,” *Journal of Materials Research*, 2014, **29(24)**, 3024–3031.

[65] J.Y. Lee, Y.S. Yun, B.C. Suh, N.J. Kim, W.T. Kim and D.H. Kim, "Comparison of Static Recrystallization Behavior in Hot Rolled Mg–3Al–1Zn and Mg–3Zn–0.5Ca Sheets," *Journal of Alloys and Compounds*, 2014, **589**, 240–246.

[66] D. Guan, X. Liu, J. Gao, L. Ma, B. Wynne and W.M. Rainforth, "Effect of Deformation Twinning on Crystallographic Texture Evolution in a Mg–6.6Zn–0.2Ca (ZX70) Alloy during Recrystallisation," *Journal of Alloys and Compounds*, 2019, **774**, 556–564.

[67] D. Guan, B. Wynne, J. Gao, Y. Huang, W.M. Rainforth, "Basal slip mediated tension twin variant selection in magnesium WE43 alloy," *Acta Materialia*, 2019, **170**, 1–14.

[68] J. Victoria-Hernández, S. Yi, D. Klaumünzer, D. Letzig, "Recrystallisation behavior and its relationship with deformation mechanisms of a hot rolled Mg-Zn-Ca-Zr alloy," *Materials Science & Engineering. A, Structural Materials: Properties, Microstructure and Processing*, 2019, **761**, 138054.

[69] J. Deng, J. Tian, Y. Zhou, Y. Chang, W. Liang, and J. Ma, "Enhanced Formability of Magnesium Alloy Rolled Plates by {10-12} Tensile Twinning and Recrystallization," *Materials*, 2022, **15(18)**, 6253.

[70] S. Wang, X. Li, S.Z. Kure-Chu, B. Deng, X. Li and X. Xiao, "Enhanced rollability of Mg alloys by directly activated {10-12} twinning during asymmetric rolling: Experiments and finite element analysis," *Materials Characterization,* 2023, **196**, 112582.

[71] M. Arul Kumar, M. Wroński, R. J. McCabe, L. Capolungo, K. Wierzbanowski, and C. N. Tomé, "Role of microstructure on twin nucleation and growth in HCP titanium: A statistical study," *Acta materialia*, 2018, **148(C)**, 123–132.

[72] W.Q. Chen, S. Deng, X.J. Zhao and S.N. Luo, "Active {11-21} and {10-12} extension twinning in a WE43 Mg alloy," *Journal of Materials Science & Technology*, 2023, **13**, 93-101.

[73] X. Li, P. Yang and L. Meng, "Analysis of The Static Recrystallization at Tension Twins in AZ31 Magnesium Alloy," *Advanced Materials Research*, 2011, **299-300**, 778-784.

[74] Y. Xin, H. Zhou, H. Yu, R. Hong, H. Zhang, and Q. Liu, "Controlling the recrystallization behavior of a Mg–3Al–1Zn alloy containing extension twins," *Materials science & engineering. A, Structural materials: properties, microstructure and processing*, 2015, **622**, 178–183.

[75] M. R. Barnett, Z. Keshavarz, A. G. Beer, and X. Ma, "Non-Schmid behaviour during secondary twinning in a polycrystalline magnesium alloy," *Acta materialia*, 2008, **56(1)**, 5–15.

[76] T.T. Liu, Q.S. Yang, N. Guo, Y. Lu and B. Song, "Stability of twins in Mg alloys – A short review," *Journal of Magnesium and Alloys*, 2020, **8(1)**, 66-77.

[77] M. Lentz, M. Risse, N. Schaefer, W. Reimers, and I. J. Beyerlein, "Strength and ductility with {10$\bar{1}$1} — {10$\bar{1}$2} double twinning in a magnesium alloy," *Nature communications*, 2016, **7(1)**, 11068–11068.

[78] É. Martin, L. Capolungo, L. Jiang, and J. J. Jonas, "Variant selection during secondary twinning in Mg–3%Al," *Acta materialia*, 2010, **58(11)**, 3970–3983.

[79] Y. Liu *et al.*, "Twin recrystallization mechanisms in a high strain rate compressed Mg-Zn alloy," *Journal of magnesium and alloys*, 2021, **9(2)**, 99–504.

[80] S. Jin, K. Marthinsen, and Y. Li, "Formation of {112$\bar{1}$1} twin boundaries in titanium by kinking mechanism through accumulative dislocation slip," *Acta materialia*, 2016, **120**, 403–414.

[81] M. M. Myshlyaev, H. J. McQueen, A. Mwembela, and E. Konopleva, "Twinning, dynamic recovery and recrystallization in hot worked Mg–Al–Zn alloy," *Materials science & engineering. A, Structural materials: properties, microstructure and processing*, 2002, **337(1)**, 121–133.

[82] D. Guan, X. Liu, J. Gao, L. Ma, B.P. Wynne, W.M. Rainforth, "Exploring the mechanism of "Rare Earth" texture evolution in a lean Mg–Zn–Ca alloy," *Scientific Reports*, 2019, **9(1)**, 7152–7152.

[83] I. Basu, T. Al-Samman, and G. Gottstein, "Shear band-related recrystallization and grain growth in two rolled magnesium-rare earth alloys," *Materials science & engineering. A, Structural materials: properties, microstructure and processing*, 2013, **579**, 50–56.

[84] N. Stanford and M. R. Barnett, "The origin of 'rare earth' texture development in extruded Mg-based alloys and its effect on tensile ductility," *Materials science & engineering. A, Structural materials: properties, microstructure and processing*, 2008, **496(1)**, 399–408.

[85] J.Y. Lee, Y.S. Yun, W.T. Kim and D.H. Kim, "Twinning and Texture Evolution in Binary Mg-Ca and Mg-Zn Alloys, Metals and Materials International," *Metals and materials international*, 2014, **20(5)**, 885–891.

[86] L.Q. Zhao *et al.*, "Development of weak-textured and high-performance Mg–Zn–Ca alloy sheets based on Zn content optimization," *Journal of alloys and compounds*, 2020, **849(C)**, 156640.

[87] M. H. Yoo, S. R. Agnew, J. R. Morris, and K. M. Ho, "Non-basal slip systems in HCP metals and alloys: source mechanisms," *Materials science & engineering. A, Structural materials: properties, microstructure and processing*, 2001, **319**, 87–92.

[88] I. Basu and T. Al-Samman, “Triggering rare earth texture modification in magnesium alloys by addition of zinc and zirconium,” *Acta materialia*, 2014, **67**, 116–133.

[89] G. Wang *et al.*, “Effects of Zn addition on the mechanical properties and texture of extruded Mg-Zn-Ca-Ce magnesium alloy sheets,” *Materials science & engineering. A, Structural materials: properties, microstructure and processing*, 2017, **705**, 46–54.

[90] Y. Tang and J. A. El-Awady, “Formation and slip of pyramidal dislocations in hexagonal close-packed magnesium single crystals,” *Acta materialia*, 2014, **71**, 319–332.

[91] L. L. Rokhlin, T. V. Dobatkina, I. E. Tarytina, E. A. Luk’yanova, and O. A. Ovchinnikova, “Recovery of an Aged Mg–Y–Nd–Zr Magnesium Alloy,” *Russian metallurgy Metally*, 2022, **2022(3)**, 200–203.

[92] M. Verdier, M. Janecek, Y. Bréchet, and P. Guyot, “Microstructural evolution during recovery in Al–2.5%Mg alloys,” *Materials science & engineering. A, Structural materials: properties, microstructure and processing*, 1998, **248(1)**, 187–197.

[93] T. Kajiura, M. Tsukamoto, and A. Yamamoto, “Same Area EBSD Observation on Early Stage of Recovery and Recrystallization in A1050 Aluminum after Cold-Rolling,” *Journal of the Japan Institute of Metals and Materials*, 2012, **76(9)**, 528–534.

[94] S. Ding, J. Zhang, S. A. Khan, and J. Yanagimoto, “Static recovery of A5083 aluminum alloy after a small deformation through various measuring approaches,” *Journal of materials science & technology*, 2022, **104**, 202–213.

[95] J. Hofstetter, S. Rüedi, I. Baumgartner, H. Kilian, B. Mingler, E. Povoden-Karadeniz, S. Pogatscher, P.J. Uggowitzer and J.F. Löffler, “Processing and microstructure–property relations of high-strength low-alloy (HSLA) Mg–Zn–Ca alloys,” *Acta Materialia*, 2015, **98**, 423–432.

[96] H. Pan, R. Kang, J. Li, H. Xie, Z. Zeng, Q. Huang, C. Yang, Y. Ren, G. Qin, “Mechanistic investigation of a low-alloy Mg–Ca-based extrusion alloy with high strength–ductility synergy,” *Acta Materialia*, 2020, **186**, 278–290.

[97] Y. Du, B. Cheng, M. Shen, “Effect of Rolling Deformation on the Microstructure and Mechanical Properties of an Extruded Mg-Zn-Ca Alloy, Journal of Materials Engineering and Performance,” *Journal of materials engineering and performance*, 2019, **28(7)**, 4357–4363.

[98] Q. Li, G. Huang, X. Huang, S. Pan, C. Tan, Q. Liu, “On the texture evolution of Mg–Zn–Ca alloy with different hot rolling paths,” *Journal of Magnesium and Alloys*, 2017, **5(2)**, 166–172.

[99] Q. Wang, B. Jiang, A. Tang, J. Fu, Z. Jiang, H. Sheng, D. Zhang, G. Huang, F. Pan, "Unveiling annealing texture formation and static recrystallisation kinetics of hot-rolled Mg-Al-Zn-Mn-Ca alloy," *Journal of Materials Science & Technology*, 2020, **43**, 104–118.

[100] Z.M. Hua *et al.*, "Development of low-alloyed Mg–Zn–Ca–Sn–Mn alloy with high strength-ductility synergy by sub-rapid solidification and hot rolling," *Journal of alloys and compounds*, 2021, **855**, 157317.

[101] K. Neh, M. Ullmann, and R. Kawalla, "Twin-Roll-Casting and Hot Rolling of Magnesium Alloy WE43," in *Procedia Engineering*, Elsevier Ltd, 2014, 1553–1558.

[102] A. P. Khrustalyov, A. Akhmadieva, A. N. Monogenov, I. A. Zhukov, E. S. Marchenko and A. B. Vorozhtsov, "Study of the Effect of Diamond Nanoparticles on the Structure and Mechanical Properties of the Medical Mg–Ca–Zn Magnesium Alloy," *Metals (Basel)*, 2022, **12(2)**, 206.

[103] I. J. Beyerlein, R. J. McCabe, and C. N. Tomé, "Effect of microstructure on the nucleation of deformation twins in polycrystalline high-purity magnesium: A multi-scale modeling study," *Journal of the mechanics and physics of solids*, 2011, **59(5)**, 988–1003.

[104] W. Chen, S. Li, K. S. Bhandari, S. Aziz, X. Chen, and D. W. Jung, "Genetic optimized Al–Mg alloy constitutive modeling and activation energy analysis," *International journal of mechanical sciences*, 2023, **244**, 108077.

[105] Z. Tong, L. Wang, G. Zhu, and X. Zeng, "Predicting Twin Nucleation in a Polycrystalline Mg Alloy Using Machine Learning Methods," *Metallurgical and materials transactions. A, Physical metallurgy and materials science*, 2019, **50(12)**, 5543–5560.

[106] M. Mito *et al.*, "Achieving superconductivity with higher T c in lightweight Al–Ti–Mg alloys: Prediction using machine learning and synthesis via high-pressure torsion process," *Journal of applied physics*, 2022, **131(10)**.

[107] D. Guan, *Processing, microstructure and mechanical behavior of bulk nanostructured Mg alloy*. University of Sheffield, 2016.

[108] Y. Q. Chai *et al.*, "Anomalous Tension Twinning Activity in Extruded Mg Sheet During Hard-Orientation Loading at Room Temperature," *Metallurgical and materials transactions. A, Physical metallurgy and materials science*, 2021, **52(2)**, 449–456.

[109] L. Zhao, X. Guo, A. Chapuis, Y. Xin, Q. Liu, and P. Wu, "Strain-Path Dependence of {10-12} Twinning in a Rolled Mg–3Al–1Zn Alloy: Influence of Twinning Model," *Metallurgical and materials transactions. A, Physical metallurgy and materials science*, 2019, **50(1)**, 118–131.

[110] S.G. Hong, S.H. Park, and C.S. Lee, “Strain path dependence of {10−12} twinning activity in a polycrystalline magnesium alloy,” *Scripta materialia*, 2011, **64(2)**, 145–148.

[111] Y. Zhu, X. Chen, K. Chen, Y. Wang, and Z. Wang, “Quasi in situ observation of twinning evolution during strain path change in magnesium alloy,” *Journal of materials research*, 2022, **37(5)**, 1125–1132.

[112] L. Wang, G. Huang, Q. Quan, P. Bassani, E. Mostaed, M. Vedani and F. Pan, “The effect of twinning and detwinning on the mechanical property of AZ31 extruded magnesium alloy during strain-path changes,” *Materials & design*, 2014, **63**, 177–184.

[113] V.R. Maarten, Strain path dependency in sheet metal: Experiments and models. University of Twente, 2009.

[114] W. Wen *et al.*, “Mechanical behavior of Mg subjected to strain path changes: Experiments and modeling,” *International journal of plasticity*, 2015, **73(C)**, 171–183.

[115] G. Proust, C. N. Tomé, A. Jain, and S. R. Agnew, “Modeling the effect of twinning and detwinning during strain-path changes of magnesium alloy AZ31,” *International journal of plasticity*, 2009, **25(5)**, 861–880.

[116] J. Lee, Y.-S. Lee, M.-G. Lee, and D. Kim, “Constitutive modelling of magnesium alloy sheets under strain path changes,” *Journal of physics. Conference series*, 2016, **734(3)**, 32135.

[117] K. Alkan, O. B. Aytuna, B. Güler, and M. Efe, “Strong strain path dependence of strain localizations and fracture in magnesium AZ31 sheet,” Journal of magnesium and alloys, 2020, **8(2)**, 472–479.

[118] C. H. Cáceres, P. Lukáč, and A. Blake, "Strain hardening due to {10 12} twinning in pure magnesium," Philosophical magazine (Abingdon, England), 2008, **88(7)**, 991–1003.

[119] I. A. Evdokimov et al., “Nanostructured Strain-Hardened Aluminum–Magnesium Alloys Modified by C60 Fullerene Obtained by Powder Metallurgy: 2. The Effect of Magnesium Concentration on Physical and Mechanical Properties,” *Russian journal of non-ferrous metals*, 2021, **62(3)**, 368–374.

[120] C. Sonat, S. He, J. Li, C. Unluer, and E.-H. Yang, “Strain hardening magnesium-silicate-hydrate composites (SHMSHC) reinforced with short and randomly oriented polyvinyl alcohol microfibers,” *Cement and concrete research*, 2021, **142**, 106354.

[121] D. Kumar, T. Mi, and E.-H. Yang, “Improving the material sustainability of strain-hardening magnesium-silicate-hydrate composite by incorporating aggregates,” *Construction & building materials*, 2023, **407**, 133576.

[122] T. Mi, D. Kumar, M. S. Faris, and E.-H. Yang, “Sustainable strain-hardening magnesium silicate hydrate composite,” *Magazine of concrete research*, 2025, 1–11.

[123] N. Dixit, K. Y. Xie, K. J. Hemker, and K. T. Ramesh, “Microstructural evolution of pure magnesium under high strain rate loading,” *Acta materialia*, 2015, **87**, 56–67.

[124] H. Somekawa and T. Mukai, “Hall–Petch Breakdown in Fine-Grained Pure Magnesium at Low Strain Rates,” *Metallurgical and materials transactions. A, Physical metallurgy and materials science*, 2015, **46(2)**, 894–902.

[125] Y. Chen, P. Mao, Z. Wang, and G. Cao, “Tensile twin evolution of Mg-3Al-1Zn magnesium alloy during high-strain rate deformation,” *Materials science and technology*, 2021, **37(18)**, 1452–1464.

[126] EBSD.com, “EBSD: Electron Backscatter Diffraction.” EBSD.com Electron Backscatter Diffraction. http://ebsd.com (Accessed: January 10, 2025)

[127] Y. Xiong, Q. Luan, K. Zheng, W. Wang, and J. Jiang, “Understanding the strain path effect on the deformed microstructure of single crystal pure aluminum,” *Metals (Basel)*, 2021, **11(8)**, 1189.

[128] J. Papillon, P. Salero, F. Mercier, D. Fabrègue and Éric Maire, “Compressive deformation behavior of dendritic Mg–Ca(–Zn) alloys at high temperature,” *Materials science & engineering. A, Structural materials: properties, microstructure and processing*, 2019, **763**, 138180.

[129] M. R. Barnett and N. Stanford, “Influence of microstructure on strain distribution in Mg–3Al–1Zn,” *Scripta materialia*, 2007, **57(12)**, 1125–1128.

[130] M. D. Nave and M. R. Barnett, “Microstructures and textures of pure magnesium deformed in plane-strain compression,” *Scripta materialia*, 2004, **51(9)**, 881–885.

[131] M. Jackson, R. J. Dashwood, L. Christodoulou, and H. M. Flower, “Application of novel technique to examine thermomechanical processing of near β alloy Ti-10V-2Fe-3Al,” *Materials science and technology*, 2000, **16(11–12)**, 1437–1444.

[132] L. Villegas-Armenta, R. A. L. Drew and M. Pekguleryuz, “The Ignition Behavior of Mg-Ca Binary Alloys: The Role of Heating Rate,” *Oxidation of Metals*, 2020, **93(5-6)**.

[133] X. Ye, Z. Suo, Z.H. Heng, B. Chen, Q.M. Wei, J. Umeda, K. Kondoh and J.H. Shen, “An in-situ study of static recrystallization in Mg using high temperature EBSD,” *Journal of Magnesium and Alloys*, 2024, **12(4)**, 1419-1430.

[134] I. Basu and T. Al-Samman, “Twin recrystallization mechanisms in magnesium-rare earth alloys,” *Acta materialia*, 2015, **96**, 111-132.

[135] M. N. Zhang *et al.*, “Anisotropic segregation-driven texture weakening in a dilute Mg-Al-Ca alloy during isothermal annealing,” *Materials research letters*, 2023, **11(9)**, 781–788.

[136] S. R. Claves and A. Deal, “Orientation Dependence of EBSD Pattern Quality,” *Microscopy and microanalysis*, 2005, **11(S02)**, 514–515.

Appendix I

A1 Channel die one-direction compressed Mg-0.2Ca-0.3Zn (at%) specimens

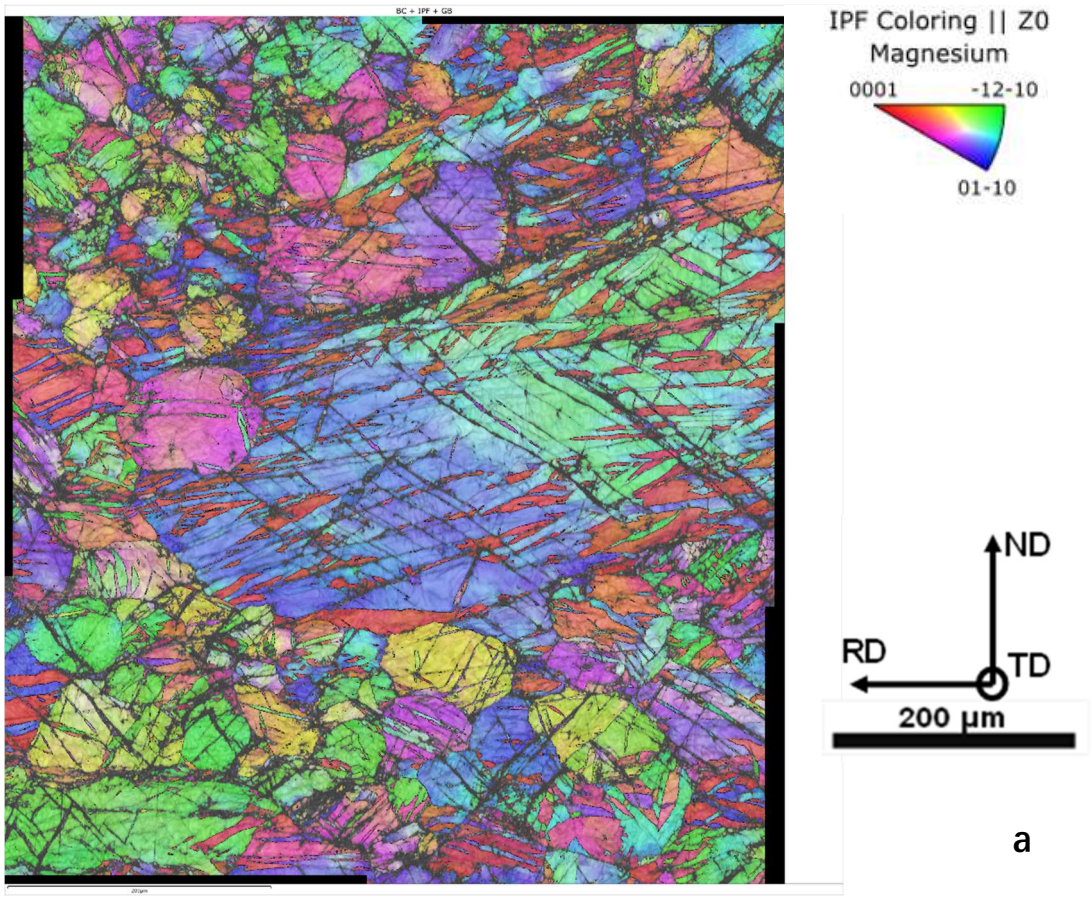

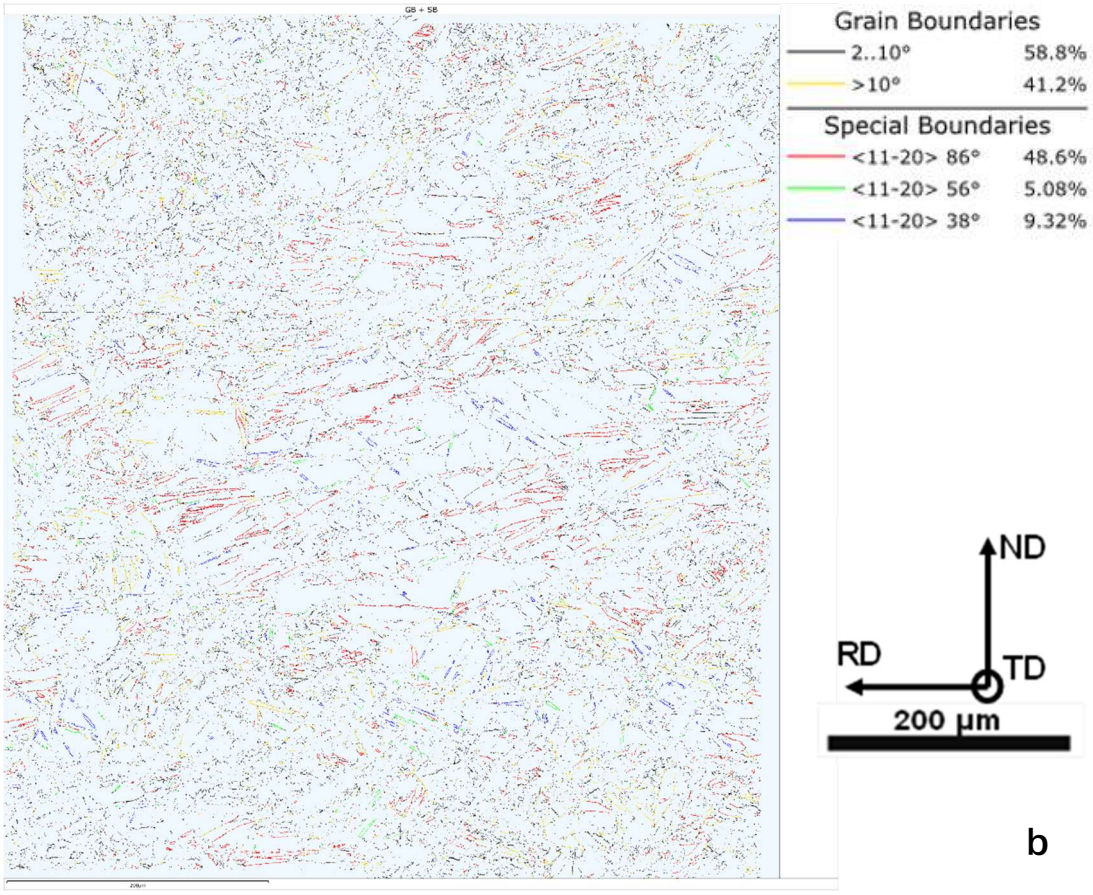
GB + SB
Grain Boundaries
2..10° 58.8%
>10° 41.2%
Special Boundaries
<11-20> 86° 48.6%
<11-20> 56° 5.08%
<11-20> 38° 9.32%
ND
RD
TD
200 µm

b

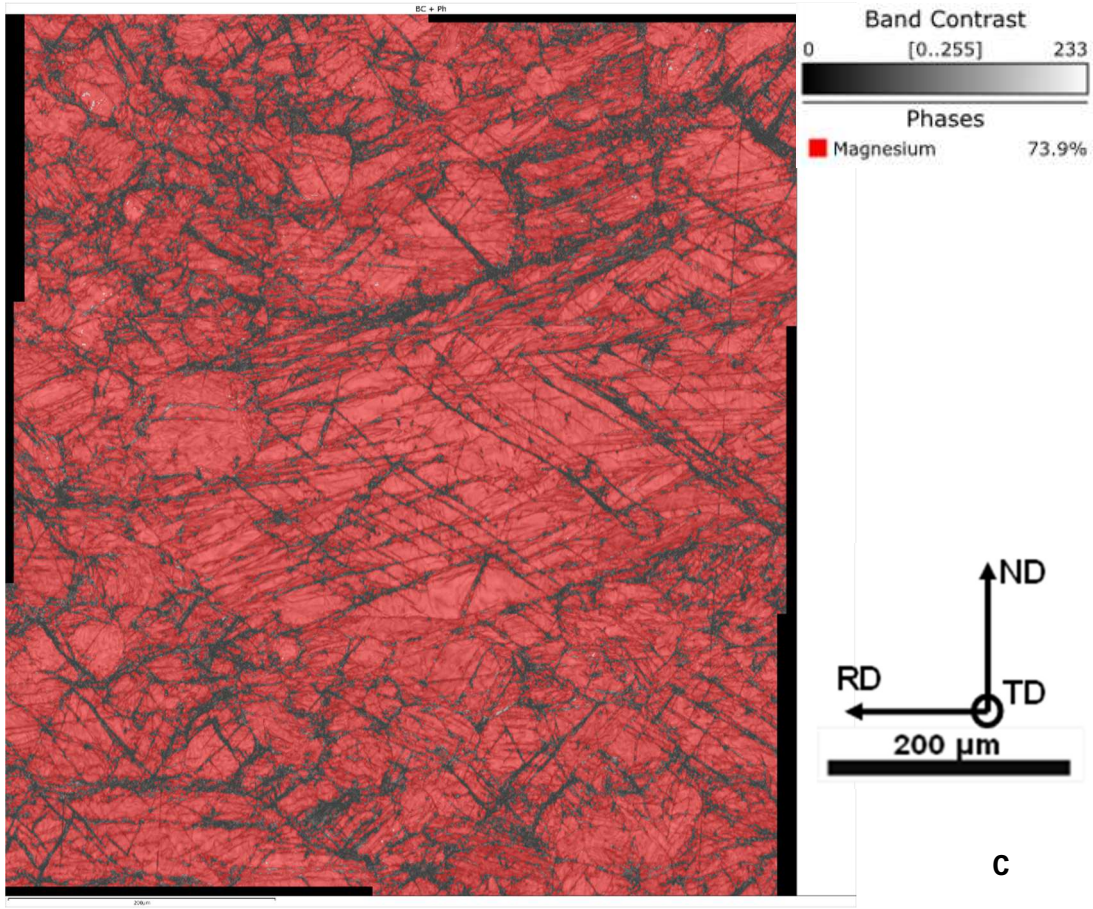
BC + Ph
Band Contrast
0 [0..255] 233
Phases
Magnesium 73.9%
ND
RD
TD
200 µm

c

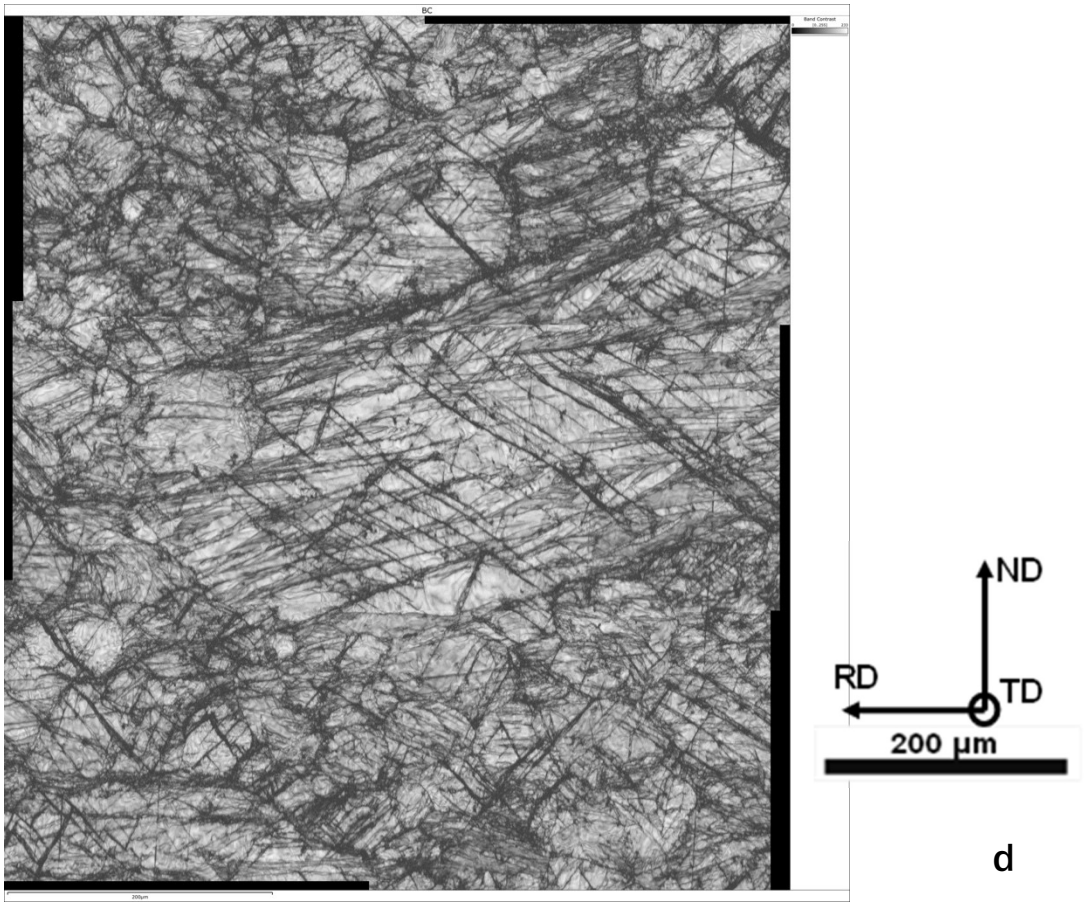
BC
ND
RD
TD
200 µm
d

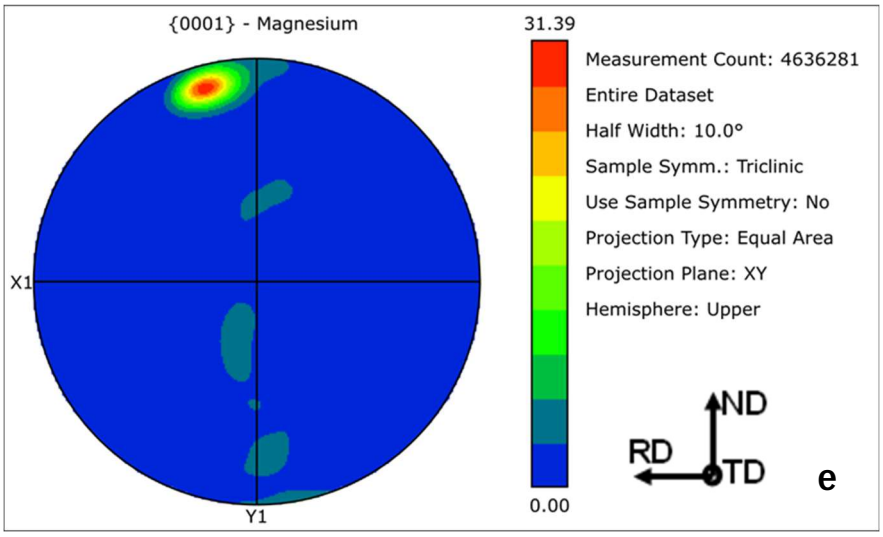
{0001} - Magnesium
31.39
0.00
Measurement Count: 4636281
Entire Dataset
Half Width: 10.0°
Sample Symm.: Triclinic
Use Sample Symmetry: No
Projection Type: Equal Area
Projection Plane: XY
Hemisphere: Upper
X1
Y1
ND
RD
TD
e

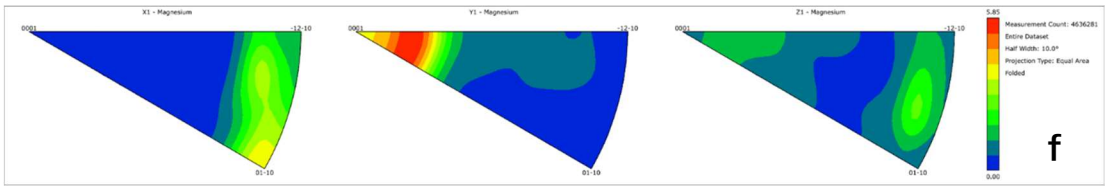
X1 - Magnesium
Y1 - Magnesium
Z1 - Magnesium
f

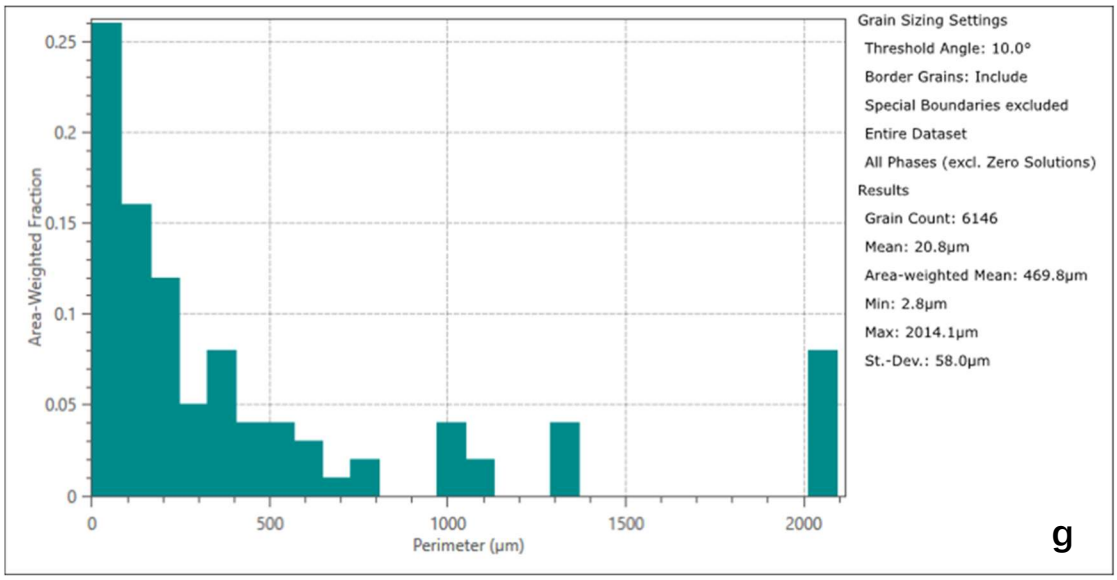

Figure A1-1 The EBSD result of the 30s annealed 1D compressed Mg-0.2Ca-0.3Zn specimen: (a) The inverse pole figure map and grain boundaries, (b) The grain boundaries and the special grain boundaries, (c) The band contrast and the phase analysis, (d) The band contrast, (e) The pole figure, (f) The inverse pole figures, (g) Grain size distribution expressed as grain boundary perimeter

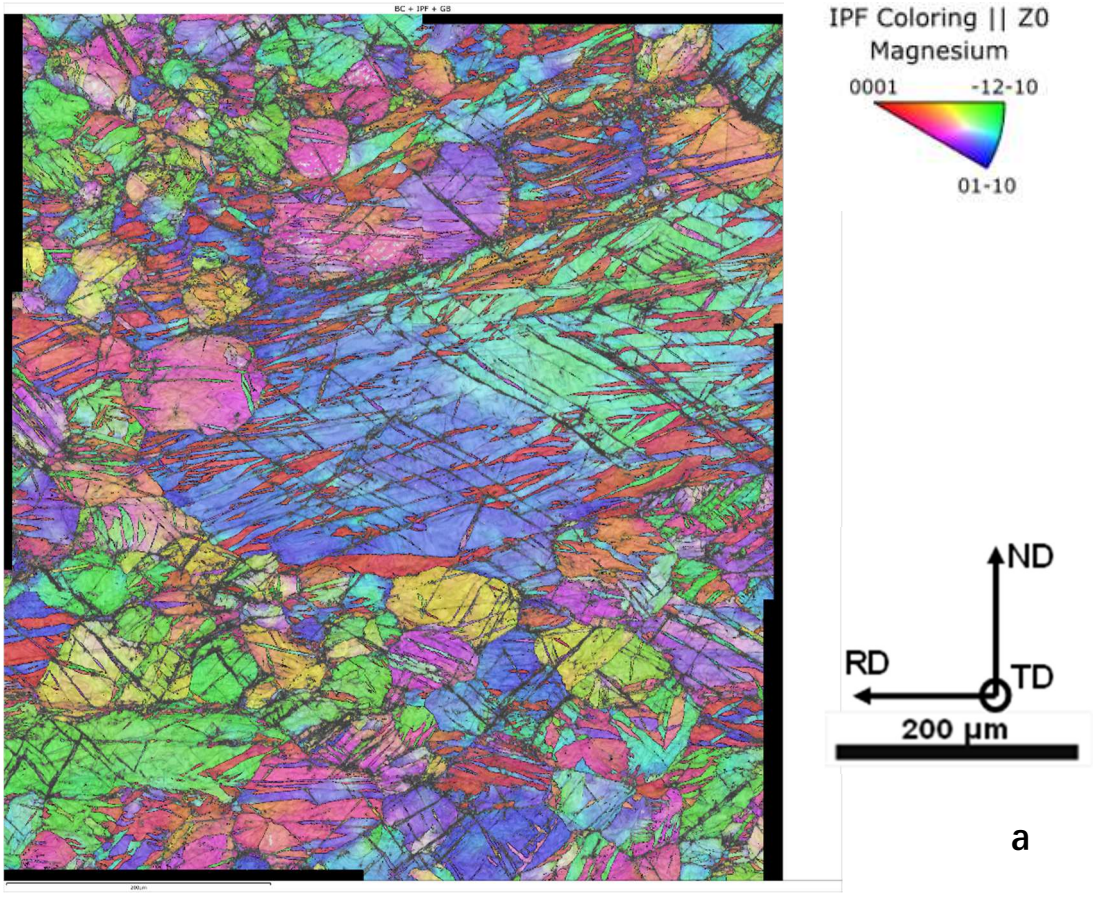

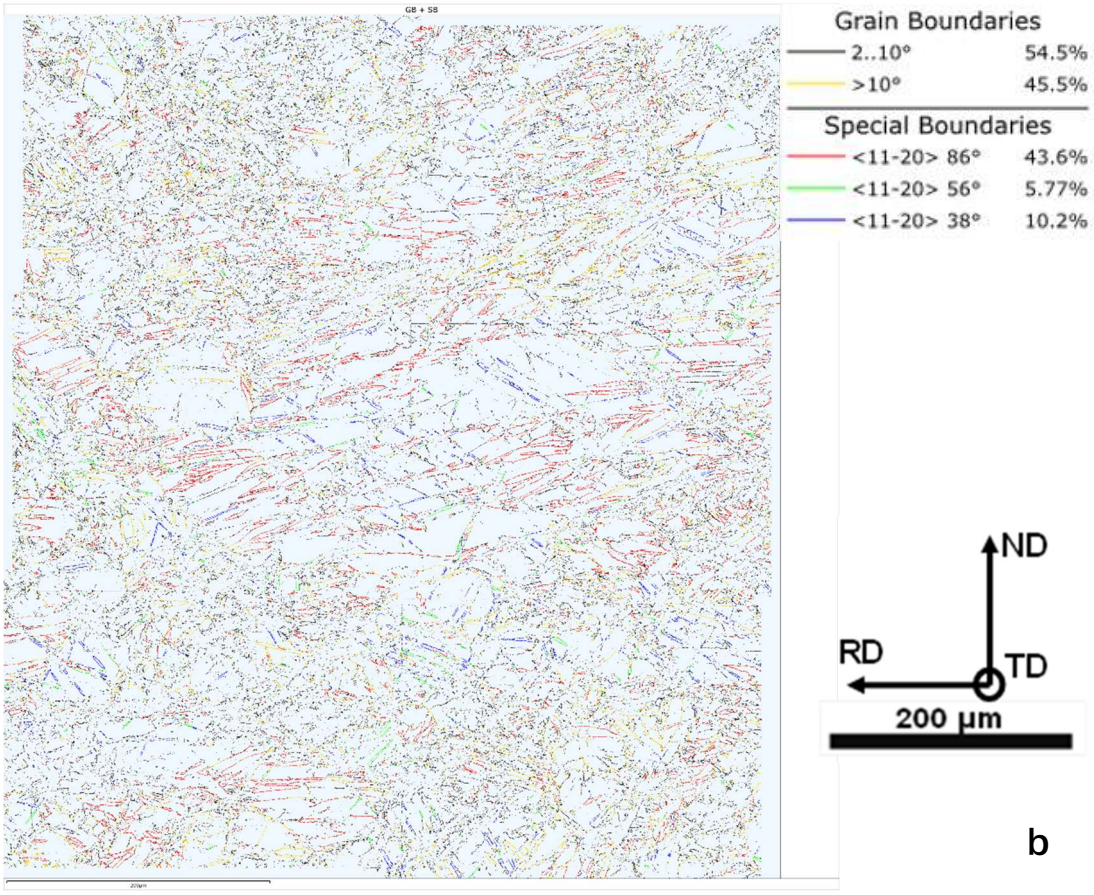
GB + SB
Grain Boundaries
2..10° 54.5%
>10° 45.5%
Special Boundaries
<11-20> 86° 43.6%
<11-20> 56° 5.77%
<11-20> 38° 10.2%
ND
RD
TD
200 µm

b

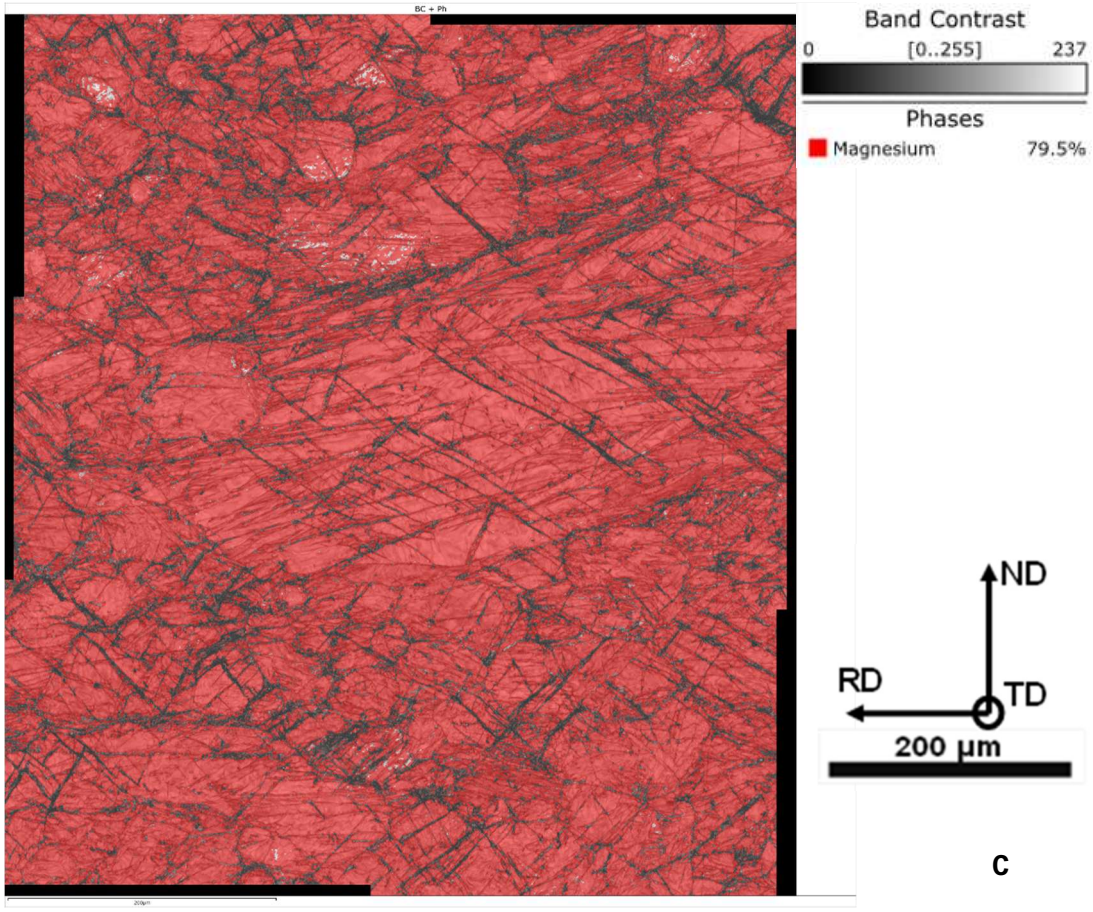
BC + Ph
Band Contrast
0 [0..255] 237
Phases
Magnesium 79.5%
ND
RD
TD
200 µm

c

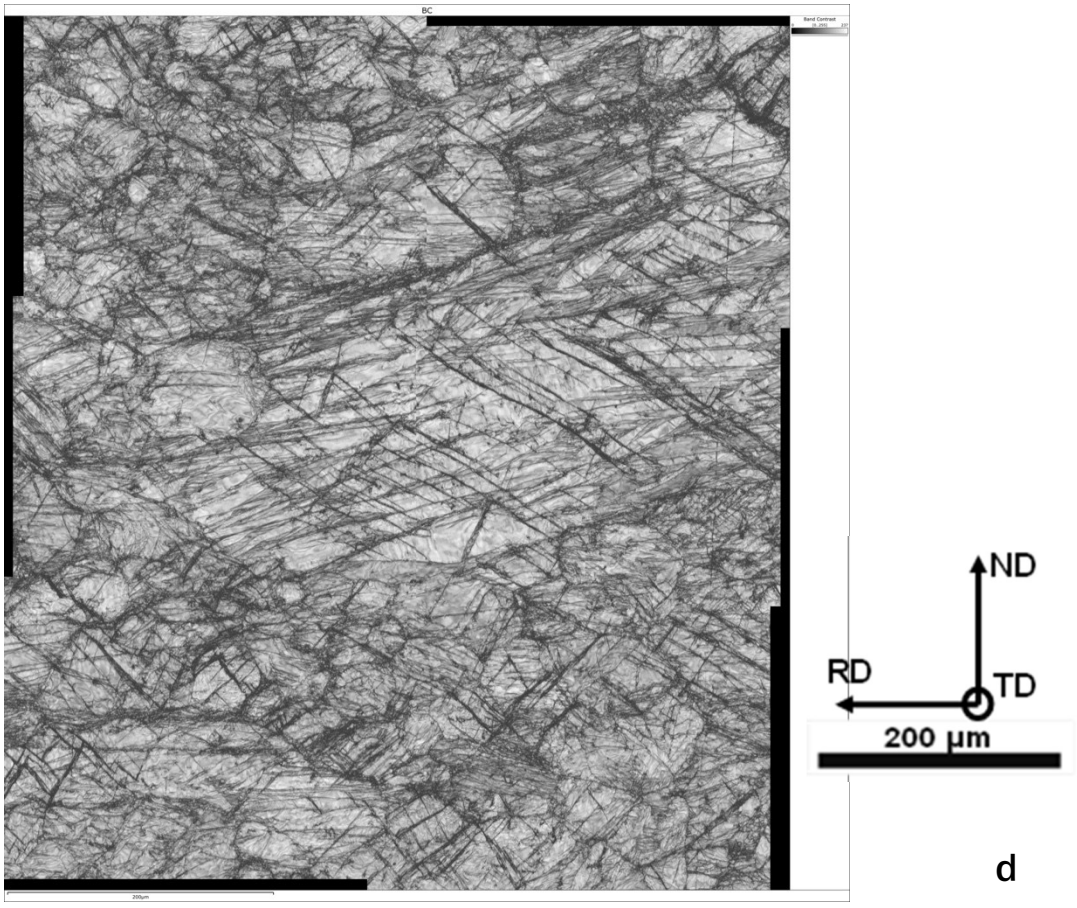
ND
RD
TD
200 µm
d

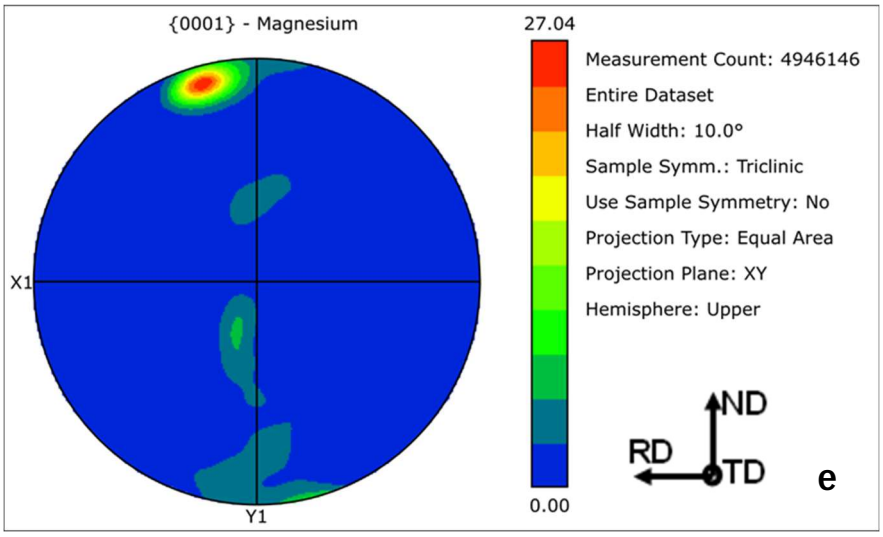
{0001} - Magnesium
27.04
0.00
X1
Y1
Measurement Count: 4946146
Entire Dataset
Half Width: 10.0°
Sample Symm.: Triclinic
Use Sample Symmetry: No
Projection Type: Equal Area
Projection Plane: XY
Hemisphere: Upper
ND
RD
TD
e

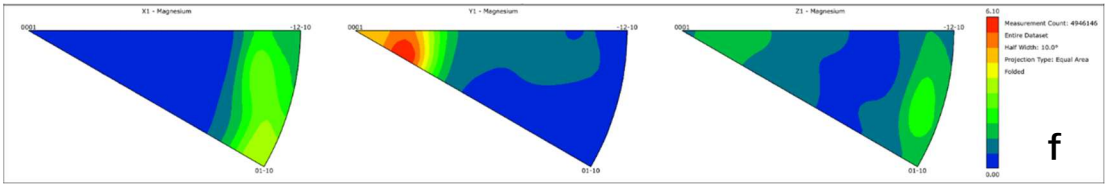
f

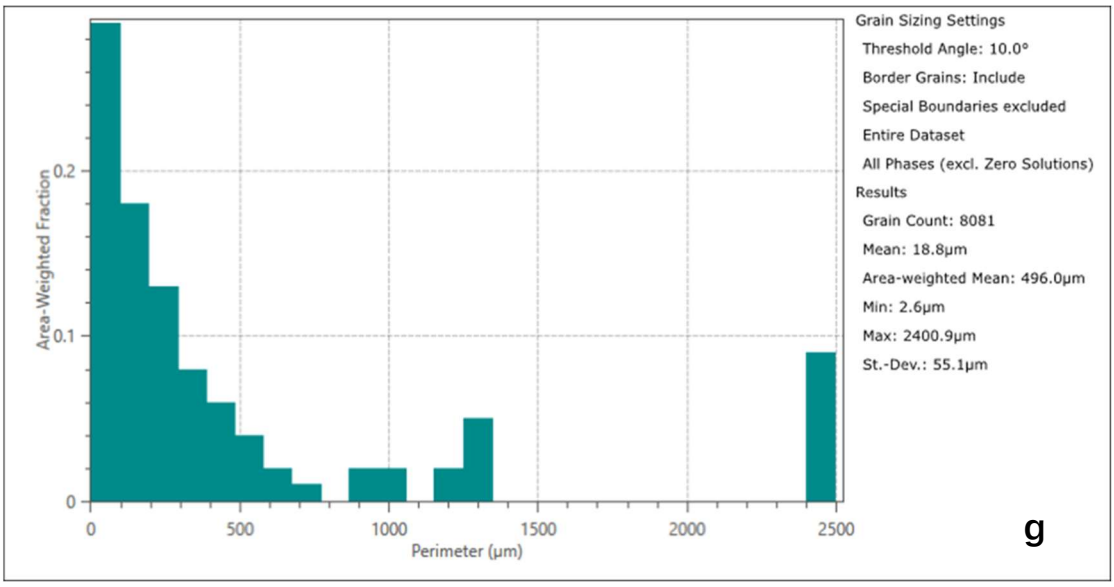

Figure A1-2 The EBSD result of the 75s annealed 1D compressed Mg-0.2Ca-0.3Zn specimen: (a) The inverse pole figure map and grain boundaries, (b) The grain boundaries and the special grain boundaries, (c) The band contrast and the phase analysis, (d) The band contrast, (e) The pole figure, (f) The inverse pole figures, (g) Grain size distribution expressed as grain boundary perimeter

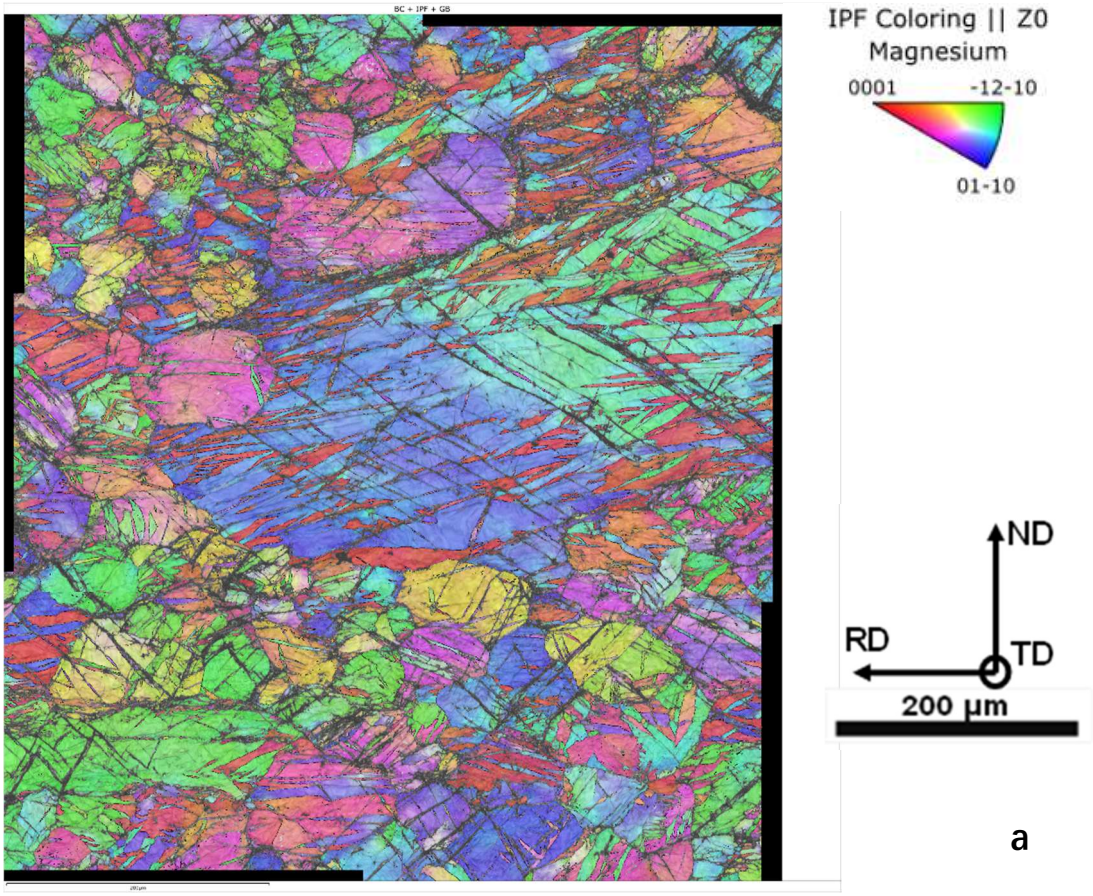

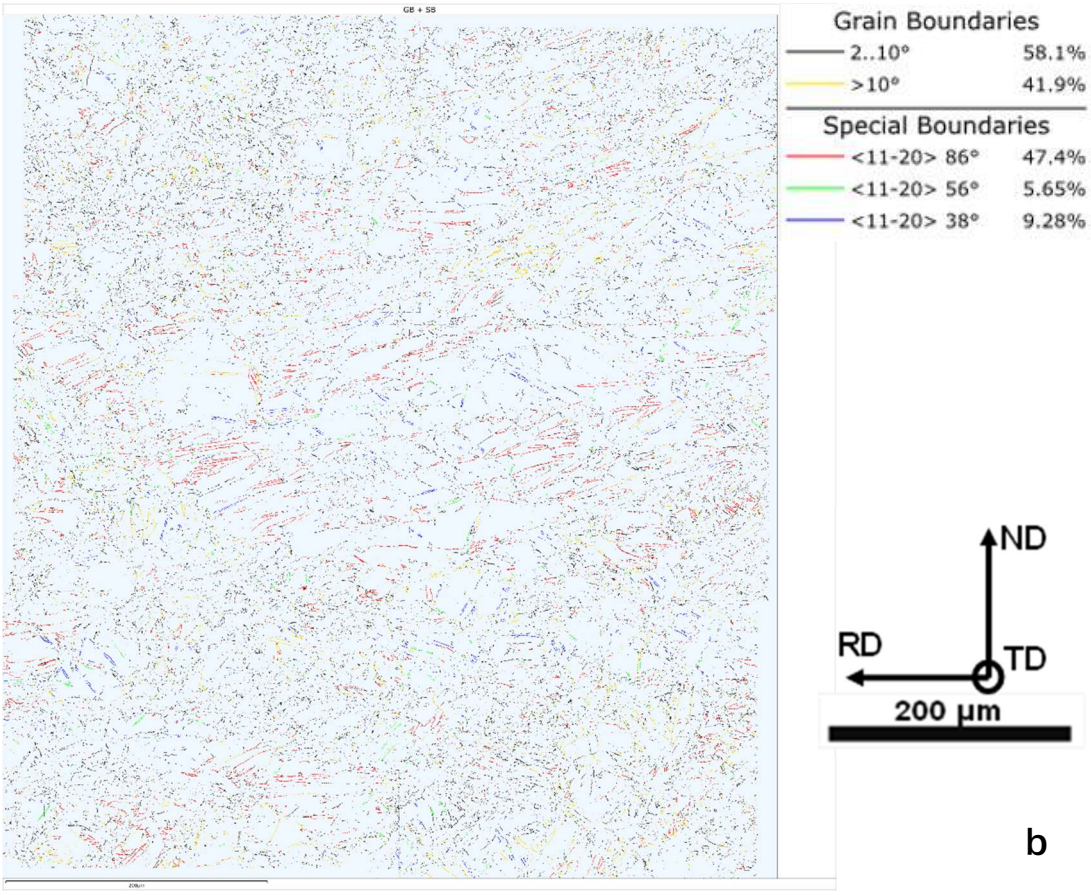
GB + SB
Grain Boundaries
2..10° 58.1%
>10° 41.9%
Special Boundaries
<11-20> 86° 47.4%
<11-20> 56° 5.65%
<11-20> 38° 9.28%
ND
RD
TD
200 µm

b

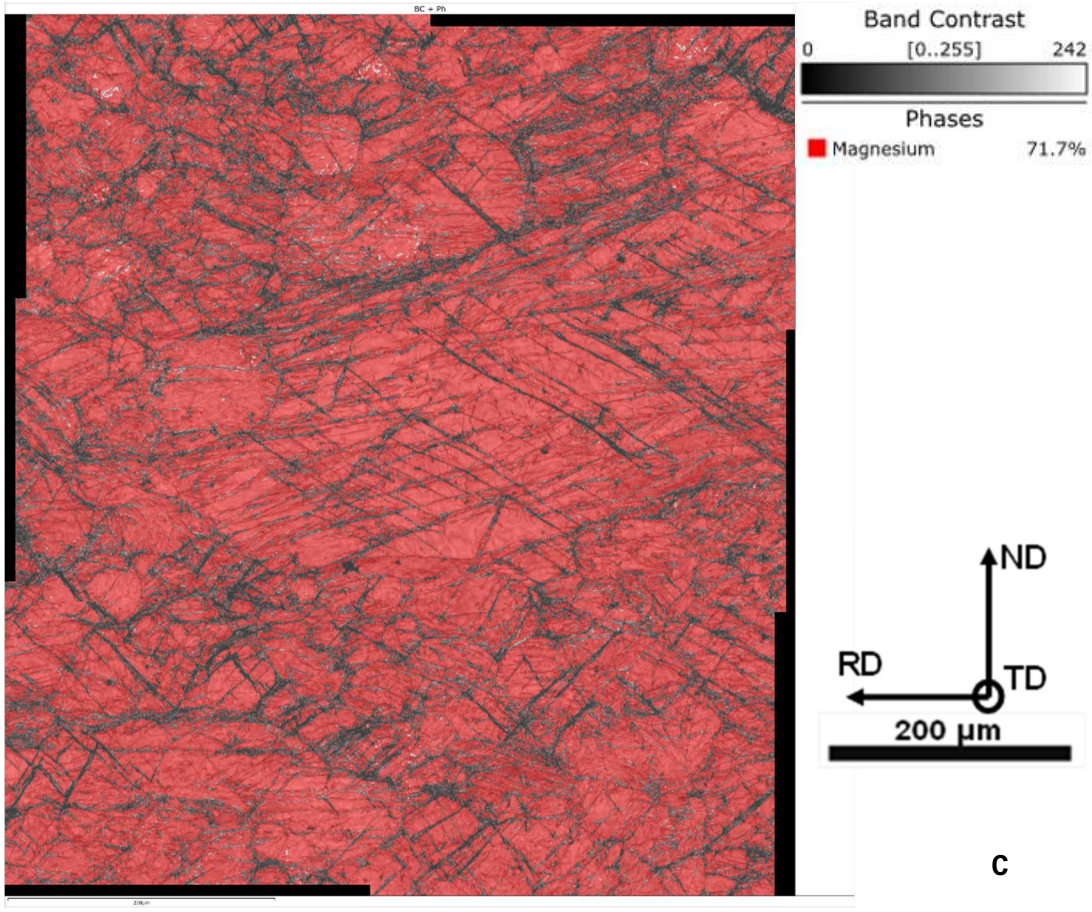
BC + Ph
Band Contrast
0 [0..255] 242
Phases
Magnesium 71.7%
ND
RD
TD
200 µm

c

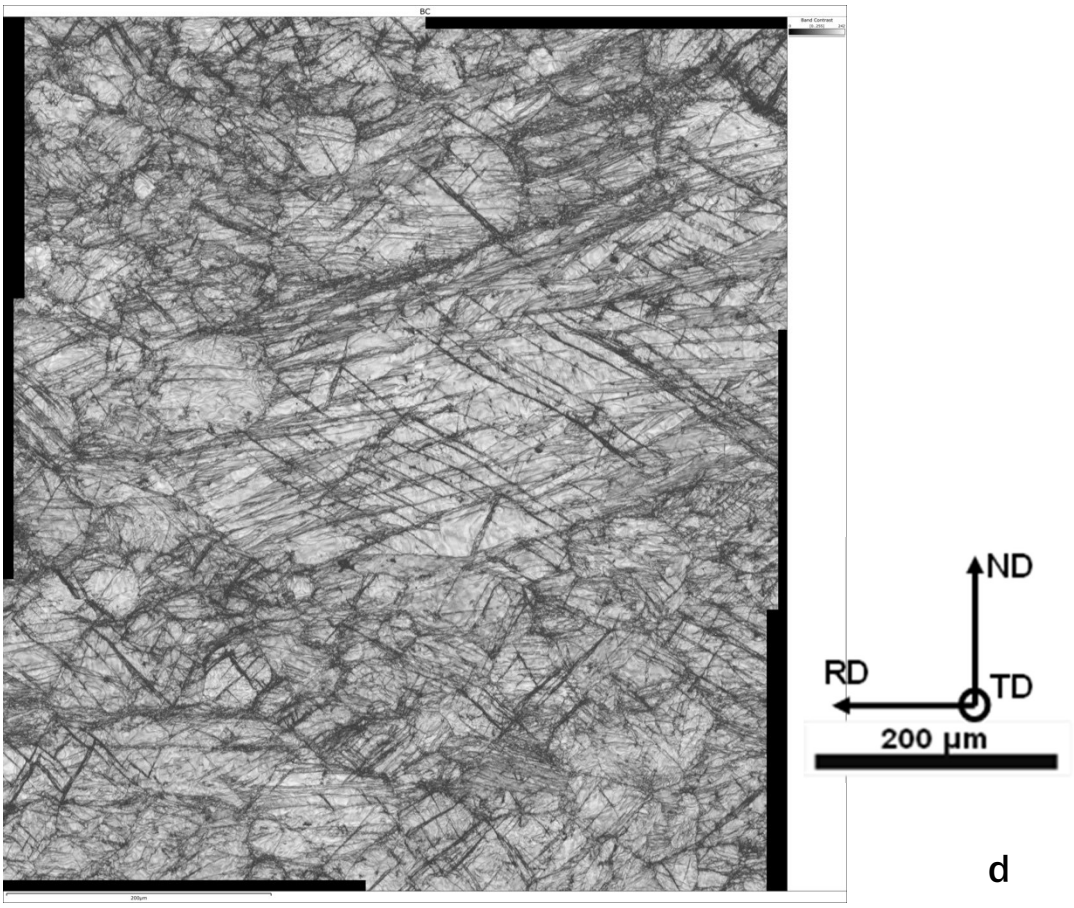
ND
RD
TD
200 µm
d

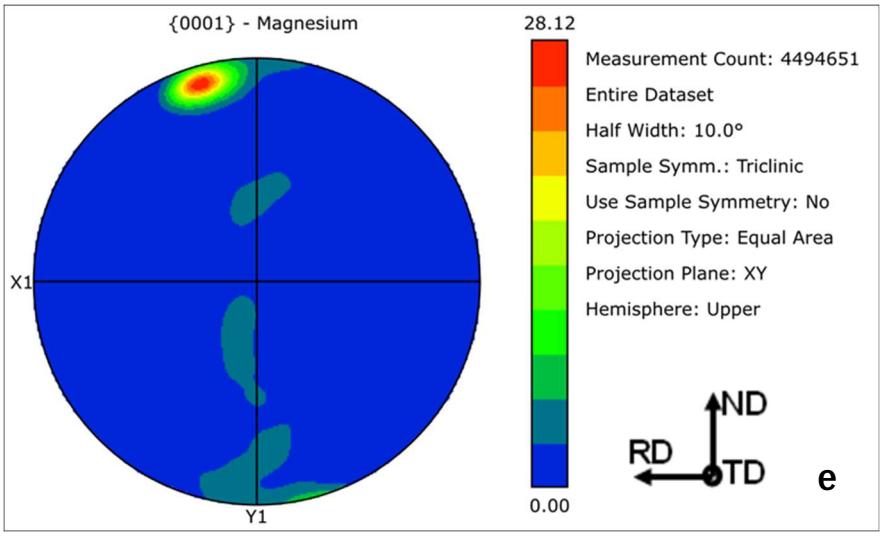
{0001} - Magnesium
28.12
0.00
X1
Y1
Measurement Count: 4494651
Entire Dataset
Half Width: 10.0°
Sample Symm.: Triclinic
Use Sample Symmetry: No
Projection Type: Equal Area
Projection Plane: XY
Hemisphere: Upper
ND
RD
TD
e

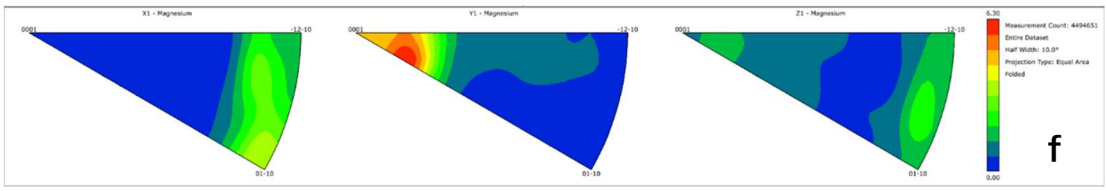
f

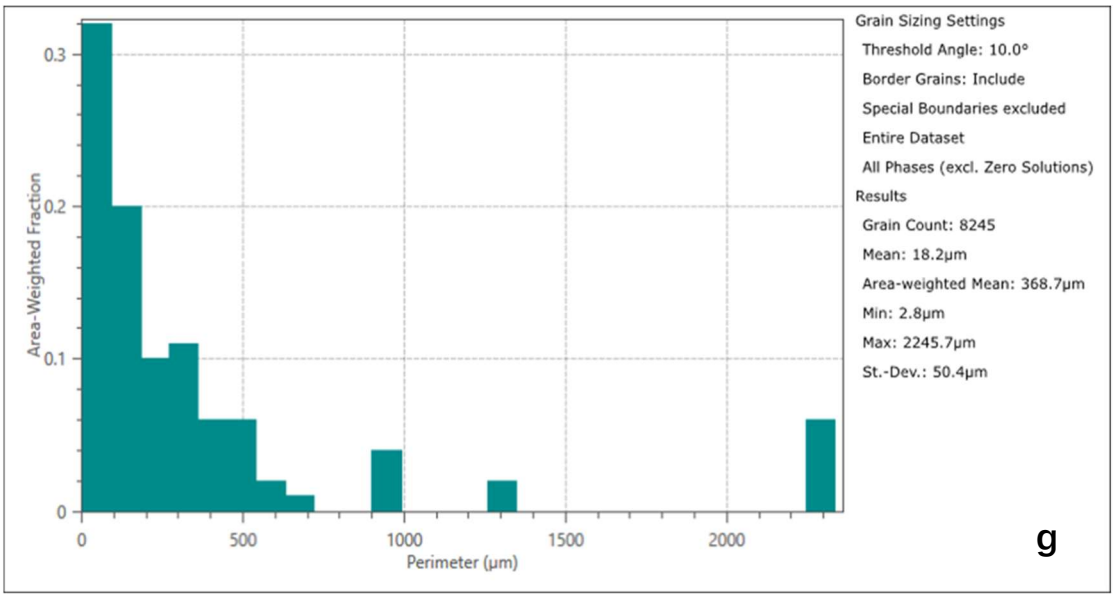

Figure A1-3 The EBSD result of the 135s annealed 1D compressed Mg-0.2Ca-0.3Zn specimen: (a) The inverse pole figure map and grain boundaries, (b) The grain boundaries and the special grain boundaries, (c) The band contrast and the phase analysis, (d) The band contrast, (e) The pole figure, (f) The inverse pole figures, (g) Grain size distribution expressed as grain boundary perimeter

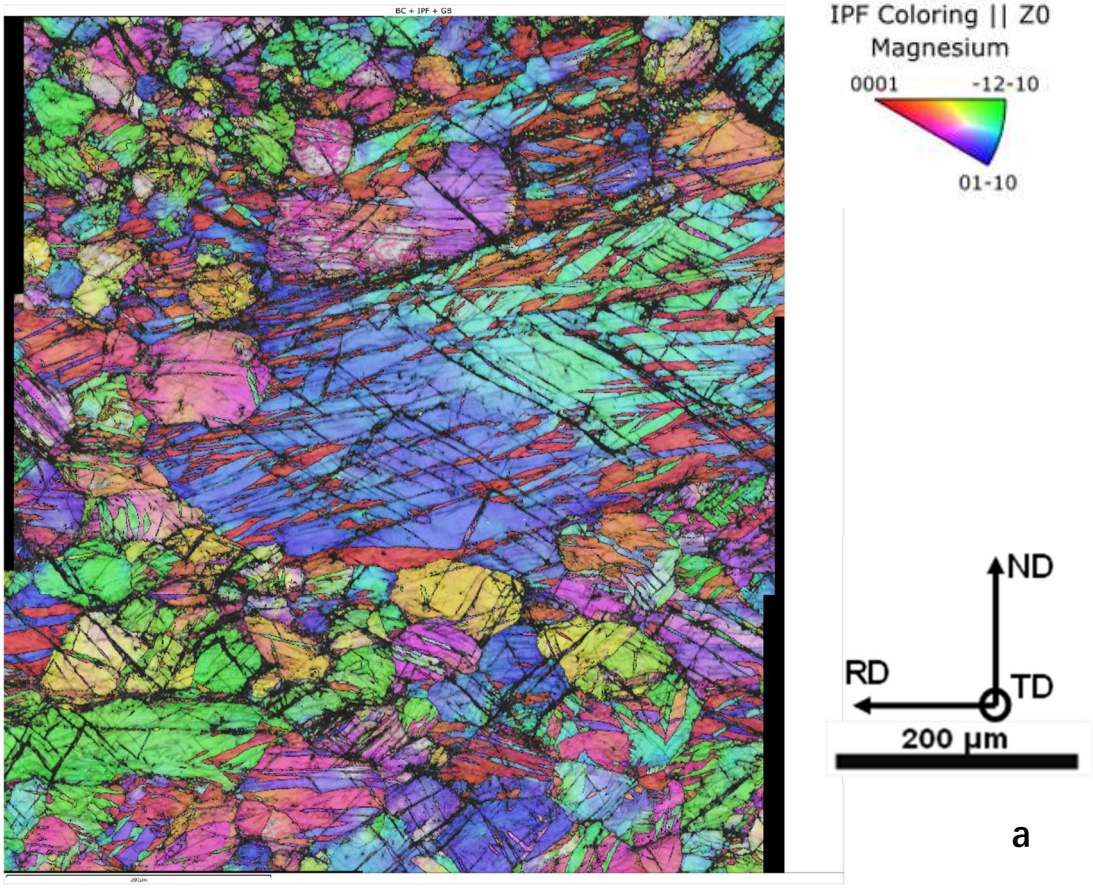

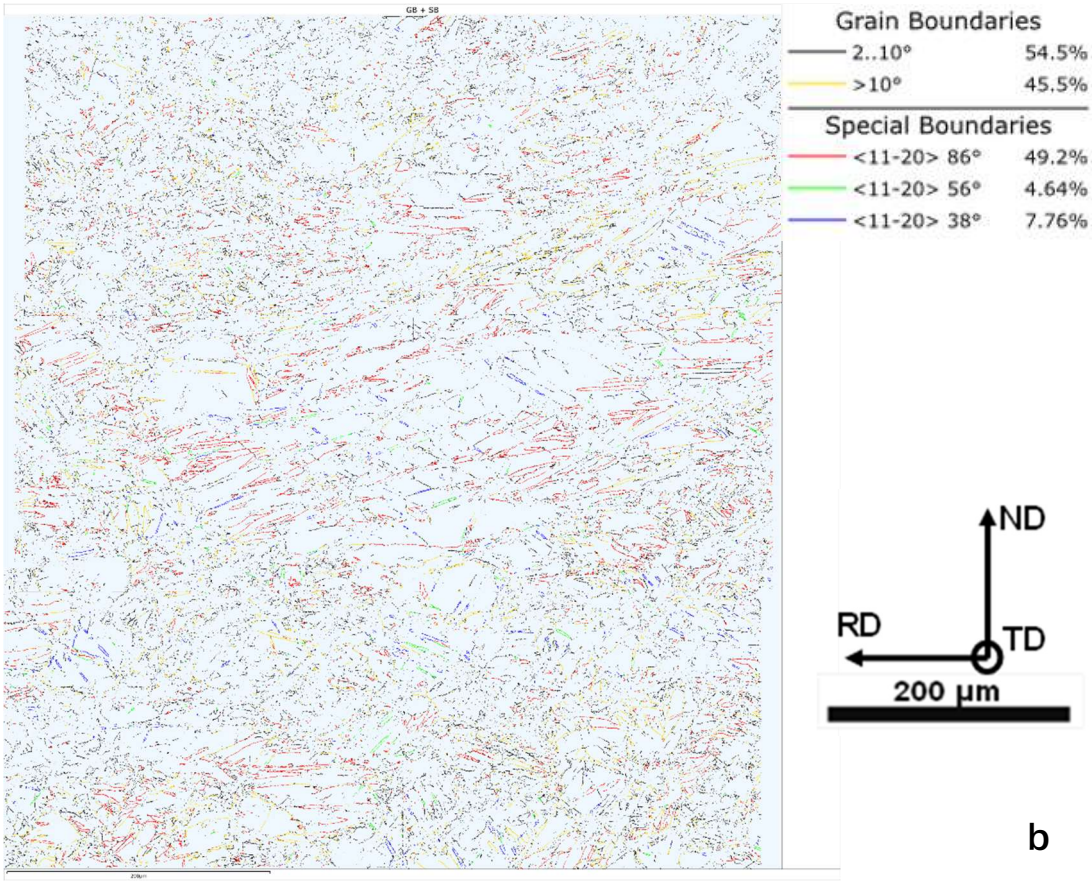
GB + S8
Grain Boundaries
2..10° 54.5%
>10° 45.5%
Special Boundaries
<11-20> 86° 49.2%
<11-20> 56° 4.64%
<11-20> 38° 7.76%
ND
RD
TD
200 µm

b

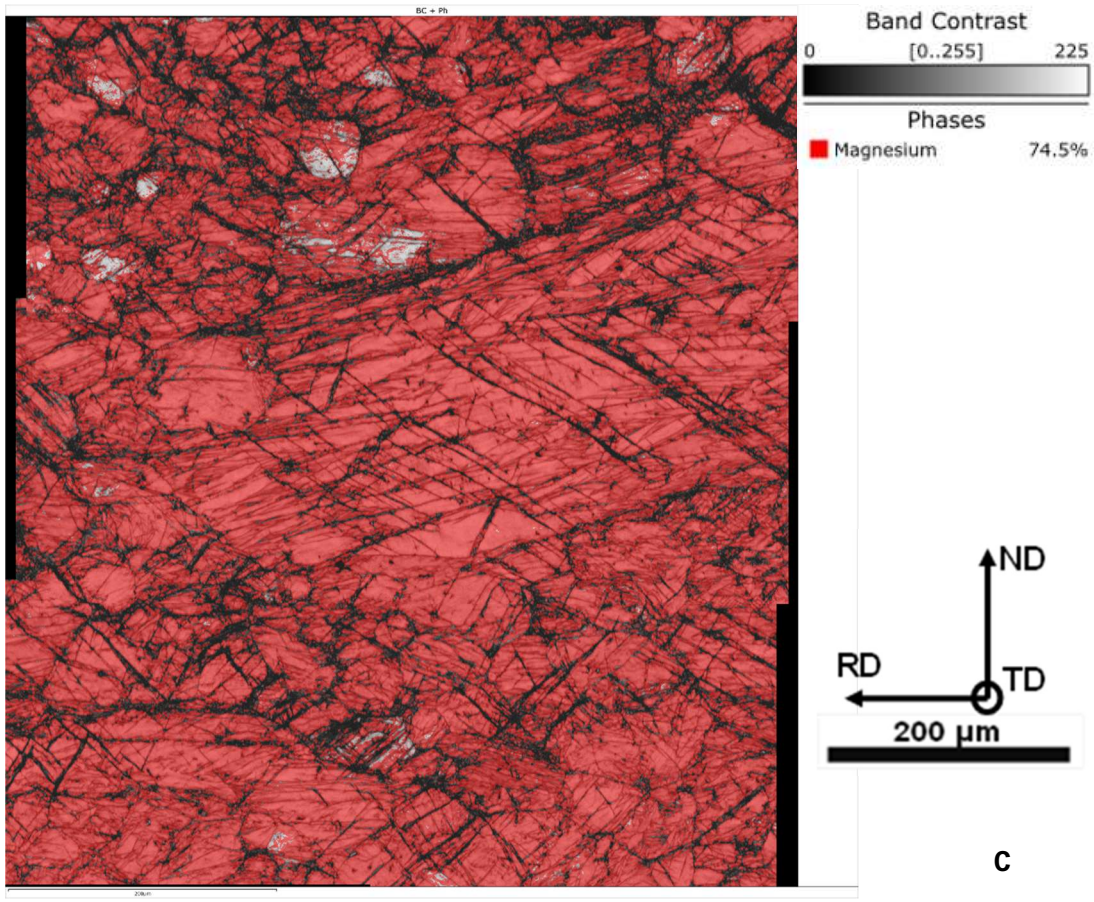
BC + Ph
Band Contrast
0 [0..255] 225
Phases
Magnesium 74.5%
ND
RD
TD
200 µm

c

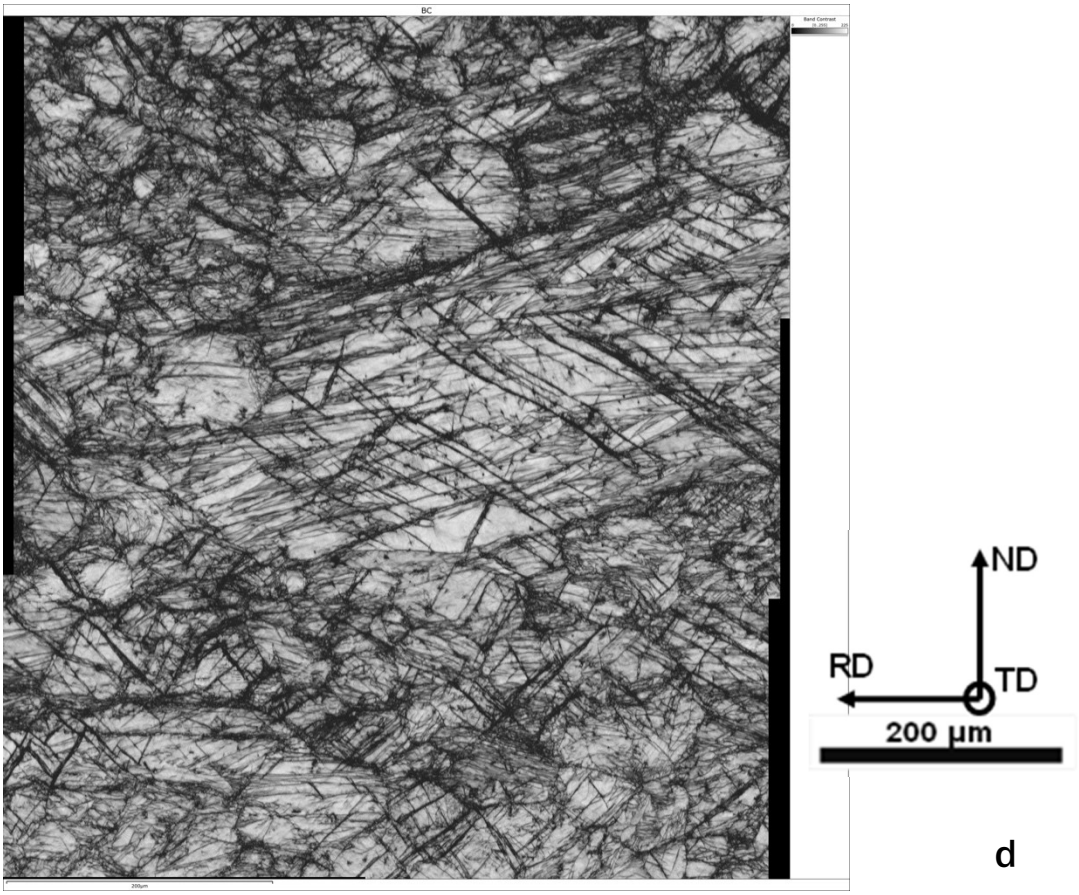
BC
ND
RD
TD
200 µm

d

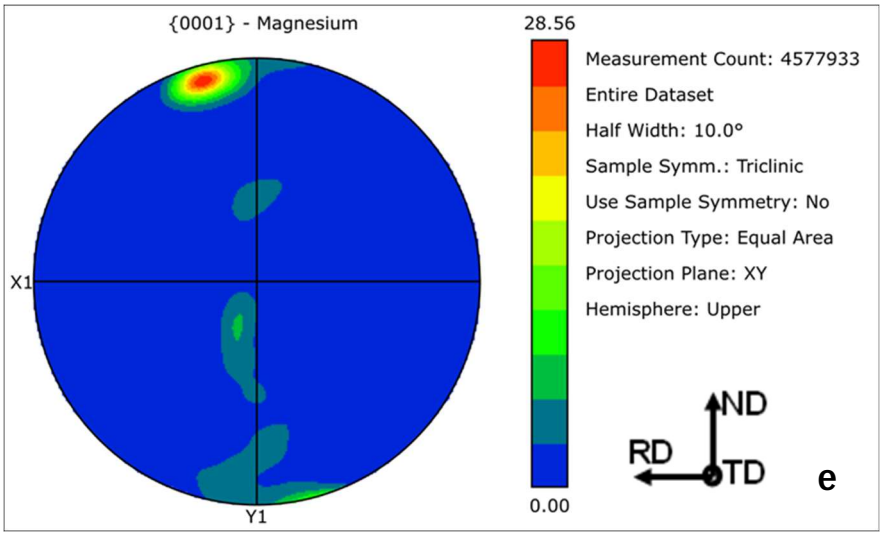
{0001} - Magnesium
28.56
0.00
X1
Y1
Measurement Count: 4577933
Entire Dataset
Half Width: 10.0°
Sample Symm.: Triclinic
Use Sample Symmetry: No
Projection Type: Equal Area
Projection Plane: XY
Hemisphere: Upper
ND
RD
TD

e

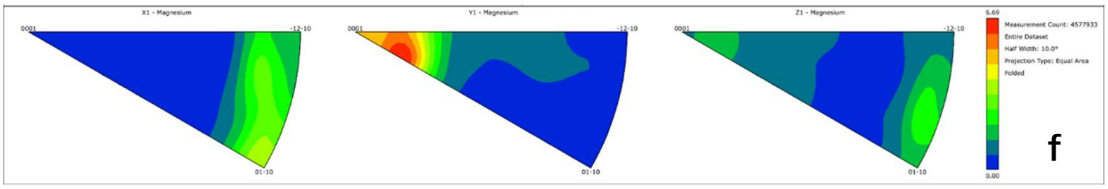

f

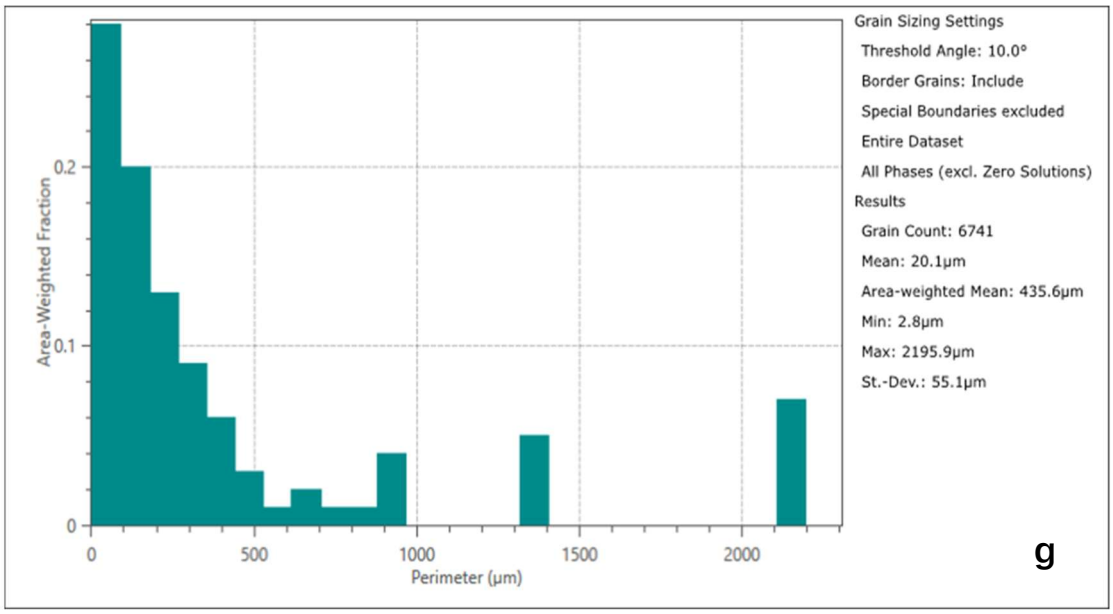

Figure A1-4 The EBSD result of the 210s annealed 1D compressed Mg-0.2Ca-0.3Zn specimen: (a) The inverse pole figure map and grain boundaries, (b) The grain boundaries and the special grain boundaries, (c) The band contrast and the phase analysis, (d) The band contrast, (e) The pole figure, (f) The inverse pole figures, (g) Grain size distribution expressed as grain boundary perimeter

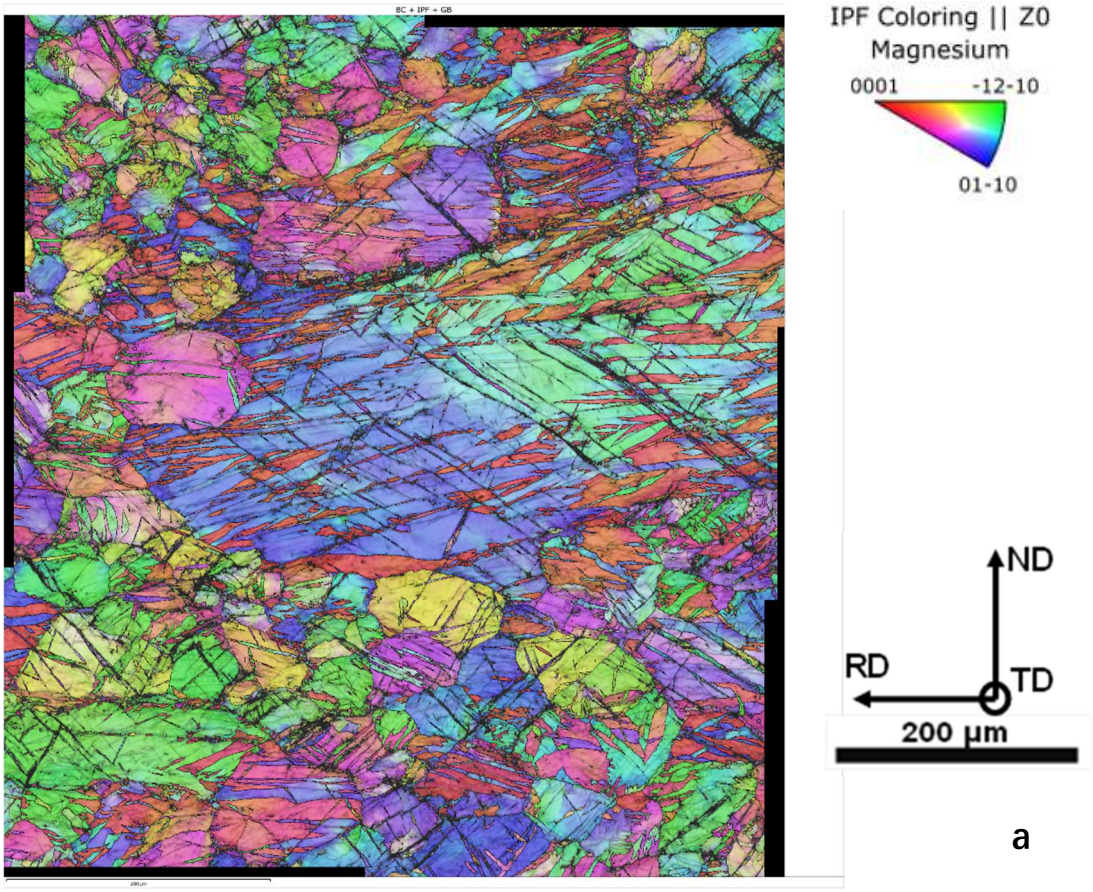

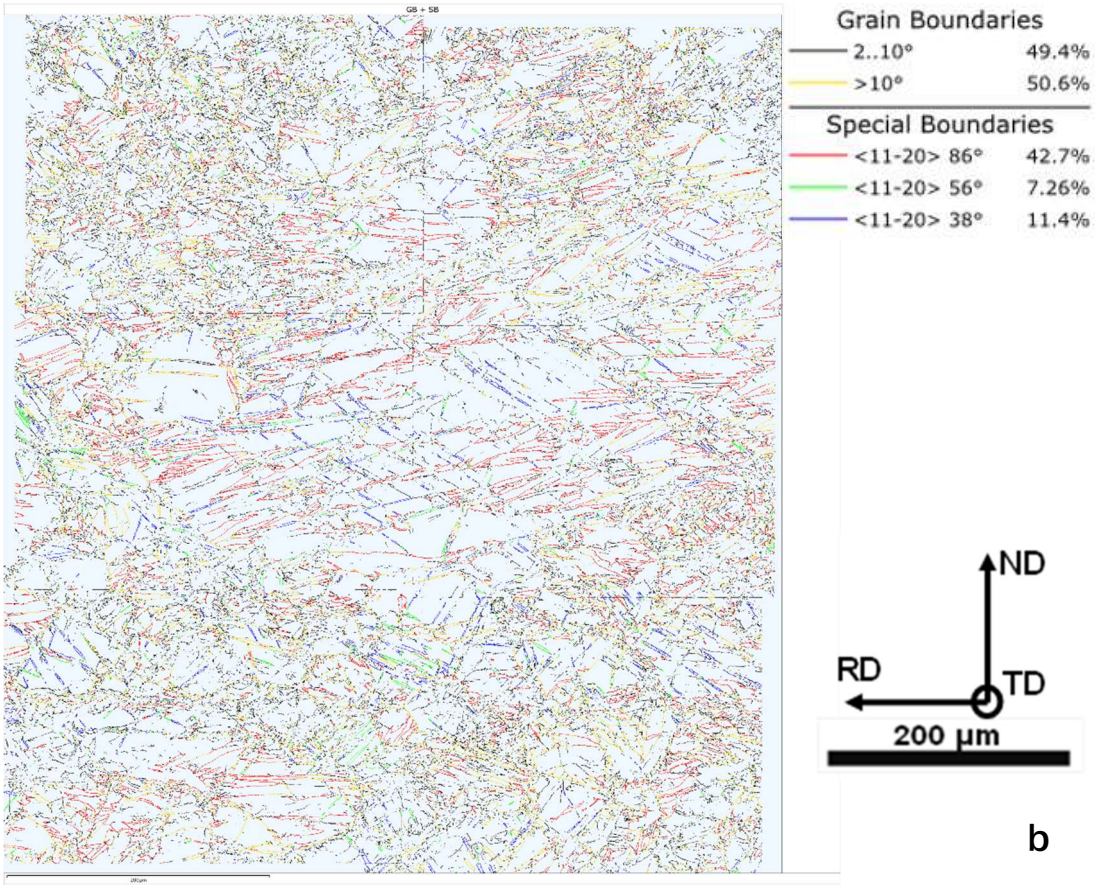
GB + SB
Grain Boundaries
2..10° 49.4%
>10° 50.6%
Special Boundaries
<11-20> 86° 42.7%
<11-20> 56° 7.26%
<11-20> 38° 11.4%
ND
RD
TD
200 µm

b

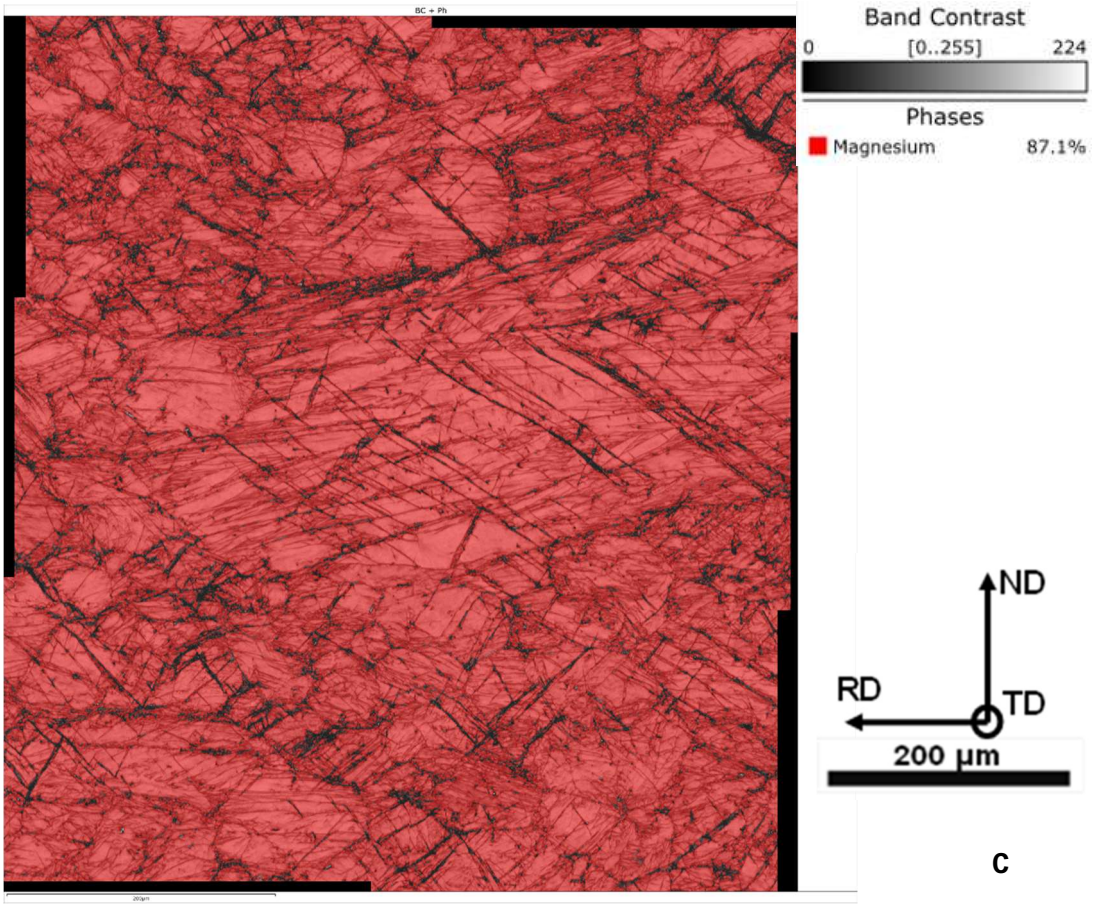
BC + Ph
Band Contrast
0 [0..255] 224
Phases
Magnesium 87.1%
ND
RD
TD
200 µm

c

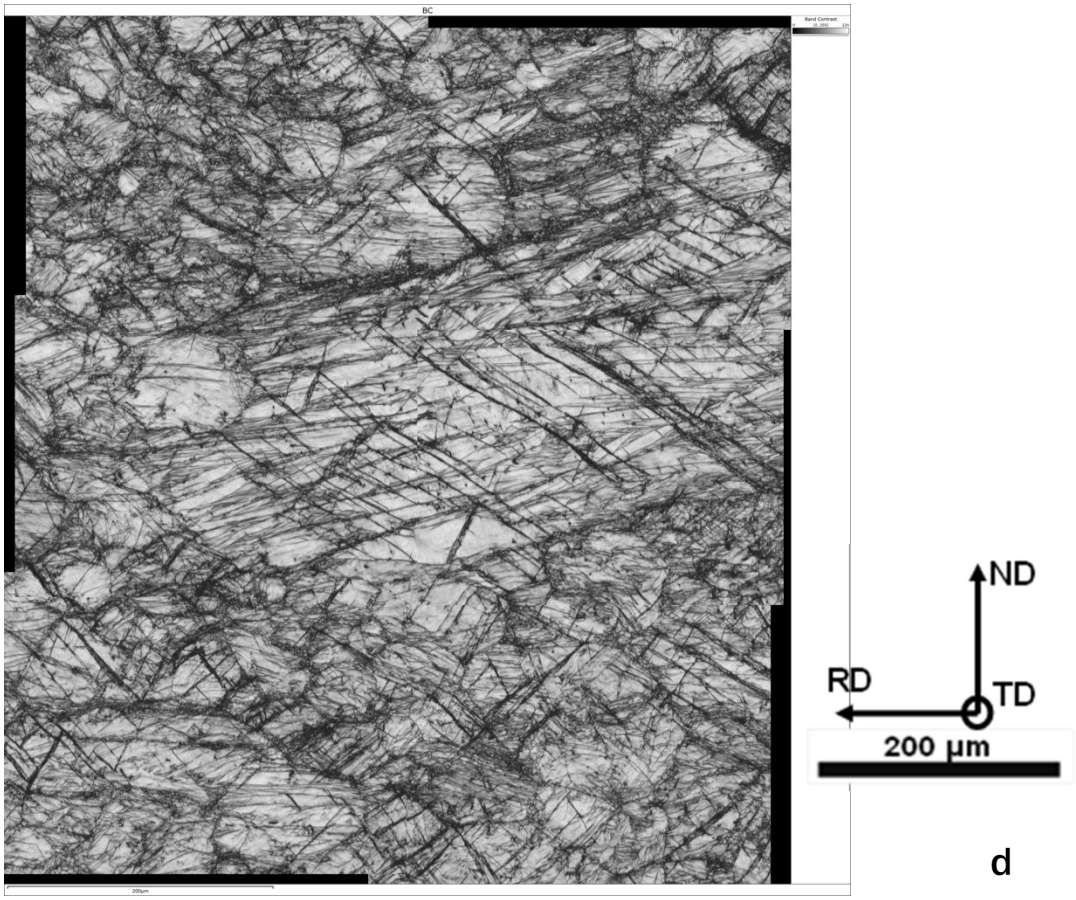
BC
ND
RD
TD
200 µm
d

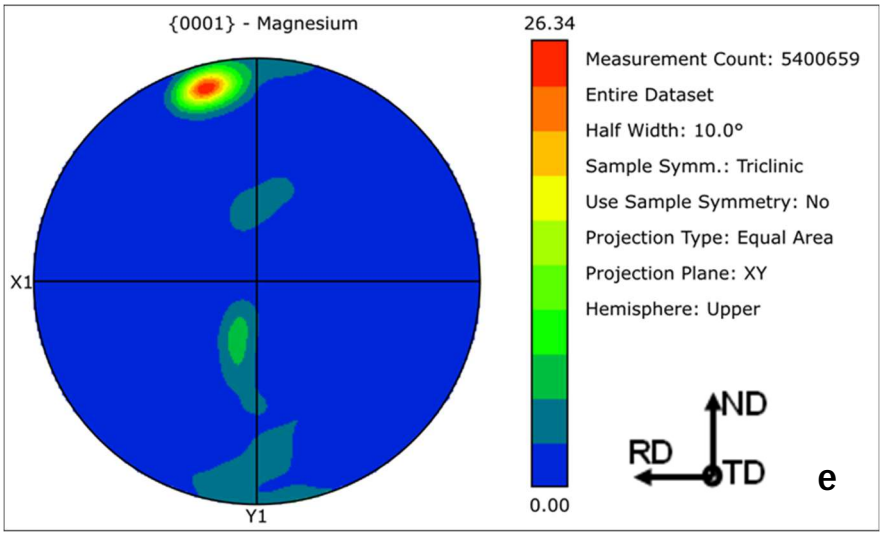
{0001} - Magnesium
26.34
Measurement Count: 5400659
Entire Dataset
Half Width: 10.0°
Sample Symm.: Triclinic
Use Sample Symmetry: No
Projection Type: Equal Area
Projection Plane: XY
Hemisphere: Upper
X1
Y1
0.00
ND
RD
TD
e

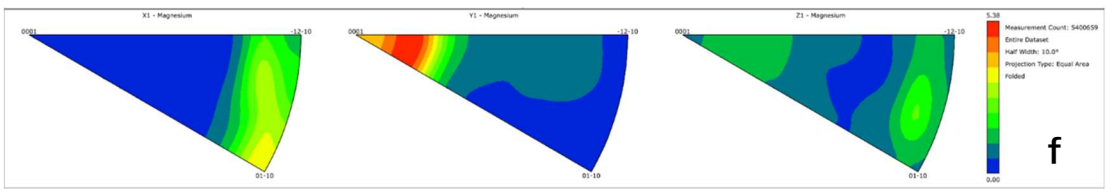
X1 - Magnesium
Y1 - Magnesium
Z1 - Magnesium
f

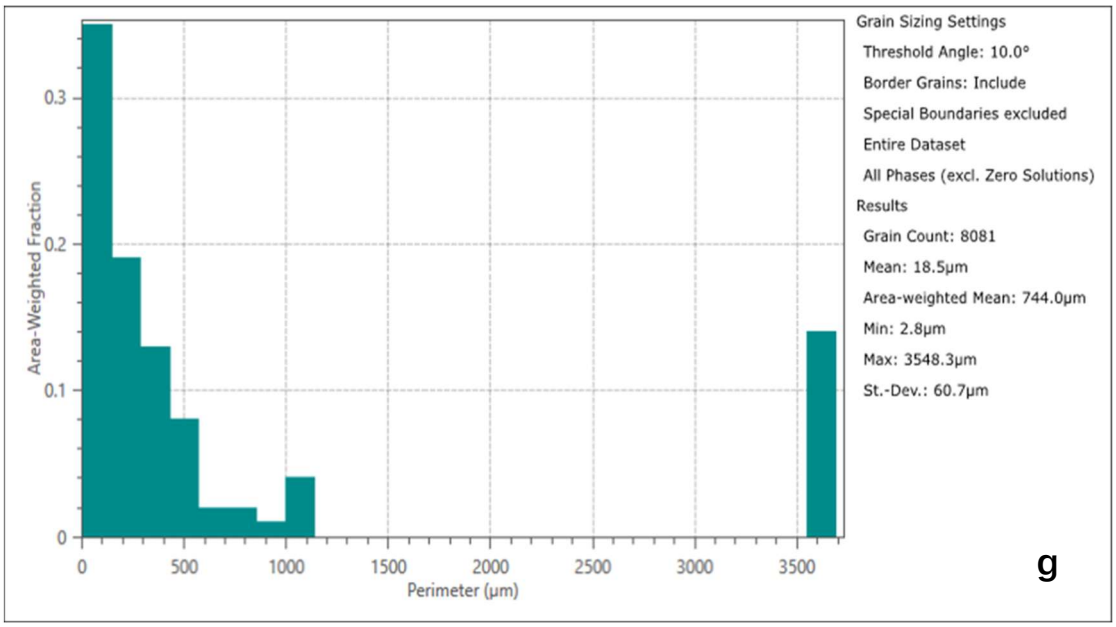

Figure A1-5 The EBSD result of the 300s annealed 1D compressed Mg-0.2Ca-0.3Zn specimen: (a) The inverse pole figure map and grain boundaries, (b) The grain boundaries and the special grain boundaries, (c) The band contrast and the phase analysis, (d) The band contrast, (e) The pole figure, (f) The inverse pole figures, (g) Grain size distribution expressed as grain boundary perimeter

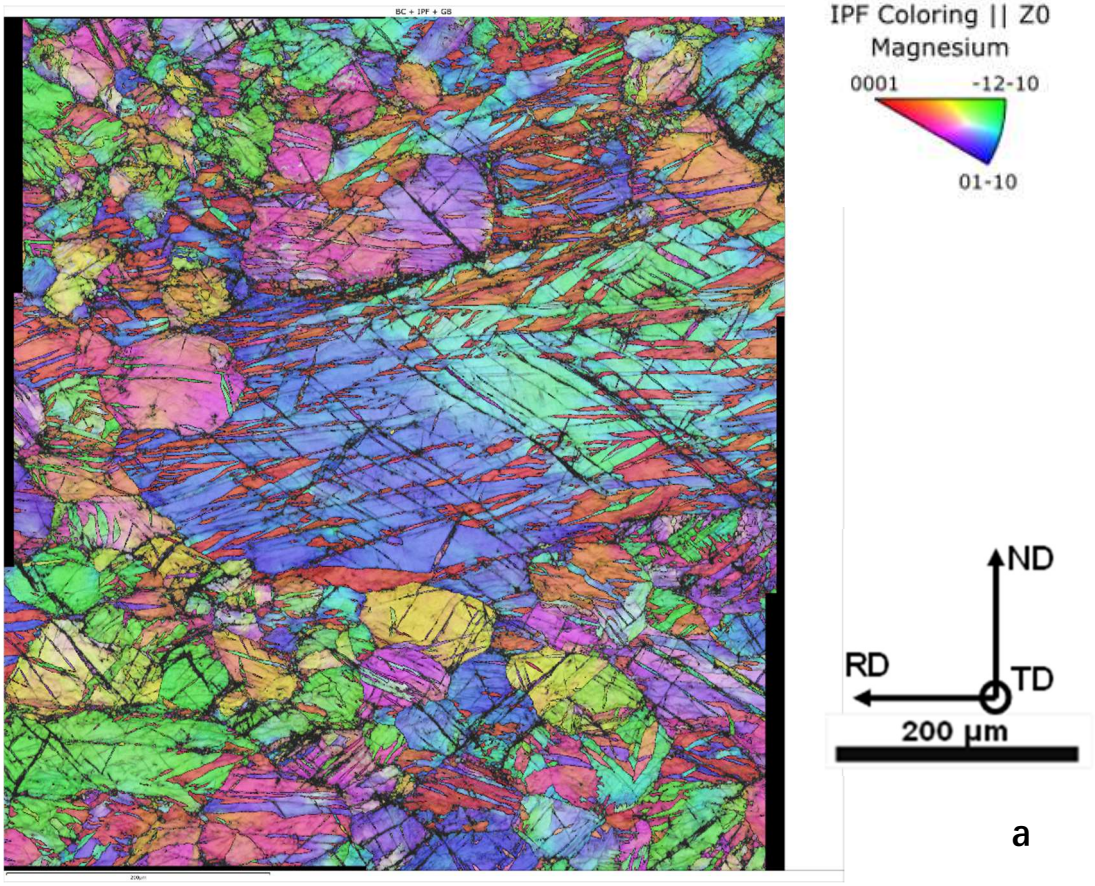

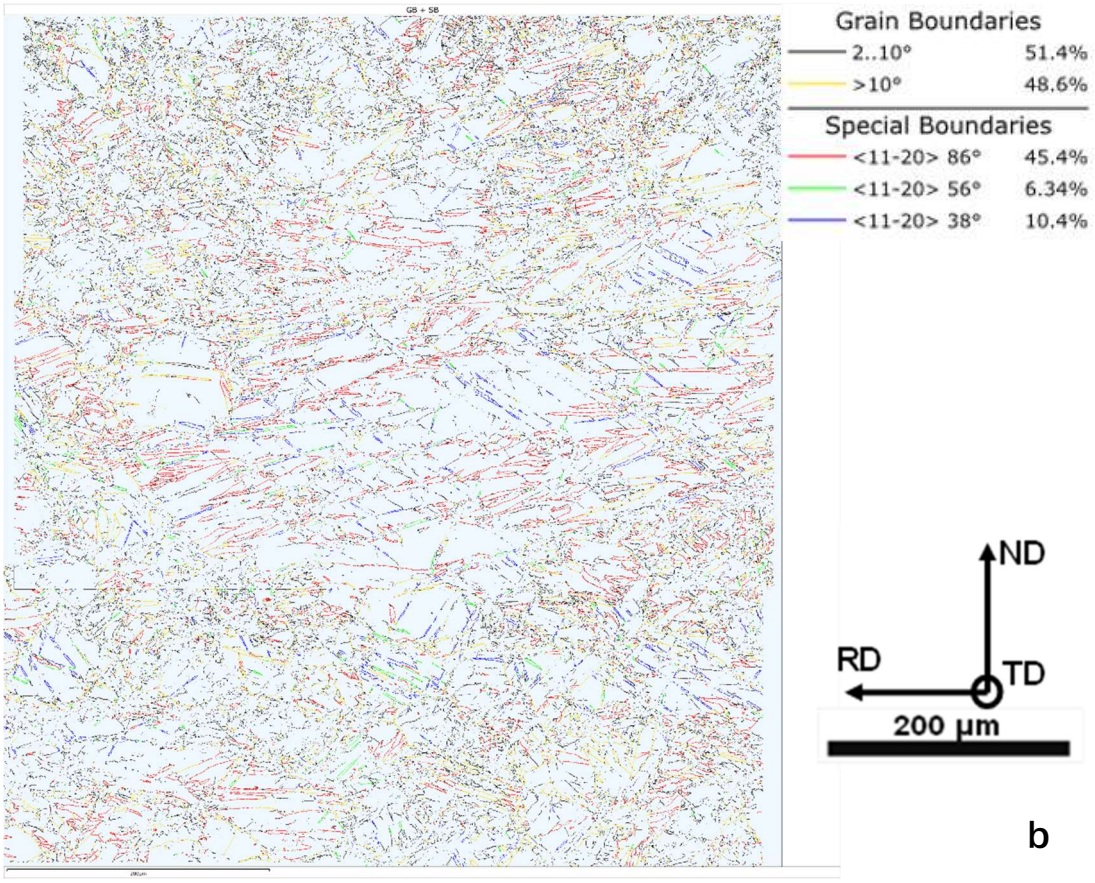
GB + SB
Grain Boundaries
2..10° 51.4%
>10° 48.6%
Special Boundaries
<11-20> 86° 45.4%
<11-20> 56° 6.34%
<11-20> 38° 10.4%
ND
RD
TD
200 µm

b

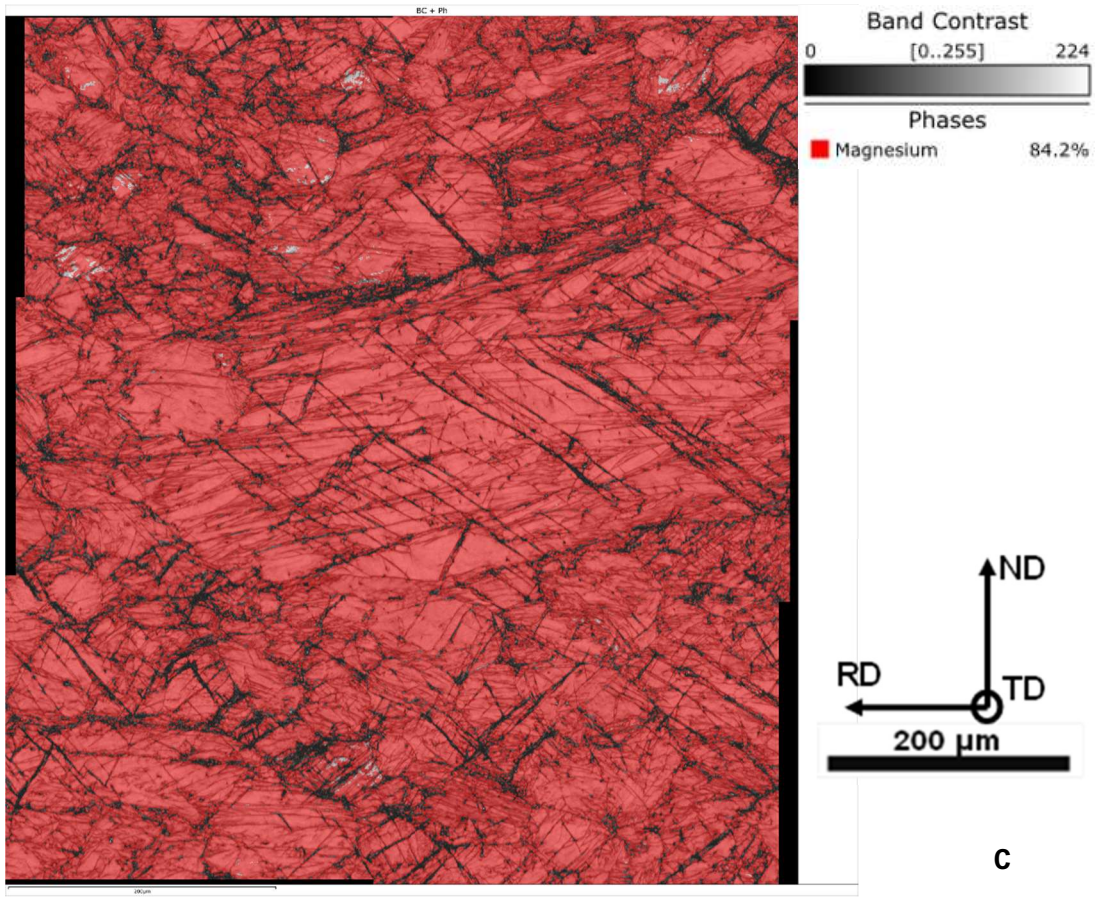
BC + Ph
Band Contrast
0 [0..255] 224
Phases
Magnesium 84.2%
ND
RD
TD
200 µm

c

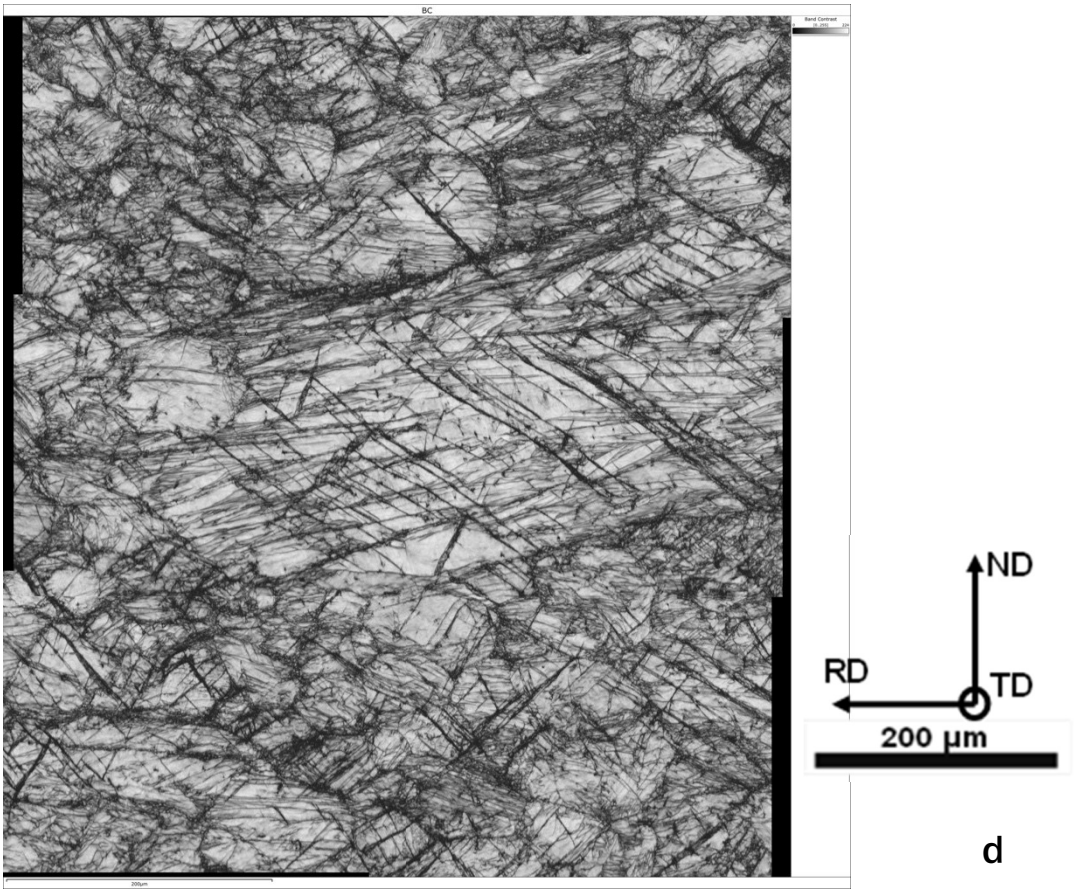
BC
ND
RD
TD
200 µm

d

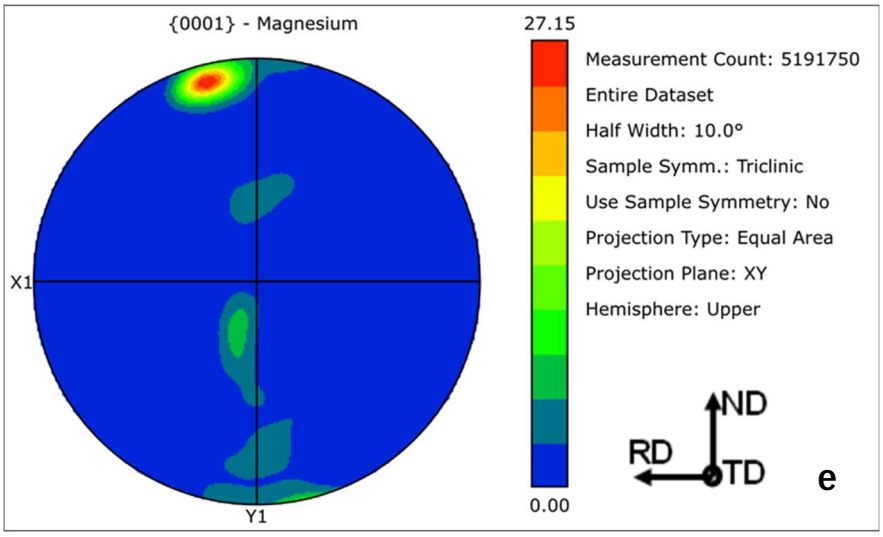
{0001} - Magnesium
27.15
0.00
X1
Y1
Measurement Count: 5191750
Entire Dataset
Half Width: 10.0°
Sample Symm.: Triclinic
Use Sample Symmetry: No
Projection Type: Equal Area
Projection Plane: XY
Hemisphere: Upper
ND
RD
TD

e

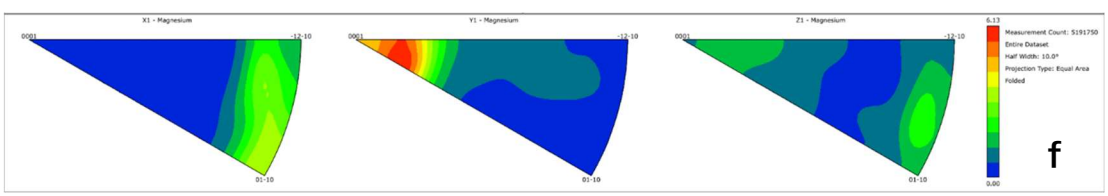
X1 - Magnesium
Y1 - Magnesium
Z1 - Magnesium
Measurement Count: 5191750
Entire Dataset
Half Width: 10.0°
Projection Type: Equal Area
Folded

f

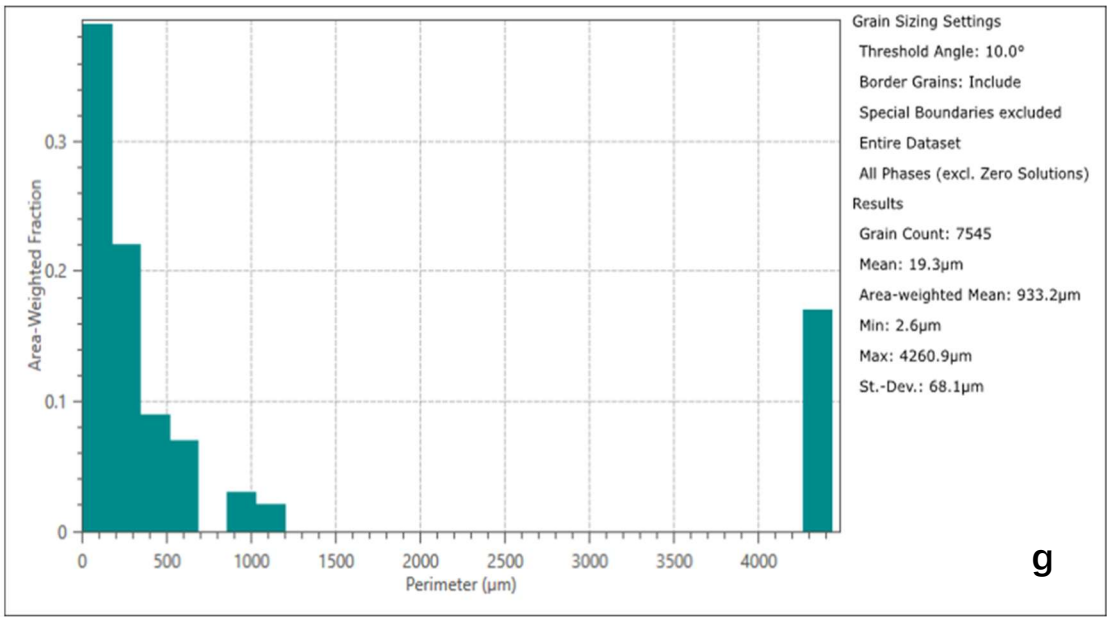

Figure A1-6 The EBSD result of the 420s annealed 1D compressed Mg-0.2Ca-0.3Zn specimen: (a) The inverse pole figure map and grain boundaries, (b) The grain boundaries and the special grain boundaries, (c) The band contrast and the phase analysis, (d) The band contrast, (e) The pole figure, (f) The inverse pole figures, (g) Grain size distribution expressed as grain boundary perimeter

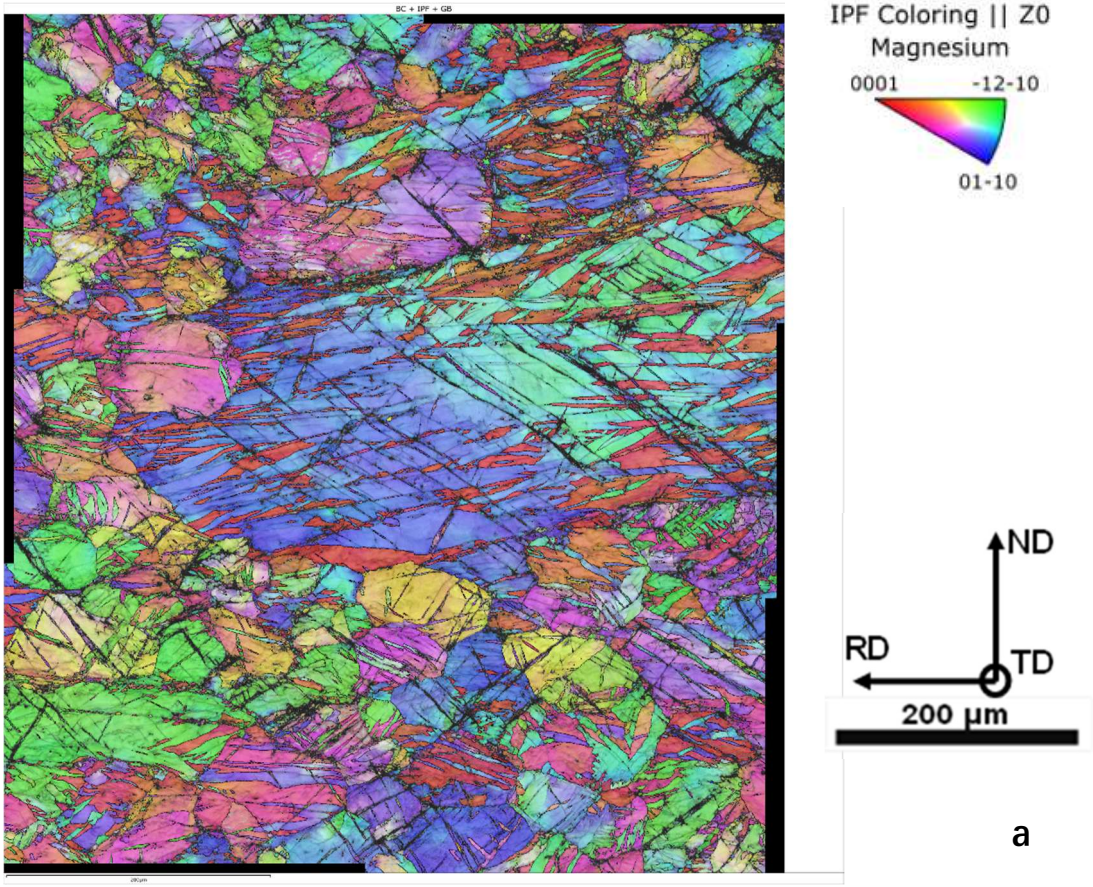

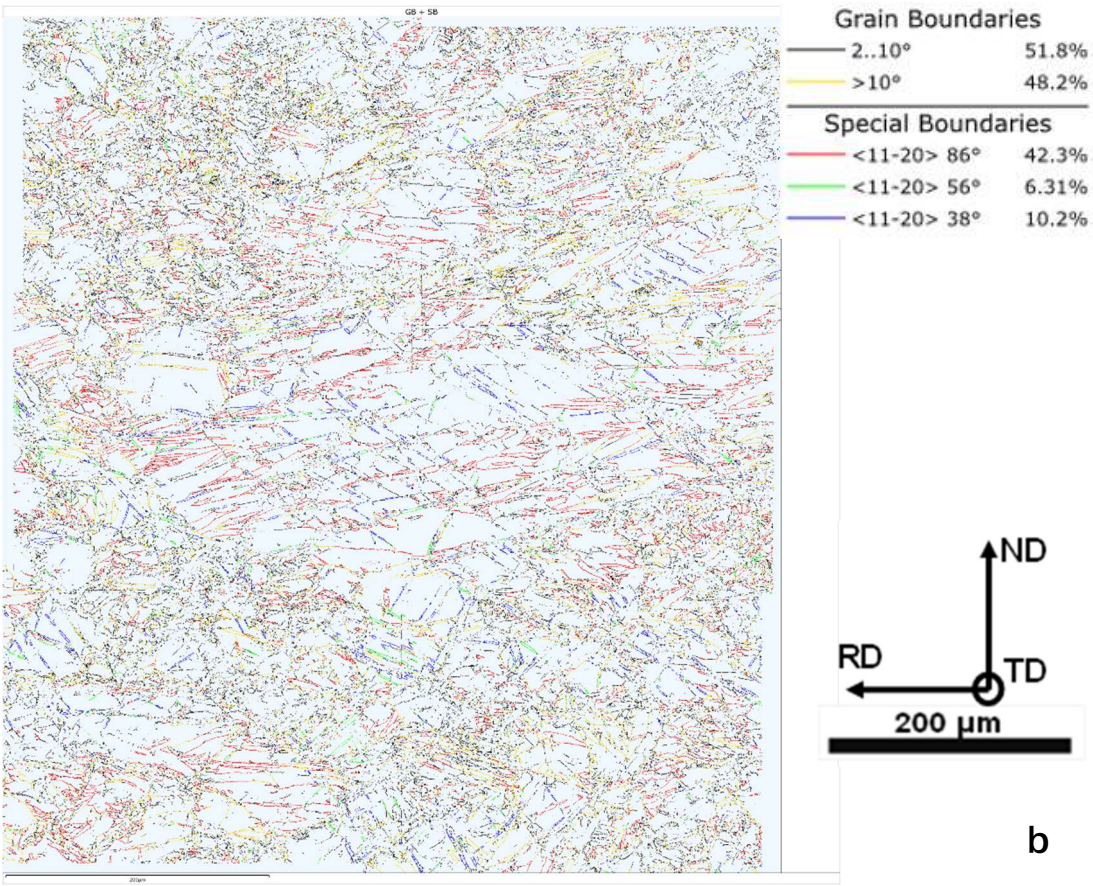
GB + SB
Grain Boundaries
2..10° 51.8%
>10° 48.2%
Special Boundaries
<11-20> 86° 42.3%
<11-20> 56° 6.31%
<11-20> 38° 10.2%
ND
RD
TD
200 µm

b

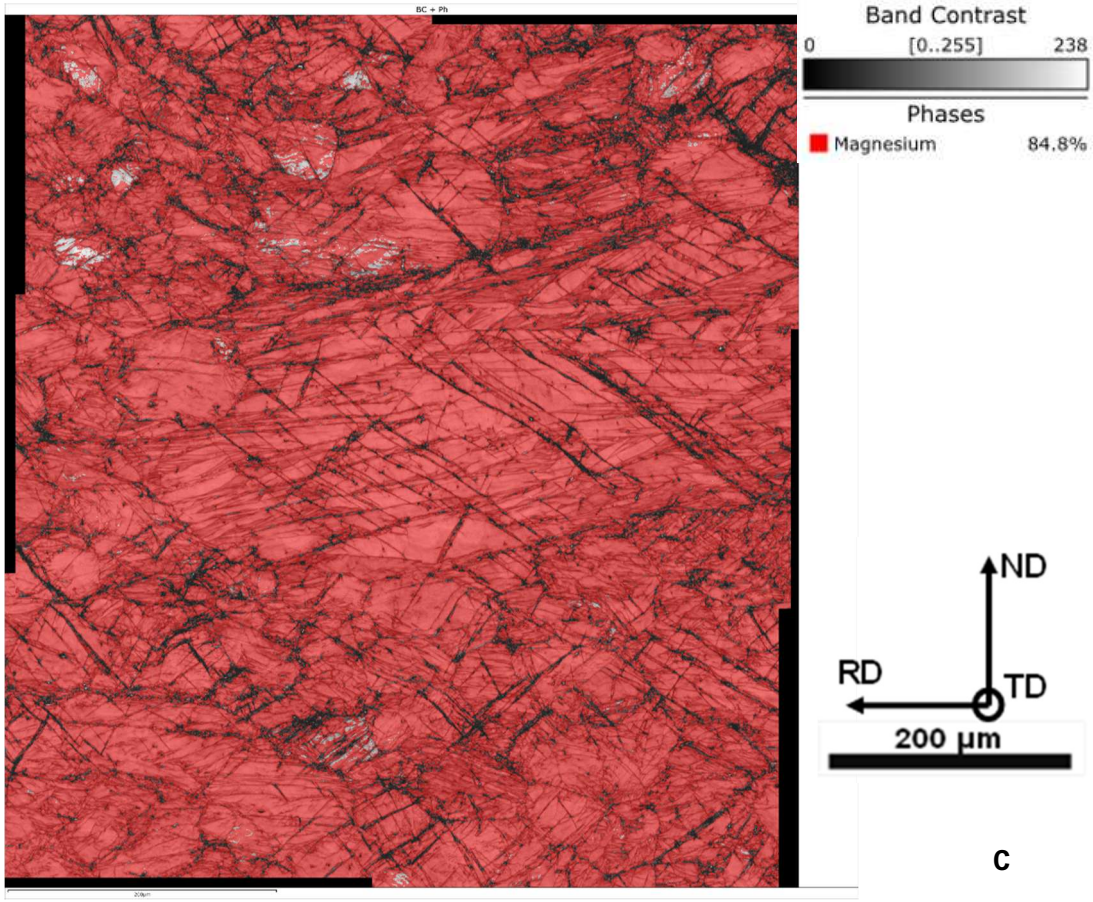
BC + Ph
Band Contrast
0 [0..255] 238
Phases
Magnesium 84.8%
ND
RD
TD
200 µm

c

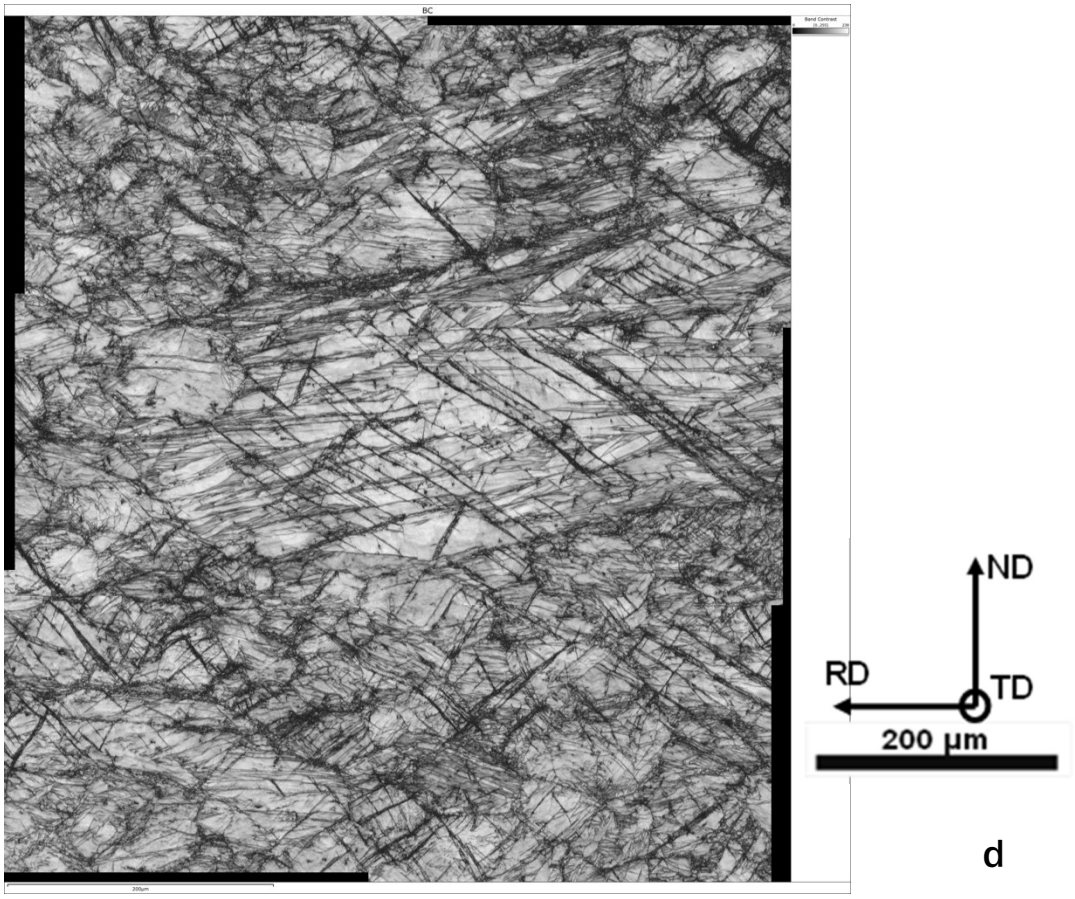
BC
ND
RD
TD
200 µm
d

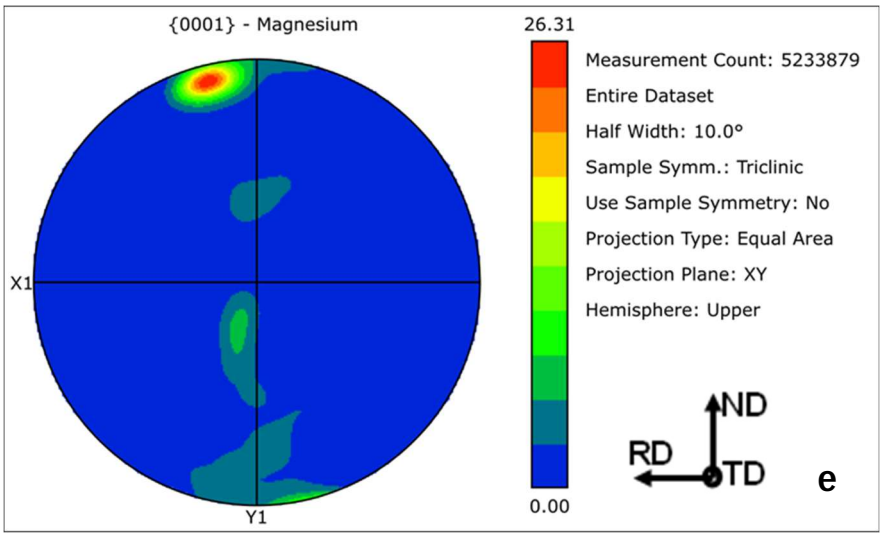
{0001} - Magnesium
26.31
Measurement Count: 5233879
Entire Dataset
Half Width: 10.0°
Sample Symm.: Triclinic
Use Sample Symmetry: No
Projection Type: Equal Area
Projection Plane: XY
Hemisphere: Upper
X1
Y1
0.00
ND
RD
TD
e

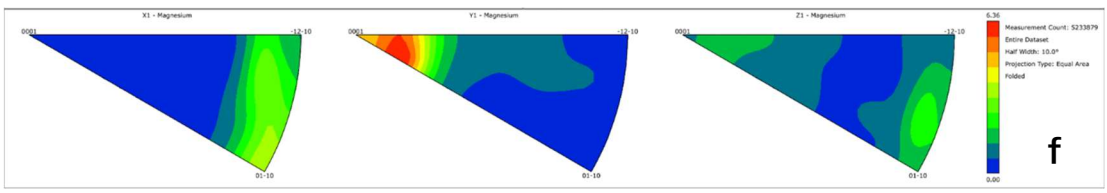
X1 - Magnesium
Y1 - Magnesium
Z1 - Magnesium
f

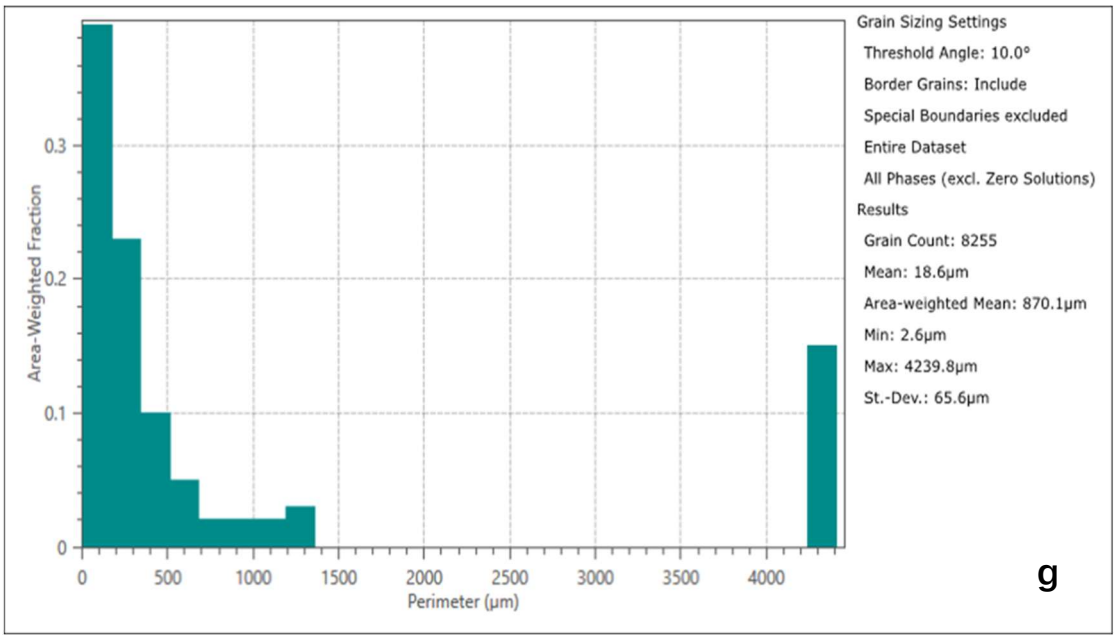

Figure A1-7 The EBSD result of the 570s annealed 1D compressed Mg-0.2Ca-0.3Zn specimen: (a) The inverse pole figure map and grain boundaries, (b) The grain boundaries and the special grain boundaries, (c) The band contrast and the phase analysis, (d) The band contrast, (e) The pole figure, (f) The inverse pole figures, (g) Grain size distribution expressed as grain boundary perimeter

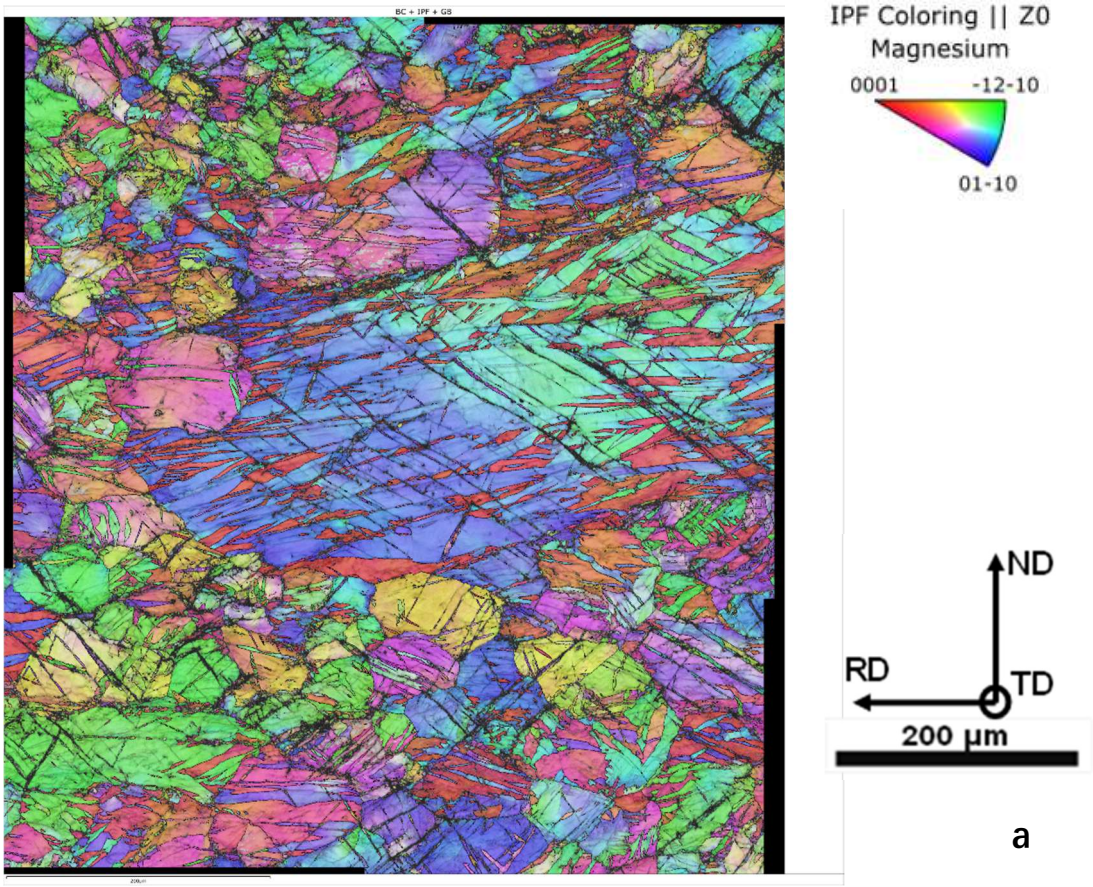

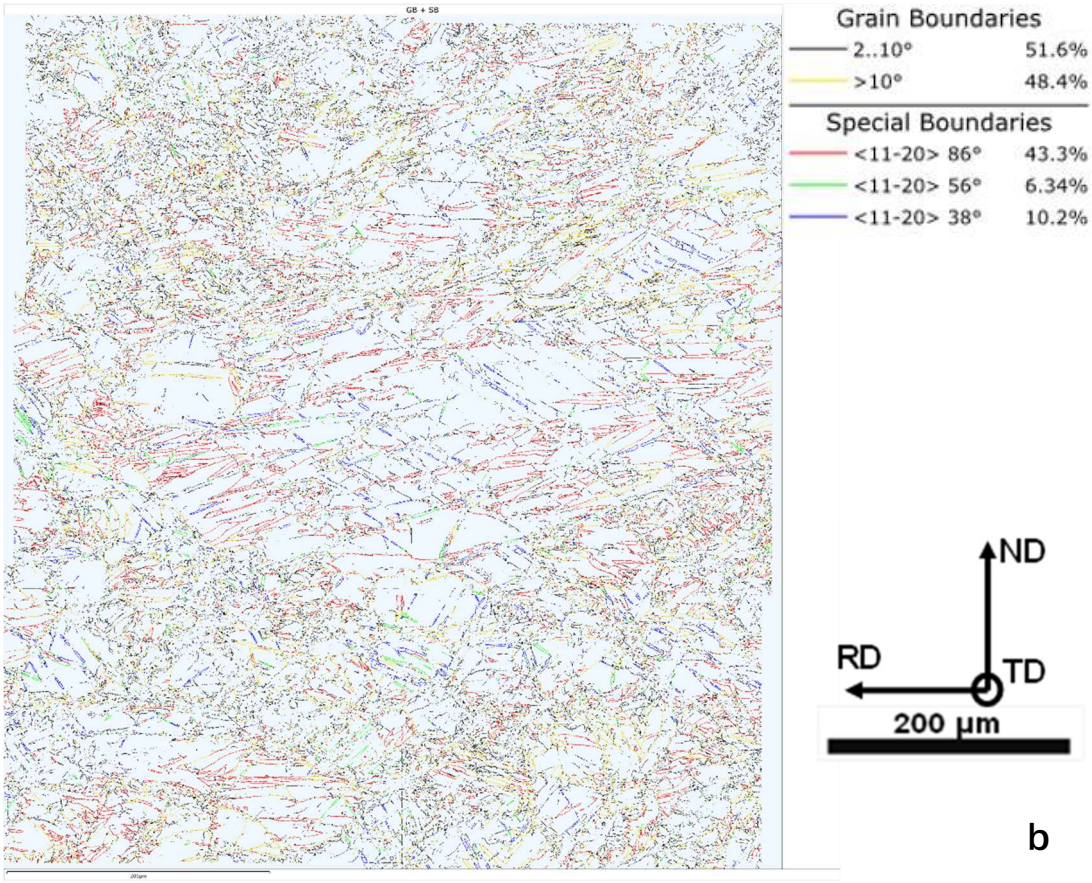
GB + SB
Grain Boundaries
2..10° 51.6%
>10° 48.4%
Special Boundaries
<11-20> 86° 43.3%
<11-20> 56° 6.34%
<11-20> 38° 10.2%
ND
RD
TD
200 µm

b

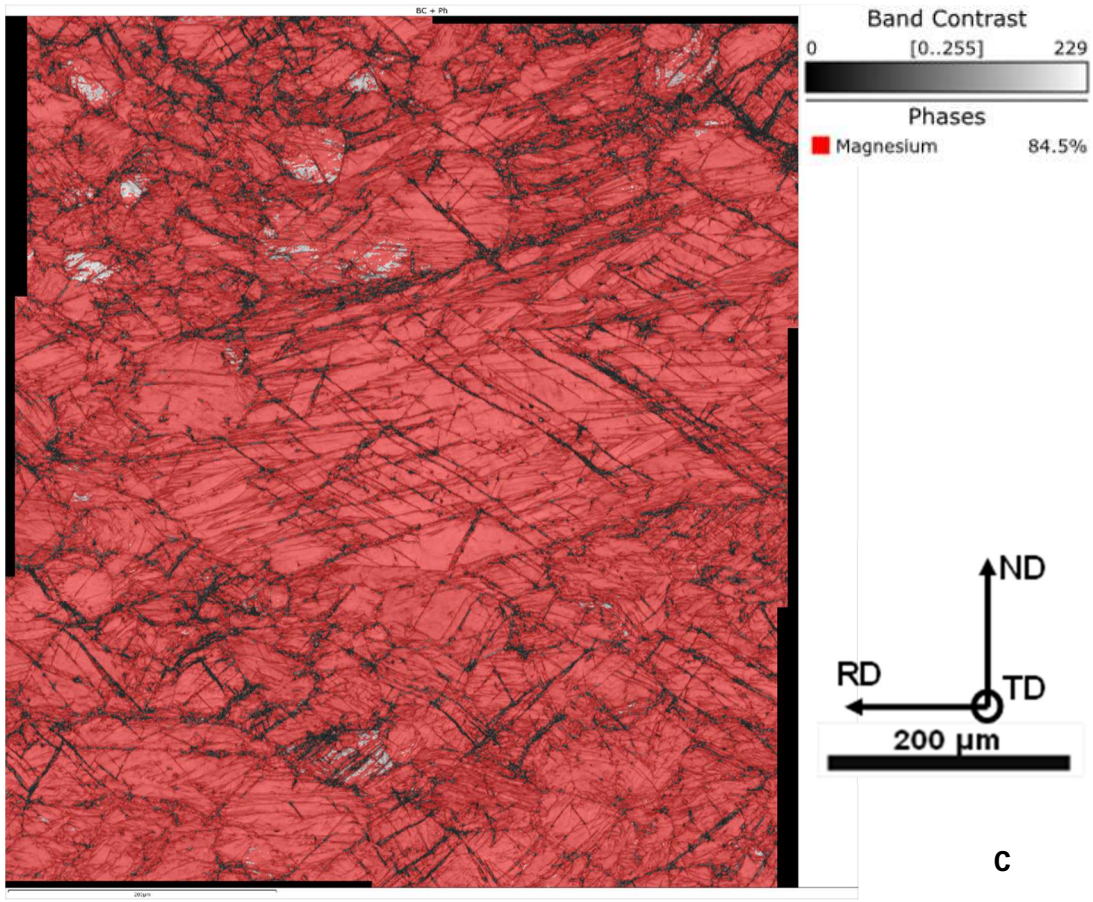
BC + Ph
Band Contrast
0 [0..255] 229
Phases
Magnesium 84.5%
ND
RD
TD
200 µm

c

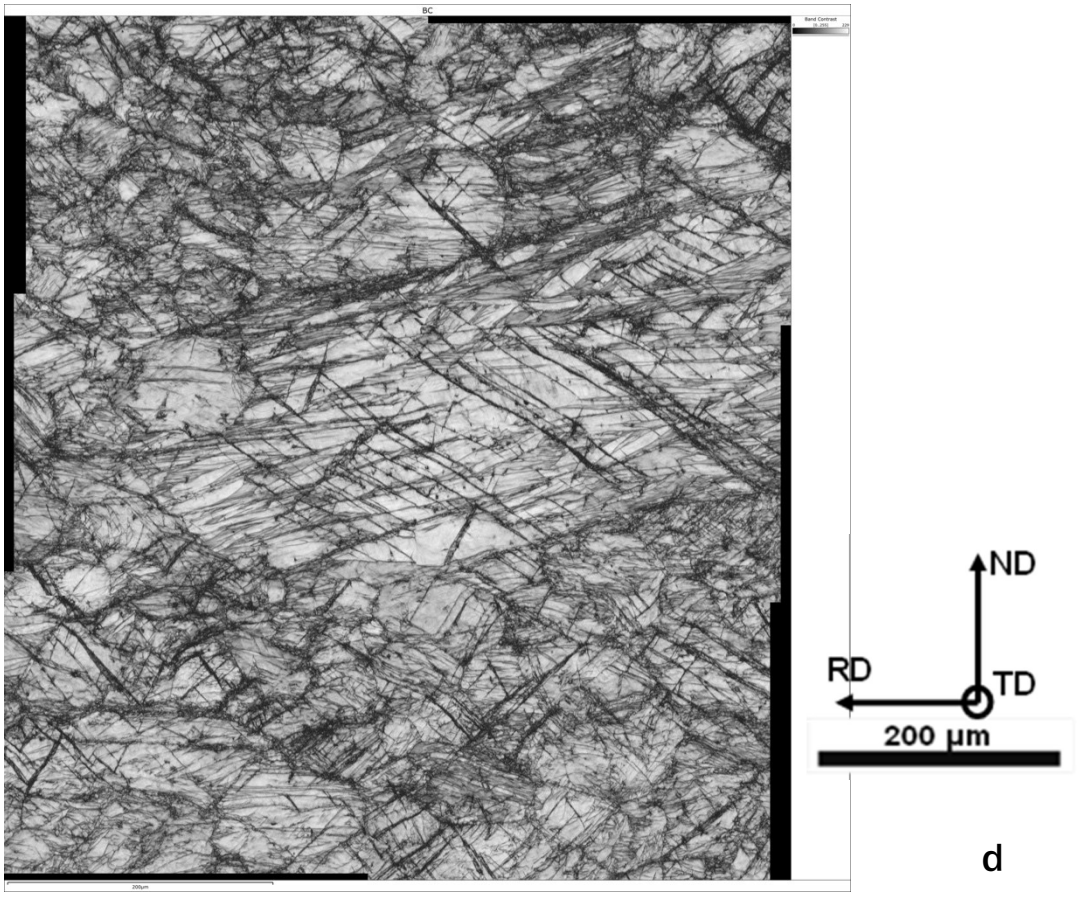
ND
RD
TD
200 µm
d

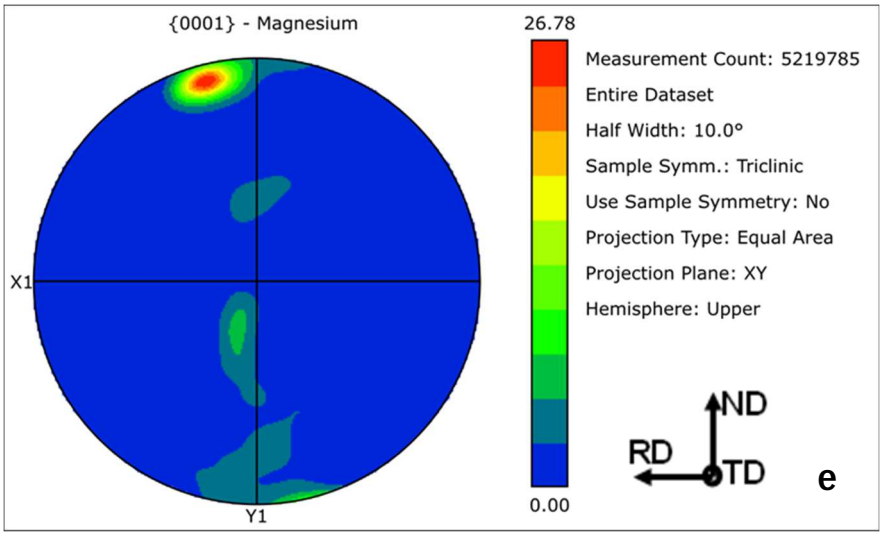
{0001} - Magnesium
26.78
Measurement Count: 5219785
Entire Dataset
Half Width: 10.0°
Sample Symm.: Triclinic
Use Sample Symmetry: No
Projection Type: Equal Area
Projection Plane: XY
Hemisphere: Upper
X1
Y1
0.00
ND
RD
TD
e

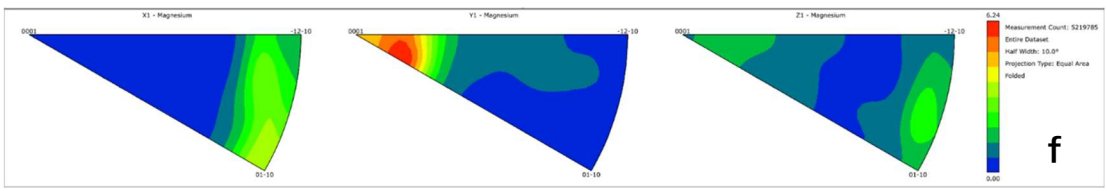
f

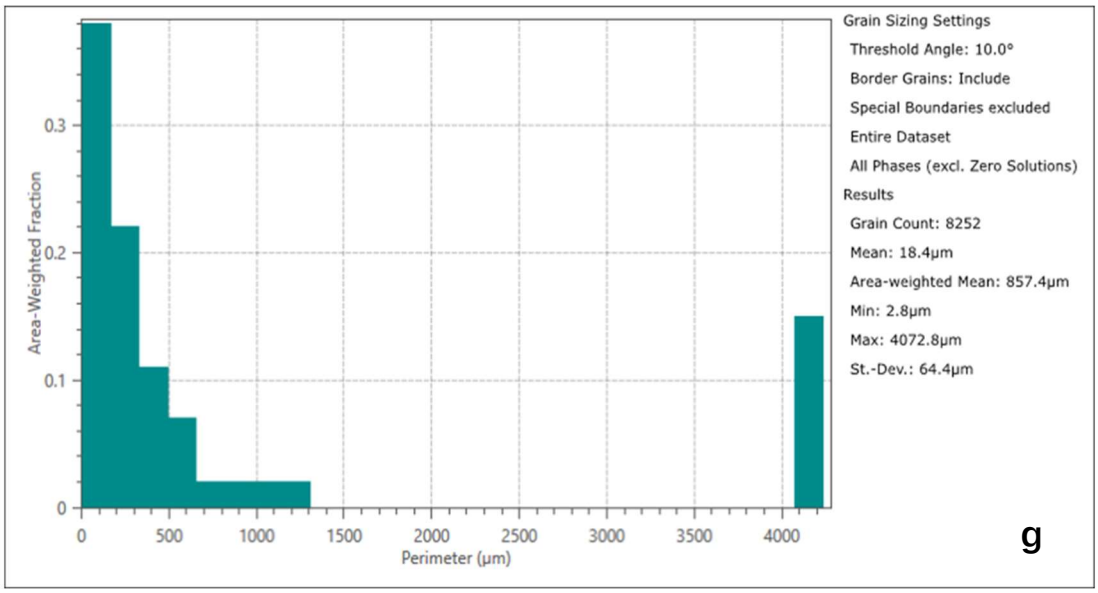

Figure A1-8 The EBSD result of the 750s annealed 1D compressed Mg-0.2Ca-0.3Zn specimen: (a) The inverse pole figure map and grain boundaries, (b) The grain boundaries and the special grain boundaries, (c) The band contrast and the phase analysis, (d) The band contrast, (e) The pole figure, (f) The inverse pole figures, (g) Grain size distribution expressed as grain boundary perimeter

A2 Channel die two-direction compressed Mg-0.2Ca-0.3Zn (at%) specimens

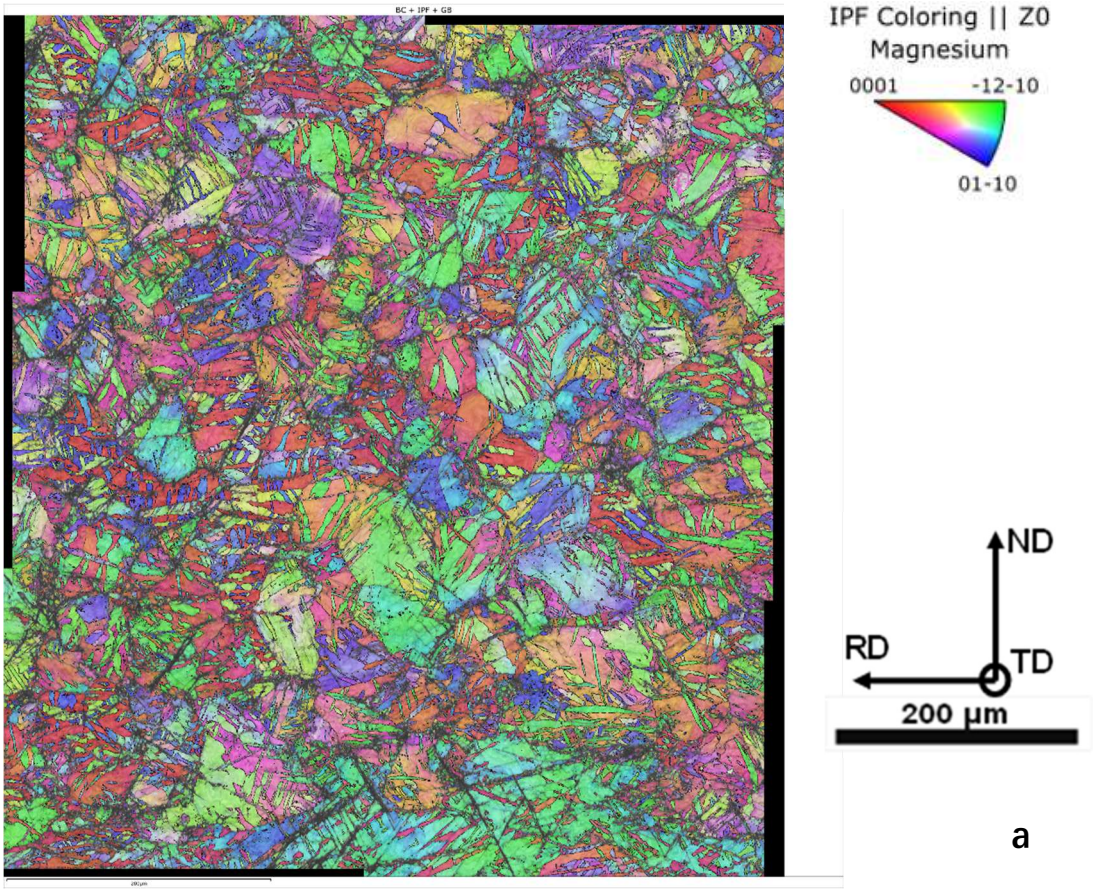

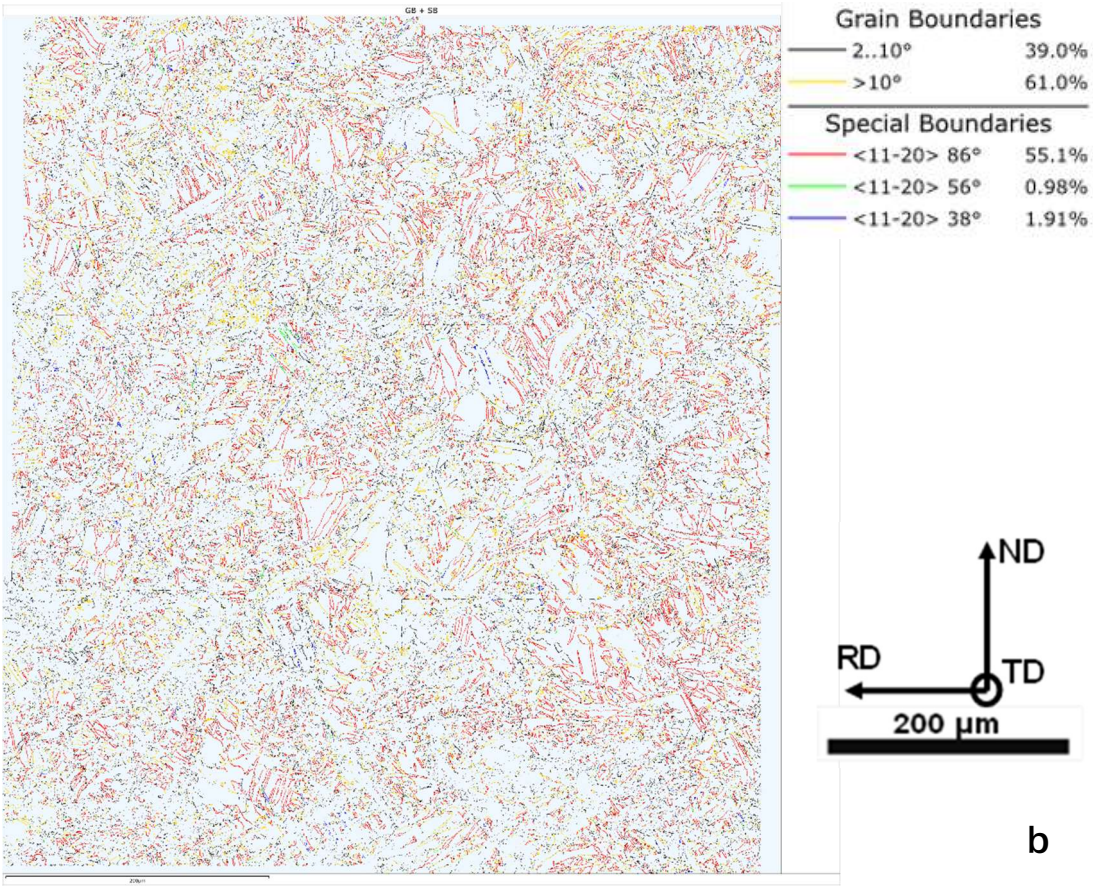
GB + SB
Grain Boundaries
2..10° 39.0%
>10° 61.0%
Special Boundaries
<11-20> 86° 55.1%
<11-20> 56° 0.98%
<11-20> 38° 1.91%
ND
RD
TD
200 µm

b

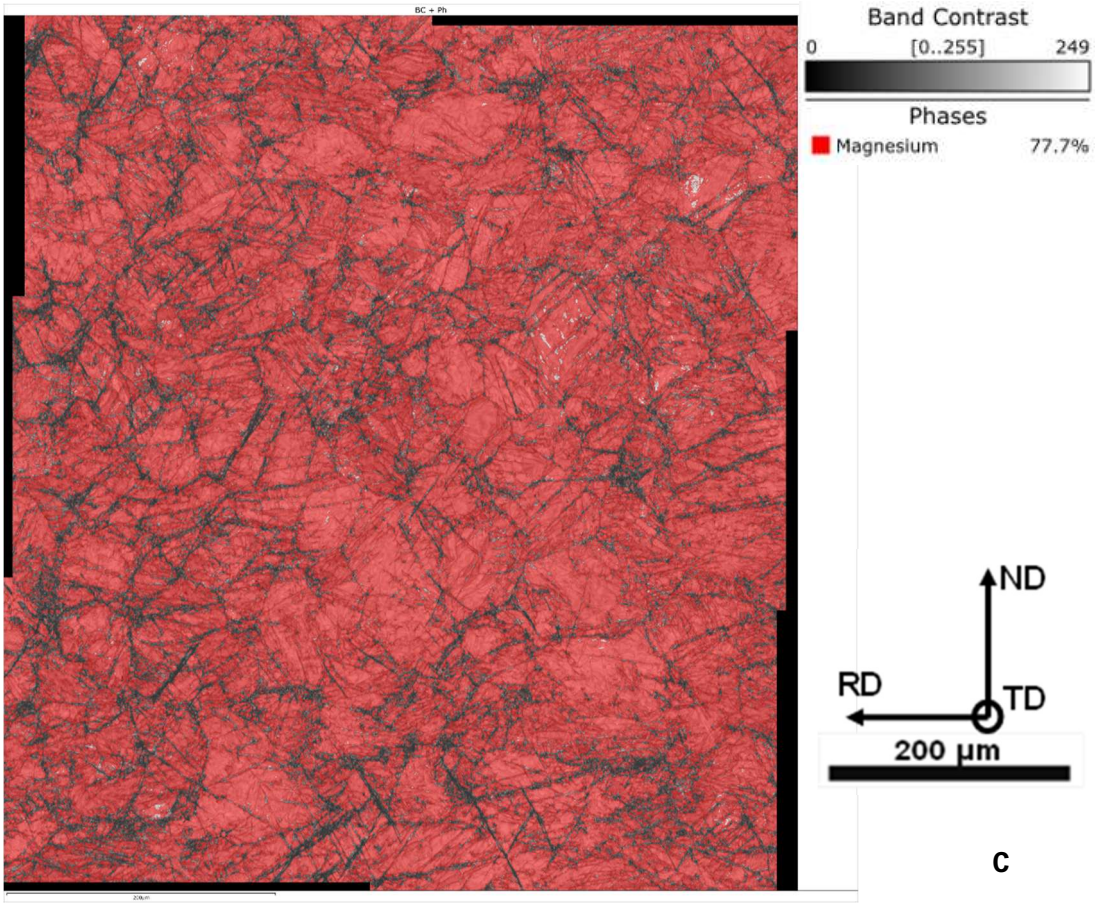
BC + Ph
Band Contrast
0 [0..255] 249
Phases
Magnesium 77.7%
ND
RD
TD
200 µm

c

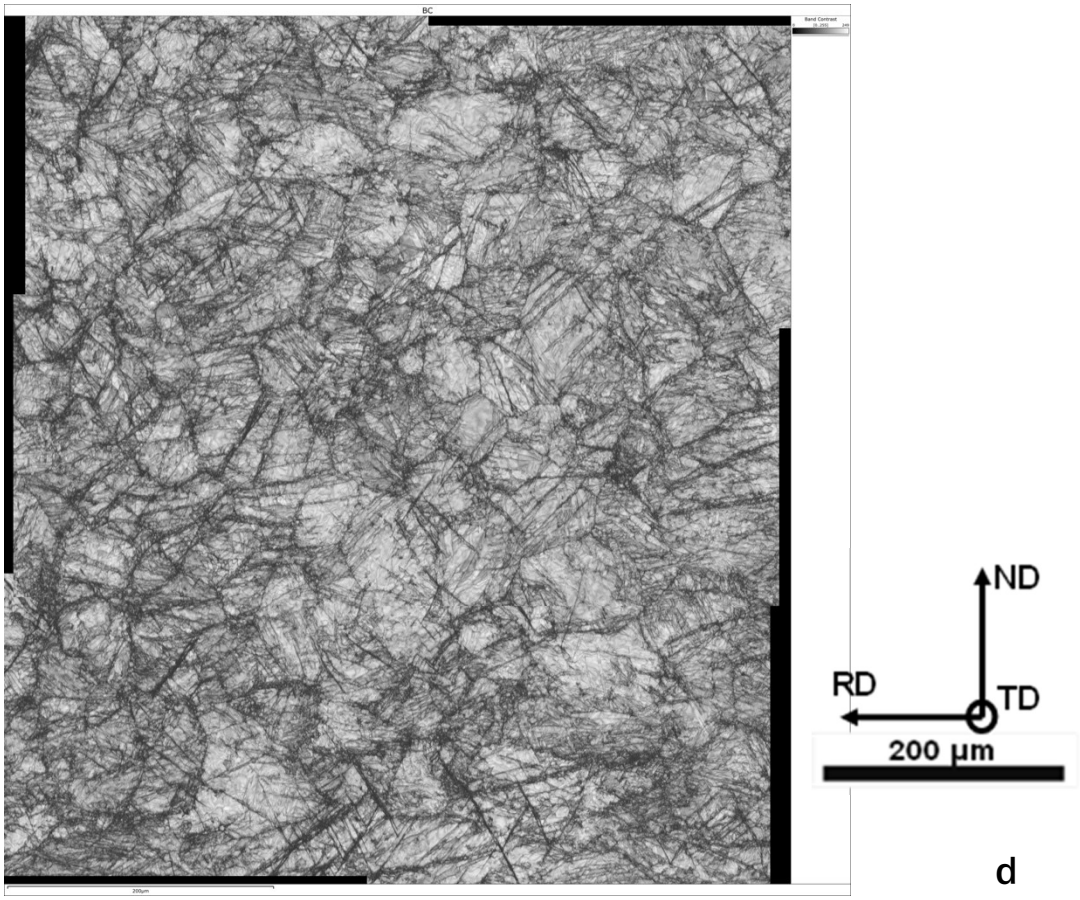
BC
ND
RD
TD
200 µm
d

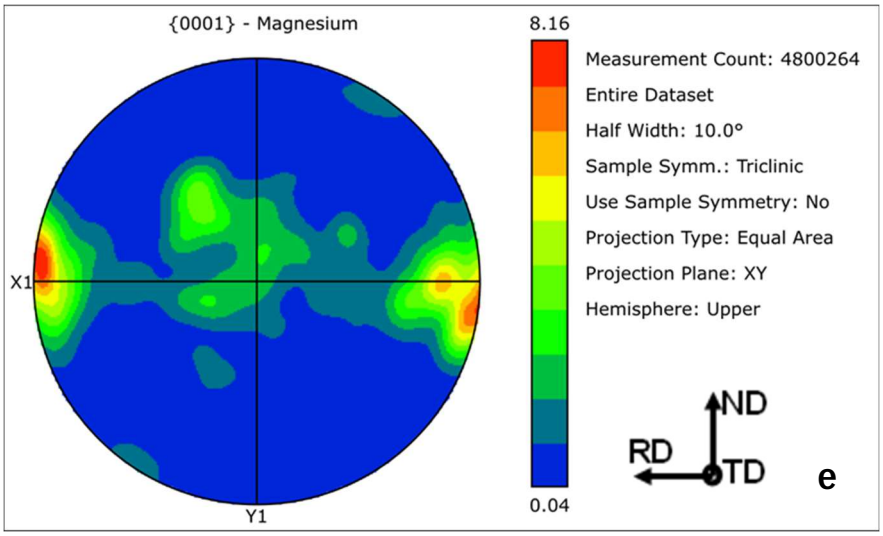
{0001} - Magnesium
8.16
0.04
X1
Y1
Measurement Count: 4800264
Entire Dataset
Half Width: 10.0°
Sample Symm.: Triclinic
Use Sample Symmetry: No
Projection Type: Equal Area
Projection Plane: XY
Hemisphere: Upper
ND
RD
TD
e

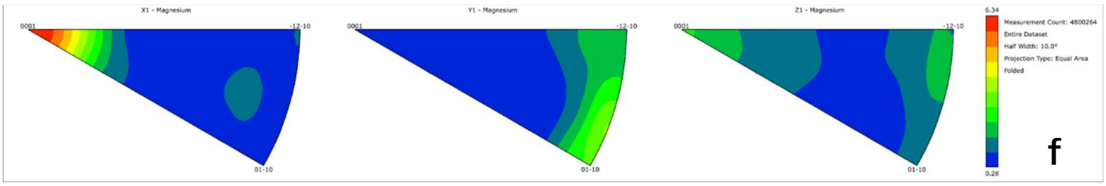
X1 - Magnesium
Y1 - Magnesium
Z1 - Magnesium
f

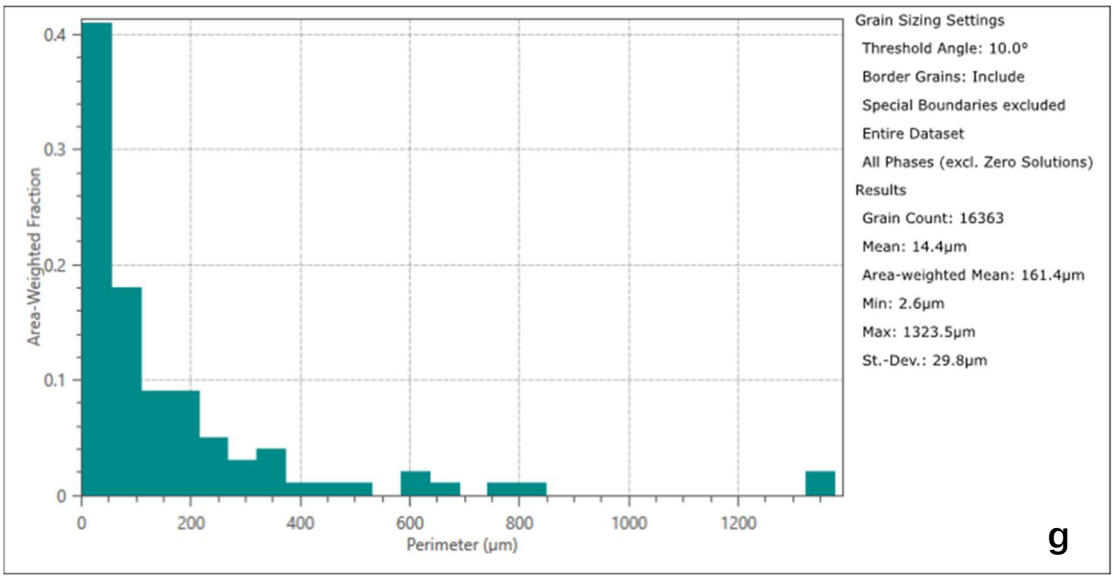

Figure A2-1 The EBSD result of the 30s annealed 2D compressed Mg-0.2Ca-0.3Zn specimen: (a) The inverse pole figure map and grain boundaries, (b) The grain boundaries and the special grain boundaries, (c) The band contrast and the phase analysis, (d) The band contrast, (e) The pole figure, (f) The inverse pole figures, (g) Grain size distribution expressed as grain boundary perimeter

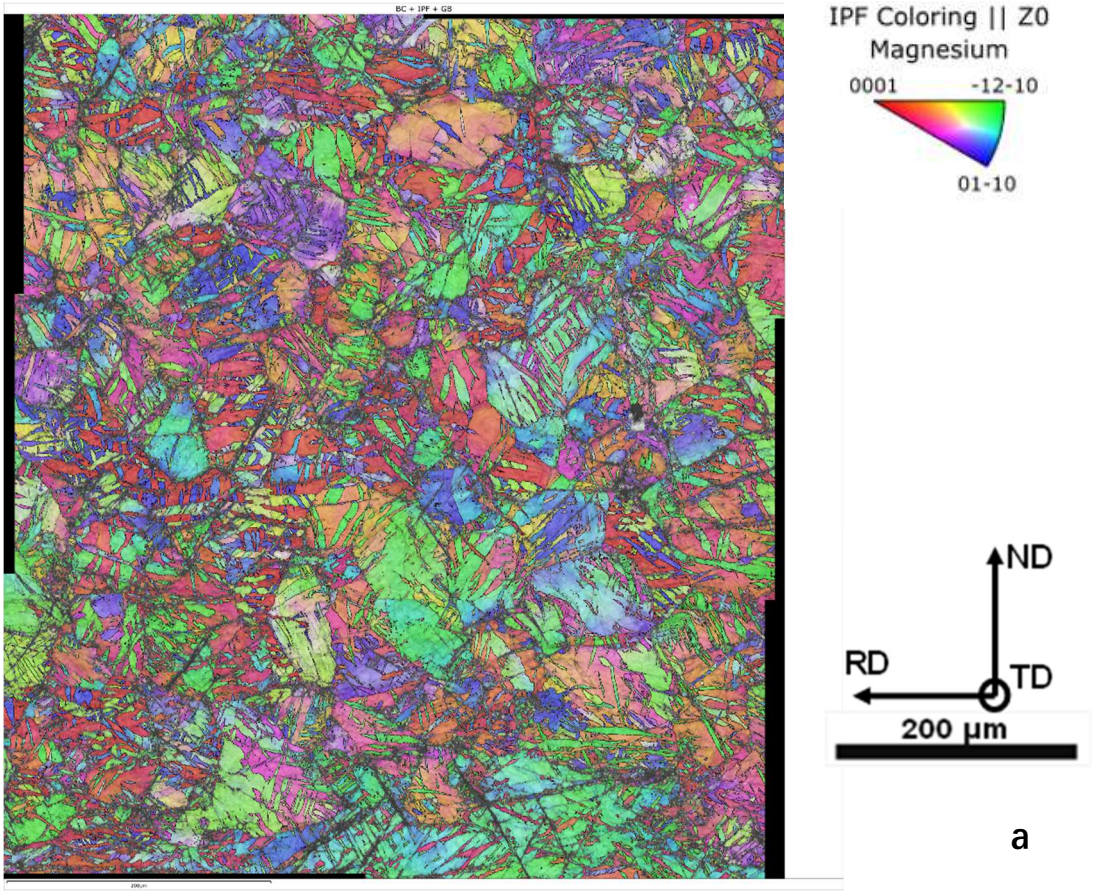

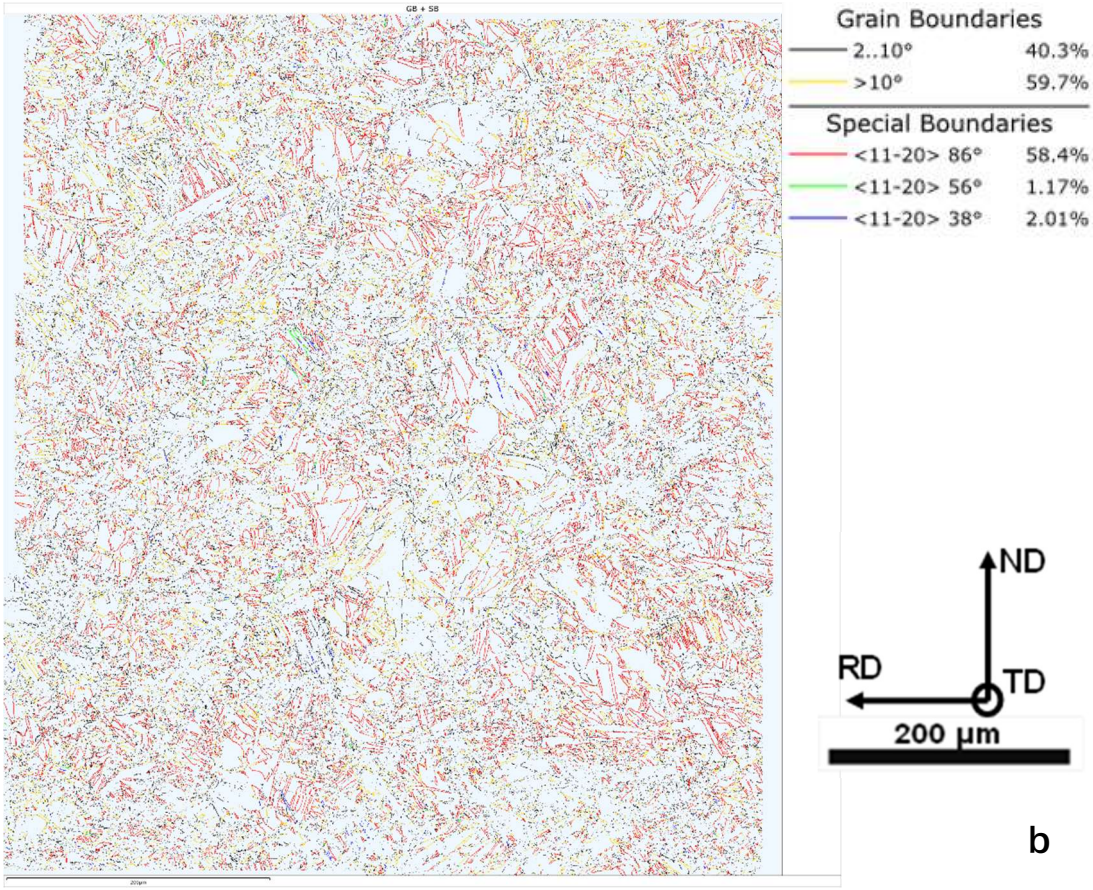
GB + SB
Grain Boundaries
2..10° 40.3%
>10° 59.7%
Special Boundaries
<11-20> 86° 58.4%
<11-20> 56° 1.17%
<11-20> 38° 2.01%
ND
RD
TD
200 µm

b

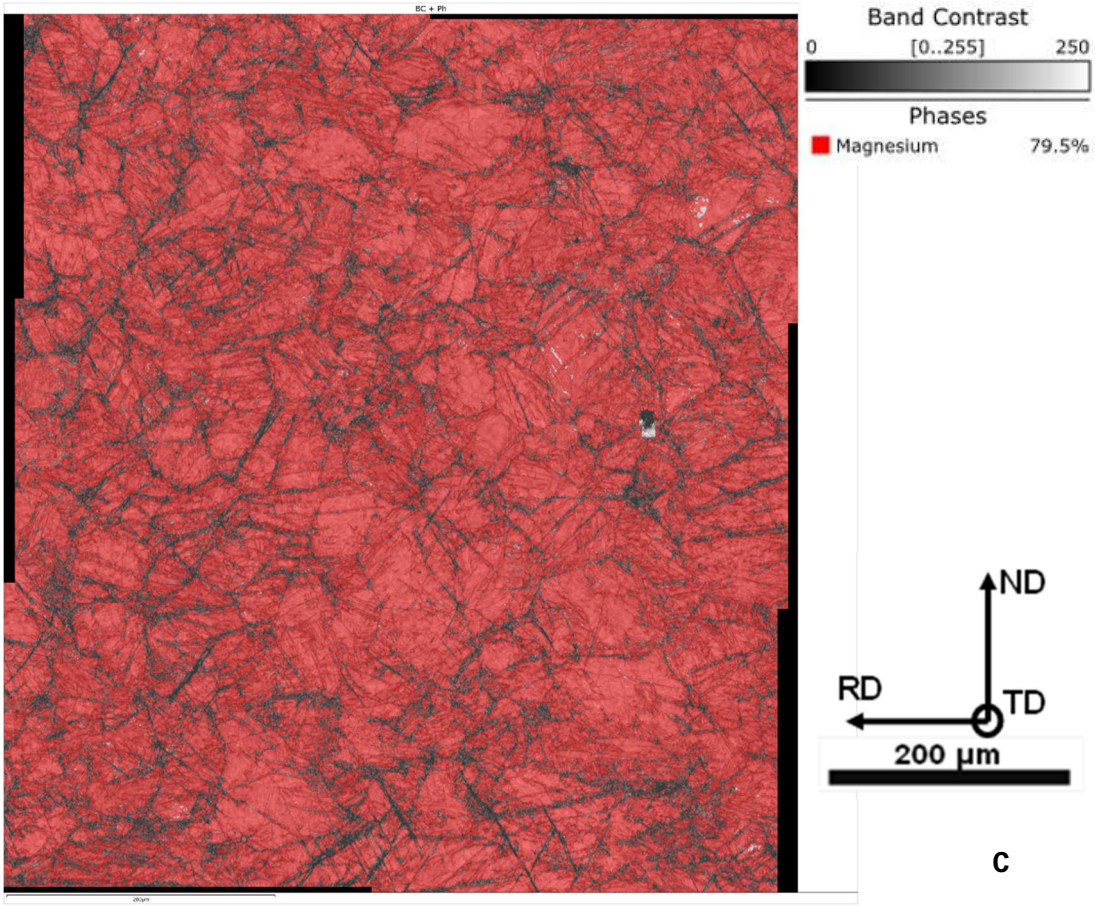
BC + Ph
Band Contrast
0 [0..255] 250
Phases
Magnesium 79.5%
ND
RD
TD
200 µm

c

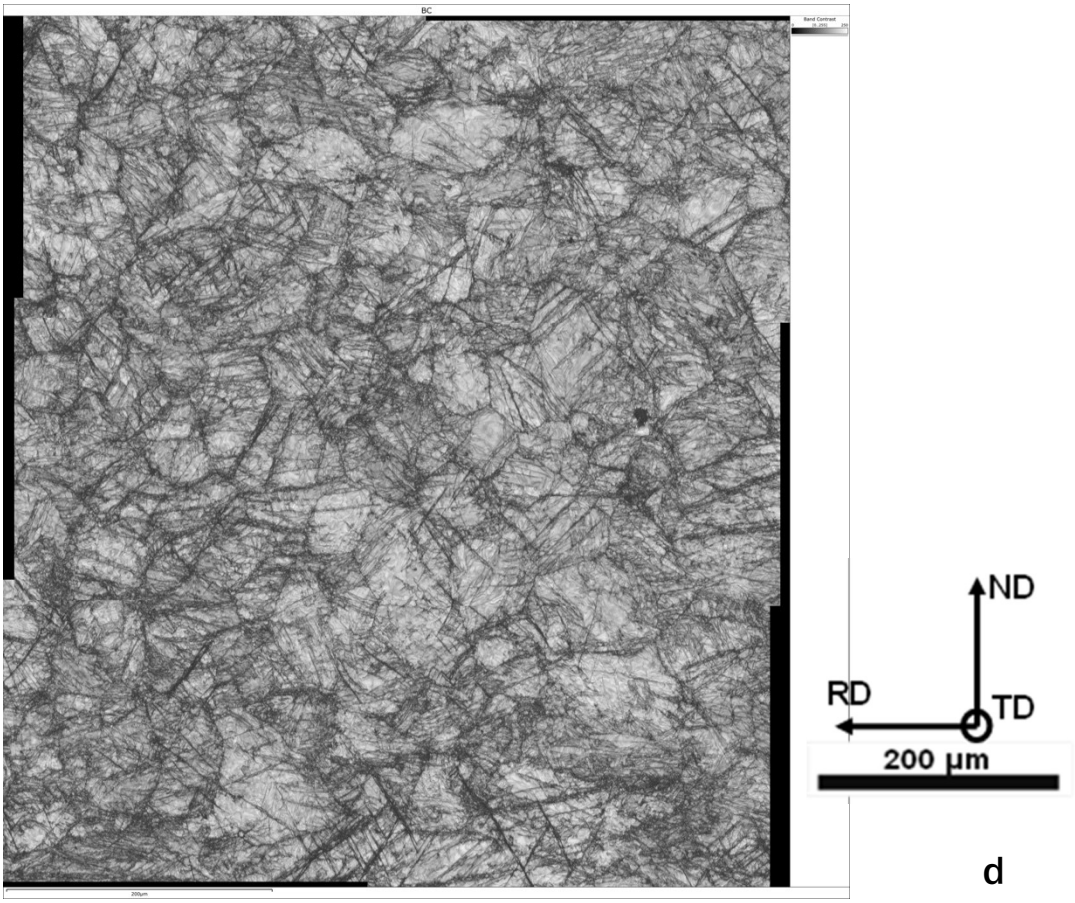
BC
ND
RD
TD
200 µm
d

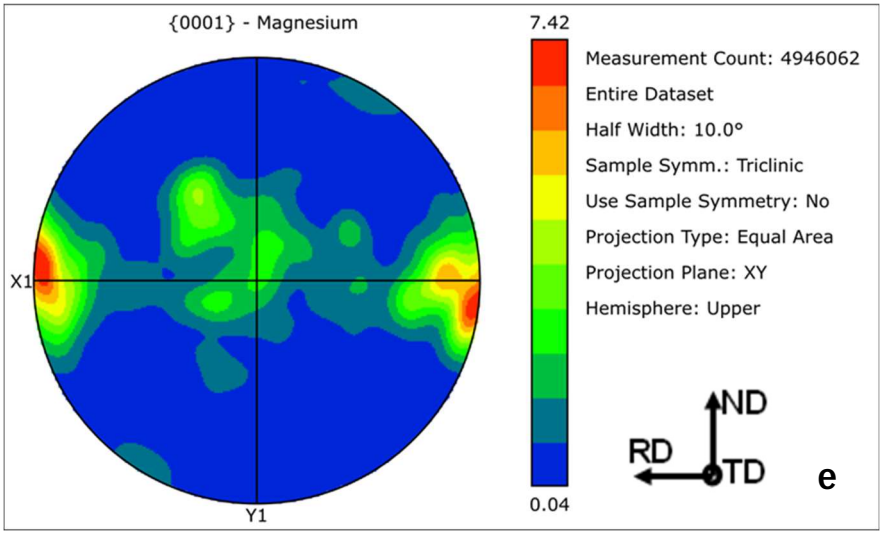
{0001} - Magnesium
7.42
0.04
Measurement Count: 4946062
Entire Dataset
Half Width: 10.0°
Sample Symm.: Triclinic
Use Sample Symmetry: No
Projection Type: Equal Area
Projection Plane: XY
Hemisphere: Upper
X1
Y1
ND
RD
TD
e

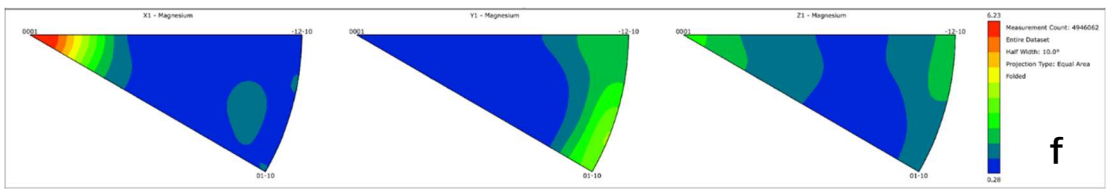
X1 - Magnesium
Y1 - Magnesium
Z1 - Magnesium
f

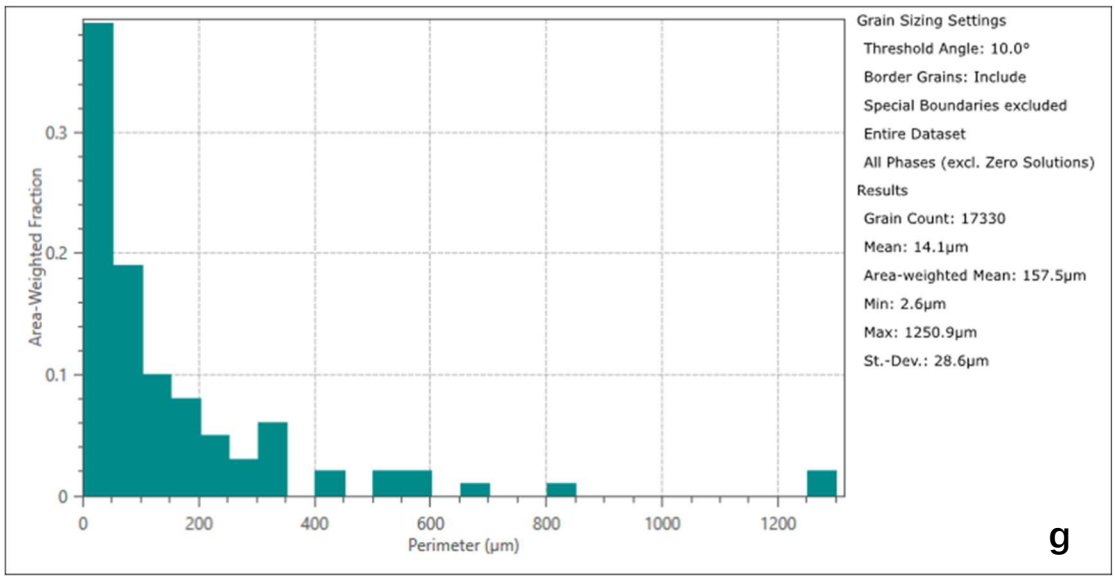

Figure A2-2 The EBSD result of the 75s annealed 2D compressed Mg-0.2Ca-0.3Zn specimen: (a) The inverse pole figure map and grain boundaries, (b) The grain boundaries and the special grain boundaries, (c) The band contrast and the phase analysis, (d) The band contrast, (e) The pole figure, (f) The inverse pole figures, (g) Grain size distribution expressed as grain boundary perimeter

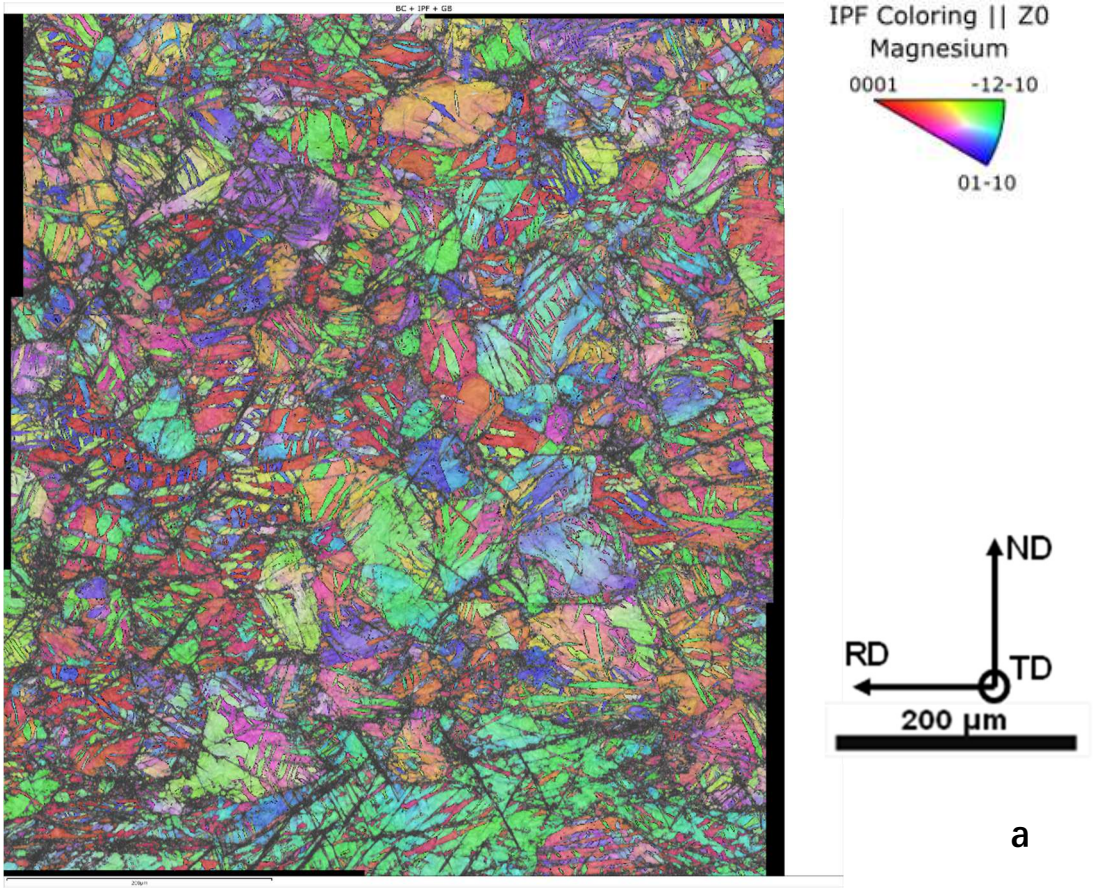

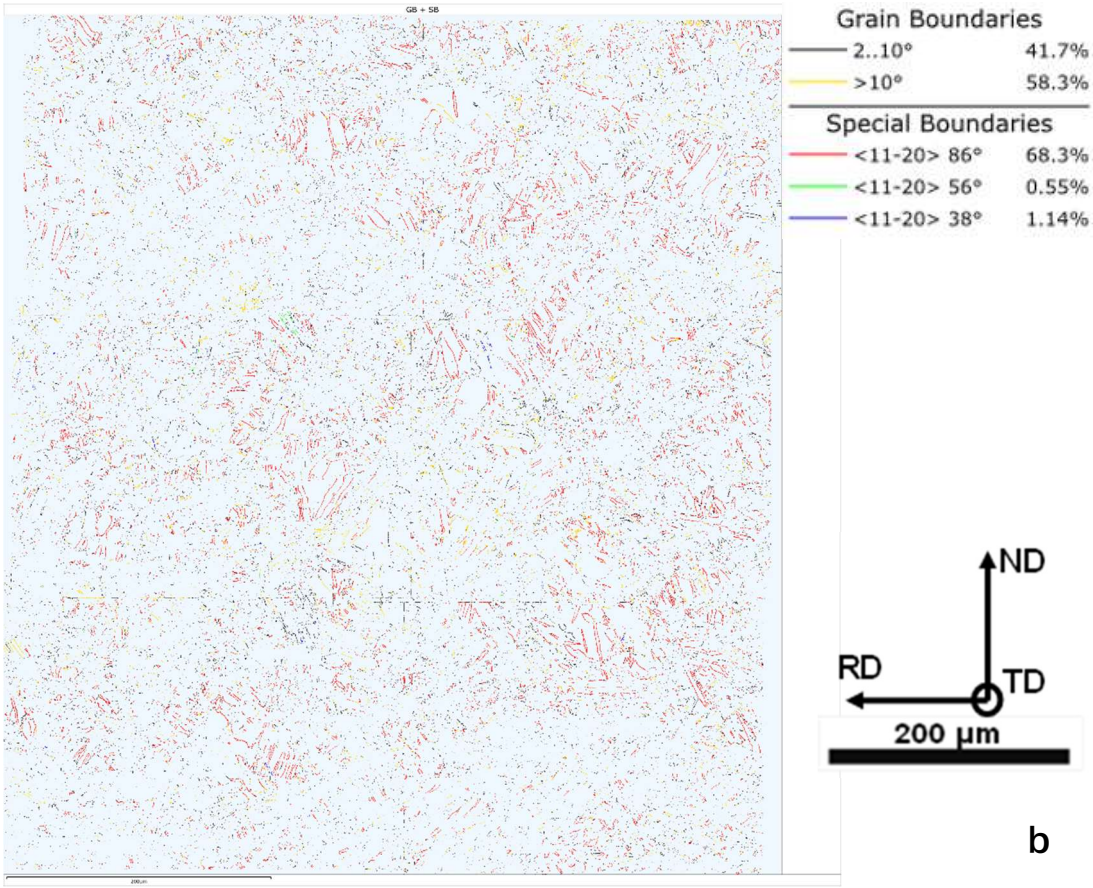
GB + SB
Grain Boundaries
2..10° 41.7%
>10° 58.3%
Special Boundaries
<11-20> 86° 68.3%
<11-20> 56° 0.55%
<11-20> 38° 1.14%
ND
RD
TD
200 µm

b

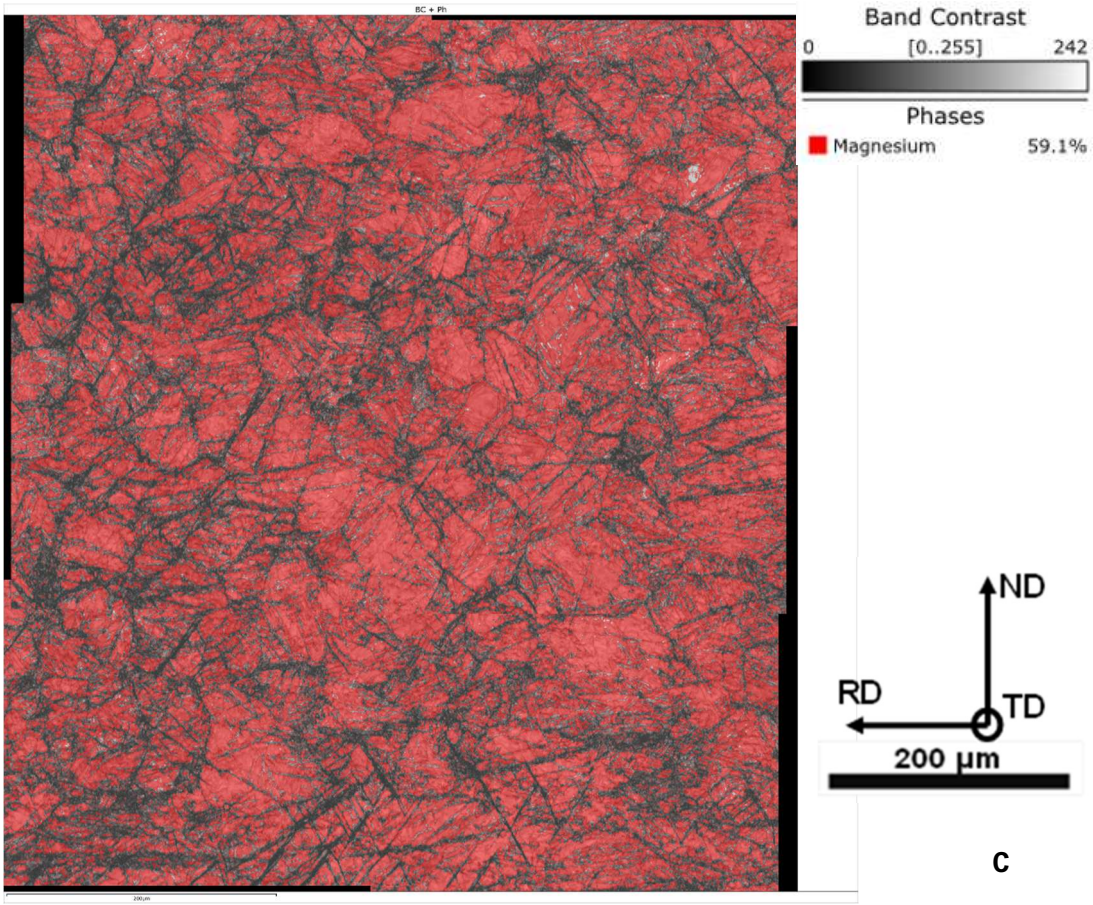
BC + Ph
Band Contrast
0 [0..255] 242
Phases
Magnesium 59.1%
ND
RD
TD
200 µm

c

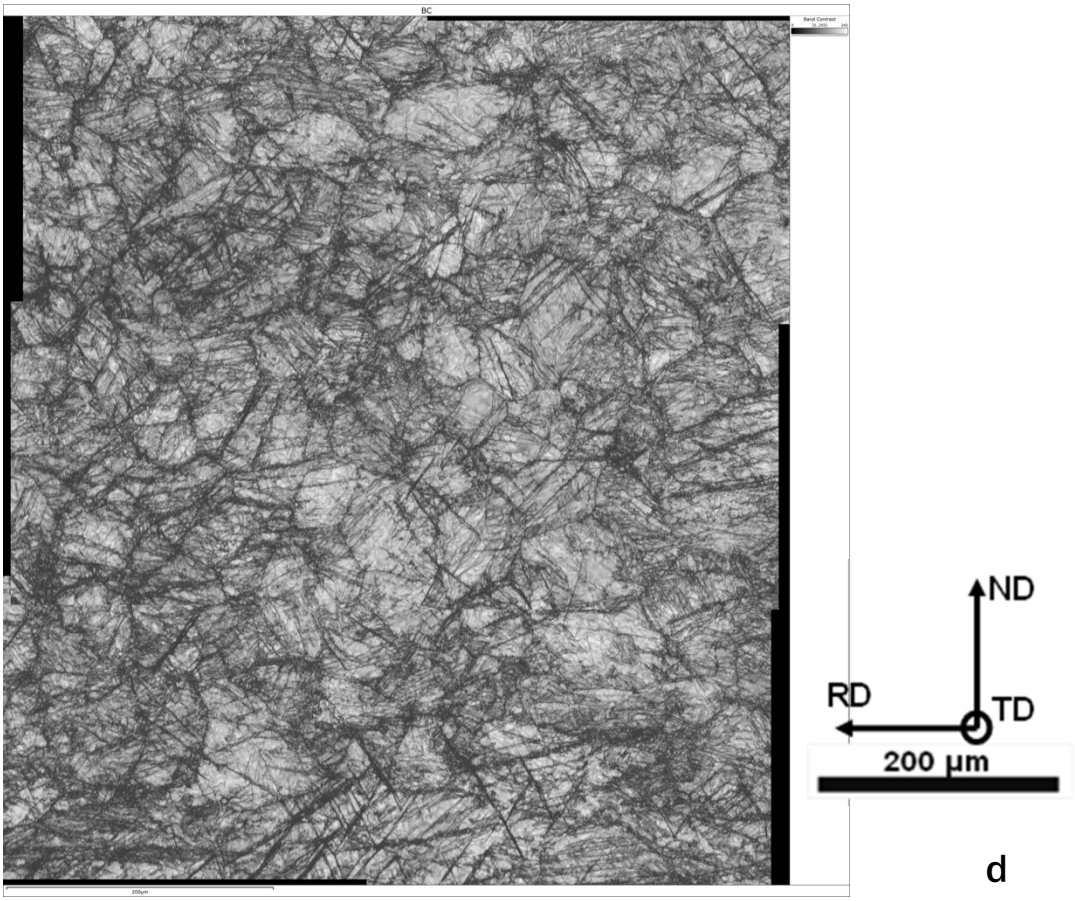
BC
ND
RD
TD
200 µm

d

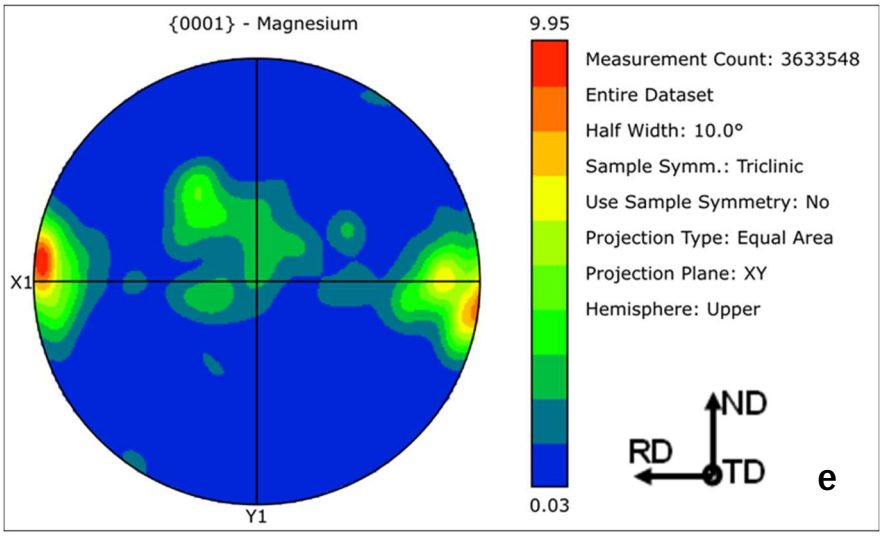
{0001} - Magnesium
9.95
0.03
Measurement Count: 3633548
Entire Dataset
Half Width: 10.0°
Sample Symm.: Triclinic
Use Sample Symmetry: No
Projection Type: Equal Area
Projection Plane: XY
Hemisphere: Upper
X1
Y1
ND
RD
TD

e

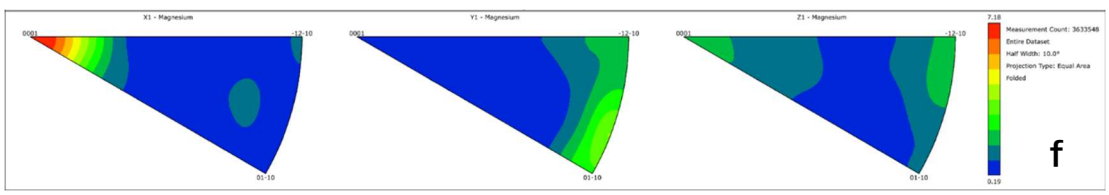
X1 - Magnesium
Y1 - Magnesium
Z1 - Magnesium
0001
-12-10
01-10
7.18
0.19
Measurement Count: 3633548
Entire Dataset
Half Width: 10.0°
Projection Type: Equal Area
Folded

f

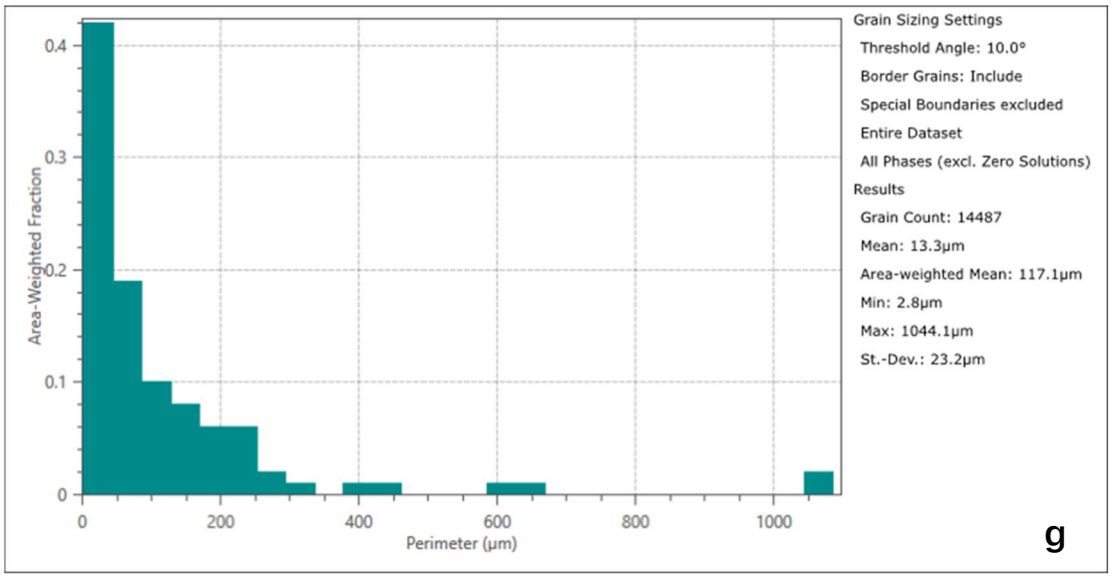

Figure A2-3 The EBSD result of the 135s annealed 2D compressed Mg-0.2Ca-0.3Zn specimen: (a) The inverse pole figure map and grain boundaries, (b) The grain boundaries and the special grain boundaries, (c) The band contrast and the phase analysis, (d) The band contrast, (e) The pole figure, (f) The inverse pole figures, (g) Grain size distribution expressed as grain boundary perimeter

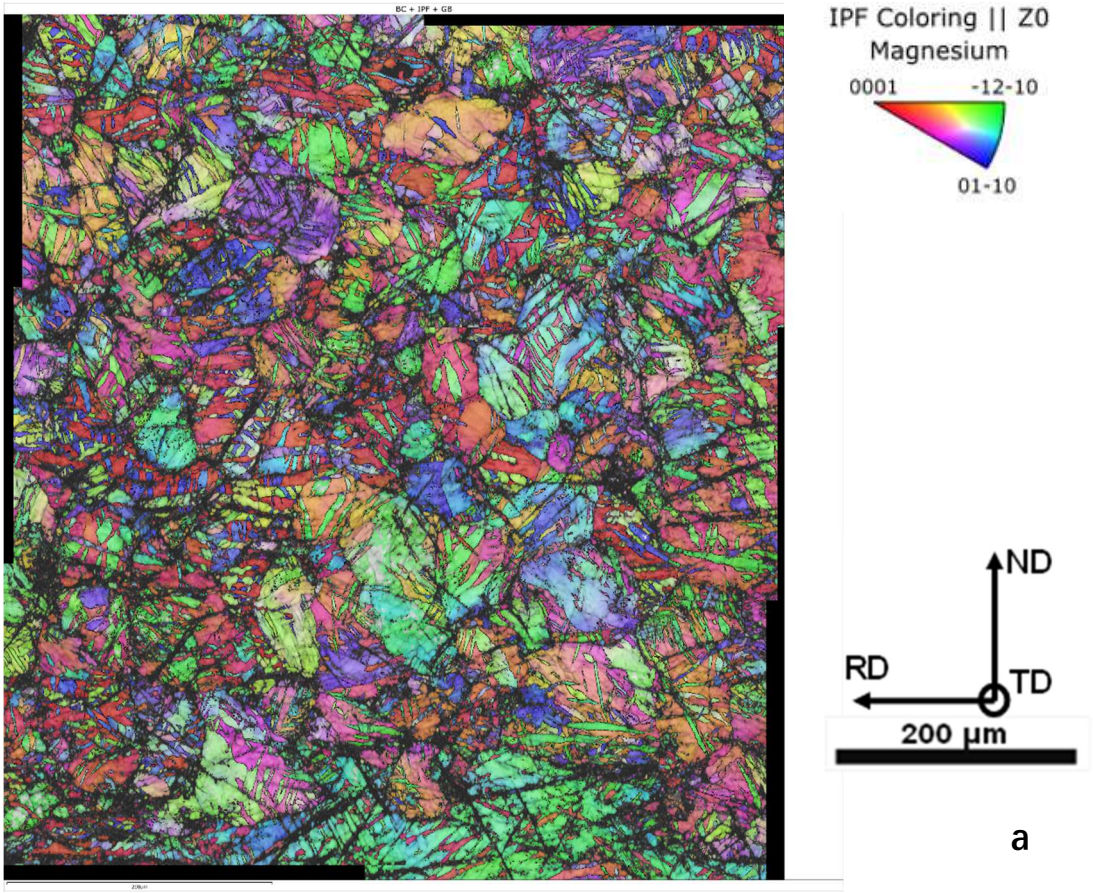

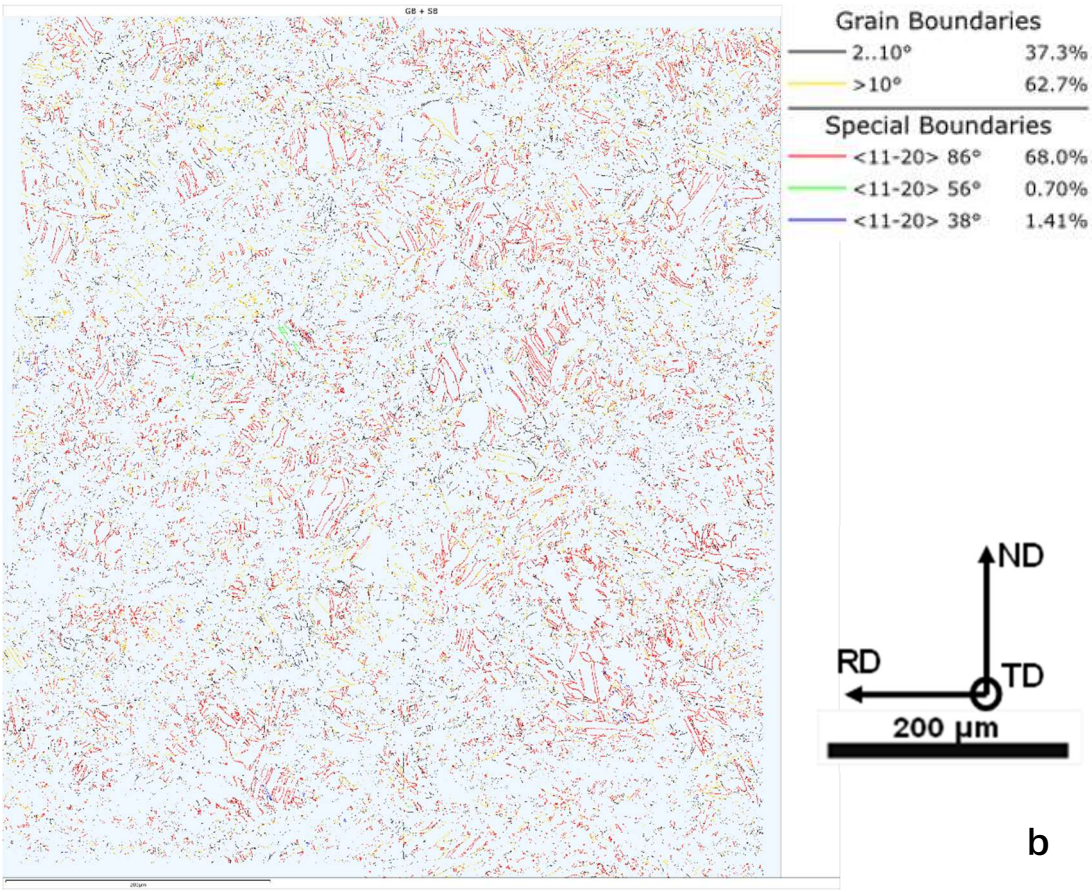
GB + SB
Grain Boundaries
2..10° 37.3%
>10° 62.7%
Special Boundaries
<11-20> 86° 68.0%
<11-20> 56° 0.70%
<11-20> 38° 1.41%
ND
RD
TD
200 µm

b

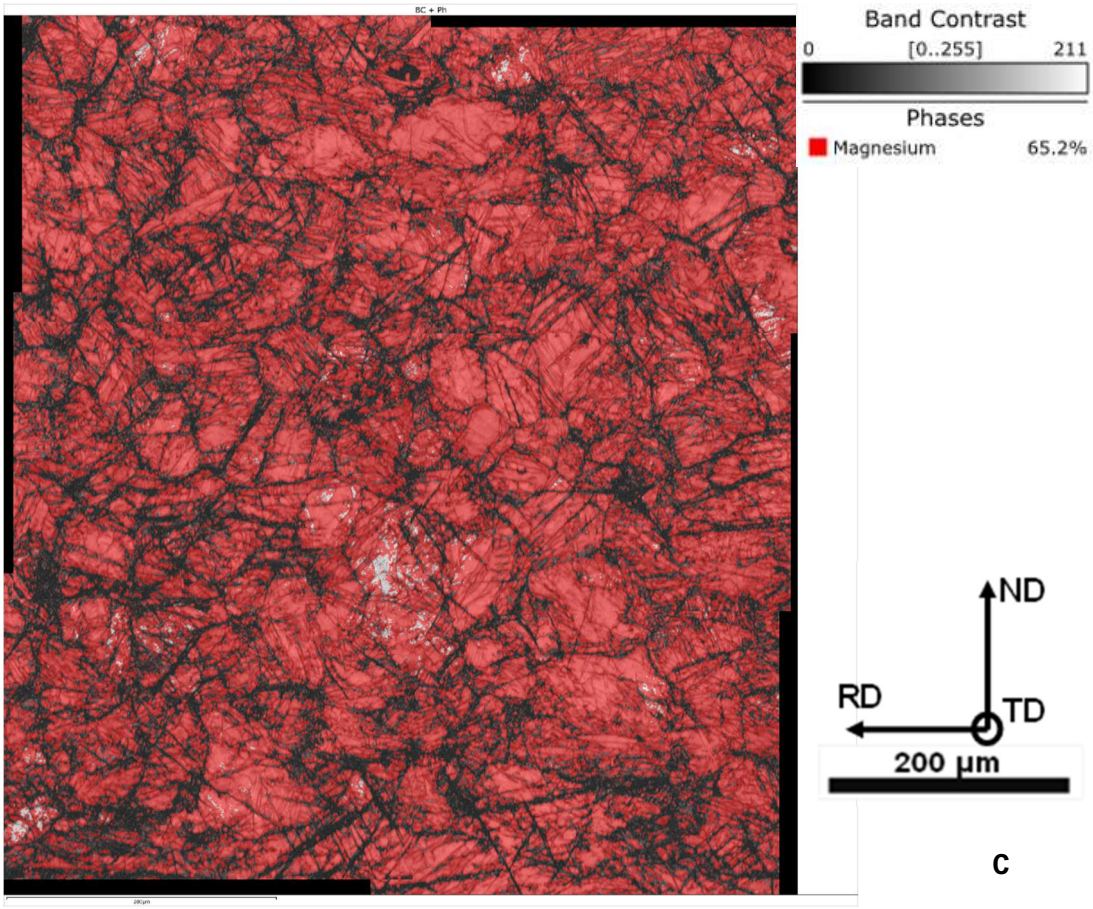
BC + Ph
Band Contrast
0 [0..255] 211
Phases
Magnesium 65.2%
ND
RD
TD
200 µm

c

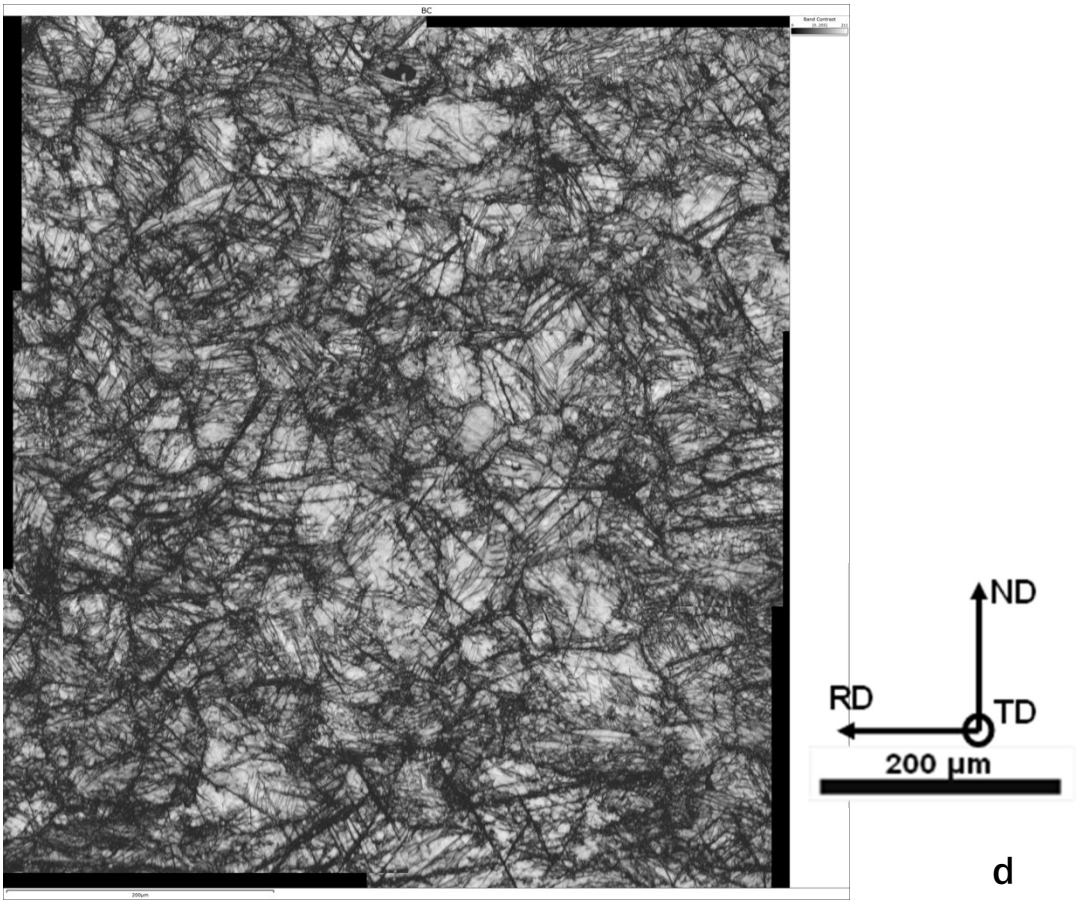
BC
ND
RD
TD
200 µm

d

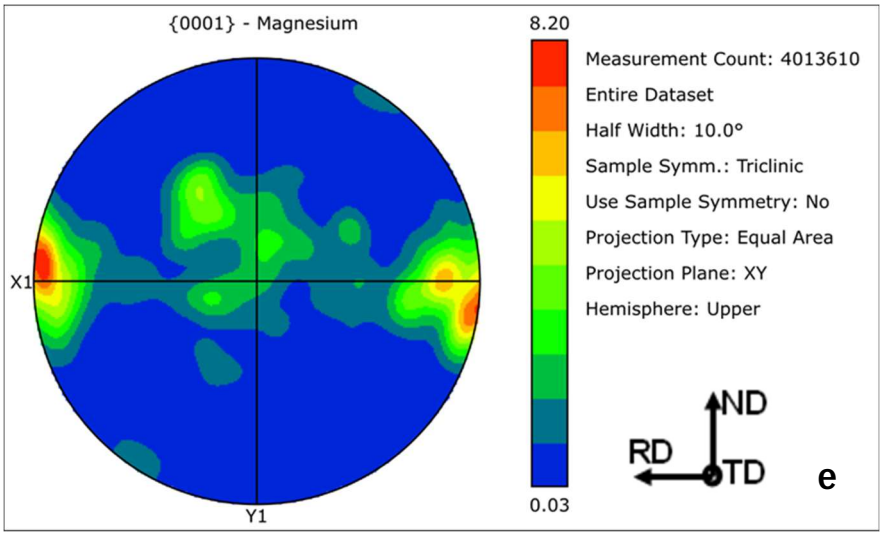
{0001} - Magnesium
8.20
0.03
Measurement Count: 4013610
Entire Dataset
Half Width: 10.0°
Sample Symm.: Triclinic
Use Sample Symmetry: No
Projection Type: Equal Area
Projection Plane: XY
Hemisphere: Upper
X1
Y1
ND
RD
TD

e

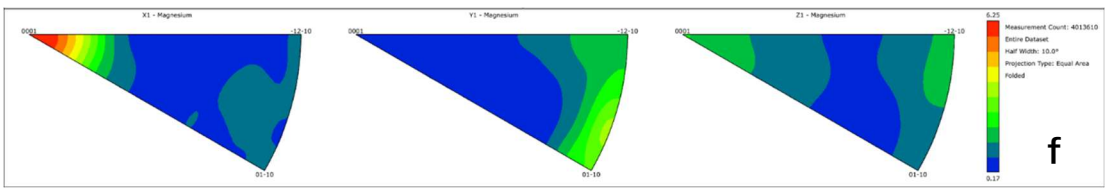
X1 - Magnesium
Y1 - Magnesium
Z1 - Magnesium
Measurement Count: 4013610
Entire Dataset
Half Width: 10.0°
Projection Type: Equal Area
Folded

f

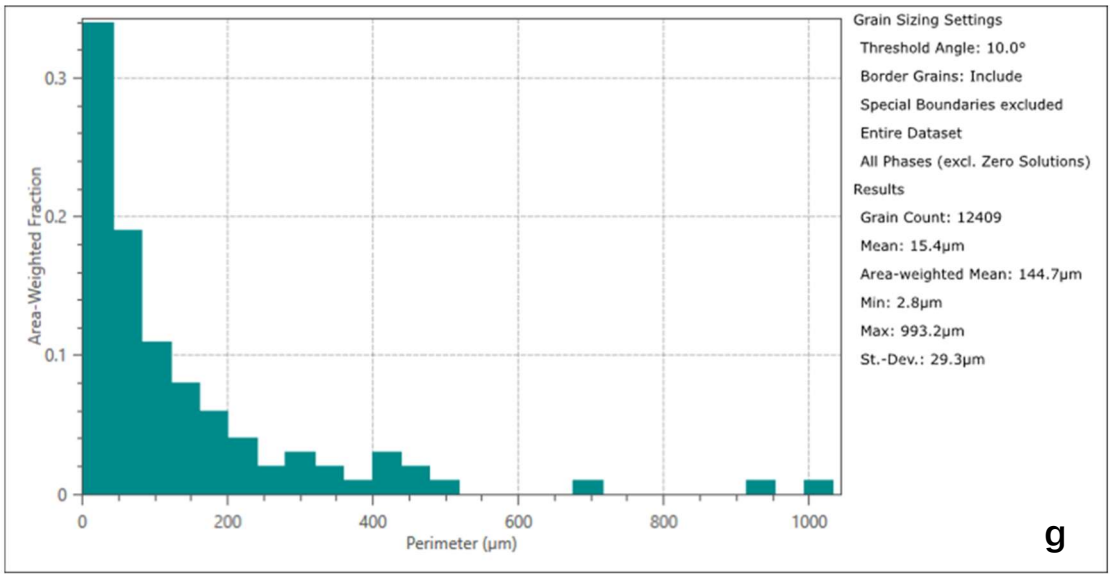

Figure A2-4 The EBSD result of the 210s annealed 2D compressed Mg-0.2Ca-0.3Zn specimen: (a) The inverse pole figure map and grain boundaries, (b) The grain boundaries and the special grain boundaries, (c) The band contrast and the phase analysis, (d) The band contrast, (e) The pole figure, (f) The inverse pole figures, (g) Grain size distribution expressed as grain boundary perimeter

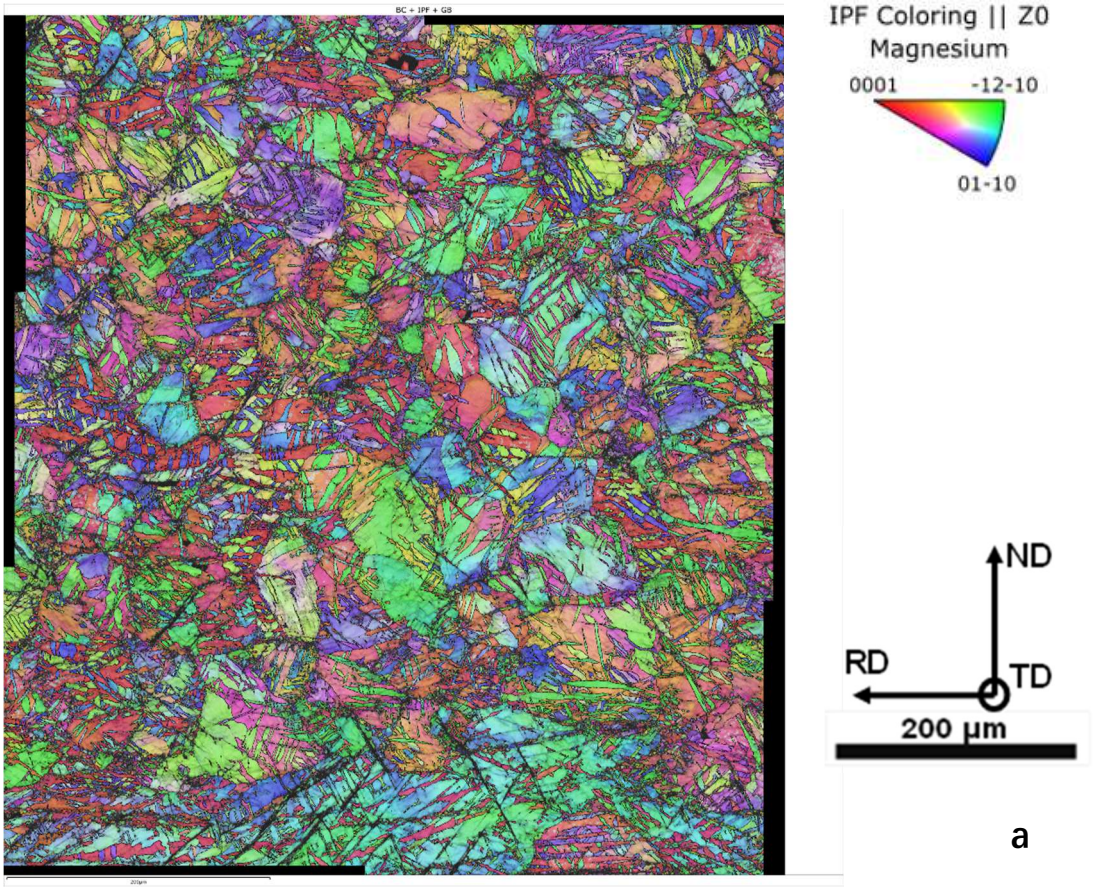

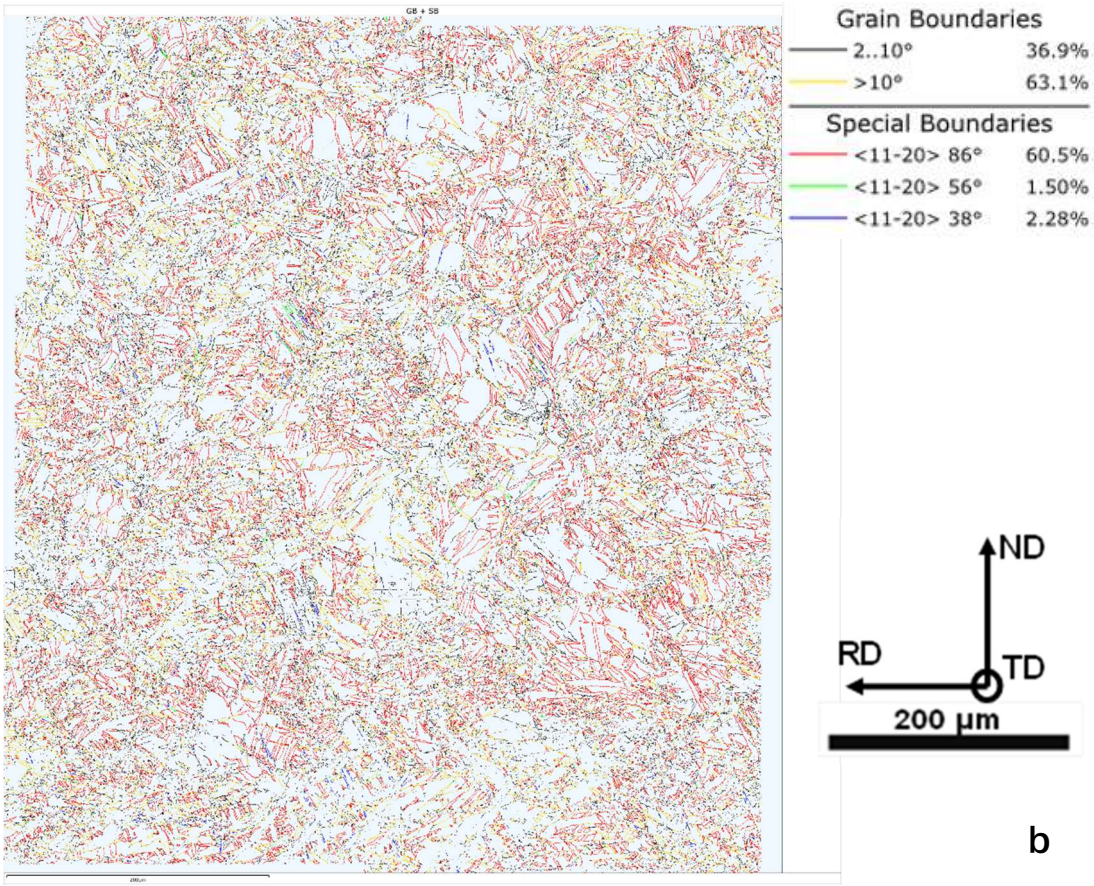
GB + S8
Grain Boundaries
2..10° 36.9%
>10° 63.1%
Special Boundaries
<11-20> 86° 60.5%
<11-20> 56° 1.50%
<11-20> 38° 2.28%
ND
RD
TD
200 µm

b

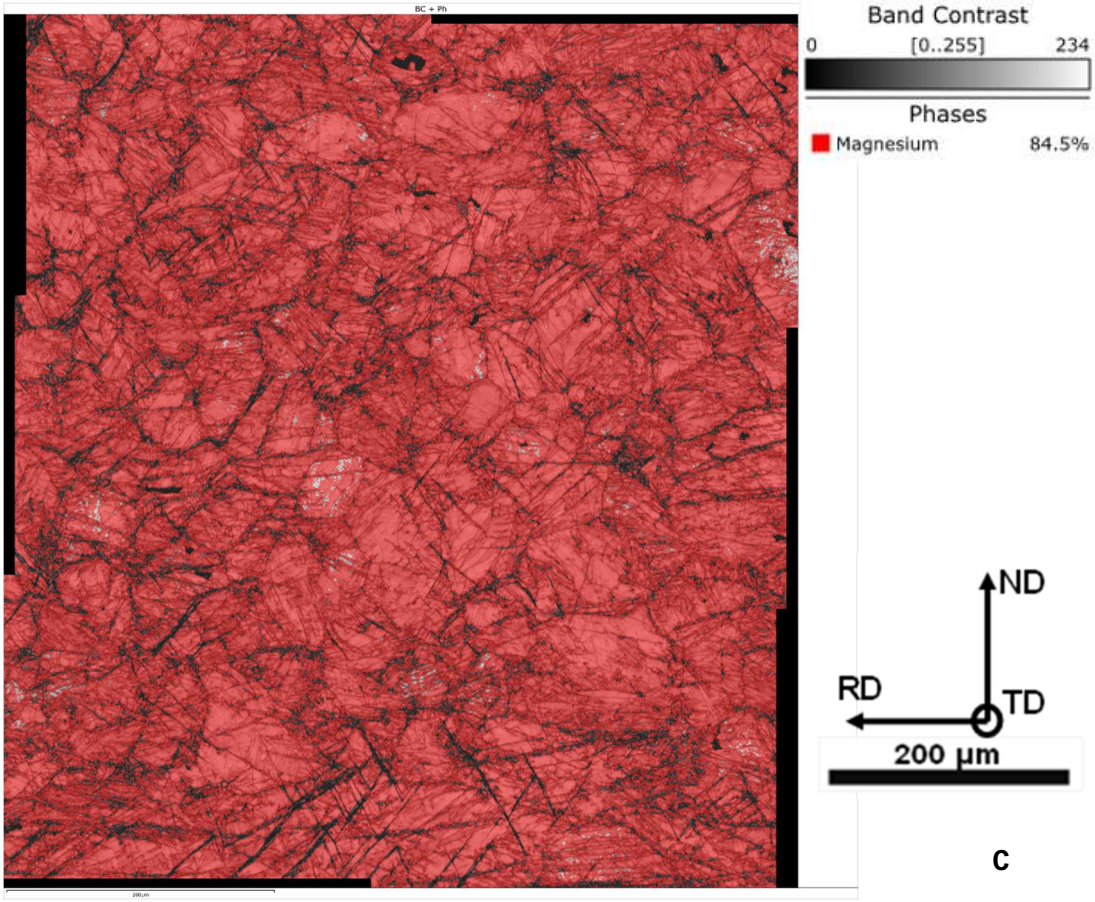
BC + Ph
Band Contrast
0 [0..255] 234
Phases
Magnesium 84.5%
ND
RD
TD
200 µm

c

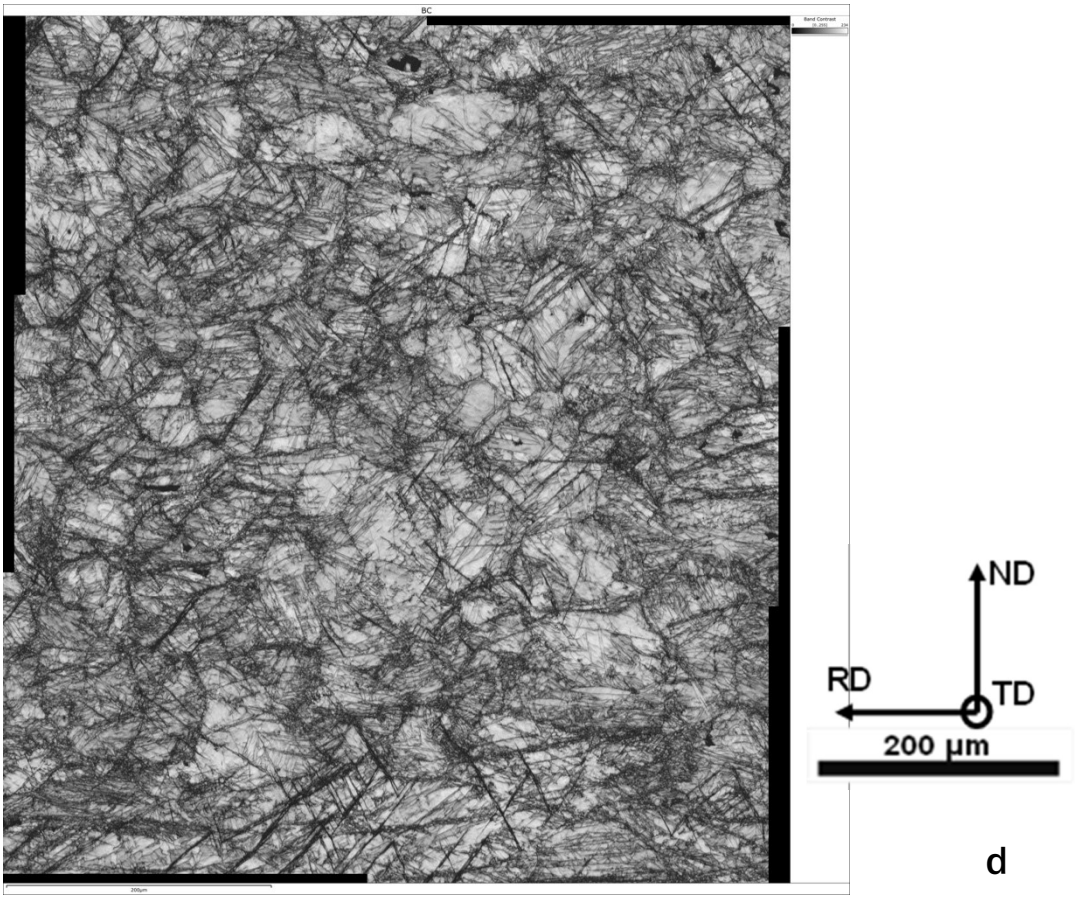
BC
ND
RD
TD
200 µm
d

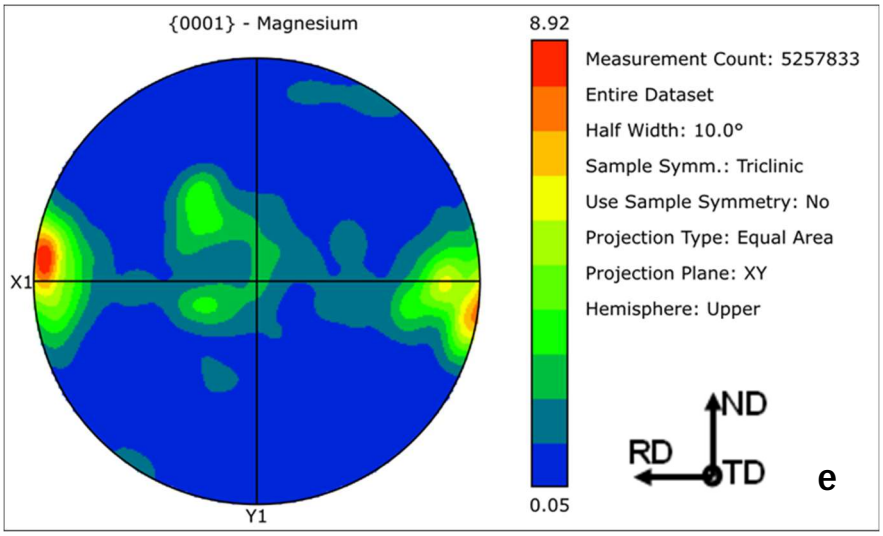
{0001} - Magnesium
8.92
0.05
Measurement Count: 5257833
Entire Dataset
Half Width: 10.0°
Sample Symm.: Triclinic
Use Sample Symmetry: No
Projection Type: Equal Area
Projection Plane: XY
Hemisphere: Upper
X1
Y1
ND
RD
TD
e

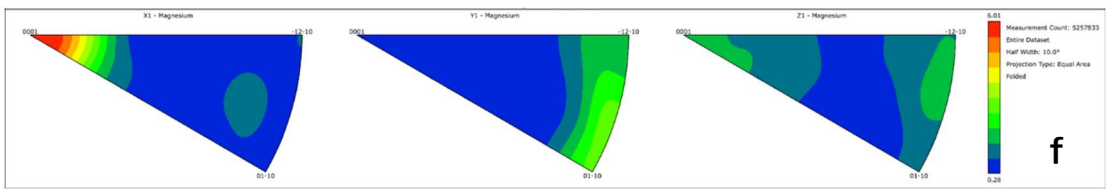
X1 - Magnesium
Y1 - Magnesium
Z1 - Magnesium
f

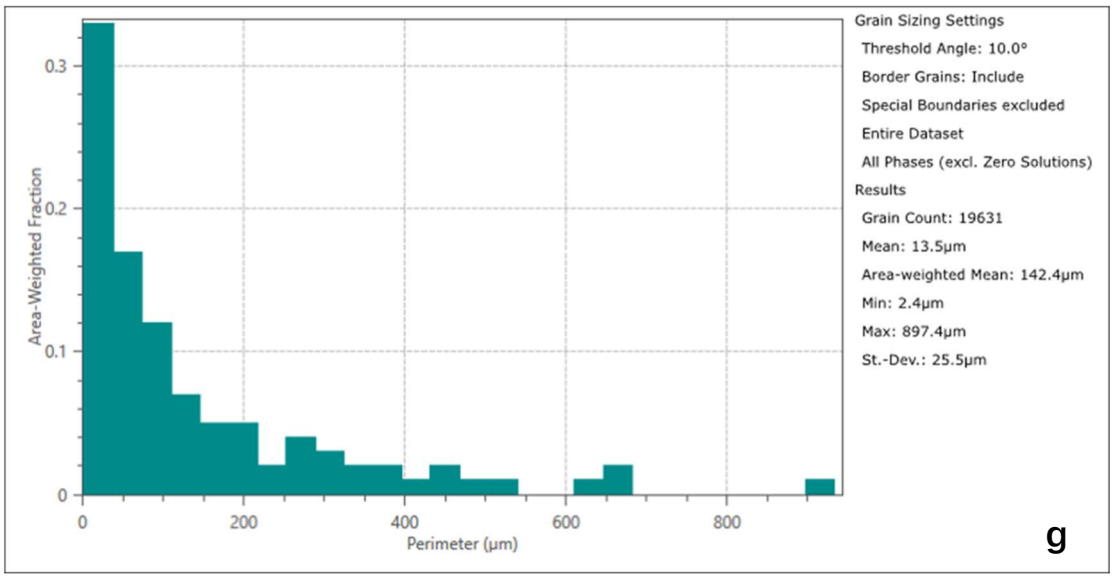

Figure A2-5 The EBSD result of the 300s annealed 2D compressed Mg-0.2Ca-0.3Zn specimen: (a) The inverse pole figure map and grain boundaries, (b) The grain boundaries and the special grain boundaries, (c) The band contrast and the phase analysis, (d) The band contrast, (e) The pole figure, (f) The inverse pole figures, (g) Grain size distribution expressed as grain boundary perimeter

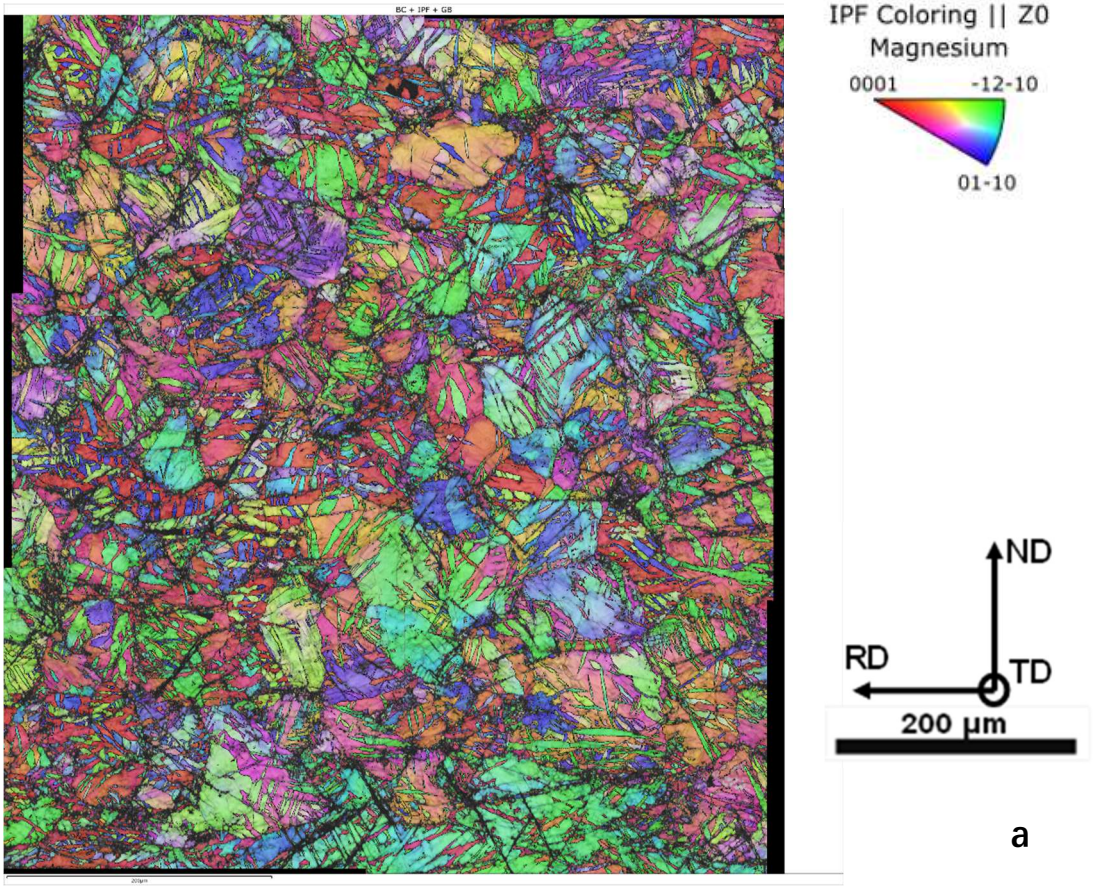

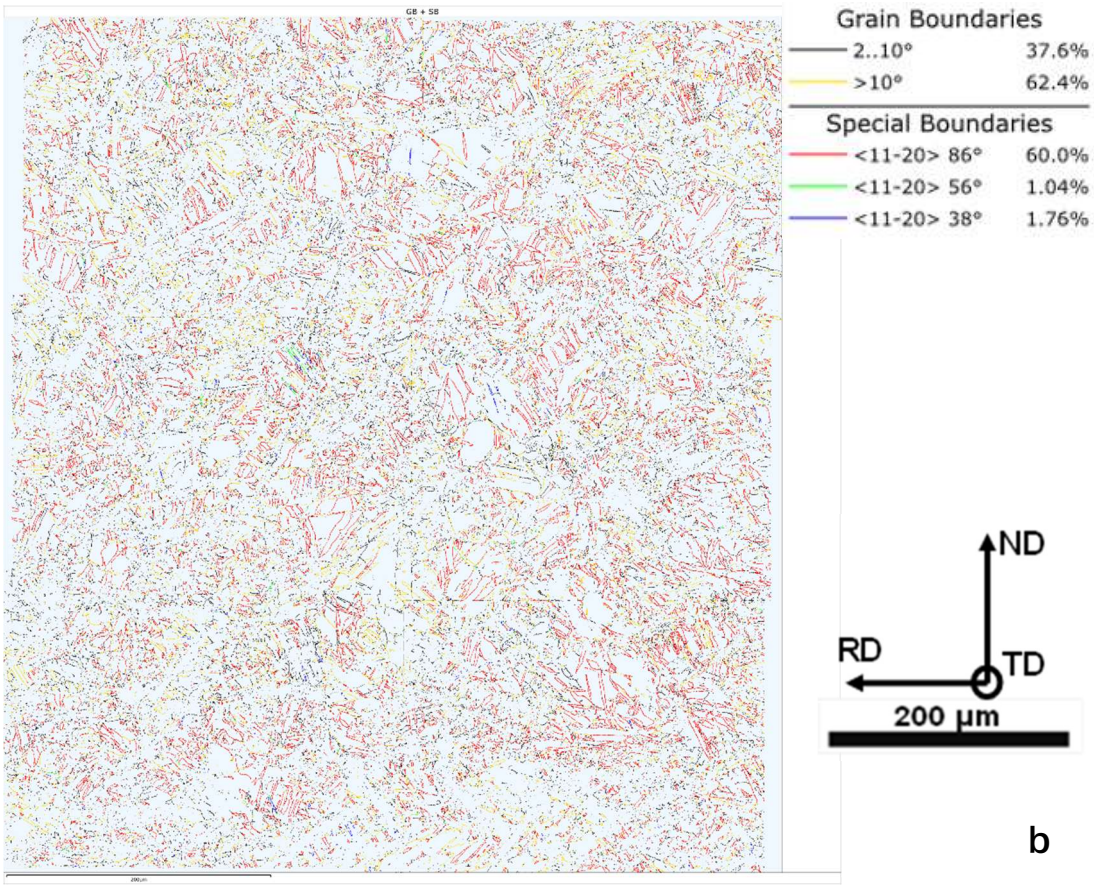
GB + S8
Grain Boundaries
2..10° 37.6%
>10° 62.4%
Special Boundaries
<11-20> 86° 60.0%
<11-20> 56° 1.04%
<11-20> 38° 1.76%
ND
RD
TD
200 µm

b

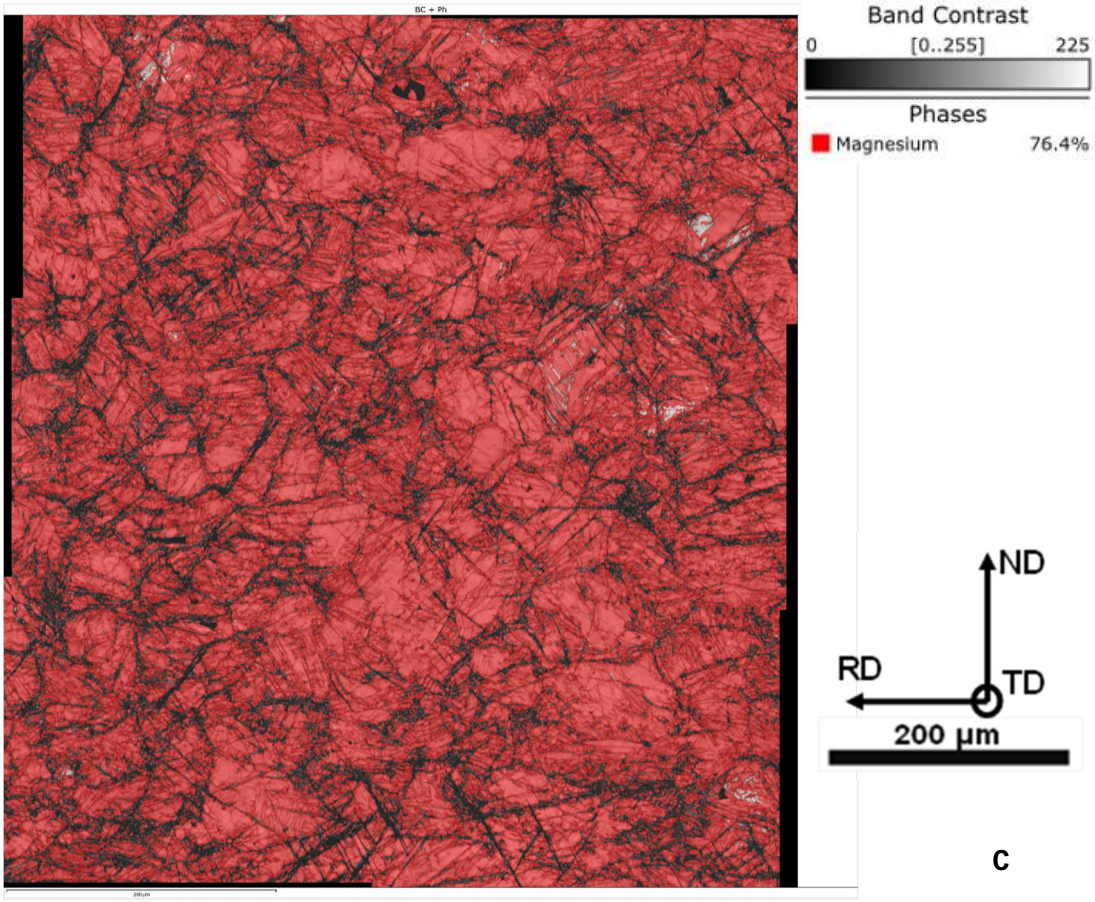
BC + Ph
Band Contrast
0 [0..255] 225
Phases
Magnesium 76.4%
ND
RD
TD
200 µm

c

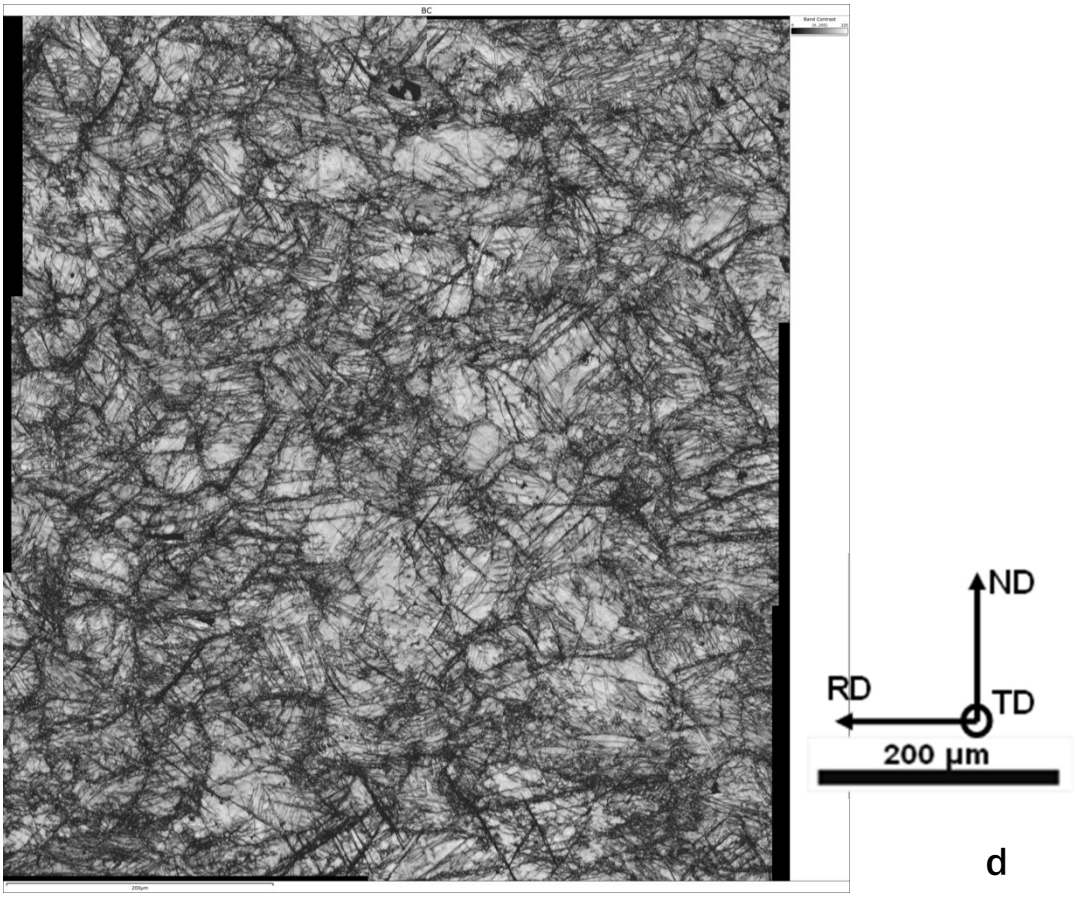
ND
RD
TD
200 µm
d

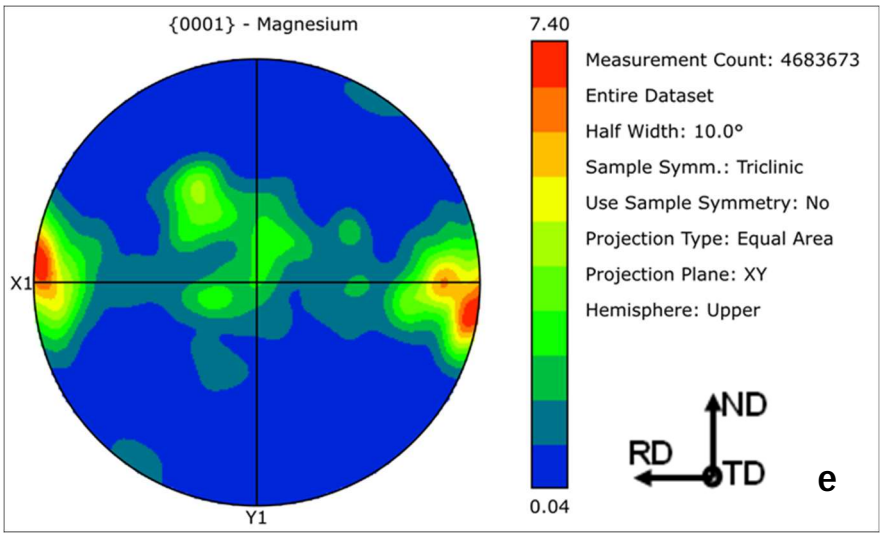
{0001} - Magnesium
7.40
0.04
Measurement Count: 4683673
Entire Dataset
Half Width: 10.0°
Sample Symm.: Triclinic
Use Sample Symmetry: No
Projection Type: Equal Area
Projection Plane: XY
Hemisphere: Upper
X1
Y1
ND
RD
TD
e

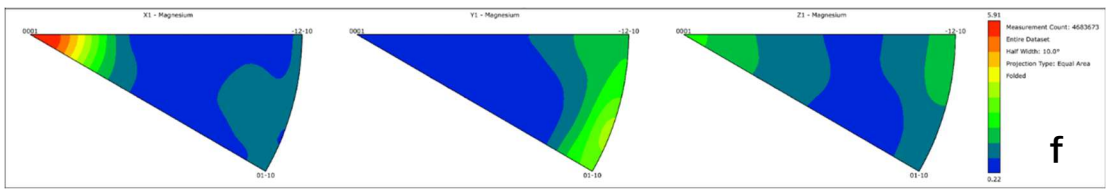
X1 - Magnesium
Y1 - Magnesium
Z1 - Magnesium
f

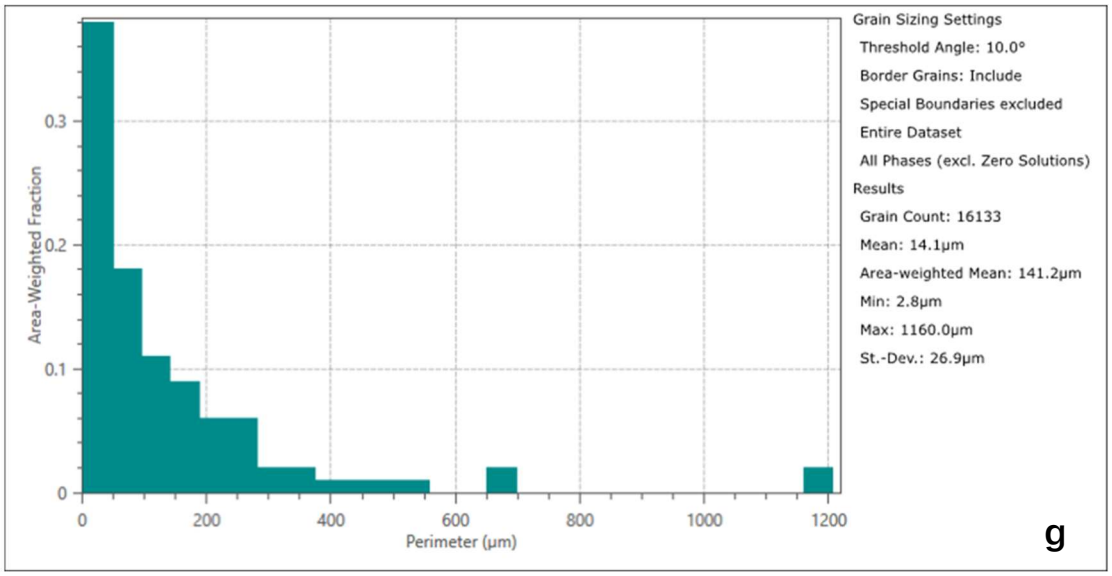

Figure A2-6 The EBSD result of the 420s annealed 2D compressed Mg-0.2Ca-0.3Zn specimen: (a) The inverse pole figure map and grain boundaries, (b) The grain boundaries and the special grain boundaries, (c) The band contrast and the phase analysis, (d) The band contrast, (e) The pole figure, (f) The inverse pole figures, (g) Grain size distribution expressed as grain boundary perimeter

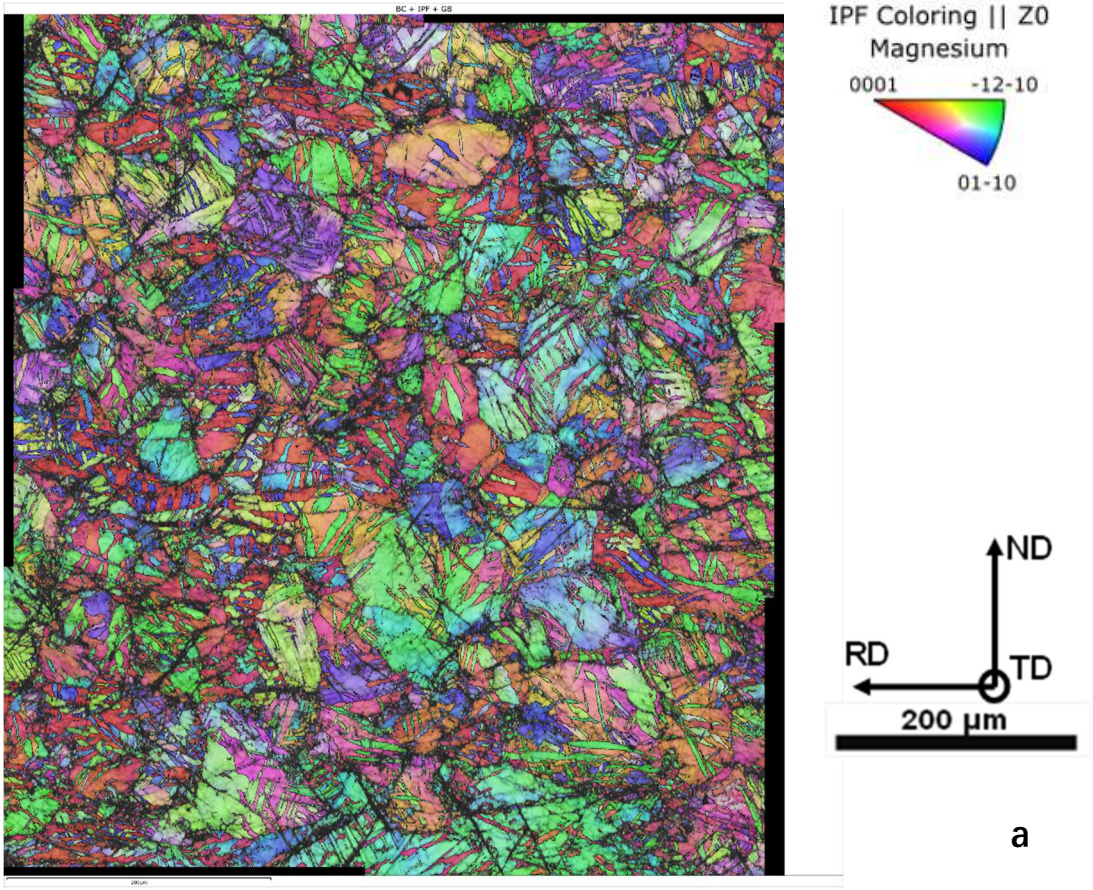

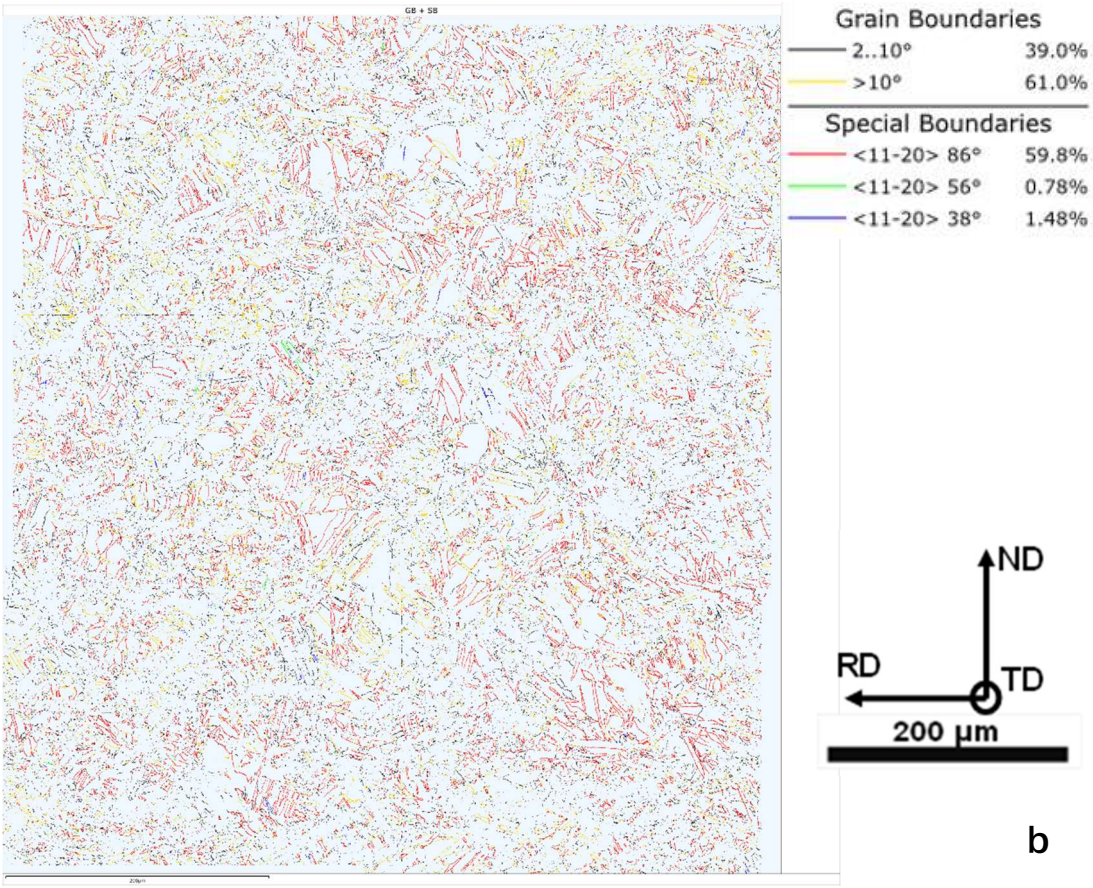
GB + SB
Grain Boundaries
2..10° 39.0%
>10° 61.0%
Special Boundaries
<11-20> 86° 59.8%
<11-20> 56° 0.78%
<11-20> 38° 1.48%
ND
RD
TD
200 µm

b

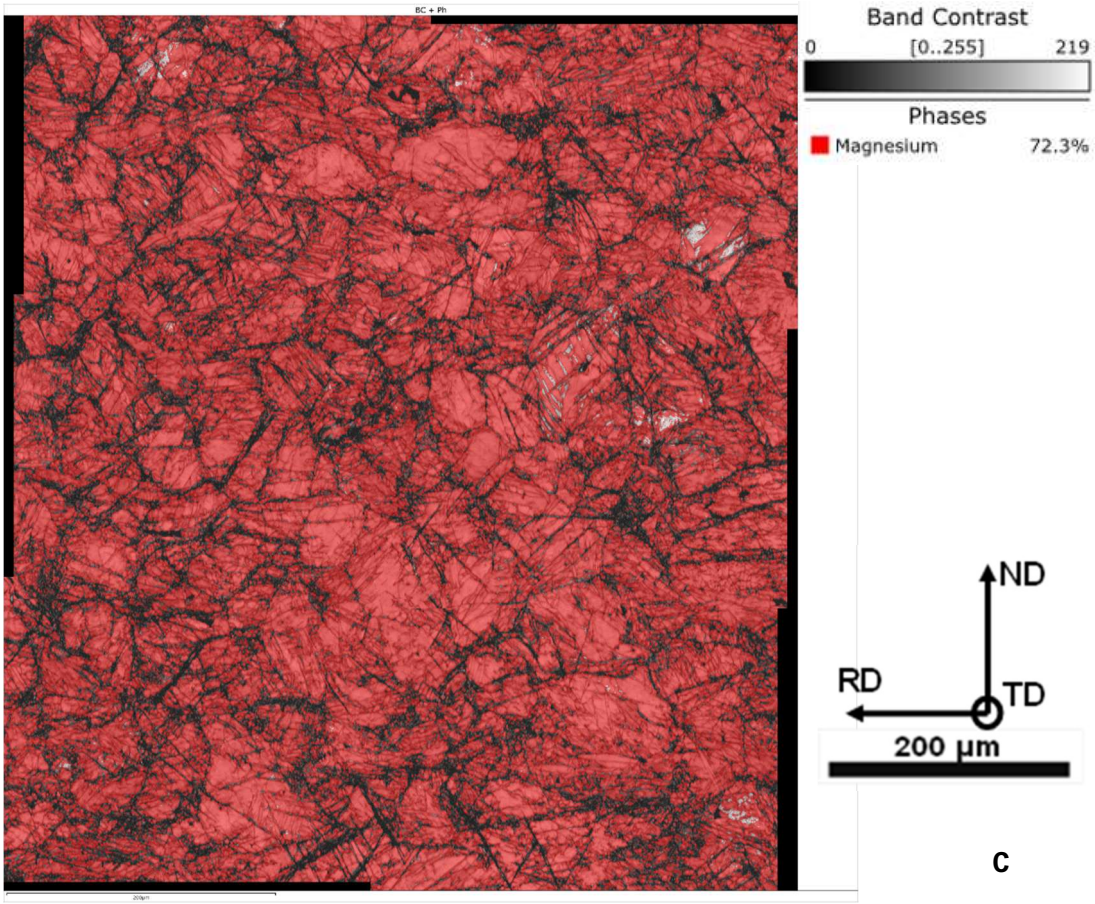
BC + Ph
Band Contrast
0 [0..255] 219
Phases
Magnesium 72.3%
ND
RD
TD
200 µm

c

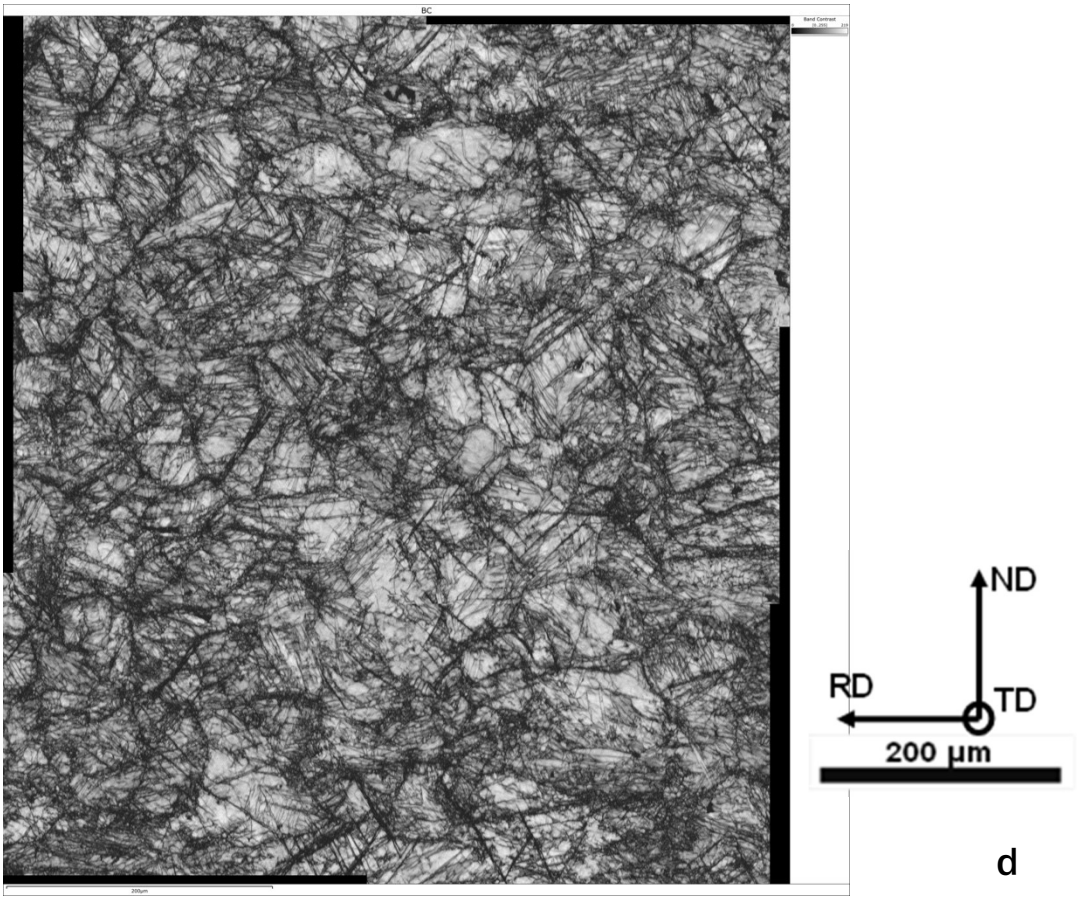
ND
RD
TD
200 µm
d

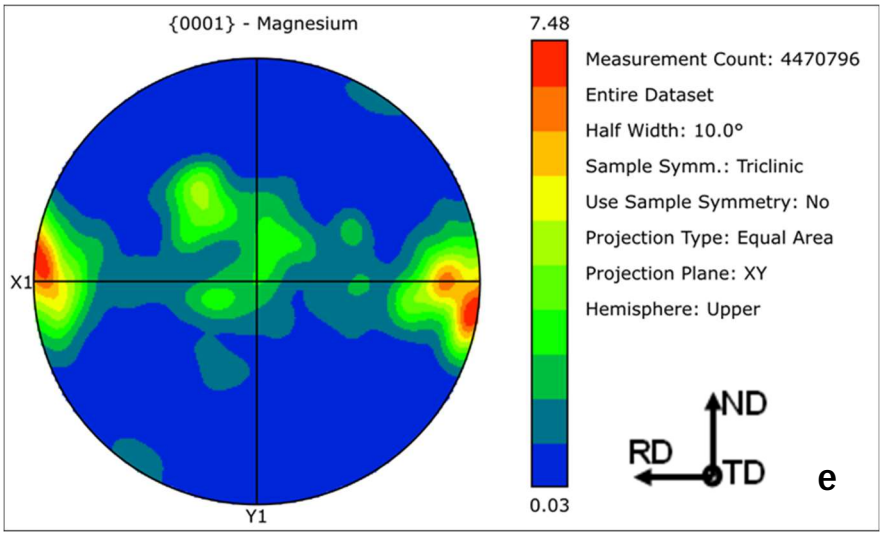
{0001} - Magnesium
7.48
0.03
X1
Y1
Measurement Count: 4470796
Entire Dataset
Half Width: 10.0°
Sample Symm.: Triclinic
Use Sample Symmetry: No
Projection Type: Equal Area
Projection Plane: XY
Hemisphere: Upper
ND
RD
TD
e

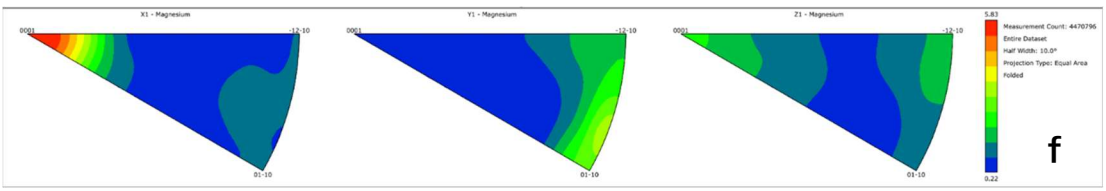
f

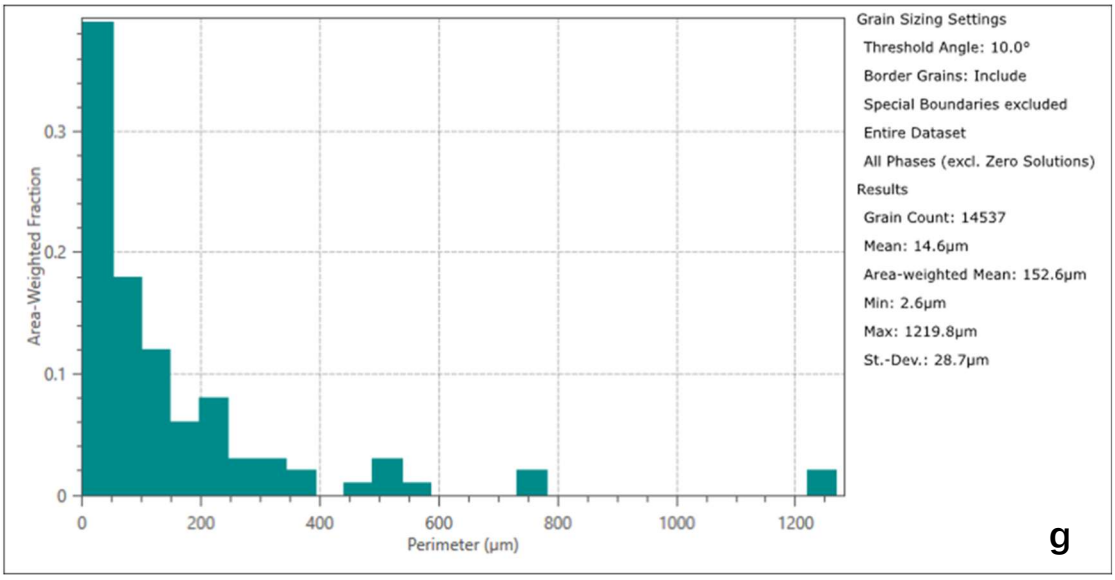

Figure A2-7 The EBSD result of the 570s annealed 2D compressed Mg-0.2Ca-0.3Zn specimen: (a) The inverse pole figure map and grain boundaries, (b) The grain boundaries and the special grain boundaries, (c) The band contrast and the phase analysis, (d) The band contrast, (e) The pole figure, (f) The inverse pole figures, (g) Grain size distribution expressed as grain boundary perimeter

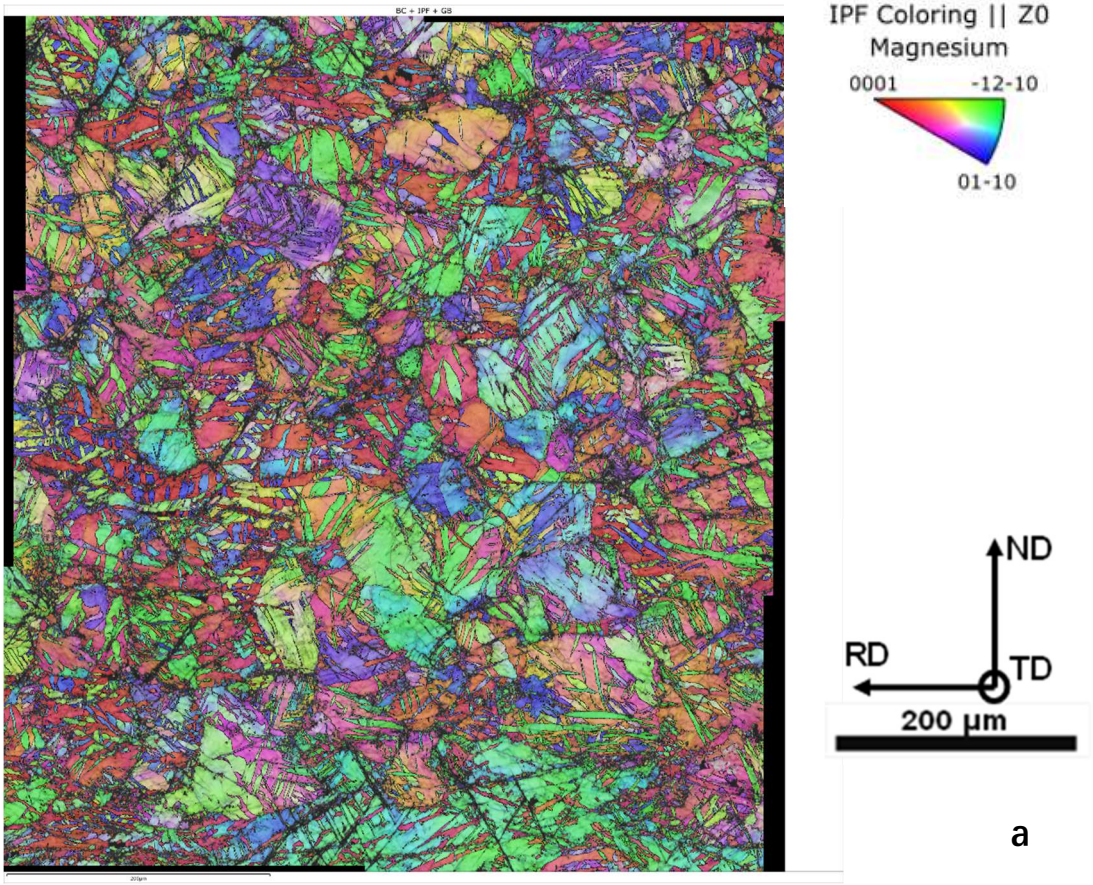

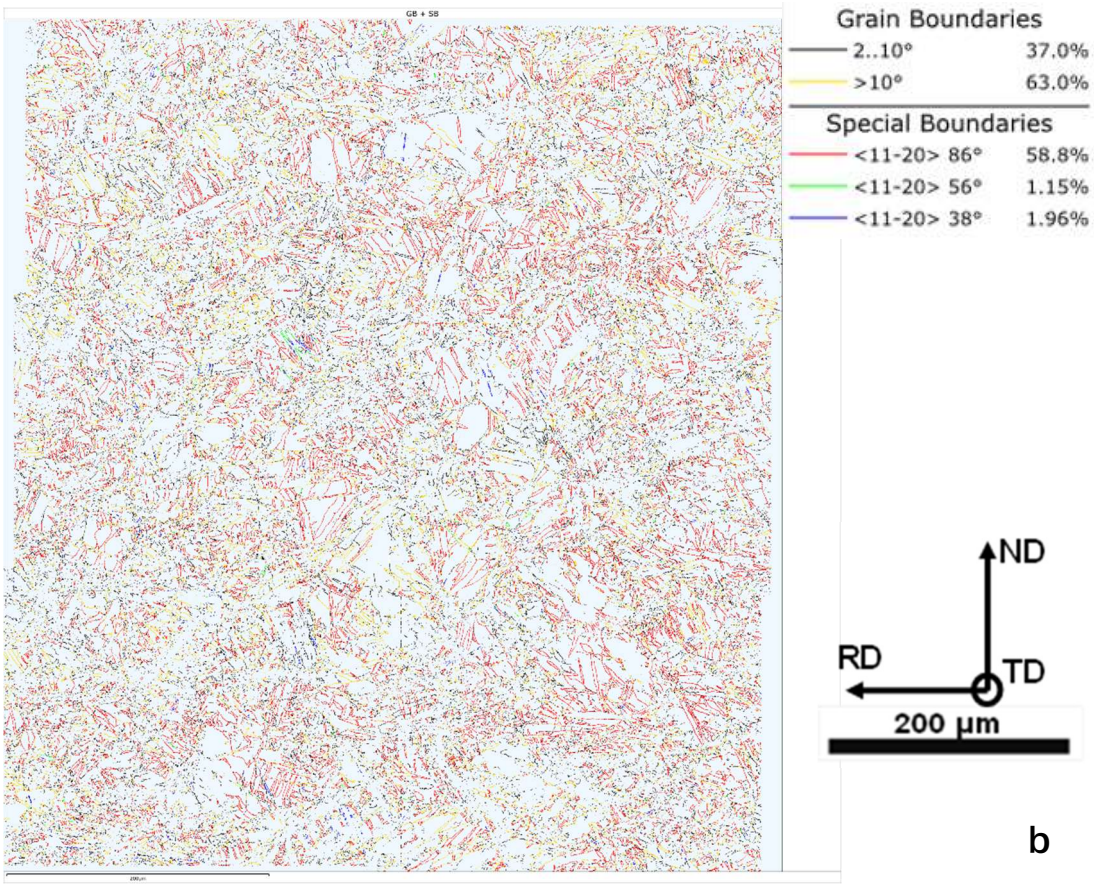
GB + SB
Grain Boundaries
2..10° 37.0%
>10° 63.0%
Special Boundaries
<11-20> 86° 58.8%
<11-20> 56° 1.15%
<11-20> 38° 1.96%
ND
RD
TD
200 µm

b

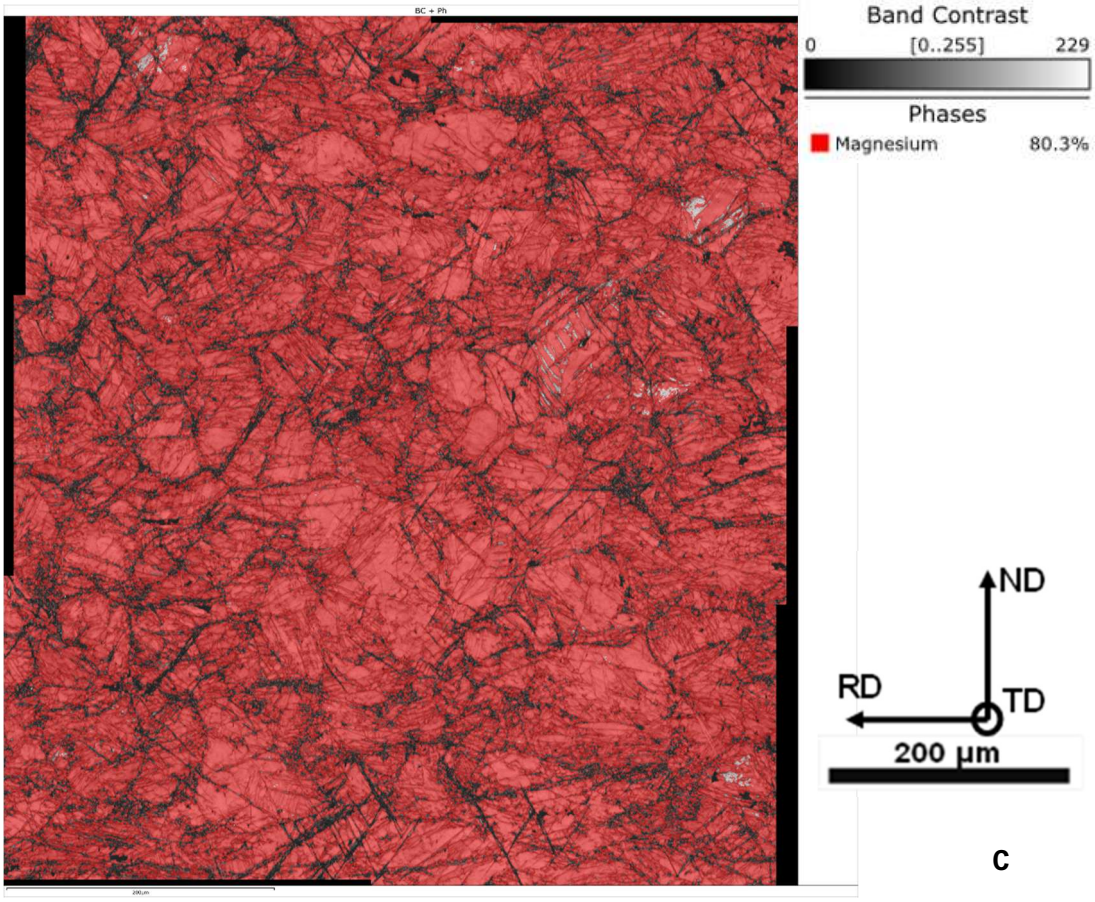
BC + Ph
Band Contrast
0 [0..255] 229
Phases
Magnesium 80.3%
ND
RD
TD
200 µm

c

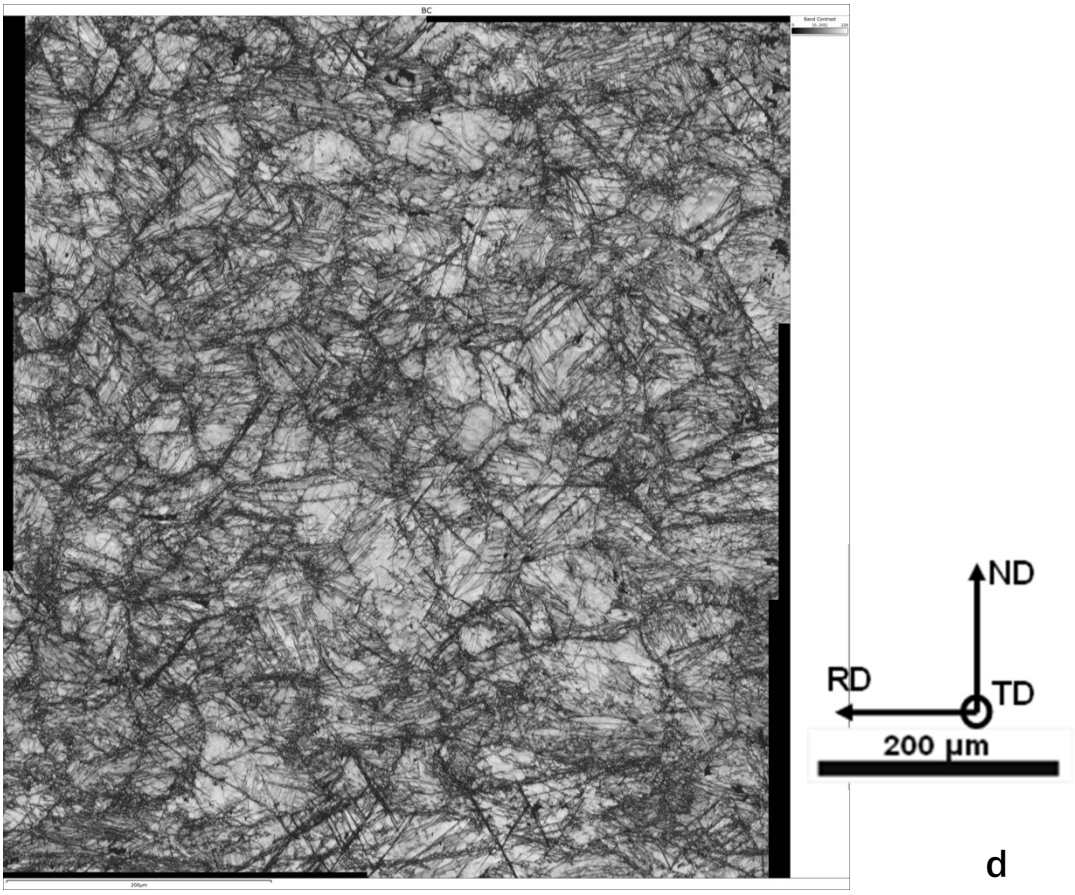
BC
ND
RD
TD
200 µm
d

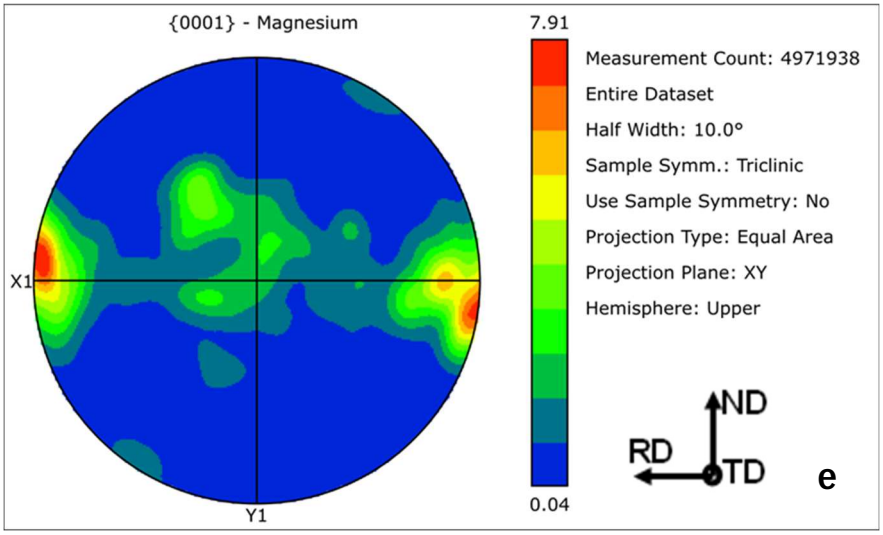
{0001} - Magnesium
7.91
0.04
Measurement Count: 4971938
Entire Dataset
Half Width: 10.0°
Sample Symm.: Triclinic
Use Sample Symmetry: No
Projection Type: Equal Area
Projection Plane: XY
Hemisphere: Upper
X1
Y1
ND
RD
TD
e

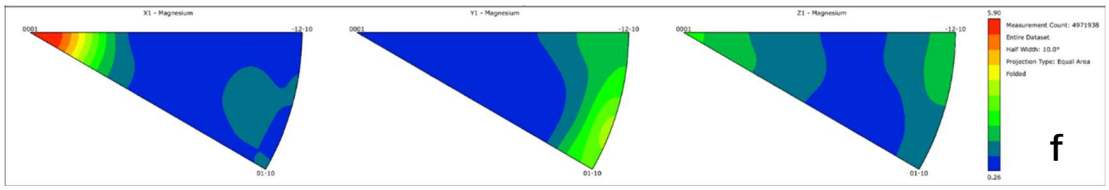
X1 - Magnesium
Y1 - Magnesium
Z1 - Magnesium
f

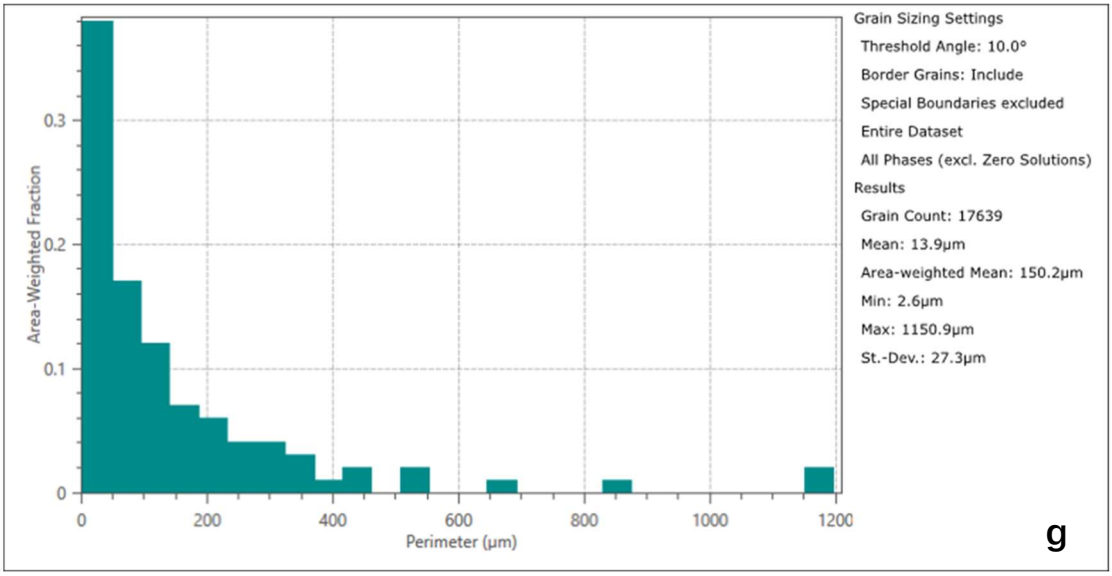

Figure A2-8 The EBSD result of the 750s annealed 2D compressed Mg-0.2Ca-0.3Zn specimen: (a) The inverse pole figure map and grain boundaries, (b) The grain boundaries and the special grain boundaries, (c) The band contrast and the phase analysis, (d) The band contrast, (e) The pole figure, (f) The inverse pole figures, (g) Grain size distribution expressed as grain boundary perimeter

A3 Channel die one-direction compressed Mg-0.1Ca-0.4Zn (at%) specimens

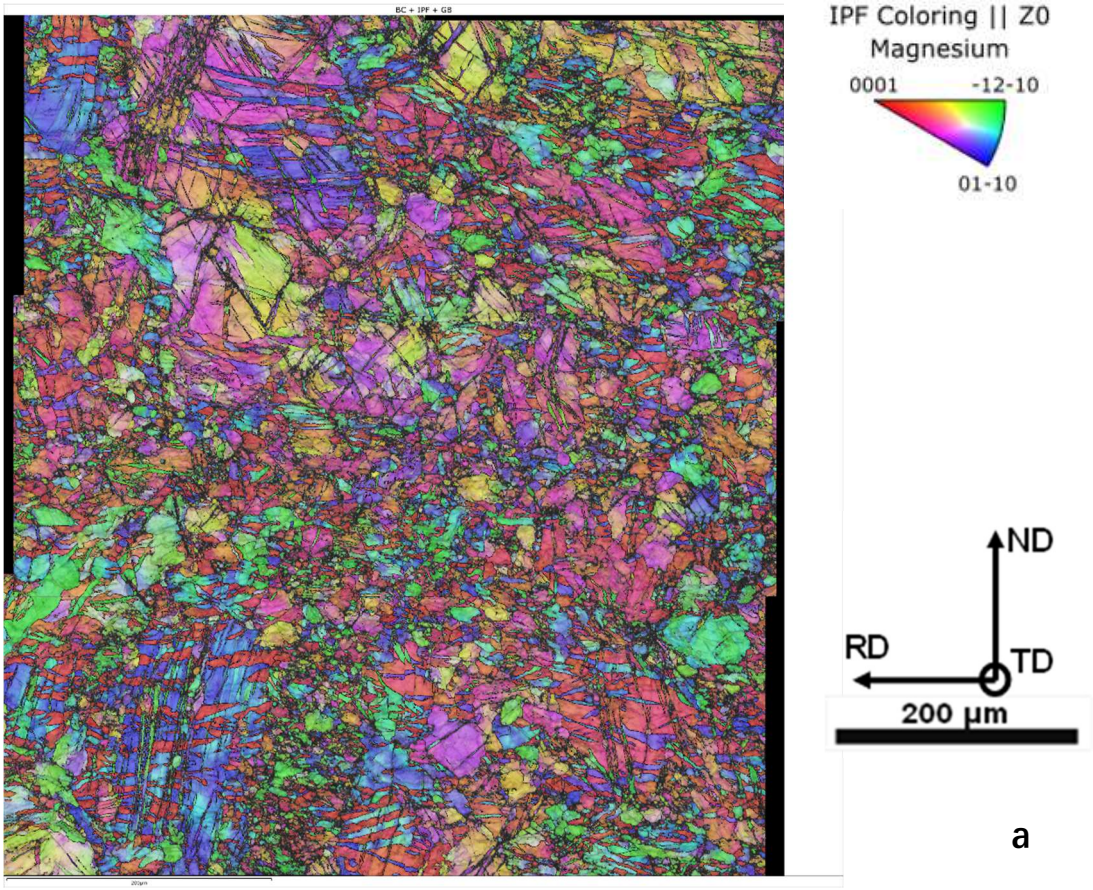

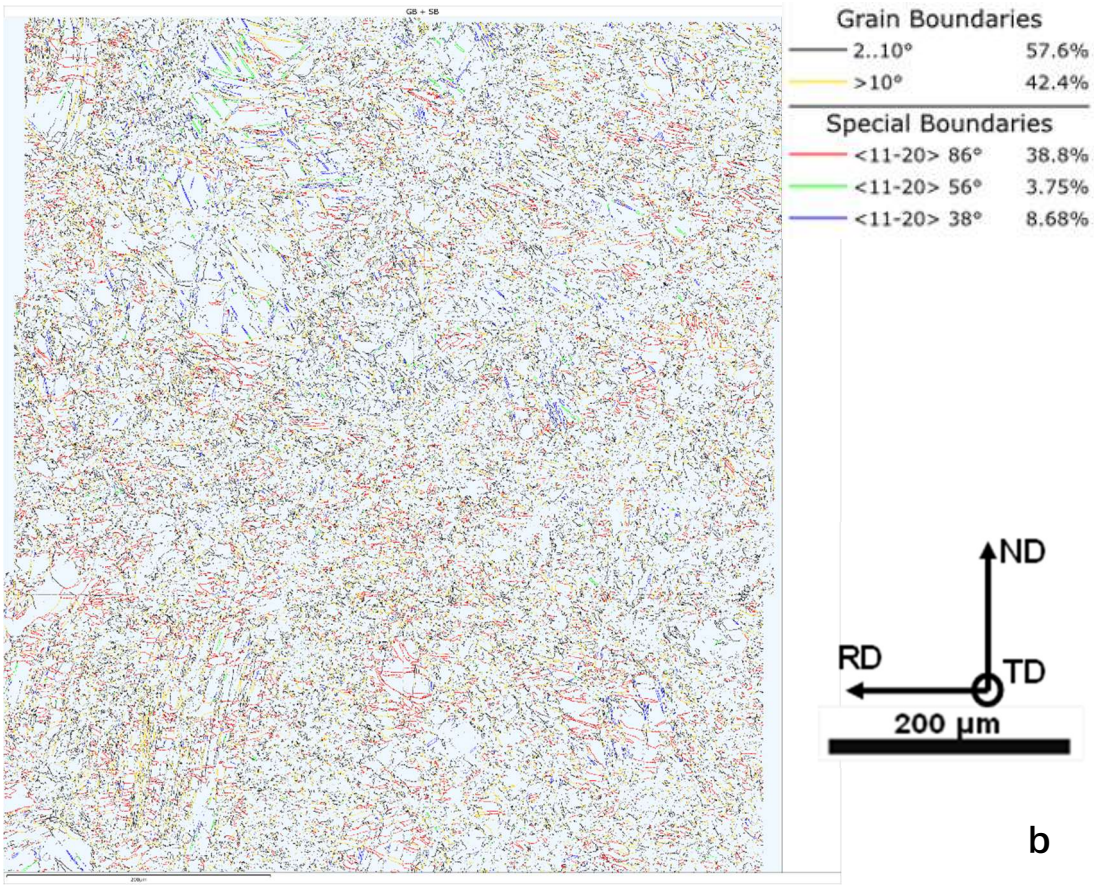
GB + SB
Grain Boundaries
2..10° 57.6%
>10° 42.4%
Special Boundaries
<11-20> 86° 38.8%
<11-20> 56° 3.75%
<11-20> 38° 8.68%
ND
RD
TD
200 µm

b

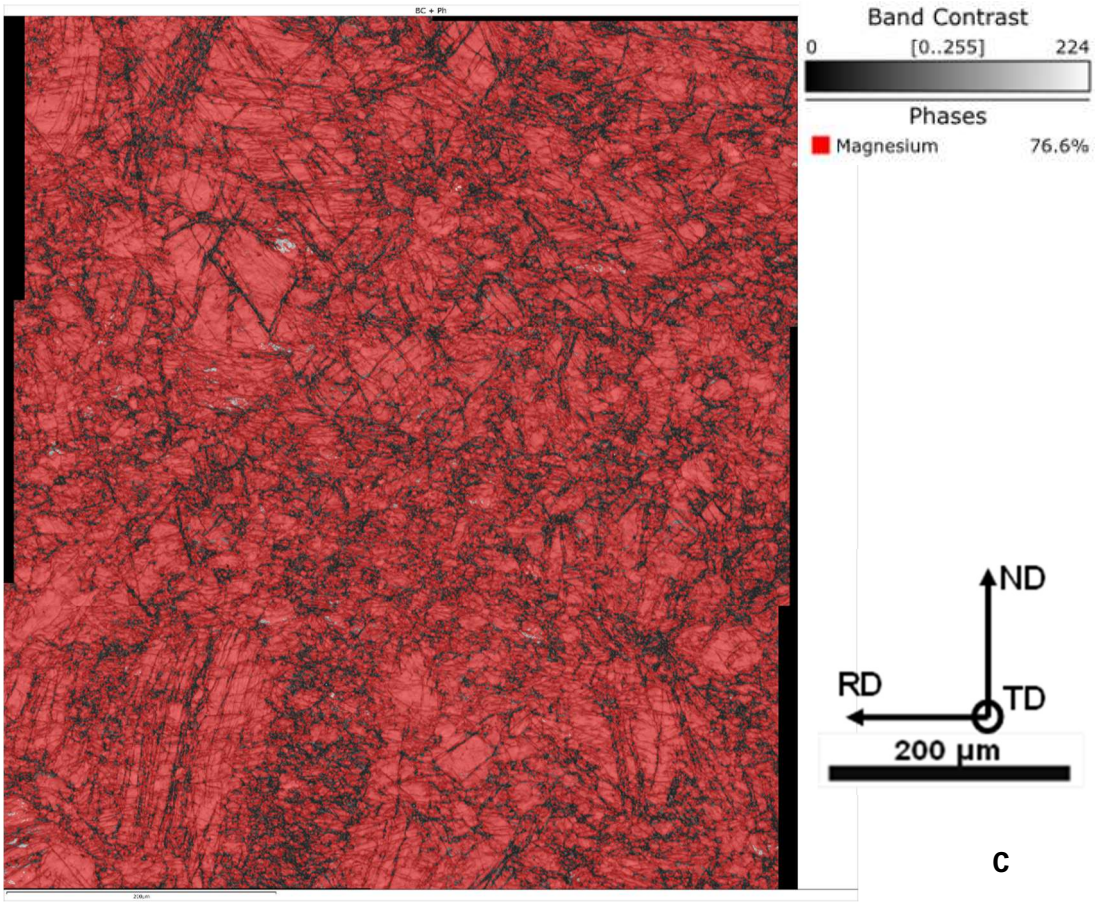
BC + Ph
Band Contrast
0 [0..255] 224
Phases
Magnesium 76.6%
ND
RD
TD
200 µm

c

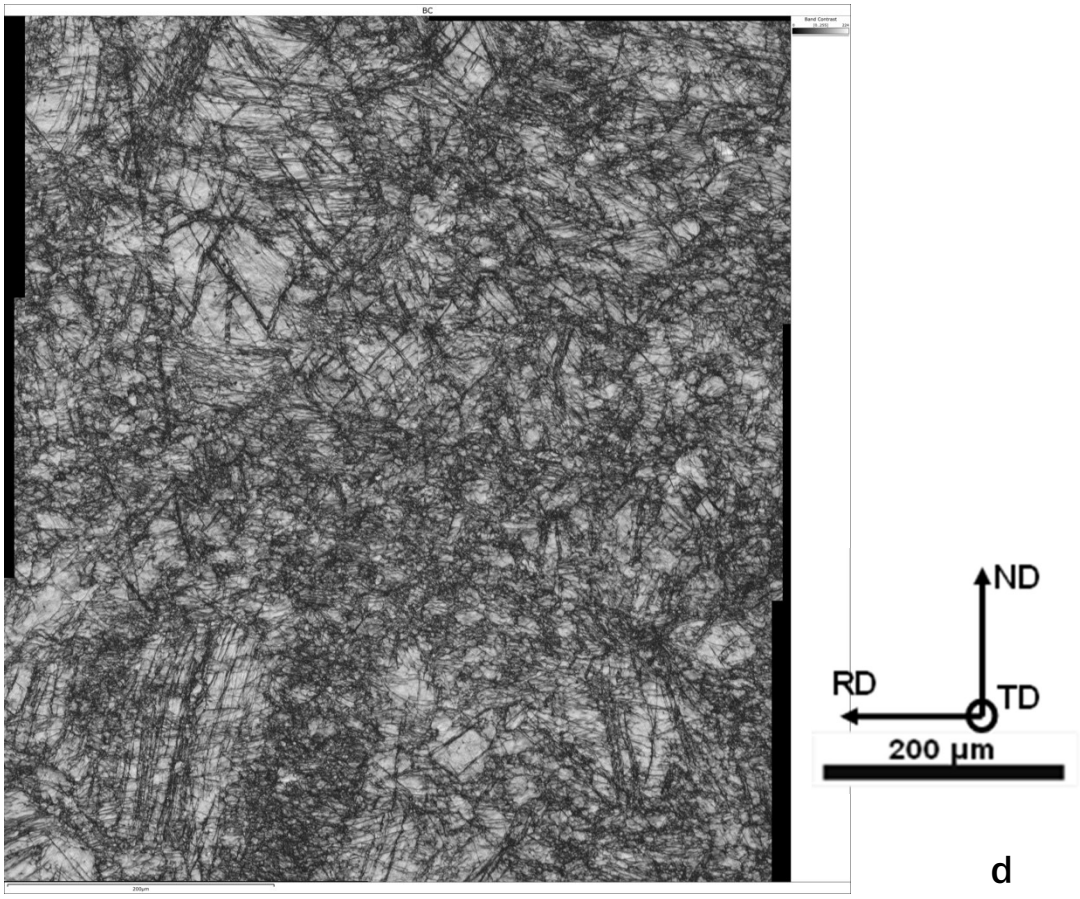
BC
ND
RD
TD
200 µm

d

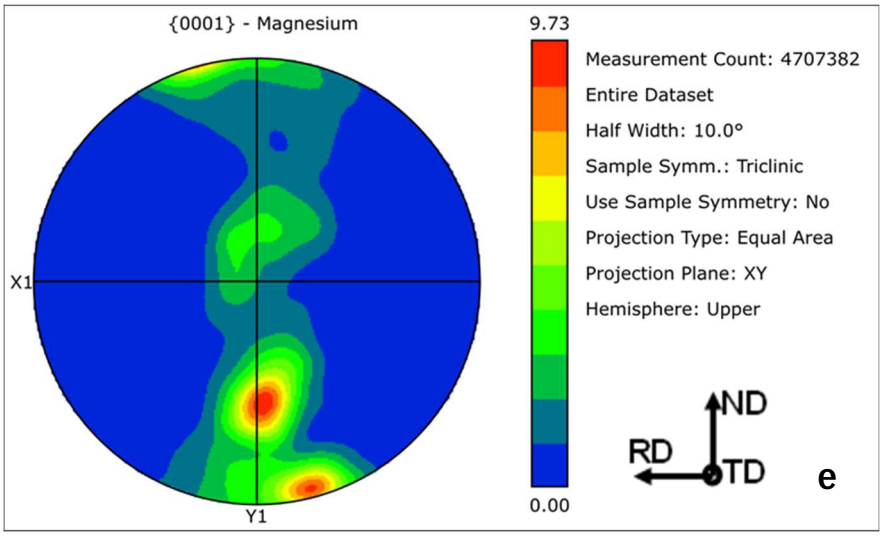
{0001} - Magnesium
9.73
0.00
Measurement Count: 4707382
Entire Dataset
Half Width: 10.0°
Sample Symm.: Triclinic
Use Sample Symmetry: No
Projection Type: Equal Area
Projection Plane: XY
Hemisphere: Upper
X1
Y1
ND
RD
TD

e

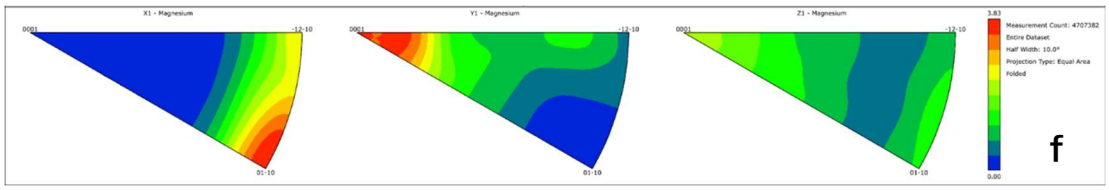
X1 - Magnesium
Y1 - Magnesium
Z1 - Magnesium
3.83
0.00

f

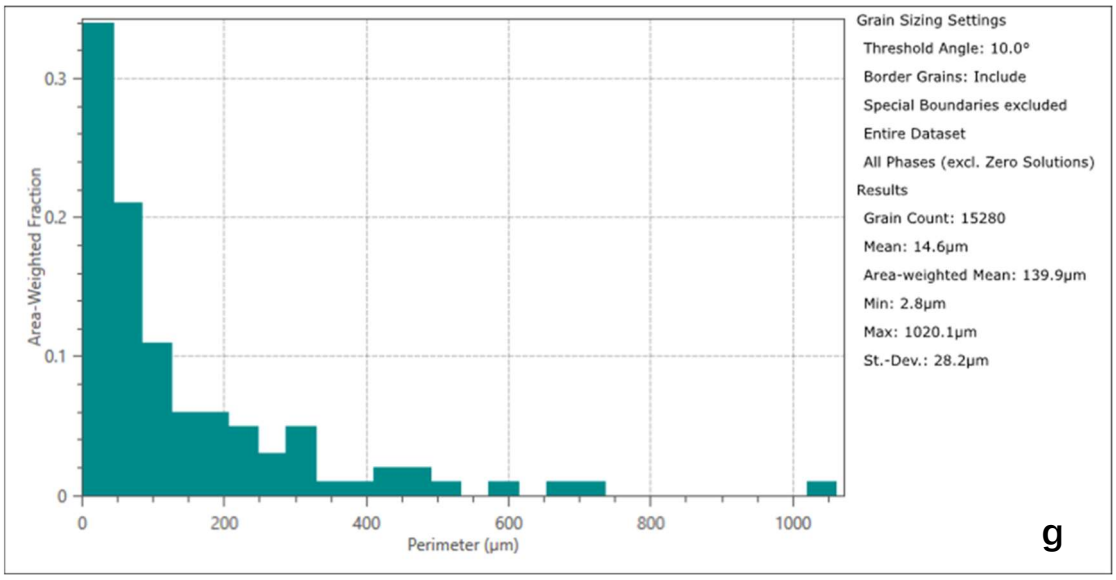

Figure A3-1 The EBSD result of the 30s annealed 1D compressed Mg-0.1Ca-0.4Zn specimen: (a) The inverse pole figure map and grain boundaries, (b) The grain boundaries and the special grain boundaries, (c) The band contrast and the phase analysis, (d) The band contrast, (e) The pole figure, (f) The inverse pole figures, (g) Grain size distribution expressed as grain boundary perimeter

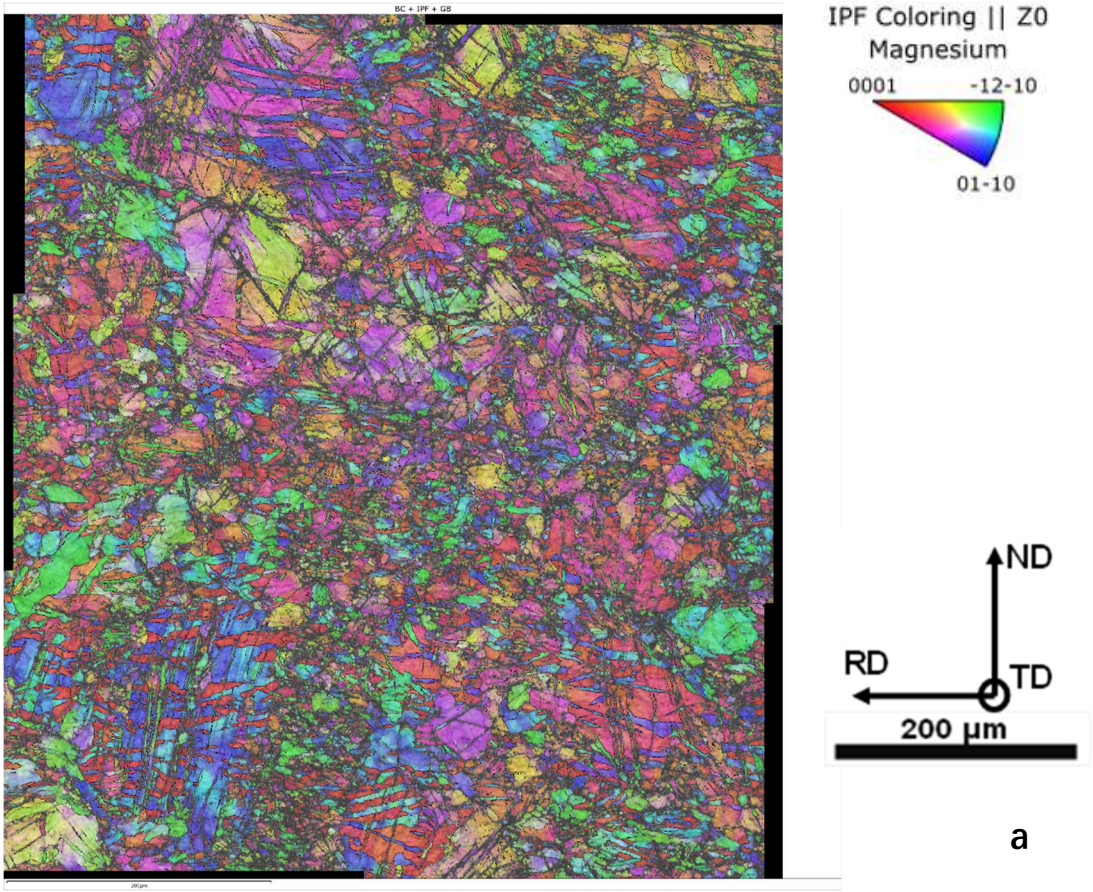

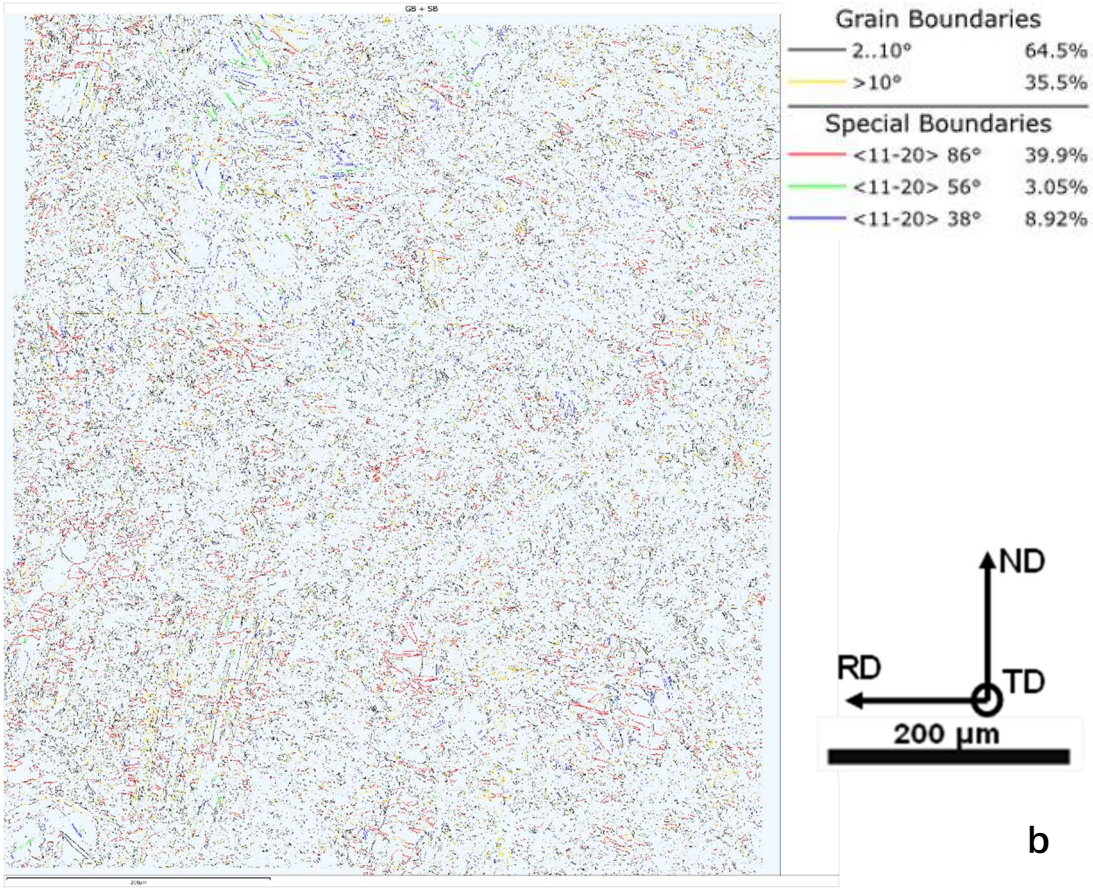
GB + SB
Grain Boundaries
2..10° 64.5%
>10° 35.5%
Special Boundaries
<11-20> 86° 39.9%
<11-20> 56° 3.05%
<11-20> 38° 8.92%
ND
RD
TD
200 µm

b

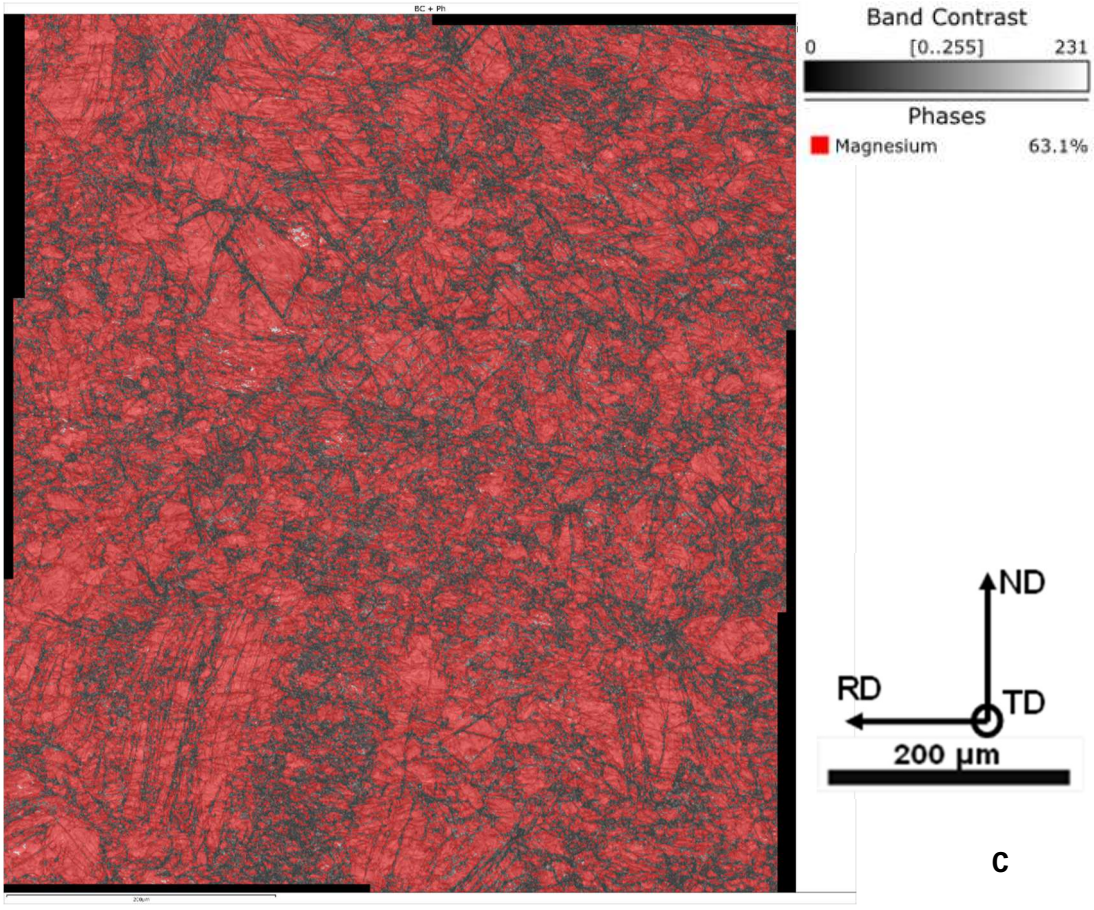
BC + Ph
Band Contrast
0 [0..255] 231
Phases
Magnesium 63.1%
ND
RD
TD
200 µm

c

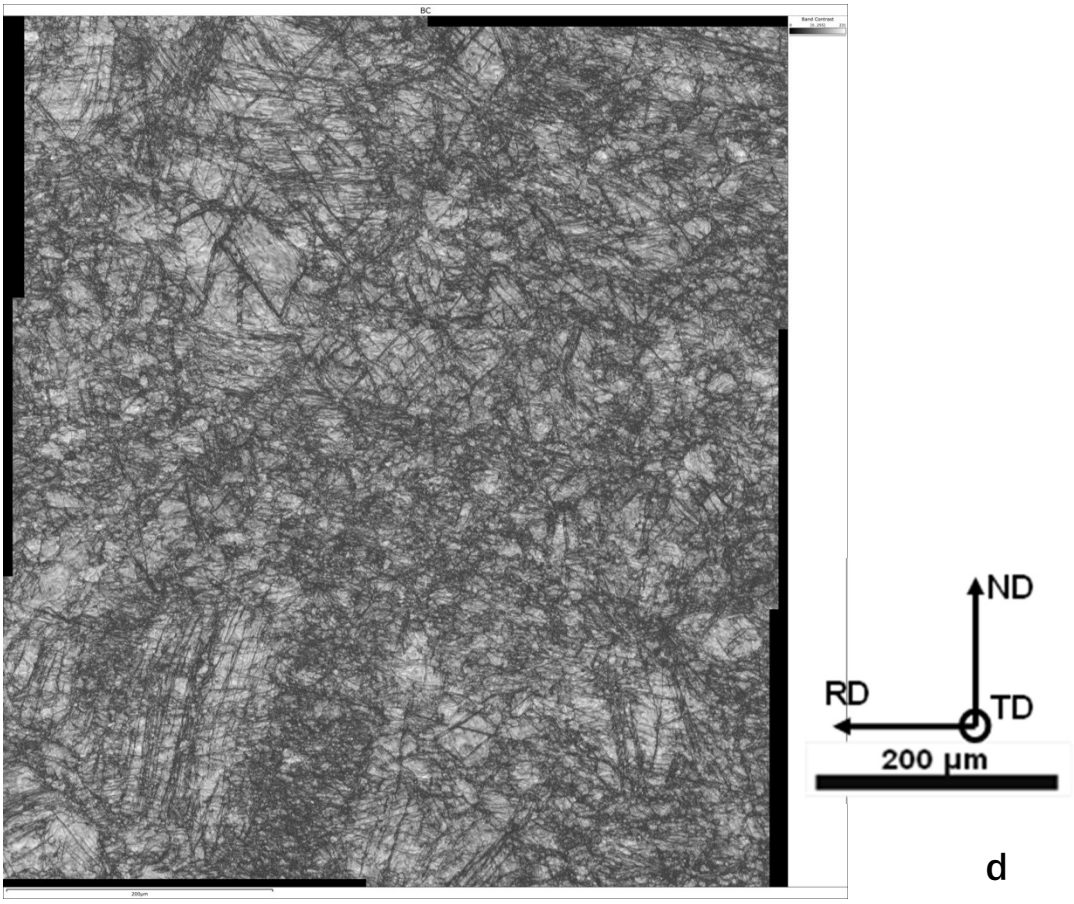
BC
ND
RD
TD
200 µm
d

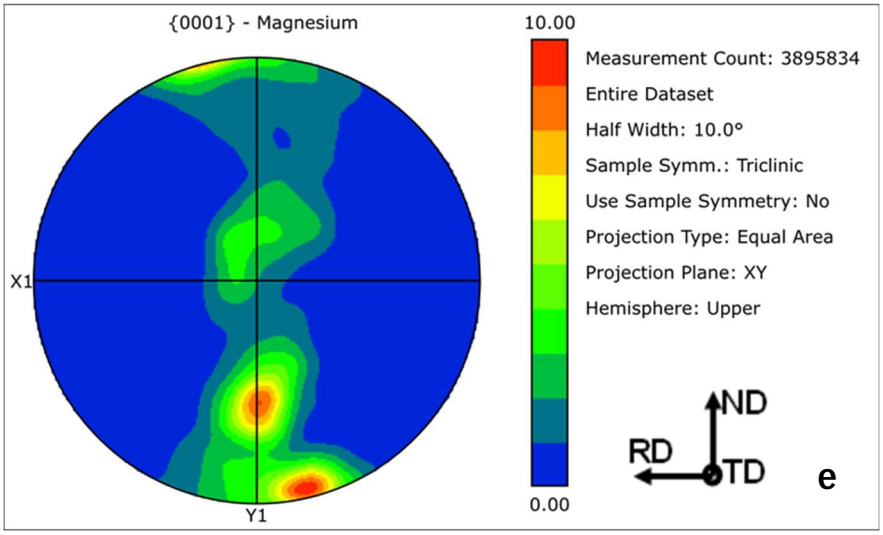
{0001} - Magnesium
10.00
0.00
X1
Y1
Measurement Count: 3895834
Entire Dataset
Half Width: 10.0°
Sample Symm.: Triclinic
Use Sample Symmetry: No
Projection Type: Equal Area
Projection Plane: XY
Hemisphere: Upper
ND
RD
TD
e

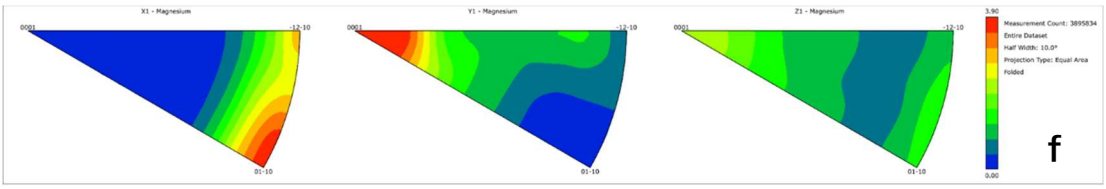
X1 - Magnesium
Y1 - Magnesium
Z1 - Magnesium
f

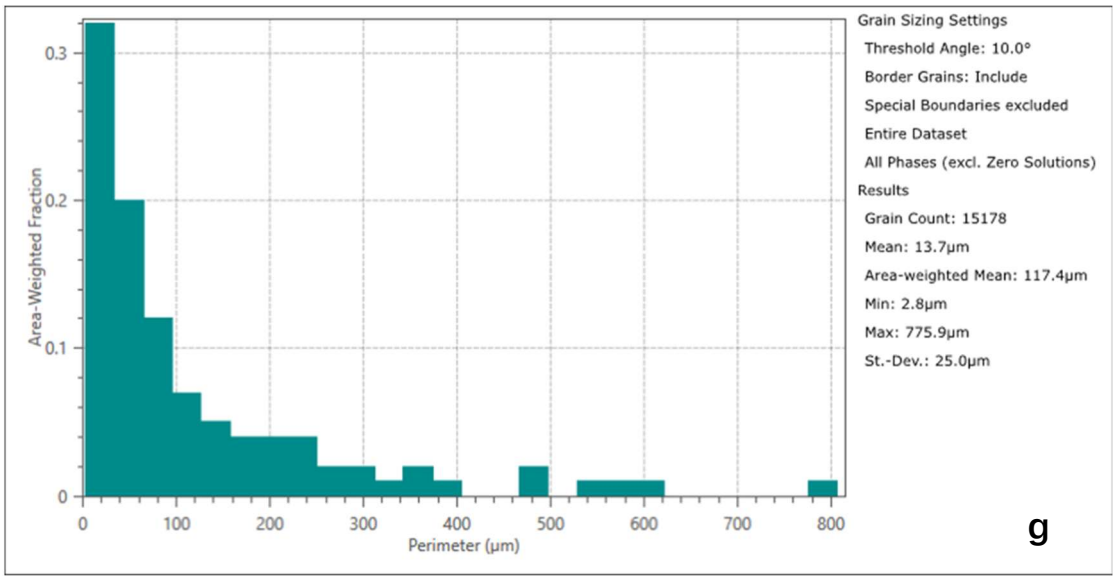

Figure A3-2 The EBSD result of the 75s annealed 1D compressed Mg-0.1Ca-0.4Zn specimen: (a) The inverse pole figure map and grain boundaries, (b) The grain boundaries and the special grain boundaries, (c) The band contrast and the phase analysis, (d) The band contrast, (e) The pole figure, (f) The inverse pole figures, (g) Grain size distribution expressed as grain boundary perimeter

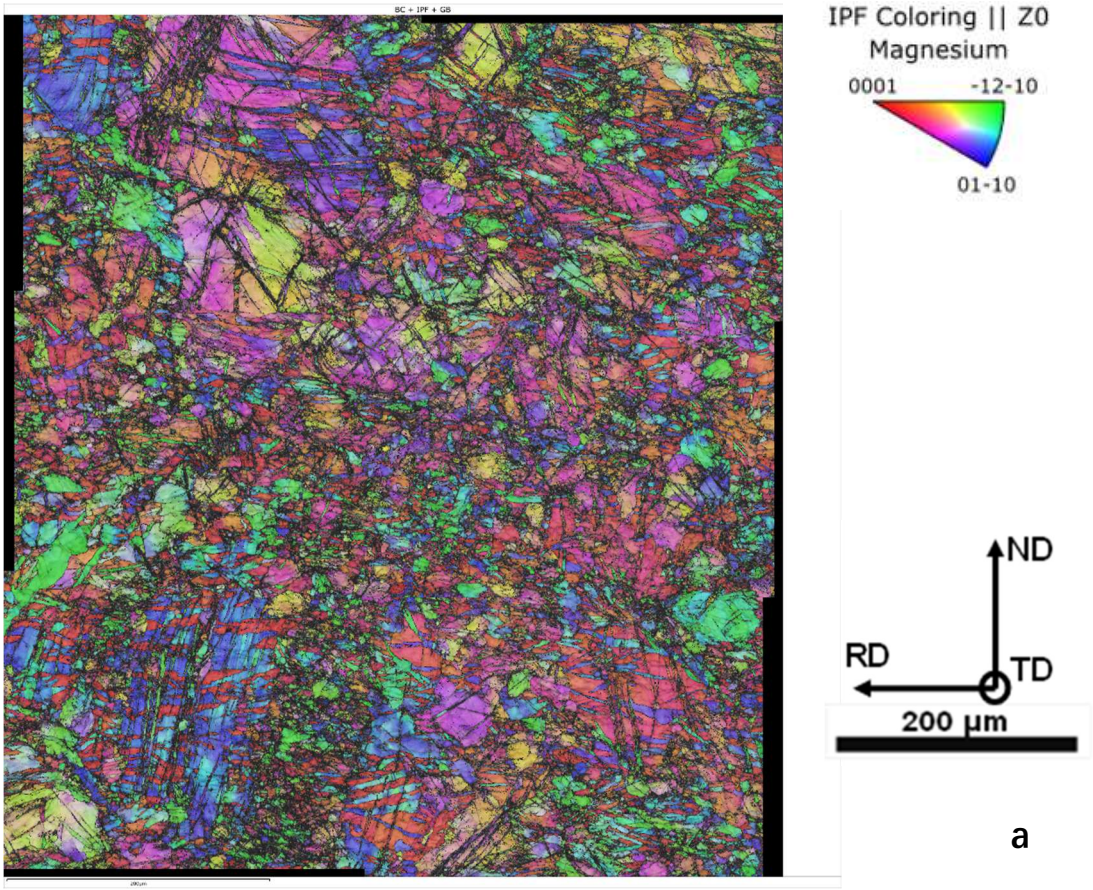

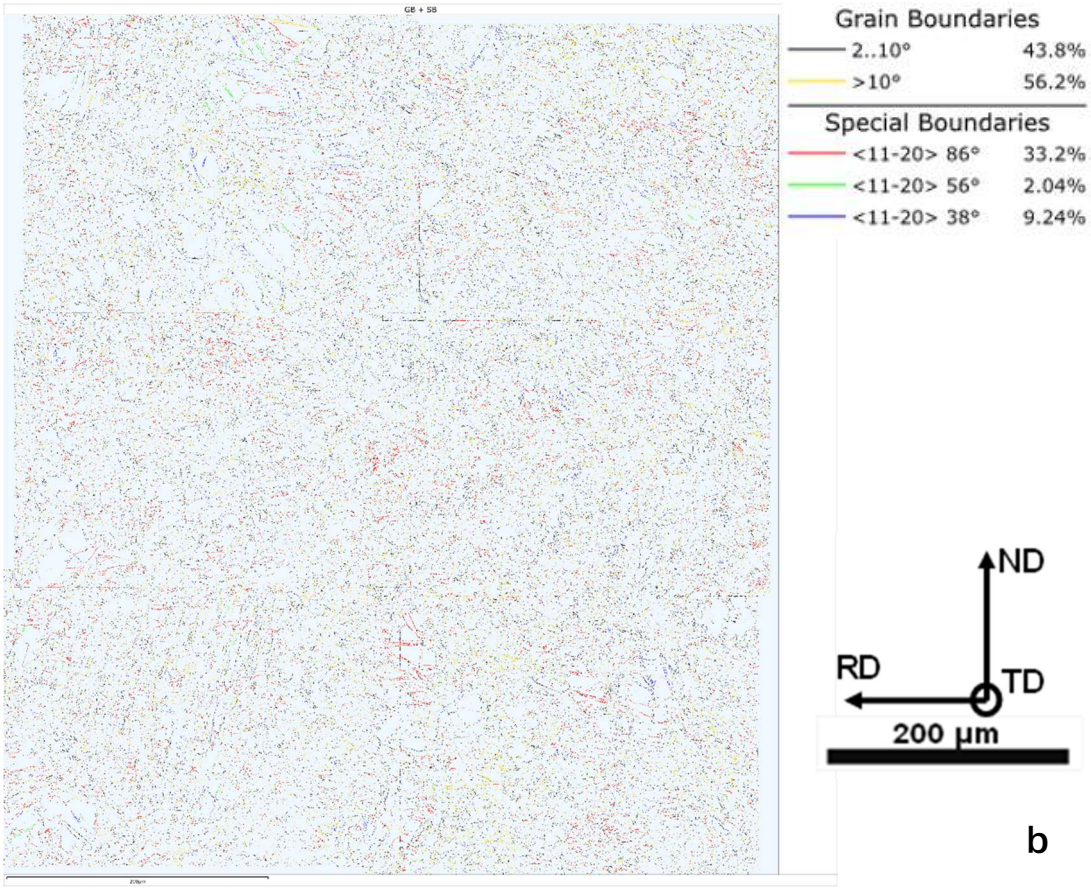
GB + SB
Grain Boundaries
2..10° 43.8%
>10° 56.2%
Special Boundaries
<11-20> 86° 33.2%
<11-20> 56° 2.04%
<11-20> 38° 9.24%
ND
RD
TD
200 µm

b

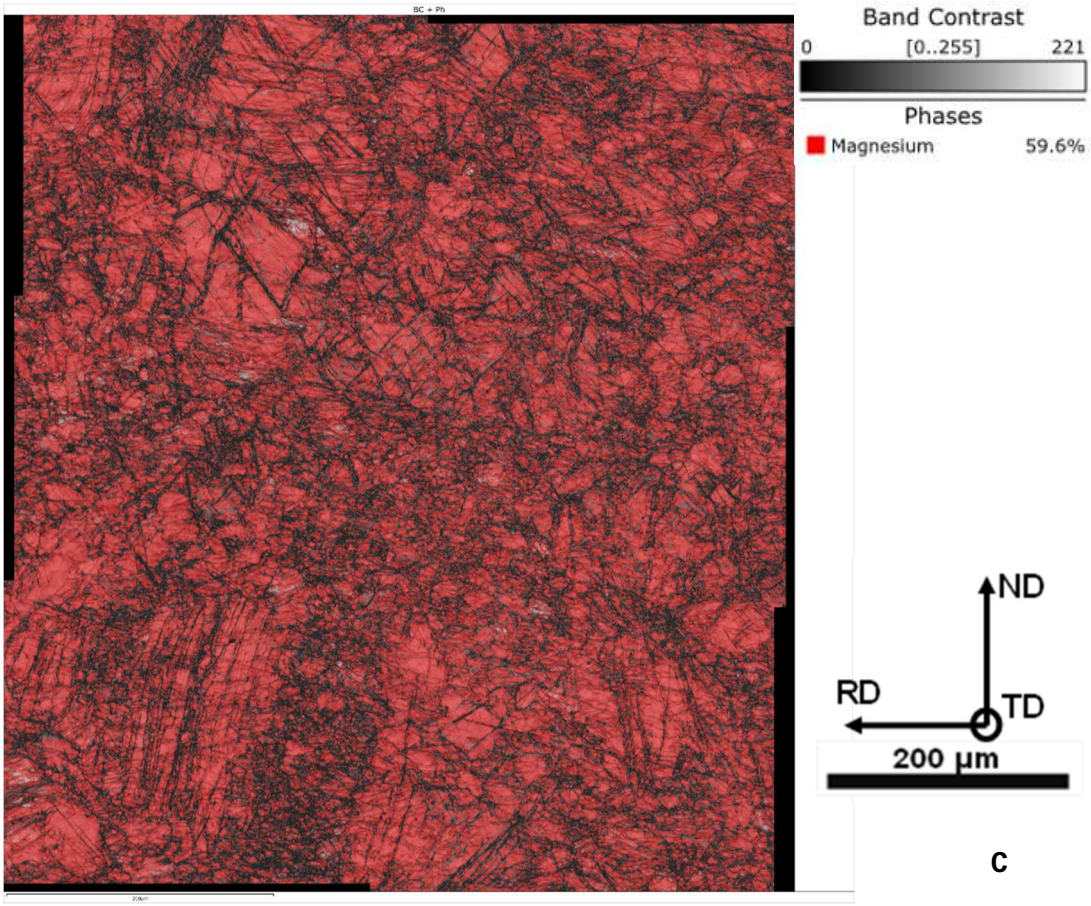
BC + Ph
Band Contrast
0 [0..255] 221
Phases
Magnesium 59.6%
ND
RD
TD
200 µm

c

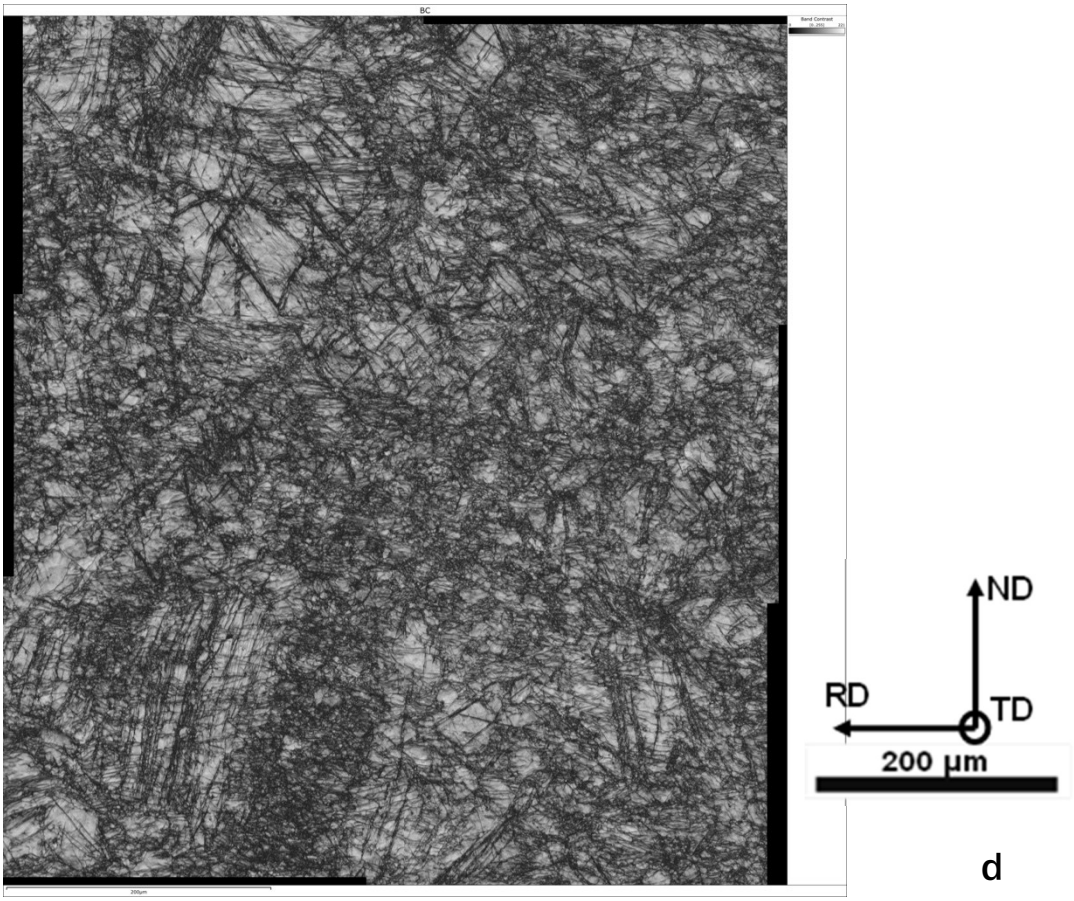
BC
ND
RD
TD
200 µm
d

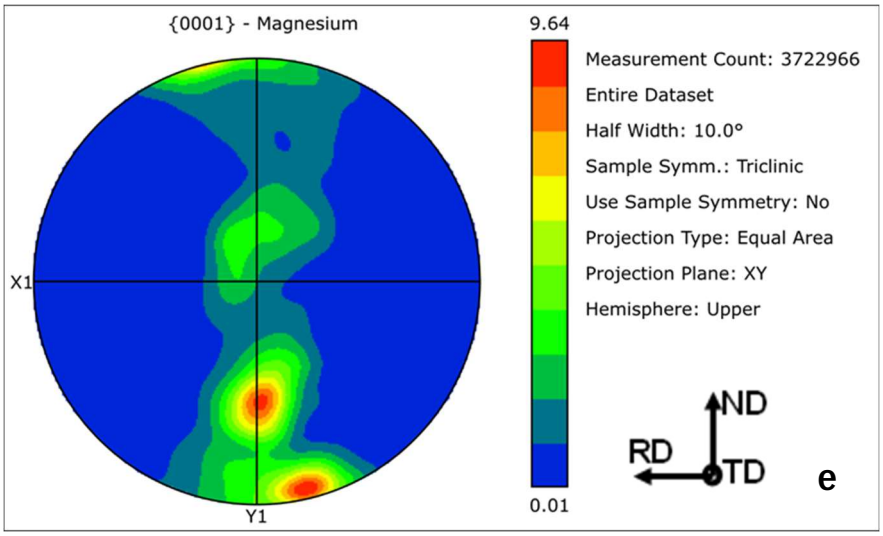
{0001} - Magnesium
9.64
0.01
X1
Y1
Measurement Count: 3722966
Entire Dataset
Half Width: 10.0°
Sample Symm.: Triclinic
Use Sample Symmetry: No
Projection Type: Equal Area
Projection Plane: XY
Hemisphere: Upper
ND
RD
TD
e

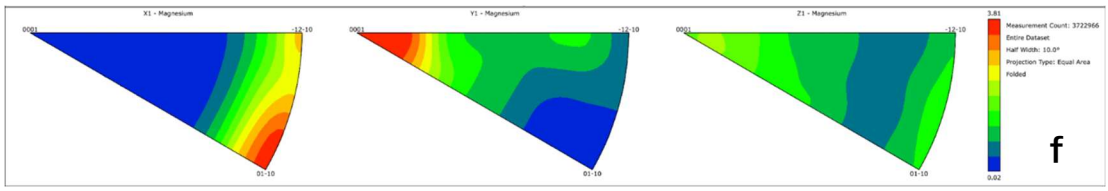
X1 - Magnesium
Y1 - Magnesium
Z1 - Magnesium
f

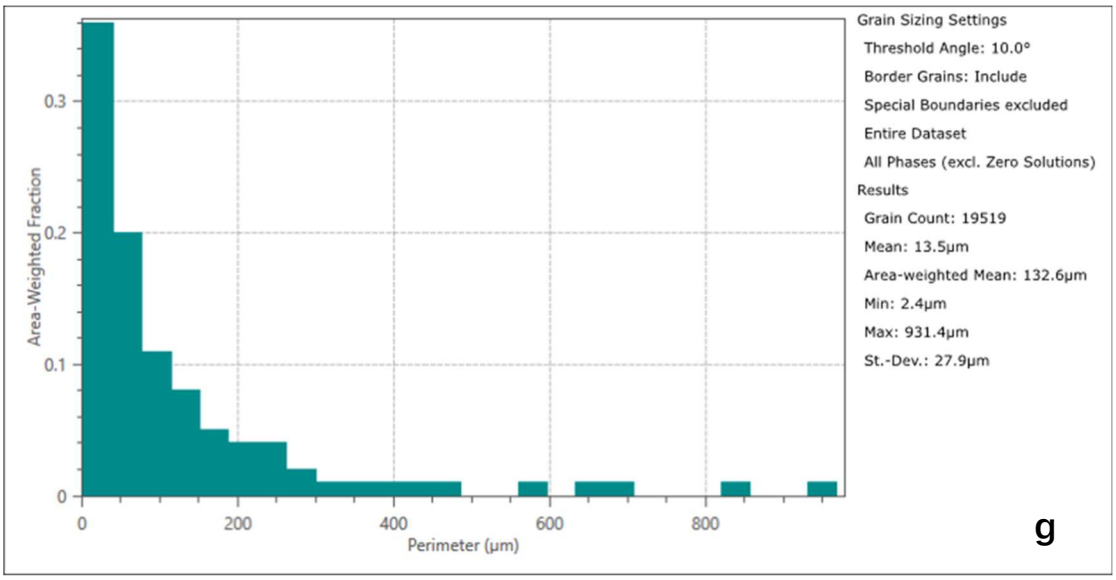

Figure A3-3 The EBSD result of the 135s annealed 1D compressed Mg-0.1Ca-0.4Zn specimen: (a) The inverse pole figure map and grain boundaries, (b) The grain boundaries and the special grain boundaries, (c) The band contrast and the phase analysis, (d) The band contrast, (e) The pole figure, (f) The inverse pole figures, (g) Grain size distribution expressed as grain boundary perimeter

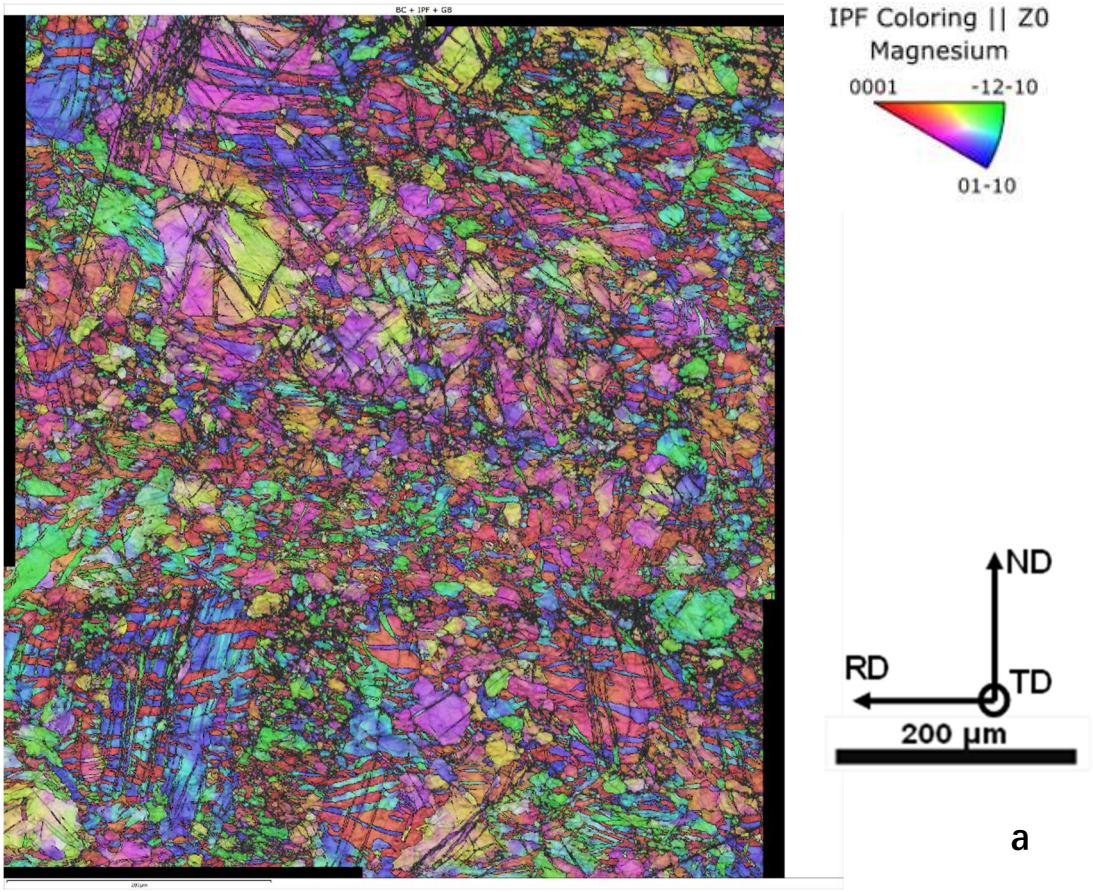

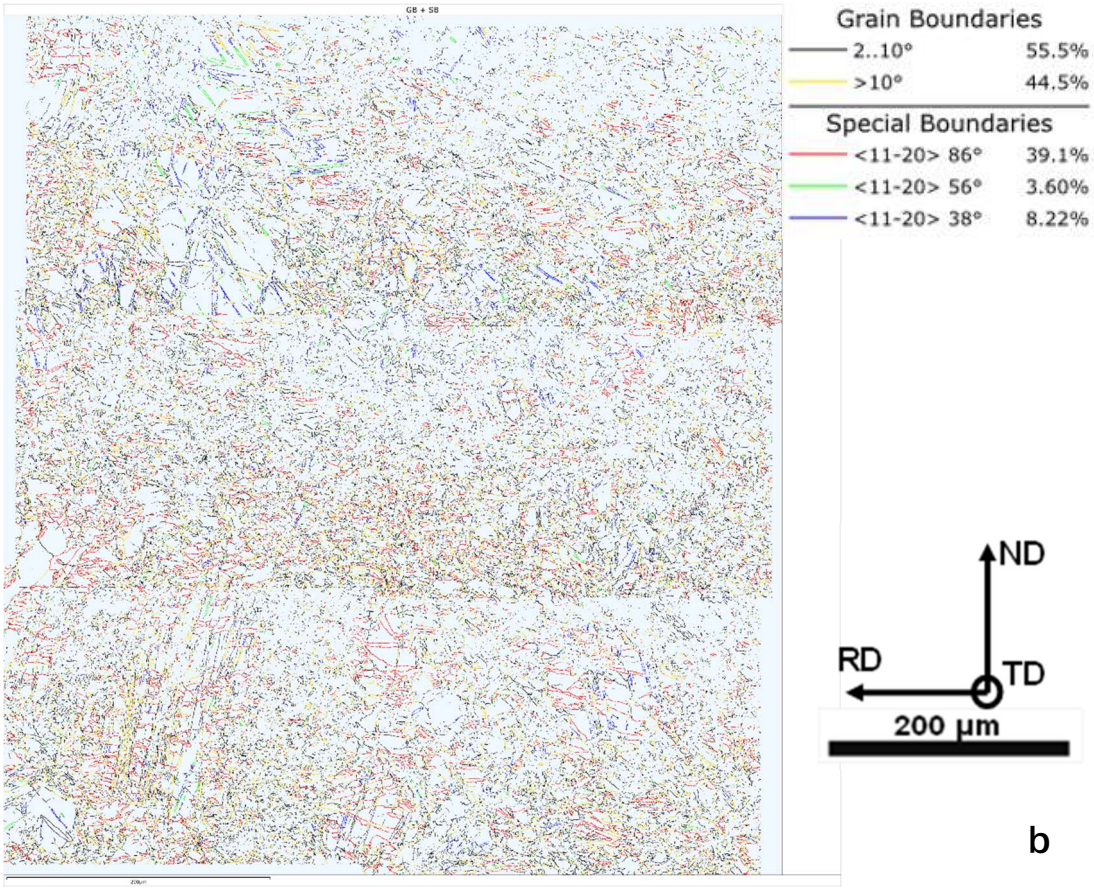
GB + SB
Grain Boundaries
2..10° 55.5%
>10° 44.5%
Special Boundaries
<11-20> 86° 39.1%
<11-20> 56° 3.60%
<11-20> 38° 8.22%
ND
RD
TD
200 µm

b

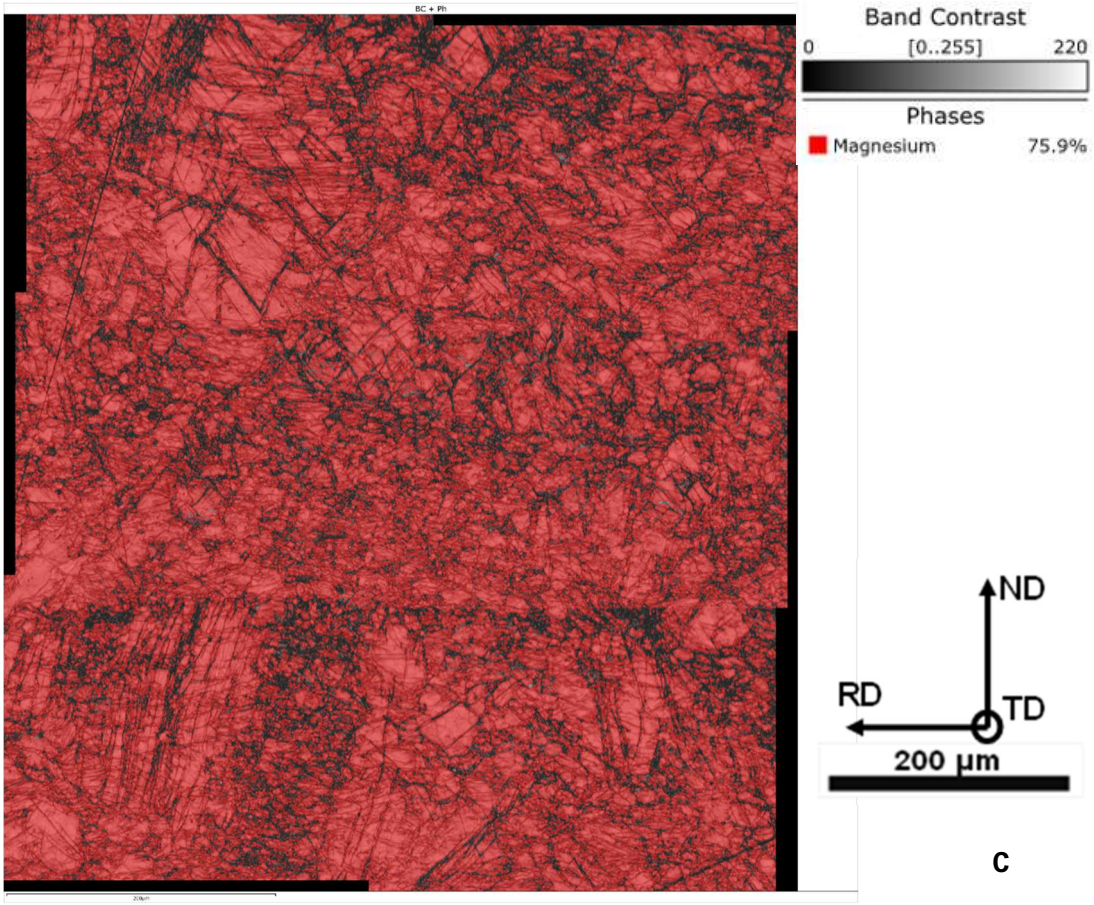
BC + Ph
Band Contrast
0 [0..255] 220
Phases
Magnesium 75.9%
ND
RD
TD
200 µm

c

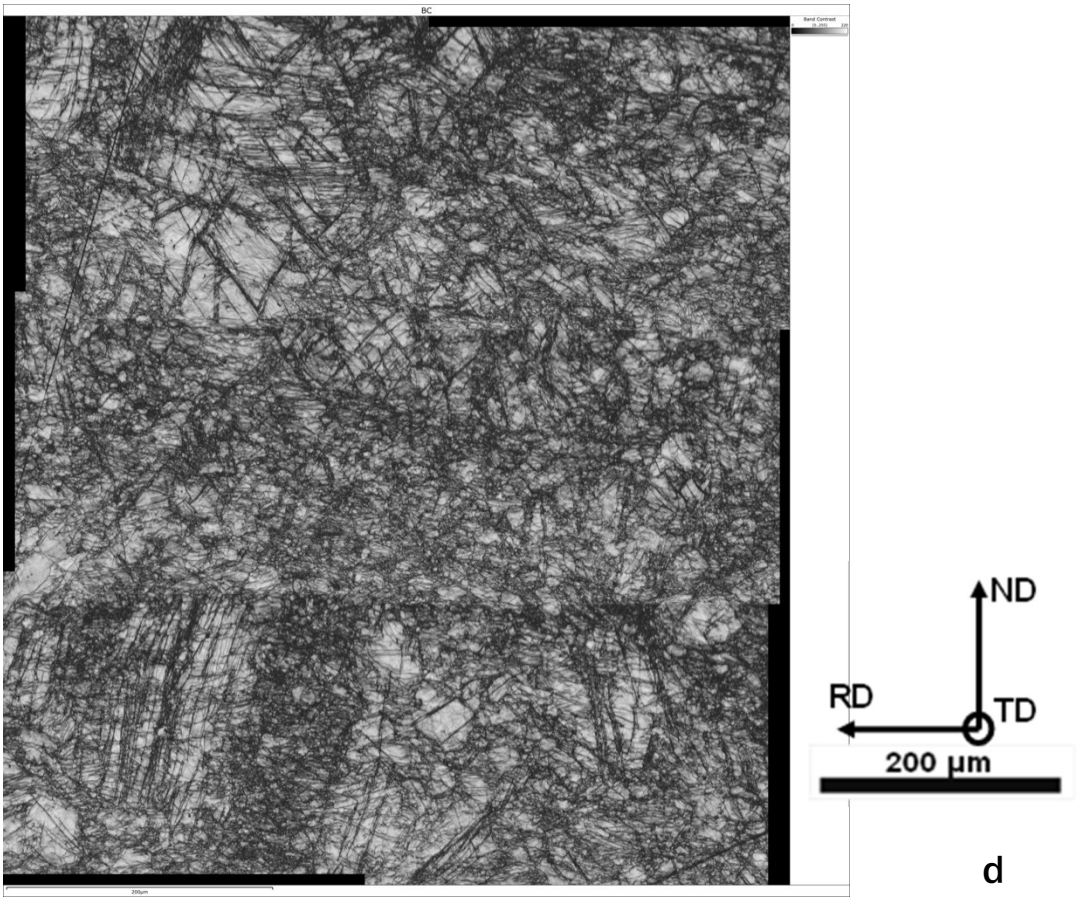
BC
ND
RD
TD
200 µm

d

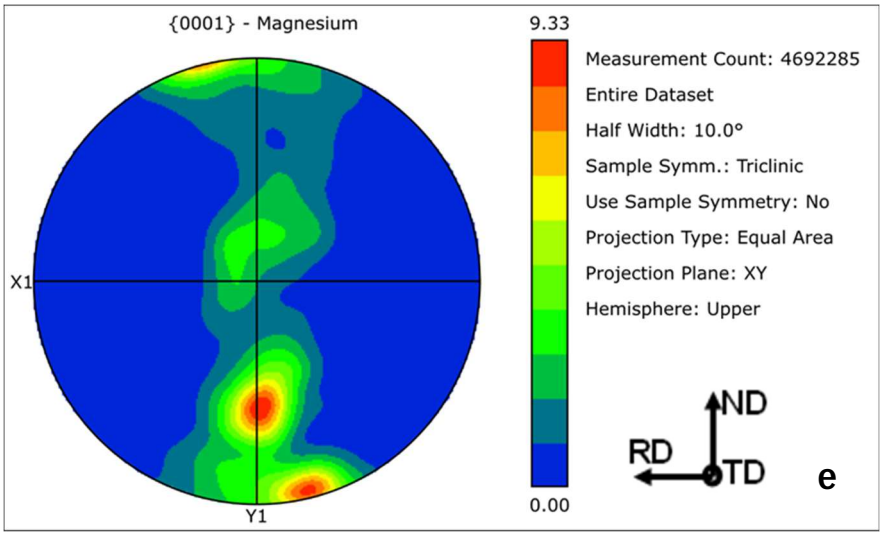
{0001} - Magnesium
9.33
0.00
Measurement Count: 4692285
Entire Dataset
Half Width: 10.0°
Sample Symm.: Triclinic
Use Sample Symmetry: No
Projection Type: Equal Area
Projection Plane: XY
Hemisphere: Upper
X1
Y1
ND
RD
TD

e

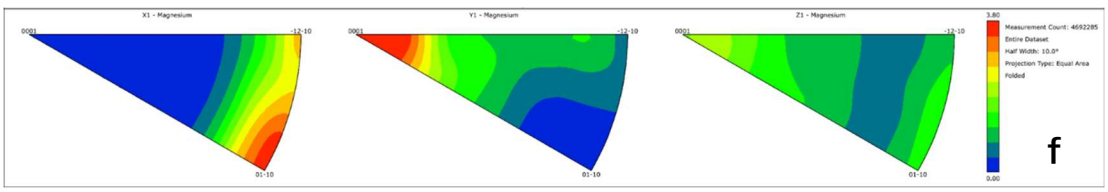
X1 - Magnesium
Y1 - Magnesium
Z1 - Magnesium
Measurement Count: 4692285
Entire Dataset
Half Width: 10.0°
Projection Type: Equal Area
Folded

f

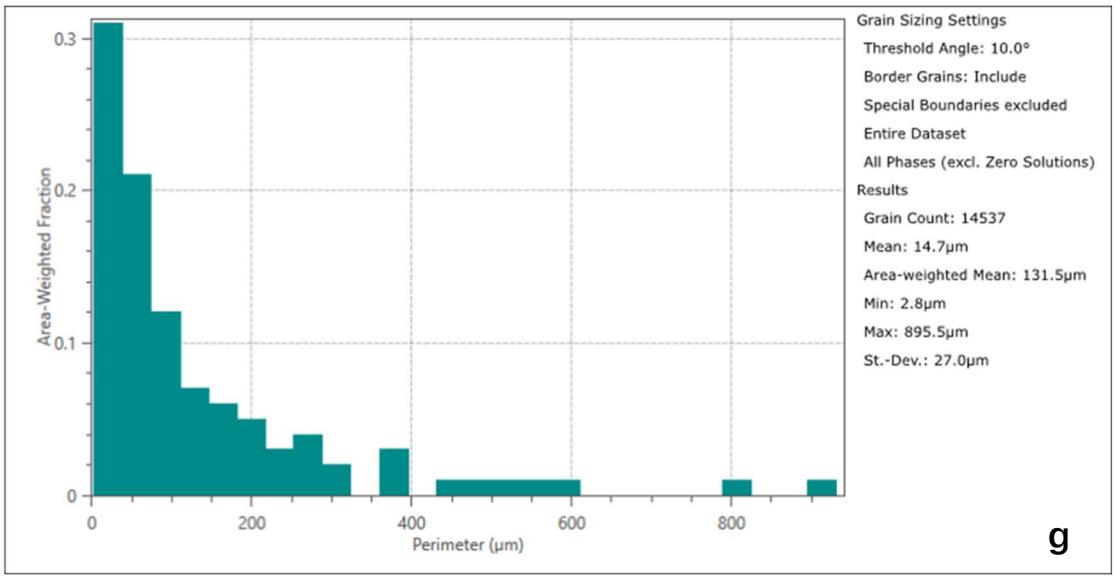

Figure A3-4 The EBSD result of the 210s annealed 1D compressed Mg-0.1Ca-0.4Zn specimen: (a) The inverse pole figure map and grain boundaries, (b) The grain boundaries and the special grain boundaries, (c) The band contrast and the phase analysis, (d) The band contrast, (e) The pole figure, (f) The inverse pole figures, (g) Grain size distribution expressed as grain boundary perimeter

A4 Channel die two-direction compressed Mg-0.1Ca-0.4Zn (at%) specimens

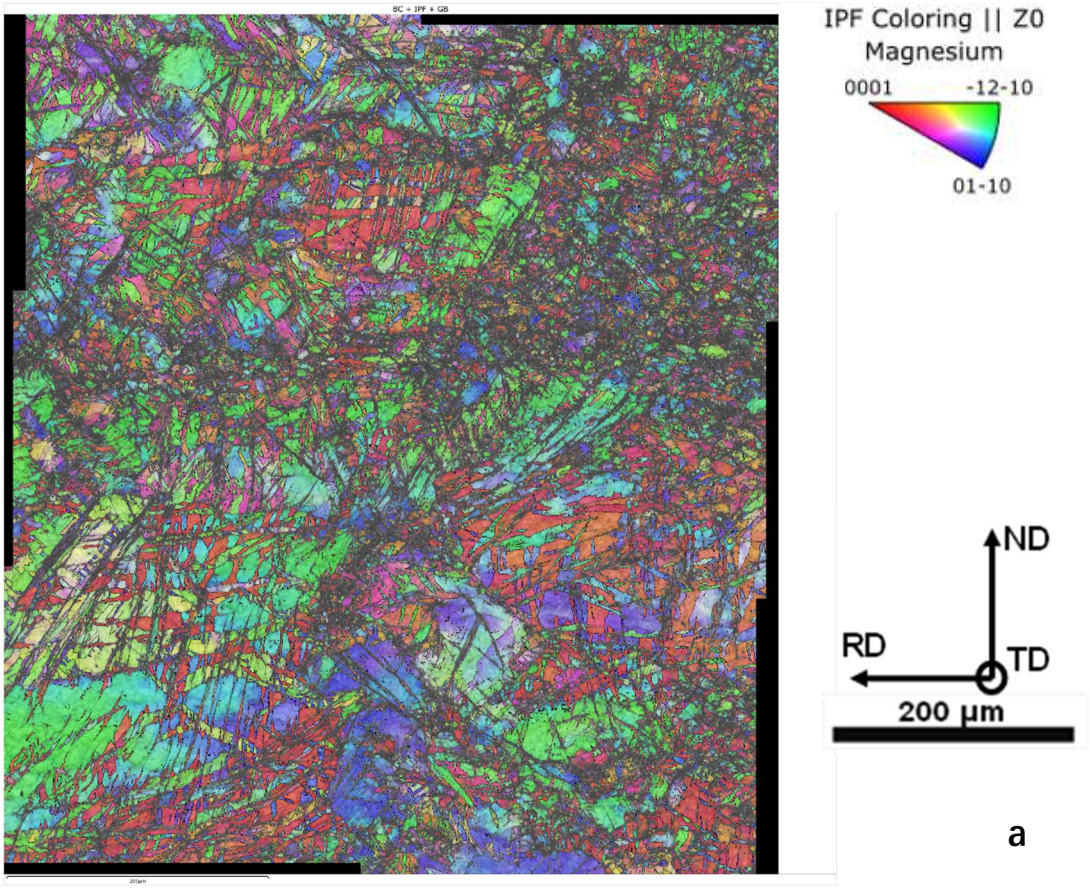

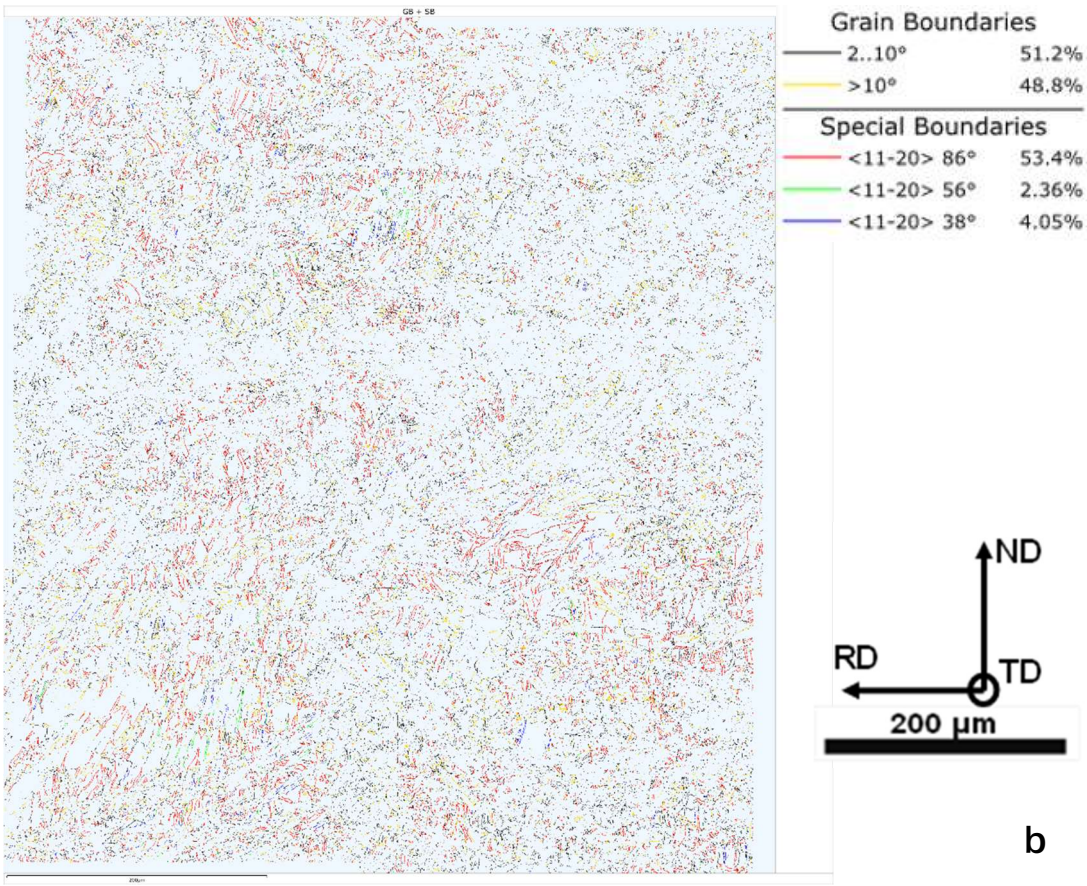
GB + SB
Grain Boundaries
2..10° 51.2%
>10° 48.8%
Special Boundaries
<11-20> 86° 53.4%
<11-20> 56° 2.36%
<11-20> 38° 4.05%
ND
RD
TD
200 µm

b

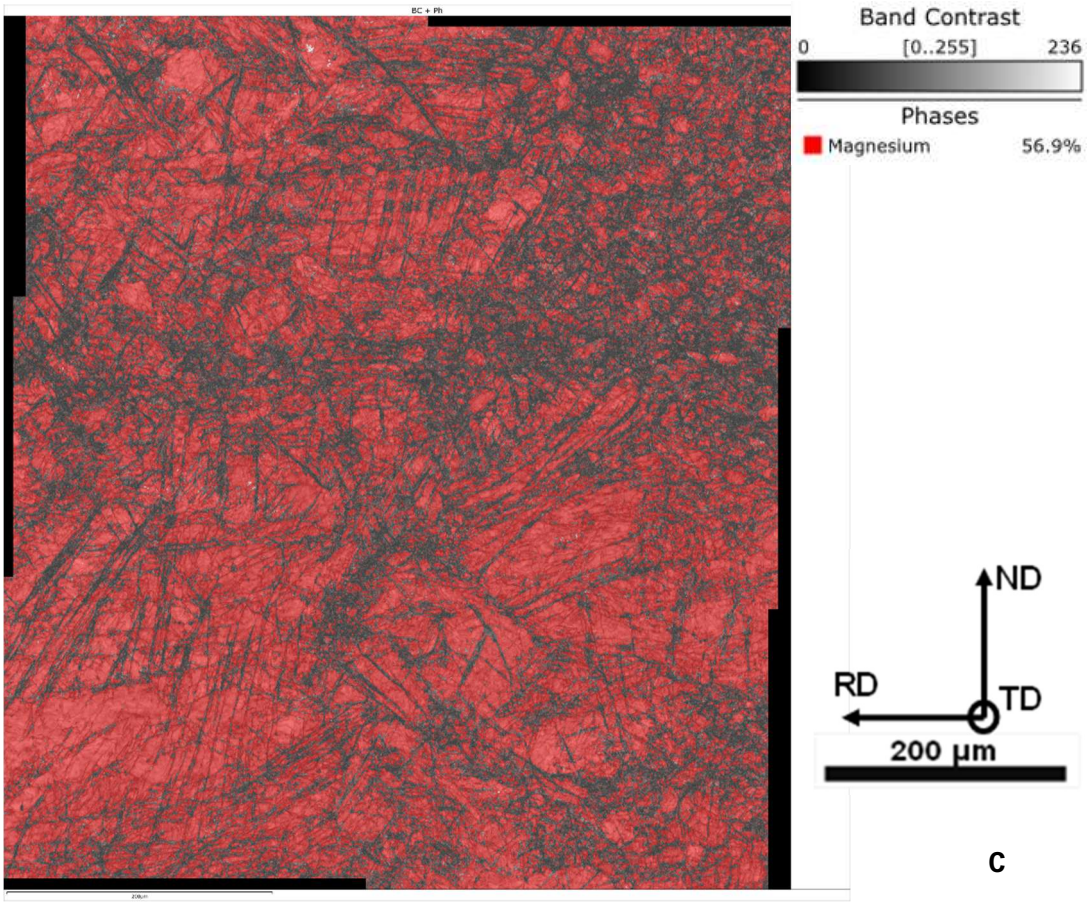
BC + Ph
Band Contrast
0 [0..255] 236
Phases
Magnesium 56.9%
ND
RD
TD
200 µm

c

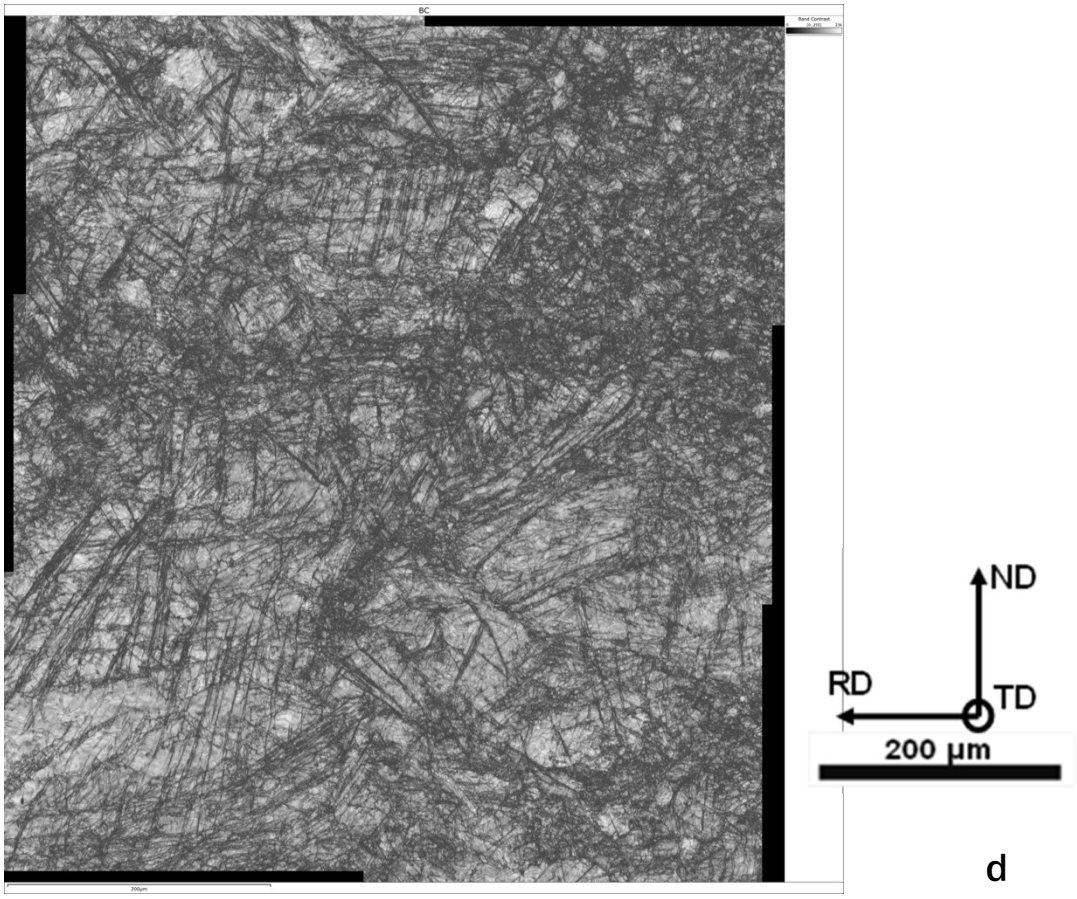
BC
ND
RD
TD
200 µm
d

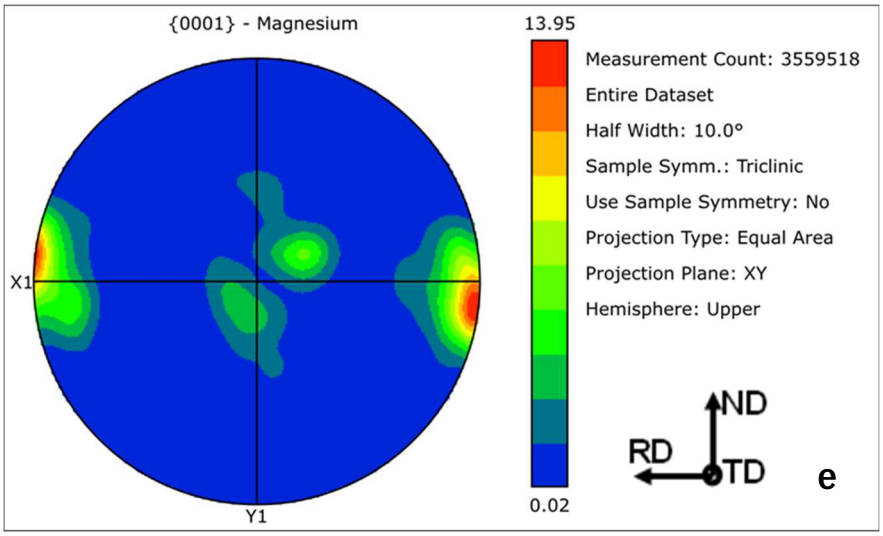
{0001} - Magnesium
13.95
0.02
Measurement Count: 3559518
Entire Dataset
Half Width: 10.0°
Sample Symm.: Triclinic
Use Sample Symmetry: No
Projection Type: Equal Area
Projection Plane: XY
Hemisphere: Upper
X1
Y1
ND
RD
TD
e

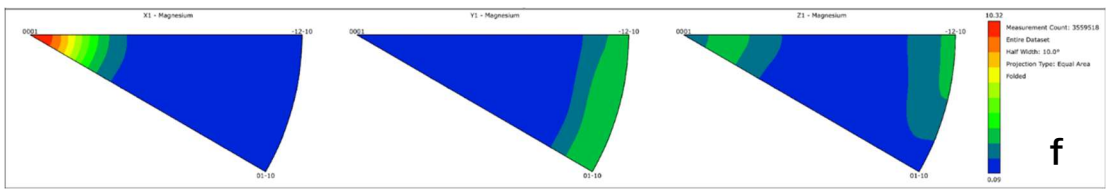
X1 - Magnesium
Y1 - Magnesium
Z1 - Magnesium
f

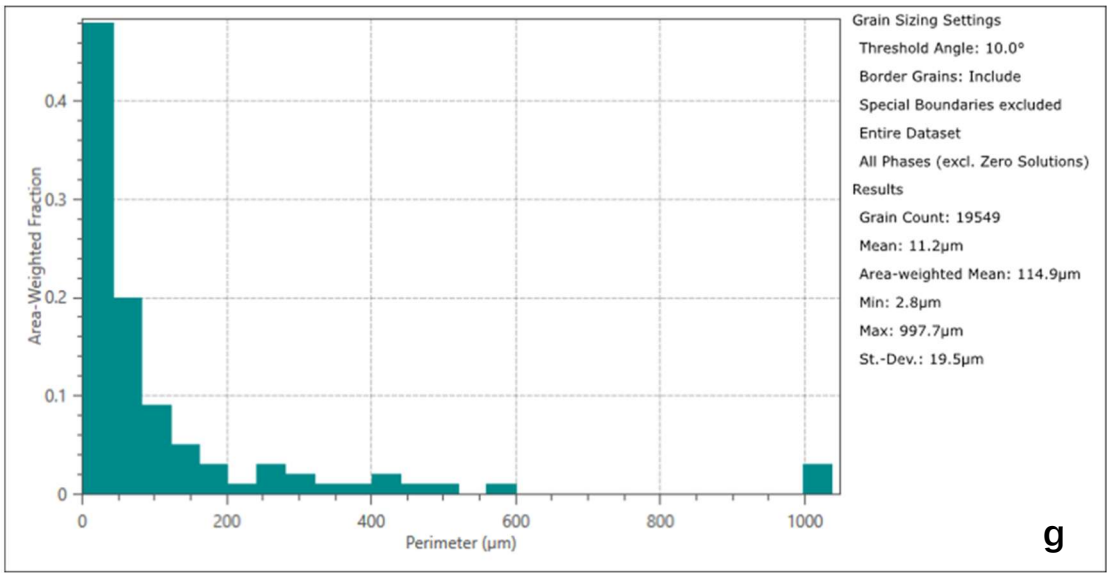

Figure A4-1 The EBSD result of the 30s annealed 2D compressed Mg-0.1Ca-0.4Zn specimen: (a) The inverse pole figure map and grain boundaries, (b) The grain boundaries and the special grain boundaries, (c) The band contrast and the phase analysis, (d) The band contrast, (e) The pole figure, (f) The inverse pole figures, (g) Grain size distribution expressed as grain boundary perimeter

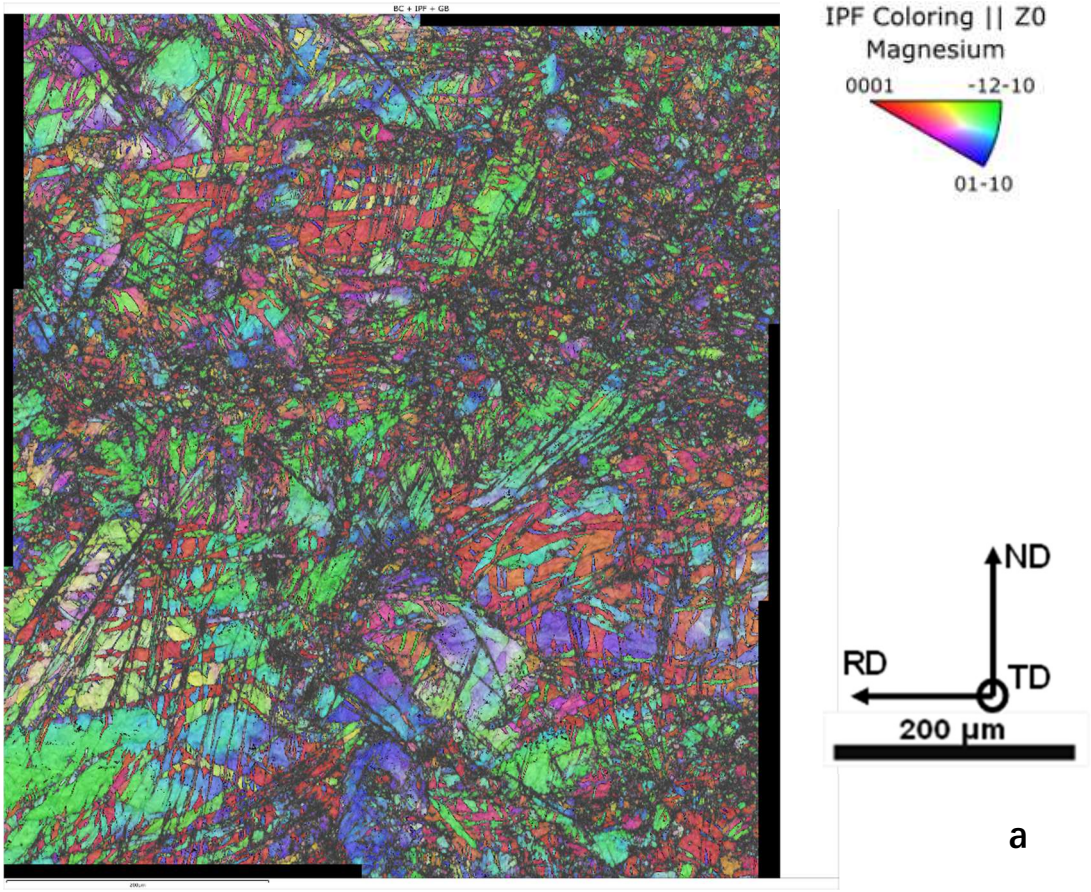

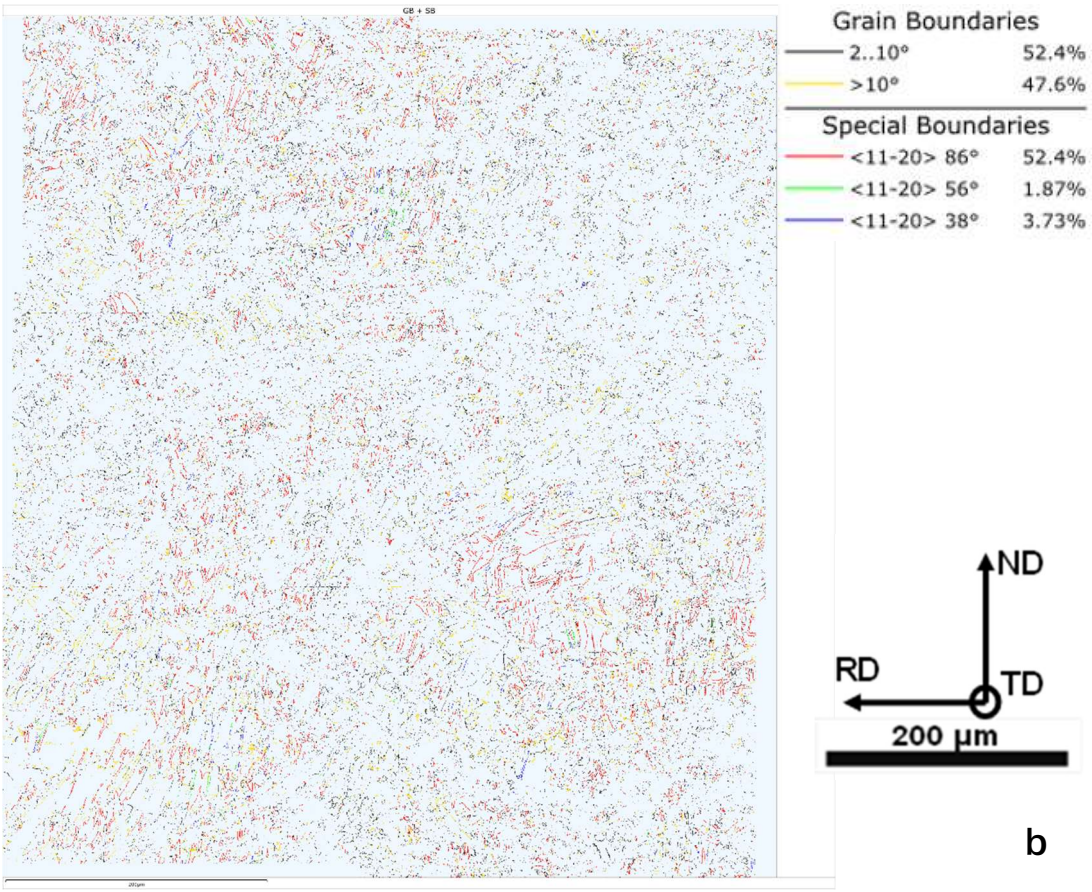
GB + SB
Grain Boundaries
2..10° 52.4%
>10° 47.6%
Special Boundaries
<11-20> 86° 52.4%
<11-20> 56° 1.87%
<11-20> 38° 3.73%
ND
RD
TD
200 µm

b

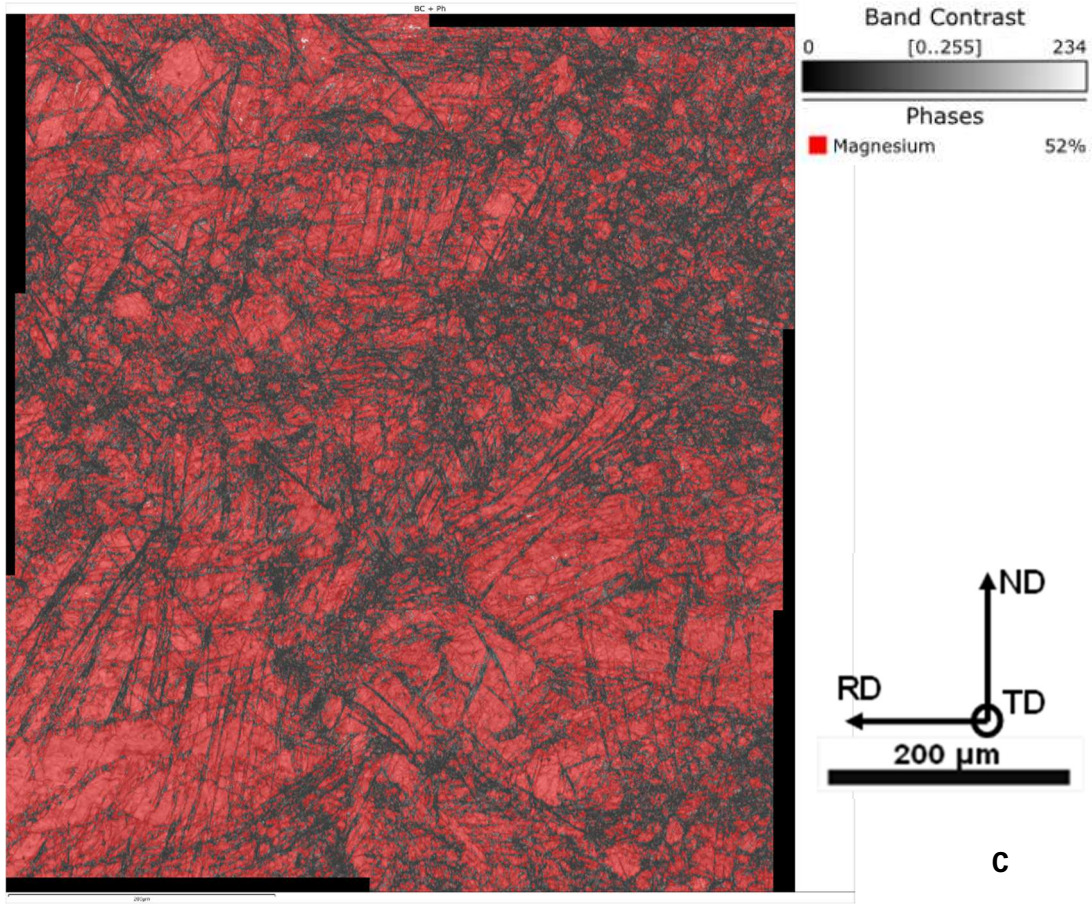
BC + Ph
Band Contrast
0 [0..255] 234
Phases
Magnesium 52%
ND
RD
TD
200 µm

c

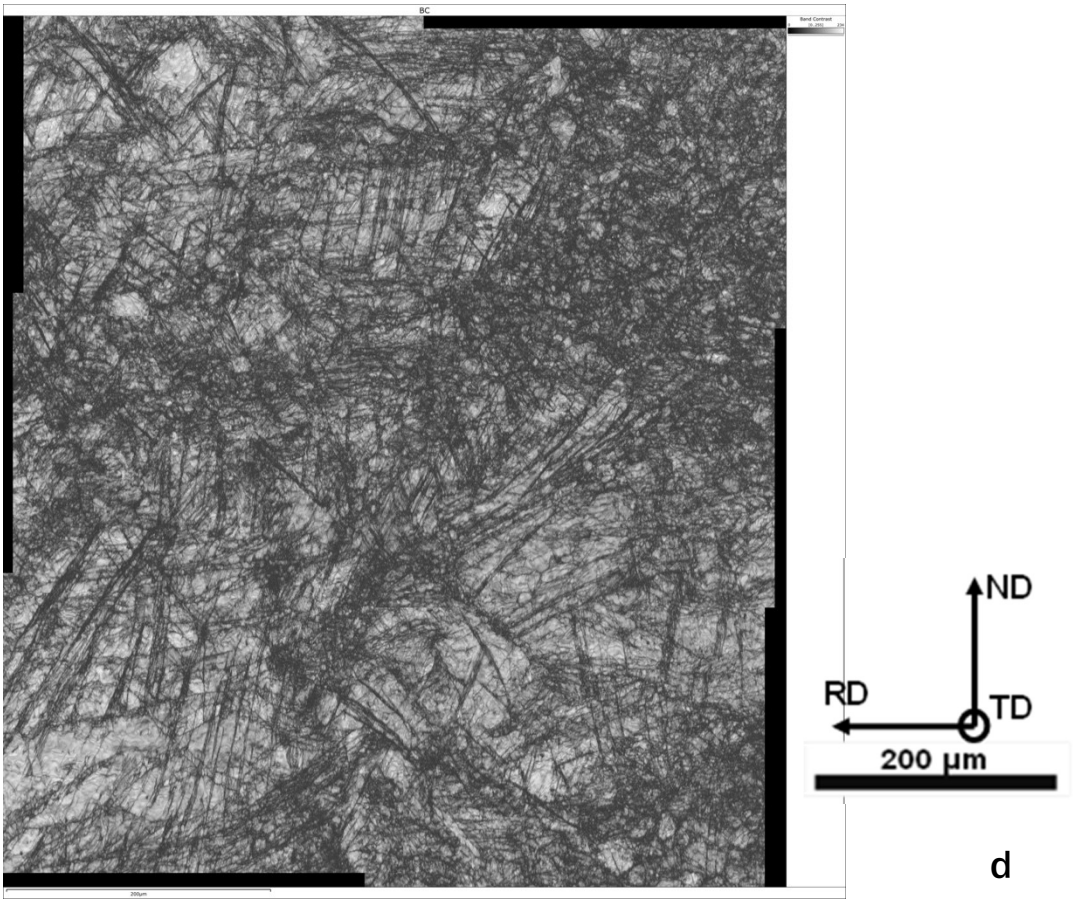
BC
ND
RD
TD
200 µm
d

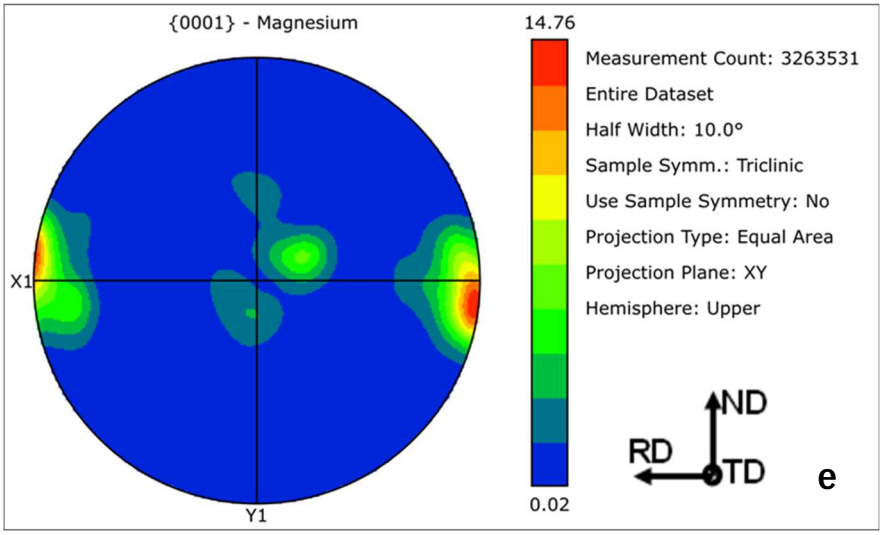
{0001} - Magnesium
14.76
Measurement Count: 3263531
Entire Dataset
Half Width: 10.0°
Sample Symm.: Triclinic
Use Sample Symmetry: No
Projection Type: Equal Area
Projection Plane: XY
Hemisphere: Upper
X1
Y1
0.02
ND
RD
TD
e

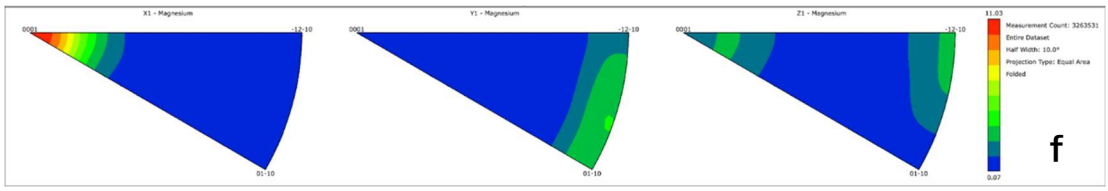
X1 - Magnesium
Y1 - Magnesium
Z1 - Magnesium
11.03
0.07
f

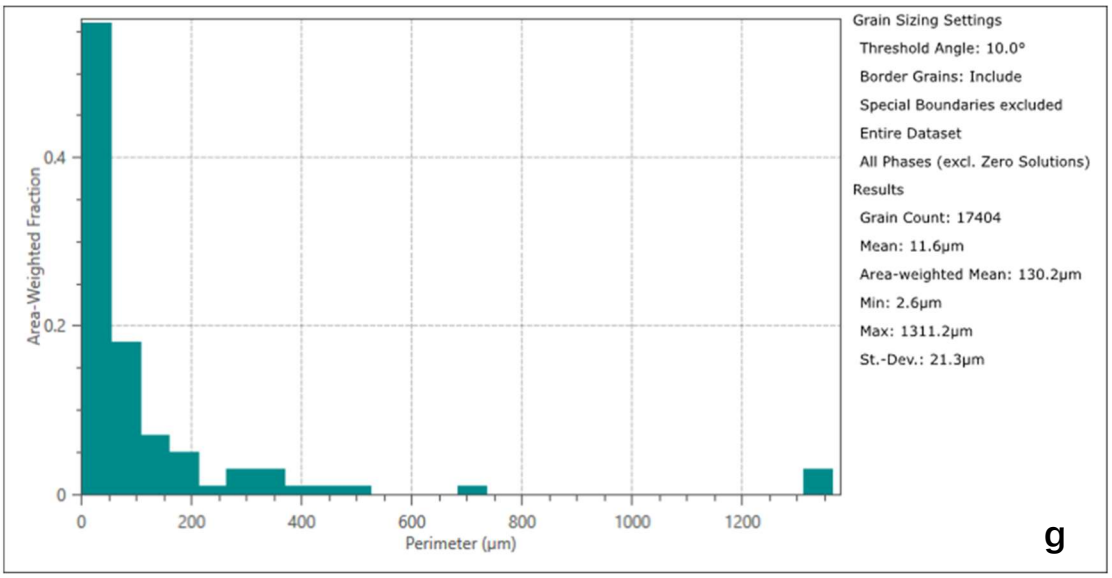

Figure A4-2 The EBSD result of the 75s annealed 2D compressed Mg-0.1Ca-0.4Zn specimen: (a) The inverse pole figure map and grain boundaries, (b) The grain boundaries and the special grain boundaries, (c) The band contrast and the phase analysis, (d) The band contrast, (e) The pole figure, (f) The inverse pole figures, (g) Grain size distribution expressed as grain boundary perimeter

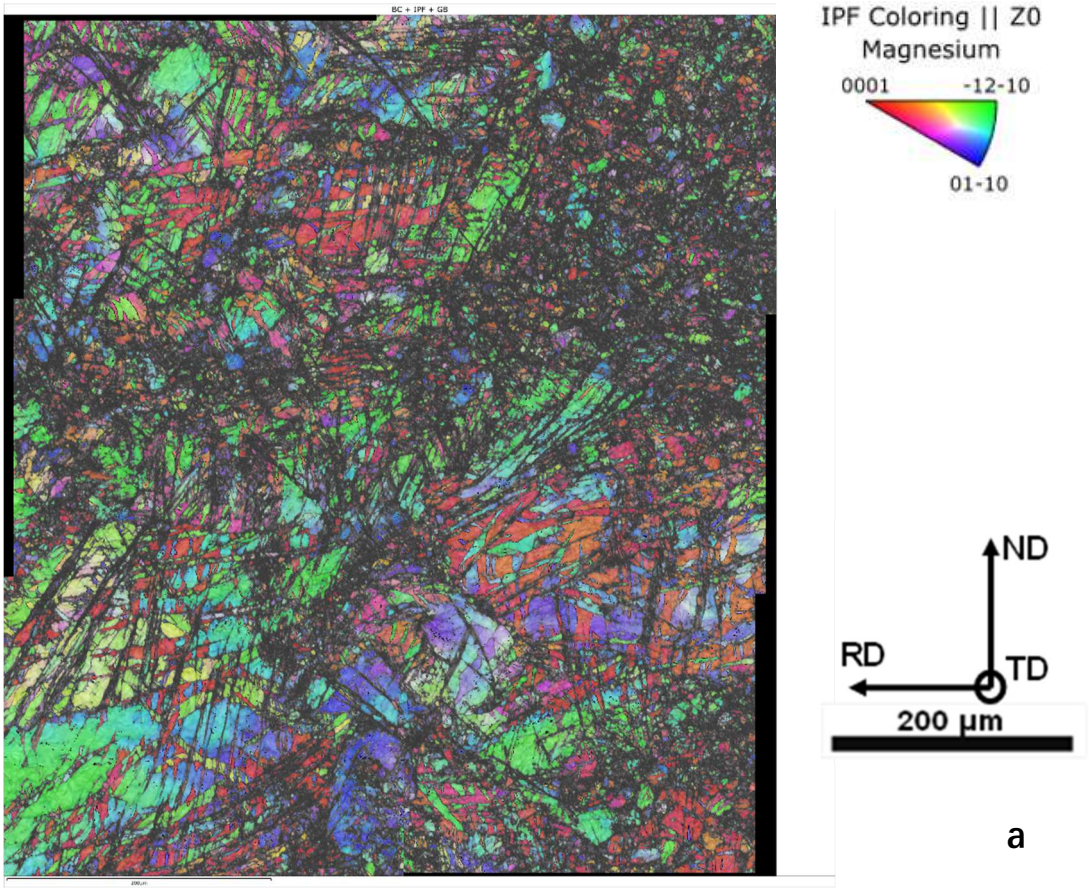

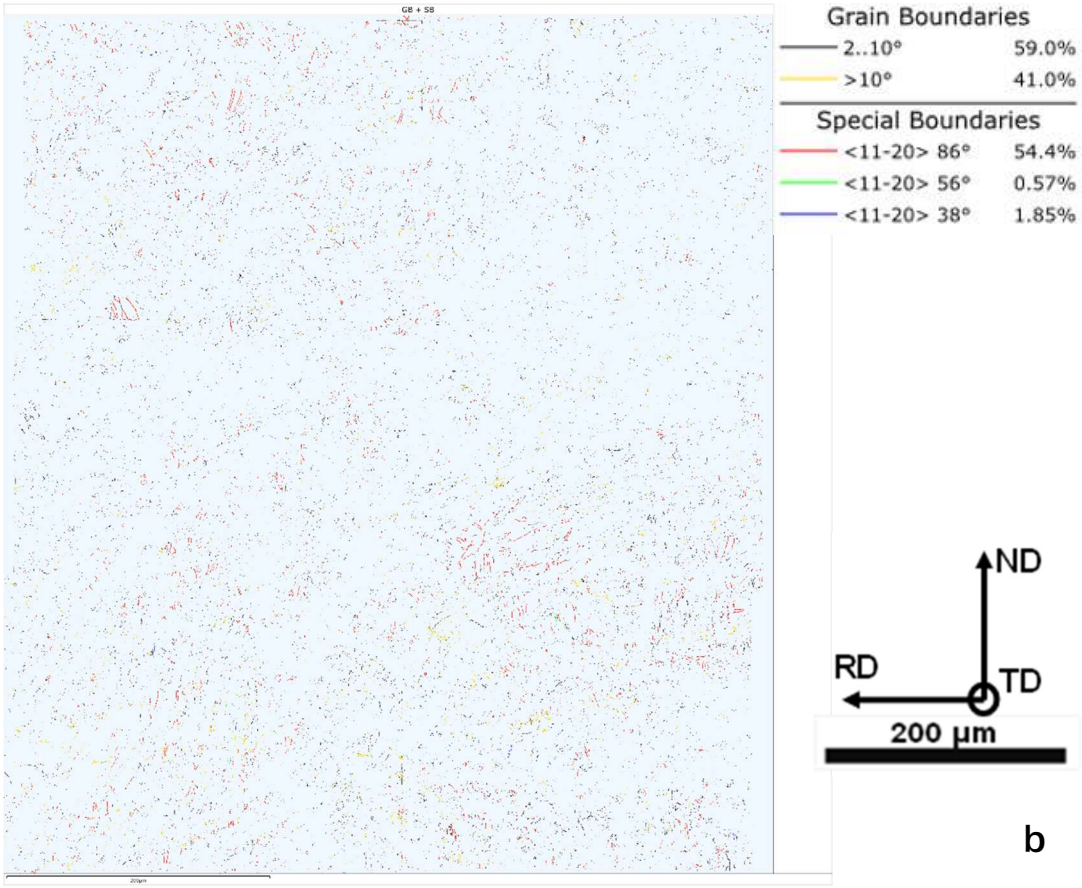
GB + SB
Grain Boundaries
2..10° 59.0%
>10° 41.0%
Special Boundaries
<11-20> 86° 54.4%
<11-20> 56° 0.57%
<11-20> 38° 1.85%
ND
RD
TD
200 µm

b

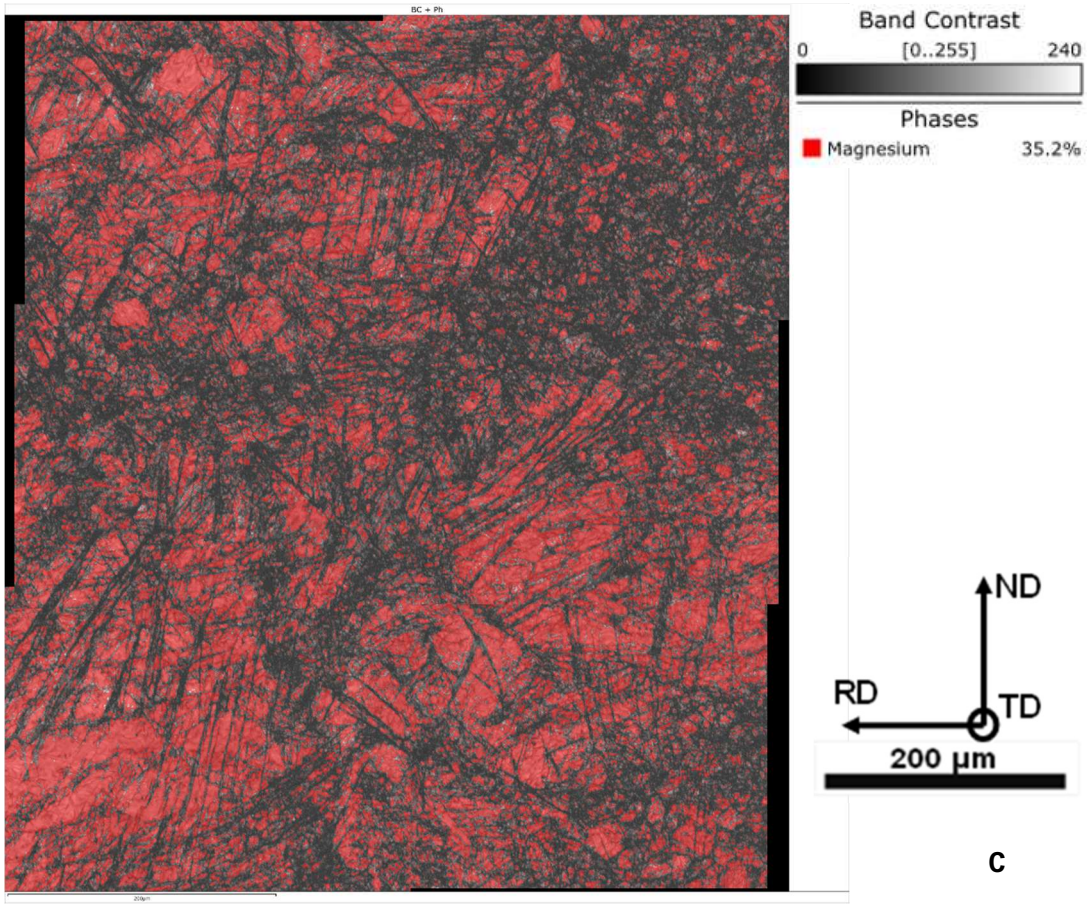
BC + Ph
Band Contrast
0 [0..255] 240
Phases
Magnesium 35.2%
ND
RD
TD
200 µm

c

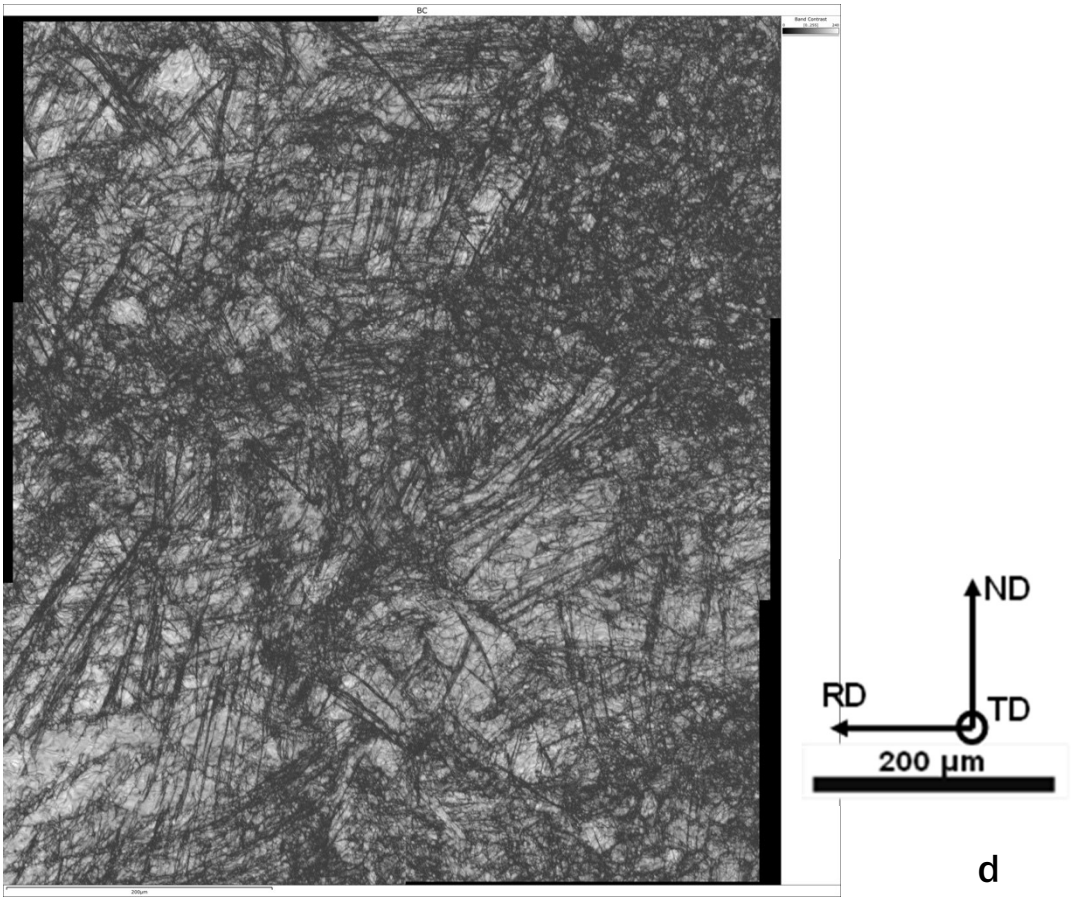
BC
ND
RD
TD
200 µm
d

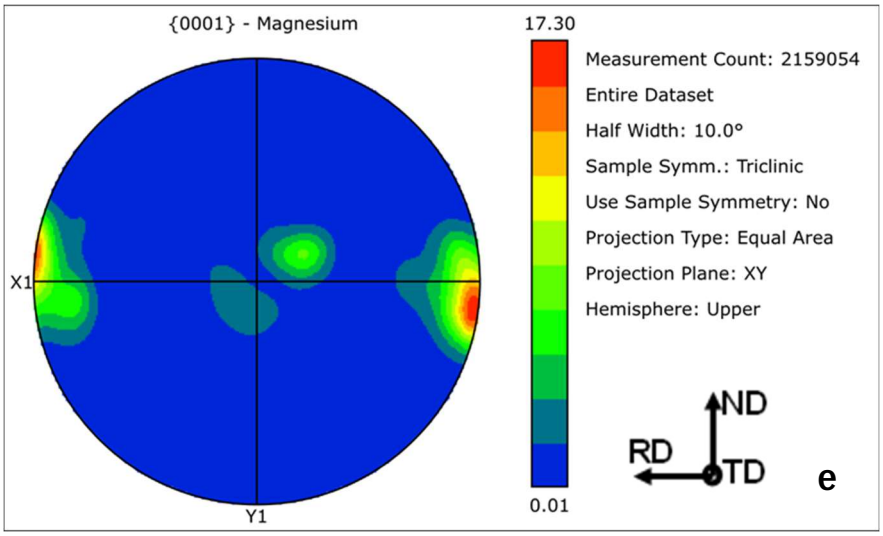
{0001} - Magnesium
17.30
0.01
Measurement Count: 2159054
Entire Dataset
Half Width: 10.0°
Sample Symm.: Triclinic
Use Sample Symmetry: No
Projection Type: Equal Area
Projection Plane: XY
Hemisphere: Upper
X1
Y1
ND
RD
TD
e

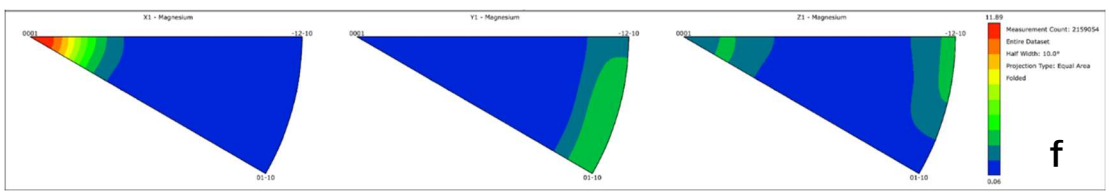
X1 - Magnesium
Y1 - Magnesium
Z1 - Magnesium
f

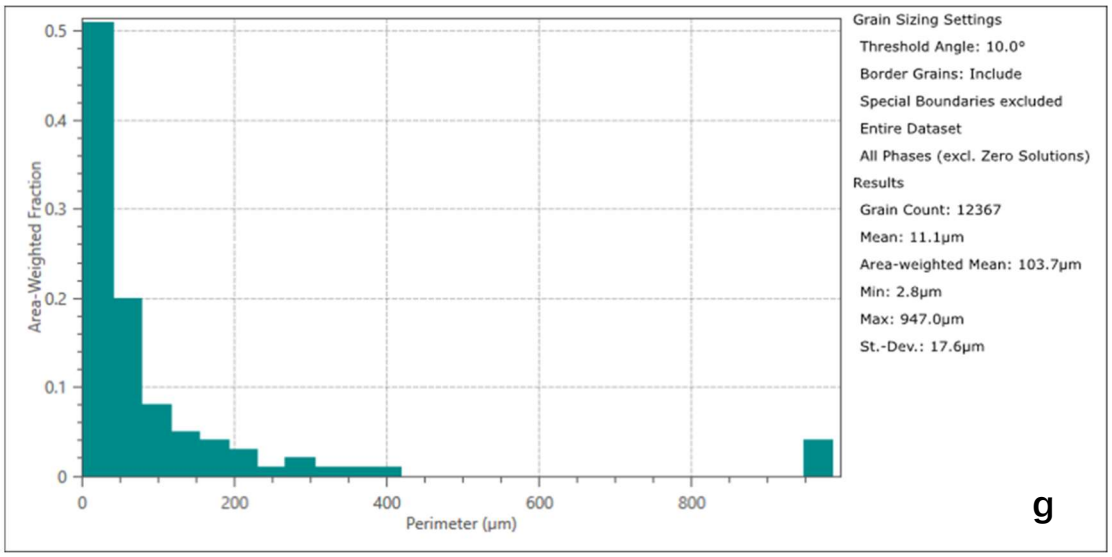

Figure A4-3 The EBSD result of the 135s annealed 2D compressed Mg-0.1Ca-0.4Zn specimen: (a) The inverse pole figure map and grain boundaries, (b) The grain boundaries and the special grain boundaries, (c) The band contrast and the phase analysis, (d) The band contrast, (e) The pole figure, (f) The inverse pole figures, (g) Grain size distribution expressed as grain boundary perimeter

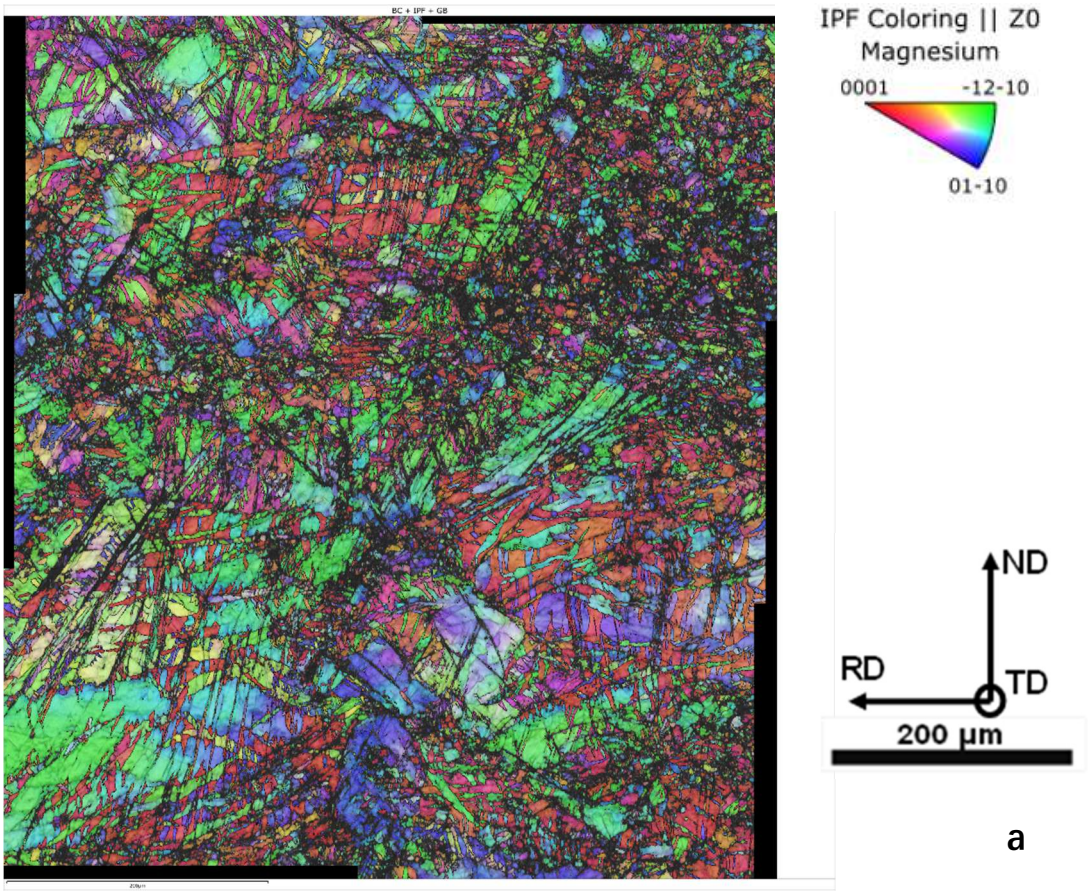

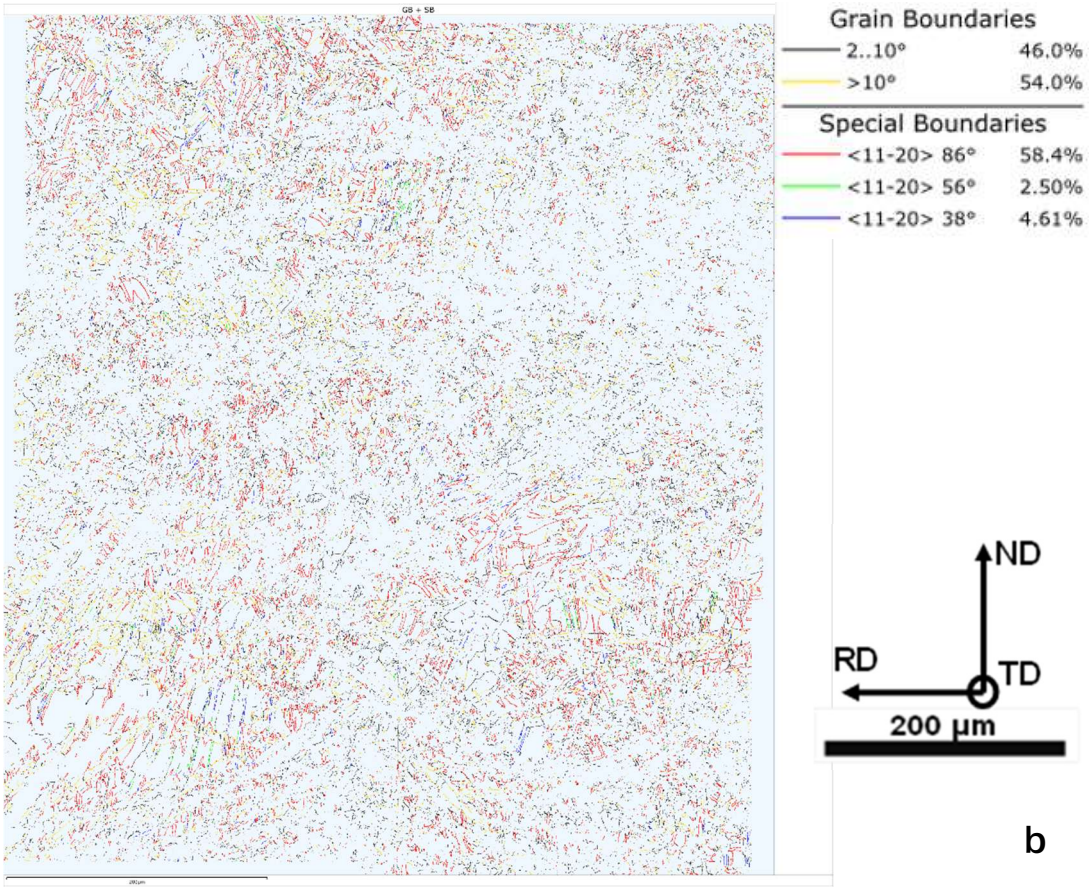
GB + SB
Grain Boundaries
2..10° 46.0%
>10° 54.0%
Special Boundaries
<11-20> 86° 58.4%
<11-20> 56° 2.50%
<11-20> 38° 4.61%
ND
RD
TD
200 µm

b

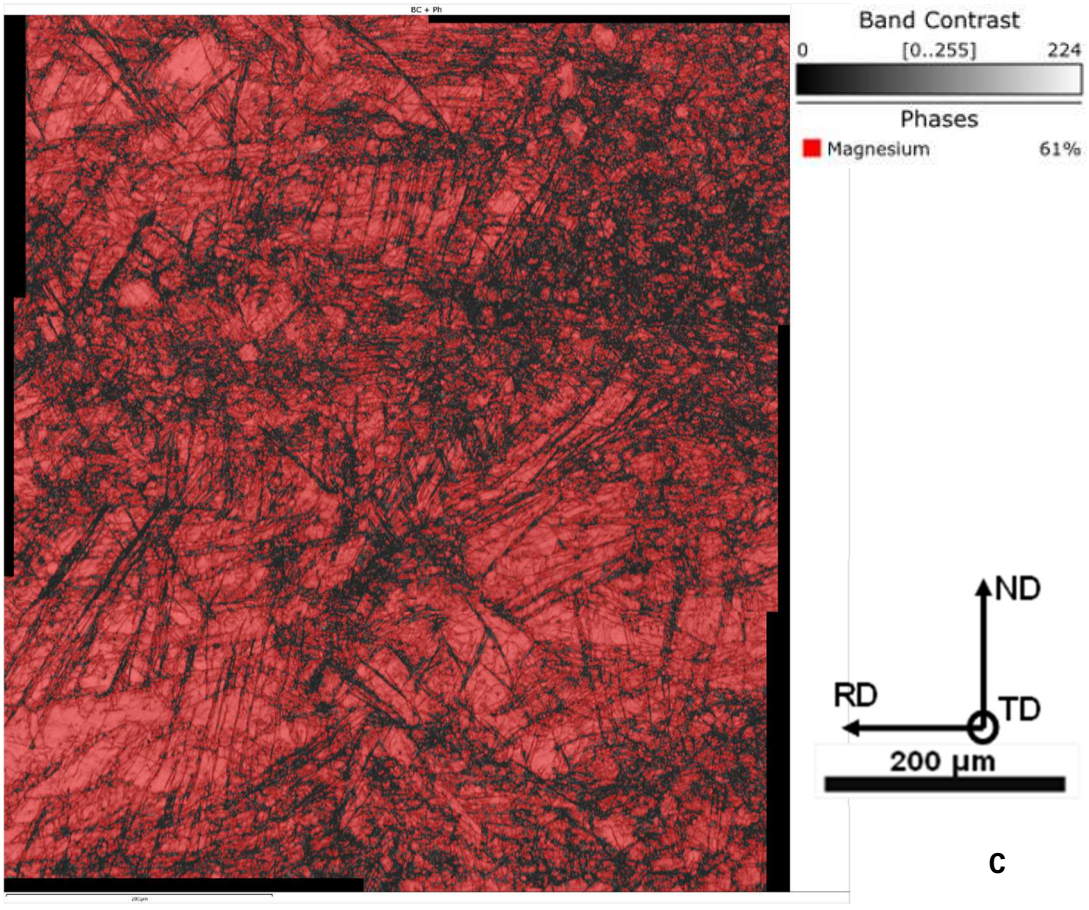
BC + Ph
Band Contrast
0 [0..255] 224
Phases
Magnesium 61%
ND
RD
TD
200 µm

c

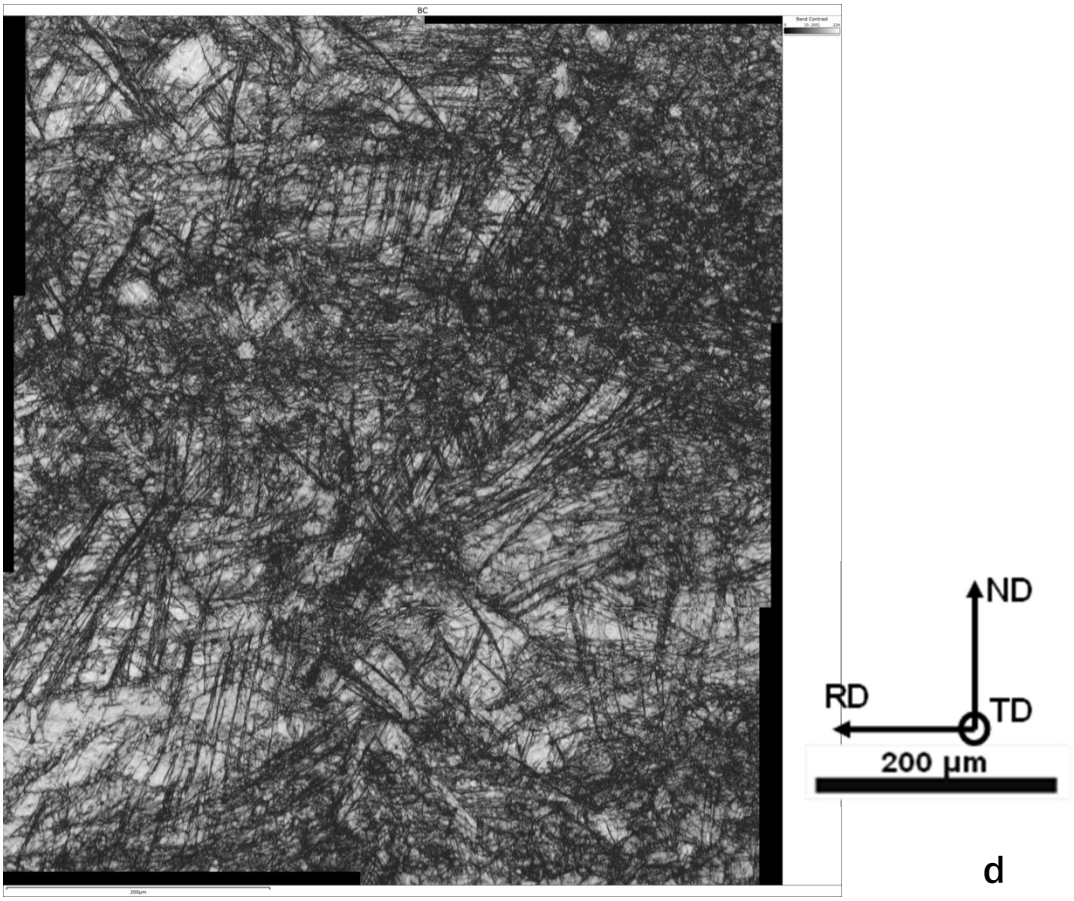
BC
ND
RD
TD
200 µm

d

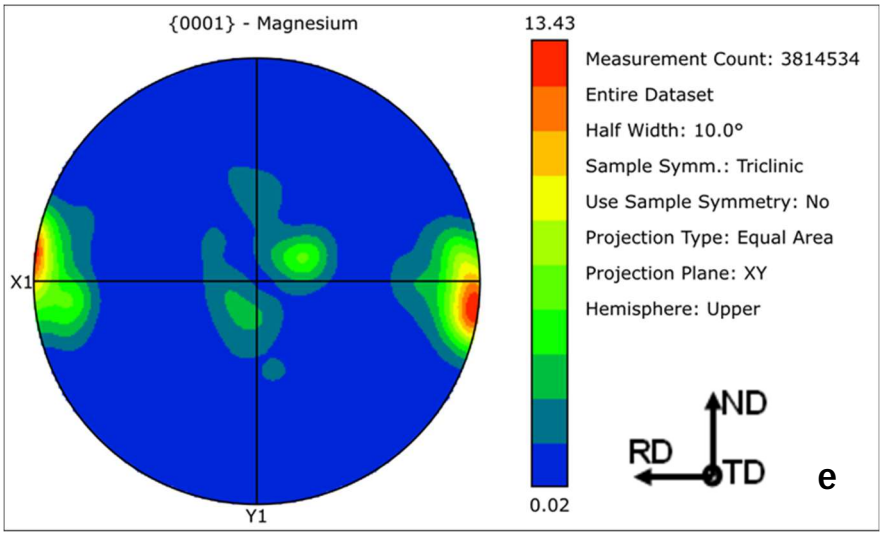
{0001} - Magnesium
13.43
Measurement Count: 3814534
Entire Dataset
Half Width: 10.0°
Sample Symm.: Triclinic
Use Sample Symmetry: No
Projection Type: Equal Area
Projection Plane: XY
Hemisphere: Upper
X1
Y1
0.02
ND
RD
TD

e

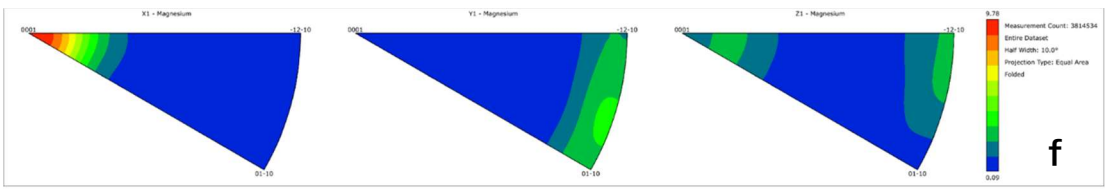
X1 - Magnesium
Y1 - Magnesium
Z1 - Magnesium
Measurement Count: 3814534
Entire Dataset
Half Width: 10.0°
Projection Type: Equal Area
Folded

f

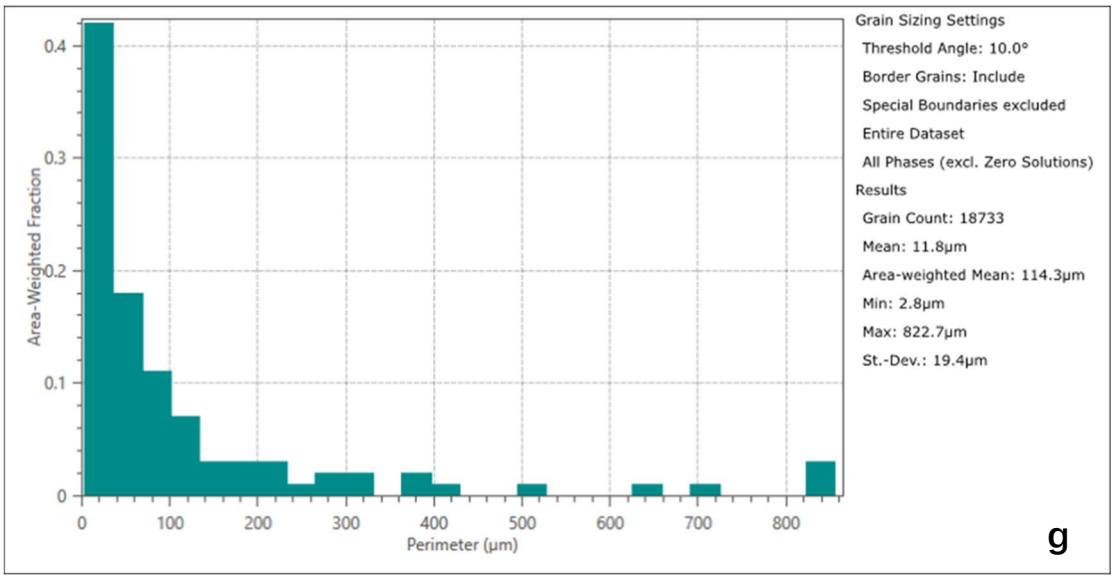

Figure A4-4 The EBSD result of the 210s annealed 2D compressed Mg-0.1Ca-0.4Zn specimen: (a) The inverse pole figure map and grain boundaries, (b) The grain boundaries and the special grain boundaries, (c) The band contrast and the phase analysis, (d) The band contrast, (e) The pole figure, (f) The inverse pole figures, (g) Grain size distribution expressed as grain boundary perimeter

A5 Channel die two-direction compressed Mg-0.5Zn (at%) specimens

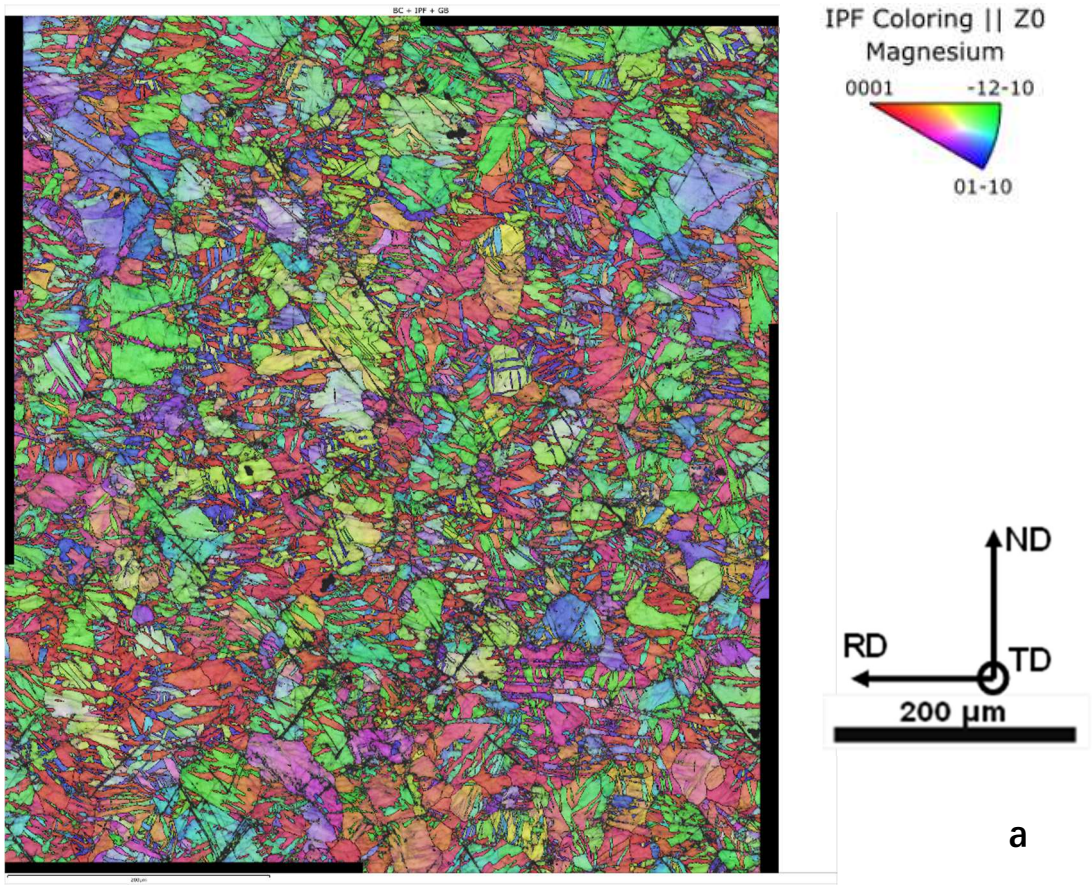

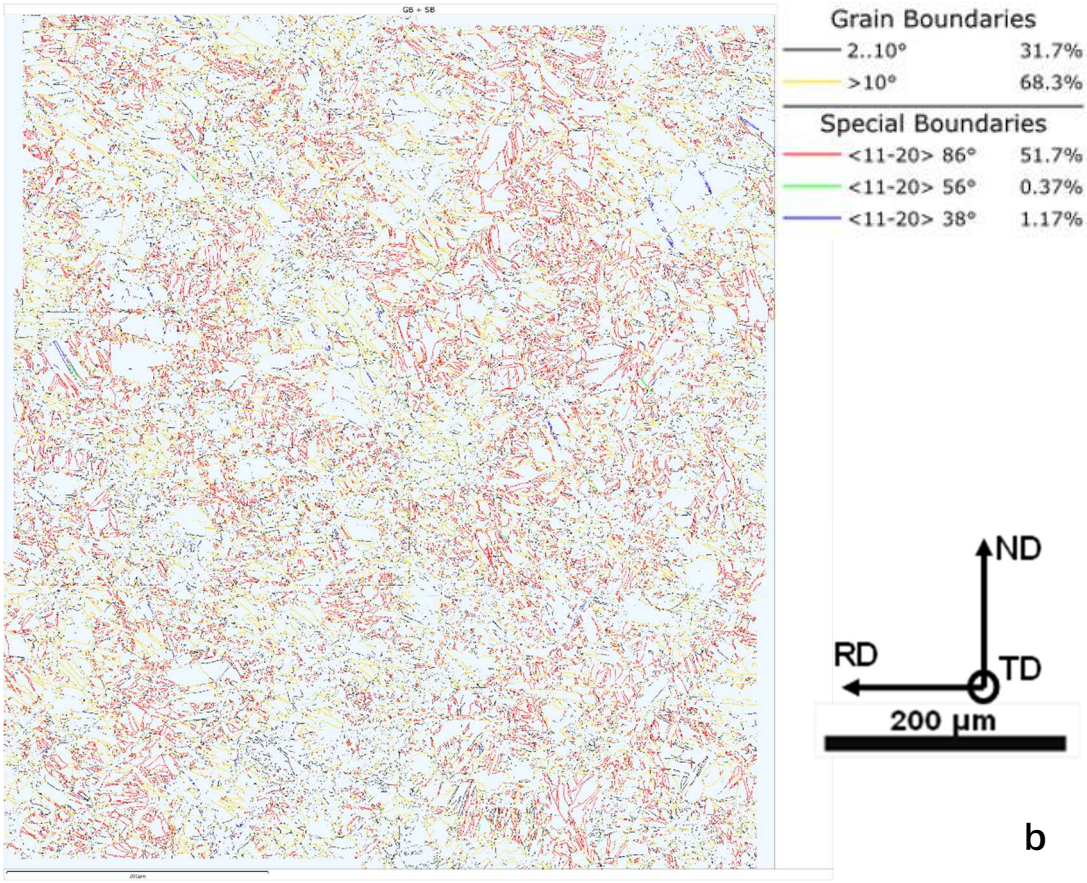
GB + SB
Grain Boundaries
2..10° 31.7%
>10° 68.3%
Special Boundaries
<11-20> 86° 51.7%
<11-20> 56° 0.37%
<11-20> 38° 1.17%
ND
RD
TD
200 µm

b

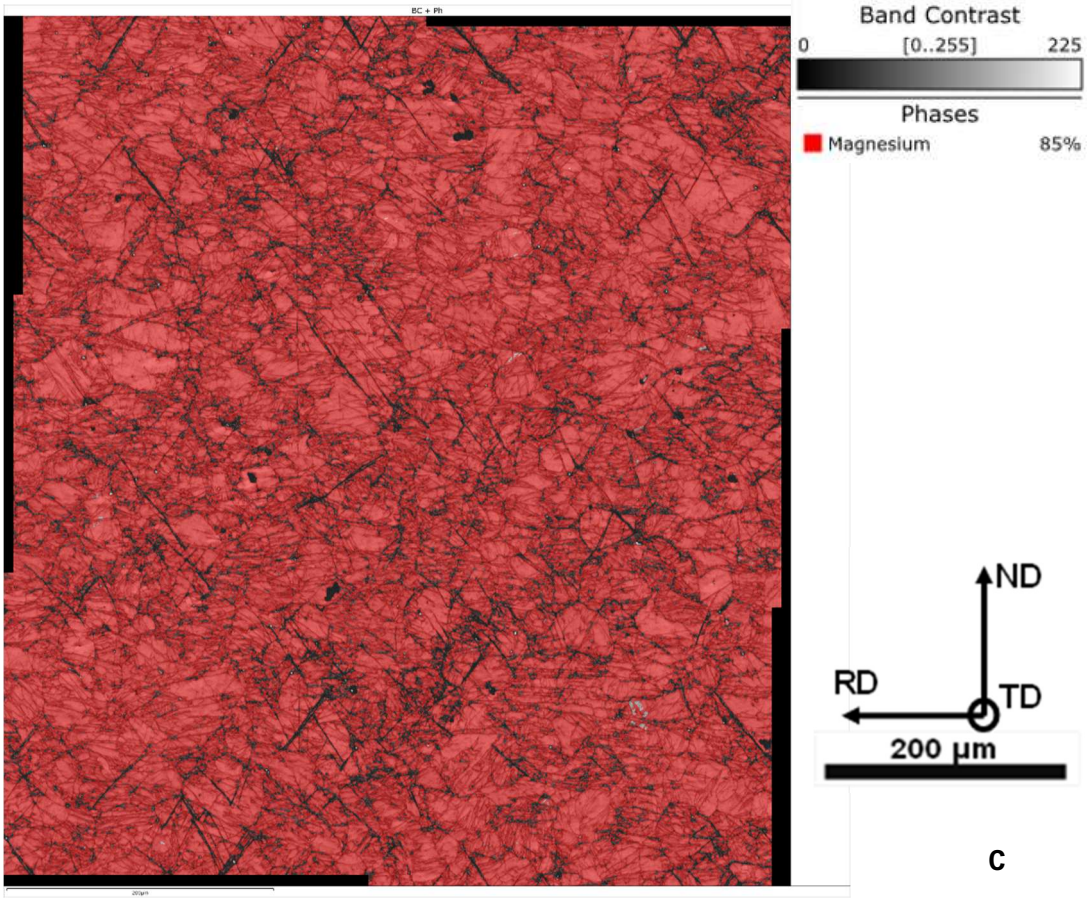
BC + Ph
Band Contrast
0 [0..255] 225
Phases
Magnesium 85%
ND
RD
TD
200 µm

c

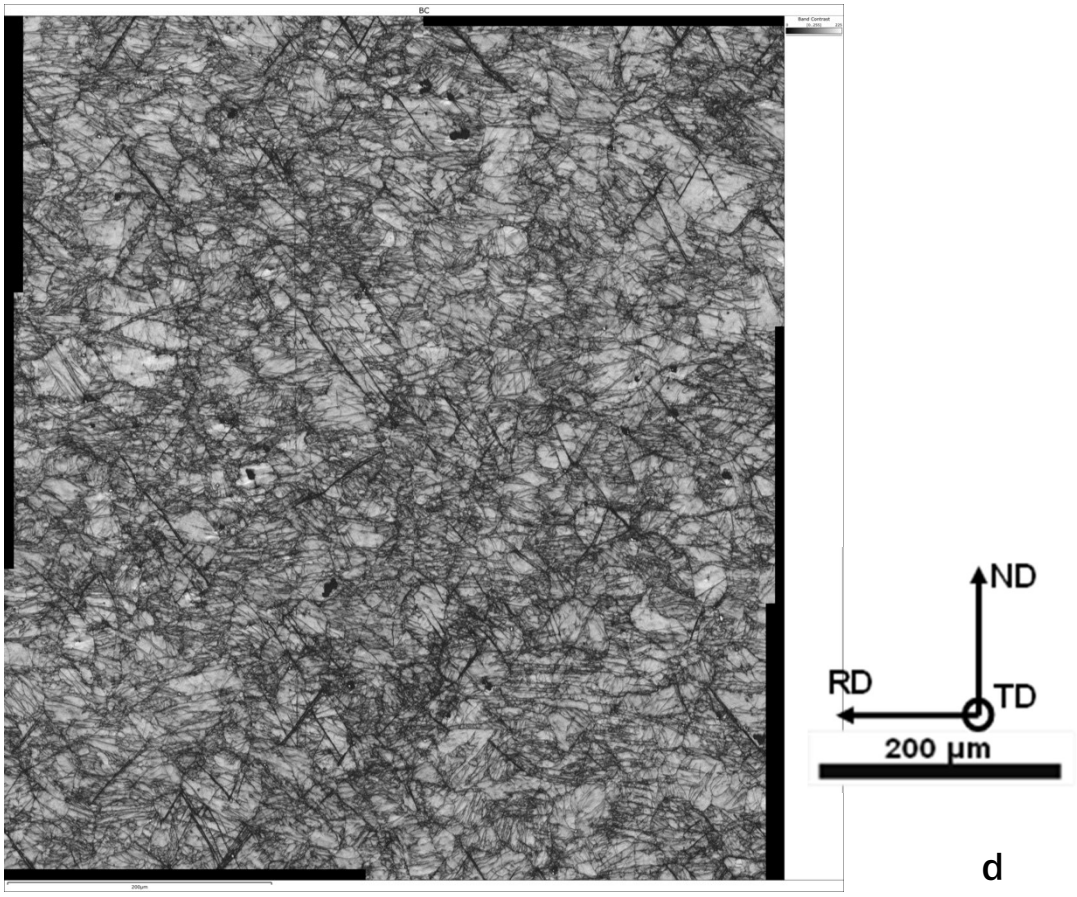
BC
ND
RD
TD
200 µm

d

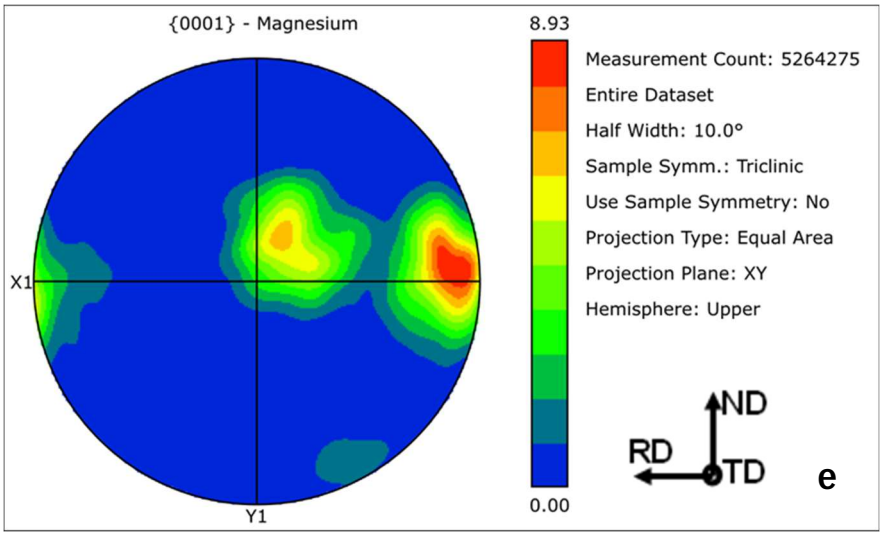
{0001} - Magnesium
8.93
0.00
Measurement Count: 5264275
Entire Dataset
Half Width: 10.0°
Sample Symm.: Triclinic
Use Sample Symmetry: No
Projection Type: Equal Area
Projection Plane: XY
Hemisphere: Upper
X1
Y1
ND
RD
TD

e

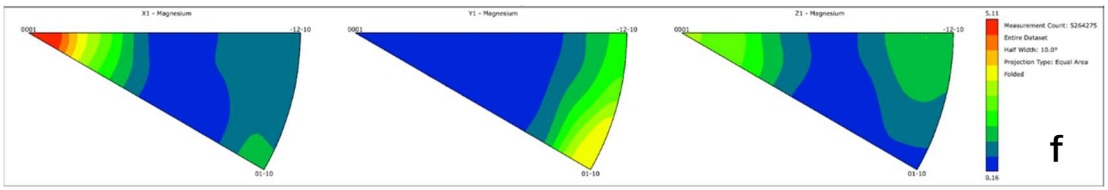
X1 - Magnesium
Y1 - Magnesium
Z1 - Magnesium

f

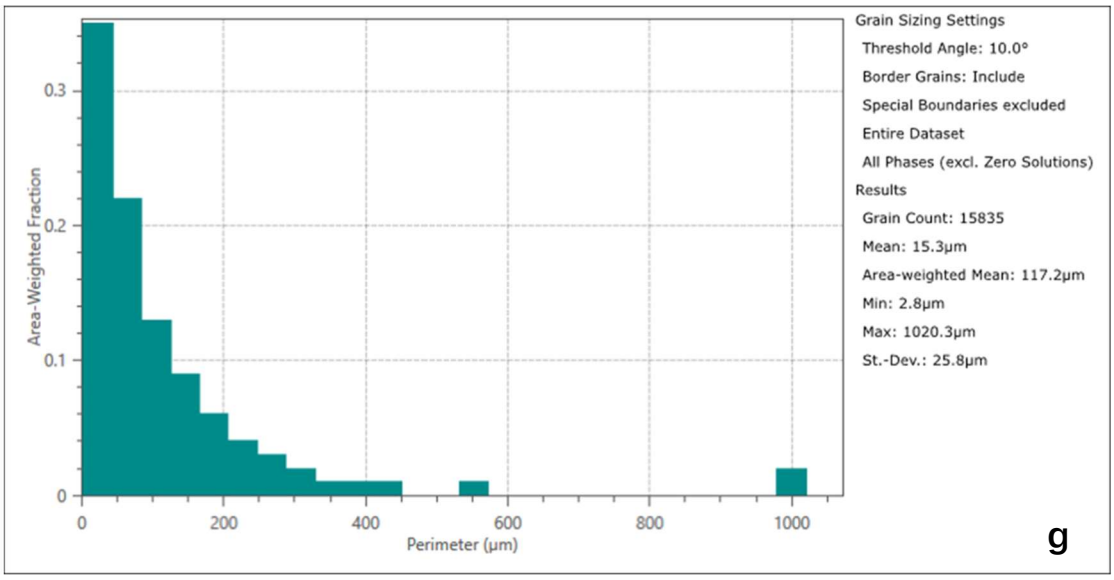

Figure A5-1 The EBSD result of the 30s annealed 2D compressed Mg-0.5Zn specimen: (a) The inverse pole figure map and grain boundaries, (b) The grain boundaries and the special grain boundaries, (c) The band contrast and the phase analysis, (d) The band contrast, (e) The pole figure, (f) The inverse pole figures, (g) Grain size distribution expressed as grain boundary perimeter

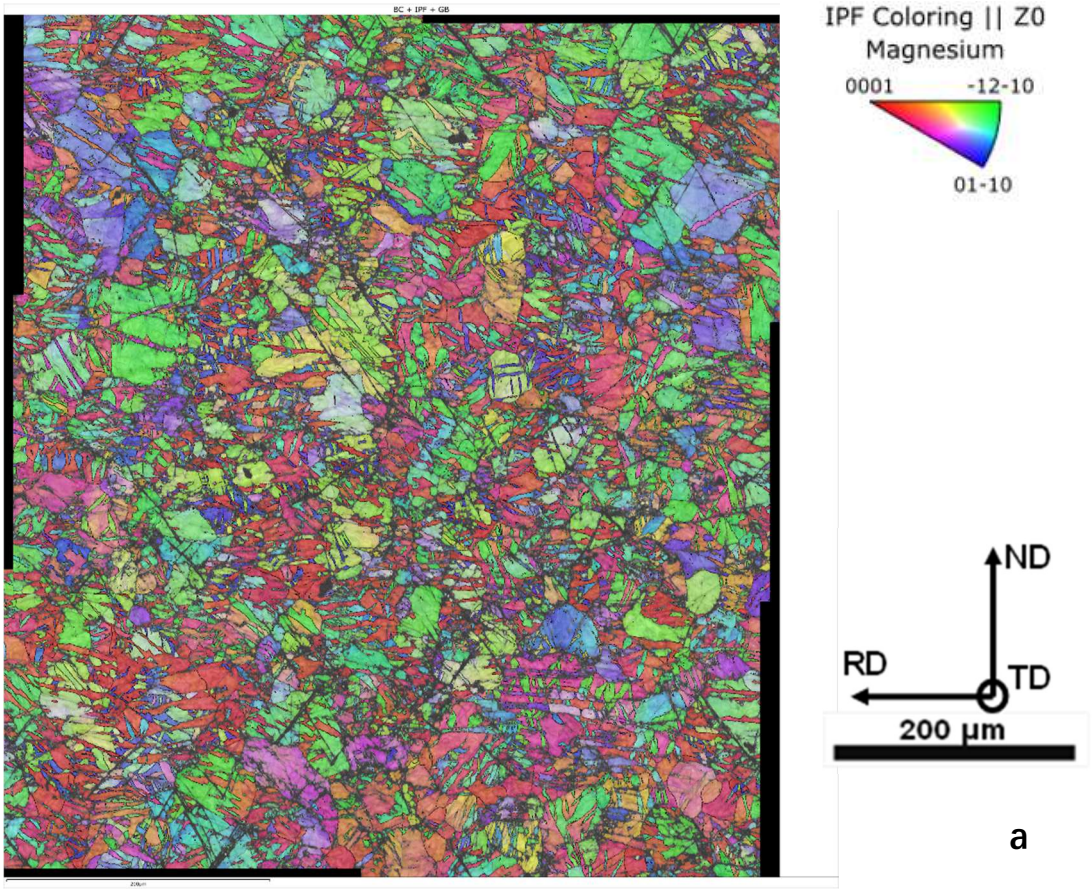

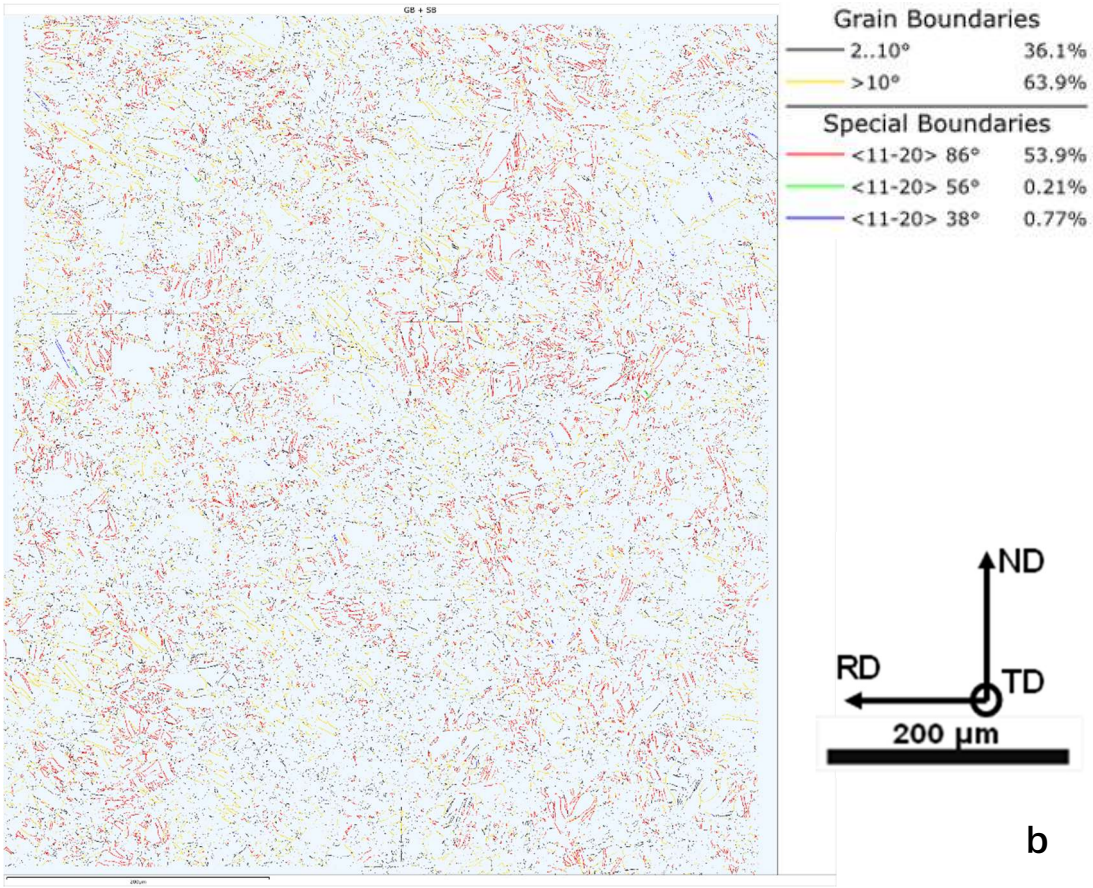
GB + SB
Grain Boundaries
2..10° 36.1%
>10° 63.9%
Special Boundaries
<11-20> 86° 53.9%
<11-20> 56° 0.21%
<11-20> 38° 0.77%
ND
RD
TD
200 µm

b

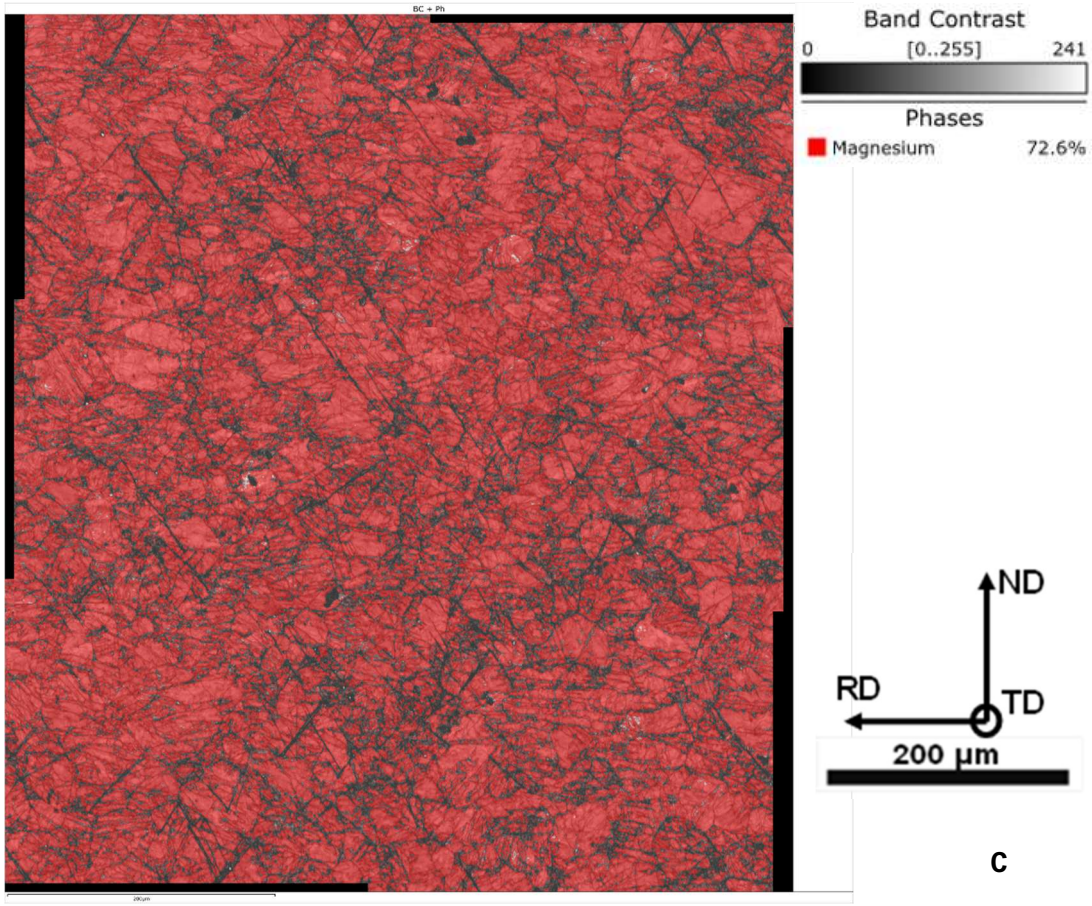
BC + Ph
Band Contrast
0 [0..255] 241
Phases
Magnesium 72.6%
ND
RD
TD
200 µm

c

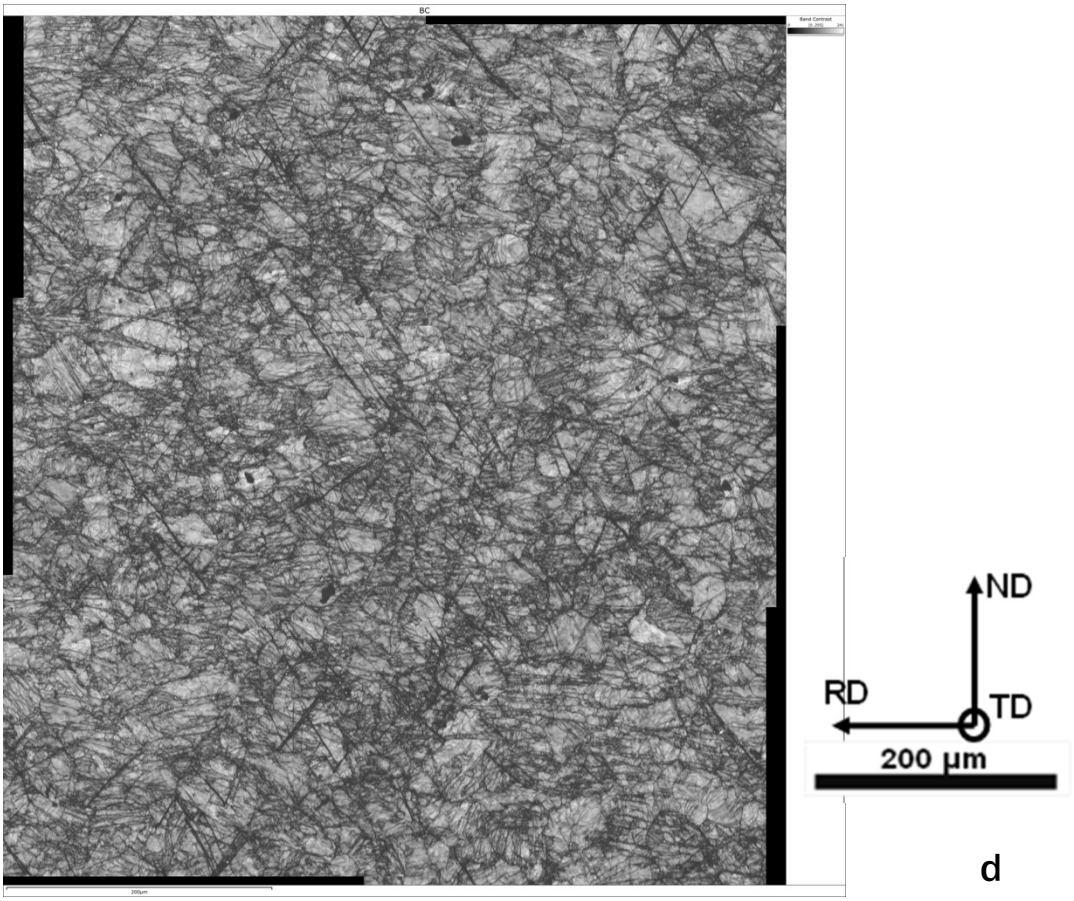
ND
RD
TD
200 µm
d

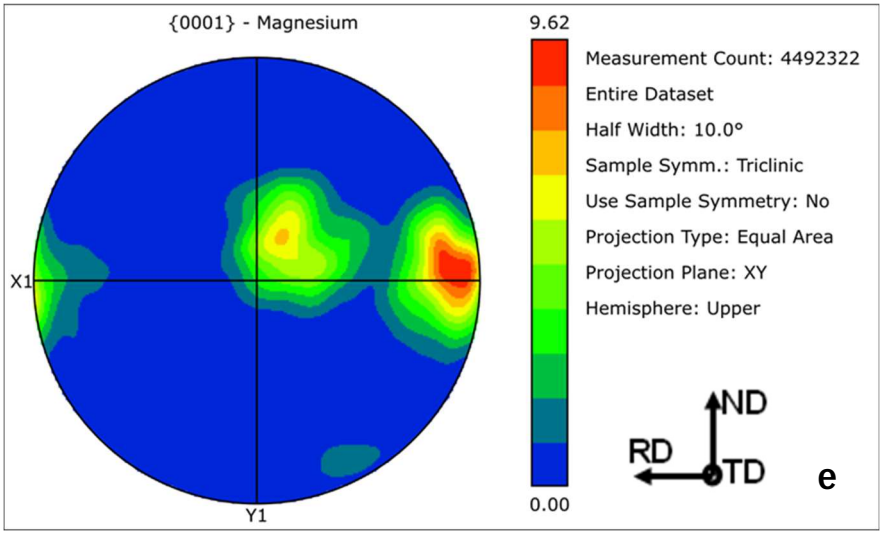
{0001} - Magnesium
9.62
0.00
Measurement Count: 4492322
Entire Dataset
Half Width: 10.0°
Sample Symm.: Triclinic
Use Sample Symmetry: No
Projection Type: Equal Area
Projection Plane: XY
Hemisphere: Upper
X1
Y1
ND
RD
TD
e

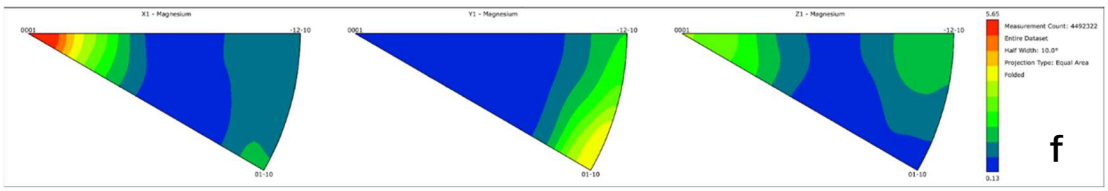
X1 - Magnesium
Y1 - Magnesium
Z1 - Magnesium
f

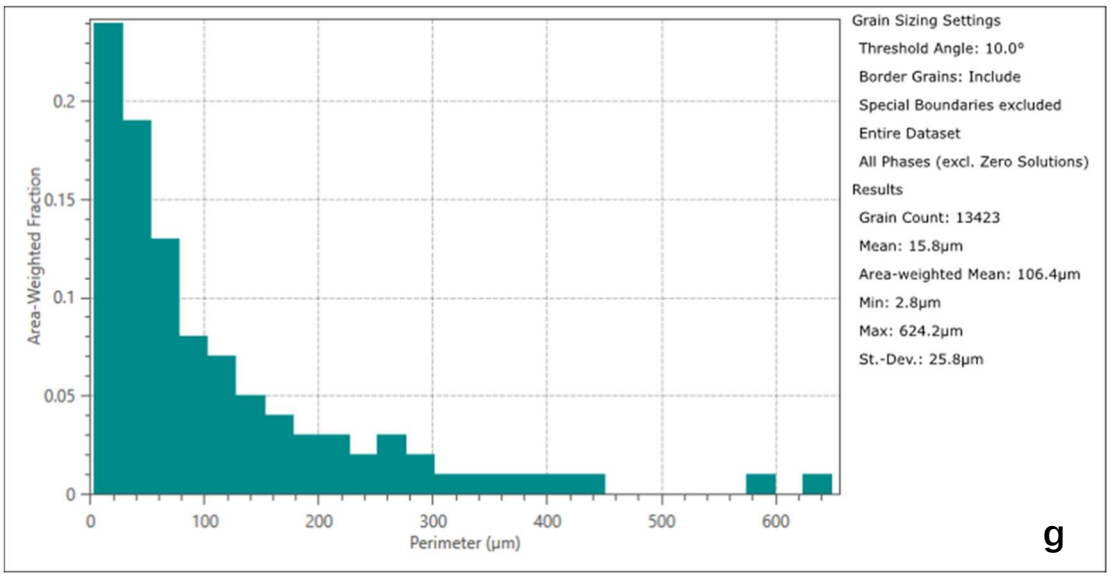

Figure A5-2 The EBSD result of the 75s annealed 2D compressed Mg-0.5Zn specimen: (a) The inverse pole figure map and grain boundaries, (b) The grain boundaries and the special grain boundaries, (c) The band contrast and the phase analysis, (d) The band contrast, (e) The pole figure, (f) The inverse pole figures, (g) Grain size distribution expressed as grain boundary perimeter

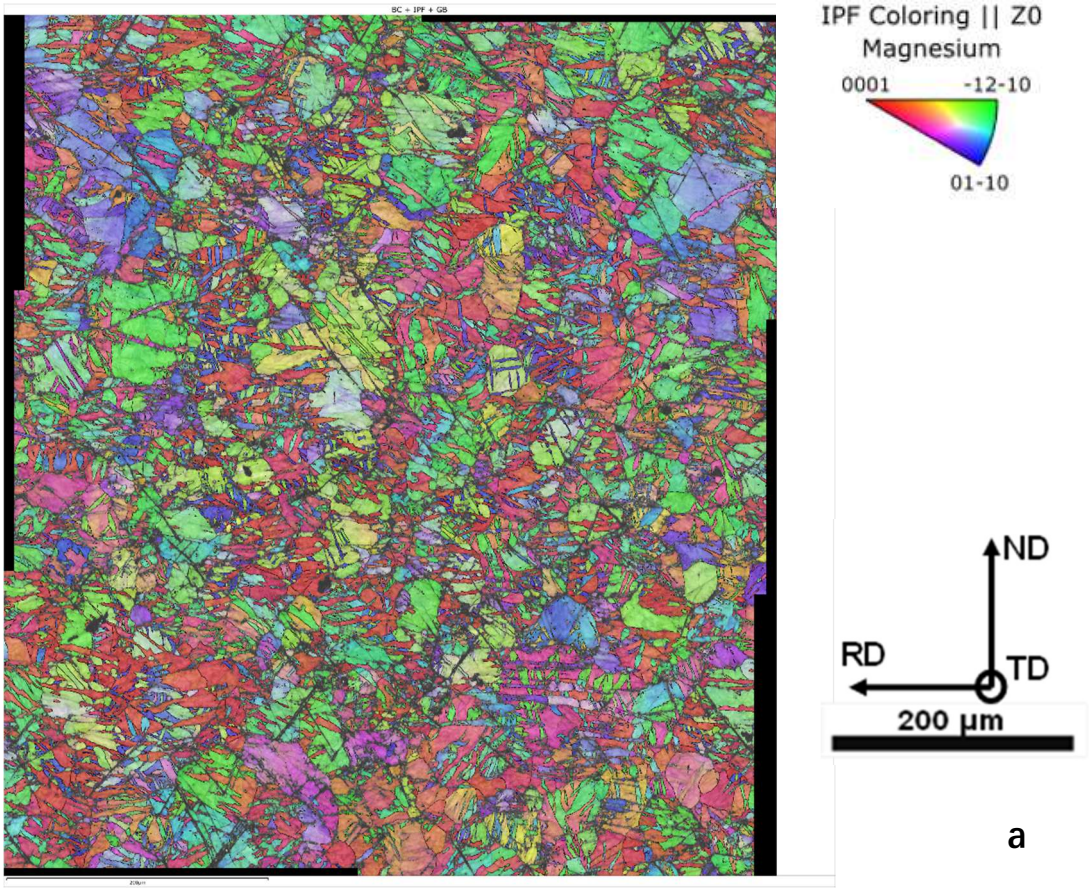

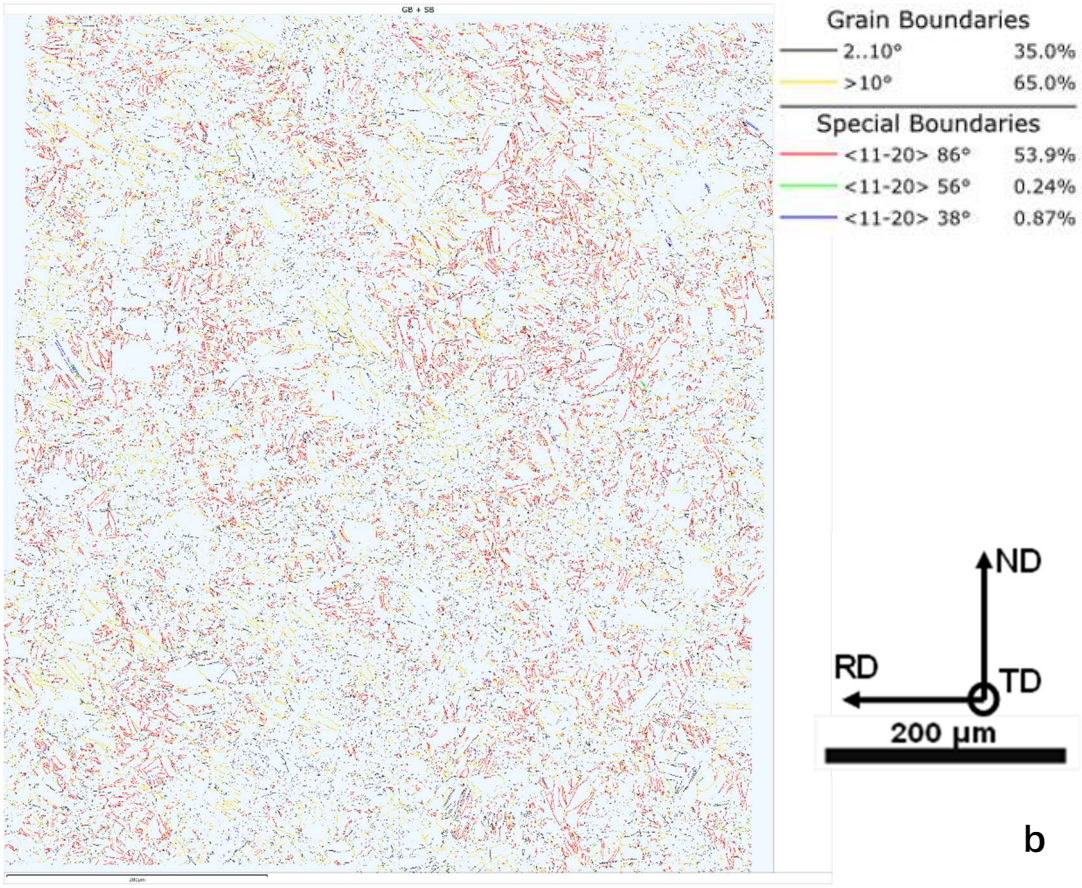
GB + SB
Grain Boundaries
2..10° 35.0%
>10° 65.0%
Special Boundaries
<11-20> 86° 53.9%
<11-20> 56° 0.24%
<11-20> 38° 0.87%
ND
RD
TD
200 µm

b

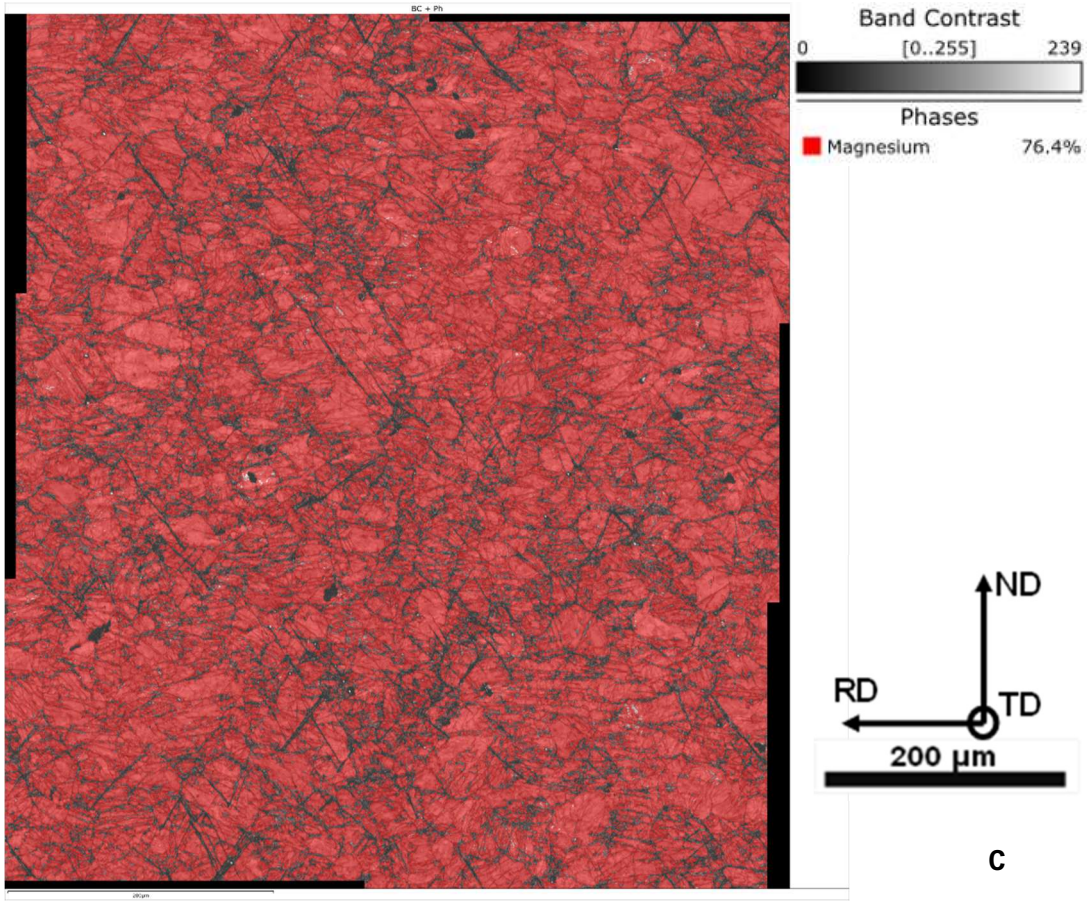
BC + Ph
Band Contrast
0 [0..255] 239
Phases
Magnesium 76.4%
ND
RD
TD
200 µm

c

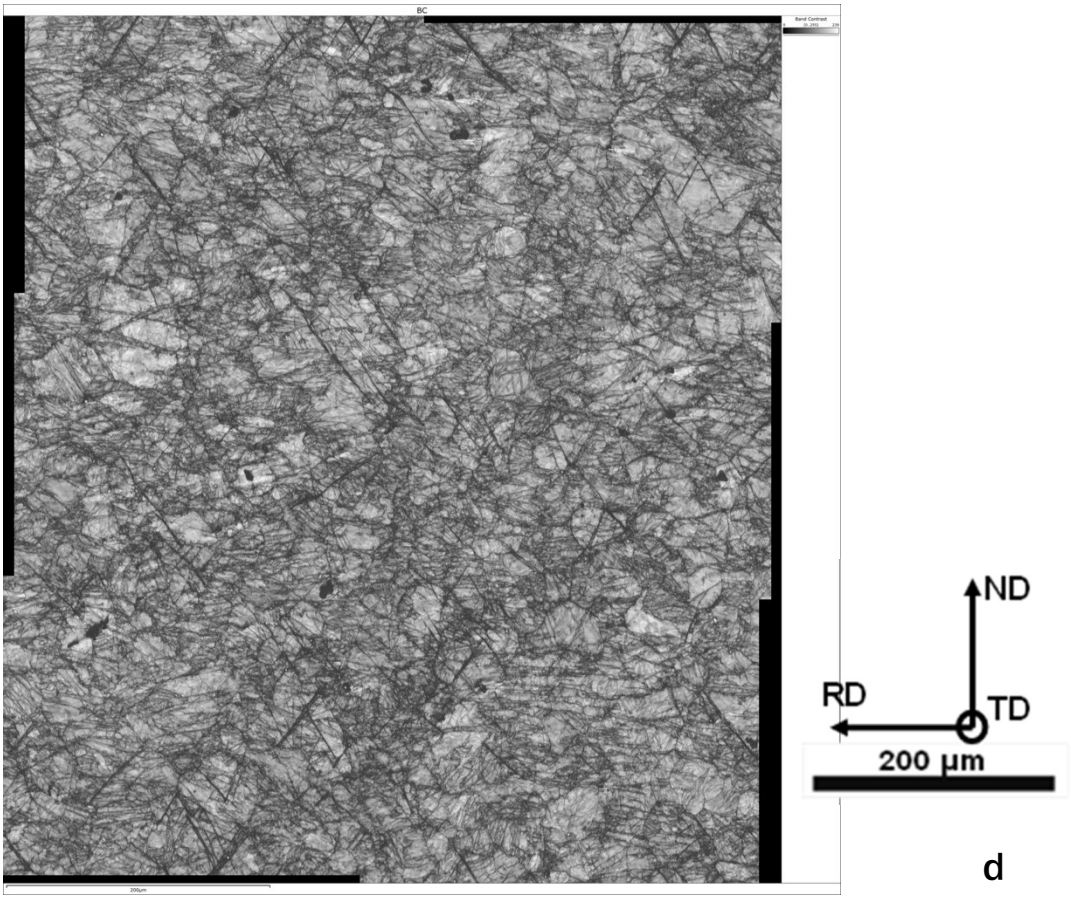
BC
ND
RD
TD
200 µm
d

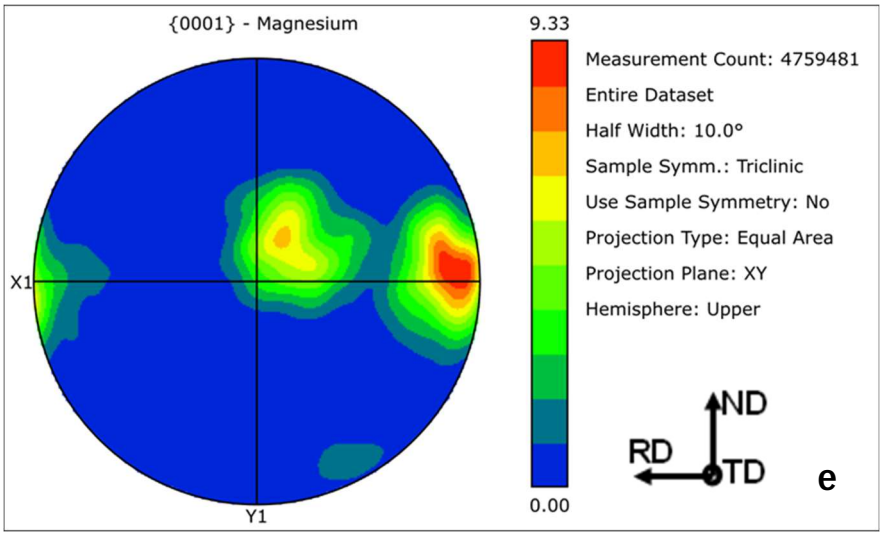
{0001} - Magnesium
9.33
0.00
Measurement Count: 4759481
Entire Dataset
Half Width: 10.0°
Sample Symm.: Triclinic
Use Sample Symmetry: No
Projection Type: Equal Area
Projection Plane: XY
Hemisphere: Upper
X1
Y1
ND
RD
TD
e

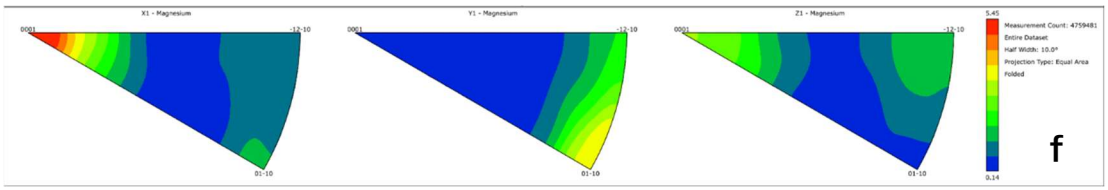
X1 - Magnesium
Y1 - Magnesium
Z1 - Magnesium
f

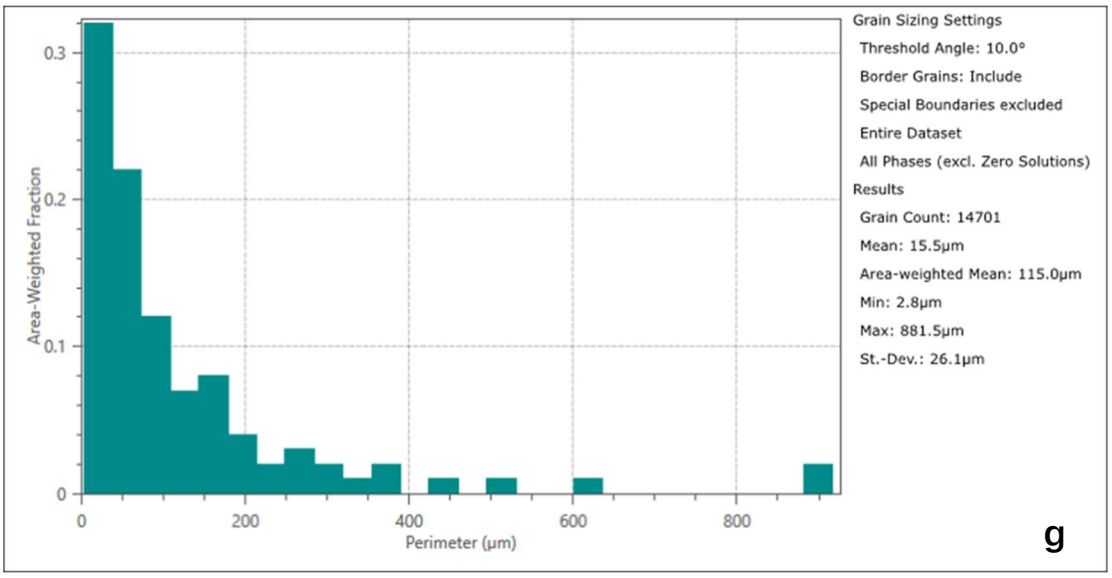

Figure A5-3 The EBSD result of the 135s annealed 2D compressed Mg-0.5Zn specimen: (a) The inverse pole figure map and grain boundaries, (b) The grain boundaries and the special grain boundaries, (c) The band contrast and the phase analysis, (d) The band contrast, (e) The pole figure, (f) The inverse pole figures, (g) Grain size distribution expressed as grain boundary perimeter